Challa S.S.R. Kumar *Editor*

Nanotechnology Characterization Tools for Biosensing and Medical Diagnosis

MATERIALS.SPRINGER.COM

Springer

Nanotechnology Characterization Tools for Biosensing and Medical Diagnosis

Challa S. S. R. Kumar
Editor

Nanotechnology Characterization Tools for Biosensing and Medical Diagnosis

With 291 Figures and 9 Tables

Springer

Editor
Challa S. S. R. Kumar
Integrated Mesoscale Architectures for Sustainable Catalysis (IMASC)
Rowland Institute of Science
Harvard University
Cambridge, MA, USA

ISBN 978-3-662-56332-8 ISBN 978-3-662-56333-5 (eBook)
https://doi.org/10.1007/978-3-662-56333-5

Library of Congress Control Number: 2018930879

Printed on acid-free paper

This Springer imprint is published by the registered company Springer-Verlag GmbH, DE part of Springer Nature.
The registered company address is: Heidelberger Platz 3, 14197 Berlin, Germany

Contents

Contributors

Haim Azhari Department of Biomedical Engineering, Technion – Israel Institute of Technology, Haifa, Israel

Nilay Bereli Department of Chemistry, Hacettepe University, Ankara, Turkey

Pratip K. Bhattacharya Department of Cancer Systems Imaging, The University of Texas MD Anderson Cancer Center, Houston, TX, USA

Daniel D. Carson Department of BioSciences, Rice University, Houston, TX, USA

Jen-Jie Chieh Institute of Electro-Optical Science and Technology, National Taiwan Normal University, Taipei, Taiwan

Dana Cialla-May Friedrich Schiller University Jena, Institute of Physical Chemistry and Abbe Center of Photonics, Jena, Germany

Pamela E. Constantinou Department of BioSciences, Rice University, Houston, TX, USA

Adil Denizli Department of Chemistry, Hacettepe University, Ankara, Turkey

Ali Derazshamshir Department of Chemistry, Hacettepe University, Ankara, Turkey

Mary C. Farach-Carson Department of Diagnostic and Biomedical Sciences, The University of Texas Health Science Center, School of Dentistry, Houston, TX, USA

Yixiao Guo Nano Biomedical Research Center, School of Biomedical Engineering, Med-X Research Institute, Shanghai Jiao Tong University, Shanghai, China

Jianhua Hao Department of Applied Physics, The Hong Kong Polytechnic University, HKSAR, Hung Hom, China

Alison J. Hobro Biophotonics Laboratory, Immunology Frontier Research Center, Osaka University, Suita City, Japan

Herng-Er Horng Institute of Electro-Optical Science and Technology, National Taiwan Normal University, Taipei, Taiwan

Jingzhe Hu Department of Cancer Systems Imaging, The University of Texas MD Anderson Cancer Center, Houston, TX, USA

Department of Bioengineering, Rice University, Houston, TX, USA

Kai-Wen Huang Department of Surgery and Hepatitis Research Center, National Taiwan University Hospital, Taipei, Taiwan

Graduate Institute of Clinical Medicine, National Taiwan University, Taipei, Taiwan

Izabella J. Jahn Leibniz Institute of Photonic Technology Jena, Jena, Germany

Chulhong Kim Department of Creative IT Engineering, Pohang University of Science and Technology, Pohang, Gyeongbuk, Republic of Korea

Jeesu Kim Department of Creative IT Engineering, Pohang University of Science and Technology, Pohang, Gyeongbuk, Republic of Korea

Shu-Hsien Liao Institute of Electro-Optical Science and Technology, National Taiwan Normal University, Taipei, Taiwan

Guofeng Liu Division of Chemistry and Biological Chemistry, School of Physical and Mathematical Sciences, Nanyang Technological University, Singapore, Singapore

Francis L. Martin School of Pharmacy and Biomedical Sciences, University of Central Lancashire, Preston, UK

Pierre L. Martin-Hirsch Department of Obstetrics and Gynaecology, Central Lancashire Teaching Hospitals NHS Foundation Trust, Preston, UK

Erdoğan Özgür Department of Chemistry, Hacettepe University, Ankara, Turkey

Department of Chemistry, Aksaray University, Aksaray, Turkey

Maria Paraskevaidi School of Pharmacy and Biomedical Sciences, University of Central Lancashire, Preston, UK

Xiaolei Peng Materials Science and Engineering Program and Texas Materials Institute, The University of Texas at Austin, Austin, TX, USA

Or Perlman Department of Biomedical Engineering, Technion – Israel Institute of Technology, Haifa, Israel

Juergen Popp Institute of Photonic Technology, Jena, Germany

Institute of Physical Chemistry and Abbe Center of Photonics, Jena, Germany

Andreea I. Radu Leibniz Institute of Photonic Technology Jena, Jena, Germany

Bharath Bangalore Rajeeva Materials Science and Engineering Program and Texas Materials Institute, The University of Texas at Austin, Austin, TX, USA

Yeşeren Saylan Department of Chemistry, Hacettepe University, Ankara, Turkey

Jianhui Sheng Division of Chemistry and Biological Chemistry, School of Physical and Mathematical Sciences, Nanyang Technological University, Singapore, Singapore

Xiangyang Shi College of Chemistry, Chemical Engineering and Biotechnology, Donghua University, Shanghai, People's Republic of China

CQM-Centro de Química da Madeira, Universidade da Madeira, Funchal, Portugal

Nicholas I. Smith Biophotonics Laboratory, Immunology Frontier Research Center, Osaka University, Suita City, Japan

Daniel Teal Department of Mechanical Engineering, Materials Science and Engineering Program, Texas Materials Institute, The University of Texas at Austin, Austin, TX, USA

Ming-Kiu Tsang Department of Applied Physics, The Hong Kong Polytechnic University, HKSAR, Hung Hom, China

Li-Min Wang Department of Physics, National Taiwan University, Taipei, Taiwan

Karina Weber Friedrich Schiller University Jena, Institute of Physical Chemistry and Abbe Center of Photonics, Jena, Germany

Nicholas Whiting Department of Cancer Systems Imaging, The University of Texas MD Anderson Cancer Center, Houston, TX, USA

Yuen-Ting Wong Department of Applied Physics, The Hong Kong Polytechnic University, HKSAR, Hung Hom, China

Liqin Xiong Nano Biomedical Research Center, School of Biomedical Engineering, Med-X Research Institute, Shanghai Jiao Tong University, Shanghai, China

Hong-Chang Yang Institute of Electro-Optical Science and Technology, National Taiwan Normal University, Taipei, Taiwan

Handan Yavuz Department of Chemistry, Hacettepe University, Ankara, Turkey

Fatma Yılmaz Department of Chemistry Technology, Abant Izzet Baysal University, Bolu, Turkey

Lingzhou Zhao Department of Nuclear Medicine, Shanghai General Hospital, Shanghai Jiao Tong University School of Medicine, Shanghai, People's Republic of China

Yanli Zhao Division of Chemistry and Biological Chemistry, School of Physical and Mathematical Sciences, Nanyang Technological University, Singapore, Singapore

School of Materials Science and Engineering, Nanyang Technological University, Singapore, Singapore

Jinhua Zhao Department of Nuclear Medicine, Shanghai General Hospital, Shanghai Jiao Tong University School of Medicine, Shanghai, People's Republic of China

Yuebing Zheng Materials Science and Engineering Program and Texas Materials Institute, The University of Texas at Austin, Austin, TX, USA

Department of Mechanical Engineering, Materials Science and Engineering Program, Texas Materials Institute, The University of Texas at Austin, Austin, TX, USA

Surface Enhanced Raman Spectroscopy for Medical Diagnostics

1

Izabella J. Jahn, Andreea I. Radu, Karina Weber, Dana Cialla-May, and Juergen Popp

Contents

List of Abbreviations

1-DT	1-Decanethiol
4-MBA	4-Mercaptobenzoic acid
AA	Ascorbic acid
AD	Alzheimer's disease
AFM	Atomic force microscopy
AFP	Alpha-fetoprotein

I. J. Jahn · A. I. Radu
Leibniz Institute of Photonic Technology Jena, Jena, Germany

K. Weber · D. Cialla-May
Friedrich Schiller University Jena, Institute of Physical Chemistry and Abbe Center of Photonics, Jena, Germany

J. Popp (✉)
Institute of Photonic Technology, Jena, Germany

Institute of Physical Chemistry and Abbe Center of Photonics, Jena, Germany
e-mail: juergen.popp@ipht-jena.de

C. S. S. R. Kumar (ed.), *Nanotechnology Characterization Tools for Biosensing and Medical Diagnosis*, https://doi.org/10.1007/978-3-662-56333-5_1

AGC	Advanced gastric cancer
AIBN	Azobis(isobutyronitrile)
ATE	Telomeric repeat complementary oligonucleotide
AuFON	Gold film-over-nanospheres
Aβ	Amyloid β
BSA	Bovine serum albumin
Ce6	Chlorin e6
CEA	Carcinoembryonic antigen
CGM	Continuous glucose monitoring
CK-MB	Creatine kinase MB
CPBT	2-Cyano-2-propyl benzodithioate
CSF	Cerebrospinal fluid
cTnI	Troponin I
cTnT	Troponin T
CVD	Cardiovascular diseases
Cy5	Cyanine 5
DNA	Deoxyribonucleic acid
DT	Decanethiol
DTNB	5,5-Dithiobis(2-dinitrobenzoic acid)
DTTC	Diethylthiatricarbocyanine iodide
EBL	Electron beam lithography
ECG	Electrocardiogram
EDC	1-Ethyl-3-(3-dimethyl-aminopropyl)carbodiimide
EGA	Clarke error grid analysis
EGC	Early gastric cancer
EGFR	Epidermal growth factor receptor
ELISA	Enzyme-linked immunosorbent assay
G−	Gram negative
G+	Gram positive
GOx	Glucose oxidase
HBsAg	Hepatitis B virus antigen
HCPCF	Hollow core photonic crystal fiber
HeLa	Human cervical cells
HEMA	2-Hydroxyethyl methacrylate
HER2	Human epidermal growth factor receptor 2
HIV-1	Human immunodeficiency virus
HPLC	High-performance liquid chromatography
HPV	Human papillomavirus
IgG	Immunoglobulin G
iMS	Inverse molecular sentinel
ISO	International Organization Standard
ITO	Indium tin oxide
LA	Lipoic acid
LoC-SERS	Lab-on-a-chip SERS
LOD	Limit of detection

MBs	Magnetic nanobeads
MGITC	Malachite green isothiocyanate
MH	6-Mercapto-1-hexanol
MI	Myocardial infarction
miR21	Micro ribonucleic acid 21
miRNA	Micro ribonucleic acid
MNP	Magnetic nanoparticle
MPBA	Mercaptophenylboronic acid
mPEG-SH	*O*-[2-(3-Mercaptopropionylamino)ethyl]-*O′*-methylpolyethylene glycol
MPS	3-Methacryloxypropyltrimethoxysilane
MRI	Magnetic resonance imaging
mRNA	Messenger ribonucleic acid
MTC	Mycobacterium tuberculosis complex
MU	11-Mercapto-1-undecanol
MUA	11-Mercaptoundecanoic acid
NHS	N-Hydroxysuccinimide
NP	Nanoparticle
NPs	Nanoparticles
NT	Naphthalenethiol
OAD	Oblique angle deposition
OSCC	Oral squamous carcinoma
PBS	Phosphate-buffered saline
PBST	Phosphate-buffered saline tween-20
PCA	Principal component analysis
pCBAA	Zwitterionic poly(carboxybetaine acrylamide)
PCN	Pyocyanin
PCR	Polymerase chain reaction
PEG	Polyethylene glycol
PEG-SH	Thiolated PEG
PET	Positron emission tomography
PLS-DA	Partial least squares discriminant analysis
RBCs	Red blood cells
Rh6G	Rhodamine 6 G
SAM	Standard addition method
SERRS	Surface-enhanced resonance Raman spectroscopy
SERS	Surface-enhanced Raman spectroscopy
SESORS	Surface-enhanced spatially offset Raman spectroscopy
TAT	Turnaround time
TGFbRII	Transforming growth factor beta receptor II
TMB	3,3′,5, 5′-Tetramethylbenzidine
TPMT	Thiopurine s-methyltransferase
TS	Telomeres substrate
VAN	Vancomycin
VEGF	Vascular endothelial growth factor

1 Definition of the Topic

Medical diagnosis requires reliable identification of very low concentration of different biomarkers specific for medical conditions in a time-effective manner. In this chapter, we summarize the work reported on the application of surface-enhanced Raman spectroscopy for the detection and the identification of different biomarkers in body fluids, tissues, or in vivo.

2 Overview

Early disease diagnosis allows for better treatment options and leads to improved patient outcomes. This is because by delaying treatment the disease can also spread to otherwise healthy organs. The consequences of this can vary, depending on the specific medical condition (i.e., Alzheimer's disease, diabetes, cancer, etc.) and on the exact time of diagnosis.

One highly promising method for fast and reliable biomarker identification is surface-enhanced Raman spectroscopy (SERS). Depending on the particular medical diagnosis requirements, different SERS approaches can be considered. That is because, as it will be discussed in this chapter, many different SERS-active substrates are available, and they can be applied within different schemes. Specifically, functionalized SERS nanoparticles can have a high biocompatibility for in vivo measurements, while different microfluidic approaches can be considered for the analysis of body fluids.

The scientific interest for assessing the potential of SERS for medical analysis and diagnosis increased during recent years. This is also demonstrated by the multiple literature reports (scientific papers, communications, reviews, and book chapters) that test and push the limits of using SERS in medicine or report on new SERS-active substrates and platforms that are continuously developed for analyzing trace amount of analytes in body fluids and tissue [1–5]. However, SERS has not yet been established as a routine analytical tool for medical diagnosis. Moreover, clinical trials and development of analytical procedures are still required. The high potential and interest for development in this direction explains the high number of publications still being reported. The current chapter summarizes some of the most promising approaches introduced during the last 5 years. A wide panel of diseases is addressed, and the best-suited SERS-based approaches are discussed for each of the topics introduced.

3 Introduction

The latest developments in the health-care field have two directions: detection and diagnosis of disease and its treatment. They are of comparable importance when it comes to achieving positive patient outcomes. In particular, the fast and correct diagnosis of a medical condition leads to more appropriate treatment decisions and

to the establishment of a care plan at an early stage of the disease, increasing the chances of successfully fighting the disease [6]. Nevertheless, for example, the direct identification of viruses and bacteria can be challenging at times. In such situations disease-specific biomarkers are targeted instead. Biomarkers, or biological markers, have been defined several times in the literature, and they are mainly described as substances, structures, or processes that can be objectively measured in the body and can be used as indicators for normal biological processes, pathogenic processes, or pharmacological responses to a therapeutic intervention (i.e., deoxyribonucleic acid (DNA), messenger ribonucleic acid (mRNA), enzymes, metabolites, transcription factors, and cell surface receptors) [7]. Frequently, during the early stages of disease, biomarkers are present in low amounts, and their reliable detection is challenging. In clinical chemistry, the specific and sensitive detection of disease biomarkers, of drug levels in biological fluids, or the assessment of enzyme activities is carried out by a multitude of analytical methods, such as high-performance liquid chromatography [8–13], mass spectrometry [11, 14, 15], or immunoassays [16–21]. Since each method has its advantages and shortcomings, the scientific community is continuously searching for new, faster, and affordable tools.

Vibrational spectroscopy, particularly Raman spectroscopy, can provide molecular fingerprint information [22–24] and is suitable for investigating biological samples because of the low scattering cross section of water molecules. Consequently, no or little sample pre-processing steps are required prior to the analysis. However, owing to the inherently weak Raman effect, the identification of target molecules present at very low concentrations is challenging. This is especially important for the early diagnosis of medical conditions. Nevertheless, the sensitivity of Raman spectroscopy can be easily enhanced by several orders of magnitude by taking advantage of the plasmonic properties of nanostructured metallic particles and performing surface-enhanced Raman spectroscopy (SERS) measurements. The two underlying mechanisms of SERS, extensively described in the literature [25–29], are the electromagnetic and the chemical enhancement mechanisms. The first mechanism explains how the molecules situated in the proximity of metallic nanoparticles (NPs) experience a strong local electromagnetic field, referred to as localized plasmon polaritons. This is caused by the resonant interaction between an incident electromagnetic wave and the oscillating charge density of the NPs. As a consequence, both the electromagnetic radiation of the laser source incident on the molecules and the intensity of the Raman-scattered photons will be enhanced. As the plasmon resonance condition for a spherical NP, $\epsilon(\lambda) = -2\epsilon_m$,[1] can be fulfilled only for materials with $\mathrm{Re}(\epsilon(\lambda)) < 0$ and $\mathrm{Im}(\epsilon(\lambda)) \approx 0$,[2] gold and silver are the most preferred metals for plasmonic nanostructure fabrication.

[1] $\epsilon(\lambda)$ is the wavelength-dependent dielectric function of the NP's material, and ϵ_m is the dielectric function of the surrounding medium.

[2] The dielectric function is a complex function with $\epsilon(\lambda) = \mathrm{Re}(\epsilon(\lambda)) + i \cdot \mathrm{Im}(\epsilon(\lambda))$, where $\mathrm{Re}(\epsilon(\lambda))$ is the real part and $\mathrm{Im}(\epsilon(\lambda))$ is the imaginary part.

The electromagnetic mechanism accounts for enhancement magnitudes up to 10^{11} [30]. However, enhancement factors of 10^{14}–10^{15} [31, 32] have been often reported in literature. This is due to the chemical enhancement mechanism to which three different processes have been suggested to contribute: (1) chemical interactions between the NP and the target molecule in the electronic ground state, (2) resonant excitation of the charge-transfer process between the target molecule and the NP, and (3) the resonance Raman enhancement. As the aim of this book chapter is to give a comprehensive overview of the SERS advancements in the field of medical diagnosis, a detailed description of the fundamental principles of the technique is beyond the purpose, and the reader is directed to the multiple extensive reviews and book chapters reported in the literature [25–29, 33, 34].

An important factor when performing SERS measurements is the choice of the SERS-active substrates to be used: planar substrates, NP suspension, core-shell structures, functionalized NPs, etc. Depending on the exact application, specific structures will be preferred. Moreover, the development of NPs that show a high biocompatibility while still maintaining their physical properties is often desirable in medical applications [35–37]. To this end, different functional layers are added to the NP to facilitate their delivery to a specific affected organ. Upon this, the destruction of the NP's core-shell structure can lead to the release of different filling materials [35], to a faster clearance of the NPs from the body, or to the induction of a highly localized electrical field in the close vicinity of the NP that increases the efficiency of in vivo biomarker detection.

In the following section, we will address some of the most relevant experimental details having a considerable impact on the outcome of the SERS measurement. Namely, details regarding Raman systems used for SERS measurements will be introduced; the commonly used SERS-active substrates and the different approaches used for SERS measurements will be summarized; the choice regarding the best-suited laser wavelength for the investigation of biological samples will be discussed; the synergy between SERS, immunoassays, and microfluidics will be presented; and finally some details regarding quantitative SERS measurements will be addressed.

4 Experimental and Instrumental Methodology

When performing SERS measurements, the experimenter is confronted with a series of measurement parameters to be considered and decided for. For example, reliable SERS results can be achieved only when the parameters of the Raman setup, the physicochemical properties of the targeted samples, the properties of SERS-active substrate, and the measurement design are all carefully considered and optimized. SERS spectra can be acquired with a large variety of commercial or in-house build Raman setups. Detectors and instrumentation in this field are in continuous development, and therefore, in the following, we will provide just a generalized view on Raman (micro)spectroscopy, highlighting some of the major factors relevant for SERS measurements. For a more detailed overview, the reader is directed to the multiple book chapters reported in the literature [38–40].

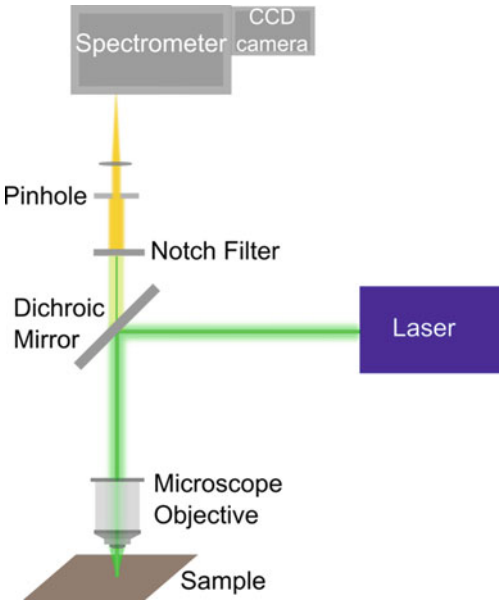

Fig. 1.1 Scheme of a confocal Raman microscope

Although the Raman effect was discovered by C. V. Raman already in 1928, only 30 years later, with the development of lasers, Raman experiments gained popularity. The introduction of charge-coupled devices (CCD) with high quantum efficiency and the establishment of confocal micro-Raman spectroscopy have further sparked the interest of scientists for this technique. For example, in Fig. 1.1 one of the many existing Raman setups is depicted. Here, a laser source provides the monochromatic light required to induce the inelastic light scattering events yielding a Raman spectrum. The excitation laser is coupled into the Raman microscope via a dichroic mirror. This element acts as a long pass filter, and it reflects with high efficiency the laser excitation light, whereas the backscattered Stokes-shifted Raman photons will be transmitted. If, however, the detection of the anti-Stokes Raman photons is desired, the setup must be equipped with a holographic beam splitter that will act as a notch filter. Further on, after the monochromatic light is reflected by the dichroic mirror, it is focused on the surface of the sample via a microscope objective. Here, the backscattered light is collected via the same objective, and it is transmitted via the dichroic mirror. The currently available coating technologies applied on dichroic mirrors reach a reflection of the elastically scattered photons of up to 95%, and thus, for a more efficient suppression of the Rayleigh line, an additional edge/notch filter is also implemented. This reduces the laser light intensity by around six orders of magnitude. The resulting filtered light crosses through a pinhole, which, if present, yields a confocal collection and reduces the background signal of the sample. Finally, the light is coupled into a spectrometer, where by the aid of gratings the beam is dispersed onto the CCD detector by deflecting each wavelength at a slightly different angle.

When deciding on the particularities of the experiment, the user can freely opt for a number of the above-enumerated components such as the excitation source to which the researcher should match the dichroic mirror and notch filter, the used microscope objective, as well as the size of the pinhole and the type of grating. Below, we will address the particularities of each of these parameters.

Generally, in order to obtain intense Raman spectra, lasers with short emission wavelengths (UV, blue, or green) are preferred as the Raman-scattering intensity is proportional to the fourth power of the frequency of the exciting laser radiation. Nonetheless, many samples show strong fluorescence when excited with these lasers and the detection of the Raman-scattered photons is inhibited. This is especially valid for biological samples, as it will be discussed in the following sections, and thus, often a red or near-infrared laser (emission above 600 nm) is preferred. Furthermore, for SERS spectroscopy, one has also to consider the localized plasmon polariton resonances of the employed SERS-active substrates in order to make use of the electromagnetic enhancement mechanism. Generally, for silver spheres blue/green laser lines are chosen, whereas for gold, wavelengths above 600 nm are applied. This can be explained by considering the dielectric function of the two metals, and it was described, among others, by, i.e., Le Ru et al. [33].

Besides carefully choosing the excitation wavelength, one has to pay attention also to the excitation power. Although the Raman intensity is proportional to the power of the used laser, limitations brought by the thermal damage of the sample have to be considered. In Raman experiments, the excitation power can vary from microwatts to several hundreds of milliwatts depending on the thermal conductivity and absorption of the sample and the measurement conditions (point scan, line scan, light sheet illumination, etc.). For SERS measurements, the applied laser power will vary also based on the employed SERS-active substrate. When measurements are performed on planar plasmonic substrates under dry conditions, laser powers in the ~20–500 microwatt range are used in order to avoid the local heating and damage of both the nanostructure and molecule. If these substrates are measured while they are incubated in the sample solution, the laser power can be increased up to 5–10 mW due to the increased heat dissipation in the presence of a liquid. For measurements carried out with microfluidic platforms, thanks to the dynamic flow, the laser intensity can be increased considerably as no sample degradation is expected.

Microscope objectives play also a key role in maximizing collection efficiency and spatial resolution. For applications where both parameters are crucial for optimal results, objectives with a high numerical aperture (above 0.8) have to be selected. Nevertheless, these objectives have generally a low working distance (at most 2–3 mm) and a reduced collection depth. Therefore, if the surface of the sample to be measured presents high roughness, information might be lost during measurements due to getting out of focus or the objective might be irreversibly contaminated due to touching the sample surface. Furthermore, one must also pay attention to the choice of the right objective for the intended excitation laser as the antireflection coatings can present different transmission characteristics for different frequencies.

Lastly, a grating with a higher number of grooves per mm (e.g., 1800 l/mm) will yield a spectrum with a high resolution (~2 cm^{-1}) but with a lower spectral range,

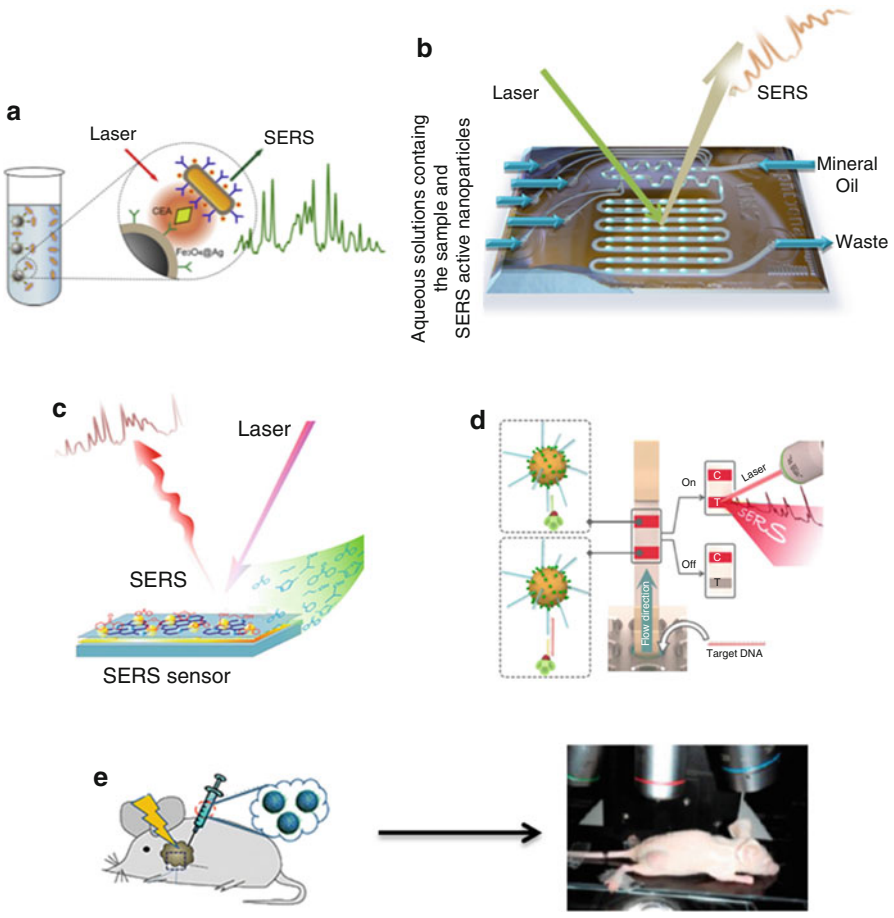

Fig. 1.2 Selected representations of the different encountered SERS measurement configurations: cuvette measurement (**a** – adapted from Rong et al. [41] with permission from Elsevier. Copyright © 2016 Elsevier); microfluidic platform measurement (**b** – adapted with permission from Hidi et al. [42]. Copyright © 2016, American Chemical Society); flat substrate-based SERS measurement (**c** – adapted with permission from Chen et al. [43]. Copyright © 2016, American Chemical Society); immunoassay-based SERS measurement (**d** – adapted from Fu et al. [44]. Copyright © 2015 Elsevier B.V., with permission from Elsevier); SERS measurement performed through the skin upon injection of the nanoparticles in laboratory mice (**e** – left image adapted with permission from Lin et al. [35]. Copyright © 2013, American Chemical Society; right image adapted with permission from Zeng et al. [37]. Copyright © 2015, American Chemical Society)

whereas a grating with, e.g., 600 l/mm will yield a lower resolution (~6–10 cm^{-1}), but it covers the whole Stokes Raman spectral range.

Overall, the excitation wavelength and power, the microscope objective, and the grating will strongly influence the outcome of the SERS measurements. Nevertheless, the choice of the SERS-active substrates and the measurement approach (see Fig. 1.2) will have also a key role. As summarized in several reviews [45–47], a large

variety of SERS-active substrates are available. As already mentioned in the previous section, the coinage metals, such as silver and gold, are the most often encountered materials for plasmonic structure fabrication. Depending on the preparation procedure, the SERS-active substrates can be classified into bottom-up, self-organizing, and top-down substrates [45–48]. Among the metal nanostructures fabricated by bottom-up procedures, there are metal colloids [49, 50], core-shell nanoparticles and structures, [35] seed-mediated growth structures [51, 52], and others. A large variety of such substrates have been fabricated owing to the relatively easy preparation protocols, the high diversity of sizes and geometries that can be developed, and the ease of use while performing the measurements. However, most of these NPs are suspended in an aqueous solution, restricting their application for fat soluble analytes. For such analytes, additional preparation steps can follow, resulting in the attachment of functional groups on the surface of the NPs, the formation of core-shell structures, or the addition of protective layers on the surface of the NPs. Still, this further increases the complexity of the preparation protocol and the time and the costs of the substrate preparation. The second category of SERS-active substrates mentioned are self-organizing substrates, which include self-assembled colloidal nanoparticle [53] clusters and arrays as well as template-based self-assembled planar nanostructures [52, 54, 55]. Finally, the top-down substrates are prepared by using a template produced by electron beam lithography (EBL) [56, 57], lift-off processes [58], and ion beam etching processes as part of lithographic methods [59]. Compared with the bottom-up procedures, the top-down substrates are less cost-effective, and the preparation protocol is more complex, but the resulting substrates have a more homogeneous size distribution and are highly reproducible and structured. Additionally, the substrates' templates can often be prepared in advance, and the final layer of the coinage metal (i.e., Ag, Au, Cu, or Pt) can be deposited on the substrate short before the actual SERS measurement is performed.

Among the measurement approaches, cuvette-based SERS measurements are the most widely spread ones. Here, the colloidal nanoparticles in aqueous suspension are mixed with the targeted analyte solved also in an aqueous solvent. Commonly, in order to efficiently enhance the Raman signal, an electrolyte is also added, which has the role to aggregate the nanoparticles and to create "hot spots." The order of mixing these three components, the ratio in which they are mixed, the type of electrolyte used, and the time lapse between mixing and measurements will highly influence the recorded SERS signal. Unfortunately, there exists no golden rule which guarantees the best results, and for each targeted molecule, the procedure is commonly optimized by the trial and error method. During the SERS measurements, objectives with a long working distance are preferred as this avoids the unwanted dipping of the microscope objective in the sample, and it offers information from a larger collection volume. The incident laser power can have values of above 1 mW up to tens of milliwatts due to the presence of the aqueous environment, and the excitation laser is focused on the water-air interface or short below it as this avoids the reabsorption of the Raman-scattered light by the sample.

If the targeted analytes are hydrophilic, scientists usually choose planar SERS-active substrates. The deposition of the analytes is done either by the drop-and-dry

approach or by incubating the substrate in the sample solution for a given time. For the first case, due to the coffee-ring effect, heterogeneous molecule layers will be obtained, while in the second case, the incubation time will strongly influence the outcome. Furthermore, in the second case, the scientist might opt to measure the substrate after it was air-dried or when it is still dipped in the solution. In all cases, most commonly Raman scans are performed in order to avoid the local heating and degradation of both the analyte and the plasmonic structure. Under dry conditions, laser powers lower than 1 mW are preferred, and objectives with a high numerical aperture are selected. These two procedures, cuvette and scanning the surface of the planar substrate, are suitable for the determination of biomarkers in body fluids. For the in vivo applications, nanoparticles are injected into the tissue of interest, or substrates are implanted below the skin and approaches like spatially offset SERS microscopy is performed.

Reproducible and automated measurement conditions are essential characteristics for the successful integration of new analytical methods in routine analysis. As mentioned above, SERS measurements with NPs in colloidal solutions are generally carried out in cuvettes, whereas in the case of the planar substrates, the analyte molecules are deposited on the metallic surface either via drop and dry or incubation. Neither of these two approaches offers the possibility to perform automated measurements, and both methods are subject to human errors. The combination of SERS with microfluidics, however, has been very promising at overcoming these limitations, and it opened a door toward a plethora of biomedical applications [60–68]. Notably, by employing microfluidics, the required reagent volumes can be considerably reduced, chemical reactions can be observed at the microscale, and sample preparation and measurements are integrated in the same platform. Among the optical methods that have been applied to record signals from such volume-reduced samples, SERS is favored because of its high sensitivity.

On the basis of literature, microfluidic platforms can be divided into two main categories: flow-through or continuous flow platforms [69–88] and segmented or droplet-based platforms [42, 68, 89–95]. In the first approach, planar substrates prepared via top-down processes can be integrated into the channel system, colloidal NPs can be injected via one of the inlet ports, or SERS-active substrates can be produced in situ. In these platforms, solvent evaporation is inhibited, the coffee-ring effect occurring in the open platforms is avoided, and the diffusion of the target molecules toward the metallic surface can be improved via, e.g., electrokinetic [96] or hydrodynamic focusing [97]. However, because the sample is permanently wetting the channel walls of the microfluidic platform, the so-called memory effect can appear, where the channel surface of the channels becomes enriched with the samples over time and the reliability of the SERS measurements can be compromised. This is one of the reasons leading to the development of droplet-based microfluidic platforms. In these platforms, cross contamination can be significantly inhibited by ensuring no or very low cross talk between the different liquid compartments by dispensing the sample and colloidal NPs into individual droplets surrounded by an immiscible liquid phase. These droplets can be trapped, sorted, mixed, or split, based on the specific experimental requirements. As droplet

formation is controlled by high precision pump systems, the method will suffer less from human-induced errors, and the SERS signals will offer reliable results.

With this approach, two of the main limitations of the SERS technique, reproducibility and automation, can be overcome. However, this is not sufficient for the selective detection of molecules in complex matrices. Generally, the SERS-active substrates will enhance the signal of any Raman-active molecule situated in their proximity. Consequently, the molecules of a complex matrix and the target molecules will compete for free binding sites on the metallic surface, and the successful detection of the molecule of interest can be inhibited. For example, when a biomarker must be detected in human blood, proteins, red blood cells, and other large molecules will block the nanostructured metallic surface. Thus, the distance between the target molecule and the enhanced electromagnetic field will be too large for the molecule to still experience the SERS effect. Increased selectivity of the metallic surface is present only toward those molecules that have functional groups with high chemical affinity for the respective metal. Namely, thiol groups, the lone pair electrons of oxygen and nitrogen atoms, and π electrons of aromatic rings show high affinity toward gold and silver. To increase the selectivity of the SERS substrates for the targeted molecules, immunoassay-based SERS platforms have been developed. The working principle of an immunoassay is based on the antigen-antibody binding reaction. The technique gains its high specificity and sensitivity from three important properties of antibodies: (1) the ability to bind to both natural and synthetic molecules, (2) specific binding, and (3) binding strength [98–101]. Immunometric assays, such as the enzyme-linked immunosorbent assay (ELISA), use two different specific antibodies that form a sandwich around the target of interest, and they are suitable for the detection of molecules with large molecular weight, such as proteins or peptides. For the low molecular weight substances, the competition design is preferred. Here, the target molecule competes with a fixed amount of tracer (labeled molecule) for a limited number of antibodies. The affinity of the target molecule for the antibody is higher than that of the tracer. Therefore, when the target molecule is present in the sample, fewer tracers will bind to the antibody than in the absence of such a molecule. Finally, after the successful formation of immunocomplexes, SERS can be used to detect the signal. Commonly, Raman reporter molecules with well-defined and strong Raman signatures are embedded in the SERS tags, and their signal rather than that of the target molecule is measured. In the following section, the reader will find many examples of the successful detection of biomarkers by means of SERS-based immunoassay platforms.

For most medical diagnosis purposes, qualitative results are not sufficient for confirming the presence of a medical condition. However, quantitative SERS measurements are still very challenging even after more than 40 years from the first reported enhanced Raman signals of pyridine on roughened metallic surfaces [102]. This stems from the fact that SERS is a surface-sensitive technique. Only the Raman signal of the molecules in the first layers on the metallic surface will be considerably enhanced. Thus, the dynamic range of the method is limited, and very seldom it extends over more than one or two orders of magnitude. At high

concentrations of the target molecules, the so-called saturation or poisoning effect appears due to the evanescent character of the local electromagnetic field. Furthermore, using the traditional quantification method based on previously established calibration curves will fail because of the batch-to-batch variation in the quality of the SERS-active substrates and because of the high chemical variability of the biological samples. Nevertheless, most of the reported SERS-based immunoassay platforms, owing to their selective binding, offer reliable quantitative measurements, while for the microfluidic SERS platforms, the standard addition was implemented to improve quantitative measurements of molecules [89]. However, most studies in the literature show results measured in a single run, and they do not address the quantification of the target molecules in clinical samples, where the concentration is unknown. Therefore, before SERS can be considered as a tool for clinical diagnosis, this challenge has to be met.

In conclusion, due to the high variety of available SERS-active substrates, the choice of the best-suited substrate is never trivial and highly depends on the specific application. A top-down substrate with a highly homogenous surface would generally present a uniform enhancement over the surface, making it easily suited for applications that require quantification and high reproducibility (e.g., cell measurements). On the other hand, a substrate with less uniform enhancement would often present hot spots with higher enhancements, which would make the substrate better suited for applications connected to single-molecule detection or microfluidic system measurements [46, 103]. Finally, functionalized colloids are easily distributed in the organism, taken up by cells, or dispersed on tissues, making them a generally good choice for in vivo medical applications. Nevertheless, in this situation, the problem of ensuring the formation of hot spots remains, and different solutions have been reported in the literature as it will be discussed below.

5 Key Research Findings

5.1 Aging-Associated Diseases

5.1.1 Neurodegenerative Diseases

Life expectancy has risen dramatically during the last century, leading to an increase in the proportion of the elderly population. This, given the progressive degeneration of the structure and function of the nervous system during aging, has increased the incidence of neurodegenerative disorders. Alzheimer's disease (AD) is the most prevalent form of late-life mental failure in humans. Since 2010, multiple SERS studies of AD have been conducted, and their results will be the subject of the present section of the chapter. However, before discussing the findings in the field, a brief summary of key factors related to AD will be presented in the following paragraphs. For an extensive discussion of AD pathology, the reader is referred to the multiple excellent review papers and books published on this topic [104–114].

AD is associated with progressive memory impairment, disordered cognitive function, and altered behavior, including paranoia, delusions, and loss of social

appropriateness, accompanied by progressive decline in language function [104–108]. The study of AD pathogenesis generated long discussions in the medical community. Nowadays, it is commonly accepted that the two main pathological hallmarks of the disease are extracellular neuritic plaques and intracellular neurofibrillary tangles. The neuritic plaques are microscopic foci of extracellular depositions consisting of amyloid β (Aβ) proteins [104]. Aβ is a 39–43-residue-long polypeptide generated through cleavage of the amyloid precursor protein by β- and γ-secretase [115]. The Aβ species associated with AD are composed of 40 or 42 residues. Aβ (1-40) has a higher concentration in AD patients, although the neurotoxicity of Aβ (1-42) is much more pronounced owing to its greater tendency to form aggregates in vivo. The question of whether the insoluble Aβ fibrils and monomeric Aβ proteins are less pathogenic than soluble, nonfibrillar assemblies (dimers, trimers, or larger oligomers) has generated an intense debate [110–112]. In addition to amyloid plaques, the AD brain contains also large, non-membrane-bound bundles of abnormal fibers composed of the microtubule-associated protein tau [113, 114] with abnormal posttranslational modifications, including phosphorylation and acetylation [116, 117]. In AD, more than 20 residues become phosphorylated, whereas in the healthy brain, 8–10 of these residues are heterogeneously phosphorylated and, therefore, do not bind to microtubules. As a consequence, dendritic spines in the AD brain become enriched in the tau protein, which might interfere with neurotransmission [118].

These two pathologies can occur independently of each other. Neurofibrillary tangles have been observed in other neurodegenerative disorders that are not associated with amyloid plaques. Similarly, Aβ aggregates were observed in brains of cognitively normal-aged individuals in the virtual absence of tangles [104]. Therefore, the gold standard for AD diagnosis to date is postmortem neuropathological confirmation. However, it is commonly accepted that the neurological changes leading to AD begin to develop decades before the earliest clinical symptoms occur. Biomarker detection has been proposed to be used for early diagnosis. The five most widely studied biomarkers of AD are decreased Aβ (1-42) concentrations in the cerebrospinal fluid (CSF), increased CSF tau levels, decreased fluorodeoxyglucose uptake assessed by positron emission tomography (PET) imaging, PET amyloid imaging, and structural magnetic resonance imaging (MRI) measurements of cerebral atrophy [105].

Aβ monomers and oligomers have been detected by electrochemical, surface plasmon resonance, colorimetric, resonance light scattering, and fluorescent sensors, as well as by ELISA and with large-scale instrumentation such as mass spectrometry [115, 119–122]. However, there is no gold standard for these assays, and the research community is strongly driven by this unmet challenge. As already described in the experimental section, the combination of SERS with immunoassays yields a platform with high specificity, sensitivity, and selectivity. Multiple groups have taken advantage of this detection principle and reported on the successful determination of Aβ and tau proteins in phosphate-buffered saline (PBS) and in artificially spiked whole-blood samples. In Fig. 1.3, an easy and straightforward approach to detect Aβ (1-40) is illustrated [123]. The platform is based on capturing Aβ (1-40) antigens by

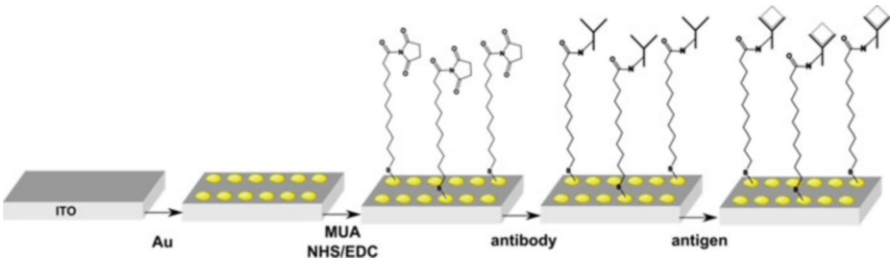

Fig. 1.3 Schematics of the SERS-based immunoassay used for Aβ (1-40) detection described by El-Said et al. [123]

antibodies immobilized on an N-hydroxysuccinimide (NHS)- and 1-ethyl-3-(3-dimethyl-aminopropyl)carbodiimide (EDC)-activated 11-mercaptoundecanoic acid (MUA) layer linked to electrochemically deposited Au NPs. This immunoassay was used for the detection and quantification of Aβ (1-40) based on its SERS spectrum, at concentrations between 100 fg/ml and 1 μg/ml in PBS, with a linear dynamic range of 100 fg/ml–1 ng/ml.

Tau, the biomarker indicating the formation of neurofibrillary tangles in the human brain, has also been successfully quantified in PBS solution by a homogenous sandwich assay combined with SERS [124]. For this, the authors used monoclonal anti-tau antibody-functionalized hybrid magnetic nanoparticle (MNP) probes and polyclonal anti-tau antibodies immobilized on gold NPs as SERS tags. Figure 1.4 illustrates schematically the working principle of the assay. In the first step, silica-coated, oleic acid-stabilized maghemite (γ-Fe_2O_3) NPs were prepared. To prevent self-polymerization of the MNPs, 3-methacryloxypropyltrimethoxysilane (MPS) in the presence of hydroquinone as a catalyzer was deposited on their surface. The MPS-modified MNPs were then coated with the chain transfer agent 2-cyano-2-propyl benzodithioate (CPBT) and azobis(isobutyronitrile) (AIBN). Grafted hybrid MNPs were obtained via the surface-mediated reversible addition-fragmentation chain transfer polymerization of 2-hydroxyethyl methacrylate (HEMA) from CPBT-modified MNPs poly(HEMA). This was followed by the cleavage of the poly(HEMA) grafted chains from the hybrid MNPs, the removal of dithiobenzoate end groups, and the addition of the monoclonal anti-tau antibody. These hybrid MNPs have a diameter of ~70 nm. As SERS tags, gold NPs with a diameter of 15 ± 8 nm, modified with a self-assembled monolayer of 5,5-dithiobis (2-dinitrobenzoic acid) (DTNB) and followed by the attachment of the polyclonal anti-tau antibody, were used. A polyclonal antibody was chosen to amplify the low signal from the target tau, as polyclonal anti-tau antibodies can recognize multiple epitopes on tau molecules. As a result, sandwich complex aggregation is induced.

To detect the tau protein, the hybrid MNPs, functionalized with the monoclonal anti-tau antibody, were added to the sample solutions. After 30 min, the resultant tau conjugated MNPs were isolated with a magnet, washed, and added to the solution containing the SERS tags. After another 30 min, the resultant sandwich complex was isolated with a magnet and SERS measurements were performed. The MNPs are not

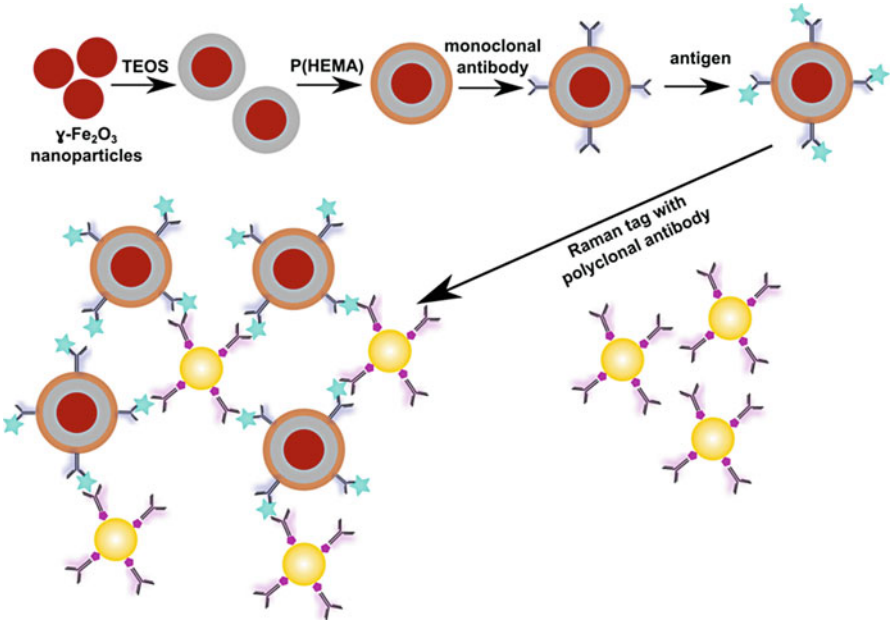

Fig. 1.4 Scheme of the preparation of sandwich assay for tau protein detection described by Zeng in et al. [124]

SERS active, and therefore, there is no plasmonic coupling between them and the SERS tags. However, it is very likely that hot spots can be generated between adjacent polyclonal anti-tau antibody-functionalized Au NPs. This is clearly supported by the appearance of Raman bands in the SERS spectrum associated with the vibrational modes of DNTB (Fig. 1.5a). Under these conditions, it is expected that by increasing the amount of tau proteins conjugated with the hybrid MNPs, the number of captured polyclonal antibody-conjugated Au NPs will also increase. The sensitivity of this immunoassay SERS platform is illustrated in Fig. 1.5b. An excellent linear response was obtained for tau concentrations between 25 fM and 500 nM. Furthermore, the cross-specificity of the assay was also tested using a solution containing equal amounts of tau, bovine serum albumin (BSA), and immunoglobulin G (IgG). As it can be seen in Fig. 1.5c, the SERS intensity obtained from the response of the mixture was strongly similar to that obtained from the sample containing only tau in solution. Therefore, BSA and IgG had no strong influence on the performance of the assay, confirming its high specificity for the tau protein.

Ideally, the assays intended to diagnose a medical condition should measure multiple indicators of the disease in biological fluids in order to avoid false-positive results. In the case of AD, this is especially important, because common dementia cases can be easily misdiagnosed as AD. Therefore, although the two assays presented above offer high sensitivity and specificity for the detection of Aβ (1-40) and tau in PBS, an assay offering multiplex measurements in biological fluids

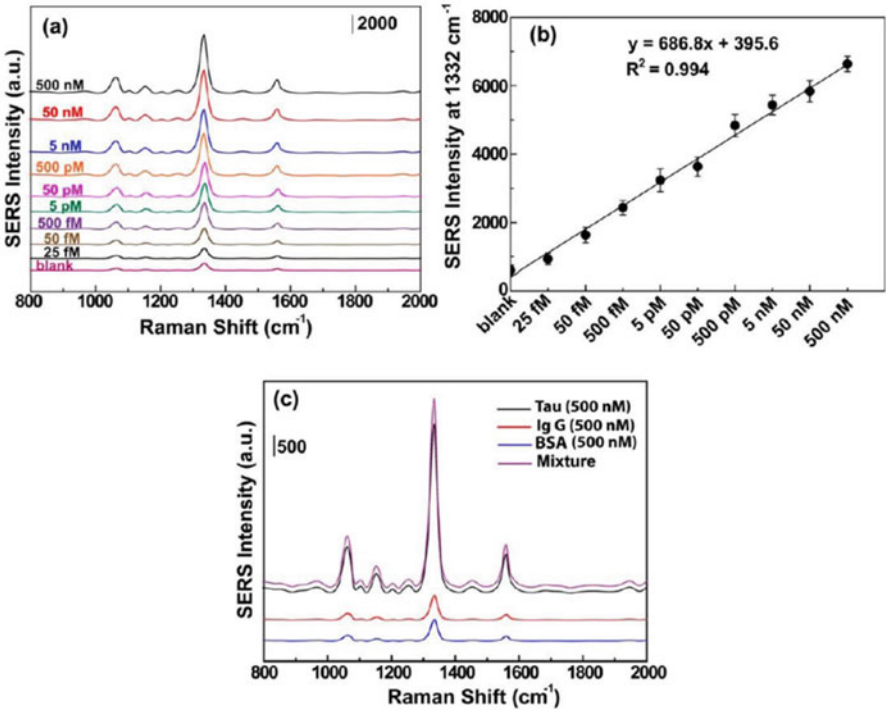

Fig. 1.5 (**a**) SERS spectra at different tau concentrations showing the Raman bands characteristic for the DNTB molecule. (**b**) Concentration-response curve of the tau assay. For each concentration four different reading of the SERS intensity was performed. (**c**) SERS spectra demonstrating the specificity of the sandwich assay for the tau protein (Adapted with permission from Zengin et al. [124]. Copyright © 2013, American Chemical Society)

is desired. Additionally, whole blood would be an attractive alternative to CSF as a biological fluid of clinical interest for biomarker detection, because it allows less expensive and invasive measurements, suitable for repeated, routine examinations. However, the Aβ (1-42) levels in plasma (~20 pg/ml) are considerably lower than those in CSF (800 pg/ml) [125, 126]; furthermore, plasma is a much more complex matrix, as it contains high amounts of different proteins, and Aβ in plasma can also be derived from peripheral tissues and not only from the brain [127]. In the case of tau, its plasma levels were ~8 pg/ml, whereas its levels in CSF were ten times higher. Furthermore, to have elevated tau protein levels in the plasma, substantial axonal injury is required; thus, high levels of tau in the plasma is a late marker of AD [128].

Keeping in mind the need for multiplex detection platforms and the low concentrations of Aβ (1-42) and tau protein in plasma, Demeritte and coworkers developed a large-scale, chemically stable, bioconjugated, multifunctional, hybrid graphene oxide platform for the separation and identification of trace levels (femtogram) of the two AD biomarkers in whole blood [129]. Their nanoplatform conjugated with anti-tau and anti-Aβ antibodies is based on magnetic core-plasmonic shell nanoparticles

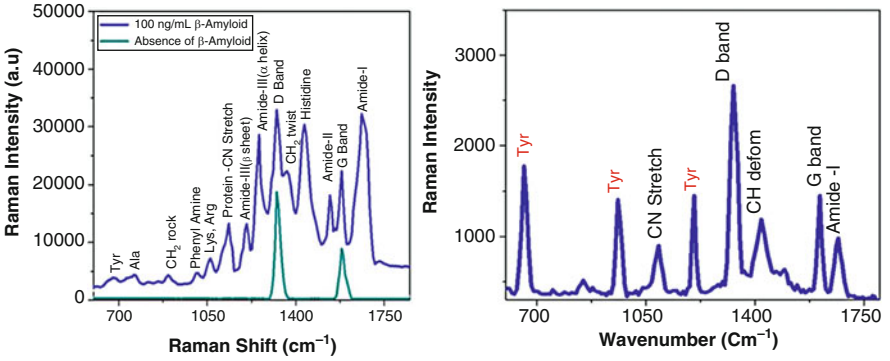

Fig. 1.6 SERS spectrum of Aβ (1-42) and tau protein measured with magnetic core-plasmonic shell NPs attached to 2D hybrid graphene oxide platforms (Adapted with permission from Demeritte et al. [129]. Copyright © 2015, American Chemical Society)

attached to 2D hybrid graphene oxide. Here, as also in the former report, the authors took advantage of the magnetic properties of their particles in order to separate them from the complex matrix and avoid autofluorescence background signals originating from blood cells. The large surface area of the graphene oxide supports high adsorption of the target molecules, and it also facilitates stable hot-spot creation between the core-shell particles. The selective capture efficiency of the assay was confirmed by using an ELISA kit, and it was estimated to be 98% for Aβ (1-42) and 97% for tau. In contrast to the previous case, SERS protein detection was performed label-free, based on their intrinsic Raman vibrational modes. The SERS spectra of Aβ (1-42) and tau are shown in Fig. 1.6, together with the background signal from the nanoplatform. In the latter case, the Raman bands were assigned to the D and G bands of graphene oxide. The SERS spectrum of Aβ (1-42) shows sharp bands assigned to the amide I, amide II, and amide III groups. The position of the amide III band is especially important, as it gives information about the structure of the protein. When the protein adopts an α-helical structure, it is shifted to high wavenumbers (~1300 cm^{-1}), whereas with β-sheet conformations, it is shifted toward the low wavenumbers (~1220 cm^{-1}). In addition to the amide bands, histidine residues, phenylalanine, and tyrosine molecules contribute to the Raman spectrum of Aβ (1-42). In the case of tau, the vibrational modes of tyrosine are strongly contributing to the Raman spectrum. Owing to the absence of amide II and amide III bands in the spectrum of tau, the two molecules can be easily discriminated based on their SERS spectrum. The sensitivity of the assay was 500 fg/ml for Aβ (1-42), with a linear dynamic range up to 1 pg/ml. For the case of tau, SERS signals were present at 100 fg/ml, but the authors do not offer information regarding the linear range.

The three examples described above demonstrate the high potential of immunoassay SERS platforms for the detection of AD biomarkers with very high sensitivity. However, SERS spectroscopy is not limited to the detection of molecules, but it can also offer valuable information about the structure and conformation of the

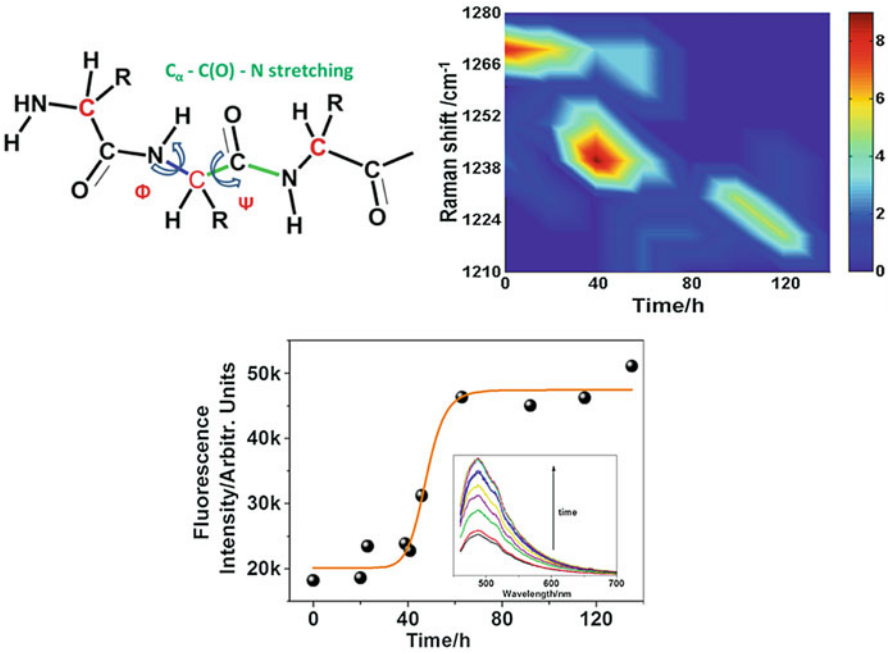

Fig. 1.7 Model of peptide secondary structure and predominately contributed Raman signal associated with the C_α–H bending motion mode. Characterization of Ab (1-42) peptide Am III frequency, with simultaneously ThT assay fluorescence measurement of Aβ (1-42) (Adapted from Wang et al. [132] with permission from Wiley)

molecules. Although this does not have a diagnostic value per se, it is often important to gather additional information of the detected molecules.

In the case of Aβ, it has been proposed that small oligomers, profibrils, Aβ-derived diffusible ligands, and heterogeneous globular species are more neurotoxic than the fibrils in late aggregation stages [130, 131]. To investigate the aggregation pathway, it is crucial to identify the conformation of the proteins accumulated in the different aggregation stages. As already mentioned above, the position of the Raman mode ascribed to the amide III vibration is sensitive to the conformation of the protein (α-helical or β-sheet). Consequently, the C_α-H and N-H bending motions of secondary structure elements, defined by the Ψ and Φ Ramachandran angles (Fig. 1.7), will be affected by the aggregation stage of the protein. In a SERS study carried out with Ag NPs coated with a silica shell, the authors were able to monitor the conformational changes occurring during aggregation by correlating the SERS measurements with the results of a thioflavin T fluorescence assay, the gold standard for assessing Aβ aggregation, and atomic force microscopy [132]. The SERS results are nicely summarized in Fig. 1.7. In the 3D plot, the Raman shift of the amide III band is shown as a function of the incubation time with Aβ (1-42) monomer in PBS at 37 °C. These results show that as the incubation time increases, the center of the Raman band shifts from higher to

lower wavenumbers. At time points below 20 h, the position of the band suggests that the structure of the protein might be flexible to form different hydrogen bonds between C_α-H and N-H. This hypothesis was confirmed by fluorescence measurements, showing no significant changes in the fluorescence intensity at times below 20 h, indicating that Aβ is still not aggregated or has only elementary aggregation forms. For incubation times at the range of 20–80 h, the fluorescence emission of thioflavin T increased exponentially, suggesting Aβ (1-42) aggregation, accompanied by the formation of β-sheet hydrophobic cores. The apparent heterogeneity of the Raman signal suggests that the aggregation process is not homogenous. After 80 h, the aggregation process reaches equilibrium and the Raman band is shifted to 1220 cm^{-1}. In conclusion, SERS is a powerful tool for structure investigation, and it is much more sensitive than classical fluorescence measurements.

5.1.2 Cardiovascular Diseases

Approximately half of the deaths in the western world are caused by cardiovascular diseases (CVD) and particularly by myocardial infarction (MI). The early diagnosis of MI will have a high impact on the health of the patients, as MI causes irreversible heart damage, and it will also significantly decrease the financial burden placed on clinical resources. MI diagnosis is performed by electrocardiogram (ECG) measurements combined with the determination of the level of cardiac specific biomarkers in patient blood [133, 134]. Troponin I (cTnI), troponin T (cTnT), myoglobin, and creatine kinase MB (CK-MB) are the most commonly monitored MI biomarkers. Myoglobin elevation above the clinical cutoff value of 70–200 ng/ml in the first 1–3 h is considered to be one of the earliest signs of MI. However, myoglobin is released by both skeletal and cardiac muscle injury, and, thus, it has low specificity [134]. CK-MB increases above the clinical cutoff value of 10 U/l 3–4 h after MI, and it is considered of medium specificity for the clinical condition [134]. For the confirmation of cardiomyocyte damage, cTnI and cTnT are considered to be the gold standard [135, 136]. The troponin complex is responsible for skeletal and cardiac muscle contraction. After myocardial damage, the individual proteins of the complex are released in the bloodstream. Nevertheless, up to 6 h have to pass since the first physical symptoms appeared to reach a concentration level above the cutoff value of 0.01–0.1 ng/ml. Based on these facts, it becomes clear that once again, as in the case of AD, it is desirable to determine the presence of more than just one biomarker to avoiding false-positive diagnoses. Optical (intensity readout, luminescence, surface plasmon resonance, SERS), electrochemical (amperometric, potentiometric, impedimetric), and paramagnetic particle-based immunosensors have been widely employed for this purpose [133, 134, 137–141].

The high sensitivity of SERS was the driving force for the development of various assays for cardiac biomarker detection. Myoglobin concentrations as low as 10 ng/ml were detected in PBS and in human urine, with a linear dynamic range of 10 ng/ml–5 μg/ml, by employing a template-free, one-step synthesis for the plasmonic structure [142]. However, the employed Ag nano-pinetree film-modified ITO substrates are not selective for myoglobin and are most probably not suitable for the detection of the molecule in blood.

ELISA assays are routinely performed for molecule detection with high specificity and sensitivity. The recently developed assays use fluorogenic, electrochemiluminescent, and real-time polymerase chain reaction to generate quantifiable signals. SERS was also considered as a signal readout method, and it was successfully applied for the quantification of the cTnT biomarker at concentrations of 2–320 pg/ml. For this, the target molecule at different concentrations was incubated in antibody-coated microplates, followed by the addition of an anti-cTnT-horseradish peroxidase conjugate, chromogen A (3,3′,5, 5′-tetramethylbenzidine (TMB)) and chromogen B (H_2O_2). As a result of the enzymatic reaction, TMB^{2+} was obtained, and it was found that its SERS intensities decreased upon decreasing the concentration of the antigen (cTnT) present in the sample.

International guidelines for cardiac biomarker detection recommend a turnaround time (TAT) of less than 1 h from the moment the patient is admitted to the hospital. A competitive immunoassay for the simultaneous detection of two cardiac biomarkers in human blood, cTnI and CK-MB, was proven to deliver results in less than 15 min, requiring a minimum sample consumption of 10 μl [143]. In this assay, monoclonal antibodies against cTnI and CK-MB were conjugated to magnetic beads, and the target antigens were immobilized on the surface of SERS tags. Therefore, the free target antigens in the sample would compete with the antigen-conjugated SERS tags for the binding sites on the surface of the magnetic particles. After binding for 7 min, the immunocomplexes were captured with a magnetic bar, and the Raman signals of the remaining SERS tags in the supernatant were measured. As reporter molecules, malachite green isothiocyanate was used for cTnI and X-rhodamine-5-(and-6)-isothiocyanate for CK-MB. The cross-reactivity between cTnI and CK-MB was also evaluated for a concentration range between 10 pg/ml and 1 μg/ml. The SERS spectra of the two reporter molecules exhibited well-separated Raman bands. Therefore, multiplex detection could be easily carried out. The clinical application of the competitive immunoassay-based SERS platform was evaluated by determining the two biomarkers in 18 blood samples collected from patients and comparing the results with data measured by a commercial assay. For the quantitative determination of the target molecules, SERS calibration curves were generated from cTnI and CK-MB dissolved in PBS. The limit of detection was 42.5 pg/ml and 33.7 pg/ml for CK-MB and cTnI, respectively. By applying the Bland-Altman and Passing-Bablok regression analysis, it was demonstrated that the differences between the results of the SERS assay and the commercial assay were in the 95% limit of agreement range. Thus, the authors were successful in developing an immunosensor with fast TAT and high specificity and with a considerably higher sensitivity than the commercially available platform.

5.1.3 Diabetes Mellitus

Glucose levels in the human body are regulated by the ability of insulin, secreted by the pancreas, to promote glucose uptake in the peripheral tissues and to suppress hepatic glucose production [144]. Type I diabetes mellitus, also referred to as juvenile diabetes, is caused by insulinopenia, and it affects 5–10% of all diagnosed patients. Type II diabetes, with a prevalence outreaching 90%, is described as an

insulin resistance. The onset of type II diabetes happens at adult age when the pancreas is not able to produce excess insulin to overcome the resistance, and its incidence increases with age. There is no established cure for this medical condition, although the state of the patients can be considerably improved by responsible glucose level monitoring. An impressive variety of glucose sensors are on the market, including point-sample and continuous monitoring devices [145–147]. Although glucose monitoring is not a diagnostic procedure per se, we consider that the high number of publications reporting SERS-based sensors for glucose monitoring [148–173] requires a separate section for highlighting the major findings in the field.

Glucose molecules do not naturally absorb onto metallic surfaces; hence different strategies had to be developed in order to detect them. The enzyme glucose oxidase (GOx) catalyzes the oxidation of glucose, generating H_2O_2 and gluconic acid. Consequently, the pH value of the microenvironment is changing. Several researchers took advantage of this reaction and developed sensors based on it. GOx was deposited on SERS-active microneedles used for in vivo glucose sensing [159]. Specifically, 0.2 mm stainless-steel acupuncture needles were covered with gold nanoshells and a microporous polystyrene layer. As the SERS reporter molecule, 4-mercaptobenzoic acid (4-MBA) was deposited before GOx was added on the surface. When the sensor was immersed in an environment containing glucose, the integrated GOx molecules could convert the target molecule to gluconic acid, which would cause a pH change. Consequently, owing to the pH-sensitive SERS signal of 4-MBA, the concentration of glucose could be indirectly assessed. This sensor showed satisfactory linear response for glucose concentrations between 2.7 and 8 mM in water. By taking into account that the normal blood glucose levels in humans are in the range of 3–6 mM [174], the sensor would allow the quantification of blood glucose at normal levels, but hypo- and hyperglycemic states cannot be quantified. In the same study, the in vivo performance of the multifunctional acupuncture needle was demonstrated on a male New Zealand rabbit. For this, the glucose-responsive multifunctional acupuncture needles were inserted in the rabbit tendon and ear vein for 30 s. The signal from different needles was measured before and after the injection of a glucose solution (5 ml, 0.75 g) via the ear vein. At the same time, reference values were measured using a commercial glucometer. Unfortunately, the authors do not provide a quantitative estimation of the glucose levels in the rabbit; however, the 4-MBA signal decreased upon increasing glucose concentration. Overall, this technique is very promising, and with further work, it could compete with other commercial devices.

Boronic acid covalently binds saccharides via the diol moieties [175]. Thus, many glucometers rely on this recognition reaction for the detection of glucose levels. In the SERS studies different isomers of mercaptophenylboronic acid (MPBA) have been widely used for capturing glucose, and also as Raman reporters for quantification purposes [153, 155, 158, 169–171]. Glucose recovery levels of 84–110% in undiluted human urine were reported by employing a nanosensor based on 4-MPBA decorated Ag NPs [171]. The working principle of the sensor relies on the aggregation of the Ag NPs induced by the 2:1 4-MPBA/glucose bonding ratio. Glucose

contains two pairs of adjacent hydroxyl groups that could bind to two 4-MPBA-modified Ag NPs. This glucose sensor showed a response time of 12 min, and its selectivity over mannose, galactose, sucrose, and fructose was also demonstrated. Two-component (4-MPBA and 1-decanethiol (1-DT)) self-assembled monolayers, serving as molecular recognition and penetration agents, have also been employed in a paper membrane-based SERS sensor [155]. Owing to the nitrocellulose layer, blood cells and proteins were captured on the surface of the membrane, and only the small molecules reached through capillary forces the sensing site. The assay time was 5 min and a glucose recovery rate of 88% was reached. The limit of detection was estimated to be 0.1 mM and the linear range 0.5–10 mM. To increase the selectivity of the glucose sensing platforms, scaffolds incorporating two boronic acid groups have also been considered [153]. Direct and selective SERS detection under physiological conditions was carried out using a gold film-over-nanosphere (AuFON) substrate, functionalized with bisboronic acid receptors incorporating two 4-amino-3-fluorophenylboronic acid units. By employing monobornic acid, the glucose molecules will be in the close proximity of the metallic surface, sensing the high electromagnetic field. On the basis of their results, the authors concluded that a bisboronic acid analogue with seven atoms separating the amide carbonyls of the receptor units showed the highest selectivity and affinity for glucose. By applying multivariate statistical analysis, a clear distinction between hypoglycemic, normal, and hyperglycemic levels was achieved.

All sensors described above rely on point measurements, where the patients are requested to test their glucose levels multiple times per day. In this manner, hypo- and hyperglycemic episodes can be hardly detected, as they might occur randomly during the day. Continuous monitoring of glucose levels is therefore highly desired for the well-being of the patients. Multiple continuous glucose monitoring (CGM) devices are already on the market. However, they can generally function up to 7 days, they require multiple calibrations, and the product description recommends the patients to verify with a regular glucometer the actual glucose levels before taking measures. At the Van Duyne laboratory, a transcutaneous glucose sensing platform relying on surface-enhanced spatially offset Raman spectroscopy (SESORS) was developed, which could reliably sense glucose in vivo in rats for more than 17 days [151, 152]. While in normal Raman measurements the excitation and signal collection sites coincide, there is an offset between the two processes in SORS. In this way, the Raman signal from the underlying layers in the investigated samples will not be overwhelmed by the signals from the surface. Thus, SERS signals originating from the transcutaneous sensors can be easily collected. Decanethiol (DT)/6-mercapto-1-hexanol (MH) self-assembled monolayers partition and localize the glucose molecules on the AgFON surface. Based on space-filling computer models, the authors suggest that dynamic pockets capturing glucose are formed from the long DT chains and the short MH chains. The reliability and accuracy of new glucose sensors are generally assessed by the Clarke error grid analysis (EGA), illustrated in Fig. 1.8. The grid is divided into five zones (A–E), with measured concentrations by a reference method on the x-axis and predicted concentrations by the new method on the y-axis. The zones have the following

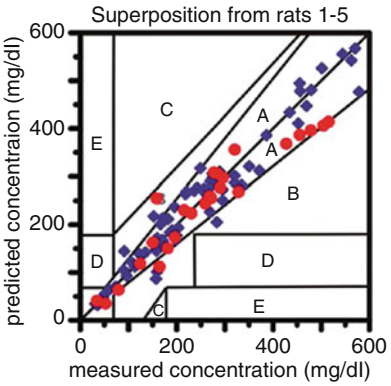

Fig. 1.8 In vivo transcutaneous SESORS glucose calibration (blue ♦) and validation (red •) data sets on five rats (Adapted with permission from Ma et al. [152]. Copyright © 2011, American Chemical Society)

significance: (A) clinically accurate measurements and treatment, (B) benign errors or no action, (C) unnecessary action, (D) lack of action, and (E) actions that are opposite to those that are clinically necessary.

Therefore, data acquired with the new method has to fall into the A and B zones in order to pass the accuracy test. Based on the plots presented in this study, this transcutaneous sensor detected hypoglycemia with an accuracy exceeding the current International Organization Standard (ISO/DIS 15197) requirements, with only one calibration in a time period of 17 days.

5.2 Cancer Diagnostics

Another important cause of a high number of deaths worldwide is cancer and cancer-related diseases. As nicely introduced in many review articles [176–178], the term cancer encompasses a large family of diseases, all characterized by uncontrolled cell growth that can potentially spread to other parts of the organism as well. Consequently, the diseases develop fast and are often diagnosed at a rather late(r) stage. Additionally, there is limited access to standard and efficient treatment, and cancer removal surgeries depend strongly on the proper assessment of the tumor borders in the affected tissue. Accordingly, cancer survival rates tend to be low, with the exact rates depending on the specific region of the world, the type of cancer, the age of the affected person, and the stage of the cancer spread [179]. To improve this, different techniques have been applied to achieve fast and reliable cancer diagnosis at an early stage, including polymerase chain reaction (PCR), ELISA, electrophoresis, SERS, micro-cantilevers, colorimetric assay, electrochemical assay, and fluorescence methods [176–178]. Each of these techniques relies on the specific identification of different cancer biomarkers present in tumor tissues, cells, or body fluids [176, 180]. Nevertheless, due to the high diversity of cancer-related diseases and

the particularities of its detection at different organs, often, detection of more than one biomarkers is required to assess whether an individual has cancer. DNA, mRNA, enzymes, metabolites, transcription factors, and cell surface receptors are some of the biomarkers used for cancer diagnosis [176, 179].

Proteins and related biomarkers released from cells and organs have been used for the detection and monitoring of cancer [181–184]. The available SERS studies for the ex vivo (cell, tissues, and body fluid measurements) identification of cancer often relies on the recognition of such biomarkers, and promising results have been reported for their ex vivo detection in cell culture [185–194]. Nevertheless, a more clinically relevant approach would rely on body fluid measurements. However, the concentration of protein biomarkers in serum during early cancer stages can be as low as 10^{-16}–10^{-12} M, making their detection rather challenging [181]. Since SERS is a molecular fingerprinting technique that can identify target molecules at very low concentrations, different SERS-based approaches have been tested to achieve this goal. Among the most straightforward approaches, SERS NPs in the form of commercially available colloids [195] or colloids prepared according to easy preparation protocols [50] were mixed with blood or serum samples, dropped on glass slides, and measured by Raman spectroscopy [195–197]. However, due to the low specificity of label-free SERS NPs, the results obtained by this procedure only partly correlated to the gold standard analysis (i.e., high-performance liquid chromatography – HPLC) [195]. Nevertheless, upon functionalization of these nanostructures, their specificity for specific cancer biomarkers increased, leading to better diagnostic results [198, 199]. In addition to pure Au or Ag nanostructures [50, 182, 195, 198], core-shell NPs have also been reported in the literature for cancer detection applications: Fe_3O_4/Au/Ag [41, 199], Au@Ag [41], or Au @ polyethylene glycol(PEG) – Au@PEG [182]. For each of these structures, specific tags were used for distinct cancer types, making the overall SERS substrate preparation protocols not universally applicable. For example, a surface-enhanced resonance Raman spectroscopy (SERRS) sensor based on sandwich immunocomplexes consisting of a mixture of Fe_3O_4@Ag NPs conjugated with capture antibody through an amidation reaction, and Au@Ag NPs conjugated with antibody using an HS-PEG-COOH/Tween 20-assisted method was tested for the detection of the colon cancer biomarker carcinoembryonic antigen (CEA) in clinical serum samples [41] (schematic representation in Fig. 1.9). For the preparation of the sandwich structure, a rather complicated and time-demanding procedure was followed. That is, the Fe_3O_4@Ag NPs were first incubated overnight in an ethanolic solution containing 10 μM MUA and 10 μM 11-mercapto-1-undecanol (MU). Then the carboxyl groups on the NP surface were activated by using a mixture of 1 mM and 5 mM sulfo-NHS, and the resulting NPs were incubated overnight in the presence of 10 μg of capture antibody. In the case of the Au@Ag NPs, upon washing three times with a buffer containing 1 μM HS-PEG-COOH and 0.01% Tween 20, the NPs were sonicated for 30 min in 25 μM diethylthiatricarbocyanine iodide (DTTC) to synthesize Raman-encoded NPs. Next, the particles were sonicated for another 30 min in 10 μL of a 1 mM mPEG-SH solution to increase their stability, suspended in a K_2CO_3 solution, vigorously mixed with 25 μM EDC and 25 μM sulfo-NHS for 15 min, and

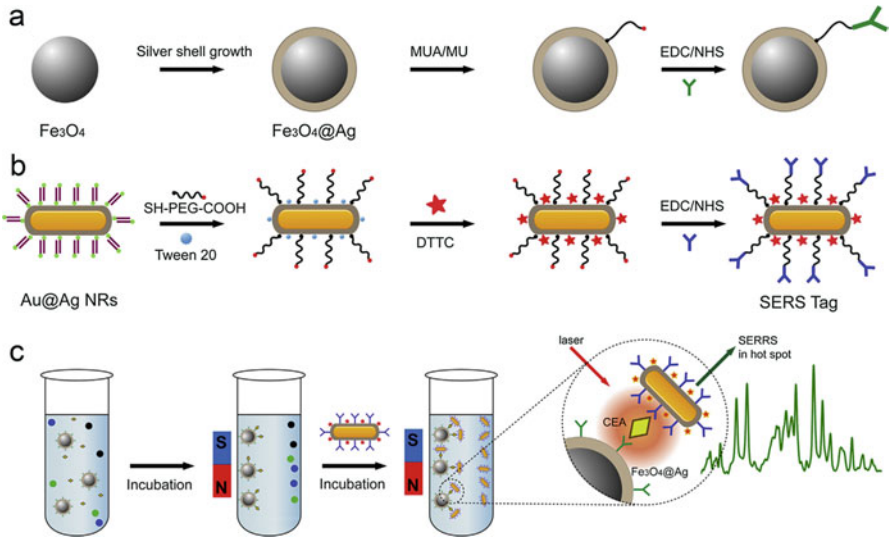

Fig. 1.9 Scheme of the preparation of sandwich assay for CEA protein detection (Reprinted from Rong et al. [41] with permission from Elsevier. Copyright © 2016 Elsevier)

re-suspended in a K_2CO_3 solution. Finally, the resulting activated NPs were incubated overnight in the presence of 10 μg of detection antibody. Thus, the preparation of the two different types of NPs required overnight incubation, making the overall NP preparation protocol rather time-consuming. However, once the NPs were available, the actual measurement protocol was rather simple. The magnetic NPs were first allowed to interact with the target solution for 30 min, and then the immune complexes were magnetically collected and washed. Subsequently, the DTTC-encoded Au@Ag were added and incubated for another 30 min. Finally, the formed sandwich complexes were washed with phosphate-buffered saline tween-20 (PBST), re-suspended in deionized water, and measured by SERS. Thus, the detection time required was approximately 1 h, which is fit for clinical application approaches.

Other commonly investigated biomarkers for cancer identification are DNA and mRNA. As in the previous case, both NP-based [200] and planar substrates-based [201] SERS immunosensors have been developed for their detection. For example, the detection of micro ribonucleic acid 21 (miR21) is often achieved by using labels such as cresyl fast violet T, Rhodamine B, Rhodamine 6G, and DTNB [201]. Nevertheless, it was recently shown [200] that by using an "OFF-to-ON" SERS inverse molecular sentinel (iMS) nanoprobe in a homogeneous assay for multiplexed detection of micro ribonucleic acid (miRNA) in a single sensing platform, no labeling is required. The starting point in the preparation of this detection scheme was the generation of Au nanostars based on a seed-mediated growth protocol introduced by Wang et al. [200], followed by Ag coating of these structures by adding 0.1 M $AgNO_3$ and 29% NH_4OH and allowing the chemicals to react for 5 min. Finally, the SERS iMS nanoprobes were produced by mixing 10 μl of a 10 μM stem-loop DNA

probe solution with 0.9 mL of 0.1 nM Ag-coated nanostars and 0.1 mL of a 2.5 mM $MgCl_2$ solution and incubating this mixture overnight at room temperature. The obtained structures were stabilized by a 30-min incubation with a 1 μM *O*-[2-(3-mercaptopropionylamino)ethyl]-*O*-methylpolyethylene glycol (mPEG-SH, 5000) solution. Following centrifugation and resuspension in Tris-HCl buffer (10 mM, pH 8.0) containing 0.01% Tween-20, the metallic surface of the nanostars was passivated with 0.1 mM MH. Subsequently, the SERS iMS nanoprobes were washed and redispersed in Tris-HCl-Tween-20 buffer. Finally, the iMS SERS signal was "turned OFF" by incubating the nanoprobes with 0.1 μM placeholder strands in PBS buffer solution containing 0.01% Tween-20 overnight at 37 °C. While performing the SERS measurements, the iMS SERS signal was "turned ON" when the structures sensed the presence of at least 1 μM miR-21 targets.

For each of the above mentioned biomarkers, SERS immunosensors are also available as planar substrates [43, 181, 184, 202–204] and within photonic crystal fiber probes [51, 182], for the detection of breast cancer biomarkers such as vascular endothelial growth factor (VEGF) [181], human epidermal growth factor receptor 2 (HER2) [184], and the wild-type and mutant mp53 protein [204] in patient blood plasma. An example of a hollow core photonic crystal fiber (HCPCF) probe used for multiplex detection of serological liver cancer biomarkers is illustrated in Fig. 1.10 [182]. Here, the fiber PCF was cut into 7 cm pieces cleaved at the ends, and its inner walls were coated with poly-L-lysine to induce active sites for the binding of the target biomarkers. The resulting fiber was then dipped in cell lysates from oral squamous carcinoma (OSCC) HER2 biomarker supernatant from Hep 3b cancer cell line for 3 min to allow for protein binding and was incubated at 4 °C for 2 h. After drying, a mixture of antibody-conjugated SERS nanotags was added into the fiber. In parallel, bio-conjugated SERS nanotags were prepared from commercially available NPs. For this, NPs were incubated with the following Raman reporter molecules: malachite green isothiocyanate (MGITC), naphthalenethiol (NT), or lipoic acid-modified cyanine 5 (Cy5), for 15 min, 1 h, or 15 min, respectively, in a ratio of 1:9. Subsequently, thiolated-carboxylated PEG (HS-PEG-CO_2H) was added and incubated for 20 min, followed by and incubation with thiolated PEG (PEG-SH) for 3 h. Upon activation of the carboxylic acid functional groups on the surface of these PEG-encapsulated NPs (by using EDC and sulfo-NHS), the resulting NPs were mixed with an additional antibody to achieve multiplexing: the alpha-fetoprotein (AFP) antibody was added to the activated Cy5 nanotag and the AIAT antibody to the MGITC nanotag. Finally, the resulting bioconjugated SERS nanotags were washed and bonded to the immobilized biomarkers in the fibers (see Fig. 1.10). In this study [182], the HCPCF was used both as a proof of concept, achieving the detection of HER2 in OSCC cancer cell lysate, and for the detection of two prominent hepatocellular carcinoma biomarkers, alpha-fetoprotein and alpha-1-anti-trypsin, in the Hep 3b cancer cell line. Furthermore, it was proposed that the HCPCF probe can be used for the analysis of saliva, tear, urine, and other body fluids for the early diagnosis of multiple diseases.

Other body fluids used for cancer biomarker detection include cervical fluids for the identification of the E7 gene of human papillomavirus (HPV) [202]; additionally,

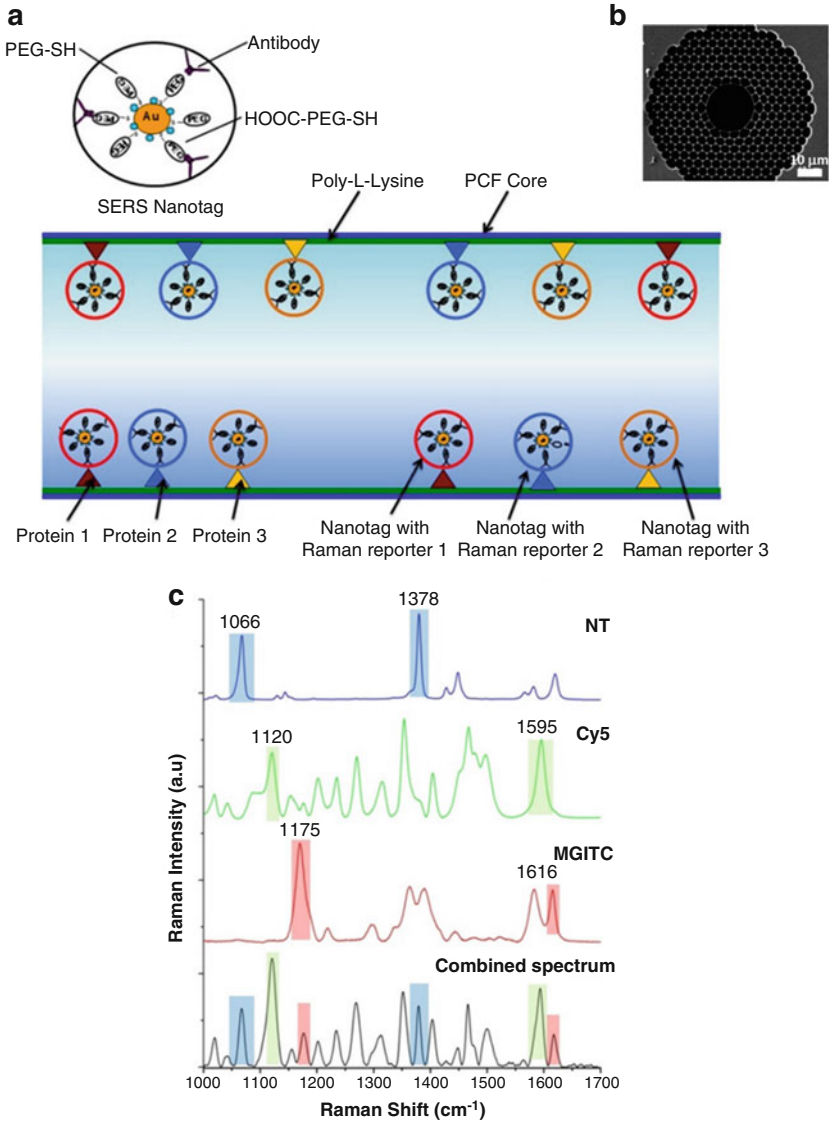

Fig. 1.10 Scheme of a hollow core photonic crystal fiber (HCPCF) probe used for multiplex detection of serological liver cancer biomarkers (**a**), SEM of the cross section of the HCPCF (**b**) and SERS spectra of individual SERS nanotags and their mixture used for the multiplexing measurements (**c**) (Adapted from Dinish et al. [182] with permission from John Wiley and Sons. Copyright © 2014 John Wiley and Sons)

breath analysis was also performed for the identification of volatile organic compound that can act as biomarkers for gastric cancer [43]. For the latter, a sensor was developed starting from a 7.5 cm clean glass, on which a 300-nm-thick Au layer was sputtered and 2 µL of a graphene oxide homogeneous solution was dropped and

dried. Following hydrazine vapor adsorption and reduction, the substrate was placed in N_2 for 30 min, and 1 μL of a 5 mM $AuCl_4^-$ solution was dried on the substrate, resulting in a Au NP distribution on the reduced graphene oxide film. The resulting SERS-active substrate was used for measurements of both simulated and real breath. To this end, the substrate was placed in a small vessel, and 50 μL liquid standard of each biomarker was added to the vessel without allowing any direct interaction between the substrate and the liquid to occur. The vessel was sealed and placed at 37 °C to allow for the liquid to vaporize and interact with the substrate, dry, and be measured. As illustrated in the simplified schematic in Fig. 1.11, statistical analysis was performed on the measured data and the results allowed for the differentiation of patients affected by early gastric cancer (EGC, stages I and II) from patients suffering from advanced gastric cancer (AGC, stages III and IV).

As is evident from the examples presented above, the drawback of these SERS-based analytical methodologies is the complexity of the protocol required for the preparation of the SERS-active substrates. Following NP preparation, functionalization and immobilization on a substrate are necessary, and the total time and complexity of the measurements increase. Nonetheless, once the SERS substrates are available, the measurements are easy to perform, and the results are available in a time-efficient manner. An alternative approach for the identification of cancer in tissues has also been reported in the literature [205–207], based on incubating the tissue with NP solutions, which does not require NP immobilization on any substrate. However, tissue measurements are by far the most invasive of the proposed methods, as the tissue must be removed from the patient before being investigated ex vivo by SERS. For the measurements, the tissue is first sliced into μm–mm thick sections [206, 207], then stained [206] or breaded [205] with NPs, and measured by mapping. It was found that upon incubation of the tissue with NPs, non-functionalized Au NPs form nano-clusters, which lead to increased Raman signals due to the formation of hot spots. On the contrary, encapsulated Au NPs (i.e., Au/SiO_2) and functionalized Au NPs are homogeneously spread over the tissue surface, increasing afferent specificity for the targeted biomarkers and lower Raman signals [205]. However, E. Cepeda-Pérez et al. [205] reported that in wet tissues, the Au/SiO_2 NPs used in their study formed aggregates in the vicinity of the biomolecules located on the tissue surface, leading to a further increase in Raman signals.

As an alternative to the abovementioned procedures, direct intra-tumoral injection of NPs (see schematic representation in Fig. 1.12) has also been used for cancer identification. Different approaches were considered here, starting from functionalization of commercially available NPs [36] and ending with the development of rather complex core-shell nanostructures [35, 208]. These complex core-shell nanostructures, depicted in Fig. 1.12, consist of Au vesicles encapsulating active compounds, such as chlorin e6 (Ce6). They were prepared starting from the generation of Au NPs by citrate reduction of $HAuCl_4$ in an aqueous phase. Subsequently, the Au NPs were dried on a glass substrate, followed by triggering the self-assembly of amphiphilic block copolymers by rehydrating of the thin Au NP film in water by sonication. Finally, Ce6 was encapsulated in the resulting Au NPs by rehydrating the structures with solutions having different concentrations of Ce6 during

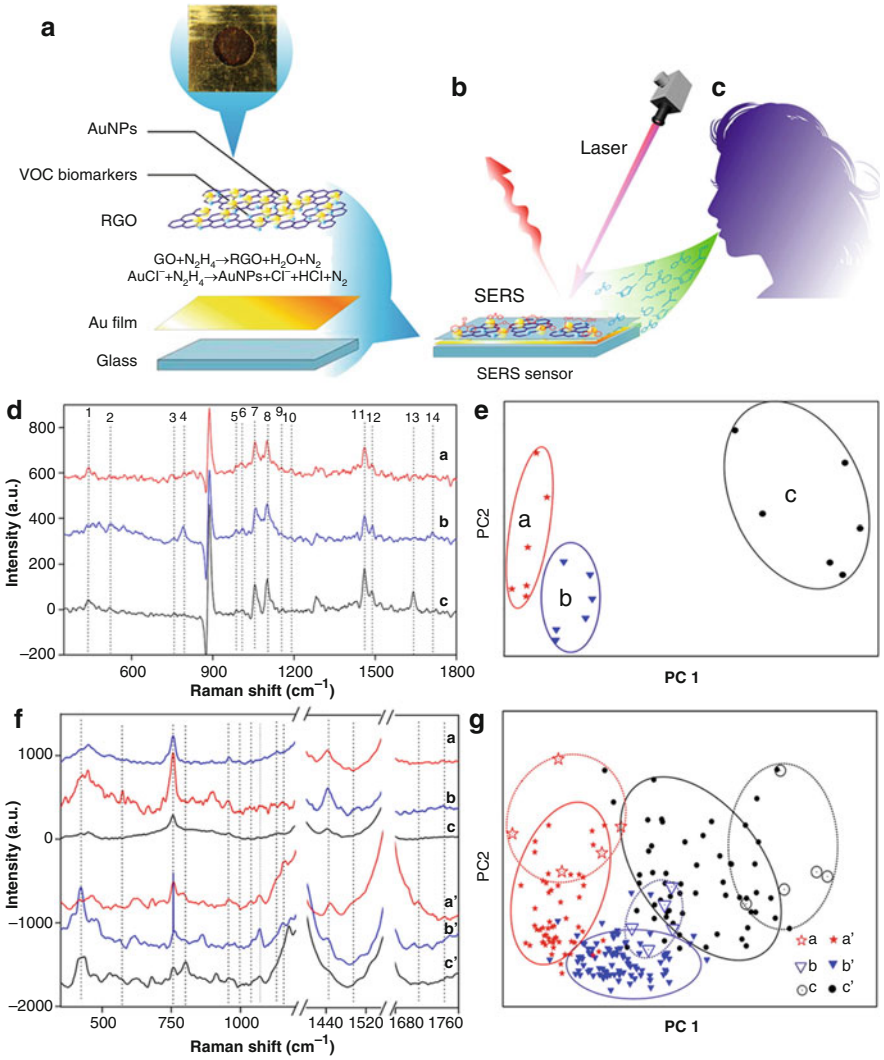

Fig. 1.11 Schematic representation of the SERS substrate preparation protocol (**a**), the SERS measurement procedure (**b**) of both simulated and real breath samples (**c**) and data analysis (**d**, **e**): the processed Raman spectra of the used biomarkers out of which 14 were associated to different vibrations that can be seen in the breath samples of healthy persons (*c*) and EGC (*b*) and AGC (*a*) patients (**d**); principal component analysis (PCA) of the data set of biomarker patterns of healthy persons (*c*) and EGC (*b*) and AGC (*a*) patients (**e**) obtained by using the mentioned bands; SERS spectra of simulated and real breath samples of healthy persons (*c*, *c*′) and EGC (*b*, *b*′) and AGC (*a*, *a*′) patients (**f**); PCA analysis of the data set of simulated and real breath samples of healthy persons (*c*, *c*′) and EGC (*b*, *b*′) and AGC (*a*, *a*′) patients (**g**) (Adapted with permission from Chen et al. [43]. Copyright © 2016, American Chemical Society)

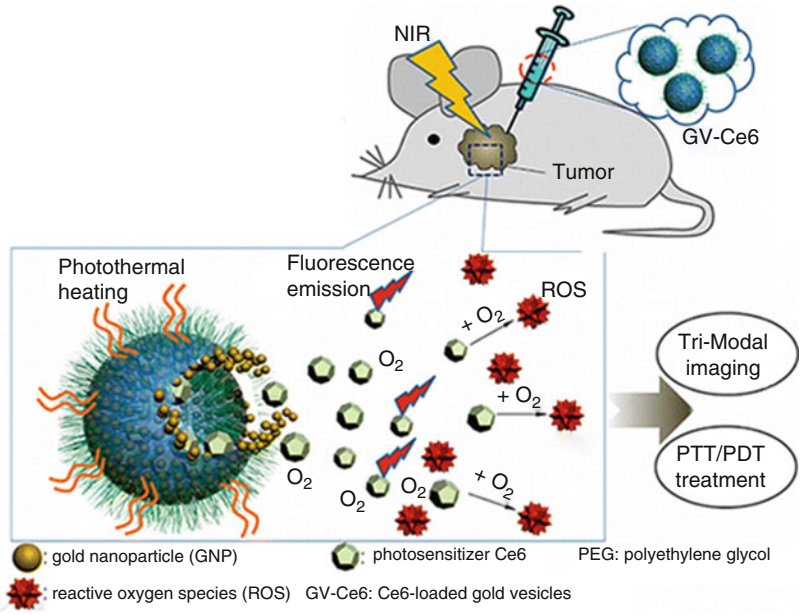

Fig. 1.12 Scheme of the preparation of sandwich assay for CEA protein detection (Adapted with permission from Lin et al. [35]. Copyright © 2013, American Chemical Society)

centrifugation of the mixtures. The resultant nanostructures were tested and characterized regarding their SERS, near-infrared spectroscopy, fluorescence, thermal, and photoacoustic properties. Moreover, it was found that laser irradiation causes them to break and to be easier cleared from the organism [208]. Additionally, during the experiments there was no significant inflammation observed in the heart, liver, spleen, lung, and kidneys, suggesting low cytotoxicity and high biocompatibility of the Au vesicles [208]. Therefore, these nanostructures are thought to represent a potentially interesting tool for cancer identification.

In a different study, the detection of the breast cancer-specific biomarkers epidermal growth factor receptor (EGFR), CD44, and transforming growth factor beta receptor II (TGFbRII) in mice was also reported [36]. To achieve this, three different reporter molecules were immobilized on the surface of commercially available 60 nm SERS NPs: malachite green isothiocyanate (MGITC), Rh6G, and Cy5. For this, solutions of 10 mM lipoic acid (LA) linker modified with Cy5, 10 mM malachite green isothiocyanate (MGITC), and 50 mM Rh6G were separately mixed with the AuNPs in a v/v ratio of x/x for 20 min. Subsequently, PEG encapsulation for antibody conjugation and protection of the nanotags was performed. Next, the carboxylic acid functional groups were activated on the surface of the resulting nanostructures by the EDC and sulfo-NHS coupling reaction. Finally, an anti-EGFR antibody was allowed to react with the activated Rh6G

nanotag, an anti-CD44 antibody with the malachite green isothiocyanate (MGITC) nanotag, and an anti-TGFbRII antibody with the Cy5 nanotag, for 2 h at 25 °C, and the samples were incubated overnight at 4 °C. Although the overall NP preparation was rather long (approximately 6 h of actual preparation time plus an overnight incubation at 4 °C), the achieved multiplexing efficiency makes the resulting NPs a potentially interesting structure. Moreover, the NP clearance by the liver and spleen was evaluated by monitoring the SERS signals in these organs for more than 72 h [36], and it was concluded that they are eliminated from the organism within 72 h from their intra-tumoral injection.

Regarding NP biocompatibility and clearance time in mice, the study of Zeng et al. [37] shows that the Ag@Au-DTTC nanostars prepared and used during the experiments had a negligible effect on tumor volume and overall body weight in mice for a period longer than 16 days (Fig. 1.13). Moreover, no inflammation in the heart, liver, spleen, lung, kidney, or intestine tissue was observed during the study. In this study, the NPs were injected through the tail vein and not directly at the tumor site. An additional study was carried out to compare the use of Ag@Au-DTTC nanostars, PBS, PBS + NIR, Ag@Au-DTTC, and Ag@Au-DTTC + NIR, and the results are summarized in Fig. 1.13. The NIR addition in the names of the different systems was used by the authors to denote that an 808 nm laser was applied for the excitation of the NPs instead of the 785 nm laser used in all other cases. Ag@Au-DTTC nanostars were prepared starting from simple, 20–30 nm Ag NPs by adding dropwise deionized water and 0.1 mM DTTC under stirring. This led to the formation of Ag-DTTC NPs, which were further mixed with 0.1 M HCl and 2.5 mM $HAuCl_4$ aqueous solutions. Then, 10 mM $AgNO_3$ and 100 mM ascorbic acid (AA) were added under vigorous stirring. Next, 0.1 mM DTTC was dropped into the NPs for the second time, while stirring, and the reaction was maintained for 10 min. Here, the addition of $AgNO_3$ was performed to generate anisotropic Au nanostars. Finally, the resulting Ag@Au-DTTC nanostars were modified with mPEG-SH by adding 2 mM mPEG-SH to the Ag@Au-DTTC nanostars under stirring and allowing them react for 30 min. Subsequently, the nanostarts were washed, redispersed in deionized water, and used for measurements.

While a few studies are introduced here, many others are available in the literature. Cancer detection is a high-interest topic, and much effort is directed toward developing methods for the reliable detection of cancer biomarkers present at low concentrations, especially at early stages of the disease.

5.3 Pathogen Detection

The early diagnosis of medical conditions caused by viruses and parasites is highly needed, especially in the cases where treatment administration during the early stage of the disease is crucial. For example, communal transmission of malaria and full recuperation of patients infected with the apicomplexan parasite *Plasmodium* species are guaranteed only when medication follows early detection. Hemozoin, a crystalline insoluble precipitate present in the red blood cells (RBCs), is considered to be a

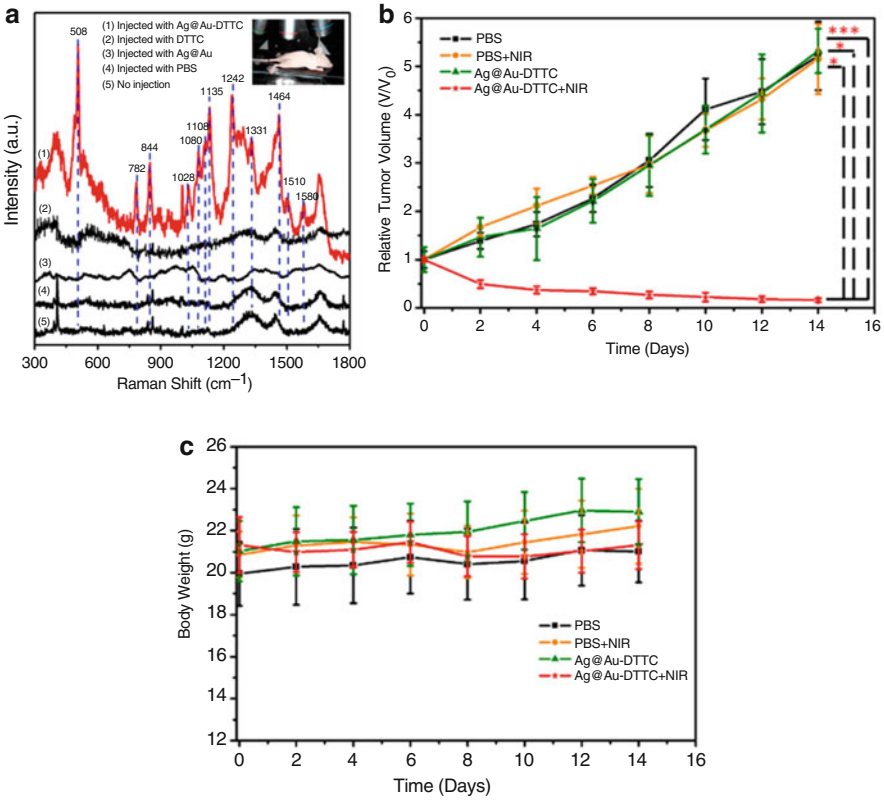

Fig. 1.13 In vivo SERS spectra of tumor-bearing mice in the control and injected with PBS buffer, Ag@Au, pure DTTC, and Ag@Au-DTTC nanostars under the excitation of a 785 nm laser (**a**); the change of relative tumor volume in different groups of PBS (under the excitation of a 785 nm laser), PBS + NIR (under the excitation of a 808 nm laser), Ag@Au-DTTC (under the excitation of a 785 nm laser), and Ag@Au-DTTC + NIR (under the excitation of a 808 nm laser) (**b**); the change of body weight in different groups of PBS, PBS + NIR, Ag@Au-DTTC, and Ag@Au-DTTC + NIR (**c**) (Adapted with permission from Zeng et al. [37]. Copyright © 2015, American Chemical Society)

biomarker for malaria diagnosis. The reference method for its detection is based on visual examination of light microscopy images of Giemsa-stained blood smears. However, a considerable amount of hemozoin precipitates have to be present in the sample in order to diagnose malaria with this method. Nevertheless, hemozoin is produced in the RBCs already during the earliest stages of the parasite lifecycle. In a period of 48 h, the parasite transitions from the merozoite stage to the ring and trophozoite stage, and then it matures to the schizont stage. During this time, the parasite digests up to 75% of the available hemoglobin, and it produces the crystalline, insoluble hemozoin. The compound is highly paramagnetic, and it has a strong Raman fingerprint, as it can be seen in Fig. 1.14. Because hemozoin is a product of hemoglobin digestion, most of the Raman bands are identical for the two molecules.

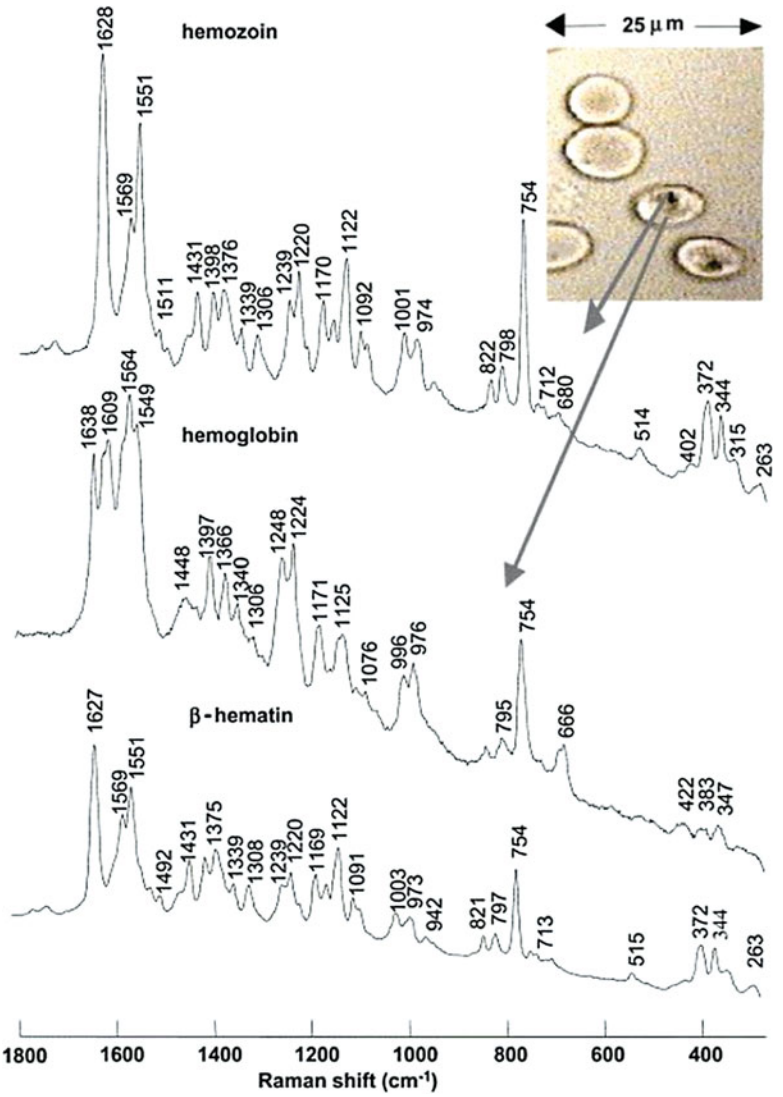

Fig. 1.14 Photomicrograph of *P. falciparum*-infected erythrocytes in the late trophozoite stage, showing vacuoles containing hemozoin. The Raman spectrum of β-hematin, a structurally identical, synthetic composite of hemozoin, is also depicted (Reprinted from Wood et al. [209] with permission from John Wiley and Sons. Copyright © 2003, American Chemical Society)

SERS, owing to its high sensitivity, can easily determine hemozoin at low concentrations, and multiple studies have reported the successful detection of the precipitates in lysed blood samples, infected RBC, or human blood, even at single parasite level [210–213]. For example, Garrett and coworkers used gold-coated butterfly wings for the detection of the malarial hemozoin pigment in the early

ring stage in lysed blood samples containing 0.005% and 0.0005% infected RBC [210]. However, because the surface of the substrate was not functionalized, hemozoin deposition from the cell lysate was random. The detection of the parasite at a concentration of 0.0005% infected RBC was achieved only by manually selecting the measurement spots on the SERS-active surface. This is a time-consuming approach, and it is not feasible for real-time measurements of a high number of samples. In another study, Chen et al. [211] performed detailed SERS investigations of normal and infected RBCs at different stages of infection. By using multivariate statistics based on principle component analysis, the authors were successful in discriminating between ring, trophozoite, and schizont stages of infected RBCs from normal RBCs. The changes observed in the SERS spectra were associated with changes of the cell membrane. Namely, during the life cycle of the parasite, the host cell plasma membrane displays a significantly decreased content of cholesterol and sphingomyelin, and an increased ratio of phospholipid to cholesterol, while a large number of proteins are exported. In this study, silver nanorods were fabricated via the oblique angle deposition method on glass microscope slides, and they were used for enhancing the weak Raman spectrum. In a recent study, Chen and coworkers reported a procedure confirming that the source of the measured SERS signal originated from a single parasite in the ring stage [212]. In order to do this, silver NPs were synthesized directly inside the parasites to ensure close proximity between the NPs and the target molecules and to avoid the necessity of lysing the parasites. Specifically, following lysis of blood cells from the infected sample, the lysate was re-suspended in $AgNO_3$ solution. Triton X-100 was mixed with hydroxylamine hydrochloride, and it was added dropwise to the $AgNO_3$ solution containing the sample. The resulting solution was smeared on glass slides covered with aluminum foil and measured with a Raman spectrometer. With the help of bright field microscopy images and the SERS spectra, the authors showed that the measurements were carried out on a single parasite level. On the basis of all the studies described above, it is clear that SERS is very promising for early malaria diagnosis. However, further work is required to design reliable platforms that can be affordable for developing countries.

Hepatitis B can lead to liver cirrhosis and hepatoma; during the last years, proteins, antibodies and antigens, and specific DNA sequences have been considered as hepatitis B biomarkers. As already demonstrated in the previous sections, the combination of immunoassays, microfluidics, and SERS yields fruitful synergy, and it was also applied for the detection of hepatitis B virus antigen (HBsAg) in human blood plasma [214]. In Fig. 1.15, the working principle of a microfluidic SERS-based immunoassay is depicted. GaN/Au-Ag was used as the capturing substrate. The substrate was modified with 6-amino-1-hexanethiol to form amino-terminated linkages. The thiolated metallic substrate was placed in the measuring chamber of the microfluidic chip fabricated on polycarbonate. A mixture of a hepatitis B virus monoclonal antibody (anti-HBsAg) and an activation solution was injected via one of the inlet ports. After 1 h, the remaining active surface was blocked by BSA, and the antibody-immobilized substrate was stored at 4 °C until the measurements were performed. The Raman reporter molecule, basic fuchsin, was designed to chemisorb

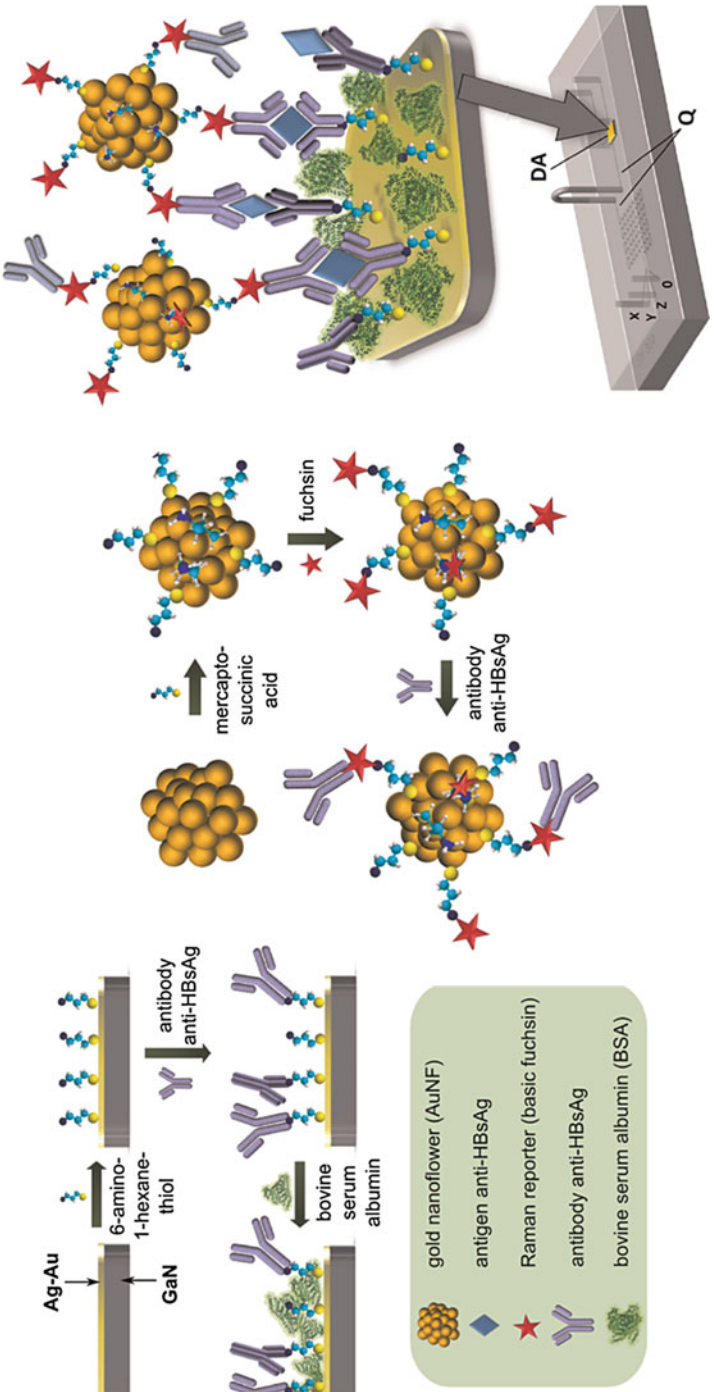

Fig. 1.15 Sequential steps for the formation of the microfluidic SERS-based immunoassay platform: capturing substrate preparation (GaN/Au-Ag modified with a thiol layer and anti-HBsAg), Raman reporter-labeled Au nanoflowers modified with anti-HBsAg, SERS detection of the sandwich interection, and integration of the assay within a microfluidic chip (Adapted from Kaminska et al. [214] with the permission of Elsevier. Copyright © 2014 Published by Elsevier)

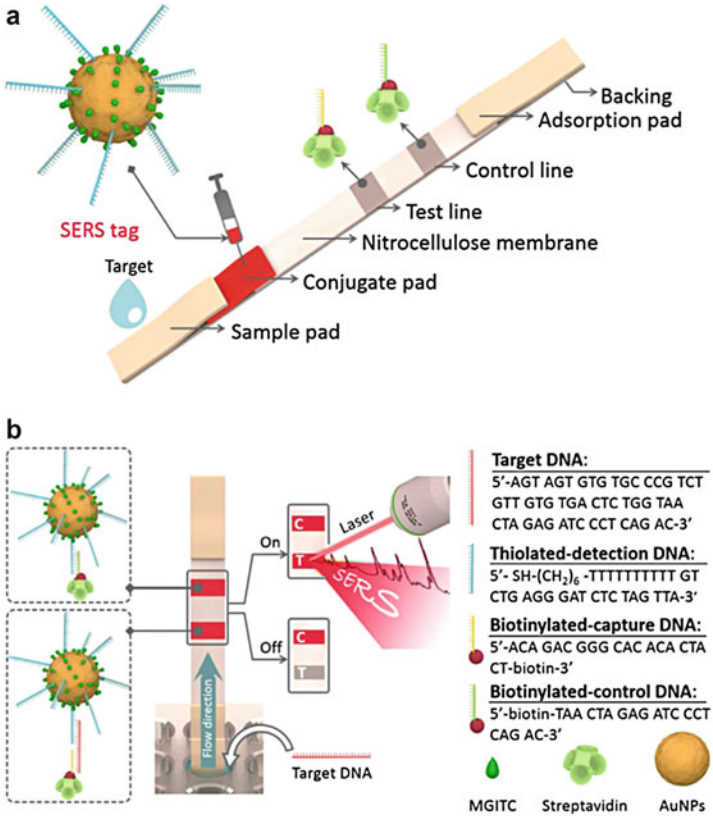

Fig. 1.16 SERS-based lateral flow assay for the quantification of HIV-1 DNA (Reprinted from Fu et al. [44]. Copyright © 2015 Elsevier B.V., with permission from Elsevier)

on thiol-modified gold nanoflowers and to covalently bind to the antibody via a terminal amino group. For the measurements, human blood samples from ten healthy volunteers were spiked with HBsAg in different concentrations. The samples were injected via the Y inlet, while the antibody-modified Raman reporter-labeled nanoflowers were supplied via the Z inlet of the microfluidic chip. After 3 min, the flows were stopped and for 30 min all reagents were incubated in the detection area of the microfluidic chip to generate the sandwich immunocomplex, which was then measured by Raman spectroscopy. A calibration curve was obtained from the SERS intensity of the Raman marker band of fuchsin. HBsAg was successfully detected at concentrations as low as 0.01 IU/ml (0.2 ng/ml corresponds to 0.05 IU/ml) with a relative standard deviation of less than 10%. In addition to this study, hepatitis B virus was also detected by employing plasmonic nanorice antennae on triangle nanoarrays [215] and spatially reinforced nano-cavity arrays [216]. A SERS-based lateral flow assay biosensor for the highly sensitive (down to 0.24 pg/ml) detection of human immunodeficiency virus (HIV-1) DNA was described by Fu and coworkers, and it is depicted in Fig. 1.16 [44]. The working principle of the platform

can be described as "DNA-conjugated Au NPs target DNA-capture DNA." Namely, on the nitrocellulose membrane, streptavidin-biotinylated capture DNA, which is complementary with a part of the target DNA, and streptavidin-biotinylated control DNA were immobilized at the test and control line, respectively. The control DNA was complementary with the detection DNA probe immobilized on the malachite green isothiocyanate (MGITC) functionalized Au NPs. The MGITC Au NPs were dispersed on the conjugated pad, which was designed to bind specifically the target DNA. The sample was applied on the sample pad and diffused toward the absorption pad due to capillary action. When the sample crossed over the conjugate pad, the target DNA, if it was present in the sample, and the detection DNA immobilized on the Au NPs hybridized to form a complex. The immunoassay complexes reaching the test line were captured by the DNA probe present there based on a second hybridization step between the target DNA and the capture DNA, yielding sandwich complexes. Finally, the excess DNA-conjugated Au NPs reached the control line and were captured by the probe DNA pre-immobilized on the strip. For quantitative analysis, SERS spectra were recorded at the test line with a bench top Raman spectrometer. The Raman characteristic bands of the Raman label molecule, MDITC, were considered for analytical performance assessment. The authors claim that a detection limit of 0.24 pg/ml was achieved based on the IUPAC regulations for LOD calculation. However, the lowest concentration that could be measured was 8 pg/ml, and it showed only low-intensity Raman bands. For an accurate estimation, measurements of solution with lower concentrations of HIV-1 DNA would be required. Furthermore, future experiments testing the feasibility of the platform to detect the target DNA in biological fluids instead of pure solvent are expected. As a simplified sample preparation protocol is of high interest for point-of-care applications, it will have a major impact on the commercialization of the device.

With more than 50 known species that can be easily spread through the air as aerosols, *Legionella* can rapidly infect a large number of people. As main clinical symptoms, acute fever appears after a short incubation period, followed by pneumonia symptoms. Therefore, rapid identification of *Legionella* is important. The study by Jing et al. [51] focuses on the discrimination between virulent and weak *Legionella* strains in five commercially available *Legionella* species (*ATCC33152 L. pneumophila*, strong virulence; *ATCC33156 L. pneumophila*, strong virulence; *ATCC43878 L. brunensis*, weak virulence; *ATCC35249 L. spiritensis*, weak virulence; and *ATCC35252 L. cherrii*, weak virulence) and three *L. pneumophila* strains (*strain 1*, strong virulence; *strain 2*, strong virulence; and *strain 3*, weak virulence) isolated from different samples. For this, the different *Legionella* strains were measured by SERS, using Au-tiopronin NPs. For the preparation of these NPs, Au NPs were first prepared by the standard citrate reduction method followed by seed growth by first mixing 0.24 ml of 15 nm Au NPs with 2.49 ml 10 mM $HAuCl_4 \cdot 3H_2O$ solution with stirring and then adding 100 ml 0.4 mM ascorbic acid at a 10 mL/min rate. Finally, excess tiopronin solution was added and allowed to react. The resulting NPs were washed and added to the *Legionella* colonies as follows: each grown colony was picked into a clean microslide onto which 5 μl NPs were added and incubated for 5–10 s before performing the SERS measurements. The results

obtained upon PCA analysis denote the potential of differentiating between *Legionella* species based on their virulence and support the notion that this technique could be further developed into an analytical tool for both environmental and medical applications.

Wu et al. [217] used a SERS Ag nanorod array substrate, fabricated by the oblique angle deposition (OAD) technique, to analyze and differentiate 27 different bacteria species, strains, and serotypes isolated from chicken carcass rinses (denoted USDACR in Fig. 1.17), patients from a medical center (denoted WRAMC in Fig. 1.17), and patients from an army medical center (denoted BAMC in Fig. 1.17. For the substrate fabrication, a glass slide was first cleaned and then positioned perpendicular to the incident vapor direction for the deposition of a 20 nm titanium film followed by a 200 nm silver film. The substrates were then rotated to an angle of 86° with respect to the incident vapor, resulting in the growth of Ag nanorods. Rods of two different thicknesses were created: 2000 nm for pristine Ag nanoroads and 800 nm for vancomycin (VAN) Ag nanoroads. Finally, the 800 nm Ag nanorods were immersed into a 1 mM vancomycin solution to achieve VAN functionalization of the 800 nm for VAN Ag nanorods. For the measurements, either a 2 ml droplet of a sample containing a single bacterial species was applied to the pristine Ag nanorod substrate or the VAN Ag nanorod substrate was immersed in 2 ml of the single-species bacterial culture for 2 h, rinsed with DI water, and measured. Upon statistical analysis of the data, different visualization procedures were tested. As shown in Fig. 1.17, it was possible to differentiate between gram-negative and gram-positive bacteria, but it was still challenging to differentiate between different serotypes of the same bacteria species.

The same SERS-active substrates were also used for the differentiation of patients infected with *Pseudomonas aeruginosa* (denoted PA+ in Fig. 1.18) and *Staphylococcus aureus* (denoted PA+/SA+ in Fig. 1.18) or patients that tested negative for *Pseudomonas aeruginosa* infections (denoted PA- in Fig. 1.18), by analyzing sputum samples [218]. Since the target analyte for *Pseudomonas aeruginosa* identification was the redox-active blue green pigment pyocyanin (PCN), PCN was extracted from sputum samples by mixing 100 μL of processed sputum with 50 μL of chloroform and then refrigerate the mixture for 2 min. Subsequently, the chloroform layer was transferred to a new tube, a 1 μl droplet of the sample was dropped on the SERS-active substrate, the contaminants on the substrate surface were removed using Ar^+ plasma generator, and the substrate was dried inside a plasma generator chamber and measured by SERS. The LOD for the SERS detection of PCN in aqueous solution was detected to be 5 ppm (2.38×10^{-8} M). This information was used together with the calibration curve obtained by measuring chloroform-treated sputum control samples spiked with different concentrations of PCN (reproduced in Fig. 1.18a) to predict the presence of *Pseudomonas aeruginosa* in patient sputum samples and to classify the patients based on this information. Upon measuring 15 patient sputum samples and using the mentioned calibration curve, it was found that the concentration of PCN ranges from 18.7 to 64.9 ppb in the PA+ samples, from 5.1 to 21.5 ppb in the PA+/SA+ samples, and from 1.1 to 2.9 ppb in the PA− samples (Fig. 1.18b). Considering that the LOD for detecting PCN was

A

Abbreviation	Bacteria species	Strains	Serotypes	Gram
AB1	*Acinetobacter baumannii*	ATCC 19606	N/A	–
AB2	*Acinetobacter baumannii*	ATTC BAA-1605	N/A	–
AB3	*Acinetobacter baumannii*	ATTC 17961	N/A	–
AB4	*Acinetobacter baumannii*	ATTC 19003	N/A	–
AB6	*Acinetobacter baumannii*	WRAMC #13	N/A	–
CK	*Citrobacter koseri*	USDACR	N/A	–
PP	*Pseudomonas putida*	USDACR	N/A	–
EC	*Escherichia coli*	USDACR	N/A	–
EF	*Enterococcus faecalis*	USDACR	N/A	+
ENC	*Enterobacter cloacae*	USDACR	N/A	–
KP1	*Klebsiella pneumoniae*	IA-525	N/A	–
KP2	*Klebsiella pneumoniae*	BAMC 07-18	N/A	–
KP3	*Klebsiella pneumoniae*	Xen-39	N/A	–
PA1	*Pseudomonas aeruginosa*	Xen-41	N/A	–
PA2	*Pseudomonas aeruginosa*	PA 01	N/A	–
SalE	*Salmonella entericat*	USDACR	Enteritidis	–
SalH	*Salmonella enterica*	USDACR	Heidelberg	–
SalI	*Salmonella enterica*	USDACR	Infantis	–
SalK	*Salmonella enterica*	USDACR	Kentucky	–
SalT	*Salmonella enterica*	USDACR	Typhimurium	–
SA1	*Staphylococcus aureus*	IQ 0070	N/A	+
SA2	*Staphylococcus aureus*	Xen 40	N/A	+
SA3	*Staphylococcus aureus*	ATCC 33591	N/A	+
SA4	*Staphylococcus aureus*	TCH 1516	N/A	+
SA5	*Staphylococcus aureus*	USDACR	N/A	+
SH	*Staphylococcus hyicus*	USDACR	N/A	+
SK	*Staphylococcus kloosii*	USDACR	N/A	+

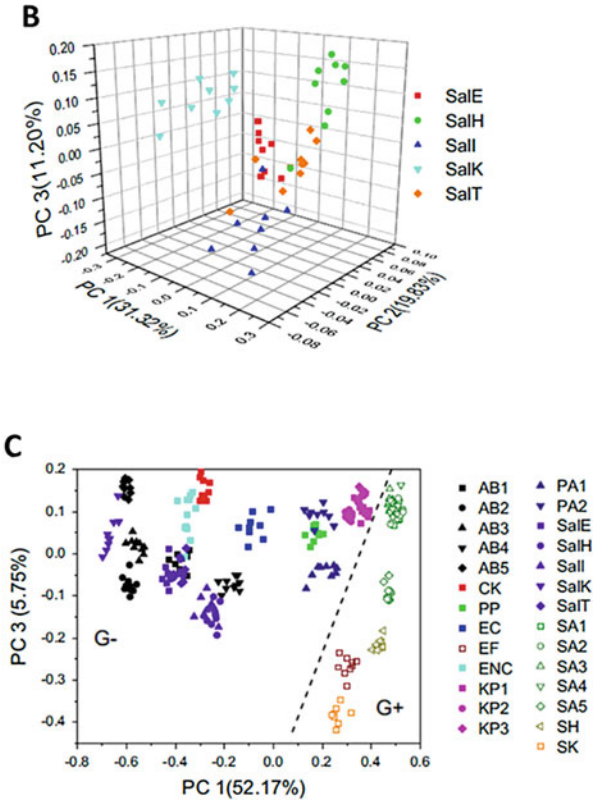

Fig. 1.17 (continued)

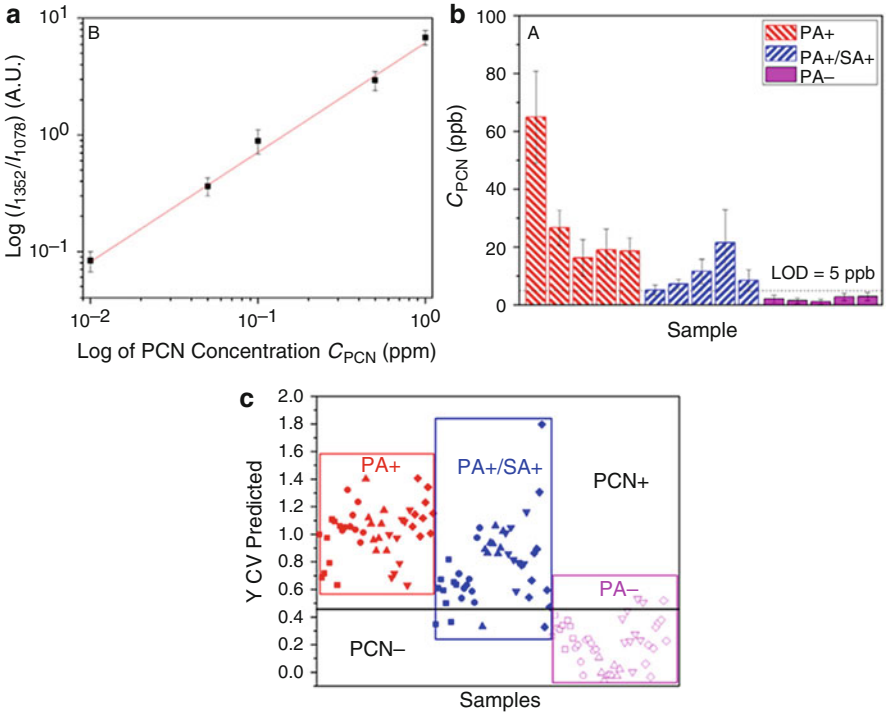

Fig. 1.18 Intensity ratio of two peaks belonging to PCN in the PCN-spiked sputum samples (**a**). Estimated PCN concentration in clinical sputum samples (**b**). PLS-DA plot of SERS spectra of the clinical sputum samples (**c**) (Reprinted from Wu et al. [218]. Copyright © 2014 Elsevier Inc., with permission from Elsevier)

5 ppm, the authors concluded that the patients in the PA− group were not infected by *Pseudomonas aeruginosa*. However, to better visualize and confirm this result, the authors also performed PLS-DA analysis on the measured data, and the results are also reproduced in Fig. 1.18c. Considering that by using the chloroform extraction procedure introduced by Wu et al. [218] the total experimental work time is approximately 5 min, this represents a promising analytical approach.

Rapid identification of bacteria has also been reported in the case of urinary tract infections and the detection of *E. Coli*, *Enterococcus faecalis*, *Staphylococcus*

Fig. 1.17 Bacteria species, strains, and serotypes isolated from chicken carcass rinses (denoted USDACR), from patients at a medical center (denoted WRAMC), and from patients at an army medical center (denoted BAMC) used during the measurements (**a**). 3D PCA score plot differentiation of five different serotypes of *Salmonella* species based on the chemometric analysis of the SERS spectra (**b**). Partial least squares discriminant analysis (PLS-DA) score plot: gram-positive (G+) bacteria are indicated as unfilled symbols, and the gram-negative (G-) bacteria are indicated as filled symbols (**c**) (Reprinted from Wu et al. [217]. Copyright © 2015 Elsevier B.V., with permission from Elsevier)

aureus, *Staphylococcus saprophyticus*, *Klebsiella pneumoniae*, *Staphylococcus haemolyticus*, and *Proteus mirabilis* [219]. In this case, however, a bacterial culture was required. The authors cultured the bacteria on nine different nutrient agar plates and incubated them for different times: 1, 2, 4, 6, 8, 10, 12, 18, and 24 h. At the end of each time frame, the bacteria were measured by SERS, using Ag NPs prepared according to a simple procedure introduced by Leopold and Lendl [50]. As already mentioned, it was found that a 1-h incubation was enough to discriminate between the different bacteria.

Differentiation of the *Mycobacterium tuberculosis* complex (MTC), including *M. tuberculosis*, *M. bovis BCG*, *M. canettii*, *M. abscessus*, and *M. szulgai*, was attempted using a bead-beating module in combination with a lab-on-a-chip SERS (LoC-SERS) system [90] and NPs prepared according to the Leopold-Lendl protocol [50]. In this study, it was found that *M. abscessus* and *M. szulgai* can be differentiated with an accuracy of 100%, whereas the bacteria in the MTC group (containing *M. bovis BCG*, *M. tb Beij*, *M. can*, and *M. tb H37Rv*) could only be differentiated as follows: *M. can* was separated from the others with an accuracy of 100%, while the separation of *M. bov BCG* and *M. tb H37Rv* only reached 75.3% by applying a principal component analysis-linear discriminant analysis (PCA-LDA) model.

As has been largely discussed in the literature, it is important to properly consider and plan the growth conditions [220] as well as the steps prior to the measurement [221] when working with cell and bacteria culture, since even small quantities of culture medium present in the sample during the SERS measurement can give rise to a strong SERS response [221] and also because more extreme culture growth conditions (i.e., starvation) can modify the main components of the cell wall. Indeed, according to a recently published study by Premasiri et al. [220], cell wall SERS spectra of bacteria that were starved before performing the measurements at 785 nm show that the cell wall is not dominated by peptidoglycan layer components such as *N*-acetyl-D-glucosamine, *N*-acetylmuramic acid, lipids, and proteins, which would be the normal cell wall composition suggested by the literature, but by molecular species such as purine phosphoribosyltransferases, enzymes that convert purine mononucleotides to purine bases. Moreover, according to this study, these purines are the result of metabolic degradation of nucleic acids and nucleotides (i.e., RNA, adenosine triphosphate, guanosine triphosphate, and other nucleotide containing molecules). They are produced when bacteria are placed in a nutrient-free environment [220]. In contrast, the cell wall SERS spectra of starved bacteria measured at 514/532 nm were nearly equivalent to those of flavin adenine dinucleotide [220]. Figure 1.19 reproduces some of the example figures presented by the authors. However, it is important to mention that the conditions of the SERS measurement play a very important role. For example, whether NPs can interact with any other part of the bacteria or whether they come in contact only with the cell wall will have an impact on the results. Also, it is important to notice whether the NPs are functionalized or not and how this induces a binding preference toward certain molecules of the cell wall. In the particular case presented above, an aggregated Au NP-covered SiO_2 SERS-active substrate was prepared by the hydrolysis of tetramethoxysilane in an acidic methanol solution of $HAuCl_4$ (containing methanol, water, and $Si(OCH_3)_4$).

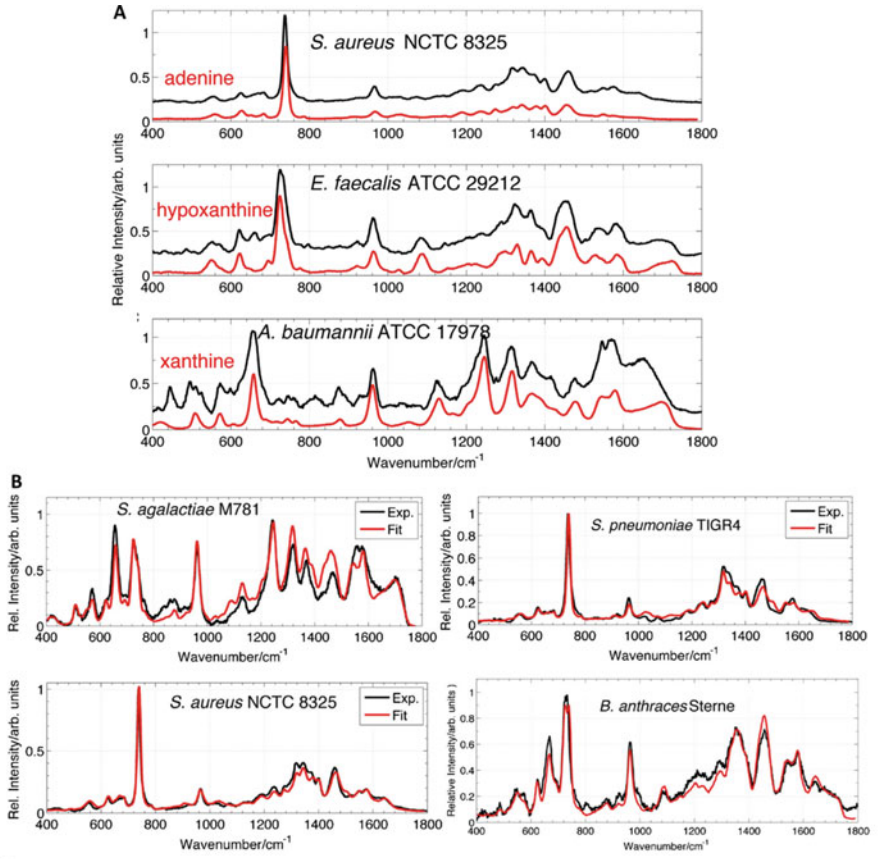

C

Organism	Source or reference	Adenine[a]	Hypoxanthine[a]	Xanthine[a]	Guanine[a]	Uric acid[a]	AMP[a]
Streptococcus agalactiae M781	ATCC	8/2	39/56	47/38	6/4	0	0
Streptococcus pneumonia TIGR4	[44]	65/62	0	3/8	0	0	32/30
Bacillus anthracis Sterne	Colorado Serum Company	27/9	45/71	0	28/20	0	0
Staphylococcus aureus NCTC 8325	[45]	75/69	0	0	8/16	0	17/15

AMP adenosine monophosphate

[a] The first number is the percent contribution of the purine component surface-enhanced Raman spectroscopy (SERS) spectrum normalized by the spectrum maximum the second number is the percent contribution scaled by the relative cross section of the purine component and is thus the relative number of purine component molecules accounting for the SERS signature

Fig. 1.19 Comparison of SERS spectra of bacterial species with model compounds (**a**). Empirically determined best fits (red) of the bacterial spectra (black) of some of the spectra shown in the left side graph of the figure (**b**). Best-fit-determined relative (%) purine contributions to the bacterial spectra on the graphs on the right upper side of the figure (**c**) (Premasiri et al. [220]. Copyright © Springer-Verlag Berlin Heidelberg 2016, with permission of Springer)

This resulted in the formation of metal-doped sol-gels, which were dried at room temperature before mixed with aqueous sodium borohydride and exposed to water-saturated air for 1 h. Subsequently, the solution was drained and the gel chips were covered with water and gently shaken for 30 min. Finally, the substrates were

incubated for 24 h in a diluted $NaBH_4$ solution for the slow growth of Au NPs. The resulting substrates were covered with a 1 μL bacteria loop and measured 2 min later [52, 220].

In the above paragraphs of this section, we presented the most promising findings on pathogen detection. Different SERS platforms were applied in these studies, starting with Leopold-Lendl colloids and microfluidic devices and reaching to SERS immunoassays and easy to prepare SERS planar substrates. Depending on the type of substrate, different measurement methods were also chosen. Both very simple measurement conditions, such as a simple mixing of the analyte with the pathogen suspension or dropping the analyte on planar substrates and measuring the resulting dried substrate, and more complicated approaches, such as microfluidic platforms, have been tested. Additionally, owing to the high resemblance of SERS spectra from pathogens belonging to the same species, statistical analysis is often required for reliable identification. Moreover, even though discrimination of pathogen species is often reported in the literature, separation of different strains belonging to one species is still challenging. However, there are numerous other reports proving the high potential of SERS for medical diagnosis of infectious diseases, and with further work carried out with clinical samples, SERS might yield a wide range of applications.

5.4 Other Fields of Application with Clinical Relevance

5.4.1 Therapeutic Drug Monitoring

The cost of medical treatments could be significantly lowered, while the patient outcome could be considerably improved, by the practice of personalized medicine. Therapeutic drug monitoring is of especially high value, as several drugs have a narrow therapeutic range and the concentration of the active agent in the human body strongly varies among individuals. Currently, different physiological indices (lipid concentrations, blood glucose, blood pressure) are routinely used to monitor the pharmacological response and determine the pharmacokinetic and pharmacodynamic characteristics of drugs. However, there are many drugs with insufficiently sensitive or no direct indicator of their therapeutic response. In these cases, therapeutic drug monitoring relies on measurements of the concentration of the prescribed xenobiotic that, with an appropriate interpretation, could directly influence the prescribing procedure and lead to the desired clinical outcome [222].

In clinical chemistry, the determination of drug levels in biological fluids is performed by methods based on chromatographic separation or immunological assays [98, 101, 223–230]. The first approach offers great specificity and sensitivity for, theoretically, all existing drugs, but it is mainly available in reference clinical laboratories and academic centers because of the high initial financial investment required. On the other hand, immunological assays (or immunoassays) are easy to integrate in a clinical setting, but they are available for only a limited number of drugs because they require specific antibodies. In recent years, multiple SERS studies for the determination of various drugs at clinically relevant concentrations in biological fluids were reported. Thanks to the high sensitivity of the method and

the narrow Raman bands, SERS is optimal for the determination of trace amounts of molecules in complex matrices. Although SERS cannot compete with chromatography for sensitivity and specificity in an academic lab setting, it finds its place in on-field applications and near-patient settings thanks to the development of high-performance portable and handheld Raman setups.

Anticancer drugs are notorious for their toxic effects when their concentration in the human body exceeds their therapeutic range. Methotrexate is generally administered at high doses (5000 mg/week) for cancer therapy. However, its action is not restricted only to cancerous cells, and a concomitant administration of leucovorin is recommended to avoid side effects. According to most medical guidelines, a plasma methotrexate concentration $\leq$0.2 μM allows the clinician to stop leucovorin administration [231]; 42 h after the start of methotrexate infusion, the target concentrations are $\leq$1 μM, while high-risk toxic effects are associated with concentrations $\geq$10 μM [232]. The direct, quantitative determination of methotrexate in diluted human serum samples spiked with different concentrations of the target drug was achieved by employing gold NP deposited on paper as SERS-active substrate [233, 234]. Specifically, a mixture of citrate-reduced gold NPs and sodium citrate, used as aggregation agent, was added to a glass vial containing a 1 cm^2 filter paper at the bottom. After 1 week, all particles were deposited on the surface of the paper. The supernatant was removed, and the paper was dried in air and stored in Milli-Q water. The relative standard deviation of the SERS signal from different analytes measured with substrates from different batches was 15%. Relative standard deviations of 10–20% are commonly reported in SERS studies and have their origin in the low homogeneity of hot spots on the solid SERS-active substrate and on the random orientation of the molecules on the metallic surface. Nevertheless, the SERS community is continuously aiming at improving this and increasing the reliability of the SERS measurements. For the determination of methotrexate with the abovementioned SERS-active substrate, calibration standards were prepared by spiking drug-free human serum with different amounts of methotrexate stock solutions. The final concentration of the drug in the fivefold diluted serum was 0.1–300 μM. The data were evaluated by employing chemometric methods, and the used model yielded a root mean square error of prediction of 31.57 μM, with an R^2 linear regression coefficient of 0.63. These values show that the method yields poor predictions, emphasizing the challenge of quantitative SERS measurements. Paclitaxel, another highly antineoplastic active drug against a wide spectrum of human malignancies, was also detected by SERS in blood plasma using microwave-treated gold film polystyrene beads [235]. Although the concentration window where the drug was detected was narrower than that of the previous case (10^{-8}–10^{-7} M), the accuracy was considerably higher (3.8×10^{-9} M). The authors attributed this great accuracy to the direct absorption of the molecule on the metallic surface owing to its high chemical affinity. However, as in the preceding case, the authors had to dilute the paclitaxel/blood mixture with ethanol to reduce strong matrix effects.

Clinical guidelines for antibiotic administration are most often derived from dose-establishing clinical trials carried out with healthy volunteers instead of patients. However, it was demonstrated that fix-dose administration will fail in the case of

patients in the intensive care unit [236]. Therefore, it is of high interest to determine the actual concentration of the active drug in the human body in order to guarantee treatment success and avoid the emergence of antibacterial resistances. The aminoglycoside tobramycin [237], the fluoroquinolone levofloxacin [42, 238], and nitroxoline [89] were successfully detected by SERS. A 1000-fold dilution of human serum samples spiked with tobramycin was required prior to SERS detection with Au NPs prepared according to the traditional citrate reduction protocol and modified with dithiobis-(2-nitrobenzoi acid) as a Raman reporter. Unfortunately, the authors did not carry out quantitative measurements, but the intense Raman spectrum recorded at 4 μM shows great promise for further studies.

SERS is a great analytical method owing to its specificity and sensitivity. However, it is challenging to achieve reproducible and automated measurement conditions. The synergy between microfluidic platforms and SERS can overcome this limitation, as demonstrated in numerous reports [60–68]. Hidi et al. took advantage of a droplet-based SERS microfluidic platform and conducted measurements on human urine samples collected from patients and healthy donors [42, 89]. As none of the donors had previously taken levofloxacin or nitroxoline, the two antibiotics were artificially added to the sample. In this way, the influence of the complex matrix on the SERS signal of the target molecules was carefully characterized. The authors first demonstrated that the two antibiotics can be successfully and reliably quantified in the complex matrix by employing silver NPs prepared at room temperature. Specifically, urinary levofloxacin concentrations in the range of 0.1–1 mM and urinary nitroxoline concentrations in the range of 3–42.8 μM were detected with a good linear response, covering the clinically relevant concentration window. The distinct detection regions for the two antibiotics were explained based on the different chemical affinity of the two molecules for the metallic surface. The detection limit for levofloxacin dissolved in high purity water was found to be 0.8 μM, whereas that for nitroxoline was 2.5 μM. The latter antibiotic showed a clear preference for binding on the metallic surface, as its detection limit was not significantly affected by the complex matrix, and this facilitated its detection.

Most of the reported SERS studies confirm that the technique can offer quantitative measurements under well-controlled, known conditions; however, very seldom the concentration of the target molecules is determined in patient samples containing an unknown amount of the molecules. This has numerous reasons. First, the chemical composition of the clinical samples varies strongly between patients, or even between samples collected from the same patient at different time points. Therefore, if no thorough sample cleanup procedure is applied, quantification based on previously established calibration curves will fail, as the SERS signal is very sensitive to the chemical species present in the sample. Second, the low batch-to-batch reproducibility of metallic NPs also inhibits the traditional quantification procedure, as signals measured with NPs of different batches cannot be reliably compared. To overcome these drawbacks, the SERS community directed its attention toward the standard addition method (SAM) [91, 239–242]. Here, all analytical measurements, including the calibration curve, are performed using the sample itself, and the slight variation between colloid batches will have no impact on the final results.

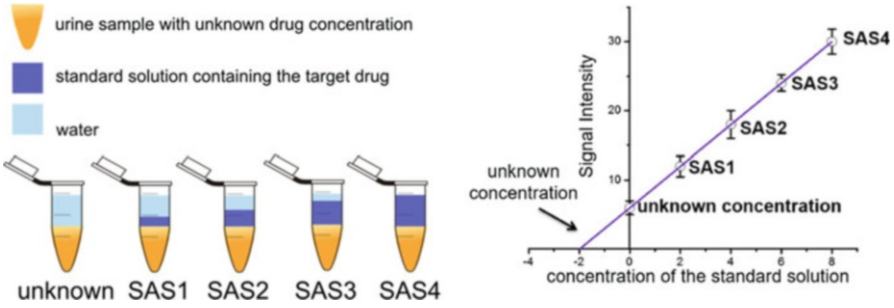

Fig. 1.20 The principle of the standard addition method: (1) equal amounts of the sample are pipetted into several volumetric flasks, (2) increasing volumes of the standard solution are added to each flask, and (3) the content of each flask is diluted with water to the same volume. The signal intensity for all flasks is measured and plotted. The intercept of the linear regression with the x-axis will give the concentration of the analyte in the unknown sample

The SAM experiments are carried out as follows: (1) equal amounts of the sample are pipetted into several volumetric flasks, (2) increasing volumes of standard are added to each flask, and (3) the content of each flask is diluted to the same volume (Fig. 1.20). Therefore, every flask contains the same concentration of the unknown sample and different concentrations of the standard solutions, which contain the same analyte as the one to be quantified. The number of flasks minus one represents the number of the standard addition steps (SAS). The signal intensity from all flasks is measured and plotted as shown in Fig. 1.20. The data are fitted by linear regression, and the x-axis intercept gives the analyte concentration in the unknown sample, which is the ratio between the intercept at $y = 0$ and the slope of the regression. By combining this method with microfluidic SERS measurements and multivariate statistical analysis, the authors were successful in determining the unknown concentration of nitroxoline in four simulated clinical samples. In the repots described above, sample dilution was carried out in order to reduce interference from the matrix molecules. Nevertheless, in a recent study, the β-blocker propranolol spiked into human serum, plasma, and urine was detected at physiologically relevant concentrations without the need for matrix dilution [243]. For this, the authors employed silver NPs synthesized according to the Lee-Meisel citrate reduction method and multivariate data analysis. In this study, stock solutions of the drug were prepared directly in the biological fluids, and serial dilutions of propranolol with each biological fluid of interest were then performed using these stock solutions in the range of 0–120 μM. In the case of the plasma samples, proteins were removed by centrifugation prior to the measurements. Metallic NPs were mixed with the samples in a 1:1 ratio, and 0.5 M sodium chloride was used as aggregation agent.

Principal component analysis of the SERS spectra demonstrated a clear differentiation between pure biofluids and biofluids spiked with varying concentrations of the target drug. To provide quantitative results, the authors used the partial least square regression method. The limit of detection for propranolol was estimated to be 0.45 μM, 0.53 μM, and 0.57 μM for serum, plasma, and urine, respectively. The

reported results showed a linear response in the 1–10 μM range for serum, 10–100 μM range for plasma, and 10–120 μM for urine. In conclusion, the authors were successful in detecting the target molecule in various biofluids with conventional silver NPs, demonstrating the high potential of SERS.

Finally, in two recent studies, approaches based on a vertical-flow paper system [244] and hierarchical zwitterion-modified SERS platforms [245] were reported and were used successfully for the detection of various drugs owing to the inhibition of substrate fouling by the components of the matrix. In the first approach, a sample droplet was applied to a membrane selected to trap serum components while transmitting the drug 5-fluorocytosine. An inkjet-fabricated paper-based SERS sensor was placed below the filtering membrane. In this way, large molecules from the serum were trapped, while the target molecule could interact with the metallic surface. The SERS signal was measured with a portable Raman spectrometer. This, and the fact that the no additional apparatus was required for sample cleanup, is very promising for bedside applications. However, it would be interesting to see the platform extend to whole-blood samples and to the determination of drug levels in clinical samples. Concerning the analytical performance of the platform for 5-fluorocytosine spiked into human serum, a limit of detection of 93 μM and linearity up to 1.16 mM were reported by the authors. An alternative strategy to avoid substrate fouling and to trap the target analytes was reported by Sun et al. [245]. In this study, the authors functionalized the optofluidic platform with two different layers. The role of the first layer was to capture the target molecule via functional thiols situated in the proximity of the SERS substrate. Thus, the surface could be enriched with substances exhibiting weak surface affinity, and the SERS signal could be enhanced. The second layer consisted of non-fouling zwitterionic poly(carboxybetaine acrylamide) (pCBAA) grafted via surface-initiated atom transfer radical polymerization, and it protected the metallic surface from the proteins in whole blood. This SERS platform could detect the anticancer drug doxorubicin when spiked into plasma sample. Doxorubicin is known to be deactivated upon protein binding; hence the detection of the free drug is of clinical interest. Owing to the presence of the polymer brush on the surface of the metallic substrate, only the unbound amount of doxorubicin could get into the close proximity of the hot spots. This phenomenon was confirmed by liquid chromatography-mass spectrometry measurements. Furthermore, doxorubicin measurements were proved to be reversible by carrying out experiments whereby drug-spiked plasma was injected into the optofluidic platform, followed by injection of pure plasma after 250 s. The continuously collected SERS spectra showed that doxorubicin detection was reversible with exponential response constants of 43 and 95 s for partitioning and departitioning, respectively. Furthermore, owing to the presence of thiol layers, the authors were successful in detecting the tricyclic antidepressant amitriptyline hydrochloride and antiseizure medications carbamazepine and phenytoin at 20 μM in spiked plasma. In conclusion, the same substrate could be used for multiple drug detection, which is a very promising approach. The scientific community is looking forward for further research developments to demonstrate the quantification power of the platform applied to clinical samples.

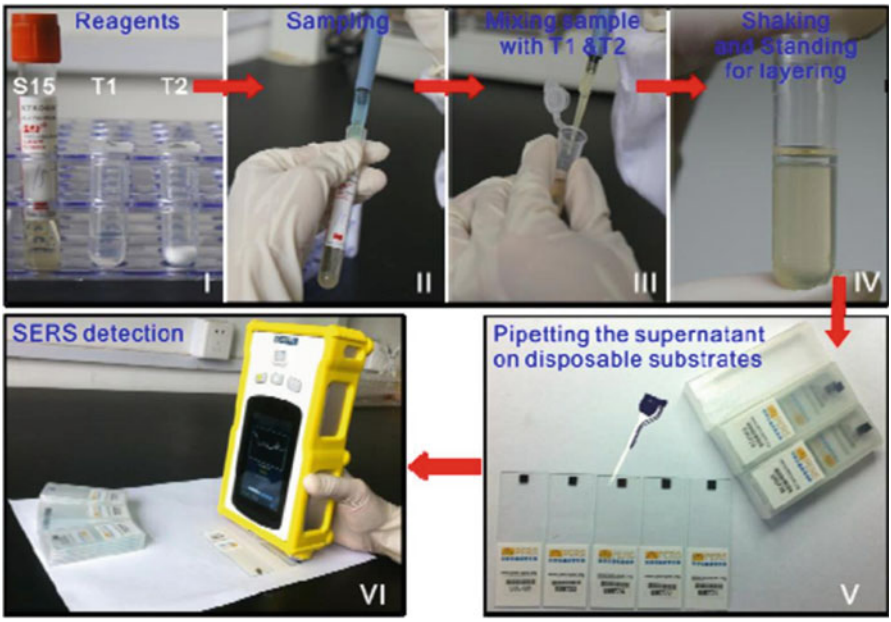

Fig. 1.21 Illustration of a portable kit for rapid SERS detection of drugs in real human urine: (*I*) the urine sample and reagents; (*II*) the sampling of certain amounts of urine; (*III*) the mixing of urine with T1 and T2; (*IV*) the layering of the mixture after fully shaking by hand; (*V*) 2 μL of the supernatant dropped and dried on 2D gold nanorods arrays, which were assembled on silicon wafer and deposited on glass slides; (*VI*) SERS detection with a handheld Raman device (Reprinted with permission from Han et al. [249]. Copyright (2015) American Chemical Society)

Although not exclusively related to the necessity of therapeutic drug monitoring, SERS was shown to be powerful also in the detection of illicit drugs. The system integration and miniaturization carried out in the last decade considerably increased the chances of Raman and SERS spectroscopy to be employed in the field of clinical forensics. Liu and coworkers published three consecutive studies during the last 3 years regarding the determination of amphetamines in human urine samples [246–249]. The group also developed a portable kit, shown in Fig. 1.21, to facilitate the multiplex determination of 3,4–methylenedioxymethamphetamine and methcathinone. The study was carried out with 30 volunteers providing urine samples. Briefly, the portable kit contains two sealed reagent containers, a standardized packet of highly reproducible gold nanorod 2D arrays on silicon wafers, and a handheld Raman device. Prior to the measurements, the human urine samples spiked with the drugs were subjected to a 3-min pretreatment. The obtained results were confirmed also by chromatographic measurements.

Overall, owing to the fingerprint specificity of Raman spectroscopy and the high sensitivity of SERS, the technique can determine therapeutic and illicit drugs at clinically relevant concentrations. However, work directed toward inhibiting the fouling of the SERS-active substrate and the specific capturing of the drugs still

needs to be performed before SERS can compete with the well-established reference methods currently used in clinical chemistry laboratories.

5.4.2 Enzyme Activity Assays

Enzymes regulate almost all metabolic processes in cells, and the assessment of their activity is crucial to either identify a special enzyme in order to prove its presence or absence in the sample or to quantify the amount of the enzyme in the sample [250]. SERS-based assays have been applied to assess the activity various enzymes, including telomerase [193, 251–253], thiopurine S-methyltransferase [254–256], and protease [257–261] activity.

Telomeres protect the ends of eukaryotic chromosomes by inhibiting the loss of base pair sequences and conserving the genetic information stored in the chromosomes [262]. Telomere activity is controlled by erosion during cell division and, in addition, determined by the telomerase activity. Telomerase or telomere terminal transferase elongates chromosomes by adding TTAGGG sequences to their ends. In normal somatic cells, this enzyme is highly suppressed; however, it was found that in more than 85% of cancerous cells, telomerase activity is enhanced. This leads to the so-called cell immortality and uncontrolled proliferation. Therefore, telomerase activity is considered an important biomarker for cancer diagnosis [263–265]. Zong and coworkers reported a dual-mode detection approach for assessing telomerase activity based on colorimetry and SERS [251]. Using telomeric elongation-assisted magnetic capturing of gold nanotags, a fast preliminary screening of the samples could be performed by the naked eye, using the colorimetric functionality, while SERS quantitative analysis could also be carried out. The platform employs two types of NPs: telomere substrate oligonucleotide (TS primer)-modified gold shell-coated magnetic nanobeads (MBs) as the capturing substrate and telomeric repeat complementary oligonucleotide (ATE)- and Raman reporter-conjugated gold NPs (Au-Tag). If the clinical sample possesses telomerase activity, then tandem telomeric repeats will be added to the TS primers on the surfaces of the MB@Au@TS particles. The elongated telomeric sequences will capture the Au-Tag NPs upon hybridization with ATE. This leads to a color change and enhancement of the SERS signal due to the aggregation of the magnetically separated NPs. If the sample does not present telomerase activity, the ATE-modified Au-Tag cannot hybridize with the MB@Au@TS, and neither a color change nor a SERS signal will be detected. Telomerase enzymes were extracted from human cervical cells (HeLa), human breast cancer cells (SKBR3, MCF7), and normal embryonic lung fibroblasts (MRC5). Quantitative analysis was carried out by diluting the cell extracts, and it was shown that telomerase activity of 1 cell/ml could be reliably detected.

Shi and coworkers recently published a very well-founded study regarding the detection of telomerase activity by SERS [193]. The authors first assessed the feasibility of their approach by performing quantitative measurements with crude telomerase extracts from HeLa cells. Then, they evaluated the selectivity of their method by measuring the telomerase activity in the cancer cell lines HeLa, HT29, and A549 and in the normal cell line HEK293. Furthermore, to test the capacity of

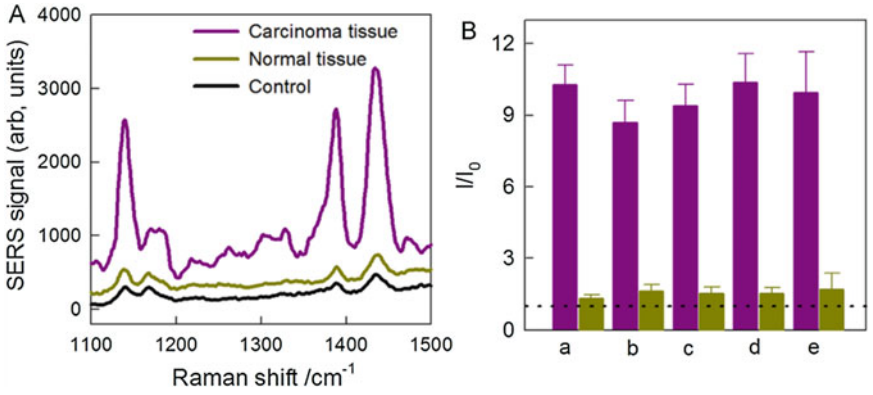

Fig. 1.22 Results of telomerase activity SERS-based platform carried out on colon cancer tissues. (**a**) SERS spectra of telomerase extracts of carcinoma tissue (purple), para-carcinoma normal tissue (green), and the heat-inactive control (black). The Raman bands originate from the vibrational modes of 4-amino-benzenethiol Raman reporter. (**b**) Histogram showing the results from five patients with colon cancer. Purple bar represents carcinoma tissue, while green bar represents para-carcinoma tissue (I_0 and I are the SERS intensities at 1440 cm^{-1} in the absence and presence of telomerase) (Reprinted from Shi et al. [193]. Copyright © 2015 Elsevier B.V. with permission from Elsevier)

their platform for ultra-early diagnosis of malignant disease, they mixed normal HEK293 cells and HeLa cells in four different ratios. Additionally, samples from colon cancer patients were also investigated, and their results were validated by the gold standard method (see Fig. 1.22). In total, five samples from patients were investigated. Finally, a telomerase inhibition assay was also carried out. For these studies, quadratic SERS signal amplification via telomerase-triggered silver NP assembly combined with ions-mediated cascade amplification was used. Namely, silica microbeads were conjugated with the telomerase substrate primer via the streptavidin-biotin binding reaction. In the presence of telomerase activity in the sample, the primer will be extended via the TTAGGG repeat units. Sulfhydryl-labeled single-stranded DNA served as the capture probe, and by hybridizing with the extended part of TSP, a long double-stranded DNA would form. This would provide numerous sulfhydryl groups for subsequent Ag NP conjugation via Ag-S bonds. This assembly works as the primary amplification element. Subsequently, the conjugated silver NPs were dissolved into Ag^+ upon the addition of H_2O_2. Ag^+ induced the aggregation of 4-amino-benzenthiol-modified gold NPs, creating highly active SERS hot spots. Based on the results presented in this study, the platform could offer reliable and valuable information for early cancer diagnosis.

In addition to telomerase activity, abnormal expression of certain proteases has also been related to the presence of cancer or Alzheimer's disease [266, 267]. Yazgan and coworkers investigated two different SERS-based platforms for the quantification of protease activity [258]. Spherical and rod-shaped gold NPs were used as SERS-active substrates, while the molecule DTNB was employed as a Raman

reporter. The first analysis platform used gold-coated glass slides conjugated with 11-MUA (11-mercaptoundeconic acid) as a support material. When the sample possessing protease activity was incubated on the surface of the platform, the covalently immobilized Raman-labeled SERS probe was released from the surface via the hydrolytic reaction catalyzed by the protease. Therefore, the SERS signal of the DTNB molecule was negatively correlated with the enzyme concentration in the sample. The second analysis platform used casein- or BSA-modified polystyrene microtiter plates, coated with the labeled SERS probe. Upon hydrolytic activity, the Raman probe with the peptide fraction was released from the surface and transferred to the supernatant. The SERS signal measured in the aliquoted supernatant positively correlated with the enzyme concentration. The platform with rodlike NPs on gold-coated glass slides yielded the best results. Namely, a linear correlation between protease activity and SERS signal in the range of 0.1–2 mU/ml and LOD and LOQ of 0.43 and 0.3 mU/ml, respectively. At the end of their study, the authors successfully quantified the protease activity in a commercial enzyme preparation. A second research group employed a novel "turn-on" SERS strategy based on non-cross-linking aggregation of gold NPs [257]. Specifically, by first stabilizing 4-MBA-modified Au NPs with a short peptide substrate, their aggregation was inhibited owing to their low isoelectric point. However, in the presence of a protease, this peptide was cleaved and the gold NPs formed hot spots, considerably enhancing the SERS signal of the reporter. Trypsin and thrombin were used as protease models, considering their importance in clinical diagnosis, and diluted human serum samples as matrix. The limit of detection was 85 fM for trypsin, and the experiments showed good selectivity over other proteases.

As described in the previous section, therapeutic drug monitoring is crucial for positive patient outcome. The pharmacokinetic and pharmacodynamic activity of drugs is often governed by the metabolic characteristics of the individual patient. In particular, the genetic differences in metabolic enzymes, such as thiopurine s-methyltransferase (TPMT), in humans have a major impact on the therapeutic response of drugs. This is the case for the immunosuppressive drug 6-mercaptopurine, which is deactivated in the presence of high TPMT activity, reducing the amount of parental drug available to form the active metabolite. Therefore, determination of TPMT activity in each patient before treatment is required in order to improve the therapeutic response. März et al. performed lab-on-a-chip SERS measurements on lysed red blood cells to assay TPMT activity [254], whereas Han et al. investigated the conversion of 6-mercaptopurine to 6-mercaptopurine-ribose in living cells by label-free SERS imaging [256]. In the first report, TPMT activity was assessed based on the methylation of 6-mercaptopurine to 6-methylmercaptopurine in lysed red blood cells. The parental drug and the metabolite developed specific Raman signatures based on which the two molecules could be clearly discriminated using linear discriminant analysis (LDA) (see Fig. 1.23). Furthermore, confirmation of TPMT activity in lysed red blood cells was obtained using a support vector machine classifier. The resulting accuracies were above 92%.

In the second study, the different orientation of 6-mercaptopurine and 6-mercaptopurine-ribose on the surface of the SERS-active Au@Ag NPs also generated

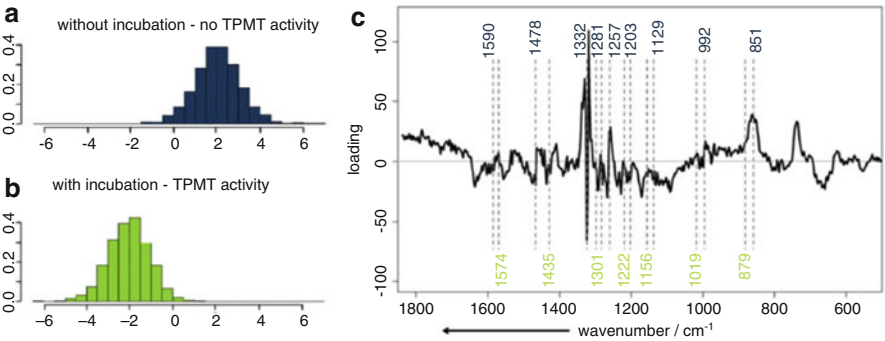

Fig. 1.23 LDA model of incubated test blood sample and test blood samples without incubation. (**a**, **b**) Histograms of LDA values of spectra from each group. (**c**) LDA loading with assignment of bands appearing in SERS spectrum of 6-mercaptopurine (blue) and 6-methylmercaptopurine (green) (März et al. [254]. Copyright © Springer-Verlag 2011, with permission of Springer)

specific Raman spectra. In this study, the authors used a straightforward ratio of two marker Raman bands to follow drug uptake and intracellular distribution, as well as metabolism. For these tests, the concentrated Au@Ag NPs were incubated with different concentrations of 6-mercaptopurine. After the removal of the free drug by centrifugation, the drug-conjugated NPs were re-suspended in culture media and incubated for 5 h with human lung adenocarcinoma cells. After washing steps to remove the loosely attached NPs, measurements were carried out at 0, 2, 4, 6, 8, 10, 16, 20, and 24 h. The authors noticed that owing to the uneven distribution of the parental drug in the cells, the transformation ratio of 6-mercaptopurine to 6-mercaptopurine-ribose was less at sites of high concentration, and it reduced at sites of low concentration. This and other SERS studies [268–285] on drug metabolism pathways can offer valuable information for drug development.

Overall, SERS offers multiple ways to monitor and assess enzymatic activity that can have a crucial impact on, i.e., cancer diagnosis, drug uptake, and drug metabolism. This is very important for improving patient outcomes and to reduce the costs associated with medical treatments.

6 Conclusions and Future Perspectives

The studies described in this chapter are just a small fraction of the publications related to SERS as an analytical method for medical diagnosis and were selected based on their significance. However, we are convinced that we did not manage to fully cover all the developments in the field, and we ask our readers who are interested in this topic to use this book chapter as a starting point for their research.

SERS was discovered more than 40 years ago. During these years, it transitioned from fundamental studies where metal-molecule interactions were investigated, such as food and environmental safety, to medical diagnosis. As demonstrated in this

chapter, SERS can be used for biomarker detection for Alzheimer's disease, myocardial infarction, diabetes, various types of cancer, and malaria, and it can offer information for therapeutic drug monitoring and enzyme activities. Despite the large number of publications, SERS is still not commercially available and is mainly used in academic research laboratories. There are multiple reasons behind this. One of the challenges is related to the preparation of SERS-active substrate. As described in the previous sections, most of the time, preparation of these substrates is labor-intensive. Additionally, their shelf life is seldom tested and needs to be considered for future studies and applications. Ideally, these platforms must offer high stability over time, reliable SERS enhancement, ease of use, and cost-efficiency. This is especially important for medical diagnosis, where a large number of samples is expected to be analyzed in a short time in non-laboratory environments, such as during field screening. Once the challenge with the platform is overcome, it could be easily combined with the existing high-performance portable Raman spectrometers. But before clinical applications, researchers must present proof that SERS brings considerable improvements as compared with chromatographic separation-based methods or traditional immunoassays. The topic is extremely interesting, and the work of researchers in the next years will demonstrate whether SERS could replace the reference methods in the clinical chemistry laboratories.

References

1. Lane LA, Qian X, Nie S (2015) SERS nanoparticles in medicine: from label-free detection to spectroscopic tagging. Chem Rev 115(19):10489–10529
2. Nima ZA et al (2014) Applications of surface-enhanced Raman scattering in advanced bio-medical technologies and diagnostics. Drug Metab Rev 46(2):155–175
3. Vo-Dinh T, Wang H-N, Scaffidi J (2010) Plasmonic nanoprobes for SERS biosensing and bioimaging. J Biophotonics 3(0):89–102
4. Wong Chi L, Dinish US, Olivo M (2015) Recent advances in SPR and SERS for sensitive translational medical diagnostics. Photonics Lasers Med 4:119–149
5. Prochazka M (2016) Medical applications of SERS. In: Prochazka M (ed) Surface-enhanced Raman spectroscopy: bioanalytical, biomolecular and medical applications. Springer International Publishing, Cham, pp 149–211
6. Recknagel P et al (2012) Liver dysfunction and phosphatidylinositol-3-kinase signalling in early sepsis: experimental studies in rodent models of peritonitis. PLoS Med 9(11):e1001338
7. Strimbu K, Tavel JA (2010) What are biomarkers? Curr Opin HIV AIDS 5(6):463–466
8. Zeng X et al (2011) Lung cancer serum biomarker discovery using label-free liquid chromatography-tandem mass spectrometry. J Thorac Oncol 6(4):725–734
9. Murph M et al (2007) Liquid chromatography mass spectrometry for quantifying plasma lysophospholipids: potential biomarkers for cancer diagnosis. In: Methods in enzymology. Academic, San Diego, pp 1–25
10. Sato Y et al (2012) Identification of a new plasma biomarker of Alzheimer's disease using metabolomics technology. J Lipid Res 53(3):567–576
11. McShane AJ, Bunch DR, Wang S (2016) Therapeutic drug monitoring of immunosuppressants by liquid chromatography–mass spectrometry. Clin Chim Acta 454:1–5

12. Baldelli S et al (2005) High-performance liquid chromatography with ultraviolet detection for therapeutic drug monitoring of everolimus. J Chromatogr B 816(1–2):99–105
13. Deters M, Kaever V, Kirchner GI (2003) Liquid chromatography/mass spectrometry for therapeutic drug monitoring of immunosuppressants. Anal Chim Acta 492(1–2):133–145
14. Peltier J et al (2016) Quantitative proteomic analysis exploring progression of colorectal cancer: modulation of the serpin family. J Proteome 148:139–148
15. Liu Y, Qing H, Deng Y (2014) Biomarkers in Alzheimer's disease analysis by mass spectrometry-based proteomics. Int J Mol Sci 15(5):7865–7882
16. Gan SD, Patel KR (2013) Enzyme immunoassay and enzyme-linked immunosorbent assay. J Investig Dermatol 133(9):1–3
17. Sun S-H et al (2015) Immunoassays for the cancer biomarker CA125 based on a large-birefringence nematic liquid-crystal mixture. Biomed Opt Express 6(1):245–256
18. Liu X et al (2008) A one-step homogeneous immunoassay for cancer biomarker detection using gold nanoparticle probes coupled with dynamic light scattering. J Am Chem Soc 130(9):2780–2782
19. Coverley D et al. (2017) A quantitative immunoassay for lung cancer biomarker CIZ1b in patient plasma. Clin Biochem 50:336–343
20. Savukoski T et al (2014) Novel sensitive cardiac troponin I immunoassay free from troponin I-specific autoantibody interference. In: Clinical chemistry and laboratory medicine (CCLM), vol 52, pp 1041–1048
21. Guirgis BSS et al (2012) Gold nanoparticle-based fluorescence immunoassay for malaria antigen detection. Anal Bioanal Chem 402(3):1019–1027
22. Popp J et al (2017) Label-free molecular imaging of biological cells and tissues by linear and non-linear Raman spectroscopic approaches. Angew Chem Int. Ed. 56:4392–4430
23. Li Y-S, Church JS (2014) Raman spectroscopy in the analysis of food and pharmaceutical nanomaterials. J Food Drug Anal 22(1):29–48
24. Dietzek B et al (2011) Introduction to the Fundamentals of Raman Spectroscopy. In: Dieing T, Hollricher O, Toporski J (eds) Confocal Raman Microscopy. Springer Berlin Heidelberg, Berlin/Heidelberg, pp 21–42
25. Schlücker S (2014) Surface-enhanced Raman spectroscopy: concepts and chemical applications. Angew Chem Int Ed 53(19):4756–4795
26. Etchegoin PG, Le Ru EC (2010) Basic electromagnetic theory of SERS. In: Surface enhanced Raman spectroscopy. Wiley-VCH Verlag GmbH & Co. KGaA, Weinheim, pp 1–37
27. Campion A, Kambhampati P (1998) Surface-enhanced Raman scattering. Chem Soc Rev 27(4):241–250
28. Cialla D et al (2012) Surface-enhanced Raman spectroscopy (SERS): progress and trends. Anal Bioanal Chem 403(1):27–54
29. Moskovits M (2005) Surface-enhanced Raman spectroscopy: a brief retrospective. J Raman Spectrosc 36(6–7):485–496
30. Xu H et al (2000) Electromagnetic contributions to single-molecule sensitivity in surface-enhanced Raman scattering. Phys Rev E 62(3):4318–4324
31. Lee HM et al (2013) Single-molecule surface-enhanced Raman spectroscopy: a perspective on the current status. Phys Chem Chem Phys 15(15):5276–5287
32. Kneipp K et al (1997) Single molecule detection using surface-enhanced Raman scattering (SERS). Phys Rev Lett 78(9):1667–1670
33. Le Ru EC, Etchegoin PG (2009) Introduction to plasmons and plasmonics, Chapter 3. In: Principles of surface-enhanced Raman spectroscopy. Elsevier, Amsterdam, pp 121–183
34. Le Ru EC, Etchegoin PG (2009) SERS enhancement factors and related topics, Chapter 4. In: Principles of surface-enhanced Raman spectroscopy. Elsevier, Amsterdam, pp 185–264
35. Lin J et al (2013) Photosensitizer-loaded gold vesicles with strong plasmonic coupling effect for imaging-guided Photothermal/photodynamic therapy. ACS Nano 7(6):5320–5329

36. Dinish US et al (2014) Actively targeted in vivo multiplex detection of intrinsic cancer biomarkers using biocompatible SERS nanotags. Sci Rep 4:4075
37. Zeng L et al (2015) Raman reporter-coupled Agcore@Aushell nanostars for in vivo improved surface enhanced Raman scattering imaging and near-infrared-triggered photothermal therapy in breast cancers. ACS Appl Mater Interfaces 7(30):16781–16791
38. Hollricher O (2011) Raman instrumentation for confocal Raman microscopy. In: Dieing T, Hollricher O, Toporski J (eds) Confocal Raman microscopy. Springer Berlin Heidelberg, Berlin/Heidelberg, pp 43–60
39. Griffiths PR (2009) Infrared and Raman instrumentation for mapping and imaging. In: Infrared and Raman spectroscopic imaging. Wiley-VCH Verlag GmbH & Co. KGaA, Weinheim, pp 1–64
40. Delhaye M et al (1996) Instrumentation A2 – Turrell, George, Chapter 3. In: Corset J (ed) Raman microscopy. Academic, London, pp 51–173
41. Rong Z et al (2016) Magnetic immunoassay for cancer biomarker detection based on surface-enhanced resonance Raman scattering from coupled plasmonic nanostructures. Biosens Bioelectron 84:15–21
42. Hidi IJ et al (2016) Toward levofloxacin monitoring in human urine samples by employing the LoC-SERS technique. J Phys Chem C 120(37):20613–20623
43. Chen YS et al (2016) Breath analysis based on surface-enhanced Raman scattering sensors distinguishes early and advanced gastric cancer patients from healthy persons. ACS Nano 10(9):8169–8179
44. Fu X et al (2016) A SERS-based lateral flow assay biosensor for highly sensitive detection of HIV-1 DNA. Biosens Bioelectron 78:530–537
45. Jahn M et al (2016) Plasmonic nanostructures for surface enhanced spectroscopic methods. Analyst 141(3):756–793
46. Lin X-M et al (2009) Surface-enhanced Raman spectroscopy: substrate-related issues. Anal Bioanal Chem 394(7):1729–1745
47. Stewart ME et al (2008) Nanostructured plasmonic sensors. Chem Rev 108(2):494–521
48. Wei X, Sebastian S (2014) Rationally designed multifunctional plasmonic nanostructures for surface-enhanced Raman spectroscopy: a review. Rep Prog Phys 77(11):116502
49. Hidi IJ et al (2015) Droplet based microfluidics: spectroscopic characterization of levofloxacin and its SERS detection. Phys Chem Chem Phys 17(33):21236–21242
50. Leopold N, Lendl B (2003) A new method for fast preparation of highly surface-enhanced Raman scattering (SERS) active silver colloids at room temperature by reduction of silver nitrate with hydroxylamine hydrochloride. J Phys Chem B 107(24):5723–5727
51. Garai E et al (2015) A real-time clinical endoscopic system for intraluminal, multiplexed imaging of surface-enhanced Raman scattering nanoparticles. PLoS One 10(4):e0123185
52. Premasiri WR et al (2005) Characterization of the surface enhanced Raman scattering (SERS) of bacteria. J Phys Chem B 109(1):312–320
53. Kang Y et al (2013) Surface-enhanced Raman scattering (SERS) spectra of hemoglobin of mouse and rabbit with self-assembled nano-silver film. Spectrochim Acta A Mol Biomol Spectrosc 108:177–180
54. Baia L et al (2006) Gold films deposited over regular arrays of polystyrene nanospheres as highly effective SERS substrates from visible to NIR. J Phys Chem B 110(47):23982–23986
55. Yüksel S et al (2015) Background-free bottom-up plasmonic arrays with increased sensitivity, specificity and shelf life for SERS detection schemes. J Phys Chem C 119(24):13791–13798
56. Huebner U et al (2011) Fabrication and characterization of silver deposited micro fabricated quartz arrays for surface enhanced Raman spectroscopy (SERS). Microelectron Eng 88(8):1761–1763
57. Radu AI et al (2016) Toward food analytics: fast estimation of lycopene and [small beta]-carotene content in tomatoes based on surface enhanced Raman spectroscopy (SERS). Analyst 141(14):4447–4455

58. Srichan C et al (2016) Highly-sensitive surface-enhanced Raman spectroscopy (SERS)-based chemical sensor using 3D graphene foam decorated with silver nanoparticles as SERS substrate. Sci Rep 6:23733
59. Jiang T-T et al (2014) Enhanced photoluminescence of CdSe quantum dots by the coupling of Ag nanocube and Ag film. Chin Phys B 23(8):086102
60. Zhou Q, Kim T (2016) Review of microfluidic approaches for surface-enhanced Raman scattering. Sensors Actuators B Chem 227:504–514
61. Chao W, Chenxu Y (2015) Analytical characterization using surface-enhanced Raman scattering (SERS) and microfluidic sampling. Nanotechnology 26(9):092001
62. Alharbi O, Xu Y, Goodacre R (2015) Detection and quantification of the opioid tramadol in urine using surface enhanced Raman scattering. Analyst 140(17):5965–5970
63. Amendola G, Pelosi P, Barbini DA (2015) Determination of pesticide residues in animal origin baby foods by gas chromatography coupled with triple quadrupole mass spectrometry. J Environ Sci Health Part B 50(2):109–120
64. Andreou C et al (2013) Rapid detection of drugs of abuse in saliva using surface enhanced Raman spectroscopy and microfluidics. ACS Nano 7(8):7157–7164
65. Bazylak G, Nagels LJ (2002) Integrated acquisition of analytical and biopharmaceutical screening data for beta-adrenergic-drugs employing diversified macrocycle supported potentiometric detection in HPLC systems. Curr Med Chem 9(16):1547–1566
66. Chung E et al (2013) Trace analysis of mercury(II) ions using aptamer-modified Au/Ag core-shell nanoparticles and SERS spectroscopy in a microdroplet channel. Lab Chip 13(2):260–266
67. Gao R et al (2014) Real-time analysis of diaquat dibromide monohydrate in water with a SERS-based integrated microdroplet sensor. Nanoscale 6(15):8781–8786
68. Gao RK et al (2016) Wash-free magnetic immunoassay of the PSA cancer marker using SERS and droplet microfluidics. Lab Chip 16(6):1022–1029
69. Yazdi SH, White IM (2012) Optofluidic surface enhanced Raman spectroscopy microsystem for sensitive and repeatable on-site detection of chemical contaminants. Anal Chem 84(18):7992–7998
70. Zhou JH et al (2012) Convenient formation of nanoparticle aggregates on microfluidic chips for highly sensitive SERS detection of biomolecules. Anal Bioanal Chem 402(4):1601–1609
71. Qi N et al (2014) Surface-enhanced Raman scattering on a zigzag microfluidic chip: towards high-sensitivity detection of As(iii) ions. Anal Methods 6(12):4077–4082
72. Yazdi SH, Giles KL, White IM (2013) Multiplexed detection of DNA sequences using a competitive displacement assay in a microfluidic SERRS-based device. Anal Chem 85(21):10605–10611
73. Yazdi SH, White IM (2012) A nanoporous optofluidic microsystem for highly sensitive and repeatable surface enhanced Raman spectroscopy detection. Biomicrofluidics 6(1):014105
74. Hwang H et al (2011) In situ dynamic measurements of the enhanced SERS signal using an optoelectrofluidic SERS platform. Lab Chip 11(15):2518–2525
75. Kim KB et al (2012) Dynamic preconcentration of gold nanoparticles for surface-enhanced Raman scattering in a microfluidic system. Small 8(3):378–383
76. Mungroo NA, Oliveira G, Neethirajan S (2016) SERS based point-of-care detection of food-borne pathogens. Microchim Acta 183(2):697–707
77. Guo YB et al (2012) Ultrasensitive optofluidic surface-enhanced Raman scattering detection with flow-through multihole capillaries. ACS Nano 6(1):381–388
78. Gao R et al (2015) Fast and sensitive detection of an anthrax biomarker using SERS-based solenoid microfluidic sensor. Biosens Bioelectron 72:230–236
79. Bailey MR et al (2015) Sheath-flow microfluidic approach for combined surface enhanced Raman scattering and electrochemical detection. Anal Chem 87(8):4347–4355
80. Choi J et al (2015) Integrated real-time optofluidic SERS via a liquid-core/liquid-cladding waveguide. RSC Adv 5(2):922–927

81. Deng Y et al (2015) Optofluidic microsystem with quasi-3 dimensional gold plasmonic nanostructure arrays for online sensitive and reproducible SERS detection. Anal Chim Acta 863:41–48
82. Lamberti A et al (2015) Metal-elastomer nanostructures for tunable SERS and easy microfluidic integration. RSC Adv 5(6):4404–4410
83. Lamberti A et al (2015) Ultrasensitive Ag-coated TiO2 nanotube arrays for flexible SERS-based optofluidic devices. J Mater Chem C 3(26):6868–6875
84. Patze S et al (2017) SERS as an analytical tool in environmental science: the detection of sulfamethoxazole in the nanomolar range by applying a microfluidic cartridge setup. Anal Chim Acta 949:1–7
85. Uusitalo S et al (2015) Performance and flow dynamics studies of polymeric optofluidic SERS sensors. J Eur Opt Soc-Rapid Publ 10:15043
86. Zhao YQ et al (2015) Plasmonic nanopillar array embedded microfluidic chips: an in situ SERS monitoring platform. J Mater Chem A 3(12):6408–6413
87. Yamaguchi A et al (2016) Dielectrophoresis-enabled surface enhanced Raman scattering on gold-decorated polystyrene microparticle in micro-optofluidic devices for high-sensitive detection. Sens Actuators B-Chem 230:94–100
88. Yüksel S et al (2016) Trace detection of tetrahydrocannabinol (THC) with a SERS-based capillary platform prepared by the in situ microwave synthesis of AgNPs. Anal Chim Acta 939:93–100
89. Hidi IJ et al (2016) Lab-on-a-chip-surface enhanced Raman scattering combined with the standard addition method: toward the quantification of nitroxoline in spiked human urine samples. Anal Chem 88(18):9173–9180
90. Muhlig A et al (2016) LOC-SERS: a promising closed system for the identification of mycobacteria. Anal Chem 88(16):7998–8004
91. Kammer E et al (2015) Quantitative SERS studies by combining LOC-SERS with the standard addition method. Anal Bioanal Chem 407(29):8925–8929
92. Piorek BD et al (2014) Discrete free-surface millifluidics for rapid capture and analysis of airborne molecules using surface-enhanced Raman spectroscopy. Anal Chem 86(2):1061–1066
93. Wu L et al (2014) Rapid and reproducible analysis of thiocyanate in real human serum and saliva using a droplet SERS-microfluidic chip. Biosens Bioelectron 62:13–18
94. Hidi IJ et al (2014) LOC-SERS: towards point-of-care diagnostic of methotrexate. Anal Methods 6(12):3943–3947
95. Kammer E et al (2014) A new calibration concept for a reproducible quantitative detection based on SERS measurements in a microfluidic device demonstrated on the model analyte adenine. Phys Chem Chem Phys 16(19):9056–9063
96. Cheng IF et al (2013) Rapid (<5 min) identification of pathogen in human blood by electrokinetic concentration and surface-enhanced Raman spectroscopy. Sci Rep 3:2365
97. Negri P et al (2013) Ultrasensitive surface-enhanced Raman scattering flow detector using hydrodynamic focusing. Anal Chem 85(21):10159–10166
98. Wu AHB (2006) A selected history and future of immunoassay development and applications in clinical chemistry. Clin Chim Acta 369(2):119–124
99. Wild D (2013) Immunoassay for beginners, Chapter 1.2. In: The Immunoassay handbook (fourth edition). Elsevier, Oxford, pp 7–10
100. Rubenstein KE, Schneider RS, Ullman EF (1972) "Homogeneous" enzyme immunoassay. A new immunochemical technique. Biochem Biophys Res Commun 47(4):846–851
101. Darwish IA (2006) Immunoassay methods and their applications in pharmaceutical analysis: basic methodology and recent advances. Int J Biomed Sci IJBS 2(3):217–235
102. Fleischmann M, Hendra PJ, McQuillan AJ (1974) Raman spectra of pyridine adsorbed at a silver electrode. Chem Phys Lett 26(2):163–166
103. Le Ru EC, Etchegoin PG (2009) Metallic colloids and other SERS substrates, Chapter 7. In: Principles of surface-enhanced Raman spectroscopy. Elsevier, Amsterdam, pp 367–413

104. Selkoe DJ (2001) Alzheimer's disease: genes, proteins, and therapy. Physiol Rev 81(2):741–766
105. Jack CR Jr et al (2010) Hypothetical model of dynamic biomarkers of the Alzheimer's pathological cascade. Lancet Neurol 9(1):119–128
106. Karran E, Mercken M, Strooper BD (2011) The amyloid cascade hypothesis for Alzheimer's disease: an appraisal for the development of therapeutics. Nat Rev Drug Discov 10(9):698–712
107. Huang Y, Mucke L (2012) Alzheimer mechanisms and therapeutic strategies. Cell 148(6):1204–1222
108. Mangialasche F et al (2010) Alzheimer's disease: clinical trials and drug development. Lancet Neurol 9(7):702–716
109. Hamley IW (2012) The amyloid beta peptide: a chemist's perspective. Role in Alzheimer's and fibrillization. Chem Rev 112(10):5147–5192
110. Benilova I, Karran E, De Strooper B (2012) The toxic A[beta] oligomer and Alzheimer's disease: an emperor in need of clothes. Nat Neurosci 15(3):349–357
111. Li S et al (2011) Soluble Aβ oligomers inhibit long-term potentiation through a mechanism involving excessive activation of extrasynaptic NR2B-containing NMDA receptors. J Neurosci Off J Soc Neurosci 31(18):6627–6638
112. Palop JJ, Mucke L (2010) Amyloid-β induced neuronal dysfunction in Alzheimer's disease: from synapses toward neural networks. Nat Neurosci 13(7):812–818
113. Grundke-Iqbal I et al (1986) Abnormal phosphorylation of the microtubule-associated protein tau (tau) in Alzheimer cytoskeletal pathology. Proc Natl Acad Sci U S A 83(13):4913–4917
114. Kosik KS, Joachim CL, Selkoe DJ (1986) Microtubule-associated protein tau (tau) is a major antigenic component of paired helical filaments in Alzheimer disease. Proc Natl Acad Sci U S A 83(11):4044–4048
115. Zhou YL et al (2016) Detection of A beta monomers and oligomers: early diagnosis of Alzheimer's disease. Chem Asian J 11(6):805–817
116. Cohen TJ et al (2011) The acetylation of tau inhibits its function and promotes pathological tau aggregation. Nat Commun 2:252–252
117. Iqbal K et al (2010) Tau in Alzheimer disease and related tauopathies. Curr Alzheimer Res 7(8):656–664
118. Hoover BR et al (2010) Tau mislocalization to dendritic spines mediates synaptic dysfunction independently of neurodegeneration. Neuron 68(6):1067–1081
119. Golde TE, Eckman CB, Younkin SG (2000) Biochemical detection of A beta isoforms: implications for pathogenesis, diagnosis, and treatment of Alzheimer's disease. BBA-Mol Basis Dis 1502(1):172–187
120. Lista S et al (2014) CSF A beta 1-42 combined with neuroimaging biomarkers in the early detection, diagnosis and prediction of Alzheimer's disease. Alzheimers Dement 10(3):381–392
121. Blennow K et al (2015) Clinical utility of cerebrospinal fluid biomarkers in the diagnosis of early Alzheimer's disease. Alzheimers Dement 11(1):58–69
122. Galozzi S, Marcus K, Barkovits K (2015) Amyloid- as a biomarker for Alzheimer's disease: quantification methods in body fluids. Expert Rev Proteomics 12(4):343–354
123. El-Said WA et al (2011) Fabrication of gold nanoparticle modified ITO substrate to detect beta-amyloid using surface-enhanced Raman scattering. J Nanosci Nanotechnol 11(1):768–772
124. Zengin A, Tamer U, Caykara T (2013) A SERS-based sandwich assay for ultrasensitive and selective detection of Alzheimer's tau protein. Biomacromolecules 14(9):3001–3009
125. Cherny RA et al (1999) Aqueous dissolution of Alzheimer's disease Aβ amyloid deposits by biometal depletion. J Biol Chem 274(33):23223–23228
126. Yoshiike Y, Akagi T, Takashima A (2007) Surface structure of amyloid-β fibrils contributes to cytotoxicity. Biochemistry 46(34):9805–9812
127. Pesaresi M et al (2006) Plasma levels of beta-amyloid (1–42) in Alzheimer's disease and mild cognitive impairment. Neurobiol Aging 27(6):904–905

128. Zetterberg H et al (2013) Plasma tau levels in Alzheimer's disease. Alzheimers Res Ther 5(2):9
129. Demeritte T et al (2015) Hybrid graphene oxide based plasmonic-magnetic multifunctional nanoplatform for selective separation and label-free identification of Alzheimer's disease biomarkers. ACS Appl Mater Interfaces 7(24):13693–13700
130. Klein WL (2002) Aβ toxicity in Alzheimer's disease: globular oligomers (ADDLs) as new vaccine and drug targets. Neurochem Int 41(5):345–352
131. Haass C, Selkoe DJ (2007) Soluble protein oligomers in neurodegeneration: lessons from the Alzheimer's amyloid [beta]-peptide. Nat Rev Mol Cell Biol 8(2):101–112
132. Wang Q, Wang YM, Lu HP (2013) Revealing the secondary structural changes of amyloid beta peptide by probing the spectral fingerprint characters. J Raman Spectrosc 44(5):670–674
133. Abdolrahim M et al (2015) Development of optical biosensor technologies for cardiac troponin recognition. Anal Biochem 485:1–10
134. Mohammed MI, Desmulliez MPY (2011) Lab-on-a-chip based immunosensor principles and technologies for the detection of cardiac biomarkers: a review. Lab Chip 11(4):569–595
135. Katrukha IA (2013) Human cardiac troponin complex. Structure and functions. Biochem Mosc 78(13):1447–1465
136. Lippi G (2013) Biomarkers of myocardial ischemia in the emergency room: cardiospecific troponin and beyond. Eur J Intern Med 24(2):97–99
137. Fathil MFM et al (2015) Diagnostics on acute myocardial infarction: cardiac troponin biomarkers. Biosens Bioelectron 70:209–220
138. Fathil MFM et al (2016) Progression in sensing cardiac troponin biomarker charge transductions on semiconducting nanomaterials. Anal Chim Acta 935:30–43
139. Han X et al (2016) Recent development of cardiac troponin I detection. ACS Sensors 1(2):106–114
140. Hasanzadeh M et al (2013) Optical immunosensing of effective cardiac biomarkers on acute myocardial infarction. Trac-Trends Anal Chem 51:158–168
141. Qureshi A, Gurbuz Y, Niazi JH (2012) Biosensors for cardiac biomarkers detection: a review. Sensors Actuators B Chem 171:62–76
142. El-Said WA, Fouad DM, El-Safty SA (2016) Ultrasensitive label-free detection of cardiac biomarker myoglobin based on surface-enhanced Raman spectroscopy. Sensors Actuators B Chem 228:401–409
143. Chon H et al (2014) SERS-based competitive immunoassay of troponin I and CK-MB markers for early diagnosis of acute myocardial infarction. Chem Commun 50(9):1058–1060
144. Sacks DB, McDonald JM (1996) The pathogenesis of type II diabetes mellitus: a polygenic disease. Am J Clin Pathol 105(2):149
145. Oliver NS et al (2009) Glucose sensors: a review of current and emerging technology. Diabet Med 26(3):197–210
146. McCrimmon R (2008) The mechanisms that underlie glucose sensing during hypoglycaemia in diabetes. Diabet Med 25(5):513–522
147. Newman JD, Turner APF (2005) Home blood glucose biosensors: a commercial perspective. Biosens Bioelectron 20(12):2435–2453
148. Perez-Mayen L et al (2016) Nanomolar detection of glucose using SERS substrates fabricated with albumin coated gold nanoparticles. Nanoscale 8(23):11862–11869
149. Zhang A et al (2012) Novel molecular specific detection of glucose using a Raman probe molecule with surface enhanced Raman scattering. Sci Adv Mater 4(10):1047–1054
150. Lin JY et al (2014) Label-free optical detection of type II diabetes based on surface-enhanced Raman spectroscopy and multivariate analysis. J Raman Spectrosc 45(10):884–889
151. Yuen JM et al (2010) Transcutaneous glucose sensing by surface-enhanced spatially offset Raman spectroscopy in a rat model. Anal Chem 82(20):8382–8385
152. Ma K et al (2011) In vivo, transcutaneous glucose sensing using surface-enhanced spatially offset Raman spectroscopy: multiple rats, improved hypoglycemic accuracy, low incident power, and continuous monitoring for greater than 17 days. Anal Chem 83(23):9146–9152

153. Sharma B et al (2016) Bisboronic acids for selective, physiologically relevant direct glucose sensing with surface-enhanced Raman spectroscopy. J Am Chem Soc 138(42):13952–13959
154. Lyandres O et al (2008) Progress toward an in vivo surface-enhanced Raman spectroscopy glucose sensor. Diabetes Technol Ther 10(4):257–265
155. Torul H et al (2015) Paper membrane-based SERS platform for the determination of glucose in blood samples. Anal Bioanal Chem 407(27):8243–8251
156. Mei L-P et al (2015) Simple electrodeposition of hierarchical gold-platinum nanothorns and their applications in electrocatalysis and SERS. Electrochim Acta 160:235–243
157. Ceja-Fdez A et al (2014) Glucose detection using SERS with multi-branched gold nanostructures in aqueous medium. RSC Adv 4(103):59233–59241
158. Torul H et al (2014) Glucose determination based on a two component self-assembled monolayer functionalized surface enhanced Raman spectroscopy (SERS) probe. Anal Methods 6(14):5097–5104
159. Dong J et al (2012) Glucose-responsive multifunctional acupuncture needle: a universal SERS detection strategy of small biomolecules in vivo. Anal Methods 4(11):3879–3883
160. Qi GH et al (2015) A highly sensitive SERS sensor for quantitative analysis of glucose based on the chemical etching of silver nanoparticles. J Opt 17(11)
161. Dinish US et al (2011) Development of highly reproducible nanogap SERS substrates: comparative performance analysis and its application for glucose sensing. Biosens Bioelectron 26(5):1987–1992
162. Qi GH et al (2016) Glucose oxidase probe as a surface-enhanced Raman scattering sensor for glucose. Anal Bioanal Chem 408(26):7513–7520
163. Severyukhina AN et al (2015) Nanoplasmonic chitosan nanofibers as effective SERS substrate for detection of small molecules. ACS Appl Mater Interfaces 7(28):15466–15473
164. Quyen TTB et al (2013) Au@SiO2 core/shell nanoparticle assemblage used for highly sensitive SERS-based determination of glucose and uric acid. J Raman Spectrosc 44(12):1671–1677
165. Yuen C, Liu Q (2014) Towards in vivo intradermal surface enhanced Raman scattering (SERS) measurements: silver coated microneedle based SERS probe. J Biophotonics 7(9):683–689
166. Al-Ogaidi I et al (2014) A gold@silica core-shell nanoparticle-based surface-enhanced Raman scattering biosensor for label-free glucose detection. Anal Chim Acta 811:76–80
167. Gupta VK et al (2013) A novel glucose biosensor platform based on Ag@AuNPs modified graphene oxide nanocomposite and SERS application. J Colloid Interface Sci 406:231–237
168. Wang XM et al (2016) A glucose biosensor based on detecting longitudinal surface plasmon resonance of gold nanorods. J Nanosci Nanotechnol 16(7):6925–6929
169. Kong KV et al (2014) Sensitive SERS glucose sensing in biological media using alkyne functionalized boronic acid on planar substrates. Biosens Bioelectron 56:186–191
170. Bi XS et al (2015) Facile and sensitive glucose sandwich assay using in situ-generated Raman reporters. Anal Chem 87(3):2016–2021
171. Sun D et al (2016) Construction of highly sensitive surface-enhanced Raman scattering (SERS) nanosensor aimed for the testing of glucose in urine. RSC Adv 6(59):53800–53803
172. Sun XC et al (2014) Functionalized aligned silver nanorod arrays for glucose sensing through surface enhanced Raman scattering. RSC Adv 4(45):23382–23388
173. Zhang YW et al (2012) One-pot green synthesis of Ag nanoparticles-graphene nanocomposites and their applications in SERS, H2O2, and glucose sensing. RSC Adv 2(2):538–545
174. Güemes M, Rahman SA, Hussain K (2015) What is a normal blood glucose? Arch Dis Child:569–574
175. James TD, Phillips MD, Shinkai S (2006) The molecular recognition of saccharides. Complexation of boronic acids with saccharides. Fluorescent sensors. Modular fluorescent sensors. Other types of sensor. Other systems for saccharide recognition. In: Boronic acids in saccharide recognition. The Royal Society of Chemistry, Cambridge, pp 3–176

176. Wu L, Qu XG (2015) Cancer biomarker detection: recent achievements and challenges. Chem Soc Rev 44(10):2963–2997
177. McAughtrie S, Faulds K, Graham D (2014) Surface enhanced Raman spectroscopy (SERS): potential applications for disease detection and treatment. J Photochem Photobiol C Photochem Rev 21:40–53
178. Ye SJ et al (2014) Enzyme-based signal amplification of surface-enhanced Raman scattering in cancer-biomarker detection. Trac-Trends Anal Chem 55:43–54
179. Bernard CPW, Stewart W (2014) World cancer report 2014. International Agency for Research on Cancer (IARC), Lyon, p 633
180. Gam L-H (2012) Breast cancer and protein biomarkers. World J Exp Med 2(5):86–91
181. Li M et al (2013) Three-dimensional hierarchical plasmonic nano-architecture enhanced surface-enhanced Raman scattering immunosensor for cancer biomarker detection in blood plasma. ACS Nano 7(6):4967–4976
182. Dinish US et al (2014) Sensitive multiplex detection of serological liver cancer biomarkers using SERS-active photonic crystal fiber probe. J Biophotonics 7(11–12):956–965
183. Vaidyanathan R et al (2015) A multiplexed device based on tunable nanoshearing for specific detection of multiple protein biomarkers in serum. Sci Rep 5:9756
184. Wang Y et al (2015) Enabling rapid and specific surface-enhanced Raman scattering immunoassay using nanoscaled surface shear forces. ACS Nano 9(6):6354–6362
185. Mandal S et al (2011) Synthesis and multidisciplinary characterization of polyelectrolyte multilayer-coated nanogold with improved stability toward aggregation. Colloid Polym Sci 289(3):269–280
186. Beqa L et al (2011) Gold nano-popcorn attached SWCNT hybrid nanomaterial for targeted diagnosis and photothermal therapy of human breast cancer cells. ACS Appl Mater Interfaces 3(9):3316–3324
187. Yang J et al (2012) Distinguishing breast cancer cells using surface-enhanced Raman scattering. Anal Bioanal Chem 402(3):1093–1100
188. Zhang P et al (2014) Novel nitrocellulose membrane substrate for efficient analysis of circulating tumor cells coupled with surface-enhanced Raman scattering imaging. ACS Appl Mater Interfaces 6(1):370–376
189. Fales AM, Yuan H, Vo-Dinh T (2013) Cell-penetrating peptide enhanced intracellular Raman imaging and photodynamic therapy. Mol Pharm 10(6):2291–2298
190. Lee S et al (2014) Rapid and sensitive phenotypic marker detection on breast cancer cells using surface-enhanced Raman scattering (SERS) imaging. Biosens Bioelectron 51:238–243
191. Freitag I et al (2016) Recognition of tumor cells by immuno-SERS-markers in a microfluidic chip at continuous flow. Analyst 141(21):5986–5989
192. Jimenez de Aberasturi D et al (2016) Surface enhanced Raman scattering encoded gold nanostars for multiplexed cell discrimination. Chem Mater 28(18):6779–6790
193. Shi ML et al (2016) SERS assay of telomerase activity at single-cell level and colon cancer tissues via quadratic signal amplification. Biosens Bioelectron 77:673–680
194. Lee M et al (2011) Highly reproducible immunoassay of cancer markers on a gold-patterned microarray chip using surface-enhanced Raman scattering imaging. Biosens Bioelectron 26(5):2135–2141
195. Perumal J et al (2015) SERS-based quantitative detection of ovarian cancer prognostic factor haptoglobin. Int J Nanomedicine 10:1831–1840
196. Feng SY et al (2011) Study on gastric cancer blood plasma based on surface-enhanced Raman spectroscopy combined with multivariate analysis. Sci China Life Sci 54(9):828–834
197. Feng SY et al (2010) Nasopharyngeal cancer detection based on blood plasma surface-enhanced Raman spectroscopy and multivariate analysis. Biosens Bioelectron 25(11):2414–2419
198. Xie H-n et al (2012) Tracking bisphosphonates through a 20 mm thick porcine tissue by using surface-enhanced spatially offset Raman spectroscopy. Angew Chem Int Ed 51(34):8509–8511

199. Yang TX et al (2014) Facile and label-free detection of lung cancer biomarker in urine by magnetically assisted surface-enhanced Raman scattering. ACS Appl Mater Interfaces 6(23):20985–20993
200. Wang H-N et al (2016) Multiplexed detection of microRNA biomarkers using SERS-based inverse molecular sentinel (iMS) nanoprobes. J Phys Chem C 120(37):21047–21055
201. Guven B et al (2014) SERS-based direct and sandwich assay methods for mir-21 detection. Analyst 139(5):1141–1147
202. Choi S et al (2015) Biochemical investigations of human papillomavirus-infected cervical fluids. Microsc Res Tech 78(3):200–206
203. Granger JH et al (2013) Toward development of a surface-enhanced Raman scattering (SERS)-based cancer diagnostic immunoassay panel. Analyst 138(2):410–416
204. Domenici F, Bizzarri AR, Cannistraro S (2012) Surface-enhanced Raman scattering detection of wild-type and mutant p53 proteins at very low concentration in human serum. Anal Biochem 421(1):9–15
205. Cepeda-Pérez E et al (2016) SERS-active Au/SiO(2) clouds in powder for rapid ex vivo breast adenocarcinoma diagnosis. Biomed Opt Express 7(6):2407–2418
206. Wang X-P et al (2016) iSERS microscopy guided by wide field immunofluorescence: analysis of HER2 expression on normal and breast cancer FFPE tissue sections. Analyst 141(17):5113–5119
207. Sinha L et al (2015) Quantification of the binding potential of cell-surface receptors in fresh excised specimens via dual-probe modeling of SERS nanoparticles. Sci Rep 5:8582
208. Song J et al (2015) Plasmonic vesicles of amphiphilic nanocrystals: optically active multifunctional platform for cancer diagnosis and therapy. Acc Chem Res 48(9):2506–2515
209. Wood BR et al (2003) Raman imaging of hemozoin within the food vacuole of *Plasmodium falciparum* trophozoites. FEBS Lett 554(3):247–252
210. Garrett NL et al (2015) Bio-sensing with butterfly wings: naturally occurring nano-structures for SERS-based malaria parasite detection. Phys Chem Chem Phys 17(33):21164–21168
211. Chen FN et al (2016) Direct detection of malaria infected red blood cells by surface enhanced Raman spectroscopy. Nanomed Nanotechnol Biol Med 12(6):1445–1451
212. Chen KR et al (2016) Review of surface enhanced Raman spectroscopy for malaria diagnosis and a new approach for the detection of single parasites in the ring stage. IEEE J Sel Top Quantum Electron 22(4)
213. Chen KR et al (2016) Towards ultrasensitive malaria diagnosis using surface enhanced Raman spectroscopy. Sci Rep 6
214. Kaminska A et al (2015) Detection of hepatitis B virus antigen from human blood: SERS immunoassay in a microfluidic system. Biosens Bioelectron 66:461–467
215. Li M et al (2013) Plasmonic nanorice antenna on triangle nanoarray for surface-enhanced Raman scattering detection of hepatitis B virus DNA. Anal Chem 85(4):2072–2078
216. Yao CK et al (2012) Spatially reinforced nano-cavity array as the SERS-active substrate for detecting hepatitis virus core antigen at low concentrations. Sens Actuators B Chem 174:478–484
217. Wu XM et al (2015) Differentiation and classification of bacteria using vancomycin functionalized silver nanorods array based surface-enhanced Raman spectroscopy and chemometric analysis. Talanta 139:96–103
218. Wu X et al (2014) Culture-free diagnostics of *Pseudomonas aeruginosa* infection by silver nanorod array based SERS from clinical sputum samples. Nanomedicine 10(8):1863–1870
219. Avci E et al (2015) Discrimination of urinary tract infection pathogens by means of their growth profiles using surface enhanced Raman scattering. Anal Bioanal Chem 407(27):8233–8241
220. Premasiri WR et al (2016) The biochemical origins of the surface-enhanced Raman spectra of bacteria: a metabolomics profiling by SERS. Anal Bioanal Chem 408(17):4631–4647
221. Marotta NE, Bottomley LA (2010) Surface-enhanced Raman scattering of bacterial cell culture growth media. Appl Spectrosc 64(6):601–606

222. Watson I et al (1997) Therapeutic drug monitoring [Editorial]. Ther Drug Monit 19(2):125
223. Muller DM, Rentsch KM (2010) Therapeutic drug monitoring by LC-MS-MS with special focus on anti-infective drugs. Anal Bioanal Chem 398(6):2573–2594
224. Humble RM et al (2015) Therapeutic drug monitoring of pentobarbital: experience at an Academic Medical Center. Ther Drug Monit 37(6):783–791
225. Carlier M et al (2015) Assays for therapeutic drug monitoring of beta-lactam antibiotics: a structured review. Int J Antimicrob Agents 46(4):367–375
226. Baranowska I, Magiera S, Baranowski J (2013) Clinical applications of fast liquid chromatography: a review on the analysis of cardiovascular drugs and their metabolites. J Chromatogr B Analyt Technol Biomed Life Sci 927:54–79
227. Aucella F et al (2013) Liquid chromatography-tandem mass spectrometry method as the golden standard for therapeutic drug monitoring in renal transplant. J Pharm Biomed Anal 86:123–126
228. Young J et al (2015) A novel immunoassay to measure total serum lymphotoxin-alpha levels in the presence of an anti-LT alpha therapeutic antibody. J Immunol Methods 424:91–99
229. Song ZR et al (2016) A validated chemiluminescence immunoassay for methotrexate (MTX) and its application in a pharmacokinetic study. Anal Methods 8(1):162–170
230. Krieg AK, Gauglitz G (2015) Ultrasensitive label-free immunoassay for optical determination of amitriptyline and related tricyclic antidepressants in human serum. Anal Chem 87(17):8845–8850
231. Guerriero E et al (2014) Unexpected overestimation of methotrexate plasma concentrations: analysis of a single center pediatric population. Ther Drug Monit 36(4):499–504
232. Widemann BC, Adamson PC (2006) Understanding and managing methotrexate nephrotoxicity. Oncologist 11(6):694–703
233. Fornasaro S et al (2016) Toward SERS-based point-of-care approaches for therapeutic drug monitoring: the case of methotrexate. Faraday Discuss 187:485–499
234. Crews KR et al (2004) High-dose methotrexate pharmacokinetics and outcome of children and young adults with osteosarcoma. Cancer 100(8):1724–1733
235. Yuen C, Zheng W, Huang ZW (2010) Low-level detection of anti-cancer drug in blood plasma using microwave-treated gold-polystyrene beads as surface-enhanced Raman scattering substrates. Biosens Bioelectron 26(2):580–584
236. Pletz M, Lipman J (2013) Clinical measures for increased creatinine clearances and suboptimal antibiotic dosing. Intensive Care Med 39(7):1322–1324
237. McKeating KS et al (2016) High throughput LSPR and SERS analysis of aminoglycoside antibiotics. Analyst 141(17):5120–5126
238. Liu SP et al (2015) Raman spectroscopy measurement of levofloxacin lactate in blood using an optical fiber nano-probe. J Raman Spectrosc 46(2):197–201
239. Xia TH et al (2014) Improving the quantitative accuracy of surface-enhanced Raman spectroscopy by the combination of microfluidics with a multiplicative effects model. Anal Methods 6(7):2363–2370
240. Villa JEL, Poppi RJ (2016) A portable SERS method for the determination of uric acid using a paper-based substrate and multivariate curve resolution. Analyst 141(6):1966–1972
241. Mamian-Lopez MB, Poppi RJ (2013) Standard addition method applied to the urinary quantification of nicotine in the presence of cotinine and anabasine using surface enhanced Raman spectroscopy and multivariate curve resolution. Anal Chim Acta 760:53–59
242. Mamian-Lopez MB, Poppi RJ (2013) Quantification of moxifloxacin in urine using surface-enhanced Raman spectroscopy (SERS) and multivariate curve resolution on a nanostructured gold surface. Anal Bioanal Chem 405(24):7671–7677
243. Subaihi A et al (2016) Rapid, accurate, and quantitative detection of propranolol in multiple human biofluids via surface-enhanced Raman scattering. Anal Chem 88 (22):10884–10892
244. Berger AG, Restaino SM, White IM (2017) Vertical-flow paper SERS system for therapeutic drug monitoring of flucytosine in serum. Anal Chim Acta 949:59–66

245. Sun F et al (2016) Hierarchical zwitterionic modification of a SERS substrate enables real-time drug monitoring in blood plasma. Nat Commun 7:9
246. Ma YM et al (2016) Surface-enhanced Raman spectroscopy on liquid interfacial nanoparticle arrays for multiplex detecting drugs in urine. Anal Chem 88(16):8145–8151
247. Robinson AM et al (2015) The development of "fab-chips" as low-cost, sensitive surface-enhanced Raman spectroscopy (SERS) substrates for analytical applications. Analyst 140(3):779–785
248. Dong RL et al (2015) Detection and direct readout of drugs in human urine using dynamic surface-enhanced Raman spectroscopy and support vector machines. Anal Chem 87(5):2937–2944
249. Han Z et al (2015) Portable kit for identification and detection of drugs in human urine using surface-enhanced Raman spectroscopy. Anal Chem 87(18):9500–9506
250. Bisswanger H (2014) Enzyme assays. Perspect Sci 1(1–6):41–55
251. Zong SF et al (2014) Colorimetry and SERS dual-mode detection of telomerase activity: combining rapid screening with high sensitivity. Nanoscale 6(3):1808–1816
252. Zong S et al (2014) Assessing telomere length using surface enhanced Raman scattering. Sci Rep 4:1–8
253. Zong S et al (2013) Ultrasensitive telomerase activity detection by telomeric elongation controlled surface enhanced Raman scattering. Small 9(24):4215–4220
254. März A et al (2011) Detection of thiopurine methyltransferase activity in lysed red blood cells by means of lab-on-a-chip surface enhanced Raman spectroscopy (LOC-SERS). Anal Bioanal Chem 400(9):2755–2761
255. Wang Y et al (2015) A SERS protocol as a potential tool to access 6-mercaptopurine release accelerated by glutathione-S-transferase. Analyst 140(22):7578–7585
256. Han GM et al (2014) Label-free surface-enhanced Raman scattering imaging to monitor the metabolism of antitumor drug 6-mercaptopurine in living cells. Anal Chem 86(23):11503–11507
257. Wu ZT et al (2015) A simple and universal "turn-on" detection platform for proteases based on surface enhanced Raman scattering (SERS). Biosens Bioelectron 65:375–381
258. Yazgan NN et al (2010) A high sensitive assay platform based on surface-enhanced Raman scattering for quantification of protease activity. Talanta 82(2):631–639
259. Yang L et al (2016) SERS determination of protease through a particle-on-a-film configuration constructed by electrostatic assembly in an enzymatic hydrolysis reaction. RSC Adv 6(93):90120–90125
260. Chen LX, Fu XL, Li JH (2013) Ultrasensitive surface-enhanced Raman scattering detection of trypsin based on anti-aggregation of 4-mercaptopyridine-functionalized silver nanoparticles: an optical sensing platform toward proteases. Nanoscale 5(13):5905–5911
261. Wu ZT et al (2013) A "turn-off" SERS-based detection platform for ultrasensitive detection of thrombin based on, enzymatic assays. Biosens Bioelectron 44:10–15
262. Cong Y-S, Wright WE, Shay JW (2002) Human telomerase and its regulation. Microbiol Mol Biol Rev 66(3):407–425
263. Dhaene K, Van Marck E, Parwaresch R (2000) Telomeres, telomerase and cancer: an up-date. Virchows Arch Int J Pathol 437(1):1–16
264. Klingelhutz AJ (1997) Telomerase activation and cancer. J Mol Med JMM 75(1):45–49
265. Smekalova EM et al (2012) Telomerase RNA biosynthesis and processing. Biochem Mosc 77(10):1120–1128
266. Lopez-Otin C, Matrisian LM (2007) Emerging roles of proteases in tumour suppression. Nat Rev Cancer 7(10):800–808
267. Duffy MJ (1992) The role of proteolytic enzymes in cancer invasion and metastasis. Clin Exp Metastasis 10(3):145–155
268. Anastasopoulos JA, Beobide AS, Voyiatzis GA (2013) Quantitative surface enhanced Raman scattering measurements at the early stage of active agent release processes. J Raman Spectrosc 44(3):401–405

269. Chen H et al (2014) SERS-fluorescence monitored drug release of a redox-responsive nanocarrier based on graphene oxide in tumor cells. ACS Appl Mater Interfaces 6(20):17526–17533
270. El-Said WA, Choi JW (2014) In-situ detection of neurotransmitter release from PC12 cells using surface enhanced Raman spectroscopy. Biotechnol Bioprocess Eng 19(6):1069–1076
271. Fang W et al (2014) pH-controllable drug carrier with SERS activity for targeting cancer cells. Biosens Bioelectron 57:10–15
272. Ganbold EO et al (2013) Raman spectroscopy of combinatory anticancer drug release from gold nanoparticles inside a single leukemia cell. J Raman Spectrosc 44(5):675–679
273. Gautier J et al (2013) SERS spectroscopic approach to study doxorubicin complexes with Fe2 + ions and drug release from SPION-based nanocarriers. Analyst 138(24):7354–7361
274. Huang J et al (2013) Tracking the intracellular drug release from graphene oxide using surface-enhanced Raman spectroscopy. Nanoscale 5(21):10591–10598
275. Ilkhani H et al (2016) Nanostructured SERS-electrochemical biosensors for testing of anticancer drug interactions with DNA. Biosens Bioelectron 80:257–264
276. Liang LJ et al (2015) In situ surface-enhanced Raman scattering spectroscopy exploring molecular changes of drug-treated cancer cell nucleus. Anal Chem 87(4):2504–2510
277. Liu L et al (2016) Smart surface-enhanced Raman scattering traceable drug delivery systems. Nanoscale 8(25):12803–12811
278. Masetti M et al (2015) Revealing DNA interactions with exogenous agents by surface-enhanced Raman scattering. J Am Chem Soc 137(1):469–476
279. Nieciecka D, Krolikowska A, Krysinski P (2015) Probing the interactions of mitoxantrone with biomimetic membranes with electrochemical and spectroscopic techniques. Electrochim Acta 165:430–442
280. Ock K et al (2012) Real-time monitoring of glutathione-triggered thiopurine anticancer drug release in live cells investigated by surface-enhanced Raman scattering. Anal Chem 84(5):2172–2178
281. Ock KS et al (2012) Label-free Raman spectroscopy for accessing intracellular anticancer drug release on gold nanoparticles. Analyst 137(12):2852–2859
282. Tian LM, Gandra N, Singamaneni S (2013) Monitoring controlled release of payload from gold nanocages using surface enhanced Raman scattering. ACS Nano 7(5):4252–4260
283. Yang J et al (2012) Tracking multiplex drugs and their dynamics in living cells using the label-free surface-enhanced Raman scattering technique. Mol Pharm 9(4):842–849
284. Yang J et al (2014) Dual-mode tracking of tumor-cell-specific drug delivery using fluorescence and label-free SERS techniques. Biosens Bioelectron 51:82–89
285. Zong SF et al (2014) Telomerase triggered drug release using a SERS traceable nanocarrier. IEEE Trans Nanobioscience 13(1):55–60

In Vivo Near-Infrared Fluorescence Imaging

2

Guofeng Liu, Jianhui Sheng, and Yanli Zhao

Contents

1 Definition of the Topic

In vivo near-infrared (NIR) fluorescence imaging used for clinical diagnostics and treatment monitoring provides a noninvasive approach for visualizing and peering deeply morphological details of tissues or living subjects with subcellular resolution.

G. Liu · J. Sheng
Division of Chemistry and Biological Chemistry, School of Physical and Mathematical Sciences, Nanyang Technological University, Singapore, Singapore

Y. Zhao (✉)
Division of Chemistry and Biological Chemistry, School of Physical and Mathematical Sciences, Nanyang Technological University, Singapore, Singapore

School of Materials Science and Engineering, Nanyang Technological University, Singapore, Singapore
e-mail: zhaoyanli@ntu.edu.sg

C. S. S. R. Kumar (ed.), *Nanotechnology Characterization Tools for Biosensing and Medical Diagnosis*, https://doi.org/10.1007/978-3-662-56333-5_2

In this chapter, we describe the applications of organic dyes, metal complexes, fluorescent biomacromolecules, and nanoparticles (such as polymers, quantum dots (QDs), carbon-based nanomaterials, upconversion nanoparticles (UCNPs), noble metal clusters, and Si-based hybrid nanoparticles) for NIR fluorescence imaging of living subjects.

2 Overview

Fluorescence is a useful noninvasive tool for visualizing the morphological details in vivo with subcellular resolution and for effective medical diagnosis and therapeutics. Except for high sensitivity and high spatial resolution, it possesses fast imaging, low-cost, and facile multiplexing properties. Thus, ideal contrast agents with bright fluorescence, desirable excitation and emission wavelength, high photostability, small size, and good biocompatibility are vital for fluorescence imaging in vivo.

However, the major obstacle of fluorescent imaging in vivo is limited by the tissue attenuation and autofluorescence. To minimize these effects, scientists have focused on NIR fluorescent probes that are excited and emitted in the spectral range of 650–950 nm, since tissues are virtually transparent and have typically no autofluorescence in this optimal NIR region. Compared with UV or visible light excitation, in vivo imaging excited from NIR light has noticeable advantages including deep penetration, weak autofluorescence, minimal photo-bleaching, and low phototoxicity. Especially, two-photon-excited fluorescence imaging on account of the anti-Stokes luminescence process provides a powerful approach to reduce autofluorescence for bioimaging. Furthermore, in vivo NIR fluorescence bioimaging is important to explore fundamental biological mechanism and pathological progression and offers key information to the disease diagnosis and therapy. An equally important issue worth to study is to invasively outline the healthy tissues from diseased ones. Thus, these methods require further optimization of design to gain effective NIR imaging agents with high brightness, excellent biocompatibility, good water solubility, and tissue-specific targeting ability.

Herein, we describe how to employ NIR fluorescent organic dyes, biomacromolecules, metal complexes, and nanoparticles (such as QDs, UCNPs, carbon-based nanomaterials, noble metal clusters, polymers, and Si-based hybrid nanoparticles) with NIR excitation or emission for fluorescence imaging in vivo in order to clearly define the physical margins of tumorous and vital tissues for disease diagnostics and therapy.

3 Introduction

Although biomedical imaging technologies have been developed for disease diagnosis and therapy, researchers still face great challenges in precisely viewing and understanding the disease processes, since these processes usually occur at the subcellular and molecular levels [1]. To date, a variety of techniques have been

used for imaging the structures and functions of bio-samples, which include ultrasound imaging, computed tomography (CT), magnetic resonance imaging (MRI), positron-emission tomography (PET), single-photon emission tomography (SPET), and optical imaging (bioluminescence and fluorescence imaging). Among these techniques, fluorescence provides a unique path to noninvasively visualize morphological details of living cells and animals with high resolution and becomes a useful tool for in vivo imaging. Unlike CT and PET imaging techniques, fluorescence imaging utilizes nonionizing and noninvasive radiation that can visualize the targeted tissue in situ with high spatiotemporal resolution in a real-time manner [2, 3].

However, there are still some limitations existing in fluorescent imaging, such as the interference from less penetration depth of light, tissue attenuation, and autofluorescence. To address these problems, various fluorescent probes with NIR excitation and emission have been continuously designed and developed. In contrast to visible light excitation for in vivo imaging, NIR light excitation possesses many merits including deep tissue penetration, weak autofluorescence, minimal photobleaching, low light scatter, and less phototoxicity, thus allowing engineered contrast agents to operate effectively by avoiding the disruptive background signal present at lower wavelengths. These properties are highly important for future clinical translation and should be maintained throughout the developmental process. These characteristics afford high signal-to-background ratio (SBR) that is recognized as the paramount parameter for successful contrast agents. High SBR paired with cost-effective lasers and detectors as well as the inherent innocuous nature of NIR light makes NIR fluorescence imaging a promising technology for further development.

Currently, many kinds of NIR fluorescent probes lie within this research focus, including small-molecule fluorophores (such as cyanines, porphyrin-based fluorophores, squaraine-based fluorophores, and metal complexes), biological species (such as fluorescent proteins and DNA aptamers), and synthetic nanoparticles (such as polymers, QDs, UCNPs, carbon-based nanomaterials, noble metal clusters, and Si-based hybrid nanoparticles).

In vivo NIR fluorescence imaging is important to explore fundamental biological mechanism and pathological progression and provides lots of important information for disease diagnosis and therapy. Specific, sensitive detection of tumors in patients is a long-standing challenge in oncology. Successful detection of small premalignant lesions and diagnosis of early-stage tumors can significantly benefit cancer treatment and improve the survival rate for patients. To improve the target-to-background ratio, fluorescent labels are typically conjugated to a tumor-targeting moiety, instead of exploiting passive dye accumulation resulting from the enhanced permeability and retention effect (EPR) of tumors. Many affinity scaffolds against cancer markers have been developed for in vivo tumor targeting, ranging from conventional antibodies and peptide-based probes to receptor-targeted natural ligands, small-molecule antagonists, and DNA or RNA aptamers. All of these representative agents must be tailored to achieve sufficient stability, specificity, and safety for human use. Before NIR imaging could be successfully employed in the clinic, contrast agents must be designed to satisfy a very particular set of parameters that are requisite to future success. The research efforts place an emphasis on improvements in terms of low

cytotoxicity, high photostability, NIR emission, two-photon excitation, and long fluorescence lifetime, which are crucial for longtime tracking of biological processes, tissue and body imaging with deep penetration and low autofluorescence, and time-resolved fluorescence imaging.

Recent advances in bioimaging provide great promises to fulfill the requirements, as targeted contrast agents have been successfully developed for visualizing both tumors and vital tissues by simultaneously utilizing spectrally different fluorophores. These tissue-specific contrast agents can be versatile warehouse to physicians for real-time intraoperative navigation and image-guided targeted therapy. NIR fluorescence light has played an important role in clinical bioimaging via providing highly specific fluorescent images of targeted tissues. Further research requires optimizing designs to gain effective NIR imaging agents with high brightness, good water solubility, excellent biocompatibility, and tissue-specific target ability.

Although there are many reviews highlighting organic fluorophores and nanoparticles for fluorescence imaging [1–56], there is still no review to systematically summarize various organic fluorophores and nanoparticles with NIR fluorescence for in vivo bioimaging. Herein, we discuss recent significant research progress about NIR fluorescent probes, including small-molecule fluorophores, biological species, and synthetic nanoparticles, for in vivo NIR fluorescence bioimaging.

4 Experimental and Instrumental Methodology

4.1 Confocal Laser Scanning Microscopy (CLSM)

CLSM is a noninvasive optical imaging technique with high contrast and resolution of images through the addition of a spatial pinhole placed at the confocal plane of the lens to eliminate out-of-focus light. This technique has been widely employed in bioimaging applications. It enables the reconstruction of three-dimensional structures from sets of images obtained at different depths within a thick object, although the penetration depth of CLSM is restricted and only acquires images one depth level at a time. Currently, CLSM has been used for fixed or slowly evolving cellular structures due to its noninvasiveness, high resolution, and real-time optical sectioning capabilities. For instance, upconversion-enabled optical microscope usually comprises an inverted microscope, an NIR (980, 915, or 808 nm) continuous wave (CW) diode laser, a charge-coupled device (CCD) camera, and optical components like dichroic beam splitter and excitation and emission filters. A CLSM setup for upconversion-based imaging based on an inverted microscope and a confocal scanning unit is depicted in Fig. 2.1 [57]. The CW laser emitting at 980 nm is conducted by galvanometer mirrors and then focused by objective lens into the specimen. Light emitted from the location of the scanning spot is deflected by the galvanometer mirrors, separated from the excitation by a reverse excitation dichroic mirror, passed through a confocal pinhole and a filter, and finally captured by a detector consisting of photomultiplier tubes. Multiplexed imaging can be simultaneously

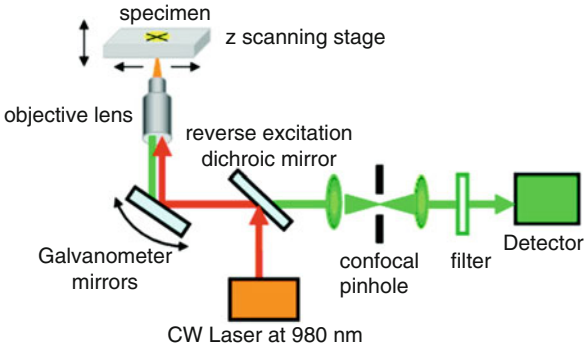

Fig. 2.1 Schematic illustration of a laser scanning upconversion luminescence microscopy (LSUCLM) system setup. The excitation laser beam pathway is depicted in red, and the emission path is displayed in green [57] (Reprinted with permission from Ref. [57], Copyright 2009 the American Chemical Society)

obtained by detecting individual emission wavelength channels. In addition, live cell incubator systems can enable long-term and real-time tracking of cells.

For upconversion luminescence (UCL) in vivo imaging, UCNP dissolved in physiological saline is injected into specially targeted site of mice. After being anesthetized, mice are imaged by utilizing an NIR optical fiber-coupled laser as the excitation source under a safe power (usually no more than 0.2 W/cm^2). A short-pass emission filter is used to prevent the interference of excitation light to the CCD camera. In vivo spectral imaging is carried out with a rate of 10 nm per step and with an enough exposure time due to rather low quantum yield of UCNPs.

4.2 Two-Photon Fluorescence Microscopy

Two-photon fluorescence (TPF) microscopy (Fig. 2.2) is a noninvasive imaging technology for cell and tissue imaging, which shows enhanced penetration depth, increased spatiotemporal resolution, diminished tissue autofluorescence interference, and reduced photodamage as compared to one-photon imaging. Unlike in the case of traditional fluorescence microscopy, the shorter wavelength of emitted light in TPF microscopy is excited by the longer wavelengths of two exciting photons. Generally, the excitation lights employed for TPF technology are in the NIR region. Using NIR light can highly minimize the scattering from the tissues, leading to an increased penetration depth for bioimaging. Meanwhile, the background signal is also greatly suppressed because of the two-photon absorption. Thus, two-photon excitation can be a superior alternative to confocal microscopy because of its deeper tissue penetration, efficient light detection, and reduced phototoxicity.

For two-photon in vivo imaging experiments, mice are first anesthetized and subsequently injected with the solution of NIR fluorescent probes at the targeted area. The images are obtained by utilizing a two-photon microscope with a tunable 680–1080 nm laser. When using zebra fish as animal models, zebra fish are first incubated with NIR fluorescent probes [59]. After washing with PBS (pH 7.4) to remove the remaining probe, TPF fluorescence images are observed under multi-photon laser scanning confocal microscope using a mode-locked titanium-sapphire laser source set at a targeted wavelength with suitable laser power.

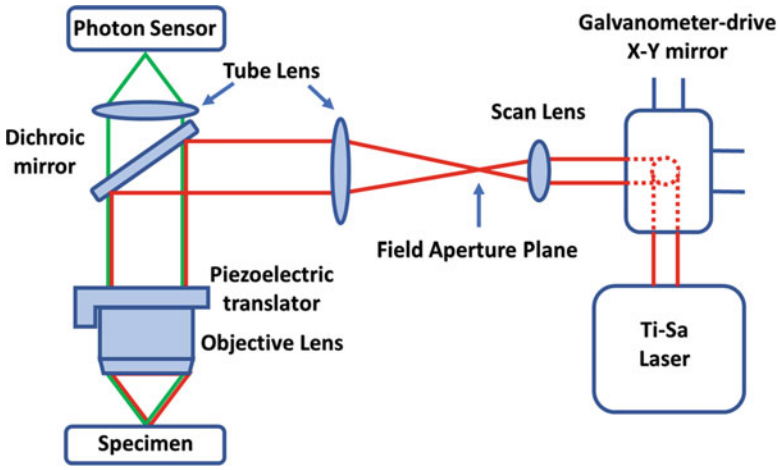

Fig. 2.2 Schematic illustration of two-photon microscope. The excitation laser beam path is shown in red, and the emission pathway is displayed in green [58] (Reproduced with permission from Annual Reviews, Copyright 2000)

4.3 Fluorescence Lifetime Imaging Microscopy (FLIM)

Apart from imaging techniques based on luminescence intensity, FLIM can offer images by measuring the emission lifetime of a signal. The main merit of FLIM is that it can provide quantitative information and monitor cellular dynamic activities with high spatial resolution [14]. Generally, a pulsed light source is necessary, and time-correlated single-photon counting (TCSPC) is adopted in common FLIM. To carry out FLIM, an external frequency-doubled picosecond Nd:YAG laser, operating at 532 nm with a pulse width of 7 ps and a frequency of 50 MHz, is coupled through a single-mode optical fiber into the Leica microscope featuring a FLIM system (Fig. 2.3). Fluorescence is measured by using a 63× oil-immersion objective and detected with an APD at a wavelength of 650–850 nm through a band-pass filter. A time-correlated single-photon counting system is applied to detect the fluorescence lifetime, where time-gated images are acquired with the SymPhoTime software.

5 Key Research Findings

5.1 Organic Fluorophores

Organic fluorophores including NIR dyes, fluorescent proteins, DNA aptamer, and metal complexes are widely used NIR-emitting molecules for bioimaging due to their versatile structures and facile synthesis. In this section, we will discuss the utilizations of these organic fluorophores for NIR imaging.

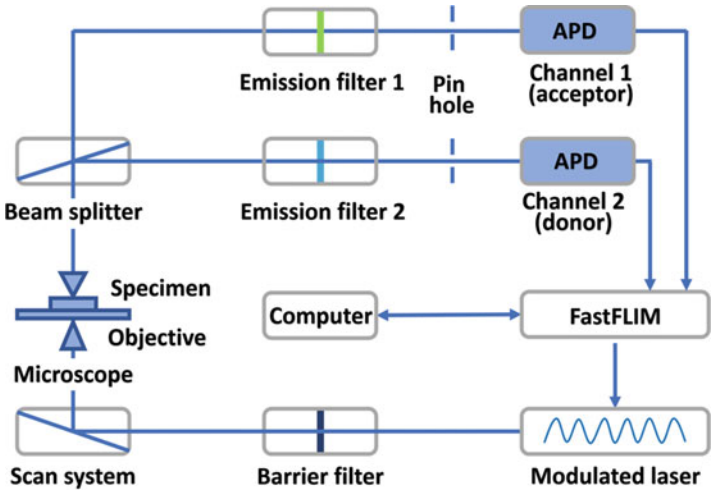

Fig. 2.3 Schematic illustration of the experimental FLIM setup

5.1.1 NIR Dyes

Inspired by fascinating colors of dyes widely used in staining, chemists and materials scientists have greatly widened the applications of fluorescent dyes for in vivo imaging [8–10, 18, 35, 39, 40, 49, 60–64]. Particularly, great zeal has been focused on NIR dyes whose absorption and emission lie in the region of 750–900 nm, since tissues are virtually transparent and have no autofluorescence in this NIR window. Up to now, a large number of NIR fluorescent dyes have been designed and developed for in vivo imaging, such as cyanines [65], porphyrin-based fluorophores [66], xanthene dyes [67, 68], squaraine rotaxanes [26], and phenothiazine-based fluorophores [69]. All of these representative agents are tailored to achieve sufficient stability, specificity, and safety for practical use [39].

Cyanine dyes, as well-known NIR fluorochromes, are usually featured by polymethine chain bridged with two aromatic heterocycles containing nitrogen [70–72]. The absorption and emission of cyanine can be adjusted to NIR region by altering the length of polymethine bridge with the addition of vinylene group to achieve about a 100 nm bathochromic shift. Generally, cyanine dyes are weakly luminescent, since the polymethine bridge in the excited state is flexible and easy to the isomerization [73]. To enhance the quantum yield of cyanine, an effective approach is to stiffen the backbone by introducing chlorocyclohexenyl moiety on the polymethine chain [71]. Traditional cyanine dyes, in essence, are easy to aggregate in aqueous solution. Fortunately, the phenomenon of self-aggregation can be largely alleviated by the introduction of two sulfonate groups to the nitrogen-containing heterocycles. Poor photostability is a major limitation for cyanine dyes, since the fluorophore molecules are quite sensitive to the dissolved oxygen. A promising approach to enhance the photostability is incorporating cyanines into the silica nanoparticles where the nanoparticle shell can effectively protect

the fluorophore molecules. Due to the excellent biocompatibility, a variety of cyanine-based dyes with NIR florescence were effectively used for medical diagnostic imaging in vivo [74–77].

A typical strategy for constructing targeted fluorescent imaging agents requires covalently conjugating the separate target and fluorophore domains. On the other hand, it is possible to develop a single NIR fluorophore-based perform with both targeting and imaging by their inherent chemical structures [76]. For instance, NIR contrast agents were developed to target cartilage with high specificity and performed well for biomedical imaging of bone in vivo [78, 79]. By conjugating with biofunctional groups, zwitterionic NIR fluorophore based on cyanine outperforms commercially available NIR fluorophores IRDye800-CW and Cy5.5 in vivo for image-guided surgery [80]. Recently, NIR fluorescence probes based on cyanine were used for noninvasive in vivo imaging of endogenous H_2S without interfering with biological autofluorescence and for detecting tumors in mice [77]. Covalently conjugating cyanine dye with human serum albumin (HSA) was also used to conduct multimodality (NIR fluorescence/photoacoustic/thermal) imaging and eliminate tumor by intravenously injecting the nanosystem into tumor-bearing mouse model [75]. In addition, it is useful to specifically image different tissues by NIR fluorophores based on their inherent chemical structures. For example, a halogenated fluorophore based on cyanine dyes with NIR emission has been synthesized to successfully identify and preserve parathyroid and thyroid glands in vivo. By means of dual-channel NIR imaging approach, parathyroid and thyroid glands can be unambiguously observed and distinguished in the coexisting blood and surrounding soft tissues [81]. Unlike cationic cyanine, pyrrolopyrrole cyanine (PPCy) is a nonionic cyanine-type dye with NIR absorption and emission, which is favorable for bioimaging after the biofunctionalization [82].

Squaraine dyes are featured with resonance-stabilized zwitterionic structures and consist of a central oxocyclobutenolate-based core linked with two aromatic or heterocyclic moieties on both sides [83–87]. Squaraines usually show sharp and intense absorption and emission bands, which are ascribed to the unique donor-acceptor-donor (D-A-D) electron-transfer structure. However, most of them are water-insoluble and emit below 600 nm with low extinction coefficients, making them unsuitable for deep tissue imaging. Furthermore, the strong tends to aggregate, and the susceptibility of the central cyclobutene ring to undergo chemical attack greatly impede their usage for in vivo imaging [83, 85–87]. These drawbacks can be favorably overcome by the physical encapsulation of squaraines in tetralactam macrocycles. Based on this strategy, various NIR-emissive squaraine dyes were synthesized for in vivo imaging [88]. For example, unsymmetrical NIR squaraines (USq) was successfully developed as an exogenously produced fluorescent probe for fluorescence and photoacoustic imaging of thiol variations in vivo [83]. USq absorbs a wavelength of 680 nm and emits a strong NIR emission at 700 nm, which is suitable for deep tissue fluorescence imaging. Dependent on the presence of different thiols, the fluorescence and photoacoustic signals can selectively disappear. Upon food uptake, bright imaging of aminothiols in blood can be confirmed by in vivo imaging (Fig. 2.4).

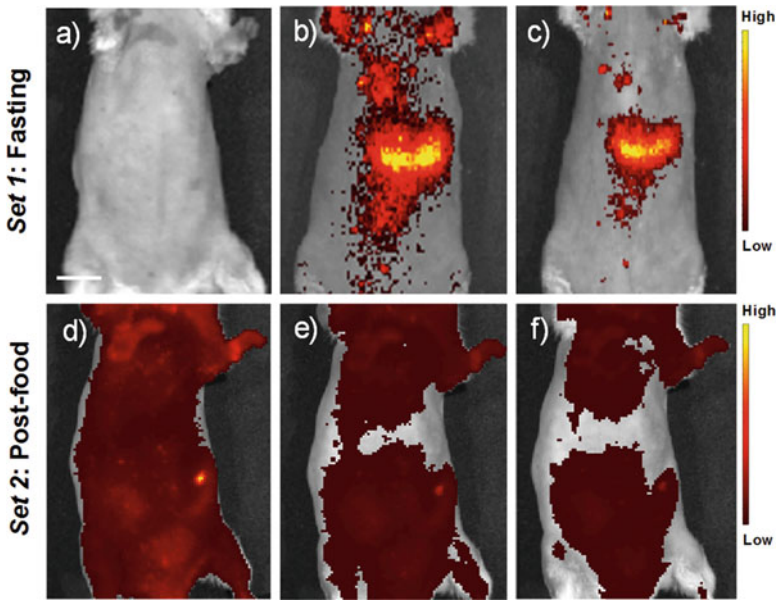

Fig. 2.4 (**a**–**f**) In vivo fluorescence images acquired from postinjection of USq in fasting (set 1) and post-food (set 2) mice [83] (Reprinted with permission from Ref. [83], Copyright 2016 the Royal Society of Chemistry)

Boron dipyrromethenes (BODIPYs) can be regarded as rigid cross-conjugated cyanine dyes with small Stokes shifts but high molar extinction coefficients [89–94]. Moreover, spectroscopic properties of BODIPYs show sharp spectra, shiny fluorescence, high quantum yields, and less influence by solvent polarity and pH [18]. Small chemical modifications on BODIPY structures could induce large emission shifts and improve water solubility as well as the extinction coefficient [72, 73, 95, 96]. The combined features of BODIPYs make them a useful platform to develop NIR-emitting contrast agents for in vivo imaging [63]. Generally, the absorption and emission of pristine BODIPY core exhibit at ~500 nm, but it can be shifted in the NIR regions via various strategies of extending the conjugation length or reducing the resonance energy [89, 90, 92]. Compared with phenyl-substituted counterpart, the absorption and emission of aza-BODIPY attached with thiophene at 1-, 3-, 5-, and 7-positions redshift to 733 and 757 nm, respectively [91]. For example, an NIR-emitting probe based on BODIPY showed non-fluorescence with Cu(II). When injected with Na_2S in mouse, it performed a remarkable fluorescence "switch on" response at 790 nm [97]. More and more NIR fluorophores based on BODIPY were successfully constructed for imaging in vivo with high selection and sensitivity [96–98]. For instance, aniline-substituted aza-BODIPY with pH-response was employed to selectively image tumor. Meanwhile, photodynamic therapy (PDT) and therapeutic self-monitoring were also achieved via encapsulating it in cRGD-functionalized micelle (Fig. 2.5) [98].

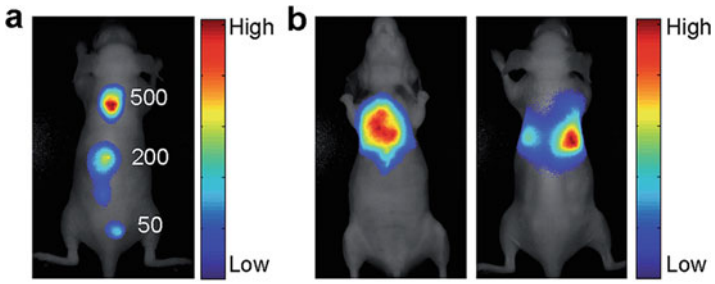

Fig. 2.5 (**a**) In vivo NIR fluorescence imaging sensitivity and (**b**) depth of U87MG cells labeled with cRGD-Net_2Br_2BDP NP [98] (Reprinted with permission from Ref. [98], Copyright 2015 the Royal Society of Chemistry)

Xanthene dyes, as a type of classical fluorophores, possess good photostability and moderate hydrophilicity [15]. After rational chemical modifications, they show excellent NIR emission and are favorable for biological imaging applications in living animals [99–102]. For example, several rhodamine-based NIR dyes were developed for imaging endogenously generated HClO in the living animals [101]. Moreover, NIR fluorescent Si-rhodamine dyes were developed to be powerful labeling tools for multicolor bioimaging [102].

Porphyrins are conjugated tetrapyrrolic macrocycles and considered as "pigments of life," thanks to their extensive presence in biological systems [103–105]. Due to outstanding and versatile features, porphyrins can be easily functionalized and undergo various supramolecular interactions [104]. The remarkable and strongly tunable luminous features of porphyrinoids enable them with a great potential for bioimaging with strong NIR emission [103]. Up to now, an effective approach to gain bright NIR fluorescence is to extend the conjugation of ring. This strategy has been demonstrated by the expansion of ring conjugation in Pt(II)-porphyrins through exploring the substituent effect in *meso* positions [105]. Porphysomes were developed from self-assembled porphyrin bilayers, which possess large extinction coefficients, structure-dependent fluorescence, and unique photothermal and photoacoustic features. The optical features and relatively good biocompatibility of porphysomes prove the multimodal potential of organic fluorophores for bioimaging and therapy [106]. For example, a cleavable folate-photosensitizer conjugate was successfully used for both NIR fluorescence imaging and PDT of cancer cells with high specificity (Fig. 2.6) [107].

Phthalocyanines, termed tetrabenzotetraazaporphyrins, are analogs of tetrabenzoporphyrins containing N atoms in the *meso* position of the ring in place of C atom. They are featured by two sets of absorption bands in the UV-Vis region. One called B band is located at around 350 nm, and the other one termed Q band is placed in the region of 600–700 nm. It should be noted that protonation could cause remarkable redshift of the Q band and accordingly the emission peak is present at

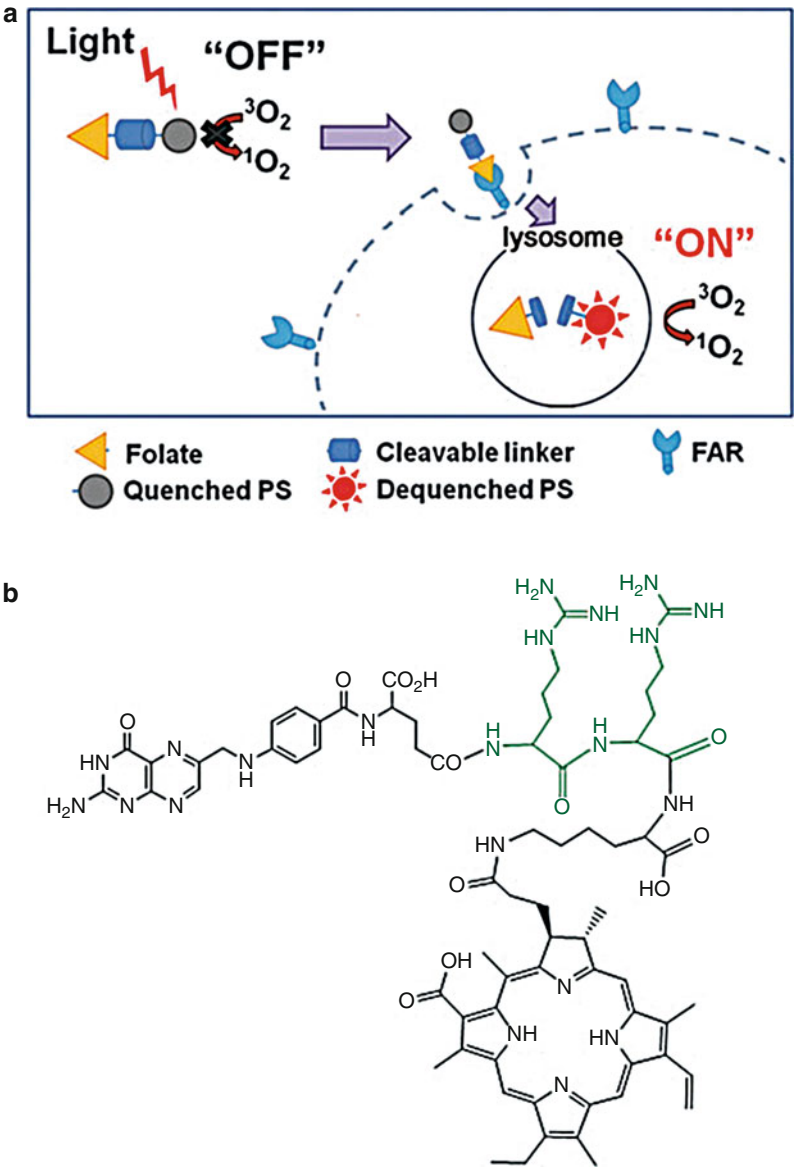

Fig. 2.6 (**a**) Schematic illustration of cleavable folate-photosensitizer conjugate for NIR fluorescence imaging and photodynamic therapy. (**b**) Chemical structure of the conjugate [107] (Reprinted with permission from Ref. [107], Copyright 2014 the Royal Society of Chemistry)

longer wavelength. Moreover, it can also achieve redshift of the fluorescence and absorption by expanding the π-conjugation structure of the macrocycle [64]. Phthalocyanines can host many metal ions in the core and undergo wide chemical modifications.

Except for the abovementioned NIR fluorescent dyes, other NIR dyes or two-photon excited fluorophores were also developed for in vivo imaging [107–111]. For example, red emitting dicyanomethylenebenzopyran probe (DCMC-N_3) was successfully used to detect the presence of HS in vivo by employing two-photon microscopy [31, 112]. NIR-II molecular fluorophores based on shielding unit-donor-acceptor-donor-shielding unit (S-D-A-D-S) structure developed very recently may offer rich opportunities to improve the performance for NIR-II bioimaging [109].

5.1.2 Metal Complexes

Transition metal complexes are a versatile type of emitters that provide a series of inherent merits over traditional fluorescent materials [62]. Firstly, they show large Stokes shifts due to the S_1-T_1 intersystem crossing, which can effectively discriminate the excitation and emission light, and prevent fluorescence quenching caused by self-absorption. Secondly, the emissive excited state displays long lifetime within the range of μs to ms. Thus, metal complexes can be used for time resolution imaging. Furthermore, metal complexes such as d^6, d^8, and d^{10} metal ions – Re(I), Os(II), Ru(II), Ir(III), Pt(II), Au(III), Au(I), and Cu(I) – possess emission in the NIR region. Metal complexes exhibit high luminescence efficiency through a rational modification of ligand frameworks including the inclusion of donor-acceptor push-pull systems, the change of the π-conjugation length, or the addition of heterocycles. Thus, metal complexes present many advantages including easily tunable chemical and photophysical properties, high emission quantum yields, long phosphorescence lifetime, large Stokes shifts, and emissive properties that are highly sensitive to subtle changes in the local environment, which collectively enable metal complexes with a great potential in bioimaging [113].

Some metal complexes show two-photon absorption. Due to the excitation of NIR light in two-photon absorption metal complexes, they possess features of deep tissue penetration, weak autofluorescence, low photo-bleaching, and low phototoxicity for bioimaging [114]. For instance, by illumination with 840 nm laser, two-photon active Zn(salen) complex was employed for imaging of living cells and organism with high signal-to-noise contrast and good membrane permeability [115, 116].

5.1.3 Fluorescent Proteins

Fluorescent proteins are widely used as contrast agents for bioimaging with high spatiotemporal resolution [48, 55, 117–119]. A prerequisite for in vivo fluorescence imaging is the safety of contrast agents. As a fluorescent probe from biological system, NIR fluorescent proteins are safe enough and would be useful to increase the sensitivity of in vivo imaging [55, 120]. For instance, fluorescent proteins were used for whole-body and deep tissue imaging to explore the metastasis, cell migration, tumor distribution, and embryogenesis.

To obtain the fluorescent proteins with NIR excitation and emission, several feasible approaches have been developed. A useful strategy is the exploration of phytochromes for NIR fluorescence imaging. Phytochromes root in plant and

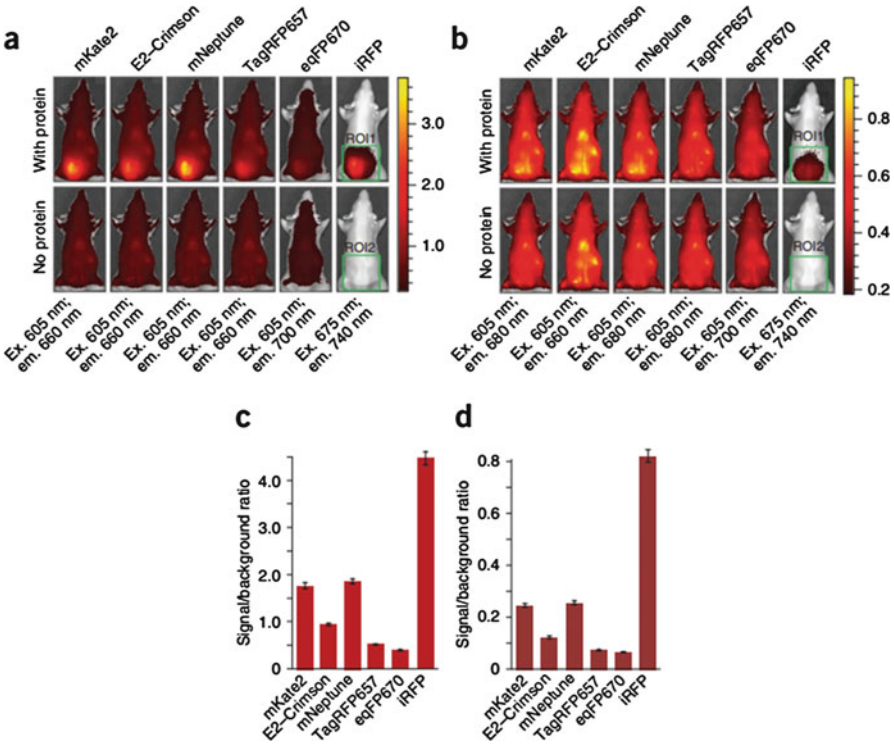

Fig. 2.7 (**a**–**d**) Comparison of near-infrared fluorescent protein (NIRFP) with far-red GFP-like proteins in mouse phantom [122] (Reprinted with permission from Ref. [122], Copyright 2011 Nature Publishing Group)

bacterial photopigments, which can absorb NIR light and emit weak fluorescence. Through chemical modifications, engineered NIR fluorescent proteins from phytochromes show excellent NIR absorption and good aqueous quantum yield [117]. For example, NIR fluorescent proteins selected by using bacterial expression method showed low toxicity in bacterial expression experiments. After distributed in mice, they presented relatively high brightness and no toxicity [121]. In contrast to far-red green fluorescent protein (GFP)-like proteins, NIR fluorescent proteins display a considerably higher SBR in mice because of their infrared-shifted spectra. NIR fluorescent probes could facilitate the imaging of biological processes in living tissues with low autofluorescence and light scattering. For example, NIR fluorescent proteins with bright luminescence were used to label live mammalian cells and show low scattering and absorption in most tissues (Fig. 2.7) [122]. The bright phytochrome-based proteins are stable and low cytotoxic and exhibit bright fluorescence in both tissues and whole animals with high SBR.

Fluorescent proteins with bright NIR emitting are undoubtedly suitable for whole-body imaging in vivo. However, it is not easy to develop fluorescent proteins with NIR emission. Proteins labeled with NIR fluorescent dyes would be an

alternative approach for targeted tumor imaging with NIR light. Epidermal growth factor receptor (EGFR) protein, a vital transmembrane protein in the family of tyrosine kinase receptors, plays an important role in physiological and pathological processes. Since aberrant overexpression of EGFR is related to many kinds of cancers, it was used for noninvasive imaging of tumor in vivo. For example, Eaff800, an EGFR-specific Affibody molecule labeled with NIR fluorescent dye IRDye800CW maleimide, was successfully used to identify A431 xenograft tumor in mice. Interestingly, combined with a human EGFR type 2 (HER_2), Eaff800 could clearly distinguish the overexpression of EGFR and HER_2 in tumors by showing different organ distribution pattern and clearance rate [123].

Fluorogen-activating proteins (FAPs) are single-chain variable fragment-based fluoromodules that bind to non-fluorescent dyes (fluorogens), yielding thousandfold fluorescence enhancements. It can specifically bind targeting moieties and activate non-fluorescent dyes to visualize tumor with low nonspecific tissue staining, high contrast, fast clearance, and good tissue penetration. Affibodies, small peptides of 58 amino acids with high affinity and specificity to target proteins, are used to conjugate organic fluorophores and fluorescent proteins (affiFAP) for in vivo tumor imaging. Alternatively, FAPs binding to triphenyl methane analogs of malachite green (MG) dyes with NIR fluorescence emission may also be helpful, where probes can be targeted to a tumor site and fluorogens added serve for fluorescence visualization. For example, an FAP/MG complex was successfully employed to prepare responsive fluorescence probes for in vivo tumor imaging. Compared with conventional fluorophore-conjugated Affibodies, preincubated affiFAP/fluorogen complex could label EGFR-enriched tumors with similar perivascular tumor distribution but with higher target specificity. Due to specific fluorescence activation upon the FAP binding, no nonspecific background fluorescence was observed. The rapid FAP/fluorogen association and probe clearance allowed either sequential administration of probe and dye or local dye application with high tumor-to-background ratio (TBR). The fluorogen activation, coupled with rapid clearance of unbound small-molecule fluorogen when employing a pre-targeting approach, should significantly reduce background fluorescence from probes. Stepwise labeling can potentially provide more temporal and spatial control during the labeling procedure [124]. This pre-targeted activation approach may substantially improve the TBR and highly enhance the sensitivity for early or residual tumor diagnosis and surgery.

Directly conjugated IR dyes possess useful properties for in vivo imaging, but the conjugation often substantially alters the circulation dynamics of targeting moieties. A new tumor-targeting probe, affiFAP, was developed, which consists of an FAP and a protein that specifically binds EGFR (Affibody) [125]. This compact molecular recognition reagent can reversibly bind and activate fluorescence of otherwise non-fluorescent dyes and allows tumor visualization with low nonspecific tissue staining. Molecular pre-targeting of affiFAP with fluorogenic dye was employed to achieve high contrast, fast clearance, and good tissue penetration. Due to the instability of proteins, fluorescent proteins are still not employed for in vivo imaging in the purified form. By coating an NIR fluorescent protein with a silica nanoshell, the obtained system showed high quantum yield and photostability due to the

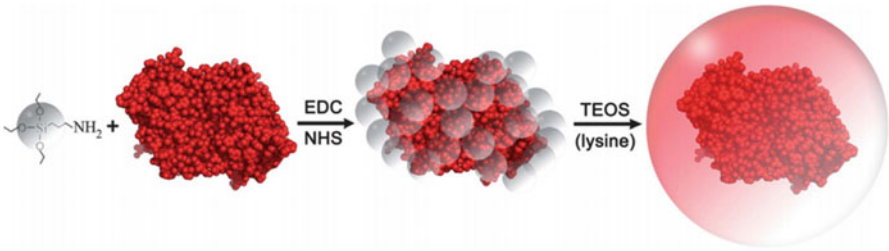

Fig. 2.8 Schematic layout of procedures for individually coating NIR fluorescent protein with a silica nanoshell [126]. *EDC* 1-ethyl-3-(3-dimethylaminopropyl)carbodiimide hydrochloride, *NHS* *N*-hydroxysuccinimide, *TEOS* tetraethyl orthosilicate (Reprinted with permission from Ref. [126], Copyright 2013 the Royal Society of Chemistry)

protection of silica shell and can be successfully used as safe and robust NIR fluorescence probe for whole-body imaging of mouse via the injection from the tail vein (Fig. 2.8) [126].

5.1.4 Aptamers

Aptamers are single-stranded DNA or RNA and can specifically recognize their targets. For instance, aptamers could be integrated into the DNA nanostructures either via base pair hybridization or as a component in the assembly procedure. DNA nanostructures have good biocompatibility, high tissue penetration, and sufficient stability in biofluids, enabling them for in vivo imaging. Due to inherent binding abilities of aptamers and superior properties of DNA nanostructures, increasing attention has been focused on the establishment of aptamer-integrated DNA nanostructures for bioimaging [19, 33, 127]. In addition, aptamers with many desirable features including small size, simple synthesis, facile chemistry, and lack of immunogenicity can specifically bind to a variety of target molecules. Aptamers, engineered with substantially enhanced biochemical functions and unique specificity, are powerful in bioimaging applications [128].

Although aptamers have emerged as promising fluorescence probes for cancer imaging, limitations including limited contrast and high background still hamper their applications in bioimaging. Aptamers, conjugated with dyes or nanoparticles as activatable probes, can change their optical properties upon biological interactions for the fluorescence imaging [127]. Thus, an activatable aptamer probe (AAP) was developed to specifically bind the membrane proteins of cancer cells, exhibiting contrast-enhanced tumor visualization in vivo (Fig. 2.9). The fluorescence of AAP can be activated by undergoing a conformational change upon targeting to cancer cells. After imaging a type of cancer cells in vivo, AAP can be specifically activated by targeted tumor cells with a considerable fluorescence enhancement. In contrast to other aptamer probes, AAP performs significantly enhanced image contrast, minimal background signals, and shorten diagnosis time [129].

Aptamers have been demonstrated for target imaging of cancer cells in vivo. However, due to limited affinity and the nuclease degradation of aptamers, typical

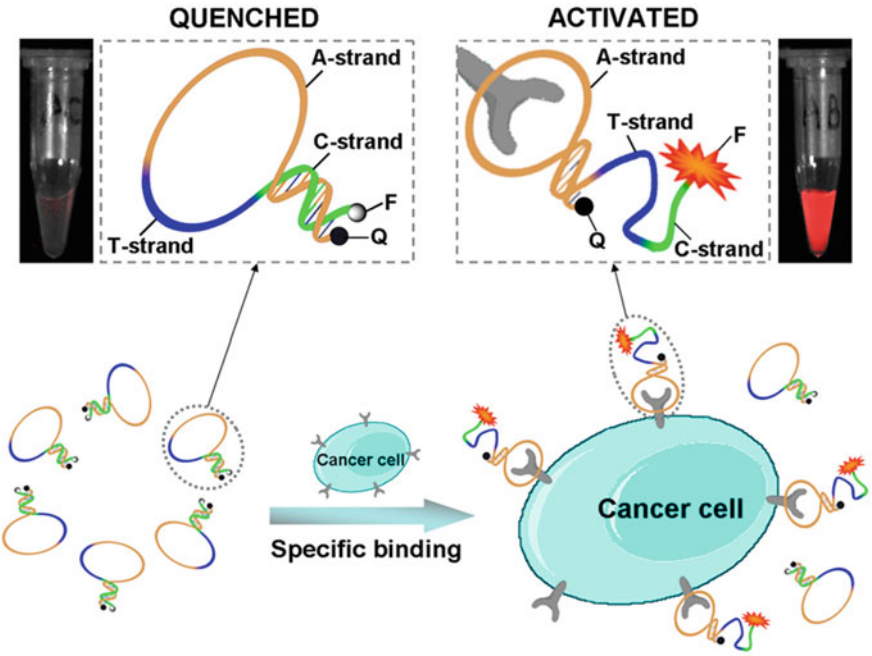

Fig. 2.9 Schematic representation of in vivo cancer imaging by using AAP on account of cell membrane protein-triggered conformation alteration [129] (Reprinted with permission from Ref. [129], Copyright 2011 National Academy of Sciences)

aptamers have not yet been used in practical in vivo imaging. Polyethyleneimine (PEI) can substantially lower the degradation rate of aptamers and improve their pharmacokinetics. Thus, PEI/aptamer molecular complexes were successfully used for tumor imaging in vivo by utilizing deoxyribonuclease (DNase)-activatable fluorescence probes (DFProbes) to detect the DNA degradation. Compared with free aptamer, the complexes exhibited excellent passive tumor targeting and prolonged circulation time in tumor-bearing mice [130].

Hybridization chain reaction (HCR), featured as multiplexed, enzyme-free, and isothermal molecular signal amplification, enables simultaneous imaging of multiple target mRNAs [131]. For instance, a multiplexed fluorescence in situ hybridization method on account of orthogonal amplification with HCR was developed to simultaneously map five target mRNAs in fixed zebra fish embryos with deep penetration, high SBR, and sharp signal localization (Fig. 2.10) [132].

5.2 Nanoparticles

Previous sections are concentrated on the advances of organic NIR fluorophores. On the other hand, there are significant advantages to locate the contrast agents inside a

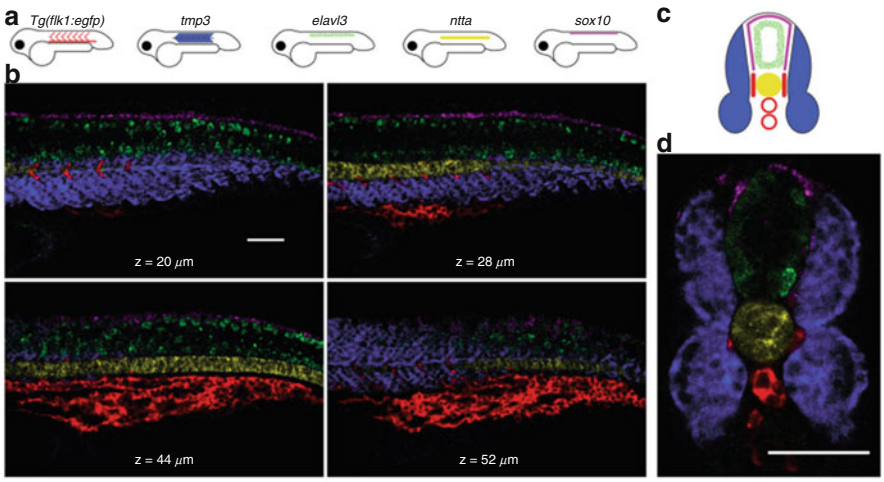

Fig. 2.10 (**a**–**d**) Multiplexed mapping in fixed whole mount and sectioned zebra fish embryos [132] (Reprinted with permission from Ref. [132], Copyright 2010 Nature Publishing Group)

nanoparticle for diagnosis and therapy. Nanoparticles with large sizes and well steric protection can effectively extend the circulation times. Generally, the preparation of nanoparticles for bioimaging contains several steps, including the synthesis, coating, surface modification, and bioconjugation. Nanoparticles with desired ligands onto their surface can be easily engineered by physical adsorption or chemisorption. Nanoparticles engineered by chemisorption not only exhibit high colloidal stability, good biocompatibility, and sufficient water solubility but also can covalently link functional groups for further bioconjugation.

The judicious design of nanoparticles with multiple functionalities has fueled significant progress in bioimaging. Fluorescent probes based on nanoparticles have blossomed in recent years thanks to their superior properties, making them hopeful alternatives to organic dyes and fluorescent proteins for cancer imaging and therapy. For instance, inorganic semiconductor QDs show much better fluorescent performance for bioimaging than traditional organic fluorophores due to their tunable emission, enhanced photostability, and high quantum yields. Thus, the rational choice of suitable nanoparticle compositions and the implement of surface functionalization would facilitate the design of fluorescent nanoparticle probes that emit enhanced fluorescence and display increased selectivity.

5.2.1 Polymer Nanoparticles

To date, polymer nanoparticles have been widely developed and used for fluorescent imaging [133–136]. In general, polymer-based nanoparticles with various morphologies can be prepared by physical encapsulation or chemical conjugation of contrast agents (such as inorganic nanoparticles or fluorescent dyes). In these nanosystems, polymers play a vital role in enhancing the aqueous stability of contrast agents,

efficiently transporting contrast agents to pathological areas, and improving the imaging [137].

Conjugated polymers (CPs), featured by a backbone with a delocalized electronic structure, were demonstrated to bind analyte receptors with obvious responses [138, 139]. To enhance the water dispersibility of neutral CPs, a variety of physical processes including nano-precipitation [140], mini-emulsion polymerization [141], and solvent extraction single emulsion [142] can be used. Usually, bare CP nanoparticles possess high photostability, good biocompatibility, and efficient permeability to cellular cytoplasm. CPs with NIR emission can be easily obtained by doping hydrophobic dyes into CP nanoparticles. Since the polymeric backbone of CPs is connected by conjugated electrons, any small perturbation of the conjugated system would result in large signal change and subsequently affect the entire assembly. Moreover, CPs with hyperbranched structures and biocompatible side chains could covalently couple many biological probes or drug molecules and efficiently transport them into live cells, which allow the diagnosis and therapy simultaneously possible. Thus, their structures and function can be tuned easily for target applications through the judicious choice of the composition and surface modification. To enhance the brightness and cell uptake efficiency, CP-based nanoparticles (CPNs) with tunable size and optics, excellent biocompatibility, and low toxicity were designed and synthesized for bioimaging [141–146].

Generally, the quantum yields of CPs would drop greatly by the nanoparticle formation. Exceptionally, cyano-substituted derivatives of poly(p-phenylene vinylene) in the aggregated film state showed efficient interchain excitonic photoluminescence in the NIR region with reasonably high quantum yields, which enabled researchers to develop NIR fluorescent probes based on CPs [147]. For instance, nanoparticle probes based on cyanovinylene backbone CPs with bright NIR fluorescence were successfully used for real-time sentinel lymph node mapping (SLNs) in mice and displayed high chromophore density and strong fluorescence, which can precisely and noninvasively identify superficial SLNs and fluorescently visualize deep SLNs (Fig. 2.11) [141].

Furthermore, polymer dots (P-dots) are an emerging class of fluorescent probes due to their large absorption coefficients, excellent brightness, high photostability, and nontoxicity [148–155]. Although the research of P-dots for bioimaging is still at an early stage, various strategies have been developed to enlarge the versatility and biofunctions of P-dots for in vivo imaging, such as tuning the emission wavelength, developing new preparation approaches, modifying the nanoparticle surface, and doping functional molecules. Recently, an emerging strategy was developed to effectively construct P-dot bioconjugates, demonstrating their features of specific cellular targeting and bio-orthogonal labeling. For example, a highly fluorescent P-dots based on CPs with benign toxicity and bright NIR emission were covalently attached with cancer-specific peptide ligands and successfully applied for target imaging of malignant brain tumors in mice (Fig. 2.12) [152].

In contrast to CPs, conjugated polyelectrolytes (CPEs) are water-soluble polymers, featuring as π-conjugated backbones and ionic side chains [12]. CPEs possess tunable size, high photostability, and good biocompatibility and can react with a

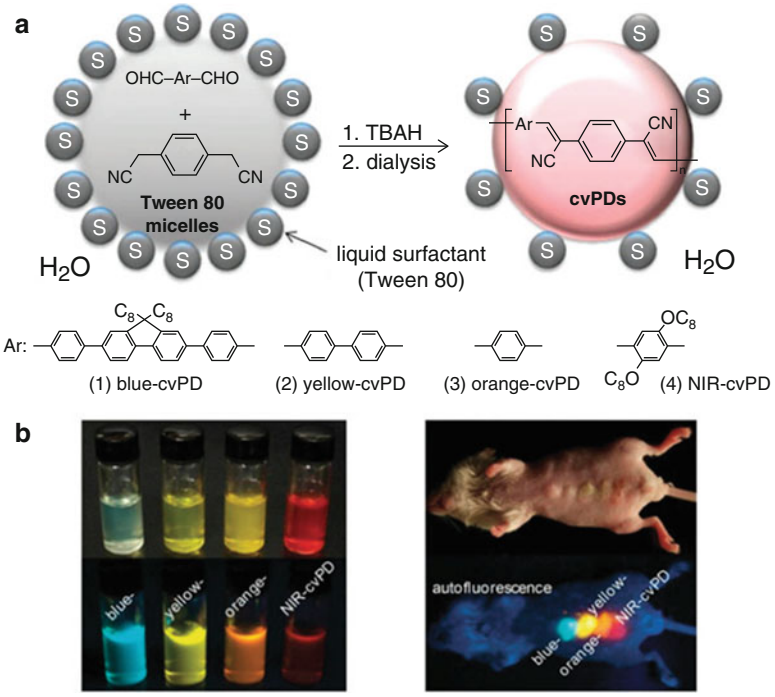

Fig. 2.11 (**a**) Schematic layout illustrating colloidal synthesis of cyanovinylene-backboned polymer dots (cvPDs). (**b**) True-color images of cvPDs (left) and a cvPD-injected live mouse (right) under room light (top) and UV excitation at 365 nm for fluorescence (bottom) [141]. TBAH, tetrabutylammonium hydroxide (Reprinted with permission from Ref. [141], Copyright 2010 the Royal Society of Chemistry)

variety of biofunctional groups and desired biorecognition elements. Similar with CPs, their absorption and emission properties can be finely tuned by backbone modifications. For example, grafted CPEs complexed with cisplatin were successfully demonstrated not only as effective contrast agents for NIR imaging in vivo but also to monitor the drug distribution in vivo by intravenous injection [156].

In addition, micellar nanocarriers containing amphiphilic block copolymers can also be developed for bioimaging, because of the drug and NIR fluorophore encapsulation capability of the hydrophobic micelle core and the biocompatibility and targeting resulted from the hydrophilic corona [157]. For example, in vivo tumor diagnosis and therapy were simultaneously achieved by using micellar nanocarriers based on the combination of pH-responsive micelle and a photosensitizer. In the system, pH-responsive micelles can efficiently deliver the encapsulated protoporphyrin IX to tumors, displaying clear imaging of tumors in vivo [158].

5.2.2 Quantum Dots

Semiconductor QDs are colloidal nanocrystals with sizes between about 1 and 10 nm close to the exciton Bohr radius. In general, each nanocrystal is composed of

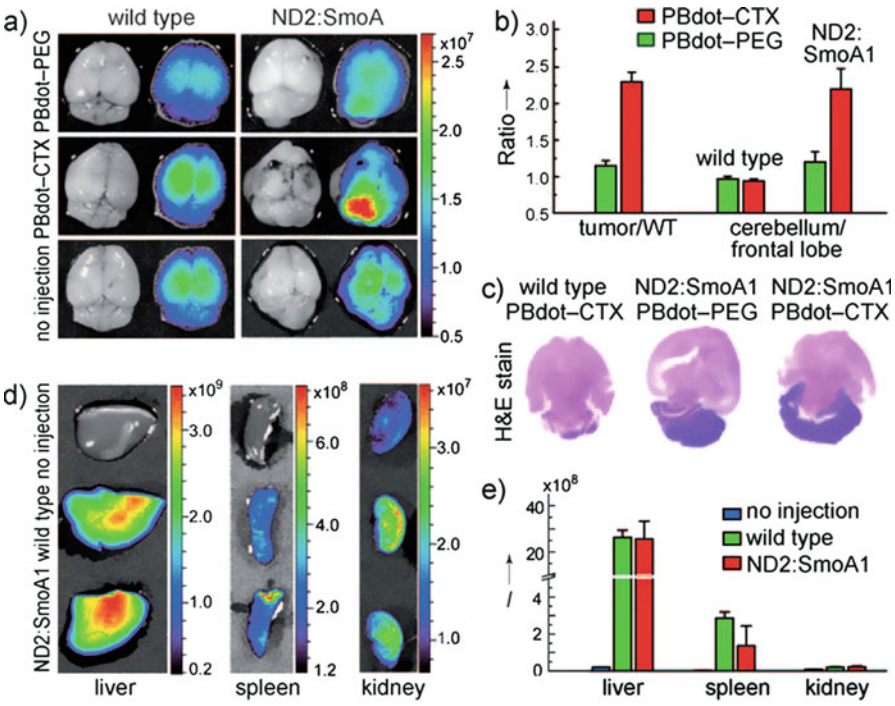

Fig. 2.12 (**a**) Fluorescence imaging of healthy brains (left) and medulloblastoma tumor ND2:SmoA1 (right) by PBdot. (**b**) Quantified fluorescence signals in ND2:SmoA1. (**c**) Histological examination of the mouse brains in (**a**). (**d**) Biophotonic images of resected livers, spleens, and kidneys from wild-type and ND2:SmoA1 mice. (**e**) Biodistribution of the PBdot probes in the resected organs [152] (Reprinted with permission from Ref. [152], Copyright 2011 Wiley-VCH Verlag GmbH & Co. KGaA, Weinheim)

elements from the periodic groups of II–VI or III–V with hundreds to thousands of atoms. They are typically synthesized from combinations of zinc(II), cadmium(II), selenide, and sulfide. QDs are famous for the quantum confinement effect, endowing them with unique size-dependent emission feature. In addition to tuning the emission wavelength of QDs by changing their size, engineered QDs with different materials can cover the spectral range from the ultraviolet to the infrared. In addition, QDs possess a lot of advantages including high photostability, strong luminescence with narrow and symmetric emission, size-tunable emission wavelength, large Stokes shift, good solution processibility, and versatile surface chemistry, which make QDs with a bright potential for NIR fluorescent imaging in vivo [36, 38, 45, 159, 160].

Most QDs applied for bioimaging are constructed with core/shell structures, where the nanocrystal core is usually coated with another material to protect and even enhance their optical properties. Meanwhile, to meet the requirement of in vivo imaging, QDs must have remarkable NIR emission, excellent biocompatibility, high photostability, and good water solubility. However, many of the existing QDs synthesized from hydrophobic conditions show water insolubility, preventing their

further bio-applications. Thus, hydrophilic modification is a vital step prior to the bioimaging application. To date, a variety of strategies developed to functionalize the hydrophobic QDs are focused on modifying their surfaces or constructing additional shells, including direct encapsulation by hydrophilic polymers, ligand exchange with hydrophilic ligands, and passivation of the QD surface. One useful approach for enhancing the dispersity of QDs in aqueous solution is the surface modification with anionic carboxylate groups. In addition, QDs with bright fluorescence and high quantum yields are important for their in vivo imaging application. QDs with narrow emission wavelength and high quantum yields are often obtained by solvothermal methods using organometallic precursors in nonpolar organic solvents. Due to the hydrophobic surface coating, QDs obtained from these methods require hydrophilic modifications for bioimaging purposes. 3-Mercaptopropionic acid-capped CdTe QDs emitted in the range 700–800 nm were prepared with microwave-assisted aqueous synthesis, and they were highly accumulated in the liver after intravenous injection. Although QDs can passively target tumorous sites in living mice resulted from EPR effect, the underlying targeting mechanism limits their applications to further distinguish tumors with different phenotypes. In this context, an active targeting strategy is important for the tumor detection by QDs [161].

Numerous methods have been developed to synthesize QDs directly in aqueous solution, since these hydrophilic QDs with lower toxicity might be more favorable for imaging in vivo. For instance, NIR Ag_2Se QDs with tunable fluorescence and low cytotoxicity were synthesized by using Na_2SeO_3, silver ions, and alanine at 90 °C in aqueous solution and subsequently used for bioimaging in living mice [163]. Moreover, such aqueous QDs with NIR emission were also employed for bioimaging in vivo with enhanced distribution, extended circulation time, and targeting tissue ability [162, 164, 165]. In another case, CdTe/CdS core/shell QDs with tunable NIR fluorescence were prepared in aqueous solution by a facile one-step method and showed high-sensitive imaging in targeted tumor sites in vivo [166]. Moreover, ultrasmall CdTe QDs with excellent water dispersibility and tunable NIR emission were synthesized by microwave method and successfully employed for tumor-targeting imaging in mice (Fig. 2.13) [162].

NIR QDs were also constructed to track the stem cells and labeled neutrophils to monitor their behavior inside living animals by noninvasive imaging [167]. For instance, due to minor autofluorescence of tissues in the second NIR region (NIR-II, 1.0–1.4 μm), Ag_2S QDs in NIR-II region were successfully used for dynamic monitoring of human mesenchymal stem cells (hMSCs) in vivo detectable of as few as 1000 cells [168]. The in situ translocation and dynamic distribution of transplanted hMSCs in the lung and liver can be detected up to 14 days with a high temporal resolution no more than 100 ms (Fig. 2.14).

In addition, NIR QDs were employed to stain the whole body of small animals with multiple color emission. For example, glutathione-coated QDs conjugated with glutathione S-transferase (GST) tagged luciferase were employed for whole-body fluorescence imaging in vivo [169]. Moreover, the sensitivity of NIR QDs was systematically investigated for in vivo imaging. Commercial Q-dot 800 QDs were

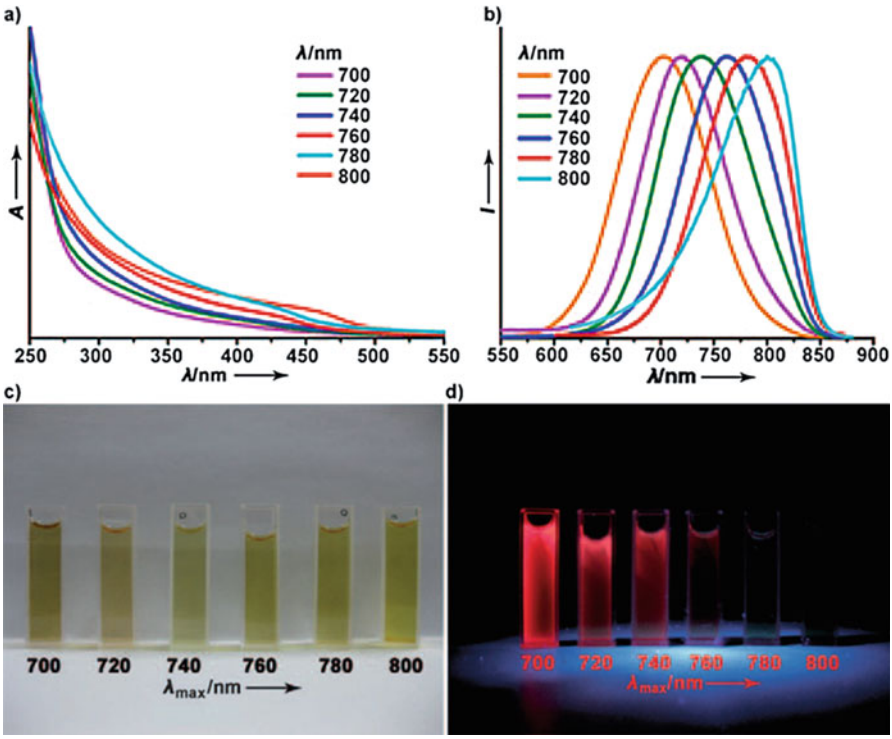

Fig. 2.13 (**a**) UV and (**b**) photoluminescence spectra of ultrasmall CdTe QDs with controllable emission in the range of 700–800 nm (λ excitation, 450 nm). Photographs of QDs in aqueous solution under (**c**) ambient light and (d) UV irradiation (λ excitation, 365 nm) [162] (Reprinted with permission from Ref. [162], Copyright 2011 Wiley-VCH Verlag GmbH & Co. KGaA, Weinheim)

conjugated with cell-penetrating peptides (CPPs) and subsequently employed to label oral carcinoma cells via endocytosis. Then, the QD-labeled cells were inoculated in several parts of nude mice in different amounts. The results displayed a sufficient signal with at least 104 QD-labeled cells, and the longest observable time extended to more than 16 days [170].

Multifunctional NIR fluorescence probes based on QDs were also developed for targeted tumor imaging in vivo [171]. Moreover, functionalized QDs have been widely explored for multimode bioimaging. Thus, it is important to develop suitable surface coatings to construct efficient QDs for bioimaging. In order to obtain functionalized QDs, a variety of surface coating methods have been applied, such as compact ligands [172], polymer immobilization [173], micellar encapsulation [174, 175], and polyethylene glycol (PEG) coating [176]. For instance, the Cerenkov luminescence of [^{64}Cu] $CuInS_2$/ZnS QDs, which were optimized by controlling the QD amount and ^{64}Cu radioactivity level, were successfully employed for in vivo tumor imaging [177]. Two-photon excitation technique is an attractive tool for in vivo tissue imaging, since it makes QD excitation in the NIR window with deep

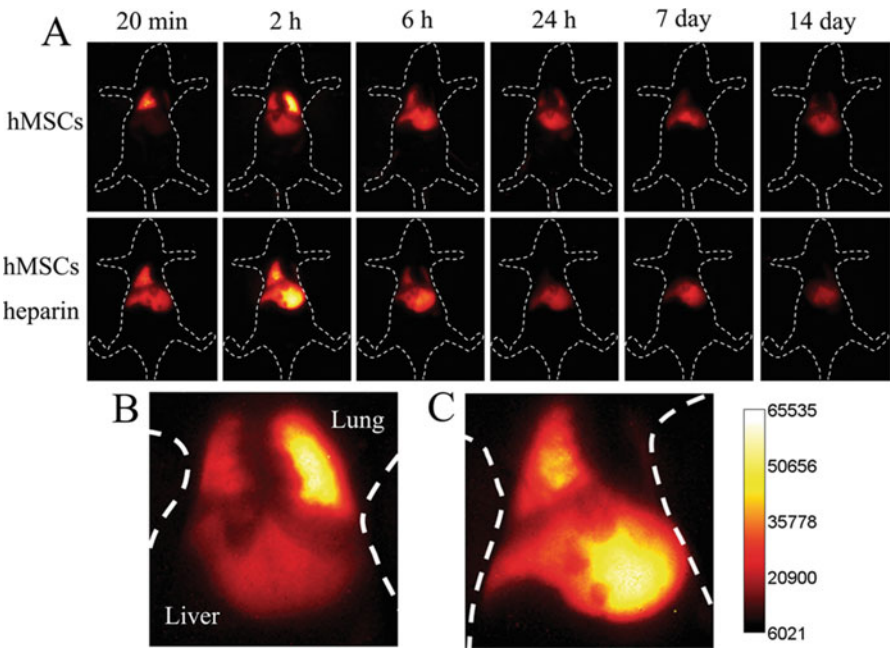

Fig. 2.14 (**a**–**c**) In vivo tracking of hMSCs via intravenous injection of Ag_2S QDs in mice [168] (Reprinted from Ref. [168], Copyright 2013 Wiley-VCH Verlag GmbH & Co. KGaA, Weinheim)

tissue penetration and negligible autofluorescence. Except for imaging QDs inside the tissue, they can also be applied for coating glass pipettes that are used to target visually identified neurons for electrophysiological studies. For example, glass pipettes coated with QDs that can exhibit excellent two-photon excitation signals were used for deep brain tissues imaging [178].

5.2.3 Carbon Dots

Carbon dots (C-dots), as fluorescent nanocarbons with sizes below 10 nm, are accidently discovered by purifying the single-walled carbon nanotubes (SWCNs) [179]. C-dots possess sp^2 character ascribed to three-dimensional nanocarbons, which are different from nanocrystalline graphite. Similar with traditional QDs, C-dots combine several favorable features such as size- and wavelength-dependent emissions, less photo-bleaching, and ease of bioconjugation. In addition, C-dots have many additional merits including easy preparation, low toxicity, easy excrement, weak protein adhesion, low disturbance by the immune system, and versatile surface chemistry. Due to the excellent photoluminescent properties and good biocompatibility, C-dots are attractive and eco-friendly candidates for bioimaging applications [46, 180–185].

Up to now, many strategies have been developed to produce C-dots in low cost and at a large scale [186–190]. Approaches for preparing C-dots can be usually classified into two categories: top-down and bottom-up approaches. Top-down

approaches for the fabrication of C-dots from prime materials like graphite powder or multi-walled carbon nanotubes (MWCNs) are generally executed under severe physical or chemical conditions such as laser ablation, arc discharge, and electrochemical oxidation [191]. Generally, C-dots obtained by laser ablating method are not fluorescent, but the surface passivation could substantially enhance their fluorescence intensity. Bottom-up approaches usually employ molecular precursors such as glucose and fructose with external energy source including ultrasonication, microwave pyrolysis, and heating. Typically, the surfaces of raw materials are oxidized by nitric acid (HNO_3) and then purified by separation processes such as centrifugation, dialysis, and electrophoresis. Besides, C-dots prepared by hybrid strategies combining elaborate functionalization with mild carbonization processing may show distinct surface functionalities.

Due to abundant carboxylic acid moieties spreading on the surface, C-dots possess sufficient water solubility and are facile to be functionalized with a variety of organic, inorganic, polymeric, and biological species. Moreover, C-dots possess great advantages including nearly isotropic shapes, ultrafine dimensions, tunable surface functionalities, as well as simple and cheap synthesis, making them highly potential in fluorescent bioimaging. However, pure C-dots are generally not fluorescent and do not display biofunction because of their poor interaction with biological species. Thus, it is important to engineer the functional surface of C-dots with tailored biological coatings for improving the fluorescence intensity [192].

Fluorescent C-dots are usually water-soluble with high photostability and good stability [193]. For instance, C-dots obtained from the passivation of commercial lampblack can be stored for up to 6 months [194]. Meanwhile, systematic cytotoxicity evaluations demonstrated that both raw C-dots and passivated C-dots exhibited low cytotoxicity at the concentration required for fluorescence bioimaging [182]. Thus, to meet the imaging application in vivo, it is important to engineer the surface functionality of C-dots with NIR emission, high quantum yield, excellent biocompatibility, and durable photostability [6].

NIR fluorescent C-dots, deemed as benign nanoprobes, have attracted great attention for imaging in vivo. It is necessary to understand the in vivo kinetic behavior of these particles which is required for clinical translation. For instance, C-dot-ZW800 conjugate was prepared by coupling C-dots with NIR dye ZW800, to monitor the in vivo kinetic behavior and the effect of tumor uptake via three injection routes: intravenous (i.v.), subcutaneous (s.c.), and intramuscular (i.m.) routes. The C-dot-ZW800 conjugate showed high photostability and rapid renal clearance with relatively low retention in the reticuloendothelial system and displayed effective passive tumor-targeted imaging with high tumor-to-background contrast (Fig. 2.15) [195].

Great efforts have been made to tailor C-dots for targeting tumors in vivo. For instance, photosensitizer-conjugated C-dots (C-dots-Ce_6) possessing excellent imaging and tumor-homing ability were successfully developed, showing simultaneous enhanced NIR fluorescence imaging and remarkable photodynamic efficacy of gastric cancer tumor in vivo (Fig. 2.16) [196]. In addition, C-dot-based hybrid nanosystems can also be used for in vivo determination of various biologically

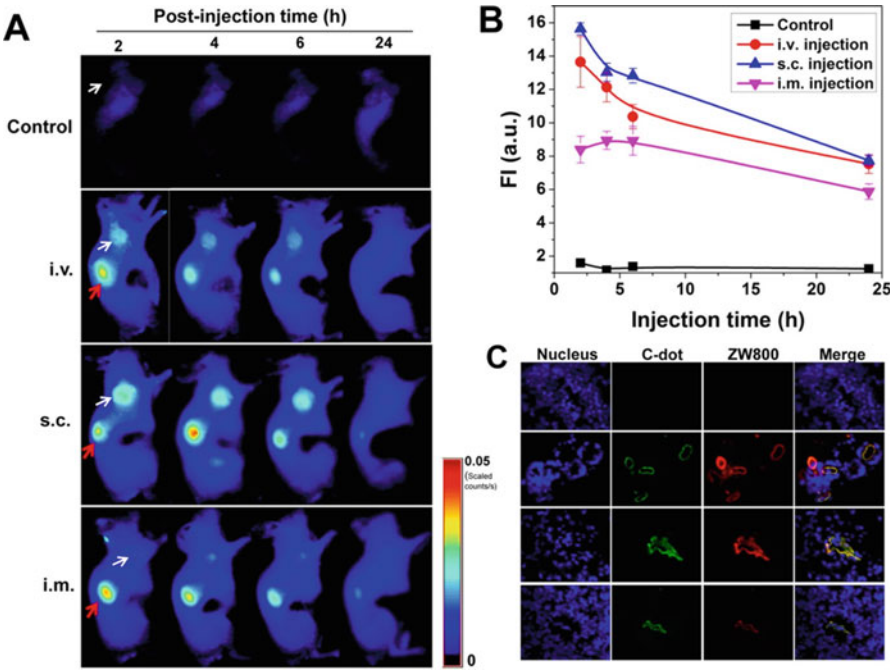

Fig. 2.15 (**a**) NIR fluorescence images of SCC-7 tumor-bearing mice obtained at different time points: control (without injection), i.v. injection, s.c. injection, and i.m. injection (white arrow points to tumor; red arrow points to the kidney). (**b**) Tumor region-of-interest analysis. (**c**) Ex vivo fluorescence images obtained to demonstrate tumor uptake of the nanoparticle conjugate [195] (Reprinted from Ref. [195], Copyright 2013 the American Chemical Society)

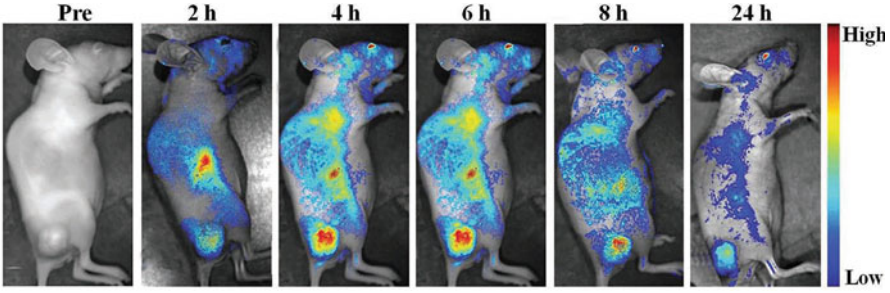

Fig. 2.16 Real-time in vivo NIR fluorescence images of intravenously injected C-dots-Ce_6 in nude mice upon time [196] (Reprinted from Ref. [196], Copyright 2012 Wiley-VCH Verlag GmbH & Co. KGaA, Weinheim)

relevant species. For example, C-dot-based two-photon fluorescent probe has been applied for imaging and biosensing of pH gradients in living tissues at depths of 65–185 μm without the interference resulted from other biological species [197].

Intravenous injection plays a vital role in the study of pharmacokinetics, biodistribution, and toxicological evaluations of C-dots. Due to the small size and high solubility, C-dots can be excreted efficiently via urine with negligible accumulation in the internal organs. For example, polymer-coated nitrogen-doped C-dots with diameters of 5–15 nm were prepared by solvothermal reaction for tumor-targeted imaging in vivo. The C-dot-based nanosystem was intravenously injected into glioma-bearing mice, displaying an enhanced accumulation within the glioma based on the EPR effect [185].

5.2.4 Carbon Nanotubes

Carbon nanotubes (CNTs) with a unique one-dimensional structure and inherently physical, mechanical, and chemical properties are classified into two structural forms: SWNTs and MWNTs [198]. In general, CNTs display NIR fluorescence with relatively low quantum yield and exhibit excellent resistance to photobleaching and low cytotoxicity.

The bandgap between each semiconducting SWNT is in the order of 1 eV, which allows for the fluorescence located in the NIR-II (900–1600 nm) region upon NIR-I excitation [199]. Furthermore, the large Stokes shift between the excitation at 550–850 nm and emission at 900–1600 nm would substantially reduce the autofluorescence resulted from biological tissues during bioimaging, providing enhanced imaging sensitivity. Despite the encouraging properties of SWNTs with NIR fluorescence, the low quantum yield of SWNTs is the main obstacle for further in vivo imaging applications. It has been demonstrated that the photoluminescence quantum yield is closely related to the length and surface coating of CNTs. Thus, the coating exchange approach can effectively enhance the quantum yield of SWCNTs, and the resulted bright fluorescence can directly visualize the small tumor vessels beneath the thick skin [200]. Enhanced fluorescence of SWNTs was also obtained from the modification with gold that shortened radioactive lifetime through resonance coupling of SWNT emission to plasmonic modes in the metal [201].

CNTs can be synthesized by various approaches including laser ablation, arc discharge, and chemical vapor deposition (CVD) [202]. Generally, CNTs obtained by laser ablation produces are clean but accompanied by relatively low yield. In contrast to laser ablation, arc discharge can produce larger quantities of CNTs but with poor purity. In contrast to arc discharge and laser ablation, CVD is relatively a mild approach for the production of CNTs with lower operated temperature and good scalability. However, MWNTs or SWNTs obtained from traditional CVD processes always show large diameter distribution and poor quality. Thus, more advanced and facile strategies for CNT production are highly desirable. Generally, the purification of SWNTs includes removing the structural impurities generated during the synthesis process and screening out SWNTs with homogeneous size distribution. Commonly used purifying techniques include acid treatment, oxidation, cutting, ferromagnetic separation, annealing, microfiltration, ultrasonication, functionalization, ultracentrifugation, and chromatographic separation.

A research advance involves the use of SWNTs as NIR-II fluorescent imaging agents [203–209]. A great number of fundamental and biological studies using CNTs

showed excitation bands ranging from 600 to 800 nm and emission bands at the range of 950–1300 nm. Fluorescent imaging in the NIR-II window holds high promise on account of minimal autofluorescence and tissue scattering. For instance, high-frame-rate video in vivo imaging can be visually observed by intravenously injecting SWNTs into mice. Compared with the conventional NIR-I window (700–900 nm) by indocyanine green, SWNTs displayed much longer remain of feature contrast and integrity with increasing feature depth by tissue phantom studies. By combining with principal component analysis (PCA), NIR-II fluorescence imaging may become a powerful way to image deep tissues with high resolution, which is useful for a wide range of applications from bioimaging to disease diagnosis [210].

Generally speaking, SWNTs used for bioimaging applications are a complex mixture of semiconducting and metallic species with random chirality, which greatly prevent simultaneous resonant excitation of all CNTs and strongly decrease the emission at a single well-defined wavelength. Based on the structure-dependent interaction of SWNTs with an allyl dextran size-exclusion gel, brightly fluorescent SWNTs consisting of predominantly (12,1) and (11,3) chirality were successfully produced and achieved for real-time NIR-II fluorescence imaging of deep organs with high-magnification imaging of hind limb vessel in mice (Fig. 2.17) [211].

To meet the requirement of cancer imaging, contrast agents should be selectively accumulated in the tumor area rather than distributions in healthy tissues. For instance, polymer-functionalized SWNTs were successfully used to achieve ultra-high accumulation in tumors with long blood circulation in vivo (Fig. 2.18) [212]. Based on the intrinsic NIR-II fluorescence of SWNTs, both video-rate imaging and dynamic contrast imaging of tumors were performed through PCA. The fluorescent imaging showed unambiguous tumor identification up to 72 h after the injection. In addition, the 3D reconstruction of SWNT distribution revealed highly passive tumor uptake of SWNTs that mainly resulted from the EPR effect. In addition, fluorescent SWNTs engineered with multifunctional M13 phage were successfully achieved for targeted fluorescence imaging of tumors, showing a great potential for specific diagnosis and therapy monitoring of hard-to-detect areas [213].

5.2.5 Graphene-Based Nanomaterials

Graphene-based nanomaterials include graphene, graphene oxide (GO), reduced graphene oxide (rGO), graphene quantum dots (GQDs), and their derivatives. Graphene, an atomically thick sheet of two-dimensional honeycomb monolayer, is the basic building block for all other dimensionalities of carbon nanomaterials, such as CNTs, fullerene, and carbon nanohorns. GO is a highly oxidized form of chemically modified graphene, which comprises of single atom thick layer of graphene sheets with hydroxyl (-OH) and epoxide (-O-) functional groups on the two accessible sides and carboxylic acid (-COOH) groups at the edges. By the reduction treatment of GO, the oxygen content, surface charge, and hydrophilicity of GO are decreased, and then rGO is produced with restored electrical conductivity and enhanced optical absorbance. GQDs are two-dimensional graphene fragments

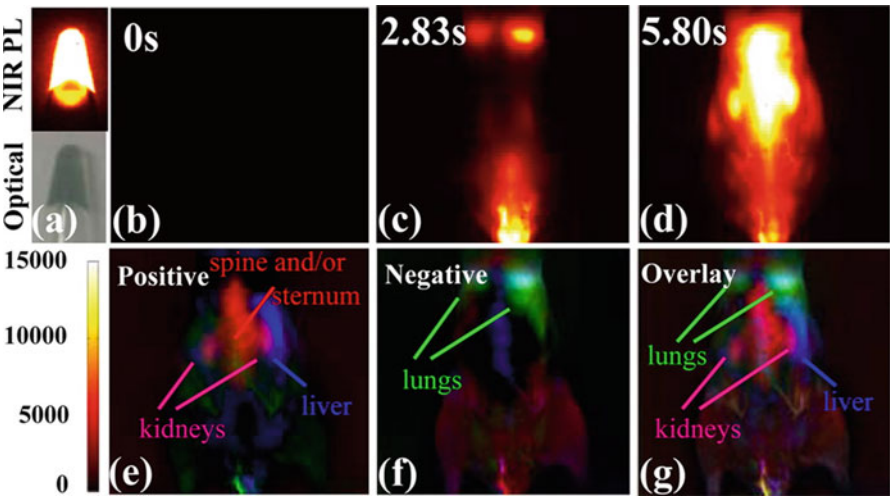

Fig. 2.17 (**a**) Optical and fluorescence images of (12,1) and (11,3) SWNT solution. (**b**) Initial NIR-II fluorescence image of nude mouse without the injection of SWNTs. (**c**, **d**) NIR-II fluorescence images after the injection of SWNTs with different time. (**e**–**g**) PCA images of positive, negative, and overlaid components. Green represents lungs, pink represents kidneys, and blue represents the liver [211] (Reprinted from Ref. [211], Copyright 2012 the American Chemical Society)

sized in 10–60 nm, usually not single-layer but multilayers (~10 layers of rGO). On account of their versatile surface functionalization and ultrahigh surface area, graphene and its derivatives can be easily functionalized by small molecular dyes, polymers, nanoparticles, drugs, or biomolecules to obtain graphene-based nanomaterials for various biomedical applications. Due to intrinsic optical properties in the visible and NIR spectral region, low cytotoxicity, intrinsic aqueous solubility, and versatile surface functionalization, graphene-based nanomaterials have attracted considerable interest for bioimaging [4, 11, 23, 42, 53, 214–218].

Graphene can be synthesized by either bottom-up or top-down strategy [219]. The bottom-up strategy mainly includes CVD, organic synthesis, and solvothermal synthesis [217]. The top-down strategy mainly involves mechanical, physical, and chemical exfoliation methods [220]. GO is typically produced by the Hummers' method through the oxidative exfoliation of graphite using $KMnO_4$/H_2SO_4. rGO can be obtained by treating GO with reducing agents, such as hydrazine, hydrazine hydrate, *L*-ascorbic acid, and so on [221]. GQDs are usually prepared by thermal oxidation of GO or other carbon precursors [11, 214].

Compared with classical QDs, GQDs have merits of low cytotoxicity, good biocompatibility, and physiological solubility and can be used directly for bioimaging without further surface functionalization or processing. In addition, GQDs have unique optical properties of upconversion fluorescence and pH dependence, which make them suitable for safe and efficient bioimaging [223]. To eliminate the autofluorescence interference of biological tissues, lots of efforts have been

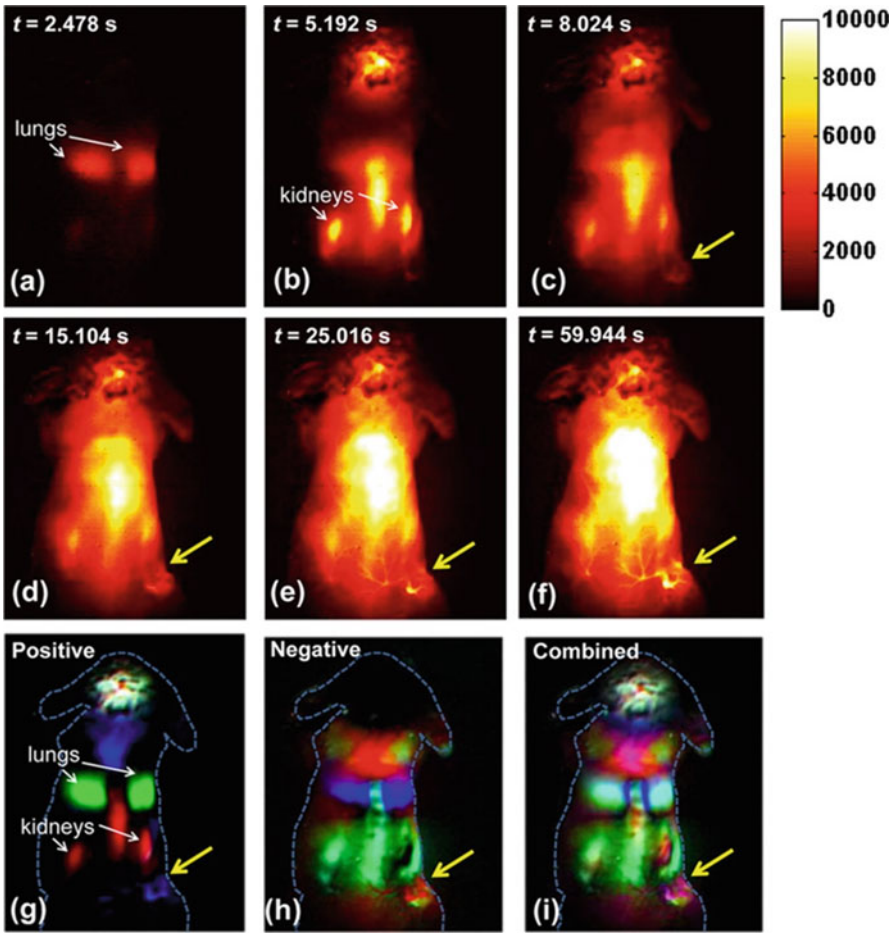

Fig. 2.18 (**a**–**i**) NIR-II fluorescence images and dynamic contrast-improved images using polymer-functionalized SWNTs based on PCA analysis. Yellow arrows indicate the tumor [212] (Reprinted from Ref. [212], Copyright 2012 the American Chemical Society)

expended in constructing NIR fluorescent GQDs for imaging in vivo [222]. For example, NIR graphene nanoparticles (GNPs) were synthesized from carbon fibers through a simple reaction. Due to the excellent biocompatibility, sufficient water solubility, and high luminescence stability, GNPs were proven to be greatly attractive NIR fluorescence probes for high-contrast bioimaging of deep tissues and organs (Fig. 2.19) [222]. In addition, GQDs with bright fluorescence emission around 815 nm were synthesized by one-step pyrolysis of *L*-glutamic acid and subsequently used to image biological targets in vivo with high sensitivity due to their large Stokes shift of 455 nm [224].

By taking advantage of photostable, nontoxic, and easy conjugation properties, GQDs can also be designed and applied for in situ drug delivery and imaging. For

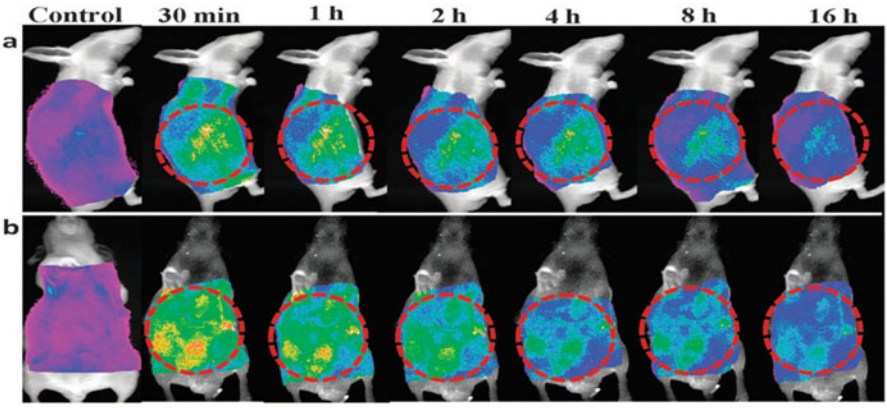

Fig. 2.19 (**a**) Side and (**b**) front view fluorescent images of mice using GNPs [222] (Reprinted from Ref. [222], Copyright 2013 the Royal Society of Chemistry)

example, biodegradable polymers, such as hyaluronic acid (HA), were selected as linkage groups for loading fluorescent species onto the surfaces of GQDs. The obtained GQD-HA composites were demonstrated as efficient targeting agents to achieve specific targeted delivery, since the tumor tissues showed more brighter fluorescence during the investigation of in vivo biodistribution in mice [225].

Two-photon fluorescent probes with bright photoluminescence are highly desirable to be able to visualize biological activities with high spatial resolution, deep tissue penetration inside living organisms, low autofluorescence, and minor photodamage. For example, nitrogen-doped graphene quantum dots (N-GQDs), obtained from a facile solvothermal method, were used as efficient two-photon fluorescent probes for deep tissue imaging [226]. The obtained N-GQDs displayed high two-photon absorption cross section, large imaging depth, and outstanding photostability. In addition, another feasible approach to improve the in vivo imaging performance in complex biological conditions is introducing a two-photon dye (TP dye) as the signal reporter. For instance, by the combination of GO with the two-photon excitation (TPE) technique, a GO/aptamer-TP dye conjugate was successfully constructed and achieved for in vivo imaging of ATP with high sensitivity and selectivity [59]. In another case, GO nanoparticles grafted with PEG polymer were injected into mouse body from the tail vein, the flow and distributions of GO nanoparticles in blood vessels can be clearly observed by using a deep-penetrating two-photon imaging technique, and the imaging depth could reach 300 μm or more (Fig. 2.20) [227].

For practical NIR imaging using functional graphene nanomaterials, real-time imaging of in vivo photo absorber distribution and monitoring of posttreatment therapeutic outcome are vital to optimize personalized cancer treatment. The development of multifunctional probes combined with therapeutic functions and imaging capabilities thus becomes important. For example, rGO-IONP-PEG, prepared from

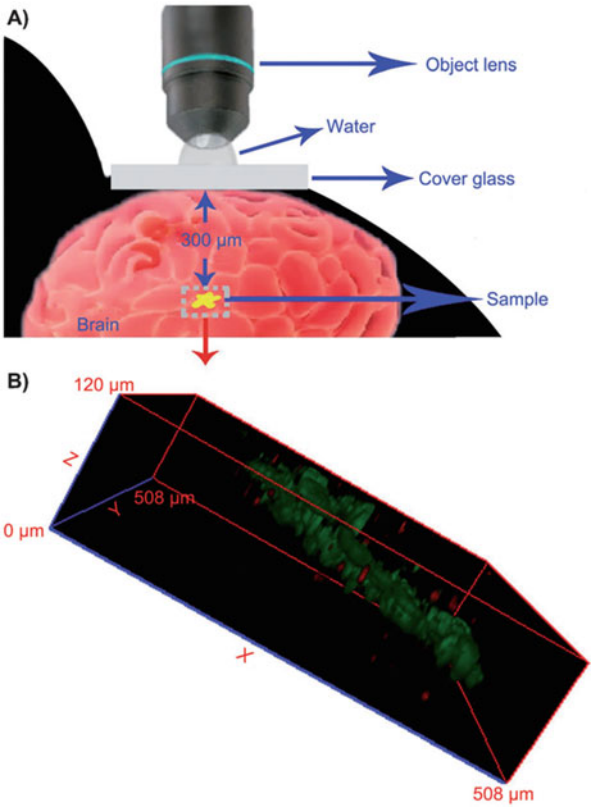

Fig. 2.20 (**a**) Two-photon luminescence microscopy and corresponding image of GO-PEG nanoparticles in a mouse brain. (**b**) A reconstructed image illustrating the three-dimensional distribution of GO-PEG nanoparticles in vivo [227] (Reprinted from Ref. [227], Copyright 2012 Wiley-VCH Verlag GmbH & Co. KGaA, Weinheim)

rGO-iron oxide hybrid nanoparticles (rGO-IONP) with PEG modification, was successfully employed for tumor imaging in vivo and triple modal imaging-guided photothermal therapy for cancer [228].

Moreover, graphene can also be developed as multifunctional nanomaterials in biomedical applications of bioimaging, diagnosis, and therapeutics. For instance, a multifunctional graphene (MFG) having water dispersible, fluorescent, and magnetic functions was developed through microwave-heated sonication-assisted method. The MFG was demonstrated as a useful in vivo imaging probe, which exhibited even distribution in whole zebra fish for in vivo imaging. Furthermore, taking advantage of the magnetic property, MFG could also be utilized in biomedical diagnostics [216]. By covalently grafting UCNPs with nanographene oxide (NGO) via bifunctional PEG and then loading phthalocyanine (ZnPc) on the surface of NGO, nanocomposites named UCNPs-NGO/ZnPc were formed. The obtained UCNPs-NGO/ZnPc can be applied not only for in vivo imaging with high contrast for diagnosis but also for generating singlet oxygen for photodynamic therapy. The nanosystem could also efficiently convert the 808 nm laser energy into thermal energy for photothermal therapy [229].

5.2.6 Nanodiamond

Fluorescent nanodiamond (FND) is an emerging nanomaterial based on sp^3-carbon for bioimaging and cell tracking [230]. FND possesses unique and well-established nitrogen-vacancy (NV) emission centers that endow it with excellent photostability and inherent biocompatibility [7, 32, 231]. NV has an absorption maximum at 550 nm, and when exposed to green-orange light, it emits bright fluorescence at 700 nm with a lifetime of more than 10 ns. In addition, the NV center is perfectly photostable without photo-bleaching and blinking and could be little affected by surface functionalization. Unlike other fluorescent nanoparticles that can be synthesized with wet chemistry methods, FND can be fabricated only by physicochemical means under extreme conditions. Together with facile surface modification on diamond nanoparticles, high sensitivity of NV centers endows these nanoparticles with unprecedented performance in bioimaging and long-term cell tracking, especially in stem cell research (Fig. 2.21) [7, 32, 34, 232, 233].

The unprecedented biocompatibility of FND was successfully evaluated and demonstrated by long-term imaging for *Caenorhabditis elegans* [234]. The toxicity assessments showed that the FND present in cells was stable and nontoxic and did not induce any change in longevity and reproductive potential of the worms. The outstanding photostability and excellent biocompatibility feature of FND enabled continuous imaging of the whole digestive system and monitoring of cellular and developmental processes of the living organism for several days.

However, to meet the requirement of practical imaging, some limitations such as weak brightness and tough bioconjugation have to be overcome. Chang et al. developed FND particles by utilizing nitrogen-rich type Ib diamonds, which showed high fluorescence and ready functionalization with proteins for cell imaging [235, 236]. Additionally, the surfaces of diamond nanostructures play an important role in determining the utility and biocompatibility of these nanostructures in biological and medical applications. The first step of diamond surface modification often involves harsh treatment with strong chemicals or plasma irradiation to introduce functional groups onto the surface. Once surface functional groups are established, various linker molecules or biomolecules, including biomarkers, therapeutic drugs, and genes, can be grafted onto the surface. The surface of diamond can be flexibly tuned through the surface modification methods such as oxidative treatment, halogenation, reduction, hydrogenation, and thiolation [237–239].

Based on the surface modifications of FND with various functional groups, including targeted probes and drugs, a multifunctional platform for combined targeting, imaging, and therapy using diamond nanoparticles was demonstrated. This combination allows simultaneous diagnosis and therapy and also enables monitoring therapeutic delivery, transport, and response. In addition, FND is chemically inert and does not release toxic chemicals even in harsh environments. Thus, these properties endow diamond nanostructures with intrinsic biocompatibility. Thanks to their inherent photochemical and chemical inertness and their emission in the NIR region, FND has been widely employed for in vivo imaging and long-term tracking as cellular biomarkers [230, 237]. For instance, FND-based platforms can be used for long-term imaging without eliminating in vivo cell migration and

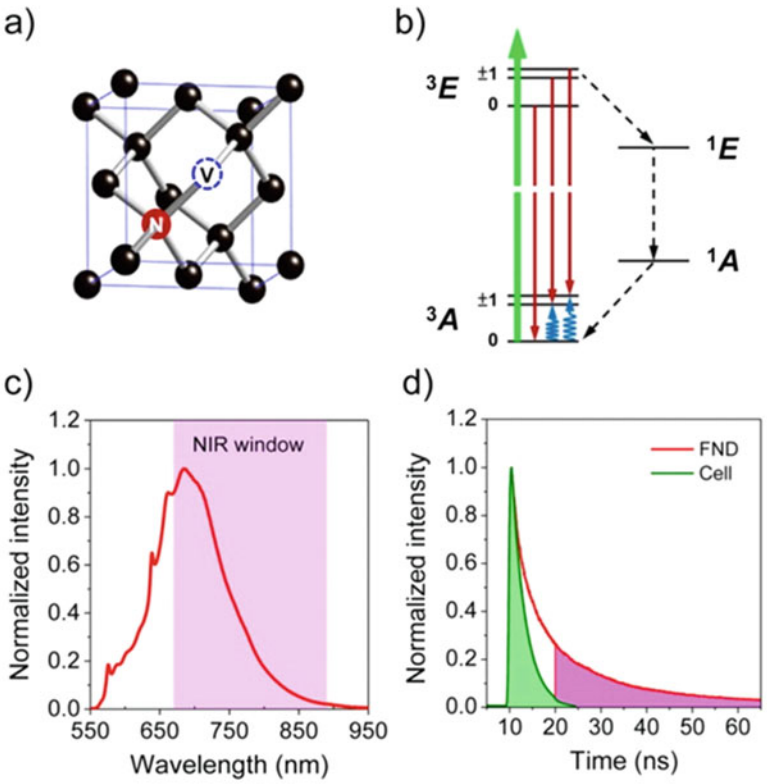

Fig. 2.21 (**a**) Structure and (**b**) energy level diagram of the NV center in diamond. The red sphere, blue dashed circle, and black spheres in (**a**) denote nitrogen, vacancy, and carbon atoms, respectively. The green, red, and blue sinusoidal and black dashed arrows in (**b**) denote optical excitation, fluorescence emission, microwave excitation, and intersystem crossing relaxation, respectively. (**c**) Comparison between the fluorescence spectrum of FND excited with a 532 nm laser and the NIR window of biological tissue. (**d**) Comparison between the fluorescence lifetime of FND in water and endogenous fluorophores in cells. Time gating at 10 ns is indicated for background-free detection [7] (Reprinted from Ref. [7], Copyright 2016 the American Chemical Society)

differentiation into type I and type II pneumocytes. Moreover, by using the combined technology of FND labeling, FLIM, and fluorescence-activated cell sorting (FACS), researchers can unequivocally monitor and identify the transplanted $CD45^{-}CD54^{+}CD157^{+}$ lung stem/progenitor cells in vivo under single-cell resolution and further quantify their engraftment and regenerative capabilities over a week (Fig. 2.22) [233].

In order to meet some demanding bioimaging applications and to integrate with existing advanced protein labeling technologies, there is a need to reduce the particle size down to at least 10 nm. FND performs in vivo tracking of cells with good sensitivity, resolution, and precision. The fluorescence intensity of NV centers sensitively depends on the ground-state spin configuration that can be tuned by

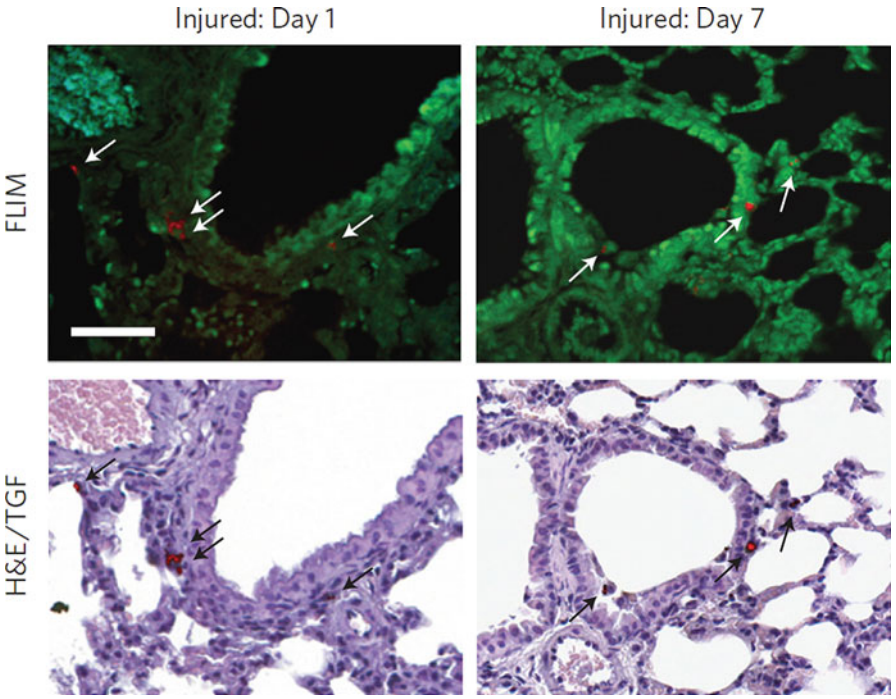

Fig. 2.22 FLIM, transforming growth factor (TGF) and corresponding bright-field hematoxylin and eosin (H&E) staining images of lung tissues using FND. White and black arrows indicate the FND-labeled lung stem/progenitor cells [233] (Reprinted from Ref. [233], Copyright 2013 Nature Publishing Group)

electron-spin magnetic resonance. By means of real-time selective fluorescence imaging of NV centers, successful long-term monitoring of a single nanodiamond in both *Caenorhabditis elegans* and mice was conducted, with extraordinary imaging contrast even in the presence of strong background autofluorescence [240].

Due to the excellent photostability and nontoxicity, FND was used as photostable labels and tracers for the intercellular transport of proteins. For example, FND coated with yolk lipoprotein complexes was successfully microinjected into intestinal cells to monitor the transportation of fat molecules and cholesterol in vivo. The results indicate that FND can be used as a safe and efficient nanocarrier for biomolecules without obviously changing the functionality of the cargos for cell-specific targeting, intercellular transport, and long-term in vivo imaging applications [232].

5.2.7 Upconversion Nanoparticles

UCNPs, featured as upconversion luminescence (UCL), are a unique class of lanthanide-doped nanoparticles with fluorescence emission upon NIR light excitation. UCL is a process where low-energy NIR light is converted to higher-energy light through the sequential absorption of multiple photons or energy transfers. Most

UCNPs consist of hexagonal $NaYF_4$ nanocrystals doped with trivalent lanthanide ions such as Er^{3+}, Yb^{3+}, or Tm^{3+}. Usually, UCNPs display multiphoton emission, and the peak wavelengths depend on the lanthanide dopant used. The size of UCNPs highly affects the quantum yields and is widely tunable in the range of 10–100 nm. Unlike in the case of C-dots, the emission wavelength of UCNPs is independent of the excitation wavelength. Remarkably, the quantum yields of UCNPs depend on both the power density of the laser and the particle size.

Compared with conventional contrast agents with downconversion, UCNPs possess a lot of merits as bioimaging probes: minimal autofluorescence, deeper penetration depth, less photodamage, hardly attacked by the immune system, narrow emission bands, tunable emission, no photo-bleaching, long luminescence lifetime at micro- to milliseconds scale, low toxicity to living systems, high cell permeability, and excellent chemical and physical stability. Due to their superior optical and chemical properties, UNCPs have been deemed as perfect fluorescent contrast agents for NIR imaging in vivo.

To use UCNPs as successful fluorescent labels, some major requirements must be met. Firstly, suitable size and uniform shape are the prerequisites for bioimaging [241]. Up to now, a number of approaches and considerable research efforts have been devoted to preparing UCNPs with different shapes and tunable sizes from 10 nm to sub-mm. Thermal decomposition and hydro(solvo)thermal synthesis are the two most common approaches for the production of uniform hydrophobic nanocrystals [242]. A variety of UCNPs with monodispersed size and uniform shapes have been successfully prepared by the modified thermal decomposition method [243, 244]. For instance, monodispersed $NaYF_4$:Yb^{3+}/Tm^{3+} nanocrystals with enhanced NIR-to-NIR upconversion photoluminescence were successfully synthesized by using a modified co-thermolysis method [241]. Unlike in the case using thermal decomposition method, highly crystalline materials can be prepared by hydro(solvo)thermal approach at much lower temperature and without the requirement of annealing process. However, the UCNPs synthesized by thermal decomposition and hydro(solvo)thermal approach are hydrophobic. Since the UCNPs as biological fluorescent probes should be water-soluble, a facile surface modification or functionalization is needed to convert hydrophobic UCNPs into hydrophilic ones for bioimaging applications. Currently, many surface modification strategies have been developed to convert the hydrophobic UCNPs into water-soluble ones. These methods include ligand exchange, cation-assisted ligand assembly, organic ligand-free synthesis, ligand oxidation reaction, layer-by-layer method, hydrophobic-hydrophobic interaction, host-guest interaction, and silanization. Generally, UCNPs processed by ligand exchange have no obvious changes for their morphology, crystallization, and chemical properties. Similarly, UCNPs treated by the ligand oxidation process also show no obvious adverse effects on the morphology and luminescence properties. Cation-assisted ligand assembly is also an efficient way to convert UCNPs into water-soluble ones. For example, oleylamine (OM)-coated $NaYF_4$:Yb,Er/Tm UCNPs are hydrophobic and can be converted into water-soluble system by cleaving OM along with the cation exchange. By taking advantage of hydrophobic-hydrophobic interaction, hydrophobic UCNPs can be converted

into hydrophilic forms by coating hydrophilic small molecules or polymers [245, 246]. Moreover, hydrophilic ligands can be linked on the surface of hydrophobic nanoparticles mediated by host-guest interactions [247]. For instance, oleic acid (OA)-coated $NaYF_4$:Yb,Er/Tm nanoparticles were successfully transferred into water-soluble forms via the robust host-guest interaction between α-cyclodextrin (α-CD) and OA [248]. The size of nanoparticles can be remained on account of hydrophobic-hydrophobic interaction and host-guest interaction. In addition, silanization is a powerful and popular tool for the surface functionalization of nanoparticles on account of high biocompatibility of silica, and silica-coated UCNPs were employed for bioimaging. Both hydrophilic and hydrophobic UCNPs can be modified with silica coating. For UCNPs with hydrophobic ligands, reverse micro-emulsion method is often employed to conduct silica coatings [249, 250], while UCNPs with hydrophilic ligands can be modified by the Stöber method [251]. Among the abovementioned surface treatment strategies, silanization is the only inorganic modification approach, offering a core/shell structure and inducing $–NH_2$, –COOH, or –SH groups for further bioconjugation. However, the sizes of UCNPs are often enlarged by the silanization.

To simplify the procedure of synthesis and posttreatment, a variety of one-step synthetic strategies [252], including polyol process assisted by hydrophilic ligands [253], hydrothermal route assisted by binary cooperative ligands (HR-BCL) [254], and ionic liquid-based synthesis [255], were used to prepare water-soluble UCNPs. In general, the one-step synthetic method can greatly simplify the procedure of reaction and posttreatment. However, UCNPs with small and uniform sizes are hardly obtained. Although usually requiring complicated posttreatment, two-step approaches are convenient for tuning the size, shape, and crystallinity of UCNPs. In short, both one-step and two-step methods for converting the hydrophobic UCNPs into hydrophilic forms are under active developments.

The application of UCNPs in fluorescence imaging of tissues and living subjects has attracted increasing attention. Unquestionably, great research progress has been achieved in the development of uniform, ultrasmall-sized, water-soluble, and surface-functionalized UCNPs with multiplexed colors and high quantum yield. However, only few UCNP examples could thoroughly meet all the requirements for in vivo imaging. There are still many challenges to synthesize UCNPs with controllable size, hydrophilic properties, and biofunctionality as fluorescence probes for in vivo imaging. To date, $NaYF_4$:Yb,Tm nanoparticles with a diameter of 11.5 nm are the smallest UCNPs obtained from solvothermal method and coated with polyacrylic acid (PAA) [256]. These hexagonal $NaYF_4$:Yb,Tm nanoparticles were successfully used for the long-term tracking of the biodistribution in vivo.

Some UCNPs are ideally suited for in vivo fluorescent bioimaging due to their merits of NIR-to-NIR upconversion. For example, core/shell α-$NaYbF_4$:Tm^{3+}/CaF_2 nanoparticles exhibited highly efficient NIR emission at ~800 nm when excited at ~980 nm, which enabled their applications for high-contrast deep tissue bioimaging [257]. However, the 980 nm laser, typically employed to trigger the upconversion process, is highly absorbed by water in biological structures and could induce severe

overheating effect. To address the issue of NIR laser-induced tissue damage, Nd^{3+} ion was introduced as NIR absorber and sensitizer in conventional Yb^{3+}-doped UCNPs [258]. The integrated $Nd^{3+} \rightarrow Yb^{3+}$ energy transfer to conventional Yb^{3+}-sensitized upconversion processes is a versatile method to extend the single NIR excitation band of Yb^{3+} to shorter wavelengths. The excited band at 808 nm could offer high upconversion excitation efficiency similar to that of 980 nm excitation, while having substantially minimized tissue overheating effect. A similar approach was proposed to excite UCNPs by using 915 nm laser light, which showed the depth range in vivo imaging [259].

UCNPs, featured with distinct narrow emissions, are deemed as good color markers to simultaneously trace different biochemical species and monitor multiple organs [260]. For instance, UCNP-dye complexes based on $NaYF_4$ nanocrystals were synthesized by simultaneously modifying with amphiphilic polymer and fluorescent dyes via physical adsorption. The obtained supramolecular UCNP-dye complexes exhibited controllable visible emission spectra ascribing to the luminescence resonance energy transfer (LRET) from UCNPs to the organic dyes upon NIR excitation and achieved multicolor UCL imaging in vivo (Fig. 2.23) [261].

Targeted monitoring and bioimaging of special chemicals in biological systems are important, since these molecules or ions often play an important role in organisms. For example, efficient and sensitive monitoring of methylmercury ($MeHg^+$) in vivo is of great importance, because a certain amount of methylmercury accumulated in the organs of animals would result in prenatal nervous system and visceral damage. Considering the superior UCL of UCNPs, cyanine dye-assembled UCNPs were synthesized for UCL sensing and bioimaging of $MeHg^+$ in vivo (Fig. 2.24) [262]. The cyanine dye hCy7, a $MeHg^+$-sensitive dye, was loaded on the surface of lanthanide UCNPs, achieving the monitoring of $MeHg^+$ in vivo with high sensitivity. Moreover, targeted tumor imaging is also important for tumor diagnosis and therapy. This target-specific recognition includes ligand-acceptor and antigen-antibody interactions. For instance, recombinant chlorotoxin-mediated $NaYF_4$:Yb,Er/Ce UCNPs showed highly specific binding of tumors and can be used to directly visualize tumors in living mice with high-contrast images [263].

Common approaches to study the deep tissue imaging of most UCNPs mainly rely on direct injection of abundant UCNPs into tissue or special site of animals, which may cause long-term biosafety issues. Thus, an advanced approach is to develop highly sensitive UCNP-based fluorescence probes for in vivo imaging. UCNP-labeled cells delivered into injured muscles would undoubtedly offer useful insights for real-time monitoring of the myoblast transplantation therapy [261]. For example, sub-10 nm Gd^{3+}-doped $NaLuF_4$ UCNPs, synthesized via thermal decomposition, were effectively used with tracking limits of 50 and 1000 UCNP-labeled cells via subcutaneous and intravenous injection, where high-contrast UCL whole-body imaging of a black mouse with a penetration depth of ~2 cm was achieved [264].

In addition, the spatiotemporal regulation of light-gated ion channels is a useful tool to study physiological pathways and develop personalized theranostic

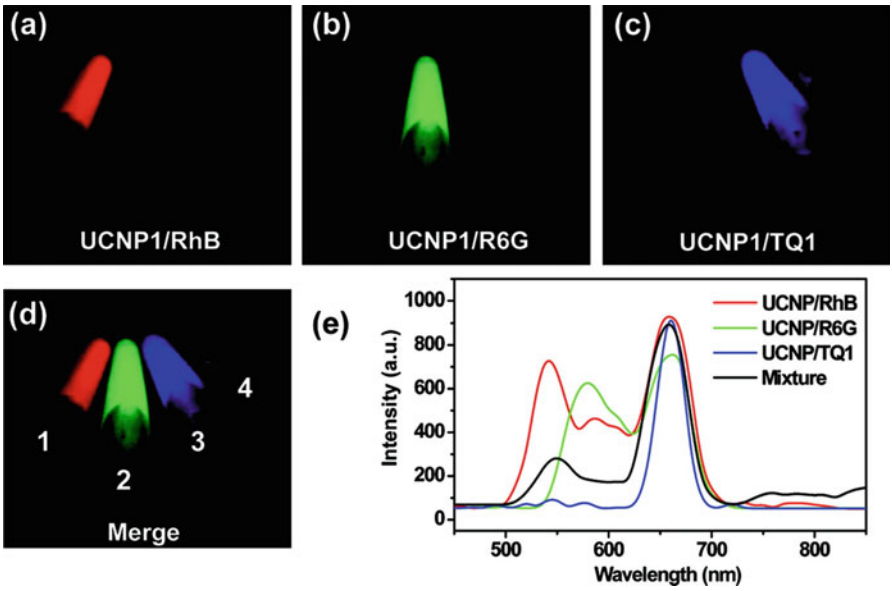

Fig. 2.23 (**a**–**e**) Multicolor UCL imaging of UCNP-dye complexes [261] (Reprinted from Ref. [261], Copyright 2011 the American Chemical Society)

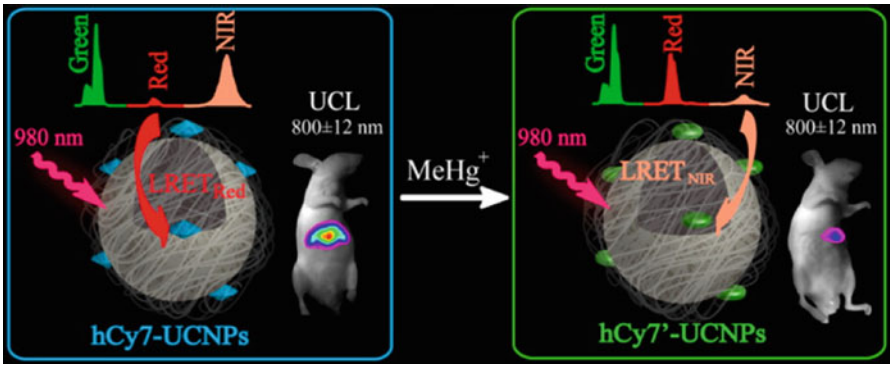

Fig. 2.24 Schematic layout of cyanine-modified UCNPs for in vivo imaging of methylmercury [262] (Reprinted from Ref. [262], Copyright 2013 the American Chemical Society)

modalities. Recently, a simple strategy based on native metabolic glyco-biosynthesis was used to achieve site-specific covalent localization of NIR light-responsive UCNPs on the cell surface through a copper-free click reaction under living conditions. Upon 808 nm light irradiation, the blue emission (at 480 nm) from UCNPs could remotely activate the photosensitive ion channel and effectively manipulate the cation influx in living zebra fish [265].

5.2.8 Noble Metal Nanoclusters

Noble metal nanoclusters (NCs), as a new type of luminescent nanomaterials, have been attracting extensive interest due to convenient surface bioconjugation and unique optical properties [266]. NCs are composed of a few to hundred atoms, and typically have diameters below 2 nm, making their dimensions between metal atoms and small nanoparticles. Since their sizes are close to the Fermi wavelength of electrons, NCs possess molecule-like properties such as discrete electronic states and size-dependent fluorescence [267]. Therefore, NCs are referred as fluorescent noble metal QDs. NCs have several distinct features including strong photoluminescence, good photostability, and large Stokes shift. To date, water-soluble NCs with different ligands and tunable emission have been developed in various biocompatible scaffolds, enabling them as useful fluorescence probes for bioimaging applications [268–275].

Various methods have been employed to prepare metal NCs with considerable quantum yield and sufficient brightness for the applications of bioimaging. However, NCs obtained from the reduction of metal ions tend to aggregate into large nanoparticles in aqueous solution. In addition, the emission properties of NCs can be easily affected by the ligands capped on the particle surface. Therefore, a judicious choice of capable agents or stabilizers is vital to obtain small metal NCs with high stability and enhanced fluorescence.

Thiol-containing small molecules are the most commonly used stabilizers in metal nanoparticle production due to the strong interaction between thiols and Au/Ag. For instance, glutathione as an excellent stabilizer was widely used to synthesize Au NCs with visible luminescence through the reduction of Au^{3+} with sodium borohydride ($NaBH_4$). Except for glutathione, a variety of thiols including tiopronin, thiolated cyclodextrin, phenylethylthiolate, and 3-mercaptopropionic acid are also good stabilizers and have been used for the preparation of metal NCs [267]. In addition, fluorescent metal NCs can also be prepared by etching large Au nanoparticles with thiols or capping agents, such as mercaptosuccinic acid. On account of their capability of sequestering metal ions from solution, both dendrimers and polymers with a mass of carboxylic acid groups were used as templates to produce metal NCs. Biomacromolecules such as DNA, peptides, and proteins were also employed to fabricate various fluorescent metal nanostructures [277–280]. Particularly, DNA oligonucleotides are excellent stabilizers for preparing small Ag NCs, due to the high affinity between silver ions and cytosine bases on single-stranded DNA.

Fluorescence imaging relies heavily on stable, biocompatible, highly specific, and sensitive markers. Conventional fluorophores such as organic dyes and fluorescent proteins with limited photostability greatly limit the long-term monitoring tests in vivo, and QDs also showed potential safety concerns for in vivo applications. In contrast, fluorescent metal NCs exhibited bright emission as well as good biocompatibility, making them attractive alternatives as fluorescent probes for bioimaging. For instance, ultrasmall bovine serum albumin-stabilized Au NCs exhibiting bright NIR fluorescence and high photostability were successfully used for in vivo

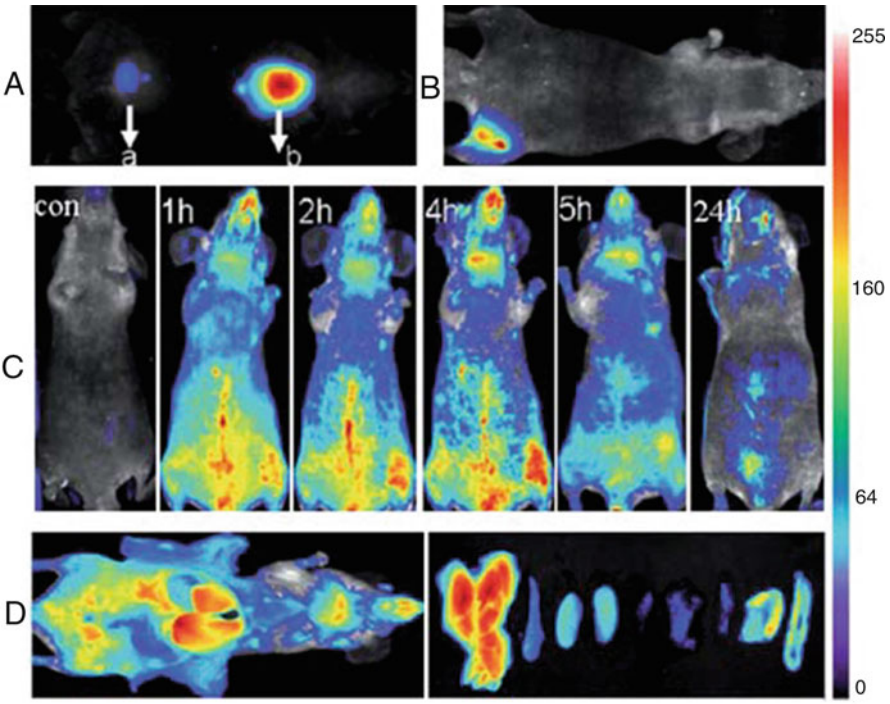

Fig. 2.25 In vivo tumor imaging upon (**a**) subcutaneous (*a*, 0.235 mg mL^{-1}; *b*, 2.35 mg mL^{-1}) and (**b**) intramuscular (2.35 mg mL^{-1}) injection of 100 μL Au NCs into mice. (**c**) Real-time in vivo fluorescence image of abdomen after intravenous injection with Au NCs (200 μL, 2.35 mg mL^{-1}) at different time. (**d**) Ex vivo optical images of a mouse treated with the injection of Au NCs (200 μL, 2.35 mg mL^{-1}) and some dissected organs [276] (Reprinted with permission from Ref. [276], Copyright 2010 the Royal Society of Chemistry)

fluorescence imaging of tumor [276]. Due to the high photostability and low toxicity, the Au NCs could be employed for continuous in vivo imaging. For example, fluorescent Au NCs were injected intravenously into mice for whole-body real-time in vivo imaging. As shown in Fig. 2.25, Au NCs showed spectrally distinguished emission with different brightness depending on locations and the dose of Au NCs injected. The fluorescence of Au NCs could also be visualized upon the injection into muscles by up to a few millimeters on account of their NIR light excitation. The fluorescence of superficial vasculature of mouse was immediately visualized after tail vein injection, remained visible after 5 h, and decreased noticeably after 24 h. Due to the EPR effect, ultrasmall Au NCs were found to accumulate at a high concentration in the tumor sites under in vivo imaging test.

It is important to develop contrast agents with efficient renal clearance for in vivo bioimaging applications. Ideal nanoparticle-based fluorescent probes should be effectively excreted out of the body, with low accumulation in normal organs and minor interference from background noise. Although NCs with hydrodynamic

diameters smaller than 10 nm are usually considered to be stealthy to the reticulo-endothelial system (RES), fluorescent NCs are still severely hampered by their slow renal clearance. To overcome the problem, 2 nm glutathione-coated luminescent Au NCs with good renal clearance were developed. In this case, less than 5% particles were accumulated in the liver, and more than 50% particles were found in urine within 24 h after intravenous injection [281]. Due to the ultrasmall size of fluorescent nanoparticles and biocompatible glutathione ligand, most of Au NCs can keep stable during blood circulation and efficiently be cleared out of the body via the kidney filtration.

In vivo fluorescence imaging of tumors is one of the most important topics in nanomedicine and biomedical engineering for early, accurate tumor diagnosis and imaging-guided surgery and therapy. Due to the facile function of engineered NCs, multimodal imaging-guided combinational phototherapy by integrating various building blocks would be used for cancer diagnosis and therapy. For example, nano-assembly of nanorods (NR) and UCNPs engineered by DNA hybridization was successfully employed for multimodal imaging and combinational phototherapy (Fig. 2.26) [282]. Upon the execution into mice, the assembly exhibited outstanding cancer-targeting ability via EPR effect and substantially eliminated the tumor for in vivo cancer therapy.

5.2.9 Fluorescent Silica Nanoparticles

Since silica nanoparticles (SiNPs) feature optical transparency, robustness, chemical and mechanical stability, low toxicity, easy excrement, and resistance to microbial attacks, they are also suitable for bioimaging [21, 56, 283–287]. However, as SiNPs are optically silent in visible and NIR region, improving their bioimaging capability is focused on doping them with other fluorescent materials to form silica-based hybrid nanomaterials. Fortunately, due to the facile modification on the surface, SiNPs are easily functionalized by lots of existing NIR fluorescent materials such as metal-organic and metallic fluorophores [288], organic dyes [22, 289–291], protein [126], UCNPs [292], and QDs [51]. Thus, different fluorescent SiNPs can be obtained by using different kinds of fluorophores.

Most fluorescent SiNPs consist of silica coating on outside of fluorophores, because silica coating enables excellent properties and enhanced performance, such as high stability over a wide range of solution pH, nontoxicity, non-swelling, and efficient light transmission. Furthermore, silica coating offers a variety of targeting ligands by covalent binding, including antibodies, peptides, sugars, and nucleotides.

Doping SiNPs with NIR fluorescent dyes is a simple and convenient approach to prepare NIR fluorescent nanoparticle probes for in vivo imaging. Recently, SiNPs were successfully used for in vivo biomedical applications. For example, 20–25 nm-sized NIR dye-doped silica nanoparticles (ORMOSIL) were synthesized by a normal micellar route and subsequently radiolabeled with iodine-124. The biodistribution of ORMOSIL determined by NIR fluorescence and radiolabeling studies in vivo displayed a major accumulation in RES in mice. Nearly all of the nanoparticles were cleared out of the body through the hepatobiliary excretion, without any sign of organ toxicity [293]. In

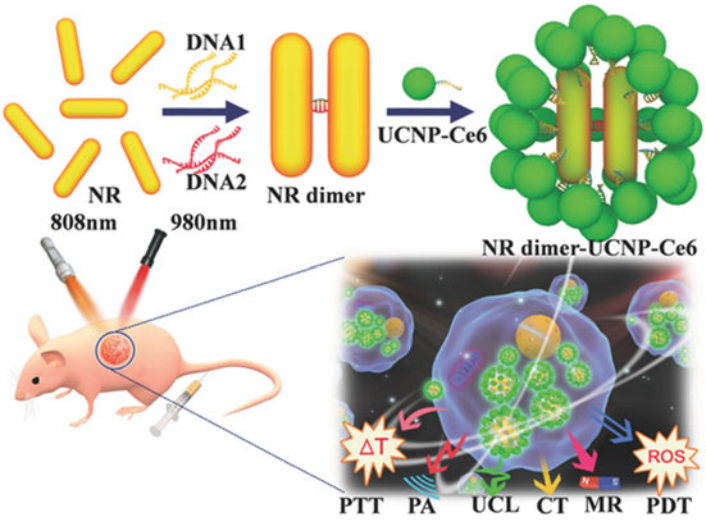

Fig. 2.26 Schematic layout of DNA-hybridized core-satellite assembly of NR dimer and UCNPs for multimodal imaging-guided combinational phototherapy [282] (Reprinted with permission from Ref. [282], Copyright 2016 Wiley-VCH Verlag GmbH & Co. KGaA, Weinheim)

addition, cyanine dye is a type of NIR dye with excellent NIR emission, but with poor photostability strongly limiting its in vivo imaging applications. A promising approach to overcome the problem is incorporating cyanines into SiNPs, where the nanoparticle shell can effectively protect the fluorophore molecules. In a similar case, a unique fluorescent system (CyN-12@NHs) constructed by amphiphilic block copolymer-based nanoscale micelles (NHs) encapsulating NIR fluorescent dye (CyN-12) exhibited good photo and chemical stability, water solubility, and bright NIR fluorescence, making it a suitable fluorescent probe for bioimaging. CyN-12@NHs also showed bright fluorescence with a long retention in tumor by injecting intratumorally into mice and displayed selective accumulation in the liver via intravenous injection [294].

Although fluorescent proteins might be the safest fluorescent probes for in vivo imaging, their instability in the purified forms strongly impeded their uses. Fortunately, near-infrared fluorescent proteins (NIRFPs) coated with a silica nanoshell, named NIRFP@silica, can increase the stability of proteins and simultaneously improve the quantum yield and photostability of the coated NIRFPs. When injected by the tail vein, NIRFP@silica with a small nanoparticle size, narrow distribution, and good dispersibility can be distributed all over the mouse body, and then efficiently eliminated through urine in 24 h, indicating its high potential as a safe and robust NIR fluorescence imaging agent for whole-body imaging. To avoid the adverse interference of pulmonary damage resulted from the aggregation/agglomeration of nanoparticles, nanoprobes with slightly bigger size than a single fluorescent protein were produced via lysine-catalyzed Stöber method [126].

A multifunctional core/satellite nanotheranostic (CSNT) constructed by decorating ultrasmall CuS nanoparticles onto the surface of a silica-coated UCNP could not

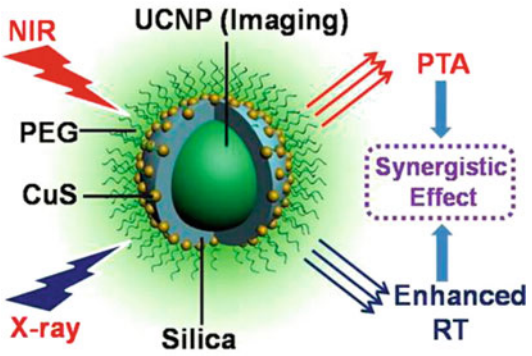

Fig. 2.27 Schematic layout of a synergistic therapy based on CSNT for enhanced radiotherapy (RT) and photothermal ablation (PTA). UCNP cores are responsible for the RT, and CuS satellites are used to convert the 980 nm laser into heat for PTA [292] (Reprinted from Ref. [292], Copyright 2013 the American Chemical Society)

only convert NIR light into heat for effective thermal ablation but also cause highly localized radiation dose boost to trigger remarkably enhanced radiation damage in vivo. Moreover, the CSNT can be used as an excellent trimodal imaging agent based on upconversion luminescence, magnetic resonance, and computer tomography technology (Fig. 2.27) [292]. Similarly, mesoporous SiO_2 can be modified by UCNPs. For example, a microcarrier (Fig. 2.28) based on mesoporous SiO_2-Nd@SiO_2@mSiO_2-NH_2@SSPI (SSPI, succinylated soy protein isolate polymer) was successfully used to noninvasively monitor the gastrointestinal drug release in vivo through the NIR-II fluorescence signals of lanthanide-based downconversion nanoparticles (DCNPs) [295].

In another example, chlorin e6 (Ce_6) photosensitizer conjugated with silica-coated gold nanoclusters (AuNC@SiO_2-Ce_6) can be used for NIR fluorescence imaging of gastric cancer tissue through intravenous injection into MDA-MB-435 breast cancer-bearing mice [296]. Moreover, the persistent emission (5–13 ms) of NIR luminescent nanoparticles made of porous silicon is long enough to permit time-resolved fluorescence imaging and can be distinguished in the time domain from signals associated with tissue autofluorescence or interfering organic chromophores [285].

Compared with other semiconductor nanocrystals, silicon quantum dots (Si QDs) possess many merits including high natural abundance of silicon, low cytotoxicity, unique size, and surface-dependent optical properties [297]. Strategies for the preparation of Si QDs generally include solution-phase-based methods, microemulsion synthesis, and thermally induced disproportionation of solid hydrogen silsesquioxane in a reducing atmosphere. The approaches for the functionalization of Si QDs include surface oxidation and etching, covalent functionalization, non-covalent functionalization, and bioconjugation [34]. Si QDs can be used in multiple cancer-related in vivo imaging, such as tumor vasculature targeting, sentinel lymph node mapping, and multicolor NIR imaging. For example, a type of Si QDs was developed through a combination of unique nanoparticle synthesis, surface functionalization, PEGylated micelle encapsulation, and bioconjugation. The encapsulated Si QDs with nanospheres showed stable luminescence and long tumor accumulation time (>40 h) in live mice [298].

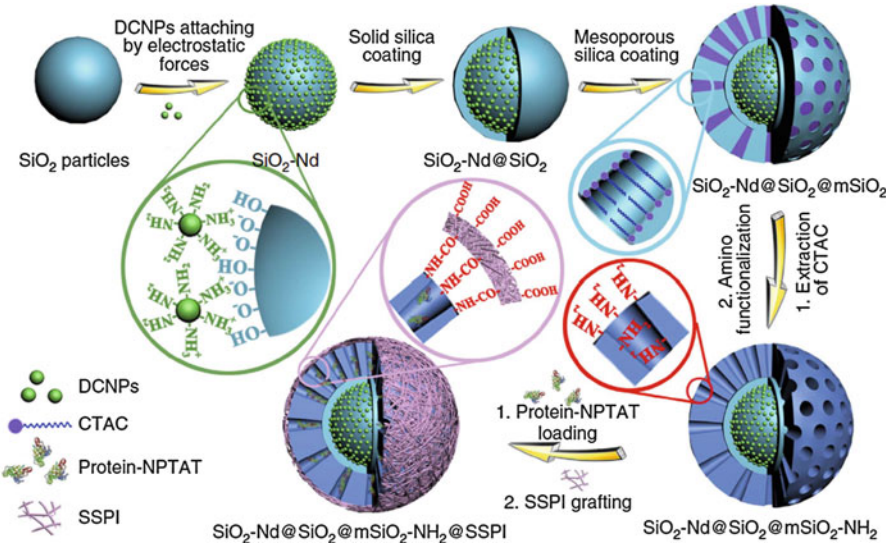

Fig. 2.28 Schematic illustration of NIR-II fluorescent mesoporous microcarrier preparation with protein drugs loading and SSPI grafting. NPTAT, nickel(II) phthalocyanine-tetrasulfonic acid tetrasodium; CTAC, cetyltrimethylammonium chloride [295] (Reprinted from Ref. [295], Copyright 2017 Nature Publishing Group)

6 Conclusions and Future Perspective

NIR fluorescence is a powerful imaging technique that not only noninvasively visualizes biological processes in cells and organisms but also permits tracking of molecules and cells in real time for disease diagnosis and treatment. Thus, ideal NIR fluorescent materials with strong luminescence, desirable excitation and emission wavelength, high photostability, small size, and good biocompatibility are pivotal for in vivo imaging. However, the lack of desirable NIR fluorescent probes is the major reason that NIR fluorescence imaging in vivo is still in its infancy of clinical diagnosis and therapy. Moreover, some problems still limit clinical applications of NIR fluorescence imaging, such as the degradation of imaging agents, the toxicity to bio-samples, and color fading.

NIR fluorescent materials with excellent photophysical properties and smart functionality are not only basic elements of theranostic techniques for biology and pathophysiology but also practically significant toward clinical applications. For optimal monitoring and deciphering of physiological structures and functions with the maximum temporal and spatial resolution as well as minimal perturbation to biological systems, NIR fluorescent probes should have high brightness, adequate water dispersibility, excellent biocompatibility, and facile bioconjugation. Among many NIR fluorescent materials, small fluorophores (such as NIR dyes and metal complexes) and fluorescent proteins have been extensively studied for bioimaging

in vivo. However, these small fluorophores and fluorescent proteins generally show photo-bleaching that limits their maximum effectiveness for long-range and three-dimensional in vivo imaging. Despite great advances that have been made in the field of NIR dyes for bioimaging, there are still a lot of rooms for further improvement. For instance, some cyanine dyes still suffer from low photostability, which should be further improved. The ease of aggregation in aqueous media greatly limits squaraines for medical and biological imaging. To improve the photostability of cyanine dyes and reduce their cell toxicity, tremendous efforts have been given to cyanine-based contrast agents. Rational incorporation of the cyanine platform with nanoparticles or polymers has provided great opportunities to efficiently monitor the biological species in tissue and animal body. The approaches for the conjugation of nanoparticles such as UCNPs or QDs could be built up to enhance the performance of NIR dyes for bioimaging.

Nanoparticles like QDs have been frequently employed for bioimaging applications. However, these QDs usually contain inherently toxic elements including cadmium and selenium that are easy to leak and harm to live organisms, which severely restrict their uses to most in vivo work and narrow their scope of applications. Furthermore, QDs with dynamic surface structures tend to aggregate in biological environments, which also constrain their physiological utilities and clinical implementation. To overcome these limitations, silicon nanocrystals, C-dots, and GQDs featuring higher photostability and better biocompatibility have been developed. On the other hand, it is not easy to tune broad photoluminescence emission for GQDs and to gain pure samples of CNTs with desirable photoluminescence intensity. Although silicon nanocrystals and C-dots have demonstrated increasing importance in the field of biological imaging, some questions regarding the complete understanding of their fluorescence mechanism and rational control of their emission characteristics still remain. Unlike these materials, the photoluminescence of nanodiamond is known to rely mainly on the formation of well-established fluorescent NV centers. However, nanodiamond possesses low extinction coefficient and their emission is not easily tunable.

As discussed in this chapter, numerous NIR fluorescent probes, including organic dyes, fluorescent proteins, and nanoparticles, have been used for fluorescence bioimaging. Most of them for bioimaging take advantage of single-photon excitation, emitting long wavelength fluorescence when excited by low wavelength light. In contrast, by using the anti-Stokes luminescence process, two-photon-excited fluorescence imaging offers a powerful approach for bioimaging of the living tissue to eliminate autofluorescence. Due to the requirement of simultaneous absorption of two coherent photons, these two-photon fluorescence materials usually exhibit narrow two-photon absorption cross sections and low two-photon emission efficiency. In addition, expensive pulsed lasers (usually a femtosecond laser) are needed for two-photon fluorescence imaging.

On account of intrinsic upconversion luminescent features and narrow emission lines, UCNPs have attracted significant attention, providing lots of uncommon opportunities in bioimaging applications. On the other hand, their drawbacks include less facile bioconjugation and larger size. The safety concern of UCNPs in

biomedical application cannot be ignored. Thus, how to design and develop safer and smarter UCNPs with enhanced quantum yields is a right research direction in this rapidly developing field. For nanosystems based on SiNPs, they have very bright fluorescence and possess excellent resistance to photo-bleaching. But, less facile multiplexing and large size hamper their practical use. Thus, it is necessary to design optimal and functional structures to enhance their biomedical performance by chemical modifications and bioconjugation, and detailed in vivo biosafety and performance investigations are also required. Furthermore, the synergistic combination of inorganic SiO_2 and organic functionalities is expected to highly facilitate the clinical translation of these nanosystems. In short, each type of fluorescent materials possesses their own merits and shortages. Choosing a right system for NIR fluorescent bioimaging depends on their performance for a specific biological task.

Acknowledgment This work was financially supported by the SingHealth-NTU Research Collaborative Grant (SHS-NTU/009/2016) and the Singapore Academic Research Fund (RG121/16 (S)).

References

1. Erathodiyil N, Ying JY (2011) Functionalization of inorganic nanoparticles for bioimaging applications. Acc Chem Res 44:925–935
2. Ueno T, Nagano T (2011) Fluorescent probes for sensing and imaging. Nat Method 8:642–645
3. Kobayashi H, Ogawa M, Alford R, Choyke PL et al (2010) New strategies for fluorescent probe design in medical diagnostic imaging. Chem Rev 110:2620–2640
4. Chengzhou Z, Dan D, Yuehe L (2015) Graphene and graphene-like 2D materials for optical biosensing and bioimaging: a review. 2D Mater 2:032004
5. Bardhan R, Lal S, Joshi A, Halas NJ (2011) Theranostic nanoshells: from probe design to imaging and treatment of cancer. Acc Chem Res 44:936–946
6. Ding C, Zhu A, Tian Y (2014) Functional surface engineering of C-dots for fluorescent biosensing and in vivo bioimaging. Acc Chem Res 47:20–30
7. Hsiao WW-W, Hui YY, Tsai P-C, Chang H-C (2016) Fluorescent nanodiamond: a versatile tool for long-term cell tracking, super-resolution imaging, and nanoscale temperature sensing. Acc Chem Res 49:400–407
8. Owens EA, Henary M, El Fakhri G, Choi HS (2016) Tissue-specific near-infrared fluorescence imaging. Acc Chem Res 49:1731–1740
9. Yuan L, Lin W, Zheng K, Zhu S (2013) FRET-based small-molecule fluorescent probes: rational design and bioimaging applications. Acc Chem Res 46:1462–1473
10. Zhu H, Fan J, Du J, Peng X (2016) Fluorescent probes for sensing and imaging within specific cellular organelles. Acc Chem Res 49:2115–2126
11. Lin J, Chen X, Huang P (2016) Graphene-based nanomaterials for bioimaging. Adv Drug Deliv Rev 105, Part B:242–254
12. Pu K-Y, Liu B (2011) Fluorescent conjugated polyelectrolytes for bioimaging. Adv Funct Mater 21:3408–3423
13. Xing P, Zhao Y (2016) Multifunctional nanoparticles self-assembled from small organic building blocks for biomedicine. Adv Mater 28:7304–7339
14. Tan G-R, Wang M, Hsu C-Y, Chen N et al (2016) Small upconverting fluorescent nanoparticles for biosensing and bioimaging. Adv Opt Mater 4:984–997
15. Kushida Y, Nagano T, Hanaoka K (2015) Silicon-substituted xanthene dyes and their applications in bioimaging. Analyst 140:685–695

16. Li J, Zhu J-J (2013) Quantum dots for fluorescent biosensing and bio-imaging applications. Analyst 138:2506–2515
17. Hahn MA, Singh AK, Sharma P, Brown SC et al (2011) Nanoparticles as contrast agents for in-vivo bioimaging: current status and future perspectives. Anal Bioanal Chem 399:3–27
18. Umezawa K, Citterio D, Suzuki K (2014) New trends in near-infrared fluorophores for bioimaging. Anal Sci 30:327–349
19. Chakraborty K, Veetil AT, Jaffrey SR, Krishnan Y (2016) Nucleic acid–based nanodevices in biological imaging. Annu Rev Biochem 85:349–373
20. Petryayeva E, Algar WR, Medintz IL (2013) Quantum dots in bioanalysis: a review of applications across various platforms for fluorescence spectroscopy and imaging. Appl Spectrosc 67:215–252
21. Du X, Li X, Xiong L, Zhang X et al (2016) Mesoporous silica nanoparticles with organo-bridged silsesquioxane framework as innovative platforms for bioimaging and therapeutic agent delivery. Biomaterials 91:90–127
22. Bae SW, Tan W, Hong J-I (2012) Fluorescent dye-doped silica nanoparticles: new tools for bioapplications. Chem Commun 48:2270–2282
23. Georgakilas V, Tiwari JN, Kemp KC, Perman JA et al (2016) Noncovalent functionalization of graphene and graphene oxide for energy materials, biosensing, catalytic, and biomedical applications. Chem Rev 116:5464–5519
24. Louie A (2010) Multimodality imaging probes: design and challenges. Chem Rev 110:3146–3195
25. Smith BR, Gambhir SS (2017) Nanomaterials for in vivo imaging. Chem Rev 117:901–986
26. Sun W, Guo S, Hu C, Fan J et al (2016) Recent development of chemosensors based on cyanine platforms. Chem Rev 116:7768–7817
27. Yang Y, Zhao Q, Feng W, Li F (2013) Luminescent chemodosimeters for bioimaging. Chem Rev 113:192–270
28. Yao J, Yang M, Duan Y (2014) Chemistry, biology, and medicine of fluorescent nanomaterials and related systems: new insights into biosensing, bioimaging, genomics, diagnostics, and therapy. Chem Rev 114:6130–6178
29. Wang L-J, Ma F, Tang B, Zhang C-Y (2017) Sensing telomerase: from in vitro detection to in vivo imaging. Chem Sci 8:2495–2502
30. Amoroso AJ, Pope SJA (2015) Using lanthanide ions in molecular bioimaging. Chem Soc Rev 44:4723–4742
31. Ashton TD, Jolliffe KA, Pfeffer FM (2015) Luminescent probes for the bioimaging of small anionic species in vitro and in vivo. Chem Soc Rev 44:4547–4595
32. Chen X, Zhang W (2017) Diamond nanostructures for drug delivery, bioimaging, and biosensing. Chem Soc Rev 46:734–760
33. Meng H-M, Liu H, Kuai H, Peng R et al (2016) Aptamer-integrated DNA nanostructures for biosensing, bioimaging and cancer therapy. Chem Soc Rev 45:2583–2602
34. Montalti M, Cantelli A, Battistelli G (2015) Nanodiamonds and silicon quantum dots: ultrastable and biocompatible luminescent nanoprobes for long-term bioimaging. Chem Soc Rev 44:4853–4921
35. Tang Y, Lee D, Wang J, Li G et al (2015) Development of fluorescent probes based on protection-deprotection of the key functional groups for biological imaging. Chem Soc Rev 44:5003–5015
36. Wegner KD, Hildebrandt N (2015) Quantum dots: bright and versatile in vitro and in vivo fluorescence imaging biosensors. Chem Soc Rev 44:4792–4834
37. Wolfbeis OS (2015) An overview of nanoparticles commonly used in fluorescent bioimaging. Chem Soc Rev 44:4743–4768
38. Wu P, Yan X-P (2013) Doped quantum dots for chemo/biosensing and bioimaging. Chem Soc Rev 42:5489–5521
39. Wu X, Zhu W (2015) Stability enhancement of fluorophores for lighting up practical application in bioimaging. Chem Soc Rev 44:4179–4184

40. Yang Z, Cao J, He Y, Yang JH et al (2014) Macro−/micro-environment-sensitive chemosensing and biological imaging. Chem Soc Rev 43:4563–4601
41. Yang Z, Sharma A, Qi J, Peng X et al (2016) Super-resolution fluorescent materials: an insight into design and bioimaging applications. Chem Soc Rev 45:4651–4667
42. Yoo JM, Kang JH, Hong BH (2015) Graphene-based nanomaterials for versatile imaging studies. Chem Soc Rev 44:4835–4852
43. Zhao Q, Huang C, Li F (2011) Phosphorescent heavy-metal complexes for bioimaging. Chem Soc Rev 40:2508–2524
44. Zhou J, Liu Z, Li F (2012) Upconversion nanophosphors for small-animal imaging. Chem Soc Rev 41:1323–1349
45. Zrazhevskiy P, Sena M, Gao X (2010) Designing multifunctional quantum dots for bioimaging, detection, and drug delivery. Chem Soc Rev 39:4326–4354
46. LeCroy GE, Yang S-T, Yang F, Liu Y et al (2016) Functionalized carbon nanoparticles: syntheses and applications in optical bioimaging and energy conversion. Coord Chem Rev 320–321:66–81
47. Liu Q, Feng W, Li F (2014) Water-soluble lanthanide upconversion nanophosphors: synthesis and bioimaging applications in vivo. Coord Chem Rev 273–274:100–110
48. Mukherjee A, Schroeder CM (2015) Flavin-based fluorescent proteins: emerging paradigms in biological imaging. Curr Opin Biotechnol 31:16–23
49. Escobedo JO, Rusin O, Lim S, Strongin RM (2010) NIR dyes for bioimaging applications. Curr Opin Chem Biol 14:64
50. Becker JS (2010) Bioimaging of metals in brain tissue from micrometre to nanometre scale by laser ablation inductively coupled plasma mass spectrometry: state of the art and perspectives. Int J Mass Spectrom 289:65–75
51. Gomes MC, Cunha Â, Trindade T, Tomé JPC (2016) The role of surface functionalization of silica nanoparticles for bioimaging. J Innov Opt Health Sci 09:1630005
52. Chen S, Wang H, Hong Y, Tang BZ (2016) Fabrication of fluorescent nanoparticles based on AIE luminogens (AIE dots) and their applications in bioimaging. Mater Horiz 3:283–293
53. Du D, Yang Y, Lin Y (2012) Graphene-based materials for biosensing and bioimaging. MRS Bull 37:1290–1296
54. Hemmer E, Venkatachalam N, Hyodo H, Hattori A et al (2013) Upconverting and NIR emitting rare earth based nanostructures for NIR-bioimaging. Nanoscale 5:11339–11361
55. Chudakov DM, Matz MV, Lukyanov S, Lukyanov KA (2010) Fluorescent proteins and their applications in imaging living cells and tissues. Physiol Rev 90:1103–1163
56. Niu J, Wang X, Lv J, Li Y et al (2014) Luminescent nanoprobes for in-vivo bioimaging. TrAC Trends Anal Chem 58:112–119
57. Yu M, Li F, Chen Z, Hu H et al (2009) Laser scanning up-conversion luminescence microscopy for imaging cells labeled with rare-earth nanophosphors. Anal Chem 81:930–935
58. So PTC, Dong CY, Masters BR, Berland KM (2000) Two-photon excitation fluorescence microscopy. Annu Rev Biomed Eng 2:399–429
59. Yi M, Yang S, Peng Z, Liu C et al (2014) Two-photon graphene oxide/aptamer nanosensing conjugate for in vitro or in vivo molecular probing. Anal Chem 86:3548–3554
60. Nagano T (2010) Development of fluorescent probes for bioimaging applications. Proc Jpn Acad Ser B 86:837–847
61. Chan J, Dodani SC, Chang CJ (2012) Reaction-based small-molecule fluorescent probes for chemoselective bioimaging. Nat Chem 4:973–984
62. Barbieri A, Bandini E, Monti F, Praveen VK et al (2016) The rise of near-infrared emitters: organic dyes, porphyrinoids, and transition metal complexes. Top Curr Chem 374:47
63. Yuan L, Lin W, Zheng K, He L et al (2013) Far-red to near infrared analyte-responsive fluorescent probes based on organic fluorophore platforms for fluorescence imaging. Chem Soc Rev 42:622–661
64. Isago H (2015) Optical spectra of phthalocyanines and related compounds: a guide for beginners. Springer, Tokyo, pp 107–132
65. Owens EA, Hyun H, Kim SH, Lee JH et al (2013) Highly charged cyanine fluorophores for trafficking scaffold degradation. Biomed Mater 8:014109

66. Park JH, Royer JE, Chagarov E, Kaufman-Osborn T et al (2013) Atomic imaging of the irreversible sensing mechanism of NO_2 adsorption on copper phthalocyanine. J Am Chem Soc 135:14600–14609
67. Chen X, Pradhan T, Wang F, Kim JS et al (2012) Fluorescent chemosensors based on spiroring-opening of xanthenes and related derivatives. Chem Rev 112:1910–1956
68. Katori A, Azuma E, Ishimura H, Kuramochi K et al (2015) Fluorescent dyes with directly connected xanthone and xanthene units. J Org Chem 80:4603–4610
69. He X, Wu X, Wang K, Shi B et al (2009) Methylene blue-encapsulated phosphonate-terminated silica nanoparticles for simultaneous in vivo imaging and photodynamic therapy. Biomaterials 30:5601–5609
70. Oushiki D, Kojima H, Terai T, Arita M et al (2010) Development and application of a near-infrared fluorescence probe for oxidative stress based on differential reactivity of linked cyanine dyes. J Am Chem Soc 132:2795–2801
71. Peng X, Song F, Lu E, Wang Y et al (2005) Heptamethine cyanine dyes with a large stokes shift and strong fluorescence: a paradigm for excited-state intramolecular charge transfer. J Am Chem Soc 127:4170–4171
72. Tasior M, O'Shea DF (2010) BF2-chelated tetraarylazadipyrromethenes as NIR fluorochromes. Bioconjug Chem 21:1130–1133
73. Pansare VJ, Hejazi S, Faenza WJ, Prud'homme RK (2012) Review of long-wavelength optical and NIR imaging materials: contrast agents, fluorophores, and multifunctional nano carriers. Chem Mater 24:812–827
74. Choi HS, Nasr K, Alyabyev S, Feith D et al (2011) Synthesis and in vivo fate of zwitterionic near-infrared fluorophores. Angew Chem Int Ed 50:6258–6263
75. Rong P, Huang P, Liu Z, Lin J et al (2015) Protein-based photothermal theranostics for imaging-guided cancer therapy. Nanoscale 7:16330–16336
76. Owens EA, Hyun H, Tawney JG, Choi HS et al (2015) Correlating molecular character of NIR imaging agents with tissue-specific uptake. J Med Chem 58:4348–4356
77. Zhang K, Zhang J, Xi Z, Li L-Y et al (2017) A new H_2S-specific near-infrared fluorescence-enhanced probe that can visualize the H_2S level in colorectal cancer cells in mice. Chem Sci 8:2776–2781
78. Hyun H, Wada H, Bao K, Gravier J et al (2014) Phosphonated near-infrared fluorophores for biomedical imaging of bone. Angew Chem Int Ed 53:10668–10672
79. Hyun H, Owens EA, Wada H, Levitz A et al (2015) Cartilage-specific near-infrared fluorophores for biomedical imaging. Angew Chem Int Ed 54:8648–8652
80. Choi HS, Gibbs SL, Lee JH, Kim SH et al (2013) Targeted zwitterionic near-infrared fluorophores for improved optical imaging. Nat Biotechnol 31:148–153
81. Hyun H, Park MH, Owens EA, Wada H et al (2015) Structure-inherent targeting of near-infrared fluorophores for parathyroid and thyroid gland imaging. Nat Med 21:192–197
82. Fischer GM, Jungst C, Isomaki-Krondahl M, Gauss D et al (2010) Asymmetric PPCys: strongly fluorescing NIR labels. Chem Commun 46:5289–5291
83. Anees P, Joseph J, Sreejith S, Menon NV et al (2016) Real time monitoring of aminothiol level in blood using a near-infrared dye assisted deep tissue fluorescence and photoacoustic bimodal imaging. Chem Sci 7:4110–4116
84. Avirah RR, Jayaram DT, Adarsh N, Ramaiah D (2012) Squaraine dyes in PDT: from basic design to in vivo demonstration. Org Biomol Chem 10:911–920
85. Hu L, Yan Z, Xu H (2013) Advances in synthesis and application of near-infrared absorbing squaraine dyes. RSC Adv 3:7667–7676
86. Beverina L, Salice P (2010) Squaraine compounds: tailored design and synthesis towards a variety of material science applications. Eur J Org Chem 2010:1207–1225
87. Anees P, Sreejith S, Ajayaghosh A (2014) Self-assembled near-infrared dye nanoparticles as a selective protein sensor by activation of a dormant fluorophore. J Am Chem Soc 136:13233–13239
88. Baumes JM, Gassensmith JJ, Giblin J, Lee J-J et al (2010) Storable, thermally activated, near-infrared chemiluminescent dyes and dye-stained microparticles for optical imaging. Nat Chem 2:1025–1030

89. A. Poirel, A. De Nicola and R. Ziessel, Oligothienyl-BODIPYs: red and near-infrared emitters, Org Lett, 2012, 14: 5696–5699
90. Ni Y, Wu J (2014) Far-red and near infrared BODIPY dyes: synthesis and applications for fluorescent pH probes and bio-imaging. Org Biomol Chem 12:3774–3791
91. Zhang X, Yu H, Xiao Y (2012) Replacing phenyl ring with thiophene: an approach to longer wavelength aza-dipyrromethene boron difluoride (Aza-BODIPY) dyes. J Org Chem 77:669–673
92. Lu H, Mack J, Yang Y, Shen Z (2014) Structural modification strategies for the rational design of red/NIR region BODIPYs. Chem Soc Rev 43:4778–4823
93. Loudet A, Burgess K (2007) BODIPY dyes and their derivatives: syntheses and spectroscopic properties. Chem Rev 107:4891–4932
94. Ulrich G, Ziessel R, Harriman A (2008) The chemistry of fluorescent bodipy dyes: versatility unsurpassed. Angew Chem Int Ed 47:1184–1201
95. Tasior M, Murtagh J, Frimannsson DO, McDonnell SO et al (2010) Water-solubilised BF2-chelated tetraarylazadipyrromethenes. Org Biomol Chem 8:522–525
96. Jiang N, Fan J, Liu T, Cao J et al (2013) A near-infrared dye based on BODIPY for tracking morphology changes in mitochondria. Chem Commun 49:10620–10622
97. Wu H, Krishnakumar S, Yu J, Liang D et al (2014) Highly selective and sensitive near-infrared-fluorescent probes for the detection of cellular hydrogen sulfide and the imaging of H_2S in mice. Chem Asian J 9:3604–3611
98. Tian J, Zhou J, Shen Z, Ding L et al (2015) A pH-activatable and aniline-substituted photosensitizer for near-infrared cancer theranostics. Chem Sci 6:5969–5977
99. McQuade LE, Ma J, Lowe G, Ghatpande A et al (2010) Visualization of nitric oxide production in the mouse main olfactory bulb by a cell-trappable copper(II) fluorescent probe. Proc Natl Acad Sci 107:8525–8530
100. Koide Y, Urano Y, Hanaoka K, Piao W et al (2012) Development of NIR fluorescent dyes based on Si–rhodamine for in vivo imaging. J Am Chem Soc 134:5029–5031
101. Yuan L, Lin W, Yang Y, Chen H (2012) A unique class of near-infrared functional fluorescent dyes with carboxylic-acid-modulated fluorescence ON/OFF switching: rational design, synthesis, optical properties, theoretical calculations, and applications for fluorescence imaging in living animals. J Am Chem Soc 134:1200–1211
102. Koide Y, Urano Y, Hanaoka K, Terai T et al (2011) Development of an Si-rhodamine-based far-red to near-infrared fluorescence probe selective for hypochlorous acid and its applications for biological imaging. J Am Chem Soc 133:5680–5682
103. Bhupathiraju NVSDK, Rizvi W, Batteas JD, Drain CM (2016) Fluorinated porphyrinoids as efficient platforms for new photonic materials, sensors, and therapeutics. Org Biomol Chem 14:389–408
104. Babu SS, Bonifazi D (2014) Self-organization of polar porphyrinoids. ChemPlusChem 79:895–906
105. Sommer JR, Shelton AH, Parthasarathy A, Ghiviriga I et al (2011) Photophysical properties of near-infrared phosphorescent π-extended platinum porphyrins. Chem Mater 23:5296–5304
106. Lovell JF, Jin CS, Huynh E, Jin H et al (2011) Porphysome nanovesicles generated by porphyrin bilayers for use as multimodal biophotonic contrast agents. Nat Mater 10:324–332
107. Kim J, Tung C-H, Choi Y (2014) Smart dual-functional warhead for folate receptor-specific activatable imaging and photodynamic therapy. Chem Commun 50:10600–10603
108. Lee H, Kim J, Kim H, Kim Y et al (2014) A folate receptor-specific activatable probe for near-infrared fluorescence imaging of ovarian cancer. Chem Commun 50:7507–7510
109. Yang Q, Ma Z, Wang H, Zhou B et al (2017) Rational design of molecular fluorophores for biological imaging in the NIR-II window. Adv Mater 29:1605497
110. Divya KP, Sreejith S, Ashokkumar P, Yuzhan K et al (2014) A ratiometric fluorescent molecular probe with enhanced two-photon response upon Zn2+ binding for in vitro and in vivo bioimaging. Chem Sci 5:3469–3474

111. Tian J, Ding L, Xu H-J, Shen Z et al (2013) Cell-specific and pH-activatable rubyrin-loaded nanoparticles for highly selective near-infrared photodynamic therapy against cancer. J Am Chem Soc 135:18850–18858
112. Sun W, Fan J, Hu C, Cao J et al (2013) A two-photon fluorescent probe with near-infrared emission for hydrogen sulfide imaging in biosystems. Chem Commun 49:3890–3892
113. Chen Y, Guan R, Zhang C, Huang J et al (2016) Two-photon luminescent metal complexes for bioimaging and cancer phototherapy. Coord Chem Rev 310:16–40
114. Zhang KY, Liu S, Zhao Q, Li F et al (2015) In: Lo KK-W (ed) Luminescent and photoactive transition metal complexes as biomolecular probes and cellular reagents. Springer, Berlin/Heidelberg, pp 131–180
115. Jing J, Chen J-J, Hai Y, Zhan J et al (2012) Rational design of ZnSalen as a single and two photon activatable fluorophore in living cells. Chem Sci 3:3315–3320
116. Xie D, Jing J, Cai Y-B, Tang J et al (2014) Construction of an orthogonal ZnSalen/Salophen library as a colour palette for one- and two-photon live cell imaging. Chem Sci 5:2318–2327
117. Shu X, Royant A, Lin MZ, Aguilera TA et al (2009) Mammalian expression of infrared fluorescent proteins engineered from a bacterial phytochrome. Science 324:804–807
118. Allison RR (2016) Fluorescence guided resection (FGR): a primer for oncology. Photodiagn Photodyn Ther 13:73–80
119. Lin MZ (2011) Beyond the rainbow: new fluorescent proteins brighten the infrared scene. Nat Method 8:726–728
120. Lecoq J, Schnitzer MJ (2011) An infrared fluorescent protein for deeper imaging. Nat Biotechnol 29:715–716
121. Shcherbo D, Shemiakina II, Ryabova AV, Luker KE et al (2010) Near-infrared fluorescent proteins. Nat Method 7:827–829
122. Filonov GS, Piatkevich KD, Ting L-M, Zhang J et al (2011) Bright and stable near-infrared fluorescent protein for in vivo imaging. Nat Biotechnol 29:757–761
123. Gong H, Kovar J, Little G, Chen H et al (2010) In vivo imaging of xenograft tumors using an epidermal growth factor receptor-specific affibody molecule labeled with a near-infrared fluorophore. Neoplasia (New York) 12:139–149
124. He J, Wang Y, Missinato MA, Onuoha E et al (2016) A genetically targetable near-infrared photosensitizer. Nat Method 13:263–268
125. Wang Y, Ballou B, Schmidt BF, Andreko S et al (2017) Affibody-targeted fluorogen activating protein for in vivo tumor imaging. Chem Commun 53:2001–2004
126. Yang Y, Xiang K, Yang Y-X, Wang Y-W et al (2013) An individually coated near-infrared fluorescent protein as a safe and robust nanoprobe for in vivo imaging. Nanoscale 5:10345–10352
127. Hong H, Goel S, Zhang Y, Cai W (2011) Molecular imaging with nucleic acid aptamers. Curr Med Chem 18:4195–4205
128. Mallikaratchy PR, Ruggiero A, Gardner JR, Kuryavyi V et al (2011) A multivalent DNA aptamer specific for the B-cell receptor on human lymphoma and leukemia. Nucleic Acids Res 39:2458–2469
129. Shi H, He X, Wang K, Wu X et al (2011) Activatable aptamer probe for contrast-enhanced in vivo cancer imaging based on cell membrane protein-triggered conformation alteration. Proc Natl Acad Sci 108:3900–3905
130. Gong P, Shi B, Zheng M, Wang B et al (2012) PEI protected aptamer molecular probes for contrast-enhanced in vivo cancer imaging. Biomaterials 33:7810–7817
131. Choi HMT, Beck VA, Pierce NA (2014) Next-generation in situ hybridization chain reaction: higher gain, lower cost, greater durability. ACS Nano 8:4284–4294
132. Choi HMT, Chang JY, Trinh LA, Padilla JE et al (2010) Programmable in situ amplification for multiplexed imaging of mRNA expression. Nat Biotechnol 28:1208–1212
133. Hu S-H, Gao X (2010) Nanocomposites with spatially separated functionalities for combined imaging and magnetolytic therapy. J Am Chem Soc 132:7234–7237

134. Zhang X, Wang S, Xu L, Feng L et al (2012) Biocompatible polydopamine fluorescent organic nanoparticles: facile preparation and cell imaging. Nanoscale 4:5581–5584
135. Wang X-d, Meier RJ, Wolfbeis OS (2012) A fluorophore-doped polymer nanomaterial for referenced imaging of pH and temperature with sub-micrometer resolution. Adv Funct Mater 22:4202–4207
136. Schreml S, Meier RJ, Kirschbaum M, Kong SC et al (2014) Luminescent dual sensors reveal extracellular pH-gradients and hypoxia on chronic wounds that disrupt epidermal repair. Theranostics 4:721–735
137. Li Y, Yang HY, Lee DS (2016) Polymer-based and pH-sensitive nanobiosensors for imaging and therapy of acidic pathological areas. Pharm Res 33:2358–2372
138. Tuncel D, Demir HV (2010) Conjugated polymer nanoparticles. Nanoscale 2:484–494
139. Xu H, Wang L, Fan C (2012) Functional nanoparticles for bioanalysis. Nanomedicine, and bioelectronic devices, vol 1. ACS symposium series, vol 1112, Chapter 4. American Chemical Society, Washington, DC, pp 81–117
140. Wu C, Szymanski C, Cain Z, McNeill J (2007) Conjugated polymer dots for multiphoton fluorescence imaging. J Am Chem Soc 129:12904–12905
141. Kim S, Lim C-K, Na J, Lee Y-D et al (2010) Conjugated polymer nanoparticles for biomedical in vivo imaging. Chem Commun 46:1617–1619
142. Li K, Liu Y, Pu K-Y, Feng S-S et al (2011) Polyhedral oligomeric silsesquioxanes-containing conjugated polymer loaded PLGA nanoparticles with trastuzumab (herceptin) functionalization for HER2-positive cancer cell detection. Adv Funct Mater 21:287–294
143. Shuhendler AJ, Pu K, Cui L, Uetrecht JP et al (2014) Real-time imaging of oxidative and nitrosative stress in the liver of live animals for drug-toxicity testing. Nat Biotechnol 32:373–380
144. Klingstedt T, Nilsson KPR (2011) Conjugated polymers for enhanced bioimaging. Biochim Biophys Acta Gen Subj 1810:286–296
145. Jeong K, Park S, Lee Y-D, Lim C-K et al (2013) Conjugated polymer/photochromophore binary nanococktails: bistable photoswitching of near-infrared fluorescence for in vivo imaging. Adv Mater 25:5574–5580
146. Ding D, Liu J, Feng G, Li K et al (2013) Bright far-red/near-infrared conjugated polymer nanoparticles for in vivo bioimaging. Small 9:3093–3102
147. Greenham NC, Moratti SC, Bradley DDC, Friend RH et al (1993) Efficient light-emitting diodes based on polymers with high electron affinities. Nature 365:628–630
148. Lyu Y, Pu K (2017) Recent advances of activatable molecular probes based on semiconducting polymer nanoparticles in sensing and imaging. Adv Sci 4:1600481
149. Zhu H, Fang Y, Zhen X, Wei N et al (2016) Multilayered semiconducting polymer nanoparticles with enhanced NIR fluorescence for molecular imaging in cells, zebrafish and mice. Chem Sci 7:5118–5125
150. Jin Y, Ye F, Zeigler M, Wu C et al (2011) Near-infrared fluorescent dye-doped semiconducting polymer dots. ACS Nano 5:1468–1475
151. Pu K, Shuhendler AJ, Rao J (2013) Semiconducting polymer nanoprobe for in vivo imaging of reactive oxygen and nitrogen species. Angew Chem Int Ed 52:10325–10329
152. Wu C, Hansen SJ, Hou Q, Yu J et al (2011) Design of highly emissive polymer dot bioconjugates for in vivo tumor targeting. Angew Chem Int Ed 50:3430–3434
153. Pu K, Chattopadhyay N, Rao J (2016) Recent advances of semiconducting polymer nanoparticles in in vivo molecular imaging. J Control Release 240:312–322
154. Liu H-Y, Wu P-J, Kuo S-Y, Chen C-P et al (2015) Quinoxaline-based polymer dots with ultrabright red to near-infrared fluorescence for in vivo biological imaging. J Am Chem Soc 137:10420–10429
155. Pu K, Shuhendler AJ, Valta MP, Cui L et al (2014) Phosphorylcholine-coated semiconducting polymer nanoparticles as rapid and efficient labeling agents for in vivo cell tracking. Adv Healthc Mater 3:1292–1298

156. Ding D, Li K, Zhu Z, Pu K-Y et al (2011) Conjugated polyelectrolyte-cisplatin complex nanoparticles for simultaneous in vivo imaging and drug tracking. Nanoscale 3:1997–2002
157. Fu L, Sun C, Yan L (2015) Galactose targeted pH-responsive copolymer conjugated with near infrared fluorescence probe for imaging of intelligent drug delivery. ACS Appl Mater Interfaces 7:2104–2115
158. Koo H, Lee H, Lee S, Min KH et al (2010) In vivo tumor diagnosis and photodynamic therapy via tumoral pH-responsive polymeric micelles. Chem Commun 46:5668–5670
159. Shen S, Wang Q (2013) Rational tuning the optical properties of metal sulfide nanocrystals and their applications. Chem Mater 25:1166–1178
160. Jing L, Kershaw SV, Li Y, Huang X et al (2016) Aqueous based semiconductor nanocrystals. Chem Rev 116:10623–10730
161. Lim SJ, Ma L, Schleife A, Smith AM (2016) Quantum dot surface engineering: toward inert fluorophores with compact size and bright, stable emission. Coord Chem Rev 320–321:216–237
162. He Y, Zhong Y, Su Y, Lu Y et al (2011) Water-dispersed near-infrared-emitting quantum dots of ultrasmall sizes for in vitro and in vivo imaging. Angew Chem Int Ed 50:5695–5698
163. Gu Y-P, Cui R, Zhang Z-L, Xie Z-X et al (2012) Ultrasmall near-infrared Ag_2Se quantum dots with tunable fluorescence for in vivo imaging. J Am Chem Soc 134:79–82
164. Wang J, Lu Y, Peng F, Zhong Y et al (2013) Photostable water-dispersible NIR-emitting CdTe/CdS/ZnS core–shell–shell quantum dots for high-resolution tumor targeting. Biomaterials 34:9509–9518
165. Wang Y, Hu R, Lin G, Law W-C et al (2013) Optimizing the aqueous phase synthesis of CdTe quantum dots using mixed-ligands system and their applications for imaging of live cancer cells and tumors in vivo. RSC Adv 3:8899–8908
166. Chen L-N, Wang J, Li W-T, Han H-Y (2012) Aqueous one-pot synthesis of bright and ultrasmall CdTe/CdS near-infrared-emitting quantum dots and their application for tumor targeting in vivo. Chem Commun 48:4971–4973
167. Kikushima K, Kita S, Higuchi H (2013) A non-invasive imaging for the in vivo tracking of high-speed vesicle transport in mouse neutrophils. Sci Rep 3:1913
168. Chen G, Tian F, Zhang Y, Zhang Y et al (2014) Tracking of transplanted human mesenchymal stem cells in living mice using near-infrared Ag_2S quantum dots. Adv Funct Mater 24:2481–2488
169. Hasegawa M, Tsukasaki Y, Ohyanagi T, Jin T (2013) Bioluminescence resonance energy transfer coupled near-infrared quantum dots using GST-tagged luciferase for in vivo imaging. Chem Commun 49:228–230
170. Yang K, Zhang F-J, Tang H, Zhao C et al (2011) In-vivo imaging of oral squamous cell carcinoma by EGFR monoclonal antibody conjugated near-infrared quantum dots in mice. Int J Nanomedicine 6:1739–1745
171. Yong K-T, Roy I, Law W-C, Hu R (2010) Synthesis of cRGD-peptide conjugated near-infrared CdTe/ZnSe core-shell quantum dots for in vivo cancer targeting and imaging. Chem Commun 46:7136–7138
172. Li C, Ji Y, Wang C, Liang S et al (2014) BRCAA1 antibody- and Her2 antibody-conjugated amphiphilic polymer engineered CdSe/ZnS quantum dots for targeted imaging of gastric cancer. Nanoscale Res Lett 9:244
173. Yuan Y, Zhang J, An L, Cao Q et al (2014) Oligomeric nanoparticles functionalized with NIR-emitting CdTe/CdS QDs and folate for tumor-targeted imaging. Biomaterials 35:7881–7886
174. Liu L, Yong K-T, Roy I, Law W-C et al (2012) Bioconjugated pluronic triblock-copolymer micelle-encapsulated quantum dots for targeted imaging of cancer: in vitro and in vivo studies. Theranostics 2:705–713
175. Liu L-w, Hu S-y, Pan Y, Zhang J-q et al (2014) Optimizing the synthesis of CdS/ZnS core/shell semiconductor nanocrystals for bioimaging applications. Beilstein J Nanotechnol 5:919–926

176. Ding H, Yong K-T, Law W-C, Roy I et al (2011) Non-invasive tumor detection in small animals using novel functional Pluronic nanomicelles conjugated with anti-mesothelin antibody. Nanoscale 3:1813–1822
177. Guo W, Sun X, Jacobson O, Yan X et al (2015) Intrinsically radioactive [^{64}Cu]CuInS/ZnS quantum dots for PET and optical imaging: improved radiochemical stability and controllable cerenkov luminescence. ACS Nano 9:488–495
178. Andrasfalvy BK, Galinanes GL, Huber D, Barbic M et al (2014) Quantum dot-based multiphoton fluorescent pipettes for targeted neuronal electrophysiology. Nat Method 11:1237–1241
179. Xu X, Ray R, Gu Y, Ploehn HJ et al (2004) Electrophoretic analysis and purification of fluorescent single-walled carbon nanotube fragments. J Am Chem Soc 126:12736–12737
180. Yang S-T, Cao L, Luo PG, Lu F et al (2009) Carbon dots for optical imaging in vivo. J Am Chem Soc 131:11308–11309
181. Baker SN, Baker GA (2010) Luminescent carbon nanodots: emergent nanolights. Angew Chem Int Ed 49:6726–6744
182. Liu J-H, Anilkumar P, Cao L, Wang X et al (2010) Cytotoxicity evaluations of fluorescent carbon nanoparticles. Nano Life 01:153–161
183. Luo PG, Sahu S, Yang S-T, Sonkar SK et al (2013) Carbon "quantum" dots for optical bioimaging. J Mater Chem B 1:2116–2127
184. Sharker SM, Kim SM, Lee JE, Jeong JH et al (2015) In situ synthesis of luminescent carbon nanoparticles toward target bioimaging. Nanoscale 7:5468–5475
185. Yuan F, Li S, Fan Z, Meng X et al (2016) Shining carbon dots: synthesis and biomedical and optoelectronic applications. Nano Today 11:565–586
186. Li H, Kang Z, Liu Y, Lee S-T (2012) Carbon nanodots: synthesis, properties and applications. J Mater Chem 22:24230–24253
187. Wang Y, Hu A (2014) Carbon quantum dots: synthesis, properties and applications. J Mater Chem C 2:6921–6939
188. Roy P, Chen P-C, Periasamy AP, Chen Y-N et al (2015) Photoluminescent carbon nanodots: synthesis, physicochemical properties and analytical applications. Mater Today 18:447–458
189. Liu X, Pang J, Xu F, Zhang X (2016) Simple approach to synthesize amino-functionalized carbon dots by carbonization of chitosan. Sci Rep 6:31100
190. Zhang J, Yu S-H (2016) Carbon dots: large-scale synthesis, sensing and bioimaging. Mater Today 19:382–393
191. Nguyen V, Si J, Yan L, Hou X (2015) Electron–hole recombination dynamics in carbon nanodots. Carbon 95:659–663
192. Wang F, Pang S, Wang L, Li Q et al (2010) One-step synthesis of highly luminescent carbon dots in noncoordinating solvents. Chem Mater 22:4528–4530
193. Li X, Wang H, Shimizu Y, Pyatenko A et al (2011) Preparation of carbon quantum dots with tunable photoluminescence by rapid laser passivation in ordinary organic solvents. Chem Commun 47:932–934
194. Li H, He X, Liu Y, Huang H et al (2011) One-step ultrasonic synthesis of water-soluble carbon nanoparticles with excellent photoluminescent properties. Carbon 49:605–609
195. Huang X, Zhang F, Zhu L, Choi KY et al (2013) Effect of injection routes on the biodistribution, clearance, and tumor uptake of carbon dots. ACS Nano 7:5684–5693
196. Huang P, Lin J, Wang X, Wang Z et al (2012) Light-triggered theranostics based on photosensitizer-conjugated carbon dots for simultaneous enhanced-fluorescence imaging and photodynamic therapy. Adv Mater 24:5104–5110
197. Kong B, Zhu A, Ding C, Zhao X et al (2012) Carbon dot-based inorganic–organic nanosystem for two-photon imaging and biosensing of pH variation in living cells and tissues. Adv Mater 24:5844–5848
198. Wang X, Liu Z (2012) Carbon nanotubes in biology and medicine: an overview. Chin Sci Bull 57:167–180

199. O'Connell MJ, Bachilo SM, Huffman CB, Moore VC et al (2002) Band gap fluorescence from individual single-walled carbon nanotubes. Science 297:593–596
200. Welsher K, Liu Z, Sherlock SP, Robinson JT et al (2009) A route to brightly fluorescent carbon nanotubes for near-infrared imaging in mice. Nat Nanotechnol 4:773–780
201. Hong G, Tabakman SM, Welsher K, Wang H et al (2010) Metal-enhanced fluorescence of carbon nanotubes. J Am Chem Soc 132:15920–15923
202. Joselevich E, Dai H, Liu J, Hata K et al (2008) In: Jorio A, Dresselhaus G, Dresselhaus MS (eds) Carbon nanotubes: advanced topics in the synthesis, structure, properties and applications. Springer, Berlin/Heidelberg, pp 101–165
203. Hong H, Gao T, Cai W (2009) Molecular imaging with single-walled carbon nanotubes. Nano Today 4:252–261
204. Liu Z, Tabakman S, Welsher K, Dai H (2009) Carbon nanotubes in biology and medicine: in vitro and in vivo detection, imaging and drug delivery. Nano Res 2:85–120
205. Wu H-C, Chang X, Liu L, Zhao F et al (2010) Chemistry of carbon nanotubes in biomedical applications. J Mater Chem 20:1036–1052
206. Huang H, Zou M, Xu X, Liu F et al (2011) Near-infrared fluorescence spectroscopy of single-walled carbon nanotubes and its applications. TrAC Trends Anal Chem 30:1109–1119
207. Liu Z, Yang K, Lee S-T (2011) Single-walled carbon nanotubes in biomedical imaging. J Mater Chem 21:586–598
208. Gong H, Peng R, Liu Z (2013) Carbon nanotubes for biomedical imaging: the recent advances. Adv Drug Deliv Rev 65:1951–1963
209. Mu B, Zhang J, McNicholas TP, Reuel NF et al (2014) Recent advances in molecular recognition based on nanoengineered platforms. Acc Chem Res 47:979–988
210. Welsher K, Sherlock SP, Dai H (2011) Deep-tissue anatomical imaging of mice using carbon nanotube fluorophores in the second near-infrared window. Proc Natl Acad Sci 108:8943–8948
211. Diao S, Hong G, Robinson JT, Jiao L et al (2012) Chirality enriched (12,1) and (11,3) single-walled carbon nanotubes for biological imaging. J Am Chem Soc 134:16971–16974
212. Robinson JT, Hong G, Liang Y, Zhang B et al (2012) In vivo fluorescence imaging in the second near-infrared window with long circulating carbon nanotubes capable of ultrahigh tumor uptake. J Am Chem Soc 134:10664–10669
213. Yi H, Ghosh D, Ham M-H, Qi J et al (2012) M13 phage-functionalized single-walled carbon nanotubes as nanoprobes for second near-infrared window fluorescence imaging of targeted tumors. Nano Lett 12:1176–1183
214. Shen H, Zhang L, Liu M, Zhang Z (2012) Biomedical applications of graphene. Theranostics 2:283–294
215. Shen J, Zhu Y, Yang X, Li C (2012) Graphene quantum dots: emergent nanolights for bioimaging, sensors, catalysis and photovoltaic devices. Chem Commun 48:3686–3699
216. Gollavelli G, Ling Y-C (2012) Multi-functional graphene as an in vitro and in vivo imaging probe. Biomaterials 33:2532–2545
217. Yang K, Feng L, Shi X, Liu Z (2013) Nano-graphene in biomedicine: theranostic applications. Chem Soc Rev 42:530–547
218. Li L, Wu G, Yang G, Peng J et al (2013) Focusing on luminescent graphene quantum dots: current status and future perspectives. Nanoscale 5:4015–4039
219. Nguyen KT, Zhao Y (2014) Integrated graphene/nanoparticle hybrids for biological and electronic applications. Nanoscale 6:6245–6266
220. Zhang H, Gruner G, Zhao Y (2013) Recent advancements of graphene in biomedicine. J Mater Chem B 1:2542–2567
221. Zhang J, Yang H, Shen G, Cheng P et al (2010) Reduction of graphene oxide vial-ascorbic acid. Chem Commun 46:1112–1114
222. Nurunnabi M, Khatun Z, Reeck GR, Lee DY et al (2013) Near infrared photoluminescent graphene nanoparticles greatly expand their use in noninvasive biomedical imaging. Chem Commun 49:5079–5081

223. Shen J, Zhu Y, Chen C, Yang X et al (2011) Facile preparation and upconversion luminescence of graphene quantum dots. Chem Commun 47:2580–2582
224. Wu X, Tian F, Wang W, Chen J et al (2013) Fabrication of highly fluorescent graphene quantum dots using L-glutamic acid for in vitro/in vivo imaging and sensing. J Mater Chem C 1:4676–4684
225. Abdullah Al N, Lee J-E, In I, Lee H et al (2013) Target delivery and cell imaging using hyaluronic acid-functionalized graphene quantum dots. Mol Pharm 10:3736–3744
226. Liu Q, Guo B, Rao Z, Zhang B et al (2013) Strong two-photon-induced fluorescence from photostable, biocompatible nitrogen-doped graphene quantum dots for cellular and deep-tissue imaging. Nano Lett 13:2436–2441
227. Qian J, Wang D, Cai F-H, Xi W et al (2012) Observation of multiphoton-induced fluorescence from graphene oxide nanoparticles and applications in in vivo functional bioimaging. Angew Chem Int Ed 51:10570–10575
228. Yang K, Hu L, Ma X, Ye S et al (2012) Multimodal imaging guided photothermal therapy using functionalized graphene nanosheets anchored with magnetic nanoparticles. Adv Mater 24:1868–1872
229. Wang Y, Wang H, Liu D, Song S et al (2013) Graphene oxide covalently grafted upconversion nanoparticles for combined NIR mediated imaging and photothermal/photodynamic cancer therapy. Biomaterials 34:7715–7724
230. Mochalin VN, Shenderova O, Ho D, Gogotsi Y (2012) The properties and applications of nanodiamonds. Nat Nanotechnol 7:11–23
231. Danilenko VV (2004) On the history of the discovery of nanodiamond synthesis. Phys Solid State 46:595–599
232. Kuo Y, Hsu T-Y, Wu Y-C, Chang H-C (2013) Fluorescent nanodiamond as a probe for the intercellular transport of proteins in vivo. Biomaterials 34:8352–8360
233. Wu T-J, Tzeng Y-K, Chang W-W, Cheng C-A et al (2013) Tracking the engraftment and regenerative capabilities of transplanted lung stem cells using fluorescent nanodiamonds. Nat Nanotechnol 8:682–689
234. Mohan N, Chen C-S, Hsieh H-H, Wu Y-C et al (2010) In vivo imaging and toxicity assessments of fluorescent nanodiamonds in caenorhabditis elegans. Nano Lett 10:3692–3699
235. Chang B-M, Lin H-H, Su L-J, Lin W-D et al (2013) Highly fluorescent nanodiamonds protein-functionalized for cell labeling and targeting. Adv Funct Mater 23:5737–5745
236. Tzeng Y-K, Faklaris O, Chang B-M, Kuo Y et al (2011) Superresolution imaging of albumin-conjugated fluorescent nanodiamonds in cells by stimulated emission depletion. Angew Chem Int Ed 50:2262–2265
237. Lin H-H, Lee H-W, Lin R-J, Huang C-W et al (2015) Tracking and finding slow-proliferating/quiescent cancer stem cells with fluorescent nanodiamonds. Small 11:4394–4402
238. Alhaddad A, Adam M-P, Botsoa J, Dantelle G et al (2011) Nanodiamond as a vector for siRNA delivery to ewing sarcoma cells. Small 7:3087–3095
239. Havlik J, Petrakova V, Rehor I, Petrak V et al (2013) Boosting nanodiamond fluorescence: towards development of brighter probes. Nanoscale 5:3208–3211
240. Igarashi R, Yoshinari Y, Yokota H, Sugi T et al (2012) Real-time background-free selective imaging of fluorescent nanodiamonds in vivo. Nano Lett 12:5726–5732
241. Chen G, Ohulchanskyy TY, Kumar R, Ågren H et al (2010) Ultrasmall monodisperse $NaYF_4$:Yb^{3+}/Tm^{3+} nanocrystals with enhanced near-infrared to near-infrared upconversion photoluminescence. ACS Nano 4:3163–3168
242. Wang Y, Cai R, Liu Z (2011) Controlled synthesis of $NaYF_4$:Yb,Er nanocrystals with upconversion fluorescence via a facile hydrothermal procedure in aqueous solution. CrystEngComm 13:1772–1774
243. Ye X, Collins JE, Kang Y, Chen J et al (2010) Morphologically controlled synthesis of colloidal upconversion nanophosphors and their shape-directed self-assembly. Proc Natl Acad Sci 107:22430–22435

244. Yang D, Li C, Li G, Shang M et al (2011) Colloidal synthesis and remarkable enhancement of the upconversion luminescence of $BaGdF_5:Yb^{3+}/Er^{3+}$ nanoparticles by active-shell modification. J Mater Chem 21:5923–5927
245. Budijono SJ, Shan J, Yao N, Miura Y et al (2010) Synthesis of stable block-copolymer-protected $NaYF_4:Yb^{3+},Er^{3+}$ up-converting phosphor nanoparticles. Chem Mater 22:311–318
246. Pedroni M, Piccinelli F, Passuello T, Giarola M et al (2011) Lanthanide doped upconverting colloidal CaF2 nanoparticles prepared by a single-step hydrothermal method: toward efficient materials with near infrared-to-near infrared upconversion emission. Nanoscale 3:1456–1460
247. Liu Q, Li C, Yang T, Yi T et al (2010) "Drawing" upconversion nanophosphors into water through host-guest interaction. Chem Commun 46:5551–5553
248. Liu Q, Chen M, Sun Y, Chen G et al (2011) Multifunctional rare-earth self-assembled nanosystem for tri-modal upconversion luminescence/fluorescence/positron emission tomography imaging. Biomaterials 32:8243–8253
249. Shan J, Kong W, Wei R, Yao N et al (2010) An investigation of the thermal sensitivity and stability of the β-$NaYF_4$:Yb,Er upconversion nanophosphors. J Appl Phys 107:054901
250. Wang F, Wang J, Liu X (2010) Direct evidence of a surface quenching effect on size-dependent luminescence of upconversion nanoparticles. Angew Chem Int Ed 49:7456–7460
251. Hu D, Chen M, Gao Y, Li F et al (2011) A facile method to synthesize superparamagnetic and up-conversion luminescent $NaYF_4$:Yb,Er/Tm@SiO_2@Fe_3O_4 nanocomposite particles and their bioapplication. J Mater Chem 21:11276–11282
252. Zhou J, Yao L, Li C, Li F (2010) A versatile fabrication of upconversion nanophosphors with functional-surface tunable ligands. J Mater Chem 20:8078–8085
253. Wang Z-L, Hao J, Chan HLW, Law G-L et al (2011) Simultaneous synthesis and functionalization of water-soluble up-conversion nanoparticles for in-vitro cell and nude mouse imaging. Nanoscale 3:2175–2181
254. Cao T, Yang Y, Gao Y, Zhou J et al (2011) High-quality water-soluble and surface-functionalized upconversion nanocrystals as luminescent probes for bioimaging. Biomaterials 32:2959–2968
255. Chen C, Sun L-D, Li Z-X, Li L-L et al (2010) Ionic liquid-based route to spherical $NaYF_4$ nanoclusters with the assistance of microwave radiation and their multicolor upconversion luminescence. Langmuir 26:8797–8803
256. Xiong L, Yang T, Yang Y, Xu C et al (2010) Long-term in vivo biodistribution imaging and toxicity of polyacrylic acid-coated upconversion nanophosphors. Biomaterials 31:7078–7085
257. Chen G, Shen J, Ohulchanskyy TY, Patel NJ et al (2012) (α-$NaYbF_4:Tm^{3+}$)/CaF_2 core/shell nanoparticles with efficient near-infrared to near-infrared upconversion for high-contrast deep tissue bioimaging. ACS Nano 6:8280–8287
258. Wang Y-F, Liu G-Y, Sun L-D, Xiao J-W et al (2013) Nd^{3+}-sensitized upconversion nanophosphors: efficient in vivo bioimaging probes with minimized heating effect. ACS Nano 7:7200–7206
259. Zhan Q, Qian J, Liang H, Somesfalean G et al (2011) Using 915 nm laser excited $Tm^{3+}/Er^{3+}/Ho^{3+}$-doped $NaYbF_4$ upconversion nanoparticles for in vitro and deeper in vivo bioimaging without overheating irradiation. ACS Nano 5:3744–3757
260. Sun L-D, Wang Y-F, Yan C-H (2014) Paradigms and challenges for bioapplication of rare earth upconversion luminescent nanoparticles: small size and tunable emission/excitation spectra. Acc Chem Res 47:1001–1009
261. Cheng L, Yang K, Shao M, Lee S-T et al (2011) Multicolor in vivo imaging of upconversion nanoparticles with emissions tuned by luminescence resonance energy transfer. J Phys Chem C 115:2686–2692
262. Liu Y, Chen M, Cao T, Sun Y et al (2013) A cyanine-modified nanosystem for in vivo upconversion luminescence bioimaging of methylmercury. J Am Chem Soc 135:9869–9876
263. Yu X-F, Sun Z, Li M, Xiang Y et al (2010) Neurotoxin-conjugated upconversion nanoprobes for direct visualization of tumors under near-infrared irradiation. Biomaterials 31:8724–8731

264. Liu Q, Sun Y, Yang T, Feng W et al (2011) Sub-10 nm hexagonal lanthanide-doped $NaLuF_4$ upconversion nanocrystals for sensitive bioimaging in vivo. J Am Chem Soc 133:17122–17125
265. Ai X, Lyu L, Zhang Y, Tang Y et al (2017) Remote regulation of membrane channel activity by site-specific localization of lanthanide-doped upconversion nanocrystals. Angew Chem Int Ed 56:3031–3035
266. N. G. Khlebtsov and L. A. Dykman, Optical properties and biomedical applications of plasmonic nanoparticles, J Quant Spectrosc Radiat Transf, 2010, 111: 1–35
267. Shang L, Dong S, Nienhaus GU (2011) Ultra-small fluorescent metal nanoclusters: synthesis and biological applications. Nano Today 6:401–418
268. Liu C-L, Wu H-T, Hsiao Y-H, Lai C-W et al (2011) Insulin-directed synthesis of fluorescent gold nanoclusters: preservation of insulin bioactivity and versatility in cell imaging. Angew Chem Int Ed 50:7056–7060
269. Polavarapu L, Manna M, Xu Q-H (2011) Biocompatible glutathione capped gold clusters as one- and two-photon excitation fluorescence contrast agents for live cells imaging. Nanoscale 3:429–434
270. Shang L, Dorlich RM, Brandholt S, Schneider R et al (2011) Facile preparation of water-soluble fluorescent gold nanoclusters for cellular imaging applications. Nanoscale 3:2009–2014
271. Gao S, Chen D, Li Q, Ye J et al (2014) Near-infrared fluorescence imaging of cancer cells and tumors through specific biosynthesis of silver nanoclusters. Sci Rep 4:4384
272. Nie LB, Xiao XY, Yang HC (2016) Preparation and biomedical applications of gold nanocluster, Jounal of Nanoscience. Nanotechnology 16:8164–8175
273. Kim Y-H, Jeon J, Hong SH, Rhim W-K et al (2011) Tumor targeting and imaging using cyclic RGD-PEGylated gold nanoparticle probes with directly conjugated iodine-125. Small 7:2052–2060
274. Mathew A, Pradeep T (2014) Noble metal clusters: applications in energy, environment, and biology. Part Part Syst Charact 31:1017–1053
275. Qiu L, Chen T, Öçsoy I, Yasun E et al (2015) A cell-targeted, size-photocontrollable, nuclear-uptake nanodrug delivery system for drug-resistant cancer therapy. Nano Lett 15:457–463
276. Wu X, He X, Wang K, Xie C et al (2010) Ultrasmall near-infrared gold nanoclusters for tumor fluorescence imaging in vivo. Nanoscale 2:2244–2249
277. Guo C, Irudayaraj J (2011) Fluorescent Ag clusters via a protein-directed approach as a Hg (II) ion sensor. Anal Chem 83:2883–2889
278. Habeeb Muhammed MA, Verma PK, Pal SK, Retnakumari A et al (2010) Luminescent quantum clusters of gold in bulk by albumin-induced core etching of nanoparticles: metal ion sensing, metal-enhanced luminescence, and biolabeling. Chem Eur J 16:10103–10112
279. Wen F, Dong Y, Feng L, Wang S et al (2011) Horseradish peroxidase functionalized fluorescent gold nanoclusters for hydrogen peroxide sensing. Anal Chem 83:1193–1196
280. Pitchiaya S, Krishnan Y (2006) First blueprint, now bricks: DNA as construction material on the nanoscale. Chem Soc Rev 35:1111–1121
281. Zhou C, Long M, Qin Y, Sun X et al (2011) Luminescent gold nanoparticles with efficient renal clearance. Angew Chem Int Ed 50:3168–3172
282. Sun M, Xu L, Ma W, Wu X et al (2016) Hierarchical plasmonic nanorods and upconversion core–satellite nanoassemblies for multimodal imaging-guided combination phototherapy. Adv Mater 28:898–904
283. Lim WQ, Phua SZ, Xu HV, Sreejith S et al (2016) Recent advances in multifunctional silica-based hybrid nanocarriers for bioimaging and cancer therapy. Nanoscale 8:12510–12519
284. Cheng S-H, Li F-C, Souris JS, Yang C-S et al (2012) Visualizing dynamics of sub-hepatic distribution of nanoparticles using intravital multiphoton fluorescence microscopy. ACS Nano 6:4122–4131
285. Gu L, Hall DJ, Qin Z, Anglin E et al (2013) In vivo time-gated fluorescence imaging with biodegradable luminescent porous silicon nanoparticles. Nat Commun 4:2326

286. Croissant JG, Qi C, Mongin O, Hugues V et al (2015) Disulfide-gated mesoporous silica nanoparticles designed for two-photon-triggered drug release and imaging. J Mater Chem B 3:6456–6461
287. Geng J, Goh CC, Qin W, Liu R et al (2015) Silica shelled and block copolymer encapsulated red-emissive AIE nanoparticles with 50% quantum yield for two-photon excited vascular imaging. Chem Commun 51:13416–13419
288. Wu Y, Shi M, Zhao L, Feng W et al (2014) Visible-light-excited and europium-emissive nanoparticles for highly-luminescent bioimaging in vivo. Biomaterials 35:5830–5839
289. Sreejith S, Ma X, Zhao Y (2012) Graphene oxide wrapping on squaraine-loaded mesoporous silica nanoparticles for bioimaging. J Am Chem Soc 134:17346–17349
290. Nguyen KT, Sreejith S, Joseph J, He T et al (2014) Poly(acrylic acid)-capped and dye-loaded graphene oxide-mesoporous silica: a nano-sandwich for two-photon and photoacoustic dual-mode imaging. Part Part Syst Charact 31:1060–1066
291. Helle M, Rampazzo E, Monchanin M, Marchal F et al (2013) Surface chemistry architecture of silica nanoparticles determine the efficiency of in vivo fluorescence lymph node mapping. ACS Nano 7:8645–8657
292. Xiao Q, Zheng X, Bu W, Ge W et al (2013) A core/satellite multifunctional nanotheranostic for in vivo imaging and tumor eradication by radiation/photothermal synergistic therapy. J Am Chem Soc 135:13041–13048
293. Kumar R, Roy I, Ohulchanskky TY, Vathy LA et al (2010) In vivo biodistribution and clearance studies using multimodal organically modified silica nanoparticles. ACS Nano 4:699–708
294. Wu X, Chang S, Sun X, Guo Z et al (2013) Constructing NIR silica-cyanine hybrid nanocomposite for bioimaging in vivo: a breakthrough in photo-stability and bright fluorescence with large stokes shift. Chem Sci 4:1221–1228
295. Wang R, Zhou L, Wang W, Li X et al (2017) In vivo gastrointestinal drug-release monitoring through second near-infrared window fluorescent bioimaging with orally delivered microcarriers. Nat Commun 8:14702
296. Huang P, Lin J, Wang S, Zhou Z et al (2013) Photosensitizer-conjugated silica-coated gold nanoclusters for fluorescence imaging-guided photodynamic therapy. Biomaterials 34:4643–4654
297. McVey BFP, Tilley RD (2014) Solution synthesis, optical properties, and bioimaging applications of silicon nanocrystals. Acc Chem Res 47:3045–3051
298. Erogbogbo F, Yong K-T, Roy I, Hu R et al (2011) In vivo targeted cancer imaging, sentinel lymph node mapping and multi-channel imaging with biocompatible silicon nanocrystals. ACS Nano 5:413–423

Real-Time Molecular MRI with Hyperpolarized Silicon Particles

3

Jingzhe Hu, Nicholas Whiting, Pamela E. Constantinou, Mary C. Farach-Carson, Daniel D. Carson, and Pratip K. Bhattacharya

Contents

Jingzhe Hu and Nicholas Whiting are contributed equally.

J. Hu
Department of Cancer Systems Imaging, The University of Texas MD Anderson Cancer Center, Houston, TX, USA

Department of Bioengineering, Rice University, Houston, TX, USA

N. Whiting · P. K. Bhattacharya (✉)
Department of Cancer Systems Imaging, The University of Texas MD Anderson Cancer Center, Houston, TX, USA
e-mail: whitingn@rowan.edu; PKBhattacharya@mdanderson.org

P. E. Constantinou · D. D. Carson
Department of BioSciences, Rice University, Houston, TX, USA
e-mail: pamela.constantinou@rice.edu; ddc3@rice.edu

M. C. Farach-Carson
Department of Diagnostic and Biomedical Sciences, The University of Texas Health Science Center, School of Dentistry, Houston, TX, USA
e-mail: Mary.C.FarachCarson@uth.tmc.edu

C. S. S. R. Kumar (ed.), *Nanotechnology Characterization Tools for Biosensing and Medical Diagnosis*, https://doi.org/10.1007/978-3-662-56333-5_3

Alternative Title
MRI with Silicon Particles

1 Definition of Topic

Magnetic resonance imaging (MRI) is an inherently insensitive imaging modality, due to low thermal spin polarization at typical clinical magnetic field strength and room temperature. Dynamic nuclear polarization (DNP) has the potential to increase the magnetic resonance signal of the underlying material by 3–4 orders of magnitude through enhanced nuclear spin alignment. In this chapter, we describe the application of the DNP technique to silicon particles and nanoparticles for background-free real-time molecular MR imaging.

2 Overview

Silicon particles, on the nanometer to micron scale, are attractive for development as biomedical imaging agents due to their biocompatibility and simple surface chemistry that is amenable to the addition of targeting moieties and therapeutic drugs. As such, they hold potential as theranostic agents that may both detect and treat diseases in real time. Because the ^{29}Si isotope is detectable using magnetic resonance imaging (MRI), silicon particles enable high-resolution, deep-tissue imaging of different disease states. Because the achievable ^{29}Si MR signal is insufficient for imaging studies under normal conditions, a method termed "hyperpolarization" can be used to temporarily increase the ^{29}Si MR signal by several orders of magnitude. This effect allows ^{29}Si MRI signal to be visualized over the course of tens of minutes (regardless of chemical environment), which is significantly longer than that of most other hyperpolarized contrast agents (on the order of tens of seconds in vivo). The long-lasting enhanced signal provides an elongated window to pursue molecular imaging studies and overcomes one of the primary drawbacks of hyperpolarized contrast agents – fast relaxation times. In this chapter, we describe the background theory, experimental conditions, and recent breakthroughs in silicon particle hyperpolarization, as they are developed for targeted molecular imaging of different disease systems.

3 Introduction

Silicon particles are biocompatible, functionalizable, and commercially available. They have been used as fluorescent imaging agents for targeting tumor vasculature [1], multistage drug delivery systems for therapeutic applications [2], as well as additives to increase food shelf life [3]. Under physiologic conditions, silicon particles degrade to orthosilicic acid ($Si(OH)_4$), which helps bone mineralization and collagen synthesis and reduces atheromatous plaques [4–9]. Orthosilicic acid ultimately exits the body through renal clearance [10]. Incidentally, ^{29}Si, a stable isotope with 4.71% natural abundance, is also MR active with a nuclear spin of 1/2 [11], thus opening the possibility of MR imaging with silicon particles.

Unfortunately, because of the poor sensitivity of MRI, direct imaging of silicon particles is not feasible. MR sensitivity of a given nucleus is proportional to the gyromagnetic ratio (γ), magnetic field strength (B_0), species concentration, as well as nuclear spin polarization (P) (Eq. 3.1). For spin 1/2 species such as ^{1}H, ^{13}C, and ^{29}Si, polarization is defined as the difference of spin populations occupying the two stationary energy levels. Since the spin populations conform to Boltzmann distribution, the polarization is extremely low under typical clinical magnetic field strength and room temperature. As a result, MRI is an inherently insensitive imaging modality with only around 10 per million protons detectable at 3 T and 25 °C. However, due to the high water concentration in tissues (~80 M), conventional proton MRI can be used to create 3D anatomical images with submillimeter resolution and excellent soft-tissue contrast [12]. For nuclei other than proton, the situation is a bit more challenging. Except at low spatial (1 cm^3) and temporal resolution (5–10 min), direct in vivo imaging of trace nuclei such as ^{29}Si is generally not feasible, due to low sample concentration, lower natural abundance, and a smaller gyromagnetic ratio compared to that of proton [13]. The conventional approach to boost sensitivity is to increase the magnetic field strength, which leads to an increasingly expensive proposition (~1 million USD/Tesla for MRI scanners). Temperature also can be lowered to achieve higher polarization, but in order to reach a high polarization, sample temperatures approaching absolute zero are needed, which is not feasible for in vivo applications.

$$P = \frac{n_+ - n_-}{n_+ + n_-} = \tan h\left(\frac{\gamma h B_0}{2k_B T}\right) \tag{3.1}$$

P = polarization for spin 1/2 nuclei; n_+ = spin population aligned with the magnetic field; n_- = spin population antiparallel to the magnetic field; γ = gyromagnetic ratio, a physical constant unique to each type of MR-active nucleus in units of MHz/Tesla; h = Planck's constant; B_0 = magnetic field strength in Tesla; T = temperature in Kelvin; k_B = Boltzmann's constant. Net polarization quickly diminishes as temperature rises above several degrees Kelvin.

One solution to the sensitivity conundrum is to hyperpolarize the silicon particles using dynamic nuclear polarization (DNP), a technique that has the potential to

increase MR sensitivity by 3–5 orders of magnitude. The DNP process requires the presence of unpaired electrons, low temperature (approaching 0 K), high magnetic field (typically >1 T), as well as a microwave source that matches the electron spin resonance frequency under the chosen magnetic field (usually GHz range). At around 3 K and 3 T, electron spin polarization approaches 100% and can be transferred to nearby nuclear spins via continuous microwave irradiation of the electron spin resonance condition. First proposed by Albert Overhauser in 1953 [14], DNP techniques are experiencing a recent resurgence, with a particular focus on ^{13}C-labeled compounds for metabolic imaging and spectroscopy. Mixed with stable radicals and after several hours of DNP, the polarization of ^{13}C-labeled pyruvic acid can reach over 64%, representing >10,000-fold signal enhancement [15]. A key development occurred in 2003 when Klaes Golman, Ardenkjaer-Larsen, and colleagues developed the first modern dissolution-DNP polarizer that allows the frozen hyperpolarized sample to be dissolved quickly in 180 °C superheated water, thus paving way for in vivo imaging applications and determination of metabolic flux in real time [16]. Recently, hyperpolarized pyruvic acid has been used in a Phase I clinical trial for prostate cancer detection and identified tumorous regions in patients that were not detected by conventional MRI [17]. For a detailed review of hyperpolarization methods and hyperpolarized ^{13}C compounds, please refer to the following articles [18, 19]. Despite the significant gain in sensitivity, the major limitation of hyperpolarized ^{13}C-labeled compounds is the typically short characteristic decay time, which only allows the hyperpolarized signal to be detected for ~1–2 min.

Silicon particles directly address this challenge with the hyperpolarized signal lasting on the order of tens of minutes. In the atmosphere, the surface of silicon particles can react with oxygen to form a thin silicon oxide (SiO_2) layer of a few nm, which contains naturally occurring surface defects [20]. Since the exposed bonds in the Si/SiO_2 interface can provide free unpaired electrons, no expensive and potentially toxic stable radicals are needed for DNP of silicon particles [20]. Under proper microwave irradiation, spin flip-flops are driven between nearby dipolar-coupled electrons and nuclei, resulting in a net transfer of spin polarization from the highly polarized surface electrons to nearby ^{29}Si nuclei, which in turn gradually hyperpolarize the core ^{29}Si nuclei via spin diffusion [21]. During depolarization, while the signal relaxation of the polycrystalline shell portion of the silicon particle is fast, depolarization of the core crystalline region is dominated by the slow spin-diffusion process, leading to a significantly long-lived hyperpolarized signal that is on the order of tens of minutes and unaffected by the in vivo environment, particle tumbling, or surface functionalizations [22]. Thus, in effect, these unique nanoparticles behave as little "spin batteries," storing the spin polarization for relatively long periods of time, ready for release on demand.

In summary, radical-free hyperpolarization of ^{29}Si nuclear spins is generated by low temperature solid-state DNP, a nuclear magnetic resonance (NMR) process for transferring spin polarization from electrons to nuclei, taking advantage of the intrinsic defect sites that naturally occur at the surface of the particles. In contrast to the hyperpolarization of conventional ^{13}C, nucleus, wherein magnetic resonance

signals are lost within 1–2 min, thus severely limiting applications in vivo, hyperpolarization of ^{29}Si produces MRI signals with a characteristic decay time in the order of tens of minutes. Furthermore, silicon-based nanoparticles are attractive due to their inert properties, biocompatibility and biodegradability. Coupled with low cost and the fact that silicon particles can be surface-modified with relative ease, hyperpolarized silicon particles have the potential to become a next-generation, high-impact MRI contrast agent.

Due to the potential benefits of developing silicon particles as hyperpolarized tracers, there has recently been increased interest in this new field. Given that the majority of work has been conducted within the last 10 years by only a handful of research groups, the authors felt that it would be worthwhile to provide an up-to-date summary of the state of hyperpolarized silicon to help inform scientists and clinicians who may wish to learn more about this technique and its relevant applications. This review serves as the initial comprehensive summary of the state of the art in silicon particle hyperpolarization, and there are currently no other reviews concerning this field. The authors hope that this will foster awareness and spur interest in hyperpolarized silicon particles and help lead to new developments and discoveries that will advance the field.

4 Methodology

4.1 Solid-State DNP Device

Even though the theoretical underpinnings of DNP are intricate, the experimental conditions are relatively straightforward to satisfy in practice. As an example, the home-built solid-state DNP device at UT MD Anderson Cancer Center is comprised of a 2.9 T superconducting magnet and in situ cryostat that maintains the sample temperature at ~3 K using a continuous flow of liquid helium (supplied from a 250 L helium dewar; application of a vacuum pump achieves temperatures lower than 4 K). The microwave source (80.9 GHz, 100 mW Gunn diode) is directed to the PTFE sample tube (~120 μL, 5 mm ID) containing silicon particles through a waveguide and slot antenna. In addition, the DC bias of the microwave source is modulated with a function generator to provide uniform irradiation across the suitable electron spin resonance spectrum ($\Delta\lambda$~60 MHz). The microwave output can be observed by a spectrum analyzer after siphoning a portion of the ~80.9 GHz radiation into a harmonic mixer, where it is mixed-down using an intermediate frequency source (8 GHz). Inside the cryostat, an in situ saddle coil enables NMR spectroscopy of the ^{29}Si nuclei in the sample, thus allowing observation of polarization buildup in real time for fundamental studies and quality control (Fig. 3.1). Unlike the commercially available dissolution-DNP polarizer "HyperSense" (Oxford Instruments), the sample remains in the solid state and requires manual removal, transport to the MRI scanner, and dissolution (if needed) prior to usage. While the HyperSense unit is capable of hyperpolarizing silicon particles, optimal DNP would require some slight modifications to the normal operating procedure.

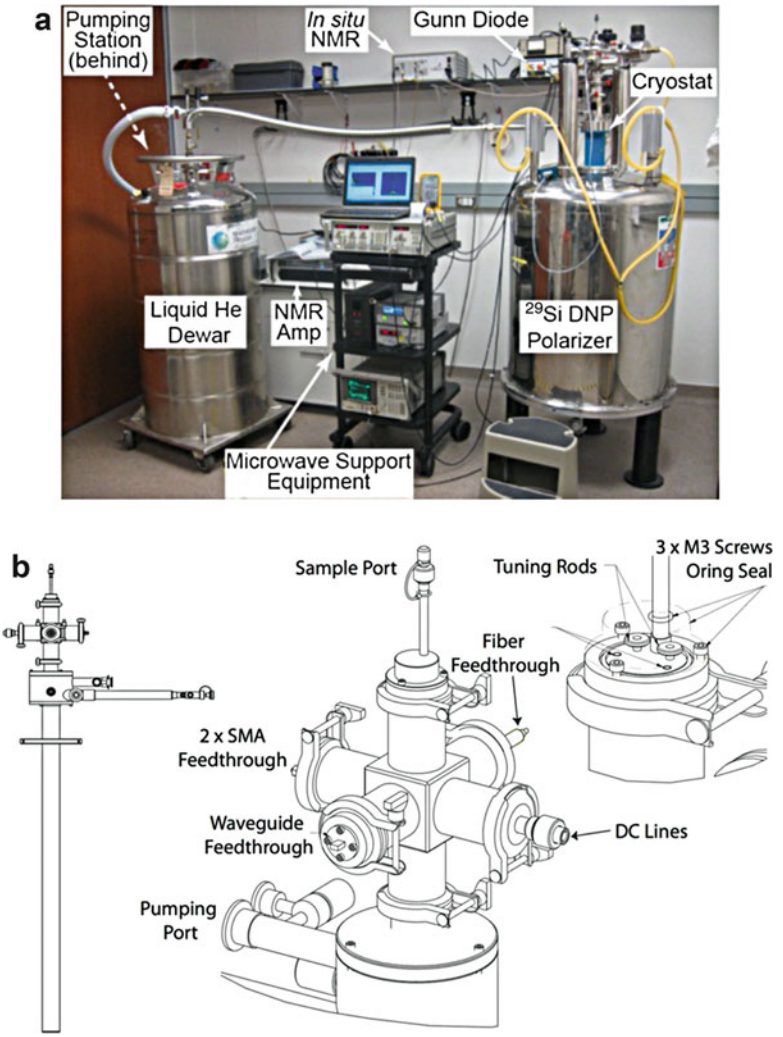

Fig. 3.1 (**a**) Solid-state DNP polarizer at UT MD Anderson Cancer Center showing relevant components (labeled) [23]. (**b**) Schematic for the cryostat showing the sample port and connections [24]

Once the sample is retrieved from the polarizer, the hyperpolarized signal begins to decay. As a result, the polarizer should be situated close to the MR scanner in order to reduce the sample transit time. In addition, there should not be zero-crossings of the magnetic field along the path to the scanner, which could instantaneously deplete the hyperpolarized signal. For preclinical animal experiments, once the sample is warmed (by hand) and suspended in ~200 μL of buffer (such as phosphate-buffered saline, "PBS"), it's ready for administration to the animal via oral gavage, intraperitoneal injection, enema, etc. [22, 23].

4.2 Silicon Particles and Surface Functionalization

Silicon particles can be sourced from a variety of methods. These typically include commercially purchased as a powder, silicon wafer that is crushed using a ball mill, or grown in-lab through chemical synthesis. The commercially available nanoscale particles are often formed via wet synthesis, plasma synthesis, or explosion synthesis and are well-characterized by the vendor. Particles can also be created in-lab through ball milling of a silicon wafer (which is either commercially purchased, grown in-house, or procured through a collaborating laboratory). The benefits of ball milling include simplicity, availability, and low price. The downsides include a heterogeneous size distribution and potential contamination by the jar/ball material. This can be particularly problematic for hyperpolarized MRI experiments, and metallic contaminants into the silicon powder can shorten the lifetime of the hyperpolarized signal while broadening the ^{29}Si NMR line [23]. Alternatively, silicon particles can be synthesized in the laboratory using a variety of established protocols (e.g., Stober method, etc.). Utilization of a collaborating laboratory can be useful for growing bespoke silicon particles, as often is the case that the research groups interested in applying hyperpolarized silicon particles are not as well versed in materials chemistry. Given the relatively low price, large available quantities (multi-gram), and quality assurances, commercially procured particles often represent the simplest route. Additional characterization should be performed for commercial nanoparticles, as aggregation can be problematic.

For the most part, the particles detailed in this review consist of elemental silicon, with a natural abundance of ^{29}Si (~4.7%). While it is possible to procure particles that are isotopically enriched in ^{29}Si (to further enhance MR signals), acquisition of such particles typically proves elusive. Some particles in the results outlined below employ silicon particles that are doped with other metals (boron, phosphorus, etc.). These internal metallic impurities provide additional free electrons that speed up the DNP process; however, they also serve as relaxation sinks as soon as DNP is concluded. This results in comparatively shorter hyperpolarized T_1 values vs. undoped silicon. The silicon particles used for DNP studies are typically exposed to the atmosphere, allowing an oxide shell to form on the surface of the particles; in the absence of internal electronic defects, this oxide layer provides the free electrons needed for DNP. To achieve the longest-lasting hyperpolarized ^{29}Si signal, the particles will consist of undoped silicon with a natural oxide surface layer; this allows the polarization to be retained in the core of the particle for tens of minutes.

Relevant characterization criteria for silicon particles used in hyperpolarization studies include the following: (1) electron microscopy (SEM or TEM) to examine particle size, shape, and aggregation; (2) electron spin resonance (ESR) spectroscopy to measure the number of available free electrons for DNP; (3) dynamic light scattering (DLS) to determine hydrodynamic size and distribution; (4) x-ray diffraction (XRD) and Raman spectroscopy to measure particle crystallinity; (5) infrared spectroscopy to monitor surface passivation; (6) nitrogen adsorption-desorption volumetric isotherm analysis to estimate particle surface area; (7) zeta potential to measure particle charge; and (8) nuclear magnetic resonance (NMR) spectroscopy

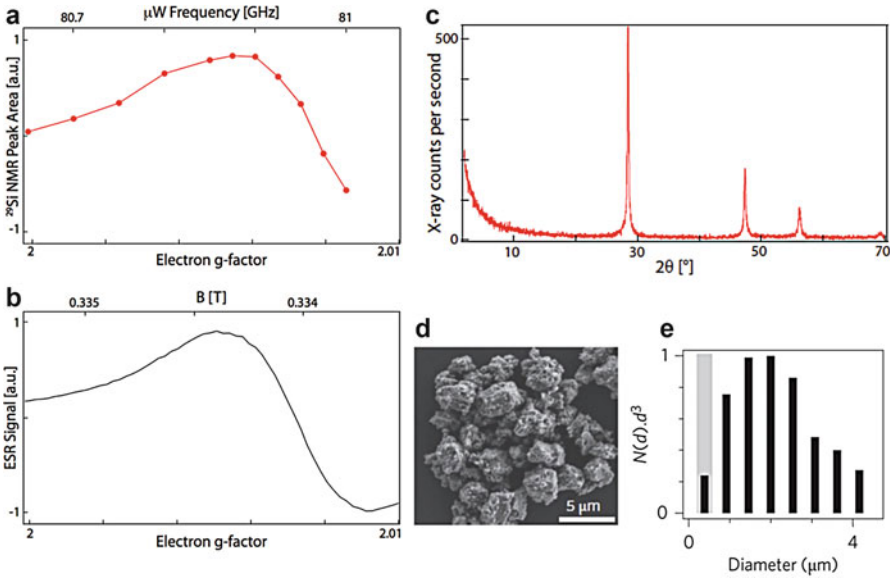

Fig. 3.2 (**a**) Microwave frequency dependence of DNP-polarized ^{29}Si NMR signal [22]. (**b**) Magnetic field dependence of ESR signal at microwave frequency of 9GHz and 3.8 K. The g-factor corresponding to flipping the sign of silicon NMR amplitude in (**a**) matches well with the crossover g-factor of ESR signal in (**b**) [22]. (**c**) Comparison of 2 μm silicon particle XRD power spectrum with peak locations of a known silicon standard (10 μm APS, NIST) shows the particles used have an approximately 80% crystallinity with an average crystallite size of 350 nm [22]. (**d**) Example SEM image of the silicon microparticles used for in vivo imaging [22]. (**e**) Volume-weighted particle size distribution determined by SEM image analysis shows an average particle size of 2 μm (black bars). The gray bar corresponds to the average crystallite size (~350 nm) as determined by powder XRD analysis

(including solid-state magic angle spinning NMR, or MAS-NMR) to determine chemical shift, linewidth, and thermal T_1 timescale [24]. These standard characterization protocols (Fig. 3.2) provide key information to determine the likelihood for successful DNP of silicon particles.

The surface silicon dioxide layer can be further utilized to functionalize the particles for a variety of biomedical applications. While different functionalization strategies may be employed, a common tactic is to aminize the surface by attaching (3-aminopropyl)-triethoxysilane, or "APTES." Successful amination can be verified through a ninhydrin test or the use of fluorescent tags. With the free amine on the particle surface, several robust functionalization strategies can be further pursued. For example, to improve hydrostability and biocompatibility, polyethylene glycol (PEG) can be used to coat the particles for in vivo studies. Furthermore, following an amine-NHS ester reaction with heterobifunctional PEG linkers, targeting moieties (such as aptamers, antibodies, or peptides) can be attached to the silicon particles via a maleimide-thiol reaction [25]. Fluorescent tags may also be incorporated to allow correlative optical imaging in addition to hyperpolarized MRI. A batch of silicon

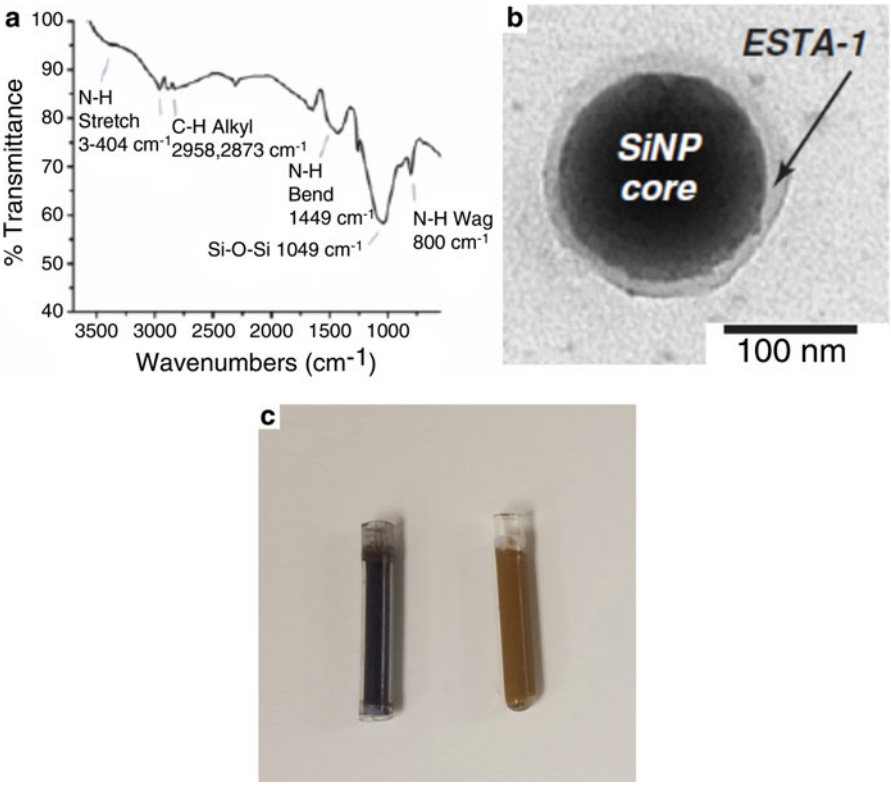

Fig. 3.3 (**a**) Infrared spectroscopy of amine-terminated trimethoxysilane silicon nanoparticles (~10 nm) [35]. (**b**) TEM of a ~70 nm silicon nanoparticle that is functionalized with an aptamer (ESTA-1) to seek out E-selectin overexpression on ovarian tumors [23]. (**c**) Photograph of example silicon particle samples: 2 μm dry-packed particles with bare surface chemistry (*left*) and 70 nm silicon particles functionalized with APTES and PEG, suspended in solution (*right*). The change in color between the samples is due to particle size differences, not surface chemistry

particles can typically be functionalized with PEG or targeting moieties within 2–3 days with minimal batch-to-batch variations. Functionalized silicon particles can be characterized using many of the physical characterization tools mentioned above (Fig. 3.3), as well as using secondary antibodies and fluorescent tags to determine primary antibody loading, and fluorescent microscopy of targeted particles in vitro.

4.3 Imaging Experiments

In order to detect hyperpolarized ^{29}Si signal using an MRI scanner, a transmit/receive MRI coil tuned to the ^{29}Si resonance frequency is needed; some examples include a ^{29}Si surface coil or ^{1}H/^{29}Si dual-tuned volume coil (Fig. 3.4). When

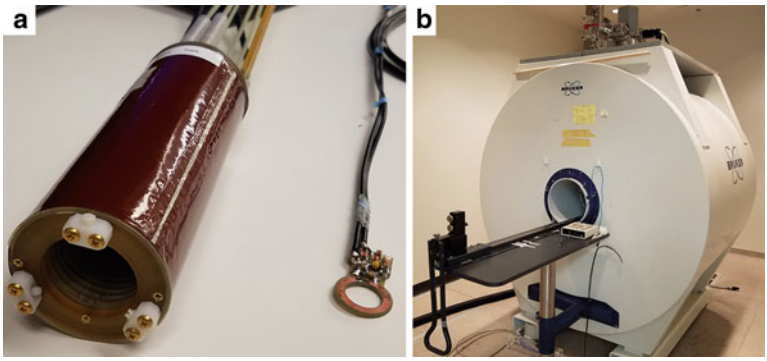

Fig. 3.4 (**a**) Example MRI coils for silicon hyperpolarization studies: volume coil (*left*) and surface coil (*right*). (**b**) Example preclinical MRI scanner (7 Tesla) for hyperpolarized ^{29}Si MRI studies

multiple scans of the sample are required, a gradient echo sequence with variable flip angle schedule is recommended. In addition, ultrashort echo time (UTE) or zero echo time (ZTE) imaging sequences [26] could be employed to offset the short T_2* (~1–2 ms) of silicon particles. Even though silicon particles have short T_2*, their T_2 can instead be on the order of several seconds [27]. As a result, a fast spin-echo sequence, such as RARE (rapid acquisition of refocused echoes), is suitable for single-shot molecular imaging applications, if the refocusing pulse is applied sufficiently fast [28]. When using spin-echo sequences for ^{29}Si imaging, a 90-degree excitation pulse is recommended, followed by a long echo train (e.g., 32) for phase encoding. Because the long echo train will disrupt the longitudinal magnetization (due to the likely inaccuracy of 180-degree pulses), it is recommended to proceed with a 90-degree excitation pulse (regardless of its deleterious effect on hyperpolarization).

Hyperpolarized ^{29}Si signal is primarily depleted through two processes: T_1 decay and signal acquisition. The hyperpolarized signal is subject to T_1 decay over time as the spins realign to thermal equilibrium. While this is true of all hyperpolarized spin systems, silicon particles benefit from a relatively long T_1 timescale, making this less critical compared to other hyperpolarized species. However, each time an MR signal is acquired (spectra or image), it nonreversibly depletes a portion of the available magnetization. Once these spins are perturbed through the application of radio wave pulses, they revert back to thermal equilibrium; the magnitude of this effect corresponds to the size of the tipping angle. Once they revert back to thermal equilibrium, the spins cannot be hyperpolarized again unless the sample is removed from the magnet and placed back into the DNP device for an appropriate amount of time (not feasible once the particles are administered in vivo). It is typical practice to minimally perturb the spins using a 10-degree pulse to acquire a ^{29}Si MR spectra prior to an imaging experiment in order to calibrate signal levels and help inform decisions regarding how long to wait prior to the imaging experiment (particularly for molecular targeting experiments).

Most imaging experiments detailed in this review consist of silicon particle samples either residing within their sample tubes (i.e. "imaging phantoms") or suspended in buffer and administered to an animal model. For the latter, care must be taken to prepare the particles for administration following DNP. Because the hyperpolarized ^{29}Si signal is constantly relaxing, and the relaxation rate changes with magnetic field (faster for lower B_0), it is best to prepare the particles for administration next to the MRI scanner (after DNP). The animal model (mice, to date) should be anesthetized (isoflurane or ketamine) and positioned on a heated MR-compatible cradle, while vital bodily functions are monitored. It should be noted that, as suspended particles are administered in vivo, they will disperse throughout the body and provide lower ^{29}Si MRI signals than when physically concentrated in one location (due to fewer silicon particles per pixel/voxel). Because of this, higher ^{29}Si nuclear spin polarization is needed for in vivo experiments compared to imaging phantoms. All animal work should be previously approved by the relevant Institutional Animal Care and Use Committee (IACUC) and carried out by trained personnel.

5 Key Research Findings

5.1 Dynamic Nuclear Polarization of Silicon Particles

While dynamic nuclear polarization of silicon particles has progressed since the early days of DNP in the 1950s [29], the field has only recently seen an increase in interest due to the emergence of potential applications in both biomedical imaging [22] and quantum computation [30]. In 2008, Dementyev et al. published their findings [31] regarding DNP in undoped silicon microparticles at lower temperatures (1.4 K) and higher magnetic fields (2.35 T) than had been previously studied [32, 33]. They found that much of the hyperpolarized signal originated from the irradiation of the electron-nuclear pairings in the amorphous regions of the silicon particles. The spin polarization then can be transferred to ^{29}Si in the crystalline lattice through spin diffusion. Optimal microwave irradiation was achievable on either side of the electron spin resonance (ESR) central frequency, albeit with opposite spin orientations. Because the crystalline cores have few paramagnetic impurities to act as relaxation agents, the spin polarization is long-lived (tens of minutes). The silicon particles (99.999% purity) ranged in size from 1 to 5 μm and were approximately 80% amorphous and 20% polycrystalline (individual crystallites >200 nm). The study also differentiated between hyperpolarized (HP) ^{29}Si signal in the amorphous regions, which relaxes under short time durations *vs*. HP ^{29}Si signal in the crystalline regions (longer time durations). While the NMR signal from the amorphous silicon provided an inhomogeneously broadened spectrum, the silicon in the crystalline sections provided a stronger, narrower ^{29}Si NMR line (Fig. 3.5a). Furthermore, under DNP conditions, the ^{29}Si NMR signal contribution from the amorphous silicon contributes to a broad NMR line (Fig. 3.5b). Because the amorphous regions of silicon relax faster than the crystalline portions, the line significantly narrows after a period of ~1 h (as the only remaining signal contribution is then from the crystalline ^{29}Si).

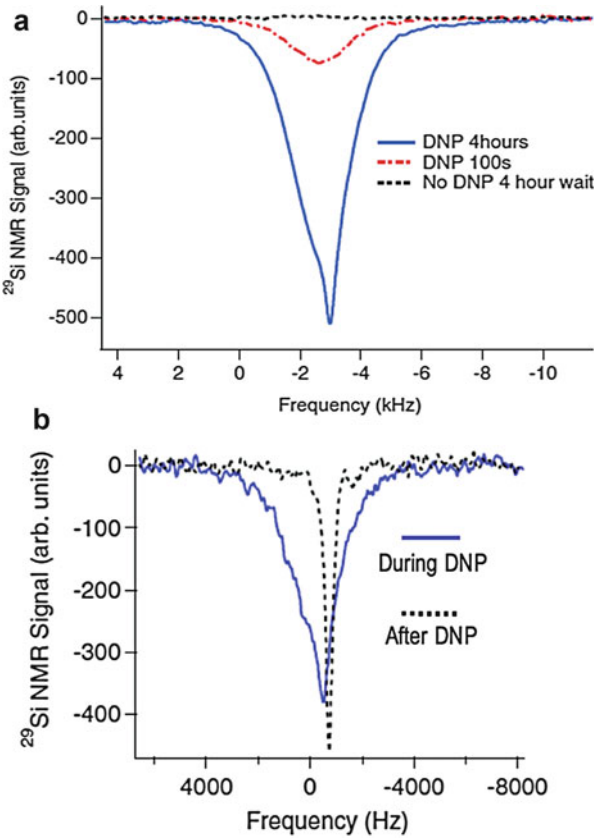

Fig. 3.5 (**a**) ^{29}Si NMR spectra of polycrystalline/amorphous silicon microparticles for different microwave irradiation times [31]; (**b**) ^{29}Si NMR spectra of polycrystalline/amorphous silicon microparticles during DNP (solid line, 1.4 K and 5-degree flip angle) *vs.* after a wait time of 1 h (dotted line, 240 K and 90-degree flip angle) [31]

The measured T_1 values for the silicon microparticles at 4.2 K was a little over 2 h and generally agreed with simulations that took into account the size of the crystallites in the particles, the spin-diffusion rate, and the natural abundance of ^{29}Si in the crystalline lattice. Overall, this work set the stage for a number of studies that employed solid-state DNP in silicon particles on the nano- to microscale, with future applications geared toward biomedical imaging and quantum computation.

5.2 T_1 Values of Nanoscale Silicon Particles

Further studies from Aptekar et al. [34] investigated the T_1 of nanoscale silicon particles at room temperature (as opposed to cryogenic temperatures) and demonstrated that the addition of surface functionalities does not affect the relaxation rate of the nuclear spin polarization. The long T_1 is a result of the low natural abundance of ^{29}Si spins that are relatively isolated within a lattice of ^{28}Si nuclei ($I = 0$). As a result, when combined with the weak dipole-dipole coupling of ^{29}Si, the absence of a quadrupolar moment, and the isotropic crystal structure, the silicon particles retain

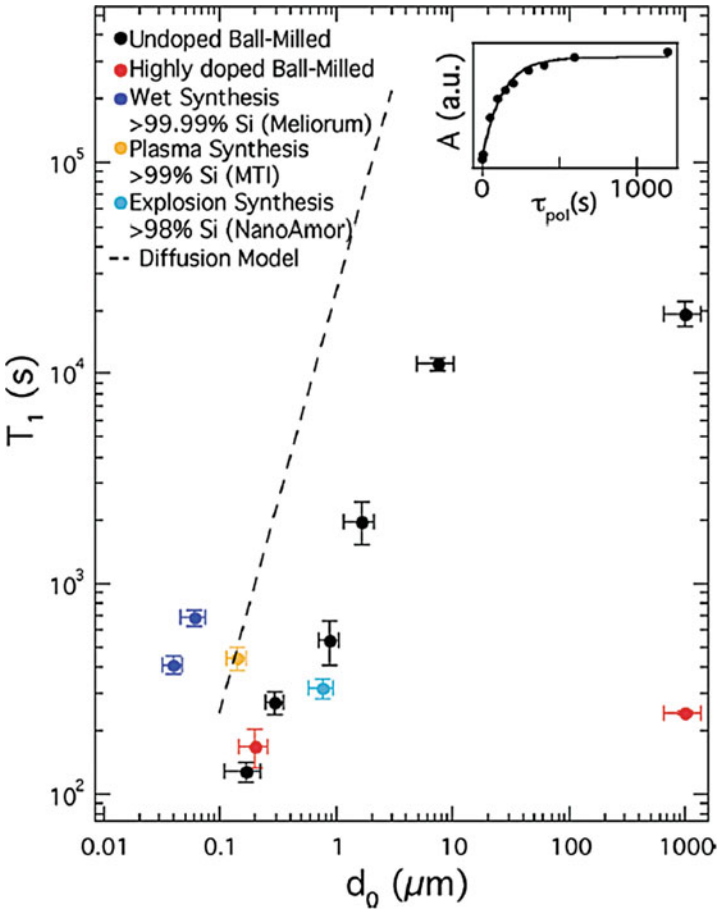

Fig. 3.6 T_1 values of silicon particles at 2.9 T vs. particle diameter (d_0). Vertical error bars from data fits; horizontal error bars relate to particle size distribution. *Inset*: polarization buildup curve for $d_0 = 0.17$ μm silicon particles. T_1 values were measured using a saturation recovery spin-echo sequence [34]

their enhanced signal for tens of minutes regardless of nanoparticle tumbling in solution. This study examined a variety of silicon particle sizes, ranging from 40 nm to 1 mm, and particles were created *via* ball-milled silicon wafers, wet synthesis, plasma synthesis, and electrical explosion synthesis. The longitudinal relaxation times of these particles (non-hyperpolarized) were measured at room temperature and at 2.9 T; the T_1 values correlated with particle size, with the larger silicon particles having the longest relaxation times (up to several hours (Fig. 3.6)). The experimentally measured values were compared to a core-shell nuclear spin-diffusion model. While the overall trends were similar, the experimentally validated results typically exhibited a slightly lower T_1 value. This is likely due to the presence

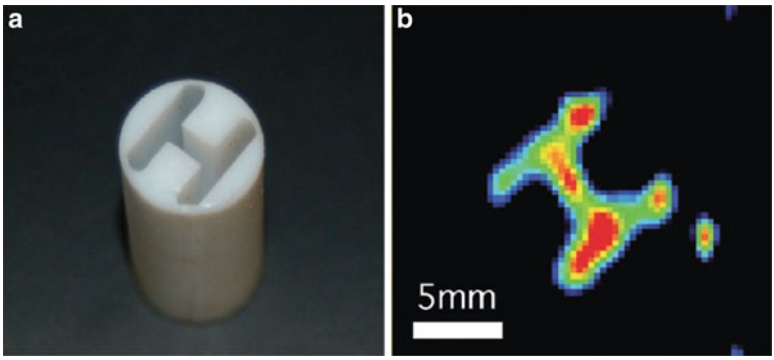

Fig. 3.7 ^{29}Si MRI scan of brute-force polarized silicon particles (1.6 μm) after transfer to room temperature in a 4.7 T MRI scanner. (**a**) An H-shaped phantom that is to be filled with the HP particles and (**b**) the corresponding ^{29}Si MRI scan [34]

of impurities within the core of the particles (which vary with particle synthesis route); the particles that contained highly doped silicon displayed a $T_1 \approx 200$ s, regardless of size (likely due to internal defects). While the T_1 value changed by two orders of magnitude across the studied particle sizes, the inhomogeneous dephasing time (T_2*) only varied by a factor of ~6×.

A sample of undoped ball-milled silicon particles (1.6 μm diameter) was hyperpolarized via the brute-force polarization technique, where the sample was exposed to low temperature (4.2 K) inside of a 5 T superconducting magnet for 60 h. This enhanced the ^{29}Si MR signal by a factor of ~16× compared to thermal equilibrium and allowed for a ^{29}Si MRI scan in an H-shaped phantom (Fig. 3.7). The same sample at thermal equilibrium (i.e., without hyperpolarization) did not produce an image under the same imaging conditions.

To further investigate the applicability of HP silicon particles for biomedical applications, the surface of the nanoparticles was treated with either (3-aminopropyl) triethoxysilane (APTES), bis-(triethoxysilyl)ethane (BTEOSE), or (3-trihydroxysilyl)propyl methylphosphonate (THPMP). Treatment with any of these surface ligands results in amination of the particles. These free amine groups are then available for further linkage to targeting moieties or therapeutic drugs (Fig. 3.8).

The amount of amine deposited on the particle surfaces was quantized by fluorescence spectroscopy using a fluorescamine reporter. These aminated particles were then further functionalized with polyethylene glycol (PEG), which improves the stability and biodistribution of the particles. The PEGylated particles were stable in phosphate-buffered saline (PBS) for a period of at least 48 h without a significant change in the hydrodynamic radius. Overall, this study determined the room temperature T_1 values for a range of silicon particle sizes, demonstrated the first MRI scan of brute-force hyperpolarized silicon particles, and confirmed that the particle surface can be functionalized for future biomedical applications.

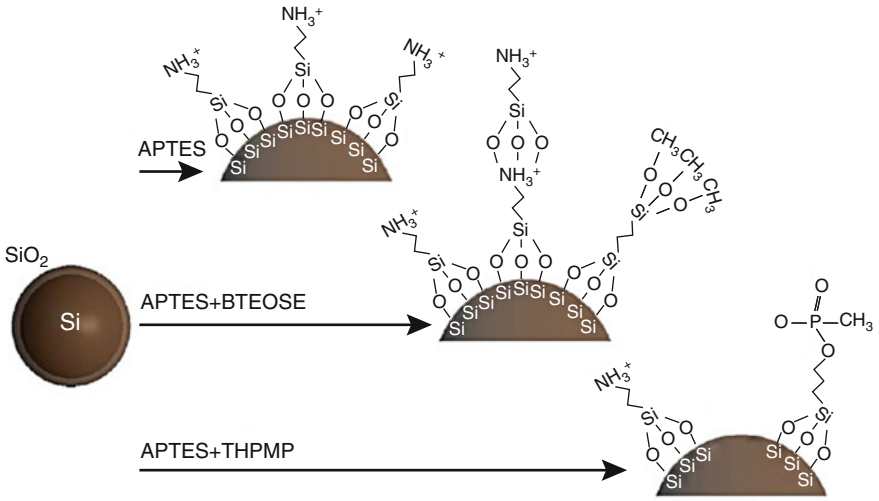

Fig. 3.8 Surface functionalization scheme for 200 nm silicon particles coupled to either APTES, APTES + BTEOSE, or APTES + THPMP. Surface amination confirmed by fluorescence spectroscopy and changes in the zeta potential (not shown) [34]

5.3 Dynamic Nuclear Polarization of Nanoscale Silicon Particles

A later study by Atkins et al. [35] extended this concept an additional step by synthesizing, characterizing, and then hyperpolarizing nanoscale silicon particles *via* DNP. This work prepared silicon nanoparticles through colloidal synthesis to produce particles with an average diameter of ~10 nm and room temperature T_1 values of ~10 min. The synthesis included a metathesis reaction of sodium silicide and silicon tetrachloride, from which only the larger particles were collected ($\leq$5 nm particles were also produced, but not included in the study). The particles were then surface passivated with different ligands (Fig. 3.9a–c) and confirmed using infrared spectroscopy. The metathesis reaction produced particles that were mostly amorphous, as confirmed by x-ray powder diffraction and Raman spectroscopy. Silicon nanoparticles terminated with aminopropyltriethoxysilane (APTMS – which allows for further conjugation via the terminal amine) were previously annealed at high temperature; these particles dispersed well in solution, were free of aggregation, and exhibited high crystallinity (Fig. 3.9e). These are among the smallest particles studied for ^{29}Si DNP and potentially open the door to advanced biomedical imaging opportunities that are not conducive to the use of microscale particles.

T_1 values for the 10 nm hyperpolarized silicon particles ranged between 5 and 10 min, which is in line with results from 60 nm silicon particles that were previously synthesized using alternative methods [36]. The amorphous (non-annealed) silicon nanoparticles exhibited slightly longer T_1's compared to the annealed APTMS-terminated particles; this could be due to the introduction of isolated point defects

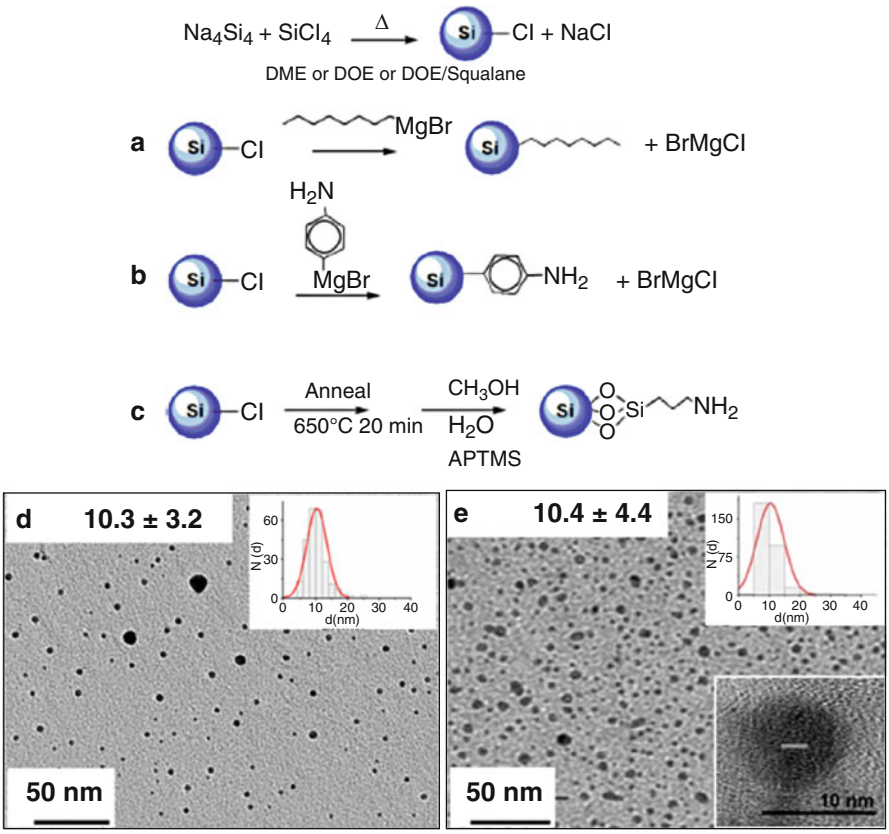

Fig. 3.9 (**a**–**c**) Synthetic schemes for the production of silicon nanoparticles; final particles are surface-functionalized with (**a**) octyl-, (**b**) 4-aminophenyl-, and (**c**) (after annealing step) aminopropyltriethoxysilane groups. (d) TEM images of silicon particles functionalized with 4-aminophenyl. (**e**) TEM images of silicon particles terminated with aminopropyltriethoxysilane. Top right insets (**d** and **e**) display size distribution of particles; bottom right inset on (**e**) shows crystallinity of annealed particles [35]

within the particle core during the annealing process. The two amorphous samples also possessed a narrower ESR linewidth compared to the annealed particles (Fig. 3.10a), indicating that the amorphous particles are likely polarized via a "single electron-single nuclei interaction" (i.e., "solid effect") rather than a "multielectron-single nuclei interaction" (i.e., "thermal mixing"). The room temperature ESR spectra correlate well with the low temperature DNP response to changes in microwave irradiation (Fig. 3.10b), and all samples provided positively enhanced ^{29}Si hyperpolarized NMR spectra after a few hours of DNP (Fig. 3.10c).

Overall, this work successfully synthesized and characterized silicon particles on the scale of 10 nm, demonstrated different surface passivation strategies, and compared the hyperpolarization characteristics of both amorphous and crystalline silicon particles. The relatively long (size-adjusted) T_1 values, small size, and

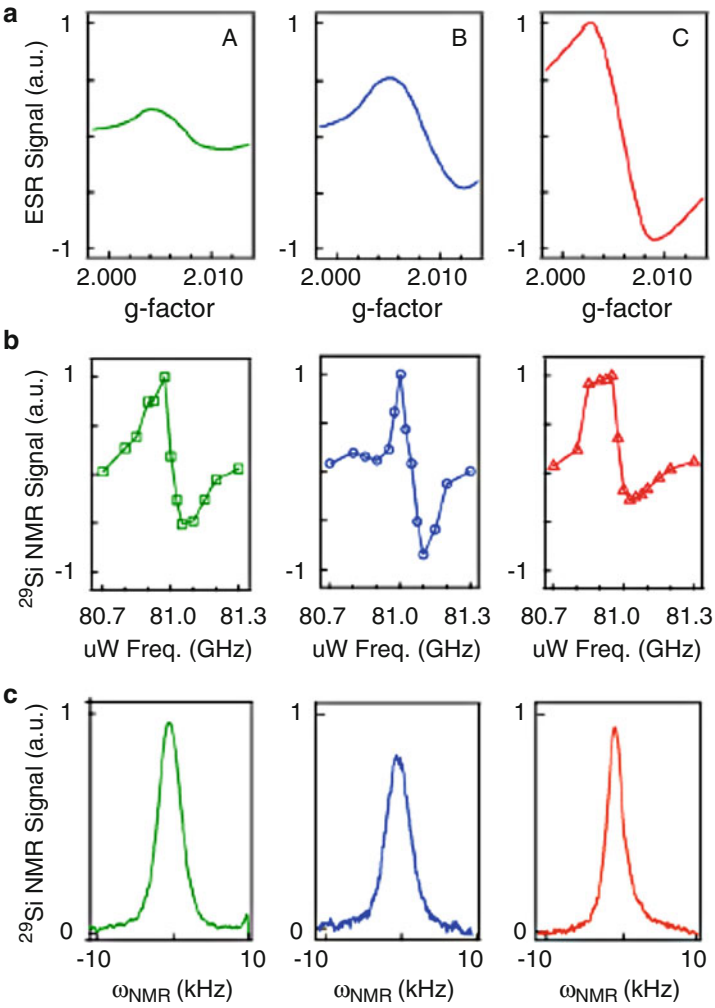

Fig. 3.10 (**a**) Electron spin resonance signal, (**b**) ^{29}Si NMR response to microwave frequency during DNP, and (**c**) ^{29}Si NMR spectra after 3 h of DNP for samples of (A) octyl-, (B) 4-aminophenyl-, and (C) APTMS-terminated silicon nanoparticles [35]

amenable surface chemistry provide promise for further development of nanoscale hyperpolarized silicon particle as biomedical imaging agents.

5.4 ^{29}Si Spin Relaxation in Particles

Additional studies regarding the relaxation of ^{29}Si MR signal were carried out by Lee et al. [21] at room temperature and low ambient magnetic fields for silicon microparticles. Previous studies had shown that the ^{29}Si T_1 increases with magnetic

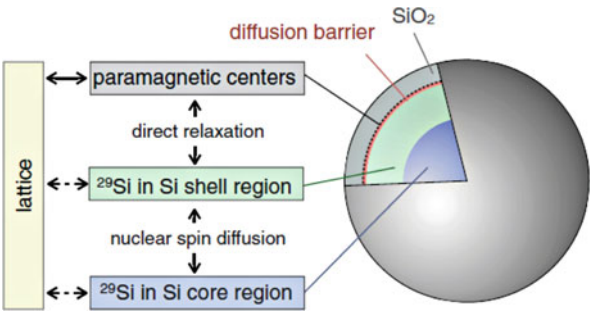

Fig. 3.11 Model of spin reservoirs and relaxation pathways in undoped silicon particles. "Core" silicon nuclei relax slowly via spin diffusion to the surface "shell region," which then relax quickly via dipolar coupling to paramagnetic centers in the silicon dioxide surface layer [21]

field strength (due to the field dependence of electron-nuclear dipolar interactions) and decreases with the addition of dopants (as they create an additional relaxation sink within the particles) [37]. The T_1 values were shown to increase with particle size, due to longer spin-diffusion time from the core to the surface (where the relaxation mostly occurs via interaction with surface defects) [34]. The work highlighted by Lee et al. demonstrated that the particles relax *via* a bi-exponential decay that consists of a slow-decaying component that is independent of magnetic field and a fast-decaying component that shows a slight inverse relationship with magnetic field strength. This new extended model of spin relaxation in silicon particles accounts for sample heterogeneity. Nuclear spin relaxation occurs at the particle surface, while the ^{29}Si spins in the core of the particle relax *via* spin diffusion to the surface.

These studies focused on silicon microparticles (5 μm diameter) made from undoped, ball-milled silicon wafer, as well as boron-doped particles of 10 μm diameter (from ball-milled silicon wafer that was doped with boron). The particles were allowed to equilibrate inside a 2.9 T magnetic field for 8 h (room temperature); then the signal decay was measured at different ambient fields (0.2 mT, 6 mT, 130 mT, and 300 mT). After fitting to a bi-exponential function, it was found that the "slow" relaxing component is indifferent to ambient field, while the "fast" relaxing component is inversely proportional to the applied field. This behavior accounts for the two populations of ^{29}Si nuclear spins that reside within the particles: the "core" spins that slowly relax via spin diffusion to the surface and the "surface" spins that relax quickly via an electron-nuclear interaction with paramagnetic defects on the oxidized particle surface (Fig. 3.11). The work also noted that the surface relaxation likely follows a three-spin process (two interacting electrons and a ^{29}Si nucleus), which matches well with experimental data.

For the boron-doped particles, both the buildup and decay of ^{29}Si nuclear spin polarization were hastened due to the readily available free electrons that were evenly dispersed throughout the particles (instead of only at the particle surface). Overall, this work established a bi-exponential decay model in undoped silicon particles that can be attributed to the placement of the ^{29}Si nuclei relative to the surface, showed that the longer relaxation time of ^{29}Si nuclei in the particle core is independent of magnetic field, and demonstrated that the surface relaxation is likely due to a three-spin process involving electron pairs.

5.5 Co-polarization of ^{1}H Using Silicon Particles as Radicals

The presence of naturally occurring electronic defects allows silicon particles to be hyperpolarized without the addition of an exogenous radical species, which are commonly used for the hyperpolarization of ^{13}C-labelled metabolites [38]. Because the majority of the electronic defects reside on the particle surface, silicon particles also may be used to hyperpolarize small molecules that reside close to the particle surface. One such instance was demonstrated by Cassidy et al. [39], where ^{1}H nuclear spins in water and water-ethanol mixtures were hyperpolarized *via* DNP while using the silicon particles as the sole source of free electrons. This technique allows DNP without the addition of contaminating radicals that can be burdensome to remove prior to in vivo MRI scans; while the radicals assist with hyperpolarization during DNP, they act as relaxation agents as soon as DNP is completed, thus shortening the T_1 value. In this instance, natural abundance (4.7% ^{29}Si) silicon powder (3 μm diameter) was compared with isotopically enriched ^{29}Si (91.4%) particles of diameter ~200 nm to determine their effects on nearby ^{1}H spins during DNP. Both types of samples were suspended in water or water-ethanol mixture. The particles were polarized at 4.2 K and 2.35 T, and the NMR coil was capable of detecting both ^{29}Si and ^{1}H frequencies.

Hyperpolarized ^{1}H NMR signal was shown to correlate with ^{29}Si NMR signal as the microwave frequency (which modulates the electron-nuclear dipolar interaction) was swept across a range that is relevant for ^{29}Si hyperpolarization (Fig. 3.12a–b). For a control sample that was absent of silicon particles, there was no change in ^{1}H NMR signal; this is indicative that the electrons present on the silicon particles contribute to the hyperpolarization of ^{1}H spins that are close to the particle surface. A second control confirmed that there was no discernable ^{1}H NMR signal from samples that consisted of dry silicon particles (i.e., absent of water), nor any changes in room temperature ^{1}H signal from non-hyperpolarized samples (over the course of 1 week). Furthermore, because both the ^{1}H and ^{29}Si signals demonstrated signal inversion at the same microwave irradiation frequency, the enhanced signal for both species was created using electrons with the same *g*-factor. The role of the surface electrons was validated further by removing the surface oxide layer with hydrofluoric acid, which resulted in a complete loss of both ^{1}H and ^{29}Si signals under DNP conditions. Because the sign of the ^{1}H and ^{29}Si NMR signals are the same, the polarization enhancement of ^{1}H came directly from the electron bath instead of dipolar interactions with the polarized ^{29}Si nuclear spins (which have an opposite gyromagnetic ratio and would result in oppositely aligned NMR peak orientations). These results indicate that the changes in ^{1}H NMR signal are caused by hyperpolarization using the silicon particles as electron sources; a schematic of this interaction is displayed in Fig. 3.12c–d. Interestingly, it was found that silicon particles that were isotopically enriched in ^{29}Si (91.4%) and of smaller diameter (200 nm) provided slower polarization transfer to ^{1}H as well as lower overall HP ^{1}H signal. This is despite the smaller enriched particles possessing a ~15× greater surface-to-volume ratio compared to the larger (3 μm), naturally abundant ^{29}Si particles. The cause of this slower buildup and overall lower ^{1}H signal is likely

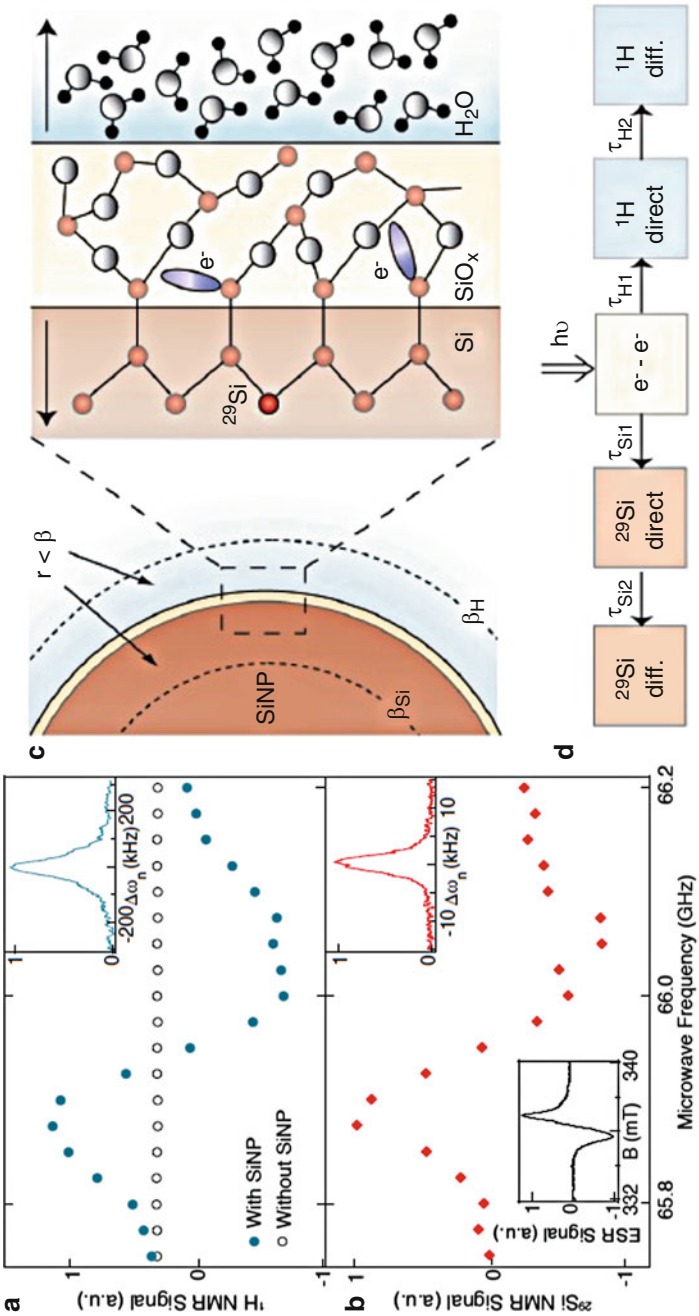

Fig. 3.12 Dependence of (**a**) ^{1}H NMR signal and (**b**) ^{29}Si NMR signal during DNP from a sample of silicon particles suspended in frozen water. Open circles in (**a**) denote the absence of silicon particles, which led to no changes in ^{1}H signal. Insets in (**a**) and (**b**) denote corresponding HP ^{1}H and ^{29}Si NMR peaks, along with the ESR spectra for the silicon particles (lower right in (**b**)) [39]. (**c**) Schematic showing DNP-active electrons around the Si/SiO_2 border in silicon particles. Arrows indicate direction of nuclear spin polarization away from the particle surface. (**d**) Thermodynamic model for hyperpolarization of ^{1}H and ^{29}Si nuclear spins both near (direct) and at a distance (diffusion) from the electron defects [39]

due to enhanced competition for the angular momentum from the polarized electrons, on account of the greater abundance of ^{29}Si nuclear spins in the sample; it may also be affected by differences in the density of surface defects between particle types. It was also estimated that the interface between direct nuclear spin polarization and polarization via spin diffusion was approximately 3 nm for ^{1}H and 4 nm for ^{29}Si; TEM images verified that the silicon dioxide layer was comprised of a similar thickness.

While the overall increase in ^{1}H NMR signal within the sample was modest, the signal enhancement for ^{1}H within 10 nm of the silicon particle surface was estimated to be ~50X higher compared to equilibrium at 4.2 K. Overall, this work demonstrates that naturally occurring electronic defects present on the surface of silicon particles can be used to directly polarize nearby ^{1}H nuclei present in solutions used to suspend the particles. This property can be developed as an easier method to remove sources of free electrons for DNP of frozen solutions, as well as study surface chemistry at the particle/solution interface.

5.6 Hyperpolarized Silicon Particles as In Vivo MRI Contrast Agents

Following these studies regarding the technique development and fundamental physics of DNP of silicon particles, more effort was contributed to their applications in biomedical imaging. Cassidy et al. [22] published seminal work showing in vivo ^{29}Si MR imaging of silicon microparticles injected into mouse models. While silicon particles had been previously used for in vivo imaging using optical methods (fluorescence) [2], radionuclides (PET scans) [40], or paramagnetic agents (^{1}H MRI) [41], no study had yet used silicon particles for ^{29}Si MR imaging in vivo. Commercially available silicon particles (polycrystalline/amorphous) with a mean diameter ~2 μm were surface-functionalized with polyethylene glycol to improve biodistribution and hydrostability (Fig. 3.13). The particles then were subjected to

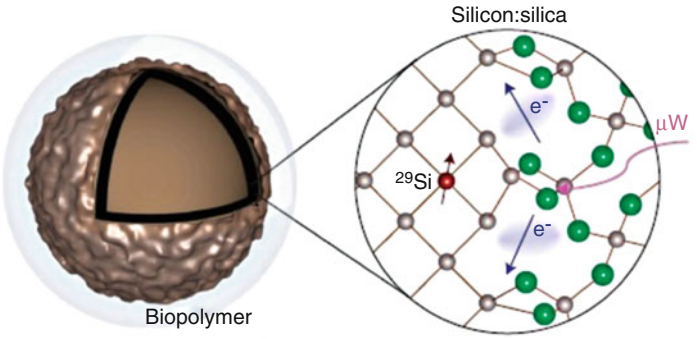

Fig. 3.13 Schematic showing the core-shell structure of silicon particles; unbound electrons on the surface polarize nearby ^{29}Si nuclei via DNP process

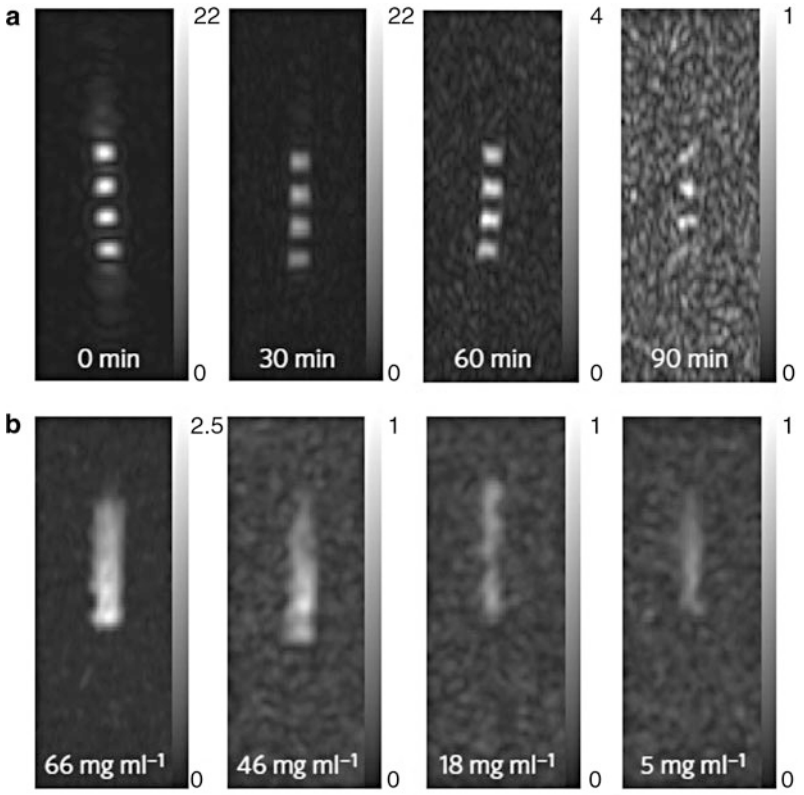

Fig. 3.14 (**a**) ^{29}Si MRI of a segmented phantom of dry silicon particles (~15 mg per segment) at different time points following DNP. (**b**) ^{29}Si MRI of cylindrical phantom with decreasing silicon particle concentration [22]

DNP at 3.4 K and 2.9 T, with spectroscopy and imaging experiments taking place in a nearby 4.7 T small animal MRI scanner.

The particles were allowed to polarize for ~18 h, and studies focused on both dry particles (in the sample tube) and PEGylated particles that were suspended in PBS and injected into mouse models. Both types of samples showed similar ^{29}Si polarization buildup times, overall signal enhancement (^{29}Si polarization ~1%), and hyperpolarized T_1 decay rates (~38 min). A positive correlation was noticed regarding time spent conducting DNP and the corresponding T_1 value; it was noted that further improvements to the T_1 could be achieved *via* improved polarization efficiency or optimized internal crystal structure of the particles. Imaging experiments were carried out in phantoms to calibrate a relevant time window for imaging (Fig. 3.14a) and particle concentration (Fig. 3.14b). It was found that HP ^{29}Si MR images were still achievable 90 min following DNP and particle concentrations as low as 5 mg/mL can be successfully imaged. Taking into account the estimated number silicon particles per image

pixel and coil geometry, an absolute ^{29}Si sensitivity of ~7×10^{-3} mol/L was calculated, which is comparable to paramagnetic MRI nanoparticle contrast agents [42].

The versatility of HP silicon particles was demonstrated further through a series of in vivo imaging scans using PEGylated silicon particles injected into mouse models (Fig. 3.15). The particles were injected into the intestinal tract, peritoneal cavity, and vasculature and into the tumor of a prostate cancer mouse model (TRAMP – transgenic adenocarcinoma of mouse prostate). Imaging the intestines and peritoneal cavity at different time points allowed visualization of the movement of the silicon particles both internal and external to the intestines. Noninvasive MRI of the intestines is typically difficult due to susceptibility artifacts as well as the use of positive and negative contrast agents (delivered orally and intravenously) in order to define the intestines. Because silicon particles are biocompatible and can be easily coupled to targeting agents, they can provide an option for molecular imaging of intestinal maladies. Particles injected directly into the *vena cava* provided an intense signal that began to lessen over the course of 1–2 min, as the particles are distributed throughout the body and taken up by the reticuloendothelial system. Injection of the particles directly into a prostate tumor showed ^{29}Si MR signal over the course of 10 min, with the particles perfusing across the tumor from the injection site in the direction of the blood flow. Areas of the tumor that did not display HP ^{29}Si signal later were confirmed to be necrotic. While this is not considered targeted molecular imaging, it is an important first step in developing silicon particles for the interrogation of cancer systems.

In vivo toxicity studies from this work indicated that the mice receiving injections of silicon particles did not exhibit decreased viability over a 2-week period following the injections, and a comparison of kidney and liver tissues, both 3 h and 2 weeks after silicon particle injections, showed clearance of particles in the longer time period (Fig. 3.16). Silicon particles are expected to degrade into silicic acid and be excreted within a few days. This confirmation of the biocompatibility and biodegradation of hyperpolarized silicon particles bodes well for their continued development as in vivo imaging probes.

The authors note that room remains to improve the particle concentration threshold and timeframe for imaging through optimization of the particle crystal structure and surface defect density; they also note potential benefits to using isotopically enriched silicon. The long in vivo ^{29}Si T_1 value may allow silicon particles to transfer polarization in situ to nuclei with a higher gyromagnetic ratio to improve the sensitivity of other MRI probes. The positive contrast, background-free signal of HP ^{29}Si can be monitored in real time using single-scan imaging acquisitions (without the need for signal averaging), and hyperpolarization allows imaging to take place in lower magnetic fields without sacrificing sensitivity. These lower fields may alleviate any concerns regarding the specific absorption rate (SAR) that may be incurred when using fast spin-echo imaging sequences for in vivo imaging (however, the relatively lower gyromagnetic ratio of ^{29}Si also reduces the likelihood of this potential issue). Overall, this work was the first demonstration that hyperpolarized silicon particles could be used for in vivo MRI and that they can provide imaging times in excess of thirty minutes, thus allowing changes in particle distribution to be monitored in real time.

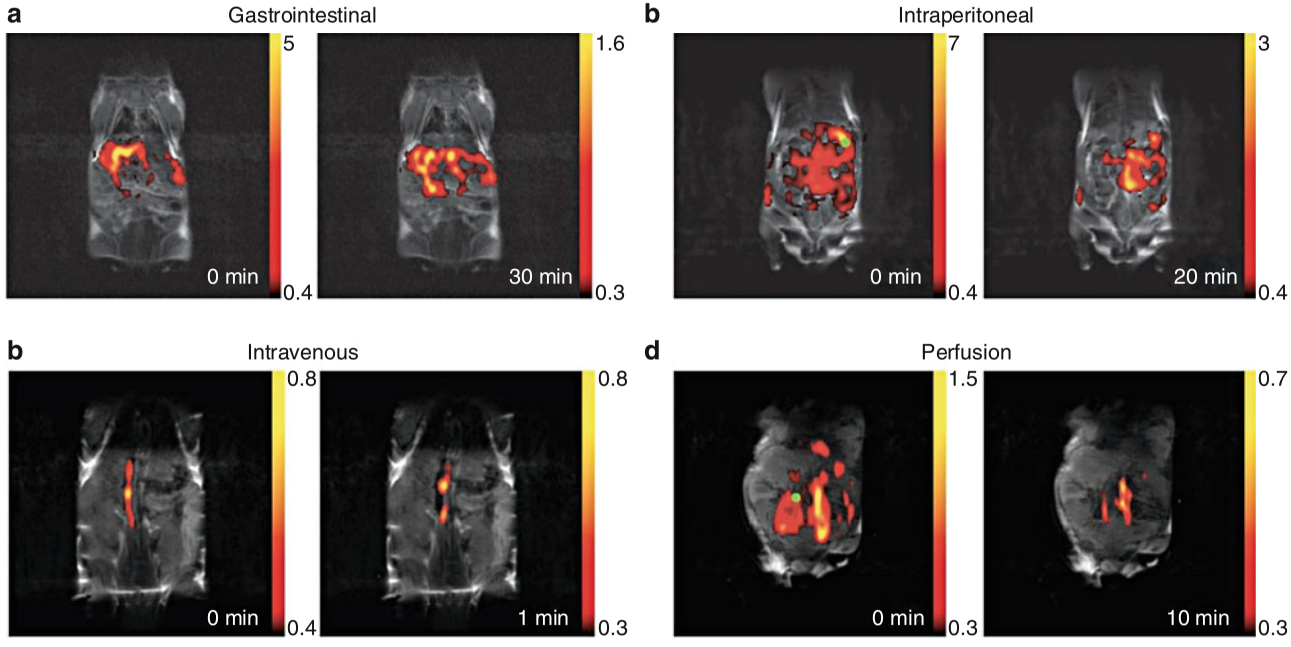

Fig. 3.15 In vivo ^{29}Si MRI of silicon particles injected (**a**) intragastrically, (**b**) intraperitoneally, (**c**) intravenously, and (**d**) directly into a prostate tumor. Green circle in (**b**), (**d**) denotes point of injection. ^{29}Si MRI (color) co-registered with ^{1}H anatomical scan (gray scale) [22]

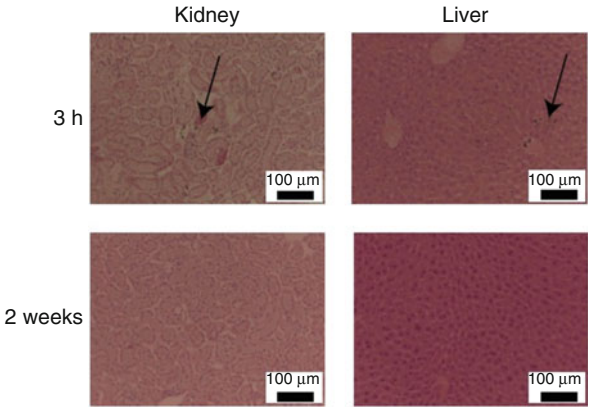

Fig. 3.16 Histology of kidney and liver tissue at a 3 h (top) and 2-week (bottom) time point following intravenous delivery of silicon particles; organs stained with hematoxylin and eosin. Arrows indicate the presence of silicon particles. Particle clearance appears to occur after longer time span as expected [22]

5.7 Development Toward Targeted Molecular Imaging

To further advance the utility of hyperpolarized silicon particles as targeted molecular imaging agents, Whiting et al. [23] published a study that focuses on the hyperpolarization characteristics and imaging procedures for targeted silicon microparticles. These 2 μm silicon particles were surface-functionalized with a thioaptamer that targets E-selectin [43] – a glycoprotein that is overexpressed on the endothelial surface of some forms of ovarian cancer. Previously, silicon and silica particles had been functionalized with E-selectin thioaptamer (ESTA-1) for optical tracking of particle binding in bone marrow [44], and ESTA-1 has been shown to bind to E-selectin with nanomolar affinity. Because E-selectin is expressed on the cell surface, binding is not dependent on endocytosis, which mitigates some of the drawbacks that occur due to the large size of the microparticles.

Initial studies compared the effect of particle size on hyperpolarization characteristics through a study of both 20 nm and 2 μm silicon particles that were not surface-functionalized (Fig. 3.17). While the 20 nm particles achieved steady-state HP ^{29}Si signal relatively quickly (~40 min), the larger microparticles were still increasing in ^{29}Si MR signal after nearly 6 h of DNP. This is expected, given the spin-diffusion model of hyperpolarization of silicon nuclei at a distance from electronic defects. However, the 2 μm particles also provided ~25x as much ^{29}Si signal compared to the 20 nm particles. This is likely due to the prevalence of endogenous electronic defects, which are necessary for DNP. While the monocrystalline nanoparticles contain some defects on their surface, the larger microparticles are polycrystalline/amorphous and likely contain a significantly larger number of defects (both on the surface and in the amorphous regions). This increase in electron defects significantly boosts the achievable ^{29}Si signal and so far has made the larger microparticles more useful for in vivo imaging studies, despite their large size and decreased mobility.

Differences in particle size also affected the relaxation rate of the hyperpolarized signal, with the smaller nanoscale particles exhibiting a T_1 on the range of 10–20 min, while the larger microparticles provided a T_1 of approximately 1 h

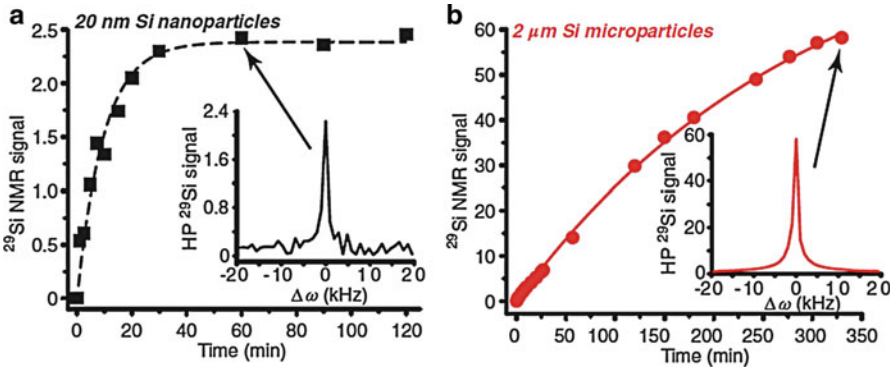

Fig. 3.17 Hyperpolarized ^{29}Si NMR signal as a function of time during DNP for samples of (**a**) 20 nm and (**b**) 2 μm silicon particles (normalized by mass). Insets: representative ^{29}Si NMR spectra for a given data point [23]

Table 3.1 Decay constant for hyperpolarized ^{29}Si NMR signal as a function of silicon particle size, surface chemistry, and time spent undergoing DNP [23]

^{29}Si hyperpolarization decay times		
SiNP size	HP T_1	DNP time
20 nm	~10 min	~80 min
30 nm	~17 min	~120 min
70 nm	~16 min	~60 min
2000 nm	~62 min	~300 min
2000 nm PEGylated	~55 min	~330 min
2000 nm ESTA-1	~56 min	~300 min

(Table 3.1). Changes to the surface chemistry of the 2 μm particles, through PEGylation or addition of ESTA-1, did not affect the overall achievable polarization level or the T_1 decay. This is expected since the ^{29}Si nuclear spins in the core of the particles are not thought to be affected by changes on the surface.

Because silicon particles represent a new "platform technology" that can interrogate a variety of diseases, it is important to optimize the delivery of particles to different organ systems. In this study, PEGylated particles were administered to normal mice via oral gavage, rectal enema, and intraperitoneal injection (Fig. 3.18a–c), with wait times between particle administration and the ^{29}Si MRI scan ranging from 5 to 30 min. For the oral gavage administration, HP ^{29}Si signal was visible in the stomach at a time point of 5 min following administration. The rectal enema provided signal in the lower intestinal tract (likely near the cecum) at a time point of 5 min after injection. The intraperitoneal injection provided signal – mostly at the site of injection – at a time point of 30 min after injection. This illustrates one potential issue with the larger microparticles – a lack of mobility, which is crucial in targeted molecular imaging. Given the long imaging window, it could be that the largest particles (which retain signal the longest) settled at the

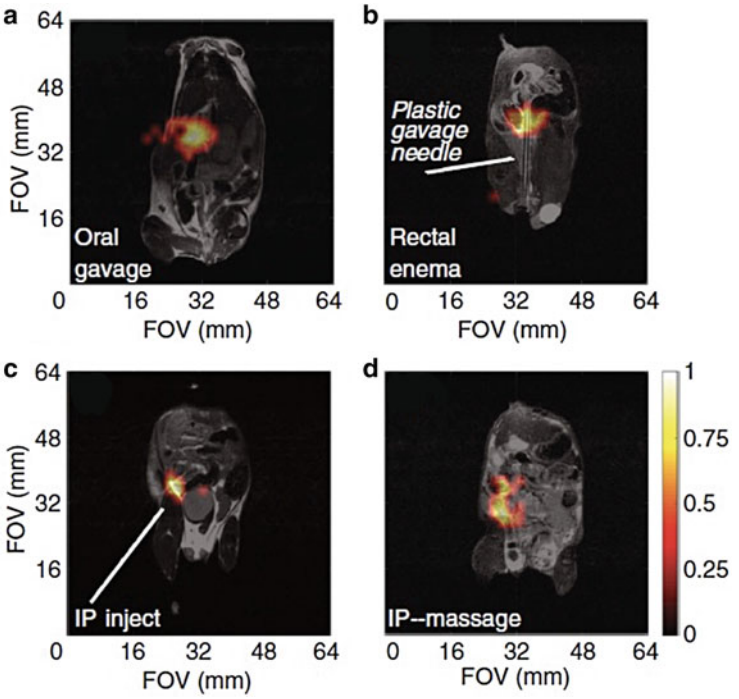

Fig. 3.18 Different administration routes of HP silicon particles (2 μm). (**a**) Oral gavage of PEGylated particles, image after 5 min. (**b**) Rectal injection of PEGylated particles, image after 5 min. (**c**) Intraperitoneal injection of PEGylated particles, image after 30 min. (**d**) Intraperitoneal injection of ESTA-1 particles into an ovarian cancer mouse model, followed by physical massage and 10 min wait time for image. ^{29}Si MRI (color) co-registered with ^{1}H anatomical (gray scale) [23]

injection site, while smaller silicon particles dispersed more readily. However, these smaller, more disperse particles did not contribute to the image due to a shorter T_1 and/or lower concentration of particles per pixel. As a follow-up, silicon particles functionalized with ESTA-1 were administered (via intraperitoneal injection) to *SKOV3* mice that contain orthotopic ovarian tumors; then the mouse's abdomen was gently massaged before waiting 10 min prior to imaging. The goal was to encourage particle mobility through physical manipulation. However, the resulting image (Fig. 3.18d) shows that while the particles moved, it was not enough to concentrate at the tumor site.

Because of these issues regarding the mobility of the large microparticles, a mouse with an orthotopic ovarian tumor (*HeyA8*) was directly injected with the ESTA-1 functionalized particles, with an image acquired 20 min following particle administration. HP ^{29}Si signal is seen throughout sections of the tumor image (Fig. 3.19), with the majority of the signal remaining relatively near to the injection site. While this does not qualify as targeted imaging, affirmation that the HP ^{29}Si signal in the targeted particles survives for at least 20 min in the tumor environment is an encouraging sign for continued development of the particles as biomedical contrast agents.

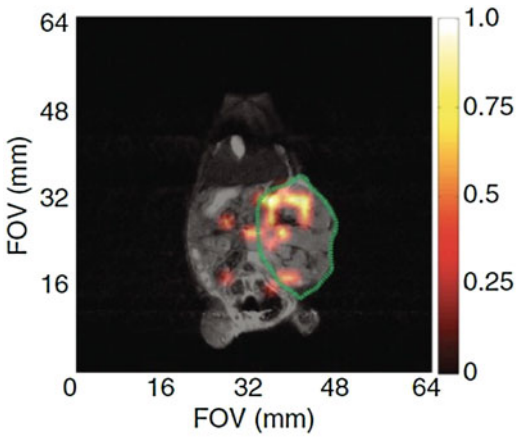

Fig. 3.19 In vivo ^{29}Si MRI of ESTA-1 functionalized 2 m silicon particles directly injected into an orthotopic ovarian tumor (HeyA8) possessed by a mouse. Single image acquired 20 min following particle injection. ^{29}Si MRI (color) co-registered with ^{1}H anatomical (gray scale) [23]

Overall, this work detailed the effects of size and surface chemistry on silicon hyperpolarization and demonstrated additional particle administration routes, as displayed by ^{29}Si imaging of targeted particles inside of an orthotopic tumor. The study also made the case for the transition from microscale to nanoscale silicon particles, as particle mobility is key in molecular imaging. Due to differences in achievable HP ^{29}Si MR signal between particle sizes, additional work is needed to achieve this goal.

5.8 ^{29}Si MRI-Guided Catheter Tracking Using Hyperpolarized Silicon Particles

In addition to their utility as targeted molecular imaging agents, hyperpolarized silicon particles also can be developed for other biomedical imaging applications. One example, recently published by Whiting et al. [45], demonstrated the utility of HP silicon microparticles for use in MRI-guided catheter tracking. There are many potential benefits using MRI to guide the movement of angiocatheters, as it allows clinicians to image the tissue/vasculature interface in three dimensions without worries of radiation exposure to the patient or hospital staff. Current methods of MRI-guided catheter tracking include active tracking of a miniature radiofrequency coil on the tip of the catheter as well as passive tracking of magnetic susceptibility differences in catheters implanted with metallic markers. While clinically useful, these methods suffer from drawbacks that include difficulty with steering catheter in vivo due to rigidity, tissue heating via radiofrequency excitations, and reliance on negative contrast that must overcome both susceptibility distortions and competition with ^{1}H background signal (when using metallic rings). Hyperpolarized silicon particles, on the other hand, are biocompatible and offer background-free positive contrast that lasts for tens of minutes without the use of ionizing radiation.

As a demonstration, 2 μm silicon particles (~50 mg) were hyperpolarized via DNP and then inserted into a large (24 Fr) urinary catheter; then the catheter was transited through a gelatin phantom (in a 50 mL centrifuge tube). Co-registered ^{29}Si

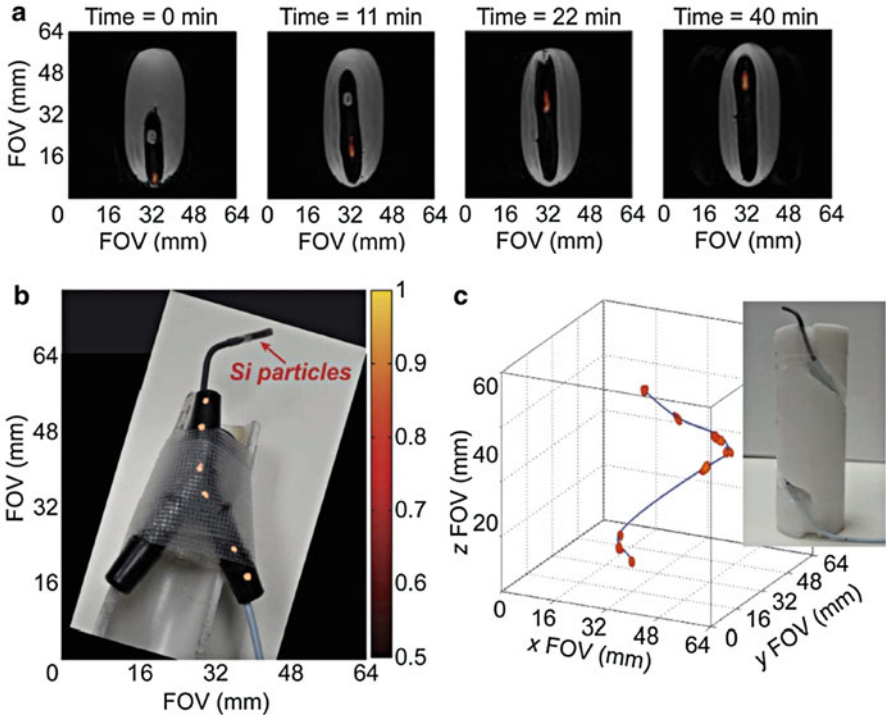

Fig. 3.20 (**a**) Co-registered ^{29}Si (color) and ^{1}H (gray scale) MR images demonstrate the transit of ~50 mg of HP silicon microparticles in a 24 Fr urinary catheter through a gelatin phantom over the course of 40 min. (**b**) ^{29}Si MRI (color) of ~6 mg of silicon particles attached to a 5 Fr urinary catheter transiting through a Y-shaped phantom (superimposed photograph) that mimics the branching of the vasculature. (**c**) ~6 mg of silicon microparticles attached to a 5 Fr angiocatheter shown moving through a spiral phantom to demonstrate 3D imaging with ^{29}Si MRI (color) [45]

and ^{1}H MR images were collected over the course of 40 min to demonstrate that the silicon particles could be used to track the movement of a catheter over long time durations (Fig. 3.20a). Separately, only ~6 mg of the microparticles were hyperpolarized and affixed to the tip of a 5 Fr angiocatheter and then moved through a 2D Y-shaped phantom (Fig. 3.20b) and a 3D spiral phantom (Fig. 3.20c), to demonstrate multidimensional tracking. The ^{29}Si MRI-guided catheters navigated the phantoms without issue and provided sufficient contrast despite possessing a fraction of the typically available magnetization (due to the small sample size).

In addition to multidimensional and longtime scale imaging, the ^{29}Si particles also were used to demonstrate the ability to monitor movement of the catheter in real time. For this study, ~50 mg of the microparticles was hyperpolarized and inserted into the tip of a large 24 Fr urinary catheter. The particles then transited through a gelatin phantom quickly, and ^{29}Si imaging provided an imaging speed of over 6 frames per second (Fig. 3.21). This frame refresh rate is similar to what is standard practice in the clinic using x-ray fluoroscopy, as a high refresh rate is necessary for

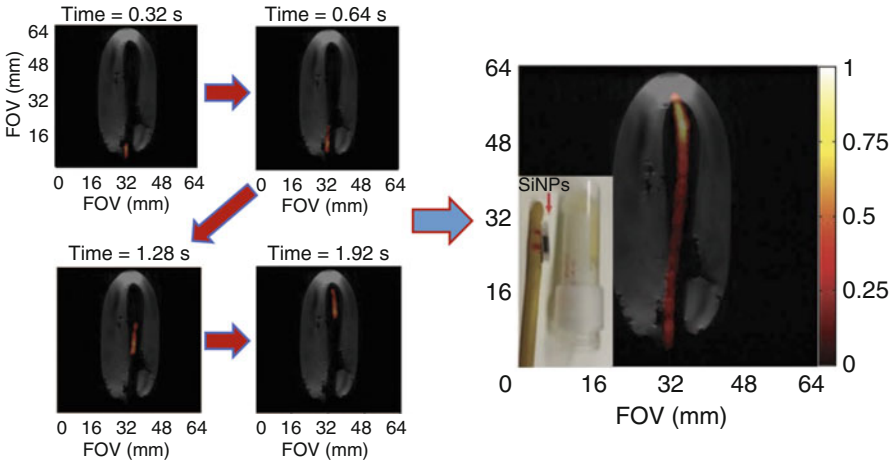

Fig. 3.21 Co-registered ^{29}Si (color) and ^{1}H (gray scale) MR images demonstrate the transit of ~50 mg of HP silicon microparticles in a 24 Fr urinary catheter through a gelatin phantom over the course of 3.2 s, with a speed of 6.25 frames per second. Larger co-registered image is a composite of twenty ^{29}Si images overlaid on a single ^{1}H image (following the experiment). Inset: photograph of the urinary catheter, silicon particle sample, and gelatin phantom [45]

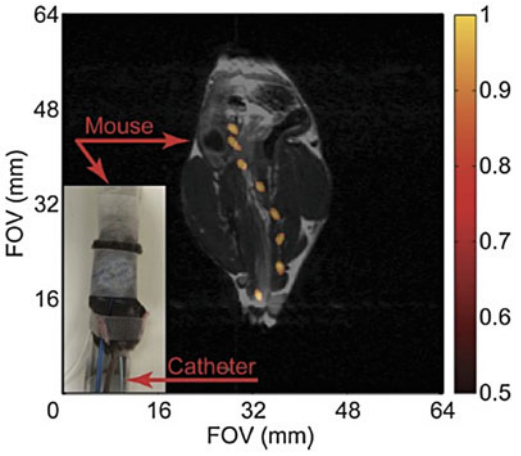

Fig. 3.22 Composite of ^{29}Si images (color) co-registered with a single ^{1}H scan (gray scale), showing the movement of a 5 Fr angiocatheter that is loaded with ~6 mg of HP silicon particles through the large intestines of a live mouse. Inset: photograph of the mouse during the procedure [45]

optimal catheter guidance. The intense imaging protocol (20 images in 3.2 s) did not completely deplete the available ^{29}Si magnetization, as the experiment was repeated immediately afterward using the same sample. These results are encouraging for real-time imaging over longer time durations.

Because the angiocatheter is similar in size to commercially available colonoscopy probes used for mice, initial in vivo ^{29}Si MRI-guided catheter tracking trials using the large intestines of a live mouse to demonstrate the capacity of this imaging procedure in a living model were pursued (Fig. 3.22). The same 5 Fr angiocatheter

was loaded with ~6 mg of hyperpolarized silicon microparticles and inserted into the rectum of a normal mouse. ^{29}Si imaging was acquired during transit of the catheter through the intestines (to near the cecum) over the course of several minutes, with a co-registered ^{1}H MR image taken at the end of the experiment. A follow-up study acquired both a ^{29}Si and ^{1}H MR image at each point in the movement, over 22 min, to show that the shape and placement of the intestines coincide with the position of the catheter tip containing HP silicon particles.

Overall, this work demonstrated an alternative biomedical imaging application for hyperpolarized silicon particles, other than targeted molecular imaging. Clinically relevant catheters were tracked in 2D and 3D, over long time durations (40 min) and in real time, as well as in phantoms and in vivo. ^{29}Si hyperpolarization provided background-free, positive contrast without the need for ionizing radiation. Continued development of this approach may allow future deployment in a clinical setting.

6 Conclusion and Future Perspective

The recent application of DNP to silicon particles for MRI signal enhancement has only been pursued over the last decade [31], yet many advances have been achieved in this short time period. Primarily, silicon particles ranging from 10 nm to several millimeters can be hyperpolarized and detected using MR imaging and/or spectroscopy [34]. The enhanced signal lasts for exceedingly long time periods (tens of minutes, up to hours) [21] and is impervious to its local chemical environment (including in vivo). This is a marked departure from most other hyperpolarized contrast agents, which typically lose their signal in <1 min when used for in vivo studies [46]. The particles can be functionalized to target a variety of disease systems by coupling targeting moieties such as antibodies or aptamers onto the particle surface [23]. This form of molecular targeting can perform a complementary function to the already-established metabolic interrogation of disease systems that is achieved with other hyperpolarized tracers.

To date, the larger polycrystalline/amorphous silicon particles provide significantly improved ^{29}Si MR signals (around 1–2% polarization) [22] compared to nanoscale particles and thus have received the majority of attention for development as biomedical imaging agents [22]. However, in order to tap the full potential of HP silicon particles as MRI contrast agents, the field will need to transition to nanoscale particles, due to their improved mobility and solubility. This will allow for true molecular targeting to occur; given the simple surface chemistry of silicon particles, they may be developed as a platform technology that can simultaneously interrogate multiple disease processes. If paired with therapeutic drugs, the silicon particles may take on a theranostic role in nanomedicine. While a few studies have shown proof-of-concept studies of hyperpolarized nanoscale silicon particles [35], the achievable ^{29}Si MR signal to date requires significant improvement to allow in vivo imaging studies. The low signal is likely due to differences in the number and placement of the endogenous electronic defects that are necessary for DNP. Ongoing efforts focus on resolving this issue to allow the nanoscale particles to be used for targeted imaging in vivo (Fig. 3.23).

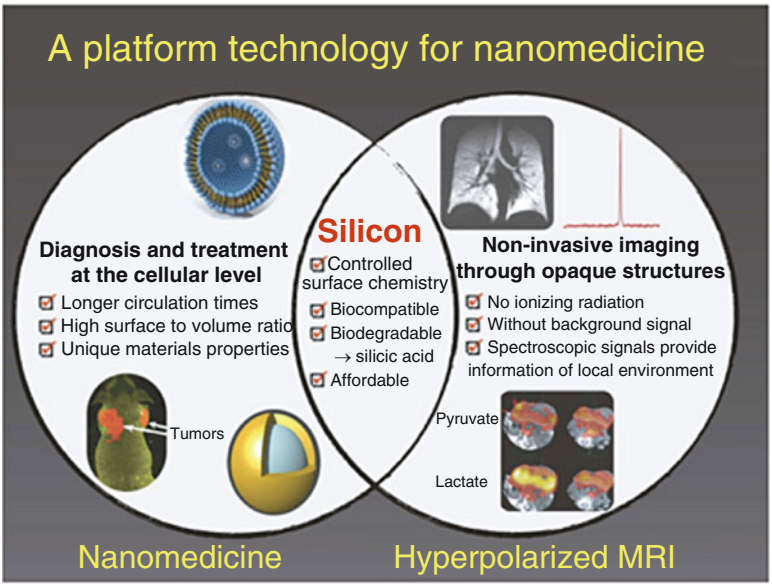

Fig. 3.23 Impact area of MRI with hyperpolarized silicon nanoparticles at intersection of nanomedicine and hyperpolarized MR

This emerging imaging modality at the intersection of nanomedicine and hyperpolarized MRI opens up the possibility of employing magnetic resonance for a "receptor-ligand" type of targeted imaging in MR that used to be in the realm of PET and SPECT, as well as for potential "spin-battery" applications for nuclear spin polarization storage [47]. Unlike widely available iron-oxide-based nanoparticles for MR applications [48, 49], ^{29}Si MRI achieves positive contrast, and, unlike the emerging modality of hyperpolarized nanodiamonds [50, 51], hyperpolarized silicon has longer-lived signal as well as well-developed surface chemistry for functionalization. Plans are underway to apply this emerging hyperpolarized imaging platform to (a) detect protein expression exclusive to pancreatic cancer stromal cells, thereby detecting pancreatic cancer at an early stage by effective lesion size amplification; (b) seek out precancerous polyps via MR colonoscopy, thereby opening a way for noninvasive MR-based colonoscopy; and (c) distinguish inflammatory from cancerous tissues.

Silicon and silica nanoparticles have a rich history of use in biomedical research for other diagnostic modalities (optical, PET, etc.) [44] and therapeutics, including clinical trials for their application as drug delivery vehicles in humans [52]. Other MRI studies using hyperpolarized media (^{13}C-labeled metabolites and ^{129}Xe gas) have found increasing relevance in the clinic for tracking disease metabolism [17] and lung ventilation/perfusion [53]. Given the success of these already-established programs, as well as the clinical need for targeted molecular imaging, the barrier to clinical translation of hyperpolarized silicon particles should be relatively low. Given the steady progression of ongoing research, it is likely that the versatility of silicon particles will be leveraged to achieve clinical relevance in the near future.

Acknowledgments We thank CPRIT RP150701, NCI R21CA185536, MD Anderson Brain Cancer Moonshot, Gulf Coast Consortium and John S. Dunn Foundation Collaborative Research Award Program, Koch Foundation, and Red and Charline McCombs Institute, MD Anderson IRG grants and institutional research startup for funding support. We also thank Julie Liu, Caitlin V. McCowan, Charles M. Marcus, Maja C. Cassidy, Niki M. Zacharias, David G. Menter, Jennifer S. Davis, Shivanand Pudakalakatti, David E. Volk, Patrick Kee, Prasanta Dutta, Amy Heimberger, David Gorenstein, Anil K. Sood, Seth Gammon, and David Piwnica-Worms for helpful discussion.

References

1. Erogbogbo F, Yong K-T, Roy I, Hu R, Law W-C, Zhao W, Ding H, Wu F, Kumar R, Swihart MT, Prasad PN (2011) In vivo targeted cancer imaging, sentinel lymph node mapping and multi-channel imaging with biocompatible silicon nanocrystals. ACS Nano 5:413–423
2. Tasciotti E, Liu X, Bhavane R, Plant K, Leonard AD, Price BK, Cheng MM-C, Decuzzi P, Tour JM, Robertson F, Ferrari M (2008) Mesoporous silicon particles as a multistage delivery system for imaging and therapeutic applications. Nat Nanotechnol 3:151–157
3. Canham LT (2007) Nanoscale semiconducting silicon as a nutritional food additive. Nanotechnology 18:185704
4. Carlisle EM (1972) Silicon: an essential element for the chick. Science 178:619–621
5. Loeper J, Goy-Loeper J, Rozensztajn L, Fragny M (1979) The antiatheromatous action of silicon. Atherosclerosis 33:397–408
6. Eisinger J, Clairet D (1993) Effects of silicon, fluoride, etidronate and magnesium on bone mineral density: a retrospective study. Magnes Res 6:247–249
7. Reffitt DM, Ogston N, Jugdaohsingh R, Cheung HFJ, Evans BAJ, Thompson RPH, Powell JJ, Hampson GN (2003) Orthosilicic acid stimulates collagen type 1 synthesis and osteoblastic differentiation in human osteoblast-like cells in vitro. Bone 32:127–135
8. Jugdaohsingh R (2007) Silicon and bone health. J Nutr Health Aging 11:99–110
9. Tanaka T, Mangala LS, Vivas-Mejia PE, Nieves-Alicea R, Mann AP, Mora E, Han H-D, Shahzad MMK, Liu X, Bhavane R, Gu J, Fakhoury JR, Chiappini C, Lu C, Matsuo K, Godin B, Stone RL, Nick AM, Lopez-Berestein G, Sood AK, Ferrari M (2010) Sustained small interfering RNA delivery by mesoporous silicon particles. Cancer Res 70:3687–3696
10. Reffitt DM, Jugdaohsingh R, Thompson RP, Powell JJ (1999) Silicic acid: its gastrointestinal uptake and urinary excretion in man and effects on aluminium excretion. J Inorg Biochem 76:141–147
11. O'Neil MJ (2013) The Merck index: an encyclopedia of chemicals, drugs, and biologicals. RSC Publishing, Cambridge, UK
12. van der Kolk AG, Hendrikse J, Zwanenburg JJM, Visser F, Luijten PR (2013) Clinical applications of 7T MRI in the brain. Eur J Radiol 82:708–718
13. Nelson SJ (2011) Assessment of therapeutic response and treatment planning for brain tumors using metabolic and physiological MRI. NMR Biomed 24:734–749
14. Overhauser AW (1953) Polarization of Nuclei in Metals. Phys Rev 92:411–415
15. Jóhannesson H, Macholl S, Ardenkjaer-Larsen JH (2009) Dynamic nuclear polarization of [1-13 C] pyruvic acid at 4.6 tesla. J Magn Reson 197:167–175
16. Ardenkjær-Larsen JH, Fridlund B, Gram A, Hansson G, Hansson L, Lerche MH, Servin R, Thaning M, Golman K (2003) Increase in signal-to-noise ratio of >10,000 times in liquid-state NMR. Proc Natl Acad Sci 100:10158–10163
17. Nelson SJ, Kurhanewicz J, Vigneron DB, Larson PEZ, Harzstark AL, Ferrone M, van Criekinge M, Chang JW, Bok R, Park I, Reed G, Carvajal L, Small EJ, Munster P, Weinberg VK, Ardenkjaer-Larsen JH, Chen AP, Hurd RE, Odegardstuen L-I, Robb FJ, Tropp J, Murray JA (2013) Metabolic imaging of patients with prostate cancer using hyperpolarized [1-^{13}C] pyruvate. Sci Transl Med 5:198ra108

18. Keshari KR, Wilson DM (2014) Chemistry and biochemistry of 13C hyperpolarized magnetic resonance using dynamic nuclear polarization. Chem Soc Rev 43:1627–1659
19. Nikolaou P, Goodson BM, Chekmenev EY (2015) NMR hyperpolarization techniques for biomedicine. Chemistry 21:3156–3166
20. Pereira RN, Rowe DJ, Anthony RJ, Kortshagen U (2011) Oxidation of freestanding silicon nanocrystals probed with electron spin resonance of interfacial dangling bonds. Phys Rev B Condens Matter 83:155327
21. Lee M, Cassidy MC, Ramanathan C, Marcus CM (2011) Decay of nuclear hyperpolarization in silicon microparticles. Phys Rev B Condens Matter 84:035304
22. Cassidy MC, Chan HR, Ross BD, Bhattacharya PK, Marcus CM (2013) In vivo magnetic resonance imaging of hyperpolarized silicon particles. Nat Nanotechnol 8:363–368
23. Whiting N, Hu J, Zacharias NM, Lokesh GLR, Volk DE, Menter DG, Rupaimoole R, Previs R, Sood AK, Bhattacharya P (2016) Developing hyperpolarized silicon particles for in vivo MRI targeting of ovarian cancer. J Med Imaging (Bellingham) 3:036001
24. Cassidy MC (2012) Hyperpolarized silicon particles as in-vivo imaging agents. at http://gradworks.umi.com/35/42/3542959.html
25. Hermanson GT (2013) Bioconjugate techniques. Academic Press, Philadelphia, PA, USA
26. Larson PEZ, Han M, Krug R, Jakary A, Nelson SJ, Vigneron DB, Henry RG, McKinnon G, Kelley DAC (2016) Ultrashort echo time and zero echo time MRI at 7T. MAGMA 29:359–370
27. Dementyev AE, Li D, MacLean K, Barrett SE (2003) Anomalies in the NMR of silicon: unexpected spin echoes in a dilute dipolar solid. Phys Rev B Condens Matter 68:153302
28. Hennig J, Nauerth A, Friedburg H (1986) RARE imaging: a fast imaging method for clinical MR. Magn Reson Med 3:823–833
29. Abragam A, Combrisson J, Solomon I (1958) Dynamic polarization of the nuclei of silicon 29 in silicon. Compt Rend 246:683–690
30. Morley GW, Warner M, Stoneham AM, Greenland PT, van Tol J, Kay CWM, Aeppli G (2010) The initialization and manipulation of quantum information stored in silicon by bismuth dopants. Nat Mater 9:725–729
31. Dementyev AE, Cory DG, Ramanathan C (2008) Dynamic nuclear polarization in silicon microparticles. Phys Rev Lett 100:127601
32. Lock H, Wind RA, Maciel GE, Zumbulyadis N (1987) 29Si dynamic nuclear polarization of dehydrogenated amorphous silicon. Solid State Commun 64:41–44
33. Henstra A, Dirksen P, Wenckebach WT (1988) Enhanced dynamic nuclear polarization by the integrated solid effect. Phys Lett A 134:134–136
34. Aptekar JW, Cassidy MC, Johnson AC, Barton RA, Lee M, Ogier AC, Vo C, Anahtar MN, Ren Y, Bhatia SN, Ramanathan C, Cory DG, Hill AL, Mair RW, Rosen MS, Walsworth RL, Marcus CM (2009) Silicon nanoparticles as hyperpolarized magnetic resonance imaging agents. ACS Nano 3:4003–4008
35. Atkins TM, Cassidy MC, Lee M, Ganguly S, Marcus CM, Kauzlarich SM (2013) Synthesis of long T_1 silicon nanoparticles for hyperpolarized ^{29}Si magnetic resonance imaging. ACS Nano 7:1609–1617
36. Cassidy MC, Aptekar JW, Lee M, Walsworth RL, Marcus CM (2009) Dynamic nuclear polarization of silicon-based nanoparticle magnetic resonance imaging agents. Proc Intl Soc Mag Reson Med 17:2457. (cds.ismrm.org
37. Bagraev NT, Vlasenko LS (1981) Optical nuclear polarization in heavy-doped silicon. Solid State Commun 40:483–485
38. Haze O, Corzilius B, Smith AA, Griffin RG, Swager TM (2012) Water-soluble narrow-line radicals for dynamic nuclear polarization. J Am Chem Soc 134:14287–14290
39. Cassidy MC, Ramanathan C, Cory DG, Ager JW, Marcus CM (2013) Radical-free dynamic nuclear polarization using electronic defects in silicon. Phys Rev B Condens Matter 87:161306
40. Tu C, Ma X, House A, Kauzlarich SM, Louie AY (2011) PET imaging and biodistribution of silicon quantum dots in mice. ACS Med Chem Lett 2:285–288

41. Ananta JS, Godin B, Sethi R, Moriggi L, Liu X, Serda RE, Krishnamurthy R, Muthupillai R, Bolskar RD, Helm L, Ferrari M, Wilson LJ, Decuzzi P (2010) Geometrical confinement of gadolinium-based contrast agents in nanoporous particles enhances T1 contrast. Nat Nanotechnol 5:815–821
42. Bouchard L-S, Anwar MS, Liu GL, Hann B, Xie ZH, Gray JW, Wang X, Pines A, Chen FF (2009) Picomolar sensitivity MRI and photoacoustic imaging of cobalt nanoparticles. Proc Natl Acad Sci U S A 106:4085–4089
43. Mann AP, Somasunderam A, Nieves-Alicea R, Li X, Hu A, Sood AK, Ferrari M, Gorenstein DG, Tanaka T (2010) Identification of thioaptamer ligand against E-selectin: potential application for inflamed vasculature targeting. PLoS One 5
44. Mann AP, Tanaka T, Somasunderam A, Liu X, Gorenstein DG, Ferrari M (2011) E-selectin-targeted porous silicon particle for nanoparticle delivery to the bone marrow. Adv Mater 23
45. Whiting N, Hu J, Shah JV, Cassidy MC, Cressman E, Millward NZ, Menter DG, Marcus CM, Bhattacharya PK (2015) Real-time MRI-guided catheter tracking using hyperpolarized silicon particles. Sci Rep 5:12842
46. Golman K, Zandt RI, Lerche M, Pehrson R, Ardenkjaer-Larsen JH (2006) Metabolic imaging by hyperpolarized 13C magnetic resonance imaging for in vivo tumor diagnosis. Cancer Res 66:10855–10860
47. Chekmenev EY, Norton VA, Weitekamp DP, Bhattacharya P (2009) Hyperpolarized (1)H NMR employing low gamma nucleus for spin polarization storage. J Am Chem Soc 131:3164–3165
48. Laurent S, Forge D, Port M, Roch A, Robic C, Vander Elst L, Muller RN (2008) Magnetic iron oxide nanoparticles: synthesis, stabilization, vectorization, physicochemical characterizations, and biological applications. Chem Rev 108:2064–2110
49. Peng X-H, Qian X, Mao H, Wang AY, Chen ZG, Nie S, Shin DM (2008) Targeted magnetic iron oxide nanoparticles for tumor imaging and therapy. Int J Nanomedicine 3:311–321
50. Dutta P, Martinez GV, Gillies RJ (2014) Nanodiamond as a new hyperpolarizing agent and its 13C MRS. J Phys Chem Lett 5:597–600
51. Rej E, Gaebel T, Boele T, Waddington DEJ, Reilly DJ (2015) Hyperpolarized nanodiamond with long spin-relaxation times. Nat Commun 6:8459
52. Santos HA (2014) Porous silicon for biomedical applications. Elsevier, Cambridge, UK
53. Fain SB, Korosec FR, Holmes JH, O'Halloran R, Sorkness RL, Grist TM (2007) Functional lung imaging using hyperpolarized gas MRI. J Magn Reson Imaging 25:910–923

ATR-FTIR Spectroscopy Tools for Medical Diagnosis and Disease Investigation

4

Maria Paraskevaidi, Pierre L. Martin-Hirsch, and Francis L. Martin

Contents

1 Definition of the Topic

Vibrational spectroscopic techniques are increasingly utilized in biomedical research. Attenuated total reflection Fourier-transform infrared (ATR-FTIR) spectroscopy has been applied extensively to investigate various diseases by determining the chemical and molecular differences coming with the disease. Being label-free, nondestructive, and inexpensive, biospectroscopy could potentially make a perfect diagnostic tool in the years to come.

M. Paraskevaidi · F. L. Martin (✉)
School of Pharmacy and Biomedical Sciences, University of Central Lancashire, Preston, UK
e-mail: flmartin@uclan.ac.uk

P. L. Martin-Hirsch
Department of Obstetrics and Gynaecology, Central Lancashire Teaching Hospitals NHS Foundation Trust, Preston, UK

C. S. S. R. Kumar (ed.), *Nanotechnology Characterization Tools for Biosensing and Medical Diagnosis*, https://doi.org/10.1007/978-3-662-56333-5_4

2 Overview

Biospectroscopy's ability to investigate and facilitate in different diseases in numerous ways has been pushing the technique toward clinical implementation over the last years. Vibrational spectroscopy could be applicable to many disease states, likely to detect most changes during transition from a normal to a pathological state or during treatment, as well as to provide novel biomarkers related to a disease. Uncertainty in clinical decision-making could thus be significantly reduced. ATR-FTIR sampling mode is preferred in many cases due to the many advantages coming with it, such as ease of sample preparation or reduced light scattering. In this chapter, we will focus on recent advances of ATR-FTIR spectroscopy in the investigation of various pathological conditions. Several review articles and book chapters have been previously written with regard to vibrational spectroscopy and its applications in disease diagnosis. Nevertheless, what is still lacking is a comprehensive report covering the field of disease-related studies that have employed ATR-FTIR spectroscopy as their main analytical approach. The focus of this chapter is, therefore, placed specifically on ATR-FTIR spectroscopy; herein, key research findings are presented after reviewing the recent literature (from 2010 onward). In addition, in an effort to illustrate the breadth and wide-ranging applications of this spectroscopic method, different types of biological materials (tissues, cells, and biofluids) have been investigated instead of focusing on one sample type only.

3 Introduction

Fourier-transform infrared (FTIR) spectroscopy is a well-established technique used to study and give information on the molecular composition of samples. It has been largely used in biomedical studies and has numerous applications including screening of high-risk populations, disease diagnosis, subtype classification, surgical margin determination as well as monitoring of drugs and disease progression/regression. By using a number of different sample types such as cells, tissues, or biofluids, vibrational spectroscopy yields information on their structural components including proteins, lipids, and carbohydrates. The way this analytical method works could be characterized as disadvantageous and advantageous at the same time, depending on the nature of research to be conducted. In particular, vibrational spectroscopy may not be capable of identifying specific molecules when compared to molecular tests, but it allows the investigation of a range of different molecules simultaneously; thus, it provides an overall status of the examined sample and is ideal for complicated diseases such as cancer, diabetes, or neurodegeneration, which are multifactorial, and studying isolated molecules alone might not give a complete answer [1].

Spectrochemical methods generate a signature fingerprint of biological material in the form of spectra. The most commonly used region for biological samples is the mid-IR region (4000–400 cm^{-1}), which includes stretching vibrations such as S–H, O–H, N–H, and C–H (3500–2500 cm^{-1}), and the so-called fingerprint region (1800–900 cm^{-1}), mainly representative of amide I/II (1600–1500 cm^{-1}), lipids

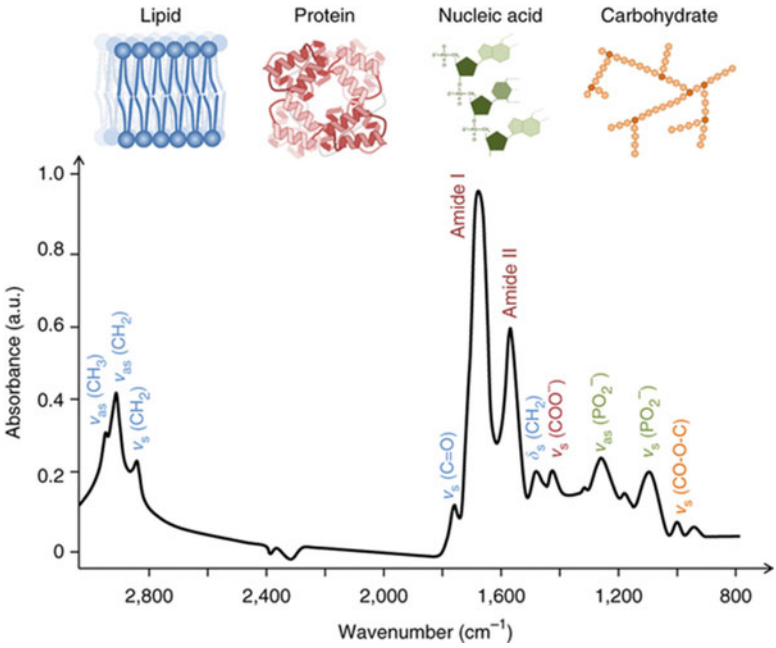

Fig. 4.1 Typical infrared spectrum of a biological sample. ν, stretching vibration; δ, bending vibration; as, asymmetric; s, symmetric. The spectrum was generated in transmission mode from a human breast carcinoma mounted on a CaF_2 slide [4]

(1750 cm^{-1}), carbohydrates (1155 cm^{-1}), asymmetric phosphate stretching vibrations (1225 cm^{-1}), and symmetric phosphate stretching vibrations (1080 cm^{-1}) (Fig. 4.1) [2, 3].

The use of FTIR in attenuated total reflection (ATR) sampling mode is a very promising approach with numerous advantages over transmission or transflection mode, namely, larger sampling area, easier sample preparation, spectral reproducibility, higher signal-to-noise (S/N) ratio, applicability to aqueous samples, and reduced light scattering. ATR-FTIR uses an internal reflection element (IRE) with a high refractive index to direct the beam to the sample; an evanescent wave is created, penetrating the sample a few microns to derive its chemical information. Therefore, the sample has to be in direct contact with the IRE (i.e., ATR crystal) (Fig. 4.2). The angle of the incident IR beam should exceed the critical angle to achieve total internal reflection; otherwise, the resulting spectrum will be a combination of ATR and external refraction (Fig. 4.3).

A number of different diseases have been thoroughly investigated by ATR-FTIR (Fig. 4.4). It would seem that the fastest growing area in vibrational spectroscopy is the diagnosis of various cancers, such as ovarian, endometrial, breast, skin, prostate, brain, colorectal, and others. The advent of IR fiber-optic probes equipped with ATR elements has also allowed for in vivo and in situ diagnostic studies of easily reached organs such as the skin, oral cavity, or colon and gastrointestinal tract through

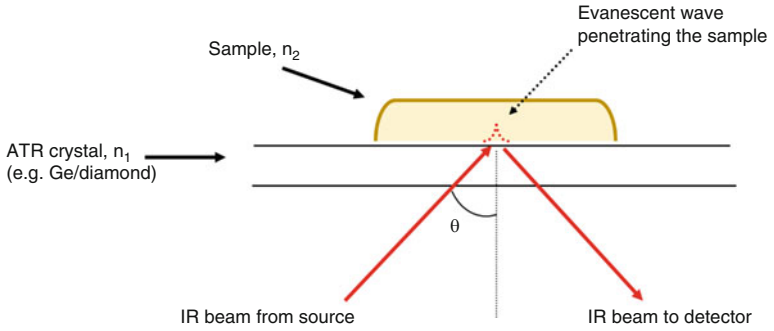

Fig. 4.2 Schematic of the ATR-FTIR sampling mode (n, refractive index; θ, angle of incidence)

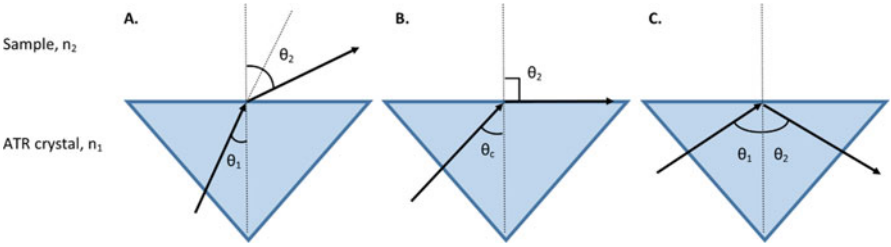

Fig. 4.3 (A) $\theta_1 < \theta_c$, refraction occurs; (B) θ_c, refraction along the boundary; (C) $\theta_1 > \theta_c$, total internal reflection occurs, (θ_c, critical angle)

colonoscopes and endoscopes [5, 6]. However, other pathological conditions have been studied as well, such as rheumatoid arthritis [7], HIV/AIDS [8], alkaptonuria [9], malaria [10], diabetes [11, 12], cystic fibrosis [13], thalassemia [14], kidney diseases [15, 16], prenatal disorders like preterm birth and premature rupture of membranes [17], and neurological diseases like Alzheimer's [18], which are also some examples of the wide-reaching applications of ATR-FTIR spectroscopy.

Suitable sample types for ATR-FTIR spectroscopy include tissues, cells, and biological fluids. Different groups have used endometrial [19], cervical [20], brain [21, 22], ovarian [23], intestine [22], lung [24], skin [25, 26], prostate [27, 28], breast [29, 30], liver [31, 32], colorectal [33], gastric [34], and esophagus [35] tissues – a method known as spectral histopathology (SHP) [36]. Various cell types and populations have also been examined, either fixed or live, derived from epithelial, nervous, muscle, or connective tissue, being either stem cells, transit-amplifying, or differentiated [4, 37–39] – this method is known as spectral cytopathology (SCP) [40]. Some of the biofluids that have been employed for ATR-FTIR analysis are whole blood [41, 42], blood plasma and serum [43–45], urine [9, 42], sputum [46], saliva [47, 48], tears [49], cerebrospinal fluid (CSF) [50], and amniotic fluid [17]. From the above sample types, readily accessible biofluids such as blood, urine, sputum, or saliva are considered ideal for clinical implementation due to the noninvasive, routine methods of collection as well as their minimal sample preparation.

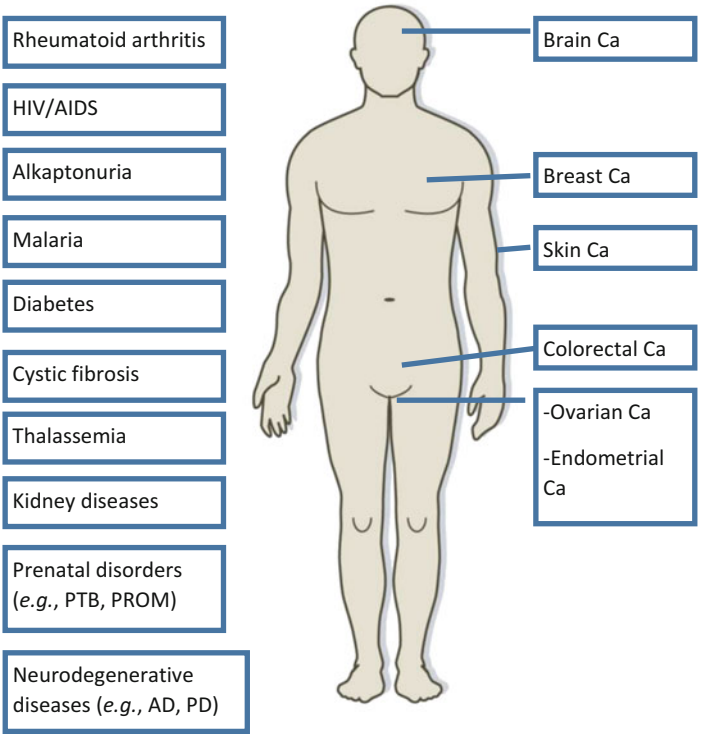

Fig. 4.4 Diseases that have been studied by ATR-FTIR include a number of different pathologies/disorders (HIV, human immunodeficiency virus; AIDS, acquired immune deficiency syndrome; PTB, preterm birth; PROM, premature rupture of membrane; AD, Alzheimer's disease; PD, Parkinson's disease; Ca, cancer)

Early disease detection is of crucial importance as, once the patient appears with clinical symptoms, the condition may already be irreversible. If at-risk individuals are identified early, it may be possible to delay/prevent further progression or provide suitable treatment/medication. As aforementioned, multifactorial diseases may require a panel of biomarkers – defined as disease-associated molecular changes in body tissues and fluids [51] – in order to better comprehend their etiology and facilitate screening and diagnosis, so that appropriate clinical intervention can begin as soon as possible. The necessity of discovering new biomarkers and techniques arises from the lack of highly sensitive and specific biomarkers for a number of diseases, as well as the limited availability of cost-effective and noninvasive tests. For instance, prostate-specific antigen (PSA) levels, used to diagnose prostate cancer in serum, provide sensitivity of ~20% for any stage of the disease and ~50% for high grade [52]; cancer antigen 125 (CA-125) levels, used as a biomarker for ovarian cancer detection in serum, provide sensitivity and specificity of ~80% and 75%, respectively, but are only elevated in half of the individuals at an early stage [53];

estrogen receptor (ECα), used in breast cancer, has varying specificity from 72% to 77% [54]; Alzheimer's disease has been shown to be diagnosed with ~95% sensitivity and ~85% specificity but only after the combination of three different biomarkers in CSF, namely, amyloid-β 42 (Aβ42), total tau, and phospho-tau-181 [55]; serum creatinine, used for screening kidney failure, provides sensitivity of ~13% for any stage and ~45% for severe kidney failure [56].

This chapter will focus on the advancements of ATR-FTIR spectroscopy as a diagnostic tool for the investigation of a variety of diseases; particular focus will be given on experimental and instrumental methodology, as well as potential pitfalls and what to avoid. An in-depth review of all the literature on ATR-FTIR since 2010, along with the key research findings, will also be included. Conclusions, limitations, and an overview of where the field of spectroscopy is heading will be presented.

4 Experimental and Instrumental Methodology

4.1 Experimental Methodology

A variety of different clinical sample types, substrates, preparation, data preprocessing, and multivariate techniques have been employed in the past toward medical diagnosis with ATR-FTIR spectroscopy. It is worth mentioning that even though there is a growing literature proving the diagnostic capability of spectroscopy, there are still many hurdles to overcome for clinical implementation; the most important is the lack of standardization and validation in large clinical trials. A very interesting paper on discovering new biomarkers of disease states that flaws could be introduced in a study even from the very first step of sample collection which could inevitably affect the results of subsequent experiments [51]. For instance, it was recently shown that use of different anticoagulants in blood plasma collection could affect spectroscopic analysis by introducing confounding peaks [57]. Continuous efforts of different groups within the spectroscopy field are made to standardize processes from the pre-analytical phase, such as sample collection/preparation, to the analytical and post-analytical phase, such as optimal spectrometer settings and data handing (Fig. 4.5). In this section, we will discuss some of the most common steps adapted as experimental procedures. The methodology presented here is not exhaustive but rather an overview of the critical steps for ATR-FTIR spectroscopy.

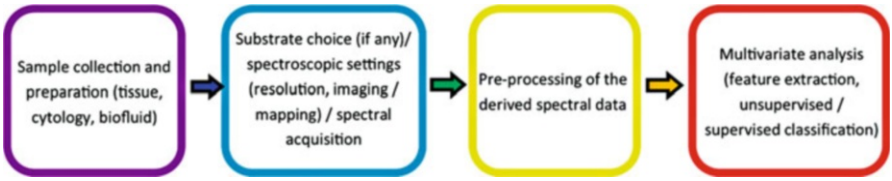

Fig. 4.5 Schematic overview of the steps followed for ATR-FTIR spectroscopy

4.1.1 Sample Collection and Preparation

Tissue: Tissue samples can be either formalin-fixed paraffin-embedded (FFPE) or snap-frozen. For FFPE tissue, the removed biopsy of interest is immersed in an aqueous formaldehyde solution (formalin), which is used as a preservative for biological material. The aim is to remove the water present in tissue and replace it with a medium that solidifies the tissue (i.e., paraffin wax) and allows fine sectioning. Paraffin is immiscible with water; thus, the tissue is first dehydrated with sequential immersions in increasing concentration of ethanol up to 100%, followed by washes in xylene, which is used to remove ethanol. Final step includes embedding of the tissue in molten paraffin wax and cooling down, which hardens the wax. FFPE blocks can be stored at room temperature.

In order for the FFPE tissue to be analyzed with spectroscopy, it needs to be sectioned from the whole tissue block with a microtome, while kept cool onto an ice block to ensure that the wax remains hard, therefore allowing easier sectioning. The tissue ribbons (8–10 μm thick) are put in a warm H_2O bath (40–44 °C) and then floated onto the substrate of choice. The slide with the tissue is then placed in a 60 °C oven for 10 min and de-waxed by immersion in fresh xylene for 5 min, thrice. Finally, immersion in acetone or 100% ethanol follows for 5 min in order to remove the xylene before air-drying in room temperature.

Snap-frozen tissue is preferred for molecular studies as it avoids the use of preservatives and paraffin that cause degradation. For snap-freezing, the tissue is first embedded in optimal cutting temperature (OCT) compound, while isopentane, cooled with liquid N_2, is then used to finally freeze the sample; 60–90 s will be enough for the OCT compound to freeze. Direct immersion of the tissue into liquid N_2 is avoided, as it would destroy cellular morphology and tissue architecture. Each sample can then be wrapped individually in labeled aluminum foil and stored at −80 °C until analysis.

To use snap-frozen tissue for spectroscopic analysis, the frozen block is mounted into a cryostat for 30 min to reach the cryostat's temperature (~ −20 °C). Then, serial sections of tissues (8–10 μm thick) are cut from the block, mounted onto the substrate of choice, and left to dry in desiccant for at least 3 h before analysis. Sections should be carefully collected in order to avoid contamination of the tissue with the OCT. Exposure to light should be minimized until the analysis to prevent tissue degradation due to oxidation.

Cytology: Cells can be either fixed in a preservative solution or live. A well-studied example of fixed cells is cervical cytology; however, the following experimental procedure could be adapted for other cell types kept in fixative buffers. Firstly, the fixative solution (e.g., ThinPrep or SurePath for cervical cells) needs to be removed as it would give unwanted peaks in the fingerprint region; to achieve this, the sample undergoes centrifugation (2000 rpm for 5 min) and the supernatant is discarded. Each sample is resuspended in distilled water and centrifuged again. This washing procedure should be repeated three times. The remaining cell pellet should be finally resuspended in 100 μl of distilled water, deposited onto a substrate of choice with a micropipette, and left to air-dry at room temperature. Another way to apply the cells onto a substrate is by cytospinning; the initial washing steps are

followed as before, and a maximum volume of 200 μl is spun in a cytospin cytocentrifuge so that the cells get squashed onto the slide. Then, they are again left to air-dry and stored in desiccant until their analysis.

Studying live cells rather than fixed ones may be a more challenging technique, but it would allow for in situ measurements and data collection of the same cell at different time points. Cells in suspension should be firstly detached from the growth substrate (e.g., flask) using trypsin and subsequently washed from medium and trypsin with phosphate-buffered saline (PBS). Live cells could then be directly seeded and grown on the ATR crystal with the use of a cell chamber, so that they form a good contact [39]. Another option would be the deposition of a drop of the cell suspension onto a substrate of choice and air-drying at room temperature. An alternative would also be to grow the cells directly onto slides that have been sterilized in 70% ethanol for an hour and rinsed with sterilized water [28]; this would, however, make the cells thin as they grow and stretch over a 2-D surface. Three-dimensional culture matrices (a tissue culture environment or device where live cells can grow in three dimensions) could provide a realistic environment to study cells; after being grown in 3-D cultures, cells should be fixed or snap-frozen as described aforementioned for the tissue samples [4]. Of course, live cells could always be directly fixed in a preservative solution – just as with cervical cytology – and prepared as aforementioned.

Biofluids: The use of biofluids in vibrational spectroscopy has increased rapidly in the last decade, providing a promising and alternative technique to tissue biopsies and cytology. Biofluids already analyzed by ATR-FTIR spectroscopy include some easily accessible, noninvasive samples such as whole blood, plasma, serum, urine, sputum, saliva, and tears as well as some more invasive, organ-specific samples such as cerebrospinal fluid (CSF) and amniotic fluid.

Blood samples are easily collected by venepuncture: whole blood requires no further treatment apart from addition of an anticoagulant [e.g., ethylenediaminetetraacetic acid (EDTA), lithium heparin, or citrate] to prevent clotting; for blood plasma samples, whole blood is collected into anticoagulant-treated tubes and then centrifuged (~1000–2000 rpm for 5–10 min) to remove cells (the resulting supernatant is the plasma); for blood serum samples, whole blood is collected into a tube without anticoagulant, left undisturbed to clot at room temperature for 15–30 min, and then centrifuged (~1000–2000 rpm for 5–10 min) to remove the clot (the resulting supernatant is the serum). Urine samples are collected and typically stored without any sample preparation. Fresh sputum sample can be obtained either by having the patient/individual expectorate into a sterile specimen cup or by following the standard protocol for sputum induction – for those who have difficulty producing sputum spontaneously. If sputum cells were to be studied in isolation, the mucus should be removed before the whole sputum specimen undergoes centrifugation (~3000 rpm for 10 min). Saliva is obtained by expectoration or by use of a cotton swab followed by centrifugation to isolate the saliva; a detailed review specifically dedicated to saliva specimen collection toward disease diagnosis was published a decade ago [58]. Tears

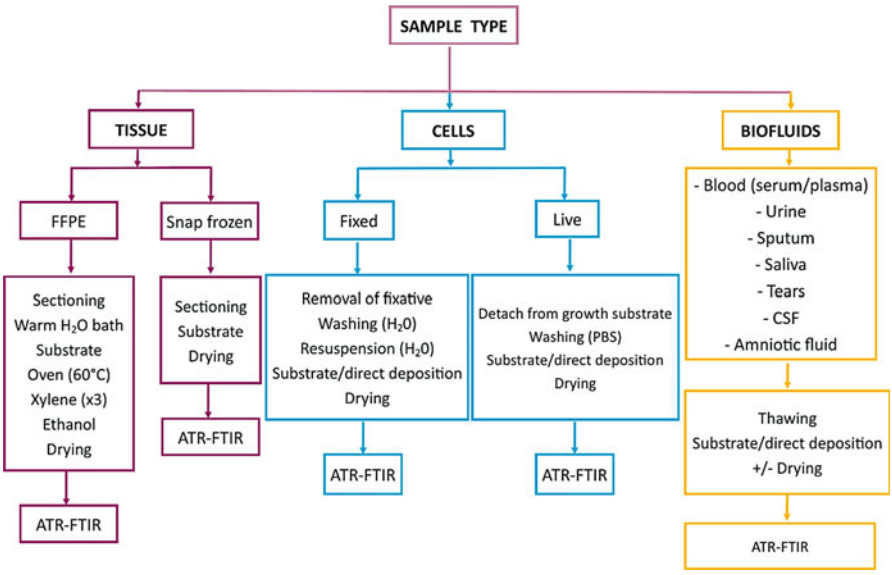

Fig. 4.6 Schematic with the basic preparation steps for different samples toward ATR-FTIR spectroscopy

should be carefully collected without additional stimulation; touching the eyelid and corneal should be avoided in order to avoid reflex tear fluid caused by stimulation. Disposable glass microcapillary tubes and polyester fiber rods have been used for tear collection. The most common collection method for CSF is by lumbar puncture followed by storage with no further sample treatment. Amniotic fluid samples are centrifuged right after collection and their supernatants are subsequently stored.

All of above biofluids are frozen at −80 °C right after their collection, unless they are immediately used. Before spectroscopic interrogation, it is crucial that samples are fully thawed. Generally, the most common method for biofluid deposition before further analysis is by drop deposition and drying either directly onto the ATR crystal or onto an appropriate IR substrate. A schematic summarizing the preparation procedures for all the sample types is shown in Fig. 4.6.

Important considerations: The pre-analytical stages for sample collection and handling can have tremendous effect on the derived spectra and subsequently the interpretation of the result; therefore, standard procedures should be followed carefully. The research community should adapt common standards and interlaboratory data integration for their findings to become clinically useful.

The quality of the samples that are stored at −80 °C could be compromised after a number of freeze-thaw cycles. Freeze-thawing should be avoided when unnecessary or at least be controlled; for instance, biofluids could be divided in aliquots of smaller volume from the initial sample. A recent study has shown the ability of FTIR to

differentiate fresh blood samples from samples that have been freeze-thawed up to five times, but could not distinguish between the five freeze-thaw cycles [57]. However, another study using mass spectrometry has found that freeze-thawing is to blame for changes in the integrity of the samples, especially after two thaws [59].

Fixative solutions, such as formalin for tissue and ThinPrep for cervical cytology, or paraffin wax used for tissue embedding, give characteristic IR spectral signatures and can easily mask biological information of a sample. Paraffin, for example, gives significant peaks at ~2954 cm^{-1}, 2920 cm^{-1}, 2846 cm^{-1}, 1462 cm^{-1}, and 1373 cm^{-1} [4]. Therefore, removal of these sample contaminants and further cleaning of the samples must be thorough. The deparaffinization and cleaning process are not always easy, and subsequent spectral analysis could be employed to exclude the spectral regions that are contaminated. When using biofluids such as blood plasma or serum, careful removal of cells should precede storage if cells are not directly investigated.

Most of the biofluid studies have used dried samples in order to remove the spectral signature of water which dominates the mid-IR region: amide I region (~1650 cm^{-1}) due to water-bending vibration and the higher region (~3000 cm^{-1}) due to –OH stretching vibrations [60]. Drying time of 1 μl of biofluid has been found to be 8 min [61], and typical volumes can range from 1 to 50 μl. However, dried samples can suffer from chemical and physical inhomogeneity which would reduce reproducibility and sensitivity [62]. When a liquid drop is dried on a surface, there is the subsequent appearance of differential crystallization known as the "coffee ring effect" where the majority of the constituents of the sample migrate to the periphery of the drop [63]. This phenomenon leads to inconsistency in the concentration across the sample and should be taken into account before spectral acquisition. Averaging multiple point spectra across the width of the outer ring has been shown to eliminate this issue [64]. Another approach is the analysis of biofluids in their liquid state without or after semidrying, which may "sacrifice" some spectral regions, but it still identifies important bands [65]. Moreover, dried samples often result in higher peaks compared to wet samples, but they have the shortcoming of the uneven distribution [4]; further research of this approach is needed.

Anticoagulants such as citrate, EDTA and lithium heparin are used for the collection of blood plasma to prevent clotting. Citrate and EDTA function by chelating calcium and preventing thiamine-dependent clotting factors from functioning, while lithium heparin binds to antithrombin III clotting factors to prevent their function [66]. Comparing the spectral signature from EDTA and citrate with lithium heparin, the latter was found to give fewer additional peaks and therefore be more appropriate for spectroscopic analysis; after dialysis of the plasma samples with a 10 kDa membrane, the peaks from EDTA seemed to be removed [57]. However, samples collected in the biobanks are used for multicenter studies, and depending on the study, different anticoagulants are preferred. For example, a different group suggested that all of the three anticoagulants are acceptable but EDTA particularly is preferred for delayed blood processing [67]. As long as the use of one anticoagulant remains consistent throughout the dataset, then this issue will be unlikely to have a great effect during spectroscopic comparison.

One of the factors that should be well-considered is the thickness of the sample under interrogation. In the ATR-FTIR sampling mode, the generated evanescent wave, which penetrates beyond the crystal to reach the sample, is ~1–2 μm within the fingerprint region, but 5% intensity still reaches at 3 μm depth. Penetration depth is dependent on the wavelength of the incident light, the refractive indices of the crystal, and the sample, as well as the incidence angle of the IR beam, and is given by the following equation:

$$d_{\mathrm{p}} = \frac{\lambda}{2\,\pi\, n_{\mathrm{IRE}} \sqrt{\sin^2\theta - \left(n_{\mathrm{samp}}/n_{\mathrm{IRE}}\right)^2}}$$

where d_{p} is the penetration depth; λ is the wavelength; n_{IRE} and n_{samp} are the refractive indices of the IRE and sample, respectively; and θ is the angle of incidence. As seen from the above equation, the pathlength is directly proportional to the wavelength so that for longer λ, we get greater penetration; therefore, ATR intensity is decreased for higher wavenumbers. Typical values of d_{p} for a biological sample are ~0.4–0.54 μm for the C–H stretching bands (lipids), 0.75–0.95 μm for amides I and II, and 1.1–1.47 μm for P–O/C–O stretching (nucleic acids and carbohydrates). A commonly used substrate in ATR-FTIR is the IR reflective low-E microscope slide (MirrIR, Kevley Technologies) mainly because of its low cost. This highly reflective slide is essentially a glass slide coated with a multilayer of tin oxide (SnO_2) and silver (Ag). Numerous studies have suggested that, in case of very thin samples, these slides could generate an electric field standing wave (EFSW) effect coming from the metallic surface (Ag), urging careful consideration of the thickness of the samples (>2–3 μm) to avoid potential spectra distortion; therefore, ATR or transmission modes were thought preferable over transflection mode [68]. However, it was also pointed out that by using suitable preprocessing methods (e.g., second derivative), distortions from this phenomenon can be efficiently reduced [40, 69]. Too-thin or too-sparse samples could also lead to low signal-to-noise (S/N) ratio [37]; thus, the samples should ideally be three- or fourfold thicker than the penetration depth, with no maximum thickness limitations. Overall, higher S/N ratio can be achieved when the sample is flat, of adequate thickness, and covers completely the ATR crystal.

4.1.2 Substrates

Substrate choice is an important consideration in IR studies of biological samples due to potential background interference. Substrates used in ATR mode include calcium fluoride (CaF_2) or barium fluoride (BaF_2) slides, MirrIR low-E slides, and zinc selenide (ZnSe) slides; aluminum-coated slides have also shown promise as a substrate in a recent, pilot study – further work with more samples would be needed to validate these results [28]. As aforementioned, caution should be exercised when using low-E slides in micro-ATR experiments to eliminate substrate artifacts generated from very thin samples; instead samples should be >2–3 μm thick. An alternative method, especially for biofluids, could be the direct deposition of a drop on the IRE as it

would avoid any substrate signal contribution. For live cells, a cell chamber can be used to facilitate cells to grow in close contact with the IRE [39].

4.1.3 Spectral Acquisition and Experimental Procedure

Different instrumentation, light sources, and detectors can be used for ATR-FTIR spectroscopy, and each one, along with other variables, could affect the S/N ratio and therefore the quality of the resulting spectra or images. Other parameters affecting the S/N ratio are the sampling aperture, number of co-additions, mirror velocity, and spectral resolution [38]. Once the samples are prepared, as abovementioned, they are deposited either directly on the ATR crystal or on the substrate of choice, and then the spectra can be collected. Generally, intimate contact of the sample with the IRE element is necessary to eliminate background artifacts. Point spectra are typically acquired from multiple locations (ten different locations is common) of each sample to minimize bias. Maps can also be generated by collection of point spectra from an area of interest. The advent of array detectors has also allowed spectral acquisition in imaging mode, which allows for simultaneous collection of spectra. The IRE should be cleaned with a disinfectant solution (e.g., Virkon solution) and distilled water or ethanol and dried every time before moving to the next sample. A background spectrum should be acquired to account for ambient and instrumental conditions. It is recommended to record a background after every sample and at regular intervals to account for atmospheric changes.

4.1.4 Spectral Preprocessing and Multivariate Analysis

Preprocessing of the acquired spectra is an essential step of all spectroscopic experiments and is used to correct problems associated with spectral acquisition, instrumentation, or even sample handling before further multivariate analysis. Depending on the study's goal (i.e., diagnostic, biomarker identification, imaging, or pattern finding), the user has to follow different pathways for the data analysis. A diagnostic approach may be more complex as it requires initial training of the classification system before further validation occurs (e.g., cross-validation).

The main preprocessing methods are de-noising, spectral correction, and normalization. Techniques for de-noising spectra are Savitzky-Golay (SG) smoothing, wavelet de-noising (WDN), and principal component analysis (PCA); the latter is more common and reduces the spectral data space to principal components (PCs) responsible for the majority of variance removing, therefore, the noise. Spectral correction can be applied to spectra with sloped or oscillatory baselines due to scattering, with resonant Mie scattering being the most pronounced effect. Preferred techniques for spectral correction include extended multiplicative scattering correction (EMSC), resonant Mie scattering correction (RMieSC), and rubberband baseline correction. Another way to correct sloped baselines is the use of first or second derivative in combination with SG smoothing; this may alter the shape of the spectra, but it resolves overlapping peaks. Normalization should follow last to account for differences such as varying thickness and concentration that are unrelated to the

biological information; amide I, amide II, and vector normalizations are common. Usually, two or three of the above methods are applied before multivariate analysis; for instance, first or second differentiation is combined with SG smoothing and followed by vector normalization [70].

Subsequently, multivariate approaches are employed to facilitate the handling of the large number of spectral data that is generated. Firstly, feature extraction (FE) is used as a data reduction technique to create new variables based on the original ones; PCA or partial least squares (PSA) are popular as FE methods. Feature selection (FS) can also be used for FE, without altering the original representation of the variables, and can be used to identify the most important wavenumbers that can be used as spectral biomarkers. Further steps include either clustering, which is an unsupervised classification method, with the class of sample being unknown, or supervised classification where the different classes are taken into account. Cluster analysis is an exploratory method and is used for pattern finding and imaging studies; some of the common approaches use k-means, fuzzy c-means, and hierarchical cluster analysis (HCA). Supervised methods estimate the class of an unknown/new dataset after training an initial dataset. Therefore, a training and a validation dataset are required; briefly, some of the supervised approaches are support machines (SVMs), artificial neural networks (ANNs), and k-nearest neighbors (k-NN). If the classifiers lack stability, models can be improved by classifier ensembles as it is accepted that no single model can solve a complex classification problem. We would advise the reader to refer to previous studies that have described the preprocessing and multivariate approaches in more detail as these were beyond the scope of this chapter [4, 38, 70–72].

4.2 Instrumental Methodology

Instrumentation varies for ATR-FTIR studies from benchtop, portable, and handheld instruments to ATR probes. Detectors and internal reflective elements (IRE) can also differ depending on the model of the instrument and the aim of the study. The majority of benchtop spectrometers make use of an inexpensive Globar infrared source. A conventional FTIR spectrometer can provide an enhanced S/N ratio using a synchrotron radiation source as it is 1000 times brighter than the Globar source; however, the combination of micro-ATR with a synchrotron source has not been demonstrated yet [39]. Enhancement of the infrared signal in ATR mode can be achieved with surface-enhanced IR absorption (SEIRA) spectroscopic approaches, according to which molecules on metal surfaces show 10–100 times stronger signal than without the metal [73–76]. This technique is complimentary to surface-enhanced Raman spectroscopy (SERS) and utilizes the surface plasmon effect from the interaction of light with metallic nanoparticles. The principle of this enhanced technique is based on the polarization of the metallic surface (e.g., gold/silver nanoparticles), which generates a local electromagnetic field stronger than the

incident IR photon field; the dipole moment of molecules is, therefore, enlarged, and IR absorption is enhanced.

Spectra can be acquired either as point spectra, which generate maps, or in imaging mode. In mapping mode, chemical information is collected from single/point spectra taken from different locations of a sample, while in imaging, the area of interest is selected and spectra are acquired simultaneously at a specific wavelength to generate pseudo-color images. In conventional ATR-FTIR, a single-element detector is used, meaning that spectra are collected point-by-point having a high S/N ratio; the resulting, high-quality spectrum is indicative of the average signal from the area that the IR light passed. In imaging mode, a large number of spectra are collected simultaneously with the use of array detectors such as linear array and focal plane array (FPA) detectors. Linear array detectors obtain an image by raster scanning of rows of a sample, whereas FPA detectors collect the IR signal from all locations. The use of these detectors in ATR decreases acquisition time by two to three times and achieves high spatial resolutions, down to diffracted-limited resolution values [77]. A fourfold increase of spatial resolution can be achieved in ATR mode, compared to transmission and transflection mode, due to the crystal's (e.g., Ge or Di) high refractive index in the mid-IR [29]. The detector of choice can be either thermal, such as the deuterated L-alanine-doped triglycine sulfate (DLaTGS), or quantum detector such as mercury cadmium telluride (MCT). Despite the latter being better than the standard DLaTGS detector, providing a higher S/N ratio with higher scanning speed and sensitivity, it also needs liquid nitrogen for cooling in contrast to the thermal detector, which operates at room temperatures.

Preliminary experiments should be conducted to find the instrument's optimal conditions before spectral acquisition. These would differ depending on the aim of the study (diagnostic or exploratory) and the preferred spectral and spatial resolution. For instance, the optimal parameters for an ATR-FTIR spectrometer with a diamond crystal of dimensions 250 μm × 250 μm and a single-element detector were found to be 8 cm^{-1} spectral resolution with mirror velocity of 2.2 kHz (1.4 mm/s) and 32 co-additions. It should be noted that resolution should not be higher than necessary, as this would increase total acquisition time significantly. Doubling the resolution, for instance, would require four times higher acquisition time to achieve the same S/N ratio, as S/N ratio of a spectrum is proportional to the square root of the number of co-additions (i.e., acquisition time).

Different accessories and configurations can be used for ATR spectroscopy with the IRE being single or multiple reflection. Single-bounce crystals have smaller sampling areas (~1.5 mm) and are used for strong absorbers and solid samples, whereas multiple-bounce materials have a broad sampling area (~6 mm) providing greater contact with the sample and are used for weaker absorbers or dilutions. Multiple reflection can provide enhanced depth of penetration and sensitivity. ATR crystals include diamond, germanium, zinc selenide, or silicon. The preferred choice for many studies is the diamond crystal due to its robustness and chemical inertness, while other crystals should be handled with caution as they could get scratched or

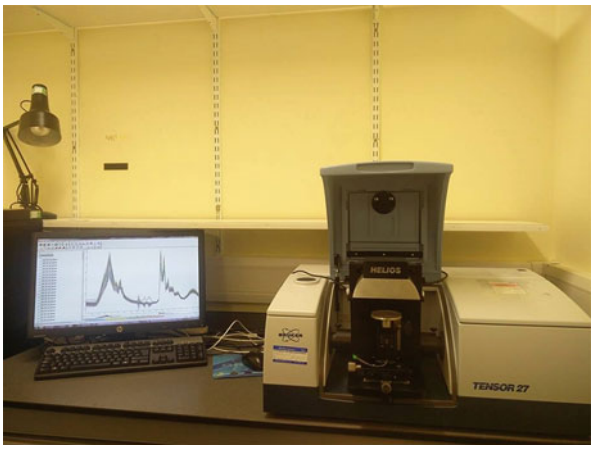

Fig. 4.7 Bruker Tensor 27 FTIR spectrometer equipped with Helios ATR attachment

broken; however, diamond comes at a higher cost. Germanium has the highest refractive index of all ATR materials (~4), which decreases penetration depth (<1 μm) in comparison to the other materials and is useful when highly absorbing molecules are studied. Other spectrometers with ATR attachments (such as the Helios ATR attachment we use for our studies – Fig. 4.7) use a magnification-limited camera to locate the area of interest; however, this configuration cannot provide microscopic features of the sample. ATR probes with IR fiber optics have been also used with various advantages over conventional ATR configurations such as flexibility, low cost, and remote acquirement of spectra (e.g., used for colonoscopes or endoscopes) [78].

A list of various types of instruments used for ATR-FTIR spectroscopy, along with some of their technical characteristics, is shown below:

4.2.1 Manufacturer: ABB Analytical

MB3000 FT-IR analyzer (left): spectral range, 485 to 8500 cm^{-1}; maximum signal-to-noise ratio, 50,000:1; resolution better than 0.7 cm^{-1}; a universal ATR sampling accessory can be used to analyze solids, liquids, pastes, and gels (right); horizontal ATR accessory is also available; solid-state laser; DTGS detector. Photo credit ABB Measurement & Analytics

4.2.2 Manufacturer: Agilent

Cary 630 FTIR Spectrometer: interchangeable sampling accessories for transmission, ATR, specular reflectance, and diffuse reflectance; ATR crystal can be diamond, germanium, or multibounce ZnSe; weights ~4 kg. © Agilent Technologies, Inc. 2011. Reproduced with permission, Courtesy of Agilent Technologies, Inc.

Cary 660 FTIR spectrometer (left): it is only available in conjunction with the Cary 610/620 FTIR microscope systems (right); the Cary 610 is a single-point FTIR

microscope (mapping), while Cary 620 is a focal plane array (FPA) (chemical imaging); the Cary 610 can be upgraded to a Cary 620 providing flexibility depending on the application; ATR accessories are also available. © Agilent Technologies, Inc. 2008. Reproduced with permission, Courtesy of Agilent Technologies, Inc.

4300 Handheld FTIR: a portable system with a variety of sampling interfaces (diffuse reflectance, external reflectance, grazing angle, diamond ATR and Germanium ATR); MCT or DTGS detector; weighs ~2kg. © Agilent Technologies, Inc. 2014. Reproduced with permission, Courtesy of Agilent Technologies, Inc.

4500 Series Portable FTIR: Compact and reliable for non-lab environments; suitable for liquids and solids; the 4500a type uses a spherical Diamond ATR crystal of one, three or five reflections depending on the application; it is ideal for the analysis of solids, liquids, pastes and gels. © Agilent Technologies, Inc. 2011. Reproduced with permission, Courtesy of Agilent Technologies, Inc.

4100 ExoScan Series FTIR (handheld): mid-IR range; suitable for diffuse, grazing angle, specular reflection or spherical ATR sampling interfaces; weighs ~3kg. © Agilent Technologies, Inc. 2011. Reproduced with permission, Courtesy of Agilent Technologies, Inc.

4200 FlexScan Series FTIR (handheld): dual module system, the optical module weighs ~1.5kg and is attached to the ~2kg electronics module by a power cable; it uses the same interferometer and optics as the 4100 ExoScan and thus has identical performance. The ATR interface is ideal for solids, liquids, pastes and gels.

5500 Series Compact FTIR: a portable system used for liquid and solid samples; the 5500a type has one, three or five reflection diamond ATRs depending on the application; single reflection diamond ATR available for solids and liquids identification; multi-reflection ZnSe ATR available for liquid analysis.

4.2.3 Manufacturer: Arcoptix

Arcoptix FTIR-FC (Fiber-Coupling): this system uses ATR fibered probes; it operates in the mid-IR; spectral range, ~5000 to 625 cm^{-1}; there are two options for detectors – MCT, 4-TE cooled, and MCT, liquid N2 cooled; ATR crystal can be

diamond or silicon; probe length, 1.5–1.7 m; ZnSe beamsplitter; solid-state laser at 850 nm; weighs 2.2 kg

4.2.4 Manufacturer: Beijing Beifen-Ruili Analytical Instrument

WQF-510A/520A FTIR Spectrometer: different accessories such as defused/specular reflection, ATR, liquid cell, gas cell, and IR microscope can be attached to the sample compartment; different types of single-reflection ATR crystals can be selected depending on the application (Zn, Se, diamond, germanium, AMTIR, silicon); multiple reflection horizontal ATR (HATR) can also be installed; spectral range, 7800 to 350 cm^{-1}; signal-to-noise ratio, ~15,000:1; DTGS detector; germanium-coated KBr; weighs 28 kg.

WQF-530 FTIR spectrometer: transmission sample holder is standard; optional accessories such as defused/specular reflection, single/multi-reflection ATR, liquid cell, gas cell, and IR microscope can be attached to the sample compartment; spectral range, 7800 to 350 cm^{-1}; signal-to-noise ratio, better than ~20,000:1; resolution, 0.85 cm^{-1}; room temperature DLaTGS detector is used as standard; a temperature stabilized, high sensitivity DLaTGS detector can optionally be used; multilayer Ge-coated KBr; weighs 24 kg.

4.2.5 Manufacturer: Bruker

LUMOS FTIR microscope: 8x objective – magnification can reach 32x by digital zooming; fully automated measurement in transmission, reflection, and ATR mode; in transmission and reflection, the ATR crystal is inserted into the objective; motorized germanium ATR crystal with internal pressure control (three different pressure steps can be software-selected to achieve optimal performance depending on the sample type); large working distance allows samples of ~40 mm thickness; high sensitive photoconductive MCT detector; DTGS detector as option.

HYPERION FTIR microscope: 20× objective; spectral range from visible (up to 25,000 cm^{-1}) to far-IR (down to 80 cm^{-1}); dedicated ATR objective; internal pressure sensor ensures optimal contact between the sample and the crystal; option to connect external accessories.

TENSOR II FTIR spectrometer: large sample compartment to accommodate any FTIR external accessory; fully automated PQ (performance qualification) and OQ (operational qualification) routines for instrument validation; it can be equipped with broadband beamsplitters to expand the spectral range either to the near- or far-IR; room temperature DTGS detector – easily exchangeable; long-life diode laser.

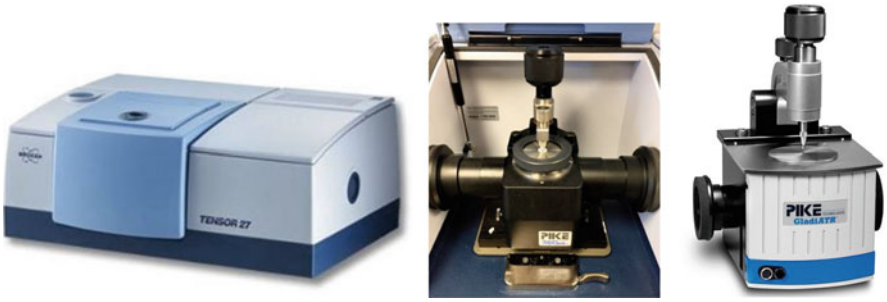

TENSOR 27/37 spectrometers: Tensor 27 is equipped with a Globar source that emits mid-IR light; Tensor 37 has both mid-IR (Globar) and near-IR (tungsten halogen lamp) sources; HeNe laser (emits red light of 633 nm) controls the position of the moving interferometer mirror and is used to determine the sampling positions; DLaTGS detectors are used in both systems with optional, liquid-N2 cooled MCT detectors; different accessories (middle, right) can be attached to the sample compartment area and allow for measurements in the ATR mode.

ALPHA FTIR spectrometers: transmission, ATR, external, and diffuse reflection sampling accessories are available; ALPHA's Platinum ATR (left) uses a single-reflection diamond ATR crystal – it is easy to clean as the pressure applicator can be rotated 360° to provide easier access to the sampling area; Eco-ATR (middle) can be used for powder, solid, paste, and liquid samples – uses a single-reflection, ZnSe ATR crystal; multireflection-ATR module (right) is designed for six internal reflections, is equipped with a horizontal ZnSe ATR crystal, and is suitable for the analysis of pastes, gels, and liquids

4.2.6 Manufacturer: Interspectrum

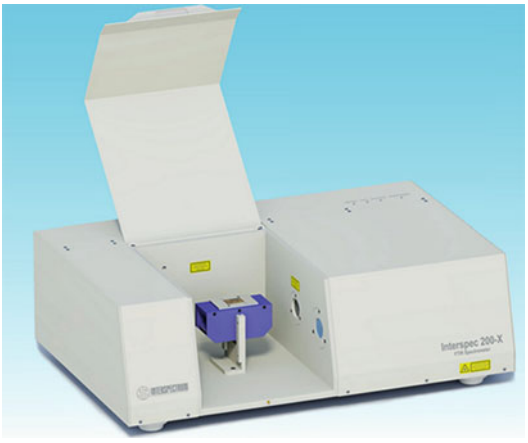

Interspec 200-X: wavelength range in mid-IR: 7000 to 400 cm^{-1}; wavelength range in near-IR: 14,000–5800 or 9000–3850 cm^{-1}; DLaTGS detector (standard) with MCT detector as optional; weighs 24 kg; signal-to-noise, 15,000:1; different accessories are also available for ATR, specular reflection, diffuse reflection, and more.

Interspec 300-X series FTIR spectrometer: portable system; wavelength range, 7000 to 400 cm^{-1}; KBr beamsplitter (standard) – ZnSe beamsplitter (optional); integrated accessories for ATR (horizontal, one bounce with a ZnSe ATR crystal), reflection and transmission measurements; DLaTGS detector; weighs 18 kg; signal-to-noise, 12,000:1.

Interspec 311 Compact FTIR spectrometer: wavelength range, 7000 to 400 cm^{-1} (KBr optics) and 5000–600 cm^{-1} (ZnSe optics); KBr beamsplitter (standard) – ZnSe beamsplitter (optional); weighs 10 kg.

Interspec 650-X Compact FTIR spectrometer: wavelength range, 7000 to 400 cm^{-1} (KBr optics) and 5000–600 cm^{-1} (ZnSe optics); KBr beamsplitter (standard) – ZnSe beamsplitter (optional); weighs 14 kg; different accessories are available or this system, e.g., horizontal one bounce ZnSe ATR accessory (left), three bounce ZnSe ATR accessory (middle), and one bounce ZnSe or diamond ATR accessory.

4.2.7 Manufacturer: JASCO

FT/IR-4000 series FTIR (left): temperature stabilized DLaTGS detector; MCT detector optional; spectral range 5000–220 cm^{-1}; manual or automatic instrument validation; accepts different accessories for the ATR sampling mode such as the ATR PRO ONE (middle) and ATR PRO ONE VIEW (right).

FT/IR-6000 series FTIR: measurements from the near-IR (15,000 cm^{-1}) to the far-IR (50 cm^{-1}); DLaTGS detector with Peltier temperature control

(standard); choice detectors, DLaTGS, MCT, indium antimonide (InSb); manual or automatic instrument validation; accepts different accessories for the ATR sampling mode.

IRT-7000 Series Microscope (left): these systems can be interfaced with the FT/IR-4000 and FT/IR-6000 Series spectrometers (right), offering advanced imaging systems; two detectors as standard, a 16-channel linear array detector for IR imaging and a single-point MCT detector; standard automatic sample stage allows analysis of a large sample area, multi-area ATR mapping, and imaging of a specific area; up to four objectives and automated switching.

IRT-5000 Series Microscope (left): it can be interfaced with the FT/IR-4000 and FT/IR-6000 Series spectrometers (right); used in the mid-IR for materials identification and forensic analysis or in the near-IR and far-IR for more fundamental research; up to two detectors can be installed: mid-band MCT detector

(optional: Peltier cooled DLaTGS); ability for transmission/reflectance or ATR mapping; automatic XYZ sample stage; multiple objectives with automatic switching.

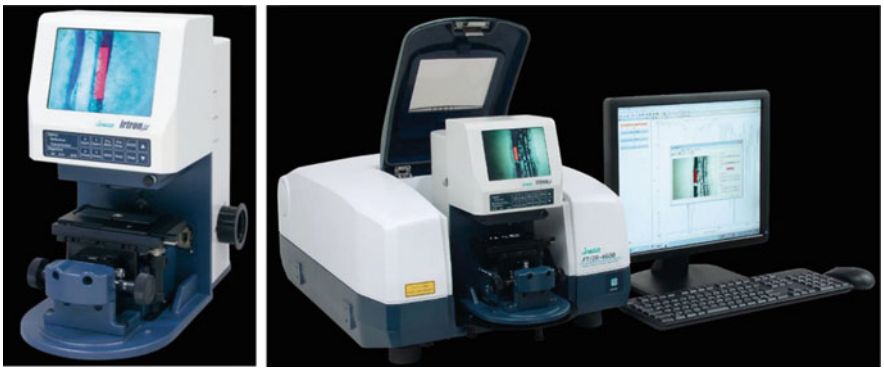

IRT-1000 Series Microscope (left): used with either FT/IR-4000 or FT/IR-6000 Series spectrometers (right); transmittance, reflectance, and ATR modes are available; DLaTGS detector in FTIR main instrument (standard) (MCT or near-IR optimized detector are optional)

4.2.8 Manufacturer: Lumex Instruments

FT-IR Spectrometer InfraLUM FT-08 (left): spectral range, 8000–350 cm^{-1}; signal-to-noise ratio > 4000; DLaTGS detector; weighs 32 kg; different accessories are available such as single (middle) and multiple (right) ATR accessories, diffuse reflectance accessory, and sample compartment microscope; the PIKE MIRacle ATR accessory (middle) is available with five different crystal types [ZnSe, diamond, germanium, silicon, and amorphous material transmitting IR radiation (AMTIR)] and can be used with liquids, solids, pastes, gels, and intractable materials; the horizontal attenuated total reflectance (HATR) accessory (right) is available with the above crystal types and can be used for liquids, semiliquids, solids.

4.2.9 Manufacturer: PerkinElmer

PerkinElmer Frontier: range of near-, mid-, and far-IR Fourier-transform spectrometers; external input and output beam options for custom experiments (left); option for multiple detectors (e.g., DTGS and MCT); different sampling accessories are available; the accessories that can be used for the ATR mode include both multiple reflection HATR and single reflection (right).

Spotlight 150i/200i FT-IR Microscopy System: operates in transmission, reflectance, and automated micro-ATR for maximum sampling flexibility; it can be upgraded to the Spotlight 400 Imaging system (shown below) to allow faster imaging and the opportunity to add ATR imaging.

Spotlight 400 FT-IR Imaging System: automated focus, stage movement, and illumination; contains a single-element MCT detector and a linear array MCT imaging detector; operates in mid-IR, near-IR, or dual range; available sampling modes are standard transmission, reflection, ATR imaging, and more; optional ATR imaging improves spatial resolution.

Spectrum Two IR Spectrometer: portable system; wavelength range, 8300–350 cm^{-1}; weighs 13 kg; DTGS detector is available.

4.2.10 Manufacturer: Shimadzu

IRTracer-100 FTIR Spectrophotometer (left): wavelength range, 7800 to 350 cm^{-1} (standard) or 12,500 to 249 cm^{-1} (optional); different accessories (right) can be used for sampling in the ATR mode; single beam; signal-to-noise ratio, 60,000:1.

IRAffinity-1S FTIR Spectrophotometer: wavelength range, 7800 to 350 cm^{-1}; allows measurements in transmission, diffuse reflection, and ATR mode; signal-to-noise ratio, 30,000:1; wide range of accessories are available as above.

4.2.11 Manufacturer: Thermo Fisher Scientific

Nicolet iS50 FT-IR Spectrometer: spectral range from far-IR to visible (15–27,000 cm^{-1}); dual source capable; ATR, Raman, and NIR modules can be used without manually changing system components; three detectors for the main sample compartment; mid-IR and far-IR diamond ATR crystal. Reproduced with permission, Courtesy of Thermo Fisher Scientific.

Nicolet iN5 FTIR microscope: detector options are medium-band MCT-A or room temperature DTGS; 10x objective, N.A. 0.71; transmission, reflection, and optional ATR modes are available; ATR options include pre-aligned, slide-on germanium or diamond crystals; integrated pressure sensor; weighs 29 kg. Reproduced with permission, Courtesy of Thermo Fisher Scientific.

Nicolet iN10 Infrared Microscope: room temperature, deuterated L-alanine-doped triglycine sulfate (DLaTGS) detector (can be replaced by a MCT detector); computer-controlled automation; configurable options: direct contact sampling with MicroTip ATR; manual or motorized stage. Reproduced with permission, Courtesy of Thermo Fisher Scientific.

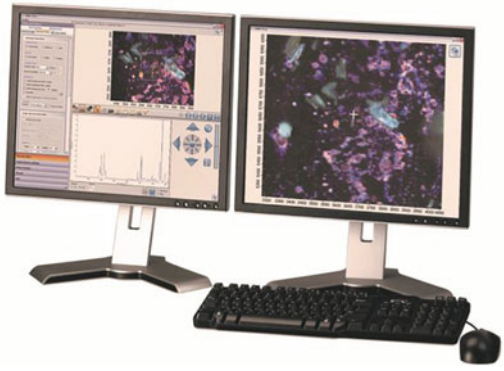

Nicolet iN10 MX Infrared Imaging Microscope: provides chemical images to enhance understanding of the chemical distribution of heterogeneous samples; DTGS detector (standard); liquid-N2 cooled MCT-A and MCT-A linear array (optional); configurable options, direct contact sampling with MicroTip ATR; best

viewing comfort with dual monitor operation. Reproduced with permission, Courtesy of Thermo Fisher Scientific.

Nicolet iS 10 FT-IR Spectrometer: spectral range 7800–350 cm^{-1} optimized, mid-IR KBr/Ge beamsplitter; 11,000–375 cm^{-1} XT-KBr/Ge extended range mid-infrared (optional); HeNe laser; deuterated triglycine sulfate (DTGS) (standard) detector; liquid-nitrogen-cooled mercury cadmium telluride (MCT) detector (optional); weighs 33 kg. Reproduced with permission, Courtesy of Thermo Fisher Scientific.

Nicolet iS 5 FT-IR Spectrometer: KBr/Ge mid-IR beamsplitter; thermally controlled diode laser; user-replaceable, source, desiccant, power supply, sample compartment windows; deuterated triglycine sulfate (DTGS) (standard) detector; weighs 10 kg. Reproduced with permission, Courtesy of Thermo Fisher Scientific.

Nicolet iS 5N FT-IR Spectrometer: near-IR diode laser; spectral range 11,000–3800 cm^{-1}; CaF2 near-IR beamsplitter; different accessories are included for transmission and ATR modes; iD5 and iD7 ATR accessories offer diamond crystal options; iD5 ATR offers a laminate-diamond crystal, plus heated and multi-bounce crystal plates for special applications; iD7 ATR has a monolithic diamond crystal for the widest spectral range and best durability; interchangeable crystal plates offer good sampling versatility; weighs 10 kg. Reproduced with permission, Courtesy of Thermo Fisher Scientific.

Nicolet Continuum Infrared Microscope: narrow-, mid-, and wide-band MCT-A detector; sampling flexibility with transmission, reflectance, and micro-ATR; chemical image analysis is possible. Reproduced with permission, Courtesy of Thermo Fisher Scientific.

5 Key Research Findings

ATR-FTIR spectroscopy is a powerful technique for the study of various biological specimens and diseases. For spectroscopy to be of diagnostic importance, it is necessary that robust biomarkers exist. For instance, a potential biomarker for cervical cancer diagnosis could be the ratio of glycogen-to-phosphate regions in cells, where increased phosphate levels and decreased glycogen levels would suggest rapid cell proliferation, in turn suggesting malignancy [79]. Apart from its use in disease diagnostics, it also extends to other fields such as screening of high-risk population to identify cells committed to develop disease, classification of different disease subtypes and severity (i.e., low-grade versus high-grade disease), determination of surgical margins, investigation of the effects of a treatment or drug, monitoring of the progression or regression of a disease, and characterization of nanomaterials. With regard to the latter specifically, ATR-FTIR has been utilized for surface characterization of nanomaterials used in biomedical applications. For instance, it has been used to identify chemical features on a surface after its modification to obtain nanosurface features; a respective study by Abbasi et al. revealed a characteristic peak at 1715 cm^{-1}, confirming the modification, and further showed that platelet adhesion was greatly reduced on the modified surface compared to the control, thus providing better blood compatibility [80]. Nanoparticles can be used to introduce drugs into specific sites due to their good uptake within cells. Therefore, Tsai et al. used ATR-FTIR spectroscopy to conduct quantitative analysis of competitive molecular adsorption on gold nanoparticles [81]. A recent study on cell sheet engineering used ATR-FTIR to successfully investigate solvent effect (optimal solvent type and ratio) on nanometric grafting of poly-N-isopropylacrylamide on the surface of polystyrene [82]. Another study explored surface modification of medical polymers which could improve biocompatibility; utilizing ATR-FTIR, normal and modified polystyrene samples (treated with plasma irradiation – oxygen and argon gases) were compared, revealing a significant difference at 3400–3700 cm^{-1} which indicated the presence of functional groups [83]. ATR-FTIR spectroscopy has been used, along with other analytical techniques, to confirm the composition of particles designed as dry-powder inhalation aerosols for targeted respiratory nanomedicine [84]. Investigation of nanoparticle surface composition is crucial in nanotoxicology, but analytical methods to probe nanoparticle surfaces in aqueous are still limited; Mudunkotuwa et al. used ATR-FTIR to study the liquid-solid interface in environmentally and biologically relevant media typically used for toxicity studies [85]. The abovementioned applications have been extremely interesting and advantageous to the scientific community and development of nanomedicine. Some examples of these are briefly reported here; however, the focus of this chapter is on studies using biological samples such as tissues, cells, and biofluids, toward investigation of various diseases.

Currently, most spectroscopic studies are proof of principle, with a small number of cases, showing the potential of the technique in the aforementioned areas; there are only a few large studies using ATR to reach ~500 subjects. In terms of sample size planning, it has been shown that 75–100 samples are required for a good but still not perfect classifier. In the case of smaller datasets, cross-validation is most appropriate as it allows for more robust results after use of different training and validation datasets for a defined number of times [86]. Herein, all of these matters and findings are discussed at more length.

5.1 Tissue

Using an ATR probe equipped with a ZnSe material, oral tissues were examined toward differentiation of malignant from healthy sites. The tumor types examined included adenoid cystic carcinoma, adenoma carcinoma, mulaepidermoid carcinoma, squamous cell carcinoma, basal cell adenocarcinoma, myoepithelioma, and pleomorphic adenoma. It was determined that normal tissue had stronger lipid (~1745 cm^{-1}) and amide I bands in contrast to malignant tissue which also had strong O–H stretching bands [5].

Via ATR-FTIR spectroscopy, Taylor et al. [19] examined endometrial tissue, from tumor and tumor-adjacent tissue, to discriminate benign from malignant areas. The spectral regions that showed significant differences were the lipid and amide I and II (indicative of secondary protein structure) regions. An accurate diagnosis based on spectroscopy would allow for an objective interpretation, eliminating the possibility of human error during microscopic histological examination.

In a preliminary study of 30 patients with lung tumor, ATR-FTIR was employed to discriminate malignant from nonmalignant lung tissue [24]. Sixty lung tissue samples (30 malignant and 30 nonmalignant) were obtained in total from 30 patients. After histological examination, it was verified that 96.7% of original grouped cases was correctly classified. The spectral bands that were mostly responsible for segregation between the two classes were related to proteins at amides I, II, and III, carbohydrates (~1120 cm^{-1}), and nucleic acids (~1085 cm^{-1}).

A recent paper by Theophilou et al. [27] revealed differences in prostate tissue collected from individuals at different time points during a 30-year period, 1983–2013. The changes were mostly attributed to DNA/RNA suggesting that phenotype of the human prostate was altered due to genotoxicity or epigenetic changes; this was also confirmed by immunohistochemical studies for DNA methylation.

Ovarian tissue has been studied with ATR-FTIR spectroscopy to reveal differences not only between benign, borderline, and cancerous tissue but also between the different carcinoma subtypes such as carcinosarcoma and clear cell [23]. Differential diagnosis of the various subtypes/grades would allow an appropriate treatment method such as surgery alone or adjuvant chemotherapy and close follow-up. Classification rates were further optimized when the different subtypes were compared in pairs.

The potential of ATR-FTIR has also been proven in the diagnosis of brain tumors using tissue sections. Gajjar et al. [21] achieved differentiation of various tumor subtypes from healthy tissue. Different ratios of important peaks were also calculated which could be utilized as potential biomarkers. For instance, decreased lipid-to-protein ratio (1740 cm^{-1} to 1400 cm^{-1}) was linked to increased tumor progression, while RNA-to-DNA ratio (1121 cm^{-1} to 1020 cm^{-1}) was reduced in meningioma and metastatic tumors when compared to normal brain tissue.

In a different study, rat tissues were analyzed by ATR-FTIR to explore their biochemical differences and composition [22]. The observed changes were consistent with the expected composition of each tissue: the brain, lung, heart, liver, intestine, and kidney. This finding could be used in pharmacological/pharmacokinetic studies to correlate the biochemical status of the sample with the changes that have occurred. For instance, this could potentially be used to follow up individuals or to monitor the effects of a specific drug to a specific tissue/organ.

Another pilot study using ATR-FTIR has shown its potential to evaluate surgical resection margin in patients with colorectal cancer. Spectra were acquired from tissue obtained from four parts: tumor sample and intestinal mucosa samples from 1 cm, 2 cm, and 5 cm away from the tumor. Spectroscopic analysis showed that spectra from the tumor area and mucosa 1 cm away from tumor were substantially different from those further away from tumor. The differences included decrease of the lipid region and increase of the protein and nucleic acid regions at the tumor and its closest site [33].

Relatively recently, ATR-FTIR spectroscopy was also used intraoperatively in fresh tissue to distinguish benign from malignant breast tissue [30]. Right after spectroscopy, the removed breast tissues were formalin-fixed and sent for histopathological examination; 50 cases were diagnosed as fibroadenoma and 50 cases as invasive ductal carcinoma. The spectroscopic results after classification showed excellent agreement with histological results, with sensitivity and specificity of 90% and 98%, respectively. These findings highlight spectroscopy as a useful investigative tool that could facilitate surgical decisions during an operation and be an alternative to pathological diagnosis of frozen or formalin-fixed tissue sections.

Biochemical changes were also monitored in normal skin tissue of mice after inducing squamous cell carcinoma (SCC) by multistage chemical carcinogenesis. SCC is a nonmelanoma skin cancer and the second most common type of skin cancer. Absorption intensities and band shifts in the peak position were altered in the neoplastic tissue, indicating changes in the secondary structural conformation of proteins. The obtained classification accuracy was 86.4% with sensitivity and specificity of 97.1% and 75.7%, respectively [26]. The authors conclude on the potential of ATR spectroscopy to facilitate diagnosis of SCC.

ATR-FTIR spectroscopy has recently been applied to understand therapeutic responses of cancer patients [87]. There is an increasing need to predict the outcome of a treatment given to cancer patients, but currently, the conventional methods include laborious, time-consuming, and subjective methods. Kalmodia et al. utilized tissue from the mouse xenograft model of retinoblastoma and nanoparticle-mediated targeted therapy (with gold nanoparticles) and showed unique spectral signatures

between treated and untreated subjects, indicating different underlying mechanisms. The results propose that ATR-FTIR could be used to monitor patients' response to cancer therapeutics.

Recent focus in spectrochemical methods has been given to the development of a cost-effective and robust substrate that would allow implementation into a clinical environment. Cui et al. have therefore employed aluminum foil as an alternative substrate, showing that it is able to perform equally or even better than the expensive, conventional substrates. Promising results in an amphibian cell and prostate tissue indicated that this readily available substrate could be used to prepare cytology and histology samples for spectroscopic interrogation without any substrate interference [28]. Undoubtedly, more research is required to achieve final and wider implementation.

5.2 Cytology

Sputum cells have been used by Lewis et al. in an attempt to develop a diagnostic tool for lung cancer [46]. Sputa from 25 lung cancer patients and 25 healthy controls were collected for this observational study; the bronchial origin of the samples was confirmed by the presence of bronchial epithelial cells in H&E-stained cells. The two classes were clearly separated after multivariate analysis with discriminating wavenumbers assigned to protein, nucleic acid, and glycogen changes and seen at 964 cm^{-1}, 1024 cm^{-1}, 1411 cm^{-1}, 1577 cm^{-1}, and 1656 cm^{-1}.

Using cervical cytology, Kelly et al. [88] used two different datasets to train and validate their classification algorithm (dataset A, samples designated as normal, low-grade, and high-grade; dataset B, low-grade samples). The authors concluded that ATR-FTIR spectroscopy could be used to correctly classify the low-grade samples (i.e., dataset B) and maybe subdivide them according to their biological progression or regression "signature." By comparing the ratio of normal/low-grade/high-grade classification per patient, this would allow earlier prediction of the progression or regression before distinct cellular changes were observable by a cytologist. For example, a patient was predicted as 42% normal/47% low-grade/11% high-grade and was negative for the human papillomavirus (HPV) which is associated with the development of cervical cancer. In case of high-grade prediction, further examination would be required as it is linked with more chances for progression.

ATR-FTIR imaging provides the highest spatial resolution, compared to transmission and transflection mode, due to the high refractive index of the IRE in the mid-IR. Walsh et al. [29] applied ATR-FTIR imaging to identify and acquire high-quality chemical information of cell types such as endothelial cells, myoepithelial cells, and terminal ductal lobular units (TDLUs) as well as structure in human breast tissues such as normal, hyperplastic, dysplastic, and malignant tissues. Changes in the structure of DNA during breast cancer were also investigated in extracted intact chromosomes from MCF-7 breast cancer cells. Results of this study pointed out

spectroscopy's ability to resolve and examine a sample at a subcellular level for a more detailed insight of a disease.

A study by Lane and Seo utilized ATR-FTIR to find the structural differences between cancerous breast cells (MCF-7 line) and normal breast cells (MCF-12G line) that contained gold nanoparticles [89]. Different concentrations of nanoparticles were applied in order to study the enhancement of the IR signal (similar to SEIRAS approach – see Instrumental Methodology). They found the nanoparticles within the cells and concluded that increased concentration resulted in sharper peaks and thus easier identification of the differences between the two groups. Findings of this specific study suggest that ATR-FTIR in combination with gold nanotechnology could be used toward cancer diagnosis.

Beta-thalassemia major (β-TM) is caused by a genetic defect in hemoglobin synthesis and results in ineffective erythropoiesis; it is also another disease that has been studied by ATR-FTIR. For the purpose of this study, bone marrow mesenchymal stem cells (BM-MSCs) were collected to investigate global structural and compositional changes in β-TM. Increased lipid, protein, glycogen, and nucleic acid levels were seen in thalassemic patients in contrast to healthy individuals, which were attributed to enhanced cell proliferation and bone marrow activity during ineffective erythropoiesis. Moreover, comparison of the BM-MSCs before and after transplant showed a significant decrease in the content of the aforementioned molecules showing the effect of the transplantation. The observed changes were confirmed by further molecular tests, such as ELISA [14].

Laboratory infected red blood cells (RBCs) have been analyzed with ATR for the detection and quantification of early-stage malaria parasite infections [10]. Early stages of the malaria parasite's life cycle were distinguished, namely, the ring and gametocyte forms, which are the only stages present in peripheral blood, with an absolute detection limit of 0.00001% parasitemia (<1 parasite / μl of blood) and quantification limit of 0.001% (10 parasites per μl). After preliminary studies to select the optimum fixative, methanol was the solution of choice among ethanol and formaldehyde solutions; the samples were then deposited and dried on the crystal. A second study from the same group used infected RBCs in their aqueous state and reported less effect of the anticoagulants compared to the dried state. The authors suggested that the effect was less pronounced presumably because the water diluted the amount of anticoagulant [66]. A large cohort clinical trial led by Wood et al. is ongoing, using portable ATR-FTIR spectrometers toward early diagnosis of asymptomatic carriers of malaria in remote, developing countries.

Another study has employed micro-ATR-FTIR imaging of fixed fibroblast cells to identify the region of the cells where spectral changes occurred upon cancer activation [90]. Predominant changes were attributed to nucleic acids and the C–H stretching of proteins and were mostly seen in the cells' cytoplasm rather than the nucleus, showing that the cells were undergoing a phenotypic change denoted by protein modification.

A more recent, large-scale study using liquid-based cytology (LBC) was conducted toward segregation of the different grades of cervical dysplasia, i.e., normal, low-grade, and high-grade. Even though a degree of crossover between

the classes was seen, attributed to the imperfect conventional screening (i.e., visual examination under the microscope), significant spectral differences were still noticeable [91]. Maximal crossover was found between normal and low-grade specimens, while the least crossover was between high-grade and normal cases, as expected.

A following study utilizing cervical cytology [37] found that ATR-FTIR spectroscopy identified more accurately the underlying disease than conventional screening. This was subsequently confirmed by histology as a "gold standard" approach; histological results were available for almost half of the cases (154 out of 322). When cytology results were used for classification, there was significant overlap between the different categories, whereas when histology results were used, the score plot showed substantially higher segregation between classes.

Using MCF-7 cells, Wu et al. [92] applied different concentrations of a chemotherapy drug (5-fluorouracil) to assess their response. With increasing drug concentration, the band at 1741 cm^{-1}, representative of membrane phospholipids, was increased and an upward shift from 1153 cm^{-1} to 1170 cm^{-1} was noted. The ratio of lipid/amide I (i.e., 1741 cm^{-1}/1640 cm^{-1}) was correlated with the percentage of apoptotic cells. The results indicate that 5-fluorouracil alters the phospholipid composition of the cell membrane, which increases permeability and fluidity, and could be utilized to drug monitoring and improvement of treatment strategies.

The impact of local treatment for precancerous lesions of the cervix has also been investigated with ATR-FTIR in cervical cells [93]. Samples were collected from before and after the treatment (6 months), and significant increase of amide I/II was shown in the posttreatment group, which was attributed to increased cellular function during wound healing from the treatment. Moreover, decreased levels of lipids in the posttreatment indicated the higher bioavailability in the population before treatment. Results from Halliwell et al. showed that excisional treatment, rather the removal of the disease, should be blamed for alterations of the biochemistry of the cervix, which is associated with the higher risk of preterm birth, evident in this population.

Detection of cell activation after treatment with an antibody [anti-CD3 (cluster of differentiation 3)] was also feasible in ATR-FTIR mode [94]. Specifically, cell activation of Jurkat T cells was detected within 75 min after the cells encountered the specific immunoglobulin molecules showing that the technique is sensitive enough to measure molecular events. Similarly, it demonstrates its use in monitoring cellular events and responses to particular agents or drugs at different time points after exposure.

A promising application of ATR-FTIR would be the spectroscopic imaging of live cells, which could facilitate in a range of biomedical purposes. Even though live cells are more of a challenge to study that fixed cytology, Andrew Chan and Kazarian [39] recently reported the advantages and developments of ATR imaging in live cells. That said, improvements in spatial resolution of the acquired images would allow for investigation of micron-sized samples and their subcellular features. A novel approach implemented by the same group has introduced optical apertures directly on the ATR objective of an infrared microscope; this allows the angle of light incidence to be controlled, modifying thus the penetration depth. As a result,

someone would be possible to derive spectral information from different thicknesses of the same sample, as well as to reduce the effects of anomalous dispersions by modifying the angle of incidence.

5.3 Biofluids

Using blood plasma and serum in a pilot study, Gajjar et al. [44] employed ATR-FTIR to diagnose endometrial and ovarian cancers. Using a classification machine, the authors were able to detect ovarian and endometrial with accuracy ~97% and ~82%, respectively. The less promising results in endometrial cancer were attributed to the fact that it is less aggressive than ovarian cancer and most of the times diagnosed in early stages when it is still confined to the uterus. Plasma was also shown to provide higher classification results than serum, which was attributed to the higher number of molecules present in this type of biofluid.

Detection of drugs was suggested in easily acquired saliva samples. Hans et al. [48] used cocaine as a commonly used drug and were able to identify it at a concentration of 0.020 mg/ml. Alcohol's spectral signature was also taken into account as it is common for drugs to get consumed alongside with alcohol. The authors showed a distinct, time-dependent decrease of the alcohol peak (i.e., sugars at ~1050 cm^{-1}) between the time point right after alcohol consumption and 2 h later. Therefore, alcohol was not considered to affect the important spectral region for cocaine detection (1800–1710 cm^{-1}). No preparation or extraction procedures were used for the saliva samples apart from the drying of the sample to eliminate the strong water absorption.

Khanmohammadi et al. were able to discriminate blood serum samples between 35 patients with renal failure and 40 healthy individuals with 95.12% accuracy [15]. The samples were analyzed without any further preparation such as drying or pre-concentration. To eliminate water interference, a background of water was first obtained which was then subtracted from the resulting spectra.

Prenatal disorders such as fetal malformations, preterm birth, and premature rupture of membranes have been investigated toward the development of an early prenatal diagnostic tool. Graça et al. [17] used amniotic fluid from second trimester pregnant women and divided them, according to their pregnancy outcomes, into healthy term pregnancies or the abovementioned disorders. The study demonstrated the ability of ATR-FTIR to accurately diagnose fetal malformations and preterm birth, while for cases or premature rupture of membranes, only minor changes were observed. The authors concluded that using predictive models and a larger cohort, it might be possible for future studies to simultaneously differentiate healthy pregnancies from potential disorders.

HIV/AIDS has been studied by ATR-FTIR in blood serum. The cohort consisted of 39 HIV-affected patients who were on antiretroviral treatment, 16 HIV-affected patients with no retroviral treatment, and 30 uninfected individuals. Both HIV-infected groups were segregated from the healthy individuals with significant differences at lipids/fatty acids (3010 cm^{-1}), carbohydrates (1299 cm^{-1};

1498 cm^{-1}), glucose (1035 cm^{-1}), and proteins (1600 cm^{-1}; 1652 cm^{-1}). Apart from the differential diagnosis of the aforementioned groups with <90% accuracy, the derived spectral biomarkers could be utilized as indicators of response to treatment and/or disease progression. The spectral data were also relatable to more sensitive metabolomic techniques such as nuclear magnetic resonance (NMR) spectroscopy and mass spectrometry (MS), which had been employed before ATR-FTIR from the same group [8].

Serum data by Hands et al. [95] showed differentiation between 311 brain tumor patients and 122 non-tumor individuals with sensitivity and specificity of 91.5% and 83.0%, respectively. The same study discriminated glioma versus meningioma, low-grade versus high-grade glioma, and groups with different organ origin of metastatic disease.

Nabers et al. [50] used an immuno-infrared-sensor in the ATR sampling mode to diagnose Alzheimer's disease (AD) in blood plasma and cerebrospinal fluid (CSF). The amide I band was specifically investigated as it reflects the overall secondary structure of amyloid-β peptides, showing a significant downshift with disease progression; the latter was attributed to increased β-sheet amyloid-β peptides. Discrimination between AD and disease control patients was achieved with accuracy 90% for CSF and 84% for plasma samples.

Rheumatoid arthritis (RA) is an autoimmune inflammatory disease with a difficult and complex diagnosis. Blood serum samples from 29 patients with RA and 40 healthy donors were collected, and ATR-FTIR spectroscopy was applied toward differentiation of the two groups. Significant differences were found in the fingerprint region as well as in a higher spectral region (3000 cm^{-1}–2800 cm^{-1}), and the two groups were classed with sensitivity and specificity of 85% and 100%, respectively [7].

Currently, a large-scale study by a diagnostics company (Glyconics Ltd.) is conducted toward diagnosis of patients with suspected respiratory disease such as chronic obstructive pulmonary disorder (COPD) in sputum samples. A preliminary diagnosis of COPD is given by spirometry, which can be insensitive and unable to distinguish between the different respiratory diseases such as COPD and asthma. Handheld ATR-FTIR systems have been used for the analysis of >500 sputum samples, showing its capacity of monitoring patients, and provide early biomarkers of acute exacerbation, which could lead to hospitalization (http://www.glyconics.com/#technology.).

6 Conclusions and Future Perspective

The field of biospectroscopy has seen tremendous progress over the last years with the focus placed extensively on disease investigation. Some of the fields that ATR-FTIR, specifically, has contributed are the development of diagnostic tools, screening of population with suspected disease, subtype classification, prediction of disease recurrence, response to treatment and personalized treatment, and much more. Despite the fact that FTIR has not yet been used for diagnosing patients

with nonspecific symptoms or for the identification of the primary origin of metastatic cancer, this possibility has been extensively discussed in a recent review [96].

Spectroscopy has been proven suitable for the differential diagnosis of various diseases with sensitivities and specificities equal (or even higher) than the ones obtained by current clinical/molecular methods. For a number of diseases, an earlier diagnosis and detection of the "warning signs" could lead to a better prognosis and immediate handling/treatment. For this reason, special attention has been given in screening of at-risk individuals before they even become symptomatic. It has been shown that this could be feasible and spectroscopy could detect changes prior to detection with conventional screening (e.g., examination of morphological changes of tissue/cells under a light microscope). One interesting example is the precancerous stages of some cancers, such as cervical or colon cancer, which may or may not progress to cancer and which spectroscopy appears to discriminate with high accuracy [37, 88, 97].

Compared to other analytical techniques which may be more sensitive, such as mass spectrometry (MS) and nuclear magnetic resonance (NMR), FTIR's ability has now been proven to generate comparable results, being able to detect and identify differential metabolites [8, 98]. The advantages of this alternative analytical method are many including high sensitivity, low cost, repeatability, and a nondestructive nature, which could render it a perfect candidate for clinical translation. In fact, it might sound surprising to someone that after all the successful applications and effort that has been put into implementation of spectroscopic techniques into the clinic, it is still not being used in routine clinical practice. The reasons for this are plenty – as already mentioned in the methodology section – including lack of standardization of techniques and sample preparation. Also, there is lack of multicenter studies with large cohort of samples (i.e., thousands), which is necessary to validate these approaches before they play a role in life-changing decisions within a clinical environment. Even though ATR is very promising, there are still several issues to be considered. As with every other analytical technique for biomarker discovery, many requirements and phases (pre-analytical, analytical, and post-analytical) need validation in independent datasets and by independent researchers before a new biomarker is approved for clinical use. In the pre-analytical phase, for example, it is important to examine whether demographic characteristics, such as age, gender, diet, or lifestyle, would affect the result. There have indeed been some examples of initially promising studies in novel biomarker discovery which were invalidated only some years after their publication [99].

A proposed scenario for clinical translation could be the use of spectroscopic methods primarily in tertiary care, with the scope that when established they will be transferred into general practice and primary care as simple and stable handheld devices, to identify patients for further examinations [53]. A recent review in vibrational spectroscopy of biological fluids states that a common mistake is to extrapolate the biomarkers' performance found in pilot studies (where a definite diagnosis of the disease has been given by gold standard methods) to the screening context [100]. Biomarker sensitivity and specificity in the screening population are expected to be much lower than in patients with confirmed disease, and thus

participants should be carefully chosen to fall into the appropriate clinical setting every time they are tested for a biomarker; this way, false-positive results would be kept at a minimum avoiding unnecessary examinations and overtreatment.

Acknowledgments We would like to thank all our collaborators over the years and all the study participants who have contributed to our research. The kind generosity of Rosemere Cancer Foundation in supporting our studies is also acknowledged; M.P. is a current recipient of one of their PhD studentships. We would also like to thank our colleagues at Lancashire Teaching Hospital NHS Trust who have selflessly facilitated many of our studies over the years. Finally, we would like to acknowledge the manufacturers for permission to copy and republish images of their instruments.

References

1. Theophilou G, Paraskevaidi M, Lima KM, Kyrgiou M, Martin-Hirsch PL, Martin FL (2015) Extracting biomarkers of commitment to cancer development: potential role of vibrational spectroscopy in systems biology. Expert Rev Mol Diagn 15(5):693–713
2. Stuart B, Infrared Spectroscopy: Fundamentals and Applications. Kirk-Othmer Encyclopedia of Chemical Technology. John Wiley & Sons, Inc. 2005; https://doi.org/10.1002/0471238961.0914061810151405.a01.pub2
3. Movasaghi Z, Rehman S, ur Rehman DI (2008) Fourier transform infrared (FTIR) spectroscopy of biological tissues. Appl Spectrosc Rev 43(2):134–179
4. Baker MJ, Trevisan J, Bassan P, Bhargava R, Butler HJ, Dorling KM et al (2014) Using Fourier transform IR spectroscopy to analyze biological materials. Nat Protoc 9(8):1771–1791
5. Mackanos MA, Contag CH (2010) Fiber-optic probes enable cancer detection with FTIR spectroscopy. Trends Biotechnol 28(6):317–323
6. Sahu R, Mordechai S (2005) Fourier transform infrared spectroscopy in cancer detection. Future Oncol 1(5):635–647
7. Lechowicz L, Chrapek M, Gaweda J, Urbaniak M, Konieczna I (2016) Use of Fourier-transform infrared spectroscopy in the diagnosis of rheumatoid arthritis: a pilot study. Mol Biol Rep 43(12):1321–1326
8. Sitole L, Steffens F, Krüger TPJ, Meyer D (2014) Mid-ATR-FTIR spectroscopic profiling of HIV/AIDS sera for novel systems diagnostics in global health. Omics J Integr Biol 18(8):513–523
9. Markus APJ, Swinkels DW, Jakobs BS, Wevers RA, Trijbels JF, Willems HL (2001) New technique for diagnosis and monitoring of alcaptonuria: quantification of homogentisic acid in urine with mid-infrared spectrometry. Anal Chim Acta 429(2):287–292
10. Khoshmanesh A, Dixon MWA, Kenny S, Tilley L, McNaughton D, Wood BR (2014) Detection and quantification of early-stage malaria parasites in laboratory infected erythrocytes by attenuated Total reflectance infrared spectroscopy and multivariate analysis. Anal Chem 86(9):4379–4386
11. Coopman R, Van de Vyver T, Kishabongo AS, Katchunga P, Van Aken EH, Cikomola J et al (2017) Glycation in human fingernail clippings using ATR-FTIR spectrometry, a new marker for the diagnosis and monitoring of diabetes mellitus. Clin Biochem 50(1–2):62–67
12. Yoshida S, Yoshida M, Yamamoto M, Takeda J (2013) Optical screening of diabetes mellitus using non-invasive Fourier-transform infrared spectroscopy technique for human lip. J Pharm Biomed Anal 76:169–176
13. Grimard V, Li C, Ramjeesingh M, Bear CE, Goormaghtigh E, Ruysschaert JM (2004) Phosphorylation-induced conformational changes of cystic fibrosis transmembrane conductance regulator monitored by attenuated Total reflection-Fourier transform IR spectroscopy and fluorescence spectroscopy. J Biol Chem 279(7):5528–5536

14. Aksoy C, Guliyev A, Kilic E, Uckan D, Severcan F (2012) Bone marrow mesenchymal stem cells in patients with beta thalassemia major: molecular analysis with attenuated total reflection-Fourier transform infrared spectroscopy study as a novel method. Stem Cells Dev 21(11):2000–2011
15. Khanmohammadi M, Garmarudi AB, Ramin M, Ghasemi K (2013) Diagnosis of renal failure by infrared spectrometric analysis of human serum samples and soft independent modeling of class analogy. Microchem J 106:67–72
16. Mulready KJ, McGoldrick D (2012) The establishment of a standard and real patient kidney stone library utilizing Fourier transform-infrared spectroscopy with a diamond ATR accessory. Urol Res 40(5):483–498
17. Graça G, Moreira AS, Correia AJV, Goodfellow BJ, Barros AS, Duarte IF et al (2013) Mid-infrared (MIR) metabolic fingerprinting of amniotic fluid: a possible avenue for early diagnosis of prenatal disorders? Anal Chim Acta 764:24–31
18. Sarroukh R, Goormaghtigh E, Ruysschaert J-M, Raussens V (2013) ATR-FTIR: a "rejuvenated" tool to investigate amyloid proteins. Biochim Biophys Acta Biomembr 1828 (10):2328–2338
19. Taylor SE, Cheung KT, Patel II, Trevisan J, Stringfellow HF, Ashton KM et al (2011) Infrared spectroscopy with multivariate analysis to interrogate endometrial tissue: a novel and objective diagnostic approach. Br J Cancer 104(5):790–797
20. Wong PTT, Lacelle S, Fung MFK, Senterman M, Mikhael NZ (1995) Characterization of exfoliated cells and tissues from human endocervix and ectocervix by FTIR and ATR/FTIR spectroscopy. Biospectroscopy 1(5):357–364
21. Gajjar K, Heppenstall LD, Pang W, Ashton KM, Trevisan J, Patel II et al (2013) Diagnostic segregation of human brain tumours using Fourier-transform infrared and/or Raman spectroscopy coupled with discriminant analysis. Anal Methods 5(1):89–102
22. Staniszewska E, Malek K, Baranska M (2014) Rapid approach to analyze biochemical variation in rat organs by ATR FTIR spectroscopy. Spectrochim Acta A Mol Biomol Spectrosc 118:981–986
23. Theophilou G, Lima KMG, Martin-Hirsch PL, Stringfellow HF, Martin FL (2016) ATR-FTIR spectroscopy coupled with chemometric analysis discriminates normal, borderline and malignant ovarian tissue: classifying subtypes of human cancer. Analyst 141(2):585–594
24. Sun X, Xu Y, Wu J, Zhang Y, Sun K (2013) Detection of lung cancer tissue by attenuated total reflection-Fourier transform infrared spectroscopy-a pilot study of 60 samples. J Surg Res 179(1):33–38
25. Kazarian SG, Chan KLA (2006) Applications of ATR-FTIR spectroscopic imaging to biomedical samples. Biochim Biophys Acta Biomembr 1758(7):858–867
26. Lima CA, Goulart VP, Côrrea L, Pereira TM, Zezell DM (2015) ATR-FTIR spectroscopy for the assessment of biochemical changes in skin due to cutaneous squamous cell carcinoma. Int J Mol Sci 16(4):6621–6630
27. Theophilou G, Lima KMG, Briggs M, Martin-Hirsch PL, Stringfellow HF, Martin FLA (2015) Biospectroscopic analysis of human prostate tissue obtained from different time periods points to a trans-generational alteration in spectral phenotype. Sci Rep 5:13465
28. Cui L, Butler HJ, Martin-Hirsch PL, Martin FL (2016) Aluminium foil as a potential substrate for ATR-FTIR, transflection FTIR or Raman spectrochemical analysis of biological specimens. Anal Methods 8(3):481–487
29. Walsh MJ, Kajdacsy-Balla A, Holton SE, Bhargava R (2012) Attenuated total reflectance Fourier-transform infrared spectroscopic imaging for breast histopathology. Vib Spectrosc 60:23–28
30. Tian P, Zhang W, Zhao H, Lei Y, Cui L, Wang W et al (2015) Intraoperative diagnosis of benign and malignant breast tissues by fourier transform infrared spectroscopy and support vector machine classification. Int J Clin Exp Med 8(1):972
31. Zohdi V, Whelan DR, Wood BR, Pearson JT, Bambery KR, Black MJ (2015) Importance of tissue preparation methods in FTIR micro-spectroscopical analysis of biological tissues:'traps for new users. PLoS One 10(2):e0116491

32. Dogan A, Lasch P, Neuschl C, Millrose MK, Alberts R, Schughart K et al (2013) ATR-FTIR spectroscopy reveals genomic loci regulating the tissue response in high fat diet fed BXD recombinant inbred mouse strains. BMC Genomics 14(1):386
33. Yao H, Shi X, Zhang Y (2014) The use of FTIR-ATR spectrometry for evaluation of surgical resection margin in colorectal cancer: a pilot study of 56 samples. Journal of. Spectroscopy 2014:4
34. Li Q-B, Sun X-J, Y-Z X, Yang L-M, Zhang Y-F, Weng S-F et al (2005) Use of Fourier-transform infrared spectroscopy to rapidly diagnose gastric endoscopic biopsies. World J Gastroenterol: WJG 11(25):3842–3845
35. Wang TD, Triadafilopoulos G, Crawford JM, Dixon LR, Bhandari T, Sahbaie P et al (2007) Detection of endogenous biomolecules in Barrett's esophagus by Fourier transform infrared spectroscopy. Proc Natl Acad Sci 104(40):15864–15869
36. Bird B, Miljkovic M, Remiszewski S, Akalin A, Kon M, Diem M (2012) Infrared spectral histopathology (SHP): a novel diagnostic tool for the accurate classification of lung cancer. Lab Investig 92(9):1358–1373
37. Gajjar K, Ahmadzai AA, Valasoulis G, Trevisan J, Founta C, Nasioutziki M et al (2014) Histology verification demonstrates that biospectroscopy analysis of cervical cytology identifies underlying disease more accurately than conventional screening: removing the confounder of discordance. PLoS One 9(1):e82416
38. Martin FL, Kelly JG, Llabjani V, Martin-Hirsch PL, Patel II, Trevisan J et al (2010) Distinguishing cell types or populations based on the computational analysis of their infrared spectra. Nat Protoc 5(11):1748–1760
39. Andrew Chan KL, Kazarian SG (2016) Attenuated total reflection Fourier-transform infrared (ATR-FTIR) imaging of tissues and live cells. Chem Soc Rev 45(7):1850–1864
40. Miljković M, Bird B, Lenau K, Mazur AI, Diem M (2013) Spectral cytopathology: new aspects of data collection, manipulation and confounding effects. Analyst 138(14):3975–3982
41. Khanmohammadi M, Ansari MA, Garmarudi AB, Hassanzadeh G, Garoosi G (2007) Cancer diagnosis by discrimination between normal and malignant human blood samples using attenuated total reflectance-Fourier transform infrared spectroscopy. Cancer Investig 25(6):397–404
42. Hoşafçı G, Klein O, Oremek G, Mäntele W (2007) Clinical chemistry without reagents? An infrared spectroscopic technique for determination of clinically relevant constituents of body fluids. Anal Bioanal Chem 387(5):1815
43. Hands JR, Dorling KM, Abel P, Ashton KM, Brodbelt A, Davis C et al (2014) Attenuated Total reflection Fourier transform infrared (ATR-FTIR) spectral discrimination of brain tumour severity from serum samples. J Biophotonics 7(3–4):189–199
44. Gajjar K, Trevisan J, Owens G, Keating PJ, Wood NJ, Stringfellow HF et al (2013) Fourier-transform infrared spectroscopy coupled with a classification machine for the analysis of blood plasma or serum: a novel diagnostic approach for ovarian cancer. Analyst 138(14):3917–3926
45. Owens GL, Gajjar K, Trevisan J, Fogarty SW, Taylor SE, Da Gama-Rose B et al (2014) Vibrational biospectroscopy coupled with multivariate analysis extracts potentially diagnostic features in blood plasma/serum of ovarian cancer patients. J Biophotonics 7(3–4):200–209
46. Lewis PD, Lewis KE, Ghosal R, Bayliss S, Lloyd AJ, Wills J et al (2010) Evaluation of FTIR spectroscopy as a diagnostic tool for lung cancer using sputum. BMC Cancer 10(1):640
47. Khaustova S, Shkurnikov M, Tonevitsky E, Artyushenko V, Tonevitsky A (2010) Noninvasive biochemical monitoring of physiological stress by Fourier transform infrared saliva spectroscopy. Analyst 135(12):3183–3192
48. Hans KM, Muller S, Sigrist MW (2012) Infrared attenuated total reflection (IR-ATR) spectroscopy for detecting drugs in human saliva. Drug Test Anal 4(6):420–429
49. Nagase Y, Yoshida S, Kamiyama K (2005) Analysis of human tear fluid by Fourier transform infrared spectroscopy. Biopolymers 79(1):18–27
50. Nabers A, Ollesch J, Schartner J, Kötting C, Genius J, Hafermann H et al (2016) Amyloid-β-secondary structure distribution in cerebrospinal fluid and blood measured by an

Immuno-infrared-sensor: a biomarker candidate for Alzheimer's disease. Anal Chem 88(5):2755–2762
51. Poste G (2011) Bring on the biomarkers. Nature 469(7329):156–157
52. Adhyam M, Gupta AKA (2012) Review on the clinical utility of PSA in cancer prostate. Indian J Surg Oncol 3(2):120–129
53. Mitchell AL, Gajjar KB, Theophilou G, Martin FL, Martin-Hirsch PL (2014) Vibrational spectroscopy of biofluids for disease screening or diagnosis: translation from the laboratory to a clinical setting. J Biophotonics 7(3–4):153–165
54. Rhodes A, Jasani B, Balaton AJ, Barnes DM, Miller KD (2000) Frequency of oestrogen and progesterone receptor positivity by immunohistochemical analysis in 7016 breast carcinomas: correlation with patient age, assay sensitivity, threshold value, and mammographic screening. J Clin Pathol 53(9):688–696
55. Humpel C (2011) Identifying and validating biomarkers for Alzheimer's disease. Trends Biotechnol 29(1):26–32
56. Swedko PJ, Clark HD, Paramsothy K, Akbari A (2003) Serum creatinine is an inadequate screening test for renal failure in elderly patients. Arch Intern Med 163(3):356–360
57. Lovergne L, Bouzy P, Untereiner V, Garnotel R, Baker MJ, Thiefin G et al (2016) Biofluid infrared spectro-diagnostics: pre-analytical considerations for clinical applications. Faraday Discuss 187(0):521–537
58. Chiappin S, Antonelli G, Gatti R, De Palo EF (2007) Saliva specimen: a new laboratory tool for diagnostic and basic investigation. Clin Chim Acta 383(1–2):30–40
59. Mitchell BL, Yasui Y, Li CI, Fitzpatrick AL, Lampe PD (2005) Impact of freeze-thaw cycles and storage time on plasma samples used in mass spectrometry based biomarker discovery projects. Cancer Informat 1:98
60. Gremlich HU, Yan B (2000) Infrared and Raman spectroscopy of biological materials, Practical Spectroscopy Series Volume 24; 2000 Sep 25, Marcel Dekker, Inc. New York, USA
61. Hands JR, Abel P, Ashton K, Dawson T, Davis C, Lea RW et al (2013) Investigating the rapid diagnosis of gliomas from serum samples using infrared spectroscopy and cytokine and angiogenesis factors. Anal Bioanal Chem 405(23):7347–7355
62. Byrne HJ, Baranska M, Puppels GJ, Stone N, Wood B, Gough KM et al (2015) Spectropathology for the next generation: quo vadis? Analyst 140(7):2066–2073
63. Deegan RD, Bakajin O, Dupont TF, Huber G, Nagel SR, Witten TA (1997) Capillary flow as the cause of ring stains from dried liquid drops. Nature 389(6653):827–829
64. Filik J, Stone N (2007) Drop coating deposition Raman spectroscopy of protein mixtures. Analyst 132(6):544–550
65. Bonnier F, Brachet G, Duong R, Sojinrin T, Respaud R, Aubrey N et al (2016) Screening the low molecular weight fraction of human serum using ATR-IR spectroscopy. J Biophotonics 9(10):1085–1097
66. Martin M, Perez-Guaita D, Andrew DW, Richards JS, Wood BR, Heraud P (2017) The effect of common anticoagulants in detection and quantification of malaria parasitemia in human red blood cells by ATR-FTIR spectroscopy. Analyst. https://doi.org/10.1039/C6AN02075E
67. Lam NYL, Rainer TH, Chiu RWK, YMD L (2004) EDTA Is A better anticoagulant than heparin or citrate for delayed blood processing for plasma DNA analysis. Clin Chem 50 (1):256–257
68. Bassan P, Lee J, Sachdeva A, Pissardini J, Dorling KM, Fletcher JS et al (2013) The inherent problem of transflection-mode infrared spectroscopic microscopy and the ramifications for biomedical single point and imaging applications. Analyst 138(1):144–157
69. Sammon C, Schultz ZD, Kazarian S, Barr H, Goodacre R, Graham D et al (2016) Spectral pathology: general discussion. Faraday Discuss 187(0):155–186
70. Trevisan J, Angelov PP, Carmichael PL, Scott AD, Martin FL (2012) Extracting biological information with computational analysis of Fourier-transform infrared (FTIR) biospectroscopy datasets: current practices to future perspectives. Analyst 137(14):3202–3215

71. Krafft C, Steiner G, Beleites C, Salzer R (2009) Disease recognition by infrared and Raman spectroscopy. J Biophotonics 2(1–2):13–28
72. Butler HJ, Ashton L, Bird B, Cinque G, Curtis K, Dorney J et al (2016) Using Raman spectroscopy to characterize biological materials. Nat Protoc 11(4):664–687
73. Glassford SE, Byrne B, Kazarian SG (2013) Recent applications of ATR FTIR spectroscopy and imaging to proteins. Biochim Biophys Acta (BBA) Proteins Proteomics 1834 (12):2849–2858
74. Ataka K, Stripp ST, Heberle J (2013) Surface-enhanced infrared absorption spectroscopy (SEIRAS) to probe monolayers of membrane proteins. Biochim Biophys Acta (BBA) Biomembranes 1828(10):2283–2293
75. JY X, Chen TW, Bao WJ, Wang K, Xia XH (2012) Label-free strategy for in-situ analysis of protein binding interaction based on attenuated Total reflection surface enhanced infrared absorption spectroscopy (ATR-SEIRAS). Langmuir 28(50):17564–17570
76. Adato R, Altug H (2013) In-situ ultra-sensitive infrared absorption spectroscopy of biomolecule interactions in real time with plasmonic nanoantennas. Nat Commun 4:2154
77. Kazarian SG, Chan KLA (2013) ATR-FTIR spectroscopic imaging: recent advances and applications to biological systems. Analyst 138(7):1940–1951
78. Mordechai S, Shufan E, Porat Katz BS, Salman A (2017) Early diagnosis of Alzheimer's disease using infrared spectroscopy of isolated blood samples followed by multivariate analyses. Analyst 142:1276
79. Walsh MJ, German MJ, Singh M, Pollock HM, Hammiche A, Kyrgiou M et al (2007) IR microspectroscopy: potential applications in cervical cancer screening. Cancer Lett 246(1–2):1–11
80. Abbasi F, Mirzadeh H, Katbab AA (2002) Bulk and surface modification of silicone rubber for biomedical applications. Polym Int 51(10):882–888
81. Tsai D-H, Davila-Morris M, DelRio FW, Guha S, Zachariah MR, Hackley VA (2011) Quantitative determination of competitive molecular adsorption on gold nanoparticles using attenuated total reflectance–Fourier transform infrared spectroscopy. Langmuir 27(15):9302–9313
82. Biazar E, Khorasani M, Daliri M (2011) Cell sheet engineering: solvent effect on nanometric grafting of poly-N-isopropylacrylamide onto polystyrene substrate under ultraviolet radiation. Int J Nanomedicine 6:295–302
83. Biazar E, Heidari M, Asefnejad A, Montazeri N (2011) The relationship between cellular adhesion and surface roughness in polystyrene modified by microwave plasma radiation. Int J Nanomedicine 6:631–639
84. Meenach SA, Vogt FG, Anderson KW, Hilt JZ, McGarry RC, Mansour HM (2013) Design, physicochemical characterization, and optimization of organic solution advanced spray-dried inhalable dipalmitoylphosphatidylcholine (DPPC) and dipalmitoylphosphatidylethanolamine poly(ethylene glycol) (DPPE-PEG) microparticles and nanoparticles for targeted respiratory nanomedicine delivery as dry powder inhalation aerosols. Int J Nanomedicine 8:275–293
85. Mudunkotuwa IA, Minshid AA, Grassian VH (2014) ATR-FTIR spectroscopy as a tool to probe surface adsorption on nanoparticles at the liquid-solid interface in environmentally and biologically relevant media. Analyst 139(5):870–881
86. Beleites C, Neugebauer U, Bocklitz T, Krafft C, Popp J (2013) Sample size planning for classification models. Anal Chim Acta 760:25–33
87. Kalmodia S, Parameswaran S, Yang W, Barrow CJ, Krishnakumar S (2015) Attenuated Total reflectance Fourier transform infrared spectroscopy: an analytical technique to understand therapeutic responses at the molecular level. Sci Rep 5:16649
88. Kelly JG, Angelov PP, Trevisan J, Vlachopoulou A, Paraskevaidis E, Martin-Hirsch PL et al (2010) Robust classification of low-grade cervical cytology following analysis with ATR-FTIR spectroscopy and subsequent application of self-learning classifier eClass. Anal Bioanal Chem 398(5):2191–2201
89. Lane R, Seo SS (2012) Attenuated Total reflectance Fourier transform infrared spectroscopy method to differentiate between normal and cancerous breast cells. J Nanosci Nanotechnol 12(9):7395–7400

90. Holton SE, Walsh MJ, Bhargava R (2011) Subcellular localization of early biochemical transformations in cancer-activated fibroblasts using infrared spectroscopic imaging. Analyst 136(14):2953–2958
91. Purandare NC, Patel II, Trevisan J, Bolger N, Kelehan R, von Bunau G et al (2013) Biospectroscopy insights into the multi-stage process of cervical cancer development: probing for spectral biomarkers in cytology to distinguish grades. Analyst 138(14):3909–3916
92. BB W, Gong YP, XH W, Chen YY, Chen FF, Jin LT et al (2015) Fourier transform infrared spectroscopy for the distinction of MCF-7 cells treated with different concentrations of 5-fluorouracil. J Transl Med 13(1):108
93. Halliwell DE, Kyrgiou M, Mitra A, Kalliala I, Paraskevaidis E, Theophilou G et al (2016) Tracking the impact of excisional cervical treatment on the cervix using biospectroscopy. Sci Rep 6:38921
94. Titus J, Filfili C, Hilliard JK, Ward JA, Unil Perera A (2014) Early detection of cell activation events by means of attenuated total reflection Fourier transform infrared spectroscopy. Appl Phys Lett 104(24):243705
95. Hands JR, Clemens G, Stables R, Ashton K, Brodbelt A, Davis C et al (2016) Brain tumour differentiation: rapid stratified serum diagnostics via attenuated total reflection Fourier-transform infrared spectroscopy. J Neuro-Oncol 127(3):463–472
96. Hughes C, Baker MJ (2016) Can mid-infrared biomedical spectroscopy of cells, fluids and tissue aid improvements in cancer survival? A patient paradigm. Analyst 141(2):467–475
97. Argov S, Ramesh J, Salman A, Sinelnikov I, Goldstein J, Guterman H et al (2002) Diagnostic potential of Fourier-transform infrared microspectroscopy and advanced computational methods in colon cancer patients. J Biomed Opt 7(2):248–254
98. Ellis DI, Goodacre R (2006) Metabolic fingerprinting in disease diagnosis: biomedical applications of infrared and Raman spectroscopy. Analyst 131(8):875–885
99. Diamandis EP (2010) Cancer biomarkers: can we turn recent failures into success? J Natl Cancer Inst 102:1462
100. Baker MJ, Hussain SR, Lovergne L, Untereiner V, Hughes C, Lukaszewski RA et al (2016) Developing and understanding biofluid vibrational spectroscopy: a critical review. Chem Soc Rev 45(7):1803–1818

Plasmofluidics for Biosensing and Medical Diagnostics

5

Xiaolei Peng, Bharath Bangalore Rajeeva, Daniel Teal, and Yuebing Zheng

Contents

X. Peng · B. B. Rajeeva
Materials Science and Engineering Program and Texas Materials Institute, The University of Texas at Austin, Austin, TX, USA

D. Teal
Department of Mechanical Engineering, Materials Science and Engineering Program, Texas Materials Institute, The University of Texas at Austin, Austin, TX, USA

Y. Zheng (✉)
Materials Science and Engineering Program and Texas Materials Institute, The University of Texas at Austin, Austin, TX, USA

Department of Mechanical Engineering, Materials Science and Engineering Program, Texas Materials Institute, The University of Texas at Austin, Austin, TX, USA
e-mail: zheng@austin.utexas.edu

C. S. S. R. Kumar (ed.), *Nanotechnology Characterization Tools for Biosensing and Medical Diagnosis*, https://doi.org/10.1007/978-3-662-56333-5_5

1 Definition of the Topic

Plasmofluidics, an extension of optofluidics into the nanoscale regime, merges plasmonics and micro-/nanofluidics for highly integrated and multifunctional lab on a chip. In this chapter, we focus on the applications of plasmofluidics in the versatile manipulation and sensing of biological cell, organelles, molecules, and nanoparticles, which underpin advanced biomedical diagnostics.

2 Overview

An improved capability of manipulating and sensing living cells, viruses, bacteria, and molecules (i.e., DNAs, proteins, and drug molecules) is significant for biomedical research and disease diagnostics in global health, primary care, and point-of-care (POC) settings. Conventional diagnostic technologies such as polymerase chain reaction (PCR) and enzyme-linked immunosorbent assay (ELISA) have been established as global gold standards. However, they have mainly been used in developed countries and major cities in developing countries due to their sophisticated instrumentation and complex operation procedures that require specially trained staffs [1, 2]. Therefore, there is still a great need for innovative portable POC devices that can provide effective high-value healthcare to underdeveloped and resource-constrained regions. Herein, we argue how plasmofluidics, a synergistic integration of plasmonics and micro-/nanofluidics, can help address current challenges in portable POC devices as well as fundamental biomedical studies. This book chapter focuses on two correlated areas: plasmofluidic tweezers and biosensors. The first part of this book chapter reviews state-of-the-art plasmofluidic tweezers for versatile manipulations of biological cells, DNAs, and proteins, including the latest strategies for overcoming the inherent drawbacks of plasmonic tweezers. The second part discusses various plasmofluidic biosensors for the detection of nucleic acids, proteins, pathogens, and drug molecules. We highlight the progress made at improving the limit of detection (LOD), response time, and accuracy for analyzing clinical samples.

3 Introduction

Infectious diseases, which are caused by bacterial (e.g., pneumonia), mycobacterial (e.g., tuberculosis), viral (e.g., HIV), fungal (e.g., candidiasis), and parasitic pathogens (e.g., malaria), have considerable impact on global economy, health, and security [1, 2]. For instance, recent years have witnessed large outbreaks of Ebola in Africa and Zika in Central and South America, and there have been serious concerns and heated debates on public health at the global scope. Cancers, which are characterized by the uncontrolled growth and spread of abnormal cells and induced by various factors such as tobacco, infectious organisms, genetic mutations, and immune conditions, are the leading cause of death for much of the US

population [3]. The threats from infectious diseases and cancers become increasingly prevalent due to factors such as changing trends in human and animal migration, increasing urbanization, environmental deterioration, and climate change. Early disease diagnosis and effective treatment have become critical for the clinical regulation and management of infectious diseases and cancers. Convectional disease diagnostics has relied on techniques such as optical microscopy, culture, immunoassays, and nucleic acid amplification [4]. A standard process for disease diagnostics includes the following steps: (a) collection and transport of biological samples such as blood, urine, and tissue swabs from the point of care; (b) analysis of the samples by experienced staffs in a centralized laboratory; and (c) notification of the results to the clinicians and patients. Due to highly frequent access to energy resources like electricity, time-consuming procedures, and need for well-trained personnel, the conventional clinical methods prelude the rapid disease detection and response at the primary care. Their drawbacks are prominently revealed in resource-limited and underdeveloped areas.

Point-of-care (POC) devices, which enable on-site test and follow-up action, are promising to improve the diagnosis and management of infectious diseases and cancers in various clinical settings. These include areas where healthcare infrastructure is limited and high-quality timely medical care is inaccessible [5, 6]. With the advancements of nanotechnologies and micro-/nanofluidic technologies, many innovative POC biosensors with optical, electrical, and mechanical interrogations have been developed. However, two major challenges, matrix effect and system integration, have prevented the further developments and uses of POC devices [4]. Most biosensors can have excellent performance with pristine samples. However, they still need to be strictly evaluated with clinical samples due to the matrix effect. Generally, the matrix of human fluids becomes more complex in infected states, which could lead to the clogging of microfluidic channels and the decrease of the transduction signals. Transformation of POC devices from proof-of-concept and benchtop to bedside care and point-of-care settings requires the system integration. However, to integrate and package various modules for sample preparation and signal detection into a fully automated and user-friendly platform remains challenging.

Plasmofluidics, which seeks to synergize plasmonics and micro-/nanofluidics for lab on a chip, is promising for advancing the next-generation POC devices that feature high compactness, high integration, and multiple functions as well as the frontiers of biomedical research [7]. With their capability of controlling light at the nanoscale beyond the diffraction limit, surface plasmons such as surface plasmon polaritons (SPPs) and localized surface plasmon resonances (LSPRs) [8] are effective at optically manipulating, sensing, and analyzing biological cells and molecules [9–11]. Micro-/nanofluidics exploit rich fluidic behaviors at the micro-/nanoscale to enable low-load, high-throughput, cost-effective, and precise delivery of analyte samples. Therefore, plasmofluidic platforms can serve the purpose of processing, sensing, and analyzing biological objects in clinical samples, paving the way toward affordable and portable healthcare devices for their uses in primary care and resource-constrained settings.

There have been several successful review articles on plasmonic biosensing and medical diagnostics [1, 12, 13]. However, a comprehensive review article focused on the emerging field of plasmofluidic sensing is not available yet. To fill the blank, our chapter covers classification, working principles, design strategies, and applications of the state-of-the-art plasmofluidic systems for sensing and medical diagnostics.

4 Experimental Methodology

4.1 Manipulations with Plasmon-Enhanced Optical Near Fields

Biosensing and medical diagnostics often rely on the capability of manipulating biological particles and molecules in fluidic environments. Three prominent techniques that exploit plasmon-enhanced optical near fields to manipulate particles and molecules in fluids have been developed: (i) SPP-based plasmonic tweezers, (ii) LSPR-based plasmonic tweezers, and (iii) plasmonic tweezers based on self-induced back-action (SIBA). Both top-down fabrication techniques such as electron beam lithography and focused ion beam lithography and bottom-up fabrication techniques such as directed assembly and self-assembly have been applied to engineer plasmonic structures for targeted tweezing platforms [14, 15].

SPPs can propagate along the metal-fluid interface with evanescent characteristics perpendicular to the interface. Accordingly, SPP-based tweezers have been used to transport and assemble microscale particles [16–18]. A patterned SPP landscape was constructed from an array of micrometer-sized gold disks on a glass substrate to achieve parallel trapping of individual particles, as shown in Fig. 5.1a [19]. The simulated trapping potential in Fig. 5.1b shows that the trapped particle on the gold disk is stabilized in a forward position along the SPP propagation direction.

Due to the localized electromagnetic fields associated with the excitation of LSPRs, LSPR-based tweezers are often applied to trap single or multiple particles near the plasmonic structures. Plasmonic nanoantennas such as nanodot pairs [20], diabolo structures [21], and bowtie structures [22] were commonly used to induce strong near-field confinement and enhancement in the nanoscale dielectric gaps known as “Hot spots,” which provide stable trapping of nanoparticles at low optical power. Trapping stiffness was enhanced by two orders of magnitude with a metal nanodot pair in a conventional optical tweezers setup, as shown in Fig. 5.1c–d [20]. Despite the localized nature of LSPRs, recent research efforts have achieved long-range transportation of particles by using arrays of plasmonic C-shaped engravings [23] and gold nanoislands with a network of “hot spots” [24].

LSPR-based tweezers exhibit limits in manipulating particles that are smaller than 100 nm due to the high-power requirement and significant thermal effects. SIBA-based plasmonic tweezers were developed to reduce the required power intensity by more than an order of magnitude [25]. As illustrated in Fig. 5.1e, a nanoaperture redshifts in its resonance wavelength when the trapped particle has a larger refractive index than solvent, enhancing the laser beam transmission through the nanoaperture. When the particle tends to escape from the aperture, a drop in the light transmission

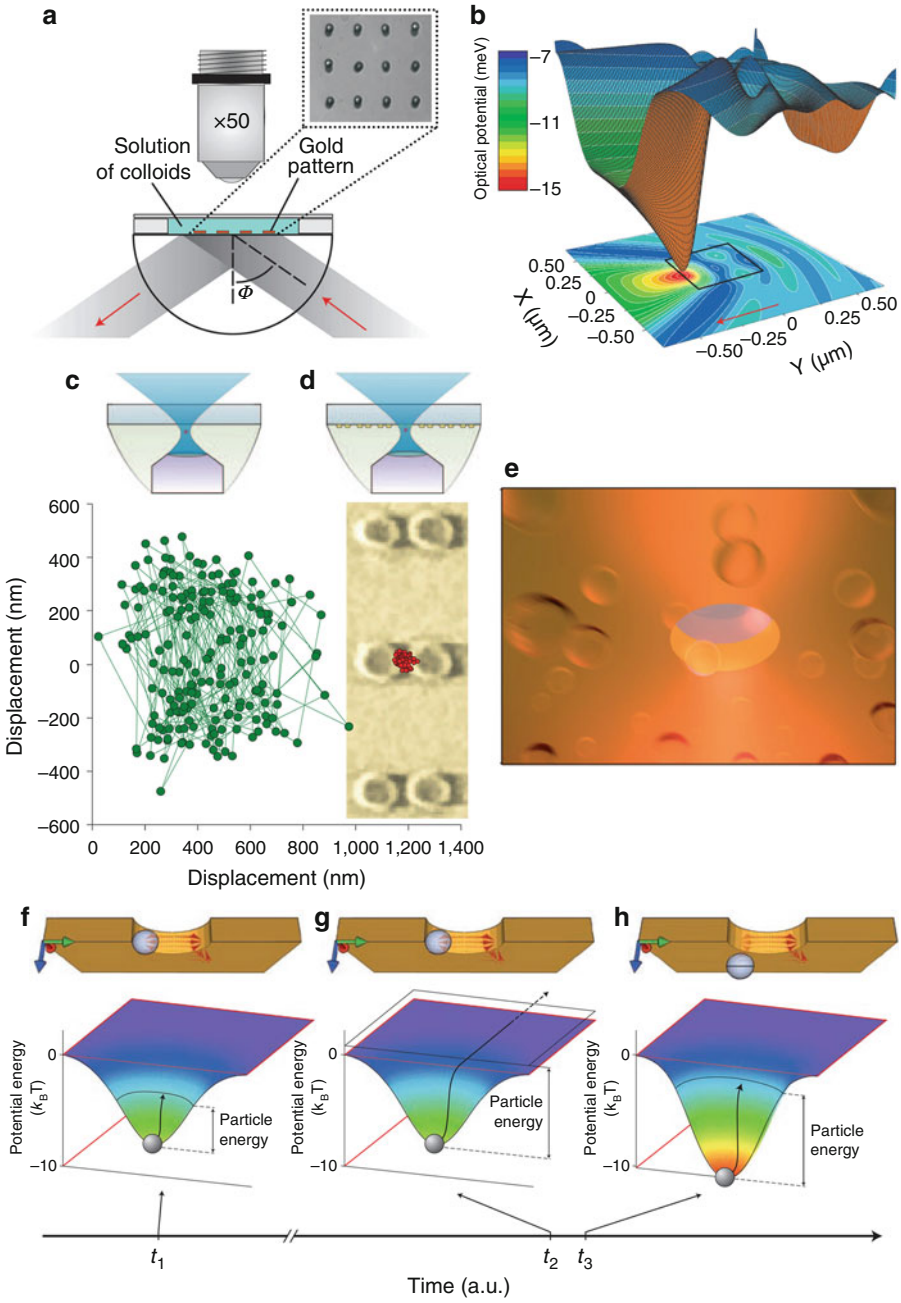

Fig. 5.1 Plasmonic tweezers based on plasmon-enhanced optical near fields. (**a**) Experimental demonstration and (**b**) simulated optical potential for parallel trapping of particles with SPP-based tweezers. Reproduced with permission [19] (Copyright 2007 Nature Publishing Group). (**c**) and (**d**)

generates a restoring force and pulls the particle back to the equilibrium position. In other words, when the particle is moving away from the optical potential well, the SIBA force will deepen the potential well and maintain the trapping state, as illustrated in Fig. 5.1f–h.

4.2 Manipulations with Plasmon-Enhanced Photothermal Effects

Along with the enhanced electromagnetic fields, surface plasmons can induce strong light absorption and photothermal effects [26]. The competing factors between light absorption and heat dissipation determine the temperature increase and spatial temperature distribution. For a spherical gold nanoparticle immersed in water and illuminated by a laser of LSPR wavelength, the temperature increase is uniform in the particle and inversely proportional to the distance outside the particle, resulting in a thermal gradient built up at the metal-water interface [26]. For metal nanoparticle arrays as illustrated in Fig. 5.2a, two heating regimes exist depending on the particle size, particle number, and geometry of the array. These are temperature confinement regime and temperature delocalization regime, as shown in Fig. 5.2b [27]. To reach the temperature confinement regime, both large spacing between nanoparticles and small illumination area are preferred.

The plasmon-assisted heating was exploited to control fluid motion at the microscale and nanoscale [28]. In typical plasmofluidic systems where the characteristic size of the plasmonic structure is very small (~100 nm), thermal diffusion of the fluid dominates in heat dissipation and thermal convection plays a minor role. As shown in Fig. 5.2c–d, the thermal convection velocity at small plasmonic structures is limited to 1–100 nm/s. In this case, the thermal convection can barely contribute to the motion of the particles in the fluidic environment. The thermal convection field can be further damped by more than one order of magnitude when the height of the fluid chamber is reduced to ~10 μm, as illustrated in Fig. 5.2e.

4.3 Plasmonic Sensing of Particles and Molecules

Optofluidic biosensing platforms based on surface plasmons have advantages of being highly integrated, miniaturized, and sensitive. SPP-based sensors typically

Fig. 5.1 (continued) Schematic illustrations of optical setup and time-resolved tracking of a bead trapped by a highly focused laser beam above a glass substrate without and with gold nanodot pairs, respectively (Reproduced with permission [20]. Copyright 2008 Nature Publishing Group). (**e**) Schematic illustration of the trapping of a single PS bead within an aperture in a thick gold film based on the SIBA mechanism (Reproduced with permission [25]. Copyright 2009 Nature Publishing Group). (**f**–**h**) Schematic illustration, together with simulated optical potential, for the working principle of SIBA-based tweezers (Reproduced with permission [10]. Copyright 2011 Nature Publishing Group)

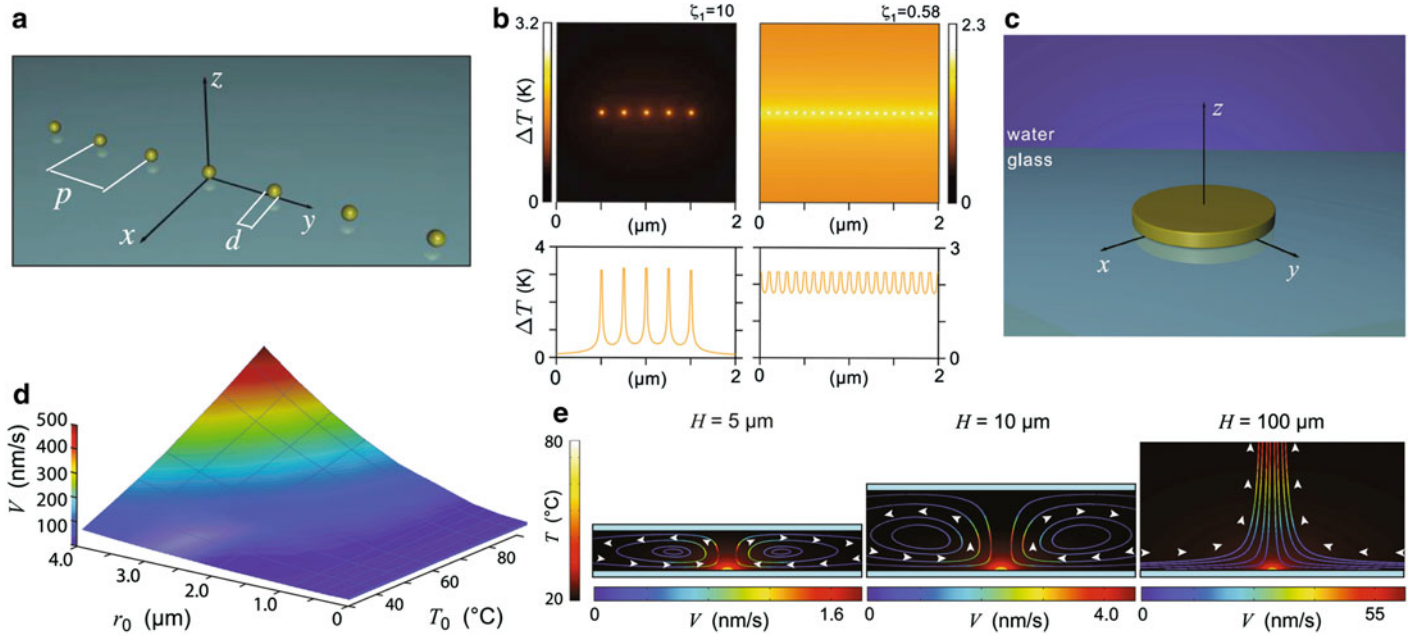

Fig. 5.2 Manipulations in fluids with plasmon-enhanced photothermal effects. (**a**) Schematic representation of a chain of gold nanoparticles on a glass substrate that is immersed in water. (**b**) Comparison of temperature confinement regime and temperature delocalization regime (Reproduced with permission [27]. Copyright 2013 American Chemical Society). (**c**) Schematic representation of a gold disk on a glass substrate that is immersed in water. (**d**) Thermal convection velocity magnitude as a function of the disk temperature and the disk radius in (**c**). (**e**) Thermal convection velocity profile as a function of the fluid chamber height (Reproduced with permission [28]. Copyright 2011 American Chemical Society)

interrogate the change in resonance angle in attenuated total internal reflection to detect target specimens and to extract binding kinetics, as shown in Fig. 5.3a [1, 29]. The specimen-binding events change the dielectric constant over the metal layer. Several approaches have been applied to excite SPPs, including prism coupling [30, 31], grating coupling [32], and waveguide coupling [33]. LSPR-based sensors utilize the strong electromagnetic response of metal nanoparticles to refractive-index changes in their surroundings [1, 12, 34, 35]. Various nanostructured metal arrays such as nanohole arrays [36, 37], nanowell arrays [38], nanocross arrays [39], nanocube arrays [40], nanomouth arrays [41], nanomushroom arrays [42], nanodisk arrays [15, 43], and nanobowtie arrays [44] have been designed for the refractive-index sensing with high figure of merit (FOM). Various techniques such as focused ion beam lithography, electron beam lithography, soft lithography, and nanosphere lithography have been employed to fabricate the large-scale arrays with good repeatability [34, 45–47].

Of particular interest are metal nanohole arrays integrated with complex fluidic structures for versatile and parallel sensing [48, 49]. On-chip nanohole array-based sensors feature simple optical instrument and high synergy with microfluidic schemes. In the flow-over mode (Fig. 5.3b), only the upper metal surfaces of the nanohole arrays are exploited like those in the convectional SPP-based sensors. Through scaling analysis and numerical simulation, Escobedo's group has found that the flow-through mode features ~10-fold enhancement of time response over the flow-over mode in typical biosensing applications [36]. Further experiments showed that the flow-through mode enabled active delivery, concentration, and sensing of analytes, leading to one order of magnitude increase in sensing efficiency and two orders of magnitude improvement in LOD [37].

In general, a LSPR biosensor consists of the following components: (i) a recognition element in conjunction with the plasmonic substrate, (ii) a transducer to convert the interaction between target and recognition element to optical or electrochemical output signals, and (iii) a system to interrogate the signals. Spectroscopic measurements are the most common approach for the signal analysis, which include (i) transmission spectroscopy (Fig. 5.3c), (ii) reflection spectroscopy (Fig. 5.3d), and (iii) dark-field scattering spectroscopy (Fig. 5.3e) [50]. Surface plasmon resonance imaging (SPRI) has been developed to perform large-area measurements at high resolution [51]. It is a label-free method of visualizing binding activities across an arrayed biochip via a video CCD camera.

Surface-enhanced Raman spectroscopy (SERS), which often arises from the strong electromagnetic field enhancement proximate to the metal surface, has proved as a powerful tool for label-free analysis of molecules. SERS interrogates Raman shifts originating from molecular vibrational energy levels [53–55]. Metal colloids, colloid aggregations in solutions, and metal nanoparticle arrays on substrates are commonly used for SERS-active sensors integrated with microfluidics [55, 56]. There are two major microfluidic approaches toward SERS-active plasmofluidic sensors: (i) mixing the sample with SERS-active colloids in a microfluidic channel

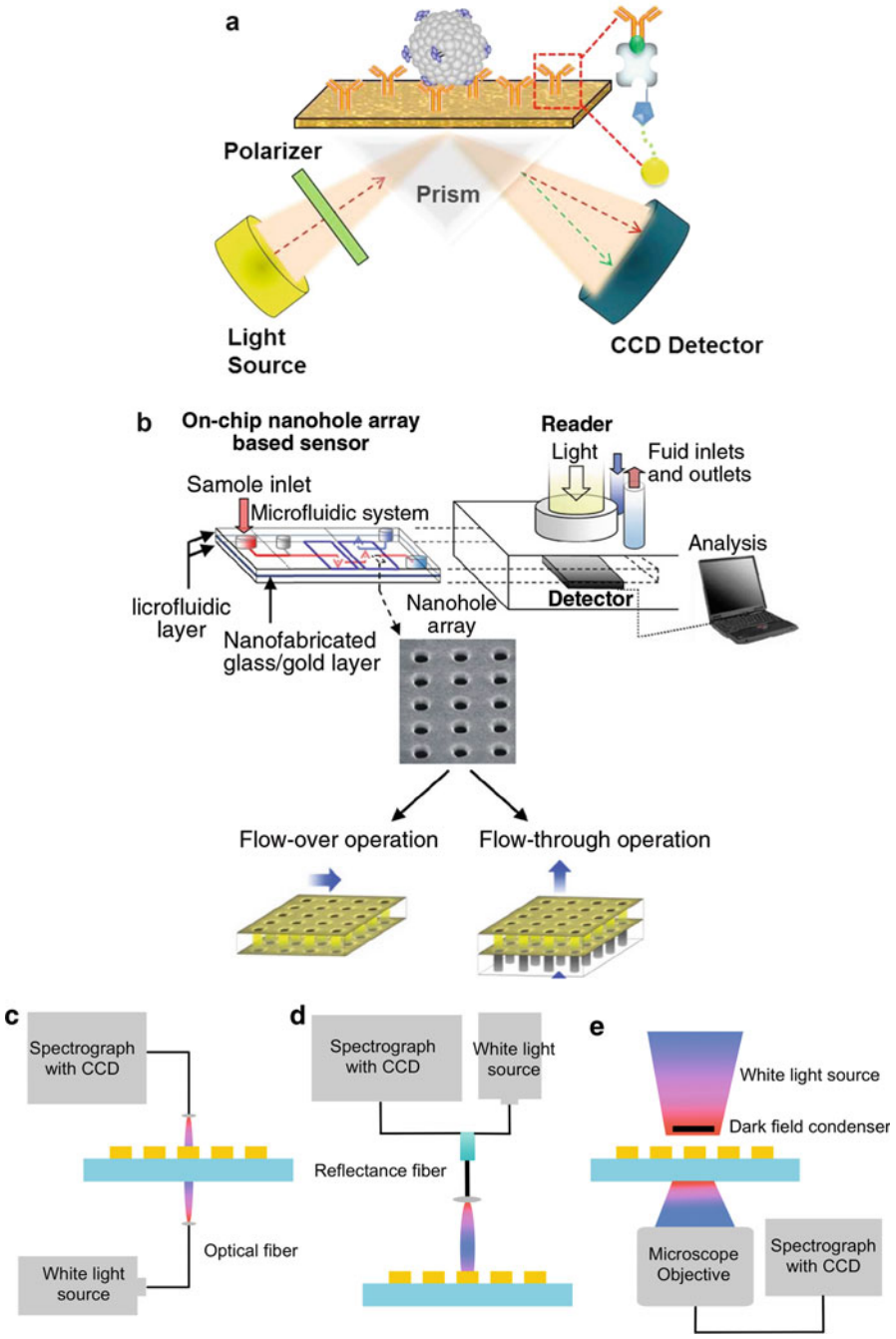

Fig. 5.3 (continued)

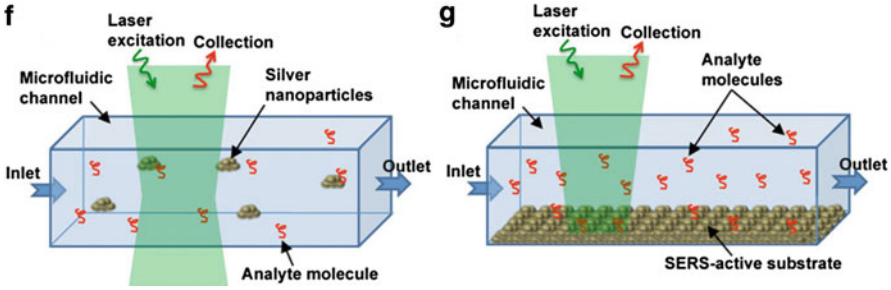

Fig. 5.3 Plasmonic sensing of biological particles and molecules. (**a**) Schematic depiction of a SPP-based sensor in the Kretschmann configuration. The metal surface is functionalized with recognition elements for selective detection. Once biological particles or molecules are captured by the metal surface, the SPP mode will be modified, and a signature in the reflected light will be probed by a detector for analysis (Reproduced with permission [1]. Copyright 2015 American Chemical Society). (**b**) Schematic depiction of an on-chip LSPR sensing platform based on metal nanohole arrays. The fluid can be transported over or through the nanoholes. The platform also includes external components such as a light source, a detector, and a fluidic actuator (Reproduced with permission [48]. Copyright 2013 RSC Publishing). Schematics of the instrumental setups for LSPR sensing that perform optical (**e**) transmission, (**f**) reflection, and (**g**) scattering measurements. (**f**–**g**) Schematic depictions of SERS-based on-chip sensors integrated with microfluidics. (**f**) Mixed solution of analytes and nanoparticles is driven through a microfluidic channel that is under laser illumination and Raman recording. (**g**) Analyte solution is driven through a microfluidic channel with a SERS-active substrate at the bottom of the channel (Reproduced with permission [52]. Copyright 2012 Springer Publishing)

(Fig. 5.3c) and (ii) driving the sample through a microfluidic channel with a SERS-active substrate at the bottom (Fig. 5.3d) [52]. Such plasmofluidic sensors have the advantages of measuring biological particles and molecules in their native watery environments. However, since the molecular adsorption or binding to the SERS-active surfaces relies on the diffusion of the analytes in solutions, the Raman signal intensities will be weaker than those of SERS based on dried samples on solid-state Raman substrates.

Various active and passive concentration techniques have been developed to improve the SERS LOD in fluidic systems [52]. Recently, we have developed a technique that uses plasmon-enhanced thermophoresis for reversible and dynamic assembly of plasmonic nanoparticles for in situ SERS analysis of molecules, as shown in Fig. 5.4a [57]. Once a temperature gradient is created on a plasmonic substrate that is illuminated with a low-power laser beam, the positive-charged nanoparticles will migrate to the hot region under a thermally induced local electrical field (Fig. 5.4b) and form nanoparticle assemblies at the laser spot (Fig. 5.4c). As shown in Fig. 5.4d, the dynamic assemblies feature a high particle density and small interparticle distance, which are suitable for the excitation of multiple electromagnetic "hot spots" for SERS with enhanced sensitivity.

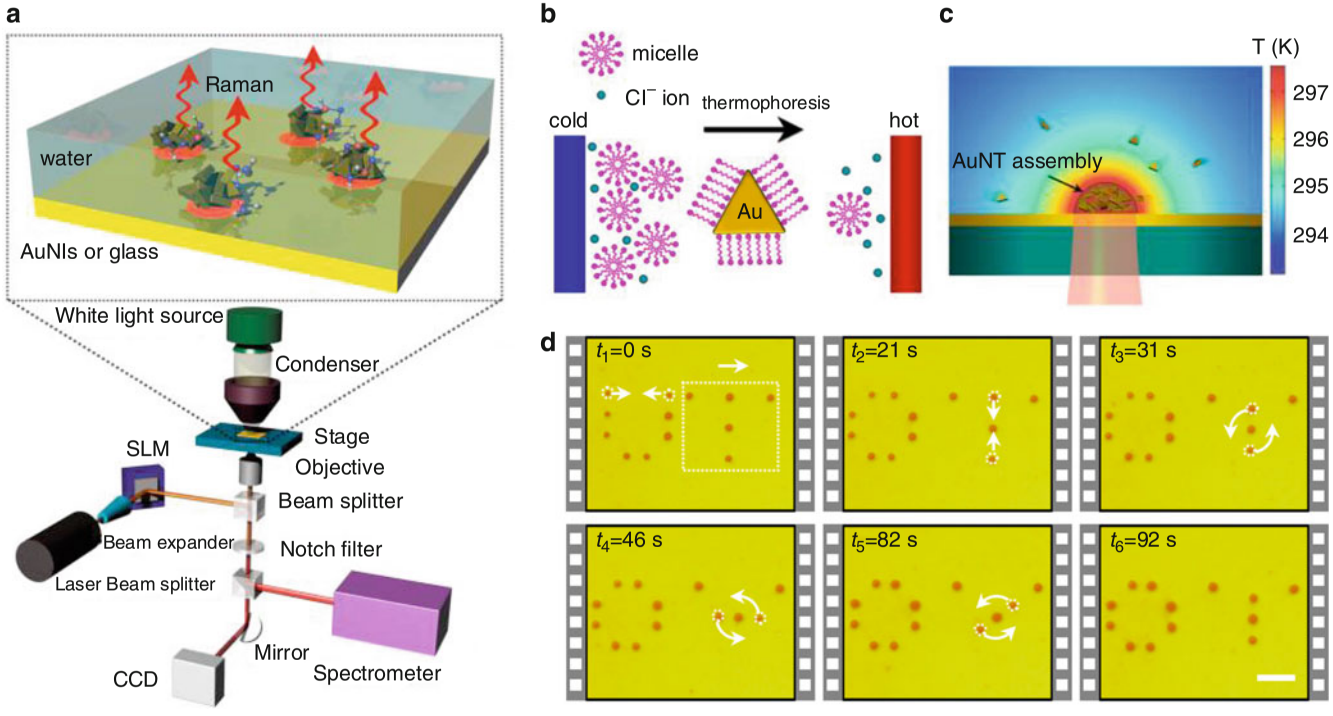

Fig. 5.4 Nanoparticle assemblies by plasmon-enhanced thermophoresis for SERS-based sensing in liquid environments. (**a**) Schematic illustration of the experimental setup for nanoparticle assembly and in situ SERS. (**b**) Migration and (**c**) assembly of positively charged metal nanoparticles in a plasmon-enhanced temperature gradient field. (**d**) Time-evolved optical images of dynamic manipulation of multiple nanoparticle assemblies (Reproduced with permission [57]. Copyright 2016 American Chemical Society)

5 Key Research Findings

5.1 Versatile Manipulations of Particles and Molecules in Plasmofluidic Systems

Manipulations of biological particles and molecules such as trapping, immobilization, and pre-concentration are becoming a critical component of biosensing and analysis in fluidic environments. Plasmonic tweezers have been employed in manipulating various bio-specimens such as cells [58, 59], DNAs [60, 61], and proteins [62–64] at high spatial resolution and low optical power. Using simple optics to create the trapping force, plasmonic tweezers can be readily incorporated into microfluidic systems to design novel plasmofluidic chips with functionalities such as single-particle trapping [57, 62], parallel trapping [58], co-trapping [63], and kinetic detection of biological objects [61, 64]. One has also recognized multiple issues of current plasmofluidic systems and proposed new solutions. First, due to the near-field nature of surface plasmons and weak thermoplasmonic convection, only particles that diffuse to the close proximity to the plasmonic structures can be captured [65]. Second, isolated plasmonic nanostructures are commonly used to avoid collective heating and particle agglomeration, preventing long-distance transportation and dynamic manipulations. Third, in contrast to conventional optical tweezers that are capable of three-dimensional (3D) manipulations, plasmonic tweezers are often limited to two-dimensional (2D) trapping of objects at the plasmonic structures. New solutions to these issues in the plasmofluidic systems include the adoption of optical components with a higher level of spatial control [66] and the exploitation of loss-induced heating at the plasmonic structures [67].

5.1.1 Plasmon-Enhanced Trapping of Single Biological Cells and Molecules

The capability of trapping fragile biological objects such as cells, DNAs, and proteins in fluids is of significant importance in cellular and molecular biotechnology. *E. coli* cells were trapped in parallel with near-infrared LSPRs on the arrays of plasmonic nanoantennas in a Kretschmann optical setup [58]. The cells were stably aligned along the antennas' long axis, and their continuous growth and division were kept over 2 h. There was no difference in the average division time between the optically trapped cells and those outside the illuminated region. In contrast, optical tweezers have challenges in trapping the *E. coli* cells for their low refraction index (1.38 for visible light) and small dimensions ($2 \times 0.8\ \mu m^2$ at infant stage).

We invented opto-thermophoretic tweezers that can achieve light-directed versatile manipulations of biological cells at an optical power 100–1000 times lower than that of optical tweezers, as illustrated in Fig. 5.5a [68]. By harnessing the permittivity gradient in the electric double layer of the charged surface of the cell membrane, we succeeded at the low-power cell trapping with a plasmon-enhanced temperature gradient field. Arbitrary spatial arrangements of cells at a resolution of ~100 nm and precise rotation of both single and multiple cells were demonstrated with an optical control system based on a digital micromirror device (DMD).

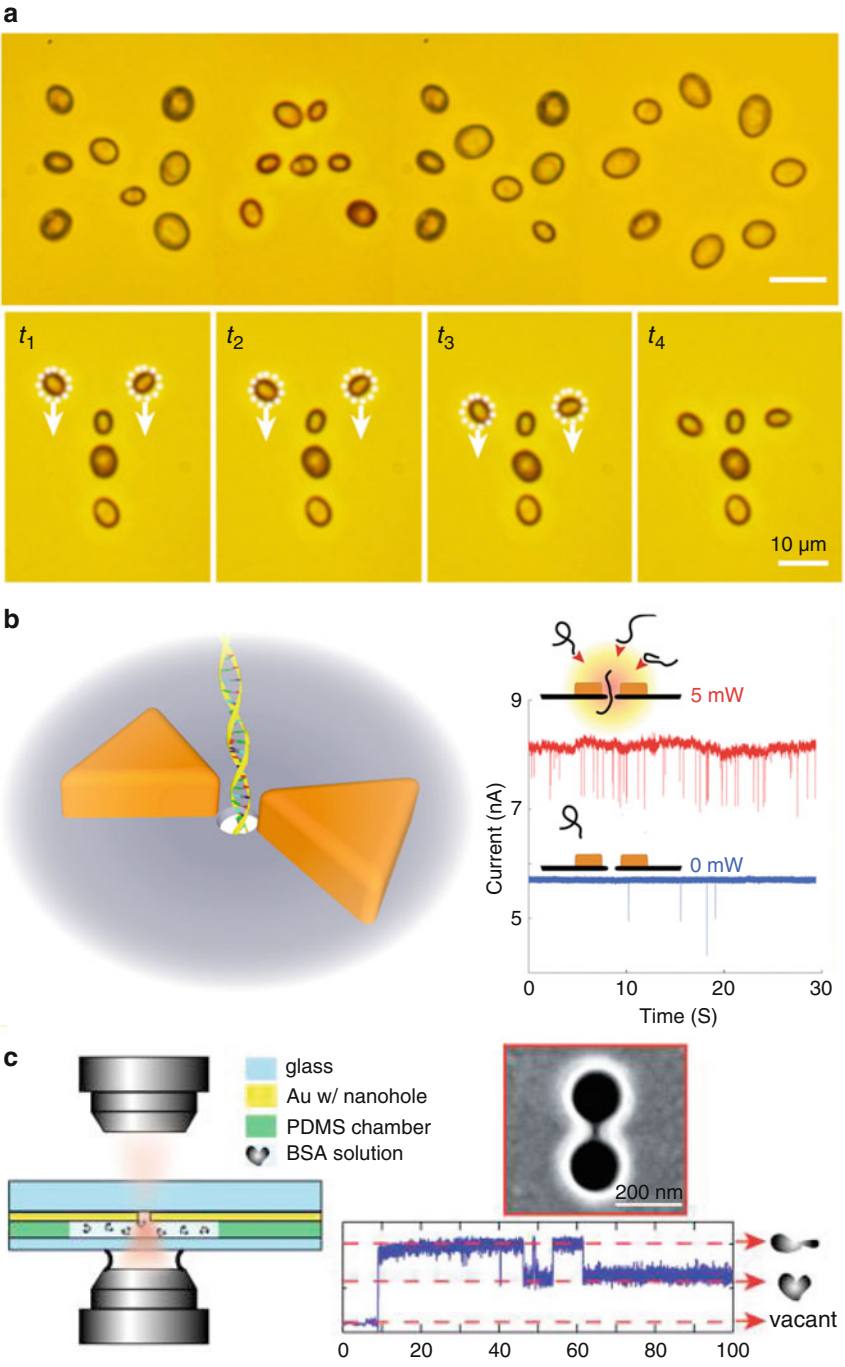

Fig. 5.5 (continued)

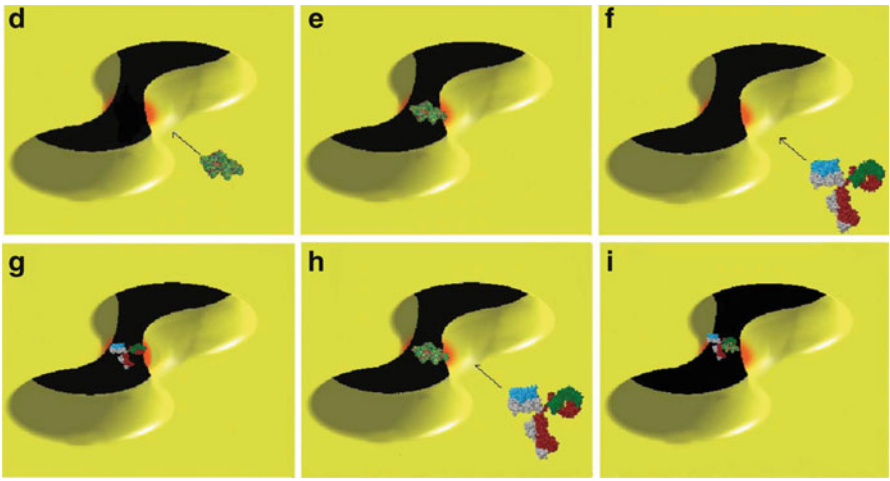

Fig. 5.5 Plasmon-enhanced trapping of biological cells, DNAs, and proteins in fluidic environments. (**a**) Parallel and dynamic trapping of yeast cells with plasmon-enhanced thermophoretic tweezers (Reproduced with permission [68]. Copyright 2017 American Chemical Society). (**b**) Trapping of single DNAs and enhancement of DNA translocation events with plasmonic excitation. The DNA translocation events are characterized by measuring the time-resolved open-pore current traces (Reproduced with permission [61]. Copyright 2014 American Chemical Society). (**c**) Two capture states and the vacant state of single-protein manipulation at the plasmonic "hot spot" of a gold double nanohole. The trapping states of the protein are monitored with time traces of the optical transmission through the double nanohole (Reproduced with permission [62]. Copyright 2011 American Chemical Society). (**d**–**i**) Schematic illustration of the co-trapping process for a BSA molecule and an anti-BSA molecule at the plasmonic "hot spot" of the double nanohole (Reproduced with permission [63]. Copyright 2013 RSC Publishing)

Optical trapping of single DNA molecules and DNA translocations in LiCl buffers were demonstrated using a solid-state plasmonic nanopore, as shown in Fig. 5.5b [61]. The nanopore is positioned between the gap of a gold bowtie antenna. The enhancement of the rate of DNA translocation events was observed and attributed to the plasmon-assisted local heating and the thermophoresis in the thermal gradient. In another example, single bovine serum albumin (BSA) molecules were trapped onto a double-hole structure with a 3.5-mW laser beam focused by a 100× oil immersion objective [62], as shown in Fig. 5.5c. The folding and unfolding states of a trapped BSA molecule were revealed by measuring the intensity of the transmitted light. The same research group demonstrated the protein-antibody co-trapping at the double-hole structure and measured the binding kinetics of the protein-ligand interaction, opening up new avenues for studying intermolecular interactions at the single-molecule level [63, 64].

5.1.2 Three-Dimensional Manipulations and Long-Range Transportation of Objects

"Ideal" tweezers for biological samples in fluidic environments should be able to rapidly deliver target objects and to achieve high-resolution 3D trapping at any

desired locations. To realize 3D low-power trapping and transportation of sub-100-nm objects over a long range, Quidant's group implemented the SIBA-based tweezers at the tip extremity of a metal-coated optical fiber, which can be raster-scanned in all three spatial directions for dynamic manipulations and simultaneously used to collect the reflected signal and identify the different trapping regimes [66], as shown in Fig. 5.6a–b. The optical-fiber-based plasmonic tweezers are attractive for in vivo applications, such as trapping proteins or viruses of interest in cells.

To solve the long-standing challenge of rapid and on-demand loading of objects at the plasmonic trapping sites, Boltasseva's group has combined the plasmonic heating and AC electrical fields for fast delivery and trapping of nanoobjects within a few seconds [65]. The coupling of the plasmon-enhanced temperature gradient and an applied AC electrical field induces an electrothermoplasmonic (ETP) flow, which leads to fluidic motion two orders of magnitude faster than the thermoplasmonic convection and greatly increases the particle capture efficiency, as shown in Fig. 5.6c–d. With their capability of rapid manipulation and concentration of DNA and protein samples, the hybrid plasmofluidic tweezers can be applied for nanoscale biosensors to improve the sensing throughput and efficiency.

5.2 High-Performance Sensing, Analysis, and Diagnostics in Plasmofluidic Systems

Benefiting from a synergy between plasmonic nanotechnology and micro-/nanofluidics, biosensors based on plasmofluidic platforms are attractive for POC devices [1, 2, 7]. They have been applied for portable sensing, analysis, and diagnostics in biomedicine and healthcare. The analytes include nucleic acids, protein, viruses, bacteria, and drugs. Tremendous efforts have been made to improve LOD, response speed, and accuracy of multiplexed identification. More innovative approaches are being developed to push proof-of-concept or benchtop prototypes into practical uses in directly analyzing bio-objects in body fluids for disease diagnosis. Herein, we focus on plasmofluidic POC sensing for DNAs/RNAs, proteins, viruses, bacteria, and drugs.

5.2.1 Detection of DNAs and RNAs

Detection and analysis of DNAs and RNAs are important for disease diagnostics as specific bacteria and viruses in complex samples can be distinguished based on their unique DNA/RNA sequences [2]. Conventional technologies for nucleic acid sensing feature high precision and optimal LOD. However, they require sophisticated instrumentation with multiple time-consuming steps, including pathogen isolation, PCR, and target identification. Plasmofluidic sensors are extensively explored to achieve precise, multiplexed, and label-free detection [31, 69–72]. Springer et al. demonstrated a SPP sensor with a four-channel flow cell (known as dispersionless microfluidics), as shown in Fig. 5.7a–b. The microfluidics suppressed the decrease of analyte concentration at the sensing area when different liquid samples were switched and thus improved the kinetic response and sensitivity [73]. Short

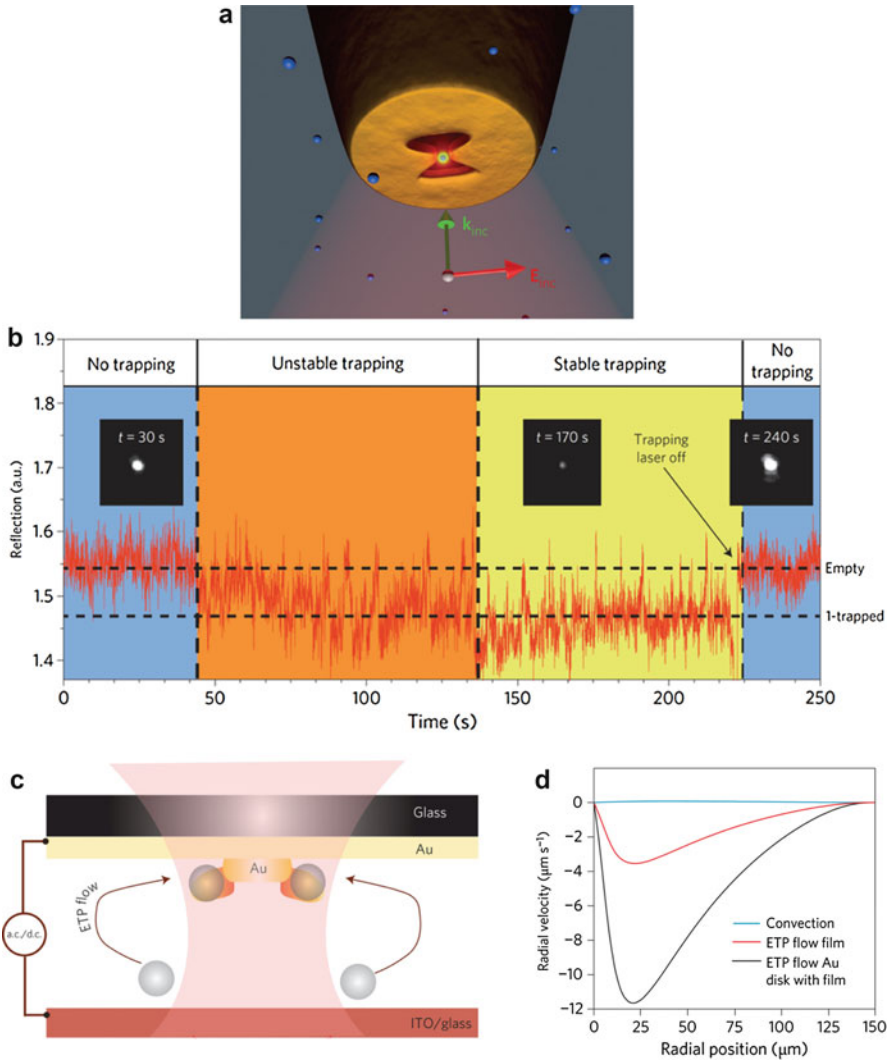

Fig. 5.6 3D manipulation and long-range transportation of objects in plasmofluidic systems. (**a**) Schematic illustration of a single particle trapped at a bowtie plasmonic aperture on the tip of an optical fiber, which is mechanically controlled to enable 3D manipulation of the trapped particle. (**b**) Dynamics of light reflection for different regimes in the 3D manipulation. Insets: Optical images of the light spots at the fiber for the different times as indicated (Reproduced with permission [66]. Copyright 2014 Nature Publishing Group). (**c**) Schematic illustration of hybrid electro-thermoplasmonic (ETP) nanotweezers. The locally heated nanoantenna induces an ETP flow under an AC electric field, which enables rapid and accurate delivery of particles to the trapping site. (**c**) Comparison of radial velocities that result from ETP flow and thermoplasmonic convection as a function of distance from the center of the laser beam (Reproduced with permission [65]. Copyright 2015 Nature Publishing Group)

sequences of DNA (20 bases) that are characteristic for *E. coli* cells were probed in less than 4 min for a concentration down to fM levels, outperforming most SPP sensors by one order of magnitude.

SERS-based plasmofluidic sensors for high-throughput detection of multiple DNAs in single assays were also developed. One example is based on self-assembled gold nanoparticles (Au NPs) on a gold nanowire (Au NW) at the presence of target DNAs [69]. Raman signal was significantly enhanced by placing the DNA molecules in the interstices of the gold-particle-on-wire structure. The structure was constructed by sequential incubation of Au NWs premodified by thiolated probe DNAs in solutions of target DNAs and Au NPs functionalized by reporter DNAs with Raman dyes (Fig. 5.7c). A high selectivity is assured because only those target DNAs with sequences complementary to the probe DNAs and the reporter DNAs can form the particle-on-wire structure for the enhanced signal of the Raman dyes. The sensor was applied for quantitative detection of DNA concentrations, multiplexed detection of bacterial DNAs, and identification of pathogenic bacteria in real clinical samples. The results on bacteria agreed well with those obtained by conventional culture-based assays, as illustrated in Fig. 5.7d.

Vo-Dinh's group devised a label-free DNA biosensor based on molecular sentinel (MS) immobilized on a metal film over nanosphere (MFON) [71, 74–76]. Upon DNA hybridization, the Raman label at the end of the MS is separated from the MFON's surface to exhibit decreased Raman signal, which works as the readout and renders high selectivity in multiplexed analysis. With the initial detection of human RSAD2 gene [71] and Ki-67 DNA [74] and the multiplexed detection of IFI27 A and IFI44L [75], the group developed the biosensor into a bioassay-on-chip platform and detected ssDNA of dengue virus (LOD ~6 attomoles), which is the culprit of dengue fever that plagues 230–390 million people each year. The platform can be combined with microfluidics for on-chip sample preparation and detection, providing a new tool for POC diagnostics and global healthcare.

Detection of microRNAs (miRNAs) has been a key topic in cancer research, diagnosis, and prognosis. miRNAs can repress gene expression in a sequence-dependent manner [77] and are associated with various human diseases such as diabetes, Alzheimer's, and cancers [78–80]. At an early stage of cancer, extremely low concentrated miRNAs circulate in human body fluid, making detection of miRNAs with improved LOD and sensitivity desirable for early disease diagnosis and implementation of new treatment options [81].

Joshi et al. designed a regenerative LSPR-based miRNA sensor for early diagnosis of pancreatic ductal adenocarcinoma (PDAC), a deadly cancer with an overall 5-year survival rate of 7%. The cancer is hard to be detected when the tumor is small and at nonmetastatic stage [82, 83]. The sensor is based on gold nanoprisms functionalized with –S-C6-ssDNAs. Direct hybridization between the –S-C6-ssDNAs and the target miRNAs forms DNA duplex (Fig. 5.7e), which increases the refractive index in local environment of the nanoprism and redshifts the LSPR peak wavelength. The high sensitivity down to 10^{-18} M for specific miRNA-10b

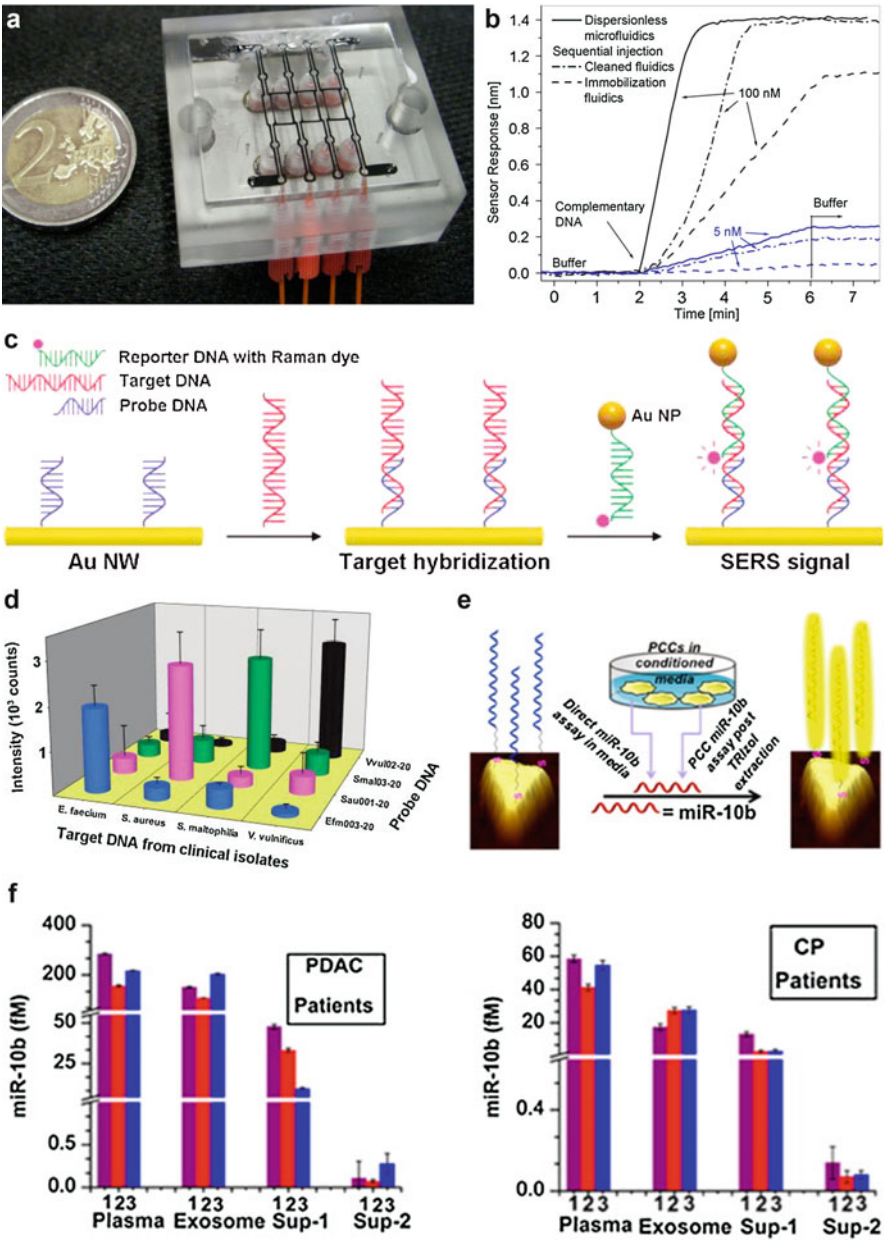

Fig. 5.7 (continued)

benefits from multiple factors: (a) atomically flat surface of the nanoprisms allowing efficient duplex formation, (b) high charge density of the duplex greatly altering the local refractive index, and (c) strong field enhancement at the tips of nanoprisms. Detection of miRNA-10b at a low concentration was achieved in pancreatic cancer cell lines, derived tissue culture media, human plasma, and plasma exosomes. Quantification of miRNA-10b in highly purified exosomes that were isolated from patients with PDAC and chronic pancreatitis (CP) was shown in Fig. 5.7f. PDAC patients had much higher miRNA-10b levels than CP patients. Integration of the sensor into microfluidics is expected to further enhance the miRNA measurements and the disease diagnosis with identifiable miRNA signatures.

5.2.2 Detection of Proteins

Proteins in biofluids such as serum are highly associated with biological functionalities. Detection of proteins and analysis of their unique sequences have high clinical relevance [84, 85]. For instance, a protein biomarker called SVEGFR-1 was increasingly expressed in patients with myelodysplastic syndromes (MDS), i.e., a diverse group of clonal disorders of the hematopoietic stem cell. Prostate-specific antigen (PSA) shows increased levels above the normal limits (4 ng mL^{-1}) in serum for possible prostate malignancy, which can be used for diagnosis and prognosis of prostate cancer [86]. Plasmofluidic immunoassays and immunosensors feature parallel, label-free, and real-time detection of proteins with high sensitivity, selectivity, multiplicity, and reproducibility [30, 87–90]. They are also applied to investigate protein-protein interaction [91], monitor live cell secretory events [92], and identify diagnosis-related cells [93].

SPP-based plasmofluidic sensors for label-free detection of proteins have recently been implemented on a smartphone platform [94]. A plasmonic sensor with dispersionless microfluidics was developed to detect protein biomarker of MDS disease (i.e., sVEGFR-1) via interaction with its high-affinity bio-receptor VEGF-A [95]. A detection limit of 25 ng/mL was achieved in 2% human blood plasma by using the sequential injection approach. However, the traditional experimental design that relies on a specific bio-receptor (known as "lock-and-key" approach) is limited by interference from molecules that are structurally or chemically alike. Moreover, most diseases are associated with multiple biomarkers, which necessitate

Fig. 5.7 Detection of DNAs and RNAs with plasmofluidic sensors. (**a**) Photograph of a four-channel flow cell for dispersionless microfluidics that was implemented in SPP-based detection of nucleic acid. (**b**) Comparison of sensor responses of different microfluidic designs in SPP-based detection of DNA E441C from *E. coli* cells (Reproduced with permission [31]. Copyright 2009 Elsevier Publishing). (**c**) Schematic illustration for the SERS-based detection of target DNAs by gold-particle-on-wire system. (d) Identification of target DNAs from clinical isolates with the gold-particle-on-wire sensor (Reproduced with permission [69]. Copyright 2010 American Chemical Society). (**e**) Schematic illustration of –S-C6-ssDNA-functionalized gold nanoprisms for LSPR-based sensing of miR-10b. (**f**) Determination of miR-10b concentration in plasma samples for three patients with PDAC and CP using the LSPR-based sensors (Reproduced with permission [83]. Copyright 2015 American Chemical Society)

the detection of a total protein distribution rather than a particular protein. To address these challenges, Choi et al. developed a "cross-reactive"-based sensor using a substrate of multiple segments of surfaces that are pre-adsorbed by different types of proteins. A distinctive pattern of SPP angle shifts arose from the interaction of the substrate with a sample of variable proteins [84]. The SPP angle pattern was used to clarify the concentration distributions of proteins and a specific biomarker, C-reactive protein (CRP), in a cocktail sample.

A more powerful way for simultaneous detection of multiple proteins is the use of protein microarrays in conjunction with surface plasmon resonance imaging (SPRI) [30]. However, protein microarrays often involve time-consuming fabrication process. Dehydrated or denatured proteins suffer a shorter lifetime of normal functionality. To overcome these problems, a multiplexed enzymatic synthesis via surface-coupled transcription-translation was employed for in vitro fabrication of protein microarrays and for their immediate use in biosensing based on a microfluidic platform, as illustrated in Fig. 5.8a–c. The plasmofluidic system includes generator, control, and detector components. Multiple RNA transcripts were created at the generator through surface reaction of RNA polymerase with adsorbed dsDNA and translated into proteins by cell-free protein synthesis. The synthesized proteins diffused to the detector element and formed protein microarrays. As a demonstration, binding of anti-GFP and antiluciferase to the protein arrays was characterized with SPRI and time-resolved absorption kinetic measurement, as shown in Fig. 5.8d–g. With multiple surface chemistries, the plasmofluidic system can be further implemented for multiplexed SPRI biosensing in clinical practices.

More challenges arise for SPP-based sensing in human serum samples due to (i) high nonspecific interaction between the sensor surface and serum proteins and (ii) matrix effects of serum such as high refractive index and viscosity that mask the binding events between the recognition elements on the sensor surface and the analytes in the serum [86]. Uludag et al. used a matrix elimination buffer to eliminate nonspecific binding of 98% serum proteins and performed a sandwich assay, in which the target proteins were sandwiched between a bottom layer of capture antibody and a top layer of antibody-modified Au NPs [86]. The Au NPs reduced the refractive-index mismatch between the buffer and the sample, leading to amplified SPP signal and enhanced sensitivity. A LOD of 0.29 ng mL^{-1} for tPSA in 75% human serum was attained, which was comparable to that achieved by a quartz crystal microbalance (QCM) sensor. SPP and QCM sensors were further combined to detect sub-attomolar human α-thrombin [96]. The sandwich immunoassays with SPP-based sensors are expected to improve early-stage cancer diagnosis and prognosis.

LSPR-based plasmofluidic sensors enable high-end miniaturization down to the single-nanoparticle scale [87, 97–100]. Zijlstra et al. reported real-time, label-free detection of single-protein binding events by monitoring the LSPR of a nanorod with an ultrasensitive photothermal assay [98]. When a single protein binds to the receptors on the surface of the nanorod, a small redshift of the longitudinal LSPR wavelength changes the absorption cross section of the nanorod at the wavelength of the heating beam, which can be measured with the transduced temperature change. Unlike the resonance Rayleigh scattering, the contrast scale of photothermal

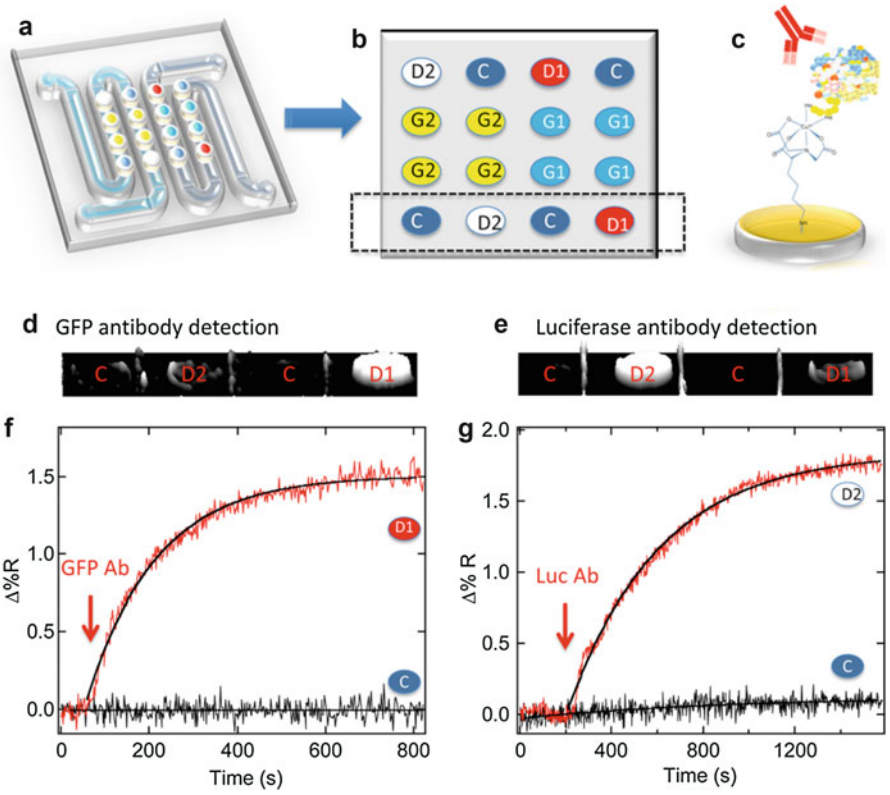

Fig. 5.8 Detection of proteins with SPP-based plasmofluidic sensors. (**a**) Schematic illustration and (**b**) spatial diagram of a GFP-luciferase DNA microarray in a dual-channel microfluidic cell. (**c**) Schematic illustration of antibody bound onto the synthesized protein array. SPRI difference images taken before and after the exposure to (**d**) anti-GFP and (**e**) antiluciferase solutions. Real-time SPRI adsorption kinetic measurement of (**f**) anti-GFP- and (**g**) antiluciferase-specific binding (Reproduced with permission [30]. Copyright 2012 American Chemical Society)

microscopy permits the measurement of mode volume that is commensurate to the size of a protein.

Ament et al. utilized single gold nanorods to monitor single-protein conformational dynamics and equilibrium coverage fluctuations [99]. The latter contain the information on the binding kinetics and nonequilibrium thermodynamics. By using a white light laser, an intensified CCD camera, and an engineered nanoparticle geometry, they achieved considerable improvement of signal-to-noise (SNR) ratio and time resolution over previous techniques to identify single-molecule binding events. Rather than utilizing passive surface binding to capture the proteins, Gordon's group used a double nanohole to actively trap single proteins and to measure the single-protein binding events [100].

LSPR biosensors based on nanoparticle ensembles and microfluidics are more suitable for clinical applications because the ensembles allow statistically significant

data analysis, relax constraints by nanoparticle variations, and enable simple instrumentation, fast data acquisition, and improved signal-to-noise ratio [87]. Plasmonic nanotechnologies such as plasmonic arrays [87, 88, 101–103] and SPRI [104, 105] and innovative microfluidic techniques such as integrated concentration gradient generator [104] and multi-well fluidic measurement [106] have been intensely pursued to detect and quantify cancer biomarkers with enhanced sensitivity, robustness, integrity, high throughput, and multiplexity.

Quidant's group developed a parallel and high-throughput LSPR-based plasmofluidic sensor that can be upgraded to a lab-on-a-chip system and be translated to clinical environments (Fig. 5.9a) [87]. For the sensor, a periodic array of gold nanorods with a bio-recognition layer was integrated with a microfluidic network. The authors applied the sensor to detect AFP and PSA, which are indicators of prostate cancers, at a LOD of as low as 5 ng/mL and a timescale of minutes. Chen et al. developed a highly integrated, multiarrayed LSPR sensor for massively parallel high-throughput detection of multiple cytokine biomarkers in a low-volume assay, as shown in Fig. 5.9b [88]. Consisting of 480 LSPR sensing spots with multistep processing for eight different samples, including manual loading, incubation, and washing, the sensor allowed quantitative measurements at concentrations ranging from 10 to 10,000 pg/mL in a 1-μL sample of serum. It also enabled multianalyte detection of ten cycles for each sample in 40 min, which is more than ten times shorter than traditional sandwich immunoassays. The sensor was further applied to measure cytokine levels of IL-6 and IL-10 in two neonates, who received cardiopulmonary bypass surgery for congenital heart disease within 24 h. The measurement was valuable for defining the postsurgery responses and predicting the anticipated assay outcomes.

Measuring binding affinities between proteins is also of fundamental interest and clinical significance. A "nanoSPR" method was proposed to simultaneously characterize the binding affinities among many macromolecular partners [91]. Briefly, multiple batches of gold nanorods functionalized with different proteins and one batch without functionalization (as a reference) were driven through the flow cell consecutively to generate a positon-encoded sensor. The encoding of the sensor was carried out by repetitive recording of the position of each randomly deposited gold nanorod, as shown in Fig. 5.9c. As a demonstration, the sensor was applied to study the interactions of three bacterial division proteins with a target protein FtsZ, which is an essential element of the division machinery in most bacterial systems. The results had an excellent agreement with those by conventional composition gradient static light scattering and fluorescence anisotropy. With the small device size, reduced sample volume, and built-in statistics, the sensor is envisioned to be a powerful tool in drug screening and discovery applications.

In light of the important role of cell secretion in a variety of physiological processes, Wu et al. developed a label-free, ultrasensitive, plasmofluidic platform based on gold nanoslits with strong Fano resonance to monitor dynamic live cell secretory activities [92]. The THP1 cells were trapped and cultured in microfluidic channels with the sensing surface of gold nanoslits ~3–5 μm away from the cell membrane. Upon stimulation with continuous lipopolysaccharide, the cells were

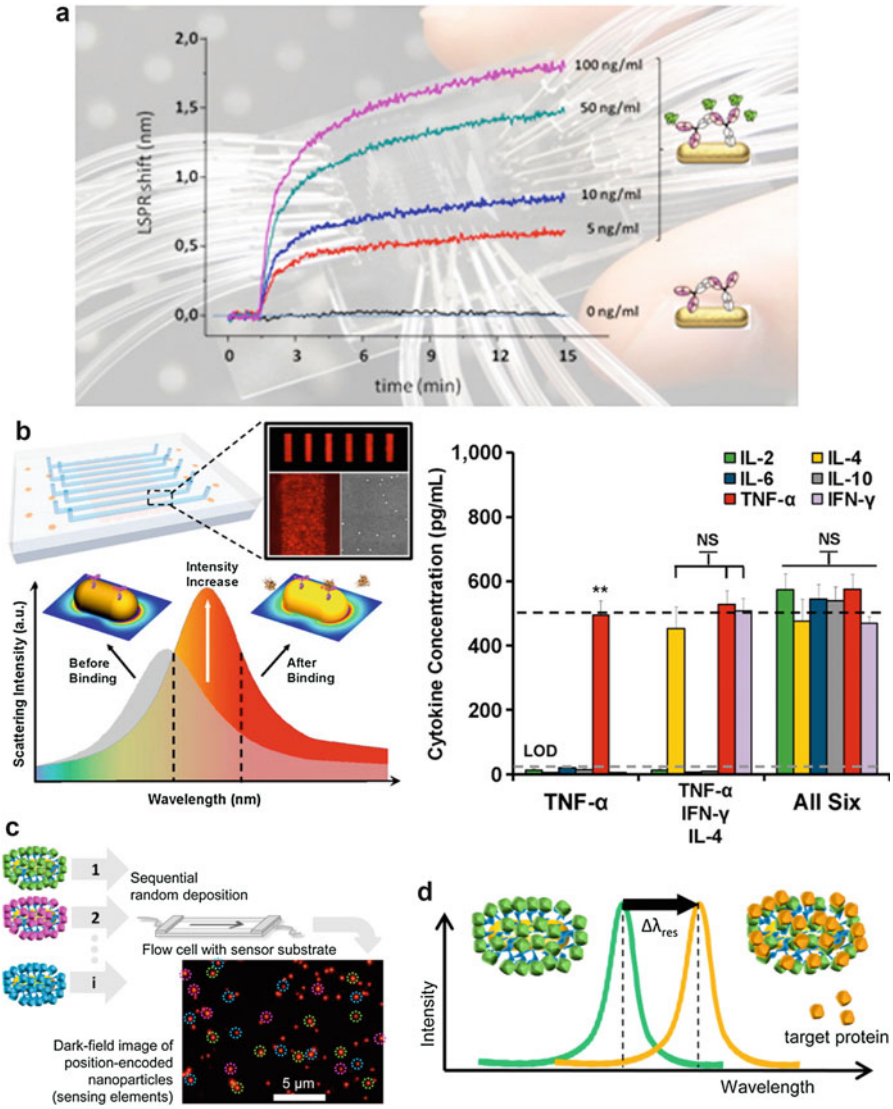

Fig. 5.9 Detection of proteins with LSPR-based plasmofluidic sensors. (**a**) Detection of prostate cancer biomarkers down to a concentration of 5 ng/mL in a complex matrix (consisting of 50% human serum) with a microfluidics-integrated LSPR-based biosensor (Reproduced with permission [87]. Copyright 2014 American Chemical Society). (**b**) Multiplex immunoassays of six cytokines in a complex serum matrix with a high-throughput, label-free, multiarrayed LSPR biosensor chip (Reproduced with permission [88]. Copyright 2015 American Chemical Society). (**c**) Simultaneous characterization of binding affinities between multiple protein partners with a LSPR biosensor. (**d**) Working principle of the characterization of binding affinities (Reproduced with permission [91]. Copyright 2014 American Chemical Society)

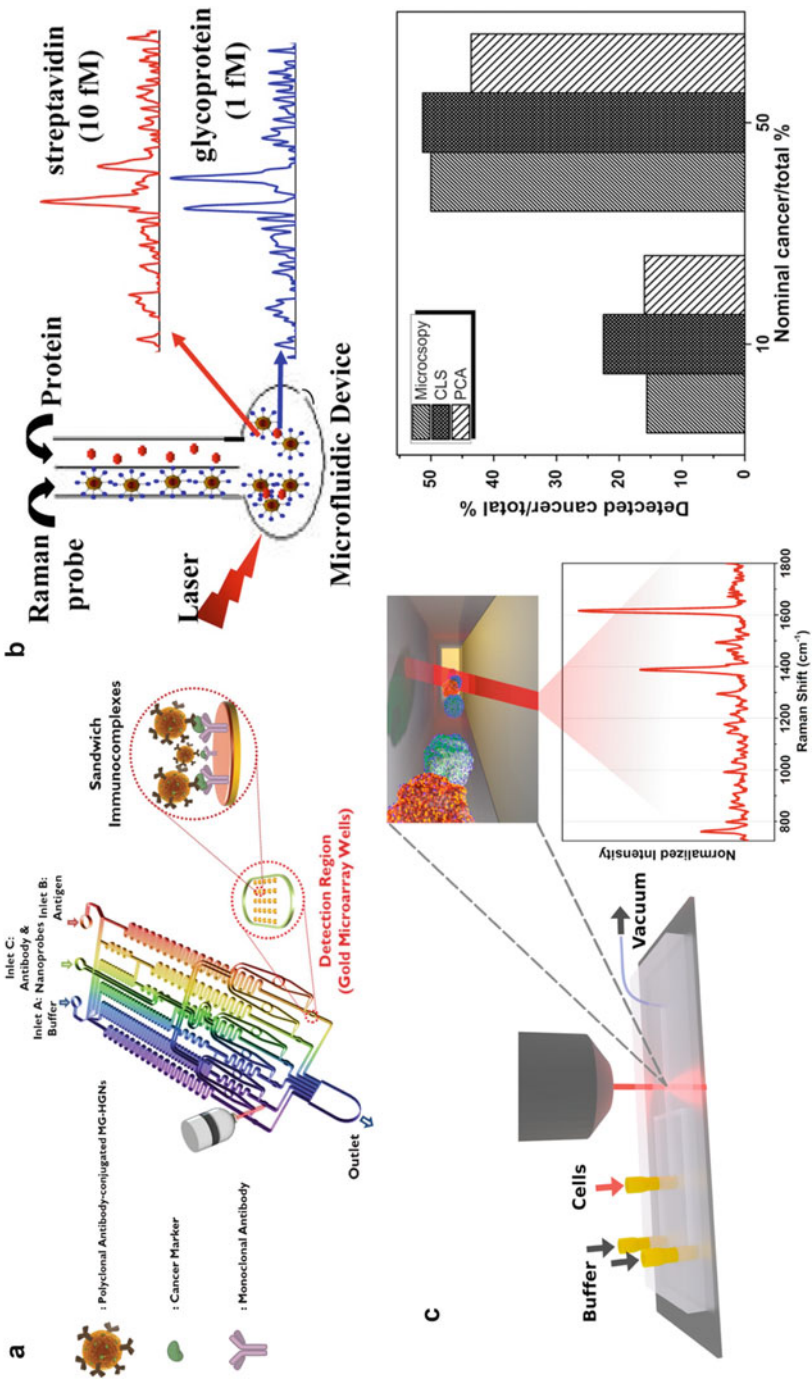

Fig. 5.10 Detection of proteins with SERS-based plasmofluidic sensors. (**a**) Schematic representation of a SERS-based immunoassay consisted of a structured gold array integrated with gradient microfluidics. The illustrations in the enlarged circles represent the formation of sandwich immunocomplexes on the surface

found to secrete MMP-9 proteins in 2 h. The plasmofluidic sensor needs less than ten cells for the study, while ELISA analysis demands at least a few thousand cells. The sensor can be applied for fundamental study of secretory events in different physiological environments and medical diagnosis of various diseases at the single-cell level.

SERS-based immunoassay is considered another promising approach for protein sensing. One of the most popular strategies uses a sandwich immunocomplex protocol with antibody-conjugated metal particles [89, 108–111]. Choo's group implemented magnetic tweezers [108] and optoelectronic tweezers [109] in a gradient microfluidic channel to form sandwich immunocomplexes for the sensitive and automatic quantitative analysis in less than 30 min. In the immunocomplexes, target antigens were sandwiched between antibody-conjugated microspheres and antibody-conjugated SERS-active nanoparticles. The magnetic tweezer-based immunoassay had a LOD of 1–10 ng/mL for rabbit IgG, and the optoelectronic tweezer-based one achieved a LOD of 98 pg/mL for alpha-fetoprotein (AFP). The same group further integrated sandwich immunoassay [110] with gradient microfluidics to achieve programmable and automatic analysis of biomarkers with small sample volume, easy sample preparation, and short assay time [89]. After the AFP antigens were captured by the immobilized antibodies on gold microwells, polyclonal anti-AFP antibody-conjugated particles were attached to form the sandwich immunocomplexes, as shown in Fig. 5.10a. A similar methodology was applied to detect hepatitis B virus antigen in human blood and blood plasma. Hepatitis B virus infection is a common cause of chronic liver disease worldwide [112]. Using a sandwich-typed immunoassay, Zou et al. detected carcinoembryonic antigen in raw blood samples with a LOD of as low as 10^{-12} M. Carcinoembryonic antigen is a wide-spectrum biomarker for diagnosis of various cancers [111].

Formation of stable electromagnetic "hot spots" in nanoparticle aggregates is another strategy for SERS-based protein analysis with high reproducibility and sensitivity. Saha et al. designed a paper-based microfluidic SERS system to detect streptavidin and glycoprotein with pico to femtomolar concentration, as shown in Fig. 5.10b [107]. Two channels with Ag/Au nanoparticles and proteins merge into a small round-shaped reaction chamber to generate SERS-active nanoparticle aggregates via protein-assisted cross-linking. Notably, the porous feature of the microchannels regulates the extent of nanoparticle aggregation and prevents the screening of "hot spots" in large aggregates.

Fig. 5.10 (continued) of a 5 × 5 array of round gold wells (Reproduced with permission [89]. Copyright 2013 RSC Publishing). (**b**) A paper-based microfluidic device for SERS-based protein detection. It involves the aggregation of Ag/Au nanoparticles at the presence of proteins (Reproduced with permission [107]. Copyright 2014 American Chemical Society). (**c**) Schematic representation of a SBT-based microfluidic system to distinguish cancer cells in a low concentration against background of normal cells. The bar graph compares cancer cell counts by microscopy, PCA, and CLS. The latter two are deconvolution strategies for analyzing the cancer-normal cell ratios with the composite Raman spectrum (Reproduced with permission [93]. Copyright 2015 American Chemical Society)

SERS protein biotags (SBTs) have been developed for identification of cells and pathogens in body fluids, which is significant for early disease detection and monitoring of patient response to therapy [93]. In the microfluidic cell identification system, two spectroscopically distinguishable SBTs that target distinct cell epitopes were used to label cells in a single focused line by hydrodynamic flow, as illustrated in Fig. 5.10c [93]. The identification was accomplished by measuring the relative signal from the cancer-specific SBT versus the cell-identifying universal control SBT. The discrimination efficiency can reach 1 cancer cell from a population of 100 normal cells due to spectroscopic richness of the Raman bands of the reporter molecules on the two SBTs and algorithmic effectiveness of the two deconvolution strategies for the composite spectrum. The SBT approach provides a continuous, low-cost, and nondestructive tumor cell identification and paves the way toward clinical cancer diagnosis at the single-cell level.

5.2.3 Detection of Pathogens

The detection of infectious agents such as viruses and bacteria is critical for public health, homeland security, and food industry [113, 115, 117]. Viruses have been responsible for a number of epidemic outbreaks (e.g., H1N1 flu and SARS) in recent years. Timely virus detection becomes essential for recognizing and controlling future epidemics. Conventional techniques such as cell culture methods, PCR, and ELISA can detect and quantify pathogens with high sensitivity and specificity [118, 119]. However, they require lab-intensive procedures, expensive equipment, and well-trained operators. Alternative biosensing techniques that can achieve reliable, accurate, and sensitive detection and analysis of pathogens under the variable settings, including source-limited settings and primary care settings, are in great need. Among the various detection platforms that use different mechanisms such as electrical, mechanical, and optical signal transduction [2, 5, 120], plasmofluidic biosensors are promising for label-free detection of infectious agents.

Wang et al. achieved label-free imaging, detection, and mass/size measurement of single viral particles with high-resolution surface plasmon resonance spectroscopy [121]. The viral particles were imaged as diffraction patterns from their scattering of SPP. The particle size and mass were determined from the image intensities. Two viruses, i.e., H1N1 influenza A/PR/8/34 and HCMV, were studied with a mass detection limit of 1 ag, which is four orders of magnitude lower than that by conventional surface plasmon resonance method.

To meet the needs for quickly recognizing and controlling epidemics, a plasmofluidic sensor was developed to detect viruses from biologically relevant media, as illustrated in Fig. 5.11a [113]. The sensor exploits plasmon-enhanced extraordinary light transmission through metal nanohole arrays and is applicable to a broad range of pathogens. It was applied to detect PT-Ebola virus in PBS buffer solution based on the consistent redshift (>14 nm) of the plasmon resonance wavelength. A 4-nm shift in resonance wavelength was observed for virus detection in biological media consisted of cell growth medium and 7% fetal calf serum. The detectable virus concentration ranges from 10^6 to 10^9 PFU/mL, which is relevant to both clinical testing and drug screening.

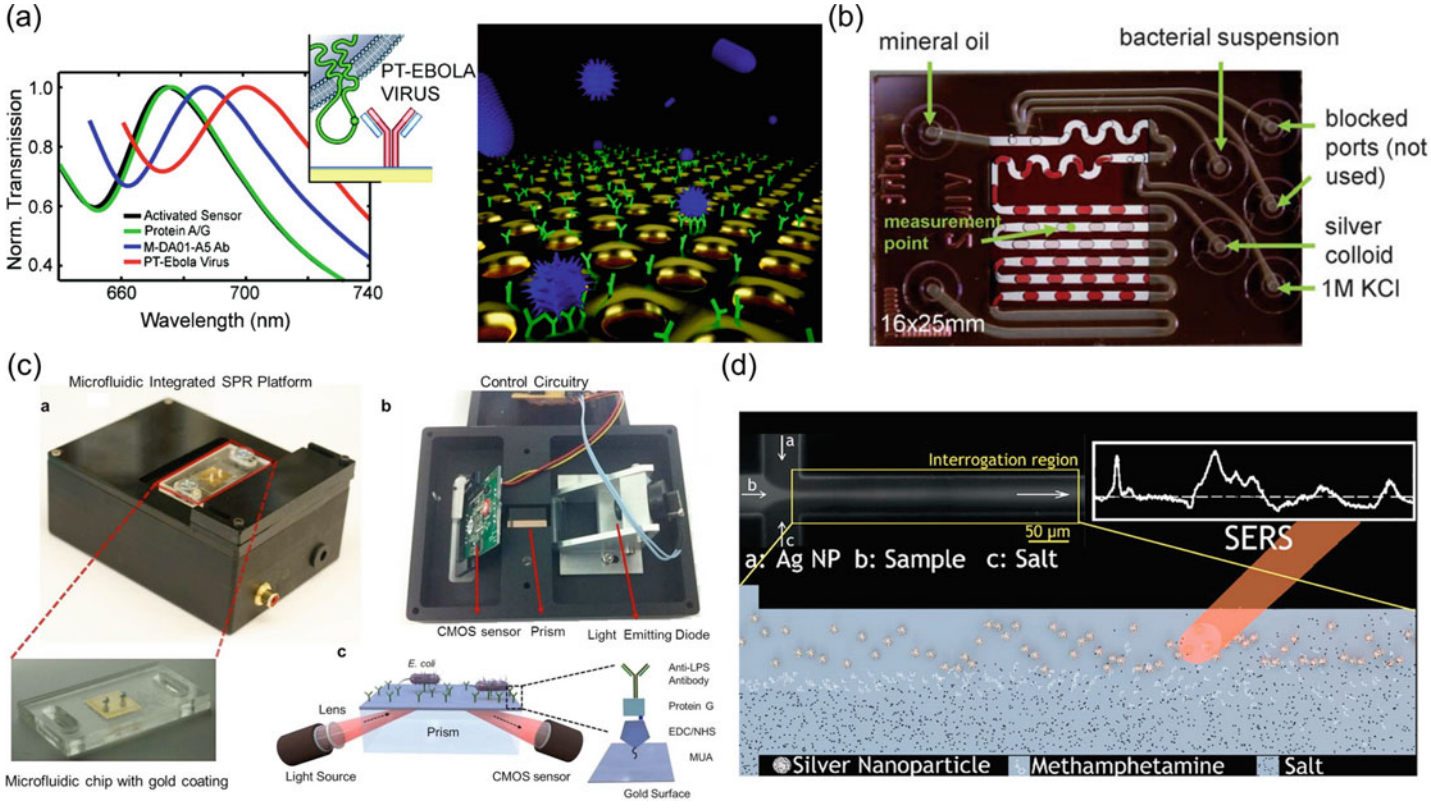

Fig. 5.11 Detection of pathogens and drugs with plasmofluidic sensors. (**a**) Detection of PT-Ebola virus using a plasmofluidic biosensor based on extraordinary optical transmission in metal nanohole arrays functionalized with M-DA01-A5 antibodies (Reproduced with permission [113]. Copyright 2010 American

Inci et al. developed a plasmofluidic platform for label-free, high-sensitive, high-specific, and reproducible HIV viral load quantification from unprocessed whole blood sample [117]. Surface chemistry and highly specific antibody immobilization were applied to capture the viruses at the electromagnetic "hot spots" and to minimize background signal from nonspecific binding of blood cells. Briefly, poly-L-lysine-modified polystyrene with terminal amine group was used as substrates to capture gold nanoparticles. The gold nanoparticles were treated with different chemicals consecutively, including 11-mercaptoundecanoic acid, *N*-ethyl-*N*-(3-dimethylaminopropyl)carbodiimide hydrochloride, N-hydroxysulfosuccinimide, NeutrAvidin, and biotinylated anti-gp120 polyclonal antibody. The antibody was positioned in a favorable orientation to have a high capture efficiency for the viruses. A SPP platform based on DNA-RNA hybridization was also developed to detect viruses plaguing plant food and feed crop plants [122].

Rapid detection of bacteria makes a difference in monitoring and preventing outbreaks of infections [2, 118]. For this purpose, Walter et al. developed microfluidic SERS to discriminate bacteria based on strain levels in a fast and reliable fashion [114]. In their plasmofluidic system, aqueous analytes and colloid solution form droplets in mineral oil, creating a segmented flow for stable optical measurements and reproducible bacterial identification, as shown in Fig. 5.11b. Besides colloidal nanoparticles, solid-state SERS substrate functionalized with recognition molecules was also employed to capture and analyze *E. coli* cells with high specificity and sensitivity [123].

Demirci's group developed a portable microfluidic SPP platform that can rapidly detect and quantify *E. coli* and *S. aureus* [115]. All the elements, including light source, optical components, CMOS sensor, circuitry, and microfluidic chip, were packaged in a portable box with dimensions of 13.5 cm × 10 cm × 5.2 cm, as shown in Fig. 5.11c. Effective capture and detection of *E. coli* at concentrations from ~10^5 to 3.2 × 10^7 CFUs/mL in PBS and peritoneal dialysis fluid were demonstrated. Multiplicity and specificity were tested with *S. aureus* in PBS solution, implying the potential of the platform for pathogen diagnostics at both POC and primary care settings.

5.2.4 Detection of Drugs

Quick and cost-effective pharmaceutical analysis can benefit healthcare, biomedicine, and food safety [124]. For example, drug screening is a critical step in new drug discovery. Detection of drug residues in food and human liquids is frequently needed

Fig. 5.11 (continued) Chemical Society). (**b**) Discrimination of bacteria based on strain levels using a six-port SERS-based plasmofluidic biosensor. Mineral oil was used as separation medium to prevent deposition of nanoparticles and analytes on the substrate (Reproduced with permission [114]. Copyright 2011 RSC Publishing). (**c**) Detection and quantification of *E. coli* cells with a portable SPP-based plasmofluidic sensor (Reproduced with permission [115]. Copyright 2015 Nature Publishing Group). (**d**) Detection of trace concentrations of drugs in saliva with a SERS-based plasmofluidic sensor. No chemical functionalization and reactants were required for the detection (Reproduced with permission [116]. Copyright 2013 American Chemical Society)

for food safety and healthcare. The capability of monitoring antibody-polypeptide reaction is desirable for multiplexed drug discovery. Chen et al. proposed a SPRI-based visualization method for monitoring antibody-polypeptide binding in a label-free and high-throughput format [125]. The plasmonic platform can support the dynamic imaging of polypeptide microarray and the time tracing of 3D histograms for monitoring antibody-polypeptide reaction on the surface.

Chiral compounds have significant impacts on pharmacological and biological processes. Effective strategies for chiral discrimination and enantioseparation are highly needed to meet the increasing need for enantiomerically pure compounds. For a pair of enantiomers, it is possible that one configuration is active drug, while the other configuration remains inactive, contributes to side effects, displays toxicity, or works as an antagonist [126, 127]. As an example, Guo et al. demonstrated α-thrombin-functionalized LSPR sensor integrated with a microfluidic chip for enantioselective analysis of melagatran. Recently, we have achieved high-sensitive label-free chiral sensing for drug molecules based on moiré chiral metamaterials [128].

Plasmofluidic sensors were also developed for label-free and rapid detection of drug residues in food and clinical samples [129]. Fernandez et al. used a portable six-channel SPP sensor to analyze antibiotic residues from different families, i.e., fluoroquinolones, sulfonamides, and phenicols, in whole milk samples [130]. The sensor showed good regenerative ability and repeatability and accomplished LODs far below the maximum residue levels established by the European Union for the antibiotics. Zhao et al. used a multichannel SPP sensor to analyze the concentrations of methotrexate, an anticancer drug, in the serum of a patient undergoing chemotherapy treatments. The results agreed with those by fluorescence polarization immunoassay [131].

Andreou et al. developed a microfluidic SERS to identify drugs at clinical levels without specialized chemicals and bio-reagents [116]. As shown in Fig. 5.11d, a laminar flow consisted of a central stream of analytes (i.e., methamphetamine) and two sheath streams of silver nanoparticle and salt solutions was created. At the interrogation region, SERS-active nanoparticle dimers and small-order aggregates with methamphetamine predominantly formed. Due to the low affinity of methamphetamine to the silver nanoparticles, the salt was added to induce the aggregation. Trace concentrations of methamphetamine in saliva were detected within minutes. The microfluidic SERS will find applications in detecting many other health-related molecules such as toxins and pollutants.

6 Conclusions and Future Perspectives

Tremendous progress has been made in plasmofluidics for biological analysis and medical diagnostics. In particular, plasmonic tweezers achieved noninvasive trapping of biological cells, DNAs, and proteins at the single-entity level. 3D manipulations were demonstrated with plasmonic tweezers based on an optical fiber tip with high-resolution mechanical motion control. Long-range and rapid delivery of nanoparticles was achieved with electrothermoplasmonics. Most of the current tweezers used microfluidic channels as passive containers for sample solutions. It is

anticipated that future plasmonic tweezers will fully reap the benefits of micro-/nanofluidics to further enhance their functionalities for biosensing and diagnostic applications. In particular, the light-fluid interactions at the nanoscale can be explored to achieve versatile multifunctional plasmofluidic tweezers [7]. Our preliminary study indicated that the plasmon-enhanced photothermal effects such as thermophoresis are one of the promising strategies for optical manipulations in variable fluidic environments.

A variety of plasmofluidic sensors has been developed to detect and analyze nucleic acids, proteins, pathogens, and drugs in life sciences, disease diagnostics, and drug discovery. Innovative microfluidic design, plasmonic engineering, and surface functionalization have led to sensitive, robust, and label-free POC biosensors. The next-generation plasmofluidic sensors are expected to target at translational and clinical applications [4]. For the purpose, the sensors need to be a highly integrated, robust, and user-friendly system that can handle a variety of clinical samples such as urine, blood, and saliva and enables POC diagnostics at field settings.

In summary, the highly interdisciplinary field of plasmofluidics presents exciting opportunities for new discoveries and POC devices. With the stronger collaborations among researchers from physics, chemistry, biology, pharmacology, and engineering, as well as clinicians and entrepreneurs, plasmofluidics for biosensing and disease diagnostics will continue to grow and contribute to global healthcare.

Acknowledgments The authors acknowledge the financial support of the Beckman Young Investigator Program and the Office of Naval Research Young Investigator Program.

References

1. Tokel O, Inci F, Demirci U (2014) Advances in plasmonic technologies for point of care applications. Chem Rev 114(11):5728–5752
2. Zhang W et al (2016) Portable point-of-care diagnostic devices. Anal Methods 8 (44):7847–7867
3. Siegel RL, Miller KD, Jemal A (2016) Cancer statistics, 2016. CA Cancer J Clin 66(1):7–30
4. Sin MLY et al (2014) Advances and challenges in biosensor-based diagnosis of infectious diseases. Expert Rev Mol Diagn 14(2):225–244
5. Pai NP et al (2012) Point-of-care testing for infectious diseases: diversity, complexity, and barriers in low- and middle-income countries. PLoS Med 9(9):e1001306
6. Han KN, Li CA, Seong GH (2013) Microfluidic chips for immunoassays. In: Cooks RG, Pemberton JE (eds) Annual review of analytical chemistry, vol 6. Annual Reviews, Palo Alto, pp 119–141
7. Wang M et al (2015) Plasmofluidics: merging light and fluids at the micro-/nanoscale. Small 11(35):4423–4444
8. Barnes WL, Dereux A, Ebbesen TW (2003) Surface plasmon subwavelength optics. Nature 424(6950):824–830
9. Zheng YB et al (2012) Molecular plasmonics for biology and nanomedicine. Nanomedicine 7(5):751–770
10. Juan ML, Righini M, Quidant R (2011) Plasmon nano-optical tweezers. Nat Photonics 5(6):349–356

11. Wang DS, Fan SK (2016) Microfluidic surface plasmon resonance sensors: from principles to point-of-care applications. Sensors 16(8):1175
12. Mayer KM, Hafner JH (2011) Localized surface plasmon resonance sensors. Chem Rev 111(6):3828–3857
13. Singh P (2016) SPR biosensors: historical perspectives and current challenges. Sensors Actuators B Chem 229:110–130
14. Huang JS, Yang YT (2015) Origin and future of plasmonic optical tweezers. Nano 5(2):1048–1065
15. Zheng YB et al (2008) Systematic investigation of localized surface plasmon resonance of long-range ordered Au nanodisk arrays. J Appl Phys 103(1):014308
16. Garcés-Chávez V, Dholakia K, Spalding GC (2005) Extended-area optically induced organization of microparticles on a surface. Appl Phys Lett 86(3):031106
17. Wang K et al (2010) Scannable plasmonic trapping using a gold stripe. Nano Lett 10(9):3506–3511
18. Wang XD et al (2013) Theoretical and experimental study of surface plasmon radiation force on micrometer-sized spheres. Plasmonics 8(2):637–643
19. Righini M et al (2007) Parallel and selective trapping in a patterned plasmonic landscape. Nat Phys 3(7):477–480
20. Grigorenko AN et al (2008) Nanometric optical tweezers based on nanostructured substrates. Nat Photonics 2(6):365–370
21. Kang J-H et al (2011) Low-power nano-optical vortex trapping via plasmonic diabolo nanoantennas. Nat Commun 2:582
22. Roxworthy BJ et al (2012) Application of plasmonic bowtie nanoantenna arrays for optical trapping, stacking, and sorting. Nano Lett 12(2):796–801
23. Zheng Y et al (2014) Nano-optical conveyor belt, part II: demonstration of handoff between near-field optical traps. Nano Lett 14(6):2971–2976
24. Lin L et al (2016) Bubble-pen lithography. Nano Lett 16(1):701–708
25. Juan ML et al (2009) Self-induced back-action optical trapping of dielectric nanoparticles. Nat Phys 5(12):915–919
26. Baffou G, Quidant R, García de Abajo FJ (2010) Nanoscale control of optical heating in complex plasmonic systems. ACS Nano 4(2):709–716
27. Baffou G et al (2013) Photoinduced heating of nanoparticle arrays. ACS Nano 7(8):6478–6488
28. Donner JS et al (2011) Plasmon-assisted optofluidics. ACS Nano 5(7):5457–5462
29. Puiu M, Bala C (2016) SPR and SPR imaging: recent trends in developing nanodevices for detection and real-time monitoring of biomolecular events. Sensors 16(6):870
30. Seefeld TH, Halpern AR, Corn RM (2012) On-chip synthesis of protein microarrays from DNA microarrays via coupled in vitro transcription and translation for surface plasmon resonance imaging biosensor applications. J Am Chem Soc 134(30):12358–12361
31. Springer T, Piliarik M, Homola J (2010) Surface plasmon resonance sensor with dispersionless microfluidics for direct detection of nucleic acids at the low femtomole level. Sensors Actuators B-Chem 145(1):588–591
32. Lee Y et al (2013) Tunable directive radiation of surface-plasmon diffraction gratings. Opt Express 21(3):2748–2756
33. Krupin O et al (2013) Biosensing using straight long-range surface plasmon waveguides. Opt Express 21(1):698–709
34. Szunerits S, Boukherroub R (2012) Sensing using localised surface plasmon resonance sensors. Chem Commun 48(72):8999–9010
35. Unser S et al (2015) Localized surface plasmon resonance biosensing: current challenges and approaches. Sensors 15(7):15684–15716
36. Escobedo C et al (2010) Flow-through vs flow-over: analysis of transport and binding in nanohole array plasmonic biosensors. Anal Chem 82(24):10015–10020
37. Escobedo C et al (2012) Optofluidic concentration: plasmonic nanostructure as concentrator and sensor. Nano Lett 12(3):1592–1596

38. Lee SY et al (2011) High-fidelity optofluidic on-chip sensors using well-defined gold nanowell crystals. Anal Chem 83(23):9174–9180
39. Verellen N et al (2011) Plasmon line shaping using nanocrosses for high sensitivity localized surface plasmon resonance sensing. Nano Lett 11(2):391–397
40. Zhang SP et al (2011) Substrate-induced Fano resonances of a plasmonic nanocube: a route to increased-sensitivity localized surface plasmon resonance sensors revealed. Nano Lett 11(4):1657–1663
41. Shen Y et al (2012) Tuning the plasmon resonance of a nano-mouth array. Nanoscale 4(18):5576–5580
42. Shen Y et al (2013) Plasmonic gold mushroom arrays with refractive index sensing figures of merit approaching the theoretical limit. Nat Commun 4:2381
43. Lin L, Zheng Y (2015) Engineering of parallel plasmonic–photonic interactions for on-chip refractive index sensors. Nanoscale 7(28):12205–12214
44. Lin L, Zheng Y (2015) Optimizing plasmonic nanoantennas via coordinated multiple coupling. Sci Rep 5:14788
45. Petryayeva E, Krull UJ (2011) Localized surface plasmon resonance: nanostructures, bioassays and biosensing-a review. Anal Chim Acta 706(1):8–24
46. Chen K et al (2015) Moiré nanosphere lithography. ACS Nano 9(6):6031–6040
47. Wu Z et al (2015) Tunable multiband metasurfaces by moire nanosphere lithography. Nanoscale 7(48):20391–20396
48. Escobedo C (2013) On-chip nanohole array based sensing: a review. Lab Chip 13(13):2445–2463
49. Im H et al (2014) Label-free detection and molecular profiling of exosomes with a nanoplasmonic sensor. Nat Biotechnol 32(5):490–495
50. Willets KA, Duyne RPV (2007) Localized surface plasmon resonance spectroscopy and sensing. Annu Rev Phys Chem 58(1):267–297
51. Wong CL, Olivo M (2014) Surface plasmon resonance imaging sensors: a review. Plasmonics 9(4):809–824
52. White IM, Yazdi SH, Yu WW (2012) Optofluidic SERS: synergizing photonics and microfluidics for chemical and biological analysis. Microfluid Nanofluid 13(2):205–216
53. Cialla D et al (2012) Surface-enhanced Raman spectroscopy (SERS): progress and trends. Anal Bioanal Chem 403(1):27–54
54. Schlucker S (2014) Surface-enhanced Raman spectroscopy: concepts and chemical applications. Angew Chem-Int Ed 53(19):4756–4795
55. Huang JA et al (2015) SERS-enabled lab-on-a-chip systems. Adv Opt Mater 3(5):618–633
56. Zhou J et al (2012) Convenient formation of nanoparticle aggregates on microfluidic chips for highly sensitive SERS detection of biomolecules. Anal Bioanal Chem 402(4):1601–1609
57. Lin L et al (2016) Light-directed reversible assembly of plasmonic nanoparticles using plasmon-enhanced thermophoresis. ACS Nano 10(10):9659–9668
58. Righini M et al (2009) Nano-optical trapping of rayleigh particles and *Escherichia coli* bacteria with resonant optical antennas. Nano Lett 9(10):3387–3391
59. Huang L, Maerkl SJ, Martin OJF (2009) Integration of plasmonic trapping in a microfluidic environment. Opt Express 17(8):6018–6024
60. Shoji T et al (2013) Permanent fixing or reversible trapping and release of DNA micropatterns on a gold nanostructure using continuous-wave or femtosecond-pulsed near-infrared laser light. J Am Chem Soc 135(17):6643–6648
61. Nicoli F et al (2014) DNA translocations through solid-state plasmonic nanopores. Nano Lett 14(12):6917–6925
62. Pang Y, Gordon R (2011) Optical trapping of a single protein. Nano Lett 12(1):402–406
63. Zehtabi-Oskuie A et al (2013) Double nanohole optical trapping: dynamics and protein-antibody co-trapping. Lab Chip 13(13):2563–2568
64. Al Balushi, A.A. And R. Gordon A label-free untethered approach to single-molecule protein binding kinetics. Nano Lett, 2014. 14(10): p. 5787–5791

65. Ndukaife JC et al (2015) Long-range and rapid transport of individual nano-objects by a hybrid electrothermoplasmonic nanotweezer. Nat Nanotechnol 11:53. Advance online publication
66. Berthelot J et al (2014) Three-dimensional manipulation with scanning near-field optical nanotweezers. Nat Nanotechnol 9(4):295–299
67. Ndukaife JC, Shalaev VM, Boltasseva A (2016) Plasmonics-turning loss into gain. Science 351(6271):334–335
68. Lin L et al (2017) Thermophoretic tweezers for low-power and versatile manipulation of biological cells. ACS Nano 11:3147
69. Kang T et al (2010) Patterned multiplex pathogen DNA detection by Au particle-on-wire SERS sensor. Nano Lett 10(4):1189–1193
70. Huang C et al (2012) Gold nanoring as a sensitive plasmonic biosensor for on-chip DNA detection. Appl Phys Lett 100(17):173114
71. Ngo HT et al (2013) Label-free DNA biosensor based on SERS molecular sentinel on nanowave chip. Anal Chem 85(13):6378–6383
72. Wang H-N, Fales AM, Vo-Dinh T (2015) Plasmonics-based SERS nanobiosensor for homogeneous nucleic acid detection. Nanomedicine 11(4):811–814
73. Homola J (2008) Surface plasmon resonance sensors for detection of chemical and biological species. Chem Rev 108(2):462–493
74. Wang H-N et al (2013) Molecular sentinel-on-chip for SERS-based biosensing. Phys Chem Chem Phys 15(16):6008–6015
75. Ngo HT et al (2014) Multiplex detection of disease biomarkers using SERS molecular sentinel-on-chip. Anal Bioanal Chem 406(14):3335–3344
76. Ngo HT et al (2014) DNA bioassay-on-chip using SERS detection for dengue diagnosis. Analyst 139(22):5656–5660
77. Mukherji S et al (2011) MicroRNAs can generate thresholds in target gene expression. Nat Genet 43(9):854–859
78. Lu J et al (2005) MicroRNA expression profiles classify human cancers. Nature 435 (7043):834–838
79. Volinia S et al (2006) A microRNA expression signature of human solid tumors defines cancer gene targets. Proc Natl Acad Sci U S A 103(7):2257–2261
80. Jeffrey SS (2008) Cancer biomarker profiling with microRNAs. Nat Biotechnol 26(4):400–401
81. Arata H, Hosokawa K, Maeda M (2014) Rapid sub-attomole microRNA detection on a portable microfluidic chip. Anal Sci 30(1):129–135
82. Joshi GK et al (2014) Highly specific plasmonic biosensors for ultrasensitive microRNA detection in plasma from pancreatic cancer patients. Nano Lett 14(12):6955–6963
83. Joshi GK et al (2015) Label-free nanoplasmonic-based short noncoding RNA sensing at attomolar concentrations allows for quantitative and highly specific assay of microRNA-10b in biological fluids and circulating exosomes. ACS Nano 9(11):11075–11089
84. Choi S et al (2011) Monitoring protein distributions based on patterns generated by protein adsorption behavior in a microfluidic channel. Lab Chip 11(21):3681–3688
85. Masson J-F, Zhao SS (2015) Plasmonic sensors for analysis of proteins and an oncologic drug in human serum. In: Vestergaard MDC et al (eds) Nanobiosensors and nanobioanalyses. Springer Japan, Tokyo, pp 305–333
86. Uludag Y, Tothill IE (2012) Cancer biomarker detection in serum samples using surface plasmon resonance and quartz crystal microbalance sensors with nanoparticle signal amplification. Anal Chem 84(14):5898–5904
87. Acimovic SS et al (2014) LSPR chip for parallel, rapid, and sensitive detection of cancer markers in serum. Nano Lett 14(5):2636–2641
88. Chen P et al (2015) Multiplex serum cytokine immunoassay using nanoplasmonic biosensor microarrays. ACS Nano 9(4):4173–4181
89. Lee M et al (2012) SERS-based immunoassay using a gold array-embedded gradient microfluidic chip. Lab Chip 12(19):3720–3727

90. He J et al (2015) Patterned plasmonic nanoparticle arrays for microfluidic and multiplexed biological assays. Anal Chem 87(22):11407–11414
91. Ahijado-Guzmán R et al (2014) Plasmonic nanosensors for simultaneous quantification of multiple protein–protein binding affinities. Nano Lett 14(10):5528–5532
92. Wu SH et al (2013) Optofluidic platform for real-time monitoring of live cell secretory activities using Fano resonance in gold nanoslits. Small 9(20):3532–3540
93. Pallaoro A et al (2015) Rapid identification by surface-enhanced Raman spectroscopy of cancer cells at low concentrations flowing in a microfluidic channel. ACS Nano 9(4):4328–4336
94. Liu Y et al (2015) Surface plasmon resonance biosensor based on smart phone platforms. Sci Rep 5:12864
95. Pimkova K et al (2012) Surface plasmon resonance biosensor for the detection of VEGFR-1-a protein marker of myelodysplastic syndromes. Anal Bioanal Chem 402(1):381–387
96. He P et al (2014) Ultrasensitive detection of thrombin using surface plasmon resonance and quartz crystal microbalance sensors by aptamer-based rolling circle amplification and nanoparticle signal enhancement. Chem Commun 50(12):1481–1484
97. Truong PL, Kim BW, Sim SJ (2012) Rational aspect ratio and suitable antibody coverage of gold nanorod for ultra-sensitive detection of a cancer biomarker. Lab Chip 12(6):1102–1109
98. Zijlstra P, Paulo PMR, Orrit M (2012) Optical detection of single non-absorbing molecules using the surface plasmon resonance of a gold nanorod. Nat Nanotechnol 7(6):379–382
99. Ament I et al (2012) Single unlabeled protein detection on individual plasmonic nanoparticles. Nano Lett 12(2):1092–1095
100. Al Balushi AA, Zehtabi-Oskuie A, Gordon R (2013) Observing single protein binding by optical transmission through a double nanohole aperture in a metal film. Biomed Opt Express 4(9):1504–1511
101. Im H et al (2012) Nanohole-based surface plasmon resonance instruments with improved spectral resolution quantify a broad range of antibody-ligand binding kinetics. Anal Chem 84(4):1941–1947
102. Cetin AE et al (2014) Handheld high-throughput plasmonic biosensor using computational on-chip imaging. Light Sci Appl 3:e122
103. Soler M et al (2016) Label-free nanoplasmonic sensing of tumor-associate autoantibodies for early diagnosis of colorectal cancer. Anal Chim Acta 930:31–38
104. Escobedo C et al (2013) Quantification of ovarian cancer markers with integrated microfluidic concentration gradient and imaging nanohole surface plasmon resonance. Analyst 138(5):1450–1458
105. Ruemmele JA et al (2013) A localized surface plasmon resonance imaging instrument for multiplexed biosensing. Anal Chem 85(9):4560–4566
106. Couture M et al (2016) 96-well plasmonic sensing with nanohole arrays. ACS Sensors 1(3):287–294
107. Saha A, Jana NR (2015) Paper-based microfluidic approach for surface-enhanced Raman spectroscopy and highly reproducible detection of proteins beyond picomolar concentration. ACS Appl Mater Interfaces 1:996–1003
108. Chon H et al (2010) On-chip immunoassay using surface-enhanced Raman scattering of hollow gold nanospheres. Anal Chem 82(12):5290–5295
109. Hwang H et al (2010) Optoelectrofluidic sandwich immunoassays for detection of human tumor marker using surface-enhanced raman scattering. Anal Chem 82(18):7603–7610
110. Lee M et al (2011) Highly reproducible immunoassay of cancer markers on a gold-patterned microarray chip using surface-enhanced Raman scattering imaging. Biosens Bioelectron 26(5):2135–2141
111. Zou K et al (2016) Picomolar detection of carcinoembryonic antigen in whole blood using microfluidics and surface-enhanced Raman spectroscopy. Electrophoresis 37(5–6):786–789
112. Kaminska A et al (2015) Detection of hepatitis B virus antigen from human blood: SERS immunoassay in a microfluidic system. Biosens Bioelectron 66:461–467

113. Yanik AA et al (2010) An optofluidic nanoplasmonic biosensor for direct detection of live viruses from biological media. Nano Lett 10(12):4962–4969
114. Walter A et al (2011) Towards a fast, high specific and reliable discrimination of bacteria on strain level by means of SERS in a microfluidic device. Lab Chip 11(6):1013–1021
115. Tokel O et al (2015) Portable microfluidic integrated plasmonic platform for pathogen detection. Sci Rep 5:9152
116. Andreou C et al (2013) Rapid detection of drugs of abuse in saliva using surface enhanced Raman spectroscopy and microfluidics. ACS Nano 7(8):7157–7164
117. Inci F et al (2013) Nanoplasmonic quantitative detection of intact viruses from unprocessed whole blood. ACS Nano 7(6):4733–4745
118. Wang S et al (2012) Portable microfluidic chip for detection of *Escherichia coli* in produce and blood. Int J Nanomedicine 7:2591–2600
119. Durmus NG et al (2013) Fructose enhanced reduction of bacterial growth on nanorough surfaces. MRS Proc 1498:73–78
120. Tasoglu S et al (2013) Manipulating biological agents and cells in micro-scale volumes for applications in medicine. Chem Soc Rev 42(13):5788–5808
121. Wang S et al (2010) Label-free imaging, detection, and mass measurement of single viruses by surface plasmon resonance. Proc Natl Acad Sci 107(37):16028–16032
122. Florschütz K et al (2013) 'Phytochip': on-chip detection of phytopathogenic RNA viruses by a new surface plasmon resonance platform. J Virol Methods 189(1):80–86
123. Srivastava SK et al (2015) Highly sensitive and specific detection of E. Coli by a SERS nanobiosensor chip utilizing metallic nanosculptured thin films. Analyst 140(9):3201–3209
124. Olaru A et al (2015) Surface plasmon resonance (SPR) biosensors in pharmaceutical analysis. Crit Rev Anal Chem 45(2):97–105
125. Chen S et al (2012) Visualization of high-throughput and label-free antibody-polypeptide binding for drug screening based on microarrays and surface plasmon resonance imaging. J Biomed Opt 17(1):0150051–0150058
126. Izake EL (2007) Chiral discrimination and enantioselective analysis of drugs: an overview. J Pharm Sci 96(7):1659–1676
127. Guo L et al (2012) Enantioselective analysis of melagatran via an LSPR biosensor integrated with a microfluidic chip. Lab Chip 12(20):3901–3906
128. Wu Z, Zheng YB (2017) Moiré chiral metamaterials. Adv Opt Mater 5. (in Press)
129. Narsaiah K et al (2012) Optical biosensors for food quality and safety assurance – a review. J Food Sci Technol 49(4):383–406
130. Fernandez F et al (2010) A label-free and portable multichannel surface plasmon resonance immunosensor for on site analysis of antibiotics in milk samples. Biosens Bioelectron 26(4):1231–1238
131. Zhao SS et al (2015) Miniature multi-channel SPR instrument for methotrexate monitoring in clinical samples. Biosens Bioelectron 64:664–670

Upconversion Nanomaterials for Biodetection and Multimodal Bioimaging Using Photoluminescence

6

Ming-Kiu Tsang, Yuen-Ting Wong, and Jianhua Hao

Contents

1 Definition of Topic

Lanthanide-doped upconversion nanomaterials are suitable for biological applications because of their near-infrared excitation property. The excitation wavelength is within the first biological window; therefore this can minimize the damage to biological samples for biomedical applications. Apart from upconversion luminescence, the doped lanthanide ions display inherent physical properties for multimodal bioimaging. The advance in nanotechnology also provides an opportunity for the synthesis of novel upconversion nanomaterial-based nanocomposites. Those hybrid

M.-K. Tsang · Y.-T. Wong · J. Hao (✉)
Department of Applied Physics, The Hong Kong Polytechnic University, HKSAR, Hung Hom, China
e-mail: jh.hao@polyu.edu.hk

C. S. S. R. Kumar (ed.), *Nanotechnology Characterization Tools for Biosensing and Medical Diagnosis*, https://doi.org/10.1007/978-3-662-56333-5_6

structures further increase the number of modalities for biodiagnostic applications. In this chapter, we introduce the key features of lanthanide-doped nanomaterials and review the recent progress in biodetection and multimodal bioimaging.

2 Overview

Photon upconversion nanomaterials are rapidly emerging in recent years owing to their unique luminescent property. Many efforts have been focused on the synthesis and surface modifications to meet the demands for biological applications. Moreover, different nanocomposite structures were formed by state-of-the-art surface chemistry. Biodetection and multimodal bioimaging are two important fields among these applications, because of the ability to visualize and analyze biological species in vitro or in vivo. First, this chapter will provide the background of lanthanide-doped upconversion nanomaterials. After that, the brief information about synthesis, surface modifications, and instrumentations will be summarized. The third part will review the recent works on biodetection and multimodal bioimaging. Finally, the chapter will be ended by illustrating the directions for future research and the current challenges faced by lanthanide-doped upconversion nanomaterials in biodetection and multimodal bioimaging.

3 Introduction

Rapid, low-cost, and sensitive biodetection system is greatly desirable, by considering the outbreak of lethal viruses and early-stage treatments. Luminescent-based assays have been regarded as a powerful tool for detection because of their high sensitivity. The conventional luminescence assays mainly rely on ultraviolet (UV)-excited emission from semiconductor quantum dots (QDs) [1–3]. However, the excitation wavelengths will pose damage to the structure of DNAs, and those damages are well-documented in literature [4]. Moreover, high-energy excitation also showed shallow penetration depths in bioimaging because of the high absorption coefficient of water and red blood cells in living animals [5]. These drawbacks paved the way for the emergence of lanthanide-doped upconversion nanocrystals (UCNCs[1]) for biodetection and bioimaging applications.

The lanthanide (Ln^{3+}) ions in UCNCs consist of partially filled inner 4f subshell and a fully filled outermost shell. The electronic configurations of the 4f orbitals present ladder-like and long-lived energy states [6]. As a result, this can facilitate sequential absorption of near-infrared (NIR) photons for upconversion luminescence (UCL). The NIR excitation falls into the biological window, and hence this allows deep penetration of excitation energy to reach the UCNCs in various biological systems. It is also important to note that the fully filled shell can shield the Ln^{3+} ions from the external environment; thus the physical properties of these elements are

[1]UCNCs and UCNPs are referred to the same material in this book chapter.

very stable. Apart from UCL, the Ln^{3+} ions also exhibit X-ray absorption property, and gadolinium ions even possess magnetism [7]. Thus, the Ln^{3+} ions doped UCNCs can be used for X-ray imaging and magnetic resonance imaging (MRI). In principle, an inorganic host material will be chosen for accommodating the doped Ln^{3+} ions in suitable proportions to realize efficient UCL. The host is usually chosen based on their lowest phonon energy [8]. To date, fluoride-based UCNCs are very popular, such as $NaYF_4$ [9–12], $NaGdF_4$ [13–15], and $NaYbF_4$ [16–18], because of their low phonon energy, high stability, and low cytotoxicity. The energy transfer upconversion is one of the popular UCL systems because of the high UCL efficiency, ytterbium (Yb), or neodymium (Nd) ions that are used to harvest the NIR photons, while a series of ions, for example, erbium (Er), thulium (Tm), and holmium (Ho), are used as activator ions to realize multicolor emissions. The development of core-shell (cs) structure brought new understandings to UCL because of the ability to spatially separate the Ln^{3+} ions [19]. The new strategy can not only tune the emission through energy migration from core to shell but also foster the doping of Nd^{3+} ions [20]. The doping of Nd^{3+} ions in the shell can shift the excitation wavelength from 980 to 808 nm; this can further enhance the penetration depth and avoid the heating effect to living cells and animals.

Despite the inherent physical properties of Ln^{3+} ions for multimodal bioimaging, those imaging modes cannot fully meet the requirements for demanding clinical imaging applications. Therefore, external moieties, ligands, or isotopes are needed to conjugate onto the surface of UCNCs for composite structures [21]. Surface modification is the fundamental knowledge for fabricating nanocomposites. The surface modifications of UCNCs had been extensively reviewed by many research groups and journals [22–27]; readers may refer to these references for more information. Our chapter discusses and reviews multimodal bioimaging and biodetection, considering the wide spectrum of biological applications of upconversion nanomaterials. Therefore, the style of this chapter can be easier for the readers to follow the latest trend of the topics in biodetection and multimodal bioimaging. Moreover, our chapter includes the experimental route and procedures for obtaining upconversion nanomaterials in a comprehensive way, while others only mentioned the principle of the synthesis briefly. A number of clinical imaging techniques, such as positron emission tomography (PET), single-photon emission computed tomography (SPECT), ultrasound imaging (USI), and photoacoustic imaging (PAI), are recently demonstrated by UCNCs-based composites. Examples will be given and further discussed in Sect. 5.1. Apart from multimodal bioimaging, the inherent luminescent properties of Ln^{3+} ions are also beneficial to sensitive and specific biodetection. The Ln^{3+} ions emit long-lived and narrowband UCL emissions; this can facilitate time-resolved biodetection by avoiding the short-lived background fluorescence. At the same time, the narrowband emissions can effectively prevent the false-positive detection signals from the quenchers in typical luminescent resonance energy transfer (LRET) or fluorescence resonance energy transfer (FRET) systems. Moreover, luminescent biodetection systems can be categorized as homogeneous and heterogeneous assays [6]. Homogeneous assays are simple, fast, and usually performed in a liquid phase without the need for washing. Therefore, it has

attracted substantial attention and being employed in a spectrum of assays [28–33]. Alternatively, heterogeneous assays are usually performed on a solid-state platform. They can enable specific recognition and high affinity between the capturing probe and the detection target; therefore the sensitivity of the type of assay is usually higher than that of homogeneous assays [34–37]. Despite the advantages, one should note that heterogeneous assays are relatively laborious and the preparation steps are tedious [38]. More examples will be provided and reviewed to further elaborate the development of biosensors in Sect. 5.2. Finally, the book chapter will be ended by conclusions and future perspectives.

4 Experimental Methodology

In this section, the essential synthetic steps in coprecipitation of $NaGdF_4$:Yb/Er@$NaGdF_4$:Yb/Nd csUCNCs will be introduced. The use of csUCNCs can not only enhance the emission intensity [39] but also enable the use of 808 nm excitation to minimize laser-heating effect to water [40]. Then, we introduce basic surface modifications for hydrophilicity. Although thermal decomposition [13, 35, 41, 42] and one-step hydrothermal synthesis [29, 36, 43–47] are common synthetic routes for UCNCs, the scope of this chapter is focused on the recent works in multimodal bioimaging and biodetection. Moreover, we have chosen the ligand-free treatment followed by polyacrylic acid (PAA) modification as an experimental example when considering the steps that are easy, and carboxylic acid is a useful functional group for further bioconjugations.

4.1 Synthesis of Core $NaGdF_4$:Yb/Er UCNCs

In a typical coprecipitation synthesis, 0.4 mmol Ln^{3+} acetates, including Gd, Yb, and Er, 4 ml oleic acid (OA), and 6 ml 1-octadecene (1-ODE) were mixed in a three-necked flask. The temperature was increased to 150 °C for 1 h to form Ln^{3+} oleate complex. After the mixture was cooled down to room temperature, 1 mmol sodium hydroxide and 1.3 mmol ammonium fluoride in methanol were injected into the reaction mixture under vigorous stirring. Then, the temperature was raised to 50 °C for removal of methanol and nucleation for 30 min. After that, the temperature was further increased to 100 °C for 10 min to degas the reaction mixture. Then, argon gas was purged via the dual gas manifold to protect the medium. The temperature was subsequently increased to 290 °C for 1.5 h. Finally, the reaction mixture was cooled down to room temperature under argon gas protection. The crude UCNCs were purified by cyclohexane and ethanol using centrifugation. After centrifugation for twice, the OA-capped core UCNCs were dispersed in cyclohexane for further use.

4.2 Synthesis of $NaGdF_4$:Yb/Er@$NaGdF_4$:Yb/Nd csUCNCs

For coating the shell, 0.4 mmol Ln^{3+} acetates, including gadolinium (Gd), ytterbium (Yb), and neodymium (Nd), 4 ml oleic acid (OA), and 6 ml 1-octadecene (1-ODE)

were mixed in a three-necked flask. The temperature was increased to 150 °C for 1 h to form Ln^{3+} oleate complex. After the mixture was cooled to room temperature, the core UCNCs in cyclohexane was transferred into the flask. Then, 1 mmol sodium hydroxide and 1.3 mmol ammonium fluoride in methanol were injected into the reaction mixture under vigorous stirring. Then, the temperature was raised up to 50 °C for removal of methanol and nucleation for 30 min. After that, the temperature was further increased to 100 °C for 10 min to degas the reaction mixture. Argon gas was purged via the dual gas manifold to protect the medium. The temperature was subsequently increased to 290 °C for 1.5 h. Finally, the reaction mixture was cooled to room temperature under argon protection. The crude UCNCs were purified by cyclohexane and ethanol using centrifugation. After centrifugation for twice, the OA-capped csUCNCs were dispersed in cyclohexane for further use.

4.3 Ligand-Free Modification of csUCNCs for Hydrophilicity

The hydrophilicity of csUCNCs is indispensable for bio-applications. This can be simply achieved by removing the hydrophobic surface oleate after successive washing the as-synthesized csUCNCs with 2 M hydrochloric acid in the presence of ethanol, water, and cyclohexane, followed by high-speed centrifugation for 30 min. The color of the csUCNCs obviously changed from brownish yellow to transparent, and the ligand-free products can be dispersed in water to form stable colloid due to the highly positive charged surface [48].

4.4 PAA Modification of csUCNCs

The as-prepared ligand-free sample can be capped with PAA due to the strong interaction between the positively charged surface and PAA. Briefly, PAA is dispersed in deionized (DI) water with 1 M sodium hydroxide. Then, ligand-free csUCNCs were added and stirred for 24 h. Then, the PAA-capped csUCNCs were purified by DI water under high speed centrifugation. The PAA-capped csUCNCs were ready for further surface modifications [49].

4.5 Photoluminescent Measurement and Surface Characterizations

The UCL property of the as-prepared PAA-UCNCs can be measured by photoluminescent technique. The excitation source was either a continuous wave (CW) 980 or 808 nm laser. The measurement was carried out in a commercial Edinburgh Instrument FLSP920 spectrometer (Fig. 6.1a). The detailed configuration of the photoluminescence spectra/lifetime measurement is shown in Fig. 6.1b. The diode laser is aligned at a perpendicular geometry with respect to the detector path.

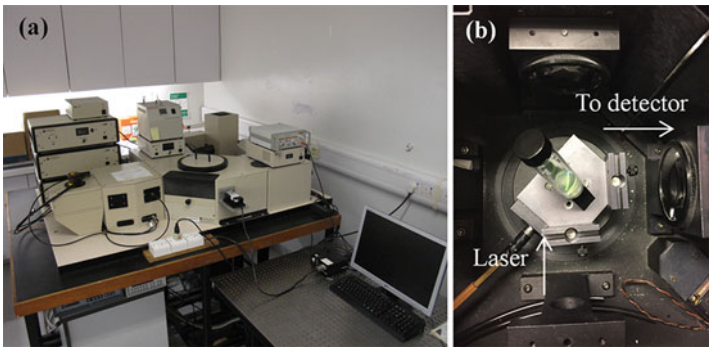

Fig. 6.1 (**a**) Photograph of Edinburgh Instrument FLSP920 spectrometer and (**b**) configuration for measuring photoluminescent spectrum of UCNCs; note that the laser is aligned perpendicularly to the optical path to detector

The dispersed UCNCs were loaded into a cuvette cell and placed at the sample holder.

In addition to possessing favorable optical property, surface functional groups are essential for tumor targeting and bioconjugation for multimodal bioimaging and biodetection, respectively. Fourier transform infrared (FTIR) spectrometry and zeta potential (ξ) measurement can evident the presence of specific surface groups. The FTIR spectrometer Vortex 70 from Bruker is shown in Fig. 6.2. The FTIR technique utilizes the absorption property of the organic bonding in the functional group to reveal the functional groups.

The Zetasizer from Malvern is shown in Fig. 6.3a; the folded capillary zeta cell (Fig. 6.3b) is used to carry 1 ml of the liquid-phase sample of the UCNCs for measurement. It is important to note that the cell is not suitable for using cyclohexane as solvent. The ξ provides the polarity of the surface to further support the existence of specific functional groups.

5 Key Research Findings

5.1 Multimodal Bioimaging Based on UCNCs

The inherent imaging modes of UCNCs are limited to UCL, MRI, and X-ray imaging owing to the doping of Ln^{3+} ions. Different functional molecules or ligands were integrated with UCNCs to form UC-based composites, meeting the increasing demand for clinical imaging modes, such as PET, SPECT, USI, and PAI. The motivation for developing multimodal bioimaging is the synergetic imaging effect so that one of the imaging modes in those systems can compensate the weakness of the others. This section will review the recent examples of multimodal bioimaging based on different combinations.

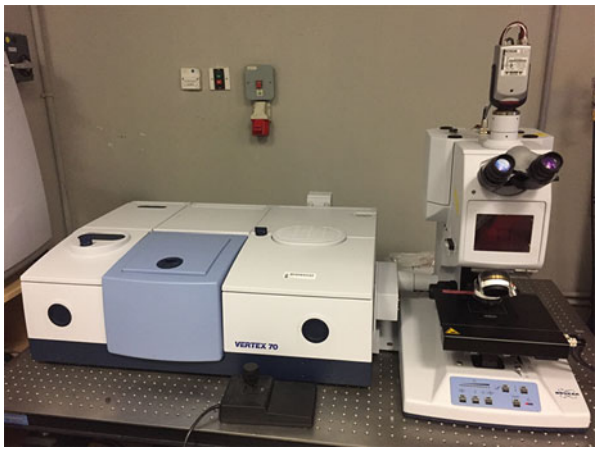

Fig. 6.2 Bruker Vortex 70 FTIR spectrometer, the system comprises of NIR and MIR light source for measurement. The MIR configuration is used for the investigation of surface organic groups on UCNCs

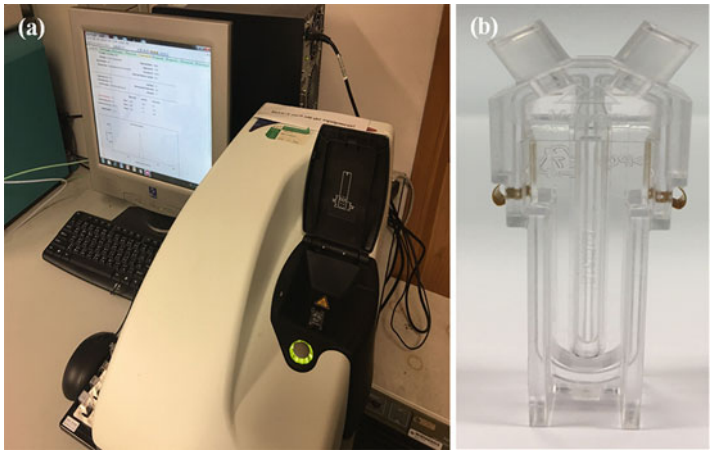

Fig. 6.3 (**a**) Zetasizer from Malvern for ξ measurement and (**b**) folded capillary zeta cell with electrodes for ξ measurement

5.1.1 Bimodal UCL and MRI System

UCL imaging is able to provide high spatial resolution and high sensitivity, but the imaging depth is relatively shallow compared to other imaging modes. MRI is a well-known imaging technique that offers high-resolution, noninvasive, and three-dimensional (3D) structural and functional information. The magnetic moments in hydrogen nuclei align along a uniform magnetic field, and a radio frequency (RF) signal will operate at the resonant frequency of the nuclei. The removal of the RF signal results in the relaxation and realignment of the nuclei. Such relaxation will emit RF signal to be measured by a conductive field coil for reconstruction of 3D MR images. However, it is important to note that MRI is further divided into T1-weighted and T2-weighted MRI which can be distinguished by the

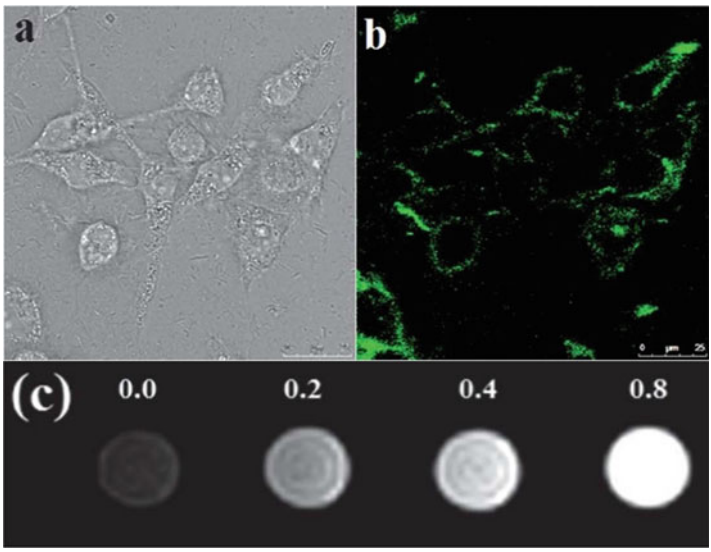

Fig. 6.4 (**a**) Bright field and (**b**) green UC fluorescent (500–600 nm) in vitro images of 100 mg mL^{-1}amine-functionalized $BaGdF_5$:Yb/Er colloidal UCNCs in HeLa cells after 24 h incubation. (**c**) T1-weighted images of $BaGdF_5$:Yb/Er UCNCs with different concentrations (mM) in water (Adapted from Ref. [46] with permission. Copyright © 2012, Royal Society of Chemistry)

relaxation mode. T1 relaxation mode measures the time required for recovery of longitudinal magnetization, while T2 relaxation mode measures time for the decay of transverse magnetization. Nevertheless, both mechanisms can provide contrast for diagnosis in MRI [50]. Our group had explored the magnetism of $Gd_2O_3:Eu^{3+}$ at different temperatures [51]. The underlying physics of the paramagnetic property of Gd^{3+} in the host was investigated at 77 and 293 K. The difference in magnetization can be ascribed to the reduced thermal fluctuation. In addition, we reported a dual mode UCL/T1-MRI bioimaging system based on amine-functionalized $BaGdF_5$:Yb/Er UCNCs [46]. Fig. 6.4 shows that the UCNCs can label HeLa cells under NIR excitation and present large longitudinal relaxation due to UCL and the paramagnetic property of the doped Ln^{3+} ions. It is worthwhile to note that surface passivation by polyethylene glycol (PEG) is preferred for in vivo investigations because PEG can increase the circulation time in the microenvironment and prevent non-specific bindings [52–56]. In a later work, Liu et al. reported a PEGylated $NaGdF_4$:Yb/Er UCNCs with antibody targeting function to image intraperitoneal tumors and subcutaneous tumors [57]. The proof-of-concept system showed promising tumor UCL imaging and T1-weighted MRI results by comparing the bare PEGylated UCNCs, antibody-modified PEGylated UCNCs, and commercialized Gd-DPTA. Owing to the active targeting ability of the antibody, the MRI contrast was greatly enhanced; this was supported by the strongly shortened T1 values. Moreover, they investigated the clearance of UCNCs by collecting the feces and urine of the mice and estimated a biological halftime of

the UCNCs of 1.4 d. Apart from T1-weighted MRI, UCNC-iron oxide-based nanocomposites were reported for T2-weighted MRI because of the strong transverse relaxation rate [58, 59]. Recently, Lee et al. reported the use of antibody-modified $NaYF_4$:Yb/Nd/Er@$NaYF_4$:Nd csUCNCs for hepatocellular carcinoma (HCC) UCL/T2-weighted MRI in an orthotopic rat model [60]. Nd^{3+} ion doping can not only harvest 808 nm laser excitation but also endow paramagnetic property to the system for MRI. They systematically proved the ability of the Nd^{3+}-doped csUCNCs and compared with ferumoxytol, which is a T2-weighted MRI contrast agent under clinical trial. Their proof-of-concept design was subsequently used in a tumor-bearing mouse for HCC surgical resection guided by UCL/T2-weighted MRI. Their results indicated that the strategy may potentially aid the surgeons' visual assessment of the surgical bed.

5.1.2 Bimodal UCL and PET or SPECT

PET scan is a well-known clinical bioimaging technique to reveal the functional information of organs. The use of radioactive isotopes and PET-CT scanner is essential to collect signal and render 3D information. Li's group presented a systematic study of fluorine-18 (^{18}F) decoration on various types of Ln^{3+} ion-doped NCs for UCL/PET [61]. The ^{18}F isotopes were attached onto the NCs due to the strong binding to Ln^{3+} ions, and only 1 min sonication was required to yield high loading of ^{18}F. ^{18}F–$NaYF_4$:Yb/Tm UCNCs were chosen for PET scan, and such scanning can reveal the real-time biodistribution of the injected UCNCs. The lymph node imaging was carried out by subcutaneously injecting at the right paw of the mice. Intense peak PET signal was detected at 30 min post-injection until 60 min (Fig. 6.5). The results indicated that the ^{18}F–UCNCs offered new opportunities for future PET scan contrast agent. On the other hand, SPECT requires radioactive tracer, which emits gamma ray photons. Subsequently, the emissions were collected by a gamma camera for 3D construction of the images. The functional information of organs can also be revealed by this type of imaging technique. For this point, one should notice that PET and SPECT are similar, yet the key difference between PET and SPECT is the use of different lifetime radioactive tracers. The lifetime of the former is shorter than the latter because of the required scanning time. The study of biodistribution of PEG-modified ^{153}Sm-$NaLuF_4$:Yb/Er UCNCs was done by Li's group (Fig. 6.6) [62]. They explored a useful strategy for changing the metabolism of nanoparticles from a liver/spleen pathway to kidney/urine pathway. In a parallel work, they reported a dual modal UCL/SPECT bioimaging system based on EDTMP-capped ^{153}Sm-$NaLuF_4$:Yb/Tm UCNCs for blood pool imaging [63]. Due to the small atomic radii of ^{153}Sm, they can be easily doped into the UCNCs without dissociation. After 30 min postinjection, the carotid artery, vertebral arteries, and superior epigastric artery of the mice were all clearly imaged. In addition, citrate-modified UCNCs and EDTMP-^{153}Sm complexes were prepared as control materials for comparing the circulation time with the EDTMP-modified UCNCs. The results indicated that EDTMP ligand but not the dissociated EDTMP-^{153}Sm moieties contribute to the extended circulation time of the UCNCs.

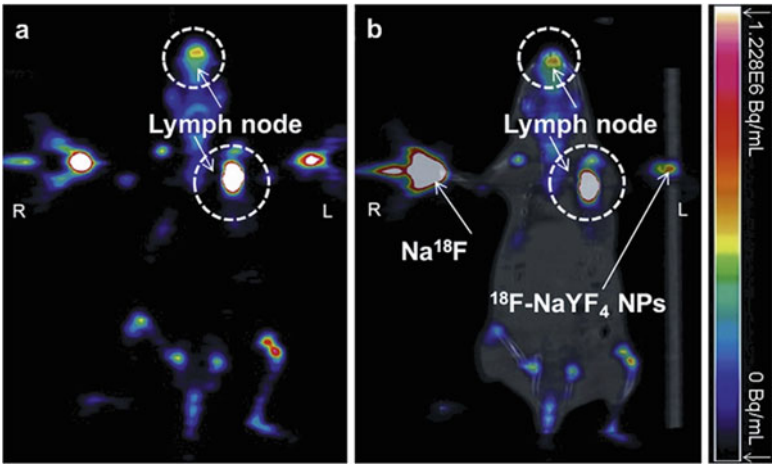

Fig. 6.5 (**a**) PET imaging and (**b**) PET/CT imaging of lymph node 30 min after subcutaneous injection of ^{18}F–UCNPs. 30 min after subcutaneous injection of 740 kBq/0.05 mL ^{18}F – UCNPs into the left paw footpad, signal in lymph node reached the peak intensity and maintained it to 60 min postinjection while as control-free $^{18}F^-$ ions injected into the right paw showed no lymphatic imaging ability (Reprinted from Ref. [61] with permission. Copyright © 2011, Elsevier)

5.1.3 Bimodal UCL and USI or PAI

USI is a well-established, simple, and noninvasive clinical imaging technique making use of the echogenicity of the tissues for imaging. Basically, US commonly sourced from a piezoelectric transducer is reflected by the targeted tissues, and the echo signals are collected to form the USI. Despite the noninvasive nature, USI is limited by the imaging depth. To overcome this challenge, lower-frequency US is needed; however images with lower resolution and poor contrast are resulted. It is also noted that some fluids of living animals, such as blood and urine, are not able to reflect US; in other words, these fluids are transparent to US and hardly produce delicate USI of the tissues. Therefore, the Food and Drug Administration (FDA)-approved microbubbles (MB) had been commercialized to meet the demand for USI contrast agents [64]. Jin et al. reported a bimodal UCL/USI contrast agent by attaching UCNCs to MBs via layer-by-layer assembly [65]. The conjugation was achieved via the electrostatic attraction of the negatively charged polyacrylic acid and the positively charged poly(allyl-amine hydrochloride). The conjugation was verified by the green UCL emission under 980 nm excitation. They further used a latex tube to stimulate the blood vessel of the human body, and enhanced US signal was observed. This work offers new opportunities for future in vivo applications. PAI is similar to USI because both imaging modes detect the acoustic wave for imaging. PAI is another emerging imaging technique in the recent year because of its high penetrating depth and high spatial resolution [66–68]. In brief, PAI is the merge of optical and acoustic imaging; the PA effect is based on the temperature rise-induced thermoelastic expansion. Such expansion produces ultrasonic waves

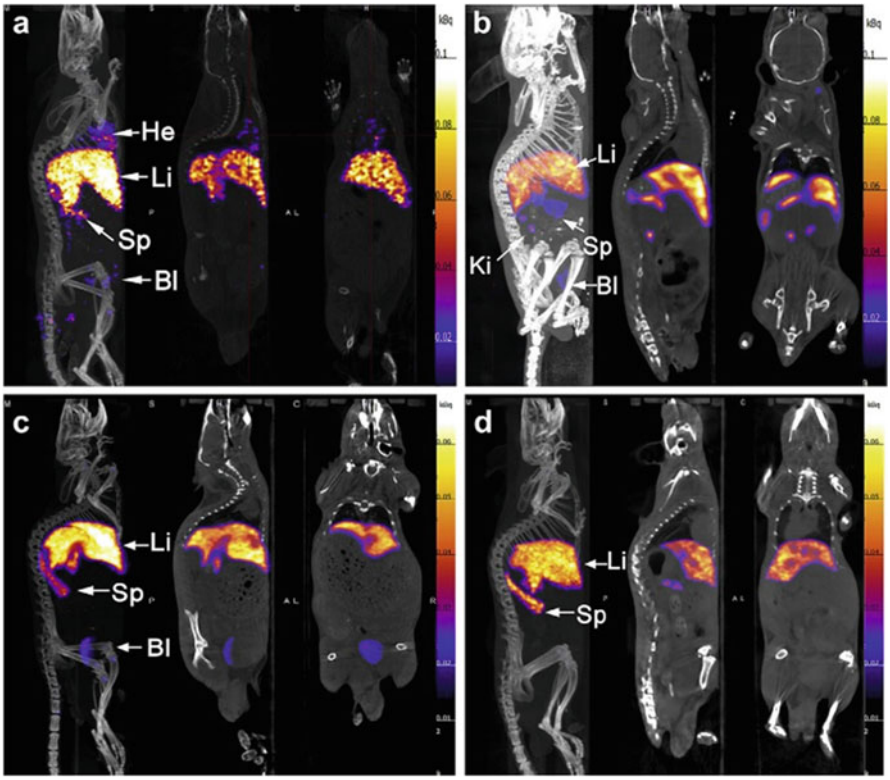

Fig. 6.6 SPECT/CT images in vivo of the Kunming mouse injected intravenously with 0.2 mL PEG-UCNPs(^{153}Sm) (2 mg/mL, 1 mCi injection/mouse) at (**a**) 0.5 h, (**b**) 1 h, (**c**) 6 h, and (**d**) 24 h. *He* heart, *Li* liver, *Sp* spleen, *Ki* kidney, *Bl* bladder (Reprinted with permission from Ref. [62]. Copyright © 2013, Elsevier)

which are subsequently transduced as imaging signal [66]. Some of the PAI-based diagnostic work needed no PA contrast agents because of the inherent PA property of the target, such as hemoglobin [69–71]. However, the use of contrast agents can enhance the contrast of the target to the background blood vessels and tissues. Moreover, contrast agents can be modified with targeting moieties or ligands for active targeting function. Early work in UCL particles-based PAI system indicated that the PA effect was due to the anisotropy and large aspect ratios [72]. In the same year, Maji et al. synthesized α-cyclodextrin (α-CD)-modified $NaYF_4$:Yb/Er UCNCs for dual modal UCL/PAI [73]. The α-CD is rationally an effective UCL quencher to give sufficient thermal expansion in water and induce PA effect. The in vivo experiment was carried out by using a nanosecond pulse laser operating at lower power so that any PA signals attributed to heating effect by 980 nm photons can be minimized. The modified UCNCs were found to uptake at the kidney of the mouse as shown in Fig. 6.7. This work opened the door for simple, low toxicity, and deep penetration UCL/PAI.

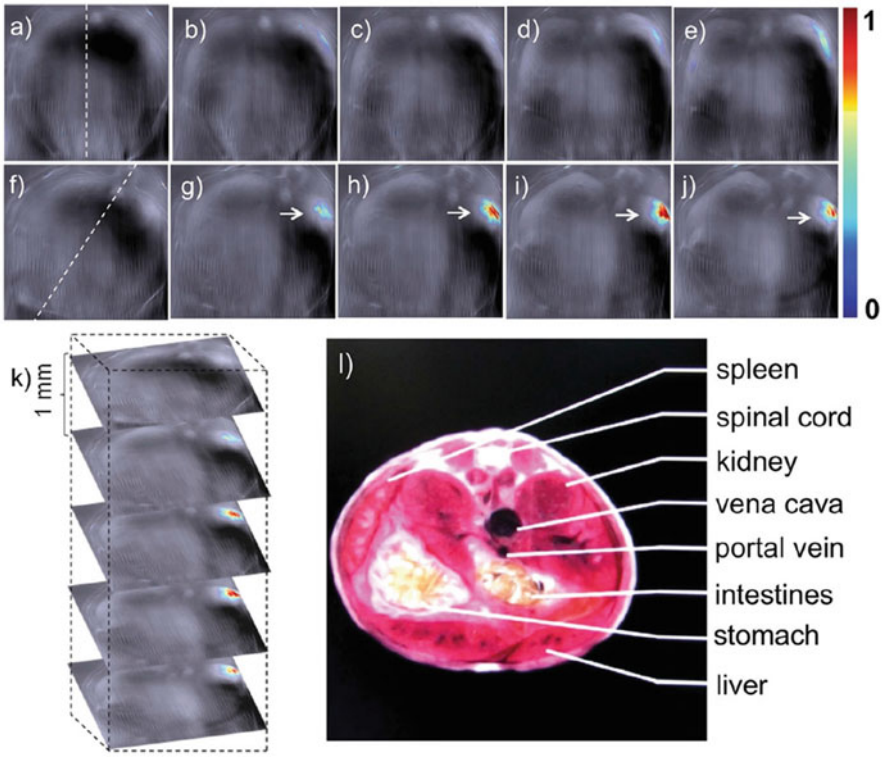

Fig. 6.7 Single-wavelength PAI of a live mouse anatomy at 980 nm. (**a**–**e**) Individual anatomy sections of the live mouse before intravenous injection of UC-α-CD. (**f**–**j**) Individual anatomy sections recorded after 35 min post-intravenous injection of UC-α-CD. Dashed lines in figures (**a**) and (**f**) indicate the positions of the mouse with respect to the viewer. Pointed areas in figures (**g**–**j**) indicate the localization of UC-α-CD. (**k**) Three-dimensional rendering of scanned area. (**l**) Schematic section corresponding to analyzed area (Adapted with permission from Ref. [73]. Copyright © 2014, Wiley)

5.1.4 Trimodal Imaging Systems: UCL, MRI, X-Ray, PET, SPECT, and PAI

The trimodal imaging systems provide additional modes compared to bimodal systems, for example, X-ray imaging cannot image soft tissue, while MRI can compensate such weakness. Therefore, trimodal bioimaging system based on these modes in UCNCs is commonly used by researchers for biodiagnostics [74–79]. Our group synthesized PEG-capped $BaGdF_5$:Yb/Er UCNCs for trimodal UCL/MRI/X-ray computed tomography (CT) by one-step hydrothermal method [44]. The simple design can integrate three modes in a single-phase material system, and the synthesis is low-cost and easy for implementation. The X-ray CT is more powerful than the ordinary X-ray imaging because of the ability to render 3D volumetric information of organs. Figure 6.8 shows the X-ray CT image of the mice after injection of PEG-UCNCs at 0–120 min. Initially, the bones of the mice were clearly seen, while no contrast was obtained in the soft tissues. At 120 min, the spleen of the mice was imaged, and the result also suggested

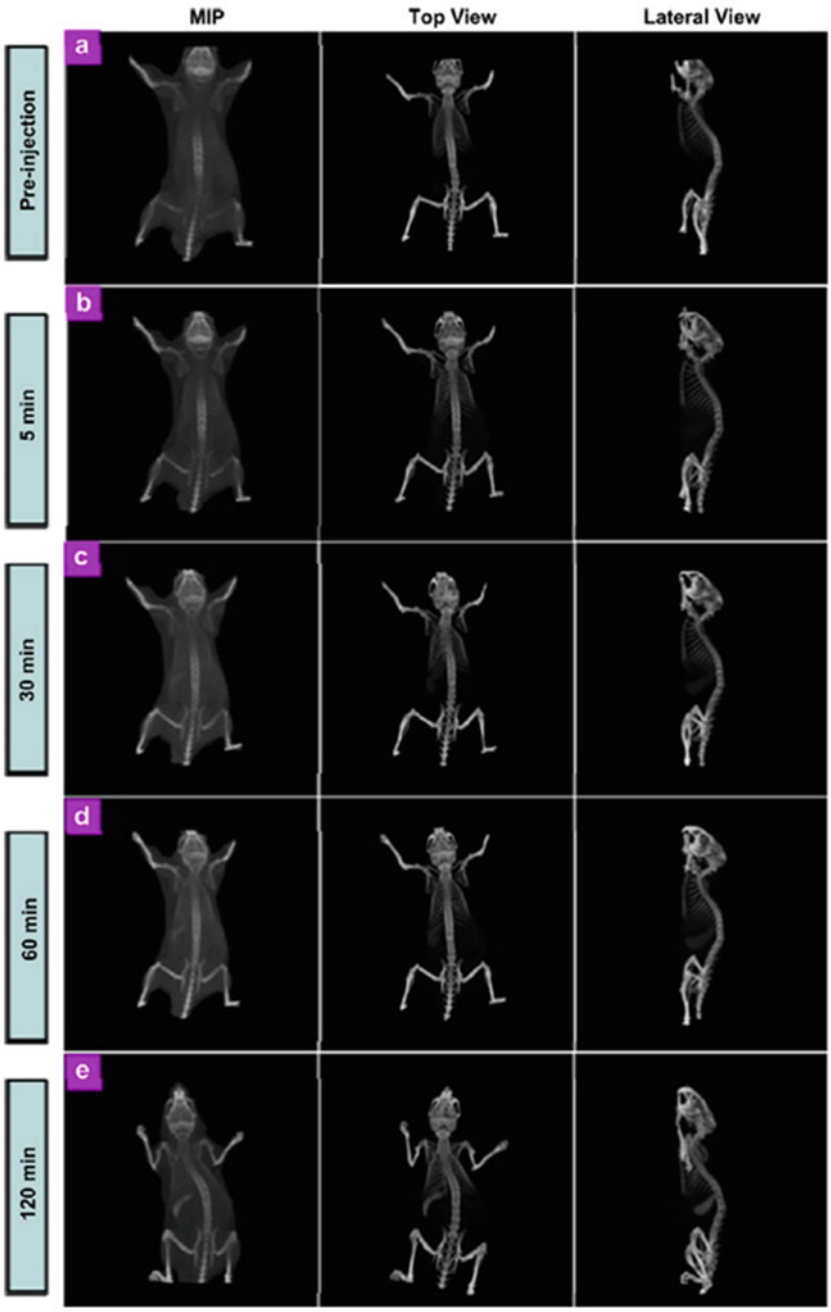

Fig. 6.8 In vivo X-ray CT imaging of a mouse before and after intravenous injection of 500 mL of PEG-modified $BaGdF_5$:Yb/Er UCNPs (0.05 M) at different time periods: (**a**) pre-injection, (**b**) 5 min, (**c**) 30 min, (**d**) 60 min, and (**e**) 120 min. The left panel: maximum intensity projection

that PEGylation can increase the circulation time. In a parallel work, Xing et al. prepared PEGylated NaY/GdF_4:Yb, Er, and Tm@SiO_2 csUCNCs decorated with gold nanoparticles (AuNPs) for trimodal imaging [80]. The addition of the silica shell layer can increase the biocompatibility and provide a versatile silane surface for further functionalization. In this case, the amine silane simply binds to AuNPs via electrostatic attraction. Apart from presenting the data from UCL, MRI, and X-ray CT images, they also worked on the Au/Y ratio for UCL intensity enhancement, in which the UCL intensity could be enhanced by 3–5 times when the Au/Y ratio was 0.274. Recently, Liu et al. showed that indocyanine green (ICG) decorated $NaYF_4$:Yb/Er@$NaYF_4$:Yb@$NaNdF_4$:Yb@$NaYF_4$@$NaGdF_4$ multi-shell UCNCs could be used for PAI/MRI/UCL imaging [81]. The system can avoid the heating effect due to 808 nm laser excitation, and ICG is a FDA-approved dye that can exhibit strong PA signal. In addition to typical UCL and MRI studies, the PAI capability of ICG was shown to be high because PA signal was detected from the concentration of 1 μg ml^{-1}. Their PAI results indicated that the system was able to image the small blood vessels under the skin with a distance range from around 4.8 to 10 mm.

5.1.5 Others

The number of imaging modes in a UCL-based nanocomposite could be more than three modes. Typically, Li's group reported the study of tumor angiogenesis by using a four-modal probe based on citrate-modified $NaLuF_4$:Yb/Tm@^{153}Sm-doped $NaGdF_4$ UCNCs, including UCL/X-ray CT/MRI/SPECT [82]. The monitoring of new blood vessels in tumors paved the way for early tumor diagnosis and better prognosis. The role of each imaging mode was distinct in this work. For example, X-ray CT and MRI revealed the structure of the tumor, the real-time quantification of the UCNCs at the tumor site was determined by using SPECT imaging, and the leaking of UCNCs from tumor vasculature was observed by UCL imaging. The study indicated that the four modalities in the UCNCs can be used for tumor angiogenesis. A recent work from Rieffel et al. showed that the imaging modality can be extended to six modes by using porphyrin-phospholipid (POP)-coated $NaYbF_4$:Tm@$NaYF_4$ with ^{64}Cu [83]. The system was able to demonstrate UCL/fluorescence (FL)/PAI/PET/X-ray CT/Cerenkov luminescence (CL). It was expected to be useful for the development of hyper-integrated imaging systems.

5.2 Luminescent Biodetections

Luminescent biodetection has been attracting substantial research attention because of their portability, ease of readout, simple operation, and high sensitivity.

Fig. 6.8 (continued) (MIP); the middle panel: the corresponding 3D volume-rendered (VR) in vivo CT images of mice; and the right panel: lateral view of 3D VR CT images (Reprinted with permission from Ref. [44]. Copyright © 2012, Elsevier)

UCL-based detection assays are more beneficial to the luminescent detections by minimizing the photodamage to linkages and biomolecules, false-positive readouts due to background, and autofluorescence. In practice, the figure of merits (FOM) to evaluate a biosensor is the limit of detection (LOD) and specificity. However, one should be aware of the differences in specific experimental conditions; such differences may affect both parameters significantly. This session will focus on reviewing the recent advances in the development of homogeneous and heterogeneous assays. Some works in homogenous detections had made breakthroughs by applying the detection schemes in cell models.

5.2.1 Homogeneous Biodetection Assays

Homogeneous assays are mainly based on the aforementioned LRET or FRET process [6]. In typical LRET or FRET process, the key components are energy donor, recognition probe, energy acceptor, and the analyte. The probe is firstly conjugated to the donor. Then, the acceptor is modified with the capturing molecules. Specific binding of the donor to the acceptor occurred as a result of mixing them with the analytes in the liquid. Finally, the changes in optical readout signals will be observed when the donor and acceptor are in close proximity. As a result, the changes in the signals will be used to quantify the amount of analyte in the samples [84, 85]. Zhang et al. designed the antibody-conjugated upconversion nanobarcode (UPNB) and secondary antibody-coated microspheres for multiplexed detection assays [86]. The design made use of the specific binding of the mouse IgG antibody-modified microspheres and the IgG-modified UPNB. However, the proof-of-concept design was not used for detection in this work. Wu et al. used a similar design for the simultaneous detection of aflatoxin B1 (AFB1) and ochratoxin A (OTA) in food samples [87]. Their competition assay design involves the use of antibody-modified magnetic nanoparticles and $NaYF_4$:Yb/Tm (Er) UCNCs. The role of the magnetic nanoparticles is to separate the unconjugated UCNCs. The LOD for AFB1 and OTA was around 0.01 ng ml^{-1}. Previous study showed that UV radiation induced reactive oxygen intermediate (ROI) to destroy nucleic acid strands and nucleobase [88]. This gained an important insight into the research of UCL-based assays. The effect of photodamage to DNA oligonucleotides (oligos) was studied by Song et al. [89] They used nitroblue tetrazolium (NBT) to detect the presence of ROI during the excitation of QDs and UCNCs because NBT can yield characteristic absorption band at 450–700 nm in the presence of ROIs. Their experiments proved that the excitation of UCNCs did not pose photodamage to the DNA oligos. Our group also worked on the detection of H7 influenza virus oligos by using amine-functionalized $BaGdF_5$:Yb/Er UCNCs and AuNPs [29]. Influenza can be rapidly spread and causes threat to human health. As a result, rapid, simple, and low-cost sensors for such virus is urgently demanding. The LRET phenomenon was evident by measuring the shift in lifetime after the UCNCs were hybridized with the oligo carrying AuNPs and the system showed a LOD of 7 pM.

Apart from DNA oligos, luminescent detection assays can also contribute to environmental pollutant detection. Li et al. presented the detection of Cu^{2+} ions in water by using mesoporous silica-coated UCNCs [90]. The rhodamine B hydrazide

(RBH) acted as a specific probe toward Cu^{2+} ions, while the silica shell can protect the probe in physiological environments, and the sensor reported a LOD of 4.6 ppb. Cyanide ions (CN^-) are more toxic pollutants in water, and the intake of such ions may inhibit respiration in mammalian cells. Yao et al. designed iridium (Ir) complex-modified $NaYF_4$:Yb/Ho UCNCs for the detection of CN^- ions [91]. The detection scheme is mainly based on the LRET process between the Ir complex and the UCNCs; the addition of CN^- ions suppressed the LRET in green emission from UCNCs and hence manifested the detection process. Moreover, the red emission was not affected by the addition of CN^- ions; therefore it was used as an internal standard for ratiometric detection. Such internal standard can avoid the external factors that may potentially affect the detection. Tu et al. reported the detection of 2,4,6-trinitrotoluene (TNT) by using $NaYF_4$:Yb/Er UCNCs and AuNPs [92]. They utilized the surface plasmonic resonance (SPR) enhancement effect on UCL to facilitate the detection scheme. The detection made use of TNT-induced AuNPs aggregation for such SPR effect. They found that the red UCL was proportional to the concentration of TNT. The specificity of the system was evaluated by mixing four types of standard nitroaromatic solutions; the results showed that their proposed system was stable and highly selective. The previous works in in vitro and in vivo detection also made significant advances. It should be noted that the microenvironment of cells or small animals is more complicated than ordinary homogeneous assays; the first difference is the salt concentration and ionic strength, and the second is the digestion of the target ion or molecules by the cells. Deng et al. designed a manganese dioxide (MnO_2) sheet-capped core-shell $NaYF_4$:Yb/Tm@$NaYF_4$ UCNCs for intracellular detection of glutathione (GSH) [30]. The detection scheme is well-illustrated in Fig. 6.9a, in which MnO_2 were selectively reduced to Mn^{2+} ions in the presence of GSH. Therefore, the UCL emission initially quenched by MnO_2 was recovered upon the addition of GSH (Fig. 6.9b). Prior to the cell work, specificity tests were carried out in the presence of different electrolytes and biomolecules. They tested the system in two cell models with GSH enhancer, and the results indicated that the model could be used for probing MnO_2 nanomaterials. Liu et al. reported an ultrasensitive in vivo sensor for the detection of hypoxia based on ruthenium(II) dichloride ($[Ru(dpp)_3]^{2+}Cl_2$)-modified $NaYF_4$:Yb/Tm@$NaYF_4$ UCNCs with hollow mesoporous silica shell [93]. Hypoxia is a phenomenon that the surrounding sites of tumors are oxygen deficient owing to enhanced tumor proliferative activity. The role of the silica was to encapsulate the oxygen-sensitive probe $[Ru(dpp)_3]^{2+}Cl_2$. The blue photons resulted from UC process at 980 nm excitation were absorbed by $[Ru(dpp)_3]^{2+}Cl_2$ via LRET to give red fluorescence. The red emission from $[Ru(dpp)_3]^{2+}Cl_2$ is inversely related to the oxygen content, enabling the proposed system to quantify the oxygen concentration. In addition to intracellular model, they worked on the zebra fish embryos by injecting the nanosensors with 2,3-butanedione (BDM) for a cerebral anoxia model into the embryos' brain (Fig. 6.10). They observed the rapid increase of luminescence until saturation in 12 min. Moreover, it is clearly showed that the sensor was able to detect hypoxia reversibly by adding fresh water to recover the oxygen content. Recently, Gu et al. developed a thiazole-derivative-functionalized $NaYF_4$:Yb/Tm/Er UCNCs for intracellular detection of Hg^{2+} ions [94]. The sensing

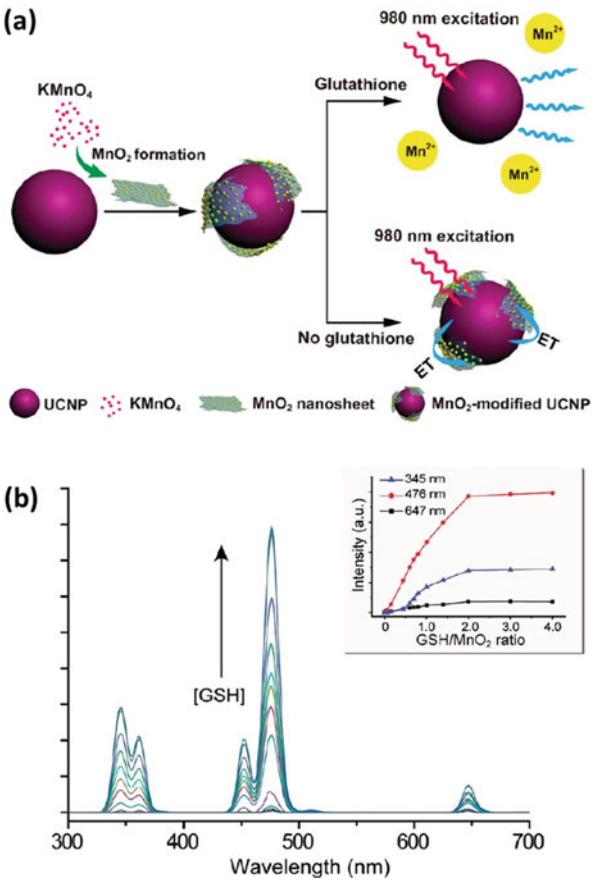

Fig. 6.9 (**a**) Schematic diagram demonstrating detection of GSH with MnO_2-nanosheet decorated UCNCs. (**b**) Photoluminescence response of MnO_2-modified $NaYF_4$:Yb/Tm@$NaYF_4$ nanoparticles as a function of GSH concentration (0–10 mM) in an aqueous solution. (Inset) Plot of luminescence intensity at 345, 476, and 647 nm, respectively, against the GSH/MnO_2 molar ratio. The spectra were recorded under excitation of a 980 nm laser at a power density of 10 W cm^{-2} (Adapted with permission from Ref. [30]. Copyright © 2011 American Chemical Society)

mechanism was based on the recovery of the green UCL emission from LRET process. The NIR emission of Tm^{3+} ions was used as the standard for ratiometric detection. Moreover, they successfully detected as low as 200 μM Hg^{2+} ions by incubating with HeLa cells.

5.2.2 Heterogeneous Biodetection Assays

Heterogeneous assays are operated on a solid-phase substrate, and they are usually more sensitive than homogeneous assays despite the need for excess washing steps. In some cases, such as lethal virus [95] and disease marker detections [34, 96, 97], a high sensitivity (or high LOD) can be beneficial to early-stage diagnostics because this can increase the survival rate. Huang et al. used $LiLuF_4$ UCNCs to detect β-subunit of human chorionic gonadotropin (β-hCG) [98]. In Fig. 6.11a, the β-hCG antigens were anchored on a microplate followed by the addition of biotinylated antibody. The avidin-modified UCNCs then specifically bind to the antibody to emit a report signal for quantification of target antigen; hence the UCL signal increased with the concentration of β-hCG (Fig. 6.11b, c). In addition, the

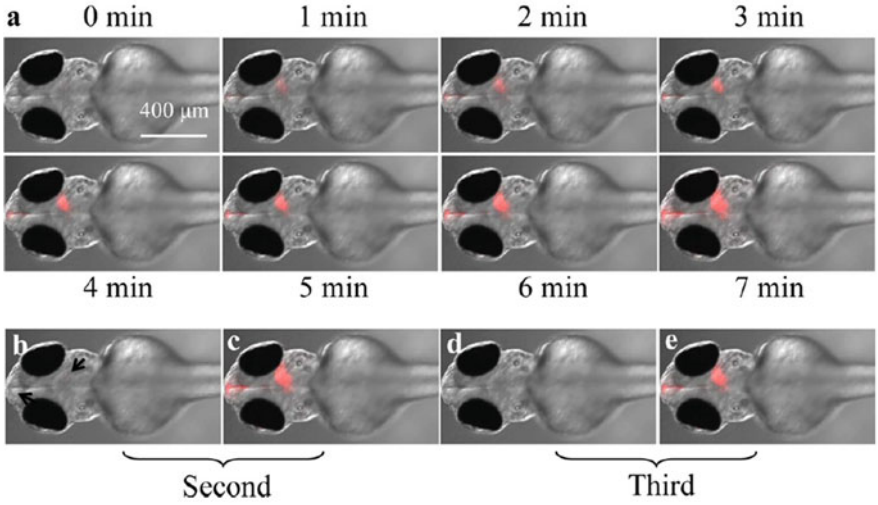

Fig. 6.10 (**a**) CLSM images of living zebra fish embryos after injection of nanosensors followed by adding BDM. UCL images were obtained for 28 min, under the excitation at 980 nm and emission at 550–650 nm. (**b**) After adding fresh water, red emission in the brain was quenched under NIR exposure, as indicated by black arrows. (**c**–**e**) Such process can be repeated for three times. All images have the same scale bar (400 μm) (Adapted from Ref. 93. Copyright © 2014, American Chemical Society)

heterogeneous assay indicated a LOD of 3.8 ng ml^{-1}, which is comparable to the β-hCG concentration in the serum of normal humans. The presence of pathogenic bacteria in food is an important issue to human health. Wu et al. developed a multiplex detection platform for simultaneous detection of three pathogenic bacteria (*Staphylococcus aureus*, *Vibrio parahaemolyticus*, and *Salmonella typhimurium*) by using $NaYF_4$ UCNCs doped with Tm, Ho, or Er and magnetic nanoparticles (Fe_3O_4 NPs) [99]. Specific sequences of aptamer were anchored on different doping of UCNCs as the probe to recognize different bacteria for multiplexed detection, while the Fe_3O_4 NPs were conjugated with complementary DNA (cDNA) oligo sequences to hybridize with the aptamer sequence partially. After the mixing of the UCNCs-aptamer probe-Fe_3O_4 with the bacteria, some of the aptamer probe captured the bacteria and forced the dissociation of the cDNA. As a result, magnetic separation could be used to collect the excess UCNCs-aptamer probe-Fe_3O_4 for quantifying the bacteria concentration indirectly. The use of magnetic separation had enhanced the sensitivity, and the assay reported a range of LOD from 10 to 25 cfu ml^{-1}. Our group also designed a novel hybrid heterogeneous assay for the ultrasensitive detection of Ebola virus oligos based on $BaGdF_5$:Yb/Er UCNCs, AuNPs, and nanoporous anodized alumina (NAAO) membrane [36]. As illustrated in Fig. 6.12, the amine-functionalized UCNCs were anchored throughout the nanochannels of the NAAO membrane, followed by the probe modifications. The targets carrying AuNPs were injected for DNA oligo hybridization. The nanosensor displayed superior LOD to homogeneous assay because the UCNPs were concentrated in the highly porous

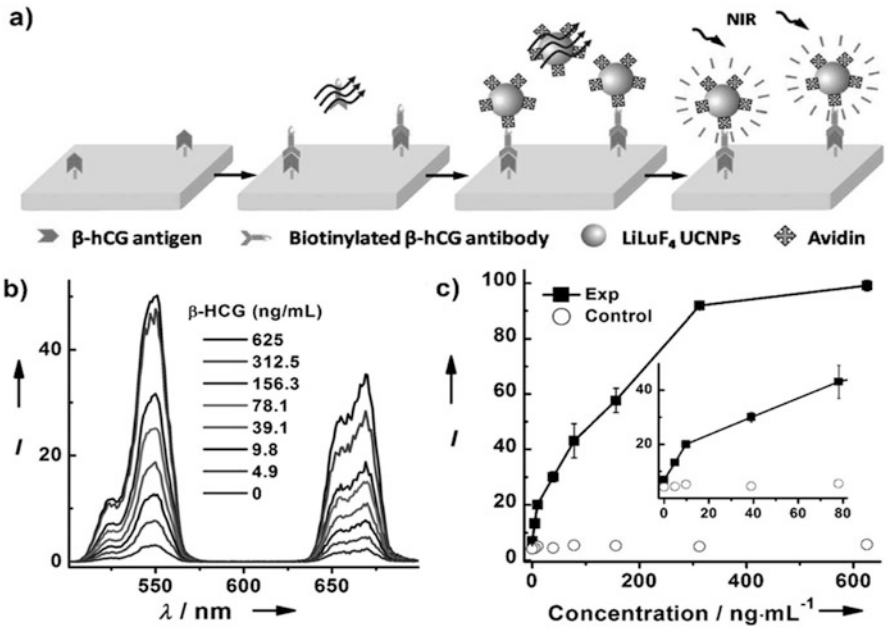

Fig. 6.11 (**a**) The process and principle of heterogeneous UCL detection of β-hCG. (**b**) UCL spectra of the bioassays using $LiLuF_4$:Yb,Er@$LiLuF_4$ core-shell UCNPs with 16 MLs as a function of β-hCG concentration, each data point represents an average of three measurements. (**c**) Calibration curve of UCL detection for the integrated UCL intensity versus the concentration of β-hCG. The control experiment was conducted using BSA instead of the β-hCG antigen as analyte under otherwise identical conditions (Reprinted with permission from Ref. [98]. Copyright © 2014, Wiley)

template; hence the light-matter interaction was enhanced due to the increased capturing. Moreover, we stepped forward to test the clinical Ebola virus sample from hospital. Importantly, the system was able to detect the virus RNA down to femtomolar (fM) scale.

6 Conclusions and Future Perspective

The book chapter had discussed and reviewed the recent development of UCNCs-based multimodal bioimaging and biodetection. Considering the intrinsic physical properties of Ln^{3+} ions in UCNCs, they can not only enjoy noninvasive UCL but also magnetism and X-ray attenuation properties. As a result, the three primary imaging modes, UCL, MRI, and X-ray imaging, can be readily achieved by using UCNCs. Although these modes possess their own drawbacks, the other modes can compensate the weaknesses of each other. Apart from the physical properties, the surface of the UCNCs played important role in the cell internalization and delivery to the diagnostic site [100]. Suitable functional groups may show enhanced

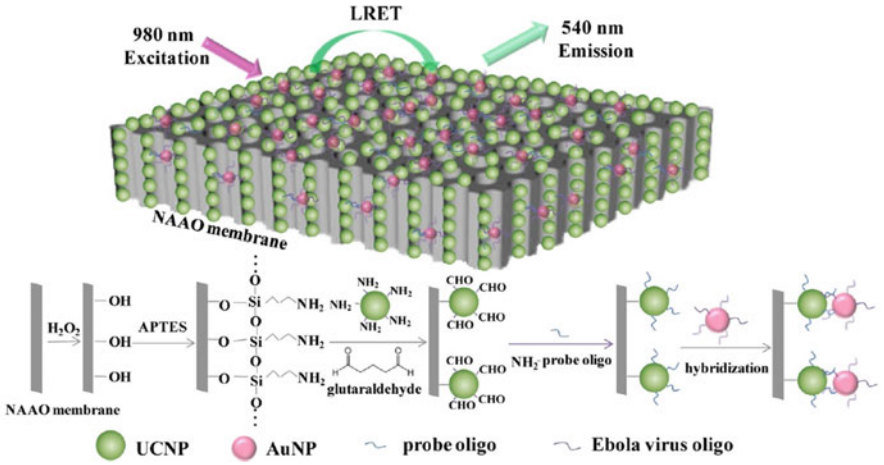

Fig. 6.12 Schematic diagram of Ebola target oligo detection based on LRET biosensor with energy transfer from UCNPs to AuNPs on NAAO membrane (Reprinted with permission from Ref. [36]. Copyright © 2016, American Chemical Society)

internalization [47, 101] and the surface should be conjugated with targeting moiety with passivation. Antibodies or peptides are usually conjugated to the surface for localized delivery to the site of interest, while PEGs are preferred to protect the UCNCs from non-specific binding [102, 103]. However, it remains a challenge for UCNCs-based contrast agents to advance into the field of real clinical trials. First, the size of UCNCs is of great concern because optimal size of tens of nanometers is favorable for internalization. Currently, the use of csUCNCs becomes a well-accepted route because such cs structure can enhance the emission intensity and shift the excitation wavelength to around 800 nm. However, it should be noted that the growth of shell layers will compensate the size factor; therefore the researches on optimizing the size while maintaining the desired optical properties should be needed to meet the requirements. The large size of UCNCs also contributes to the clearance issue in living animals; hence it eventually leads to other toxicity issues. The toxicity and clearance is a crucial issue that hampers the further advance of UCNCs for clinical trials [104]. Xiong et al. had done a 115-day in vivo distribution of PAA-UCNCs examination in a mice [105]. The results indicated the toxicity of UCNCs was low. More similar or in-depth studies are required to establish the database for UCNCs toxicity. Nevertheless, one of the merits of multimodal imaging is to avoid the need of injecting multiple contrast agents for different imaging studies.

For biodetection, UCL-based assays have been developed as an alternative to conventional fluorescent assays. The key advantage mainly stems from the use of NIR excitation, because NIR is transparent to biological species and hence poses minimal photodamage. Numerous proof-of-concept homogeneous and heterogeneous assays were reported for the detection of disease and tumor markers and virus DNA oligos. The test by using clinical samples from hospitals is essential

because this can deviate the testing conditions from the ideal experimental conditions; the results can appeal more to real and on-site detection conditions [106]. Apart from clinical samples, the reliability of the reported biosensors is another key issue because those data can validate a detection scheme or device. The sampling and disturbance test data may be provided for such purpose. Another direction is to fabricate small devices based on the proof-of-concept experiment because luminescent assays belong to quick test that should allow easy operations and access for the public. The development of luminescent assay cannot replace the existing well-known PCR (polymerase chain reaction)-based and ELISA (enzyme-linked immunosorbent assay) techniques. Instead, luminescent assay should play a role for rapid screening because the strength of the assay is simplicity, considering the availability of cheap and compacted light sources as well as detectors. Moreover, the relevant studies of microarray biosensors had produced high impacts in recent years. These arrays can simultaneously detect different types of analytes [107]. The coupling of microarray technique with UCL can further realize the potential ability of UCL for rapid, sensitive, and simple detection schemes.

Acknowledgment This work was supported by the Hong Kong Ph.D. Fellowship Scheme Fund Innovation and Technology Support Programme (Project No. ITS/057/15) and Research Grants Council of Hong Kong (GRF No. PolyU 153281/16P).

References

1. Chan WCW, Maxwell DJ, Gao X, Bailey RE, Han M, Nie S (2002) Luminescent quantum dots for multiplexed biological detection and imaging. Curr Opin Biotechnol 13(1):40–46
2. Nozik AJ, Beard MC, Beard JM, Law M, Ellingson RJ, Johnson JC (2010) Semiconductor quantum dots and quantum dot arrays and applications of multiple exciton generation to third-generation photovoltaic solar cells. Chem Rev 110(11):6873–6890
3. Olutas M, Guzelturk B, Kelestemur Y, Gungor K, Demir HV (2016) Highly efficient nonradiative energy transfer from colloidal semiconductor quantum dots to wells for sensitive noncontact temperature probing. Adv Funct Mater 26(17):2891–2899
4. Rass K, Jorg R (2008) UV damage and DNA repair in malignant melanoma and nonmelanoma skin cancer. In: Jorg R (ed) Sunlight, Vitamin D and skin cancer. Springer, New York, pp 162–174
5. Weissleder RA (2001) Clearer vision for *in vivo* imaging progress continues in the development of smaller, more penetrable probes for biological imaging. Nat Biotechnol 19(4):316–317
6. Zheng W, Huang P, Tu D, Ma E, Zhu H, Chen X (2015) Lanthanide-doped upconversion nanobioprobes: electronic structures, optical properties, and biodetection. Chem Soc Rev 44(6):1379–1415
7. Tsang M-K, Bai G, Hao J (2015) Stimuli responsive upconversion luminescence nanomaterials and films for various applications. Chem Soc Rev 44(6):1585–1607
8. Haase M, Schäfer H (2011) Upconverting nanoparticles. Angew Chem Int Ed 50(26):5808–5829
9. Wang Z-L, Hao J, Chan HLW, Wong W-T, Wong K-L (2012) A strategy for simultaneously realizing the cubic-to-hexagonal phase transition and controlling the small size of $NaYF_4$:Yb^{3+}, Er^{3+} nanocrystals for *in vitro* cell imaging. Small 8(12):1863–1868

10. Dai Y, Ma P, Cheng Z, Kang X, Zhang X, Hou Z, Li C, Yang D, Zhai X, Lin J (2012) Up-conversion cell imaging and pH-induced thermally controlled drug release from $NaYF_4$: Yb^{3+}/Er^{3+}@hydrogel core-shell hybrid microspheres. ACS Nano 6(4):3327–3338
11. Zhou J-C, Yang Z-L, Dong W, Tang R-J, Sun L-D, Yan C-H (2011) Bioimaging and toxicity assessments of near-infrared upconversion luminescent $NaYF_4$:Yb, Tm nanocrystals. Biomaterials 32(34):9059–9067
12. Yi Z, Li X, Xue Z, Liang X, Lu W, Peng H, Liu H, Zeng S, Hao J (2015) Remarkable NIR enhancement of multifunctional nanoprobes for *in vivo* trimodal bioimaging and upconversion optical/T2-weighted MRI-guided small tumor diagnosis. Adv Funct Mater 25(46):7119–7129
13. Naccache R, Chevallier P, Lagueux J, Gossuin Y, Laurent S, VanderElst L, Chilian C, Capobianco JA, Fortin M-A (2013) High relaxivities and strong vascular signal enhancement for $NaGdF_4$ nanoparticles designed for dual MR/optical imaging. Adv Healthc Mater 2(11):1478–1488
14. He M, Huang P, Zhang C, Hu H, Bao C, Gao G, He R, Cui D (2011) Dual phase-controlled synthesis of uniform lanthanide-doped $NaGdF_4$ upconversion nanocrystals via an OA/ionic liquid two-phase system for *in vivo* dual-modality imaging. Adv Funct Mater 21(23):4470–4477
15. Tsang M-K, Zeng S, Chan HLW, Hao J (2013) Surface ligand-mediated phase and upconversion luminescence tuning of multifunctional $NaGdF_4$:Yb/Er materials with paramagnetic and cathodoluminescent characteristics. Opt Mater 35(12):2691–2697
16. Zhao L, Kutikov A, Shen J, Duan C, Song J, Han G (2013) Stem cell labeling using polyethylenimine conjugated (α-$NaYbF_4$:Tm^{3+})/CaF_2 upconversion nanoparticles. Theranostics 3(4):249–257
17. Zhan Q, Qian J, Liang H, Somesfalean G, Wang D, He S, Zhang Z, Andersson-Engels S (2011) Using 915 nm laser excited $Tm^{3+}/Er^{3+}/Ho^{3+}$- doped $NaYbF_4$ upconversion nanoparticles for *in vitro* and deeper *in vivo* bioimaging without overheating irradiation. ACS Nano 5(5):3744–3757
18. Wang C, Cheng L, Liu Z (2011) Drug delivery with upconversion nanoparticles for multifunctional targeted cancer cell imaging and therapy. Biomaterials 32(4):1110–1120
19. Wang F, Deng R, Wang J, Wang Q, Han Y, Zhu H, Chen X, Liu X (2011) Tuning upconversion through energy migration in core-shell nanoparticles. Nat Mater 10(12):968–973
20. Wang Y-F, Liu G-Y, Sun L-D, Xiao J-W, Zhou J-C, Yan C-H (2013) Nd^{3+}-sensitized upconversion nanophosphors: efficient *in vivo* bioimaging probes with minimized heating effect. ACS Nano 7(8):7200–7206
21. Bai G, Tsang M-K, Hao J (2016) Luminescent ions in advanced composite materials for multifunctional applications. Adv Funct Mater 26(35):6330–6350
22. Sedlmeier A, Gorris HH (2015) Surface modification and characterization of photon-upconverting nanoparticles for bioanalytical applications. Chem Soc Rev 44(6):1526–1560
23. Feng W, Han C, Li F (2013) Upconversion-nanophosphor-based functional nanocomposites. Adv Mater 25(37):5287–5303
24. Chen G, Qiu H, Prasad PN, Chen X (2014) Upconversion nanoparticles: design, nanochemistry, and applications in theranostics. Chem Rev 114(10):5161–5214
25. Gai S, Li C, Yang P, Lin J (2014) Recent progress in rare earth micro/nanocrystals: soft chemical synthesis, luminescent properties, and biomedical applications. Chem Rev 114 (4):2343–2389
26. Feng W, Zhu X, Li F (2013) Recent advances in the optimization and functionalization of upconversion nanomaterials for *in vivo* bioapplications. NPG Asia Mater 5(12):e75
27. Muhr V, Wilhelm S, Hirsch T, Wolfbeis OS (2014) Upconversion nanoparticles: from hydrophobic to hydrophilic surfaces. Acc Chem Res 47(12):3481–3493
28. Jo E-J, Mun H, Kim M-G (2016) Homogeneous immunosensor based on luminescence resonance energy transfer for glycated hemoglobin detection using upconversion nanoparticles. Anal Chem 88(5):2742–2746

29. Ye WW, Tsang M-K, Liu X, Yang M, Hao J (2014) Upconversion luminescence resonance energy transfer (LRET)-based biosensor for rapid and ultrasensitive detection of avian influenza virus H7 subtype. Small 10(12):2390–2397
30. Deng R, Xie X, Vendrell M, Chang Y-T, Liu X (2011) Intracellular glutathione detection using MnO_2-nanosheet-modified upconversion nanoparticles. J Am Chem Soc 133 (50):20168–20171
31. Zhang C, Yuan Y, Zhang S, Wang Y, Liu Z (2011) Biosensing platform based on fluorescence resonance energy transfer from upconverting nanocrystals to graphene oxide. Angew Chem Int Ed 50(30):6851–6854
32. Li H, Shi L, Sun D, Li P, Liu Z (2016) Fluorescence resonance energy transfer biosensor between upconverting nanoparticles and palladium nanoparticles for ultrasensitive CEA detection. Biosens Bioelectron 86:791–798
33. Jin B, Wang S, Lin M, Jin Y, Zhang S, Cui X, Gong Y, Li A, Xu F, Lu TJ (2017) Upconversion nanoparticles based FRET aptasensor for rapid and ultrasenstive bacteria detection. Biosens Bioelectron 90:525–533
34. Xu S, Dong B, Zhou D, Yin Z, Cui S, Xu W, Chen B, Song H (2016) Paper-based upconversion fluorescence resonance energy transfer biosensor for sensitive detection of multiple cancer biomarkers. Sci Rep 6:23406
35. Xu J, Zhou S, Tu D, Zheng W, Huang P, Li R, Chen Z, Huang M, Chen X (2016) Sub-5 nm lanthanide-doped lutetium oxyfluoride nanoprobes for ultrasensitive detection of prostate specific antigen. Chem Sci 7(4):2572–2578
36. Tsang M-K, Ye W, Wang G, Li J, Yang M, Hao J (2016) Ultrasensitive detection of ebola virus oligonucleotide based on upconversion nanoprobe/nanoporous membrane system. ACS Nano 10(1):598–605
37. Hlaváček A, Farka Z, Hübner M, Horňáková V, Němeček D, Niessner R, Skládal P, Knopp D, Gorris HH (2016) Competitive upconversion-linked immunosorbent assay for the sensitive detection of diclofenac. Anal Chem 88(11):6011–6017
38. Zhang F (2015) In: Lockwood DJ (ed) Photon upconversion nanomaterials, vol 44. Springer, Berlin/Heidelberg
39. Wang F, Wang J, Liu X (2010) Direct evidence of a surface quenching effect on size-dependent luminescence of upconversion nanoparticles. Angew Chem Int Ed 49(41):7456–7460
40. Jayakumar MKG, Idris NM, Huang K, Zhang Y (2014) A paradigm shift in the excitation wavelength of upconversion nanoparticles. Nanoscale 6(15):8441–8443
41. Boyer J-C, Vetrone F, Cuccia LA, Capobianco JA (2006) Synthesis of colloidal upconverting $NaYF_4$ nanocrystals doped with Er^{3+}, Yb^{3+} and Tm^{3+} via thermal decomposition of lanthanide trifluoroacetate precursors. J Am Chem Soc 128(23):7444–7445
42. Liu R, Tu D, Liu Y, Zhu H, Li R, Zheng W, Ma E, Chen X (2012) Controlled synthesis and optical spectroscopy of lanthanide-doped $KLaF_4$ nanocrystals. Nanoscale 4(15):4485–4491
43. Chan C-F, Tsang M-K, Li H, Lan R, Chadbourne FL, Chan W-L, Law G-L, Cobb SL, Hao J, Wong W-T, Wong K-L (2014) Bifunctional up-converting lanthanide nanoparticles for selective *in vitro* imaging and inhibition of cyclin D as anti-cancer agents. J Mater Chem B 2(1):84–91
44. Zeng S, Tsang M-K, Chan C-F, Wong K-L, Hao J (2012) PEG modified $BaGdF_5$:Yb/Er nanoprobes for multi-modal upconversion fluorescent, *in vivo* X-ray computed tomography and biomagnetic imaging. Biomaterials 33(36):9232–9238
45. Wong H-T, Tsang M-K, Chan C-F, Wong K-L, Fei B, Hao J (2013) *In vitro* cell imaging using multifunctional small sized $KGdF_4$:Yb^{3+},Er^{3+} upconverting nanoparticles synthesized by a one-pot solvothermal process. Nanoscale 5(8):3465–3473
46. Zeng S, Tsang M-K, Chan C-F, Wong K-L, Fei B, Hao J (2012) Dual-modal fluorescent/magnetic bioprobes based on small sized upconversion nanoparticles of amine-functionalized $BaGdF_5$:Yb/Er. Nanoscale 4(16):5118–5124

47. Tsang M-K, Chan C-F, Wong K-L, Hao J (2015) Comparative studies of upconversion luminescence characteristics and cell bioimaging based on one-step synthesized upconversion nanoparticles capped with different functional groups. J Lumin 157:172–178
48. Bogdan N, Vetrone F, Ozin GA, Capobianco JA (2011) Synthesis of ligand-free colloidally stable water dispersible brightly luminescent lanthanide-doped upconverting nanoparticles. Nano Lett 11(2):835–840
49. Tian J, Zeng X, Xie X, Han S, Liew O, Chen Y, Wang L, Liu X (2015) Intracellular adenosine triphosphate deprivation through lanthanide-doped nanoparticles. J Am Chem Soc 137 (20):6550–6558
50. Sprawls P (2000) Magnetic resonance imaging: principles, methods, and techniques. Medical Physics, Madison
51. Wong H-T, Chan HLW, Hao JH (2009) Magnetic and luminescent properties of multifunctional GdF_3:Eu^{3+} nanoparticles. Appl Phys Lett 95(2):022512–022514
52. Chen H, Qi B, Moore T, Colvin DC, Crawford T, Gore JC, Alexis F, Mefford OT, Anker JN (2014) Synthesis of brightly PEGylated luminescent magnetic upconversion nanophosphors for deep tissue and dual MRI imaging. Small 10(1):160–168
53. Liu B, Li C, Ma P, Chen Y, Zhang Y, Hou Z, Huang S, Lin J (2015) Multifunctional $NaYF_4$:Yb,Er@$mSiO_2$@Fe_3O_4-PEG nanoparticles for UCL/MR bioimaging and magnetically targeted drug delivery. Nanoscale 7(5):1839–1848
54. Wang C, Cheng L, Xu H, Liu Z (2012) Towards whole-body imaging at the single cell level using ultra-sensitive stem cell labeling with oligo-arginine modified upconversion nanoparticles. Biomaterials 33(19):4872–4881
55. Chen C, Kang N, Xu T, Wang D, Ren L, Guo X (2015) Core-shell hybrid upconversion nanoparticles carrying stable nitroxide radicals as potential multifunctional nanoprobes for upconversion luminescence and magnetic resonance dual-modality imaging. Nanoscale 7(12):5249–5261
56. Idris NM, Gnanasammandhan MK, Zhang J, Ho PC, Mahendran R, Zhang Y (2012) *In vivo* photodynamic therapy using upconversion nanoparticles as remote-controlled nanotransducers. Nat Med 18(10):1580–1585
57. Liu C, Gao Z, Zeng J, Hou Y, Fang F, Li Y, Qiao R, Shen L (2013) Magnetic/upconversion fluorescent $NaGdF_4$:Yb,Er nanoparticle-based dual-modal molecular probes for imaging tiny tumors *in vivo*. ACS Nano 7(8):7227–7240
58. Xia A, Gao Y, Zhou J, Li C, Yang T, Wu D, Wu L, Li F (2011) Core-shell $NaYF_4$:Yb^{3+},Tm^{3+}@Fe_xO_y nanocrystals for dual-modality T_2-enhanced magnetic resonance and NIR-to-NIR upconversion luminescent imaging of small-animal lymphatic node. Biomaterials 32(29):7200–7208
59. Zeng L, Xiang L, Ren W, Zheng J, Li T, Chen B, Zhang J, Mao C, Li A, Wu A (2013) Multifunctional photosensitizer-conjugated core–shell Fe_3O_4@$NaYF_4$:Yb/Er nanocomplexes and their applications in T_2-weighted magnetic resonance/upconversion luminescence imaging and photodynamic therapy of cancer cells. RSC Adv 3(33):13915–13925
60. Lee J, Gordon AC, Kim H, Park W, Cho S, Lee B, Larson AC, Rozhkova EA, Kim D (2016) Targeted multimodal nano-reporters for pre-procedural MRI and intra-operative image-guidance. Biomaterials 109:69–77
61. Sun Y, Yu M, Liang S, Zhang Y, Li C, Mou T, Yang W, Zhang X, Li B, Huang C, Li F (2011) Fluorine-18 labeled rare-earth nanoparticles for positron emission tomography (PET) imaging of sentinel lymph node. Biomaterials 32(11):2999–3007
62. Cao T, Yang Y, Sun Y, Wu Y, Gao Y, Feng W, Li F (2013) Biodistribution of sub-10 nm PEG-modified radioactive/upconversion nanoparticles. Biomaterials 34(29):7127–7134
63. Peng J, Sun Y, Zhao L, Wu Y, Feng W, Gao Y, Li F (2013) Polyphosphoric acid capping radioactive/upconverting $NaLuF_4$:Yb,tm,^{153}Sm nanoparticles for blood pool imaging *in vivo*. Biomaterials 34(37):9535–9544
64. Martin KH, Dayton PA (2013) Current status and prospects for microbubbles in ultrasound theranostics. Wiley Interdiscip Rev Nanomed Nanobiotechnol 5(4):329–345

65. Su L, Gong X, Wang S, Jin B, Lin M, You M, Zong Y, Wan M, Xu F (2015) Microbubble embedded with upconversion nanoparticles as a bimodal contrast agent for fluorescence and ultrasound imaging. Nanotechnology 26(34):345601
66. Nie L, Chen X (2014) Structural and functional photoacoustic molecular tomography aided by emerging contrast agents. Chem Soc Rev 43(20):7132–7170
67. Wang LV, Hu S (2012) Photoacoustic tomography: *In vivo* imaging from organelles to organs. Science 335(6075):1458–1462
68. Lee D, Koo H, Sun I, Ryu JH, Kim K (2012) Multifunctional nanoparticles for multimodal imaging and theragnosis. Chem Soc Rev 41(7):2656–2672
69. Hu S, Maslov K, Wang LV (2011) Second-generation optical-resolution photoacoustic microscopy with improved sensitivity and speed. Opt Lett 36(7):1134–1136
70. Yao J, Wang L, Yang J, Maslov KI, Wong TTW, Li L, Huang C, Zou J, Wang LV (2015) High-speed label-free functional photoacoustic microscopy of mouse brain in action. Nat Methods 12(5):407–410
71. Wang L, Maslov K, Wang LV (2013) Single-cell label-free photoacoustic flowoxigraphy *in vivo*. Proc Natl Acad Sci 110(15):5759–5764
72. Sheng Y, Liao L-D, Thakor N, Tan MC (2014) Rare-earth doped particles as dual-modality contrast agent for minimally-invasive luminescence and dual-wavelength photoacoustic imaging. Sci Rep 4:6562
73. Maji SK, Sreejith S, Joseph J, Lin M (2014) Upconversion nanoparticles as a contrast agent for photoacoustic imaging in live mice. Adv Mater 26(32):5633–5638
74. Shen J-W, Yang C-X, Dong L-X, Sun H-R, Gao K, Yan X-P (2013) Incorporation of computed tomography and magnetic resonance imaging function into $NaYF_4$: Yb/Tm upconversion nanoparticles for *in vivo* trimodal bioimaging. Anal Chem 85(24):12166–12172
75. Xia A, Chen M, Gao Y, Wu D, Feng W, Li F (2012) Gd^{3+} complex-modified $NaLuF_4$-based upconversion nanophosphors for trimodality imaging of NIR-to-NIR upconversion luminescence, X-ray computed tomography and magnetic resonance. Biomaterials 33(21):5394–5405
76. Liu Z, Dong K, Liu J, Han X, Ren J, Qu X (2014) Anti-biofouling polymer-decorated lutetium-based nanoparticulate contrast agents for *in vivo* high-resolution trimodal imaging. Small 10(12):2429–2438
77. Dai Y, Xiao H, Liu J, Yuan Q, Ma P, Yang D, Li C, Cheng Z, Hou Z, Yang P, Lin J (2013) *In vivo* multimodality imaging and cancer therapy by near-infrared light-triggered trans-platinum pro-drug-conjugated upconverison nanoparticles. J Am Chem Soc 135 (50):18920–18929
78. Xiao Q, Zheng X, Bu W, Ge W, Zhang S, Chen F, Xing H, Ren Q, Fan W, Zhao K, Hua Y, Shi J (2013) A core/satellite multifunctional nanotheranostic for *in vivo* imaging and tumor eradication by radiation/photothermal synergistic therapy. J Am Chem Soc 135(35):13041–13048
79. Xue Z, Yi Z, Li X, Li Y, Jiang M, Liu H, Zeng S (2017) Upconversion optical/magnetic resonance imaging-guided small tumor detection and *in vivo* tri-modal bioimaging based on high-performance luminescent nanorods. Biomaterials 115:90–103
80. Xing H, Bu W, Zhang S, Zheng X, Li M, Chen F, He Q, Zhou L, Peng W, Hua Y, Shi J (2012) Multifunctional nanoprobes for upconversion fluorescence, MR and CT trimodal imaging. Biomaterials 33(4):1079–1089
81. Liu Y, Kang N, Lv J, Zhou Z, Zhao Q, Ma L, Chen Z (2016) Deep photoacoustic/luminescence/magnetic resonance multimodal imaging in living subjects using high- efficiency upconversion nanocomposites. Adv Mater 28(30):6411–6419
82. Sun Y, Zhu X, Peng J, Li F (2013) Core-shell lanthanide upconversion nanophosphors as four-modal probes for tumor angiogenesis imaging. ACS Nano 7(12):11290–11300
83. Rieffel J, Chen F, Kim J, Chen G, Shao W, Shao S, Chitgupi U, Hernandez R, Graves SA, Nickles RJ, Prasad PN, Kim C, Cai W, Lovell JF (2015) Hexamodal imaging with porphyrin-phospholipid-coated upconversion nanoparticles. Adv Mater 27(10):1785–1790
84. Bünzli J-CG (2010) Lanthanide luminescence for biomedical analyses and imaging. Chem Rev 110(5):2729–2755

85. Eliseeva SV, Bünzli J-CG (2010) Lanthanide luminescence for functional materials and bio-sciences. Chem Soc Rev 39(1):189–227
86. Zhang F, Haushalter RC, Haushalter RW, Shi Y, Zhang Y, Ding K, Zhao D, Stucky GD (2011) Rare-earth upconverting nanobarcodes for multiplexed biological detection. Small 7(14):1972–1976
87. Wu S, Duan N, Zhu C, Ma X, Wang M, Wang Z (2011) Magnetic nanobead-based immunoassay for the simultaneous detection of aflatoxin B1 and ochratoxin A using upconversion nanoparticles as multicolor labels. Biosens Bioelectron 30(1):35–42
88. Anas A, Akita H, Harashima H, Itoh T, Ishikawa M, Biju V (2008) Photosensitized breakage and damage of DNA by CdSe-ZnS quantum dots. J Phys Chem B 112(32):10005–10011
89. Song K, Kong X, Liu X, Zhang Y, Zeng Q, Tu L, Shi Z, Zhang H (2012) Aptamer optical biosensor without bio-breakage using upconversion nanoparticles as donors. Chem Commun 48(8):1156–1158
90. Li C, Liu J, Alonso S, Li F, Zhang Y (2012) Upconversion nanoparticles for sensitive and in-depth detection of Cu^{2+} ions. Nanoscale 4(19):6065–6071
91. Yao L, Zhou J, Liu J, Feng W, Li F (2012) Iridium-complex-modified upconversion nanophosphors for effective LRET detection of cyanide anions in pure water. Adv Funct Mater 22(13):2667–2672
92. Tu N, Wang L (2013) Surface plasmon resonance enhanced upconversion luminescence in aqueous media for TNT selective detection. Chem Commun 49(56):6319–6321
93. Liu J, Liu Y, Bu W, Bu J, Sun Y, Du J, Shi J (2014) Ultrasensitive nanosensors based on upconversion nanoparticles for selective hypoxia imaging *in vivo* upon near-infrared excitation. J Am Chem Soc 136(27):9701–9709
94. Gu B, Zhou Y, Zhang X, Liu X, Zhang Y, Marks R, Zhang H, Liu X, Zhang Q (2016) Thiazole derivative-modified upconversion nanoparticles for Hg^{2+} detection in living cells. Nanoscale 8(1):276–282
95. Kale V, Päkkilä H, Vainio J, Ahomaa A, Sirkka N, Lyytikäinen A, Talha SM, Kutsaya A, Waris M, Julkunen I, Soukka T (2016) Spectrally and spatially multiplexed serological array-in-well assay utilizing two-color upconversion luminescence imaging. Anal Chem 88(8):4470–4477
96. Sirkka N, Lyytikäinen A, Savukoski T, Soukka T (2016) Upconverting nanophosphors as reporters in a highly sensitive heterogeneous immunoassay for cardiac troponin I. Anal Chim Acta 925:82–87
97. Zhao P, Wu Y, Zhu Y, Yang X, Jiang X, Xiao J, Zhang Y, Li C (2014) Upconversion fluorescent strip sensor for rapid determination of *Vibrio anguillarum*. Nanoscale 6(7):3804–3809
98. Huang P, Zheng W, Zhou S, Tu D, Chen Z, Zhu H, Li R, Ma E, Huang M, Chen X (2014) Lanthanide-doped $LiLuF_4$ upconversion nanoprobes for the detection of disease biomarkers. Angew Chem Int Ed 53(5):1252–1257
99. Wu S, Duan N, Shi Z, Fang C, Wang Z (2014) Simultaneous aptasensor for multiplex pathogenic bacteria detection based on multicolor upconversion nanoparticles labels. Anal Chem 86(6):3100–3107
100. Sun Y, Feng W, Yang P, Huang C, Li F (2015) The biosafety of lanthanide upconversion nanomaterials. Chem Soc Rev 44(6):1509–1525
101. Jin J, Gu Y, Man CW, Cheng J, Xu Z, Zhang Y, Wang H, Lee VH, Cheng SH, Wong W (2011) Polymer-coated $NaYF_4$:Yb^{3+},Er^{3+} upconversion nanoparticles for charge-dependent cellular imaging. ACS Nano 5(12):7838–7847
102. Shi Y, Shi B, Dass AVE, Lu Y, Sayyadi N, Kautto L, Willows RD, Chung R, Piper J, Nevalainen H, Walsh B, Jin D, Packer NH (2016) Stable upconversion nanohybrid particles for specific prostate cancer cell immunodetection. Sci Rep 6:37533
103. Xing H, Zheng X, Ren Q, Bu W, Ge W, Xiao Q, Zhang S, Wei C, Qu H, Wang Z, Hua Y, Zhou L, Peng W, Zhao K, Shi J (2013) Computed tomography imaging-guided radiotherapy

by targeting upconversion nanocubes with significant imaging and radiosensitization enhancements. Sci Rep 3:1751
104. Gnach A, Lipinski T, Bednarkiewicz A, Rybka J, Capobianco JA (2015) Upconverting nanoparticles: assessing the toxicity. Chem Soc Rev 44(6):1561–1584
105. Xiong L, Yang T, Yang Y, Xu C, Li F (2010) Long-term *in vivo* biodistribution imaging and toxicity of polyacrylic acid-coated upconversion nanophosphors. Biomaterials 31(27):7078–7085
106. Kumar AA, Hennek JW, Smith BS, Kumar S, Beattie P, Jain S, Rolland JP, Stossel TP, Chunda-Liyoka C, Whitesides GM (2015) From the bench to the field in low-cost diagnostics: two case studies. Angew Chem Int Ed 54(20):5836–5853
107. Miller MB, Tang YW (2009) Basic concepts of microarrays and potential applications in clinical microbiology. Clin Microbiol Rev 22(4):611–633

Label-Free Raman Imaging

7

Alison J. Hobro and Nicholas I. Smith

Contents

1 Definition of the Topic

Label-free Raman imaging is a noninvasive spectroscopic method for investigating the nature and distribution of molecular species within a sample. In this chapter, we describe the applications of conventional Raman imaging, as well as the related techniques of coherent anti-Stokes Raman scattering (CARS) and stimulated Raman scattering (SRS) imaging for medical, life sciences, and other biological applications.

A. J. Hobro (✉) · N. I. Smith
Biophotonics Laboratory, Immunology Frontier Research Center, Osaka University, Suita City, Japan
e-mail: ajhobro@ifrec.osaka-u.ac.jp

C. S. S. R. Kumar (ed.), *Nanotechnology Characterization Tools for Biosensing and Medical Diagnosis*, https://doi.org/10.1007/978-3-662-56333-5_7

2 Overview

The application of Raman imaging to a wide range of biological materials has shown very promising results and is now providing biological insights that are not available to other methods. In this chapter, we first discuss typical experimental considerations for Raman, CARS, and SRS biological imaging in terms of sample preparation, instrumentation and measurement parameters, data processing, and data analysis approaches. Secondly, we discuss the recent applications of Raman, CARS, and SRS imaging of biological materials ranging from human cells and tissues for disease diagnosis to nonmammalian samples including plants, shellfish, algae, and nematode worms. The three techniques have been used to investigate wide-ranging topics from organism development, disease progression, drug uptake and metabolism, the effects of environmental pollution and toxin effects on cells, all the way through to testing the quality of food products, drugs, and even biologically derived charcoal. Finally, information obtained from Raman, CARS, and SRS images can be complimented by other techniques, and we discuss various multimodal imaging approaches that have been employed for biological analysis.

3 Introduction

Raman spectroscopy is based on the inelastic scattering of light, i.e., where incident and scattered photons have different energies, or frequencies, after interaction with matter. The frequency shift between the incident and scattered photons is indicative of the vibrational level of a molecule [1]. Therefore, a Raman experiment gives rise to a spectrum containing information about the chemical bonds present in a sample and can be thought of as a "fingerprint" of a sample. Raman spectroscopy has been used to characterize many different sample types in fields as wide ranging as materials science, organometallic chemistry, and geology [2]. However, key instrumentation advances such as the advent of laser-based Raman spectrometers in the 1960s [3] and their combination with optical microscopes in the 1970s opened up applications in fields that had often proved challenging with weaker excitation sources [4], including the analysis of biological materials.

Subsequent developments in instrumentation have improved the speed of collection to such levels where, in the last few years, it has been possible to measure Raman images, where each pixel contains a Raman spectrum with sufficient signal to noise for subsequent data analysis, within a few minutes. This has facilitated the application of Raman imaging to many types of biological samples, including live cells and tissues, providing information on the spatial distribution as well as the nature of the chemical components of the sample. Some studies have also shown that time-lapse Raman imaging is possible (for examples, see [5–7]) providing additional temporal information on changes in chemical distribution and composition.

Raman spectroscopy has a number of advantages over other analytical imaging techniques such as fluorescence imaging. In general, Raman spectroscopy is nondestructive, meaning that a sample can be measured multiple times, for Raman-based

time-lapse imaging or for subsequent measurements with other analytical techniques. In contrast to many biological assays, this allows Raman measurement while the sample continues to carry out its normal function, e.g., cells can be reimplanted and continue to develop. Raman spectra can be collected from samples in many forms such as liquids, including aqueous solutions, soft and hard tissues, solids, and powders. Samples can be relatively simple compositions, as may be found in a pharmaceutical tablet, or more complex mixtures of components that may be present in tissue sections or whole organisms. This flexibility in sample format means that sample preparation steps are often simple and can be kept to a minimum to avoid inducing noticeable changes in the sample under investigation. In addition, it is possible to measure samples in conditions that mimic, or are close to, the normal sample environment, particularly useful for in vitro cell or in vivo tissue analyses, for example.

One of the main advantages of Raman spectroscopy is that it does not require the use of labels to identify sample components, which is particularly beneficial where the presence of a label may perturb the sample. This means that no prior knowledge of the sample composition is needed to perform a Raman experiment and Raman spectroscopy therefore has the potential to measure previously unknown components in a sample. (It is worth noting that although Raman spectroscopy can be performed on labeled samples, including Raman-active dyes, deuterium-labeled samples, and molecular tags that produce bands in the silent region (e.g., [8]), these are not routinely applied in Raman experiments.) The imaging studies outlined in this chapter have all been restricted to those that do not use labels, including deuterium labeling, or the use of signal enhancement, e.g., from surface plasmons, utilized in techniques such as tip-enhanced Raman scattering (TERS) or surface-enhanced Raman scattering (SERS). Readers interested in biological applications of these enhanced Raman techniques are referred to several recent reviews on the topic (e.g., [9–11]). In addition, the other imaging techniques described in the multimodal Raman section have been limited to those that also do not require any sample labeling.

With improvements in the speed of Raman imaging measurements in recent years, there has been a corresponding increase in the number of published studies using Raman imaging, particularly for biological applications. While there are a number of recent reviews detailing the current status of Raman imaging for particular topics within bioanalysis, such as focusing on plant biology, hard tissue applications, and so on, this chapter aims to showcase the wide range of biological and medical-related applications utilizing Raman imaging. Although this chapter primarily focuses on spontaneous Raman imaging, there are several other label-free Raman techniques available that can vastly improve imaging speed, but at a trade-off of spectral resolution and range. CARS and SRS are the most well-known approaches and use coherent nonlinear effects to boost the measured signal. As such, an overview of the implementation and types of results obtained with CARS and SRS is also included. Raman, CARS, and SRS can all, potentially, be combined with other techniques to provide additional information on the nature of the sample under investigation. Therefore, the final section of this chapter focuses on recent

developments in combining Raman-based imaging modalities with other imaging techniques including infrared spectroscopy, mass spectrometry, digital holographic microscopy, and Brillouin imaging.

In the following chapters, we will outline some of the main considerations Raman, CARS, and SRS imaging including sample preparation (Chap. 2.1), instrumentation (Chap. 2.2), and data analysis (Chap. 2.3). In Chap. 3, we summarize the key research findings in the last few years, primarily from 2010 onward, in the fields of Raman (Chap. 3.1), CARS and SRS (Chap. 3.2), and combined imaging approaches (Chap. 3.3) for applications in biosensing and medical diagnosis.

4 Experimental and Instrumental Methodology

4.1 Sample Preparation

Raman spectroscopy can be performed on a wide range of different sample types from solutions such as tears, blood, plasma, and other bodily fluids (see Baker et al. [12] for a recent review) to solid materials including teeth and bones (see Gamsjaeger et al. [13] for a review). In terms of imaging studies, Raman has been used to study a wide range of both soft and hard tissues in organisms ranging from humans and other mammals to plants, fungi, and bacteria. Each of these sample types has their own preparation constraints, and some example protocols have been outlined in a recent review [14]. Some general considerations for both soft and hard tissues are discussed below.

4.1.1 Sample Considerations

While sample preparation for Raman imaging is usually straightforward, there are some factors that should be considered to ensure good-quality images. In general, it is more challenging to perform Raman spectroscopy on dark-colored samples than it is for lighter-colored or transparent samples, as darker colors can absorb the excitation laser light resulting in damage to the sample. For example, Zhang et al. noted Raman spectroscopy of black hair was difficult due to the melanin content which absorbed the laser light resulting in sample destruction and so restricted their analyses to lighter-colored hair [15]. Therefore, on darker pigmented samples, it may be necessary to limit the excitation laser power used to prevent sample damage or shift the wavelength to a nonabsorbing region, both of which can have an effect on the signal-to-noise quality of the generated Raman spectra.

In many exploratory Raman studies, it can be useful to compare the Raman images obtained with other imaging techniques, one of the most established being fluorescence imaging. Fluorescence imaging (unless limited to autofluorescence) requires the use of labels, either through the use of dyes, immunostains, or expression of fluorescent proteins such as green fluorescent protein (GFP) in the cells or tissues of interest. In general, the presence of these labels will generate a broad fluorescence signal that completely obscures the Raman bands in a spectrum. This precludes the use of pre-stained samples for Raman, i.e., any fluorescence labels

should be added after the Raman imaging has been performed, and means that Raman imaging cannot routinely be applied to cells or tissues from transgenic animals expressing fluorophores.

Currently, most Raman imaging of cells has been based on those in 2D cell culture, i.e., individual cells or monolayers of cells. However, in the last few years the possibilities of using 3D cell cultures have emerged. With continuing advancements in fields such as scaffold engineering and tissue fabrication [16], or tumor tissue architecture [17], for example, the ability to measure biomolecules, cells, and tissues in 3D will be a key tool for future research in these areas. While the practicalities of successful 3D cell culture preparation are beyond the scope of this chapter, it is worth noting that it has already been shown that Raman spectra of sufficient quality for analysis can be obtained from within both spheroidal 3D cultures, approximately 300 μm depth, and cells embedded in a matrix, at approximately 120 μm depth when using 785 nm excitation [18]. The effects of the laser excitation wavelength on the penetration depth achievable are discussed in more detail in the Raman instrumentation section. In a similar manner, imaging of both hard and soft tissue has often required sectioning the sample to produce thinner, and often flatter, subsections of the sample for analysis. Depending on the strength of the sample, sectioning can result in tearing, fracturing, or other distortions to the sample. As such, developments in imaging of 3D cell cultures may also be useful for imaging of tissues by reducing the need for sectioning or may have an impact on the applications of Raman imaging in surgery, for example, where tissue sectioning prior to measurement is not possible.

4.1.2 Live Versus Preserved Samples

While it can be argued that imaging live samples, in conditions close to their natural environment, is most desirable, it is not always possible to do so. Examples where imaging live samples is not feasible include the use of nonsimultaneous multiple imaging techniques where movement in the sample between measurements will affect image registration, where the phenomenon under investigation occurs faster than the time taken to collect an image, or where samples must be collected in a different location to the imaging measurement, e.g., tissues collected during surgery or from tissue banks. In circumstances where samples need to be preserved prior to measurement, determining which fixation method to use can be a challenging question. A number of studies have investigated fixation and cryopreservation methods for cells [19, 20] including oocytes [21] and tissues [22–24] in terms of their effects on sample morphology and biochemical composition as well as on Raman spectra and image quality. Chemical fixation methods, such as formalin fixation, and cytocentrifugation have been shown to preserve the cell in a state close to that of live cells, while air-drying results in more distinct changes [19]. When using chemical-based fixation methods for cells, aldehyde-based fixation protocols perform better than alcohol-based methods, and parameters such as the temperature of the fixation media also influence the quality of both the Raman images and spectra [20]. In tissues, common fixation, embedding, and dewaxing procedures can lead to a loss of lipid content, with the consequence that other cellular

components such as proteins are relatively enriched in the resulting spectra [23]. Depending on the tissue, xylene removal may not be completely effective, resulting in some paraffin signal present throughout the sample, and may be particularly prevalent in some tissue types. This paraffin residue can also affect the interpretation of molecules in the tissue section that have a spectral overlap with paraffin, such as phospholipids [22]. However, the spectra are still detailed enough to allow for clear determination of different tissue layers in skin [24] and colon tissue [22], for example.

Although not commonly analyzed by Raman imaging, it is also possible to measure biofluids, and for imaging, this would generally mean that the biofluid would be dried out on a suitable sample carrier so that variations in sample composition can be measured. When using this approach, it is important to consider the concentration of the sample deposited onto the sample carrier as greater homogeneity in the distribution of components is seen for more dilute samples, as was shown for proteins in synovial fluid [25].

4.1.3 Sample Substrates and Imaging Environment

The substrate that a sample is placed on for measurement can influence the Raman spectrum, especially if the sample is relatively thin, for low numerical apertures, or if Raman spectra from z-positions close to the substrate are needed. Many plastics, such as those used for cell culture dishes, are not suitable for Raman imaging as they give rise to very strong Raman spectra. Glass microscope slides and coverslips can be a suitable option, particularly when using longer excitation wavelengths, although most glass slides do produce some broad bands below approximately 1000 cm^{-1} which can be particularly noticeable in spectra collected close to the glass surface. Quartz microscope slides and coverslips also give rise to relatively weak, broad Raman bands, but these tend to cover a more limited wavenumber range than those observed with glass substrates, making quartz a good option. In terms of cell imaging, cell culture dishes with either glass or quartz bottoms are available, allowing cell culture and Raman measurements to be performed on the same substrate, minimizing the environmental change experienced by the cells. Good-quality CaF_2 exhibits a strong Raman band at approximately 321 cm^{-1} but does not give rise to strong bands in the fingerprint or high wavenumber regions, particularly when using visible excitation [26, 27]. Therefore CaF_2 slides can also be used for Raman imaging in cases where the low wavenumber regions are not required. Other common sample carriers may not always be suitable for Raman imaging, depending on the nature of the sample. For example, cells do not appear to proliferate well on ZnSe [28], while other substrates may alter the Raman signal obtained, e.g., MirrIR Low-E glass slides can increase the Raman signal via reflections but require measurements to be performed in a transflection orientation [29] which may not always be desirable.

Depending on the sample, the substrate may need to be treated in order that the sample adheres to the substrate. This is common for cell imaging where the substrate is coated with compounds, often proteins such as gelatine [30] or poly-L-lysine,

which cells often adhere to better than the bare substrate. For other samples, such as nonadherent cells, samples may have to be embedded in a matrix prior to measurement. Example matrix materials include cellulose, methylcellulose, collagen, glycerol, and complex matrices such as Matrigel. However, it should be noted that all of these matrix compounds produce Raman spectra of their own, and so careful selection of the right matrix material should be based on minimizing the spectral overlap with the sample of interest.

Hard tissues and many preserved samples can be measured in air. However, for live samples, and indeed some preserved samples, they should be immersed in liquid during the Raman imaging experiment in order to prevent the sample drying out. Raman spectra are not strongly affected by the presence of water, allowing the use of aqueous solutions for sample immersion. Although water may be suitable for some preserved samples, for most live sample imaging and particularly for longer-term imaging, additional salts and sugars are needed to maintain the health of the sample. Simple buffers such as phosphate-buffered saline supplemented with an energy source such as glucose do not generally make a significant contribution to the Raman spectrum of the immersed sample. It is also possible to measure samples in common culture media such as RPMI 1640, DMEM, MEM, etc. as long as they do not contain colored indicators such as phenol red, which create significant background contributions to the Raman spectra, often completely swamping any Raman signals from the sample. Supplemented culture media, e.g., with fetal bovine serum added, can still be used during Raman imaging experiments, but depending on the concentration of the supplemented compounds, they may contribute to the Raman spectrum.

4.1.4 Sample Number and Statistical Significance of Results

Finally, when designing any experiment that uses human or animal samples, or other samples that are in limited supply, it is important to consider the number of samples that should be analyzed. For exploratory studies, the sample number may not be as important, but for any studies from which conclusions about human health, disease markers, purity assessments, and so on are drawn, it is important to ensure that a sufficient number of samples are analyzed to ensure the conclusions drawn are robust and unbiased. The number of samples that will be required for a particular study is dependent on several factors including the type of samples, the hypothesis or scientific question under investigation, and the confidence limits required for reporting the data. More information on the parameters affecting the appropriate number of samples for a study and methods to determine appropriate samples sizes have been outlined previously (e.g., [31–33]). With spectroscopic data in mind, detailed information on the selection of the appropriate number of statistically independent samples for use in classification models has been provided by Beleites et al. While they focus on classifier training and testing, the points covered are also applicable to other experiments (i.e., where classifier training is not used) including where limited sample numbers are available [34].

4.2 Instrumentation

4.2.1 Raman Instrumentation

The components of typical Raman microscopes have been comprehensively described in recent reviews by Butler et al., Krafft et al., and Pence and Mahadevan-Jansen [14, 35, 36]. Therefore, in this chapter we have concentrated on those elements of particular importance for the analysis of biological specimens and the developments in instrumentation that are specific for imaging microscopes.

Raman spectroscopy can be achieved using excitation wavelengths from the UV, through the visible range, and into the infrared with the wavelength employed influencing several aspects of the Raman spectra obtained from biological samples. Using near-infrared (NIR) excitation wavelengths avoids the problems of fluorescence, partly due to the fact that the excitation photon energy is lower and cannot drive the same transitions to fluorescing excited states that occur with visible photon energies. Additionally the Raman spectrum and fluorescence do not overlap significantly [37] and NIR light penetrates deeper into tissues such as skin [38], compared with visible and UV light. However, as the efficiency of most CCD detectors is lower in the NIR region, and the Raman intensity is inversely proportional to the 4th power of the excitation wavelength, acquiring Raman spectra with good signal to noise in the NIR can require relatively long collection times [37]. Measurements taken with excitation lasers operating in the visible region, therefore, benefit from increased Raman intensities and better detector efficiencies; however, this is at the cost of increased overlap with fluorescence contributions to the Raman spectrum. Despite this, many of the studies discussed in 3.1 have been performed with visible excitation, both in the green and red regions of the electromagnetic spectrum. The UV region of the spectrum generally suffers less from fluorescence contributions [37] but, due to the high energy of the excitation light, can cause photodamage and photodegradation of the sample. Deep UV imaging is not commonly carried out due to the risk of sample damage. However, under carefully controlled conditions, it is possible and generates Raman images rich in information on nucleic acid bases and aromatic amino acids. Adding Lanthanide ions can also significantly extend the sample lifetime under deep UV imaging conditions [39]. The choice of excitation laser may also depend on the sample under investigation as resonance enhancement of Raman signals can occur when the excitation wavelength is close to an electronic absorption band in the sample [40]. As examples of molecules of biological interest, resonance Raman spectra of nucleic acid bases and aromatic amino acids can be recorded with UV excitation, while carotenoids such as β-carotene and heme-based molecules generate resonance Raman spectra at visible wavelengths [40, 41].

Raman measurements were initially performed as point-based measurements (see Fig. 7.1a for a basic overview of a Raman microscope), which eventually led to the ability to capture high-quality spectra from distinct points in biological samples using confocal detection around the early 1990s, where the techniques were referred to as “microspectroscopy” rather than “imaging” [42]. The approach was initially very limited in terms of speed: if the detector is only one dimensional and the acquisition time for a single Raman spectra is in the order of seconds, then modest

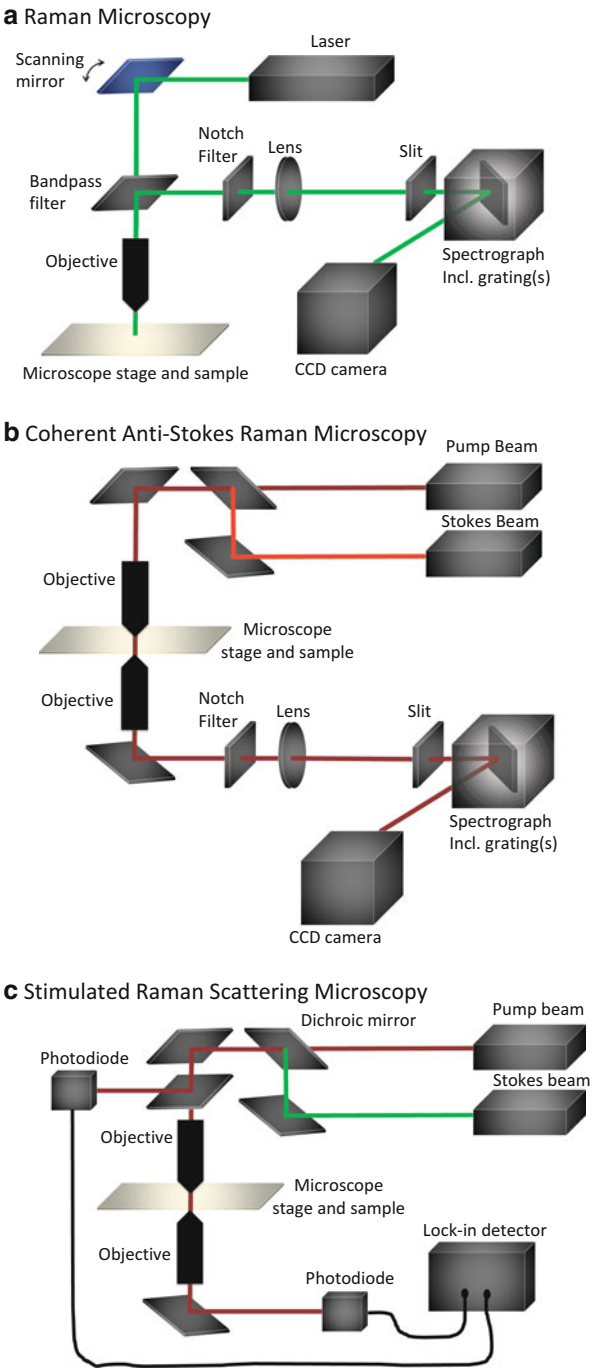

Fig. 7.1 Basic outline of instrumentation for (**a**) Raman, (**b**) CARS, and (**c**) SRS microscopes. In all cases, many optical components such as lenses and filters have been omitted for simplicity. In addition, only the laser path is represented, and indications of laser beam width, polarization, etc.,

sized Raman images could take hours to acquire (e.g., 100 × 100 pixels, 1 s per pixel, ~3 h). Especially for biological samples, where higher power may result in sample damage, and even fixed samples that may degrade over long measurement times, there has been a strong need for faster Raman imaging. Significantly faster biological images can be obtained by using a line-shaped focus with a two-dimensional detector, modality [43], allowing the observation of biological dynamics with a time scale of minutes, such as apoptosis [44]. The 2D detector allows for the parallel acquisition of all spectra from each point in the line-shaped focus. For the current state of the art, high-end deep-cooled CCDs can collect more than 90% of the incoming light, the laser excitation can be applied up to the limits of sample damage, and the numerical aperture (capture angle) of the microscope objectives is effectively maximized; the imaging speed for diffraction limited images by spontaneous Raman can be on the order of minutes per cell and not substantially faster unless some other factors are exploited. One intuitively obvious way to improve imaging speed is to reduce the sampling points. Interestingly, this does not always result in a significant degradation of the final image. Spectra taken from points in cells separated by much more than the diffraction limit can show notably different features [45], but in general, the oversampling in order to maximize resolution includes a large amount of redundant spectral measurements that are not significantly different from their adjacent pixels. This depends of course on the spatial variability of the sample but also results from the physics of the microscope itself, where the point spread function blurs each measured point. To avoid excessive blur, oversampling is common, but for more uniform samples, where the differences from region to region are more gradual, such requirements can be relaxed in order to speed up the measurement time. Even for highly heterogeneous samples, intentionally undersampling and using compressed sensing reconstruction techniques can be

Fig. 7.1 (continued) are not shown. (**a**) Raman microscopy. Laser light is directed to the sample on the microscope stage via a microscope objective, illuminating a point on the sample. Backscattered light is directed via a bandpass filter through a notch filter (rejecting light that is the same wavelength as the laser excitation) and slit (controlling the amount and angle of the light entering the spectrograph) before dispersion of the light, via gratings, and collection on the CCD camera. The addition of cylindrical lenses in the system, in conjunction with a 2D detector, results in parallel collection of spectra from all points along a line illumination on the sample. (**b**) CARS microscopy. Many different instrumentation approaches have been used for CARS microscopy, and so only a stylized version is given here. Two laser wavelengths, a pump beam and Stokes beam, are directed to the sample via a microscope objective. The output light is collected via a second objective and detected via a spectrograph and CCD camera. Generation of the two laser wavelengths is often done using a pulsed laser in conjunction with an optical parametric oscillator (OPO) or optical parametric amplifier (OPA) or in conjunction with a photonic crystal fiber. (**c**) SRS microscopy. Similarly to CARS, SRS employs two laser wavelengths, a pump beam and a Stokes beam, with the intensity of one beam modulated. These beams are directed to the sample via a microscope objective where (in the presence of a resonant vibrational mode) some degree of modulation is transferred between the two beams. The light is collected via a second microscope objective and the change in modulation of the beams detected via photodiodes attached to a lock-in amplifier

very powerful in optimizing the total information acquired for a given amount of measurement time and laser power [46].

For larger samples, particularly tissue sections, even with improvements mentioned above, measurement times with full imaging can still be prohibitive. Various approaches to better "target" the Raman measurements to specific regions of interest have been suggested in order to further reduce measurement times required. The majority of these approaches involve combining Raman imaging into a multimodal system where other analysis techniques provide an overview of the sample (discussed in more detail in the multimodal imaging section) allowing Raman measurements to be taken from the regions of interest identified by the other modality. By using scanning mirrors, it is possible to select regions in a cell and determine how much spatial information to average from the sample, which can result in improved Raman spectra compared to single point or even full imaging [47]. Another approach is to use the Raman data collected as a means of determining the next measurement points. Rowlands et al. implemented this approach by first taking two spectra at random. Next they calculated a cubic spline interpolant and a Kriging interpolant between these two points. Depending on the result from the Kriging interpolant calculation, the next measurement point is taken as either the position furthest from those already measured or the position with the largest difference between the two interpolants. The process is repeated with the new measurement points until the difference between the two interpolants reaches an acceptably small level. The increase in overall measurement speed is based on the assumption that these two interpolant values will converge in areas where there is little variation in sample features. This should result in fewer measurement points taken in these regions while concentrating the measurements in areas with higher variability [48]. An alternative method for reducing the number of spectral measurements required to analyze a sample is to employ compressed sensing approaches, where a signal can be reconstructed from a sparse subset of data points. This approach has recently been applied to hyperspectral Raman images, without the need for microscope modifications. High-resolution and relatively low-noise Raman images could be reconstructed from five times less data point sampling than would be used in conventional image Raman imaging, increasing the speed of measurement. The reduced exposure time for the sample has added benefits of reducing photobleaching on sensitive samples [46].

4.2.2 Coherent Anti-Stokes Raman Scattering (CARS) Instrumentation

The discussion so far has been concentrated on spontaneous Raman scattering, whereby an incident photon is scattered according to the vibrational bonds in the sample. The excitation light does not need to be coherent, although in practice, lasers provide the most efficient narrow bandwidth and easily focused excitation fields. The low Raman scattering cross section for most biological materials means that the techniques require large photon flux, optimized collection geometries (i.e., high NA lenses), and sensitive detectors. With excitation powers approaching the limits of sample damage, one approach to improve signal is to tune the laser excitation to resonate with a vibrational band of interest. This then requires coherent excitation

and is usually implemented with pulsed lasers. Pulsed lasers have the additional advantages of having high peak power, which is necessary to drive the nonlinear interactions, and are usually tunable. Coherent Raman techniques have limitations in the ability to measure and quantitatively interpret rich spectral information, but rather than competing directly with spontaneous Raman spectroscopy in terms of spectral range and resolution, they are usually exploited for their strengths, which include the ability to provide high-speed, high-contrast spectral imaging. Until now, the most common way to use nonlinear coherent effects to boost the Raman signal has been to use coherent anti-Stokes Raman scattering (CARS) that can be used as an imaging mode [49]. It is also possible to combine CARS in a complementary manner with spontaneous Raman spectroscopy to provide detailed spectra from one mode, with high signals from the CARS mode [50].

CARS imaging is implemented by using two wavelengths of laser excitation, one is the pump beam which drives a molecular excitation to a virtual state, which can then be driven, by stimulated excitation, down to a vibrational state by a Stokes beam (Fig. 7.1b). The molecule can then be excited to a higher virtual state and driven by stimulated emission down to the ground state. When the frequency difference between the two incident beams is resonant with a vibrational transition in the sample, the output signal increases. With the pathways involving virtual states, the process occurs essentially instantaneously, following a four-wave mixing process, rather than following actual excitation and de-excitation transitions which occur in fluorescence. This means that the output CARS light is coherent and directional. This has implications for detection methods including the possibility of gating the detection to reduce background signals, as well as control of the wave front and optimizing detection efficiency, while maintaining polarization. It also makes the process highly nonlinear with regard to the incident laser intensities. These points allow a degree of optical sectioning which, in conjugation with the near-infrared wavelengths, allows imaging in tissue samples that are difficult to image by spontaneous Raman imaging. For CARS, the fact that the anti-Stokes shift is used means that the output signal is also far away from the Stokes fluorescence typically generated from the sample.

While CARS imaging is a relatively complex imaging mode, in its most basic form, it provides only the spatial contrast resulting from a single vibrational mode. In practice this can be useful, but the ability to record multiple bands, or an entire spectrum, remains a key strength of spontaneous Raman imaging. CARS research has therefore pushed toward acquiring hyperspectral information. There are two instrumental approaches to achieving hyperspectral CARS imaging. One is to change the laser wavelength to achieve the signals for each vibrational modes of interest. The second is to use a broadband source to produce multiple excitations of vibrational modes [51].

The rapid pace of development in CARS techniques means that there are a large amount of different reports using different variations in instrumentation, and a full discussion is beyond the scope of this current work. However, key features of CARS include the spectral selectivity and high-speed imaging capability [52]. The inherent nonlinearity in CARS can also be exploited to increase both spatial and spectral resolution by measuring the onset of saturation in the CARS signals [53].

4.2.3 Stimulated Raman Scattering (SRS) Instrumentation

There are multiple ways in which coherent excitation and nonlinearity can be exploited to achieve high signals in Raman measurements. Aside from CARS techniques, discussed above, pulsed laser excitation can be used to stimulate Raman scattering, known as SRS. SRS can be used as a rapid imaging modality, with tunable selectivity for bands of interest. A good overview of the technique, with an explanation of the differences between SRS, CARS, and spontaneous Raman scattering, is available [52]. A significant advantage of SRS over CARS is the reduced background signal contribution. In terms of implementation, SRS uses two pulsed laser beams at pump and Stokes frequencies (Fig. 7.1c), and the intensity of one of the pulsed beams is modulated. Due the nonlinear interaction of the two laser beams, which occurs in the presence of a resonant vibrational mode at the laser focus, a degree of modulation is transferred from one beam to the other. This can then be detected using a lock-in amplifier and is related to the amount and type of vibrational modes in the sample, producing imaging contrast. SRS shares some of the overall limitations of CARS in the sense that it is challenging to acquire full spectra, but a number of different approaches have been made toward this goal [54]. High frame rate imaging, while stepping the spectral collection range, has already been demonstrated at video rates and above [55].

4.3 Data Analysis

4.3.1 Data Pre-processing

Interpretation of Raman spectra, especially Raman spectra acquired during imaging (which tend to have lower signal-to-noise levels than point spectra), usually requires some level of pre-processing before analysis, either by visual inspection of the spectra or by subsequent analysis by chemometric algorithms. Many of the points for consideration have also been discussed in a recent review by Byrne et al. [56], and particular attention to how experimental parameters affect Raman peak intensities, and hence Raman quantification, has been addressed by Kumar et al. [57]. Ideally, when analyzing Raman spectra, there should be no contribution to the spectra from any source other than the sample. While it is not always feasible to remove all other influences to the spectra, pre-processing steps aim to remove non-sample contributions as much as possible. Roughly, the sources of influence on the spectra arise from the instrument, the substrate, and the sample itself.

The exact performance of Raman instruments will vary slightly from machine to machine and will also change over time for an individual instrument particularly where maintenance procedures such as laser alignment or replacement of components are performed. Therefore, in order to allow comparisons between measurements, both those taken on the same instrument and those taken on different instruments, it is advisable to regularly asses the response of the Raman instrument(s) used and, as and when necessary, correct parameters such as data point spacing and scattering intensities [56]. There are various approaches to calibrate Raman instruments, for example, Slater et al. have outlined a calibration procedure

with the following steps: (1) wavelength calibration using a neon standard, (2) intensity calibration using a tungsten-halogen standard, (3) laser wavelength calibration using a Raman standard, and (4) validation of the calibration using the Raman standard. They suggest cyclohexane as a good Raman standard, using the 801.1 cm^{-1} Raman band [58], but other materials with a well-characterized Raman spectrum (particularly in terms of band position(s) and intensities) such as silicon are often used as well. It should be noted that using a homogenous sample to calibrate a Raman imaging system may obfuscate optical aberrations that appear when a spatially variant sample is then used after calibration/alignment. Therefore the quality of both spatially resolved components in the image and their spectral features should always be carefully evaluated in acquired data, even when alignment and calibration metrics appear correct. Where it is necessary to compare Raman spectra that have been measured with different excitation wavelengths, calibration procedures such as that suggested by Bocklitz et al. [59] can be used.

Other sources of spectral variation in the Raman spectrum originating from the instrument response include electronic sources of noise such as detector sensor variations, cosmic rays, dark current, and readout noise, which are always present to some degree but are often unpredictable contributions to the spectra. In order to reduce the influence of these sources of noise to the data, Raman images can be filtered or smoothed. Cosmic rays often strike the detector during long measurement times, causing errors that are large but usually very localized. They can then be removed by a local application of a median filter, with a threshold (typically several standard deviations) so that the majority of the data (i.e., the locations where no cosmic rays exist) is not altered in any way. As a 3D hyperstack, Raman images can be smoothed in the spectral domain, the spatial (x-y) domain, or both. Smoothing in the spatial domain is of limited use, since noise will be present throughout the spectral vector represented by one pixel, but smoothing in the spectral domain is commonly used. Depending on the spectrometer resolution, slit width, and laser wavelength, the spectrometer resolution is often less than would be implied by simply looking at the output spectra, and a more realistic (and less noisy) spectra can be produced by smoothing appropriately, considering all of these parameters. Loess fitting and other techniques are commonly employed but are beyond the scope of this current work. In general, however, it should be noted that the output from smoothing procedures should result in removal of noise, without the removal of features interest. Oversmoothing in the spectral domain will result in a loss of biochemical information, while oversmoothing in the spatial domain will lead to blurring of images.

Even with careful selection of a sample carrier, there will usually be some contribution to the Raman spectrum from the sample substrate. There are several ways to remove the background contributions in the spectrum. One method is to select a region of the image where no sample is present, extract an average Raman spectrum from this region, and then subtract this average from each pixel in the image. However, depending on the exact proportion of contributions from the sample and background to each pixel in the image, this may require careful implementation of baseline correction and normalization prior to background subtraction. It can also easily force some pixel values to become negative, which can be problematic for analysis since no real optical signal should be

measured as negative. Another method to remove substrate influence in the Raman spectrum is to use chemometric algorithms such as independent component analysis (ICA) that identify the background contributions as one spectral component [56]. While subtraction approaches can be useful when samples are imaged in simple media or matrices, it should be noted that background subtraction becomes more difficult when samples are imaged in more complex media. This is due to the mismatch between the sample and the surrounding media in terms of composition, particularly where substances are present in the media that are not present in the sample, as subtraction will result in negative contributions to the Raman spectrum of the sample for these substances. It is worth considering that even for simple media, the water "concentration" will be higher outside the sample, and so background subtraction to remove media contributions to the sample spectrum should also be normalized carefully before subtraction.

Some distortions to the Raman spectra can originate from the sample itself and also need to be addressed during spectral pre-processing. Autofluorescence often results in an increased background signal, particularly in the fingerprint region of the Raman spectrum. As most fluorophores have distinct excitation and emission ranges, autofluorescence can be avoided by the choice of excitation laser used. However, this is not always practical, especially if multiple fluorophores are present in the same sample, and the influence of the autofluorescence has to be dealt with once the spectrum is recorded. If the autofluorescence is relatively uniform across an image, for example, if it originates from the sample substrate, it is usually possible to remove the bulk of its influence by background subtraction. However, many compounds within the cell generate some level of autofluorescence. Examples include NAD(P)H, collagen, elastin, and flavins [60]. As these will not be uniformly distributed throughout the cell, it is harder to remove their influence, and baseline correction methods are perhaps the most effective solution. However, as the autofluorescence can be a signature of the compounds in the cell, it is not always desirable to remove it, since it can provide meaningful biological information [61].

One of the issues with analysis of tissue sections, and to a certain extent cells, particularly when using chemometric analysis methods, is the effect arising from the edges of the cell/tissue [30, 62]. Spectra originating from these regions can suffer from a number of problems including baseline distortions and widely varying proportions of sample versus background/substrate from pixel to pixel [62]. The high spectral variability in these regions, as compared to the bulk of the tissue, results in a large number of clusters/components that have little biological meaning. Strategies to overcome this and to focus on the relevant differences in the sample include controlling the number of clusters or components so that the edge of the tissue is described by distinct clusters that do not influence the interpretation of the bulk of the sample [30, 62]. Sample thickness can also affect Raman spectra, either through different volumes of sample being probed at each pixel or through out-of-focus effects [63]. A few studies have overcome the out-of-focus effects by using optical profilometry methods to assess the 3D topography of the sample, directing the measurement of the Raman spectra to always be taken from the top layer of the sample [63, 64]. Normalization of spectra, either through the use of an internal

standard or through vector normalization, can reduce the spectral differences induced by sample thickness differences but should always be applied after other corrections (background subtraction, baseline correction, and so on) [56].

4.3.2 Data Visualization and Analysis

Raman images of biological samples contain a wealth of information in terms of both chemical contributions and spatial distribution, and visualizing the data is an important step in interpreting this information. A common way to represent the data contained in a Raman hyperspectral dataset involves producing false color images based on the spectral information contained at each pixel in the image, e.g., the area under a Raman band, Raman band intensity at a given wavelength, the ratio between two Raman band intensities, or similar characteristics of the Raman spectra. Multiple false-colored images can be overlaid to compare the distribution of molecules represented by Raman bands at different wavelengths.

Ashton, Hollywood, and Goodacre [65] have shown, using a "rainbow" lookup table (also known as "jet") that is often the default color lookup table (LUT) for many image plotting software packages, the importance of the way in which the data is plotted in avoiding over-interpreting the data or missing features of interest. Using the simulated data shown in Fig. 7.2, they show that four different images can be obtained from the same dataset depending on how the false color is implemented. As the authors point out, there is no "right" or "wrong" image here; rather each image is able to answer different questions about what is contained within the data. The example, shown in Fig. 7.2, shows this. Image (a) with a significantly truncated range can answer the question "is this an animal?" (b) with a slightly increased maximum can answer "what animal is this?" (c) covering the full range of counts can answer "is there more than one animal here?" as a bird-like shape is also present on the zebra. And finally (D) with discrete blocks of color for the scaling, rather than the continuous scaling in the other three images, shows two bird shapes and so is able to answer the question "how many animals are in the image?" [65]. This illustrates that the appearance of "objects" in the data can be highly dependent on not only the type of analysis performed but on something as simple as the false color LUT applied when showing the image. Although the data shown in this example is analogous to that of a single peak area/intensity/ratio plot, the points raised are also pertinent to overlaid images and to any scale-based images produced during chemometric analyses, for example, PCA scores images.

4.3.3 Chemometric Analysis Methods

Chemometric analysis methods aim to clarify components in the data and separate them from noise, as well as provide other statistical tools such as classification of features into groups. There are many chemometric analysis methods that can be applied to Raman spectroscopy, many of which can also be adapted for the analysis of Raman images. Chemometric algorithms are often classified in several ways. They can be univariate, based on one measurement point (wavelength/Raman shift), or can be multivariate, incorporating multiple measurement points in the analysis. They can either be hard classification methods, where a spectrum (or image pixel)

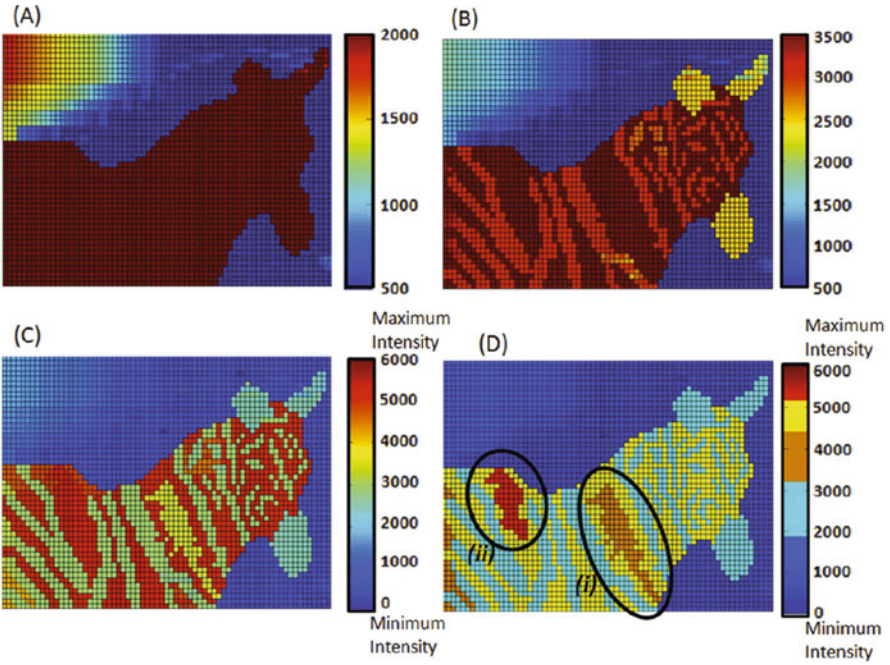

Fig. 7.2 A comparison of rainbow-shaded images constructed from a simulated Raman map with an intensity range of (**a**) 500–2000 counts, (**b**) 500–3500 counts, (**c**) minimum to maximum intensity, and (**d**) minimum to maximum intensity but using discrete colors to form the color ramp, (i) and (ii) identify the position of the bird shapes discussed in the text. Color bars are shown to the left of each image (Figure reproduced from [65] published by the Royal Society of Chemistry)

can only belong to one class, or they can be soft classification methods where a spectrum or pixel can belong to more than one class. Finally, they can be unsupervised, where no a priori information is used, or can be supervised, where information, for example, in the form of a reference spectrum, is required for the analysis. There are numerous articles that compare and contrast the various methods that have been applied to Raman spectroscopy (e.g., [56, 66–71]) to which the reader is referred to for further details. In this chapter, discussion has been limited to a brief overview of those analysis methods most commonly applied to Raman imaging as evidenced by the studies discussed in Sect. 3.

Principal component analysis (PCA) looks for a fundamental set of independent variables in a dataset [72], thereby reducing the dimensionality of a dataset. PCA produces a set of principal components (PCs) where PC1 describes the largest variation in the dataset, PC2 describes the second largest variation in the dataset, and so on. In terms of Raman imaging, PCA produces a score for each pixel/spectrum along with a loading vector, containing spectral information on the variance in the dataset, for each PC. The loading vectors contain both negative and positive peaks and, depending on the complexity of the sample, can be challenging to interpret [56]. The score values for each pixel can be used to create false color multivariate

images showing the distribution of each of the PCs in a similar manner to the univariate plots produced by Raman band intensities/peak areas, etc.

Hierarchical cluster analysis (HCA) is a method for grouping spectra together into clusters based on their similarities to each other often by calculating Euclidian or Mahalanobis distances [68]. In terms of Raman imaging, each pixel can be assigned to a particular color based on which cluster the spectrum belongs to, creating a false color map showing the location of spectra in each cluster. Selection of the number of clusters is normally user defined, meaning that determining the number of clusters can be somewhat subjective, although consideration of the spectral differences between average spectra for each cluster and the standard deviation for spectra described by one cluster can help determine how many clusters are appropriate.

Vertex component analysis (VCA) is based on unmixing hyperspectral datasets to find their reference components, also known as end-members. VCA is based on the end-members being vertices of a simplex in 3D space, meaning that all other data points can be described in terms of these end-members [73]. For Raman imaging, this means identifying the spectra that are the most "different" from each other and producing false-colored images (one per end-member) that then describe the abundance of that end-member at each pixel in the image. The end-member images can be overlaid to produce a composite image. As for HCA, many of the implementations of VCA require the number of end-members to be user defined.

Multivariate curve resolution (MCR) is another method for elucidating the pure signals from a data matrix of mixed measurements, based on the idea that the mixture is a bilinear model of pure signal contributions, or at least the variation in the dataset can be described by a bilinear model. Raman images must be unwrapped prior to MCR analysis and the results reformed into images [74]. Thus MCR produces distribution images and corresponding spectra for each of the pure components identified during the MCR analysis.

K-means clustering is another clustering method that aims to reduce a data set into a defined number of groups. The process starts with "k" number of groups consisting of a random data point. Subsequent data points are added to the group whose mean is closest to that of the data point, and the mean of each group is adjusted as new data points are added [75]. For Raman imaging, k-means clustering can be used to produce false-colored maps, with each pixel assigned to a single cluster, as well as also generating an average spectrum for each cluster.

5 Key Research Findings

5.1 Key Research Findings in Raman Imaging

5.1.1 Cell State and Metabolism

The use of Raman imaging for analysis of cells and tissues, particularly when used for many of the applications to human health and disease discussed later, is dependent on understanding the origins of the Raman signals generated. The simplest way to do this is to compare cell and tissue spectra to the spectra of individual cellular

components. This is relatively straightforward when the sample has a simple composition but can be challenging where a large number of different molecular species are all contributing to the overall signal. One way to tackle this complexity, particularly for cellular imaging, although the same can be applied to tissue imaging, is to identify marker bands or spectral profiles for classes of molecules, such as a lipid or protein signature. An alternative approach, depicted in Fig. 7.3, is to compare Raman and fluorescence images in order to identify spectral profiles for different cellular compartments and organelles [76]. Ramoji et al. have also shown that false color Raman images can identify some of the same cellular features as classical staining methods in leukocytes [77]. In another example, this time exploiting the resonance Raman effect, the colocalization of cytochromes B and C has been used to pinpoint the location of mitochondria in yeast cells [78]. A more recent study has taken hierarchical cluster analysis (HCA) of Raman images and matched the distribution of each of the components generated in terms of the best overlap they have with corresponding fluorescence images. In doing so, Raman spectra that are related to each of the fluorescent stains used can be generated and can then be used as training data/reference spectra for further analysis of Raman images, without the need for the fluorescent staining of later samples [79].

One of the main applications of resonance Raman imaging in a biological context has been for the study of cytochromes. As key components of the electron transport chain, cytochrome molecules have been used as indicators of living cells, particularly with regard to their redox states. Okada et al. followed the diffusion and oxidative state of cytochrome C during apoptosis and showed that these changes are independent of cell morphology [6]. The redox state of mitochondrial

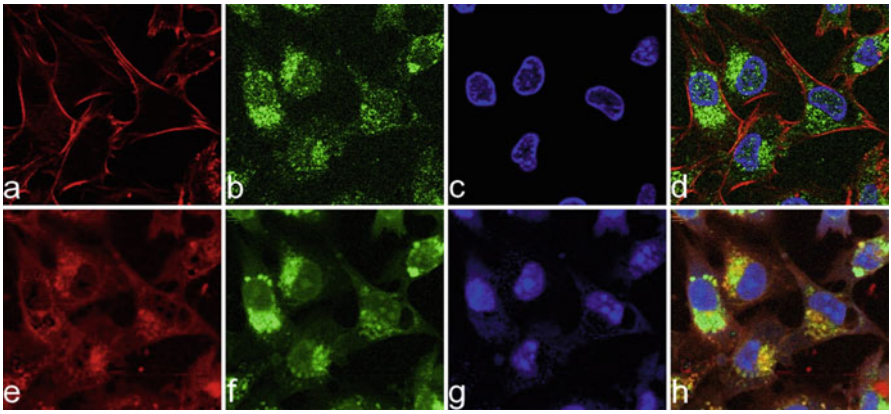

Fig. 7.3 Comparison of immunofluorescence images (**a**–**d**) and Raman-based images (**e**–**h**) measured by Klein et al. The red channels reflect actin, green channels reflect Golgi, and the blue channels reflect the nucleus. There are differences in distribution between the Raman signals and that of the fluorescence images, particularly in terms of actin distribution (correlation between **a** and **e** = 0.36, **b** and **f** = 0.74, **c** and **g** = 0.71). However, the combination of the components can provide a multichannel Raman image with a high degree of similarity to the fluorescence images [76] (Reproduced from Elsevier [76])

cytochromes in cardiomyocytes has also been estimated, based on the Raman intensities originating from cytochromes c, c1, and b, with reduced forms providing more intense Raman signals than the oxidized forms [80].

Several groups showed that with careful consideration of experimental conditions, it is possible to image live cells multiple times, allowing changes in the cells to be recorded at different time points (e.g., [5–7]). Pully et al. showed that changes in carotenoids induced by exposure to light could be detected before other changes in cell health, such as blebbing – a process that was accompanied by spectral changes in DNA and proteins. They also noted that some of the main constraints on time-lapse imaging studies are the control of nutrients, temperature, and pH of the cellular environment [5].

Raman spectroscopy has commonly been employed to discriminate between different cell types. Raman images characterizing the chemical composition (primarily heme, vitamin A and lipid content) of several types of cells originating from the liver (liver sinusoidal endothelial cells, hepatocytes, and hepatic stellate cells) have been used to identify each cell type [81]. Spectral differences were also used to classify different cell types/classes that may typically be present in blood from cancer patients, such as leukocytes, leukemic cells, and tumor cells [82]. The biochemical differences in Raman spectra of lymphocytes have been used to discriminate between T and B lymphocytes [83], and Raman imaging of murine stem cell colonies was able to identify nuclei and cytoplasm within the cells, as well as the extracellular matrix between the cells [84]. Raman imaging is also capable of distinguishing between different microorganisms, as shown by the identification of *Bacillus subtilis*, *Staphylococcus epidermidis*, and *Saccharomyces cerevisiae* from a mixture of all three species [85].

Identification of the current metabolic or activation states of cells can be a key step in understanding the course of diseases occurring when these normal processes go wrong. Raman imaging can determine the activation state of B lymphocytes, with a decrease in phospholipid content associated with activation [86]. Ghita et al. proposed that the differentiation status of neural stem cells could also be determined by nucleic acid Raman bands, specifically those indicating the levels of cytoplasmic RNA present, with higher concentrations seen in neural stem cells compared with glial cells [87]. Raman imaging has been used to assess the quality of human sperm, with healthy sperm exhibiting higher-intensity Raman bands associated with DNA and mitochondria, compared with sperm that had undergone UV-induced damage [88]. Chinese hamster ovary cells can be used for the production of proteins and monoclonal antibodies with Raman imaging able to discriminate between the different cell lines, as well as potentially able to indicate high-producing cell lines via the presence of a protein-rich signal that the authors attribute to the endoplasmic reticulum (ER) [89]. Raman imaging has also been used to characterize the communication between different cell types, with actin and DNA content and distribution shown to be important in the immunological synapse that forms between dendritic cells and T lymphocytes [90].

Raman imaging of the cell cycle provides information on the different states of a cell during normal cellular processes. An early study was able to identify the cell

cycle stage based on the Raman spectra obtained. However, the study suffered from problems in identifying the nuclear boundary which, as the authors pointed out, could be addressed by increasing spatial resolution of the Raman images but at the cost of the time taken for the measurements [91]. Shulze et al. were able to study the nucleus in detail, particularly in terms of the RNA and DNA distributions [92]. Combining Raman measurements with a second modality to identify the nucleus prior to Raman imaging has been suggested as a method for speeding up the Raman imaging [91]. Hsu et al. used such an approach, combining Raman measurements with autofluorescence imaging to follow the division of cells during cytokinesis and interphase [93].

5.1.2 Cancer Studies

Many cancer studies are performed on tissue sections, meaning that there is a mix of cell types included within each sample. As Raman imaging provides information on biochemical composition and spatial distribution, it can be used to identify the presence of different cell types within a tissue section. One such study showed that, in colon cancer tissue sections, Raman spectra could be used to identify erythrocytes (rich in heme but lacking other protein or lipid bands), lymphocytes (rich in lipids), connective tissue, and carcinoma (distinguished by differences in protein and DNA content). Although some researchers tend to avoid using 532 nm excitation for biological tissues in order to try and avoid the increased fluorescent background signal, this study found that the regions with this increased background also provided useful biological information as they correlated with areas where p53, a tumor suppressor protein, was active [61].

A different approach, focusing on the spatial distribution of molecules within breast tissue, has been used to assess a number of cell parameters including the size and dimensions of the cell and nucleus, distance between neighboring cells and Voronoi tessellation in order to characterize breast cancer cell types [94]. Larraona-Puy et al. have looked at the different distribution of key molecules in different tissue types, using a classification model based on bands associated with collagen, proline, protein backbone, and DNA to identify regions of the skin. Not only were they able to classify regions of normal tissue such as hair follicles, epidermis, and dermis, closely matching that of histologically stained tissue sections, but they could also identify regions of basal cell carcinoma [95].

Many cancer studies using Raman imaging have focused on the strength of, or lack of, particular signals in the Raman spectra. For example, in a study of cancerous and noncancerous tissue from salivary glands, the noncancerous tissue did not reflect the β-sheet protein content seen in the cancerous samples [96]. The presence of cancer cells in tissue, based on the acetylation and methylation of lysine residues in proteins contained in the cancer cells, has also been proposed [97]. On a cellular level, the presence and distribution of myeloperoxidase in both normal and abnormal promyelocytes, along with its absence in myeloblasts, could be used to identify each cell type as shown in Fig. 7.4. The numbers of each cell type found in bone marrow and peripheral blood smears can then be used for the diagnosis of myelodysplastic syndrome and acute myeloid leukemia [98].

Surmaki et al. noted that while many studies of cancer identification or development have concentrated on protein-based changes, lipids and carotenoid molecules are also significant players in the cell; in particular with regard to cancer development, they both have antioxidant properties that are important in the control of reactive oxygen species. In their study, Surmaki et al. used Raman maps to identify regions of carotenoids, lipids, and proteins with spectral differences seen for ductal and lobular carcenomas. They also noted that Raman images will incorporate information from the extracellular matrix, as well as the cells, providing additional information on the cellular environment [99]. Other studies have also focused on carotenoids and lipids in breast cancer, particularly looking at the nature of the lipids present in terms of saturation [100]. The ratio of the intensity of the nucleic acid peak at 785 cm^{-1} and the tryptophan peak at 752 cm^{-1} has also been proposed as a simple method for identifying skin tumors [101].

As cancer development is a multistep process, biochemical changes detected by Raman imaging can appear in areas that appear to be normal in morphological terms, with such changes potential markers for the early stages of the disease [102]. For example, an increased amount of lipid droplets in breast cancer cells has been correlated with the aggressiveness of cancer, suggesting that fatty acid synthesis could be an indicator of cancer development, particularly in the early stages of the disease [103]. An increase in lipid droplets has also been implicated in the development of colorectal cancer [104]. Raman imaging has also shown increased lipid content, lipid saturation, and phospholipid content in cells expressing high levels of the Her2/neu receptor, a proto-oncogene implicated in breast cancer, leading Hartsuiker et al. to suggest that the fatty acid content may be an indicator of metastatic potential in cells [105]. The metastasis of cancer cells from the primary tumor to secondary sites around the body is often associated with the later stages of cancer progression and can reflect poorer outcomes for the patient. The presence of metastatic cancer cells can also cause complications at the secondary site. Raman imaging has been used to monitor the effects of metastatic breast cancer cells on endothelial cells in the aorta of mice, where Raman analysis indicated an 18% increase in proteins and a 4% decrease in lipids for metastatic cancer cells. This change in endothelial cell composition may be a factor in the alteration of vasodilation that the authors note is associated with this disease stage [106].

There is currently a push to take Raman spectroscopy into the clinic, particularly to determine if tissue is cancerous to ensure all cancerous tissue is removed, while saving as much healthy tissue as possible, during surgery [107]. One of the main limitations for implementing Raman imaging in this context is the time required for measurements. However, advances such as the selective sampling approach outlined by Rowlands et al. [48] have been applied to basal cell carcinoma [107] and breast cancer tissue [108] potentially bringing the measurement time for large tissue sections, on the order of 1×1 cm^2, down to as little as 20 min [107].

5.1.3 Lifestyle Diseases and Aging

Lifestyle diseases, including diabetes, atherosclerosis, hypertension, strokes, and heart attacks, are often linked to unhealthy lifestyle choices such as a high-calorie

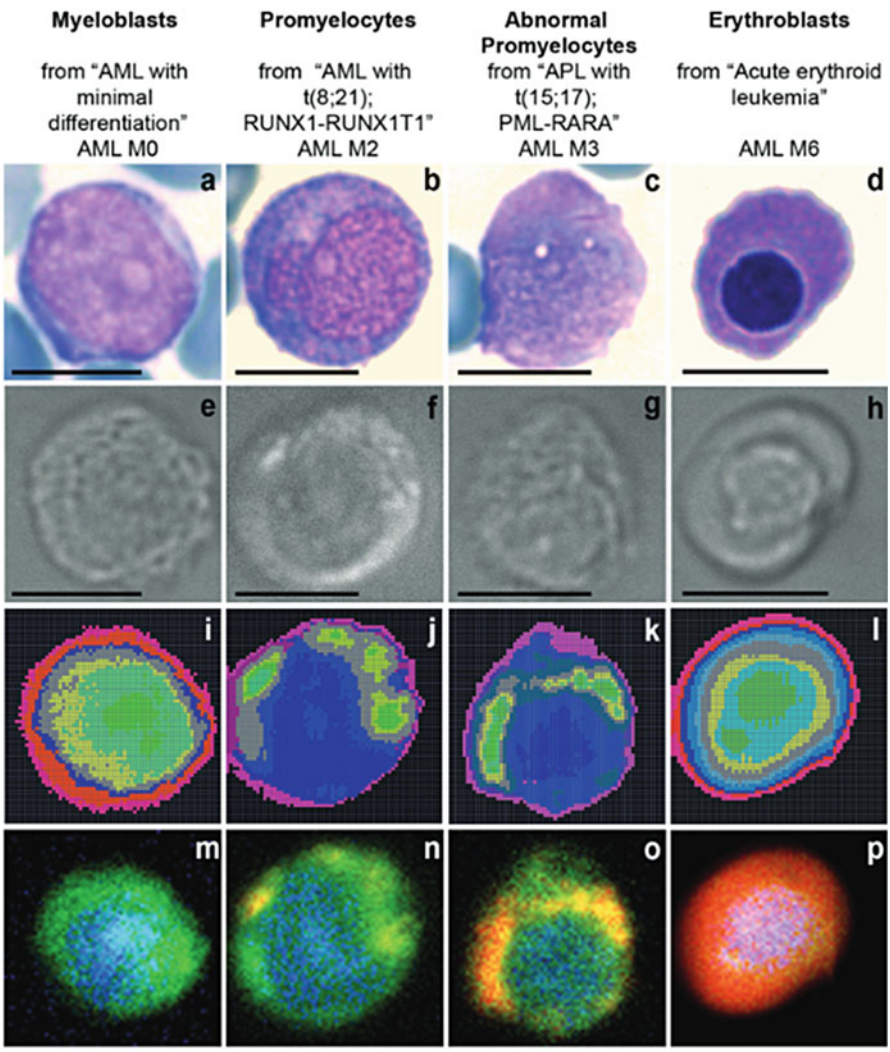

Fig. 7.4 Raman images from acute myeloid leukemia cells analyzed by Vanna et al. (**a**–**d**) Cells stained with May-Grünwald-Giemsa stain. (**e**–**h**) Bright field images before Raman measurement. (**i**–**l**) Hierarchical cluster analysis images. (**m**–**p**) multivariate images created from specific bands relating to nucleus (blue) and cytoplasm (green). For images (**m**–**o**), the presence of myeloperoxidase is shown in red. For image (**p**) the presence of hemoglobin is shown in red. Scale bar represents 10 μm (Figure reproduced from [98] with permission from the Royal Society of Chemistry)

diet rich in fats and sugars, lack of exercise, as well as factors such as smoking and alcohol consumption. These diseases tend to manifest in later life and are becoming more prevalent, particularly in industrialized societies. The risk factors for many of these diseases are shared, and the presence of some of these diseases themselves can

also be additional risk factors for other lifestyle diseases. For example, diabetes itself, along with the accumulation of lipids or cholesterol and endothelial damage, is an added risk factor for many other lifestyle diseases. Czamara et al. exploited the sensitivity of Raman to lipids to investigate the calcification process associated with aortic stenosis, finding colocalization between lipid and calcium (hydroxyapatite) even for the very small mineral deposits [109].

The relatively strong Raman signals generated by lipids in cells and tissues have been particularly beneficial for studies of atherosclerosis in both mouse models and human tissues. Kochan et al. [110] were able to show that while the livers of normal mice showed only small areas that were rich in lipids, the livers of atherosclerotic mice were rich in lipids, as were the livers of diabetic mice. In addition, even though the spectral overlap between vitamin A, essential for cell health [111, 112], and heme complicated matters, they were also able to visualize the vitamin A content in the mouse livers, highlighting a decrease in vitamin A content in early stages of disease [110]. Similar results were observed in the brains of mice where lipid to protein ratios were increased in animals in advanced stages of the disease [113]. A change in the structure of proteins contained within endothelial cells has been indicated to contribute to the stiffness of these cells during hypertension. Raman imaging has also identified changes in overall protein structure, α-helix and β-sheet [114], and amino acid composition [115], in mouse models of hypertension and atherosclerosis.

Raman imaging has been used to investigate the effects of sunlight on skin tissue. In a study by Ali et al., the lack of DNA bands in the basal layer was taken as evidence of DNA damage as a result of the solar radiation. The use of chemometric analysis methods also showed irradiation-induced changes in lipid content in the stratum corneum and the dermis [62].

Early identification of the complications of aging, such as the onset of Alzheimer's or Parkinson's diseases, is important in managing the disease progression and, consequently, the patient's quality of life. Raman imaging has been used with the aim of resolving controversy surrounding the potential presence of amyloid-beta (Aβ) protein, characteristic of Alzheimer's disease, in the cornea of affected patients. If Aβ was present in the eye, this could be an easily accessible tissue to monitor, in contrast to the brain. Techniques, such as staining, had given both positive and negative results for different researchers. Michael et al. then used Raman imaging to characterize the β-sheet to protein ratio for regions in the hippocampus with Aβ plaques or tangles, unaffected regions of the hippocampus, and the cornea. They found that the ratio was elevated in the regions where plaques and tangles were present, but unaffected areas of both the brain and the cornea had lower ratios, indicating no Aβ is present in the cornea [116].

5.1.4 Infectious Diseases

Identifying the presence of infective agents, such as bacteria or parasites, is important for implementing appropriate treatment, while analyzing the corresponding immune response of the infected cells and tissues provides information that may be beneficial for designing drug treatments or vaccines. Raman imaging has been used in a number of studies investigating the presence of bacteria in mammalian

cells. For example, the growth of *Staphylococcus aureus* has been tracked over a 24-h time period, with internalization of the bacteria confirmed via multiple images taken at different planes through the cell to create a 3D image [117]. Both 2D and 3D imaging approaches were used to identify cellular changes associated with *Mycobacterium gordonae*, with the lipid response in the mammalian cells suggested to originate from lipid-filled phagosome or lipid bodies [118].

Raman imaging of *Neospora caninum* parasite infection in human brain microvascular endothelial cells was able to indicate the location of the parasite within cells through identification of the parasite nucleus and lipid-rich regions thought to be the parasite membrane. In addition, the presence of a Raman band at 1554 cm^{-1} was attributed to the presence of lysozyme, indicating Raman imaging can also identify a step in the immune response of the infected cells [119]. *Toxoplasma gondii* is another protozoan parasite that is known to infect a wide range of hosts and cell types. Cells infected with *T. gondii* showed increased protein and lipid content, suggesting these molecules are part of the cellular response to the parasite. However, increases in nucleic acid content in the Raman spectra were noted to be proportional to the parasite proliferation, therefore originating from the parasite itself [120]. In malaria, *Plasmodium* parasites produce hemozoin, a crystalline form of heme, during catabolisis of hemoglobin in infected red blood cells. Hemozoin gives rise to resonance Raman signals when using green excitation wavelengths, allowing low concentrations to be detected within cells. Imaging the presence of hemozoin in erythrocytes is possible, even though erythrocytes also contain high concentrations of hemoglobin, due to the small spectral differences between the two substances [121]. Macrophages, forming part of the immune defense, are known to engulf hemozoin particles released into the bloodstream during malaria, and Raman imaging has been used to identify the presence of hemozoin inside macrophages, along with characterizing the corresponding cellular rearrangements and changes in biochemical composition of the macrophage cells [122].

5.1.5 Drug Treatments and Interactions

The effectiveness of drug treatment is dependent on the chemicals reaching the target site in cells, tissues, and/or organs. Once in the appropriate location, the action of the drug will induce changes, potentially both chemical and morphological, in the surrounding cells and tissues. Conversely, if drugs accumulate in the wrong site, the induced changes in the surrounding cells and tissues will manifest as undesirable side effects. As Raman spectroscopy does not require a priori knowledge of the sample, it is an ideal method to monitor cellular changes induced by drug interactions. Chloroquine is used as a drug treatment for *Plasmodium* infections that cause malaria. Raman imaging of infected erythrocytes has been used to probe the oxygenation state of hemoglobin as a marker for the effects of the chloroquine exposure [123]. Oxygenation of heme-based molecules has also been used as a marker for the presence of *Clostridium difficile* infection. Infection also results in altered protein and threonine contributions to the Raman spectra, attributed to the presence of inflammation, with the threonine signal reduced after antibiotic treatment [124]. Raman spectroscopy has been used to monitor the effects of drug

treatments in models of disease by monitoring vitamin A levels in hepatic stellate cells [125].

Other studies have noted that Raman imaging can monitor the effects of cancer drugs such as panitumumab on cells, allowing an assessment of their efficacy, even when the mode of action of the drug is not fully understood [126]. Anthracycline compounds are also potential therapies for cancer, as they inhibit topoisomerase, and have been shown to induce changes in the spectra originating from the cell nucleus in a concentration-dependent manner [127]. Two structurally related compounds, nobiletin and 5-demethylnobiletin, have been shown to have different effects, suggesting different modes of action, on cancer cell lines. Raman imaging studies showed that nobiletin induced changes in Raman bands originating from nucleic acids, while 5-demethylnobiletin affected localized lipids [128]. Nucleic acids were also the target for the action of indinavir and lopinavir in cervical cancer cells [129], and both nucleic acid and protein secondary structure changes were seen in myeloma cells after treatment with bortezomib, a proteasome inhibitor [130].

Photodynamic therapies, where a drug taken up into a cell or tissue is activated by light exposure to produce free radicals or reactive oxygen species to induce cell death in nearby cells, are used for cancer treatments. Brozek-Pluska et al. have used Raman imaging to identify the cancer cell composition, track the uptake of hematoporphyrin, and assess the effects on the surrounding tissue after photoactivation. They found cancerous regions were richer in saturated acids and proteins such as mammaglobin A and that cancerous cells took up larger amounts of hematoporphyrin compared to noncancerous regions of the tissue. Additionally, they showed that the Raman intensity of proteins and lipids in the surrounding regions did not alter significantly after photoactivation [131]. Raman imaging has also been able to show that cells with oncogenic mutations do not respond to drug treatments such as erlotinib, in the same way as normal cells do [132], indicating Raman analyses can provide insights into drug resistance as well as drug responses.

Depending on the chemical structure and concentration of a drug, it can be possible to directly measure the presence of the drug in the cell, facilitating simultaneous measurement of the drug position and the response of the surrounding regions of the cell. In drugs containing C≡O bonds, by integrating across 1945–1965 cm^{-1}, the drug location can be visualized, since that spectral region does not overlap with signals from a typical cell. The drug location can be an important step in determining its mode of action, and, in this case, the authors were able to show that the drug accumulates both inside and directly surrounding the nucleus [133]. Although exhibiting some overlap with cell-based vibrations, the C=O bond in the cancer drug paclitaxel has also been used as an effective marker to track the number of cells taking up the drug and its location at different exposure times [134]. Another Raman imaging study, based on understanding the metabolism of erlotinib which contains a C≡C bond, have indicated that it is possible to assess how drugs are modified within the cell, after desmethyl-erlotinib was detected inside exposed cells [135].

The composition of drugs can be measured via Raman imaging, providing information on both the nature and the distribution of active ingredients, other tablet

ingredients such as binding or dilution agents, and the nature of the polymer coating (if present). Vukosavljevic et al. used this approach to look at the composition of tablets containing verapamil hydrochloride, a calcium channel blocker, and were able to determine that drug release occurs through pores that form in the polymer coating of the tablet [64]. In order to understand the process of drug transfer from topologically applied drugs, e.g., those contained in lotions or creams, Goto, Morita, and Terada have used Raman imaging to follow the crystallization of components from creams containing urea as the active ingredient [136].

Modeling the uptake of nanoparticles is another potential application where Raman imaging can provide insight into the cellular response to particulate matter. Nanoparticles are sometimes employed as vehicles for drug delivery into cells, and Chernenko et al. have used Raman imaging to follow the uptake and metabolism of two nanocarriers (poly-(-caprolactone) (PCL) and poly(lactic-co-glycolic acid) (PLGA)) tracking their location within HeLa cells via Raman bands characteristic for the two molecules [137]. A significant impact of nanoparticles on human health is the potential detrimental effect on our cells and organs from environmental pollutants. Particulate matter in air, for example, has been shown to contribute to lung cancer [138]. Taking the subcellular environment and induced changes in metabolism as potential indicators of a toxic response, Dorney et al. investigated the local environment of polystyrene nanoparticles that were taken up into the cytoplasm of human lung adenocarcinoma cells [139]. Raman imaging studies of fibroblasts and macrophages showed differences in nanoparticle uptake when exposed to TiO_2 nanoparticles, with fibroblasts storing the nanoparticles in small vesicles, whereas the macrophages, with a higher uptake of nanoparticles, distributed them in much larger vesicles [140]. Other studies have suggested that nanoparticles such as TiO_2 and α-FeO(OH) can pass across the nuclear membrane and accumulate in the nucleus [141]. Extending these studies into multicellular organisms, cyanobacteria have been shown to internalize TiO_2 nanoparticles [142]. The uptake of TiO_2 nanoparticles by *Caenorhabditis elegans* has shown that despite the increase in sample complexity, Raman imaging can still provide information on the position of the nanoparticles as well as the changes they induce in the nematode itself, particularly with respect to proteins [143].

5.1.6 Hard Tissues

Raman imaging has been used to study various aspects of tooth structure in humans and primates. A recent study concentrated on the ratios of carbonate and phosphate in the dentine – enamel junction, as well as determining the presence of collagen as part of the organic component of teeth [144]. The composition of enamel in teeth determines tooth strength with hypomineralization linked to increased porosity, faster wear, and increased susceptibility to decay. Healthy enamel was shown to have strong spectral features attributed to phosphate-rich minerals, whereas lesions exhibited both carbonate substitution in the mineral components and an increase in protein content [145]. Similar mineral substitution has also been shown in sea urchin teeth where a simple band shift was sufficient to determine the presence of Mg^{2+} within the $CaCO_3$ crystal structure [146]. In direct clinical applications, Raman

imaging has identified the presence of pyrophosphate an atypical femoral fracture, with no pyrophosphate observed for control samples [147].

A particularly intriguing study used Raman imaging to assess structural defects created during tooth formation, based on the idea that these defects could be used as an assessment of illnesses and other stressors occurring during the early years of child development. The authors correlated the information from Raman imaging and other analytical techniques, such as mass spectrometry, with that of medical and behavioral data that noted the occurrences of stressful events in the lives of primates. Raman imaging was able to identify small features, primarily changes in protein and biomineral structure, that were not visible via light microscopy, and the resolution provided by the Raman images meant the size of the defect, and therefore the length of time the stressful event lasted could be estimated [148].

The repair of teeth, using resins, has also been studied by Raman imaging. Toledano et al. investigated dentin adhesive systems in terms of their ability to induce remineralization at the dentin interface [149]. In a further study, they found mechanical stresses (modeling the effect of chewing or grinding on the remineralization process) resulted in alterations of the mineral/matrix ratio [150].

Several studies have investigated the process of mineralization during bone cell differentiation. Hashimoto et al. followed the mineralization process during the first 72-h of cell differentiation, using Raman imaging to locate the presence of hydroxyapatite [151]. In a further study, they showed that the β-carotene concentration was proportional to the degree of mineralization, suggesting the presence of β-carotene could be used as an indicator for the initiation of mineralization. In addition, they also monitored cytochrome C as an indicator of apoptosis, with the onset of apoptosis in different cells linked to the fluctuations in cytochrome C intensity seen in the Raman spectra [7]. In another study of the mineralization process of bone nodules, Raman imaging identified the transition of hydroxyapatite from amorphous to crystalline during the 28-day monitoring period [152]. Extending this to more direct medical applications, Gao et al. monitored human mesenchymal stem cells, placed on a scaffold that would be implanted during bone regeneration therapies, to assess the effects of such a scaffold on osteogenic differentiation. They observed two stages of mineralization over a 28-day period and also noted that the mineralization process in cells on the scaffold was slightly delayed compared to that of cells on culture plates [153]. Of consequence for bioengineering, Raman imaging has shown that other substrates can also affect stem cells including strontium ion incorporation in bioactive glass resulting in increases in lipid rafts and cellular and membrane cholesterol [154].

Hair is an easily accessible sample for analysis. Wei et al. have investigated the potential for hair samples to provide information on the health status of an individual, namely, those suffering from rectal cancer. They found that different sections of the hair may be more useful than others for such studies in that there were little differences in cuticle between healthy people and cancer patients. The cortex and medulla, on the other hand, both showed changes in proteins, with cancer patient's hair reflecting lower protein content in the cortex, less α-helical, and more β-sheet proteins in the medulla [155]. Other hair studies have focused on the distribution of

particular compounds such as squalene, a lipid produced by skin cells in humans, noting it is primarily in the cortex [156]. Franzen et al. have also used Raman imaging to study the hair follicle, as it allows easy penetration into the skin for drugs, etc. They characterized the follicle in terms of the hair, sebum, and skin dermis and epidermis structures in both humans and pigs, as porcine skin is often used as a model for the human skin [63].

5.1.7 Plants, Algae, Molluscs, Bacteria, Fungi, and Small Multicellular Organisms

In plants, Raman imaging has primarily been used to investigate the composition of plant cell walls and other structural elements, with a focus on molecules including lignin and polysaccharides such as pectin and cellulose. The lignin and total carbohydrate content of cell walls in poplar trees has been described by Pererra et al. [157]. Analysis of Norway spruce and Scots pine showed similar lignin and cellulose distributions between both species, but spruce trees showed higher amounts of lignin-coniferyl aldehyde/alcohol groups in the secondary cell wall compared to the middle lamella and primary cell wall. Pine, on the other hand, showed comparable lignin-coniferyl aldehyde/alcohol content in the secondary cell wall and middle lamella, while the primary cell wall reflected lower levels [158]. The cell wall architecture in different regions of *Miscanthus sinensis* cv. has also been investigated with Raman imaging, providing information on the orientation of cellulose fibers with respect to the fiber axis [159]. The orientation of cellulose fibers was also important in brittle culm rice plant mutants, where cellulose fibers are arranged in a random orientation, as opposed to the parallel orientation found in wild-type plants [160]. Cellulose is an important source of ethanol for fuel during fermentation, and Chu et al. used Raman imaging to show that NaOH treatment of *Miscanthus* × *giganteus* samples removed lignin while leaving the cellulose behind [161]. Vermaak et al. have also imaged the distribution of molecules within plants, focusing on the steroidal glycoside p57 which has potential appetite suppressant properties, and found that p57 is primarily found in the inner fleshy part of the plant with low amounts in the outer layers [162]. In addition to the main plant, pollen grains are also amenable to Raman imaging studies. Analysis of intact grains provides information on the composition of the pollen grain walls, and molecular information on the substructure of the grains can be obtained from Raman images of sectioned grains [163].

Using tomatoes as a model system, Chylinska et al. identified the presence and distribution of pectin, cellulose, and polysaccharide molecules [164]. Tomatoes were also the focus for a recent study into ester cross-linking in cutin [165]. The distribution of pectins, cellulose, and hemicellulose in apples has been determined at different time points during the growth and storage of the fruit. These components are relatively evenly distributed throughout the young fruit. As the fruit matures, the pectins become more concentrated in the edges of the cell walls. During storage, the pectin distribution, once again, becomes more evenly distributed [166]. The distribution of plant cell wall polymers, namely, pectin and lignin, in different parts of the plant *Phormium tenax* is shown in Fig. 7.5. Higher pectin content in the lower

regions of the plant (Fig. 7.5 P1) was attributed to higher water content. This was not found in higher regions of the plant (Fig. 7.5 P3 and P4), which show a higher lignin content, reduced water content, and increased mechanical stability [167]. The distribution of lipids and lignin has also been used to understand the waterproofing characteristics of *Arabidopsis* plants [168]. The rhizosphere bacterium *Pantoea* sp. YR343 has been studied in terms of its co-culture with *Arabidopsis thaliana*, with Raman imaging able to distinguish wild-type and mutant bacteria via the resonance Raman contributions originating from carotenoids [169].

Raman imaging has been used to study algae, for example, to determine the proportions of silica, inorganic and organic components found in the cell walls of diatoms [170]. Monitoring the ratio of biomolecules in crops intended for producing biofuels is an important step in ensuring a good-quality fuel, for example, with a high calorific content, is produced. Chiu et al. used Raman imaging to assess the lipid and carbohydrate content in algal cells when subjected to stress. They showed that the lipid-to-carbohydrate ratio is affected by the nature of the stress applied, with nitrogen depletion resulting in increased carbohydrate content, but nitrogen depletion in combination with an increase in salinity increased the lipid content [171]. Polysaccharides are also a key component of fungi as well as plants and algae, and a recent study illustrated the ability of Raman imaging to simultaneously measure multiple polysaccharide components, including α- and β glucans and mannan, from fungal spores [172].

Raman imaging has also been used to investigate the nature and distribution of biochemicals within multicellular, living organisms. The connections between hard and soft tissues in molluscs have also been visualized by Raman imaging to investigate the interface between the living tissue and shell [173]. Raman imaging can also be used to study the whole organism as shown by Nakamura, Hotta, and Oka who followed the development of the *Ciona intestinalis* (sea squirt) embryo during development from the two-cell stage through to the tail bud stage. They were able to identify muscle and ectoderm at multiple stages throughout the development and to discriminate these cells from others that had divided from the same parent cell but that had different developmental fates [174]. Nematodes are particularly accessible samples for Raman imaging as they are usually semitransparent. Raman imaging has also been employed to assess the changes in *Radopholus similis* nematodes, a banana plant parasite, to the anigorufone compounds produced by the banana plants in response to a nematode infection. Exposed nematodes showed an increase in lipid-rich droplets which the authors suggest may be a defense mechanism to limit the toxic effects of the anigorufone on the nematode [175].

5.1.8 Food and Drug Quality and Safety

Raman imaging has been used in a number of studies investigating the distribution of components within the sample. Smith et al. have imaged the distribution of fat, protein, and water in processed cheese, along with additives such as trisodium citrate, starch, and paprika. [176]. Carotenoids are responsible for the color in fruit and vegetables such as tomatoes and peppers and are an important part of our diets as they have protective capabilities including antioxidant properties and vitamin A

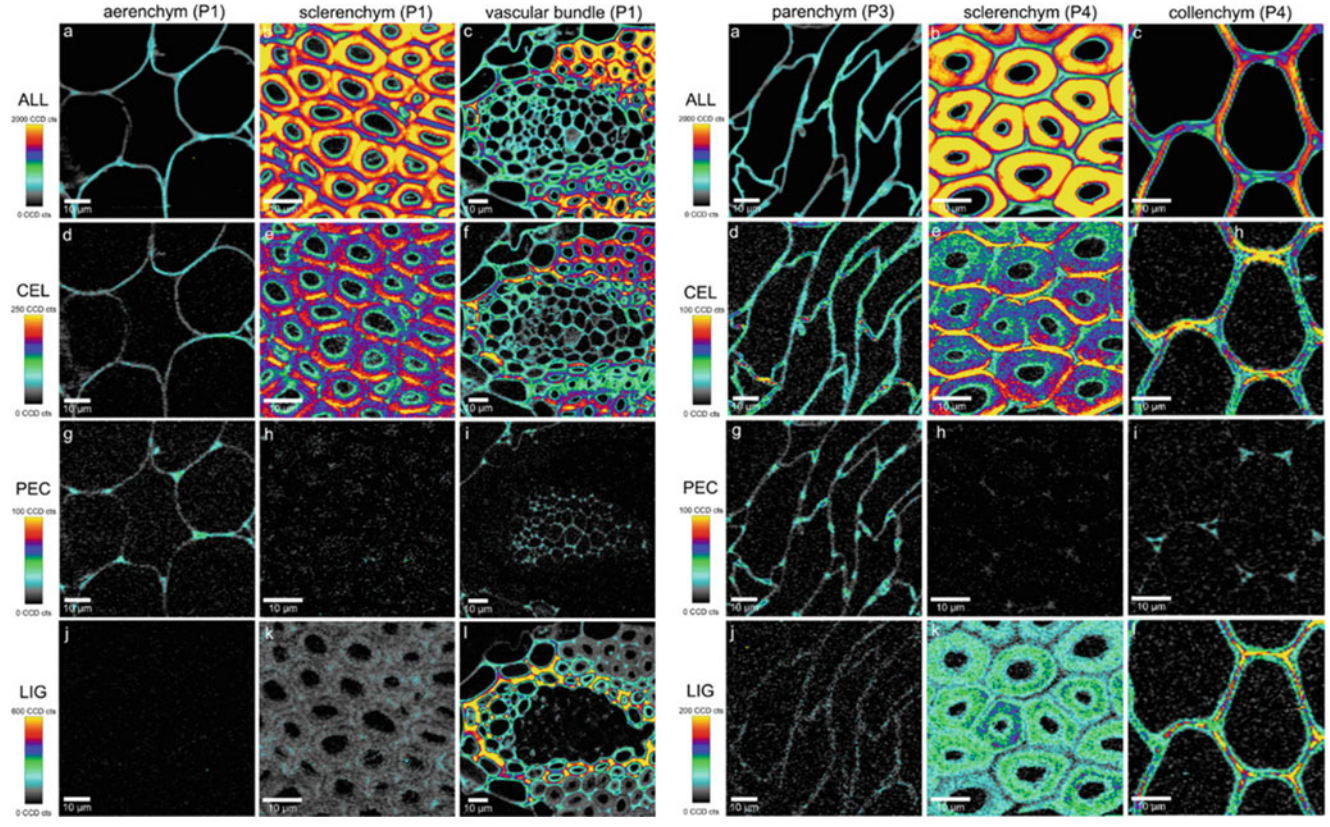

Fig. 7.5 Raman images obtained from different regions of the *Phormium tenax* plant. P1 is in the lower region of the stem, P3 from the upper region of the stem, and P4 from the leaf. ALL: intensities calculated by integrating between 2769 and 3087 cm^{-1} representing all cell wall polymers. CEL: intensities calculated by

activity. Raman imaging has been used to study the nature and subcellular location of carotenoids in chili peppers, as the subcellular location has been proposed to affect the dietary availability of the carotenoids. Carotenoids were located in lipid bodies that were outside of the chromoblast. The pepper varieties studied (four red and one orange when ripe) were found to contain different carotenoid compounds. For example, lutein was the main carotenoid component of Costeno-Amarillo, whereas NuMex Heritage 6-4 was rich in β-carotene [177].

The incidence of several food scandals in recent years, such as melamine in powdered milk in China and horse meat in meat products in the UK and Europe, has raised questions about the origins and quality of our food products. A number of studies have shown that Raman imaging can be a useful tool for quality control and the identification of contaminants in a number of food items. Quin et al. tested the potential for Raman imaging to determine the presence of contaminants such as ammonium sulfate, dicyandiamide, urea, and melamine in dry milk. Taking advantage of the well-defined Raman spectrum of the contaminants, compared to the broader-featured milk powder spectrum, they could simultaneously detect these contaminants at concentrations between 0.1% and 5.0% [178]. Extending this, Dhakal et al. tested the potential for Raman imaging to determine the presence of melamine in spiked samples of skimmed milk powder. Using a thresholding approach on the images, they were able to detect melamine at concentrations as low as 0.005% [179].

The compound benzylisothiocyanate (BITC) has antimicrobial properties. Clement et al. used Raman imaging to investigate the action of BITC when incorporated into food packaging, with a focus on its effects on the food-borne mold *Aspergillus ochraceus*. They showed BITC-induced spectral changes associated with most classes of macromolecule – saccharides, proteins, lipids, amino acids, and so on – indicating BITC disrupts multiple cellular processes in *A. ochraceus*, which will ultimately lead to the death of the microbe [180].

Not all food adulterations are dangerous to human health such as those that involve the substitution of one food product with another, usually cheaper, food product. Eksi-Kocak et al. have noted that pistachio nuts, as a more expensive crop, are often bulked out by the addition of green peas which exhibit similar green-colored kernels. They were able to use spectral feature differences observed across small areas of Raman images to identify the presence of both pistachio and green pea in mixtures of different proportions [181].

Raman imaging has also been applied to the analysis of drug mixtures in both genuine and counterfeit tablets. Kwok and Taylor compared genuine Cialis tablets, containing the active ingredient tadalafil and binding agents lactose monohydrate

Fig. 7.5 (continued) integrating between 1075 and 1114 cm^{-1} reflecting changes in cellulose orientation. PEC: intensities calculated by integrating between 842 and 872 cm^{-1} reflecting pectin content. LIG: intensities calculated by integrating between 1641 and 1546 cm^{-1} reflecting lignin content (Reproduced from Springer [167])

and microcrystalline cellulose, to two fake tablets. These fake tablets were found to contain talk, starch, calcium sulfate, and several unknown ingredients in addition to varying amounts of the active ingredient. They were also able to show that the genuine tablets had a much more even distribution of the ingredients compared to the counterfeit tablets [182]. Sacré et al. showed that the spatial differences in the chemical distribution of sildenafil in counterfeit and genuine Viagra tablets were not sufficient to discriminate between the two groups; however, the presence of lactose was a clear marker for counterfeit tablets [183].

5.2 Key Research Findings in Nonlinear Raman Imaging

5.2.1 Coherent Anti-Stokes Raman Scattering (CARS) Imaging

The sensitivity of CARS to lipids has been shown to visualize the accumulation of lipids in adipocytes with higher definition and at an earlier stage to oil red O staining commonly used for marking lipids [184]. This sensitivity has meant that CARS imaging has predominantly focused on areas where the presence of lipids or lipid metabolism is a key component of the sample. Bradley et al. have used CARS to monitor the early stages of early embryo development. They tracked the distribution of lipid droplets showing that the early embryo, at the two and four cell stages, exhibit small lipid droplets. As development continues, cells exhibit fewer droplets but these are larger in size. They also noted that the composition of the lipid droplets varied, with different ratios of saturated and unsaturated lipids found in droplets from the same embryo [185]. Unsaturated fatty acids were the focus of another study that investigated the nature of the fatty acids that were involved in the transport of yolk lipoprotein into *C. elegans* oocytes. Through the analysis of mutants deficient in polyunsaturated fatty acid synthesis, the authors were able to determine that omega-6 fatty acids were a key regulator of this fatty acid delivery process [186].

Jüngst et al. exploited the sensitivity of CARS to lipids in order to monitor the fusion process of lipid droplets in adipocytes, observing the cells over a 120-h period. They found that the increase in size of lipid droplets was mainly due to fusion of smaller droplets, rather than being due to synthesis of new lipids. They showed that the transfer of material was from the smaller droplets to the larger droplets, with the rate of transfer dependent on a number of parameters including the relative size difference and the diameter of the smaller droplet [187]. A similar study also monitored lipid droplets during the development of adipocytes, this time illustrating that the nature of fatty acids present in the cell culture medium can influence the fatty acid composition of the lipid droplets. The maturation stage of the adipocyte was also shown to be a determining factor in the speed of the cellular response to the change in fatty acid composition of the extracellular environment [188]. The manifestation of many lifestyle diseases is accompanied with changes in lipid signals. CARS imaging has identified increased lipid signals in brain samples from mice suffering from Alzheimer's disease [189].

Lipid droplets are also important in algae, and Cavonius et al. were able to identify three phases in the synthesis process. They employed time gating in order

to measure the lipid signals despite the strong pigmentation from the chloroplasts, but they did note that, when measuring time-lapse images of live algal systems, the extended exposure to the CARS excitation light is likely to have an effect on the light harvesting of the chloroplasts [190].

The myelin sheath surrounding nerves also gives rise to strong CARS signals due to its fat content. Berlanger et al. used CARS to image the myelin content of the spinal cord in live mice [191]. Turcotte et al. used polarization-resolved CARS to study myelination in live zebra fish and to assess promyelination drugs [192]. CARS imaging of lipids had also been used to indirectly measure the sweating process by covering a small area of skin with an exogenous oil, thereby filling the sweat pores. The oil can then be imaged as it is flushed out by the discharge of sweat [193]. Although CARS-based research is dominated by lipid imaging, a few studies have been engaged in determining the distribution of other molecular classes. Wang et al. looked at the distribution of pheomelanin, responsible for red hair pigmentation, in melanocytes, amelanotic melanomas, and a red-haired mouse model [194].

As with conventional Raman imaging, CARS can be used as a method to assess the impact of nanoparticle uptake on tissues. Johnston et al. were able to locate the presence of both TiO_2 and Au nanoparticles in macrophages, hepatocytes, and live animals with the CARS signals able to visualize both the cells and the position of the nanoparticles [195]. An investigation into the uptake of environmental microplastics by crabs has also used CARS to locate the particles within the crab [196].

Some CARS studies have also used spontaneous Raman measurements (usually point spectra) to provide spectral information while still retaining the speed of CARS measurement. This approach has been used to identify brain tumors, with tumor boarders and regions of infiltration imaged at the cellular level. The CARS signal was moderately reduced in metastatic tumors and markedly reduced in the glioblastoma regions, with Raman spectroscopy showing that this reduction in CARS signal was due to a lower lipid content in the tumors [197]. FAST (femtosecond adaptive spectroscopic techniques) CARS imaging and Raman spectroscopy have been used in conjunction to distinguish between polarized and non-polarized epithelia in breast tissue, based on the lipid ordering present [17]. In studies of breast and prostate cancer cells, CARS images showed an increase in the number and size of lipid droplets, while Raman spectroscopy indicated an increase in saturation of the lipids present, after treatment with the drugs medroxyprogesterone acetate or synthetic androgen R1881 [198].

A method for increasing the spectral information provided by CARS is to measure broadband CARS, which produces spectra that are more akin to conventional Raman spectra, with the first report showing a vibrational spectrum covering the region from 600 to 3200 cm^{-1} [199]. This opens up the technique for more detailed investigation of protein structure, as the peak shifts associated with α-helix, β-sheet, and other protein structural forms can be measured. Bito et al. found that the cortex of hair is mainly α-helical, while the cuticle is richer in β-sheet and random coil structures, with an α-helix to β-sheet transition observed after chemical and mechanical treatments [200]. Several recent studies have begun to explore the possibilities of combining CARS with chemometric analysis techniques. Lin et al.

applied PCA to CARS images of the meibum lipids produced by meibomian glands in the eyelid, using the lipid composition to identify the different functional regions within the gland [201]. El-Mashtoly et al. focused on the 2700–3000 cm^{-1} region and used a random forest approach to automate identification of common cellular organelles such as the endoplasmic reticulum, lipid droplets, nucleus, and nucleolus [202].

5.2.2 Stimulated Raman Scattering (SRS) Imaging

SRS has been used to visualize different biomolecules within food products. Roeffaers et al. were able to image the two phases in mayonnaise, fat and water, as an example of a simple emulsion. SRS images could also be obtained from cheese and a soy-based drink which have extra components, proteins and carbohydrates, as well as fat and water [203]. In plants, SRS has been shown to discriminate between different wax components, cellulose and pectins [204], and to assess effects of maleic acid treatment on lignins in cell walls of poplars [205]. SRS has also been used to investigate the uptake of the fungicides azoxystrobin and chlorothalonil in plants, both of which contain C≡N bonds allowing clear identification of the peaks in the "silent region" of the spectrum [206].

Egawa et al. have used SRS to study pig and human skin with a particular focus on the various stages of differentiation in keratinocytes [207]. SRS has also been used to monitor the changes occurring in mammalian tissues during disease manifestation. Tian et al. studied the nerve degeneration occurring in amyotrophic lateral sclerosis (ALS) in mouse models of the disease. They found changes in the peripheral myelin, with lipid depositions appearing in ALS-affected individuals. In addition, they monitored the effects of treatment with minocycline, a drug known to slow the progression of ALS in mice, which appeared to reduce the number of lipid deposits observed, but did not reduce them to the levels seen in unaffected individuals [208]. SRS has also been used to investigate the lipids present in ovarian cancer stem cells, with cells such as ALDH+/CD133+ cells that have high tumorigenic and metastatic potential [209] found to have a high degree of unsaturated lipids [209]. Li et al. also noted that the degree of saturation in lipids could be indicative of the metabolism after noting COV362 cells grown in a monolayer had lower levels of lipid unsaturation compared to those grown as spheres [210]. Many molecules give rise to Raman signals between 2800 and 3000 cm^{-1}, but Lu et al. have exploited the small shifts in position for each of the main classes of molecules to measure signals from DNA with SRS. They showed that it was possible to measure SRS signals from DNA in a sample of mixed components, within a cell, and within skin samples, as well as using SRS time-lapse imaging to monitor chromosome dynamics [211].

As with CARS, a few recent studies have been extending the analysis of SRS signals through the application of chemometric analyses. Satoh et al. have used PCA, concentrating on the 2800–3100 cm^{-1} region, to visualize acetaminophen-induced liver injury in mice [212]. Datta et al. used VCA to identify lipid droplets within a protein matrix when investigating metabolism and oxidative stress in cardiomyocytes derived from pluripotent stem cells [213].

5.3 Multimodal Imaging

Although the speed at which Raman imaging can be performed has increased with developments such as line scanning and improvements in detector sensitivity, it is still slow in comparison to many cellular processes. One way to compensate for this is to combine Raman with other modalities that have faster imaging capabilities and provide additional information on the nature of the sample. Multimodal approaches to Raman measurement can ideally combine two or more techniques that are applied to the sample simultaneously, so that the information between the different modes can be most easily compared. The instrumental challenges of that approach can be significant [214], but highly useful measurements can still come from multimodal techniques carried out sequentially on a sample [215]. Indeed, by relaxing the constraint of measuring simultaneous multimodal information, a wider variety of modalities may be used. For example, fluorescent staining measured following Raman can be a very useful validation technique.

One of the big challenges with multimodal imaging is the image registration between different measurement techniques. This is particularly problematic where one modality is used to provide information on what another modality is measuring as differences in the z-resolution, and probed volume will mean that there will be differences in the morphological and, potentially, molecular species measured by each technique [79, 214].

5.3.1 Raman and Infrared (IR) Spectroscopy

Raman and IR spectroscopies are both forms of vibrational spectroscopy, but as Raman imaging is based on a scattering process and IR imaging is based on absorption, they can be used to provide complimentary information on a sample. IR imaging is much more sensitive to the presence of water, meaning that it can be difficult to measure aqueous samples, restricting many of the studies to tissue sections or other samples that can be dried prior to measurement.

Garip et al. have used both Raman and IR imaging to investigate the changes in rat liver during treatment with simvastatin. Both Raman and IR images showed varying decreases in lipids and proteins, leading to an overall increased lipid:protein ratio, and Raman analysis also suggested a relative increase in DNA to proteins. The authors concluded that simvastatin causes notable damage to the liver, possibly through oxidative stress mechanisms [216]. Lau et al. used Raman and IR in conjunction to study the distribution of biomolecules within *Steinernema kraussei* nematode worms. Due to the different measurement configurations, confocal Raman images provided high spatial resolution images in a single plane through the nematode. IR images performed in transmission mode, on the other hand, provided complementary information in terms of the biochemical composition of the whole thickness of the worm [217].

In terms of hard tissues, Raman and IR imaging have been used in conjunction to study untreated human hair with both techniques providing information on the protein secondary structure and lipid composition of hair fibers. In addition, due to the fact that Raman is sensitive to disulfide linkages, Raman images also provided

information on keratin, which is rich in cysteine amino acids [15]. Bone tissue engineering was the focus of a study concentrating on determining the biocompatibility of a composite made from hydroxyapatite and β-glucan. Here, Raman imaging was used in conjunction with infrared spectroscopic imaging to investigate the differences between the composite and decalcified bone, identifying subtle changes in the mineral composition and a decrease in phosphate contributions with increasing age of the sample [218]. Chia et al. have also used Raman and IR imaging to study the formation of biochar (produced by heating biomass in limited oxygen environments) used as a soil additive. FTIR was able to show the effects of mineral additives on heat-induced chemical changes in the biochar, while Raman data provided information on the carbon structure in biochar and mineral-enriched biochar [219].

Raman and IR imaging have also been combined with additional modalities. Caine et al. added CARS and fluorescence imaging in order to investigate the alterations to the brain caused by a stroke. Raman provided high spatial resolution imaging of the lipid acyl groups revealing that the neuropil within in the peri-infarct zone showed reduced amount of lipid acyl groups. CARS showed that both the ischemic infarct and the surrounding peri-infarct zone were mainly devoid of myelinated axons. This information was complimented by IR and fluorescence imaging of the same areas [220]. Palombo et al. combined the chemical information obtained from Raman and IR imaging with Brillouin imaging, providing information on the mechanical properties, primarily the viscoelasticity, of Barrett's esophagus samples [221].

5.3.2 Raman and Mass Spectrometry (MS) Imaging

In recent years, mass spectrometry imaging has been applied to a number of biological samples (for a recent review, see Spengler et al. [222]) with a small number of studies looking to combine the mass-based sample information from MS with the vibrational information from Raman imaging. Lanni et al. combined secondary ion mass spectrometry (SIMS) with Raman in order to image bacterial biofilms of *Pseudomonas aeruginosa*, identifying components such as quinolones in the sample [223]. Ahlf et al. used an alternative MS modality, matrix-assisted laser desorption ionization (MALDI), combined with Raman for the analysis of 3D cell cultures. In this case, unlike Lanni et al., Ahlf et al. did not directly correlate the Raman and MS images, instead analyzing both modalities with PCA and then correlating the components obtained. For both techniques, the main variation, identified by the first principal component, identified the necrotic core of the culture, while the second component was associated with the proliferating edge [224]. Bocklitz et al. have proposed a workflow for combining Raman imaging with MALDI-based MS imaging, using a larynx carcinoma sample as their target. In this workflow, Raman images were compared to the H&E-stained images, with Raman identifying two layers in the epithelium attributed to differences in metabolic state. MALDI images were then taken from regions where the Raman and pathologist classifications were in agreement and from regions where the two did not agree, with m/z values from the MALDI imaging providing additional information to aid in classifying the tissue [225].

5.3.3 Raman and Atomic Force Microscopy (AFM)

AFM probes the mechanical properties of a sample such as viscoelasticity, stiffness, and topography [226]. Recently, the information provided by AFM imaging has been used to try and decouple the molecular concentration of components within cells from the topography of the sample in Raman images, as a move toward quantitative Raman measurements that are completely independent of sample thickness. In this case, correlated Raman and AFM images were used to produce quantitative maps of the cellular distribution of components such as proteins and RNA [227]. Correlated AFM and Raman images have also been used to study the effects of ex vivo treatment methods, particularly those commonly used in cell fixation protocols, on human erythrocytes [228]. Raman and AFM have also been used to assess the oxidation state of heme in erythrocytes [229].

Raman and AFM studies have often included IR imaging analyses as well. One such study used all three techniques to investigate the content and distribution of usnic acid, which has potential antibiotic properties, in three different species of lichen [230]. Raman imaging and AFM have also been used in conjunction with IR images to study mycobacterium and gram-negative bacteria, *Pseudomonas putida* and *Escherichia coli* in co-culture [231].

5.3.4 Raman and Digital Holographic Microscopy (DHM)/Quantitative Phase Imaging

Digital holographic microscopy (DHM) is a quantitative, label-free, and noninvasive technique that provides information in terms of the phase shifts induced by a sample [232]. DHM can be performed at high frame rates, making it an ideal complement to the relatively slow collection times required for Raman imaging. The implementation of a dual DHM and Raman system has been achieved using the same light source for sequential measurements [233] and by using two light sources and spectral separation allowing for simultaneous measurements from the two modalities [232]. The quantitative phase image information provided by DHM has been used to screen red blood cells infected with malaria, identifying cells of interest which can then be further analyzed by Raman to provide chemical and spatial distribution of hemozoin, for example [233]. Simultaneous measurements have provided information on the classes of biomolecules that give rise to the phase signals. Raman spectra of cells are often lipid-rich, with moderate-intensity bands from proteins and smaller contributions from other molecules such as nucleic acids. On the other hand, proteins and nucleic acids generate a significant proportion of the contrast in phase images, while the contribution from lipids is less intense. This highlights an additional aspect of the complementarity between the two imaging modes [232]. The combination of Raman and DHM has also been used to assess the health of bovine sperm cells during selection for artificial insemination. In this case, the morphology of the cells, provided by DHM, gave insight into the health of the sperm, and the Raman images and spectra were used to identify the X-carrying and Y-carrying sperm [234].

5.3.5 CARS, Second Harmonic Generation (SHG), and Two-Photon Emission Fluorescence (TPEF)

CARS has often been used in conjunction with second harmonic generation (SHG) and two-photon emission fluorescence (TPEF) imaging. This triple combined approach has been used to study the muscle tissue changes induced by cold shock in crustaceans, with CARS providing information on the ER, cisternae, and T-tubules [235]. All three techniques are able to identify the epidermis, dermis, and subcutis in the human skin, but Heuke et al. demonstrated that an overlay of all three images combined provided clear delineation between the tissue types, illustrating this with example regions including a sweat gland, sebaceous gland, hair bulb, and blood vessels [60]. In cancer applications, the three techniques have been used to discriminate between normal, desmoplastic tissue and cancerous lesions in the lung [236] and to identify normal tissue, tumor, and necrotic tissue in the kidney [237]. In atherosclerosis studies, CARS has been used in conjunction with TPEF and SHG to study the plaque deposits [238, 239]. The vitamin A content of pig liver has also been investigated with all three modalities where CARS produced images of the vitamin A droplets, fluorescence imaging highlighted the hepatocytes and liver sinusoids, and SHG showed the location of connective tissues [240]. Chernovskaia et al. combined CARS at two different wavelengths, with TPEF also at two different wavelengths and SHG to provide in total five image channels for the investigation of inflammation in diseases such as Crohn's disease and inflammatory bowel syndrome as shown in Fig. 7.6. The authors used the information from these combined modalities to predict different levels of chronicity, architecture, and activity associated with the samples [241].

CARS and TPEF have been used together to study the reorganization of the major classes of biomolecules in cells during the cell cycle. Along with quantitative analysis of concentrations of these molecules at particular points in the cell provided by Raman spectra, the study showed that proteins are inhomogenously distributed throughout the cell and that lipids tend to be more abundant at the edges of the cell. In addition, only the local concentration of DNA was found to fluctuate during the mitosis and G1 phases of the cell cycle [242].

CARS and SHG have been used to provide complimentary information on fibrosis in nonalcoholic fatty liver disease with SHG providing information on the nature of the fibrosis and CARS identifying the liver fat [243]. In a mouse model of obesity, both techniques were used to visualize the increase in size of adipocytes induced by high fat and fructose diets [244]. The combination of CARS and SHG has also been employed in several studies centered on proteins. Fibrin hydrogels are one type of substrate used as a scaffold in regenerative medicine, and Mortati et al. used SHG and CARS to follow the collagen production of mesenchymal stem cells, as an indicator of cell differentiation, and corneal fibroblasts in 3D cultures on these scaffolds [245]. Brackmann et al. used CARS and SHG in combination to investigate orange fruits/vegetables such as sweet potatoes, carrots, and mangos, with CARS used to visualize the carotenoids and SHG highlighting the starch granules in each sample [246]. Brackmann et al. also looked at the interaction of cells with a matrix, this time investigating the interactions of smooth muscle cells with a cellulose matrix in terms of how they compress the matrix [247].

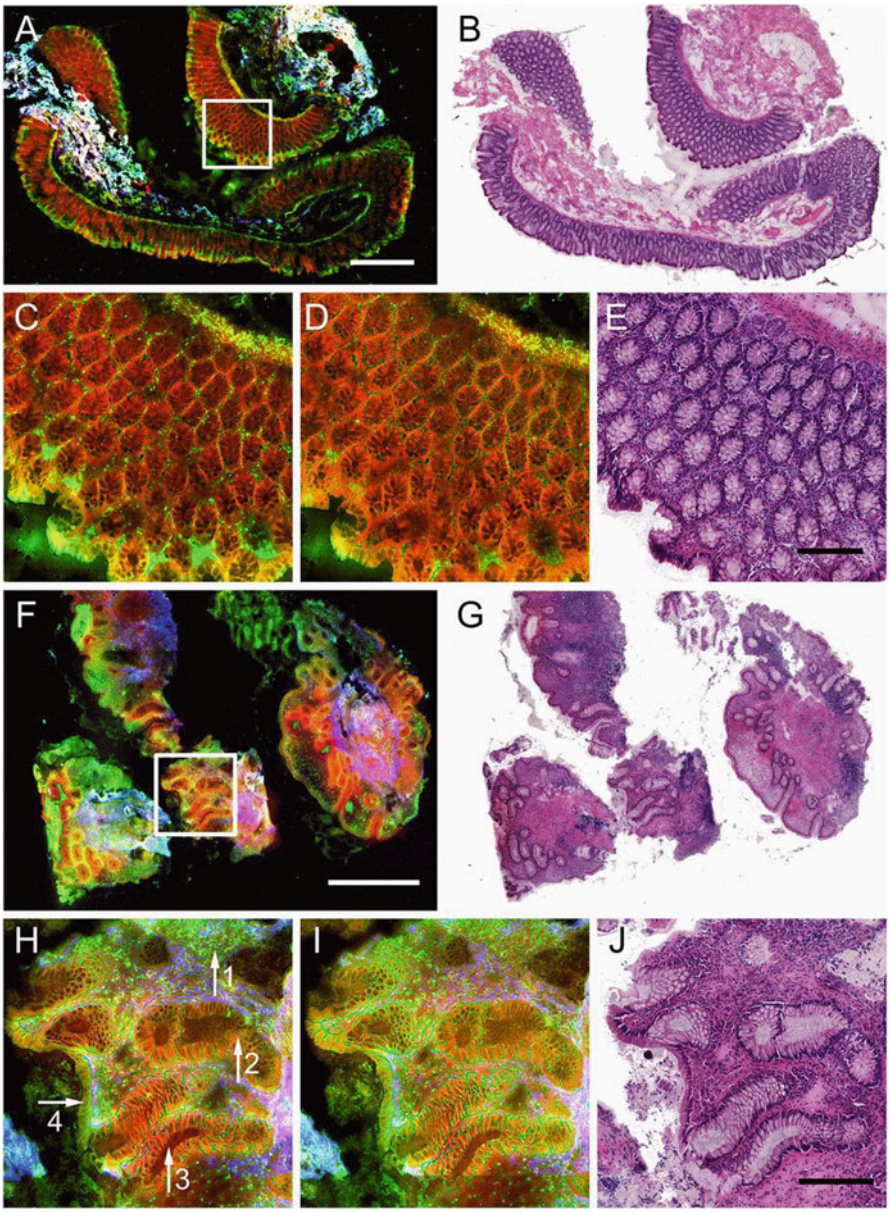

Fig. 7.6 Multimodal images (**a**, **c**, **d**, **f**, **h**, **i**) and corresponding H&E-stained tissue sections (**b**, **e**, **g**, **j**) of normal (**a**–**e**) and diseased (**f**–**j**) colon mucosa. Sub-figures (**a**) and (**f**) show multimodal images acquired with CARS at 2930 cm^{-1}, TPEF at 503–548 nm, and SHG. Sub-figures (**c**) and (**h**) show details from (**a**) and (**f**) represented by the white boxes. Sub-figures (**d**) and (**i**) show multimodal images corresponding to sub-figures (**c**) and (**h**), respectively, that were acquired with the combination of CARS at 2850 cm^{-1}, TPEF at 426–490 nm, and SHG. Red, CARS; green, TPEF; blue, SHG. White scale bar represents 1 mm and black scale bar 250 μm. Arrows:

Mansfield et al. have compared CARS and SRS for imaging of superficial zone chondrocytes showing that SRS provides a spectrum closer to that of the Raman and also gives rise to a clearer image. They then went on to combine TPEF, SHG, and SRS imaging to investigate the structure of cartilage, with three SRS channels providing images of carbonate, phosphate, and CH stretching. The TPEF images provided information on autofluorescence, while the SHG images highlighted the collagen fibers [248].

6 Conclusions and Future Perspectives

Raman imaging has been applied to a wide range of sample types and fields of research that all have an impact on human health. That includes a growing variety of applications including fundamental studies of biological reactions, through the assessment and quantification of disease states and the impact of environmental toxins on biological systems or more indirectly through determining the quality of foodstuffs and drugs. Future developments in Raman imaging will, no doubt, continue to expand the applications of Raman analyses to other fields of biochemical analysis.

In terms of applications for medical diagnosis, many studies have shown the potential for Raman in characterizing changes in cells and tissues that can be thought of as markers for diseases as wide ranging as cancer, atherosclerosis, dental lesions, and parasitic infections. The next stage will be to expand these small-scale studies to larger sample sizes and more complex sample groups (e.g., samples from patients who exhibit symptoms from multiple medical conditions) with a view to applying Raman-based diagnostics in clinics and surgeries. In many cases, this will involve the development of smaller, dedicated instruments and the development of automated software for determining the status of a sample. While much of the instrumentation currently being developed for use in surgery or other clinical settings are primarily concerned with recording single point spectra, the information provided by Raman mapping and imaging studies is useful when developing such probes [249], particularly in terms of the spatial distributions and concentrations of the key molecules of interest in a given sample.

In terms of instrumentation, it is challenging to directly improve the amounts of acquired Raman signal, since for many setups, detector sensitivity, grating efficiencies, and so on are relatively close to what might be expected theoretically. Instead, improvements in Raman imaging are likely to come from improving the speed of measurement via measures such as increased degree of parallel acquisition (i.e., in the same way that line scanning drastically improved Raman imaging speed, other improvements might be implemented) or by increasing resolution [250]. Additionally, improvements are already underway by use of smart selective sampling, compressed

Fig. 7.6 (continued) 1, lymphocytes, increase overall fluorescence, loss of crypt density; 2, crypt branching; 3, irregularities of crypts' shape; 4, flattened epithelial layer facing the lumen (Figure reproduced from Nature Publishing Group [241])

sensing, or other techniques to reduce the number of spectra required to construct an image. In essence, these directions involve the optimization of the desired information content that can be measured in a constrained set of parameters, where laser power, sample damage, and measurement time are all crucial considerations. The optimum measurement would then provide the best answer to a given hypothesis, by optimizing the measurement protocol according to the physical constraints. Most current work does not take this approach, partly because the optimum measurement may require a flexible and customizable imaging system. There is then a trade-off between the best-case measurement approaches and practical considerations. Nevertheless, we can expect significant improvements in Raman imaging, with increased attention to exploiting these factors. In addition, combining Raman imaging with other modalities, providing correlated but nonredundant information, will be important in future studies, particularly where the other modalities measure different characteristics of the sample, compared to the Raman spectra. In terms of live sample imaging, complimentary modalities with high frame rates will be particularly useful characterizing sample changes taking place during the Raman imaging measurement, currently on the order of a few minutes for a typical cell.

The complimentary information obtained from multimodal imaging, particularly when measurements are taken simultaneously, will also further our understanding of what biochemical information is contained within the Raman images. As Raman spectra contain contributions from all Raman-active molecules in a sample, they are rich in information but complex to interpret. Chemometric algorithms are very useful for decomposing the spectra into various types of components, but these component spectra are also composed of contributions from mixtures of molecules. Therefore, correlating Raman images with those obtained from other techniques will allow us to more accurately identify the nature of the molecules contributing to particular Raman signals. This knowledge can be transferred back to single modality Raman studies, allowing more detailed interpretation of the biochemical composition of samples.

References

1. Smith E, Dent G (2005) Modern Raman spectroscopy a practical approach. Wiley, Chichester
2. Grasselli JG, Snavely MK, Bulkin BJ (1980) Applications of Raman spectroscopy. Phys Rep 65(4):231–344
3. Mantsch HH (2013) The road to medical vibrational spectroscopy – a history. Analyst 138(14):3863–3870
4. Edwards HGM (2009) Raman spectroscopy of inorganic materials in art and archaeology: spectroscopic analysis of historical mysteries. In: Yarwood J, Douthwaite R, Duckett SB (eds) Spectroscopic properties of inorganic and organometallic compounds. Techniques, materials and applications. RSC Publishing, Cambridge, UK
5. Pully VV, Lenferink ATM, Otto C (2011) Time lapse Raman imaging of single live lymphocytes. J Raman Spectrosc 42(2):167–173
6. Okada M, Smith NI, Palonpon AF, Endo H, Kawata S, Sodeoka M, Fujita K (2012) Label-free Raman observation of cytochrome C dynamics during apoptosis. Proc Natl Acad Sci U S A 109(1):28–32

7. Hashimoto A, Yamaguchi Y, Chiu L-d, Morimoto C, Fujita K, Takedachi M, Kawata S, Murakami S, Tamiya E (2015) Time-lapse imaging of osteoblast differentiation. Sci Rep 5:12529
8. Yamakoshi H, Dodo K, Palonpon A, Ando J, Fujita K, Kawata S, Sodeoka M (2012) Alkene-tag Raman imaging for visualisation of mobile small molecules in living cells. J Am Chem Soc 134(51):20681–20689
9. Ando J, Fujita K (2013) Metallic nanoparticles as SERS agents for biomolecular imaging. Curr Pharm Biotechnol 14(2):141–149
10. Laing S, Gracie K, Faulds K (2016) Multiplex in vitro detection using SERS. Chem Soc Rev 45(7):1901–1918
11. Lane LA, Qian X, Nie S (2015) SERS nanoparticles in medicine: from label-free detection to spectroscopic tagging. Chem Rev 115(19):10489–10529
12. Baker MJ, Hussain SR, Lovergne L, Untereiner V, Hughes C, Lukaszewski RA, Thiéfin G, Sockalingum GD (2016) Developing and understanding biofluid vibrational spectroscopy: a critical review. Chem Soc Rev 143:2238–2247
13. Gamsjaeger S, Mendelsohn R, Boskey AL, Gourion-Arsiquaud S, Klaushofer K, Paschalis EP (2014) Vibrational spectroscopic imaging for the evaluation of matrix and mineral chemistry. Curr Osteoporos Rep 12(4):454–464
14. Butler HJ, Ashton L, Bird B, Cinque G, Curtis K, Dorney J, Esmonde-White K, Fullwood NJ, Gardner B, Martin-Hirsch PL, Walsh MJ, McAinsh MR, Stone N, Martin FL (2016) Using Raman spectroscopy to characterise biological materials. Nat Protoc 11:664–687
15. Zhang G, Senak L, Moore DJ (2011) Measuring changes in chemistry, composition and molecular structure within hair fibres by infrared and Raman spectroscopic imaging. J Biomed Opt 16(5):056009
16. Teodori L, Crupi A, Costa A, Diaspro A, Melzer S, Tarnok A (2017) Three-dimensional imaging technologies: a priority for the advancement of tissue engineering and a challenge for the imaging community. J Biophotonics 10(1):24–45
17. Yue S, Cárdenas-Mora JM, Chaboub LS, Lelièvre SA, Cheng J-X (2012) Label-free analysis of breast tissue polarity by Raman imaging of lipid phase. Biophys J 102(5):1215–1223
18. Charwat V, Schütze K, Holnthoner W, Lavrentieva A, Gangnus R, Hofbauer P, Hoffmann C, Angres B, Kasper C (2015) Potential and limitations of microscopy and Raman spectroscopy for live cell analysis of 3D cultures. J Biotechnol 205:70–81
19. Draux F, Gobinet C, Sulé-Suso J, Trussardi A, Manfait M, Jeannesson P, Sockalingum GD (2010) Raman spectral imaging of single cancer cells: probing the impact of sample fixation methods. Anal Bioanal Chem 397(7):2727–2737
20. Hobro AJ, Smith NI (2017) An evaluation of fixation methods: spatial and compositional cellular changes observed by Raman imaging. Vib Spectrosc 91:31–45
21. Bogliolo L, Murrone O, Piccinini M, Ariu F, Ledda S, Tilocca S, Albertini DF (2015) Evaluation of the impact of vitrification on the actin cytoskeleton of in vitro matured ovine oocytes by means of Raman microspectroscopy. J Assist Reprod Genet 32(2):185–193
22. Gaifulina R, Maher AT, Kendall C, Nelson J, Rodriguez-Justo M, Lau K, Thomas GM (2016) Label-free Raman spectroscopic imaging to extract morphological and chemical information from a formalin-fixed, paraffin-embedded rat colon tissue section. Int J Exp Pathol 97(4):337–350
23. Ali SM, Bonnier F, Tfayli A, Lambkin H, Flynn K, McDonagh V, Healy C, Lee TC, Lyng FM, Byrne HJ (2013) Raman spectroscopic analysis of human skin tissue sections ex-vivo: evaluating the effects of tissue processing and dewaxing. J Biomed Opt 18(6):061202
24. Ali SM, Bonnier F, Lambkin H, Flynn K, McDonagh V, Healy C, Lee TC, Lyng FM, Byrne HJ (2013) A comparison of Raman, FTIR and ATR-FTIR microspectroscopy for imaging human skin tissue sections. Anal Methods 5:2281–2291
25. Esmonde-White KA, Esmonde-White FWL, Morris MD, Roessler BJ (2014) Characterisation of biofluids prepared by sessile drop formation. Analyst 139(11):2734–2741
26. Palonpon AF, Ando J, Yamakoshi K, Dodo K, Sodeoka M, Kawata S, Fujita K (2013) Raman and SERS microscopy for molecular imaging of live cells. Nat Protoc 8:677–692
27. Gasparov L, Jegorel T, Loetgering L, Middey S, Chakhalian J (2014) Thin film substrates from the Raman spectroscopy point of view. J Raman Spectrosc 45(6):465–469

28. Draux F, Jeannesson P, Beljebbar A, Tfayli A, Fourre N, Manfait M, Sule-Suso J, Sockalingum GD (2009) Raman spectral imaging of single living cancer cells: a preliminary study. Analyst 134(3):542–548
29. Fogarty SW, Patel II, Martin FL, Fullwood NJ (2014) Surface-enhanced Raman spectroscopy of the endothelial cell membrane. PLoS One 9(9):e106283
30. Bonnier F, Knief P, Lim B, Meade AD, Dorney J, Bhattacharya K, Lyng FM, Byrne HJ (2010) Imaging live cells grown on a 3D collagen matrix using Raman microspectroscopy. Analyst 135(12):3169–3177
31. Lachin JM (1981) Introduction to sample size determination and power analysis for clinical trials. Control Clin Trials 2(2):93–113
32. Lenith RV (2001) Some practical guidelines for effective sample size determination. Am Stat 55(3):187–193
33. Dell RB, Holleran S, Ramakrishnan R (2002) Sample size determination. ILAR J 43(4):207–213
34. Beletes C, Neugebauer U, Bocklitz T, Krafft C, Popp J (2013) Sample size planning for classification models. Anal Chim Acta 760:25–33
35. Krafft C, Schie IW, Meyer T, Schmitt M, Popp J (2016) Developments in spontaneous and coherent Raman scattering microscopic imaging for biomedical applications. Chem Soc Rev 45(7):1819–1849
36. Pence I, Mahadevan-Jansen A (2016) Clinical instrumentation and applications of Raman spectroscopy. Chem Soc Rev 45(7):1958–1979
37. Thorley FC, Baldwin KJ, Lee DC, Batchelder DN (2006) Dependence of the Raman spectra of drug substances upon laser excitation wavelength. Journal of Raman Spectroscopy 37(1–3):335–341
38. Meesters AA, Pitassi LHU, Campos V, Wolkerstorfer A, Dierickx CC (2014) Transcutaneous laser treatment of leg veins. Lasers Med Sci 29(2):481–492
39. Kumamoto Y, Fujita K, Smith NI, Kawata S (2016) Deep-UV biological imaging by lanthanide ion molecular protection. Biomed Opt Express 7(1):158–170
40. Efremov EV, Ariese F, Gooijer C (2008) Achievements in resonance Raman spectroscopy review of a technique with a distinct analytical chemistry potential. Anal Chim Acta 606(2):119–134
41. Spiro TG, Strekas TC (1974) Resonance Raman spectra of heme proteins. Effects of oxidation and spin state. J Am Chem Soc 96(2):338–345
42. Puppels GJ, de Mul FFM, Otto C, Greve J, Robert-Nicoud M, Arndt-Jovin DJ, Jovin TB (1990) Studying single living cells and chromosomes by confocal Raman microspectroscopy. Nature 347(6290):301–303
43. De Grauw CJ, Otto C, Greve J (1997) Line-scan Raman microspectrometry for biological applications. Appl Spectrosc 51(11):1607–1612
44. Hamada K, Fujita K, Smith NI, Kobayashi M, Inouye Y, Kawata S (2008) Raman microscopy for dynamic molecular imaging of living cells. J Biomed Opt 13(4):044027
45. Pascut FC, Goh HT, Welch N, Buttery LD, Denning C, Notingher I (2011) Non-invasive detection and imaging of molecular markers in live cardiomyocytes derived from human embryonic stem cells. Biophys J 100(1):251–259
46. Pavillon N, Smith NI (2016) Compressed sensing laser scanning microscopy. Opt Express 24(26):30038–30052
47. Pavillon N, Smith NI (2015) Maximizing throughput in label-free microspectroscopy with hybrid Raman imaging. J Biomed Opt 20(1):016007
48. Rowlands CJ, Varma S, Perkins W, Leach I, Williams H, Notingher I (2012) Rapid acquisition of Raman spectral maps through minimal sampling: applications in tissue imaging. J Biophotonics 5(3):200–229
49. Zumbusch A, Holtom GR, Xie XS (1999) Three-dimensional vibrational imaging by coherent anti-stokes Raman scattering. Physics Review Letters 82:4142–4145
50. Becker K, Kiefer J (2016) Combined spontaneous stokes and coherent anti-stokes Raman scattering spectroscopy. Applied Physics B 122:127

51. Kano H, Segawa H, Okuno M, Leproux P, Couderc V (2016) Hyperspectral coherent Raman imaging – principle, theory, instrumentation and applications to life sciences. J Raman Spectrosc 47(1):116–123
52. Camp CH Jr, Cicerone MT (2015) Chemically sensitive bioimaging with coherent Raman scattering. Nat Photonics 9:295–305
53. Yonemaru Y, Palonpon AF, Kawano S, Smith NI, Kawata S, Fujita K (2015) Super-spatial- and -spectral-resolution in vibrational imaging via saturated coherent anti-stokes Raman scattering. Phys Rev Appl 4:014010
54. Prince RC, Frontiera RR, Potma EO (2017) Stimulated Raman scattering: from bulk to nano. Chem Rev 117(7):5070–5094
55. Ozeki Y, Umemura W, Otsuka Y, Satoh S, Hashimoto H, Sumimura K, Nishizawa N, Fukui K, Itoh K (2012) High-speed molecular spectral imaging of tissue with stimulated Raman scattering. Nat Photonics 6:845–851
56. Byrne HJ, Knief P, Keating ME, Bonnier F (2016) Spectral pre and post processing for infrared and Raman spectroscopy of biological tissues and cells. Chem Soc Rev 45(7):1865–1878
57. Kumar S, Verma T, Mukherjee R, Ariese F, Somasundaram K (2016) Umapathy Raman and infrared microscopy: towards quantitative evaluation for clinical research by ratiometric analysis. Chem Soc Rev 45(7):1879–1900
58. Slater JB, Tedesco JM, Fairchild RC, Lewis IR (2001) Raman spectrometry and its adaptation to the industrial environment. In: Lewis IR, Edwards HGM (eds) Handbook of Raman spectroscopy from the research laboratory to the process line. CRC Press, Boca Raton
59. Bocklitz TW, Dörfer T, Heinke R, Schmitt M, Popp J (2015) Spectrometer calibration protocol for Raman spectra recorded with different excitation wavelengths. Spectrochim Acta A Mol Biomol Spectrosc 149:544–549
60. Heuke S, Vogler N, Meyer T, Akimov D, Kluschke F, Röwert-Huber H-J, Lademann J, Dietzekand B, Popp J (2013) Multimodal mapping of human skin. Br J Dermatol 169(4):794–803
61. Mavarani L, Petersen D, El-Mashtoly SF, Mosig A, Tannapfel A, Kötting C, Gerwert K (2013) Spectral histopathology of colon cancer tissue sections by Raman imaging with 532 nm excitation provides label-free annotation of lymphocytes, erythrocytes and proliferating nuclei of cancer cells. Analyst 138(14):4035–4039
62. Ali SM, Bonnier F, Ptasinski K, Lambkin H, Flynn K, Lyng FM, Byrne HJ (2013) Raman spectroscopic mapping for the analysis of solar radiation induced skin damage. Analyst 138(14):3946–3956
63. Franzen L, Mathes C, Hansen S, Windbergs M (2013) Advanced chemical imaging and comparisons of human and porcine hair follicles for drug delivery by confocal Raman microscopy. J Biomed Opt 18(6):061210
64. Vukosavljevic B, De Kinder L, Siepmann J, Muschert S, Windbergs M (2016) Novel insights into controlled drug release from coated pellets by confocal Raman microscopy. J Raman Spectrosc 47(7):757–762
65. Ashton L, Hollywood KA, Goodacre R (2015) Making colourful sense of Raman images of single cells. Analyst 140(6):1852–1858
66. Shinzawa H, Awa K, Kanematsu W, Ozaki Y (2009) Multivariate data analysis for Raman spectroscopic imaging. J Raman Spectrosc 40(12):1720–1725
67. Bonifacio A, Beleites C, Vittur F, Marsich E, Semeraro S, Paoletti S, Sergo V (2010) Chemical mapping of articular cartilage sections with Raman mapping employing uni- and multi-variate methods for data analysis. Analyst 135(12):3193–3204
68. Matthäus C, Chernenko T, Quintero L, Miljković M, Milane L, Kale M, Amiji M, Torchilin V, Diem M (2010) Raman micro-spectral imaging of cells and intracellular drug delivery using nanocarrier systems. In: Dieing T, Hollrichter O, Toporski J (eds) Confocal Raman microscopy. Springer, Berlin
69. Miljković M, Chernenko T, Romeo MJ, Bird B, Matthäus C, Diem M (2010) Label-free imaging of human cells: algorithms for image reconstruction of Raman hyperspectral datasets. Analyst 135(8):2002–2013

70. Hedegaard M, Matthäus C, Hassing S, Krafft C, Diem M, Popp J (2011) Spectral unmixing and clustering algorithms for assessment of single cells by Raman microscopic imaging. Theor Chem Accounts 130(4):1249–1260
71. Vajna B, Patyi G, Nagy Z, Bódis A, Farkas A, Marosi G (2011) Comparison of chemometric methods in the analysis of pharmaceuticals with hyperspectral Raman imaging. J Raman Spectrosc 42(11):1977–1986
72. Hotelling H (1933) Analysis of a complex of statistical variables into principal components. Warwick & York, Baltimore
73. Nascimento JMP, Bioucas Dias JM (2005) Vertex component analysis: a fast algorithm to unmix hyperspectral data. IEEE Trans Geosci Remote Sens 43(4):898–910
74. De Juan A, Jaumot J, Tauler R (2014) Multivariate curve resolution (MCR). Solving the mixture analysis problem. Anal Methods 6(14):4964–4976
75. MacQueen J (1967) Some methods for classification and analysis of multivariate observations. In: Proceedings of the fifth berkeley symposium on mathematical statistics and probability. Statistics, vol 1. University of California Press, Berkeley, pp 281–297
76. Klein K, Gigler AM, Aschenbrenner T, Monetti R, Bunk W, Jamitzky F, Morfill G, Stark RW, Schlegel J (2012) Label-free live cell imaging with confocal microscopy. Biophys J 102(2):360–368
77. Ramoji A, Neugebauer U, Bocklitz T, Foerster M, Kiehntopf M, Bauer M, Popp J (2012) Towards a spectroscopic hemogram: Raman spectroscopic differentiation of the two most abundant leukocytes from peripheral blood. Anal Chem 84(12):533–5342
78. Kakita M, Kaliaperumal V, Hamaguchi H (2012) Resonance Raman quantification of the redox state of cytochromes B and C in vivo and in vitro. J Biophotonics 5(1):20–24
79. Krauß SD, Petersen D, Niedieker D, Fricke I, Freier E, El-Mashtoly SF, Gerwert K, Mosig A (2015) Colocalization of fluorescence and Raman microscopic images for the identification of subcellular compartments: a validation study. Analyst 140(7):2360–2368
80. Brazhe NA, Treiman M, Brazhe AR, Find NL, Maksimov GV, Sosnovtseva OV (2012) Mapping of redox state of mitochondrial cytochromes in live cardiomyocytes using Raman microspectroscopy. PLoS One 7(9):e41190
81. Kochan K, Kus E, Filipek A, Szafrańska K, Chlopicki S, Baranska M (2017) Label-free spectroscopic characterisation of live liver sinusoidal endothelial cells (LSECs) isolated from the murine liver. Analyst 142(8):1308–1319
82. Neugebauer U, Clement JH, Bocklitz T, Krafft C, Popp J (2010) Identification and differentiation of single cells from peripheral blood by Raman spectroscopic imaging. J Biophotonics 3(8–9):579–587
83. Hobro AJ, Kumagai Y, Akira S, Smith NI (2016) Raman spectroscopy as a tool for label-free lymphocyte cell line discrimination. Analyst 141(12):3756–3764
84. Zuser E, Chernenko T, Newmark J, Miljković M, Diem M (2010) Confocal Raman microspectral imaging (CRMI) of murine stem cell colonies. Analyst 135:3030–3033
85. Ashton L, Lau K, Winder CL, Goodacre R (2011) Raman spectroscopy: lighting up the future of microbial identification. Future Microbiol 6(9):991–997
86. Mazur AI, Monahan JL, Miljkovic M, Laver N, Diem M, Bird B (2013) Vibrational spectroscopic changes of B-lymphocytes upon activation. J Biophotonics 6(1):101–109
87. Ghita A, Pascut FC, Mather M, Sottile V, Notingher I (2012) Cytoplasmic RNA in undifferentiated neural stem cells: a potential label-free Raman spectral marker for assessing the undifferentiated status. Anal Chem 84(7):3155–3162
88. Meister K, Schmidt DA, Bründermann E, Havenith M (2010) Confocal Raman microspectroscopy as an analytical tool to assess the mitochondrial status in human spermatozoa. Analyst 135(6):1370–1374
89. Mateu BP, Harreither E, Schosserer M, Puxbaum V, Gludovacz E, Borth N, Gierlinger N, Grillari J (2016) Label-free live cell imaging by confocal Raman spectroscopy identifies CHO host and producer cell lines. Biotechnol J 12(1):1600037
90. Zoladek AB, Johal RK, Garcia-Nieto S, Pascut F, Shakesheff KM, Ghaemmaghami AM, Notingher I (2010) Label free molecular imaging of the immunological synapse between dendritic and T-cells by Raman micro-spectroscopy. Analyst 135(12):3205–3212

91. Konorov SO, Schulze HG, Piret JM, Blades MW, Turner RFB (2013) Label-free determination of the cell cycle phase in human embryonic stem cells by Raman microspectroscopy. Anal Chem 85(19):8996–9002
92. Schulze HG, Konorov SO, Piret JM, Blades MW, Turner RFB (2013) Label-free imaging of mammalian cell nucleoli by Raman microspectroscopy. Analyst 138(12):3416–3423
93. Hsu J-F, Hsieh P-Y, Hsu H-Y, Shigeto S (2015) When cells divide: label-free multimodal spectral imaging for exploratory molecular investigation of living cells during cytokinesis. Sci Rep 5:17541
94. Yang Y, Li F, Gao L, Wang Z, Thrall MJ, Shen SS, Wong KK, Wong STC (2011) Differential diagnosis of breast cancer using quantitative, label-free and molecular vibrational imaging. Biomed Opt Express 2(8):2160
95. Larraona-Puy M, Ghita A, Zoladek A, Perkins W, Varma S, Leach IH, Koloydenko AA, Williams H, Notingher I (2011) Discrimination between basal cell carcinoma and hair follicles in skin tissue sections by Raman microspectroscopy. J Mol Struct 993(1–3):57–61
96. Brozek-Pluska B, Kopec M, Niedzwiecka I, Morawiec-Sztandera A (2015) Label free determination of lipid composition and secondary protein structure of human salivary noncancerous and cancerous tissues by Raman microspectroscopy. Analyst 140(7):2107–2113
97. Brozek-Pluska B, Kopec M, Abramczyk H (2016) Development of a new diagnostic Raman method for monitoring epigenetic modifications in the cancer cells of human breast tissue. Anal Methods 8(48):8542–8553
98. Vanna R, Ronchi P, Lenferink ATM, Tresoldi C, Morasso C, Mehn D, Bedoni M, Picciolini S, Terstappen LWMM, Ciceri F, Otto C, Gramatica F (2015) Label-free imaging and identification of typical cells of acute myeloid leukaemia and myelodysplastic syndrome by Raman microspectroscopy. Analyst 140(4):1054–1064
99. Surmacki J, Brozek-Pluska B, Kordek R, Abramczyk H (2015) The lipid-reactive oxygen species phenotype of breast cancer. Raman spectroscopy and mapping, PCA and PLSDA for invasive ductal carcinoma and invasive lobular carcinoma. Molecular tumorigenic mechanisms beyond the Warburg effect. Analyst 140(7):2121–2133
100. Brozek-Pluska B, Kopec M, Surmacki J, Abramczyk H (2015) Raman microspectroscopy of noncancerous and cancerous breast tissues: identification and phase transitions of linoleic and oleic acids by Raman low temperature studies. Analyst 140(7):2134–2143
101. Piredda P, Berning M, Boukamp P, Volkmer A (2015) Subcellular Raman microspectroscopic imaging of nucleic acids and tryptophan for distinction of normal human skin cells and tumorigenic keratinocytes. Anal Chem 87(13):6778–6785
102. Kumar P, Bhattacharjee T, Pandey M, Hole A, Ingle A, Krishna CM (2016) Raman spectroscopy in experimental oral carcinogenesis: investigation of abnormal changes in control tissues. J Raman Spectrosc 47(11):1318–1326
103. Abramczyk H, Surmacki J, Kopeć M, Olejnik AK, Lubecka-Pietruszewska K, Fabianowska-Majewska K (2015) The role of lipid droplets and adipocytes in cancer. Raman imaging of cell cultures: MCF10A, MCF7 and MDA-MB-231 compared to adipocytes in cancerous breast tissue. Analyst 140(7):2224–2235
104. Tirinato L, Liberale C, Di Franco S, Candeloro P, Benfante A, La Rocca R, Potze L, Marotta R, Ruffilli R, Rajamanickam VP, Malerba M, De Angelis F, Falqui A, Carbone E, Todaro M, Medema JP, Stassi G, Di Fabrizio E (2015) Lipid droplets: a new player in colorectal cancer stem cells unveiled by spectroscopic imaging. Stem Cells 33(1):35–44
105. Hartsuiker L, Zeijen NJL, Terstappen LWMM, Otto C (2010) A comparison of breast cancer tumor cells with varying expression of the Her2/neu receptor by Raman spectroscopic imaging. Analyst 135(12):3220–3226
106. Pacia MZ, Buczek E, Blazejczyk A, Gregorius A, Wietrzyk J, Chlopicki S, Baranska M, Kaczorc A (2016) 3D Raman imaging of systemic endothelial dysfunction in the murine model of metastatic breast cancer. Anal Bioanal Chem 408:3381–3387
107. Kong K, Rowlands CJ, Varma S, Perkins W, Leach IH, Koloydenko AA, Pitiot A, Williams HC, Notingher I (2014) Increasing the speed of tumour diagnosis during surgery with selective scanning Raman microscopy. J Mol Struct 1073:56–65

108. Kong K, Zaabar F, Rakha E, Ellis I, Koloydenko A, Notingher I (2014) Towards intra-operative diagnosis of tumours during breast conserving surgery by selective-sampling Raman microspectroscopy. Phys Med Biol 59(20):6141–6152
109. Czamara K, Natorska J, Kapusta P, Baranska M, Kaczor A (2015) Raman microspectroscopy of human aortic valves. Investigation of the local and global biochemical changes associated with calcification in aortic stenosis. Analyst 140(7):2164–2170
110. Kochan K, Marzec KM, Chruszcz-Lipska K, Jasztal A, Maslak E, Musiolik H, Chłopicki S, Baranska M (2013) Pathological changes in the biochemical profile of the liver in atherosclerosis and diabetes assessed by Raman spectroscopy. Analyst 138(14):3885–3890
111. Marzec KM, Kochan K, Fedorowicz A, Jasztal A, Chruszcz-Lipska K, Dobrowolski JC, Chlopicki S, Baranska M (2015) Raman microimaging of murine lungs: insight into the vitamin A content. Analyst 140(7):2171–2177
112. Büntemeyer H, Lehmann J (2001) The role of vitamins in cell culture media in animal cell technology: from target to market. In: ESACT proceedings, vol 1. Springer Netherlands, pp 204–206
113. Kochan K, Chrabaszcz K, Szczur B, Maslak E, Dybas J, Marzec KM (2016) IR and Raman imaging of murine brains from control and ApoE/LDLR$^{-/-}$ mice with advanced atherosclerosis. Analyst 141(18):5329–5338
114. Pacia MZ, Mateuszuk L, Chlopicki S, Baranska M, Kaczor A (2015) Biochemical changes of the endothelium in the murine model of NO-deficient hypertension. Analyst 140(7):2178–2184
115. Rygula A, Pacia MZ, Mateuszuk L, Kaczor A, Kostogrys RB, Chlopickiad S, Baranska M (2015) Identification of a biochemical marker for endothelial dysfunction using Raman spectroscopy. Analyst 140(7):2185–2189
116. Michael R, Otto C, Lenferink A, Gelpi E, Montenegro GA, Rosandić J, Tresserra F, Barraquer RI, Vrensen GFJM (2014) Absence of amyloid beta in lenses of Alzheimer's patients: a confocal Raman study. Exp Eye Res 119:44–53
117. Große C, Bergner N, Dellith J, Heller R, Bauer M, Mellmann A, Popp J, Neugebauer U (2015) Label-free imaging and spectroscopic analysis of intracellular bacterial infections. Anal Chem 87(4):2137–2142
118. Silge A, Abdou E, Schneider K, Meisel S, Bocklitz T, Lu-Walther H-W, Heintzmann R, Rösch P, Popp J (2015) Shedding light on host niches: label-free in situ detection of *Mycobacterium gordonae* via carotenoids in macrophages by Raman microspectroscopy. Cell Microbiol 17(6):832–842
119. Kong K, Rowlands CJ, Elsheikha H, Notingher I (2012) Label-free molecular analysis of live Neospora caninum tachyzoites in host cells by selective scanning microspectroscopy. Analyst 137(18):4119–4112
120. Naemat A, Elsheikha HM, Al-sandaqchi A, Kong K, Ghita A, Notingher I (2015) Analysis of interaction between the apicomplexan protozoan *Toxoplasma gondii* and host cells using label-free Raman spectroscopy. Analyst 140(3):756–764
121. Hobro AJ, Konishi A, Coban C, Smith NI (2013) Raman spectroscopic analysis of malaria disease progression via blood and plasma samples. Analyst 138(14):3927–3933
122. Hobro AJ, Pavillon N, Fujita K, Ozkan M, Coban C, Smith NI (2015) Label-free Raman imaging of the macrophage response to the malaria pigment hemozoin. Analyst 140 (7):2350–2359
123. Kozicki M, Creek DJ, Sexton A, Morahan BJ, Wesełucha-Birczyńska A, Wood BR (2015) An attenuated total reflection (ATR) and Raman spectroscopic investigation into the effects of chloroquine on *Plasmodium falciparum* infected red blood cells. Analyst 140(7):2236–2246
124. Czepiel J, Kozicki M, Panasiuk P, Birczyńska M, Garlicki A, Wesełucha-Birczyńska A (2015) *Clostridium difficile* the hospital plague. Analyst 140(7):2513–2522
125. Kochan K, Marzec KM, Maslak E, Chlopicki S, Baranska M (2015) Raman spectroscopic studies of vitamin A content in the liver: a biomarker of a healthy liver. Analyst 140(7):2074–2079
126. El-Mashtoly SF, Yosef HK, Petersen D, Mavarani L, Maghnouj A, Hahn S, Kötting C, Gerwert K (2015) Label-free Raman spectroscopic imaging monitors the integral physiological relevant drug responses in cancer cells. Anal Chem 87(14):7297–7304

127. Majzner K, Wojcik T, Szafraniec E, Lukawska M, Oszczapowicz I, Chlopicki S, Baranska M (2015) Nuclear accumulation of anthracyclines in the endothelium studied by bimodal imaging: fluorescence and Raman microscopy. Analyst 140(7):2302–2310
128. Zhang H, Zheng J, Liu A, Xiao H, He L (2016) Label-free imaging and characterisation of cancer cell responses to polymethoxyflavones using Raman microscopy. J Agric Food Chem 64(51):9708–9713
129. Kim D-H, Jarvis RM, Allwood JW, Batman G, Moore RE, Marsden-Edwards E, Hampson L, Hampson IN, Goodacre R (2010) Raman chemical mapping reveals site of action of HIV protease inhibitors in HPV16 E6 expressing cervical carcinoma cells. Anal Bioanal Chem 398(7):3051–3061
130. Kang JW, Singh SP, Nguyen FT, Lue N, Sung Y, So PTC, Dasari RR (2016) Investigating effects of proteasome inhibitor on multiple myeloma cells using confocal Raman microscopy. Sensors 16(12):2133
131. Brozek-Pluska B, Kopec M (2016) Raman microspectroscopy of hematoporphorins, imaging of the non-cancerous and the cancerous human breast tissues with photosensitisers. Spectrochim Acta A Mol Biomol Spectrosc 169:182–191
132. Yosef HK, Mavarani L, Maghnouj A, Hahn S, El-Mashtoly SF, Gerwert K (2015) In vitro prediction of the efficacy of molecularly targeted cancer therapy by Raman spectral imaging. Anal Bioanal Chem 407(27):8321–8331
133. Meister K, Niesel J, Schatzschneider U, Metzler-Nolte N, Schmidt DA, Havenith M (2010) Label-free imaging of metal-carbonyl complexes in live cells by Raman microspectroscopy. Angew Chem Int Ed 49(19):3310–3312
134. Salehi H, Derely L, Vegh A-G, Durand J-C, Gergely C, Larroque C, Fauroux M-A, Cuisinier FJG (2013) Label free detection of anticancer drug Paclitaxel in living cells by confocal Raman microscopy. Appl Phys Lett 102(11):113701
135. El-Mashtoly SF, Petersen D, Yosef HK, Mosig A, Reinacher-Schick A, Kötting C, Gerwert K (2014) Label-free imaging of drug distribution and metabolism in colon cancer cells by Raman microscopy. Analyst 139(5):1155–1161
136. Goto N, Morita Y, Terada K (2016) Deposits from creams containing 20% (w/w) urea and suppression of crystallisation (part 3): novel analytical methods based on Raman spectroscopy for the characterisation of deposits and deposition phenomena of creams containing 20% (w/w) urea. Chem Pharm Bull 64(8):1099–1107
137. Chernenko T, Matthäus C, Milane L, Quintero L, Amiji M, Diem M (2009) Label-free raman spectral imaging of intracellular delivery and degradation of polymeric nanoparticle systems. ACS Nano 3(11):3552–3559
138. Raaschou-Nielsen O, Andersen ZJ, Beelen R, Samoli E, Stafoggia M, Weinmayr G, Hoffmann B, Fischer P, Nieuwenhuijsen MJ, Brunekreef B, Xun WW, Katsouyanni K, Dimakopoulou K, Sommar J, Forsberg B, Modig L, Oudin A, Oftedal B, Schwarze PE, Nafstad P, De Faire U, Pedersen NL, Östenson C-G, Fratiglioni L, Penell J, Korek M, Pershagen G, Eriksen KT, Sørensen M, Tjønneland A, Ellermann T, Eeftens M, Peeters PH, Meliefste K, Wang M, Bueno-de-Mesquita B, Key TJ, de Hoogh K, Concin H, Nagel G, Vilier A, Grioni S, Krogh V, Tsai M-Y, Ricceri F, Sacerdote C, Galassi C, Migliore E, Ranzi A, Cesaroni G, Badaloni C, Forastiere F, Tamayo I, Amiano P, Dorronsoro M, Trichopoulou A, Bamia C, Vineis P, Hoek G (2013) Air pollution and lung cancer incidence in 17 European cohorts: prospective analyses from the European Study of Cohorts for Air Pollution Effects (ESCAPE). Lancet Oncol 14(9):813–822
139. Dorney J, Bonnier F, Garcia A, Casey A, Chambers G, Byrne HJ (2012) Identifying and localising intracellular nanoparticles using Raman spectroscopy. Analyst 137(5):1111–1119
140. Bräutigam K, Bocklitz T, Silgea A, Dierker C, Ossig R, Schnekenburger J, Cialla D, Rösch P, Popp J (2014) Comparative two- and three-dimensional analysis of nanoparticle localisation in different cell types by Raman spectroscopic imaging. J Mol Struct 1073:44–50
141. Ahlinder L, Ekstrand-Hammarström B, Geladi P, Osterlund L (2015) Large uptake of titania and iron oxide nanoparticles in the nucleus of lung epithelial cells as measured by Raman imaging and multivariate classification. Biophys J 105(2):310–319

142. Cherchi C, Chernenko T, Diem M (2011) Impact of nano titanium dioxide exposure on cellular structure of anabaena variabilis and evidence of internalisation. Environ Toxicol Chem 30(4):861–869
143. Iannarelli L, Giovannozzi AM, Morelli F, Viscotti F, Bigini P, Maurino V, Spoto G, Martra G, Ortel E, Hodoroaba V-D, Rossi AM, Diomede L (2016) Shape engineered TiO2 nanoparticles in *C. elegans*. A Raman imaging based approach to assist tissue-specific toxicological studies. RSC Adv 6(74):70501–70509
144. Alebrahim MA, Krafft C, Popp J (2015) Raman imaging to study structural and chemical features of the dentine enamel junction. IOP Conf Ser: Mater Sci Eng 92:012014
145. Fraser SJ, Natarajan AK, Clark ASS, Drummond BK, Gordon KC (2015) A Raman spectroscopic study of teeth affected with molar – incisor hypomineralisation. J Raman Spectrosc 46(2):202–210
146. Masic A, Weaver JC (2015) Large area submicron chemical imaging of magnesium in sea urchin teeth. J Struct Biol 189(3):269–275
147. Shabestari M, Eriksen EF, Paschalis EP, Roschger P, Gamsjaeger S, Klaushofer K, Berzlanovich A, Nogues X, Puig L, Diez-Perez A (2017) Presence of pyrophosphate in bone from an atypical femoral fracture site: a case report. Bone Reports 6:81–86
148. Austin C, Smith TM, Farahani RM, Hinde K, Carter EA, Lee J, Lay PA, Kennedy BJ, Sarrafpour B, Wright RJ, Wright RO, Arora M (2016) Uncovering system-specific stress signatures in primate teeth with multimodal imaging. Sci Rep 6:18802
149. Toledano M, Aguilera FS, Osorio E, Cabello I, Osorio R (2014) Microanalysis of thermal-induced changes at the resin-dentin interface. Microsc Microanal 20(4):1218–1233
150. Toledano M, Cabello I, Aguilera FS, Osorio E, Osorio R (2015) Effect of in vitro chewing and bruxism events on remineralisation at the resin-dentin interface. J Biomech 48(1):14–21
151. Hashimoto A, Chiu L-d, Sawada K, Ikeuchi T, Fujita K, Takedachi M, Yamaguchi Y, Kawata S, Murakami S, Tamiya E (2014) In situ Raman imaging of osteoblastic mineralisation. J Raman Spectrosc 45(2):157–161
152. Ghita A, Pascut FC, Sottile V, Notingher I (2014) Monitoring the mineralization of bone nodules in vitro by space- and time-resolved Raman microscopy. Analyst 139(1):55–58
153. Gao Y, Xu C, Wang L (2016) Non-invasive monitoring of the osteogenic differentiation of human mesenchymal stem cells on a polycaprolactone scaffold using Raman imaging. RSC Adv 6(66):61771
154. Autefage H, Gentleman E, Littmann E, Hedegaard MA, Von Erlach T, O'Donnell M, Burden FR, Winkler DA, Stevens MM (2015) Sparse feature selection methods identify unexpected glabal cellular response to strontium containing materials. Proc Natl Acad Sci U S A 112 (14):4280–4285
155. Wei X, Wang X, Fang Y, Huang Q (2013) Comparison of hair from rectum cancer patients and from healthy persons by Raman microspectroscopy and imaging. J Mol Struct 1048:83–87
156. Wu Y, Chen G, Ji C, Hoptroff M, Jones A, Collins LZ, Janssen H-G (2016) Gas chromatography – mass spectrometry and Raman imaging measurement of squalene content and distribution in human hair. Anal Bioanal Chem 408(9):2357–2362
157. Perera PN, Schmidt M, Chuck PJ, Adams PD (2011) Blind image analysis for the compositional and structural characterisation of plant cell walls. Anal Chim Acta 702(2):172–177
158. Hänninen T, Kontturi E, Vuonnen T (2011) Distribution of lignin and its coniferyl alcohol and coniferyl aldehyde groups in *Picea abies* and *Pinus sylvestris* as observed by Raman imaging. Phytochemistry 72(14–15):1889–1895
159. Ma J, Lv X, Yang S, Tian G, Liu X (2015) Structural insight into cell wall architecture of *Miscanthus sinensis* using correlative microscopy approaches. Microsc Microanal 21(5):1304–1313
160. Sun L, Singh S, Joo M, Vega-Sanchez M, Ronald P, Simmons BA, Adams P, Auer M (2016) Non-invasive imaging of cellulose microfibril orientation within plant cell walls by polarised Raman microspectroscopy. Biotechnol Bioeng 113(1):82–90

161. Chu L-Q, Masyuko R, Sweedler JV, Bohn PW (2010) Base-induced delignification of miscanthus × giganteus studied by three-dimensional confocal Raman imaging. Bioresour Technol 101(13):4919–4925
162. Vermaak I, Viljoen AM, Hamman JH, Baranska M (2010) The potential application of FT-Raman spectroscopy for the quantification and mapping of the steroidal glycoside P57 in *Hoodia gordonii*. Phytochem Lett 3(3):156–160
163. Zimmermann B, Bağcıoğlu M, Sandt C, Kohler A (2015) Vibrational microspectroscopy enables chemical characterisation of single pollen grains as well as comparative analysis of plant species based on pollen ultrastructure. Planta 242(5):1237–1250
164. Chylińska M, Szymańska-Chargot M, Zdunek A (2014) Imaging of polysaccharides in the tomato cell wall with Raman microspectroscopy. Plant Methods 10:14
165. Philippe G, Gaillard C, Petit J, Geneix N, Dalgalarrondo M, Bres C, Mauxion J-P, Franke R, Rothan C, Schreiber L, Marion D, Bakan B (2016) Ester cross-link profiling of the cutin polymer of wild-type and cutin synthase tomato mutants highlights different mechanisms of polymerisation. Plant Physiol 170(2):807–820
166. Szymańska-Chargot M, Chylińska M, Pieczywek PM, Rösch P, Schmitt M, Popp J, Zdunek A (2016) Raman imaging of changes in polysaccharide distribution in the cell wall during apple fruit development and senescence. Planta 243:935–945
167. Richter S, Müssig J, Gierlinger N (2011) Functional plant cell wall design revealed by the Raman imaging approach. Planta 233(4):763–772
168. Mateu BP, Hauser MT, Heredia A, Gierlinger N (2016) Waterproofing in Arabidopsis: following phenolics and lipids in situ by confocal Raman microscopy. Front Chem 4:10
169. Polisetti S, Bible AN, Morrell-Falvey JL, Bohn PW (2016) Raman chemical imaging of the rhizosphere bacterium Pantoea sp. YR343 and its co-culture with *Arabidopsis thaliana*. Analyst 141(7):2175
170. Kammer M, Hedrich R, Ehrlich H, Popp J, Brunner E, Krafft C (2010) Spatially resolved determination of the structure and composition of diatom cell walls by Raman and FTIR imaging. Anal Bioanal Chem 398(1):509–517
171. Chiu L-d, Ho S-H, Shimada R, Ren N-Q, Ozawa T (2017) Rapid in vitro lipid/carbohydrate quantification of single microalgal cell by Raman spectral imaging to reveal salinity-induced starch-to-lipid shift. Biotechnol Biofuels 10:9
172. Noothalapati H, Sasaki T, Kaino T, Kawamukai M, Ando M, Hamaguchi H, Yamamoto T (2016) Label-free chemical imaging of fungal spore walls by Raman microscopy and multivariate curve resolution analysis. Sci Rep 6:27789
173. Yoo HY, Iordachescu M, Huang J, Hennebert E, Kim S, Rho S, Foo M, Flammang P, Zeng H, Hwang D, Waite JH, Hwang DS (2016) Sugary interfaces mitigate contact damage where stiff meets soft. Nat Commun 7:11923
174. Nakamura MJ, Hotta K, Oka K (2013) Raman spectroscopic imaging of the whole *Ciona intestinalis* embryo during development. PLoS One 8:e71739
175. Hölscher D, Dhakshinamoorthy S, Alexandrov T, Becker M, Bretschneider T, Buerkert A, Crecelius AC, De Waele D, Elsen A, Heckel DG, Heklau H, Hertweck C, Kai M, Knop K, Krafft C, Maddula RK, Matthäus C, Popp J, Schneider B, Schubert US, Sikora RA, Svatoš A, Swennen RL (2014) Phenalenon-type phytoalexins mediate resistance of banana plants (musa spp.) to the burrowing nematode *Radopholus similis*. Proc Natl Acad Sci U S A 111 (1):105–110
176. Smith GPS, Holroyd SE, Reid DCW, Gordon KC (2017) Raman imaging processed cheese and its components. J Raman Spectrosc 48(3):374–383
177. Kilcrease J, Collins AM, Richins RD, Timlin JA, O'Connell MA (2013) Multiple microscopic approaches demonstrate linkage between chromoplast architecture and carotenoid composition in diverse *Capsicum annum* fruit. Plant J 76(6):1074–1083
178. Qin J, Chao K, Kim MS (2013) Simultaneous detection of multiple adulterants in dry milk using macroscale Raman chemical imaging. Food Chem 138(2–3):998–1007

179. Dhakal S, Chao K, Qin J, Kim M, Chan D (2016) Raman spectral imaging for quantitative contaminant evaluation in skim milk powder. Food Meas 10(2):374–386
180. Clemente I, Aznar M, Nerín C (2016) Raman imaging spectroscopy as a tool to investigate the cells damage on *Aspergillus ochraceus* caused by an antimicrobial packaging containing benzylisothiocyanate. Anal Chem 88(9):4772–4779
181. Eksi-Kocak H, Mentes-Yilmaz O, Boyaci IH (2016) Detection of green pea adulteration in pistachio nut granules by using Raman hyperspectral imaging. Eur Food Res Technol 242(2):271–277
182. Kwok K, Taylor LS (2012) Analysis of counterfeit Cialis tablets using Raman microscopy and multivariate curve resolution. J Pharm Biomed Anal 66:126–135
183. Sacré P-Y, Deconinck E, Saerens L, De Beer T, Courselle P, Vancauwenberghe R, Chiap P, Crommen J, De Beer JO (2011) Detection of counterfeit Viagra by Raman microspectroscopy imaging and multivariate analysis. J Pharm Biomed Anal 56(2):454–461
184. Smus JP, Moura CC, McMorrow E, Tare RS, Oreffo ROC, Mahajan S (2015) Tracking adipogenic differentiation of skeletal stem cells by label-free chemically selective imaging. Chem Sci 6(12):7089–7096
185. Bradley J, Pope I, Masia F, Sanusi R, Langbein W, Swann K, Paola B (2016) Quantitative imaging of lipids in live mouse oocytes and early embryos using CARS microscopy. Development 143:2238–2247
186. Chen W-W, Yi Y-H, Chien C-H, Hsiung K-C, Ma T-H, Lin Y-C, Lo SJ, Chang T-C (2016) Specific polyunsaturated fatty acids modulate lipid delivery and oocyte development in *C. elegans* revealed by molecular-selective label free imaging. Sci Rep 6:32021
187. Jüngst C, Klein M, Zumbusch A (2013) Long term live cell microscopy studies of lipid droplet fusion dynamics in adipocytes. J Lipid Res 54(12):3419–3429
188. Di Napoli C, Pope I, Masia F, Langbein W, Watson P, Borri P (2016) Quantitative spatiotemporal chemical profiling of individual lipid droplets by hyperspectral CARS microscopy in living human adipose-derived stem cells. Anal Chem 88(7):3677–3685
189. Lee JH, Kim DH, Song WK, Oh M-K, Ko D-K (2015) Label-free imaging and quantitative chemical analysis of Alzheimer's disease brain samples with multimodal multiphoton non-linear optical microscopy. J Biomed Opt 20(5):056013
190. Cavonius L, Fink H, Kiskis J, Albers E, Undeland I, Enejder A (2015) Imaging of lipids in microalgae with coherent anti-stokes Raman microscopy. Plant Physiol 167(3):603–616
191. Belanger E, Crépeau J, Laffray S, Vallée R, De Koninck Y, Côté D (2012) Live animal myelin histomorphometry of the spinal cord with video-rate multimodal nonlinear microendoscopy. J Biomed Opt 17(2):021107
192. Turcotte R, Rutledge DJ, Bélanger E, Dill D, Macklin WB, Côté D (2016) Intravital assessment of myelin molecular order with polarimetric multiphoton microscopy. Sci Rep 6:31685
193. Chen X, Gasecka P, Formanek F, Galey J-B, Rigneault H (2016) In vivo single human sweat gland activity monitoring using coherent anti-stokes Raman scattering and two-photon excited autofluorescence microscopy. Br J Dermatol 174(4):803–812
194. Wang H, Osseiran S, Igras V, Nichols AJ, Roider EM, Pruessner J, Tsao H, Fisher DE, Evans CL (2016) Invivo coherent Raman imaging of the melanomagenesis-associated pigment pheomelanin. Sci Rep 6:37986
195. Johnston HJ, Mouras R, Brown DM, Elfick A, Stone V (2015) Exploring the cellular and tissue uptake of nanomaterials in a range of biological samples using multimodal non-linear optical microscopy. Nanotechnology 26(50):505102
196. Watts AJR, Lewis C, Goodhead RM, Beckett SJ, Moger J, Tyler CR, Galloway TS (2014) Uptake and retention of microplastics by the shore crab *Carcinus maenas*. Environ Sci Technol 48(15):8823–8830
197. Uckermann O, Galli R, Tamosaityte S, Leipnitz E, Geiger KD, Schackert G, Koch E, Steiner G, Kirsch M (2014) Label-free delineation of brain tumours by coherent anti-stokes Raman scattering microscopy in an orthotopic mouse model and human glioblastoma. PLoS One 9(9):e107115
198. Potcoava MC, Futia GL, Aughenbaugh J, Schlaepfer IR, Gibson EA (2014) Raman and coherent anti-stokes Raman scattering microscopy studies of changes in lipid content and composition in hormone treated breast and prostate cancer cells. J Biomed Opt 19(11):111065

199. Parekh SH, Lee YJ, Aamer KA, Cicerone MT (2010) Label-free cellular imaging by broadband coherent anti-stokes Raman scattering microscopy. Biophys J 99(8):2695–2704
200. Bito K, Okuno M, Kano H, Tokuhara S, Naito S, Masukawa Y, Leproux P, Couderc V, Hamaguchi H (2012) Protein secondary structure imaging with ultrabroadband multiplex coherent anti-stokes Raman scattering microspectroscopy. J Phys Chem B 116(4):1425–1457
201. Lin C-Y, Suhalim JL, Nien CL, Miljković MD, Diem M, Jester JV, Potma EO (2011) Picosecond spectral coherent anti-stokes Raman scattering with principal component analysis of Meibomian glands. J Biomed Opt 16(2):021104
202. El-Mashtoly SF, Niedieker D, Petersen D, Krauss SD, Freier E, Maghnouj A, Mosig A, Hahn S, Kötting C, Gerwert K (2014) Automated identification of subcellular organelles by coherent anti-stokes Raman scattering. Biophys J 106(9):1910–1920
203. Roeffaers MBJ, Zhang X, Freudiger CW, Saar BG, van Ruijven M, van Dalen G, Xiao C, Xie XS (2011) Label-free imaging of biomolecules in food products using stimulated Raman microscopy. J Biomed Opt 16(2):021118
204. Littlejohn GR, Mansfield JC, Parker D, Lind R, Perfect S, Seymour M, Smirnoff N, Love J, Moger J (2015) In vivo chemical and structural analysis of plant cuticle waxes using SRS microscopy. Plant Physiol 168(1):18–28
205. Zeng Y, Zhao S, Wei H, Tucker MP, Himmel ME, Mosier NS, Meilan R, Ding S-Y (2015) In situ micro-spectroscopic investigation of lignin in poplar cell walls pretreated by maleic acid. Biotechnol Biofuels 8:126
206. Mansfield JC, Littlejohn GR, Seymour MP, Lind RJ, Perfect S, Moger J (2013) Label-free chemically specific imaging in planta with stimulated Raman scattering microscopy. Anal Chem 85(10):5055–5063
207. Egawa M, Tokunaga K, Hosoi J, Iwanaga S, Ozeki Y (2016) In situ visualisation of intracellular morphology of epidermal cells using stimulated Raman scattering microscopy. J Biomed Opt 21(8):086017
208. Tian F, Yang W, Mordes DA, Wang J-Y, Salameh JS, Mok J, Chew J, Sharma A, Leno-Duran E, Suzuki-Uematsu S, Suzuki N, Han SS, Lu F-K, Ji M, Zhang R, Liu Y, Strominger J, Shneider NA, Petrucelli L, Xie XS, Eggan K (2016) Monitoring peripheral nerve degeneration in ALS by label-free stimulated Raman scattering imaging. Nat Commun 7:13283
209. Conley SJ, Wicha MX (2013) Breast cancer stem cells: from theory to therapy. In: Sell S (ed) Stem cells handbook. Humana Press, Totowa
210. Li J, Condello S, Thomes-Pepin J, Ma X, Xia Y, Hurley TD, Matei D, Cheng J-X (2017) Lipid desaturation is a metabolic marker and therapeutic target of ovarian cancer stem cells. Cell Stem Cell 20(3):1–12
211. Lu F-K, Basu S, Igras V, Hoang MP, Ji M, Fu D, Holtom GR, Neel VA, Freudiger CW, Fisher DE, Xie XS (2015) Label-free DNA imaging in vivo with stimulated Raman scattering microscopy. Proc Natl Acad Sci U S A 112(37):11624–11629
212. Satoh S, Otsuka Y, Ozeki Y, Itoh K, Hashiguchi A, Yamazaki K, Hashimoto H, Sakamoto M (2014) Label-free visualisation of acetaminophen-induced liver injury by high-speed stimulated Raman scattering spectral microscopy and multivariate image analysis. Pathol Int 64(10):518–526
213. Datta R, Heylman C, George SC, Gratton E (2016) Label-free imaging of metabolism and oxidative stress in human induced pluripotent stem-cell derived cardiomyocytes. Biomed Opt Express 7(5):1690–1701
214. Pavillon N, Smith NI (2015) Implementation of simultaneous quantitative phase with Raman imaging. EPJ Tech Instrum 2(5):1–11
215. Petibois C (2010) Imaging methods for elemental, chemical, molecular and morphological analysis of single cells. Anal Bioanal Chem 397:2051–2065
216. Garip S, Bayari SH, Severcan M, Abbas S, Lednev IK, Severcan F (2016) Structural effects of Simvastatin on rat liver tissue. Fourier transform infrared and Raman microspectroscopic studies. J Biomed Opt 21(2):025008
217. Lau K, Hobro A, Smith T, Thurston T, Lendl B (2012) Label-free non-destructive in situ biochemical analysis of nematode *Steinernema kraussei* using FPA-FTIR and Raman spectroscopic imaging. Vib Spectrosc 60:34–42

218. Sroka-Bartnicka A, Kimber JA, Borkowski L, Pawlowska M, Polkowska I, Kalisz G, Belcarz A, Jozwiak K, Ginalska G, Kazarian SG (2015) The biocompatibility of carbon hydroxyapatite/β-glucan composite for bone tissue engineering studied with Raman and FTIR spectroscopic imaging. Anal Bioanal Chem 407(25):7775–7785
219. Chia CH, Gong B, Joseph SD, Marjo CE, Munroe P, Rich AM (2012) Imaging of mineral enriched biochar by FTIR, Raman and SEM-EDX. Vib Spectrosc 62:248–257
220. Caine S, Hackett MJ, Hou H, Kumar S, Maley J, Ivanishvili Z, Suen B, Szmigielski A, Jiang Z, Sylvain NJ, Nichol H (2016) A novel multimodal platform to image molecular and elemental alterations in ischemic stroke. Neurobiol Dis 91:132–142
221. Palombo F, Madami M, Fioretto D, Nallala J, Barr H, David A, Stone N (2016) Chemico-mechanical imaging of Barratt's oesophagus. J Biophotonics 9(7):694–700
222. Spengler B (2015) Mass spectrometry imaging of biomolecular information. Anal Chem 87 (1):64–82
223. Lanni EJ, Masyuko RN, Driscoll CM, Dunham SJB, Shrout JD, Bohn PW, Sweedler JV (2014) Correlated imaging with C60-SIMS and confocal Raman microscopy: visualisation of cell-scale molecular distributions in bacterial biofilms. Anal Chem 86(21):10885–10891
224. Ahlf DR, Masyuko RN, Hummon AB, Bohn PW (2014) Correlated mass spectrometry imaging and confocal Raman microscopy for studies of three dimensional cell culture sections. Analyst 139(18):4578–4585
225. Bocklitz TW, Bräutigam K, Urbanek A, Hoffmann F, von Eggeling F, Ernst G, Schmitt M, Schubert U, Guntinas-Lichius O, Popp J (2015) Novel workflow for combining Raman spectroscopy and MALDI-MSI for tissue based studies. Anal Bioanal Chem 407(26):7865–7873
226. Gavara N (2017) A beginner's guide to atomic force microscopy probing for cell mechanics. Microsc Res Tech 80(1):75–84
227. Boifor R, Sinjab F, Strohbuecker S, Sottile V, Notingher I (2016) Towards quantitative molecular mapping of cells by Raman microscopy: using AFM for decoupling molecular concentration and cell topography. Faraday Discuss 187:199–212
228. Ashgari-Khiavi M, Wood BR, Mechler A, Bambery KR, Buckingham DW, Cooke BM, McNaughton D (2010) Correlation of atomic force microscopy and Raman microspectrscopy to study the effects of ex vivo treatment procedures on human red blood cells. Analyst 135 (3):525–530
229. Marzec KM, Rygula A, Wood BR, Chlopicki S, Baranska High-resolution M (2015) Raman imaging reveals spatial location of heme oxidation sites in single red blood cells of dried smears. J Raman Spectrosc 46(1):76–83
230. Liao C, Piercey-Normore MD, Sorensen JL, Gough K (2010) In situ imaging of usnic acid in selected Cladonia spp by vibrational spectroscopy. Analyst 135(12):3242–3248
231. Tang M, McEwen GD, Wu Y, Miller CD, Zhou A (2013) Characterisation and analysis of mycobacteria and gram-negative bacteria and co-culture mixtures by Raman micro-spectroscopy, FTIR and atomic force microscopy. Anal Bioanal Chem 405(5):1577–1591
232. Pavillon N, Hobro AJ, Smith NI (2013) Cell optical density and molecular composition revealed by simultaneous multimodal label-free imaging. Biophys J 105(5):1123–1132
233. Kang JW, Lue N, Kong C-R, Barman I, Dingari NC, Goldfless SJ, Niles JC, Dasari RR, Feld MS (2011) Combined confocal Raman and quantitative phase microscopy system for biomedical diagnosis. Biomed Opt Express 2(9):2484–2492
234. Ferrara MA, Di Caprio G, Managò S, De Angelis A, Sirleto L, Coppola G, De Luca AC (2015) Label-free imaging and biochemical characterisation of bovine sperm cells. Biosensors 5(2):141–157
235. Ibrahim A, Hage CH, Souissi A, Leray A, Héliot L, Souissi S, Vandenbunder B (2015) Label-free microscopy and stress responses reveal the functional organisation of *Pseudodiaptomus marinus* copepod myofibrils. J Struct Biol 191(2):224–235
236. Xu X, Cheng J, Thrall MJ, Liu Z, Wang X, Wong STC (2013) Multimodal non-linear optical imaging for label-free differentiation of lung cancerous lesions from normal and desmoplastic tissues. Biomed Opt Express 4(12):2855

237. Galli R, Sablinskas V, Dasevicius D, Laurinavicius A, Jankevicius F, Koch E, Steiner G (2014) Non-linear optical microscopy of kidney tumours. J Biophotonics 7(1–2):23–27
238. Meyer T, Baumgartl M, Gottschall T, Pascher T, Wuttig A, Matthäus C, Romeike BFM, Brehm BR, Limpert J, Tünnermann A, Guntinas-Lichius O, Dietzek B, Schmitti M, Popp J (2013) A compact microscope setup for multimodal nonlinear imaging in clinics and its application to disease diagnostics. Analyst 138(14):4048–4057
239. Matthäus C, Cicchi R, Meyer T, Lattermann A, Schmitt M, Romeike BFM, Krafft C, Dietzek B, Brehm BR, Pavone FS, Popp J (2014) Multimodal non-linear imaging of atherosclerotic plaques differentiation of triglyceride and cholesterol deposits. J Innov Opt Health Sci 7(5):1450027
240. Legesse FB, Heuke S, Galler K, Hoffmann P, Schmitt M, Neugebauer U, Bauer M, Popp J (2016) Hepatic vitamin A content investigation using coherent anti-stokes Raman scattering microscopy. ChemPhysChem 17(24):4043–4051
241. Chernavskaia O, Heuke S, Vieth M, Friedrich O, Schürmann S, Atreya R, Stallmach A, Neurath MF, Waldner M, Petersen I, Schmitt M, Bocklitz T, Popp J (2016) Beyond endoscopic assessment in inflammatory bowel disease: real-time histology of disease activity by non-linear multimodal imaging. Sci Rep 6:29239
242. Pliss A, Kuzmin AN, Kachynski AV, Prasad PN (2010) Non-linear optical imaging and microspectrometry of the cell nucleus through the cell cycle. Biophys J 99(10):3483–3491
243. Pirhonen J, Arola J, Sädevirta S, Luukkonen P, Karppinen S-M, Pihlajaniemi T, Isomäki A, Hukkanen M, Yki-Järvinen H, Ikonen E (2016) Continuous grading of early fibrosis in NAFLD using label free imaging: a proof of concept study. PLoS One 11:e0147804
244. Haluszka D, Lőrincz K, Kiss N, Szipőcs R, Kuroli E, Gyöngyösi N, Wikonkál NM (2016) Diet-induced obesity skin changes monitored by in vivo SHG and ex vivo CARS microscopy. Biomed Opt Express 7(11):4480–4489
245. Mortati L, Divieto C, Sassi MP (2012) CARS and SHG microscopy to follow collagen production in living human corneal fibroblasts and mesenchymal stem cells in fibrin hydrogel 3D cultures. J Raman Spectrosc 43(5):675–680
246. Brackmann C, Bengtsson A, Alminger ML, Svanberg U, Enejder A (2011) Visualisation of β-carotene and starch granules in plant cell using CARS and SHG microscopy. J Raman Spectrosc 42(4):586–592
247. Brackmann C, Dahlberg J-O, Vrana NE, Lally C, Gatenholm P, Enejder A (2012) Non-linear microscopy of smooth muscle cells in artificial extracellular matrices made of cellulose. J Biophotonics 5(5–6):404–414
248. Mansfield J, Moger J, Green E, Moger C, Winlove CP (2013) Chemically specific imaging and in-situ chemical analysis of articular cartilage with stimulated Raman scattering. J Biophotonics 6(10):803–814
249. Kallaway C, Almond LM, Barr H, Wood J, Hutchings J, Kendall C, Stone N (2013) Advances in the clinical application of Raman spectroscopy for cancer diagnosis. Photodiagn Photodyn Ther 10(3):207–219
250. Watanabe K, Palonpon AF, Smith NI, Chiu L-d, Kasai A, Hashimoto H, Kawano S, Fujita K (2015) Structured line illumination Raman microscopy. Nat Commun 6:10095

MRI and Ultrasound Imaging of Nanoparticles for Medical Diagnosis

8

Or Perlman and Haim Azhari

Contents

1 Definition of the Topic

Magnetic resonance imaging (MRI) and ultrasound (US) are two prominent medical imaging modalities. They are extensively and routinely used in various medical fields, such as cardiology, embryology, neurology, and oncology. In this chapter we describe the application of nanoparticles for MRI and US image enhancement. Moreover, the utilization of nano-scaled compounds for multimodal MRI-US imaging, allowing further increase of diagnosis certainty, is depicted.

O. Perlman · H. Azhari (✉)
Department of Biomedical Engineering, Technion – Israel Institute of Technology, Haifa, Israel
e-mail: azhari@technion.ac.il

C. S. S. R. Kumar (ed.), *Nanotechnology Characterization Tools for Biosensing and Medical Diagnosis*, https://doi.org/10.1007/978-3-662-56333-5_8

2 Overview

Imaging is a key method for obtaining medical diagnosis. To improve pathology detection ability, intravenous injections of contrast media are often performed. Such materials change a specific physical property of the tissue to which they reach, resulting in improved image contrast.

The developments in the field of nanotechnology have created vast opportunities for improved medical care, in the disciplines of diagnosis and treatment as well. The extremely small nanoparticles' (NPs) size and their high surface area to volume ratio impact various physical properties. This includes mechanical, magnetic, and optical characteristics, as well as allowing improved tumor targeting.

Here, we describe the utilization of NPs in two imaging modalities: US and MRI. These two modalities provide a vast spectrum of clinical applications, are extensively used, and are both non-ionizing in nature. The comparison and added value of NPs over conventional contrast agents will be described herein with an up-to-date review of relevant research. Finally, nano-scaled compounds allowing multimodal MRI-US will be reviewed, and future perspective will be given.

3 Introduction

Imaging is a process in which a certain property of an object is mapped to create a representative image. In medicine, several tissue properties are suitable for imaging purposes, such as atomic number in X-ray computed tomography (CT), proton density and spin relaxation in MRI, and acoustic impedance in US [1]. The image can represent an integrated physical property along a certain dimension (e.g., chest image in X-ray) or a cross-sectional slice (as in MRI and CT), depicting the inner structure of the body. In addition, several imaging protocols and image reconstruction techniques allow the representation of three-dimensional (3D) images. In several modalities, such as single photon emission computed tomography (SPECT), positron emission tomography (PET), and X-rays, the acquisition procedure involves the use of ionizing radiation. The two modalities discussed here, MRI and ultrasound are both non-ionizing in nature and considered hazardless.

The use of diagnostic imaging is highly common in the clinic [2], since correct and early detection of pathology has immense impact on prognosis. An essential factor for pathology detection is the existence of sufficient contrast between normal and abnormal tissue. To increase the differentiation ability, contrast agents are frequently used. In certain modalities, administration of contrast materials may reach 50% of all imaging sessions [3]. A common target for contrast enhancement is blood vessels. After an injection of a contrast media intravenously, veins/arteries are highlighted, allowing an improved examination of their condition. Under such conditions, blockages or impaired vessels are more easily detected, as poor contrast agent uptake is clearly visible. Contrast agents are used also in cardiology [4] and gastrointestinal tract disorders detection where contrast agents can also be

administered orally [5]. The utilization of contrast agents is naturally of great importance in tumor detection and characterization [6].

The term NPs commonly relate to particles with two or three dimensions of 1–100 nm in size [7, 8]. Nonetheless, this term is also often used for defining size ranges of 10–1000 nm size range [9], 1–50 nm diameter [10], and even less than 1 micron [11]. The remarkable developments and rapid expansion of the field of nanotechnology have brought staggering opportunities to medical imaging.

The prominent advantages that NPs hold include:

1. *Increased passive tumor accumulation ability.* Tumor-related blood vessels are commonly leaky, with pores of minimum 100 nm in size [12], and typically of less than 780 nm in diameter [13]. This characteristic, known as the enhanced permeability and retention (EPR) effect, does not occur in non-pathologic tissues and consequently leads to NPs accumulation in tumors [14]. To achieve increased tumor penetration using the above described mechanism, long circulation time of the NPs is required. This can be obtained by various manners, e.g., by poly (ethylene glycol) (PEG) encapsulation [15] and dextran coating [16].
2. *Active targeting and efficient drug carrying ability.* The high surface-to-volume ratio of NPs can be utilized for efficient conjunction ability to targeting ligands [17], including folic acid [18], insulin, and peptides. In addition, NPs can be conjugated to drugs, with an increased loading capacity [19].
3. *Tunable imaging parameters*. The extremely small size of the NPs yields also unique physical properties, e.g., by quantum mechanics-related effects [20]. Moreover, by controlling the synthesis procedure to yield particles in different sizes and morphologies, the imaging properties can be tuned to allow superior contrast generation [21, 22].

Accordingly, nano-scaled contrast agents are vastly investigated in all imaging modalities used in the clinic [23]. Prominent composites include gold nanoparticles in CT [24], nanobubbles in ultrasound [25], radiolabeled nanoparticles for PET and SPECT [26, 27], and iron oxide nanoparticles in MRI [28].

Another rapidly growing research trend is the exploitation of a single nano-compound for imaging using two or more different modalities. Using such materials, each imaging technique provides its added value, resulting in a more comprehensive evaluation of the pathologic state, and increased diagnosis certainty. Moreover, using a single contrast agent administration for several modalities prevents the physiological stress stemming from multiple dosages [29].

Several review papers have been published covering topics such as nano-scaled ultrasound contrast agents [30], nano-scaled MRI contrast agents [31], and multimodal contrast agents [32]. This chapter provides a unique step-by-step explanation of the physical background behind the mechanism of nanoparticles as contrast agents for MRI and ultrasound. It is structured to gradually add the needed building blocks for introducing the reader to the current state-of-the-art research in the field of multimodal MRI-ultrasound nano-agents. It is directed and oriented to provide a fundamental picture of the MRI and US nano-imaging field and outlines recently published relevant work.

4 Experimental and Instrumental Methodology

4.1 Magnetic Resonance Imaging (MRI)

MRI is an imaging method which utilizes magnetization properties of the studied tissue to generate images. When subjected to a strong magnetic field, some atom nuclei react in response to radio waves transmitted toward them at a specific frequency (termed the "resonance frequency") by absorbing them and then emitting detectable radio waves. This phenomenon is termed "nuclear magnetic resonance (NMR)." In most medical applications, imaging is based on the NMR of the hydrogen nucleus, i.e., a proton.

In order to explain MRI in simple terms, it is preferable to consider a voxel of tissue. Within such a voxel, (which dimensions are typically about one cubic millimeter), there are numerous hydrogen atoms. Each hydrogen proton can be approximated by a positive electric charge which spins around the proton axis. Resulting from this electric loop, a small magnetic field is generated around the hydrogen proton. Each hydrogen proton has its "private" magnetic field aimed at an arbitrary direction in space. Since magnetic fields are directional, they add up like vectors. Thus, in such random distribution of the small magnetic fields of the hydrogen protons, the resultant magnetization of the voxel is nearly zero (neglecting the earth's magnetic field). When placed within the strong magnetic field of the MRI scanner (denoted as B_0) which strength is commonly between 0.1 and 7 [Tesla] (one Tesla is about 20,000 times the magnetic field of the earth), these numerous magnetic fields are aligned with the MRI field, somewhat similar to a compass needle aligning with the magnetic field of earth. As a result, the voxel becomes "magnetized" with a magnetic moment per volume denoted as M_0 (see Fig. 8.1). This magnetic moment linearly depends on the strength of the magnetic field B_0 and the number of hydrogen protons per volume (termed "proton density").

Next, consider the magnetization vector M_0 of that voxel. This vector is positioned along the z-axis of a stationary frame of reference, which aligns with the magnetic

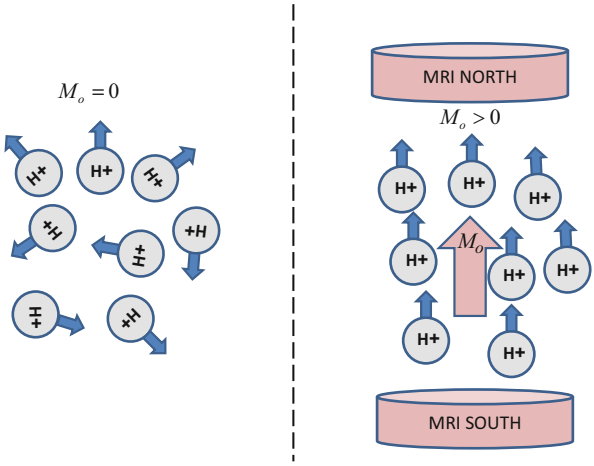

Fig. 8.1 (Left) The magnetic fields of the hydrogen protons in a voxel are randomly oriented in space; hence, the resulting magnetic moment is nulled. (Right) When placed within the MRI, they reorient and the resulting magnetic moment is M_0

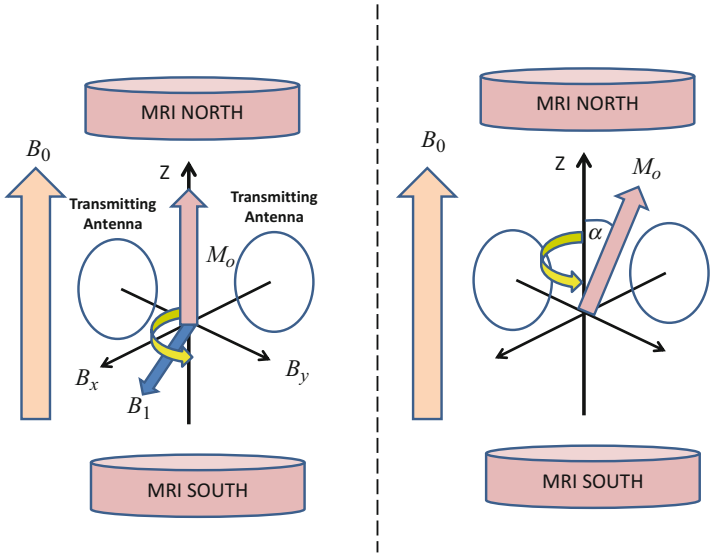

Fig. 8.2 (Left) When two orthogonal antennas transmit radio waves as explained in the text, a B_1 field which rotates about the z-axis at the resonance frequency is generated. (Right) As a result, the magnetization vector M_0 is tilted by an angle α from the z-axis

field of the MRI, i.e., B_0. Two transmission antennas are then positioned along the corresponding x and y axes. The first antenna transmits a field $B_x = B_1 \cdot \cos(\omega_0 t)$ while the second transmits a field $B_y = B_1 \cdot \sin(\omega_0 t)$. This results in a magnetic field B_1 which is located at the x-y plane and rotates around the z-axis with an angular frequency ω_0 which equals to the resonance frequency. This causes a tilt of the voxel magnetization vector M_0 by an angle α from the z-axis (see Fig. 8.2). The magnitude of this angle depends on the strength of the field B_1 and the transmission duration.

When the B_1 transmission is stopped, the tilted magnetization vector M_0 retains its rotation but also begins a realignment process with the z-axis. M_0 has two components: M_z which is aligned with the MRI magnetic field B_0 and M_{xy} which rotates perpendicularly to that field, i.e., in the x-y plane. The rotation frequency is the resonance frequency ω_0. Next, the two transmission antennas are replaced by receiving antennas with the same configuration as shown in Fig. 8.2. Since M_{xy} is actually a rotating magnetic field, it induces currents/voltage in the receiving antennas. These are the signals from which the MRI image is generated.

The contrast in an MRI image is generated by the differences in the signals emitted from the different voxels at a specific acquisition time. This specific time point is designated as echo time (TE). The differences between different materials or tissue types stem mainly from three characteristic properties: (i) proton density which relates to the number of hydrogen protons in the voxel, (ii) spin-lattice relaxation which relates to the realignment of the magnetization vector with the z-axis (see Fig. 8.3) and is characterized by a time constant T_1, and (iii) spin-spin

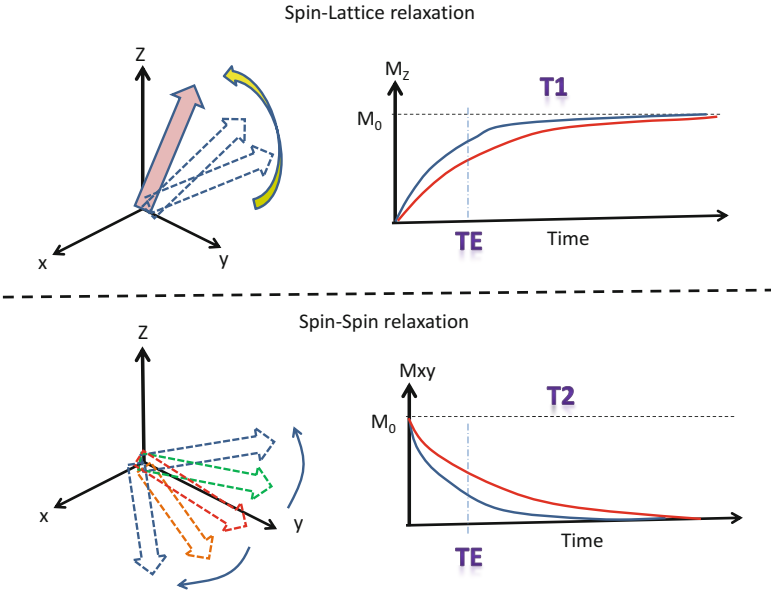

Fig. 8.3 (Top left) Spin-lattice relaxation. (Top right) The response of the vertical magnetization component M_z is time dependent and differs for each material. (Bottom left) Spin-spin relaxation. (Bottom right) The response of the transverse magnetization component M_{xy} is time dependent and differs for each material

relaxation which relates to the dephasing of the transverse magnetization M_{xy} components (see Fig. 8.3) and is characterized by a time constant T_2.

Images are generated by using special spatial encoding magnetic fields called "gradients." The process of image data acquisition is termed "pulse sequence." There are numerous pulse sequences; each sequence emphasizes a different property of the tissue. If the image emphasizes the number of protons per volume, it is termed "proton density weighted." And similarly there are T1- or T2-weighted images.

Two exemplary preclinical MRI scanning systems are depicted in Fig. 8.4, along with a typical mouse positioning MRI cradle.

4.2 Ultrasonic Imaging

Ultrasonic waves are actually sound waves which frequency exceeds 20 KHz (the upper limit for the human ear). Commonly, the frequencies used for medical imaging are in the lower MHz range, i.e., 1–10 MHz. These waves carry mechanical energy which travels at the speed of sound through matter. Typically, in soft tissues, the speed of sound is about 1500 [m/s]. The variations in the speed of sound can be used to characterize and image different tissue types.

Fig. 8.4 (Top left) Preclinical 1 T MRI system (Aspect, Israel), composed of a permanent magnet. (Top right) Preclinical 9.4 T MRI system (Bruker, Germany). (Bottom) Bruker MRI compatible mouse positioning bed. Anesthesia is provided using a chamber into which the mouse head is inserted. The bed is heated to a user-defined temperature, and respiration can be monitored by placing a sensor close to the mouse chest

Sound waves stem from a rapid change in the local pressure at their origin and carry their energy as a perturbation in the medium pressure. Accordingly, their amplitude is measured in pressure units, i.e., Pascal. When traveling through a homogeneous medium, ultrasonic waves are attenuated exponentially with a characteristic attenuation coefficient α. Thus, if the initial amplitude is P_0, at a distance x from the origin, the amplitude will be:

$$P(x) = P_0 \cdot e^{-\alpha x} \tag{8.1}$$

The attenuation coefficient varies from one tissue type to another; therefore, α can be used for tissue characterization and as a source of contrast in imaging as well. Importantly, the attenuation coefficient increases in the lower MHz range almost linearly. Consequently, when the frequency is increased, the penetration range into the tissue decreases rapidly.

Another important tissue property that is relevant to imaging is termed the "acoustic impedance." Marked as Z, it is defined by the multiplication of the tissue density ρ by its speed of sound C, i.e.:

$$Z = \rho \cdot C \tag{8.2}$$

When traveling from one tissue to another, the ultrasonic waves encounter a change in the acoustic impedance. As a result an echo is generated. The ratio between the echo amplitude P_R and the amplitude of the impinging wave P_I is called the reflection coefficient R and is given by:

$$R = \frac{P_R}{P_I} = \frac{Z_2 - Z_1}{Z_2 + Z_1} \tag{8.3}$$

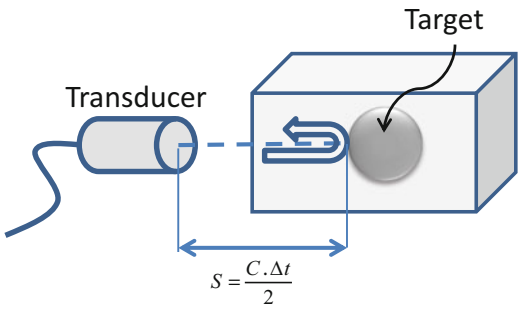

Fig. 8.5 Ultrasonic waves transmitted from the transducer will be reflected from a target having different acoustic impedance. The echo amplitude depends on the reflection coefficient, and the distance is calculated from the travel time of the waves back and forth

where Z_1 and Z_2 are the acoustic impedances of the first and second tissues, respectively. As can be noted, the absolute value of R ranges between 0 and 1; thus, if $Z_2 \gg Z_1 \Rightarrow \mathrm{R} \approx 1$, such as the case for metal implants or bones relative to soft tissues, strong echoes will be reflected. On the other hand, one can note that also when $Z_2 \ll Z_1 \Rightarrow \mathrm{R} \approx -1$, such as the case for air next to soft tissues or blood, the reflection coefficient is high and strong echoes will be obtained. (The negative sign merely indicates phase change.)

The amplitude P_T of the wave that travels through the boundary between the two tissues into the second one is given by the transmission coefficient:

$$T = \frac{P_\mathrm{T}}{P_\mathrm{I}} = \frac{2Z_2}{Z_2 + Z_1} \tag{8.4}$$

In most of the cases, ultrasonic imaging is based on measurements of the reflected echoes. The basic principle is depicted schematically in Fig. 8.5. A transducer, which is commonly made of a piezoelectric material, transmits a short ultrasonic wave into the body. The wave travels at the speed of sound C. Whenever it encounters a change in the acoustic impedance (Eq. 8.2), an echo is reflected (Eq. 8.3). The echo travels back to the transducer. Its amplitude and time of arrival Δt are registered. The distance S to the reflection point is estimated using the equation:

$$S = C \cdot \frac{\Delta t}{2} \tag{8.5}$$

To obtain a two-dimensional (2D) image, the acoustic beam sweeps through the object. This is commonly done using a fan-shaped configuration as depicted in Fig. 8.6. At every transmission angle, the echoes reflected from the object along that beam are collected and stored. The time elapsed from the ultrasonic pulse transmission to each detected echo is translated into distance using Eq. 8.5. The 2D location is determined by accounting for the transmission azimuth as well (see Fig. 8.6). The amplitude of the echo is graphically presented by assigning a gray level value to the relevant pixel. The stronger the echo the brighter is the pixel.

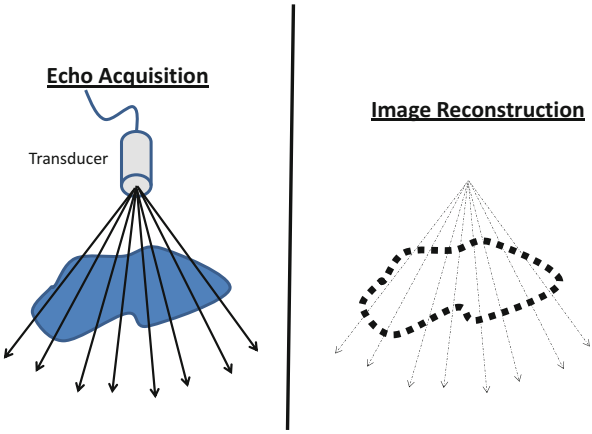

Fig. 8.6 (Left) In order to obtain a 2D image, ultrasonic pulses are transmitted along multiple directions through the object. The echoes reflected along each transmission direction are collected and registered. (Right) An image is reconstructed by depicting each echo as a bright pixel at the corresponding spatial location

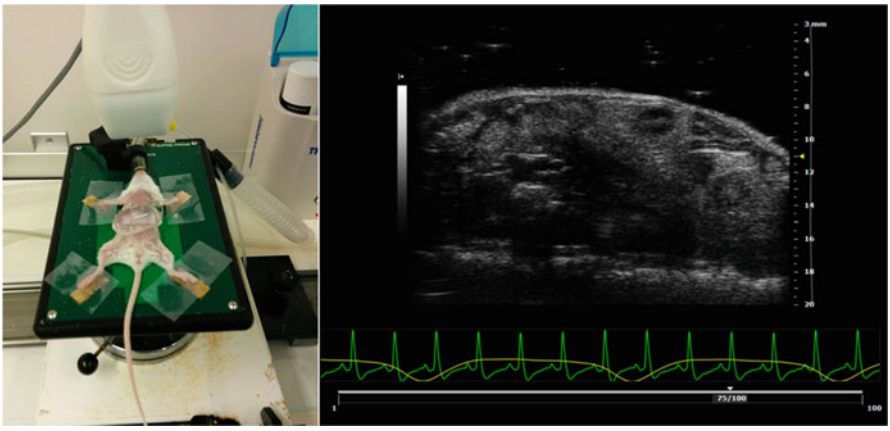

Fig. 8.7 (Left) Mouse positioning and imaging setup (VisualSonics, CA). The limbs are positioned atop electrodes, providing online ECG display. The surface is heated to a user-defined temperature, and anesthesia is applied via a facial mask. The mouse-imaged area is shaved and depilated, and a coupling gel is applied. (Right) A B-mode (reflected waves) ultrasound image of the mouse abdomen scanned using Vevo 2100 high-frequency ultrasound scanner (VisualSonics, CA)

An example of murine in vivo ultrasound experimental setup, as well as a typical pulse-echo (B-scan) image, is shown in Fig. 8.7.

Much less common is the use of through-transmission imaging. With this method, the time required for the ultrasonic waves to travel from one side of the scanned object to another and their amplitudes are registered. From this information two types of images can be generated (see Fig. 8.8): (i) a projection image, which is actually an acoustic shadow of the object, and (ii) a computed tomography (CT) cross-section, which can be reconstructed when collecting projections around the object. The latter is basically similar to X-ray CT images, but the reconstructions map the speed of sound

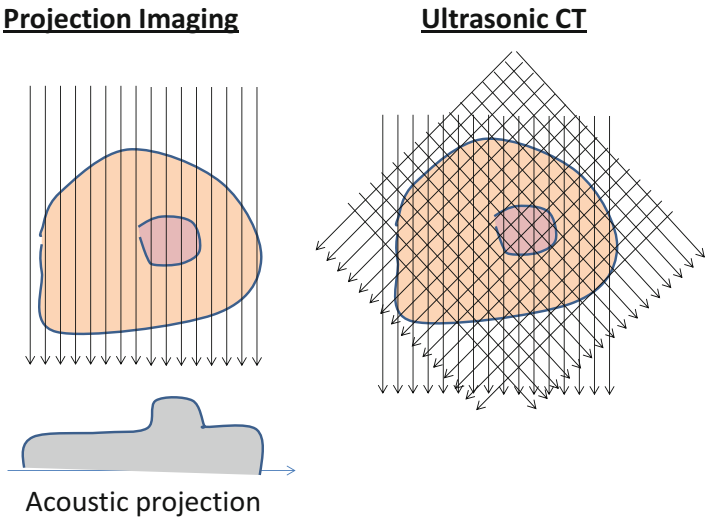

Fig. 8.8 (Left) By measuring the travel times and amplitudes of through transmitted waves, an acoustic projection (shadow) is obtained. (Right) By collecting projections from around the body, a computed tomography (ultrasonic CT) images can be obtained

or acoustic attenuation coefficient. An exemplary dedicated breast scanning system which is based on through-transmission ultrasound is depicted in Fig. 8.9.

5 Key Research Findings

This part will include three major subsections: (i) nanotechnology-based US imaging tools for medical diagnosis, (ii) nanotechnology-based MRI imaging tools for medical diagnosis, and (iii) nano-scaled compounds for multimodal MRI-US imaging. Each subsection begins by describing the main principles of contrast agent enhancement mechanisms relevant to the specific modality, including examples of conventional contrast agents. Next, representative and up-to-date findings (mainly from the years 2010–2016), related to nano-scaled contrast agents, will be described.

5.1 Nanotechnology-Based Ultrasound Imaging Tools for Medical Diagnosis

5.1.1 General Principles of Ultrasound Contrast-Enhancing Mechanism

The conventional contrast agents for ultrasonography are gas-filled microbubbles (MBs), a few microns size. The core can be made of air or other gases such as fluorocarbon and sulfur hexafluoride. The coating can be composed of albumin, a phospholipid shell, a polymer, or other materials aimed to increase the bubbles'

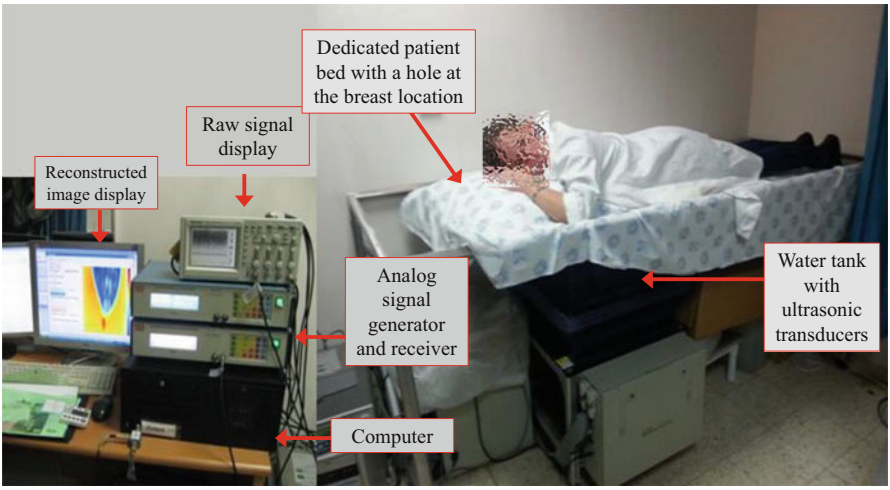

Fig. 8.9 Through-transmission ultrasound system components. (Left) The electronic boxes and computerized elements. (Right) A patient is positioned atop a dedicated bed, with a hole through which the breast is inserted. The examined breast is immersed in a water container, and ultrasonic transducers perform 2D/3D acoustic projection or computed tomography scanning. Generously contributed by Ilana Katz-Hanani from the Technion – Israel Institute of Technology

stability in the vascular system [33]. As the acoustic impedance of the MBs is negligible compared to biological tissues, they are highly echogenic. In other words, the impedance mismatch of the bubble with the blood causes an almost complete reflection of the acoustic energy back to the ultrasonic transducer. Moreover, the bubbles resonate in response to ultrasonic irradiation and yield a nonlinear effect generating subharmonic and higher harmonic signals. To further increase the MBs signal-to-noise ratio (SNR), signal processing means can be implemented on the acquired raw radiofrequency (RF) acoustic signals, for obtaining images depicting specific harmonics only [34]. As the MBs are retained in the blood for several minutes without crossing the endothelium [35], their main clinical application is vascular imaging. In cardiology, MBs can assist in assessing the heart function, improve the visualization of the cardiac chambers' borders, detect thrombus or ischemia, etc. [36]. Vascular flow quantification may also be obtained by MBs destruction. This can be achieved using a high mechanical index pulse transmission [37] and analysis of the refilling rate. Difference in vascular flow characteristics can also assist in tumor detection and evaluation, e.g., in the liver [38].

In attempts to reduce the size of ultrasound contrast agents for obtaining the benefits of the nano-scale, as described in Sect. 3, five major research paths were investigated. In the straightforward approach, a downscaled version of a microbubble is synthesized, i.e., a gas-containing nanobubble. Another approach replaces the gas core with a liquid. Although the liquid content, which is termed nanodroplet, is less echogenic than gas, it can be vaporized into an increasingly echogenic microbubble after tumor penetration. Two additionally attractive methods are the

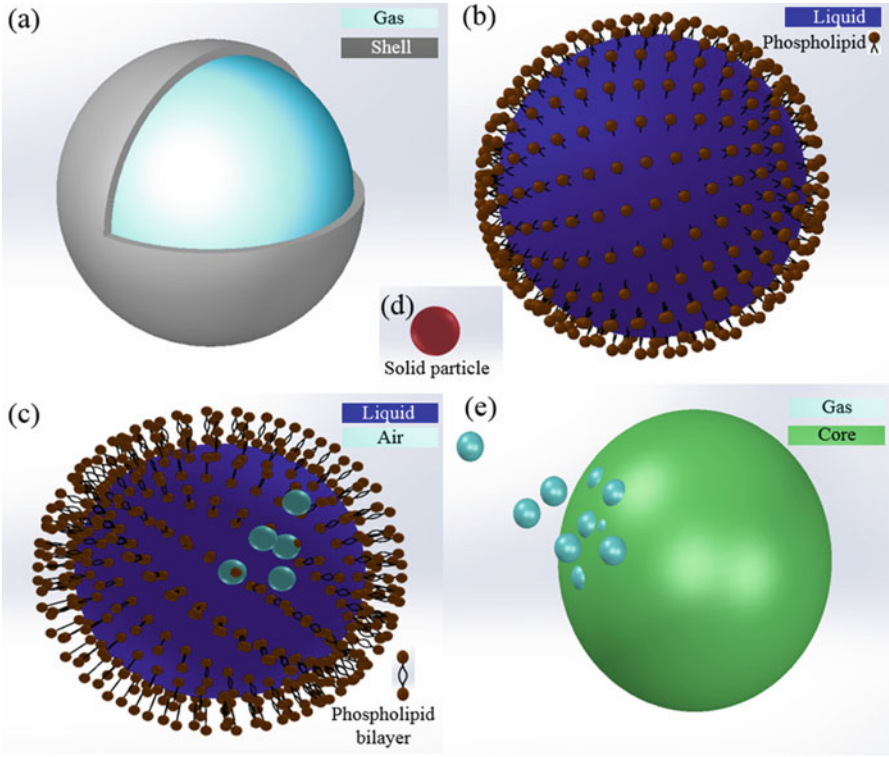

Fig. 8.10 Schematic illustration of nano-scaled ultrasound contrast agents. (**a**) Gas core nanobubble – gas (typically fluorocarbon) is trapped in a polymer or a lipid shell. (**b**) Nanodroplet – a liquid core nanoparticle, which can be vaporized into a gas-containing microbubble. The shell may be a phospholipid layer, as illustrated. (**c**) Echogenic liposome. The echogenicity is assumed to occur from air inside the liquid phase or the lipid bilayer. (**d**) Solid nanoparticle. (**e**) Gas-generating nanoparticle

synthesis of echogenic liposomes and the utilization of gas-generating nano-scaled substances. Finally, attempts to use solid nanoparticles as ultrasound contrast agents were performed. The commonly used nano-structure shells were composed of either a polymer or a single/double layer lipid. Figure 8.10 illustrates the main element of each approach. In the following subsections, we shall further elaborate on each contrast agent type and describe the representative works recently performed.

5.1.2 Gas Core Nanobubbles

As stated earlier, the intuitive way to obtain a nano-scaled US contrast agent is to synthesize a smaller version of a microbubble. When studying the capabilities of aptamer-conjugated nanobubbles (486 nm), ex vivo 40 dB enhancement was demonstrated [39]. It shall be noted that a 40 MHz transducer was used and that the nucleic acid ligands were designed to target human acute lymphoblastic leukemia, while the echogenic core was composed of perfluoropropane (C_3F_8) gas. The

necessary question at this point is weather the abovementioned contrast is suitable for in vivo applications and its comparability to conventional agents.

A comparative study between 435 nm C_3F_8-filled nanobubbles and clinically used microbubbles (SonoVue®, for which the average particle size is of 2.5 μm) demonstrated higher contrast improvement and longer imaging duration when using the nanobubbles [40]. This was demonstrated both in vitro and in vivo, using gastric cancer xenograft in mice. A further support for the in vivo ability of C_3F_8-filled nanobubbles was demonstrated in [41], as bubbles of 200–650 nm generated contrast improvement in an in vivo breast tumor mice model. Researchers from the same group have also synthesized similar nanobubbles but with a more uniformly distributed size (478.2 ± 29.7 nm), conjugated to tumor targeting agents [42].

In another mice study [43], gas-containing polymer nanobubbles (521 nm) demonstrated contrast in the kidney, liver, and tumor which was comparable to SonoVue® microbubbles. Moreover, the improved contrast imaging duration was longer in the NPs' case. The NPs' ability to load gene therapy agents and to efficiently transfect them in vitro was better than that of compared liposomes.

Polymers offer a biodegradable, biocompatible, and stable shell choice for nanobubbles. Commonly, the FDA-approved polymer poly(lactic-*co*-glycolic acid) (PLGA) is used [44]. In an in vitro study, 1D ultrasound scans (A-mode) at 10 MHz of PLGA air-filled nanocapsules (370 nm, 45 μg/ml) demonstrated 15 dB signal enhancement [45]. In another study, perfluorocarbon gas-filled PLGA bubbles (approximately 700 nm in diameter) generated contrast improvement when injected to tumor-bearing mice, under harmonic imaging [46].

A formulation of smaller gas-filled nanobubbles (200 nm in diameter), composed of C_3F_8 core, lipid-shelled nanobubbles, with the surfactant pluronic, was reported in [47]. In a later comparative study [48], the echogenicity of these nanobubbles was reported as comparable and in some cases superior to the clinically used Definity® microbubbles.

A unique biological approach was suggested by Shapiro et al. [49], which derived gas vesicles of 45–250 nm width and 100–600 nm length from bacteria and archaea (Fig. 8.11). In vitro studies demonstrated these gas-filled substances' ability to enhance the ultrasonic signal in both the fundamental frequency and higher harmonics. As with microbubbles, the vesicles were destructible using high pressure pulses. Similar to other NPs, aggregation of the vesicles resulted in an increased signal. In vivo mice studies using nontargeted intravenously injected vesicles demonstrated increased liver and inferior vena cava contrast.

5.1.3 Nanodroplets

Nanodroplets are liquid core composites. Although they can be synthesized to a size as small as 200 nm, their echogenicity is lower than gas core NPs [30], due to their reduced compressibility. In order to increase contrast ability, after the NPs accumulate in a cancerous tissue, they can be phase-shifted by vaporization into gas-containing microbubbles. It was demonstrated that acoustic radiation, generated by a 5 MHz transducer, was able to transform decafluorobutane (DFB) nanodroplets of 200–600 nm diameter, into microbubbles [50].

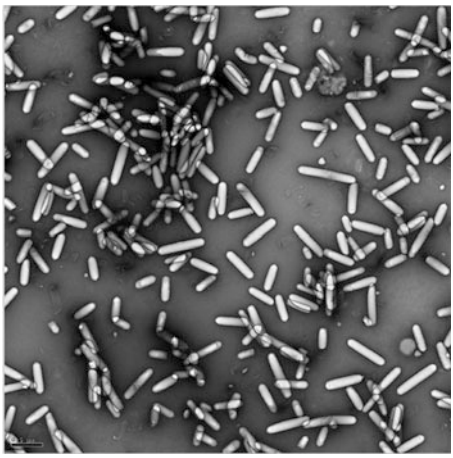

Fig. 8.11 Transmission electron microscopy (TEM) image of purified gas vesicles from *Anabaena flos-aquae*. Generously contributed by Prof. Mikhail Shapiro from California Institute of Technology

In another study, a liquid core of perfluorooctyl bromide (PFOB) was encapsulated in a shell of PLGA, with a PEGylated phospholipid-modified surface [51]. In this work, dosages of 50 mg/mL nanocapsules, 200 μL in volume and 200 nm in size, were injected into gel-containing chambers, intravenously (IV) through the retro-orbital sinus and intratumoral to tumor-bearing mice (human pancreatic cancer cells). Although the in vitro and intratumor experiments demonstrated improved contrast, the IV injections did not result in any improved tumor visualization. While histological studies demonstrated some particles residing in the tumor, the lack of IV injection-related contrast may stem from the relatively big particle size, preventing the accumulation of high particle dosage in the tumor.

A recently developed method enabled the synthesis of a mixed solution containing nanodroplets and gas core nanobubbles [52]. In vitro 15 MHz examination demonstrated that the solution resulted in an improved backscatter compared to liposomes, and in vivo 40 MHz mouse aorta imaging demonstrated clearly visible contrast improvement.

In various cases, the stimulator for the nanodroplets vaporization into microbubbles is diagnostic ultrasound with sufficiently high mechanical index. A spatially specific approach was recently suggested, in which low intensity focused ultrasound was used [53]. The researchers showed that acoustic transmission of 1 MHz focused ultrasound, applied for 2 min at 3.2 W/cm^2 intensity, was able to phase change nanodroplets into microbubbles located in a subcutaneously implanted mice tumor, yielding visibly detectable image brightening. In addition, the conjugation of folate to the nanodroplets (average diameter of 321 nm) resulted in significantly improved tumor targeting ability.

5.1.4 Echogenic Liposomes (ELIPs)

Echogenic liposomes (ELIPs) are phospholipid vesicles that contain gas either in their lipid section or in their liquid center [54, 55]. Compared to gas core NPs, they are more stable and mechanical pressure durable [56]. In an in vitro study, the

acoustic characteristics of ELIPs were examined using a broadband stationary pulse-echo methodology [57]. The resulting contrast agent efficiency was at the same range as commercially available microbubbles, when comparing the scattering-to-attenuation ratio. It should be noted that the synthesized ELIPs' solution contained a large number of 65 nm in diameter particles, but the general size distribution was rather wide, containing also particles with a diameter of a few microns.

In another study, a physiological flow phantom containing porcine plasma was used to evaluate ELIPs suitability for blood pool contrast enhancement [58]. Acquired B-mode images indeed detected improved image contrast (mean digital intensity of approximately 20 dB).

A vascular application was suggested for the ELIPs, by using their conjunction to atherosclerosis-related inflammatory markers [59]. The concept was demonstrated in an in vivo porcine study, in which the ELIPs yielded enhanced signal at the diseased artery site, when imaged using intravascular ultrasound (IVUS). In a different study, tissue plasminogen activator (tPA) was loaded into ELIPs, providing dual imaging therapy capabilities [60]. An occlusive thrombus was produced in the aorta of rabbits. The thrombus site was detected using real-time B-scan mode, following the injection of the ELIPs. A 2-min ultrasound transmission with a mechanical index of 0.4 was then performed to release the blood clots breakdown agents. Blood flow velocity recovery was measured using pulsed Doppler. The loaded ELIPs demonstrated a significant image brightening effect as well as faster and more efficient blood flow velocity improvement (indicating the thrombolytic therapy effect).

5.1.5 Gas-Generating Nanoparticles

A different and unique method for generating NP-based US contrast is engineering an agent capable of releasing gas either spontaneously, in a response to specific pathology, or when sensing a clinically important molecule.

Polymeric NPs were demonstrated as potential candidates for such substances. According to the study depicted in [61], carbonate dioxide nanobubbles were formed on the surface of a polymeric nanoparticle. As reported, the bubbles have gradually merged into microbubbles. This potentially should occur at the tumor site, post penetration using the EPR effect. The gas-generating polymeric NPs were 200–500 nm in size, and increased echogenicity was demonstrated using subcutaneous injection to the lower backs of mice, as well as intratumoral injection. The duration of ultrasound signal increase was around 12.5 min, followed by gradual decrease.

In a selectively activated gas release study [62], the researchers synthesized a 500 nm silica core particle, coated by a layer of enzymes that catalyze the decomposition of hydrogen peroxide (H_2O_2) to microbubbles. The clinical importance of H_2O_2 stems from its association with various diseases, including inflammation. The nanospheres were injected near a subcutaneous abscess in rats and generated well-detectable microbubbles.

Recently, a different group of researchers synthesized poly(vanillin oxalate) particles of 550 nm diameter, capable of releasing CO_2 when triggered by H_2O_2 [63]. Since ischemia/reperfusion injury is also associated with H_2O_2 production, the

particles were able to detect the injury site by releasing echogenic bubbles in an injured liver mice model. Moreover, the particles released vanillin that demonstrated therapeutic ability.

In another recently published work, a pluronic-based nanocarrier, containing calcium carbonate particles, was reported as suitable for ultrasonic tumor imaging [64]. The complex size was characterized as 160 nm at physiological conditions and was able to generate CO_2. Imaging at 10 MHz frequency demonstrated in vitro echogenicity as well as tumor enhancement in mice 1 h post intravenous injection. Characterization of the gas formation in various pH conditions demonstrated increased efficiency at acidic conditions, which are typical in some tumor cases.

5.1.6 Solid Nanoparticles

Although solid NPs are not expected to cause nonlinear ultrasound phenomena, several attempts were made to examine their suitability to serve as US contrast enhancers. Silica nanospheres of 100 nm were examined using 30 MHz B-scan [65]. Agarose phantom experiments demonstrated the particles visualization, and IV injections of the particles to mice yielded image brightening of the liver. This brightening persisted for 1.5 h. Nevertheless, the average gray-scale change was only around 30%, and the visual effect was rather mild.

Another solid NPs examined for ultrasonography are polylactic acid (PLA) NPs (250 nm diameter) [66]. PLA is a biodegradable, FDA-approved material [67]. The NPs were conjugated to breast cancer cells targeting agents. B-scan images of the PLA-nanoparticles containing cells demonstrated image brightening; however, the obtained effect was of less than 25%.

In a later study, the advantages of solid materials (increased durability over time to ultrasonic radiation as opposed to collapsible bubbles) were incorporated with the high echogenicity of gas-filled substances [68]. Silica and silica-boron perfluoropentane (PFP)-filled nanoparticles were synthesized, with 500 nm in diameter. The NPs were injected into the thighs of rabbits, yielding a well-visualized signal for 4 days. The authors suggested that the ability of the NPs to maintain their location without collapsing for long time periods may be useful for marking and visualizing the borders of breast cancer during surgical procedures.

In a later study by the same group of researchers, 500 nm iron-silica nanoshells were filled with PFP [69]. The particles were visible for 10 days after intratumoral injection in ex vivo breast tissue as well as in mice tumors.

Although the ability to maintain a fixed anatomical location for long time periods is an advantage in the clinical case of surgical-related tumor delineation, it constitutes a disadvantage for the application of systematically administering faster-degrading contrast agents (e.g., for tumor detection). To address this issue, it was suggested to use phosphate-based glass nanospheres (200–500 nm in diameter) [70]. The particles were imbedded in matrigel and injected into mice flanks. The resulting images demonstrated around fourfold signal increase by injecting 2 mg/mL of the composite. In addition, phantom studies showed that the particles imaging life was about 4 h.

Multi-walled carbon nanotubes (20–30 nm diameter, 400 nm length) were investigated as harmonic imaging and B-scan ultrasound contrast agents [71]. The particles brightened the injection region in ex vivo porcine livers and hearts, as well as in in vivo porcine bladder.

Additional studies in which solid-based NPs were investigated for ultrasound imaging include iron oxide and copper oxide NPs. As these two cases involve MRI imaging as well, they are described in the multimodal imaging section (5.3.2).

5.2 Nanotechnology-Based Magnetic Resonance Imaging Tools for Medical Diagnosis

5.2.1 General Principles of MRI Contrast-Enhancing Mechanism

The prevailing mechanism for MRI contrast improvement using exogenous media is relaxation time shortening. The inverse of the longitudinal (spin-lattice) relaxation time r_1:

$$r_1 = \frac{1}{T_1} \quad [\text{ms}]^{-1} \tag{8.6}$$

and the inverse of the transversal (spin-spin) relaxation time r_2:

$$r_2 = \frac{1}{T_2} \quad [\text{ms}]^{-1} \tag{8.7}$$

can be empirically estimated with respect to various particle concentration, yielding a quantitative estimate of the contrast agent ability to shorten the relaxation time (occasionally termed as molar relaxivity), with the units of $[\text{mM}^{-1}\text{s}^{-1}]$.

An ideal T1 contrast agent will have an r_2/r_1 ratio which is close to one [72] and a high r_1 value. On the contrary, the higher the r_2/r_1 ratio is, the more efficient the contrast agent is for T2 imaging [73].

The most prevalent and routinely used contrast agents in clinical MRI are gadolinium-based compounds which shorten the T1 relaxation time of nearby water molecules. This effect thereby yields a brightened region which is termed as "positive contrast." Although the exact longitudinal relaxivity may be different for various products, the characteristic value for these materials is 5 $\text{mM}^{-1}\text{s}^{-1}$ [74]. A known limitation of gadolinium-based agent injection is the possible clinical complication, to which renal disease patients are susceptible. As gadolinium administration to such population may cause nephrogenic systemic fibrosis, it should be highly avoided [75].

Another paramagnetic metal that is used for positive contrast generation is manganese. The application of manganese-based agents to the liver and to the gastrointestinal tract was previously approved for clinical use [76].

Moving to the nano-scale, three main research paths are prevalent in the literature: (i) the implementation of a gadolinium-based nano-composite, as discussed in Sect.

5.2.2; (ii) the use of T1-related contrast agents which are manganese-based NPs, as discussed in Sect. 5.2.3; and (iii) the use of iron oxide nanoparticles (IONPs) which are the most popular NPs in MRI [77, 78], as discussed in Sect. 5.2.4.

Although not the focus of this section, it should be noted that several additional nano-scaled materials, which are not based on the relaxation mechanism of MRI, are increasingly developed. Two main examples are the utilization of non-proton-based imaging. For example, in a mice study utilizing ^{19}F MRI, perfluorocarbon nano-emulsions were targeted to venous thrombosis, resulting in contrast to noise ratio improvement [79]. In another example, nano-scaled chemical exchange saturation transfer (CEST) agent dendrimers, 5 nm in size, presented a significant contrast improvement for over an hour, after injection into mice brain tumors [80].

5.2.2 Gadolinium-Based Nanoparticles

As stated above, the intuitive approach for engineering a nano-scaled MRI contrast agent would be to synthesize a nano-scaled version of a gadolinium-based composite. PEGylated gadolinium oxide (Gd_2O_3) NPs of less than 10 nm were synthesized for cell labeling [81]. Under a magnetic field of 1.41 *T*, the NPs presented a relatively high r_1 relaxivity of 14.2 $mM^{-1}s^{-1}$, while characterized by a close to one (1.21) r_2/r_1 ratio. When brain cancer cells were labeled with the particles, their in vivo detection in mice brains was feasible. The effect of coating on the longitudinal relaxivity of Gd_2O_3 NPs was examined in [82]. It was found that polyvinyl pyrrolidone (PVP) coating yielded a high value of r_1 relaxivity, 12.123 $mM^{-1}s^{-1}$, whereas oleic acid-based coating yielded only 0.5397 $mM^{-1}s^{-1}$. The PVP-coated Gd_2O_3 NPs were later injected to tumor-bearing mice. Although the tumor contrast improvement was not very dominant, the liver blood vessels visualization improved, as well as the kidney contrast.

In another approach, gadolinium molecules were loaded into PEG-coated liposomes of less than 100 nm [83]. The particles yielded an approximately 30% contrast improvement in a murine tumor model, as well as improved liver positive contrast. The synthesis of gadolinium-encapsulated carbon dots (12 nm) resulted in a longitudinal relaxivity of 5.88 $mM^{-1}s^{-1}$ at 7 T [84]. When conjugated to a targeted ligand, the particles demonstrated tumor enhancement in a murine model.

Recently, a squared-shaped, PEG-coated, 24 nm, gadolinium-based nano-composite was synthesized for gastrointestinal tract imaging [85]. It presented a high longitudinal relaxivity value at 1.4 T ($r_1 = 16.4$ $mM^{-1}s^{-1}$) and yielded distinct brightening of a rabbit stomach for more than an hour, after oral administration.

5.2.3 Manganese-Based Nanoparticles

In 2007, MnO nanoparticles of various sizes were reported as possible MRI T1 contrast agents [86]. The researchers synthesized particles of 7, 15, 20, and 25 nm in size and found that the r_1 values increased as the particles became smaller (maximal value of 0.37 $mM^{-1}s^{-1}$ at 3 T for the 7 nm agent). After injecting the particles to mice, the kidney contrast improved as well as the visualization of various brain structures. On a brain tumor model, nontargeted MnO particles yielded image brightening in various brain regions (attributed to impaired blood-brain barrier), whereas targeted MnO particles resulted in specific contrast enhancement in the tumor.

In a later study, the molar $r1$ relaxivity of MnO-based composites was increased (0.99 $mM^{-1}s^{-1}$ at 11.7 T), by using mesoporous silica coating [87]. The authors hypothesized that the improved T1-related effect stems from the ability of water molecules to penetrate the coating. These particles (diameter = 86 nm) were used to label mesenchymal stem cells transplanted in mice brains and were ultimately visualized as a white dot in a T1-weighted scan.

A further improvement in r_1 value was later presented (3.55 $mM^{-1}s^{-1}$), when yolk/shell hollow particles of manganese-based and platinum particles (40–50 nm core) were synthesized [88]. In vitro cell studies, however, revealed that the resulting composites are more cytotoxic than solid MnO particles.

Recently, a nano-scaled composite containing manganese and graphene, functionalized with dextran was synthesized [89]. It demonstrated a very high relaxivity value of 92 $mM^{-1}s^{-1}$. The blood vessels of mice were brightened for about 2 h post the NPs injection on 7 T magnetic field.

5.2.4 Iron Oxide-Based Nanoparticles

Iron oxide nanoparticles (IONPs) are characterized by an extremely high r_2 molar relaxivity value, rendering them excellent T2/T2* contrast agents. They are capable of altering image contrast even in relatively small concentrations. The common composites are magnetite (Fe_3O_4) and maghemite (γ-Fe_2O_3), but other variants are also under research [90].

Feridex®, a dextran-coated iron oxide nano-agent, was the first FDA-approved iron-based contrast agent [91] and was used for liver tumor detection. Iron is naturally taken by the liver Kupffer cells and macrophages in general [92]. When a liver pathology exists, the anomalous cell (as in a tumor or metastasis) does not contain macrophage-related activity; therefore the healthy parts of the liver are darkened when they absorb the IONPs, while the diseased region remains bright [93].

An important pathology that does involve macrophages' activity is inflammation. By injecting IONPs intravenously, their accumulation in inflamed regions can be detected. The utilization of this concept was demonstrated in an inflammatory bowel disease (IBD) rat model [94]. Using T2-weighed imaging after ultra-small (3–5 nm) IONPs IV injection, inflamed colon regions were well visualized and corresponded to histology findings. In a later work, IBD-induced mice were injected with macrophage-labeled IONPs. The particles manifested as reduced signal regions with an approximately 50% reduction at the intestine, and their visualization was strongly correlated with clinical score [95]. Other macrophage-related applications of IONPs include infection studies, renal inflammation, and heart conditions [96].

As stated earlier, the main and most significant effect of IONPs is T2/T2* shortening, which stems from creating local field inhomogeneity. The IONPs cause a susceptibility difference relative to their physiological surroundings. Such effect is manifested as image darkening, also termed as negative contrast (see Fig. 8.12). The disadvantage of this phenomenon is the difficulty in distinguishing IONPs' related dark regions, from natural image voids and artifacts. Nevertheless, several approaches were investigated for achieving IONPs' positive image contrast (brightened regions). To begin with, the transverse and longitudinal molar relaxivity

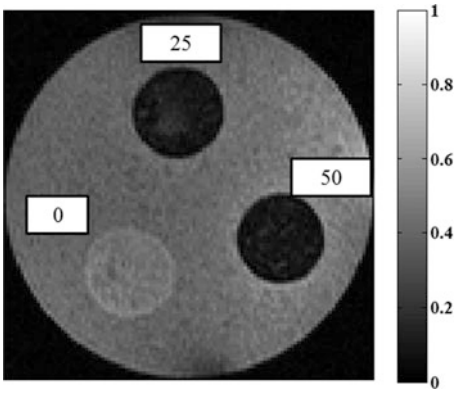

Fig. 8.12 An MRI image of IONPs phantom. The three equal-sized circles correspond to the IONPs target cylinders embedded in an agar phantom: control (no IONPs) region, 25 μg/mL IONPs region, and 50 μg/mL IONPs region. Note the substantial image darkening associated with the nanoparticles

values of the previously FDA-approved Feridex IONP-based contrast agents are 120 $mM^{-1}s^{-1}$ and 10.1 $mM^{-1}s^{-1}$, respectively [97]. As the r_2/r_1 ratio is higher than 10 in this case, the T2/T2* effect is mostly dominant. Ferumoxytol, on the other hand, is an FDA-approved iron supplement for anemia patients, with relaxivity values of $r_1 = 38\ mM^{-1}s^{-1}$ and $r_2 = 83\ mM^{-1}s^{-1}$ [98]. Given the smaller r_2/r_1 ratio in this case, the compound is useful for both T1 and T2 imaging, using T1-weighted and T2-weighted pulse sequences, respectively. Ferumoxytol was investigated for various angiography-related positive contrast applications [99]. It was found to provide distinct image brightening, as long as the particles are diluted enough, to prevent susceptibility-related, T2* artifacts (stemming from the high r_2 value). The capability of ferumoxytol in improving cancer detection in children and young adults was evaluated in a 22-subject human trial [100]. Whole-body diffusion-weighted images were fused with T1-weighted images after the IONP administration, yielding tumor detection and staging abilities, comparable to those of PET/CT.

Another approach for obtaining positive contrast using IONPs is using special MRI pulse sequences that will selectively excite the water surrounding the IONPs [101]. Using this approach, images depicting the IONPs' location only (visualized as white regions) can be obtained. Other proposed methods were based on post-processing of phase images [102] and ultrashort echo time [103].

Recently, selective positive contrast imaging of IONPs was suggested, using acoustically induced rotary saturation [104]. According to this approach, the imaged area is acoustically vibrated or displaced, while applying a modified spin-lock imaging protocol. The IONPs create a substantial susceptibility effect, yielding a change in the local field; hence, if displaced at the relevant frequency (with respect to the spin-lock frequency), they may produce a signal change, proportional to their concentration. The concept was demonstrated in phantoms, with 10 nm maghemite NPs. The minimal detected concentration was 20 μg/mL Fe, and the resulting images contained color overlay of the IONPs only, atop T2-weighted conventional images.

To summarize this section, a list of related NPs and their effect is outlined in Table 8.1.

Table 8.1 Recently published examples of MRI NPs research

Nanoparticle type	Clinical application (imaging target)	Core size (nm)	Additional study information	References
Gadolinium-based	Gastrointestinal tract	24	Rabbit study	[85]
	Kidney and liver	2.9	Gadolinium oxide NPs	[82]
	Tumor	12	Gadolinium-encapsulated carbon dots; mice study	[84]
	Brain therapy monitoring	–	Gadolinium-functionalized nanographene oxide, mice study	[105]
Iron-based	Tumor angiogenesis	5.14	Polymer-coated IONPs, mice study	[106]
	Tumor necrosis	Less than 30	Human study + mice study	[98]
	Tumor apoptosis	128.4	Magnetite aggregates	[107]
	Ovarian cancer	9.2	Folic acid targeting, mice	[108]
	Atherosclerosis	24	Zinc-doped ferrite nanoparticles, rat model	[109]
	Inflammatory bowel disease	3–5	Rat model	[94]
		–	Mice	[95]
	Brain tumors	30	Human study	[110]
	Alzheimer's disease	Less than 100	Mice study Curcumin-conjugated IONPs	[111]
	Lymph node	Less than 59	Human study	[112]
	Liver	22	Fe_5C_2 $r_2 \approx 973 mM^{-1}s^{-1}$	[113]
	Pancreatic cancer	110–130	$Fe_3O_4@SiO_2$ modified with anti-mesothelin antibody, mice study	[114]
		10.3	Mice study, milk protein-coated particles	[115]
Manganese-based	Monitoring apoptotic area in brain injury	–	Rats study	[116]
	Brain and kidney	7–25	Mice study $r_1 = 0.12 - 0.37\ mM^{-1}s^{-1}$	[86]
	Tumor	8	Mice study $r_1 \approx 0.6\ mM^{-1}s^{-1}$	[117]
		100	Mice study $r_1 \approx 10.2\ mM^{-1}s^{-1}$	[118]

(*continued*)

Table 8.1 (continued)

Nanoparticle type	Clinical application (imaging target)	Core size (nm)	Additional study information	References
Others	Liver	12	Combination of gadolinium, manganese and iron oxide, dual T1 and T2 contrast, mice study	[119]
	Cell labeling	Around 200	PLGA-perfluorooctyl bromide NPs, ^{19}F-MRI, mice study	[120]
	Venous thrombosis	Less than 165	Perfluorocarbon nanoemulsions, ^{19}F-MRI, mice study	[79]
	Brain tumors	5	CEST contrast agent, mice study	[80]

5.3 Nano-Scaled Compounds for Multimodal MRI-Ultrasound Imaging

Multimodal imaging, namely, the ability to image the same object with more than one imaging modality, is a rapidly growing field of research. A prominent example in terms of hardware is the usage of PET/CT scanners, which offers the ability to fuse metabolic and highly specific functional images with high-resolution anatomical images. In the field of nano-scaled contrast agents, the ability to use a single composite for more than one modality can significantly improve diagnosis certainty. As an illustration, consider IONPs which are administered to an MRI-scanned patient. In case a relatively high concentration of the IONPs reaches a diseased site, a dark image void may appear. To clinically ensure that the visualized darkening is not the result of a random artifact, a second image obtained by a modality which is based on a different physical process may provide a definitive answer. For example, if the IONPs could also generate a well-discernible image contrast in US as well as MRI, the patient could undergo two consecutive examinations if needed, confirming the suspected diagnosis.

The main research conducted in engineering nano-scaled complexes, capable of providing a dual-modal imaging by both MRI and US, can be divided into two main categories: (i) embedding an MRI metal-based, relaxation time-altering nano-agents, such as gadolinium-based, manganese-based, or iron-based, into a nano-scaled ultrasound contrast agent, such as nanobubble, nanodroplet, and ELIP, and (ii) attempting to find an "as-is" nano-agent which will be suitable for US imaging as well as MRI, without any required modifications.

5.3.1 Metal in Bubble Dual-Modal Composites

Initially, extensive research was conducted in attempting to trap the most commonly used MRI NPs – IONPs, in the most commonly used ultrasound contrast agent – namely, microbubbles [121, 122]. The resulting composite dimensions were in many cases larger than a micron. Although larger than the defined nano-scale, this type of agents will be shortly described here due to their impact on later detected nano-based complexes which provided dual-modal capability. One such example is the synthesis

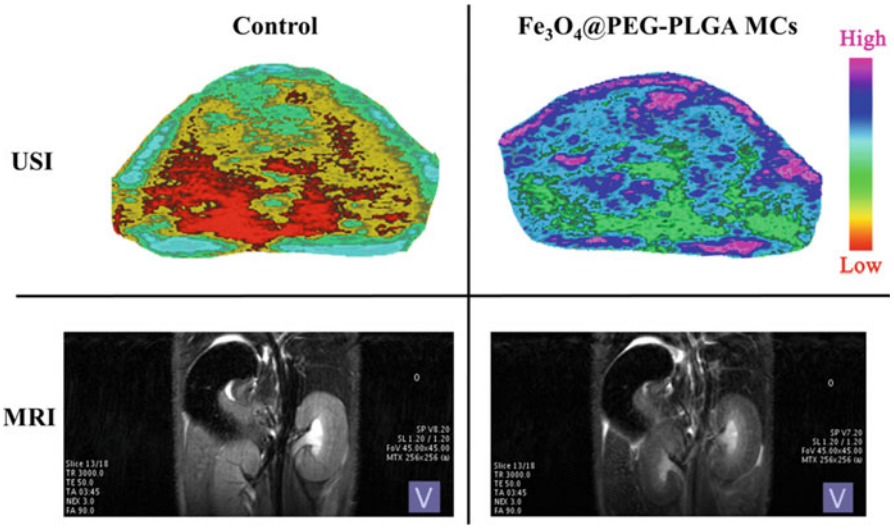

Fig. 8.13 In vivo ultrasound images of mouse liver (top) and MRI images of mouse kidneys (bottom), after injection of control saline (left) and Fe_3O_4@PEG-PLGA microcapsules (right). Generously contributed by Prof. Decheng Wu from the Institute of Chemistry, Chinese Academy of Sciences

of IONPs in a fluorocarbon gas core, polymer-shelled microbubbles [123]. The resulting complex size could be tuned between 450 and 1300 nm in size, but the ultrasound contrast was found to degrade as the size was reduced. The suitability of the composite for dual-modal imaging was demonstrated in rat livers. Although deviating from the scope of this chapter, it should be noted that one of the advantages of such bubble-based complexes is the capability to load them with therapeutic materials. For example, various studies embedded antitumor medications in bubbles [124]. Figure 8.13 depicts a representative example of iron oxide in microcapsules multimodal ultrasound-MRI study [122]. As can be noted, the administered complex agent results in both increased ultrasound echogenicity and MRI contrast alteration (commonly T2/T2*-related image darkening).

As mentioned earlier, the main limitation in the aforementioned complexes is the relatively large agent size, preventing efficient tumor accumulation. Several recent works succeeded, nonetheless, to obtain smaller contrast agent sizes. Huang et al. [125] synthesized bubbles with an approximate size of 200 nm. The outer shell was made of polyacrylic acid (PAA) and pluronic F127. The inner volume contained embedded iron oxide NPs and entrapped PFP gas. The nanobubbles demonstrated increased B-scan ultrasound contrast in vivo (subcutaneous tumor-bearing mouse), as well as MRI T2-shortening effect. The incorporation of IONPs to the nanobubbles demonstrated an improvement in the US contrast, with respect to gas-only bubbles. In addition, when a magnet was positioned next to the tumor, the nanobubbles presented improved selective accumulation.

In another work, IONPs were embedded in water instead of gas and encapsulated in a methoxy PEG-PLA shell [126]. An in vitro study has demonstrated that the acoustic attenuation increased with the IONPs concentration. By the same concept, other nano-size ultrasound contrast-enhancing complex types can be used to trap a magnetic nano-metal element, thus resulting in a multimodal imaging contrast agent. Based on the nanodroplet mechanism (see Sect. 5.1.3), IONPs were embedded in a polymer shell with a phase-changing liquid core [127]. As IONPs are sensitive to laser irradiation, near-infrared energy was used to convert the liquid core into gas and resulted in an acoustic contrast improvement, in addition to the T2-based MRI contrast. The concept was illustrated on mice livers and tumors. In another study, SPIO containing nano-droplets enhanced liver US-MRI signal, while the phase change from liquid core nanobubbles to gas core microbubbles was triggered using ultrasound [128].

Another example of ultrasonic agent embedded with metallic MRI agent is the combination of gadolinium with mesoporous silica NPs. The resulting 200 nm in size compound, demonstrated multimodal enhancing abilities for stem cells imaging [129].

5.3.2 Multimodal Solid Nanoparticles

Although the previously mentioned, bubble-like structure complexes resulted in noticeable MRI and US contrast improvement, they suffer from two main shortcomings: the complex size is typically larger than 100 nm, and the synthesis procedure may be complicated. These reasons motivated several studies, in which the suitability of the "as-is," smaller than 100 nm, metallic nanoparticle with MRI and ultrasound imaging was examined. In a rat brain tumor model, animals were administered with IONPs and imaged using MRI (resulting in T2 image darkening). Next, ultrasound images of the ex vivo removed brains were taken, demonstrating brighter tumors when SPIO was administered (with respect to control or gadolinium administration) [130]. In a later similar study, ex vivo rat brain imaging after IONPs injection allowed improved visualization of the central nervous system (CNS) lesions, which corresponded to the detected locations on MRI [131]. In a later study, however, B-scan ultrasound of IONPs did not result in a satisfying and distinct contrast improvement [132].

Another method, developed for improving the ultrasonic detection ability of IONPs is magneto-motive ultrasound (MMUS) [133]. According to this approach, a magnetic generator is placed under the imaged organ. After IONPs injection and their arrival to the designated pathology-suspected area, the magnetic field vibrates the particles, which in turn can be detected by ultrasound. In a consecutive study, IONPs were detected in rats sentinel lymph nodes using MRI imaging in vivo and MMUS *postmortem* [134].

A different approach was recently suggested for IONPs ultrasonic detection. Since the underlying physical property of the conventional B-mode ultrasound (backscatter) was not sufficient for the particles unequivocal detection [132], the effect of the particles on other acoustic characteristics was examined [135]. The study found that IONPs do not affect the acoustic attenuation in a clinically relevant concentration range. However, they increased the speed of sound (SOS) of the

examined object in a linear manner. This acoustic property can be imaged using the through-transmission ultrasound method (see Sect. 4.2). In a set of in vitro and ex vivo experiments, the feasibility of IONPs' detection via SOS change was demonstrated, while MRI of the same particles, with similar concentration, verified multimodal contrast capabilities.

Another type of "as-is" solid NPs suitable for both MRI and through-transmission ultrasound are copper oxide (CuO) NPs [136]. These 7 nm in diameter particles yielded T1-based contrast improvement on an agar-based phantom at 9.4 T while providing concentration-dependent through-transmission ultrasound enhancement. In contrary to IONPs, the dominant physical property affected by the CuO presence was the acoustic attenuation.

A summary of this section is outlined in Table 8.2.

Table 8.2 Recently published examples of multimodal US-MRI NPs studies

Nanoparticle type	Clinical application (imaging target)	Core size (nm)	Additional study information	References
IONPs in microbubble	Liver	400–1300	Rat study, polymer shell-encapsulating fluorocarbon gas and IONPs	[123]
	Liver, kidney, and spleen	3.7 micron	Magnetite in PEG-PLGA microcapsules, mice study	[122]
	Tumor	Larger than a micron	Maghemite in a polymer-based microbubble	[121]
	Tumor lymph node	868	A chemotherapeutic drug was also encapsulated	[124]
IONPs combined with US nano-agent	General imaging (in vitro study)	50–200	In vitro study, IONPs in liquid core, PEG-PLA-based shell	[126]
	Liver and tumor	374	IONPs embedded in the polymeric shell of a phase-changing liquid core, near-infrared irradiation activated	[127]
	Tumor	200	IONPs in polymeric thermo-sensitive nanobubble	[125]
	Liver	385	IONPs embedded in a nanodroplet, ultrasound shifted to a microbubble	[128]
Gadolinium combined with US nano-agent	Stem cells	200	Cardiac tissue enhancement after silica-Gd-nanoparticle-labeled stem cell injection, mice study	[129]
	Tumor	100–400	Hollow silica nanospheres combined with gadolinium, mice study	[137]

(*continued*)

Table 8.2 (continued)

Nanoparticle type	Clinical application (imaging target)	Core size (nm)	Additional study information	References
Multimodal solid NPs	Brain	62	Ex vivo rat brains imaged using SPIO on B-mode ultrasound and T2-weighted MRI	[130, 131]
	Kidney	87	Magneto-motive ultrasound of IONPs	[133]
	Sentinel lymph nodes	31 and 67	Magneto-motive ultrasound *postmortem* and MRI in vivo	[134]
	In vitro and ex vivo studies performed so far	7–10	Through-transmission ultrasound and MRI	[135, 136]
Others	Human pancreatic islets tracking	170–213	Perfluorocarbon NPs for ^{19}F MRI and US imaging	[138]

6 Conclusions and Future Perspective

The field of nano-scaled contrast agent development has attracted extensive and international research efforts. Nevertheless, the only FDA-approved and commercially available ultrasound/MRI nano-scaled contrast agent today is iron oxide [139]. Several main limitations hamper the bridge-crossing between the preclinical vast research effort and the clinical implementation: (i) the toxicity profile of the nano-agents has to be thoroughly defined and biocompatibility well proven [140] for obtaining regulatory approvals; (ii) for reproducibility, as slight changes in particle morphology may alter its efficiency and physiological behavior, the manufacturing process needs to be precisely repeated for each new batch [141]; and (iii) the targeting ability must be sufficient, namely, great percentages of the injected dose ultimately arriving the target site, allowing clear differentiation between healthy and pathological tissue.

Another obstacle, for de facto translation of a discovered nano-scaled contrast agent into a routine clinical practice use, is the "proof-of-concept" approach. In other words, the majority of studies provide an initial investigation of a newly developed material by means of in vitro cell cultures and most typically murine studies. However, once completed, no further investigations and consecutive research on larger animals/clinical trials are commonly conducted.

In terms of ultrasound nano-agents, it shall be noted that the majority of studies described relatively large materials, in many cases exceeding 500 nm. As the probability of benefiting from the associated EPR effect increases for smaller NPs [142], it is highly desirable to reduce the size of US-dedicated agents. In that sense, solid nanoparticles could provide a possible solution.

In summary, it should be noted that the fascinating multidisciplinary knowledge, integrated in the field of nano-scaled contrast agents, requires expertise in various fields. In the endeavor to obtain a major nano-progress, scientific multidisciplinary teamwork plays a critical role [31].

References

1. Wolbarst AB, Hendee WR (2006) Evolving and experimental technologies in medical imaging. Radiology 238(1):16–39
2. Smith-Bindman R, Miglioretti DL, Johnson E, Lee C et al (2012) Use of diagnostic imaging studies and associated radiation exposure for patients enrolled in large integrated health care systems, 1996–2010. JAMA 307(22):2400–2409
3. Beckett KR, Moriarity AK, Langer JM (2015) Safe use of contrast media: what the radiologist needs to know. Radiographics 35(6):1738–1750
4. Vandsburger MH, Epstein FH (2011) Emerging MRI methods in translational cardiovascular research. J Cardiovasc Transl Res 4(4):477–492
5. Fidler JL, Guimaraes L, Einstein DM (2009) MR imaging of the small bowel 1. Radiographics 29(6):1811–1825
6. Sun MR, Ngo L, Genega EM, Atkins MB et al (2009) Renal cell carcinoma: dynamic contrast-enhanced MR imaging for differentiation of tumor subtypes – correlation with pathologic findings 1. Radiology 250(3):793–802
7. Farkas J, Christian P, Urrea JAG, Roos N et al (2010) Effects of silver and gold nanoparticles on rainbow trout (*Oncorhynchus mykiss*) hepatocytes. Aquat Toxicol 96(1):44–52
8. Bihari P, Vippola M, Schultes S, Praetner M et al (2008) Optimized dispersion of nanoparticles for biological in vitro and in vivo studies. Part Fibre Toxicol 5(1):14
9. Mohanraj V, Chen Y (2006) Nanoparticles-a review. Trop J Pharm Res 5(1):561–573
10. Moreno-Manas M, Pleixats R (2003) Formation of carbon– carbon bonds under catalysis by transition-metal nanoparticles. Acc Chem Res 36(8):638–643
11. Kayser O, Lemke A, Hernandez-Trejo N (2005) The impact of nanobiotechnology on the development of new drug delivery systems. Curr Pharm Biotechnol 6(1):3–5
12. Wang AZ, Langer R, Farokhzad OC (2012) Nanoparticle delivery of cancer drugs. Annu Rev Med 63:185–198
13. Hobbs SK, Monsky WL, Yuan F, Roberts WG et al (1998) Regulation of transport pathways in tumor vessels: role of tumor type and microenvironment. Proc Natl Acad Sci 95(8):4607–4612
14. Fang J, Nakamura H, Maeda H (2011) The EPR effect: unique features of tumor blood vessels for drug delivery, factors involved, and limitations and augmentation of the effect. Adv Drug Deliv Rev 63(3):136–151
15. Li S-D, Huang L (2010) Stealth nanoparticles: high density but sheddable PEG is a key for tumor targeting. J Control Release 145(3):178
16. Moore A, Marecos E, Bogdanov A Jr, Weissleder R (2000) Tumoral distribution of long-circulating dextran-coated iron oxide nanoparticles in a rodent model 1. Radiology 214 (2):568–574
17. Nune SK, Gunda P, Thallapally PK, Lin Y-Y et al (2009) Nanoparticles for biomedical imaging. Expert Opin Drug Deliv 6(11):1175–1194
18. Li L, Gao F, Jiang W, Wu X et al (2016) Folic acid-conjugated superparamagnetic iron oxide nanoparticles for tumor-targeting MR imaging. Drug Deliv 23(5):1726–1733
19. Grenha A, Gomes ME, Rodrigues M, Santo VE et al (2010) Development of new chitosan/carrageenan nanoparticles for drug delivery applications. J Biomed Mater Res A 92(4):1265–1272
20. Alivisatos P (2004) The use of nanocrystals in biological detection. Nat Biotechnol 22(1):47–52

21. Zhou L, Gu Z, Liu X, Yin W et al (2012) Size-tunable synthesis of lanthanide-doped Gd_2O_3 nanoparticles and their applications for optical and magnetic resonance imaging. J Mater Chem 22(3):966–974
22. Zhao Z, Zhou Z, Bao J, Wang Z et al (2013) Octapod iron oxide nanoparticles as high-performance T2 contrast agents for magnetic resonance imaging. Nat Commun 4:2266
23. Baetke SC, Lammers T, Kiessling F (2015) Applications of nanoparticles for diagnosis and therapy of cancer. Br J Radiol 88(1054):20150207
24. Popovtzer R, Agrawal A, Kotov NA, Popovtzer A et al (2008) Targeted gold nanoparticles enable molecular CT imaging of cancer. Nano Lett 8(12):4593–4596
25. Yin T, Wang P, Zheng R, Zheng B et al (2012) Nanobubbles for enhanced ultrasound imaging of tumors. Int J Nanomedicine 7(2):895–904
26. Liu Y, Welch MJ (2012) Nanoparticles labeled with positron emitting nuclides: advantages, methods, and applications. Bioconjug Chem 23(4):671–682
27. Polyák A, Hajdu I, Bodnár M, Trencsényi G et al (2013) 99m Tc-labelled nanosystem as tumour imaging agent for SPECT and SPECT/CT modalities. Int J Pharm 449(1):10–17
28. Morana G, Salviato E, Guarise A (2007) Contrast agents for hepatic MRI. Cancer Imaging 7 (Spec No A):S24–S27
29. Louie A (2010) Multimodality imaging probes: design and challenges. Chem Rev (Washington, DC, United States) 110(5):3146–3195
30. Deshpande N, Needles A, Willmann JK (2010) Molecular ultrasound imaging: current status and future directions. Clin Radiol 65(7):567–581
31. Gao Z, Ma T, Zhao E, Docter D et al (2016) Small is smarter: nano MRI contrast agents–advantages and recent achievements. Small 12(5):556–576
32. Lee D-E, Koo H, Sun I-C, Ryu JH et al (2012) Multifunctional nanoparticles for multimodal imaging and theragnosis. Chem Soc Rev 41(7):2656–2672
33. Albrecht T, Blomley M, Bolondi L, Claudon M et al (2004) Guidelines for the use of contrast agents in ultrasound. January 2004. Ultraschall Med 25(04):249–256
34. Chang PH, Shun K, Wu S-J, Levene HB (1995) Second harmonic imaging and harmonic Doppler measurements with Albunex. IEEE Trans Ultrason Ferroelectr Freq Control 42(6):1020–1027
35. Calliada F, Campani R, Bottinelli O, Bozzini A et al (1998) Ultrasound contrast agents: basic principles. Eur J Radiol 27:S157–S160
36. Blomley MJ, Cooke JC, Unger EC, Monaghan MJ et al (2001) Microbubble contrast agents: a new era in ultrasound. Br Med J 322(7296):1222
37. Potdevin T, Fowlkes J, Moskalik A, Carson P (2004) Analysis of refill curve shape in ultrasound contrast agent studies. Med Phys 31(3):623–632
38. Claudon M, Dietrich CF, Choi BI, Cosgrove DO et al (2013) Guidelines and good clinical practice recommendations for contrast enhanced ultrasound (CEUS) in the liver–update 2012. Ultraschall Med 34(01):11–29
39. Wang C-H, Huang Y-F, Yeh C-K (2011) Aptamer-conjugated nanobubbles for targeted ultrasound molecular imaging. Langmuir 27(11):6971–6976
40. Fan X, Wang L, Guo Y, Tong H et al (2013) Experimental investigation of the penetration of ultrasound nanobubbles in a gastric cancer xenograft. Nanotechnology 24(32):325102
41. Cai WB, Yang HL, Zhang J, Yin JK et al (2015) The optimized fabrication of nanobubbles as ultrasound contrast agents for tumor imaging. Sci Rep 5:13725
42. Yang H, Cai W, Xu L, Lv X et al (2015) Nanobubble–affibody: novel ultrasound contrast agents for targeted molecular ultrasound imaging of tumor. Biomaterials 37:279–288
43. Tong H-P, Wang L-F, Guo Y-L, Li L et al (2013) Preparation of protamine cationic nanobubbles and experimental study of their physical properties and in vivo contrast enhancement. Ultrasound Med Biol 39(11):2147–2157
44. Makadia HK, Siegel SJ (2011) Poly lactic-co-glycolic acid (PLGA) as biodegradable controlled drug delivery carrier. Polymers 3(3):1377–1397
45. Néstor M-M, Kei N-PE, Guadalupe N-AM, Elisa M-ES et al (2011) Preparation and in vitro evaluation of poly (D, L-lactide-co-glycolide) air-filled nanocapsules as a contrast agent for ultrasound imaging. Ultrasonics 51(7):839–845

46. Zhang X, Zheng Y, Wang Z, Huang S et al (2014) Methotrexate-loaded PLGA nanobubbles for ultrasound imaging and synergistic targeted therapy of residual tumor during HIFU ablation. Biomaterials 35(19):5148–5161
47. Krupka TM, Solorio L, Wilson RE, Wu H et al (2009) Formulation and characterization of echogenic lipid– pluronic nanobubbles. Mol Pharm 7(1):49–59
48. Wu H, Rognin NG, Krupka TM, Solorio L et al (2013) Acoustic characterization and pharmacokinetic analyses of new nanobubble ultrasound contrast agents. Ultrasound Med Biol 39(11):2137–2146
49. Shapiro MG, Goodwill PW, Neogy A, Yin M et al (2014) Biogenic gas nanostructures as ultrasonic molecular reporters. Nat Nanotechnol 9(4):311–316
50. Sheeran PS, Wong VP, Luois S, McFarland RJ et al (2011) Decafluorobutane as a phase-change contrast agent for low-energy extravascular ultrasonic imaging. Ultrasound Med Biol 37 (9):1518–1530
51. Díaz-López R, Tsapis N, Santin M, Bridal SL et al (2010) The performance of PEGylated nanocapsules of perfluorooctyl bromide as an ultrasound contrast agent. Biomaterials 31(7):1723–1731
52. Peyman SA, McLaughlan JR, Abou-Saleh RH, Marston G et al (2016) On-chip preparation of nanoscale contrast agents towards high-resolution ultrasound imaging. Lab Chip 16(4):679–687
53. Liu J, Shang T, Wang F, Cao Y et al (2017) Low-intensity focused ultrasound (LIFU)-induced acoustic droplet vaporization in phase-transition perfluoropentane nanodroplets modified by folate for ultrasound molecular imaging. Int J Nanomedicine 12:911
54. Nguyen AT, Wrenn SP (2014) Acoustically active liposome-nanobubble complexes for enhanced ultrasonic imaging and ultrasound-triggered drug delivery. Wiley Interdiscip Rev Nanomed Nanobiotechnol 6(3):316–325
55. Raymond JL, Luan Y, Peng T, Huang S-L et al (2016) Loss of gas from echogenic liposomes exposed to pulsed ultrasound. Phys Med Biol 61(23):8321
56. Liang H, Blomley M (2003) The role of ultrasound in molecular imaging. Br J Radiol 76:S140
57. Kopechek JA, Haworth KJ, Raymond JL, Douglas Mast T et al (2011) Acoustic characterization of echogenic liposomes: frequency-dependent attenuation and backscatter. J Acoust Soc Am 130(5):3472–3481
58. Radhakrishnan K, Haworth KJ, Huang S-L, Klegerman ME et al (2012) Stability of echogenic liposomes as a blood pool ultrasound contrast agent in a physiologic flow phantom. Ultrasound Med Biol 38(11):1970–1981
59. Kim H, Moody MR, Laing ST, Kee PH et al (2010) In vivo volumetric intravascular ultrasound visualization of early/inflammatory arterial atheroma using targeted echogenic immunoliposomes. Investig Radiol 45(10):685
60. Laing ST, Moody M, Smulevitz B, Kim H et al (2011) Ultrasound-enhanced thrombolytic effect of tissue plasminogen activator–loaded echogenic liposomes in an in vivo rabbit aorta thrombus model – brief report. Arterioscler Thromb Vasc Biol 31(6):1357–1359
61. Kang E, Min HS, Lee J, Han MH et al (2010) Nanobubbles from gas-generating polymeric nanoparticles: ultrasound imaging of living subjects. Angew Chem Int Ed 49(3):524–528
62. Olson ES, Orozco J, Wu Z, Malone CD et al (2013) Toward in vivo detection of hydrogen peroxide with ultrasound molecular imaging. Biomaterials 34(35):8918–8924
63. Kang C, Cho W, Park M, Kim J et al (2016) H_2O_2-triggered bubble generating antioxidant polymeric nanoparticles as ischemia/reperfusion targeted nanotheranostics. Biomaterials 85:195–203
64. Kim M, Lee JH, Kim SE, Kang SS et al (2016) Nanosized ultrasound enhanced-contrast agent for in vivo tumor imaging via intravenous injection. ACS Appl Mater Interfaces 8(13):8409–8418
65. Liu J, Levine AL, Mattoon JS, Yamaguchi M et al (2006) Nanoparticles as image enhancing agents for ultrasonography. Phys Med Biol 51(9):2179
66. Liu J, Li J, Rosol TJ, Pan X et al (2007) Biodegradable nanoparticles for targeted ultrasound imaging of breast cancer cells in vitro. Phys Med Biol 52(16):4739

67. Ji Y, Li X-T, Chen G-Q (2008) Interactions between a poly (3-hydroxybutyrate-co-3-hydroxyvalerate-co-3-hydroxyhexanoate) terpolyester and human keratinocytes. Biomaterials 29(28):3807–3814
68. Liberman A, Martinez HP, Ta CN, Barback CV et al (2012) Hollow silica and silica-boron nano/microparticles for contrast-enhanced ultrasound to detect small tumors. Biomaterials 33(20):5124–5129
69. Liberman A, Wu Z, Barback CV, Viveros R et al (2013) Color doppler ultrasound and gamma imaging of intratumorally injected 500 nm iron–silica nanoshells. ACS Nano 7(7):6367–6377
70. Foroutan F, Jokerst JV, Gambhir SS, Vermesh O et al (2015) Sol–gel synthesis and electrospraying of biodegradable (P_2O_5) 55–(CaO) 30–(Na_2O) 15 glass nanospheres as a transient contrast agent for ultrasound stem cell imaging. ACS Nano 9(2):1868–1877
71. Delogu LG, Vidili G, Venturelli E, Ménard-Moyon C et al (2012) Functionalized multiwalled carbon nanotubes as ultrasound contrast agents. Proc Natl Acad Sci 109(41):16612–16617
72. Lee GH, Chang Y (2015) Magnetic properties, water proton relaxivities, and in-vivo MR images of paramagnetic nanoparticles. J Korean Phys Soc 67(1):44–51
73. Weissleder R (1994) Liver MR imaging with iron oxides: toward consensus and clinical practice. Radiology 193(3):593–595
74. Raymond KN, Pierre VC (2005) Next generation, high relaxivity gadolinium MRI agents. Bioconjug Chem 16(1):3–8
75. Kuo PH, Kanal E, Abu-Alfa AK, Cowper SE (2007) Gadolinium-based MR contrast agents and nephrogenic systemic fibrosis 1. Radiology 242(3):647–649
76. Pan D, Caruthers SD, Senpan A, Schmieder AH et al (2011) Revisiting an old friend: manganese-based MRI contrast agents. Wiley Interdiscip Rev Nanomed Nanobiotechnol 3(2):162–173
77. Amsalem Y, Mardor Y, Feinberg MS, Landa N et al (2007) Iron-oxide labeling and outcome of transplanted mesenchymal stem cells in the infarcted myocardium. Circulation 116(Suppl 11): I-38–I-45
78. Bar-Shir A, Avram L, Yariv-Shoushan S, Anaby D et al (2014) Alginate-coated magnetic nanoparticles for noninvasive MRI of extracellular calcium. NMR Biomed 27(7):774–783
79. Temme S, Grapentin C, Quast C, Jacoby C et al (2015) Non-invasive imaging of early venous thrombosis by 19F MRI using targeted perfluorocarbon nanoemulsions. Circulation. https://doi.org/10.1161/CIRCULATIONAHA.114.010962
80. Lesniak WG, Oskolkov N, Song X, Lal B et al (2016) Salicylic acid conjugated dendrimers are a tunable, high performance CEST MRI NanoPlatform. Nano Lett 16(4):2248–2253
81. Faucher L, Tremblay Ml, Lagueux J, Gossuin Y et al (2012) Rapid synthesis of PEGylated ultrasmall gadolinium oxide nanoparticles for cell labeling and tracking with MRI. ACS Appl Mater Interfaces 4(9):4506–4515
82. Fang J, Chandrasekharan P, Liu X-L, Yang Y et al (2014) Manipulating the surface coating of ultra-small Gd_2O_3 nanoparticles for improved T 1-weighted MR imaging. Biomaterials 35(5):1636–1642
83. Bertini I, Bianchini F, Calorini L, Colagrande S et al (2004) Persistent contrast enhancement by sterically stabilized paramagnetic liposomes in murine melanoma. Magn Reson Med 52(3):669–672
84. Chen H, Wang GD, Tang W, Todd T et al (2014) Gd-encapsulated carbonaceous dots with efficient renal clearance for magnetic resonance imaging. Adv Mater (Weinheim, Germany) 26(39):6761–6766
85. Perera VS, Chen G, Cai Q, Huang SD (2016) Nanoparticles of gadolinium-incorporated Prussian blue with PEG coating as an effective oral MRI contrast agent for gastrointestinal tract imaging. Analyst 141(6):2016
86. Na HB, Lee JH, An K, Park YI et al (2007) Development of a T1 contrast agent for magnetic resonance imaging using MnO nanoparticles. Angew Chem 119(28):5493–5497
87. Kim T, Momin E, Choi J, Yuan K et al (2011) Mesoporous silica-coated hollow manganese oxide nanoparticles as positive T 1 contrast agents for labeling and MRI tracking of adipose-derived mesenchymal stem cells. J Am Chem Soc 133(9):2955–2961
88. An K, Na HB, Park YI, Choi SH et al (2015) Hollow MnOxPy and Pt/MnOxPy yolk/shell nanoparticles as a T 1 MRI contrast agent. J Colloid Interface Sci 439:134–138

89. Kanakia S, Toussaint J, Hoang DM, Lee S et al (2014) Towards an advanced graphene-based magnetic resonance imaging contrast agent: sub-acute toxicity and efficacy studies in small animals. Sci Rep 5:17182–17182
90. Bao G, Mitragotri S, Tong S (2013) Multifunctional nanoparticles for drug delivery and molecular imaging. Annu Rev Biomed Eng 15:253–282
91. Wu Y, Briley K, Tao X (2015) Nanoparticle-based imaging of inflammatory bowel disease. Wiley Interdiscip Rev Nanomed Nanobiotechnol 8:300–315
92. Raynal I, Prigent P, Peyramaure S, Najid A et al (2004) Macrophage endocytosis of superparamagnetic iron oxide nanoparticles: mechanisms and comparison of ferumoxides and ferumoxtran-10. Investig Radiol 39(1):56–63
93. Van Beers B, Gallez B, Pringot J (1997) Contrast-enhanced MR imaging of the liver. Radiology 203(2):297–306
94. Frericks BB, Wacker F, Loddenkemper C, Valdeig S et al (2009) Magnetic resonance imaging of experimental inflammatory bowel disease: quantitative and qualitative analyses with histopathologic correlation in a rat model using the ultrasmall iron oxide SHU 555 C. Investig Radiol 44(1):23–30
95. Wu Y, Briley-Saebo K, Xie J, Zhang R et al (2014) Inflammatory bowel disease: MR-and SPECT/CT-based macrophage imaging for monitoring and evaluating disease activity in experimental mouse model – pilot study. Radiology 271(2):400–407
96. Neuwelt A, Sidhu N, Hu C-AA, Mlady G et al (2015) Iron-based superparamagnetic nanoparticle contrast agents for MRI of infection and inflammation. Am J Roentgenol 204(3): W302–W313
97. Aryal S, Key J, Stigliano C, Ananta JS et al (2013) Engineered magnetic hybrid nanoparticles with enhanced relaxivity for tumor imaging. Biomaterials 34(31):7725–7732
98. Aghighi M, Golovko D, Ansari C, Marina NM et al (2015) Imaging tumor necrosis with ferumoxytol. PLoS One 10(11):e0142665
99. Bashir MR, Bhatti L, Marin D, Nelson RC (2015) Emerging applications for ferumoxytol as a contrast agent in MRI. J Magn Reson Imaging 41(4):884–898
100. Klenk C, Gawande R, Uslu L, Khurana A et al (2014) Ionising radiation-free whole-body MRI versus 18 F-fluorodeoxyglucose PET/CT scans for children and young adults with cancer: a prospective, non-randomised, single-centre study. Lancet Oncol 15(3):275–285
101. Cunningham CH, Arai T, Yang PC, McConnell MV et al (2005) Positive contrast magnetic resonance imaging of cells labeled with magnetic nanoparticles. Magn Reson Med 53(5):999–1005
102. Zhao Q, Langley J, Lee S, Liu W (2011) Positive contrast technique for the detection and quantification of superparamagnetic iron oxide nanoparticles in MRI. NMR Biomed 24(5):464–472
103. Wang L, Zhong X, Qian W, Huang J et al (2014) Ultrashort echo time (UTE) imaging of receptor targeted magnetic iron oxide nanoparticles in mouse tumor models. J Magn Reson Imaging 40(5):1071–1081
104. Zhu B, Witzel T, Jiang S, Huang SY et al (2016) Selective magnetic resonance imaging of magnetic nanoparticles by acoustically induced rotary saturation. Magn Reson Med 75(1):97–106
105. Yang H-W, Huang C-Y, Lin C-W, Liu H-L et al (2014) Gadolinium-functionalized nanographene oxide for combined drug and microRNA delivery and magnetic resonance imaging. Biomaterials 35(24):6534–6542
106. Cui Y, Zhang C, Luo R, Liu H et al (2016) Noninvasive monitoring of early antiangiogenic therapy response in human nasopharyngeal carcinoma xenograft model using MrI with rgD-conjugated ultrasmall superparamagnetic iron oxide nanoparticles. Int J Nanomedicine 11:5671
107. Yuan Y, Ding Z, Qian J, Zhang J et al (2016) Casp3/7-instructed intracellular aggregation of Fe_3O_4 nanoparticles enhances T2 MR imaging of tumor apoptosis. Nano Lett 16(4):2686–2691
108. Zhang H, Li J, Hu Y, Shen M et al (2016) Folic acid-targeted iron oxide nanoparticles as contrast agents for magnetic resonance imaging of human ovarian cancer. J Ovarian Res 9(1):19

109. Chaudhary R, Roy K, Kanwar RK, Walder K et al (2016) Engineered atherosclerosis-specific zinc ferrite nanocomplex-based MRI contrast agents. J Nanobiotechnol 14(1):6
110. Dósa E, Guillaume DJ, Haluska M, Lacy CA et al (2010) Magnetic resonance imaging of intracranial tumors: intra-patient comparison of gadoteridol and ferumoxytol. Neuro Oncol 13:251. https://doi.org/10.1093/neuonc/noq172
111. Cheng KK, Chan PS, Fan S, Kwan SM et al (2015) Curcumin-conjugated magnetic nanoparticles for detecting amyloid plaques in Alzheimer's disease mice using magnetic resonance imaging (MRI). Biomaterials 44:155–172
112. Pouw JJ, Grootendorst MR, Bezooijen R, Klazen CA et al (2015) Pre-operative sentinel lymph node localization in breast cancer with superparamagnetic iron oxide MRI: the SentiMAG multicentre trial imaging subprotocol. Br J Radiol 88(1056):20150634
113. Cowger TA, Tang W, Zhen Z, Hu K et al (2015) Casein-coated Fe_5C_2 nanoparticles with superior r2 relaxivity for liver-specific magnetic resonance imaging. Theranostics 5(11):1225
114. Liu F, Le W, Mei T, Wang T et al (2016) In vitro and in vivo targeting imaging of pancreatic cancer using a Fe_3O_4@ SiO_2 nanoprobe modified with anti-mesothelin antibody. Int J Nanomedicine 11:2195
115. Huang J, Qian W, Wang L, Wu H et al (2016) Functionalized milk-protein-coated magnetic nanoparticles for MRI-monitored targeted therapy of pancreatic cancer. Int J Nanomedicine 11:3087
116. Jeon TY, Kim JH, Im GH, Kim J-H et al (2016) Hollow manganese oxide nanoparticle-enhanced MRI of hypoxic-ischaemic brain injury in the neonatal rat. Br J Radiol 89(1067):20150806
117. Luo Y, Yang J, Li J, Yu Z et al (2015) Facile synthesis and functionalization of manganese oxide nanoparticles for targeted T1-weighted tumor MR imaging. Colloids Surf B: Biointerfaces 136:506–513
118. Huang H, Yue T, Xu K, Golzarian J et al (2015) Fabrication and evaluation of tumor-targeted positive MRI contrast agent based on ultrasmall MnO nanoparticles. Colloids Surf B: Biointerfaces 131:148–154
119. Kuo Y-T, Chen C-Y, Liu G-C, Wang Y-M (2016) Development of bifunctional gadolinium-labeled superparamagnetic nanoparticles (Gd-MnMEIO) for in vivo MR imaging of the liver in an animal model. PLoS One 11(2):e0148695
120. Vu-Quang H, Vinding MS, Xia D, Nielsen T et al (2016) Chitosan-coated poly (lactic-co-glycolic acid) perfluorooctyl bromide nanoparticles for cell labeling in 19 F magnetic resonance imaging. Carbohydr Polym 136:936–944
121. Duan L, Yang F, Song L, Fang K et al (2015) Controlled assembly of magnetic nanoparticles on microbubbles for multimodal imaging. Soft Matter 11(27):5492–5500
122. Xu S, Yang F, Zhou X, Zhuang Y et al (2015) Uniform PEGylated PLGA microcapsules with embedded Fe_3O_4 nanoparticles for US/MR dual-modality imaging. ACS Appl Mater Interfaces 7(36):20460–20468
123. Song S, Guo H, Jiang Z, Jin Y et al (2015) Self-assembled microbubbles as contrast agents for ultrasound/magnetic resonance dual-modality imaging. Acta Biomater 24:266–278
124. Niu C, Wang Z, Lu G, Krupka TM et al (2013) Doxorubicin loaded superparamagnetic PLGA-iron oxide multifunctional microbubbles for dual-mode US/MR imaging and therapy of metastasis in lymph nodes. Biomaterials 34(9):2307–2317
125. Huang H-Y, Hu S-H, Hung S-Y, Chiang C-S et al (2013) SPIO nanoparticle-stabilized PAA-F127 thermosensitive nanobubbles with MR/US dual-modality imaging and HIFU-triggered drug release for magnetically guided in vivo tumor therapy. J Control Release 172(1):118–127
126. Xu B, Dou H, Tao K, Sun K et al (2011) "Two-in-one" fabrication of Fe_3O_4/MePEG-PLA composite nanocapsules as a potential ultrasonic/MRI dual contrast agent. Langmuir 27(19):12134–12142
127. Zhao Y, Song W, Wang D, Ran H et al (2015) Phase-shifted PFH@ PLGA/Fe_3O_4 nanocapsules for MRI/US imaging and photothermal therapy with near-infrared irradiation. ACS Appl Mater Interfaces 7(26):14231–14242

128. Cheng X, Li H, Chen Y, Luo B et al (2013) Ultrasound-triggered phase transition sensitive magnetic fluorescent nanodroplets as a multimodal imaging contrast agent in rat and mouse model. PLoS One 8(12):e85003
129. Kempen PJ, Greasley S, Parker KA, Campbell JL et al (2015) Theranostic mesoporous silica nanoparticles biodegrade after pro-survival drug delivery and ultrasound/magnetic resonance imaging of stem cells. Theranostics 5(6):631
130. Nolte I, Vince GH, Maurer M, Herbold C et al (2005) Iron particles enhance visualization of experimental gliomas with high-resolution sonography. Am J Neuroradiol 26 (6):1469–1474
131. Linker R, Kroner A, Horn T, Gold R et al (2006) Iron particle–enhanced visualization of inflammatory central nervous system lesions by high resolution: preliminary data in an animal model. Am J Neuroradiol 27(6):1225–1229
132. Oh J, Feldman MD, Kim J, Condit C et al (2006) Detection of magnetic nanoparticles in tissue using magneto-motive ultrasound. Nanotechnology 17(16):4183
133. Mehrmohammadi M, Oh J, Mallidi S, Emelianov SY (2011) Pulsed magneto-motive ultrasound imaging using ultrasmall magnetic nanoprobes. Mol Imaging 10(2):102. https://doi.org/10.2310/7290.2010.00037
134. Evertsson M, Kjellman P, Cinthio M, Fredriksson S et al (2014) Multimodal detection of iron oxide nanoparticles in rat lymph nodes using magnetomotive ultrasound imaging and magnetic resonance imaging. IEEE Trans Ultrason Ferroelectr Freq Control 61(8):1276–1283
135. Perlman O, Azhari H (2017) Ultrasonic computed tomography imaging of iron oxide nanoparticles. Phys Med Biol 62(3):825
136. Perlman O, Weitz IS, Azhari H (2015) Copper oxide nanoparticles as contrast agents for MRI and ultrasound dual-modality imaging. Phys Med Biol 60(15):5767
137. An L, Hu H, Du J, Wei J et al (2014) Paramagnetic hollow silica nanospheres for in vivo targeted ultrasound and magnetic resonance imaging. Biomaterials 35(20):5381–5392
138. Barnett BP, Ruiz-Cabello J, Hota P, Ouwerkerk R et al (2011) Use of perfluorocarbon nanoparticles for non-invasive multimodal cell tracking of human pancreatic islets. Contrast Media Mol Imaging 6(4):251–259
139. Thakor AS, Jokerst JV, Ghanouni P, Campbell JL et al (2016) Clinically approved nanoparticle imaging agents. J Nucl Med 57(12):1833–1837
140. Scheinberg DA, Grimm J, Heller DA, Stater EP et al (2017) Advances in the clinical translation of nanotechnology. Curr Opin Biotechnol 46:66–73
141. Kiessling F, Mertens ME, Grimm J, Lammers T (2014) Nanoparticles for imaging: top or flop? Radiology 273(1):10–28
142. Gu FX, Karnik R, Wang AZ, Alexis F et al (2007) Targeted nanoparticles for cancer therapy. Nano Today 2(3):14–21

Magnetic Tools for Medical Diagnosis

9

Jen-Jie Chieh, Shu-Hsien Liao, Li-Min Wang, Kai-Wen Huang, Hong-Chang Yang, and Herng-Er Horng

Contents

J.-J. Chieh (✉) · S.-H. Liao · H.-C. Yang · H.-E. Horng
Institute of Electro-Optical Science and Technology, National Taiwan Normal University, Taipei, Taiwan
e-mail: jjchieh@ntnu.edu.tw

L.-M. Wang
Department of Physics, National Taiwan University, Taipei, Taiwan

K.-W. Huang
Department of Surgery and Hepatitis Research Center, National Taiwan University Hospital, Taipei, Taiwan

Graduate Institute of Clinical Medicine, National Taiwan University, Taipei, Taiwan

C. S. S. R. Kumar (ed.), *Nanotechnology Characterization Tools for Biosensing and Medical Diagnosis*, https://doi.org/10.1007/978-3-662-56333-5_9

1 Definition of the Topic

Magnetic tools here are defined as the nanotechnologies for medical diagnosis, including in vitro diagnostics, ex vivo examination, and in vivo imaging by using magnetic nanoparticles (MNPs). In this chapter, we describe the mechanism, instrumentation, and medical results of different advanced magnetic tools.

2 Overview

Different developed magnetic tools based on MNPs are proposed for medical diagnosis, for example, in vitro diagnosis, in vivo diagnosis, and ex vivo diagnosis. In each magnetic technology, the mechanism and key research findings are introduced.

MNPs possess biosafety, excellent magnetic properties such as superparamagnetism characteristics, and cheap cost. Hence, numerous biomedical applications cover diagnosis, imaging, cell sorting, drug delivery, and hyperthermia treatment.

Current magnetic technologies still have some limitations, for example, high cost and maintenance of high-field magnetic resonance imaging (MRI), etc. To avoid these drawbacks, magnetic technologies introduced here were based on the unique characteristics of MNPs, rather than magnetic characteristics of materials. These introduced magnetic tools contain immunomagnetic reduction assay, vibrating sample magnetometer, low-field nuclear magnetic resonance and magnetic resonance imaging, blocking-temperature bioassay, scanning superconducting quantum interference device (SQUID) biosusceptometry, and ultrasound-induced magnetic imaging.

3 Introduction

For many medical applications, covering diagnosis, imaging, treatment, and drug delivery, the nanotechnologies were usually developed based on the utility of nanoparticles or nanomaterials. With the advantages of nanoparticles, such as good circulation, targeting, etc., the medical diagnosis and imaging could be promoted to achieve the high sensitivity and specificity, for example, the early detection of tumors or the accuracy positioning tumors. In comparison with radioactive [1], optical [2], and ultrasound [3] types of nanoparticles, MNPs [4] have been frequently used in clinics as commercial reagents of in vivo imaging (Ferucarbotran, Resovist, Germany) or examination (Sienna+, Endomagnetics, UK; MF-CEA-0061, MagQu, Taiwan) because of crucial advantages, such as biosafety [5, 6], molecular imaging [7], the ability of distribution manipulation [8], hyperthermia [9], and drug delivery [10].

MNPs usually could be mainly divided into some groups of metallic ones [11, 12], gadolinium ones [13], and iron oxide ones [14]. In metallic nanoparticles, cobalt nanoparticles always possess higher magnetic moment, but their biosafety is less appropriate for biomedical applications. Iron platinum nanoparticles, encapsulated with phospholipid coating, have significantly better T2 relaxivities than iron oxide ones. However, the intracellular biodegradation produces cytotoxic iron for iron

platinum nanoparticles, rather than safer iron ions for iron oxides ones. Iron-catalyzed decomposition of hydrogen peroxide into reactive oxygen species results in membrane lipid oxidation, damage to DNA and proteins, and tumor death [15]. Similarly, gadolinium-based nanoparticles are currently the common MRI contrast agent, but their toxicity has been warned by FDA recently [13]. Iron oxide nanoparticles, also named as ferrite nanoparticles, are composed of Fe_3O_4 or γ-Fe_2O_3 in the core and surfactants, silica, silicones, or phosphoric acid derivatives in the coating to increase their stability in solution.

For the sensing ultrasmall and ultrafew MNPs, the sensitive detection mechanism, including the magnetic sensor and the mechanism of signal transfer, is usually the key role. The SQUID is the most sensitive magnetic sensor currently. Its common configuration is the superconducting loops containing Josephson junctions, where a RF SQUID sensor possesses one Josephson junction and a DC SQUID sensor has two ones.

Due to composed superconducting materials, the cooling refrigerants are liquid nitrogen and liquid helium, and then SQUID sensor cooling by the former and the later was so-called high and low critical temperature (T_c) sensor. In general, the former can achieve the sensitivity of 10^{-13} T, and the latter is 10^{-14} (Fig. 9.1). The low-T_c SQUID could detect the neuro signal of a human brain and usually constitute of magnetoencephalography. Although the sensitivity of the high-T_c SQUID is worse than low-Tc one, it could detect the ultrafew MNPs. Besides, the high-T_c SQUID sensor is powerfully applied in biomedical laboratories and hospitals because the liquid nitrogen has much cheaper and simpler requirement of dewar container.

Even though SQUIDs are very sensitive, the dewar thickness and vacuum gap always increase the sensing distance between SQUID sensor and samples, largely decreasing the detection sensitivity based on Biot–Savart law. In order to avoid the drawback, the mechanism of the flux transfer was proposed to enhance the detected magnetic signal, i.e., the magnetic flux [16]. The transfer coil was composed of two parts (Fig. 9.2). One is the pickup coil composed of copper wires at the room temperature that could be closed to the sample as soon as possible, and the other is the input coil cooled at liquid nitrogen which could offer the amplified magnetic flux surrounding a SQUID sensor. The magnetic field (B_p) of the sample induces the induction voltage at the pickup coils, and then its current flows to the input coil and generates the magnetic field (B_i) for the SQUID detection. Hence, it could be effectively suppressed that the decay of magnetic signals results from the distance between the sample and the SQUID sensor.

Due to the room temperature, the thermal noise of the pickup up is worse than those of the input coil but inhibited by some methods, like few turns or the refrigerant cooling [17]. In addition, the amplified times of the flux transfer is defined as follows:

$$\frac{B_i}{B_p} = \frac{\omega L_i n_p \pi r_p^2}{n_p \pi r_i^2 \sqrt{\left(R_p + R_i\right)^2 + \left(\omega L_p + \omega L_i\right)^2}} \tag{9.1}$$

where L, R, n, r, and ω are the inductance, resistance, number of turns, radius of the coil, and the angular frequency, respectively. Subscripts of p and i separately indicate the pickup coil and input coil.

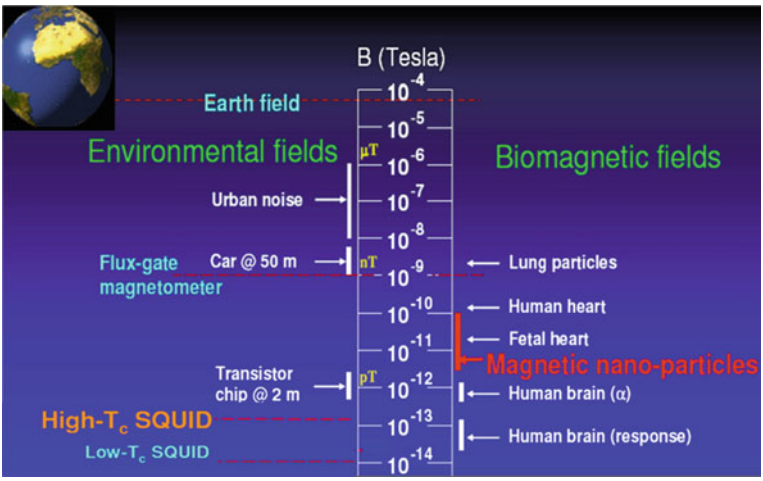

Fig. 9.1 The sensitivity and applications of the SQUID sensors

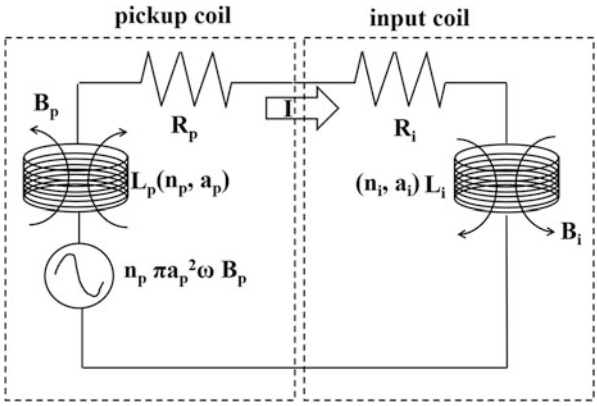

Fig. 9.2 Flux coupling from the sample to the SQUID sensor [16]

4 Advanced Magnetic Tools

Medical diagnosis is the first medical procedure of screening positive condition or determining which disease. Besides, it is also the last one to evaluate the treatment effect. In addition to physical examination, popular diagnostic procedures are examination of body fluids, pathology inspections, imaging, etc. Although some methodologies have been clinically applied in these diagnostic procedures, the improved approaches than current ones are still expected to meet the gradually serious clinical requirement, such as more biosafety, high sensitivity and specificity, rapidness, low cost, etc. Due to MNPs with many mentioned advantages, some MNP-based approaches have been developed, for example, immunomagnetic reduction assay,

vibrating sample magnetometer, and bioassay using blocking temperature for in vitro diagnosis and low-field NMR/MRI for in vivo and ex vivo diagnosis.

4.1 Immunomagnetic Reduction Assay

In comparison with current immunoassays, the advanced magnetic immunoassay, named as immunomagnetic reduction (IMR), has several powerful advantages, for example, the wash-free assay, the high specificity without optical interference of biomaterials, one-antibody utility opposite to two ones used in sandwich enzyme-linked immunosorbent assay (ELISA), longer lifetime than fluorescent labels of optical-based methodologies, and much biosafety opposite to gamma-radioactive isotopes used in radioimmunoassay.

IMR has been widely applied in many complete diseases, such as Down syndrome [18], Parkinson disease [19], hepatocellular carcinoma (HCC) [20], Alzheimer's disease [21–23], vascular endothelial growth factor related to some tumor diseases [24], Hb and HbA1c [25], nervous necrosis virus [26], H5N1 virus [27], orchid viruses [28], etc. [29].

4.1.1 Mechanism

MNPs are composed of Fe_3O_4 in core, dextran surfactant, and bioprobe coating, such as H1N2 (Fig. 9.3). Bioprobe-coated MNPs and their solvent constitute the magnetic reagent. The preparation step is to mix the magnetic reagent and the liquid sample with the target biomolecules. Consequently, an IMR instrument is to measure the variation of alternating current (ac) magnetic susceptibility χ_{ac} of the mixture from the entire free-of-bioconjugation state to partial bioconjugation state [30]. The IMR mechanism is that the bioconjugation effect results in the magnetic clusters formed by some target molecular and conjugated MNPs as well as larger bioprobe-coated MNPs, possessing the reduced χ_{ac}, i.e., the slower response with ac excitation fields (H_{ac}). Further, the scale of bioconjugation effect is proportion to the amount of target biomolecules. Hence, the representative analyzed IMR factor was defined as follows. $\chi_{ac,o}$ and $\chi_{ac,\varphi}$ are the χ_{ac} of the mixture before and after the bioconjugation of target molecular in concentration, denoted as φ, separately:

$$\mathrm{IMR}\ (\%) = \left(\chi_{ac,\,o} - \chi_{ac,\,\varphi}\right)/\chi_{ac,\,o} \times 100\% \tag{9.2}$$

The χ_{ac} variation of the mixture of magnetic reagent and H1N2 solution with time is plotted in Fig. 9.4 [31]. Here, anti-H1N2-coated MNPs was assayed H1N2 biomolecules. The round dots denoted the $\chi_{ac,o}$, average of 66.18, before the MNP–H1N2 bioconjugation. Consequently, the cross dots showed scattering χ_{ac} because bioprobe-coated MNPs conjugated H1N2 biomolecules. Finally, the dynamic χ_{ac} achieved stable state, denoted as square dots, for mean $\chi_{ac,\varphi}$ of 64.54. Hence, IMR (%) was 2.48%, larger than the standard deviation of 0.09%.

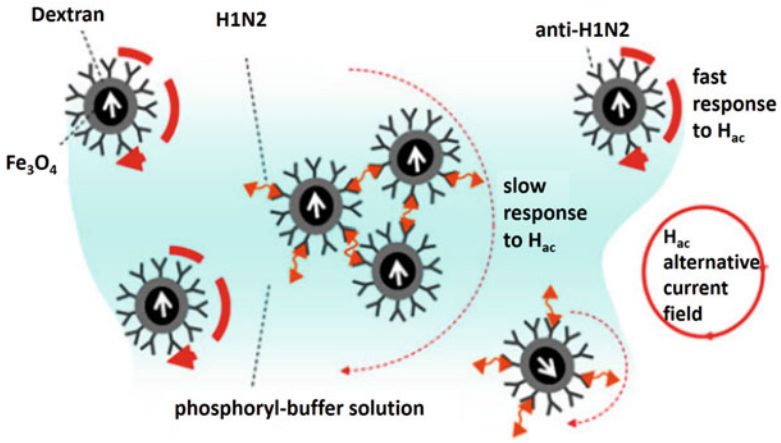

Fig. 9.3 IMR mechanism. MNPs with and without bioconjugation, and magnetic clusters possess different χ_{ac} under H_{ac}

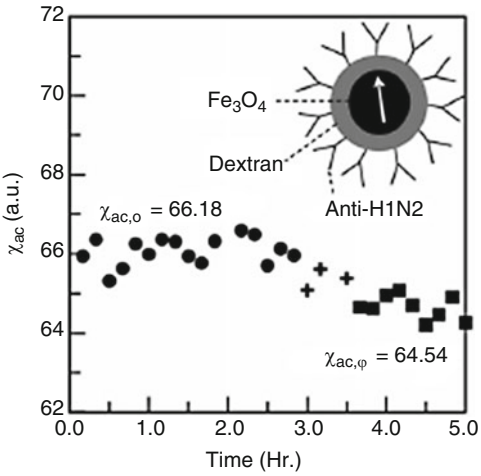

Fig. 9.4 The bioconjugation process of IMR. Here, the concentration of magnetic reagent is 0.1 emu/g. 40-μL. MNPs with the anti-H1N2 bioprobe for assaying H1N2 biomolecules. The H1N2 sample is 60-μL and 3.2-HAU/50-μL. $\chi_{ac,o}$ and $\chi_{ac,\varphi}$ are the χ_{ac} of the mixture before and after the bioconjugation of target molecular in concentration, denoted as φ, separately [31]

Hence, IMR is associated with several unique advantages in immunoassay. First, the wash-free feature due to the measurement of χ_{ac} difference between unbounded and biotarget-bounded MNPs is simplifying the IMR assay process; opposite to the physical intensity, this washing step for the removal of the unbound target biomolecules or unbounded MNPs massively happens to popular immunoassay, such as ELISA. Secondary, the high specificity results from the bounded interference biomaterials to MNPs with weaker conjugation force could be removed by the centrifugal force of the rotating MNPs using ac magnetic field, instead of the washing steps utilized in other immunoassays. Third, only one type of bioprobe, rather two ones in sandwich ELISA, is used. Fourth, with dynamic

labeling MNPs instead of static labeling materials of both fluorescent and radioactive indicators, IMR is a direct and homogeneous assay, which typically exhibits high reliability levels. Fifth, because the reduction in χ_{ac} can be accurately measured to correspond with the concentration of the target biomolecules, the concentration of the biomolecules can be quantified.

4.1.2 Experimental and Instrumental Methodology

The instrumentation principle of the mixed frequency was introduced at first. Consequently, the electrical type and SQUID type of IMR instruments were illustrated.

Instrumentation Principle

The instrumentation principle contained several features [32]. By applying an external ac field H_{ac} with a certain frequency f, the sample expressed the ac magnetization M_{ac}, i.e., χ_{ac}, due to the definition of M_{ac}/H_{ac}, for the detection. To prevent the detection of the signal contributed by the external H_{ac}, the features of the IMR instrumentation contain the gradient pickup coils, wired in opposite directions, and two excitation coils for the H_{ac}, exhibited at mixed frequencies of $mf_1 + nf_2$ with m and n being integers (Fig. 9.5). Consequently, the M_{ac} was also responsive to each H_{ac} at mixed frequencies of $mf_1 + nf_2$, and only one at around 20 kHz was chosen to evaluate the signal variation with time (Fig. 9.6).

Electrical Type of IMR Instrument

The excitation and detection devices for IMR (Fig. 9.5) were common for all types of IMR instruments. For the electrical type, the root-mean-square value of H_{ac} at target mixed frequency was around 2×10^{-4} T. The readout and amplified electronics are connected between the pickup coils and the data acquisition for the spectrum analysis. The typical example was the magnetic immunoassay analyzer (XacPro-E, MagQu).

SQUID Type of IMR Instrument

- **Single-channel**

The excitation and detection devices for IMR (Fig. 9.5) were common for all types of IMR instruments. For the SQUID type, the excitation and detection coils were similar with the electrical type of the IMR instrument. However, the pickup coils were connected to an input coil surrounding a high-transition temperature (high-T_c) rf SQUID sensor, rather than the readout and amplified electronics for the electrical type of the IMR instrument. It followed the mentioned mechanism of the flux transfer (in the section of 3 "Introduction") [33]. Hence, the configuration could be divided into the sample part and the sensor part in magnetically shielded boxes with different shielded factors (Fig. 9.7). Consequently, the SQUID type of IMR instrument was very stable for long-time detection of the tiny signal variation due to the ultrafew biomolecules conjugated to bioprobe-coated MNPs. The signal from the SQUID electronics was similarly fed to the data acquisition for the spectrum analysis.

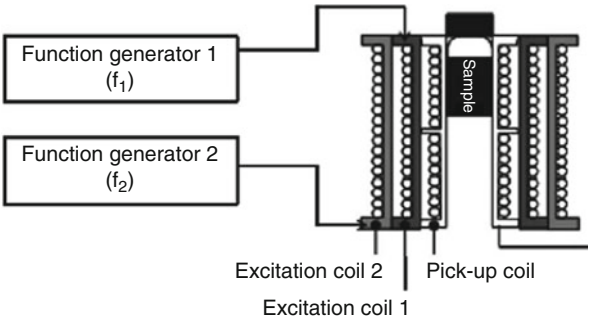

Fig. 9.5 Schematic diagram of the excitation and detection devices for IMR [32]

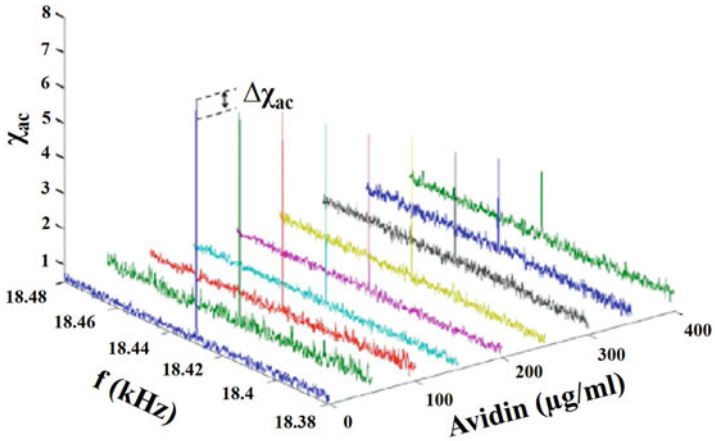

Fig. 9.6 The detected M_{ac} at a mixed frequency $mf_1 + nf_2$ in the spectra varied with the concentration of biotarget avidin. The magnetic reagent was 1 ml and 0.39 emu/g [32]

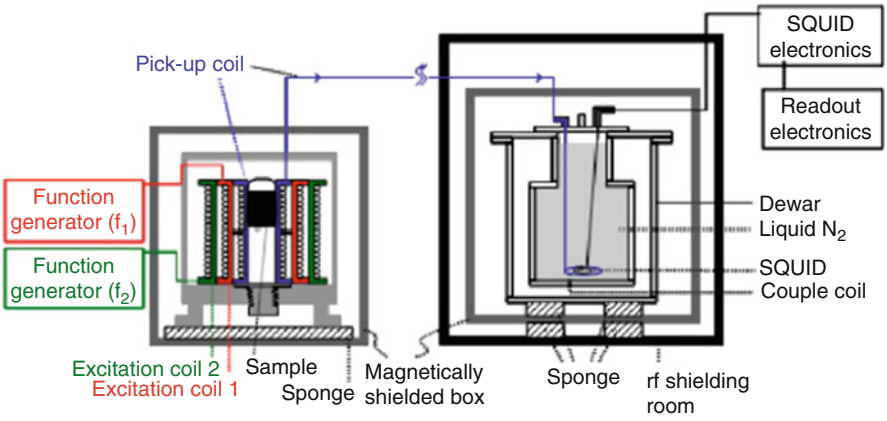

Fig. 9.7 Scheme of the single-channel SQUID IMR instrument [33]

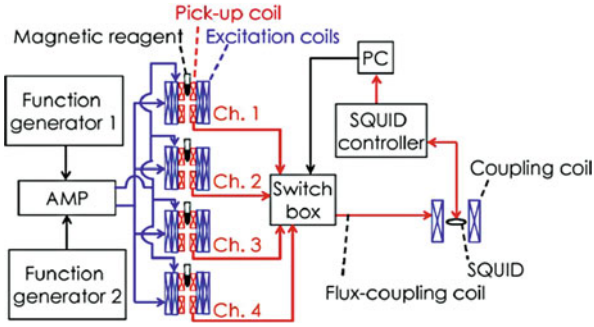

Fig. 9.8 Scheme of four-channel SQUID IMR instrument [34]

- **Four-channel**

The difference between the single-channel and four-channel of the SQUID IMR instrument was the electrical signal to input and output the common configuration of the excitation and detection devices (Fig. 9.8) [34]. For the two excitation coils of H_{ac} at different frequencies in each channel, the excitation signals at two frequencies were not only generated from function generators but also amplified by the amplifier. For the pickup coils in each channel, the detection signal of each channel, as denoted with Ch. 1 to Ch. 4, was fed into the input coil of the mechanism of the flux transfer (in the section of 3 "Introduction") in turns.

4.1.3 Key Research Findings

The major features of IMR were introduced with some examples of assaying target molecules.

High Specificity

The feature of high specificity was verified by using the magnetic reagent of anti-H5N1-coated MNPs for the assays on the samples of inactive H5N1 virus and pure H5N1 protein as well as the similar interferences of pure H1N1 protein and pure H3N1 protein individually [27]. Here, the magnetic reagent of 100 μl and 0.3 emu/g was separately mixed with two samples and interferences of 20 μl using a vortex for 2 min. Consequently, the single-channel SQUID IMR instrument was utilized to measure χ_{ac} variation of the mixture with time. Finally, the standard curve of the magnetic reagent of anti-H5N1-coated MNPs was found with the dependence of the IMR factor, denoted as $\Delta\chi_{ac}/\chi_{ac,o} \equiv (\chi_{ac,o} - \chi_{ac,\varphi})/\chi_{ac,o} \times 100$, on various concentration φ of inactive H5N1 virus, as shown in Fig. 9.9. The consistence between the standard curve and the IMR factor of assaying pure H5N1 protein proved the reliability. Further, the high specificity was verified with the IMR factors in noise levels, while pure H1N1 protein and pure H3N1 protein in high concentration of 200 pg/ml were assayed.

The specificity comparison between IMR and popular ELISA was studied by assaying alpha-fetoprotein (AFP) mixed with some interference materials, including hemoglobin (Hb), conjugated bilirubin (C-BL), triglyceride (TG), and vascular

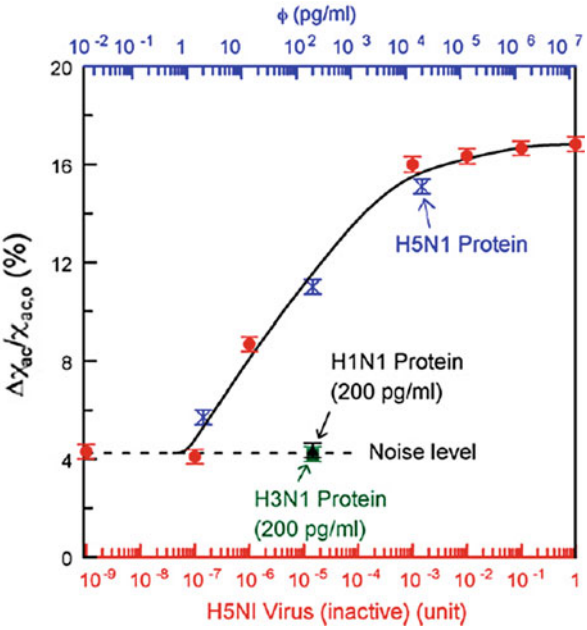

Fig. 9.9 The IMR factor $\Delta\chi_{ac}/\chi_{ac,o}$ for inactive H5N1 virus (labeled with ●) in various concentration in the red coordinates of the lower x-axis as well as H5N1 protein (labeled with ×) in various concentration and H1N1 and H3N1 proteins (labeled with ▲ and ■) of 200 pg/ml in the blue coordinates of upper x-axis [27]

Table 9.1 The utilized interference materials in the IMR and ELISA assays for AFP biomarkers [20]

Interfering material	Related disease	Normal reference level	Concentration used
Hemoglobin	Hemolysis	<500 μg/mL	600 μg/mL
			1000 μg/mL
Conjugated bilirubin	Jaundice	<2 μg/mL	5 μg/mL
			10 μg/mL
Triglyceride	Hypertriglyceridemia	500–1500 μg/mL	2000 μg/mL
Vascular endothelial growth factor	Malignancy	<0.05 ng/mL	0.1 ng/mL

endothelial growth factor (VEGF) [20]. For these interference materials, the concentrations and related disease are listed in Table 9.1. And the AFP concentration in each sample is 500 ng/mL. The sample of the pure AFP solution without interference materials was labeled with "None," and other samples of the AFP solution with interference materials were labeled with concentration and abbreviation of interference materials in Fig. 9.10. The results of IMR assay for these samples were shown in Fig. 9.10a. The IMR (%) of all samples which exhibit around 2.27% indicates no detectable interference was shown for IMR assay on AFP. Oppositely, the results of ELISA assay for these samples in Fig. 9.10b show that the optical densities (OD) 450 are 0.07 ± 0.003 for the pure AFP solution labeled with "None," higher than 0.45 for

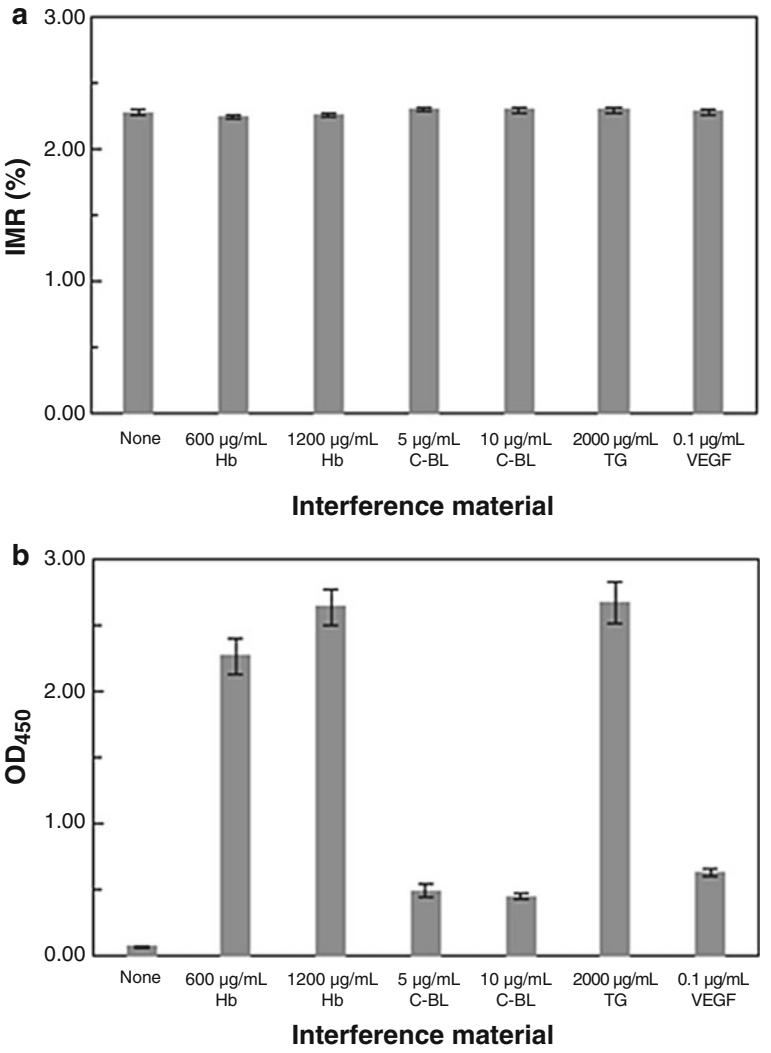

Fig. 9.10 Interference materials to (**a**) IMR (%) and (**b**) ELISA, respectively. The AFP concentration in each sample is 500 ng/mL, and the pure AFP solution is labeled with "None" [20]

the AFP solution with interference materials. The reasons were illustrated as follows. The interference materials always contribute the nonspecific binding, for example, the AFP solution with Hb/C-BL/TG is faintly red/orange/white. The sample color seriously affects the emission/transmission/absorption of fluorescent markers in the optical-examined ELISA. Oppositely, the magnetic signals are independent of any sample color. In addition, to suppress this false-positive result, the ELISA mechanism only depends on the repeated washing process, but the IMR mechanism applies the centrifugal force to break down the weak bioconjugation between interference

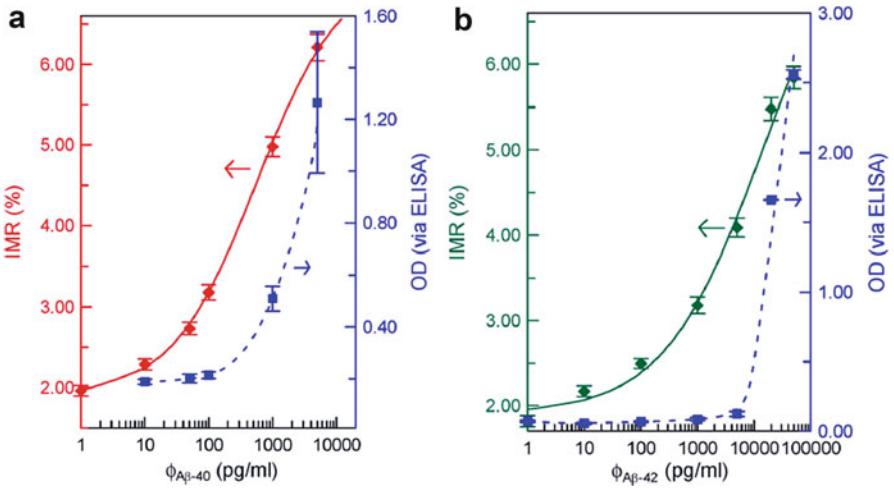

Fig. 9.11 The dependence of IMR signal and OD via ELISA on (**a**) $\Phi_{A\beta\text{-}40}$ and (**b**) $\Phi_{A\beta\text{-}42}$, respectively [34]

materials and bioprobe-coated MNPs. The former has limited improvement even though massive manpower and time are consumed. The latter absolutely removed interference materials.

High Sensitivity

The sensitivities of IMR and ELISA were compared in Fig. 9.11 [34]. The IMR and OD value via ELISA increased with the concentrations of Aβ-40 and Aβ-42, $\Phi_{A\beta\text{-}40}$ and $\Phi_{A\beta\text{-}42}$, in Fig. 9.11a and b, separately. However, the OD value has no significant variation with $\Phi_{A\beta\text{-}40}$ and $\Phi_{A\beta\text{-}42}$, while $\Phi_{A\beta\text{-}40}$ and $\Phi_{A\beta\text{-}42}$ are lower than 100 and 10,000 pg/ml. The IMR sensitivities of $\Phi_{A\beta\text{-}40}$ and $\Phi_{A\beta\text{-}40}$ achieve near 1 pg/ml and 10 pg/ml. It indicated that the detectable concentration of the SQUID IMR instrument is lower than ELISA by two orders of magnitude for $\Phi_{A\beta\text{-}40}$ and four orders of magnitude for $\Phi_{A\beta\text{-}42}$. Since the concentrations of $\Phi_{A\beta\text{-}40}$ and $\Phi_{A\beta\text{-}42}$ in cerebrospinal fluid (CSF) for Alzheimer's disease patients are at the level of tens to hundreds of pg/ml, [35, 36], the concentrations in blood are expected to be much lower than tens of pg/ml. The Aβ-40 and Aβ-42 in CSF could be assayed by ELISA and IMR, but the Aβ-40 and Aβ-42 in blood must be done by IMR. The sampling CSF is too dangerous to accept by patients, but sampling blood is much safer to screen Alzheimer's disease by assaying Aβ-40 and Aβ-42 in blood instead of CSF.

The Universal Model of IMR with Biotarget Concentrations

Similar to the analysis methods in other immunoassay [37–39], the relationship between IMR value and concentration φ of target biomolecules follows such behavior so-called logistic function:

Table 9.2 Fitted parameters A, B, φ_o, and ρ of the IMR-φ curve for various biomolecules. The utilized antibody type for the IMR assay is also listed [40]

Biomolecule	Antibody type	Parameter			
		A	B	ϕ_o	ρ
HIN2	Polyclonal	1.06	3.65	0.024	0.64
H3N1	Polyclonal	0.96	5.34	0.060	0.50
GST-TRIM33	Polyclonal	0.63	3.23	69.46	0.86
GM-CSF	Monoclonal	0.81	14.53	0.819	0.77
Chloramphenicol (CAP)	Monoclonal	0.65	6.26	2.24	0.94
Leuco-malachite green (LMG)	Monoclonal	0.75	8.86	1.78	1.01

$$\mathrm{IMR}(\%) = \frac{\mathrm{A} - \mathrm{B}}{1 + \left(\frac{\phi}{\phi_o}\right)^{\rho}} + \mathrm{B} \tag{9.3}$$

Table 9.2 shows the parameters A, B, φ_o, and ρ for viruses (e.g., swine influenza virus H1N2 and H3N1), protein (e.g., GST-TRIM33), cytokine (e.g., human GM-CSF), and small-molecule chemical (e.g., chloramphenicol and leucomalachite green). As the concentration φ of target biomolecules was as low as zero, the IMR value achieves the parameter A, i.e., the value of the noise level. Oppositely, as φ becomes very high, the saturated IMR value comes to the parameter B. Besides, as φ is φ_o, the IMR value approaches the middle between the parameter A and the parameter B. The assay sensitivity is usually defined as the concentration, while the IMR factor is 1.5 times as the noise level [40].

The lower/higher values of ρ related to the suppressed/enhanced type of collective bioconjugation between bioprobe-coated MNPs and biomolecules. For example, viruses H1N2 or H3N1 are much bigger than protein, cytokine, and chemicals in Table 9.2 by two orders of magnitude. Hence, bioprobe-coated MNPs are always conjugated to few virus particles. It results in the suppressed type of collective binding effect and the low ρ.

The logistic behavior for the IMR-φ curve is feasible for different biomolecules or chemicals with variant values of parameters A, B, φ_o, and ρ. By scaling IMR signal to (IMR − A)/(B − A), and φ to φ/φ_o, the relationships between the normalized IMR of IMR_{nor} and the normalized concentration φ/φ_o are found [40]:

$$\mathrm{IMR}_{nor} = (\mathrm{IMR} - \mathrm{A})/(\mathrm{B} - \mathrm{A}) = 1 - \frac{1}{1 + \phi^{\rho}}\phi = \phi/\phi_o \tag{9.4}$$

With Eq. 9.4 and Table 9.2, the $\mathrm{IMR}_{nor} - \varphi$ curves for assaying various biomolecules are universal, as shown in Fig. 9.12. It indicates the χ_{ac} reduction occurred from the MNP conjugation to target molecules with the concentration of target molecules is universal for different biomolecules.

4.1.4 Conclusions and Future Perspective

Based on bioprobe-coated MNPs, the IMR assay possesses some advantages of high sensitivity, high specificity, easy operation, etc. in comparison with the popular

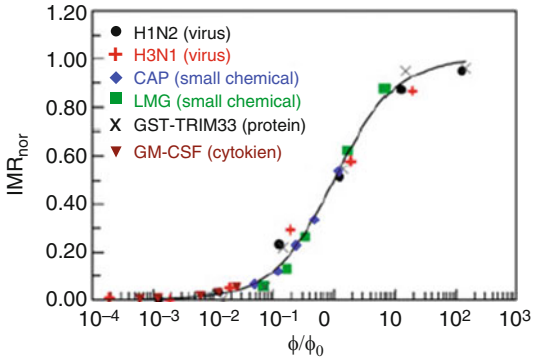

Fig. 9.12 Universal dependence of the normalized IMR IMR_{nor} on the concentration for various biomolecules [40]

ELISA. Especially, the SQUID IMR instrument was ultrahighly sensitive for the early diagnosis of the biomarkers in blood of Alzheimer's diseases. In addition, the characteristic curve of normalized IMR factor was universal for different categories of biomolecules. These results reveal the diverseness and promising feasibility of IMR for clinic or field-try applications.

4.2 Vibrating Sample Magnetometer

4.2.1 Mechanism

A vibrating sample magnetometer (VSM) [41, 42] is a scientific instrument for magnetization (M)–field (H) curves, named as the hysteresis curve, of materials. While the M variation of bioprobe-coated MNPs between bound to and free of biomarkers was examined by a VSM, the biomarker concentration in the tested sample was determined. The working principle was illustrated in Fig. 9.13. While tested samples without biomarkers were mixed with bioprobe-coated MNPs, the magnetic dipole of each bioprobe-coated MNP separately aligned parallel to the external field. By contrast, if tested samples with biomarkers, the biomarker was conjugated to one or some bioprobe-coated MNPs to form the magnetic cluster. For the mixture of bioprobe-coated MNPs and test sample, the total weight kept constant, but the magnetic moment varied with magnetic characteristics of all bioprobe-coated MNPs in separate or cluster state [43]. Hence, the M, defined as the ratio of the magnetic moment to the weight, could be used an indicator for the evaluation of the biomarker concentration. From the Langevin function, the M of all bioprobe-coated MNPs at a low magnetic field increases with the formation of magnetic clusters [43], but the M of each separate MNP is kept constant. In other words, the M of the mixture of nonmagnetic biomarkers and bioprobe-coated MNPs increased occurred from the conjugating of nonmagnetic biomarkers to one or some separate bioprobe-coated MNPs (i.e., the formation of magnetic cluster), rather than by adding any magnetic materials. Furthermore, more biomarkers led to an increased cluster formation, which increased the M of the mixture.

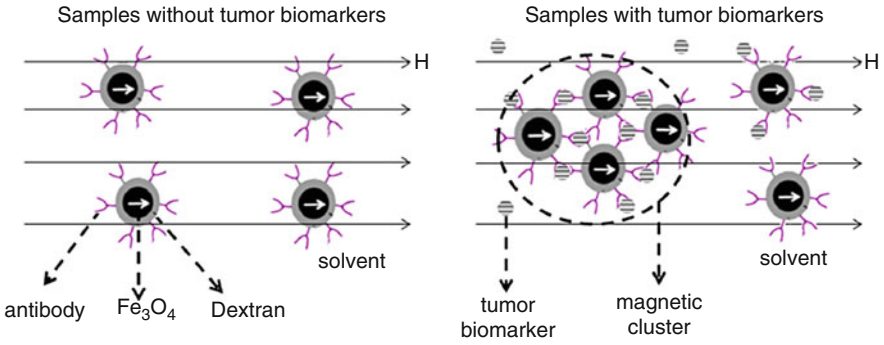

Fig. 9.13 Scheme of the biomarker evaluation with bioprobe-coated MNPs under the *H*. The mechanism is the formation of magnetic clusters caused by the conjugation of biomarkers to bioprobes coated on MNPs. Magnetic clusters exhibited greater DC susceptibility than single MNP [44]

In comparison with immunomagnetic reduction (IMR), the working principles of IMR and VSM assays are consistent in the magnetic characteristics variation under the formation of the magnetic cluster, i.e., the decrease of AC susceptibility and the increase of DC susceptibility. The former was measured with the IMR assay, and the latter was proportion to M, measured by a VSM. More biomarkers contributed to the higher number of magnetic clusters. Hence, for IMR and VSM assay, the variation of the measured intensity with biomarker concentration could be analyzed with the Langevin function.

4.2.2 Experimental and Instrumental Methodology

The configuration of a VSM includes two mechanisms of excitation and sensing (Fig. 9.14). The excitation mechanism is to magnetize the sample in different field strengths by an electromagnet and vibrate sinusoidally by a vibration motor. The sensing mechanism is to transfer the generated fluxes from the magnetized sample to the induced voltage by the pickup coils and a lock-in amplifier, analyzing at the vibration frequency.

The commercial VSM (Hystermag, MagQu Co., Taiwan) with the vibration frequency at 30 Hz, similar to several tens of hertz in general commercial VSMs, was utilized to measure the hysteresis curve. The standard solvents of phosphate-buffered saline (PBS) with biomarkers of different concentrations were tested to find the standard curve of the VSM assay at first. Consequently, the human serum was examined and analyzed with the founded standard curve. For the study of HCC [44], AFP antigens of clinical tumor biomarkers were solved with the PBS solvent to simulate the serum of normal and HCC patients with the concentration (Φ_{AFP}) range of 0–5000 ppb, covered most clinical ranges.

For comparison with the performance of AC-susceptibility-based IMR [20], the examination dose was the same, namely, 60 μl in the tested solution and 0.1 emu/g and 40 μl in anti-AFP-coated MNPs (AFP reagent, MagQu Co., Taiwan), which

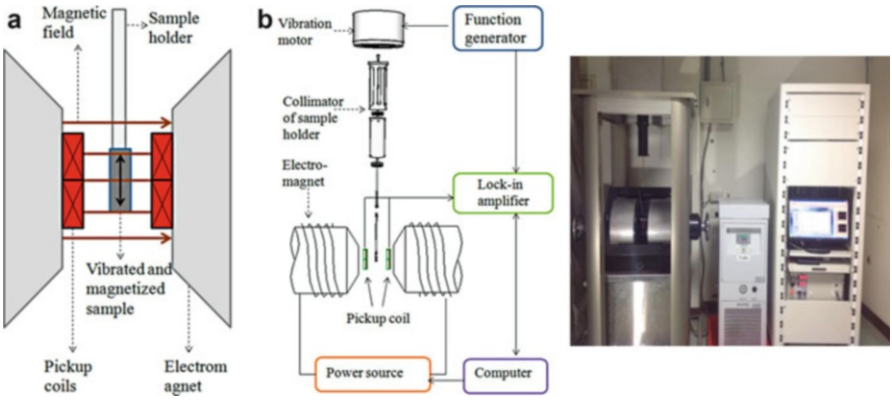

Fig. 9.14 VSM (**a**) instrumentation principle. (**b**) The utilized commercial VSM product (Hystermag, MagQu Co., Taiwan)

contained MNPs with hydrodynamic diameters of 48.6 ± 9.8 nm and a saturation magnetization (M_s) of 92 emu/g [45].

4.2.3 Key Research Findings

For samples mixing AFP-antibody-coated MNPs and the test solutions, the *M–H* curves in Fig. 9.15 show some features. In addition to the common expression of superparamagnetism, the variation of saturation fields (H_s) was discussed.

For a low Φ_{AFP} of 0–20 ppb, H_s was at approximately 0.2 T. In comparison with the popular Resovist magnetic reagent (SHU 555A, Schering Deutschland GmbH, Germany), H_s was higher than 0.5 T [46]. The difference of H_s came from the discrepancy of the magnetic core size of MNPs [14], which was 9% for the utilized AFP reagent by magnetic force microscopy (SPA400, Seiko Instruments, Inc., Japan) in the preliminary study and 65% for the Resovist MNR [46].

Similarly, for a high Φ_{AFP} of over 20 ppb, the H_s increased with Φ_{AFP}, for example, 0.4 T at 100 ppb and higher than 0.5 T at 500–5000 ppb. It was explained with the same theory of the discrepancy of the magnetic core size of MNPs. Due to larger magnetic clusters with the increased effect core size, a high Φ_{AFP} induced more or larger magnetic clusters. Consequently, the discrepancy was enhanced, and then the H_s increased [43, 46].

$M_{sub\text{-}T}$ at 0.5 T of sub-Tesla increased with Φ_{AFP} was shown in Fig. 9.16. Further, the following logistic function was utilized to clearly explain the relationship between the experimental $M_{sub\text{-}T}$ and Φ_{AFP}:

$$M_{sub-T} = \frac{A}{\left(1 + \frac{\phi_{AFP}}{C}\right)^{B}} + D \tag{9.5}$$

where A, B, C, and D are −0.617, 1.042, 8723, and 0.653, respectively. The fitting line expressed a flat region and a steep slope at low Φ_{AFP} and high Φ_{AFP} values,

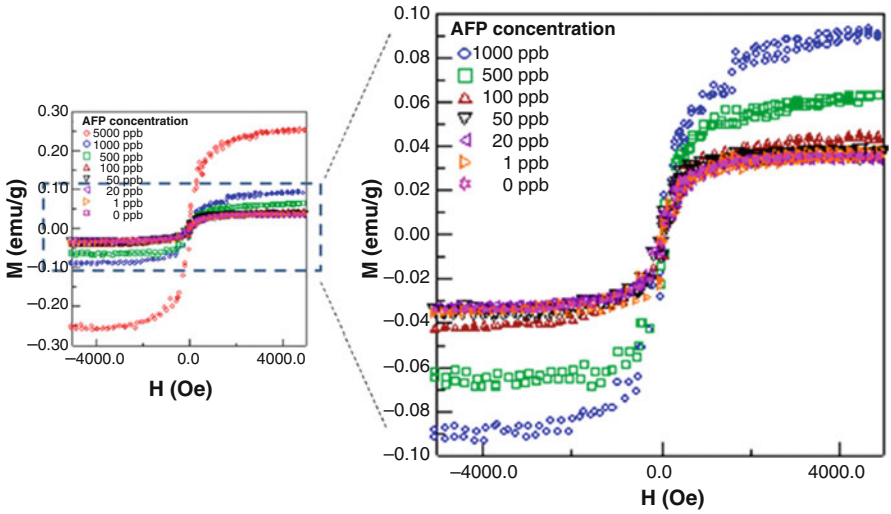

Fig. 9.15 M-H curves of only Φ_{AFP} in PBS [44]

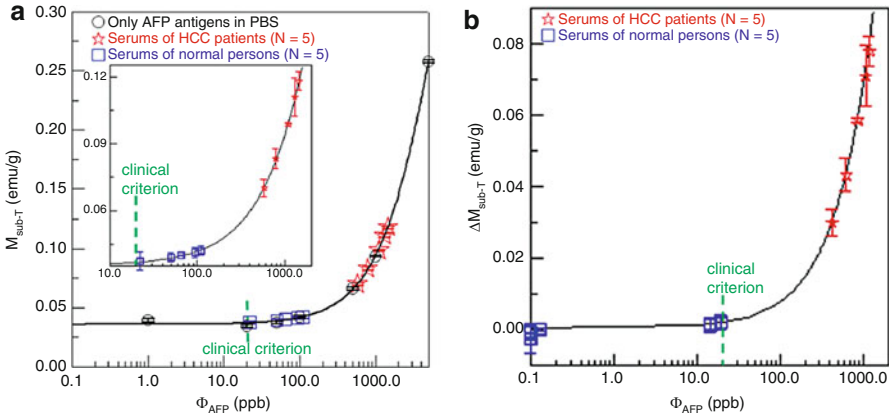

Fig. 9.16 The markers of only AFP antigens in PBS and serum of HCC patients and normal persons were marked in (**a**) the curve of $M_{sub\text{-}T}$ in relation to Φ_{AFP} and (**b**) the calibration curve of $\Delta M_{sub\text{-}T}$ in relation to Φ_{AFP} [44]

separately. Due to the measurement error of $M_{sub\text{-}T}$ within 1×10^{-3} emu/g, the lowest reliable Φ_{AFP} was nearly 25.3 ppb. In other words, the detected $M_{sub\text{-}T}$ remained at 0.03 emu/g while Φ_{AFP} lower than the sensitivity of 25.3 ppb, the same as the M_s of the mixture of anti-AFP-coated MNPs and the PBS solvent with zero Φ_{AFP}.

Besides, the tested serums of five HCC patients and five normal persons are labeled in Fig. 9.16a and analyzed for the Φ_{AFP} values using Eq. 9.5. Initially, the

obtained Φ_{AFP} values of all normal persons and HCC patients exceeded the clinical criterion of 20 ppb, as shown in the inset in Fig. 9.3a. It indicated the Φ_{AFP} values were overevaluated by the measured $M_{sub\text{-}T}$. It could be explained with some reasons. One is the false-positive phenomenon that the conjugation to anti-AFP MNPs was nontarget biomolecules, rather than AFP antigens. The vibration force by a VSM was contributed to shake the entire of the bound nontarget molecules and anti-AFP MNP together with the solvent flow, rather than the large and fixed biosensor in other works [47]. Hence, the vibration force of the VSM, opposite to the centrifugal force by IMR, has the limited suppression of the nonspecific conjugation.

To overcome the overevaluated phenomenon, the false-positive $M_{sub\text{-}T}$ value was evaluated from the average $M_{sub\text{-}T}$ value of normal persons, contributed from fewer Φ_{AFP} than 20 ppb and nonspecific molecules. The calibration factor of $\Delta M_{sub\text{-}T}$, defined as the difference between the $M_{sub\text{-}T}$ value of a tested person and the average $M_{sub\text{-}T}$ value of normal persons, was used as the calibrated Φ_{AFP} to mark in the calibrated fitting curve (Fig. 9.16b). And the fitting curve in Fig. 9.3b was obtained by subtracting the sum values of A and D in Eq. 9.5 for zero Φ_{AFP} from the measured $M_{sub\text{-}T}$. Consequently, $\Delta M_{sub\text{-}T}$ of 2.25×10^{-3} emu/g was used as the criterion for discriminating HCC patients. And all the calibrated Φ_{AFP} of the five normal persons and five HCC patients was, respectively, less than and higher than 20 ppb. Here, two negative $\Delta M_{sub\text{-}T}$ values were meaninglessly expressed in the lowest Φ_{AFP} in Fig. 9.16b. Besides, as the evaluation of screening criterion, the value of the average $M_{sub\text{-}T}$ value of normal persons is more meaningful if the number of normal persons increases.

4.2.4 Conclusions and Future Perspective

The mechanism of a VSM assay was to measure the increased M of the magnetic cluster, formed from the conjugation of biomarkers to some bioprobe-coated MNPs. The formation of magnetic cluster induced not only the variation of the DC M for a VSM assay but also that of AC magnetic susceptibility for a IMR assay. The clear demarcation between the normal and HCC groups indicated the feasibility of using $\Delta M_{sub\text{-}T}$ as the primary analysis factor for identifying risk Φ_{AFP} in HCC serums.

4.3 Bioassay Using Blocking Temperature

4.3.1 Mechanism

According to the Néel–Brown theory, the reversal of the magnetic moment of single-domain particles is governed by the rate of flipping an energy barrier; this process is thermally activated and can be described by relaxation time τ, which follows the Néel–Arrhenius equation [48, 49]:

$$\tau = \tau_0 \exp\left({}^{U}/_{k_B T}\right) \tag{9.6}$$

where τ_0 is the attempt time, k_B is the Boltzmann constant, and U is the energy barrier. The behavior depends on the type of superparamagnetic nanoparticle and the strength of interparticle interactions. In past studies [50–52] using Eq. 9.6, the MNP

system is static when τ becomes much longer than the measurement time τ_m and then appears to be blocked at temperatures below T_B. The superparamagnetic and blocked states can be observed at temperatures above and below T_B, respectively. Here, T_B corresponds to the temperature at $\tau = \tau_m$ and can be calculated as [50]

$$T_B = \frac{U}{k_B \ln(\tau_m/\tau_0)} \tag{9.7}$$

where the typical values for τ_0 are 10^{-9}~10^{-10} s [53], and τ_m is typically 100 s for DC measurements, and $U = KV$ (the energy barrier proportional to the volume of the particle), in which K is the magnetic anisotropy constant and V is the magnetic core volume of the MNP. Below T_B, the rate of thermally activated processes becomes insufficient for the system to achieve equilibrium; thus, the MNP magnetic moment remains blocked in a metastable state.

Looking deeper into the thermally activated relaxation behavior via Eqs. 9.6 and 9.7, one can see that T_B is also governed by U, which influences the magnetism in BMNs. U is dominated by K, which describes the dependence of the internal energy on the direction of the magnetization orientation and thus should depend on the magnetocrystalline structure and interparticle interactions in BMNs under an applied field. Figure 9.17 shows the ZFC $M(T)$ curves for a sample with 10 ppm of AFP under various applied fields, from which we can see that T_B is indeed field dependent [54].

The correlation between H and T_B has been discussed in many studies [55–57]. A simple analytical expression describing the functional behavior is

$$T_B(H) = \frac{KV}{k_B \ln(\tau_m/\tau_0)} \left(1 - \frac{H}{H_K}\right)^{\alpha} \tag{9.8}$$

where H_K is the anisotropic field and α is approximately 1.5 [58]. This model simplifies a complex situation by replacing the many-body problem with a single-particle description and may be strictly valid for noninteracting systems.

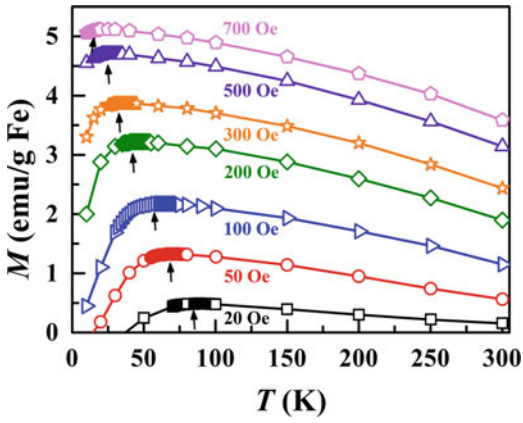

Fig. 9.17 ZFC $M(T)$ curves for a sample with 10 ppm of AFP under various fields. The arrow denotes the maximum point in the ZFC $M(T)$ curve [54]

The simplified expression of Eq. 9.8 does not describe the $T_B(H)$ curves well because of the interparticle interactions, as expected from previous MFM results. Recently, a simple modification of the random anisotropy model was proposed [57]. This model is applied to magnetic polycrystalline systems by considering interparticle interactions. According to this model, the correlation length L_H between interacting particles describes a correlation volume within which a number of particles contribute to magnetic anisotropy to generate an average anisotropy condition. Therefore, Eq. 9.8 can be rewritten as [58]

$$T_B = \frac{K\pi\left[D^3 + x\left(L_H^3 - D^3\right)\right]}{6k_B \ln(\tau_m/\tau_0)\left[1 + x\left(L_H^3 - D^3\right)/D^3\right]^{\frac{1}{2}}}\left\{1 - \frac{H_{DC}M_s\left[1 + x\left(L_H^3 - D^3\right)/D^3\right]^{\frac{1}{2}}}{2K}\right\}^{\frac{3}{2}} \tag{9.9}$$

where x represents the nanoparticle volume fraction of the magnetic phase and D is the particle diameter. Furthermore, all these parameters are related to L_H and are field dependent according to the relationship:

$$L_H = D + \sqrt{\frac{2A_{eff}}{H_{DC}M_s + C}} \tag{9.10}$$

where A_{eff} represents interaction intensity, which corresponds to the intergrain exchange constant A for nanocrystalline alloys [59]. Parameter C should give the interaction intensity variation with particle concentration, where C is set to zero to consider a system with strong interactions.

In addition, the T_B also depends on the antigen concentration φ_{AFP}. The behavior shows logistic function given by [38]

$$T_B = \frac{A - B}{1 + \left(\frac{\varphi_{AFP}}{\varphi_0}\right)^{\beta}} + B \tag{9.11}$$

This universal logistic function provides a basis to estimate unknown amounts of biomolecules [31]. Multiple categories of bio-entities, for example, proteins, viruses, small-molecule chemicals, and cytokines, have all been shown to behave similarly despite being different from each other, resulting in a general logistic function for all biotargets. The present concentration-dependent T_B also shows the behavior of a logistic function, which provides a foundation for assaying unknown amounts of biomolecules.

4.3.2 Experimental and Instrumental Methodology

The MNPs used in this study were dextran-coated Fe_3O_4. The MNPs were prepared as previously reported [60]. Oxidizing the Fe_3O_4-coated dextran with $NaIO_4$ to generate aldehyde groups, –CHO caused the dextran to react with the antibody through –CH=N– and covalently conjugate with the antibody. The unbound

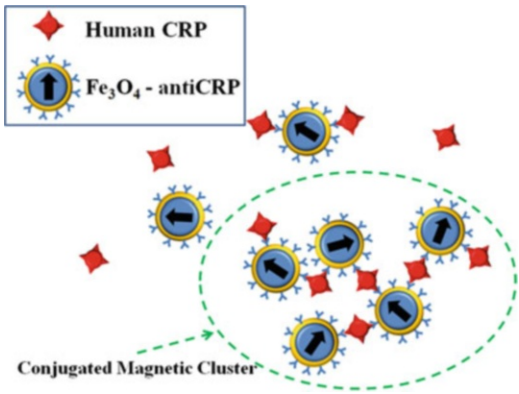

Fig. 9.18 Schematic diagram depicting conjugation of CRP and Fe_3O_4-antiCRP nanoparticles to form Fe_3O_4-antiCRP-CRP clusters [61]

antibodies were magnetically separated from the conjugated BMNs. The biotarget was the antibody. The experiment used samples consisting of the Fe_3O_4 antibody (40 μL) mixed with antigen (60 μL). The antigen concentration of the 60 μL antigen solution was varied. The samples were incubated in Eppendorf tubes for 2 h at room temperature. Figure 9.18 shows a schematic diagram depicting conjugation of CRP (antigens) and Fe_3O_4-antiCRP (Fe_3O_4 antibody) nanoparticles to form Fe_3O_4-anti-CRP-CRP clusters. More clusters of antibody–antigen-combined BMNs are expected to form in a sample with a higher concentration of antigen [61], and Fig. 9.19 shows TEM images of CRP, Fe_3O_4-antiCRP nanoparticles, and conjugated Fe_3O_4-antiCRP-CRP clusters [61]. After incubation, 1 μL of each mixed sample was dropped on a filter paper, dried, and then measured under various applied magnetic fields using a SQUID sensor.

4.3.3 Key Research Findings

Figure 9.20 shows the $M-H$ curves of samples with 0.2 and 10 ppm of AFP antigen at 300 K, demonstrating the superparamagnetic behavior of the BMNs. M_S of the samples increases with AFP concentration [54]. M_S varies with AFP concentration, suggesting that magnetic interparticle interactions occur between BMPs because AFP is nonmagnetic. In addition to M_S, the inset of Fig. 9.20 shows the normalized magnetization $M/M_{max}(H)$ curves for the corresponding samples; before saturation, the normalized magnetization of the sample with 0.2-ppm AFP is higher than that of the one with 10-ppm AFP. This indicates that samples with different AFP concentrations possess different intensities of magnetic interactions within their magnetic clusters. Other studies of clustered Fe_3O_4-antibody nanoparticles with antigen-like CRP also showed an increase of M_S with CRP concentration [60].

Recent research has suggested that dipolar interactions are long range and anisotropic, and the dipole interaction energy may increase magnetic ordering and T_B of MNPs [62]. Regarding concentrated MNPs, in which the particles are in very close proximity, the exchange coupling effect could result in the overlap of magnetic orbitals and atomic surface spins [63]. The exchange coupling effect also raises both the anisotropy and T_B of MNPs. Furthermore, because of their antibody–antigen

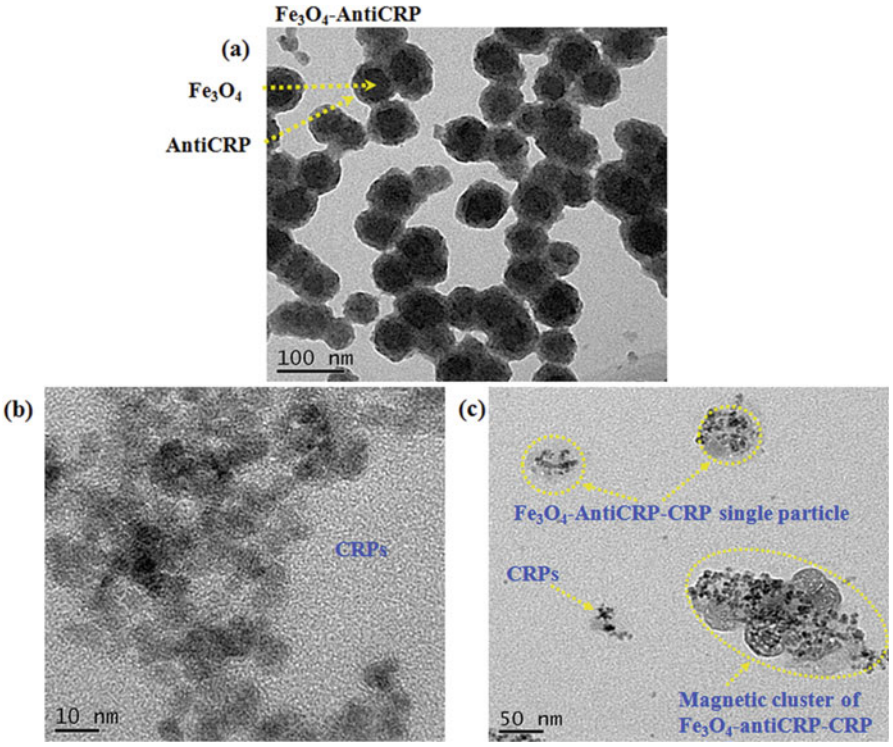

Fig. 9.19 TEM images of (**a**) Fe_3O_4-antiCRP nanoparticles, (**b**) CRP, and (**c**) conjugated Fe_3O_4-antiCRP-CRP clusters [61]

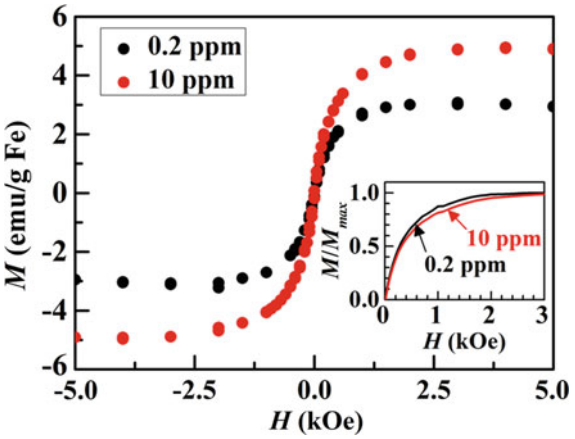

Fig. 9.20 Magnetization as a function of the magnetic field measured at 300 K for samples with 0.2 and 10 ppm of AFP. The inset shows the normalized magnetization of these two samples [54]

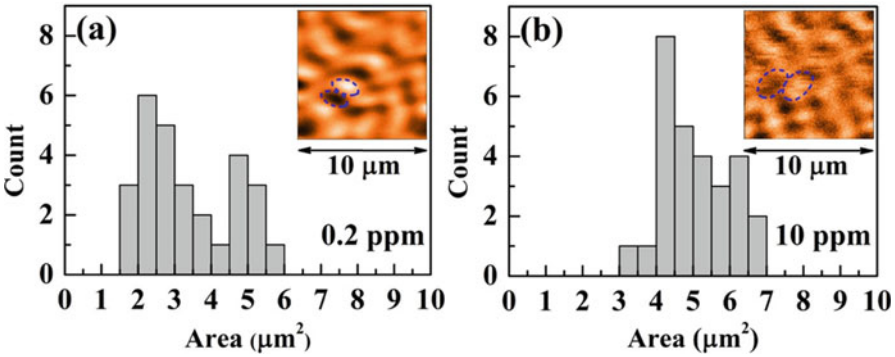

Fig. 9.21 Histogram of magnetic domain size distribution obtained from MFM for samples with (**a**) 0.2 and (**b**) 10 ppm of AFP. The insets show the MFM images of MNP clusters of the corresponding samples. The dashed lines schematically indicate one half of the magnetic domain region [54]

interactions, samples with higher antigen concentrations are expected to possess stronger interparticle interactions, which will cause greater magnetic anisotropy. T_B would be dominated by the magnetic anisotropy energy and thus should be related to the magnetic interactions between MNPs.

Figure 9.21a and b shows histograms of the magnetic domain size distribution of samples with 0.2 and 10 ppm of AFP, respectively, obtained from magnetic force microscopy (MFM) [54], and the insets show the MFM images of MNP clusters for the corresponding samples. If the MFM image contrast is changed, then one can observe dark and bright regions in the images that correspond to one half of the magnetic domain region, allowing us to easily calculate the domain size of the samples. The domain area was statistically estimated from the data in Fig. 9.21a and b, giving mean domain areas of 3.38 and 5.05 μm^2 for the samples with 0.2 and 10 ppm of AFP, respectively. The dependence of magnetic domain size on antigen concentration also implies the different intensities of magnetic interactions in samples with different antigen concentrations. The TEM results also agree with the formation of a large antibody–antigen-conjugated magnetic cluster that was observed [61].

Returning to the observed decrease of M_S in samples with lower AFP antigen concentrations, it was recently reported that the magnetism of Fe_3O_4 MNPs is weak after coating with a carbon shell and depends on both the core size and shell thickness [64]. The lower M_S compared with that of bulk Fe_3O_4 is exacerbated by decreased core size and suggestive of a surface-related mechanism [65]. For example, spin canting has been proposed as the mechanism for the M_S decrease [66]. Spin canting causes a highly disordered spin surface and is related to shell thickness (corresponding to the average particle distance) [65]. Analogous to the low M_S in MNPs, we thus infer that the observed decrease of M_S in samples with lower AFP concentration can be attributed to the magnetic disorder at the magnetic domain/cluster boundaries. The formation of a smaller antibody–antigen-conjugated magnetic cluster should result in a higher content of boundaries, leading to the lower M_S.

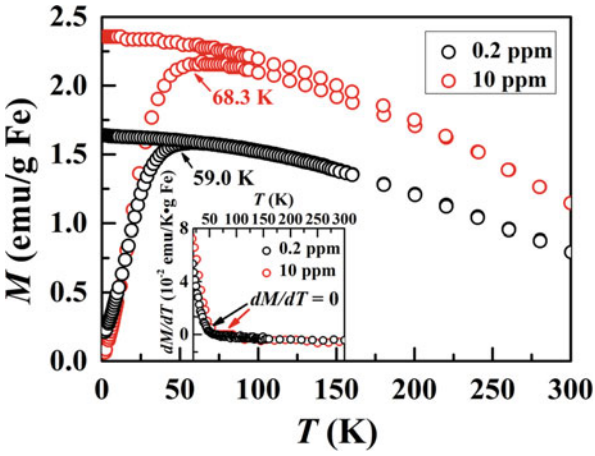

Fig. 9.22 Zero-field-cooled and field-cooled magnetization curves of samples with 0.2 and 10 ppm of AFP measured in a magnetic field of 100 Oe. The inset shows the first differential of these two samples. The T_B site is defined as the value of dM/dT equal to zero [54]

MNPs are typically characterized by the saturating behavior of their field-cooled (FC) magnetization curves and obvious maximum in their zero-field-cooled (ZFC) magnetization curves at low temperature. The temperature at which the maximum ZFC magnetization is obtained is the so-called average T_B of MNPs [55, 67]. Figure 9.22 shows the ZFC and FC magnetization curves for the samples with 0.2 and 10 ppm of AFP in 100 Oe field, and the inset shows the first differential dM/dT of these two samples, and T_B is the temperature at which dM/dT equals zero [54]. The obtained T_B for the samples with 0.2 and 10 ppm of AFP is approximately 59.0 and 68.3 K. According to Eq. 9.7, the K values are 9.07×10^3 and 1.05×10^4 erg/cm^3 for the samples with 0.2 and 10 ppm of AFP, respectively [54, 68]. K increases with AFP concentration, which confirms our inference that K of the magnetic clusters depends on AFP concentration.

Figure 9.23a, b shows the T_B dependence on field and the fits of Eqs. 9.8, 9.9, and 9.10 to the experimental data for samples with 0.2 and 10 ppm of AFP [54]. For $M_S = 11.77 \pm 1.72$ (12.58 ± 1.82) emu/cm^3, which corresponds to 3.14 ± 0.46 (3.35 ± 0.49) emu/g Fe, $A_{eff} = 1.11 \pm 0.14 \times 10^{-9}$ ($7.06 \pm 2.31 \times 10^{-10}$) erg/cm, and $K = 7.83 \pm 0.45 \times 10^3$ ($8.82 \pm 0.59 \times 10^3$) erg/cm^3 for the sample with 0.2 ppm (10 ppm) of AFP, the expression of Eq. 9.9 of the interacting model provides a good description of the field-dependent T_B for samples both with 0.2 and 10 ppm of AFP. As expected, the obtained values of M_S, A_{eff} and K for the sample with 10 ppm of AFP are indeed larger than those for the sample with 0.2 ppm of AFP. The slight deviation of the fitted and experimental M_S values may originate from the uncertainty of the effective particle correlation volume used to estimate volume/mass magnetization. This result again indicates that interparticle interactions can indeed be induced via the antibody–antigen combinations between BMNs.

Recent studies of 2D arrays of colloidal iron oxide nanoparticles [68] and $CoO/CoFe_2O_4$ core/shell nanoparticles [69] also show that $T_B(H)$ is influenced by interparticle interactions, which suggests that the interparticle interactions in these

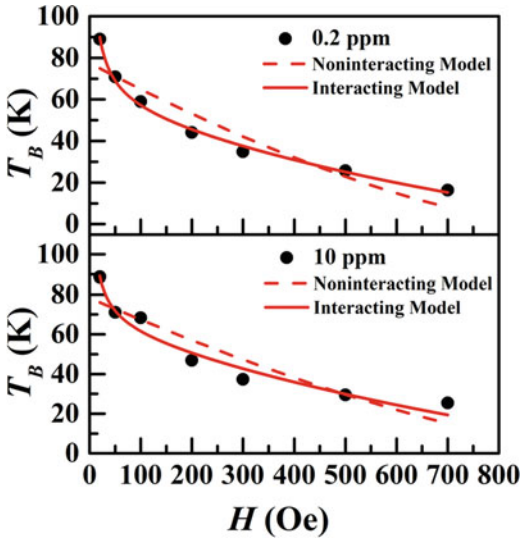

Fig. 9.23 Field dependence of the blocking temperature for samples with (**a**) 0.2 and (**b**) 10 ppm of AFP. Fits using Eq. 9.8 (dashed lines) and the interacting model given by Eqs. 9.9 and 9.10 (solid lines) [54]

systems arise from dipolar and interfacial exchange interactions, respectively. These results prompted us to examine the interparticle interactions in our BMN samples more closely. It is known that in a sample of randomly distributed nanoparticles with average magnetic moment μ and average separation d, the dipole interaction energy E_d of a particle with n nearest neighbors is of the order of $E_d \approx n(\mu_0/4\pi)(\mu^2/d^3)$, where μ_0 is the permeability of free space [62, 70]. In MNPs, dipole interactions can result in ordering of the magnetic moments of the nanoparticles below critical temperature T_o, where $T_o = E_d/k_B$ [70].

Considering their M_S of ~0.3 emu/g, the average particle diameter of our Fe_3O_4 nanoparticles of ~35 nm, and the density of Fe_3O_4 of 5.18 g/cm^3, we can estimate that the average magnetic moment μ for one Fe_3O_4 nanoparticle in our BMN samples is $\mu \approx 3762\ \mu_B$, where μ_B is the Bohr magneton. Assuming that $n = 12$ and $d = 35$ nm for a close-packed structure of the considered nanoparticles, we obtain E_d of ~3.4×10^{-23} J, which corresponds to ~2.5 K. According to the low obtained temperature of T_o, we can infer that the classic dipolar interactions between the antibody–antigen-combined BMNs do not play a major role in their magnetic behavior, unlike in iron oxide MNPs with a very small d of ~8 nm [67, 71]. Different kinds of interparticle coupling, such as classic dipolar interactions, Ruderman–Kittel–Kasuya–Yosida-like coupling, direction exchange interactions, and superexchange interactions, as reviewed by Mørup et al. [70], have been used to describe the magnetic properties of MNPs. Even though Eq. 9.9 can describe the observed $T_B(H)$ behavior, it should be noted that Eq. 9.9 is a purely phenomenological approach that does not determine whether classical dipolar or exchange coupling dominates. Currently, the kinds of magnetic

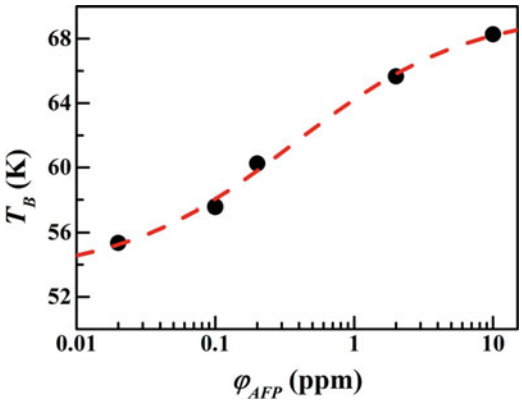

Fig. 9.24 Variation of blocking temperature T_B with respect to AFP concentration φ_{AFP}. The dashed line is a fitting based on Eq. 9.11 [54]

interactions between MNPs require refining because of the limited information available. Here, stronger magnetic interactions are expected to yield more parallel alignments in a sample with a higher concentration of AFP, resulting in larger M_S and magnetic domains, as shown above in Figs. 9.20 and 9.21.

The AFP concentration φ_{AFP} dependences of T_B and the fit obtained using Eq. 9.11 are displayed in Fig. 9.24 [54]. The results show that the AFP assay sensitivity can be enhanced to 20 ppb through measurement of the T_B of BMNs. Recently, different methods have been proposed to detect AFP concentrations in human serum, such as a photoelectrochemical immunoassay [72], fluoroimmunoassay [73, 74], and localized surface plasmon-coupled fluorescence [75]. Because these methods rely on a linear response range of a signal to calibrate the AFP concentration, they show a narrow detection range (0.05−100 ppb) even though they exhibit high sensitivity in detecting AFP levels. Such a narrow detection range would make it difficult to use these methods to detect AFP concentrations in blood exceeding 0.2 ppm. A wide detection range can be obtained because of the logistic function behavior of T_B, which demonstrates that T_B can be an index for bioassays to determine AFP concentrations using BMN reagents.

4.3.4 Conclusions and Future Perspective

In summary, we have an assay for antigen concentration based on the antigen and antibody coated onto BMN using M_S measurements, the magnetic domain images of clusters, and T_B. In particular, the T_B characteristics of samples with different antigen concentrations could be described by the interacting model. These results were attributed to the interparticle interactions and Néel motions of the magnetic moments in BMNs, which are dominated by the magnetic interactions between the conjugated Fe_3O_4-antibody BMNs. At the same time, the T_B values follow a logistic function with respect to antigen concentration. This method provides a potential platform for assaying a wide variety of targets, including viruses, proteins, and tumor markers.

4.4 Low-Field Nuclear Magnetic Resonance/Magnetic Resonance Imaging

4.4.1 Mechanism

Nuclear Magnetic Moments

The spin angular momentum and magnetic moment vectors are related to each other by $\boldsymbol{\mu} = \gamma \mathbf{J}$, where γ is a physical constant known as the gyromagnetic ratio. For example, $\gamma = 2.675 \times 10^8$ ras/s/T (42.58 MHz/T) for ^{1}H, while $\gamma = 2.516 \times 10^8$ ras/s/T (40.05 MHz/T) for ^{19}F. Based on the theories of quantum mechanics, the magnitude of $\boldsymbol{\mu}$ is $\mu = \gamma\hbar\,(I\,(I+1))^{1/2}$, where $\hbar$ is Planck's constant h (6.6×10^{-34} J-s) divided by 2π and I is the nuclear spin quantum number. For ^{1}H,^{13}C,^{19}F, and ^{31}P nuclei, $I = 1/2$, and such a spin system is called a spin-1/2 system. A nucleus is NMR active only if $I \neq 0$.

When an external magnetic field of strength B_0 is applied for an object in the z-direction such that $\mathbf{B_0} = B_0\,\mathbf{k}$, the z-component of $\boldsymbol{\mu}$ becomes certain due to the B_0 field and signs given by $\mu_z = \gamma\, m_I\, \hbar$, where m_I is the magnetic quantum number. For a spin-1/2 system, I and m_I are equal to 1/2 and $\pm 1/2$.

The torque of $\boldsymbol{\mu}$ in an external magnetic field is given by $\boldsymbol{\mu} \times B_0\mathbf{k}$ and equal to the rate of change of its angular momentum. That is, $\frac{d\,\vec{J}}{dt} = \vec{\mu} \times B_0\,\vec{k}$ and can be rewritten by $\frac{d\,\vec{\mu}}{dt} = \gamma\,\vec{\mu} \times B_0\,\vec{k}$. The solution can be expressed by

$$\begin{aligned} \mu_{xy}(t) &= \mu_{xy}(0)\, e^{-i\gamma B_0 t} \\ \mu_z(t) &= \mu_z(0) \end{aligned} \tag{9.12}$$

where the $\mu_{xy}(0)$ and $\mu_z(0)$ are the initial values of μ_{xy} and μ_z. The angular frequency of nuclear precession is $\omega_0 = \gamma\, B_0$, which is known as Larmor frequency.

Bulk Magnetization

The vector sum of all the microscopic magnetic moments, **M**, in the object can be described by $\mathbf{M} = \Sigma\boldsymbol{\mu}$. Spins in different directions have different energy of interaction with the external magnetic field $\mathbf{B_0}$. According to the quantum theory, $E = -\,\boldsymbol{\mu}\cdot\mathbf{B_0} = -\,\mu_z B_0 = -\,\gamma\, m_I\, \hbar\, B_0$, and the energy difference between the two spin states is given by $\Delta E = E_{\downarrow} - E_{\uparrow} = \gamma\,\hbar\,B_0$ for a spin-1/2 system. The spin population difference in the two spin states can be calculated according to the Boltzmann relationship:

$$\frac{N_{\uparrow}}{N_{\downarrow}} = e^{\left(\frac{\Delta E}{KT_S}\right)} \tag{9.13}$$

where $N_{\uparrow}$ is the number of pointing-up spins, $N_{\downarrow}$ is number of pointing-down spins, T_s is absolute temperature of the spin system, and K is Boltzmann constant (1.38×10^{-23} J/K). In practice, $\Delta E \ll K\ T_s$. Therefore, $\frac{N_{\uparrow}}{N_{\downarrow}} \approx 1 + \frac{\gamma\hbar B_0}{KT_S}$ and

$N_\uparrow - N_\downarrow \approx N_S \frac{\gamma\hbar B_0}{2KT_S}$, where N_S is the total number of spin in the object. Therefore the bulk magnetization can be written by $M = \mu\left(N_\uparrow - N_\downarrow\right) \approx N_S \frac{\gamma^2\hbar^2 B_0}{4KT_S}$.

Pulse Excitation

Commonly NMR experiments are performed using short pulses of excitation. Consider the response of a sample initially polarized in an external field B_0 along the pulse, $\mathbf{B_1}(t) = B_1\,\mathbf{i} \times u(t_p - t) \times \cos\omega t$, where u(t) is a step function. After the pulse is terminated, M_z keeps its new value, $M_z = M\cos\omega_1 t_p$, while the transverse components evolve that $M_x = v(t)\sin\omega t$ and $M_y = v(t)\cos\omega t$, where $v(t) = M\sin\omega_1 t_p \cos\Delta\omega t$. The angle of tilt$\alpha$ is equal to $\gamma B_1 t_p$ which is controlled by the duration of the pulse t_p and the field intensity. A typical value of t_p for a $\pi/2$ pulse for a proton with excitation amplitude $B_1 = 10^{-4}$ T is 58 μs.

The Bloch Equation

The behavior of *M* in an external magnetic field is described by the Bloch equation as the form $\frac{d\vec{M}}{dt} = \gamma\,\vec{M} \times \vec{B} - \frac{M_x\,\vec{i} + M_y\,\vec{j}}{T_2} - \frac{\left(M_z - M_{z,0}\right)\vec{k}}{T_1}$, where $M_{z,0}$ is the thermal equilibrium value for **M**. T_1 and T_2 are the time constant characterizing the relaxation process of a spin system after it has been disturbed from its thermal equilibrium state.

Free Precession and Relaxation

After magnetized spin has been perturbed from its thermal equilibrium state by a RF pulse, it will return to its thermal equilibrium state. The transverse and longitudinal relaxations are described by the Bloch equation. In the Larmor-rotating frame, it can be noted by $\frac{dM_{z'}}{dt} = -\frac{M_{z'} - M_{z,0}}{T_1}$ and $\frac{dM_{x'y'}}{dt} = -\frac{M_{x'y'}}{T_2}$. After solving the equations, the transverse and longitudinal magnetization components can be described as follows:

$$M_{x'y'}(t) = M_{x'y'}(0_+)\ e^{-t/T_2} \tag{9.14}$$

$$M_{z'}(t) = M_{z,0}\left(1 - e^{-t/T_1}\right) + M_{z'}(0_+)\ e^{-t/T_2}$$

where $M_{x',\,y'}(0_+)$ and $M_{z'}(0_+)$ are the magnetizations on the transverse plane and along the z-axis after an RF pulse. The trajectory of the tip of M during the relaxation period as observed in the laboratory frame is shown in Fig. 9.25. The evolution of the transverse magnetization is characterized by an exponential decay e^{-t/T_2} and a precession about the B_0 field $e^{-i\omega t}$. The length of the free precession period depends on the T_2 value.

4.4.2 Experimental and Instrumental Methodology

Instruments and Parameters

The SQUID-based NMR system consists of SQUID magnetometer, low-pass filter, signal amplifier, pre-polarization field, static field, and a pulsed field as shown in

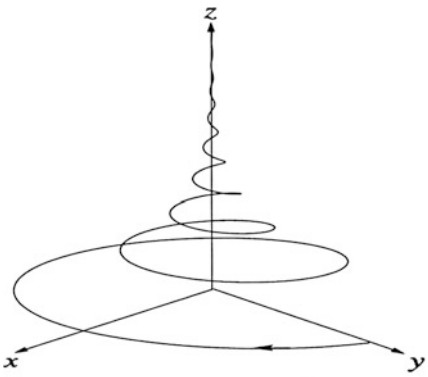

Fig. 9.25 The trajectory of the tip of **M** during the relaxation period as observed in the laboratory frame

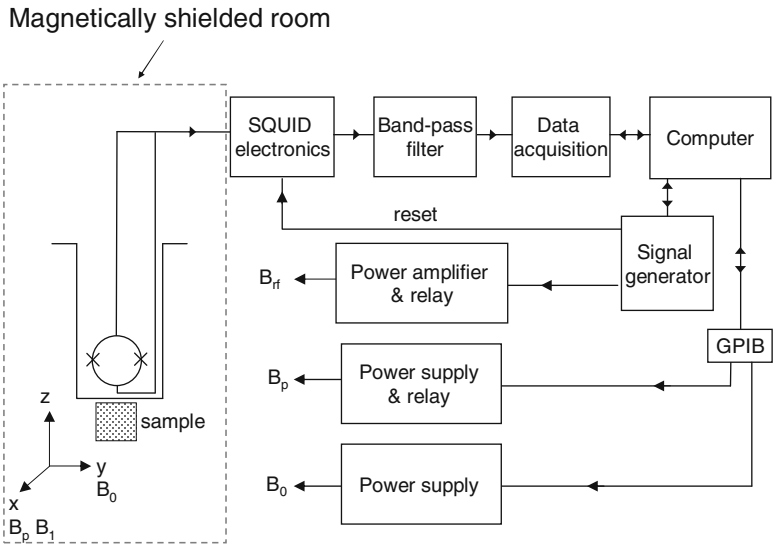

Fig. 9.26 Schematics of the HTS SQUID-based NMR spectrometer

Fig. 9.26. The magnetometer is purchased from Conductus Inc. with a magnetic field sensitivity of 100 fT/Hz$^{1/2}$ at 1 kHz and 300 fT/Hz$^{1/2}$ at 400 Hz. The magnetometer was operated in the flux-locked loop without a tuned input loop. The voltage across the SQUID was amplified by a low-noise amplifier at room temperature. After further amplification, the signal was integrated and fed back via a resistor into a coil inductively coupled to the SQUID. The voltage across the resistor was further amplified, filtered, and fed into the data acquisition system. The NMR control unit produced audio frequency pulses that were amplified by the power amplifier. A direct current (dc) power supply (Agilent E3634A) provided the Helmholtz pairs to generate the pre-polarization field up to 0.01 T. The diameter of the pre-polarization

coil was 30 cm, while the diameter of the uniform measuring field was 80 cm. The field homogeneity at the center of the pre-polarization coils was greater than 0.1% and 1% in a cubic volume of $2 \times 2 \times 2$ cm^3 and $8 \times 8 \times 8$ cm^3, respectively. The field homogeneity at the center of the pre-polarization coils was greater than 0.2% in a cube volume of $8 \times 8 \times 8$ cm^3. The strength of the static measuring field was varied from 8.9 μT to 165 μT in the y-direction. The resonating magnetic field was perpendicular to the static field and consisted of a pair of square coils with a side length of 18 cm.

Measurement Process

The pulsed NMR detection scheme is illustrated in Fig. 9.27. The pre-polarization field, B_p, up to 0.01 T was applied along the x-direction, while a uniform measuring $\mathbf{B_o}$ field in microtesla was applied along the y-direction. Both B_p and $\mathbf{B_o}$ fields were produced with Helmholtz pairs. The time to polarize the magnetization was several seconds. Power amplifiers and dc power supplies can easily couple the flux into SQUID magnetometers; therefore relays were used to isolate the noises coupled from the power amplifier and dc power supplies. Without relay, the SQUID can be unlocked due to the coupled noise from the equipment. Additionally, the SQUID was reset after applying the pre-polarization field to stabilize the SQUID operation. After the pre-polarization of magnetization, the field was ramped down directly, and the field decayed to zero in 70 ms. To prevent the induced field from affecting the

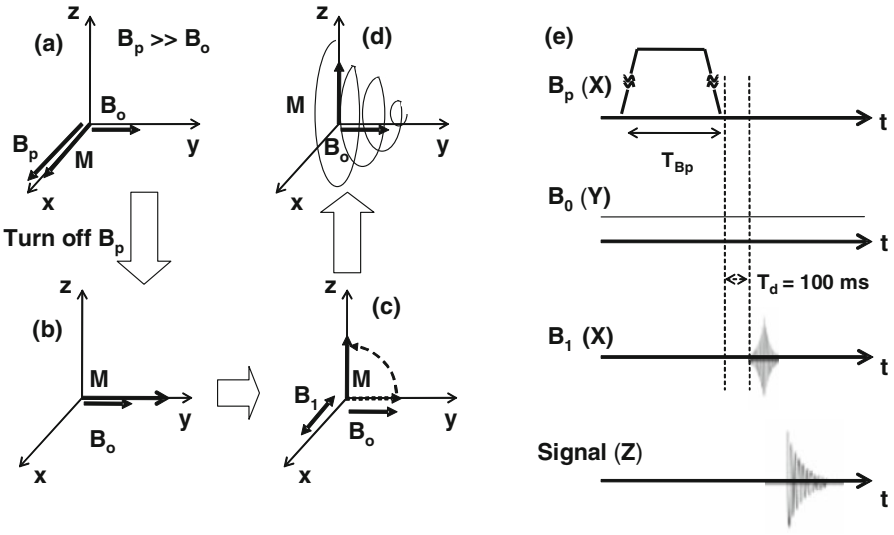

Fig. 9.27 The NMR detection scheme with (**a**) the $\mathbf{B_p}$ field up to 0.01 T is applied along the x-direction, while the uniform measuring $\mathbf{B_o}$ field in microtesla is applied along the y-direction; (**b**) after the $\mathbf{B_p}$ is turned off, the magnetization, **M**, relaxes to y-direction; (**c**) the pulses B_1 field is used to excite the **M** to z-direction; (**d**) the **M** relaxes in μT $\mathbf{B_o}$ field; and (**e**) the NMR sequences are used in the SQUID-based NMR detection

pulsed excitation field, the pulsed excitation field B_1 was turned on after a time interval T_d of 100 ms. The free induction decay signal of the processing magnetization of the samples was detected in a uniform measuring $\mathbf{B_o}$ field.

4.4.3 Key Research Findings

The magnetic fluid consisted of magnetic nanoparticle, surfactant, and solvent. The magnetic nanoparticle such as Fe_3O_4 is paramagnetic material. Therefore, it produce external magnetic field at a magnetic field. For NMR and MRI experiment, the produced external magnetic field disturbs the homogeneity of the static field nearby the magnetic nanoparticles and reduces the longitudinal relaxation time and transverse relaxation time. The shorter relaxation time means that the weaker NMR signal or the darker image for MRI. Therefore, it can be used for a contrast agent to enhance the contact between with or without magnetic nanoparticle.

Figure 9.28a shows the NMR spectrum of the magnetic fluid with different concentrations. The signal intensity is decreased with the increase of the concentration. In order to verity the influence of the magnetic nanoparticle, the T_2^* of different

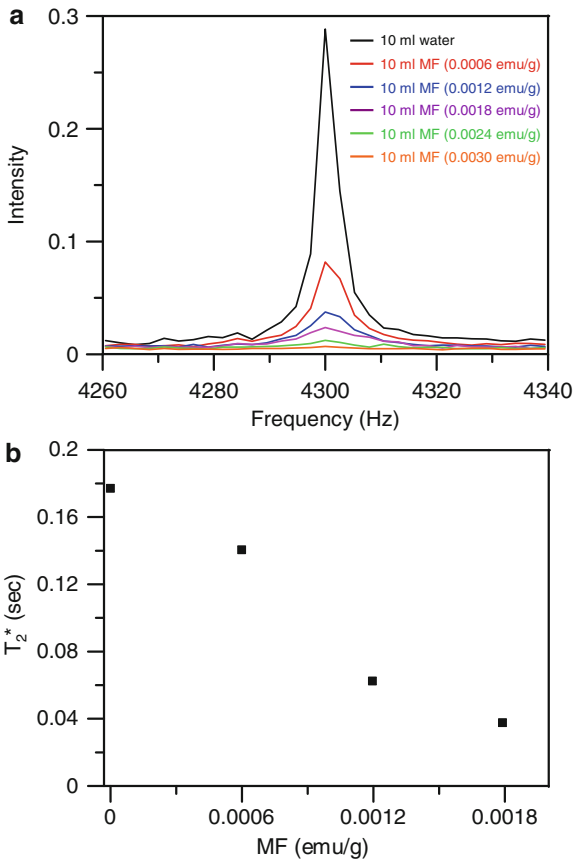

Fig. 9.28 (**a**) The NMR spectrum of the 10-ml water and magnetic fluid with different concentrations. (**b**) The T_2^* of the water and magnetic fluid with different concentrations

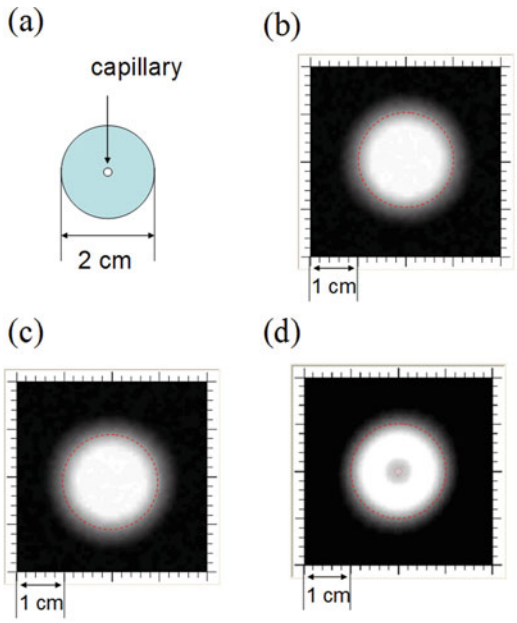

Fig. 9.29 (**a**) The cylindraceous sample which has a capillary in the center. The two-dimensional MR images when the capillary filled with (**b**) water, (**c**) air, and (**d**) magnetic fluid

concentrations has been calculated from the FID signals and shown in Fig. 9.28b. The T_2^* is also decreased with the increase of concentration. The decrease of T_2* leads into the reduction of the NMR intensity in the spectrum. In general the reason of the decrease of T_2^* is due to the field inhomogeneity. The field inhomogeneity causes the dephase of the nuclear spin and cancels the total magnetization. Therefore the T_2^* is decreased. In our case, the MNPs float around the water. They produce an external magnetic field and cause the field inhomogeneity.

Although the magnetic fluid causes the field inhomogeneity and decreases the NMR signal, it is able to be a maker and increases the locally spatial resolution. We put a capillary which the I.D. is 1.1 mm and O.D. is 1.5 mm in the center of a cylinder as shown in Fig. 9.29a. Figure 9.29b–d shows the three cases of the MR image which the capillary is filled with water, air, or magnetic fluid which the concentration is 0.3 emu/g. The images of Fig. 9.29b, c are seem to the same because the spatial resolution of our high-T_c SQUID MRI system is about 3 mm which is much larger than the size of capillary. Therefore, the capillary filled with water or air cannot be identified. However, the capillary filled with the magnetic fluid leads into a dark area in the MR image as shown in Fig. 9.29d. It means that the magnetic fluid not only decreases the NMR signal itself but also causes the field inhomogeneity around the magnetic fluid. Therefore the dark area is larger than the spatial resolution of our system and can be imaged. The magnetic fluid can point out the specific position and increase the locally spatial resolution.

Figure 9.30 shows the T_1-weighted images taken by using procedures by using the high-T_c SQUID-detected imager. The images were taken at $T_{Bp} = 0.2$, 0.4, 0.7,

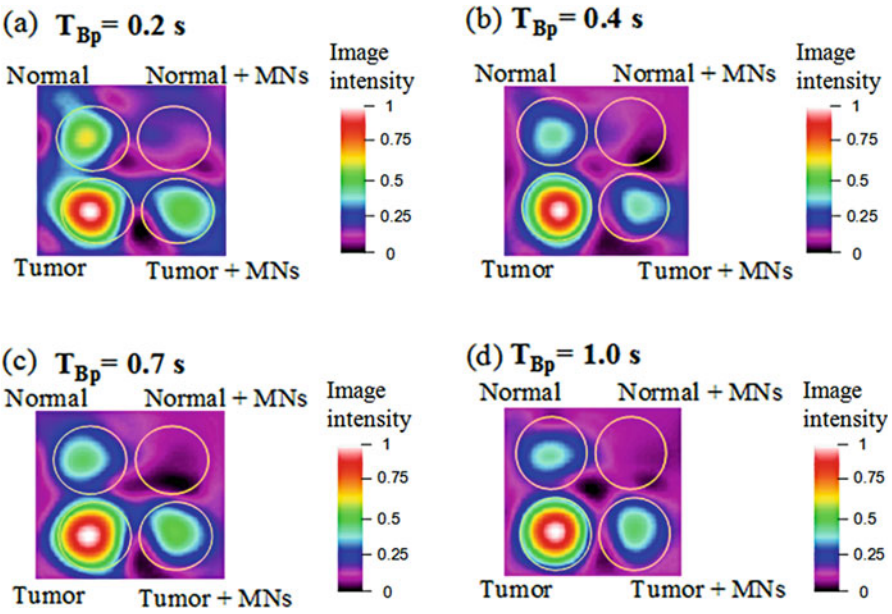

Fig. 9.30 T1-weighted images at TBP (**a**) 0.2 s, (**b**) 0.4 s, (**c**) 0.7 s, and (**d**) 1 s [76]

and 1.0 s [76]. We can obtain the image intensities of different tissue, I_{Tumor}, I_{Normal}, $I_{Tumor\ +\ MNS}$, and $I_{Normal\ +\ MNS}$, from the MR images and compare the image contrast by calculating the intensity ratio defined by the ratio of the image intensities between different tissues. It was found that the intensity ratio, I_{Tumor}/I_{Normal}, of the image = 1.8 at T_{BP} = 0.2 s and that the I_{Tumor}/I_{Normal} increases monotonically to 2.5 at T_{Bp} = 1 s. The estimated intensity ratio, $I_{Tumor\ +\ MNS}/I_{Normal\ +\ MNS}$, of the image = 1.8 at T_{BP} = 0.2 s, and the $I_{tumor\ +\ MNs}/I_{normal\ +\ MNs}$ increases monotonically to 92 at T_{Bp} = 1 s. The antibody-activated MNs significantly reduced the intensity of the normal region and the image contrast in the tumor region.

Figure 9.31 shows the MR images for a rat carrying the tumor at t = 0 and t = 24 h. The rat was injected with 1 ml of 0.06 emu/g of the Fe_3O_4-antiAFP MNs to study the effects of antibody-activated MNs on the image contrast. The MR images were taken with a 7 T MR imager at t = 0 and t = 24 h after injecting the Fe_3O_4-AntiAFP into the rat. The tumor and the normal regions used to estimate the intensity ratio are marked in the images. The intensity ratio, the I_{Tumor}/I_{Normal}, is equal to 2.2 at t = 0 before injecting MNs into rats, which indicates the absence of Fe_3O_4-AntiAFP MNs is in the tissues. The intensity ratio, $I_{Tumor+MNs}/I_{Nomal+MNs}$, is enhanced to 12.6 when a certain amount of the Fe_3O_4-AntiAFP MNs has targeted the tumor at t = 24 h. An enhancement of the image contrast due to the presence of MNs in the tissues is demonstrated. To further estimate the MNs accumulated in the tumor region, a scanning scan of high-T_c SQUID alternating current susceptometry [77] was applied to measure the magnetic signal from MNs.

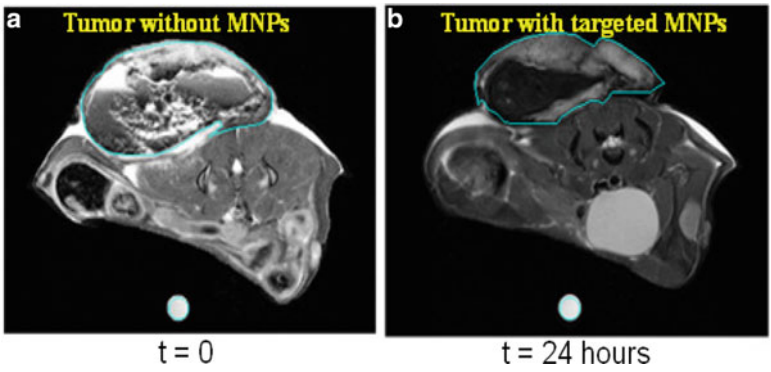

Fig. 9.31 The MR images of a rat carrying the tumor by using a 7 T–MRI imager at (**a**) t = 0 and (**b**) 24 h [76]

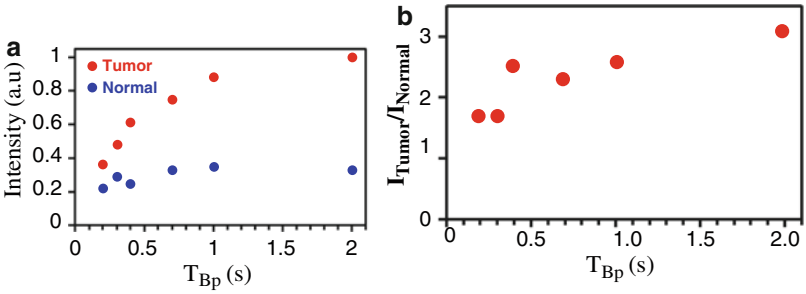

Fig. 9.32 (**a**) I_{tumor} and I_{normal} and (**b**) as a function of T_{BP} [76]

Figure 9.32a shows I_{Tumor} and I_{Normal}, derived from the intensity of images, as a function of T_{BP}. The intensities are detected with the high-T_c SQUID-based NMR/MRI, and the intensity was normalized to 1 for the liver tumor at $T_{BP} = 2$ s. Figure 9.32b shows the intensity ratio, I_{Tumor}/I_{Normal}, as a function of T_{BP}. It was found that the intensity ratio $I_{Tumor}/I_{Normal} = 0.35$ at $T_{BP} = 0.2$ s and I_{Tumor}/I_{Normal} increased to 3.2 at $T_{BP} = 2.0$ s, which are consistent with the reported data [78, 79]. The intensity ratio estimated from the 7 T MRI (7 T–MRI) is $(I_{Tumor}/I_{Normal})_{7T} = 2.2$. The SQUID-detected $I_{Tumor}/I_{Normal} = 2\sim3$ at $T_{BP} = 1$ to $T_{BP} = 2$ s, which is comparable with the $I_{Tumor}/I_{Normal} = 2.2$ estimated from the 7 T–MRI. Although the spatial resolution of T_1-weighted MRI in a low magnetic field cannot compete with that of a high-field MRI, the image contrast is quite comparable with that of 7 T–MRI. The data shows that the T_1-weighted MRI in low magnetic fields shows promise in discriminating tumors.

4.4.4 Conclusions and Future Perspective

In low-field NMR and MRI, the enhanced T_1-weighted contrast images were found. The $I_{tumor+MNS}/I_{normal+MNs}$ is enhanced by a factor of 30.6 when a certain amount

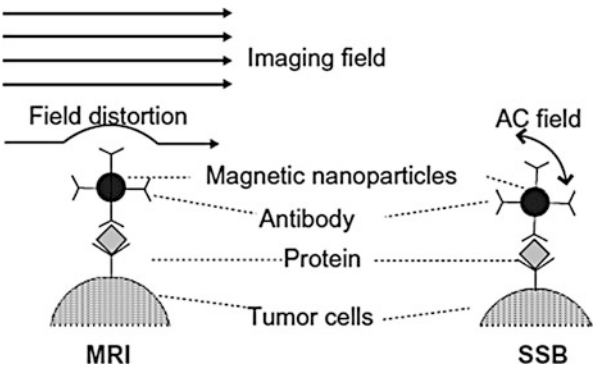

Fig. 9.33 Illustration of mechanism of (**a**) MRI and (**b**) SSB examination for antibody-mediated MNPs on liver tumor tissue [82]

of the Fe_3O_4-antiAFP MNs had targeted tumor tissues. Enhancing the tumor discrimination in the T_1-weighted images using antibody-activated MNs is demonstrated in low magnetic fields. Using antibody-activated MNs shows promises for enhancing tumor discrimination.

4.5 Scanning SQUID Biosusceptometry

4.5.1 Mechanism

The working principles of bound MNPs as image contrasts for MRI and scanning SQUID biosusceptometry (SSB) were compared in Fig. 9.33. For MRI, the DC high field is distorted bound MNPs, and then labeled tumors can be identified by darkening the image brightness. Numerous iron ions, biodegraded from MNPs, distorted the field, too [80]. This effect is especially valuable for the preoperative diagnosis of liver tumors because of the complexity of liver tissue [81].

For SSB, the AC magnetic field induced bound MNPs to express the AC susceptibility, i.e., the detected magnetic signals. In comparison with the IMR, the mechanism of AC magnetic field was the common, but the field strength, the frequency, and the field frequency composition were different due to the requirement of in vitro and noninvasive examination for the IMR and SSB. In comparison with MNP hyperthermia, both the strength and frequency of the AC field were much higher than IMR and SSB to generate heat from the out-of-phase magnetic susceptibility of MNPs.

4.5.2 Experimental and Instrumental Methodology

Instrumentation Setup

In general, the coregistration of the structural imaging and functional magnetic imaging has the complete diagnosis information. In other words, the 2D distribution of bound MNPs should be mapped to body photos. A dual-imaging model of SSB composed of a scanning probe and a SQUID sensor unit was developed for optical and magnetic imaging (Fig. 9.34). This scanning probe unit was composed of the sensing part and the excitation part. The former was the first-order vertical pickup

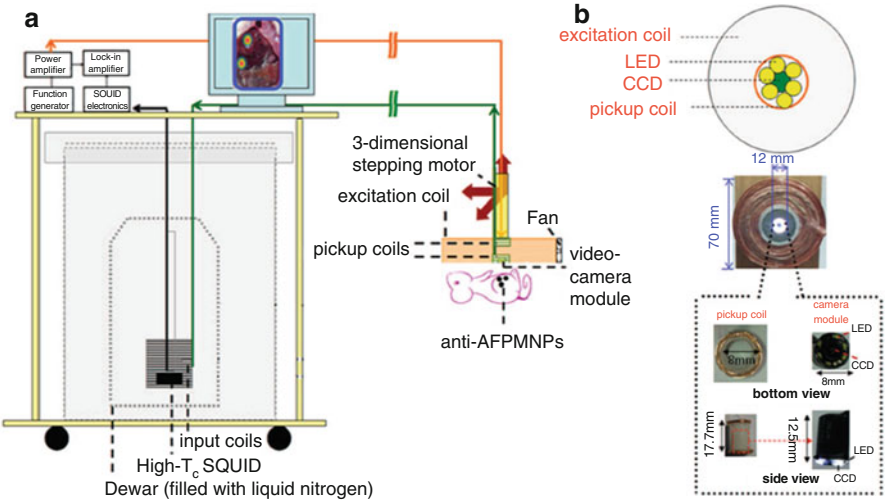

Fig. 9.34 The dual-model SSB for simultaneous optical imaging and magnetic imaging. (**a**) Scheme for the examination of tumor rats. (**b**) Bottom view of the scanning probe [84]

coils surrounding the charge-coupled device (CCD) module (Singapsy Enterprise Corp., Taiwan). The former was inserted into the latter of the circular excitation coil. A cooling fan was attached to the scanning probe unit. The excitation field strength and frequency of the excitation coil were set at 120 Oe and 400 Hz, respectively. The excitation exhibited low risk because the product of these two excitation parameters was substantially smaller than the biosafety criterion [83]. And the magnetic fields did not influence the work of the CCD module with the light-emitting diodes for lighting, while the scanning probe was close to the scanned torso. With a three-directional step motor, the 7-cm-diameter scanning probe unit can be operated as a robotic scanner for fast scanning along the torso.

For the dual-imaging model signals generated from the scanning probe, the optical video from the CCD module was recorded using a personal computer, but the magnetic signal was transferred by the connection of pickup coils to the input coil and to be detected by a high critical temperature SQUID magnetometer (JSQ GmbH, Germany). The magnetic signal was amplified approximately 29-fold with the typical conducting transfer coil of connecting pickup coils and the input coil [16] at first and amplified by the SQUID sensor secondarily. The SQUID sensor was cooled with a liquid nitrogen refrigerant in a dewar and shielded with a set of shielding cans. These parts constructed the SQUID unit. For the entire dual-imaging model SSB, the sensitivity achieved approximately 3 pT√Hz.

The construction of an optical image was processed in three steps. At first, a panoramic photograph was automatically converted from the recorded video of each scanning line. Subsequently, a single line image was generated from only the approximately central two third region of the panoramic photograph. Finally, by combining all line images, a two-dimensional optical image was constructed. And

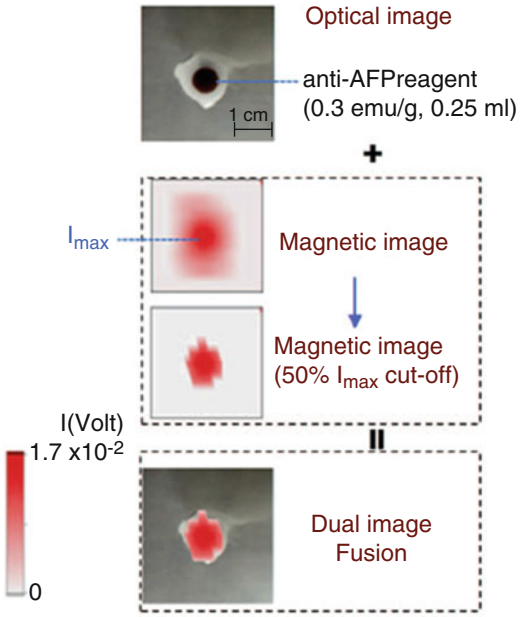

Fig. 9.35 Microtest tubes filled with anti-AFP reagents for dual-model imaging. The image process for the optical image, the magnetic images composed of I and only I larger than 50%, and the fused image [84]

the magnetic imaging was constructed by arranging the magnetic signals to the probe positions in turns. However, the magnetic image was always larger than the MNP distribution due to the magnetic field far away from magnetized MNPs. To study the modification of magnetic images, a microtest tube (Eppendorf Corp., NY, USA) filled with 0.3 emu/g and 0.25 g, approximately 28% of the injection dose for tumor rats, was imaged. Figure 9.35 shows the optical image for the top-down view of this microtest tube and the magnetic images for the 2D distribution of filled MNPs. Between two magnetic images of red spots, the upper one was composed of all raw signal intensity I, whereas the lower one was filtered signals where I is higher than 50% of the peak signal intensity I_{max} in this red spot. The spatial contour error between the red spot in the filtered magnetic image and the brown circle in the optical image is within 3 mm. Oppositely, the upper magnetic spot has more signals with I lower than 50% of I_{max}, distributed spherically from MNPs for a larger area than the optical image. Hence, the filter ratio of 50% I_{max} in the same red spot was selected to construct magnetic image. Further, the integral of I, defined as the product of the sum of I values greater than 50% of I_{max} and the pixel spacing, was used as the analysis factor of the magnetic image.

4.5.3 Key Research Findings

SSB Versus MRI

To prove the proposed working principles of MNPs detected by MRI and SSB (Fig. 9.36), rats were anesthetized using an inhalation system and measured before and after the injection of the anti-AFP reagent of 0.3 emu/g and 0.9 g through the tail

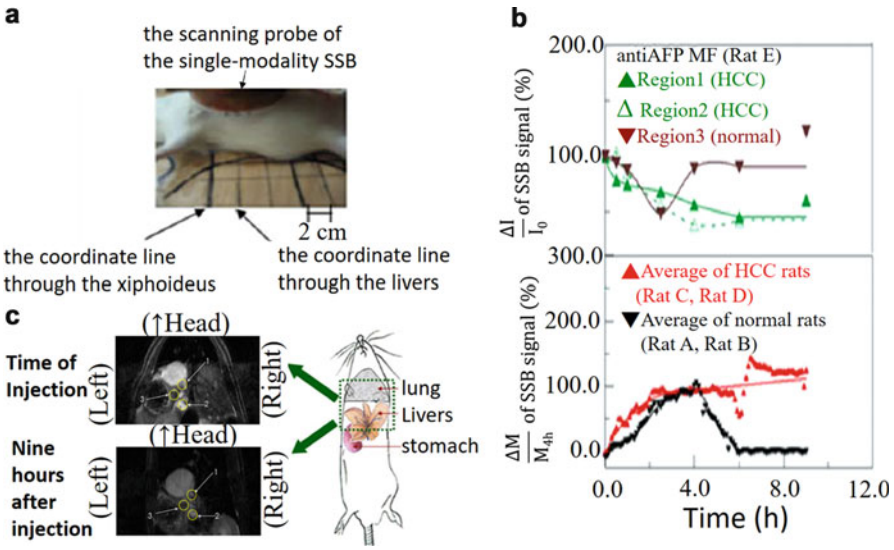

Fig. 9.36 In vivo examination of anti-AFP MNPs in the livers between by MRI and by SSB. (**a**) The alignment of the SSB probe for long-term examination. (**b**) MRI images of livers at 0 h and 9 h for the tumor rat (Rat E). (**c**) Analysis of $\Delta I/I_0$ using MRI in Regions 1, 2 (representing HCC tissue), and 3 (representing normal tissue with yellow outlines) for Rat E and of $\Delta M/M_{4h}$ using SSB for Rats A and B and Rats C and D [82]

vein. Two normal rats (Rat A and B) and two tumor rats with liver tumors (Rat C and D), also named as HCC, were statically and continuously measured by the single-modality SSB (Fig. 9.36a) [82], and one more tumor rat (Rat E) was imaged by a 3-T MRI system (Bruker, Ettlingen, Baden-Wurttemberg, Germany) (Fig. 9.36b).

In the SSB, the maximal signals by scanning the rat abdomen in a path of 2-cm interval from the xiphoideus (Fig. 9.36a) were defined as the signal of the liver center [82]. The measured intensity is proportional to the magnetization (expressed as M). However, the normalized magnetization variation $\triangle M/M_{4h}$, defined as the difference of the ΔM magnetization between any time and the time of injection (0 h) normalized by the magnetization at 4 h after injection M_{4h}, was used to compare injected normal rats and HCC rats. The results (Fig. 9.36c) show that the normalized magnetization $\Delta M/M_{4h}$ of normal and HCC rats increased rapidly within the first 2 h and remained at the maximal level until the fourth hour. However, $\Delta M/M_{4h}$ of normal rats decreased to its initial value after approximately the sixth hour and then subsequently maintained the level. Oppositely, $\Delta M/M_{4h}$ of HCC rats continued to increase gradually after the fourth hour.

In MRI, T_2-weighted axial images were at 1-mm intervals. Three liver regions (Region 1, Region 2, and Region 3, Fig. 9.36b) were selected and marked with a yellow circle to calculate the average intensity (expressed as I) of the entire circle. And the background black in each image was used as the reference signal. The

normalized intensity variation $\triangle I/I_0$ (defined as the $\triangle I$ intensity difference between any time and the time of injection over the initial intensity I_0 at 0 h) was used to analyze the MNP amount. $\Delta I/I_0$ of the HCC tissue in Regions 1 and 2 decreased to the lowest level at approximately the fourth hour and remained at this level, but $\Delta I/I_0$ in the normal tissue in Region 3 returned to its initial value at the fourth hour. In comparison between MRI and SSB, the signal variation showed the consistence in the metabolism for normal rats or tissue and the saturation targeting around 6 h for HCC rats or tissue but the difference in positive trend for SSB and in negative one for MRI. This proved the mentioned working principle comparison between the SSB and the MRI.

In Vivo/Ex Vivo Imaging

The secondary case of in vivo tests was to image the interior liver tumors within the liver lobes in a supine position at 0 h and 24 h and with their abdomens exposed at 24.5 h (Fig. 9.37a). The former simulated the preoperative diagnosis, and the latter did for the surgical navigation. The fused image shows that red spots were few at 0 h but clearly observable in the liver region at 24 h. And the results at 24.5 h expressed nearly identical red spots due to the skin without the influence on magnetic imaging.

Consequently, the ex vivo test was to image both the stacked and separated liver lobes after immersed in diluted formalin (concentration = 10%) for 1 week (Fig. 9.37b). It simulated the on-site discrimination of the positive needle biopsy. The ex vivo fused image showed the red spot of stacked livers was similar to that of the exposed livers in the in vivo fused image, except none in the lower-left region (Fig. 9.37a). This difference why a strong I in the in vivo fused image was probably because the lower-left part of the stacked livers was highly sustained by the other organs in the body for the short detection distance. Oppositely, a weak I in the ex vivo fused image that occurred from the lower-left part of the stacked livers was fixed in the formalin without the support of other organs.

In the fused image of separated liver lobes, dark spots in Lobes 1–4, and the red spot with the lowest intensity covered most of Lobe 5 (Fig. 9.37b). The positive imaging results were confirmed by the expression of abundant pink cytoplasms, representative of only cytoplasm in fast-growing tumor cells, in the HE stain and at least one brown region, indicating AFP antibodies, in the AFP stain in Lobes 1–4. Further, with the discrimination assistance of the stain results, the division of the imaging results into positive and negative groups could be determined with the integral of I at 0.10 volt.mm^2 (Fig. 9.37c).

SSB Versus Immunohistochemistry

Although the puncturing is the golden standard for tumor discrimination, immunohistochemistry (IHC), usually using fluorescent indicators for labeling and optical observation, with the fluorescent, always spent much time and manpower of pathologists, especially experienced ones, due to the precision focus variation in the observation of fluorescent microscope (Fig. 9.38). To prove the feasibility of the

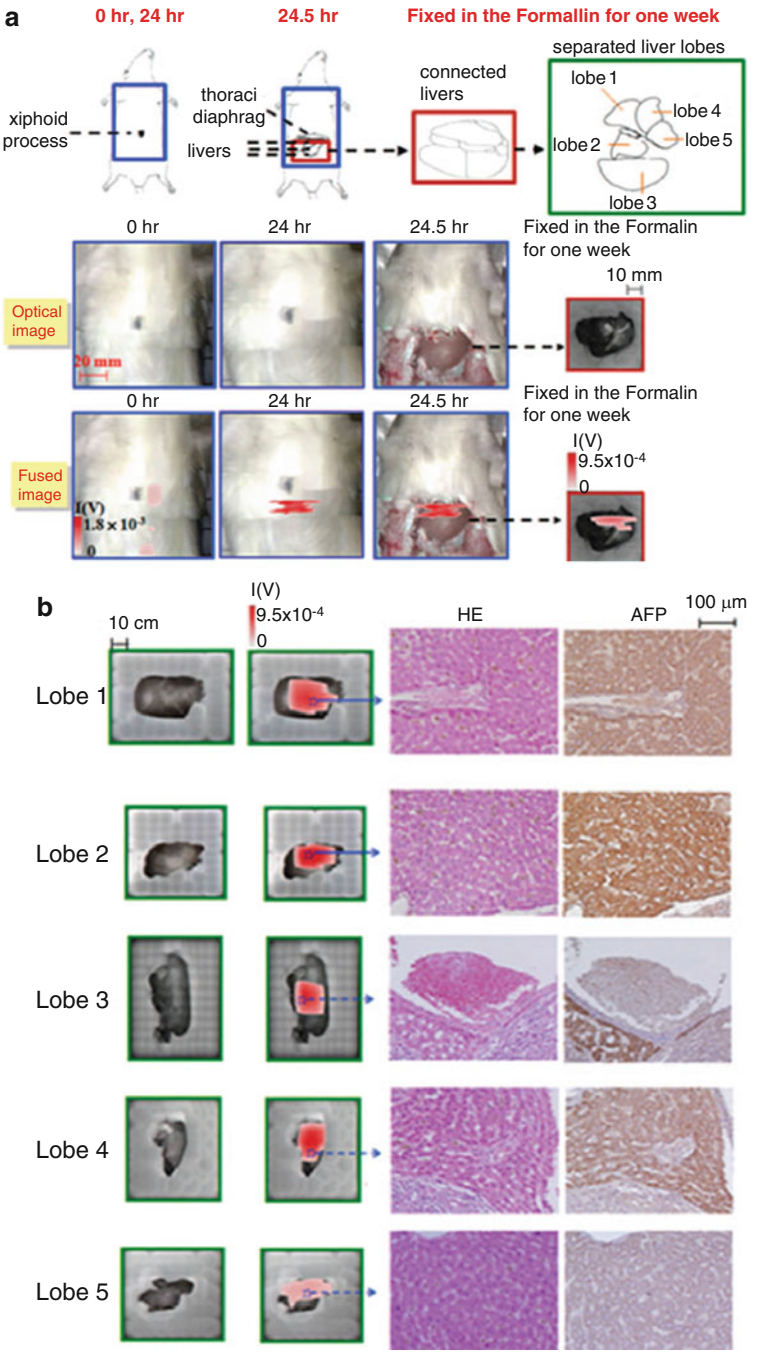

Fig. 9.37 (continued)

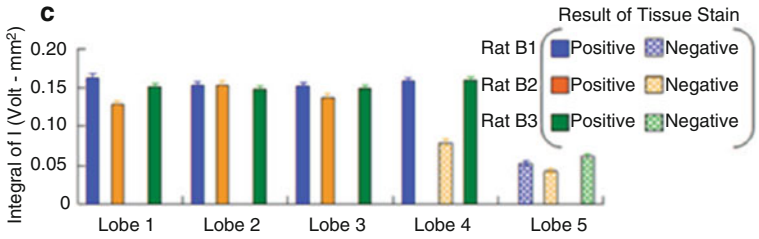

Fig. 9.37 The animal test for three tumor rats with liver tumors in the liver. (**a**) In vivo imaging for one tumor rat in a supine position at 0 h and 24 h and with its belly opened at 24.5 h. Ex vivo imaging for both the stacked block and separated lobe livers with the formalin fixation for 1 week. (**b**) Confirmation between dual-imaging SSB and tissue staining. The former was the red-spot region. The latter was HE and AFP stain. (**c**) Determination of the criterion between the positive and negative groups. By judging tissue staining of separated liver lobes (Lobes 1–5) of three tumor rats (Rats B1–3), the criterion of the integral of *I* by dual-imaging SSB was determined [84]

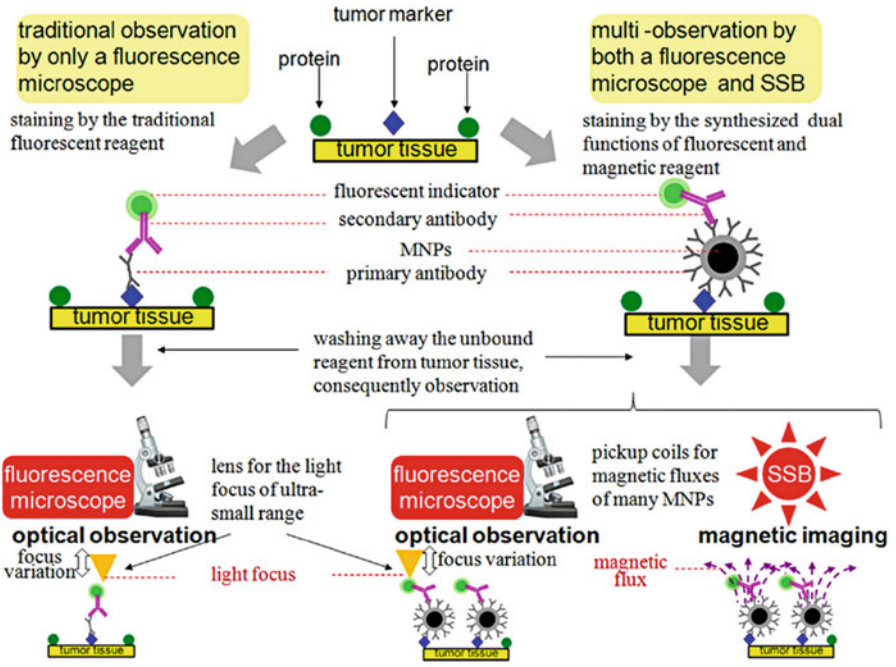

Fig. 9.38 Flowchart comparison between the current single-modality examination of IHC (left) by the fluorescent microscope and the proposed dual-modality examination of IHC (right) by the SSB and fluorescent microscope [86]

automatic IHC imaging with the dual-imaging SSB, bioprobe-coated MNPs connecting to the fluorescent indicators were used as dual-modality indicators for the confirmation of traditional IHC with the manual observation. Here, anti-carcinoembryonic antigen (anti- CEA) served as a primary antibody for the study

of colorectal cancer, the second-leading cause of cancer death in adults worldwide. And the excitation and emission wavelengths for the observed green hues of the fluorescence indicator were 358 nm and 461 nm, respectively. Consequently, two neighboring tissue slices on different microscope slides were separately immersed in the synthesized single and dual-modality reagents for approximately 5 min and then washed to clean the unbound reagents. Subsequently, microscope slides were examined by SSB for imaging the whole tissue slices in several seconds (the scanning area of 4 cm × 4 cm in the speed of 10 mm/s) and a fluorescence microscope (IX70, Olympus, Japan) for observing five points on each tissue slice in nearly 30 min.

Before any type of staining processes, no tissue slice exhibited red spots in the coregistered magnetic and optical image obtained by SSB or green spots in the fluorescent images (Fig. 9.39). After staining, for the single-modality reagent, still none exhibited in the coregistered SSB image. However, numerous green spots were found for points 1–3 and 5, but none for point 4, in the fluorescent images. This was no magnetic materials in the single-modality of the traditional IHC reagent. For the dual-modality reagent, the distribution of green spots in the fluorescent image was similar with those stained with single-modality reagent and also expressed red spots in the coregistered SSB image. The consistence between dual-modalities indicated that potentiality of rapid and automatic IHC for numerous clinical tissue by dual-imaging SSB and manual inspection for some negative-discrimination samples by a fluorescent image.

Furthermore, the coregistered images were used for the quantitative analysis of tumor cell amount of the entire microscope slide, by derivation from the measured sum intensity of the red spots. The derivation was found in two databases. One was the relationship between measured sum intensity and the MNP amount, obtained from the test results that different amounts of dried MNPs shaped into a 10-mm diameter circle on microscope slides at the same measurement distance of 2 mm were analyzed for the measured sum intensity by the dual-imaging SSB. The other was the basis of the average quantum of MNPs targeting one universal cell [87]. With these conversion standards, the tumor cells on the tissue could be quantified to approximately 10^{10} with an error of approximately 5×10^8 (Fig. 9.40). In addition, at fastest detection speed within 0.5 min, the minimum amount of tumor cells on the microscope slide was nearly 2×10^8, and this is suitable for high-sensitivity and high-throughput pathological examinations.

4.5.4 Conclusions and Future Perspective

In the mechanism, all the results of the in vivo examinations of MRI and SSB and biopsy assays exhibit the same dynamics of magnetic labeling. It verified that simple MNPs with anti-AFP coating expressed magnetic characteristics of AC susceptibility other than the distortion of the imaging field. Therefore, SSB based on the examination of AC susceptibility can be used as the instruments of intraoperative examination or other clinical requirements, extending the utilities of single magnetic modal MNPs.

In addition, a novel dual-imaging model SSB by integrating an optical camera and magnetic SSB was developed to fuse low-field magnetic images of MNP distributions and optical images for simultaneous functional and structural imaging. The feasibility of this novel dual-imaging model SSB was verified by the favorable

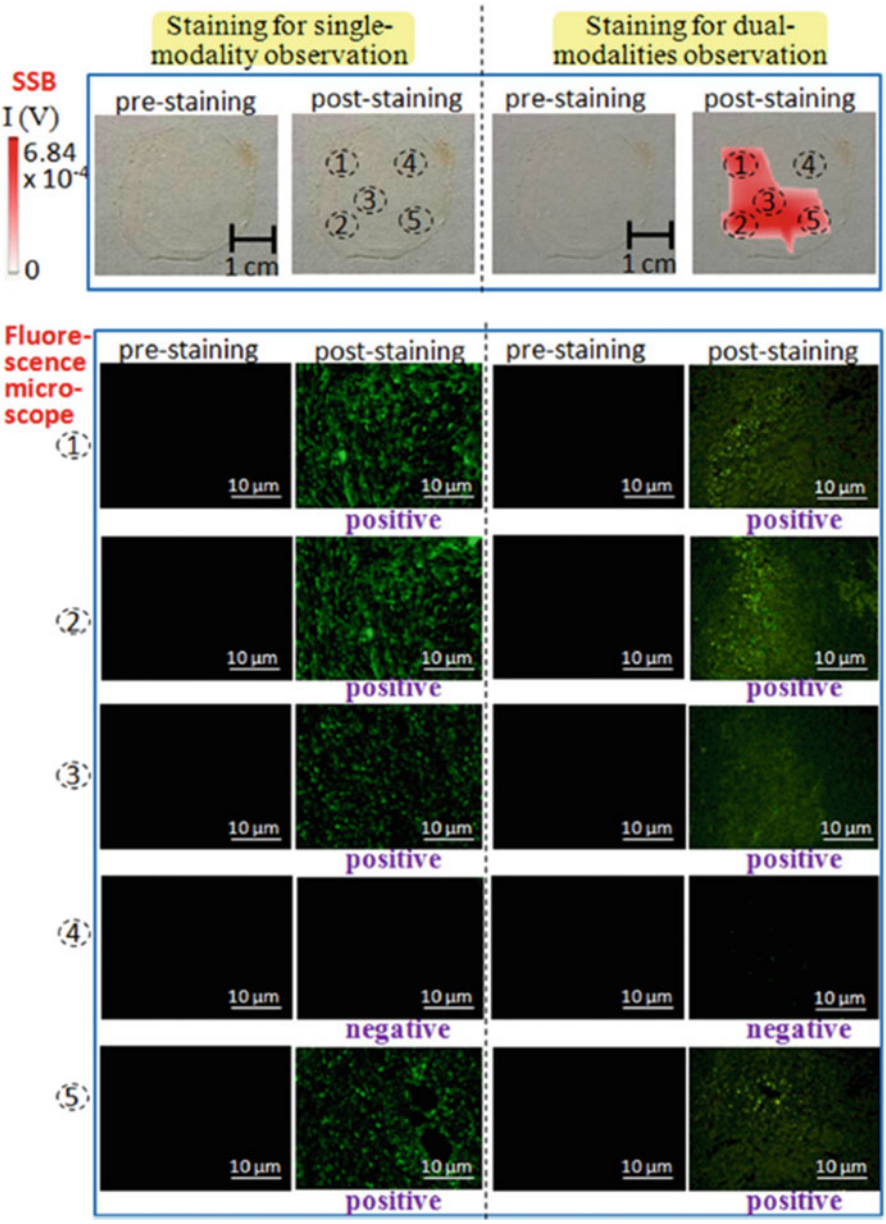

Fig. 9.39 Result of comparison between the staining reagent for the traditional single-modality examination of IHC (left) and the staining reagent for the proposed dual-modality examination of IHC (right) [86]

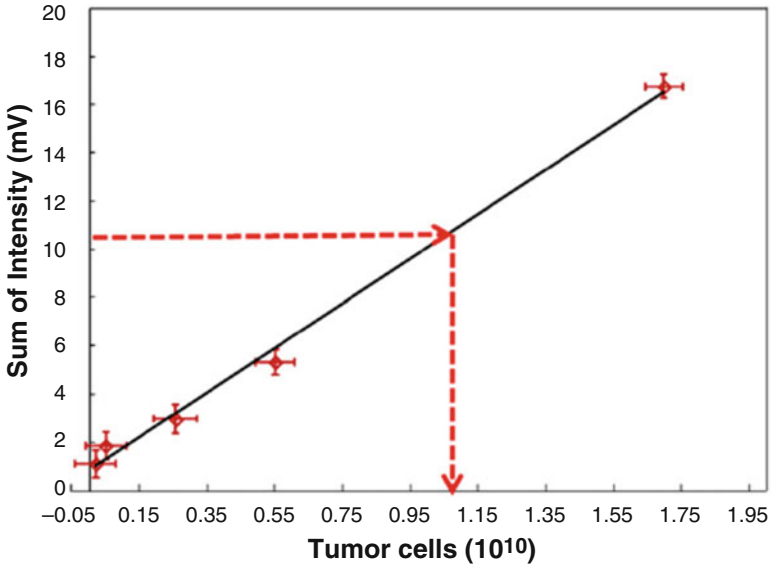

Fig. 9.40 Quantitative discrimination of tumor cells by conversion to the quantum of the MNPs on the tissue samples from the sum intensity of the red spots in the SSB images, as well as the average quantum of the MNPs targeting one universal cell [85, 86]

spatial agreement in animal tests, as well as confirmation from tissue staining. Hence, the application of imaging technologies of simple Fe_3O_4 MNPs was expanded from preoperative diagnosis by MRI to intraoperative positioning of tumors and preoperative imaging in clinics by using this novel dual-imaging model SSB, demonstrating the high potential of this method in the surgical navigation of MNP-targeted tumors in future clinical applications.

Besides, the current methodology for IHC entails using only a bioprobe-coated fluorescent reagent and requires experienced pathologists to validate the qualitative analysis obtained through time-consuming observations through a fluorescence microscope. In addition to the current methodology for IHC, the present study proposes a dual-modality methodology for achieving quick quantitative pathological analyses. Therefore, large-scale IHC analyses in hospital pathology departments can be quickly screened using SSB. If necessary, only certain samples comprising the few screened amount of tumor cells could be confirmed by an experienced pathologist.

In conclusion, this study demonstrates that using SSB is suitable for in vivo screening and in vitro examinations. Compared to using MRI, in vivo screening of HCC labeled with anti-AFP MNPs using SSB is more cost-efficient, easier to conduct, and more significant. These advantages increase the popularity of in vivo screening and reduce the costs of MNP reagents for patients. The number of MNPs measured in tissues was consistent with that of the biopsy test. These results further demonstrate the feasibility of in vivo screening of HCC in animals and clinical diagnosis in the future.

4.6 Ultrasound-Induced Magnetic Imaging

4.6.1 Mechanism

In MNPs of imaging contrast by current magnetic imaging, there are some disadvantages to be avoided. For example, the high-field MRI has deficiencies such as the limited time resolution, a vague image region with iron ions from MNP biodegradation, and two imaging times for analyzing the image brightness of MNPs between preinjection and postinjection. Similarly, magnetic particle imaging based on the nonlinear response of MNPs [88, 89] achieved high spatial resolution and 3D tomography of MNP distribution. However, the field of view and sample size were limited by the high-field gradient. Hence, the mechanism of high field or high-field gradient of MRI or magnetic particle imaging commonly consumes high cost and maintenance as well as high power.

Conversely, the MNP magnetization of a lower field or pulse consistently requires a highly sensitive magnetic sensor, so-called the superconducting quantum interference device. Magnetic relaxometry [90] detects the relaxation of MNPs after a strong pulse field. However, the particle characteristics, including size, temperature, and whether it is bound to tissue, strongly influence the results, but those of each MNP within an animal or human body are complex.

Another low-field imaging technology at approximately 100 Oe is the SSB [82, 84] based on AC magnetic susceptibility. Although the dual-imaging type of SSB has been applied in in vitro and in vivo animal tests, the future clinical diagnosis and surgical navigation for deep tumors also require the consumption of high power. Commonly, these two low-field imaging procedures achieve only 2D imaging.

To avoid these advantages of imaging MNPs, a novel mechanism of ultrasound-motivated magnetic imaging (Fig. 9.41) was proposed. Labeled MNPs on target tumors are magnetized under a DC magnetic field. The ultrasound chips and pickup coils are used to vibrate MNPs and detect the ultraweak magnetic signals of MNPs, respectively. The ultrasound excitation and magnetic detection devices are integrated

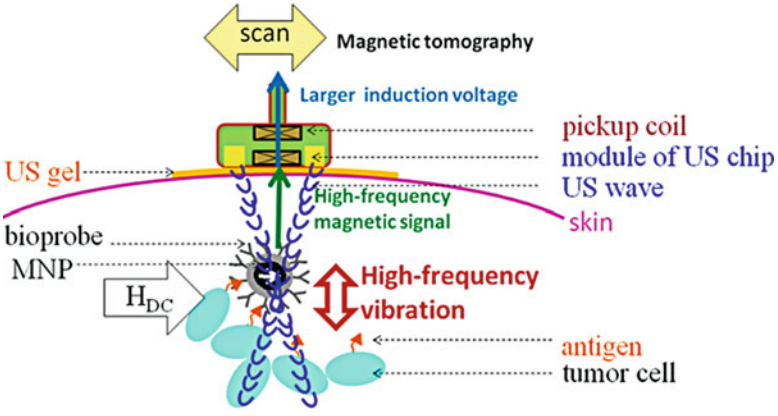

Fig. 9.41 Mechanism of the ultrasound-motivated magnetic imaging [91]

in a small probe. Consequently, labeled MNPs on target tumors were imaged for tumor imaging by mechanically moving the integrated probe in 2D or by electrically varying the ultrasound focus in 3D. The reasons why the excitation of MNPs utilized the ultrasound instead of the magnetic AC field are explained as follows. The first is that the ultrasound is markedly superior to the magnetic field in the characterization of the transportation attenuation. The second is that the inducted AC voltage of a pickup coil increases with the frequency based on Faraday's law of induction. Generally, the generation of a high-frequency magnetic excitation field by AC electromagnetic coils always consumes large power because the coil impedance increases with the frequency. By contrast, ultrasound-motivated magnetic imaging divides a high-frequency magnetic excitation field into two parts of the high-frequency ultrasound excitation field and the DC magnetic excitation field. Both the ultrasound part by ultrasound piezoelectric chips and DC magnetic part by coils or magnet consume relatively much low excitation power. It is mentioned that superparamagnetic MNPs are the focus material; a low DC magnetic field around several thousands of gauss can achieve the saturation magnetization of MNPs [44, 46]. In comparison with the ultrasound imaging, ultrasound-motivated magnetic imaging is to image MNPs, rather than the biological tissue, that is, to work as a type of functional rather than structural imaging with limited specificity of tumor discrimination as ultrasound imaging or MRI. Hence, ultrasound-motivated magnetic imaging makes up the ultrasound imaging for achieving complete medical imaging.

In comparison with the gold standard of DC magnetic-characterization instrument, vibration sample magnetometer [41, 42], both the ultrasound-motivated magnetic imaging and a vibration sample magnetometer have the common mechanism, that is, the generation of a detected magnetic signal by vibrating samples. The difference is that a vibration sample magnetometer utilizes a mechanical vibration motor and a linking holder to shake the sample at the low frequency, typically less than 100 Hz. Consequently, it presents disadvantages, for example, the radon error of measured magnetic signal from the misalignment of the sample on the long and vibrated holder in the magnetic field and the low induction voltage of a pickup coil caused by a low-frequency vibration of a mechanical motor. Hence, the detection structure of a vibration sample magnetometer thus far has limited the application in detection of magnetic samples, unable for magnetic imaging. Oppositely, the ultrasound-motivated magnetic imaging by an ultrasound vibration wave can easily manipulate the vibration energy to spatially focus on the distribution of MNPs through only the biological tissue itself, rather than the additional vibration holder and alignment mechanism in a vibration sample magnetometer.

In addition, this mechanism is very different from the pulsed magnetomotive ultrasound imaging [93]. It used a high-intensity pulsed magnetic field to excite cells or tissue labeled with MNPs. Consequently, the ultrasound imaging is used to monitor the mechanical response of the tissue (i.e., tissue displacement) to an externally applied magnetic field. Summarily, the pulsed magnetomotive ultrasound imaging has three differences from these works. One is the excitation method of the high-intensity pulsed magnetic field, rather than the low-power ultrasound and the

no-power DC magnetic field. The secondary is the pulse repetition frequency of tens of Hz up to kilohertz, rather than several megahertz. The third is the imaging technology by the ultrasound, rather than the magnetic imaging.

4.6.2 Experimental and Instrumental Methodology

The platform was composed of the instrument unit, the superconducting quantum interference device (SQUID) unit, and the probe unit (Fig. 9.42). The instrument unit and the SQUID unit were the same as the SSB. In the probe unit, a light and compact module of ultrasound chips existed for three ultrasound focuses at three depths. Besides, the magnet set with the uniform field in one horizontal direction was designed to magnetize MNPs.

The unique feature was the mechanism of exciting MNPs. Different from an AC magnetic field to magnetize MNPs in the magnetic discipline, it utilized a DC magnetic field to magnetize MNPs and an ultrasound field to vibrate MNPs. Besides, 12 ultrasound modules for three ultrasound focuses at three depths at 5, 10, and 15 mm were involved. For each focus depth, four ultrasound modules with tilt ultrasound chips ($2 \times 2 \times 0.4$ mm in size, 0.014 g in weight, and 5 MHz at operation frequency) were aligned in the distance of 4.55, 9, and 13.5 mm from the center of the scanning probe. The scanning probe possessed compact size of 3 cm in diameter and the light weight of approximately 5 g, not as heavy as several kilograms and as large as 7 cm for the probe unit of the SSB with the excitation coil [5, 84]. It was powerful for the clinical requirement. Moreover, the ultrasound-motivated magnetic

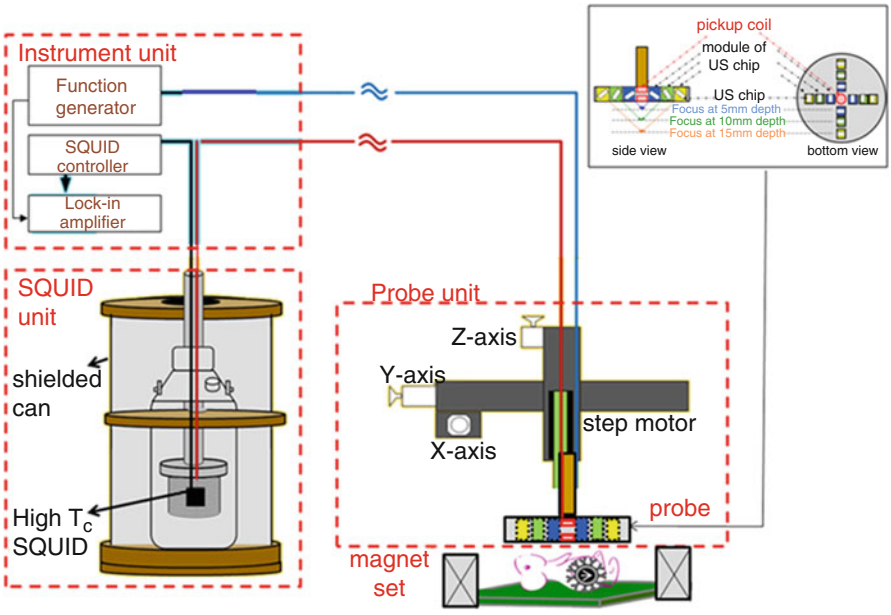

Fig. 9.42 Platform for the ultrasound-motivated magnetic imaging [91]

imaging showed absolute biosafety caused by a DC magnetization of only several thousands of Oe for achieving the saturation magnetization of MNPs, rather than AC magnetization with the consideration of power biosafety [83]. In the sensing mechanism of the probe unit, it was the first-order vertical pickup coils surrounded by 12 ultrasound modules. With the transfer coil [16], the magnetic signal was sensed by a sensitive SQUID sensor (JSQ GmbH, Germany). The sensitivity of approximately 87 pT/√Hz was primarily.

4.6.3 Key Research Findings

Table 9.3 shows the context of the phantom tests and the animal tests. In Fig. 9.43a, the ultrasound phantom and a polylactic-acid tube were inserted into a ring of the magnet set, where the alignment of each magnet in this ring set followed the Halbach array [18] to generate the uniform direction of a magnetic field. In phantom tests, the scanning probe touched the thin film of ultrasound gel on the upper surface of the phantom and polylactic-acid tube; scanned around the shape centers of anti-AFP MNP distributions in a 3×3 cm area, at a speed of 1 mm/step by an $x - y$ step motor. In each scanning step, three ultrasound foci were switched in turns to vibrate

Table 9.3 Phantom and animal tests in this study [91]

Test type	Test context
Phantom tests	Sample conditions
	Dried anti-AFP MNPs of approximately 60 μg Fe were deposited on thin gauzes of 0.1 mm in thickness for the circle, triangle, and square of 1 cm in side length or diameter. The field strengths in Anti-AFP MNP distribution were approximately 67,277, 68,153, and 68,790 A/m
	Imaging cases
	(Case P1) The circle, triangle, and square of Anti-AFP MNPs located in the depth of 5, 10, and 15 mm from the upper surface of the phantom
	(Case P2) The gaps between two circle shapes of Anti-AFP distribution in the depth of 10 mm varied 1, 3, and 5 mm
Animal tests	Imaging tumors
	(Case A1) A liver tumor ($12 \times 7 \times 12$ mm in length, width, and height) was implanted on the back of the anesthetized rat
	(Case A2) Liver tumors were implanted in rat livers
	Dose of magnetic reagent
	(Case A1) Directly injecting magnetic reagent (2.01×10^{-2} m^3/kg and 750 μl) into the liver tumor
	(Case A2) Indirectly injecting magnetic reagent (3.77×10^{-3} m^3/kg and 1 ml) into the tail vein
	Magnetization field
	(Case A1) The cascade of porous polylactic-acid ring and the ring magnet provided 221,338, 218,949, and 62,102 A/m in depth of 5, 10, and 15 mm from the upper surface
	(Case A2) This U-type of magnet ring generated major magnetic field of 179,140~210,987 A/m and 105,096 A/min one direction for the x-y plane of 5, 10, and 15 mm deep

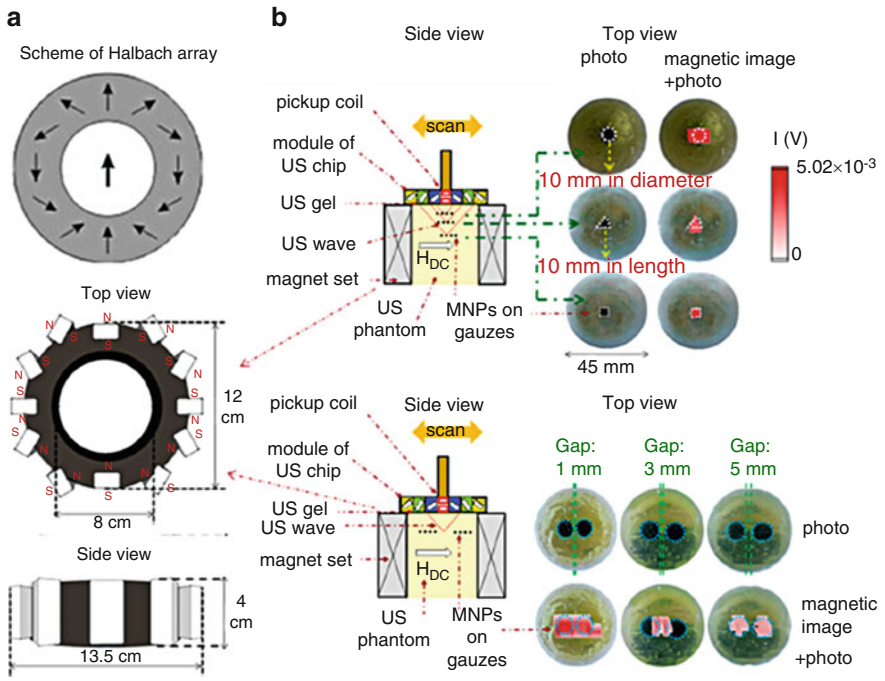

Fig. 9.43 Phantom tests. (**a**) The utilized magnet set and the uniform fields of 67,277, 68,153, and 68,790 A/m at depths of 5, 10, and 15 mm. (**b**) Three red shapes – a circle, triangle, and square □ of MNPs at depths of 5, 10, and 15 mm are similar to the black ones in the photos. (**c**) For separated MNP distributions of 1 cm in diameter, 10-mm deep, and with gaps of 1, 3, and 5 mm, a large and strong red spot was not distinguishable for the gap of 1 mm, but two connected or separated red spots were distinguishable for the gaps of 3 and 5 mm [91]

three anti-AFP MNP distributions at different depths, separately. The total imaging spent approximately 45 min. In Fig. 9.43b, it shows that three red spots of magnetic images in Case P1were close to white-dotted lines, i.e., the boundary of the real anti-AFP MNP distributions. The favorable consistency shows the feasibility for identifying tumors at different distances. In Fig. 9.43c, it shows a large red rectangle, two connected circles, and two separate circles for the gap of 1, 3, and 5 mm, separately. It indicates identifying separated tumors by this ultrasound-induced magnetic imaging was feasible. With the well discrimination of MNP distribution in different shapes and depths (Case P1) (Fig. 9.43b) and different gaps (Case P2) (Fig. 9.43c), magnetic tomography for MNP-labeled tumors could be achieved. With current simulation results of the beam pattern of each ultrasound focus, the thickness of one magnetic planar tomography may be defined as 5 mm due to the vertical distribution of ultrasound intensities larger than 50% of the maximum intensity around 5 mm.

In Case A1, anti-AFP MNPs were bound to liver tumors by directly injecting a magnetic reagent into a liver tumor implanted on the back of an anesthetized rat.

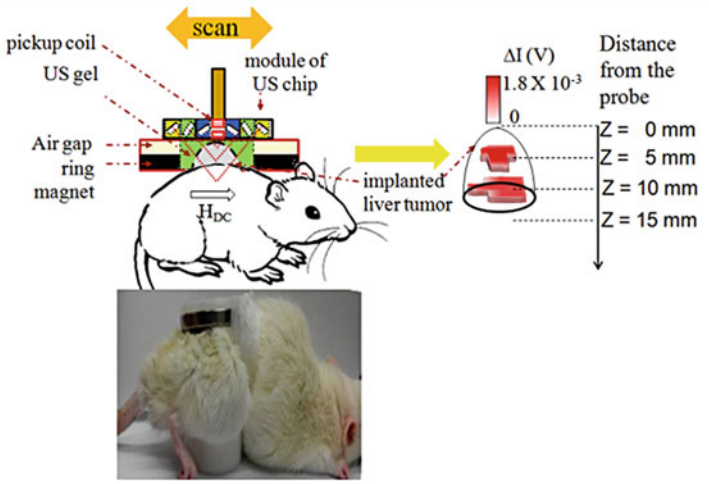

Fig. 9.44 Animal test of the implanted tumor on rat back. Anti-AFP MNPs were bound to liver tumors by directly injecting a magnetic reagent (1.6 emu/g and 750 μl) into a liver tumor (12 × 7 × 12 mm in length, width, and height) implanted on the back of an anesthetized rat. In addition, the ultrasound gel and the cascade of a porous polylactic-acid ring and a commercial ring magnet were inserted into the tumor on the rat back. The red spots of magnetic tomography at depths of 5 and 10 mm within tumors were apparent but seldom appeared at a depth of 15 mm [91]

Next, the tumor on the back of the rat was surrounded by a cascade of a commercial ring magnet (15 mm in inner diameter and 6 mm in thickness) and a polylactic-acid ring (1.5 mm in inner diameter and 5 mm in thickness), which was porous to prevent any vibration of the ring magnet from the ultrasound chips of the probe. The ultrasound gel filled the gap between the liver tumor and the cascade. The probe touched the thin film of the ultrasound gel and imaging with the same scanning speed and switching sequence of three ultrasound foci as the phantom tests. It expended approximately 7 min. In Fig. 9.44, the magnetic signals of anti-AFP MNPs were revealed with ΔI, defined as the intensity difference between preinjection and postinjection. It shows that two apparent red spots and hardly-visible one at two high and the lowest depths because numerous and fewest separately distributed within the back tumor and the rat's tumor and the rat's body. The magnetic tomography is reasonable because the external magnetic fields of the ring magnet surrounding the tumors attracted anti-AFP MNPs to remain within the tumors. The feasibility of clear identifying tumors was proved.

In Case A2, liver tumors were implanted in rat livers. The commercial ultrasound imager (DP-50vet, Mindray Corp., China) was used to observe each vertical tomography livers at first and then to model rough 3D livers (Fig. 9.45a). Consequently, the horizontal ultrasound tomography at depths of 5, 10, and 15 mm was sliced from the rough 3D model. The anesthetized rat was injected with a magnetic reagent through the tail veins of a rat and imaged inside a U-shaped magnet ring with magnetic horizontal fields with an open hole for the 40 × 40 mm scanning region of the probe.

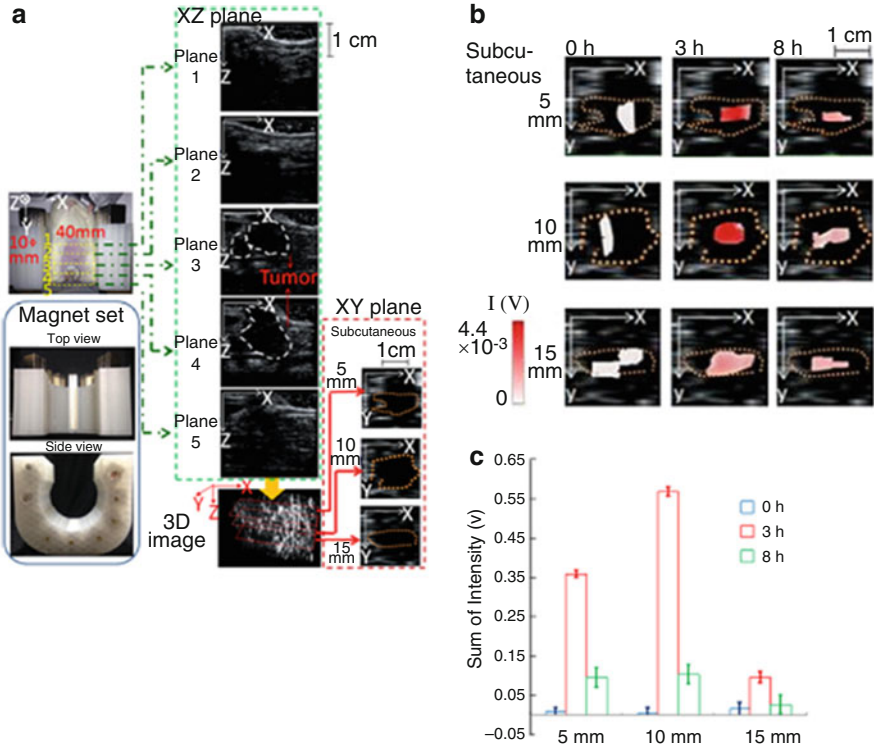

Fig. 9.45 Animal test of the implanted tumor in rat livers. (**a**) The U-type of magnet set, based on the Halbach array, for one major direction of a magnetic field, was fabricated to magnetize MNPs within rat livers. The ultrasound and probe of the ultrasound-motivated magnetic imaging platform scanned the abdomen region of 40 × 40 mm. Five ultrasound x-z planes were used to construct the 3D ultrasound image, which could be used to slice three ultrasound x-y planes at subcutaneous depths of 5, 10, and 15 mm. (**b**) The coregistrations of three magnetic tomographies and ultrasound x-y planes at subcutaneous depths of 5, 10, and 15 mm are shown. (**c**) Between magnetic spots at subcutaneous depths of 5, 10, and 15 mm, the sum of intensity was almost the same at 0 h (preinjection), the highest at 3 h postinjection, and exhibited decay at 8 h postinjection [91]

The scanning speed and switching sequence of three ultrasound foci were the same with the phantom tests. In Fig. 9.45b, it shows almost no coregistered magnetic tomography signs of red spots in 5-, 10-, and 15-mm-deep ultrasound images at 0 h. At 3 h, the coregistered magnetic sign ultrasound images showed apparent red spots at 5 and 10 mm but a light red spot at 15 mm. At 8 h, the coregistered signs show light-red and smaller spots at 5-, 10-, and 15-mm deep. Further, red spots of the functional magnetic tomography are distributed within the white dashed lines of the structural ultrasound images. Some possibilities exist to illustrate the image difference. One is the targeting amounts of anti-AFP MNPs enough for only the central regions of liver tumors near hepatic arteries. Some of the injected anti-AFP MNPs circulated away from liver tissue. Another possible reason was that the outer tissue

may have been fibrosis or dead liver tumors and then difficultly targeted by anti-AFP MNP targeting. Regardless, a difference between magnetic images of MNPs and ultrasound imaging exists. The magnetic images were more reliable for the distribution of live tumors because the former plays the functional role, whereas the latter is a structural image. Hence, the high-possibility region of liver tumors was marked with the distinct expression.

In Fig. 9.45c, for three depths, the sum of magnetic intensity of red spots was almost similar at 0 h; it reached its highest value at 3 h postinjection and exhibited decay at 8 h postinjection. It was explained as follows. At 0 h, the magnetic background came from magnetic proteins in livers, for example, ferritin protein. At 3 h postinjection, MNPs circulated to livers. At 8 h postinjection, only some of the remaining anti-AFP MNPs were bound to liver tumors, and others circulated away from the livers or were biodegraded by macrophages [5]. Actually, the imaging distance of the ultrasound-induced magnetic imaging is not limited to any specific depth, for example, the discussion depth of 15 mm here. Some factors, such as the vibration amplitude and the amount of targeted anti-AFP MNPs, influence the limitation depth.

4.6.4 Conclusions and Future Perspective

The interdisciplinary mechanism of ultrasound-induced magnetic imaging and a platform for magnetic tomography at different depths were verified. From the results of the phantom tests, two connected or separated red spots were minimally distinguishable with a gap of 3 mm. From the results of the animal tests, the image overlap between the ultrasound-induced magnetic imaging and the ultrasound images was favorable. The proposed ultrasound-induced magnetic imaging has the potential for popularity in biomedical applications due to the low-power consumption and sufficient spatial resolution.

5 Conclusion and Future Perspective

Due to MNPs with many superior characteristics, some advanced magnetic tools, for example, immunomagnetic reduction assay, vibrating sample magnetometer, bioassay using blocking temperature, low-field nuclear magnetic resonance/magnetic resonance imaging, scanning SQUID biosusceptometry, and ultrasound-induced magnetic imaging, have been developed for medical diagnostics. In addition to the mentioned in vitro diagnostics, ex vivo examination, and in vivo imaging, MNPs and other developing magnetic tools have powerful potentiality for the medical applications.

References

1. Sohn SY, Choi JH, Kim NK, Joung JY, Cho YY, Park SM, Kim TH, Jin SM, Bae JC, Lee SY, Chung JH, Kim SW (2014) The impact of iodinated contrast agent administered during

preoperative computed tomography scan on body iodine pool in patients with differentiated thyroid cancer preparing for radioactive iodine treatment. Thyroid 24(5):872–877
2. Gibbs-Strauss SL, Nasr KA, Fish KM, Khullar O, Ashitate Y, Siclovan TM, Johnson BF, Barnhardt NE, Tan Hehir CA, Frangioni JV (2011) Nerve-highlighting fluorescent contrast agents for image-guided surgery. Mol Imaging 10(2):91–101
3. Paefgen V, Doleschel D, Kiessling F (2015) Evolution of contrast agents for ultrasound imaging and ultrasound-mediated drug delivery. Front Pharmacol 6:197
4. Jianga W, Yang HC, Yang SY, Horng HE, Hung JC, Chen YC, Hong CY (2004) Preparation and properties of superparamagnetic nanoparticles with narrow size distribution and biocompatible. J Magn Magn Mater 283(2–3):210–214
5. Tseng WK, Chiech JJ, Yang YF, Chiang CK, Chen YL, Yang SY, Horng HE, Yang HC, Wu CC (2012) A noninvasive method to determine the fate of Fe_3O_4 nanoparticles following intravenous injection using scanning SQUID biosusceptometry. PLoS One 7(11):e48510
6. Jun YW, Lee JH, Cheon J (2008) Chemical design of nanoparticle probes for high-performance magnetic resonance imaging. Angew Chem Int Ed 47(28):5122–5135
7. Thomas R, Park IK, Jeong YY (2013) Magnetic iron oxide nanoparticles for multimodal imaging and therapy of cancer. Int J Mol Sci 14(8):15910–15930
8. Nacev A, Weinberg IN, Stepanov PY, Kupfer S, Mair LO, Urdaneta MG, Shimoji M, Fricke ST, Shapiro B (2015) Dynamic inversion enables external magnets to concentrate ferromagnetic rods to a central target. Nano Lett 15(1):359–364
9. Kumar CSSR, Mohammad F (2011) Magnetic nanomaterials for hyperthermia-based therapy and controlled drug delivery. Adv Drug Deliv Rev 63(9):789–808
10. McBain SC, Yiu HHP, Dobson J (2008) Magnetic nanoparticles for gene and drug delivery. Int J Nanomedicine 3(2):169–180
11. Grass RN, Stark WJ (2006) Gas phase synthesis of fcc-cobalt nanoparticles. J Mater Chem 16(19):1825–1830
12. Taylor RM, Huber DL, Monson TC, Ali AMS, Bisoffi M, Sillerud LO (2011) Multifunctional iron platinum stealth immunomicelles: targeted detection of human prostate cancer cells using both fluorescence and magnetic resonance imaging. J Nanopart Res 13(10):4717–4729
13. Rogosnitzky M, Branch S (2016) Gadolinium-based contrast agent toxicity: a review of known and proposed mechanisms. Biometals 29(3):365–376
14. Lu AH, Salabas EL, Schüth F (2007) Magnetic nanoparticles: synthesis, protection, functionalization, and application. Angew Chem Int Ed 46(8):1222–1244
15. Xu C, Yuan Z, Kohler N, Kim J, Chung MA, Sun S (2009) FePt nanoparticles as an Fe reservoir for controlled Fe release and tumor inhibition. J Am Chem Soc 131(42):15346–15351
16. Kondo T, Itozaki H (2004) Normal conducting transfer coil for SQUID NDE. Supercond Sci Technol 17(3):459–462
17. Tsukamoto A, Saitoh K, Suzuki D, Sugita N, Seki Y, Kandori A, Tsukada K, Sugiura Y, Hamaoka S, Kuma H, Hamasaki N, Enpuku K (2005) Development of multisample biological immunoassay system using HTS SQUID and magnetic nanoparticles. IEEE Trans Appl Supercond 15(2):656–659
18. Lee NC, Yang SY, Chieh JJ, Huang PT, Chang LM, Chiu YN, Huang AC, Chien YH, Hwu WL, Horng HE, Chiu MJ (2017) Blood beta-amyloid and tau in down syndrome: a comparison with Alzheimer's disease. Front Aging Neurosci 8:316
19. Yang SY, Chiu MJ, Lin CH, Horng HE, Yang CC, Chieh JJ, Chen HH, Liu BH (2016) Development of an ultra-high sensitive immunoassay with plasma biomarker for differentiating Parkinson disease dementia from Parkinson disease using antibody functionalized magnetic nanoparticles. J Nanobiotechnol 14(1):41
20. Huang KW, Yang SY, Hong YW, Chieh JJ, Yang CC, Horng HE, Wu CC, Hong CY, Yang HC (2012) Feasibility studies for assaying alpha-fetoprotein using antibody- activated magnetic nanoparticles. Int J Nanomedicine 7:1991–1996
21. Chiu MJ, Chen YF, Chen TF, Yang SY, Yang FPG, Tseng TW, Chieh JJ, Chen JCR, Tzen KY, Hua MS, Horng HE (2014) Plasma tau as a window to the brain – negative associations with

brain volume and memory function in mild cognitive impairment and early Alzheimer's disease. Hum Brain Mapp 35(7):3132–3142
22. Chiu MJ, Yang SY, Horng HE, Yang CC, Chen TF, Chieh JJ, Chen HH, Chen TC, Ho CS, Chang SF, Liu HC, Hong CY, Yang HC (2013) Combined plasma biomarkers for diagnosing mild cognition impairment and Alzheimer's disease. ACS Chem Neurosci 4(12):1530–1536
23. Chiu MJ, Yang SY, Chen TF, Chieh JJ, Huang TZ, Yip PK, Yang HC, Cheng TW, Chen YF, Hua MS, Hong HE (2012) New assay for old markers – plasma beta amyloid of mild cognitive impairment and Alzheimer's disease. Curr Alzheimer Res 9(10):1142–1148
24. Yang CC, Huang KW, Yang SY, Chen HH, Chen TC, Ho CS, Chang SF, Chieh JJ, Horng HE, Hong CY, Yang HC (2013) Development for high-accuracy in-vitro assay of vascular endothelial growth factor using nano-magnetically labeled immunoassay. J Nanomater 2013:695276
25. Hsieh WP, Chieh JJ, Yang CC, Yang SY, Chen PY, Huang YH, Hong YW, Horng HE (2013) Stability study for magnetic reagent assaying Hb and HbA1c. J Magn Magn Mater 326:147–150
26. Lu MW, Yang SY, Horng HE, Yang CC, Chieh JJ, Hong YW, Hong CY, Yang HC, Wu JL (2012) Immunomagnetic reduction assay for nervous necrosis virus extracted from groupers. J Virol Methods 181(1):68–72
27. Yang SY, Chieh JJ, Wang WC, Yu CY, Lan CB, Chen JH, Horng HE, Hong C-Y, Yang HC, Huang W (2008) Ultra-highly sensitive and wash-free bio-detection of H5N1 virus by immunomagnetic reduction assays. J Virol Methods 153(2):250–252
28. Yang SY, Jian ZF, Chieh JJ, Horng HE, Yang HC, Huang IJ, Hong CY (2008) Wash-free, antibody-assisted magnetoreduction assays of orchid viruses. J Virol Methods 149(2):334–337
29. Yang SY, Chieh JJ, Yang CC, Liao SH, Chen HH, Horng HE, Yang HC, Hong CY, Chiu MJ, Chen TF, Huang KW, Wu CC (2013) Clinic applications in assaying ultra-low concentration bio-markers using HTS SQUID-based AC magnetosusceptometer. IEEE Trans Appl Supercond 23(3):1600604–1600604
30. Chieh JJ, Huang KW, Chuang CP, Wei WC, Dong JJ, Lee YY (2016) Immunomagnetic reduction assay on des-gamma-carboxy prothrombin for screening of hepatocellular carcinoma. IEEE Trans Biomed Eng 63(8):1681–1686
31. Yang CC, Yang SY, Chieh JJ, Horng HE, Hong CY, Yang HC (2012) Universal behavior of biomolecule-concentration-dependent reduction in AC magnetic susceptibility of bioreagents. IEEE Magn Lett 3:1500104
32. Hong CY, Wu CC, Chiu YC, Yang SY, Horng HE, Yang HC (2006) Magnetic susceptibility reduction method for magnetically labeled immunoassay. Appl Phys Lett 88(21):212512
33. Chieh JJ, Yang SY, Jian ZF, Wang WC, Horng HE, Yang HC, Hong CY (2008) Hyper-high-sensitivity wash-free magnetoreduction assay on biomolecules using high- Tc superconducting quantum interference devices. J Appl Phys 103(1):014703
34. Chiu MJ, Horng HE, Chieh JJ, Liao SH, Chen CH, Shih BY, Yang CC, Lee CL, Chen TF, Yang SY, Hong CY, Yang HC (2011) Multi-Channel SQUID-based ultra-high-sensitivity in-vitro detections for bio-markers of Alzheimer's disease via immunomagnetic reduction. IEEE Trans Appl Supercond 21(3):477–480
35. Andreasen N, Blennow K (2002) β-amyloid (Aβ) protein in cerebrospinal fluid as a biomarker for Alzheimer's disease. Peptides 23(7):1205–1211
36. Tapiola T, Alafuzoff I, Herukka SK, Parkkinen L, Hartikainen P, Soininen H, Pirttilä T (2009) Cerebrospinal fluid β-amyloid 42 and tau proteins as biomarkers of Alzheimer-type pathologic changes in the brain. Arch Neurol 66(3):382–389
37. Healy MJR (1972) Statistical analysis of radioimmunoassay data. Biochem J 130(1):207–210
38. Frantzen F, Faaren AL, Alfheim I, Nordhei AK (1998) Enzyme conversion immunoassay for determining total homocysteine in plasma or serum. Clin Chem 44(2):311–316
39. Herr AE, Throckmorton DJ, Davenport AA, Singh AK (2005) Onchip native gel electrophoresis-based immunoassays for tetanus antibody and toxin. Anal Chem 77(2):585–590
40. Yang CC, Yang SY, Chieh JJ, Horng HE, Hong CY, Yang HC (2012) Universal behavior of biomolecule-concentration-dependent reduction in AC magnetic susceptibility of bioreagents. IEEE Magn Lett 3:1500104, 6157673

41. Smith DO (1956) Development of a vibrating-coil magnetometer. Rev Sci Instrum 27(261):261–268
42. Foner S (1959) Versatile and sensitive vibrating-sample magnetometer. Rev Sci Instrum 30(7):548–557
43. Visuthikraisee V, Bertsch GF (1996) Spin-rotation coupling in ferromagnetic clusters. Phys RevA 54(6):5104–5109
44. Chieh JJ, Huang KW, Shi JC (2015) Sub-Tesla-field magnetization of vibrated magnetic nanoreagents for screening tumor markers. Applied Physics Letters 16(7):073703
45. Cornell RM, Schwertmann U (2003) The iron oxides: structure, properties, reactions, occurrences and users. VCH Publishers, Weimheim
46. Khandhar AP, Ferguson RM, Arami H, Krishnan KM (2013) Monodisperse magnetite nanoparticle tracers for in vivo magnetic particle imaging. Biomaterials 34(15):3837–3845
47. Johnson BN, Mutharasan R (2014) Reduction of nonspecific protein adsorption on cantilever biosensors caused by transverse resonant mode vibration. Analyst 139(5):1112–1120
48. Neel L (1949) Theorie du trainagemagnetique des ferromagnetiquesen grains fins avec application aux terrescuites. Ann Geophys 5:99–136
49. Brown WF (1963) Thermal fluctuations of a single-domain particle. Phys Rev 130 (5):1677–1686
50. Bean CP, Livingston JD (1959) Superparamagnetism. J Appl Phys 30(4):S120–S129
51. Wernsdorfer W, Orozco EB, Hasselbach K, Benoit A, Barbara B, Demoncy N, Loiseau A, Pascard H, Mailly D (1997) Experimental evidence of the néel-brown model of magnetization reversal. Phys Rev Lett 78(9):1791–1794
52. Zhang YD, Budnick JI, Hines WA, Chien CL, Xiao JQ (1998) Effect of magnetic field on the superparamagnetic relaxation in granular Co-Ag samples. Appl Phys Lett 72(16):2053–2055
53. Dickson DPE, Reid NMK, Hunt C, Williams HD, El-Hilo M, O'Grady K (1993) Determination of f0 for fine magnetic particles. J Magn Magn Mater 125(3):345–350
54. Wang CY, Yang TW, Shen D, Chen KL, Chen JM, Liao SH, Chieh JJ, Yang HC, Wang LM (2017) Bioassay using blocking temperature: Interparticle interactions between biofunctionalized magnetic nanoparticles conjugated with biotargets. Appl Phys Lett 110 (13):133701
55. Zheng RK, Gu H, Xu B, Zhang XX (2006) The origin of the non-monotonic field dependence of the blocking temperature in magnetic nanoparticles. J Phys Condens Matter 18 (26):5905–5910
56. Zhang XX, Wen GH, Xiao G, Sun S (2003) Magnetic relaxation of diluted and self-assembled cobalt nanocrystals. J Magn Magn Mater 261(1–2):21–28
57. Knobel M, Nunes WC, Winnischofer H, Rocha TCR, Socolovsky LM, Mayorga CL, Zanchet D (2007) Effects of magnetic interparticle coupling on the blocking temperature of ferromagnetic nanoparticle arrays. J Non-Cryst Solids 353(8–10):743–747
58. Nunes WC, Socolovsky LM, Denardin JC, Cebollada F, Brandl AL, Knobel M (2005) Role of magnetic interparticle coupling on the field dependence of the superparamagnetic relaxation time. Phys Rev B 72(21):212413
59. Löffler JF, Braun HB, Wagner W (2000) Magnetic correlations in nanostructured ferromagnets. Phys Rev Lett 85(9):1990–1993
60. Huang KW, Chieh JJ, Shi JC, Chiang MH (2015) Assaying carcinoembryonic antigens by normalized saturation magnetization. Nanoscale Res Lett 10(1):277
61. Chen KL, Chen JH, Liao SH, Chieh JJ, Horng HE, Wang LM, Yang HC (2015) Magnetic clustering effect during the association of biofunctionalized magnetic nanoparticles with biomarkers. PLoS One 10(8):e0135290
62. Bedanta S, Kleemann W (2009) Supermagnetism. J Phys D Appl Phys 42(1):013001
63. Kumar PA, Ray S, Chakraverty S, Sarma DD (2013) Engineered spin-valve type magnetoresistance in Fe_3O_4-$CoFe_2O_4$ core-shell nanoparticles. Appl Phys Lett 103(10):102406
64. Shi D, Yang H, Ji S, Jiang S, Liu X, Zhang D (2015) Preparation and characterization of core-shell structure Fe_3O_4@C magnetic nanoparticles. Proc Eng 102:1555–1562

65. Krycka KL, Borchers JA, Booth RA, Ijiri Y, Hasz K, Rhyne JJ, Majetich SA (2014) Origin of surface canting within Fe_3O_4 nanoparticles. Phys Rev Lett 113(14):147203
66. Lima E Jr, Brandl AL, Arelaro AD, Goya GF (2006) Spin disorder and magnetic anisotropy in Fe_3O_4 nanoparticles. J Appl Phys 99(8):083908
67. Schmidtke C, Eggers R, Zierold R, Feld A, Kloust H, Wolter C, Ostermann J, Merkl JP, Schotten T, Nielsch K, Weller H (2014) Polymer-assisted self-assembly of superparamagnetic iron oxide nanoparticles into well-defined clusters: controlling the collective magnetic properties. Langmuir 30(37):11190–11196
68. Knobel M, Nunes WC, Socolovsky LM, Biasi ED, Vargas JM, Denardin JC (2008) Superparamagnetism and other magnetic features in granular materials: a review on ideal and real systems. J Nanosci Nanotechnol 8(6):2836–2857
69. Lavorato GC, Peddis D, Lima E Jr, Troiani HE, Agostinelli E, Fiorani D, Zysler RD, Winkler EL (2015) Magnetic interactions and energy barrier enhancement in core/shell bimagnetic nanoparticles. J Phys Chem C 119(27):15755–15762
70. Mørup S, Hansen MF, Frandsen C (2010) Magnetic interactions between nanoparticles. Beilstein J Nanotechnol 1(1):182–190
71. De Toro JA, Normile PS, Lee SS, Salazar D, Cheong JL, Muñiz P, Riveiro JM, Hillenkamp M, Tournus F, Tamion A, Nordblad P (2013) Controlled close-packing of ferrimagnetic nanoparticles: an assessment of the role of interparticle superexchange versus dipolar interactions. J Phys Chem C 117(19):10213–10219
72. Wang GL, Xu JJ, Chen HY, Fu SZ (2009) Label-free photoelectrochemical immunoassay for α-fetoprotein detection based on TiO_2/CdS hybrid. Biosens Bioelectron 25(4):791–796
73. Ye Z, Tan M, Wang G, Yuan J (2006) Development of functionalized terbium fluorescent nanoparticles for antibody labeling and time-resolved fluoroimmunoassay application. Talanta 65(1):206–210
74. Wang RY, Lu XN, Ma W (2002) Non-competitive immunoassay for alpha-fetoprotein using micellar electrokinetic capillary chromatography and laser-induced fluorescence detection. J Chromatogr B 779(2):157–162
75. Chang YF, Chen RC, Lee YJ, Chao SC, Su LC, Li YC, Chou C (2009) Localized surface plasmon coupled fluorescence fiber-optic biosensor for alpha-fetoprotein detection in human serum. Biosens Bioelectron 24(6):1610–1614
76. Yang HC, Huang KW, Liao SH, Horng HE, Chieh JJ, Chen HH, Chen MJ, Chen KL, and Wang LM (2013) Enhancing the tumor discrimination using antibody-activated magnetic nanoparticles in ultra-low magnetic fields. Appl Phys Lett 102: 013119
77. Tu L, Jing Y, Li Y, Wang JP (2011) Real-time measurement of Brownian relaxation of magnetic nanoparticles by a mixing-frequency method. Appl Phys Lett 98(21):213702
78. Liao SH, Yang HC, Horng HE, Chieh JJ, Chen KL, Chen HH, Chen JY, Liu CI, Liu CW, Wang LM (2013) Time-dependent phase lag of biofunctionalized magnetic nanoparticles conjugated with biomarkers studied with alternating current magnetic susceptometor for liquid phase immunoassays. Appl Phys Lett 103(24):243703
79. Liao SH, Liu CW, Yang HC, Chen HH, Chen MJ, Chen KL, Horng HE, Wang LM, Yang SY (2012) Spin-spin relaxation of protons in ferrofluids characterized with a high-Tc SQUID-detected magnetometer in microtesla fields. Appl Phys Lett 100(23):232405
80. Liao SH, Huang KW, Yang HC, Yen CT, Chen MJ, Chen HH, Horng HE, Yang SY (2010) Characterization of tumors using SQUID-detected nuclear magnetic resonance and imaging. Appl Phys Lett 97(26):263701
81. Ssalamah AB, Uffmann M, Saini S, Bastati N, Herold C, Schima W (2009) Clinical value of MRI liver-specific contrast agents: a tailored examination for a confident non-invasive diagnosis of focal liver lesions. Eur Radiol 19(2):342–357
82. Huang KW, Chieh JJ, Horng HE, Hong CY, Yang HC (2012) Characteristics of magnetic labeling on liver tumors with anti-alpha-fetoprotein-mediated Fe_3O_4 magnetic nanoparticles. Int J Nanomedicine 7:2987–2996

83. Atkinson WJ, Brezovich IA, Chakraborty DP (1984) Usable frequencies in hyperthermia with thermal seeds. IEEE Trans Biomed Eng BME-31(1):70–75
84. Chieh JJ, Huang KW, Lee YY, Wei WC (2015) Dual-imaging model of SQUID biosusceptometry for locating tumors targeted using magnetic nanoparticles. J Nanobiotechnol 13(1):11
85. Chieh JJ, Huang KW, Lee YD, Horng HE, Yang HC, Hong CY (2012) In vivo screening of hepatocellular carcinoma using the ac susceptibility of antialphafetoprotein-activated magnetic nanoparticles. PLOS ONE 7(10):e46756
86. Huang KW, Chieh JJ, Liao SH, Wei WC, Hsiao PY, Yang HC, Horng HE (2016) Rapid and quantitative discrimination of tumour cells on tissue slices. Nanotechnology 27(23):235101
87. Wilhelm C, Gazeau F (2008) Universal cell labelling with anionic magnetic nanoparticles. Biomaterials 29(22):3161–3174
88. Gleich B, Weizenecker J (2005) Tomographic imaging using the nonlinear response of magnetic particles. Nature 43(7046):1214–1217
89. Weizenecker J, Gleich B, Rahmer J, Dahnke H, Borgert J (2009) Three-dimensional real-time in vivo magnetic particle imaging. Phys Med Biol 54(5):L1–L10
90. Adolphi NL, Butler KS, Lovato DM, Tessier TE, Trujillo JE, Hathaway HJ, Fegan DL, Monson TC, Stevens TE, Huber DL, Ramu J, Milne ML, Altobelli SA, Bryant HC, Larson RS, Flynn ER (2012) Imaging of Her2-targeted magnetic nanoparticles for breast cancer detection: comparison of SQUID-detected magnetic relaxometry and MRI. Contrast Media Mol Imaging 7(3):308–319
91. Huang KW, Chieh JJ, Yeh CK, Liao SH, Lee YY, Hsiao PY, Wei WC, Yang HC, Horng HE (2017) Ultrasound-induced magnetic imaging of tumors targeted by biofunctional magnetic nanoparticles. ACS Nano 11(3):3030–3037
92. Mehrmohammadi M, Oh J, Mallidi S, Emelianov SY (2011) Pulsed magneto-motive ultrasound imaging using ultrasmall magnetic nanoprobes. Mol Imaging 10(2):102–110
93. Mehrmohammadi M, Shin TH, Qu M, Kruizinga P, Truby RL, Lee JH, Cheon J, Emelianov SY (2013) In vivo pulsed magneto-motive ultrasound imaging using high-performance magnetoactive contrast nanoagents. Nanoscale 5(22):11179–11186

Surface Plasmon Resonance Sensors for Medical Diagnosis

10

Yeşeren Saylan, Fatma Yılmaz, Erdoğan Özgür, Ali Derazshamshir, Nilay Bereli, Handan Yavuz, and Adil Denizli

Contents

Y. Saylan · A. Derazshamshir · N. Bereli · H. Yavuz · A. Denizli (✉)
Department of Chemistry, Hacettepe University, Ankara, Turkey
e-mail: denizli@hacettepe.edu.tr

F. Yılmaz
Department of Chemistry Technology, Abant Izzet Baysal University, Bolu, Turkey

E. Özgür
Department of Chemistry, Hacettepe University, Ankara, Turkey

Department of Chemistry, Aksaray University, Aksaray, Turkey

C. S. S. R. Kumar (ed.), *Nanotechnology Characterization Tools for Biosensing and Medical Diagnosis*, https://doi.org/10.1007/978-3-662-56333-5_10

1 Definition of the Topic

Surface plasmon resonance (SPR) sensors have fascinated impressive attention to detect clinically related analytes in recent years. SPR sensors have also multiple advantages over existing conventional diagnostic tools such as easy preparation, no requirement of labeling, and high specificity and sensitivity with low cost, and they provide real-time detection capability. There are some articles and reviews in literature focusing on the applications of SPR-based sensors for the diagnosis of medically important entities such as proteins, cells, viruses, disease biomarkers, etc. These articles generally give information about the determination of these structures, whereas this presented manuscript combines recent literature for most of the medically important structures together including proteins, hormones, nucleic acids, whole cells and drugs that especially the latest applications of SPR sensors for medical diagnosis to follow up new strategies and discuss how SPR strategy is brought to solve the medical problems.

2 Overview

A large number of potential analytical difficulties in various fields that can be easily figured out by the tools are called sensors. Medical and health problems have emerged because of the increasing population with a high risk of chronic and infection diseases such as heart disease, stroke, cancer, tuberculosis that need to be solved for public health.

This chapter is structured according to the principle of SPR, the importance of SPR in medical diagnosis, key research findings according to the diagnosis of diseases, and conclusions and future perspective. Latest strategies and novel applications are focused in this chapter by a discussion on how SPR technology is brought to solve the medical problems.

3 Introduction

The detection of clinically relevant molecules such as proteins, hormones, nucleic acids, cells, and drugs is essential to understanding their biological and physiological functions and also to developing medical diagnostics tools. These molecules accomplish many biological functions, including storing and transmitting genetic information, regulating biological activities, transporting molecules, and catalyzing reactions. Moreover, they can be used as biomarkers in the diagnosis of many diseases [1]. Analytical devices, called sensors, consist of a transducer and recognition elements capture a specific analyte for the analysis of a sample mixture to evaluate their composition, structure and function by converting biological responses into electrical signals are called sensors. Regarding the transduction principles, sensors can be classified as optical [2–4], electrochemical [5–7], mass [8–10], magnetic [11–13], and micromechanical [14–16].

Development of optical sensors has been fascinating in the past two decades, due to their immunity to electromagnetic interference and ability to perform remote sensing and to supply multiple detections with one device. Sensors utilize a variety of optical sensing methods that include chemiluminescence, fluorescence, light absorption and scattering, reflectance, and surface plasmon resonance and can be separated into two classes: label-based and label-free.

Industrious labeling methods may hinder with the function of a molecule in spite of label-based detections with the detection limit value down to a single molecule which is extremely sensitive. Quantitative studies are challenging because of the fluorescence signal bias due to the few fluorophores on each molecule, which cannot be correctly controlled. In opposing, binding-induced refractive index changes are measured with the label-free detections [17].

Surface plasmon resonance (SPR) is a very suitable technology to detect clinical analytes for a number of aims. Due to the detection that depends on refractive index changes, specific bindings are quantified as they happen without time-consuming washes of unbounds, and this feature reduces time-to-result compared with other technologies. In addition, the detection does not base on labeling of the target molecules. Because the labeling of a target may alter its binding affinity and kinetics properties and also increase the complexity of the reaction and the cost of the process. Furthermore, SPR is able to detect many clinical analytes directly. It can be used to improve detection sensitivity, selectivity, and/or refractive index resolution. SPR only needs basic optics that can be miniaturized to a size that is suitable for medical diagnosis. Besides, the non-specific interactions with SPR surface in a complex mixture can be reduced by the ability to have multiple reference surfaces that may be used to correct background signals [18].

4 Experimental and Instrumental Methodology

4.1 Principle of Surface Plasmon Resonance

Refractive index changes occur in the very close vicinity of a metal surface of the SPR sensors. This function generally appears between two transparent media and then measured by a simple and direct sensing onto the SPR sensors. Plane-polarized light can undergo total internal refraction when the beam enters into the higher refractive index medium at above its critical angle. Under optimal conditions, electromagnetic field component of the light, which is penetrating into the gold film, is called an evanescent wave. The interaction of this wave with free oscillating electrons at the metal surface will produce the excitation of surface plasmons at a specific angle of incidence and results in a decline of the reflected light intensity subsequently [19].

Utilization of the optical phenomenon, SPR, has seen extensive growth since its initial observation by Wood in the early 1900s [20]. It was initially exploited for a variety of spectroscopic and physical characterizations including enhanced holography [21], surface-enhanced Raman scattering or coherent anti-Stokes Raman scattering, and surface plasmon microscopy for high contrast imaging of thin dielectric

films [22–24]. SPR is a simple and direct sensing technique that can be used to probe refractive index changes that occur in the very close vicinity of a thin metal film surface [25]. This technique utilizes a thin film of metal between two transparent media of different refractive index to function as an optical sensor surface. Above a critical angle, a plane-polarized light beam entering the higher refractive index medium can undergo total internal refraction. Under these conditions, an electromagnetic field component of the light called the evanescent wave will penetrate into the gold film. At a specific angle of incidence, the interaction of this wave with free oscillating electrons at the gold film surface will cause the excitation of surface plasmons, resulting subsequently in a decrease in the reflected light intensity. This phenomenon is called surface plasmon resonance and occurs only at a specific angle known as the resonant angle. This SPR angle is modified by the addition of the analyte onto the gold film surface, thereby allowing the monitoring of binding events. From a practical standpoint, the Kretschmann prism arrangement is the most frequently employed geometry in SPR.

An estimation of the penetration depth is given by the following expressions [26]:

$$d_{\mathrm{p}} = \frac{\lambda}{4\pi\sqrt{\eta_1^2 \sin^2\theta - \eta_2^2}} \tag{10.1}$$

where η_1 and η_2 are the refractive index of medium 1 and medium 2, respectively. Typically, this will be approximately equal to one-fourth of the incident light wavelength.

The light that is p-polarized with respect to the metal surface is launched into the prism for coupling to the metal film only p-polarized light can be utilized for plasmon generation because this particular polarization has the electric field vector oscillations normal to the metal film. This is referred to as the transverse magnetic wave of the electron plasma along the flat metal surface [27, 28]. In contrast, the s-polarized transverse electric polarization cannot generate surface plasmons since its electric field vector is orientated parallel to the metal film. The wave vector of the oscillations, K_{sp}, is given by the expression:

$$K_{\mathrm{sp}} = \frac{\omega}{c}\sqrt{\frac{\varepsilon_{\mathrm{m}}\varepsilon_{\mathrm{s}}}{\varepsilon_{\mathrm{m}} + \varepsilon_{\mathrm{s}}}} \tag{10.2}$$

where ω is the frequency of the oscillations, c is the speed of light, ε_{s} is the dielectric function of the sample medium adjacent to the metal surface, and ε_{m} is the dielectric function of the metal. The wave vector for a component of incident light can be described by the equation:

$$K_{\mathrm{x}} = \frac{\omega}{c}\eta \sin\theta \tag{10.3}$$

where θ is the angle of incidence of the light onto the metal film and η the refractive index of the prism. Surface plasmons, which oscillate and propagate along the upper

surface of the metal film, absorb some of the p-polarized light energy from the evanescent field to change the total-internal-reflection light intensity Ir. Therefore, a plot of Ir versus incidence (or reflection) angle (θr) produces an angular intensity profile that exhibits a sharp dip at the resonance angle.

The surface plasmon wave vector can be related to the refractive index of the medium on the near vicinity of the metal film by simplification of the equation. Disregarding the imaginary portion of ε, K_{sp} can be rewritten as:

$$K_{sp} = \frac{\omega}{c}\sqrt{\frac{\eta_m^2 \eta_s^2}{\eta_m^2 + \eta_s^2}} \tag{10.4}$$

where η_m is the refractive index of the metal and η_s is the refractive index of the sample. The imaginary component of the complex refractive index term can be related to absorbance.

4.2 Importance of SPR in the Medical Diagnosis

SPR technology first emerged many years ago, and then many scientists that include chemists, biologists, physicists, and medical doctors have joined to use the SPR as a novel application in various fields, such as doping analysis [29], diagnosis [30], food safety [31], laboratory medicine [32], etc. Among them, definitely, clinical studies have also been investigated as an effective application area. Superior features of the SPR technology enable several advantages involving detecting of the target molecules in real-time, label-free analysis, need low sample amount, quantitative reply, and high sensitivity and reusability. These features make SPR technology desirable for point-of-care diagnostics that can do fast and multi-analyte detection [33]. In this chapter, the key research findings that include protein, hormone, nucleic acid, cell, and drug detection for several diseases were summarized according to the latest literature.

5 Key Research Findings

5.1 Protein Detection

Clinically relevant proteins which have very important features to diagnose the level of related diseases are needed trusty methods to detect them in complex mixtures. Detection of proteins leads to molecularly targeted therapy and also measures a therapeutic reaction. The SPR sensors supply an applicable system for clinical analysis [34, 35]. The most recent studies based on SPR sensor to detect proteins for a number of diseases were focused in this part.

There are too many different cancer types associated with deregulated genes and signaling pathways. Successful diagnosis of early stage cancer and follow-up

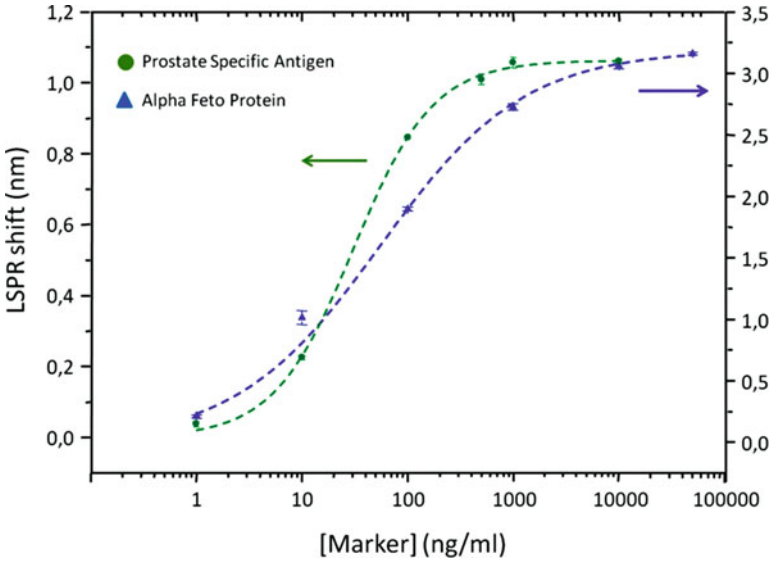

Fig. 10.1 Parallel sensor response for the detection of alpha-fetoprotein and prostate-specific antigen cancer markers [38]

treatment is vital for cancer biomarkers detection. SPR sensors offer a promising platform for rapidly target analysis, which can be used for cancer diagnosis, prognosis, and drug monitoring. They have lately performed for molecular signature profiling, dynamic functional analysis, tumor cell enrichment and purification [36]. The art of synthesizing SPR-based sensing materials has largely been improved by the recent advancements in the area of functional nanomaterials and has offered tunable surface plasmon characteristics meant for specific purposes. The trend for the use of label-free and reusable functionalized nanomaterials has greatly improved sensing capabilities of different cancer biomarkers, and the doors have been widely opened to design multiplexed analysis platforms [37].

Eight microfluidic channels based thirty-two sensing sites for monitoring cancer biomarker such as a prostate specific antigen and human alpha-fetoprotein up to a concentration of 500 pg/mL was designed by Aćimović and collaborators [38]. As seen in Fig. 10.1, they first considered alpha-fetoprotein (blue curve) and observed small fluctuations in concentration of alpha-fetoprotein in human serum below the clinically significant level. To detect alternative markers, they demonstrated (green curve) whole detection of prostate-specific antigen to show quick sensing platform for detection of analyte in the ng/mL concentration range in a matter of minutes with outstanding reproducibility.

The detection of prostate-specific antigen was also performed with UV polymerization method based on the micro-contact imprinting technique by prostate-specific antigen-imprinted SPR sensor [39]. They performed the prostate-specific antigen detection with standard prostate-specific antigen solutions in a concentration range

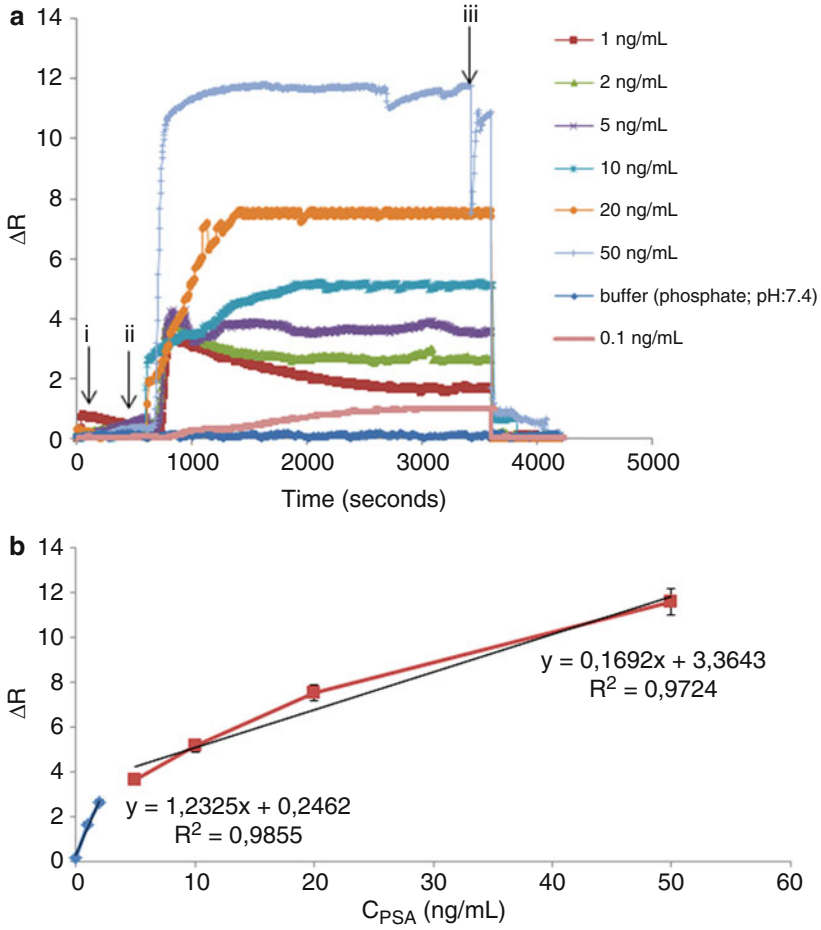

Fig. 10.2 (**a**) The prostate-specific antigen detection, (**b**) calibration curve for prostate-specific antigen detection measured with the SPR sensor [39]

of 0.1–50 ng/mL and found the limit of detection (LOD) value as 91 pg/mL. As seen in Fig. 10.2a, they equilibrated with phosphate buffer (i), injected with the analyte solutions (ii), and desorbed with glycine – HCl (iii). They also obtained high correlation coefficients after performing different samples (Fig. 10.2b). They applied ten clinical serum samples to the SPR sensor and obtained the results; 98% agreement with ELISA method without important differences at the 0.05 level was indicated.

Point-of-care diagnostic sensor for total prostate-specific antigen detection in human serum samples using SPR sensor platforms was developed by Uludag et al. [40]. They used a sandwich assay on an SPR sensor based on antibody-modified nanoparticles to detect the different concentration of total prostate-specific antigen in human serum. They calculated K_D value as 9.46×10^{-10} M, designating an excellent affinity of the antibody employed in their assay. They showed that the

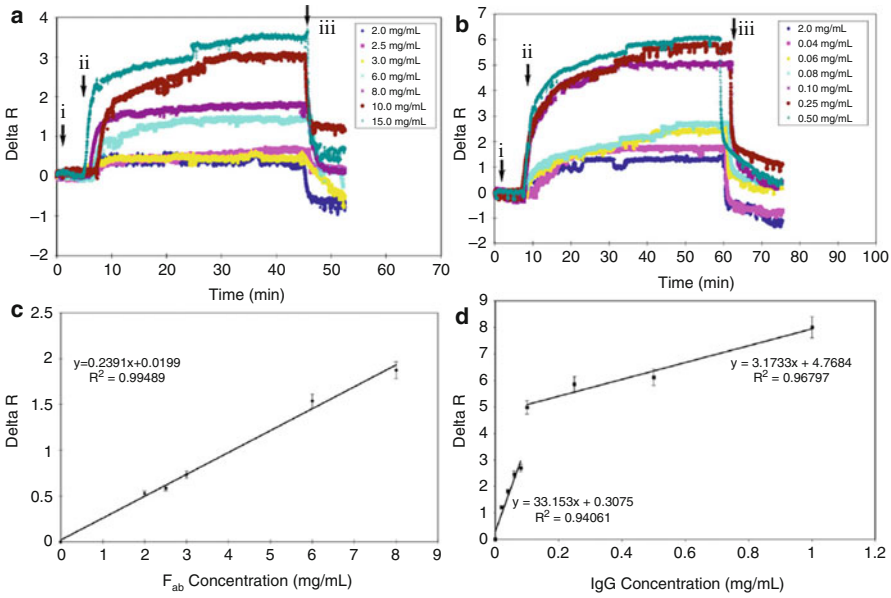

Fig. 10.3 The (**a**) F_{ab}, (**b**) IgG detection, reflectivity vs (**c**) F_{ab}, and (**d**) IgG concentration dependency of the SPR chip response [42]

developed immunoassay-based SPR sensor could be successfully utilized to patient's serum samples as clinical application.

Immunoglobulins (Ig) used in in vivo diagnostics have gained significant notice among health authorities over the world. For this purpose, detection of human IgG in human serum by polymeric nanoparticles fixed to SPR sensor was indicated by Türkoğlu and collaborators [41]. They also performed kinetic studies by using IgG samples with different concentration (0.05–2.0 mg/mL). They observed that the reflectivity value was increased from 0.3 to 2.5 in parallel to IgG concentration that increased from 0.05 to 2.0 mg/mL when the IgG samples were applied.

Ertürk and coworkers prepared F_{ab} fragments imprinted SPR sensor to detect human IgG [42]. F_{ab} fragments were digested with papain and collected by fast protein liquid chromatography system, and then collected F_{ab} fragments reacted with the specific monomer (N-methacryloyl-l-histidine methyl ester) to prepare nanofilm on SPR sensor surface in the existence of cross-linker (ethylene glycol dimethacrylate) and functional monomer (2-hydroxyethylmethacrylate). IgG detection studies were carried out by using a different concentration of aqueous IgG solutions. They also performed selectivity experiments of the F_{ab} imprinted SPR sensor by employing bovine serum albumin (BSA), IgG, and F_{ab} and F_c fragments in singular and multiple mixtures (Fig. 10.3). According to their results, they found the LOD value as 56 ng/mL.

Rheumatoid arthritis identified with common chronic joint inflammation is an autoimmune disease. The anti-cyclic citrullinated peptide is IgG antibodies which

act as a significant role in the diagnosis of this disease. Dibekkaya et al. prepared anti-cyclic citrullinated peptide imprinted SPR sensor to detect cyclic citrullinated peptide antibodies [43]. They examined the selectivity experiments by utilizing IgM and BSA. They calculated maximum reflection, LOD, association (K_a), and dissociation (K_d) constants as 1.079 RU/mL, 0.177 RU/mL, 0.589 RU/mL, and 1.697 mL/RU, respectively.

Hepatitis B virus infection is still an important global problem. The feasibility of SPR sensor was tested by Chung and collaborators to the diagnosis of human hepatitis B virus antibodies [44]. They optimized the baseline stability and the dilution factor of serum samples for SPR sensor application with phosphate buffer saline and 0.5% Tween 20 solution. They estimated the baseline stability as 69.79° with a standard deviation of 0.32 millidegree. They calculated that SPR change of 120 millidegree equaled to protein binding of 1 ng/mm^2. Samples of hepatitis B virus antibodies were used to prepare a standard curve. They used secondary antibodies to test the sensitivity of the SPR sensor. They claimed that the LOD value of the SPR sensor for the medical diagnosis was very similar to the ELISA kit for the diagnosis of hepatitis.

Diagnosis of hepatitis B surface antibody in human serum by hepatitis B surface antibody imprinted polymeric film, which was attached to the SPR sensor, was prepared by Uzun et al. [45]. They performed kinetic studies using the hepatitis B surface antibody-positive human serum. They found the LOD value as 208.2 mIU/mL. Nonimmunized, hepatitis B surface antibody-negative serum was used for performing control experiments of the SPR sensor. Results obtained by control experiments showed that SPR sensor did not give any noticeable response to hepatitis B surface antibody-negative serum.

Inflammatory bowel disease patients are treated with therapeutic monoclonal antibody, infliximab, and therapeutic outcomes are monitored infliximab trough concentrations. Lu et al. reported an assay by employing an in-house fiber-optic SPR sensor for the infliximab determination in serum [46]. They observed that SPR response was increased by using gold nanoparticles functionalized with another set of infliximab-specific antibodies. They obtained the calibration curves with a series of infliximab concentrations spiked in the buffer and serum with the LOD values of 0.3 and 2.2 ng/mL, consequently. They claimed that their results were compared with ELISA resulting in outstanding Pearson and intraclass correlation coefficients of 0.998 and 0.983.

Immobilization of a human growth hormone on the self-assembled monolayer-based SPR sensor for specific antihuman growth hormone antibodies detection using the combination of three different physical phenomena in the same channel of the SPR was performed by Ramanaviciene et al. [47]. Detection of the specific antihuman growth hormone antibodies using secondary assay format on the same domain of the SPR sensor was shown successfully by simultaneous exploitation of several techniques. They performed the secondary antibody binding to the immune complex formed between the immobilized human growth hormone and different concentrations of antihuman growth hormone (from 0.098 to 39.47 nM) at pH 7.4 by SPR study. Finally, they calculated LOD value as 0.051 nM for SPR system.

Exosomes that have the suitable features for cancer diagnostics such as molecular contents of the movement of the cell, which they create in spite of the exosomes detection, are technically contesting. Quantitative analyses of exosomes by an approach were described by Im and coworkers [48]. They functionalized the nanoholes with antibodies for a description of the exosome surface and lysate proteins to produce nanoplasmonic exosome assay, which was based on transmission SPR. They examined exosome-binding kinetics and calculated the constants K_a, K_d, and k_D as 1.6×10^7 M^{-1} s^{-1}, 4.8×10^{-4} s^{-1}, and 3.6×10^{-11} M, respectively. They observed binding constant as approximately 36 pM and claimed that this value was lower than that of individual antigen-antibody binding (1 nM). They improved the sensitivity by this approach to operating when integrated with miniaturized optics and retrieval of exosomes. They found that exosomes having the potential for diagnostics originated from ovarian cancer cells could be specified by their expression of CD24 and EpCAM by analyzing ascites samples from ovarian cancer.

The other study which described the growth of a sensor to detect folic acid protein using graphene-based SPR sensor was described by He and coworkers [49]. The exceptional properties of graphene were exploited to construct the SPR sensor for folate biomarker sensing in serum. The specific recognition of folic acid protein is based on the interactions between folic acid receptors integrated through π-stacking on the graphene-coated SPR sensor and the folic acid protein analyte in serum. Sensing capabilities for folate biomarkers were kept by a simple post-adsorption of human serum and bovine serum albumin mixtures onto the folic acid-modified sensor resulting in a highly antifouling interface. They examined the different concentration of folic acid (10 fM–1 pM) and declared that sensor allowed fM detection of folic acid protein, a detection limit well adapted and promising for quantitative clinical analysis.

Amplification technique by using magnetic nanoparticles with core-shell structure for an SPR sensor was presented by Liang et al. [50]. The detection of α-fetoprotein based on a sandwich immunoassay by immobilizing a primary α-fetoprotein antibody on the SPR sensor surface of a polymeric film employing magnetite-gold-α-fetoprotein antibody conjugates as the amplification reagent was developed by them. Calibration curve of magnetite-gold-α-fetoprotein secondary antibody conjugates amplification for α-fetoprotein detection to produce a correlation in the range of 1.0–200.0 ng/mL with a LOD value 0.65 ng/mL was obtained. Through the use of magnetite-gold-α-fetoprotein antibody conjugates as an amplifier, important increment in sensitivity was provided.

Cardiac biomarkers detection acts a significant function in the diagnosis and risk stratification of patients with chest pain and acute myocardial infarction. Myoglobin, creatine kinase-myocardial band, and cardiac troponins are the markers used to diagnose acute myocardial infarction. SPR sensor combined with the advantages of molecular imprinting-based synthetic receptors was developed by Osman et al. [51]. Myoglobin imprinted polymeric film produced onto the SPR sensor interacted with protein solutions in the concentration range from 0.1 μg/mL to 10 μg/mL (Fig. 10.4a). They observed a fast response when the myoglobin sample solution

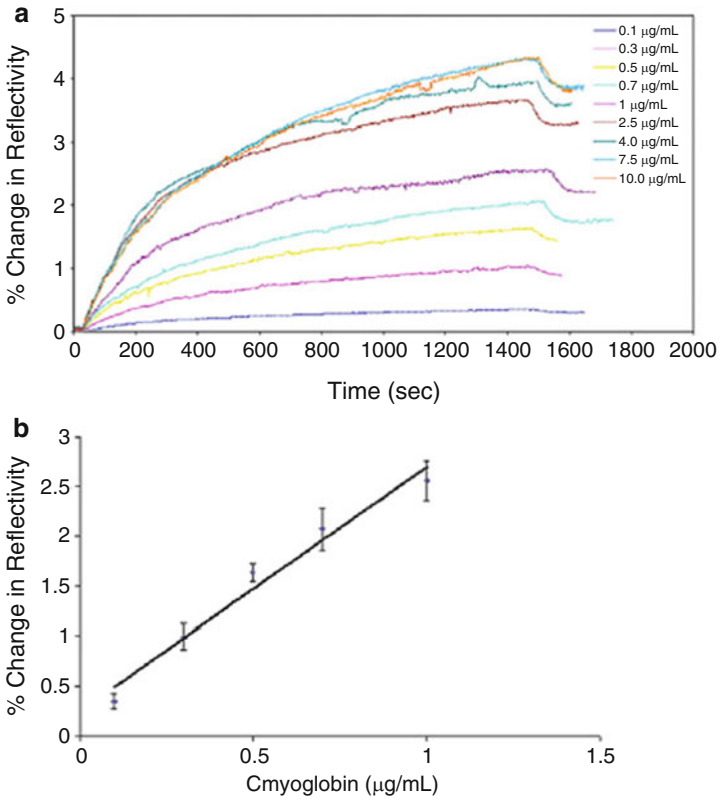

Fig. 10.4 (**a**) The sensorgrams and (**b**) concentration dependency of the SPR sensor [51]

arrived at the SPR sensor. They also observed that the SPR sensor response was increased when the concentration of myoglobin was increased as well. Figure 10.4b described the linearity of the SPR sensor in the range of 0.1 μg/mL–1.0 μg/mL. They calculated the LOD and limit of quantification (LOQ) values as 26.3 ng/mL and 87.6 ng/mL, respectively. They also used the SPR sensor to detect myoglobin in serum. They diluted the blank solution with a 1/15 ratio and spiked the samples with 0.3, 0.5, 0.7, and 1.0 μg/mL myoglobin in the same dilution ratio. They determined the myoglobin concentration in the diluted serum as 42.6 ng/mL. Their results showed that the SPR sensor could determine the myoglobin concentration with high accuracy when compared with the ELISA method (58.3 ng/mL).

Lysozyme detection has gained importance because the alteration of lysozyme levels can be used as a marker for some diseases such as meningitis, leukemia, several kidney problems, and rheumatoid arthritis. Lysozyme imprinted polymeric nanoparticles, which were modified on the SPR sensor, were represented by Sener et al. [52]. They detected lysozyme in both aqueous and natural complex sources even if lysozyme concentration was as low as 32.2 nM. They calculated the LOD, K_a, and K_d values as 84 pM, 108.71 nM^{-1}, and 9.20 pM, respectively.

Pregnancy-connected plasma protein A2 is a metalloproteinase that acts multiple roles in fetal development and postnatal growth. Bocková and coworkers presented the SPR sensor for plasma protein A2 detection in blood samples by using both single surfaces referencing method and sandwich assay with functionalized gold nanoparticles [53]. They also demonstrated that this SPR sensor had an ability to detect plasma protein A2 in blood plasma with 3.6 ng/mL LOD value. The researchers characterized the performance of the SPR sensor and evaluate its cross-reactivity to a plasma protein A2 analogue.

Alzheimer's disease is defined by the amyloid β-protein oligomerization as an early event. There is a risk of overdiagnosis employing sequence-specific antibodies oppose to toxic fibrillary and monomeric amyloid β-protein by current diagnostic methods. Murakami et al. gave much attention to developing more accurate diagnostics such as conformation-specific antibodies against neurotoxic amyloid β-protein oligomers [54]. They observed that the ratio of toxic to total amyloid β-protein in the cerebrospinal fluid of Alzheimer's disease patients was higher than in control molecules as determined by ELISA.

Selective laminin-5 determination using SPR sensor that depended on the specific interaction of laminin-5 with rabbit polyclonal antibody was performed as a new method by Sankiewicz et al. [55]. They showed that the reply range of the SPR sensor was between 0.014 and 0.1 ng/mL and calculated LOD value as 4 pg/mL. They also determined the laminin-5 concentration in blood plasma to examine the potential application of the SPR sensor. They compared the results with ELISA method, and according to their results, the plasma samples of bladder cancer patients gave more concentrated results with SPR sensor than by ELISA. The study showed that there is a clear difference in laminin-5 concentration in healthy people and patients with bladder cancer.

A self-assembled monolayer of protein chimeras to display an array of oriented antibodies on a microelectronic sensor for influenza nucleoprotein detection was described by Brun and coworkers as a new strategy [56]. They characterized their system with the structural and functional features of the bio-interface by SPR. Furthermore, they also showed that the non-covalent structure could render the dissociation of binding antibodies irreversible by chemical cross-linking in situ without attacking the antibody function.

Liu and colleagues demonstrated a fiber-optic SPR sensor that depended on the smartphone platforms by connecting the optical and sensing elements to a phone case [57]. They showed that the SPR sensor could be installed or removed from the smartphones. They also exhibited the accuracy and repeatability measurements by detecting several concentrations of antibody binding to a functionalized sensing element for smartphone-based SPR platform performance. Validation experiments resulted through contrast experiments with a commercial SPR instrument.

Rapid and reliable detection of procalcitonin by a molecularly imprinted polymer on the gold surface of SPR sensor was reported by Sener et al. [58]. According to this method, procalcitonin molecules were attached with the polymeric solution containing 2-hydroxyethylmethacrylate and ethylene glycol dimethacrylate on the SPR sensor after immobilization onto the glass slide, and then the polymerization

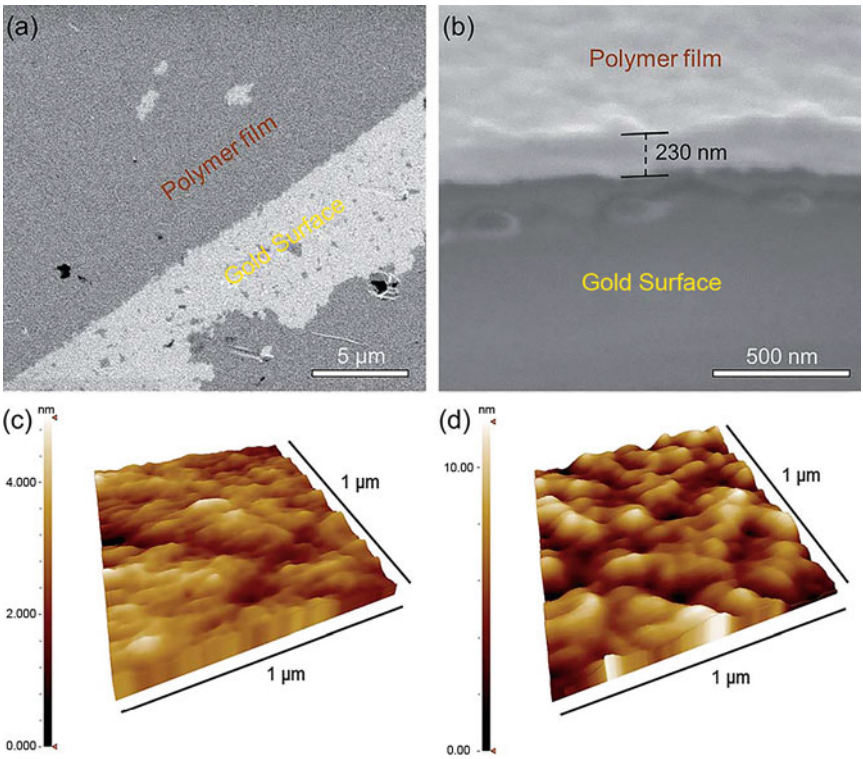

Fig. 10.5 (**a** and **b**) SEM images of procalcitonin imprinted polymer nanofilm, AFM images of (**c**) bare, and (**d**) procalcitonin imprinted SPR sensor surfaces [58]

process was initiated via UV light. Specific molecular binding sites were obtained after the removal of procalcitonin. They first characterized the SPR sensor (Fig. 10.5) and used for detection studies. The detection studies by using procalcitonin solutions in phosphate buffer and artificial blood plasma at diverse concentrations were performed after the characterization of the micro-contact imprinted SPR sensor. They also showed that the SPR sensor could detect low concentration of procalcitonin in both phosphate buffer and artificial blood plasma with a LOD value of 9.9 ng/mL.

5.2 Hormone Detection

Diagnosis of the endocrine diseases is generally difficult and needs to directly monitor and make measure hormone levels. Hormone detection demonstrates the talent of SPR technology to supply attractive answers in this clinical field and is provided in some recent studies by different groups [59].

Cenci et al. produced a library of molecularly imprinted nanoparticles to target the N-terminus of the hormone hepcidin-25 whose serum levels correlate with iron

dis-metabolisms and doping. They immobilized the molecularly imprinted nanoparticles onto the NeutrAvidin™ SPR sensor chip [60]. They studied the responses of the SPR sensor to hepcidin-25 and observed the low K_d values for the interaction of molecularly imprinted nanoparticles with hepcidin-25, but none for the molecularly imprinted nanoparticles and non-regulative hepcidin-20. They acquired the linearity with the logarithm of hepcidin-25 concentration in the range of 7.2–720 pM, and LOD value was 5 pM.

Zhang and coworkers developed a water-compatible molecularly imprinted polymer film with suitable monomers, cross-linker, polystyrene nanoparticles, and template for testosterone detection in urine [61]. Artificial urine and human urine incubation on the molecularly imprinted polymer film and the non-imprinted film was used to estimate undetectable non-specific adsorption. Testosterone detection was recorded with the LOD value down to 10^{-15} g/mL, which was regarded as one of the lowest values among the SPR sensors. The selectivity studies of molecularly imprinted polymer film were performed with the similar molecules to the testosterone such as progesterone and estradiol. They also showed that the SPR sensor had extreme stability and reproducibility over 8 months of storage at 25 °C which was better than protein-based sensors.

Vashist and his collaborators prepared SPR sensor for rapid immunoassay of procalcitonin with high detection sensitivity and reproducibility [62]. The activated protein A was dispensed on a potassium hydroxide-treated gold-coated SPR sensor surface and bound covalently in 30 min. They calculated the values of LOD and LOQ of the SPR sensor as 4.2 ng/mL and 9.2 ng/mL, respectively. They also claimed that the SPR sensor was capable of detecting procalcitonin in real sample matrices and patient samples with high precision.

Trevino et al. prepared the one and multiple analyte SPR systems for two gonadotropic hormones and luteinizing hormone from untreated human urine [63]. They found the lowest LOD values as 8 mIU/mL and 14 mIU/mL for luteinizing hormone and gonadotropic hormones in human urine. They also searched that the stability of the SPR sensor signals through more than hundred trials. They tested the comparison of the calibration curves for the three different SPR sensors. They observed that the reproducibility of chip-to-chip was exceptional and calculated the mean variation coefficients of 4.2% and 3.7% for gonadotropic hormones and luteinizing hormone, respectively.

The same research group has carried out studies to determine four pituitary hormones such as human thyroid-stimulating, growth, follicle-stimulating, and luteinizing hormones by using a portable SPR sensor [64]. They displayed the performance of the SPR sensor in different solutions ranging from 1 to 6 ng/mL. They injected the growth hormone samples to produce SPR signal due to the phosphate buffer and non-specific binding of serum components. They also obtained a calibration curve and the analytical characteristics. Their SPR sensor allowed the growth hormone determination in serum with different concentrations. Their results showed that the SPR sensor was suitable for practical and fast clinical diagnosis of growth hormone deficiency.

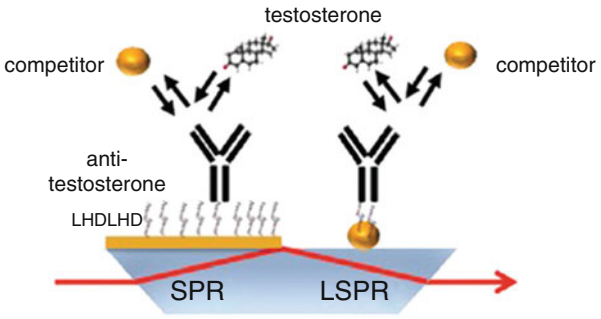

Fig. 10.6 Scheme of SPR and localized SPR systems on testosterone detection [66]

A fiber-optic SPR sensor was presented by Srivastava et al. for endocrine disruption biomarker detection [65]. They employed antibody immobilization on the SPR sensor surface. They prepared various concentrations of the biomarker in the range of 1.0–25 ng/mL and also performed control experiments with similar molecules. They found the LOD and sensitivity values of the SPR sensor as 1 ng/mL and 0.48 ng/mL in aqueous solution, respectively. Their fiber optic of the SPR sensor was fixed in a flow cell, and the flow cell had the supplies for sample input and output. Acetone-soaked optical tissue was used to wipe the ends, after fixing the fiber into the flow cell. Tungsten-halogen light source producing polychromatic light was coupled to the input end of the SPR fiber sensor probe with the help of a microscope objective of 0.65 NA to save the SPR sensorgram.

Yockell-Lelièvre and coworkers reported two sensing platforms utilizing functionalized gold nanoparticles to detect testosterone with SPR and localized SPR [66]. They provided a study based on the surface chemistries that can produce stable detection systems before detecting testosterone by employing four-channel SPR sensor system. As shown in Fig. 10.6, the SPR sensor was produced on a film on the prism, while the localized SPR sensor was originated by a monolayer gold nanoparticles immobilization on the prism. Development of the SPR and localized SPR sensors was depended on the competition of free testosterone with a testosterone-biotin. The basis of the competition assay for both SPR and localized SPR sensors relies on gold nanoparticles immobilized with testosterone-biotin. When high testosterone concentrations were applied to the SPR and localized SPR systems, the binding of a competitor to the SPR and localized SPR sensor was declined, and thus they observed a lower response.

Trade-offs between sensitivity, specificity, experiment range and time, instrumentation, sample carrier, and storage requirements with challenges for several SPR sensor applications were discussed by Sanghera et al. [67]. They calculated the LOD value of SPR sensor as 0.5 nM. They tested the insulin binding features of SPR sensor that called Protean Bio-Rad XPR36 at different pH values. They applied the insulin sample to the SPR sensor with a contact time of 300 s and a dissociation time of 400 s, at a flow rate of 25 μL/min at pH 7. They extended contact and dissociation time to improve sensitivity with same flow rate. They evaluated insulin concentration effect

on the produced signal intensity by SPR, and they declared that the more extensive contact and association times permitted, the better distinction for the different concentrations than the shorter times.

5.3 Nucleic Acid Detection

Many nucleotidic molecules of interest in medical diagnostics have been determined by nucleic acid that depended on SPR sensors. Eukaryotic chromosome ends are defended from undesired degradation, recombination, or end-to-end fusion by telomerase cap. Sharon and coworkers described the telomerase activity in human cells for the analysis of sensor involves the telomerase activity [68]. Telomerase activity was detected by their amplified SPR sensor. They did the telomerization in the mixture of the telomerase and the nucleotide, which results in the formation of telomeres on the SPR sensor surface modified with gold film-coated glass slides, and altered the surface dielectric properties that resulted in a shift in the SPR spectrum. As represented in Fig. 10.7a–d, they detected the telomerase extracted from 18 293 T cells/μL by using SPR spectra and observed the reflectance changes by sensorgrams corresponding to the different numbers of 293 T cell extracts.

Diltemiz et al. prepared SPR sensor for recognition of DNA. They reported that not only the detection of guanosine and guanine but also the DNA sequencing assay is possible with molecularly imprinted SPR sensor [69]. The binding experiments by ligand and guanosine and guanine imprinted polymers with respect to guanine and double-strand DNA were also included in their studies. They calculated the affinity constants for guanosine and guanine imprinted SPR sensors by plotting adsorption isotherms of adenosine, guanosine, guanine, adenine, single-strand DNA, and double-strand DNA, and the results were shown in Fig. 10.8.

The computationally assisted method was suggested based on the aptamer and protein interaction with the purpose of well-organized screening and selection of aptamers by Turner and collaborators [70]. They generated the computationally derived binding scores by screening a formed library of mutated DNA sequences based on the beginning from the data on the 15-mer thrombin-binding aptamer. They chose thrombin-binding aptamer and three other mutated oligonucleotides according to their binding score. They compared the analytical behaviors of the four oligonucleotide sequences employing signal amplitude, sensitivity, linearity, and reproducibility by reducing the ionic strength in order to match the simulated condition. They showed that their experimental results were in agreement with the simulation findings.

Highly infectious and rapidly spreadable through contact, bacterial meningitis is a dangerous infection of the meninges of the brain and spinal cord, which can even cause death. The report about SPR sensor was presented by Kaur and coworkers to detect *Neisseria meningitidis* DNA by utilizing laboratory assembled SPR sensor [71]. In their study, they immobilized the single-stranded probe DNA on SPR sensor surface. They provided the change in optical features at gold-zinc oxide interface by the DNA hybridization on the SPR sensor surface. A continuous shift in the dip angle of the SPR reflectance because of the dielectric properties changes of zinc

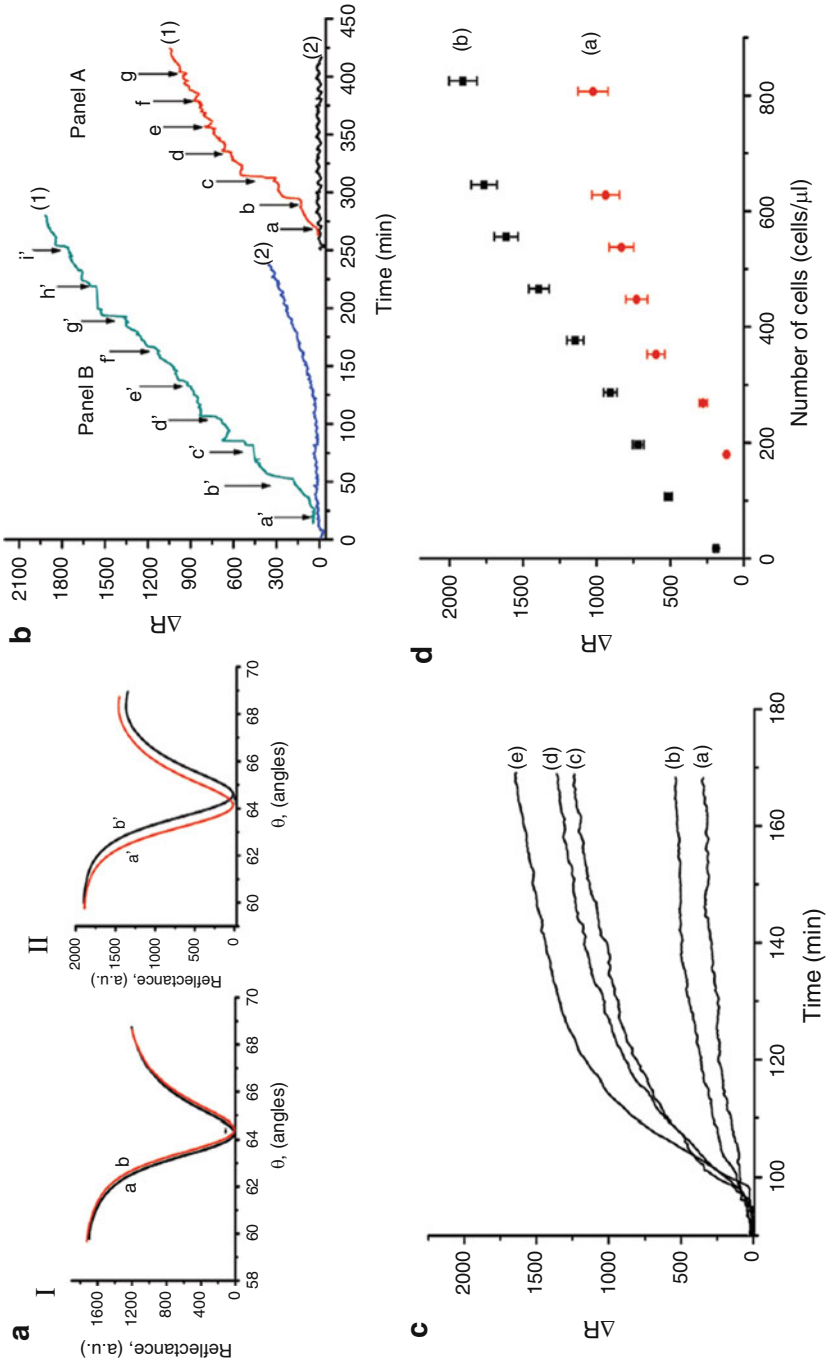

Fig. 10.7 The reflectivity responses in different steps [68]

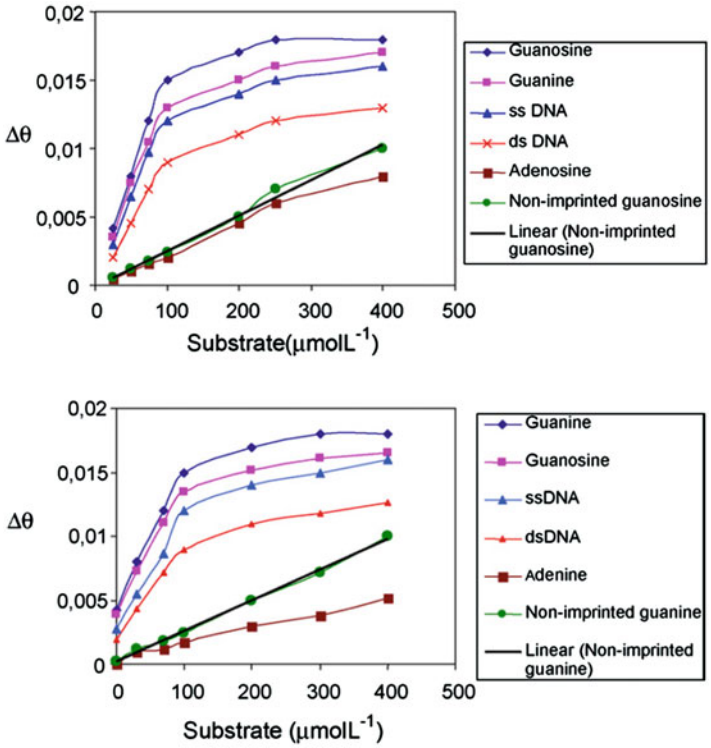

Fig. 10.8 The adsorption isotherms and selectivity of molecularly imprinted SPR sensors [69]

oxide matrix owing to the interaction between complementary DNA strands was observed with increase in the concentration of DNA. Furthermore, a continuous decline in the value of R_{min} with an increase in oligonucleotide concentration was also observed, which showed the binding between the probe and DNA. They obtained a linear response toward meningitides DNA over the concentration range from 10 to 180 ng/μL with a LOD value (5 ng/μL).

DNA arrays are priceless devices for sensing applications such as diagnostic DNA detection and gene expression analysis. Untagged oligonucleotide targets adsorbed to the array molecules can be detected by SPR imaging system. A template-directed polymerase extension of a surface array element was described as a new method by Gifford and coworkers [72]. They claimed that it is possible to obtain 10–100 attomole of polymerase outcome, representing as low as 0.25% of a monolayer by using their technique. Their system allowed detecting DNA present in low amounts in a sample with the partially unknown sequence. As seen in Fig. 10.9, they spotted the different ratios of probe DNA and T^{30} onto the glass surface above the gold spots and showed the binding of nanoparticles to the surface-bound DNA by a percent reflectivity change with the line profile indicated by the black line at the left inset.

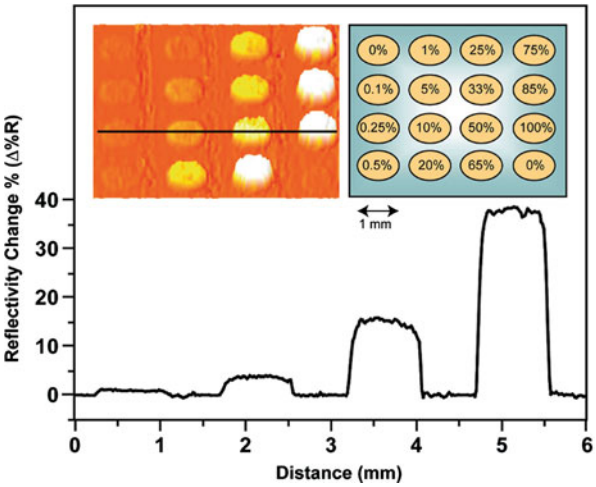

Fig. 10.9 The nanoparticle-based SPR imaging [72]

D'Agata et al. represented a detection strategy for genomic DNA that associated with the β-thalassemia disease [73]. Direct fluxing of DNA samples into each of the SPR imaging fluidic systems to let the direct interaction of each of the samples with different probes complementary to the normal and mutated DNA sequences was performed (Fig. 10.10). They declared that these different probes were functional both to distinguish between normal, homozygous, and heterozygous DNAs as well as to keep away the use of external controls which were difficult to be acquired for this application. Normal, homozygous, or heterozygous DNAs were each permitted to interact with the two different PNA probes, and obtained specific SPR imaging response patterns provided a robust experiment control.

The aptasensor that depended on the inactivation of surface plasmon enhancement of fluorescent probes modified to gold nanoparticle-bound aptamers was reported by Cho and colleagues [74]. They claimed that this sensing system measured the target directly at the clinically relevant range from 1.25 pM to 1.25 mM with high specificity and stability. Their results showed a good agreement within the limit of the ELISA kit for clinical sample experiments. The unfolded VEGF165 aptamer was bound to poly-L-lysine-coated gold nanoparticle surface as electrostatically in the lack of target molecules as shown in Fig. 10.11a. In addition Fig. 10.11b reflected that the interactions of the VEGF165 aptamer to its target induced the reversible conformation to modify the aptamer and the declined electrostatic binding force. An irreversible detachment of the aptamer from the GNP surface was caused by the target-binding interaction of the aptamer, which avoided the SEF effect of Cy3B (Fig. 10.11c).

5.4 Whole Cell Detection

Dengue is a crucial febrile disease, which is induced by the dengue virus and inserted into a host by a female *Aedes aegypti* mosquito and globally identified as one of the

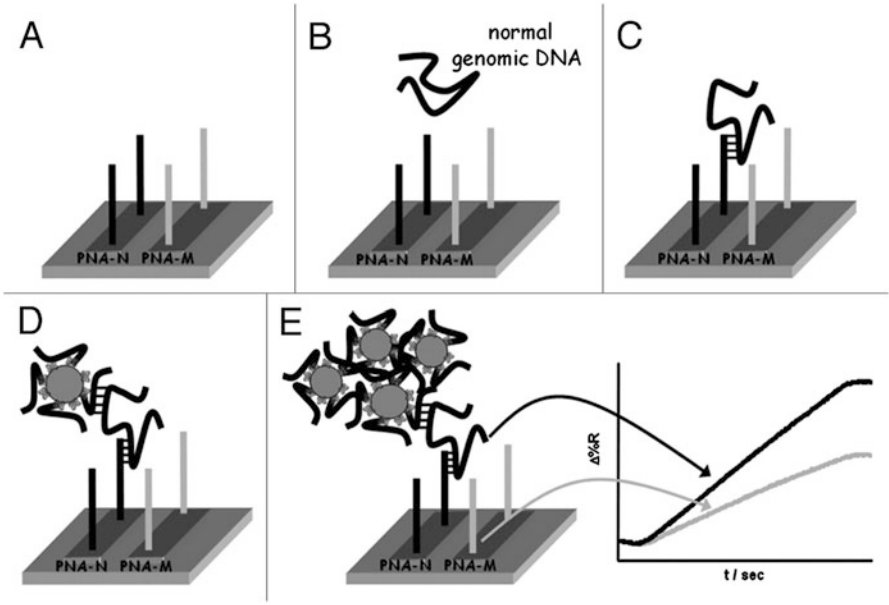

Fig. 10.10 The description of the nanoparticle-enhanced SPR imaging strategy [73]

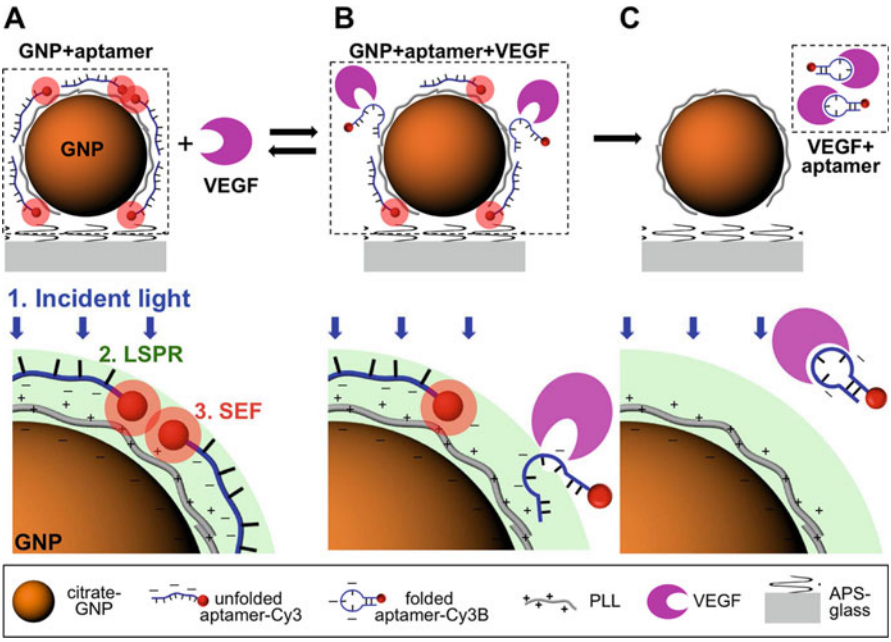

Fig. 10.11 The detection mechanism scheme of the aptasensor for VEGF165 [74]

most important vector-borne diseases. Anti-dengue virus detection in serum samples was proposed as a rapid method based on SPR by Jahanshahi and colleagues [75]. They claimed that their system, known as 10 min detection of immunoglobulin M-based dengue diagnostic test, could be applied rapidly and easily. They used different dengue virus serotypes as ligands on SPR sensor. They obtained 83–93% sensitivity, and 100% specificity for 1 ml from a patient was needed to indicate SPR angle variation to determine the ratio of each dengue serotype in samples.

Adenovirus detection was carried on by utilizing plastic and natural antibodies to refer three different strategies investigations. The implementation of a molecularly imprinted method for detection of viruses with the combination of sensors was described by Altintas et al. [76]. They used the SPR sensor as affinity receptor with the concentration range of 0.01–20 pM for the adenovirus detection and found the LOD value as 0.02 pM. They also performed the conduction of cross-reactivity studies with MS2 phage as a control virus and achieved high specificity.

Clinical diagnosis of canine distemper virus causing viral disease that influences dogs and many other carnivores is hard because of the broad spectrum of signs that may be confounded with other respiratory and enteric diseases of dogs. Basso et al. developed an SPR sensor to detect canine distemper virus [77]. They obtained a sensorgram after modification steps and the canine distemper virus concentration with a linear range from 1.1 to 116.0 ng/mL. They claimed that their SPR sensor showed a good reproducibility.

Avian influenza virus detection is needed because it causes H5N1 influenza infection in animals and humans. Bai and coworkers made research based on an SPR sensor for avian influenza virus H5N1 detection [78]. They fabricated the SPR sensor by using aptamers and then modified the gold surface of the SPR sensor coated with streptavidin. According to their results, the aptamers captured avian influenza virus H5N1 in a sample solution, which caused a refraction index increase, and the refraction index value was linearly related to the avian influenza virus concentration in the scale of 0.128 to 1.28 haemagglutination unit.

SPR sensor was developed to detect hemagglutinin which is a major protein of influenza A virus by Diltemiz et al. [79]. They modified SPR sensor surfaces with thiol groups and then 4-aminophenyl boronic acid, and the sialic acid mixture was immobilized on sensor surfaces. They employed aqueous hemagglutinin solutions to determine binding features of sensors to influenza A virus. They also calculated LOD values for SPR sensor as 1.28×10^{-1} μM, in the 95% confidence interval.

Molecularly imprinted SPR sensor to target the bacteriophage MS2 was developed by Altintas et al. [80] to detect waterborne viruses. They obtained an excellent affinity between the artificial ligand and the target (Fig. 10.12a). As shown in Fig. 10.12b, molecularly imprinted SPR sensor surface was renewed by using 0.1 M HCl (R1) and 20 mM NaOH (R2). In addition, blue line reflected the phage binding on molecularly imprinted SPR sensor, whereas red line represented the MS2 phage binding on molecularly imprinted SPR sensor in Fig. 10.12c. According to their results, they claimed that a regenerative molecularly imprinted virus detection SPR sensor was successfully promoted and provided an alternative and specific detection technology for the waterborne viruses leading to high disease and death rates all over the world.

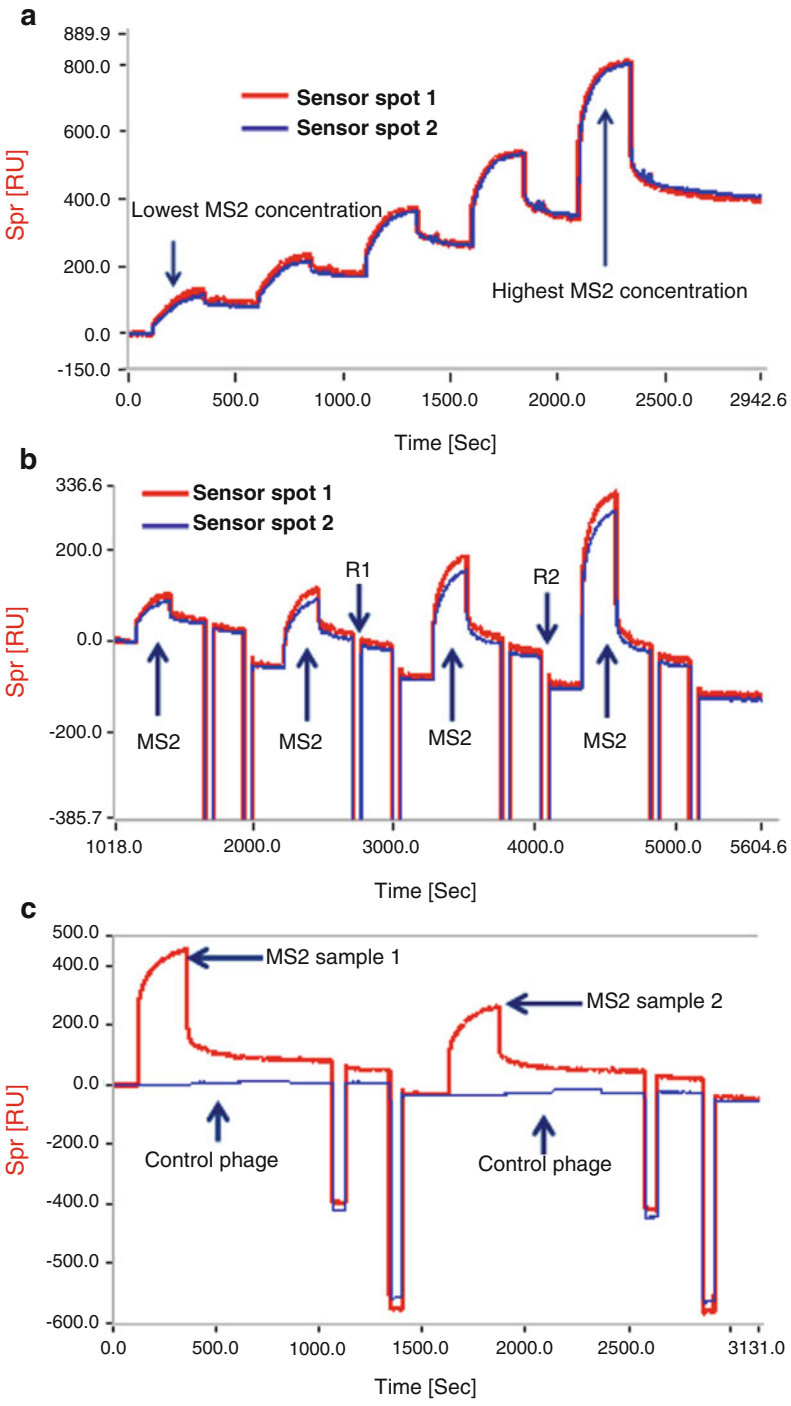

Fig. 10.12 The sensorgrams of the (**a**) continuous, (**b**) regenerative virus binding experiments, (**c**) cross-reactivity test using phage as control [80]

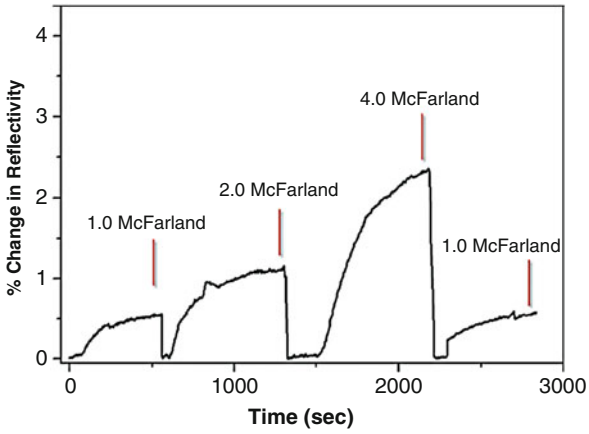

Fig. 10.13 The sensorgrams of the SPR sensor against the apple juice spiked with *Escherichia coli* at different concentrations [82]

Riedel and his research group offered SPR sensor to develop a new-generation medical diagnostic technologies [81]. They introduced an SPR sensor based on diagnosing different stages of Epstein–Barr virus infections in clinical serum samples and showed that the detection of the antibodies against three different antigens present in the virus was achieved by their study. The interference of the fouling from serum during the measurements was prevented by coating the SPR sensor with an antifouling layer of a polymer brush. Attachment of receptors by hybridization of complementary oligonucleotides allowed the SPR sensor surface regeneration after measurements by disrupting the complementary pairs above the melting temperature of oligonucleotides.

The detection of pathogenic bacteria is necessary to prevent infections and also life-threatening illnesses. Yılmaz et al. described a molecularly imprinted SPR sensor to detect *Escherichia coli* from water sources [82]. They choose amino acid-based molecule to provide similar interaction as in natural antibodies. After the polymerization, they first characterized the SPR sensor surface and then obtained a linear behavior as 98.79% at different *Escherichia coli* concentrations in the range of 0.5–4.0 McFarland. They also performed the real sample experiments with apple juice (Fig. 10.13). According to their results, the increment of the concentration of *Escherichia coli* gave rise to an increment in SPR sensor reflectivity.

Wang and collaborators displayed an SPR sensor for *Escherichia coli* O157: H7 detection [83]. In their system, *Escherichia coli* O157: H7 cells and goat polyclonal antibodies for *Escherichia coli* O157: H7 were incubated, and then the *Escherichia coli* O157: H7 cells were removed by a centrifugation step. Their results exhibited that the signals were oppositely correlated with the concentration of *Escherichia coli* O157: H7 cells in a scale from 3.0×10^4 to 3.0×10^8 CFU/mL. They compared the SPR sensor and ELISA to capture *Escherichia coli* O157: H7, and the LOD value was decreased by one order of magnitude. They commented that their method simplified bacterial cell detection and has the capacity to provide an efficient option for detecting *Escherichia coli* O157: H7 and other pathogens.

Karoonuthaisiri et al. aimed to display how filamentous M13 bacteriophages expressing 12-mer peptides could work in SPR sensor to detect the foodborne bacterium *Salmonella* [84]. They examined different factors for the successful

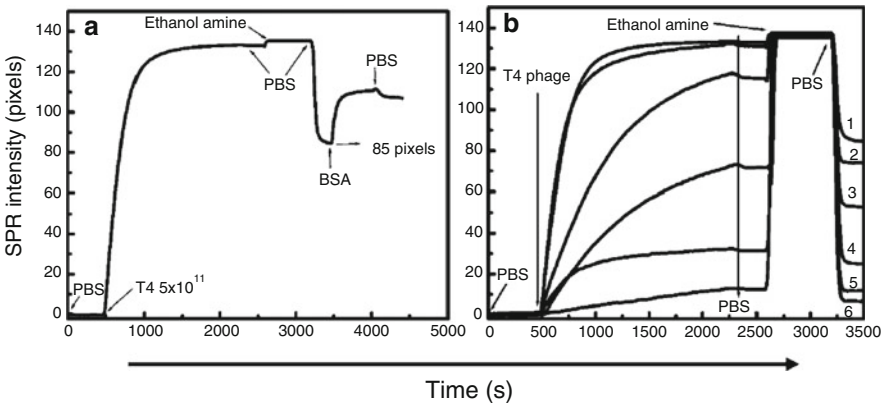

Fig. 10.14 The sensorgrams of the SPR sensor for (**a**) covalent immobilization of T4 phage, (**b**) covalent immobilization of different concentrations of T4 phages [85]

bacteriophage detection by SPR sensor. They used citric–Na_2HPO_4 buffer at pH 3.0–7.4 as an immobilization buffer for four different bacteriophage clones (MSal020401, MSal020404, MSal020417, and LM0205P01H01). They obtained low cross-reactivity and LOD values of 8.0×10^7 and 1.3×10^7 CFU/mL for one-time and five-time. Feasibility of label-free SPR assay for rapid pathogen detection by employing M13 bacteriophages expressing target-specific peptides was proved by their studies.

A T4 bacteriophage assay and SPR system were developed by Arya et al. as a specific receptor and transduction system to detect *Escherichia coli* K12 bacteria [85]. They used dithiobis(succinimidyl propionate) to immobilized T4 phages onto gold SPR sensor surfaces by utilizing self-assembled monolayer. They demonstrated that SPR sensor could detect the *Escherichia coli* K12 with high specificity against non-host *Escherichia coli* NP10 and NP30. They obtained the maximum host bacterial capture when T4 phages concentration was used as 1.5×10^{11} PFU/mL for immobilization. Figure 10.14a showed the plot of the SPR sensor response versus time induced by the chemical modification of the phages on the SPR sensor surfaces. Also, they recorded the responses of the SPR sensor for the binding properties by employing different concentrations of T4 phage solution. The number of curves from 1 to 6 had 5×10^{11}, 1.5×10^{11}, 1×10^{11}, 8×10^{10}, 5×10^{10}, and 1×10^{10} PFU/mL concentration in Fig. 10.14b.

Kuo et al. developed SPR sensing system for differentiation of cell detection in living cells due to the differences of the cell surfaces optical features [86]. Evaluation of the mesenchymal stem cells osteogenic differentiation by SPR system application was reported, and a linear relationship with a high correlation coefficient between the duration of osteogenic induction and the difference in refractive angle shift was observed. They used a He-Ne laser that penetrated through a polarizer and a beam splitter. The one was detected by a photodiode, while the other one was coupled by a prism for generation of surface plasmon wave by which the angle shift was detected

with a photodiode. At the end of the study, they emphasized that their SPR system could define osteogenic maturation of mesenchymal stem cells in a live cell as a label-free manner without cell breakage.

Yanase and collaborators reported that huge changes of refractive index by living cells could be detected with SPR sensor systems [87]. They performed the refractive index visualization of individual living cells by the prepared SPR imaging sensor. Developed SPR imaging sensor could detect reactions of individual rat basophilic leukemia cells and mouse keratinocyte cells in response. Furthermore the reactions of individual human basophils isolated from patients in response to an allergen could be detected also by the SPR sensor system. They obtained that SPR signals by the binding of anti-DNP IgE and DNP-HSA to rat basophilic leukemia cells were cultured on the surface of the SPR sensor. According to their results, the SPR system could visualize several stimuli, inhibitors effect, and conditions on cell reactions as a change of intracellular refractive index distribution at single cell levels.

The same research group also presented an SPR imaging system that had a multiple sensing with a hydrophobic membrane to detect basophils that were isolated from patients [88]. They only used a microliter of patient's blood and detected specific reactions of human receptor-expressing mast cells in response to antigens. SPR imaging system might be an excellent throughput screening system of type I allergy, not only for freshly prepared basophils but also for sera stored in clinical practices, and was claimed as a functional device for their studies. The refractive index changes of receptor-expressing mast cells were observed by the SPR imaging sensor. In addition, they obtained the time course of refractive index changes in the area with receptor-expressing mast cells in the presence or absence of anti-IgE.

5.5 Drug Detection

High affinity synthetic receptors can be used to detect drugs in clinical diagnosis studies. Altintas et al. prepared SPR sensors by using molecularly imprinted polymers that were combined with computational simulation [89]. They first synthesized the metoprolol imprinted polymers and then produced SPR sensor to sensing metoprolol. Metoprolol is a blocker drug that is detected by SPR sensor in the range of 1.9 ng/mL–1.0 μg/mL with a correlation coefficient of 0.97. They also developed a regeneration method for the reusability of SPR sensor. They calculated the K_d as 1.35×10^{-10} M by using Langmuir isotherm model. They also determined the stability experiment by measuring the size and quality of the receptor periodically during 6 months. Their results showed the success of computationally modeled receptor with SPR sensor for drug detection and monitoring.

The same research group members synthesized nanoparticles by using SPR sensor that are based on molecular imprinting method for diclofenac detection [90]. They measured the size of nanoparticles as around 132.3 nm with 0.1 of polydispersity index that confirms the property of the nanoparticles. After that, they immobilized the nanoparticle onto the SPR sensor surface via covalent coupling with EDC/NHS and detected diclofenac in the range of 1.24–80 ng/mL by the SPR

sensor. They also performed the efficiency of SPR sensor by using functionalized diclofenac with gold nanoparticles and free diclofenac. Glycine–hydrochloric acid solution was used to regenerate the SPR sensor surfaces. Subsequent analyses performed by them indicated the stability of the sensor surface. They obtained the K_d value as 1.48×10^{-9} M. At the end, they examined the cross-reactivity studies against other pharmaceuticals by employing the SPR sensor.

Yockell-Lelièvre and his collaborators achieved to detect methotrexate with a plasmon-coupling assay [91]. They immobilized the gold nanoparticles onto the sensor inserted in a portable four-channel localized SPR reader and competition of free methotrexate and folic acid. They claimed that their sensor system allowed measuring methotrexate according to the total internal reflection plasmonic spectroscopy. Color changes can be visible to the naked eye for methotrexate by the huge shifts of the plasmon-coupling assay.

Pernites et al. developed the chemosensitive sensor to detect naproxen, paracetamol, and theophylline by employing non-covalent molecularly imprinted polymers [92]. Monofunctional and bifunctional hydrogen bonding terthiophene and carbazole monomers series were compared for imprinting these drugs. They characterized the prepared surfaces by several techniques and confirmed the templating and release of the drug from the cross-linked conducting polymer film.

Pernites and coworkers also prepared a sensor to detect theophylline by molecularly imprinted polymeric film [93]. They monitored the formation of the electropolymerized molecularly imprinted polymeric film by electrochemical SPR sensor allowing examination of the simultaneous changes in electrochemical and optical properties of the film (Fig. 10.15). They obtained a calibration curve of the SPR sensor for theophylline detection with a 10–50 μM^{-1} range and LOD value of 3.36 μM^{-1}.

Golub and collaborators used SPR sensor based on metallic nanoparticles for cocaine detection by using aptasensor configuration [94]. As seen in Fig. 10.16, their sensors were depended on utilizing two anti-cocaine aptamer subunits, where one subunit was assembled on a gold support, acting as an SPR-active surface, and the second aptamer subunit was labeled with other nanoparticles (Pt, CdS, Au). In different configurations, quantitative analysis of cocaine was estimated by the addition of cocaine resulting in the formation of supramolecular complexes between the nanoparticle-labeled aptamer subunits and cocaine on the metallic surface. Detection of cocaine by the electrocatalyzed reduction was exhibited by the complex formation between the supramolecular Pt nanoparticles aptamer subunits and cocaine molecules. In addition, the generated photocurrents by the CdS nanoparticle-labeled aptamer subunits-cocaine complex also allowed the photoelectrochemical detection of cocaine. They showed that all aptasensors were able to analyze cocaine with a LOD value in the range of 10^{-6}–10^{-5} M.

Wang et al. investigated an application of case study that depended on Mach–Zehnder configuration and SPR sensor for drug screening, calculating reaction kinetic constants, inhibition effect and cytotoxicity analysis [95]. They selected cetuximab as a target molecule and measured with a sensitivity of 10^{-6} and stability of 6×10^{-7} refractive index unit in 80 min in SPR sensor. Reaction kinetic constants of cetuximab binding to epidermal growth factor receptor was calculated as $1.75 \pm 0.29 \times 10^{-3}$ S^{-1}

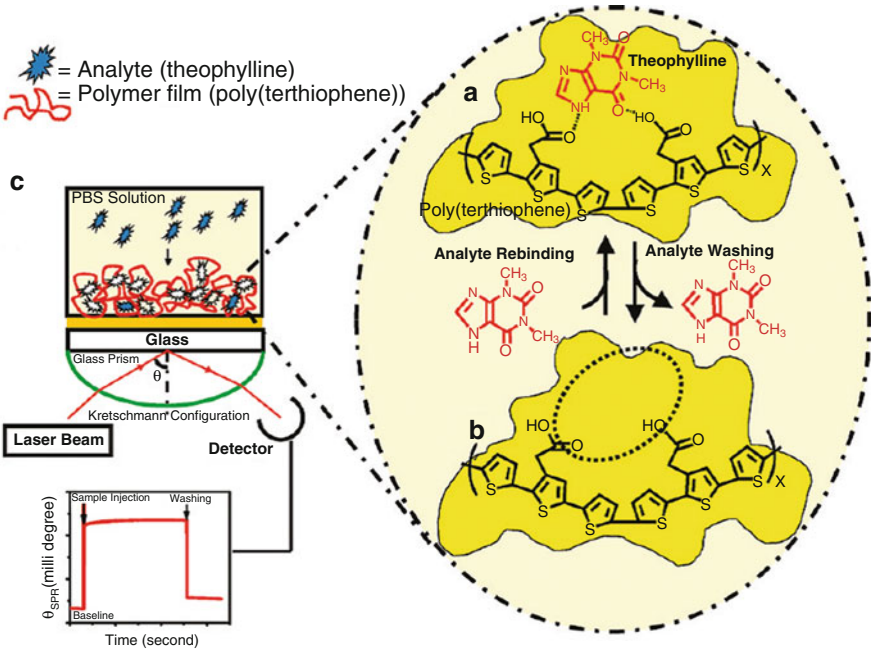

Fig. 10.15 (**a**) Molecular imprinting of theophylline, (**b**) formation of the cavity after washing, (**c**) SPR setup for sensing of theophylline [93]

and 4.19 ± 0.58 nM. Their results showed that cetuximab could block epidermal growth factor receptor binding to its two ligands, epidermal growth factor, and epidermal growth factor receptor-transforming growth factor. They tested this effect in three cell lines of lung adenocarcinoma, colon cancer, and breast cancer.

Evaluation of the influence of some gene expressions on anti-tumor drug cytotoxicity by Wang and coworkers provided the mechanism effect of connexin 43 as a tumor suppressor gene [96]. They used an SPR sensor to determine the influence of connexin 43 expressions on cisplatin cytotoxicity in different cancer cell lines. Their results exhibited that the SPR response curves had two stages. They showed that the changes which were related to connexin 43 expression in the first hour were interpreted by the SPR responses. In the second stage, the SPR response slowly decreased that was related to apoptosis. They compared the SPR measurements from several conventional biological assays with their system, and the results showed that cellular response to cisplatin in the period of oxidative stress could be affected by the connexin 43 expression.

Sari et al. developed an SPR sensor to determine erythromycin in the aqueous solution [97]. They combined the three techniques that were mini-emulsion polymerization, molecular imprinting, and SPR. They obtained R^2 and LOD values as 0.99 and 0.29 ppm, respectively. They also determined the selectivity property of this SPR sensor by using kanamycin sulfate, neomycin sulfate, and spiramycin. They claimed that the SPR sensor had low cost, was rapid, and provided reliable results in order to be used in the detection of erythromycin from aqueous solution.

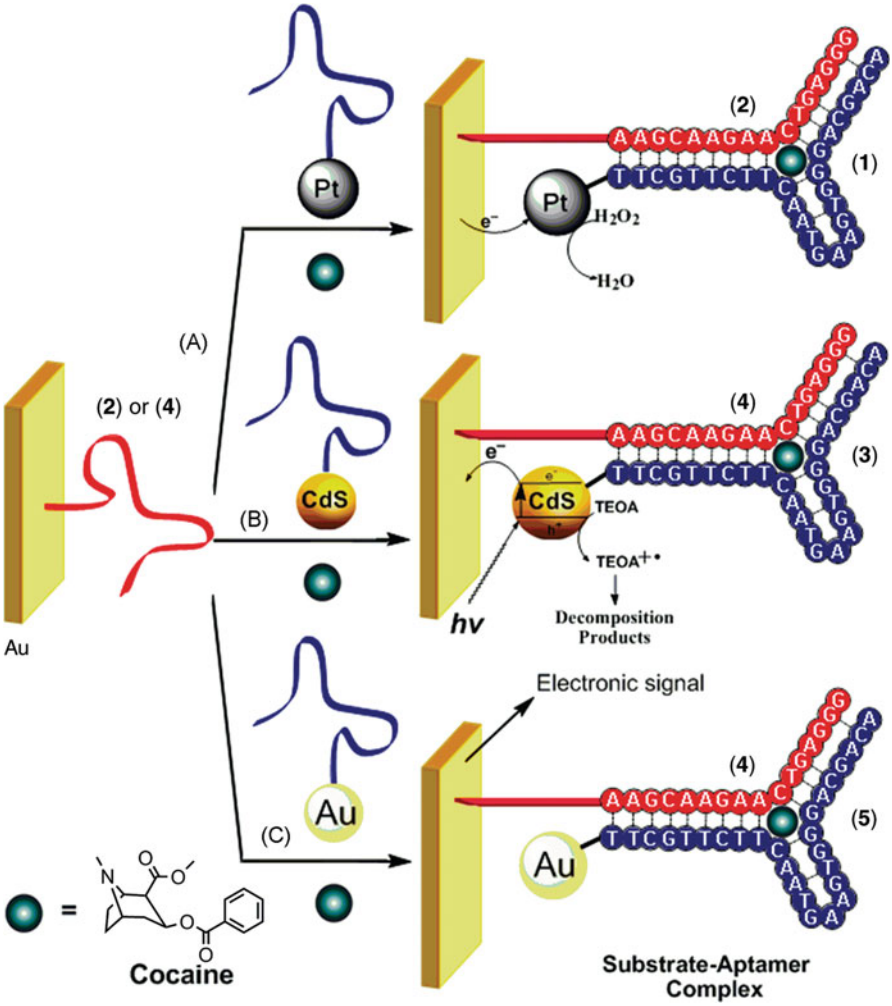

Fig. 10.16 (**a**) Electrochemical, (**b**) photoelectrochemical, and (**c**) SPR analysis [94]

6 Conclusions and Future Perspectives

Up to now, more than 40,000 publications related to SPR sensors were reported by ISI Web of Knowledge. When the assignment of the topics was analyzed, the impacts of the technologies were critically on medical diagnosis. Recently, the researchers demonstrated that the several studies on applications of real samples has performed.

In this chapter, different kinds of platforms and emerging technological inventions like coupling between SPR system and nanoparticles, microfluidics, or designing chips, analytical performance improvements for clinical diagnosis were

considered. As a case study, hormones detection associated with the endocrine disorders, protein biomarkers in relation to cancer and cardiac diseases, and immune system disease diagnoses by antibody detection were discussed. In addition, nucleic acid sensing was reviewed for genetic disorders and pathogens detections. Finally, immunosensing approaches were discussed for pathogens detection.

Innovative surface chemistry development and antifouling strategies guarantee decreased non-specific binding, which is necessary for biological fluids analysis with reduced sample pretreatment, dilution, heat, or filtration. In summary, SPR sensors propose comparable analytical performances to conventional methods used in medical diagnosis by ensuring real-time monitoring, label-free detection, parallel analysis, high-throughput analysis, little sample pretreatment, fast responses, and low cost. Considering these reasons, it is believed, in the near future, SPR will appear as an efficient, powerful, and alternative system for daily routine clinical analysis by opening also new horizons for future developments in personalized medicine and in point-of-care diagnostics. So far, published information originated from academic studies and the application of SPR sensors for medical diagnosis will obtain momentum in the next future.

References

1. Labib M, Sargent EH, Kelley SO (2016) Electrochemical methods for the analysis of clinically relevant biomolecules. Chem Rev 116:9001–9090
2. Stojanović I, Schasfoort RBM, Terstappen LWMM (2014) Analysis of cell surface antigens by surface plasmon resonance imaging. Biosens Bioelectron 52:36–43
3. Saylan Y, Yılmaz F, Derazshamshir A, Yılmaz E, Denizli A (2017) Synthesis of hydrophobic nanoparticles for real-time lysozyme detection using surface plasmon resonance sensor. J Mol Recognit 30:e2631.1–7
4. Saylan Y, Akgönüllü S, Çimen D, Derazshamshir A, Bereli N, Yılmaz F, Denizli A (2017) Surface plasmon resonance nanosensors based on molecularly imprinted nanofilm for detection of pesticides. Sensors Actuators B Chem 241:446–454
5. Ronkainen NJ, Halsall HB, Heineman WR (2010) Electrochemical biosensors. Chem Soc Rev 39:1747–1763
6. Guerreiro GV, Zaitouna AJ, Lai RY (2014) Characterization of an electrochemical mercury sensor using alternating current, cyclic, square wave and differential pulse voltammetry. Anal Chim Acta 810:79–85
7. Campuzanoa S, Kuralay F, Lobo-Castañón MJ, Bartošík M, Vyavaharea K, Paleček E, Haake DA, Wang J (2011) Ternary monolayers as DNA recognition interfaces for direct and sensitive electrochemical detection in untreated clinical samples. Biosens Bioelectron 26(8):3577–3583
8. Atay S, Pişkin K, Yılmaz F, Çakır C, Yavuz H, Denizli A (2016) Quartz crystal microbalance based biosensors for detecting highly metastatic breast cancer cells via their transferrin receptors. Anal Methods 8:153–161
9. Çiçek Ç, Yılmaz F, Özgür E, Yavuz H, Denizli A (2016) Molecularly imprinted quartz crystal microbalance sensor (QCM) for bilirubin detection. Chemosensors 4(4):21–34
10. Sener G, Ozgur E, Yılmaz E, Uzun L, Say R, Denizli A (2010) Quartz crystal microbalance based nanosensor for lysozyme detection with lysozyme imprinted nanoparticles. Biosens Bioelectron 26:815–821
11. Wang Y, Li J, Viehland D (2014) Magnetoelectrics for magnetic sensor applications: status, challenges and perspectives. Mater Today 17(6):269–275

12. Melzer M, Karnaushenko D, Lin G, Baunack S, Makarov D, Schmidt OG (2015) Direct transfer of magnetic sensor devices to elastomeric supports for stretchable electronics. Adv Mater 27(8):1333–1338
13. Zhang Y, Shen J, Yang H, Yang Y, Zhou Z, Yang S (2015) A highly selective magnetic sensor for Cd^{2+} in living cells with (Zn, Mn)-doped iron oxide nanoparticles. Sensors Actuators B Chem 207:887–892
14. Peiker P, Oesterschulze E (2015) Geometrically tuned wettability of dynamic micromechanical sensors for an improved in-liquid operation. Appl Phys Lett 107(10):101903–101907
15. Borin D, Melli M, Zilio SD, Toffoli V, Scoles G, Toffoli G, Lazzarino M (2014) How to engineer superhydrophobic micromechanical sensors preserving mass resolution. Sensors Actuators B Chem 199:62–69
16. Hu KM, Zhang WM, Shi X, Yan H, Peng ZK, Meng G (2016) Adsorption-induced surface effects on the dynamical characteristics of micromechanical resonant sensors for in situ real-time detection. J Appl Mech 83(8):081009–081020
17. Guo X (2012) Surface plasmon resonance based biosensor technique: a review. J Biophotonics 5(7):483–501
18. Fu E, Chinowsky T, Nelson K, Yager P (2008) Chapter 10: SPR imaging for clinical diagnostics. In: Handbook of surface plasmon resonance. Royal Society of Chemistry, Cambridge, pp 313–332
19. Caucheteur C, Guo T, Albert J (2015) Review of plasmonic fiber optic biochemical sensors: improving the limit of detection. Anal Bioanal Chem 407:3883–3897
20. Wood RW (1902) On a remarkable case of uneven distribution of light in a diffraction grating spectrum. Philos Mag 4:396–402
21. Cowan JJ (1972) The surface plasmon resonance effect in holography. Opt Commun 5:69–72
22. Schneider FW (1982) Non-linear Raman spectroscopy and its chemical applications. Biological applications of resonance CARS, Reidel Publishing Company Dordrecht: Holland/Boston: USA/London: England vol 93, pp 445–459
23. Rothenbausler B, Knoll W (1988) Surface–plasmon microscopy. Nature 332:615–617
24. Hickel W, Knoll W (1989) Surface plasmon microscopic imaging of ultrathin metal coatings. Acta Metall 37:2141–2144
25. Otto A (1968) Excitation of nonradiative surface plasma waves in silver by the method of frustrated total reflection. Z Phys 16:398–410
26. Buck RP (1990) Biosensor technology: fundamentals and applications. Marcel Dekker, New York
27. Szentirmay Z (1992) Surface plasmon spectroscopy of metal/dielectric structures. Spectrochim Acta 48:9–17
28. Welford K (1991) Surface plasmon-polaritons and their uses. Opt Quant Electron 23:1–27
29. Gutiérrez-Gallego R, Llop E, Bosch J, Segura J (2011) Surface plasmon resonance in doping analysis. Anal Bioanal Chem 401:389–403
30. Masson JF (2017) Surface plasmon resonance clinical biosensors for medical diagnostics. ACS Sens 2(1):16–30
31. Situ C, Mooney MH, Elliott CT, Buijs J (2010) Advances in surface plasmon resonance biosensor technology towards high-throughput, food-safety analysis. TrAC Trends Anal Chem 29:1305–1315
32. Helmerhorst E, Chandler DJ, Nussio M, Mamotte CD (2012) Real-time and label-free bio-sensing of molecular interactions by surface plasmon resonance: a laboratory medicine perspective. Clin Biochem Rev 33:161–173
33. Tokel O, Yildiz UH, Inci F, Durmus NG, Ekiz OO, Turker B, Cetin C, Rao S, Sridhar K, Natarajan N, Shafiee H, Dana A, Demirci U (2015) Portable microfluidic integrated plasmonic platform for pathogen detection. Sci Rep 5:9152–9161
34. Laocharoensuk R (2016) Development of electrochemical immunosensors towards point-of-care cancer diagnostics: clinically relevant studies. Electroanalysis 28:1716–1729
35. Ouellet E, Lund L, Lagally E (2013) Chapter 30: Multiplexed surface plasmon resonance imaging for protein biomarker analysis. In: Microfluidic diagnostics. Methods in molecular biology, Springer Science+Business Media, LLC, Berlin/Heidelberg, Germany vol 949. pp 473–490

36. Kirsch J, Siltanen C, Zhou Q, Revzin A, Simonian A (2013) Biosensor technology: recent advances in threat agent detection and medicine. Chem Soc Rev 42:8733–8769
37. Ranjan R, Esimbekova EN, Kratasyuk VA (2017) Rapid biosensing tools for cancer biomarkers. Biosens Bioelectron 87:918–930
38. Aćimović SS, Ortega MA, Sanz V, Berthelot J, Garcia-Cordero JL, Renger J, Maerkl SJ, Kreuzer MP, Quidant R (2014) LSPR chip for parallel, rapid, and sensitive detection of cancer markers in serum. Nano Lett 14:2636–2641
39. Ertürk G, Özen H, Tümer MA, Mattiasson B, Denizli A (2016) Microcontact imprinting based surface plasmon resonance (SPR) biosensor for real-time and ultrasensitive detection of prostate specific antigen (PSA) from clinical samples. Sensors Actuators B Chem 224:823–832
40. Uludag Y, Tothill IE (2012) Cancer biomarker detection in serum samples using surface plasmon resonance and quartz crystal microbalance sensors with nanoparticle signal amplification. Anal Chem 84:5898–5904
41. Türkoğlu EA, Yavuz H, Uzun L, Akgöl S, Denizli A (2013) The fabrication of nanosensor-based surface plasmon resonance for IgG detection. Artif Cells Nanomed Biotechnol 41:213–221
42. Ertürk G, Uzun L, Tümer MA, Say R, Denizli A (2011) Fab fragments imprinted SPR biosensor for real-time human immunoglobulin G detection. Biosens Bioelectron 28(1):97–104
43. Dibekkaya H, Saylan Y, Yılmaz F, Derazshamshir A, Denizli A (2016) Surface plasmon resonance sensors for real-time detection of cyclic citrullinated peptide antibodies. J Macromol Sci, Part A: Pure Appl Chem 53:585–594
44. Chung JW, Kim SD, Bernhardt R, Pyun JC (2005) Application of SPR biosensor for medical diagnostics of human hepatitis B virus (hHBV). Sensors Actuators B Chem 111(112):416–422
45. Uzun L, Say R, Ünal S, Denizli A (2009) Production of surface plasmon resonance based assay kit for hepatitis diagnosis. Biosens Bioelectron 24:2878–2884
46. Lu J, Stappen TV, Spasic D, Delport F, Vermeire S, Gils A, Lammertyn J (2016) Fiber optic-SPR platform for fast and sensitive infliximab detection in serum of inflammatory bowel disease patients. Biosens Bioelectron 79:173–179
47. Ramanaviciene A, German N, Kausaite-Minkstimiene A, Voronovic J, Kirlyte J, Ramanavicius A (2012) Electrochemical and electroassisted chemiluminescence methods based immunosensor for the determination of antibodies against human growth hormone were performed as comparative studies by surface plasmon resonance. Biosens Bioelectron 36:48–55
48. Im H, Shao H, Park YI, Peterson VM, Castro CM, Weissleder R, Lee H (2014) Label-free detection and molecular profiling of exosomes with a nanoplasmonic sensor. Nat Biotechnol 32(5):490–495
49. He L, Pagneux Q, Larroulet I, Serrano AY, Pesquera A, Zurutuza A, Mandler D, Boukherroub R, Szunerits S (2017) Label-free femtomolar cancer biomarker detection in human serum using graphene-coated surface plasmon resonance chips. Biosens Bioelectron 89:606–611
50. Liang RP, Yao GH, Fan LX, Qiu JD (2012) Magnetic Fe3O4@Au composite-enhanced surface plasmon resonance for ultrasensitive detection of magnetic nanoparticle-enriched α-fetoprotein. Anal Chim Acta 737:22–28
51. Osman B, Uzun L, Beşirli N, Denizli A (2013) Microcontact imprinted surface plasmon resonance sensor for myoglobin detection. Mater Sci Eng C 33:3609–3614
52. Sener G, Uzun L, Say R, Denizli A (2011) Use of molecular imprinted nanoparticles as biorecognition element on surface plasmon resonance sensor. Sensors Actuators B Chem 160:791–799
53. Bocková M, Song XC, Gedeonová E, Levová K, Kalousová M, Zima T, Homola J (2016) Surface plasmon resonance biosensor for detection of pregnancy associated plasma protein A2 in clinical samples. Anal Bioanal Chem 408(26):7265–7269
54. Murakami K, Tokuda M, Suzuki T, Irie Y, Hanaki M, Izuo N, Monobe Y, Akagi K-i, Ishii R, Tatebe H, Tokuda T, Maeda M, Kume T, Shimizu T, Irie K (2016) Monoclonal antibody with conformational specificity for a toxic conformer of amyloid β42 and its application toward the Alzheimer's disease diagnosis. Sci Rep 6:29038–29050

55. Sankiewicz A, Romanowicz L, Laudanski P, Zelazowska-Rutkowska B, Puzan B, Cylwik B, Gorodkiewicz E (2016) SPR imaging biosensor for determination of laminin-5 as a potential cancer marker in biological material. Anal Bioanal Chem 408:5269–5276
56. Brun APL, Soliakov A, Shah DSH, Holt SA, McGill A, Lakey JH (2015) Engineered self-assembling monolayers for label free detection of influenza nucleoprotein. Biomed Microdevices 17:49–59
57. Liu Y, Liu Q, Chen S, Cheng F, Wang H, Peng W (2015) Surface plasmon resonance biosensor based on smart phone platforms. Sci Rep 5:12864–12873
58. Sener G, Ozgur E, Rad AY, Uzun L, Say R, Denizli A (2013) Rapid real-time detection of procalcitonin using a microcontact imprinted surface plasmon resonance biosensor. Analyst 138:422–428
59. Mariani S, Minunni M (2014) Surface plasmon resonance applications in clinical analysis. Anal Bioanal Chem 406:2303–2323
60. Cenci L, Andreetto E, Vestri A, Bovi M, Barozzi M, Iacob E, Busato M, Castagna A, Girelli D, Bossi AM (2015) Surface plasmon resonance based on molecularly imprinted nanoparticles for the picomolar detection of the iron regulating hormone Hepcidin-25. J Nanobiotechnol 13:51–66
61. Zhang Q, Jing L, Zhang J, Ren Y, Wang Y, Wang Y, Wei T, Liedberg B (2014) Surface plasmon resonance sensor for femtomolar detection of testosterone with water-compatible macroporous molecularly imprinted film. Anal Biochem 463:7–14
62. Vashist SK, Marion Schneider E, Barth E, Luong JHT (2016) Surface plasmon resonance-based immunoassay for procalcitonin. Anal Chim Acta 938:129–136
63. Treviño J, Calle A, Rodríguez-Frade JM, Mellado M, Lechuga LM (2009) Single- and multi-analyte determination of gonadotropic hormones in urine by surface plasmon resonance immunoassay. Anal Chim Acta 647:202–209
64. Treviño J, Calle A, Rodríguez-Frade JM, Mellado M, Lechuga LM (2009) Surface plasmon resonance immunoassay analysis of pituitary hormones in urine and serum samples. Clin Chim Acta 403:56–62
65. Srivastava SK, Verma R, Gupta BD, Khalaila I, Abdulhalim I (2015) SPR based fiber optic sensor for the detection of vitellogenin: an endocrine disruption biomarker in aquatic environments. Biosens J 4:1–5
66. Yockell-Lelièvre H, Bukar N, McKeating KS, Arnaud M, Cosin P, Guo Y, Dupret-Carruel J, Mouginb B, Masson JF (2015) Plasmonic sensors for the competitive detection of testosterone. Analyst 140:5105–5112
67. Sanghera N, Anderson A, Nuar N, Xie C, Mitchell D, Klein-Seetharaman J (2017) Insulin biosensor development: a case study. Int J Parallel Emergent Distrib Syst 32(1):119–138
68. Sharon E, Freeman R, Riskin M, Gil N, Tzfati Y, Willner I (2010) Optical, electrical and surface plasmon resonance methods for detecting telomerase activity. Anal Chem 82:8390–8397
69. Diltemiz SE, Denizli A, Ersöz A, Say R (2008) Molecularly imprinted ligand-exchange recognition assay of DNA by SPR system using guanosine and guanine recognition sites of DNA. Sensors Actuators B Chem 133:484–488
70. Bini A, Mascini M, Mascini M, Turner APF (2011) Selection of thrombin-binding aptamers by using computational approach for aptasensor application. Biosens Bioelectron 26:4411–4416
71. Kaur G, Paliwal A, Tomar M, Gupta V (2016) Detection of Neisseria meningitidis using surface plasmon resonance based DNA biosensor. Biosens Bioelectron 78:106–110
72. Gifford LK, Sendroiu IE, Corn RM, Luptak A (2010) Attomole detection of mesophilic DNA polymerase products by nanoparticle-enhanced surface plasmon resonance imaging on glassified gold surfaces. J Am Chem Soc 132:9265–9267
73. D'Agata R, Breveglieri G, Zanoli LM, Borgatti M, Spoto G, Gambari R (2011) Direct detection of point mutations in nonamplified human genomic DNA. Anal Chem 83:8711–8717
74. Cho H, Yeh EC, Sinha R, Laurence T, Bearinger J, Lee L (2012) Single-step nanoplasmonic VEGF165 aptasensor for early cancer diagnosis. ACS Nano 6:7607–7614

75. Jahanshahi P, Zalnezhad E, Sekaran SD, Adikan FRM (2014) Rapid immunoglobulin M-based dengue diagnostic test using surface plasmon resonance biosensor. Sci Rep 4:3851–3858
76. Altintas Z, Pocock J, Thompson KA, Tothill IE (2015) Comparative investigations for adenovirus recognition and quantification: plastic or natural antibodies? Biosens Bioelectron 74:996–1004
77. Basso CR, Tozato CC, Ribeiro MCM, Junior JPA, Pedros VA (2013) A immunosensor for the diagnosis of canine distemper virus infection using SPR and EIS. Anal Methods 5:5089–5096
78. Bai H, Wang R, Hargis B, Lu H, Li Y (2012) A SPR aptasensor for detection of avian influenza virus H5N1. Sensors 12:12506–12518
79. Diltemiz SE, Ersöz A, Hür D, Keçili R, Say R (2013) 4-Aminophenyl boronic acid modified gold platforms for influenza diagnosis. Mater Sci Eng C 33:824–830
80. Altintas Z, Gittens M, Guerreiro A, Thompson KA, Walker J, Piletsky S, Tothill IE (2015) Detection of waterborne viruses using high affinity molecularly imprinted polymers. Anal Chem 87:6801–6807
81. Riedel T, Rodriguez-Emmenegger C, Santos Pereira A, Bědajánková A, Jinoch P, Boltovets PM, Brynda E (2014) Diagnosis of Epstein–Barr virus infection in clinical serum samples by an SPR biosensor assay. Biosens Bioelectron 55:278–284
82. Yilmaz E, Majidi D, Ozgur E, Denizli A (2015) Whole cell imprinting based Escherichia Coli sensors: a study for SPR and QCM. Sensors Actuators B Chem 209:714–721
83. Wang Y, Ye Z, Si C, Ying Y (2011) Subtractive inhibition assay for the detection of E. coli O157:H7 using surface plasmon resonance. Sensors 11:2728–2739
84. Karoonuthaisiri N, Charlermroj R, Morton MJ, Oplatowska-Stachowiak M, Grant IR, Elliott CT (2014) Development of a M13 bacteriophage-based SPR detection using Salmonella as a case study. Sensors Actuators B Chem 190:214–220
85. Arya SK, Singh A, Naidoo R, Wu P, McDermott MT, Evoy S (2011) Chemically immobilized T4-bacteriophage for specific Escherichia coli detection using surface plasmon resonance. Analyst 136:486–492
86. Kuo YC, Ho JH, Yen TJ, Chen HF, Lee OKS (2011) Development of a surface plasmon resonance biosensor for real-time detection of osteogenic differentiation in live mesenchymal stem cells. PLoS One 6(7):e22382–e22389
87. Yanase Y, Hiragun T, Yanase T, Kawaguchi T, Ishii K, Hide M (2013) Application of SPR imaging sensor for detection of individual living cell reactions and clinical diagnosis of type I allergy. Allergol Int 62:163–169
88. Yanase Y, Hiragun T, Yanase T, Kawaguchi T, Ishii K, Kumazaki N, Obara T, Hide M (2014) Clinical diagnosis of type I allergy by means of SPR imaging with less than a microliter of peripheral blood. Sens Bio-Sens Res 2:43–48
89. Altintas Z, France B, Ortiz JO, Tothill IE (2016) Computationally modelled receptors for drug monitoring using an optical based biomimetic SPR sensor. Sensors Actuators B Chem 224:726–737
90. Altintas Z, Guerreiro A, Piletsky SA, Tothill IE (2015) NanoMIP based optical sensor for pharmaceuticals monitoring. Sensors Actuators B Chem 213:305–313
91. Yockell-Lelièvre H, Bukar N, Toulouse JL, Pelletiera JN, Masson JF (2016) Naked-eye nanobiosensor for therapeutic drug monitoring of methotrexate. Analyst 141:697–703
92. Pernites RB, Ponnapati RR, Felipe MJ, Advincula RC (2011) Electropolymerization molecularly imprinted polymer (E-MIP) SPR sensing of drug molecules: pre-polymerization complexed terthiophene and carbazole electroactive monomers. Biosens Bioelectron 26:2766–2771
93. Pernites RB, Ponnapati RR, Advincula RC (2010) Surface plasmon resonance (SPR) detection of theophylline via electropolymerized molecularly imprinted polythiophenes. Macromolecules 43:9724–9735

94. Golub E, Pelossof G, Freeman R, Zhang H, Willner I (2009) Electrochemical, photoelectrochemical, and surface plasmon resonance detection of cocaine using supramolecular aptamer complexes and metallic or semiconductor nanoparticles. Anal Chem 81:9291–9298
95. Wang Y, Zhang C, Zhang Y, Fang H, Min C, Zhu S, Yuan XC (2015) Investigation of phase SPR biosensor for efficient targeted drug screening with high sensitivity and stability. Sensors Actuators B Chem 209:313–322
96. Wang Y, Zhang S, Zhang C, Zhao Z, Zheng X, Xue L, Liu J, Yuan XC (2016) Investigation of an SPR biosensor for determining the influence of connexin 43 expression on the cytotoxicity of cisplatin. Analyst 141:3411–3421
97. Sari E, Üzek R, Duman M, Denizli A (2016) Fabrication of surface plasmon resonance nanosensor for the selective determination of erythromycin via molecular imprinted nanoparticles. Talanta 150:607–614

Photoacoustic Imaging Tools for Nanomedicine

11

Jeesu Kim and Chulhong Kim

Contents

1 Definition of the Topic

Photoacoustic imaging is a biomedical imaging method that has grown explosively over the last decades. Functional molecular and morphological information of biological molecules, cells, tissues, and organs can be obtained through photoacoustic images. In addition to endogenous light absorbing chromophores, various exogenous contrast agents have been developed to obtain molecular photoacoustic images. Thus, this technology has been soon popular in nanomedicine. This chapter introduces various types of photoacoustic imaging systems and recent trends in photoacoustic image-guided nanomedicine.

J. Kim · C. Kim (✉)
Department of Creative IT Engineering, Pohang University of Science and Technology, Pohang, Gyeongbuk, Republic of Korea
e-mail: chulhong@postech.edu; chulhong@postech.ac.kr

C. S. S. R. Kumar (ed.), *Nanotechnology Characterization Tools for Biosensing and Medical Diagnosis*, https://doi.org/10.1007/978-3-662-56333-5_11

2 Overview

Molecular imaging has been widely explored for detecting early cancer, monitoring drug delivery, and evaluating therapeutic efficacy. Among various molecular imaging methods, photoacoustic imaging (PAI) has received great interest in recent decades. PAI combines optical and ultrasound imaging concepts and thus can provide several promising advantages in molecular imaging:

1. PAI is noninvasive and completely free from ionizing radiation.
2. PAI penetrates much deeper than conventional optical imaging methods.
3. PAI provides both functional molecular information, based on light absorption, and morphological information of living tissues.
4. PAI is relatively cheap and easy to implement in combination with conventional ultrasound imaging techniques.

Because of these advantages, PAI has found a wide variety of uses in biomedical research, including tracking single cells in blood vessels, mapping vasculature networks, imaging cancer at the molecular level, monitoring drug delivery, and evaluating therapeutic efficiency. In these biomedical studies, both endogenous and exogenous contrasts have been used. Typical endogenous chromophores include oxyhemoglobin, deoxy-hemoglobin, lipid, melanin, and water. To acquire deep tissue images with enhanced contrast, various exogenous contrast agents have been developed and applied, including organic dyes, gold nanoparticles, carbon nanotubes, and organic nanostructures.

In what follows, we describe (1) the basic principles of PAI, (2) various types of PAI systems, (3) recent trends in contrast agents, and (4) applications of contrast-enhanced PAI.

3 Introduction

In the last few decades, molecular imaging has been widely used in biomedical research such as studying cancer physiopathology, studying brain hemodynamics, enhancing diagnostic accuracy, developing new drugs, and monitoring therapeutic efficacy. Various biomedical imaging modalities have been developed and applied for these purposes.

Among these molecular imaging methods, pure optical imaging has been most extensively investigated because it is cost-efficient, is simple to implement, offers real-time imaging, and is noninvasive [1]. Optical imaging provides molecular information about biological tissues with high optical contrast. However, because of the strong light scattering in biological tissues, pure optical imaging methods suffer from a shallow imaging depth of typically ~1 mm, the so-called diffusion limit.

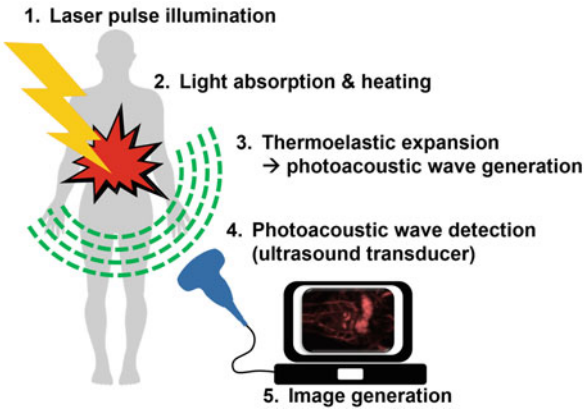

Fig. 11.1 The basic principles of photoacoustic imaging

PAI is a biomedical imaging modality that breaks the diffusion limit. As noted above, PAI has attracted great interest in recent decades due to its noninvasiveness, non-ionizing radiation, and relatively inexpensive and easy implementation. The underlying principle of PAI is the photoacoustic (PA) effect, a series of energy transductions from light to acoustic waves [2]. Figure 11.1 shows the basic principles of PAI. When a short laser pulse (typically a few nanoseconds) illuminates the object, its light absorbing substances capture the light energy. Rapidly alternating expansion and contraction via thermoelastic expansion generate acoustic waves, which propagate in all directions. Conventional ultrasound (US) transducers detect the generated acoustic waves, from which PA images are then generated.

Because PAI combines optical and US imaging concepts, it can penetrate much deeper than conventional optical imaging methods and still maintain high US resolution [2–5]. PAI inherits strengths of both optical and US imaging methods and thus can visualize both functional and morphological information of biological substances, including molecules, cells, tissues, and organs [6–8]. In addition, by scaling its spatial resolution and imaging depth, PAI can be used for applications ranging from molecular biology to clinical practice [4].

Because of these advantages, PAI has been widely utilized in both preclinical and clinical biomedical research. Typical preclinical studies include (1) visualizing organelles, such as melanosomes and mitochondria; (2) mapping vasculature networks and lymphatic systems; (3) tracking single cells, including melanoma cells and red blood cells; and (4) conducting molecular cancer imaging, monitoring drug delivery, and evaluating therapeutic efficiency. In the clinic, PAI is usually integrated with a US machine to visualize and stage breast cancers and melanoma [9–13].

In all of these biomedical studies, maximizing the PA signals in deep tissues is desired. From the principles of the PAI, the initial pressure P [Pa] of a PA wave is proportional to four parameters:

$$P \propto \Gamma(T)\sigma\mu_a F \tag{11.1}$$

In Eq. 11.1, $\Gamma(T)$ is the Gruneisen coefficient (which depends on the local temperature), σ [dimensionless] is the energy conversion efficiency from light to heat in the range of $0 \leq \sigma \leq 1$, μ_a [cm^{-1}] is the optical absorption coefficient (which depends on the concentration and the excitation wavelength), and F [Wm^{-2}] is the fluence of light. Because of the linearly proportional relationship between the initial pressure of the PA wave and the four parameters, the PA signal can be easily enhanced by increasing one of the four parameters. Especially, increasing the optical absorption coefficient by using optically absorbing contrast agents is an efficient way to increase the sensitivity of the PA signals.

Endogenous contrast agents, including oxyhemoglobin, deoxy-hemoglobin, lipid, melanin, and water, can be utilized for in vivo PA images. However, these substances unfortunately do not strongly absorb near-infrared (NIR) light (wavelengths between 650 and 1000 nm), which penetrates deeply in biological tissues [14]. To acquire deep tissue PA images, exogenous contrast agents that absorb NIR light are necessary.

Methylene blue and indocyanine green (ICG), organic dyes approved for human uses by the US Food and Drug Administration (FDA), have been applied for PAI in vivo [15–17]. However, these small molecules circulate quickly and their light absorbing capability is relatively weak. To overcome these limitations, several gold nanostructures, carbon nanotubes, and quantum dots have been extensively synthesized and applied because they have exceptionally strong optical absorption and can be easily modified for specific applications [18–24]. Yet these types of nanoparticles are not biodegradable and thus pose continuing safety concerns. As alternatives, various organic nanoparticles, such as colored microbubbles, liposomal nanoformulations, and polymeric nanostructures, have recently been developed for contrast-enhanced PA imaging.

So far, several articles have reviewed PAI systems and nanoparticles for contrast-enhanced PA imaging [2, 4, 5]. This chapter introduces various scales of PAI systems and focuses on recent trends in organic nanostructures and their applications. By exploring the recent trends and therapeutic applications, we can discover the future direction of contrast-enhanced PA imaging.

4 Experimental and Instrumental Methodologies

4.1 Photoacoustic Imaging Systems

PAI systems for preclinical animal studies are of two main types: PA microscopy (PAM) and PA computed tomography (PACT). PAM systems generally utilize point-by-point raster scanning of a single-element focused transducer to acquire volumetric images [25–28]. The imaging speed of PAM is relatively slow, because the light and the transducer both need to be scanned to get a single image. In contrast, PACT systems use various configurations of array transducers, such as linear, arc, ring, and circular arrays [29–31]. The parallel detection provided by array transducers enables real-time image generation, but mathematical reconstruction may generate artifacts.

PACT has also been developed with clinically available transducers [12, 32–34]. In particular, clinically promising PAI systems have recently been developed with commercial USI platforms [10, 11, 35, 36].

4.1.1 Photoacoustic Microscopy (PAM)

In PAM, 1D depth-resolved PA signals are obtained by using a single-element focused transducer, and then 2D and 3D images are acquired by point-by-point scanning. The transverse resolution of PAM is scaled by controlling the acoustic or optical focus, while the axial resolution depends on the center frequency of the transducer. PAM systems are generally utilized for label-free vasculature mapping in small animals. The main advantage of PAM is that images can be obtained without mathematical reconstruction algorithms that generate artifacts. However, the imaging speed and penetration depth are respectively limited by the mechanical raster scanning and optical diffusion.

Figure 11.2a is a schematic of an acoustic-resolution PAM (AR-PAM) system [25, 26]. The system can achieve multiscale PA images by selecting US transducers with different center frequencies (Fig. 11.2b). PA images from a 5-MHz transducer have axial and transverse resolutions of 590 and 150 μm, respectively. By using a 40-MHz transducer, the axial and transverse resolutions are improved to 85 and 50 μm, respectively. However, the imaging depth is reduced from ~30 mm (5 MHz) to ~3 mm (40 MHz). In vivo spectroscopic whole-body PA images of small animals can be acquired by extending the scanning region and tuning the excitation wavelengths.

As another type of PAM, optical-resolution PAM (OR-PAM) systems have been investigated (Fig. 11.3a) [27]. In OR-PAM, the transverse resolution is improved to several micrometers by controlling the focal spot size of the light to be narrower than that of the transducer (Fig. 11.3b). Similar to conventional optical imaging methods, the imaging depth of OR-PAM is limited because the optical focusing cannot be maintained beyond the optical mean free path (~1 mm). Therefore, OR-PAM is usually used for imaging shallow regions of biological tissues, such as the ears, eyes, and brains of mice.

The main disadvantage of a PAM system is its slow imaging speed, which is due to the mechanical scanning mechanism. To improve the scanning speed, laser scanning methods have been used in several PAM systems. In particular, laser scanning using a microelectromechanical system (MEMS) mirror can significantly enhance the imaging speed. The excitation laser and photoacoustic waves are aligned confocally and scanned by a MEMS mirror [29, 38]. To acquire volumetric images, elevational scanning is added by using a motorized stage. A PAM system that uses a 2-axis waterproof MEMS mirror has also been demonstrated recently (Fig. 11.4a) [37]. The fast scanning mechanism enables acquiring real-time PA images without sacrificing the high SNR and high spatial resolution. The real-time imaging capability of the system has been tested by detecting a flowing stream of carbon nanoparticles in a silicone tube (Fig. 11.4b). Further, in vivo PA images of a mouse ear clearly visualized individual red blood cells as well as small blood vessels (Fig. 11.4c).

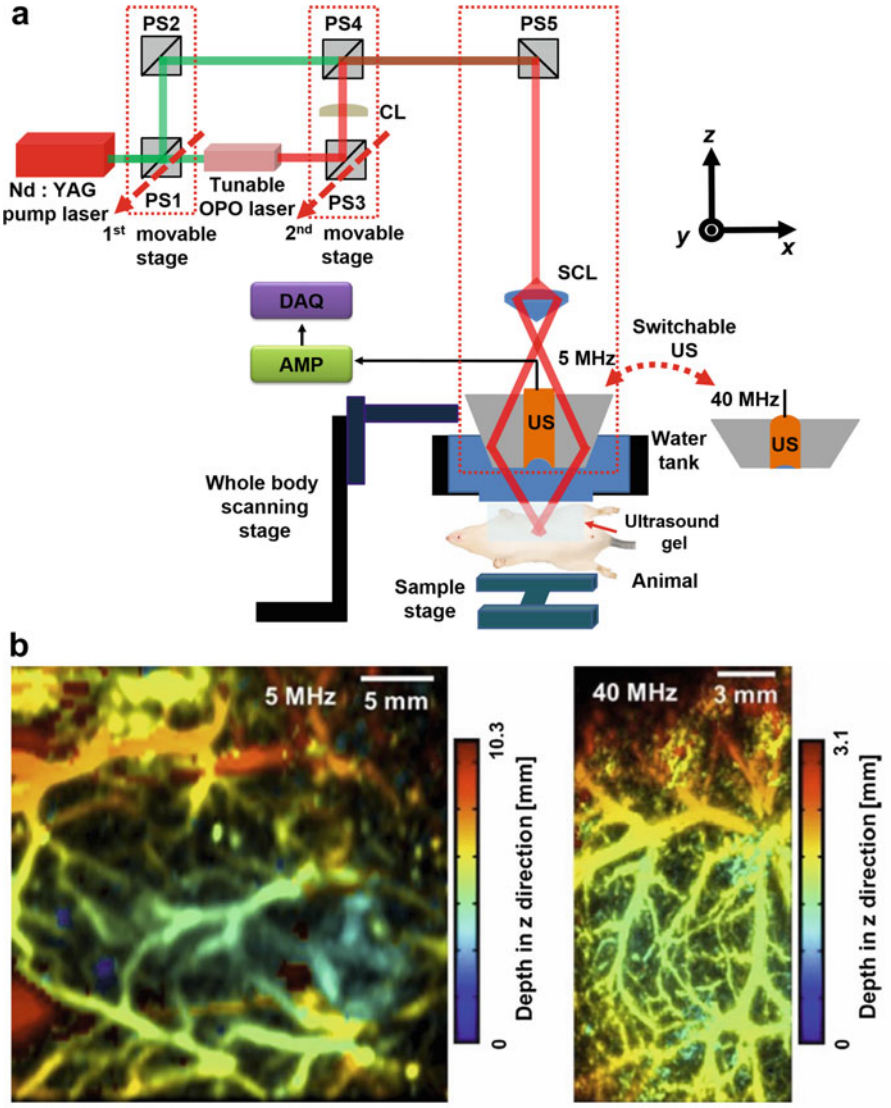

Fig. 11.2 (**a**) Schematic of an acoustic-resolution photoacoustic microscopy system. OPO, optical parametric oscillator; PS, prism; CL, collimating lens; SCL, spherical conical lens; US, ultrasound transducer; AMP, amplifier; and DAQ, data acquisition. (**b**) In vivo multiscale photoacoustic images of a rat's vascular networks (Reprinted with permission from Ref. [26])

4.1.2 Photoacoustic Computed Tomography (PACT)

In PACT, 2D images are acquired by using various types of array transducers and corresponding image reconstruction algorithms. Because the array performs parallel acoustic detection, the image can be generated significantly faster. The laser

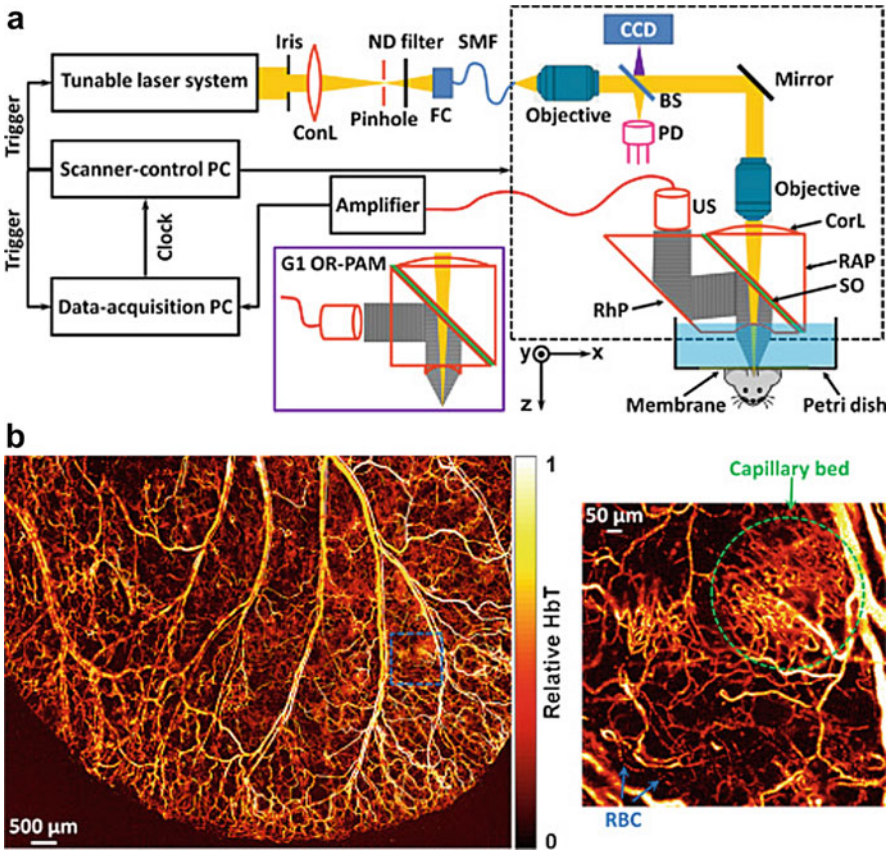

Fig. 11.3 (**a**) Schematic of an optical-resolution photoacoustic microscopy system. ConL, condenser lens; ND, neutral density filter; FC, fiber collimator; SMF, single-mode fiber; CCD, charge-coupled device; BS, beam splitter; PD, photodiode; CorL, correction lens; RAP, right-angle prism; SO, silicone oil; RhP, rhomboid prism; and US, ultrasound transducer. (**b**) In vivo photoacoustic images of a mouse ear. RBC, red blood cell (Reprinted with permission from Ref. [27])

repetition rate and data acquisition (DAQ) channel capacity determine the imaging speed of PACT. Therefore, if a large number of DAQ channels and a fast laser are used, PACT can provide real-time tomographic images of small animals. However, PACT has relatively poor spatial resolution because the illumination is moderately focused and the ultrasound transducers acquire signals over the entire image plane. In addition, image reconstruction algorithms may produce artifacts that degrade image quality.

As an example of a PACT system, a system using a full-ring array has been developed (Fig. 11.5a) [39, 40]. The beam path of the excitation laser is controlled to produce either external or internal illumination. For external illumination, the laser is delivered using prisms, as in previous imaging systems. For internal illumination,

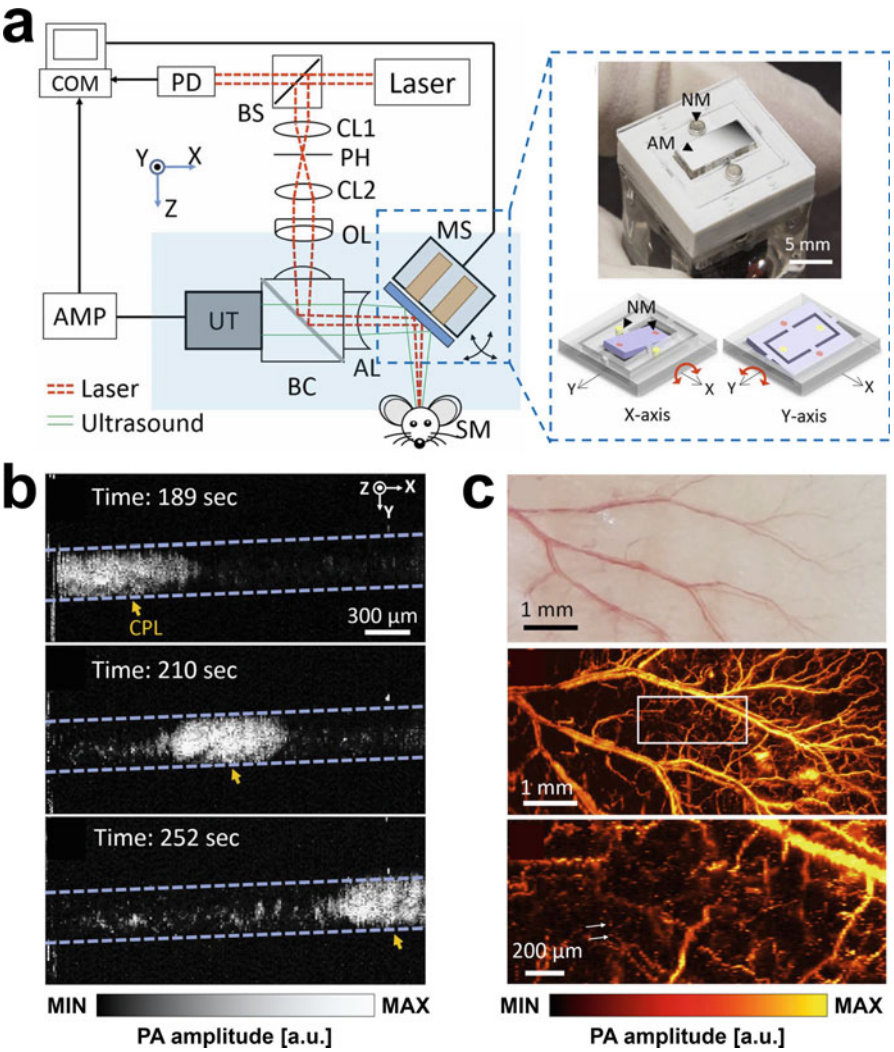

Fig. 11.4 (**a**) Schematic of a MEMS mirror-based PAM system. NM, neodymium magnet; AM, aluminum mirror; COM, computer; PD, photodiode; BS, beam splitter; AMP, amplifier; UT, ultrasound transducer; CL, condenser lens; PH, pin hole; OL, objective lens; BC, beam combiner; AL, acoustic lens; MS, MEMS scanner; and SM, sample. (**b**) In vitro PA images of carbon particles flowing in a silicone tube. CPL, carbon particles lump. (**c**) Photograph and in vivo photoacoustic images of vasculature in a mouse ear (Reprinted with permission from Ref. [37])

the laser is delivered into the subject animal's mouth through a multimode optical fiber, and the light propagates toward the brain. This system utilizes a full-ring array transducer that has 512 elements with a center frequency of 5 MHz. A 512-channel preamplifier is provided at the front end, but the analog-to-digital converter has only

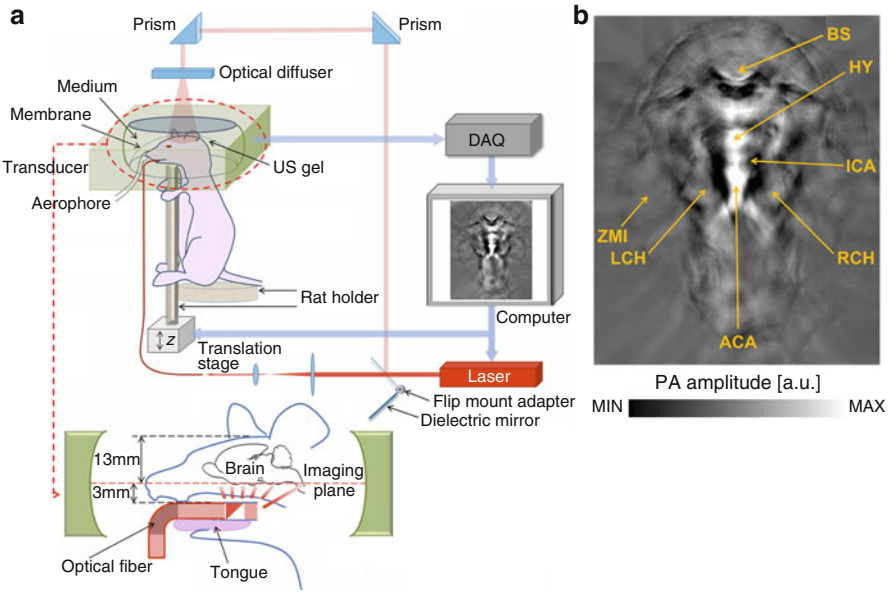

Fig. 11.5 (**a**) Schematic of a full-ring array-based photoacoustic computed tomography system. US, ultrasound; DAQ, data acquisition. (**b**) Noninvasively acquired photoacoustic image of a rat brain. BS, brain stem; HY, hypothalamus; ICA, internal carotid artery; ACA, anterior cerebral artery; RCH, right cerebral hemisphere; LCH, left cerebral hemisphere; and ZMI, zygomatic muscle interface (Reprinted with permission from Ref. [40])

64 channels. Thus eight laser shots are required to achieve one complete 2D image, acquired at a frame rate of 0.9 Hz. This system can also produce 3D images by scanning the samples vertically. Figure 11.5b shows a mouse brain PA image that was acquired noninvasively.

Arc-array-based PACT also has been developed (Fig. 11.6a). The system uses a 64-element arc-array transducer with a 3.1-MHz center frequency, a 0.7-mm gap between each element, and 152 degrees of overall angular aperture [30, 41, 42]. This system can produce 3D whole-body images by rotationally scanning the transducer (Fig. 11.6b). A full-circle (360 degrees) rotation takes 8 min, acquiring data from 32 laser shots at each imaging position for averaging. The angular gaps between imaging positions are 2.4 degrees, which represents 150 angular steps and 9600 virtual transducer positions. Figure 11.6b is a volumetric PA image of a female mouse using a 755-nm alexandrite laser. The volumetric image clearly visualizes the inferior vena cava and surrounding blood vessels. Both kidneys and the spleen are also visualized.

Figure 11.7a is a schematic of another arc-array-based PACT system [33, 43–46]. The system utilizes a 64-, 128-, or 256-element transducer with a center frequency of 5 MHz. The overall view angles of these transducers are respectively

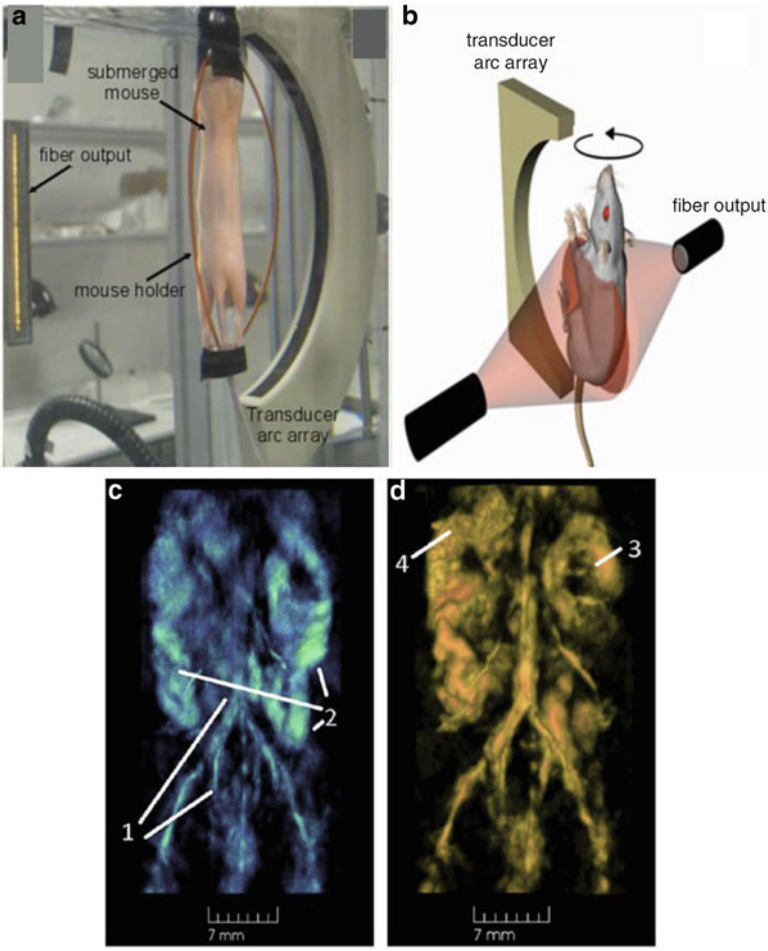

Fig. 11.6 (**a**) Photograph of an arc-array-based photoacoustic computed tomography system. (**b**) A schematic of the experimental geometry. (**c**) and (**d**) In vivo whole-body photoacoustic images of a mouse using excitation wavelengths of (**c**) 800 and (**d**) 1064 nm. 1, central and peripheral circulatory system; 2, intestine; 3, right kidney; and 4, spleen (Reprinted with permission from Refs. [41, 42])

172, 270, and 270 degrees. The radius of all the transducer arrays is 40 mm. The image reconstruction speed for a single slice is less than 1 ms, but the relatively slow pulse repetition rate (10 Hz) of the laser limits the frame rate. To enhance the signal-to-noise ratio (SNR) and to investigate the optically absorbing characteristics of the target object, the system can average ten signals and acquire signals from five optical wavelengths [46]. In this case, obtaining one multispectral PA image takes 17 s. The main difference from the previously introduced system is the scanning mechanism for achieving 3D images. This system linearly scans the samples, while the previous

one rotationally scans the transducer. In vivo transversal PA images of a mouse were acquired using transducers with various numbers of elements (Fig. 11.7b) [33]. Internal organs are clearly identified by comparison with the corresponding ex vivo cryoslice images. Increasing the number of elements improves the resolution of PA images. For example, the diameter of the sagittal sinus is measured as 600, 550, and 450 μm in the images acquired using 64-, 128-, and 256-element transducers, respectively.

PACT systems that use clinically applicable transducers have been developed. In particular, several breast imaging systems have been developed to visualize, identify, and diagnose cancers. Figure 11.8a is a schematic of a breast scanner consisting of a 512-element hemispherical-array US transducer with a center frequency of 5 MHz [34, 47]. The hemispherical-array transducer is positioned beneath the cup of the scanner, and then a laser beam with a wavelength of 756 nm illuminates the target tissues through an articulated arm. The transducer is scanned continuously in a spiral pattern (Fig. 11.8b) by using a 2-axis (XA) scanning stage. The PA signals at each position are acquired, and then 3D images are reconstructed by the back projection algorithm. Figure 11.8c shows vasculature networks of a human breast, clearly visualized in vivo with a spatial resolution of 420 μm and an image acquisition time of 12 s.

The two systems in Fig. 11.9 are other PAI implementations for breast imaging, in which a glass plate and a plate array transducer gently compress a human breast and then PA mammography is performed [12, 48]. The first system uses a rectangular 2D array transducer with 600 elements (20 elements horizontally and 30 elements vertically) and a center frequency of 2 MHz (Fig. 11.9a). A Ti:Sa laser pumped with Q-switched Nd:YAG laser illuminates the target in both direction, and the generated PA signals are detected on one side by the 2D array transducer. A polymethylpentene and a polymethyl methacrylate plates hold the patient's breast. A nanocomposite gel is applied to enhance the acoustic impedance matching. Figure 11.9b shows in vivo B-mode US and maximum amplitude projected PA images acquired from breast cancer patients. The reconstructed PA images visualize the blood vessels in the cancer region.

In the second system, the signal receiving transducer has 590 elements, arranged in a roughly circular grid with a center-to-center distance of 3.175 mm (Fig. 11.9c). A Q-switched Nd:YAG laser is coupled into a light delivery system and then illuminates the breast sample. The output position of laser delivery system is controlled by a motor controller. Similar to the previous system, a glass plate and a 2D array transducer hold the patient's breast, and a conventional US gel is added for acoustic coupling. The generated photoacoustic signals are gathered by the transducer and then reconstructed to an average intensity projected PA image (Fig. 11.9d). To enhance the signal-to-noise ratio, 128 images are acquired and averaged. In the PA image, high contrast signals are clearly visualized in lesion area.

These breast imaging systems are promising for clinical use, but they may not be applicable for other parts of the body due to their breast-specific design. One approach that overcomes this limitation is shown schematically in Fig. 11.10a a PAI system with a handheld imaging probe [32]. The fiber-guided laser beam is delivered onto the center of

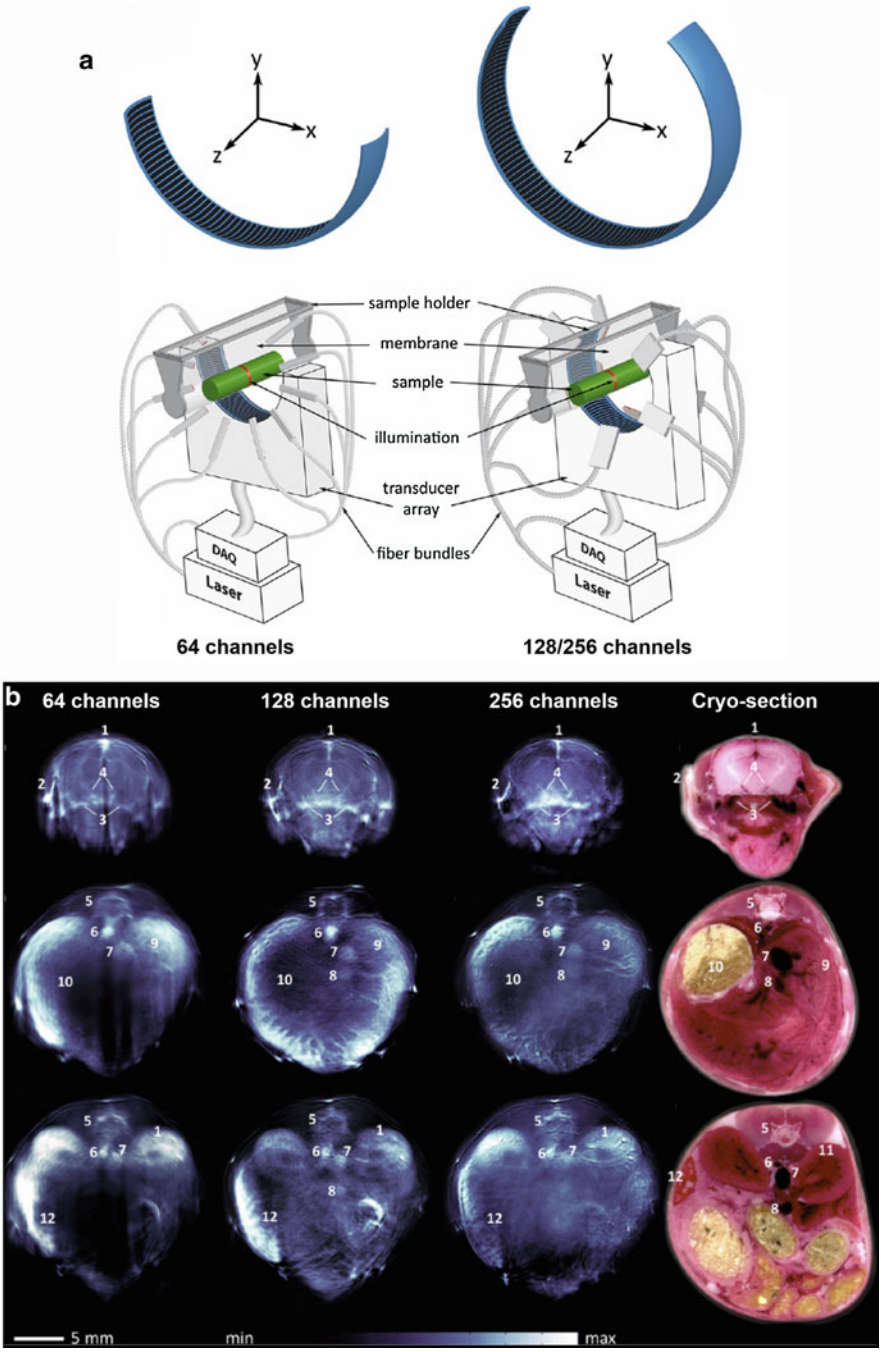

Fig. 11.7 (continued)

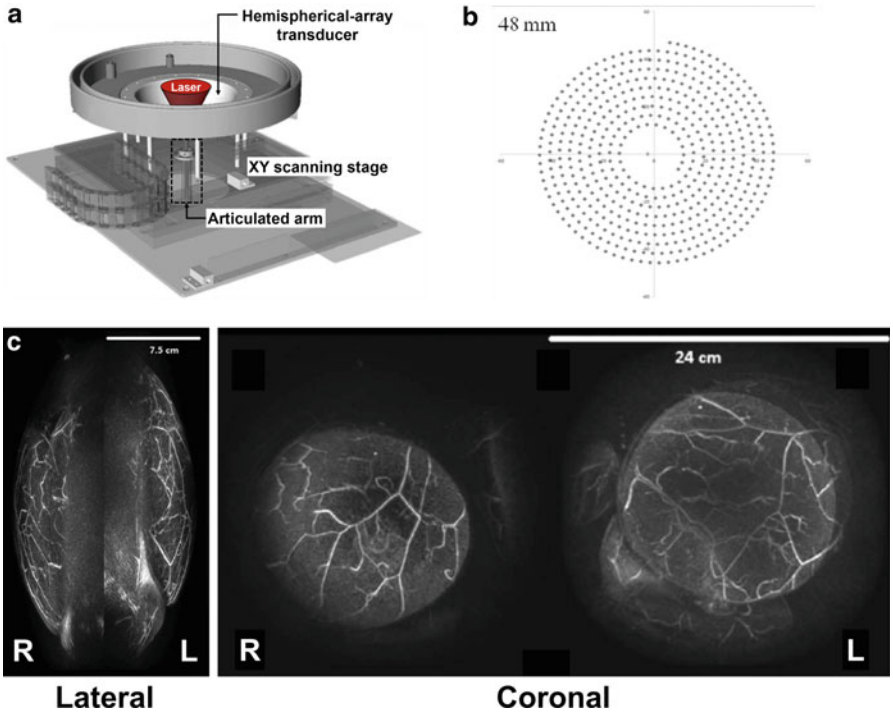

Fig. 11.8 (**a**) Schematic of a hemispherical-array-based photoacoustic tomography system. (**b**) The spiral scanning pattern of the transducer. (**c**) In vivo maximum intensity projected photoacoustic images in the lateral and coronal planes. R, right; L, left (Reprinted with permission from Ref. [47])

the spherical transducer surface, where 256 piezoelectric elements, with a center frequency of 4 MHz, collect the volumetric ($15 \times 15 \times 7$ mm^3) PA data. A 32-channel DAQ system is used for saving data; thus eight laser shots are required to obtain one volumetric image. Fortunately, real-time imaging is enabled by the relatively fast (up to 50 Hz) pulse repetition rate of the laser. Figure 11.10b presents in vivo whole-body images of mice acquired with this system [50]. Maximum amplitude projected images in various planes verify the real-time volumetric imaging capability of the system. By changing the excitation wavelengths, the system can also be used to distinguish endogenous chromophores with different optical absorption characteristics

Fig. 11.7 (**a**) Schematic of an arc-array-based photoacoustic computed tomography system. (**b**) In vivo transversal photoacoustic images and corresponding ex vivo cryo-sections of a mouse at various heights, acquired with various numbers of elements. 1, sagittal sinus; 2, temporal artery; 3, extracranial blood vessel; 4, deep cerebral vessel; 5, spinal cord; 6, aorta; 7, vena cava; 8, vena porta; 9, liver; 10, stomach; 11, kidney; and 12, spleen (Reprinted with permission from Ref. [43])

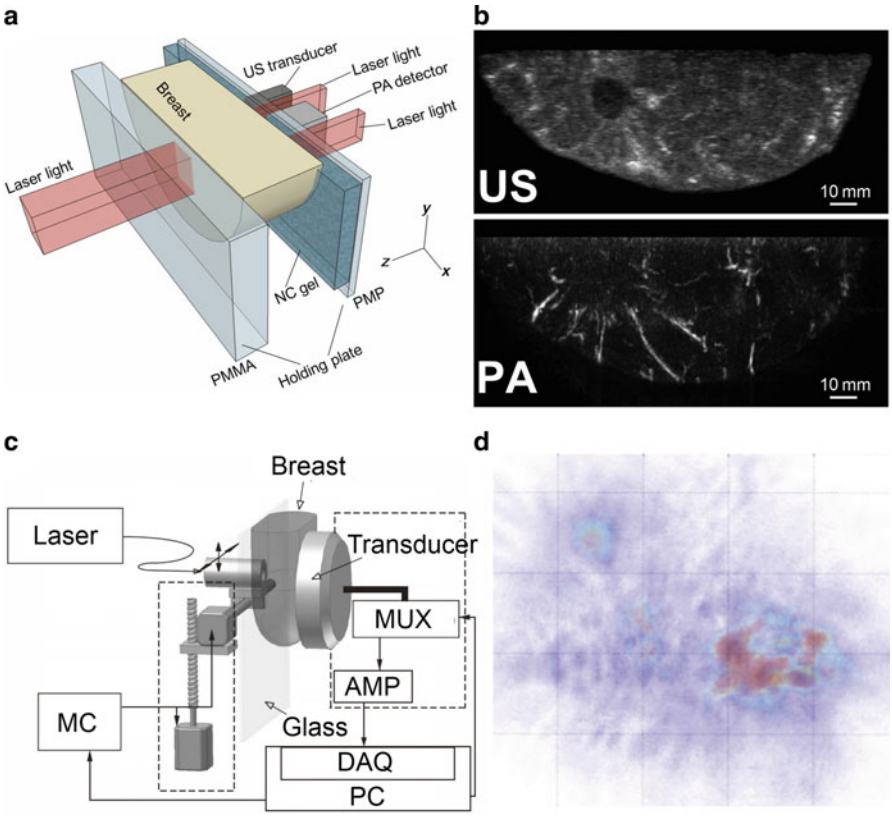

Fig. 11.9 (**a**) Schematic of a photoacoustic mammography system. PMP, polymethylpentene; PMMA, polymethyl methacrylate; and NC, nanocomposite. (**b**) In vivo B-mode US and maximum amplitude projected PA images of human breast cancer. PA, photoacoustic; and US, ultrasound. (**c**) Schematic of the photoacoustic mammoscope. MUX, multiplexer; AMP, amplifier; DAQ, data acquisition; PC, personal computer; and MC, motor controller. (**d**) Average intensity projection of a volumetric PA image of a human breast (Reprinted with permission from Refs. [12, 48, 49])

(Fig. 11.10c). The three main endogenous chromophores (i.e., oxyhemoglobin, deoxyhemoglobin, and melanin) are distinguished by multispectral analysis. By providing five-dimensional imaging (3D volume, time, and wavelength), the system shows great potential for conducting numerous biomedical studies.

4.1.3 Photoacoustic Imaging Systems Combined with Clinical Ultrasound Imaging Platforms

Because the signal reception and image generation mechanisms of PAI are identical to those of USI, they are often combined into a dual imaging modality [9, 51, 52]. Such a combined PA and US imaging (PAUSI) system can share a conventional US transducer. More importantly, PAI and USI can respectively provide functional molecular information and structural information of biological tissues. This

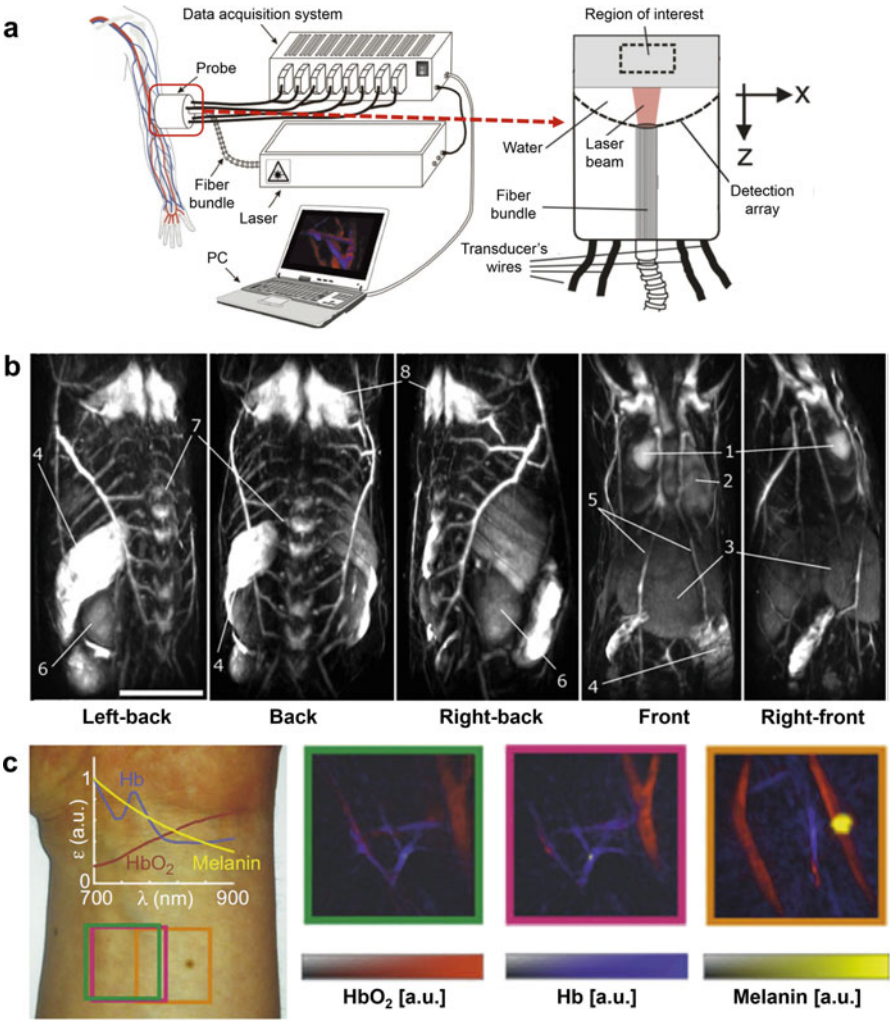

Fig. 11.10 (**a**) Schematic of a multispectral real-time photoacoustic imaging system and a handheld imaging probe. (**b**) In vivo maximum amplitude projected photoacoustic images of mice in various planes. 1, left atrium; 2, cardiac ventricles; 3, liver; 4, spleen; 5, thoracic vessels; 6, kidney; 7, spine; 8, brown adipose tissue. (**c**) Photograph of a human forearm and real-time PA signals from three different endogenous chromophores: HbO2, oxyhemoglobin; Hb, deoxyhemoglobin; and melanin (Reprinted with permission from Refs. [32, 50])

complementary information can enhance diagnostic accuracy and thereby help the clinicians establish an effective treatment plan.

One of the major issues of PAUSI system is compactness of laser, which determines the mobility of the system and directly related to the clinical availability of the system. A PAUSI system that uses a compact laser system has recently been developed (Fig. 11.11a) [53]. The diode-pumped laser measures

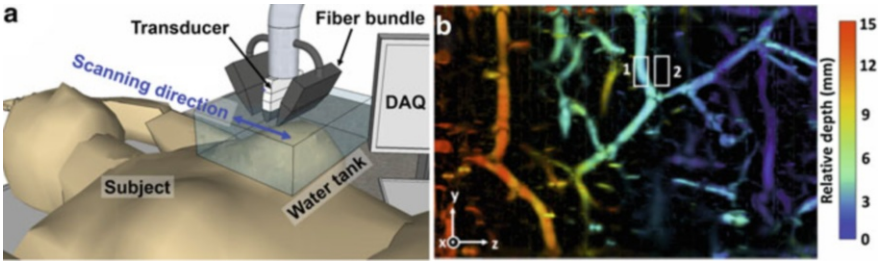

Fig. 11.11 (**a**) Illustration of breast imaging. (**b**) Depth-encoded maximum amplitude projected photoacoustic image of vasculature in a human breast. Color represents relative depth from the transducer surface (Reprinted with permission from Ref. [53])

$13 \times 14 \times 7$ cm^3 and weighs 2.4 kg. Moreover, the system utilizes an ultrasound research platform (Vantage, Verasonics) which can be programmed to acquire PA images as well as US images. Thus PAI and USI are fully integrated in a single platform. The laser beam is guided to the imaging surface and then integrated with a linear array US transducer with a center frequency of 5 MHz (ATL/Philips L7–4). By scanning in an elevational direction, volumetric data and corresponding maximum amplitude projected images are reconstructed. As Fig. 11.11b shows, the vasculature networks in a human breast are clearly visualized with a quantified SNR of 36 dB, which is calculated by using the signals in white rectangular 1 and 2 as signal and noise, respectively. Nevertheless, while the system has successfully demonstrated in vivo PA imaging using a compact laser, it is still based on an US research platform rather than on a clinical US imaging system.

Yet another preclinical commercial PAI system (Vevo LAZR, FujiFilm VisualSonics) combines a portable laser system and a conventional US imaging system [35]. A linear array US transducer (MS250, FujiFilm VisualSonics) and an optical fiber bundles are assembled into a handheld probe (Fig. 11.12a). A NIR Nd:YAG laser with wavelengths ranging from 680 to 970 nm generates 20-Hz pulsed illumination. Because there are 256 transducer elements and 64 receiving channels, four laser shots are required to achieve one B-mode PA image. Consequently, the frame rate of PAI is 5 Hz. By scanning the imaging probe in an elevational direction, volumetric PA images can be acquired (Fig. 11.12b). The system also can investigate spectral analysis by tuning the excitation wavelengths. However, due to its high-frequency transducer (21 MHz), this system is more suitable for preclinical animal imaging than human imaging.

Clinical US imaging systems also can be combined with PA imaging. Fig. 11.13a is a photograph of an integrated PAUSI system which consists of a clinical US system (iU22, Philips Healthcare) and an Nd:YAG-pumped dye laser [10]. The laser beam is delivered through bifurcated fiber bundles and then integrated with a linear array US transducer that has a center frequency of 6 MHz (L8–4, Philips Healthcare). The raw data are extracted from a modified DAQ module and then

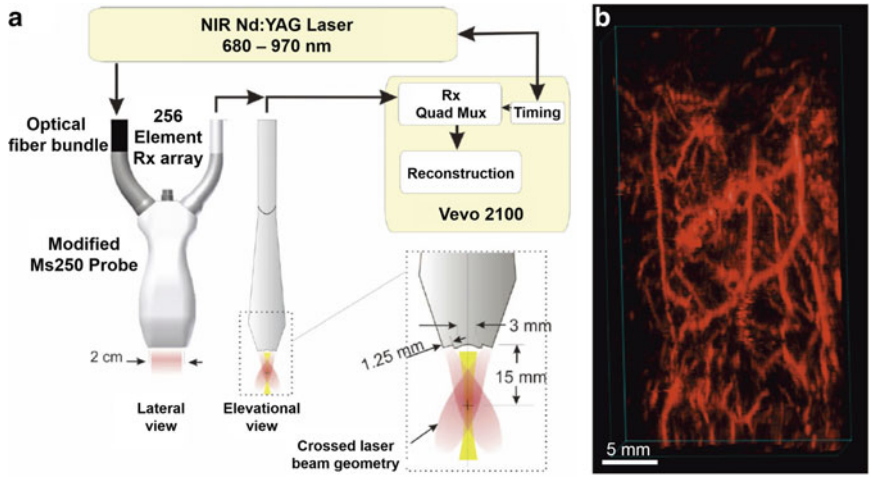

Fig. 11.12 (**a**) Schematic of the integrated transducer array and signal processing procedure in a commercialized photoacoustic imaging system. (**b**) Projection view of 3D photoacoustic data of vasculature networks in the lower abdominal region of a mouse (Reprinted with permission from Ref. [35])

reconstructed to yield PA and US images by using the Fourier beamforming algorithm (Fig. 11.9b). Although the system successfully integrates PAI with a clinical US machine, its main drawback is its large size. The Nd:YAG-pumped dye laser is too big to use in clinics. In addition, PAI has not been fully integrated with the US machine: the DAQ board has been modified to extract raw data, and therefore additional DAQ and image reconstruction modules are required.

Figure 11.13b shows a recently developed PAUSI system that combines an FDA-cleared US machine (EC-12R, Alpinion Medical Systems) and a transportable laser [11]. Wavelength-tuned laser illumination is delivered via a bifurcated fiber bundle and then integrated with US transducers. This system provides four types of transducers, which are linear array (L3–12, center frequency of 8.5 MHz, Alpinion Medical Systems), convex array (SC1–6, center frequency of 3.8 MHz, Alpinion Medical Systems), phased array (SP1–5, center frequency of 3.1 MHz, Alpinion Medical Systems), and endocavity (EC3-10H, center frequency of 7.5 MHz, Alpinion Medical Systems). More importantly, this PAUSI system has a programmable platform, so users can implement specific operational sequences. PA, US, and overlaid PAUS images are displayed in real time at a frame rate of 5 Hz with the linear array transducer. Raw channel data can be extracted, so offline investigation is also possible. As with the previously introduced systems, volumetric images are obtained by scanning the imaging probe in an elevational direction (Fig. 11.13c). Blood vessels in a human forearm were clearly visualized in both maximum amplitude projected and cross-sectional images. Based on its programmable platform, the system can be applied to various clinical studies.

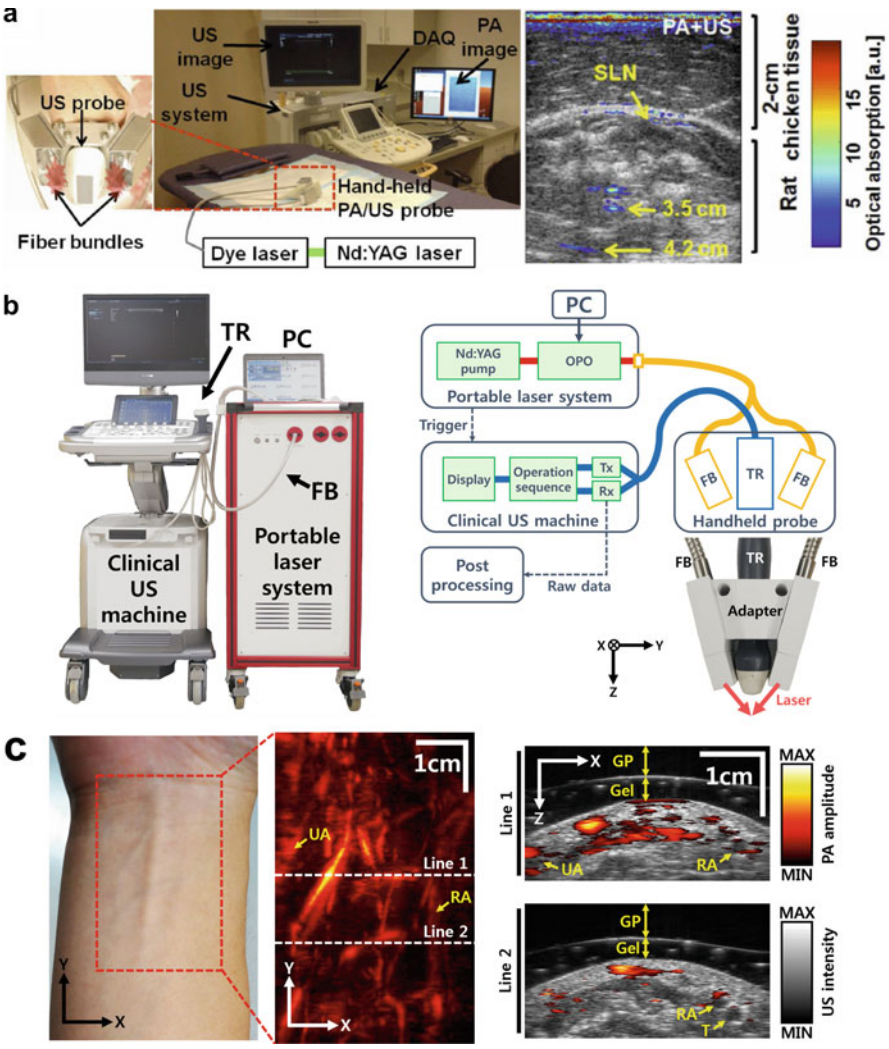

Fig. 11.13 (**a**) Photograph of a clinical photoacoustic and ultrasound imaging system and an image of rat sentinel lymph node overlaid with chicken breast tissue. PA, photoacoustic; US, ultrasound; DAQ, data acquisition; and SLN, sentinel lymph node. (**b**) Photograph and schematic of the programmable clinical photoacoustic and ultrasound imaging system. TR, ultrasound transducer; FB, fiber bundle; PC, personal computer; and OPO, optical parametric oscillator. (**c**) Photograph and in vivo photoacoustic images of a human forearm. In the maximum amplitude projected PA image (center), the cross-sectional images corresponding to the position of Line 1 and 2 are displayed on the right. GP, gelatin pad; Gel, ultrasound gel; UA, ulnar artery; RA, radial artery; and T, tendon (Reprinted with permission from Ref. [10, 11])

5 Key Research Findings

5.1 Organic Nanoparticles as Contrast Agents for Photoacoustic Imaging

It follows from the principles of PAI that optically absorbing contrast agents efficiently enhance the SNR of images. The optical absorption capacity of endogenous chromophores, such as oxyhemoglobin, deoxy-hemoglobin, melanin, water, and lipid, is not strong in the NIR region, but due to optical transparency, the penetration depth of light is maximized in that region [14]. Therefore, for deep tissue imaging, an obvious approach is to use exogenous contrast agents that absorb NIR light.

For this purpose, organic dyes such as methylene blue and indocyanine green (ICG) have been used for some time now [15–17]. Although these molecules are biocompatible and biodegradable, they are limited by their quick circulation time and relatively weak light absorption. To overcome these limitations, gold nanoparticles of several shapes, quantum dots, and carbon nanotubes have been widely investigated. These nanoparticles absorb light strongly and can be easily modified for molecular targeting or drug loading [18–24]. However, they raise long-term safety concerns, such as biodegradation and heavy metal toxicity. Gold nanoparticles have been considered biocompatible, but still have biodegradability problems. It has been reported that more than 40% of administered gold nanoparticles are accumulated in internal organs such as the liver, spleen, and lung [54]. Small-sized nanoparticles, typically ~10 nm in diameter, do not accumulate in these organs. However, when the size of the contrast agent is small, the light absorption is low and the PA signal is reduced. To overcome this problem, small nanoparticles that aggregate in response to the microenvironment of the target tissue, such as the low pH of a tumor site, have been used. However, the synthesis of such nanoparticles is complicated. Therefore, recent trends in contrast agents are shifting toward organic nanostructures such as colored microbubbles, liposomal nanoformulations, and polymeric nanostructures.

5.1.1 Colored Microbubbles and Nanobubbles

PAI is usually combined with other biomedical imaging methods. Among them, USI is the most commonly integrated method because it shares the same signal reception and image generation procedure. Along with the integration of PA and US methods, dual-mode contrast agents for molecular imaging have also been developed. One standard contrast agent for USI is microbubbles, which have been used in various clinical applications, including cardiac chamber visualization, Doppler signal enhancement, microvascular perfusion assessment, tumor detection, and drug delivery [55]. For performing dual-mode imaging, organic dyes or nanoparticles that absorb light have been utilized to enhance the NIR light absorption of microbubbles. This section discusses the synthesis and evaluation of various colored microbubbles and nanobubbles as dual-mode contrast agents.

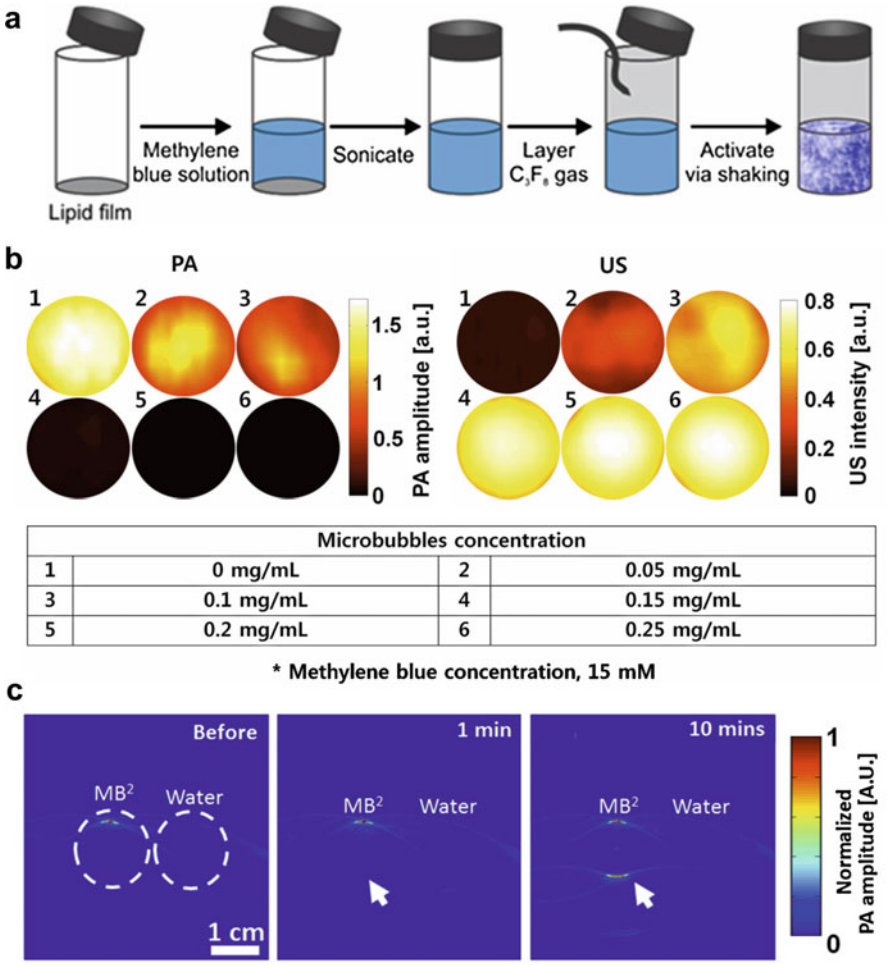

Fig. 11.14 (**a**) Schematic for synthesizing methylene blue microbubbles (MB^2). (**b**) Photoacoustic and ultrasound images of MB^2 solutions with various microbubble concentrations at a methylene blue concentration of 15 mM. (**c**) Photoacoustic images of MB^2 solution before and after sonication (Reprinted with permission from Ref. [56])

As the first example, M. Jeon et al. developed a composition of a methylene blue microbubble (MB^2) [56]. As shown in Fig. 11.14a, MB^2 was easily synthesized by combining methylene blue and microbubbles. Lipid films containing 1,2-dipalmitoyl-*sn*-glycero-3-phosphocholine (DPPC), 1,2-dipalmitoyl-sn-glycero-3-phosphate (DPPA), and 1,2-dipalmitoyl-sn-glycero-3-phosphoethanolamine-N-[methoxy(polyethylene glycol)-5000] were hydrated with methylene blue solution. After sonication, a layer of C_3F_8 gas was added and mechanically agitated to form microbubbles. Since both methylene blue and microbubbles are contrast agents commonly used in PA and US imaging, respectively, MB^2 can provide dual-mode

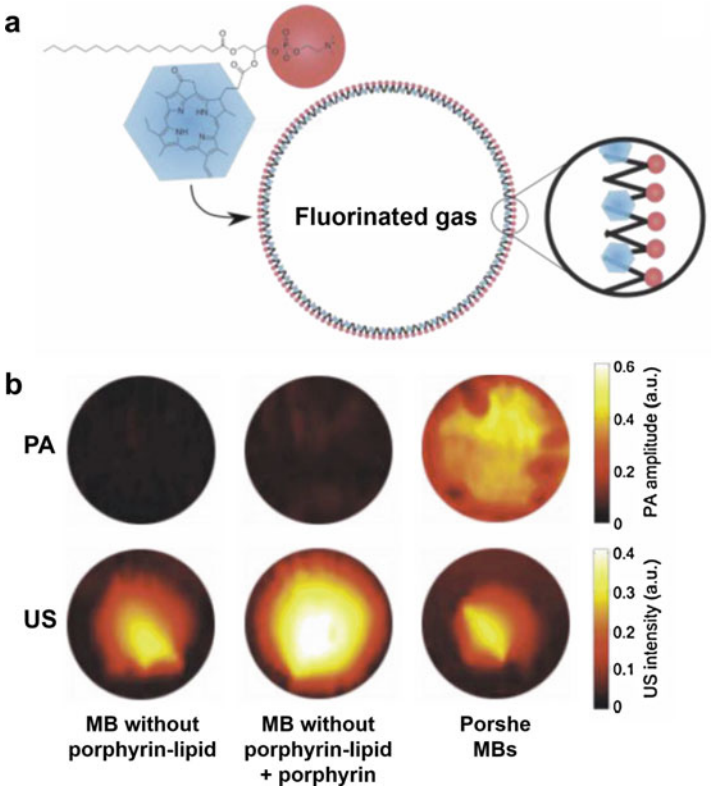

Fig. 11.15 (**a**) Schematic of Porsche MBs. (**b**) PA and US images of three different configurations of MBs. PA, photoacoustic; US, ultrasound; and MB, microbubble (Reprinted with permission from Ref. [57])

contrast. By controlling the concentration of microbubbles in MB^2, the PA amplitude and US intensity can be varied. Fig. 11.14b shows that increasing microbubble concentration at a fixed methylene blue concentration decreases PA amplitude and increases US intensity. In addition, high-power US waves from a US transducer can burst the microbubbles in MB^2, resulting in a significant increase in the PA signal (Fig. 11.14c). Therefore, MB^2 can provide acoustically triggered PA signals.

As another way to increase the optical absorption of microbubbles, organic dyes or light absorbing nanoparticles are used to form a microbubble shell layer. E. Hyunh et al. developed a microbubble formulation with a porphyrin-lipid shell (a Porsche microbubble) [57]. As shown in Fig. 11.15a, a lipid film consisting of the porphyrin-lipid 1-stearoyl-2-pyropheophorbide-sn-glycero-3-phosphocholine and the phospholipid 1,2-distearoyl-sn-glycero-3-phosphocholine (DSPC) was rehydrated with a solution of phosphate-buffered saline (PBS) and polyoxyethylene-40 stearate (PEG40S). After the lipid film had dispersed in the solution, a commercial activator produced lipid-encapsulated microbubbles in the aqueous solution. Due to high

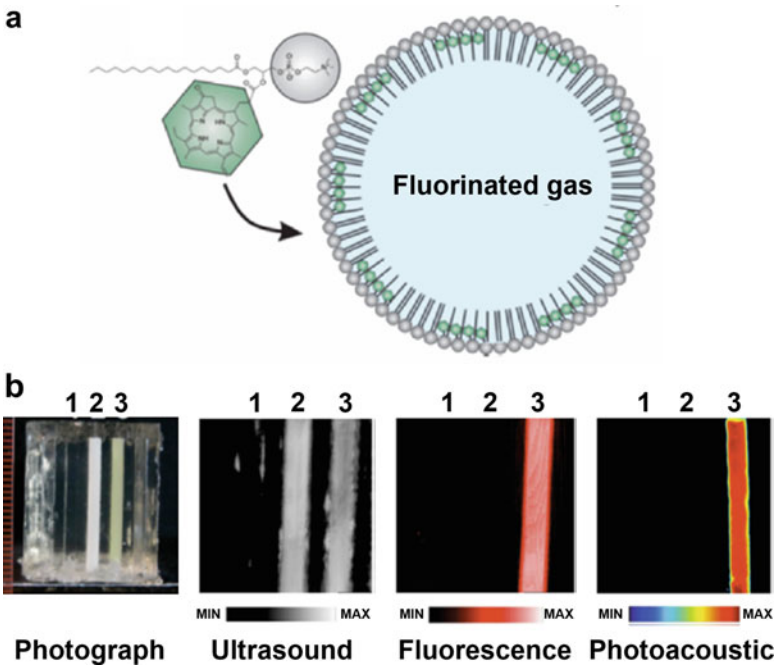

Fig. 11.16 (**a**) Illustration of trimodal porphyrin-phospholipid microbubbles. (**b**) Photograph, ultrasound, fluorescence, and photoacoustic images of three samples: (1) PBS only, (2) pure microbubbles, and (3) trimodal porphyrin-phospholipid microbubbles (Reprinted with permission from Ref. [58])

density of the shell layer, the normally fluorescent porphyrins are self-quenched, and the Porsche microbubbles generate PA signals. To evaluate the self-quenching of porphyrins, PA and US images were acquired of microbubbles without porphyrin-lipid, of microbubbles mixed with only free porphyrins, and of Porsche microbubbles (Fig. 11.15b). The Porsche microbubbles generate stronger PA signals than the other two types of microbubbles, whereas strong US signals are generated by all the microbubble types. These results demonstrate that the lipid-conjugated porphyrins in the microbubble shell effectively generate PA signals.

The Porsche microbubble has been improved to perform as a trimodal (US, PA, and fluorescence) contrast agent by increasing the porphyrin content in the microbubble shell. A lipid film containing porphyrin-lipid, DSPC, and 1,2-distearoyl-sn-glycero-3-phosphoethanolamine-N-[methoxy(polyethylene glycol)-2000] (DSPE-PEG_{2000}) was rehydrated with a solution of propylene glycol, glycol, and PBS. After sonication, C_3F_8 gas was added and the solution was then stirred for 45 s to form microbubbles. As Fig. 11.16a shows, the increased porphyrin content generates ordered aggregation, which in turn generates fluorescence (FL) signals. The feasibility of trimodal imaging was verified by capturing US, PA, and FL images of the Porsche microbubbles (Fig. 11.16b). PBS and pure microbubbles were also imaged.

Both kinds of microbubbles were clearly visible in US images, whereas only the trimodal Porsche microbubble was visible in the PA and FL images.

K. Wilson et al. fabricated another example of contrast enhancing agents, perfluorocarbon (PFC) nanobubbles that enclose plasmonic nanoparticles [59]. When a pulsed laser illuminates the nanobubbles, the plasmonic nanoparticles absorb light and generate heat and pressure waves, which cause a vaporization of the nanobubbles from liquid to gas (steps 2–3 in Fig. 11.17a). The consequent formation of larger bubbles instantly induces high amplitude PA signals. After the vaporization, the continued laser illuminations generate PA signals via thermal expansion (step 4–5 in Fig. 11.17a). In addition, the PFC bubbles also provide US contrast by acoustic impedance mismatch between the generated bubbles and surrounding medium, which is maintained for a while (step 6 in Fig. 11.17a). Figure 11.17b shows in vivo PA and US images of PFC nanobubble-injected region. The result shows that the PA amplitudes in vaporization step are higher than that in thermal expansion step. The US contrast enhancement of PFC nanobubbles is also verified.

To enhance the clinical availability, A. Hannah et al. replaced plasmonic nanoparticles in the PFC nanobubbles to ICG, which is an FDA-approved organic dye [60]. Solutions of ICG and tetrabutylammonium iodide (TBAI) in chloroform were prepared and mixed. The ICG-TBAI solution was added dropwise into the emulsion of blank droplets, which contains a PFC core encapsulated in albumin shell. The chloroform in solution was evaporated by a vacuum tube. After 30 min of evaporating, a remaining solution was centrifuged. The synthesis of the ICG-loaded PFC nanobubbles was completed after dilution of the centrifuged solution. Figure 11.17c shows both PA and US images of three types of ICG-loaded bubbles in water. The developed ICG-loaded perfluorocarbon nanobubbles are completely biocompatible and improve the contrast in both PA and US images.

In this section, we have reviewed the synthesis and evaluation of colored microbubbles and nanobubbles as multimodal contrast agents for biomedical imaging. Because microbubbles have been utilized as standard contrast agents for USI, colored microbubbles have great potential for clinical applications. The optical absorption properties, physical properties, and multimodal imaging capabilities of the agents discussed here are summarized in Table 11.1.

5.1.2 Liposomal Nanoformulations

Due to their biocompatibility, biodegradability, and ease of drug loading, liposomal nanoformulations have widely been extensively investigated for drug delivery [61, 62]. However, to be utilized in PAI, optically absorbing substances must be conjugated, encapsulated, or layered in liposomal structures because the liposomal nanoformulations do not absorb light. In this section, several liposomal nanoformulations are introduced as PA contrast agents.

As an example of liposomal nanoformulation, N. Lozano et al. developed a liposomal ICG (LipoICG), which has good biodegradability and biocompatibility because of FDA-approved ICG and clinically relevant PEGylated liposomes [63]. Lipid films containing $_{L}$-α-phosphatidylcholine, hydrogenated (HSPC),

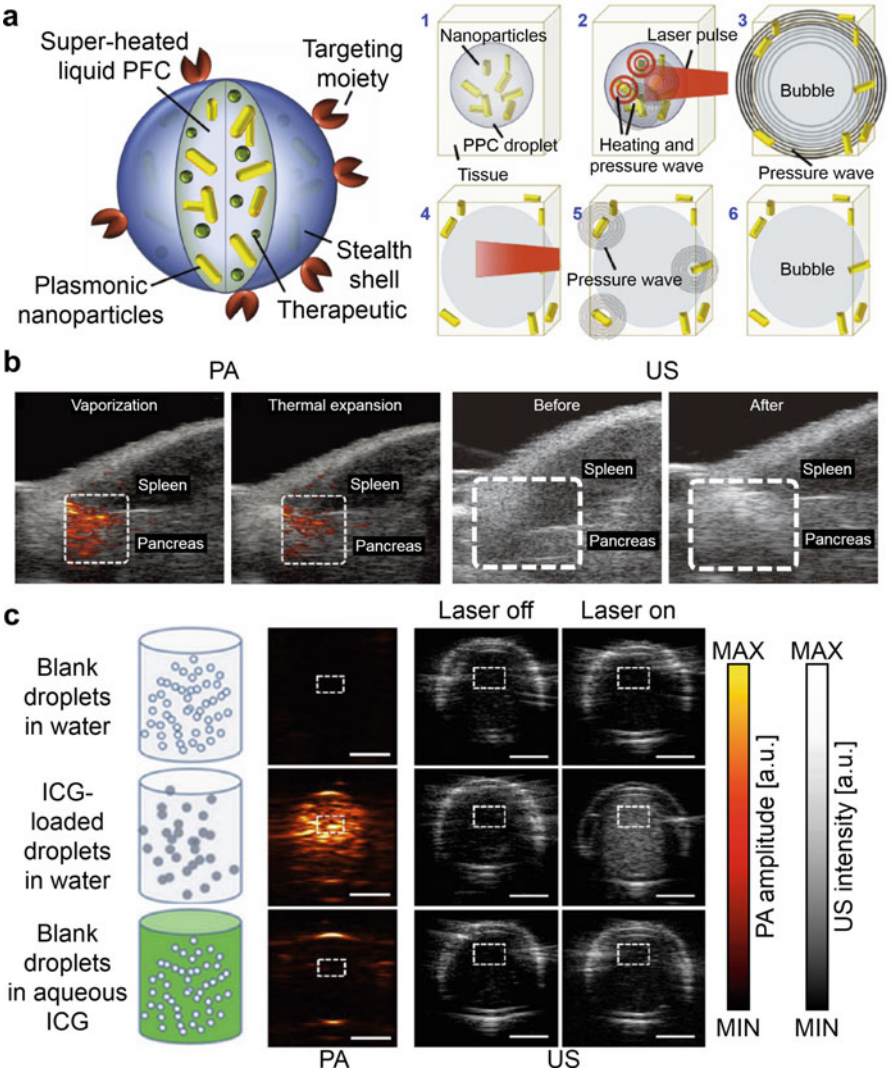

Fig. 11.17 (**a**) Schematic of the dual-mode contrast agent concept of liquid PFC nanobubbles. PFC, perfluorocarbon. (**b**) In vivo overlaid PA/US and US images of PFC nanobubble-injected region. (**c**) Diagram, PA, and US images of samples of three types of droplets. PA, photoacoustic; US, ultrasound; and ICG, indocyanine green (Reprinted with permission from refs [59, 60])

cholesterol, and DSPE-PEG_{2000} were hydrated in 5% ICG-containing dextrose solution. LipoICG was fabricated by removing free ICG. As shown in Fig. 11.18a, LipoICG with three different concentrations (25, 50, and 75 μM) of loaded ICG absorb more light and induce a red spectral shift of 20 nm, compared to free ICG of the same concentration. The moderate FL quantum yield of ICG enables dual-mode

Table 11.1 Optical absorption properties, physical properties, and multimodal imaging capabilities of colored microbubbles and microbubbles. PA, photoacoustic; US, ultrasound; and FL, fluorescence

	Optical absorption agent	Shell composition	Excitation wavelength [nm]	Size [μm]	Multimodal imaging capability
MB^2	Methylene blue	Lipid	667	~3	PA, US
Porshe	FL quenched porphyrin	Porphyrin–lipid	700	~2.7	PA, US
Trimodal Porshe	FL quenched porphyrin	Porphyrin–lipid	704	2-6	PA, US, FL
ICG-loaded PFC nanobubble	Indocyanine green	Perfluorocarbon	780	~0.6	PA, US

contrast in PA and FL imaging. Dual-mode images of CD-1 mice were acquired after intravenous injection of LipoICG (Fig. 11.18b). The LipoICG was further modified to target tumor cells by using the anti-MUC-1 "humanized" monoclonal antibody (MoAb) hCTM01 (Fig. 11.18c) [64]. To test the tumor targeting capability of the LipoICG, in vivo PA images were acquired from tumor-bearing mice (Fig. 11.18d). The targeted LipoICGs were intravenously injected into mice bearing HT-29 human colon adenocarcinoma and mice bearing 4 T1 murine breast cancer. After injection, the accumulations of LipoICG in tumors were verified from multispectral PA images. In addition, targeted drug delivery can be performed by encapsulating doxorubicin (DOX) within the LipoICG. This combination of targeted imaging and drug delivery techniques enables monitoring of drug accumulation in tumor regions.

J. F. Lovell et al. developed a self-assembled porphyrin-phospholipid bilayer, called porphysome (Fig. 11.19a) [65]. An acylation reaction between lysophosphatidylcholine and pyropheophorbide generated porphyrin-lipid conjugates which constituted the porphysome. The porphyrin-lipid conjugates were located in the alkyl side chain and thus the amphipathic structure was maintained. The porphysome was formed by self-assembly and extrusion of the porphyrin-lipid conjugates in an aqueous buffer. The porphysome was a nanovesicle with a liposome-like structure that had excellent biodegradability, biocompatibility, and loading capacity. In the structure of the porphysome, two separate monolayers of porphyrin formed a bilayer shell with a gap of 2 nm. Due to the high density of porphyrin in the interlayer, the strong FL quantum yield of porphyrin was quenched. As a result, the porphysomes produced strong photoacoustic signals by efficiently converting absorbed light to heat. This high NIR absorption and structurally dependent FL quenching allow porphysomes to be used as a PA and FL dual-mode contrast agent (Fig. 11.19b). The lymphatic systems were clearly imaged in PA images at 15 min after intradermal injection of the porphysomes. FL images were also acquired after intravenous injection of porphysomes in tumor-bearing rats. As the porphysomes accumulated and unquenched, a strong FL signal was observed in the tumor region.

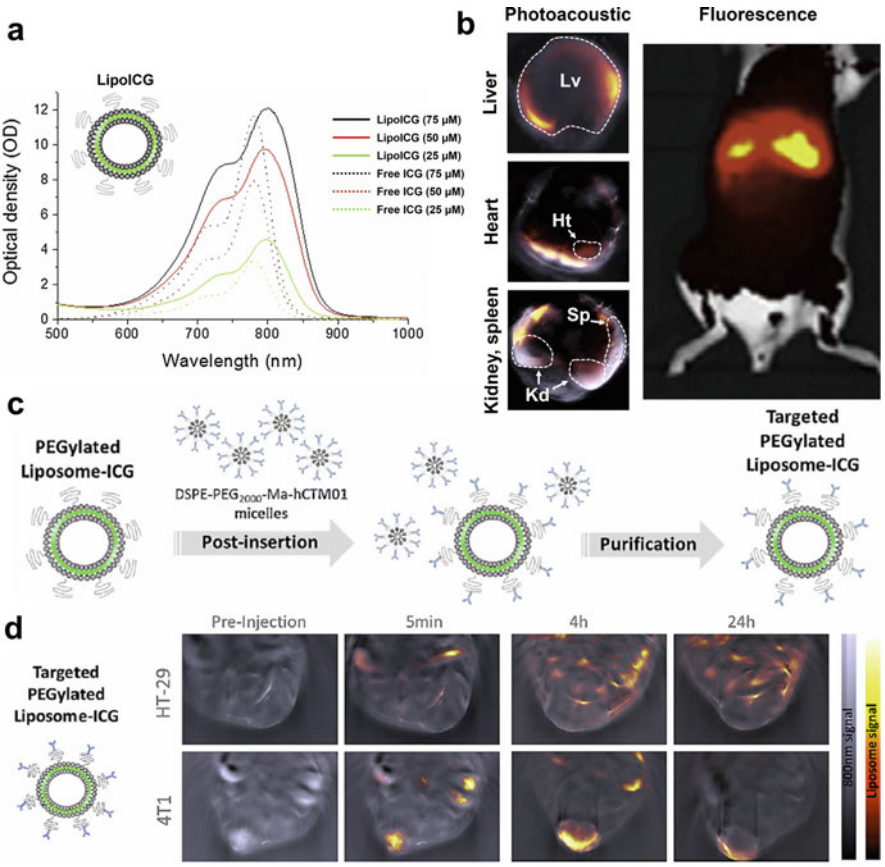

Fig. 11.18 (**a**) Absorption spectra of LipoICG. ICG, indocyanine green; LipoICG, liposomal ICG. (**b**) In vivo transversal photoacoustic images and whole-body fluorescence images of CD-1 mice after injection of LipoICG. Lv, liver; Ht, heart; Sp, spleen; and Kd, kidney. (**c**) Schematic depiction of the synthesis of the targeted LipoICG. (**d**) In vivo photoacoustic images of tumor-bearing mice before and after injection of tumor-targeted LipoICG (Reprinted with permission from Refs. [63, 64])

J. Rieffel et al. introduced another porphyrin-phospholipid (PoP) bilayer-coated nanoparticle, called a PoP-coated upconversion nanoparticle (PoP-UCNP), as a hexamodal contrast agent (Fig. 11.20a) [66]. To synthesize PoP-UCNPs, oleic acid-capped UCNPs were coated with phospholipids for dispersal in water. Thin PoP-UCNP films were hydrated with water and then sonicated. Similar to the previously introduced porphysomes, high-density packing of porphyrins in the PoP bilayer induced FL quenching and generated PA contrast. The FL quantum yield of porphyrin was recovered by adding a detergent that destroyed the bilayer structure of the PoP shell. The PoP-UCNPs were labeled for positron emission tomography (PET) and Cerenkov luminescence (CL) by simply incubating them with ^{64}Cu [67]. The core shell of

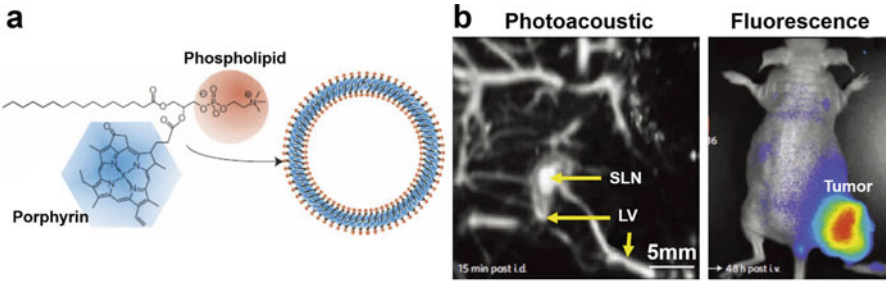

Fig. 11.19 (**a**) Schematic of a porphysome, a self-assembled phospholipid-porphyrin bilayer. (**b**) Photoacoustic and fluorescence images of porphysomes in vivo. SLN, sentinel lymph node; LV, lymphatic vessel (Reprinted with permission from Ref. [65])

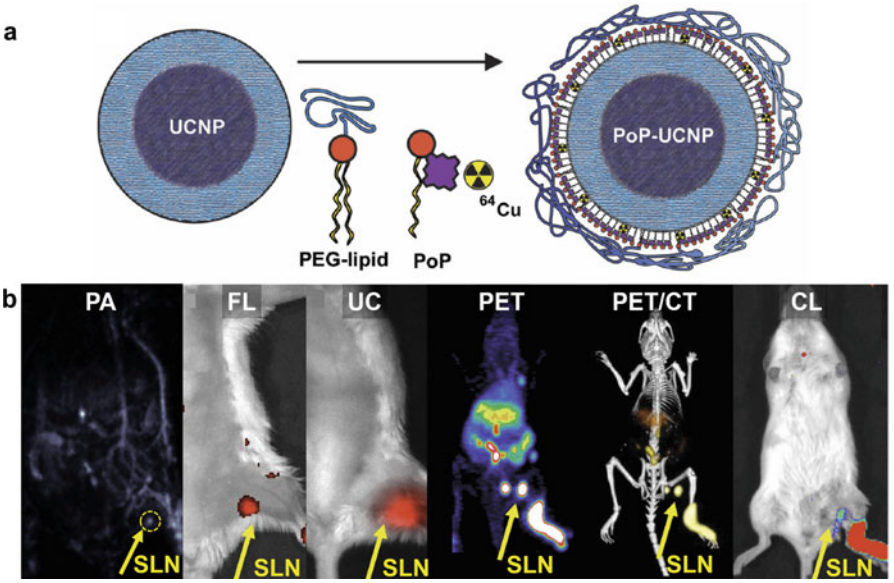

Fig. 11.20 (**a**) Schematic of the PoP-UCNP. UCNP, upconversion nanoparticle; PoP, porphyrin-phospholipid; and PEG, polyethylene glycol. (**b**) In vivo hexamodal images of mice after injection of PoP-UCNPs. PA, photoacoustic; FL, fluorescence; UC, upconversion luminescence; PET, positron emission tomography; CT, X-ray computed tomography; CL, Cerenkov luminescence; and SLN, sentinel lymph node (Reprinted with permission from Ref. [66])

$NaYbF_4$:Tm-$NaYF_4$ was used for upconversion (UC) luminescence imaging. In addition, the massed electron content was detected by X-ray computed tomography (CT). To validate the hexamodal contrast of the PoP-UCNP, in vivo images of contrast-enhanced lymphatic system were acquired using six different imaging modalities (PA, FL, UC, PET, PET/CT, and CL) (Fig. 11.20b). In each image, the PoP-UCNPs in the sentinel lymph nodes (SLNs) are visualized (yellow arrow in each image).

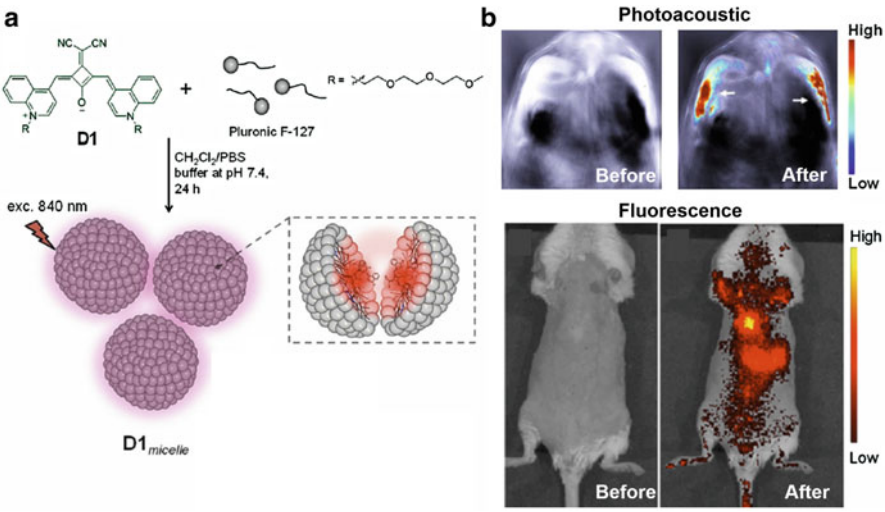

Fig. 11.21 (**a**) Schematic of $D1_{micelle}$ and a single micelle containing D1. (b) In vivo photoacoustic and fluorescence images of mice before and after injection of $D1_{micelle}$ (Reprinted with permission from Ref. [68])

Micelles have also been investigated for encapsulating optically absorbing substances. S. Sreejith et al. encapsulated an NIR-absorbing squaraine dye termed D1 inside micelles [68]. D1 is a 4-methyl-quinolium-based dicyanovinyl-substituted squaraine with oxyethylene side chains (Fig. 11.21a). D1 and concentrated Pluronic F-127 surfactant were dissolved in dichloromethane, and then PBS buffer at pH 7.4 was added. After stirring at room temperature for 24 h, dichloromethane evaporation formed D1-encapsulated micelles ($D1_{micelle}$). The feasibility of dual-mode contrast using $D1_{micelle}$ was tested by acquiring in vivo PA and FL images of mice before and after intravenous injection of $D1_{micelle}$ (Fig. 11.21b). In both PA and FL images, clear and constant enhancement in the liver could be observed in the abdominal region after injection of $D1_{micelle}$. The result shows the in vivo dual-mode imaging capability of $D1_{micelle}$.

D. Zhang et al. developed another example of a micelle-encapsulated nanoparticle [69]. A photosensitizer (chlorin e6, Ce6) and a poly[2,6-(4,4-bis-(2-ethylhexyl)-4H–cyclopenta[2,1-b;3,4-b']-dithiophene)-alt-4,7-(2,1,3-benzothiadiazole)] (PCPDTBT) dot were co-loaded in lipid micelles (Pdots/Ce6@lipid-Gd-DOTA micelles) by the self-assembly of gadolinium-1,4,7,10-tetraacetic acid-modified phospholipid-PEG lipid (lipid-Gd-DOTA) and 1-palmitoyl-2-stearoylsn-glycero-3-phosphatidylcholine (HSPC) (Fig. 11.22a). PCPDTBT is an organic semiconducting π-conjugation polymer with no heavy metal toxicity [70]. Further, its strong NIR absorption enables both photothermal therapy (PTT) and photodynamic therapy (PDT), as well as contrast-enhanced PAI. The Pdots/Ce6@lipid-Gd-DOTA micelles provide dual-mode contrast for PA and magnetic resonance (MR) imaging

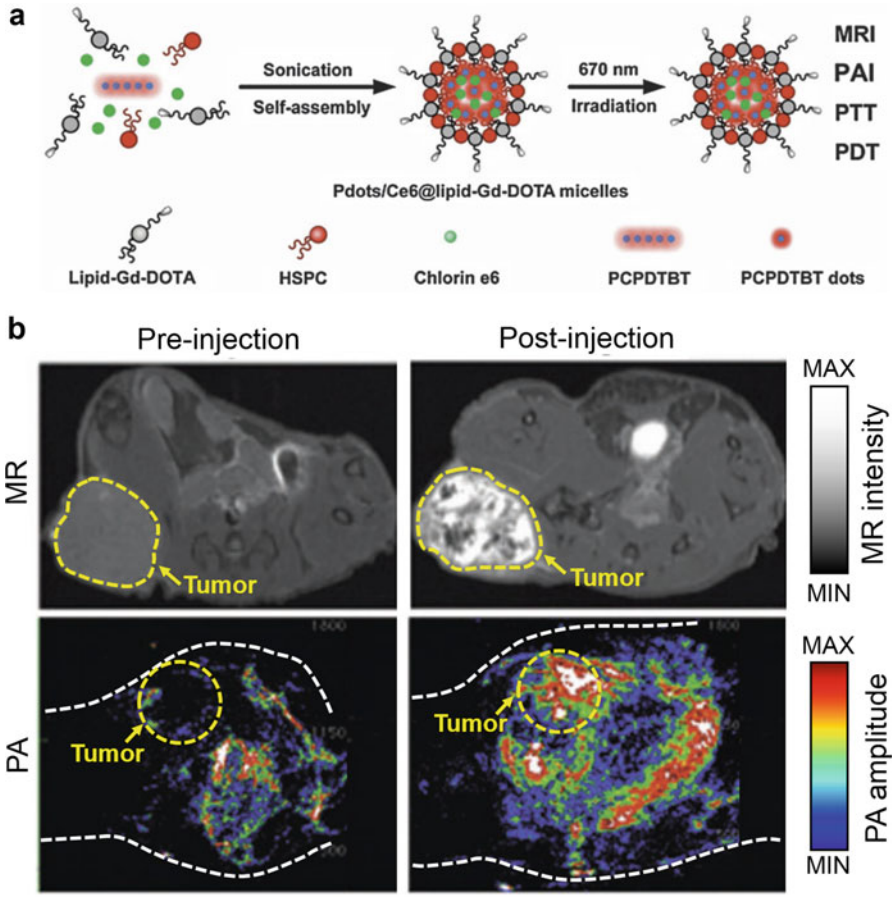

Fig. 11.22 (**a**) Fabrication of Pdots/Ce6@lipid-Gd-DOTA micelles. MRI, magnetic resonance imaging; PAI, photoacoustic imaging; PTT, photothermal therapy; and PDT, photodynamic therapy. (**b**) T1-weighted MR and PA images of mice before and after injection of Pdots/Ce6@lipid-Gd-DOTA micelles. The yellow dashed boundaries represent tumor region, and the white dashed line represents boundary of mice (Reprinted with permission from Ref. [69])

(Fig. 11.22b). In addition, PTT and PDT can be performed by using a single laser illumination with a wavelength of 670 nm.

In this section, we have reviewed the synthesis and evaluation of liposomal nanoformulations as PA contrast agents and discussed their multimodal imaging and therapeutic capabilities. Liposomal nanoformulations can be trackable drug delivery tools with good biocompatibility and biodegradability. The optical absorption, physical, and functional properties of the discussed liposomal nanoformulations are summarized in Table 11.2.

Table 11.2 Optical absorption, physical, and functional properties of the discussed liposomal nanoformulations. PA, photoacoustic; FL, fluorescence; UC; upconversion; CL, Cerenkov luminescence; PET, positron emission tomography; CT, X-ray computed tomography; MR, magnetic resonance; DOX, doxorubicin; PTT, photothermal therapy; and PDT, photodynamic therapy

	Optical absorption agent	Excitation λ [nm]	PA sensitivity	Size [nm]	Multimodal imaging capability	Therapeutic capability
LipoICG	Indocyanine green	800	~ 0.6 μM	~130	PA, FL	Targeted DOX delivery
Porphysome	FL quenched porphyrin	680	~25 pM	~100	PA, FL	PTT, PDT
PoP-UCNP	FL quenched porphyrin	675	–	~74	PA, FL, UC, CL, PET, CT	–
$D1_{micelle}$	Squaraine dye	840	–	~100	PA, FL	–
Pdots/ Ce6@lipid-Gd-DOTA	Pdots	670	~1.6 μg/mL	~36	PA, MR	PTT, PDT

5.1.3 Organic Polymeric Nanostructures

The biocompatibility, adjustable size, and photostability of organic polymeric nanostructures have recently spurred their development as biomedical contrast agents. In addition, by synthesizing optically absorbing organic polymeric nanostructures, contrast agents that are free from heavy metal toxicity have recently been developed and explored for PAI.

K. Pu et al. transformed semiconducting π-conjugating polymers (SPs), which have strong NIR absorption, into nanoparticles for dual-mode PA and FL imaging [70]. A photovoltaic SP derivative, poly(cyclopentadithiophene-alt-benzothiadiazole) SP (SP1), was assembled to semiconducting polymer nanoparticles (SPNs) through nanoprecipitation assisted by DPPC (Fig. 11.23a). The SPNs generate stronger PA signals than conventional PA contrast agents such as gold nanoparticles. In addition, because they are made from organic and biologically inert substances, SPNs are completely free from heavy metal toxicity and are biocompatible. The feasibility of the SPNs as dual-mode contrast agents was tested by acquiring in vivo lymph node images of mice (Fig. 11.23b–c). SPNs were intravenously injected into healthy mice, and, after 24 h, both PA and FL images were acquired. Accumulated SPNs in lymph nodes were clearly visualized in both PA and FL images.

SPNs were further synthesized to enhance PA contrast by using diketopyrrolopyrrole (DPP)-based SPs [71]. SPNs with three types of SP (SP2–SP4) were synthesized and compared with the previously described SPN1 (Fig. 11.23d). DSPE-PEG_{2000} was added to achieve an excellent in vivo distribution of SPNs in living animals. DPP-based SPNs (SPN2–SPN4) have lower FL quantum yields than SPN1, so their PA signals are stronger (Fig. 11.23e). In particular, SPN4 produces the brightest PA signal because it has the lowest FL quantum yield.

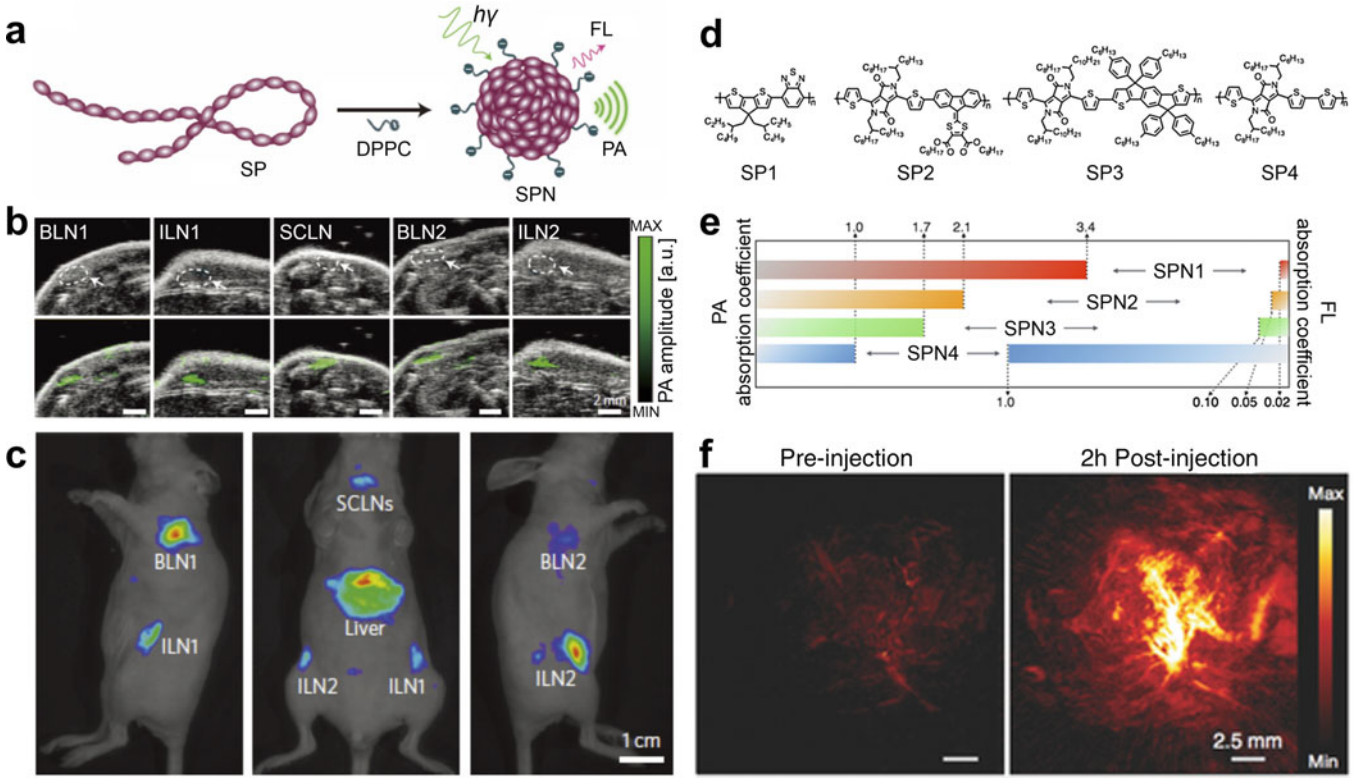

Fig. 11.23 (**a**) Schematic of the synthesis of SPNs through nanoprecipitation. SP, semiconducting π-conjugating polymers; SPN, semiconducting polymer nanoparticle; DPPC, 1,2-dipalmitoyl-sn-glycero-3-phosphocholine; PA, photoacoustic; and FL, fluorescence. (**b**) and (**c**) Transversally sliced ultrasound and PA/US overlaid images (**b**) and corresponding FL images (**c**) of lymph nodes in a mouse. US, ultrasound; BLN, brachial lymph nodes; ILN, inguinal lymph

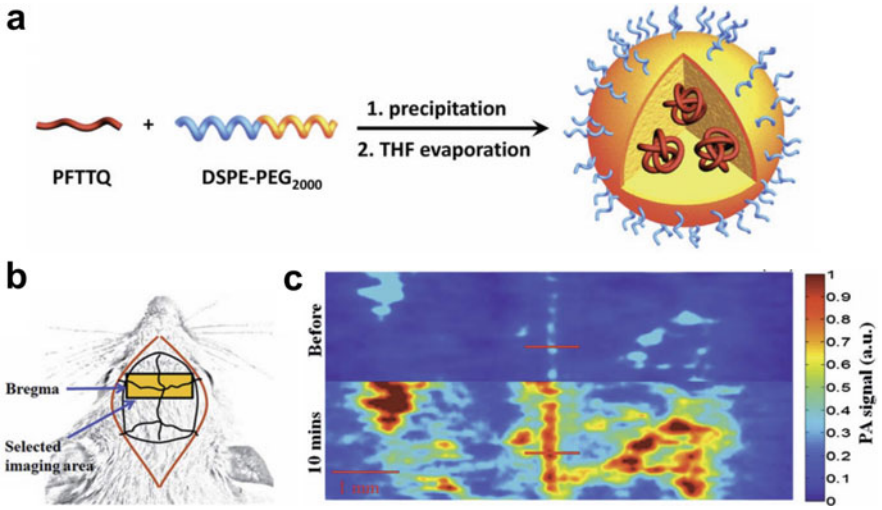

Fig. 11.24 (**a**) Schematic of the synthesis of PFTTQ NPs. THF, tetrahydrofuran. (**b**) Schematic of photoacoustic imaging of rat brain vasculature. (**c**) In vivo PA images of cortical vasculature in rats before and after injection of PFTTQ NPs. PA, photoacoustic (Reprinted with permission from Ref. [72])

To evaluate its PA imaging capability, contrast-enhanced PA images of a tumor were acquired before and after intravenous injection of SPN4 (Fig. 11.23f). Before injection, weak PA signals were detected due to intrinsic optical absorption from blood vessels. After injection, the PA signal in the tumor region was significantly increased.

As another example of an organic polymer, J. Liu et al. synthesized a conjugated polymer (CP) via Suzuki polymerization of poly[9,9-bis(4-(2-ethylhexyl) phenyl)fluorene-*alt*-co-6,7-bis(4-(hexyloxy)phenyl)-4,9-di(thiophen-2-yl)-thiadiazoloquinoxaline] (PFTTQ) [72]. These CPs have good biocompatibility and photostability. In addition, due to their π-conjugated structures, the CPs have strong NIR absorption and a low FL quantum yield, which make them very attractive as potential organic contrast agents for PAI. The PFTTQ was encapsulated into a $DSPE\text{-}PEG_{2000}$ matrix (Fig. 11.24a). A tetrahydrofuran solution consisting of PFTTQ and $DSPE\text{-}PEG_{2000}$ was added to water and sonicated. The sonication entangled hydrophobic DSPE segments in PFTTQ chains and transformed hydrophobic PEG chains to a hydrophilic phase. The sample was stirred overnight to evaporate tetrahydrofuran and then purified with a syringe filter to achieve

Fig. 11.23 (continued) nodes; and SCLN, superficial cervical lymph nodes. (**d**) Structural diagram of SP1 and DPP-based SPs (SP2–4). DPP, diketopyrrolopyrrole. (**e**) Normalized photoacoustic and fluorescence intensities at 710 nm. (**f**) In vivo photoacoustic images of a tumor region before and after injection of SPN4 (Reprinted with permission from Refs. [70, 71])

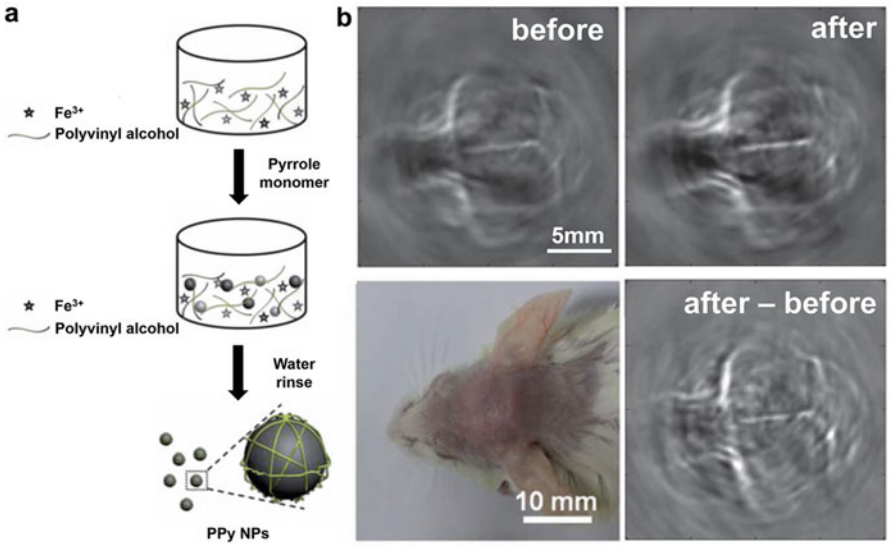

Fig. 11.25 (**a**) Schematic of PPy NP fabrication. (**b**) Photograph and in vivo photoacoustic images of a mouse brain before and after injection of PPy NPs (Reprinted with permission from Ref. [74])

PFTTQ-loaded DSPE-PEG_{2000} nanoparticles (PFTTQ NPs), which are dispersible i n aqueous solution. The PFTTQ NPs were retro-orbitally injected to acquire PA i mages of blood vessels in the superior sinus region of rats (Fig. 11.24b). The PA i ntensities of the blood vessels increased by three times after PFTTQ NPs were i njected (Fig. 11.24c). PFTTQ NPs could be utilized for targeted imaging by further conjugating them with targeting ligands [73]. In addition, due to their low FL quantum yield, the PFTTQ NPs could also be used for PTT.

Z. Zha et al. developed polypyrrole nanoparticles (PPy NPs) as an organic contrast agent for PAI [74]. PPy NPs have been used for various biomedical applications that take advantage of their excellent photostability and biocompatibility [75]. Monodisperse PPy NPs were prepared through chemical oxidation polymerization (Fig. 11.25a). Polyvinyl alcohol (PVA) solution and $FeCl_3$ were used in the synthesis process as a stabilizer and an initiator, respectively. $FeCl_3 \cdot 6H_2O$ was poured into the PVA solution and stirred. After 1 h for equilibration, pyrrole monomer was added to the sample, polymerization proceeded for 4 h with stirring, and finally the PPy NPs were extracted from the solution by centrifugation. To evaluate the PAI contrast enhancing capability of the PPy NPs, mouse brains were imaged before and after intravenous injection. As seen in Fig. 11.25b, after injection, PA intensities of the brain vasculature are considerably enhanced. The enhancement can be better evaluated in the differential image, which was obtained by pixel-by-pixel subtracting PA images between before and after injection. The results show that PPy NPs have great potential for contrast-enhanced PAI. In addition, PPy NPs could also be used for PTT of tumors, with good photostability [76].

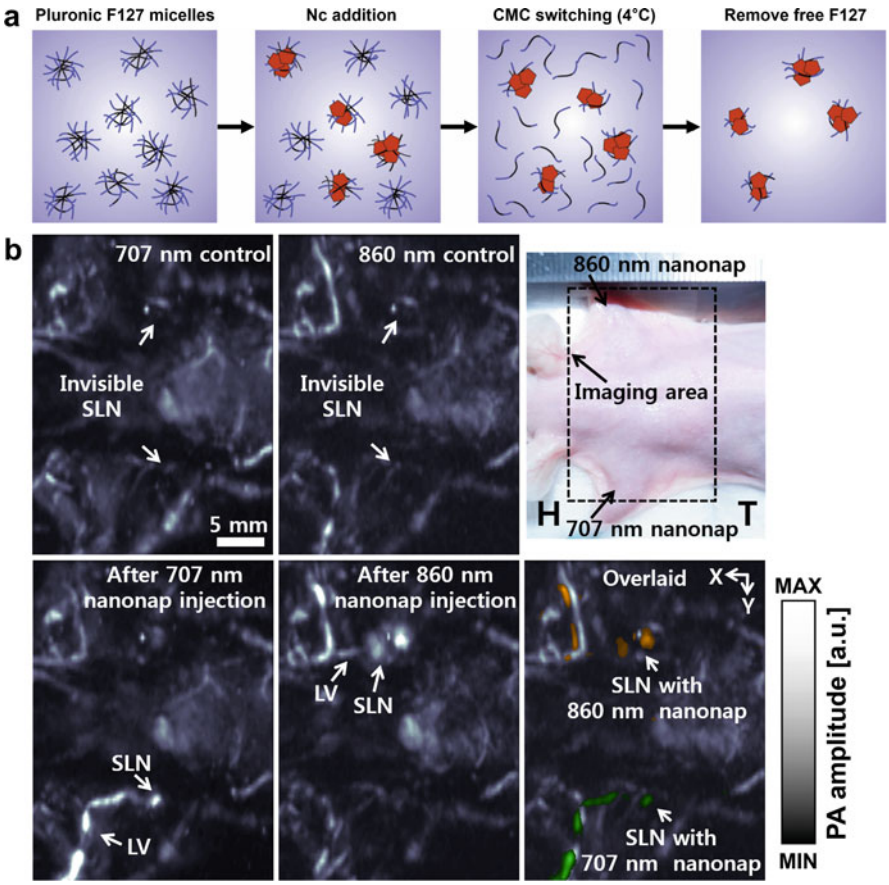

Fig. 11.26 (**a**) Synthesis of nanoformulated naphthalocyanine (nanonaps). Nc, naphthalocyanine; CMC, critical micelle concentration. (**b**) In vivo simultaneous dual-color photoacoustic images of SLNs in a mouse after injection of dual-color nanonaps. SLN, sentinel lymph node; LV, lymphatic vessel; H, head; and T, tail (Reprinted with permission from Refs. [77, 78])

Y. Zhang et al. demonstrated an organic nanoformulated naphthalocyanine (nanonap) as a PAI contrast agent with excellent NIR absorption [77]. As shown in Fig. 11.26a, organic naphthalocyanines were diluted in pluronic (poly (oxyethylene)-poly(oxypropylene)-poly(oxyethylene)) (PEO-PPO-PEO) F127, which is an FDA-approved biocompatible surfactant, and then self-assembled into photostable nanoparticles. Centrifugation was performed to remove aggregations, and then the sample was diluted in sodium cholate. Unincorporated F127 was removed by critical micelle concentration switching. The nanonaps have unique advantages in multicolor PAI due to their wide spectral tuning range, narrow spectral bandwidth, and non-shifting spectral stability at high concentrations. To test the feasibility of multicolor imaging with nanonaps, dual-color PA images of SLNs in mice were acquired in vivo (Fig. 11.26b). Nanonaps with absorption peaks of

707 and 860 nm were respectively injected in the left and right forepaws. Before injection, both SLNs and lymphatic vessels were invisible because their optical absorptions were low. After injection, lymphatic vessels and SLNs were clearly delineated by their corresponding wavelengths: lymphatic systems in the left axillary region were visualized with an excitation wavelength of 707 nm, and lymphatic systems in the right axillary region were visualized with an excitation wavelength of 860 nm. Overlaid PA images, which represent the two independent lymphatic systems, were obtained by combining the images.

Due to their biocompatibility and biodegradability, bioinspired polymers are promising for fabricating contrast agents in biomedical imaging. Melanin has great possibility for a contrast agent for PA imaging due to its exceptionally strong optical absorption in the NIR as well as the visible region. Q. Fan et al. synthesized melanin nanoparticles (MNPs) for use as a tumor-targeted multimodal contrast agent for PA, PET, and MRI [79]. As shown in Fig. 11.27a, melanin granules were dissolved in 0.1 N NaOH solution and then neutralized by adding 0.1 N HCl solution under sonication, yielding water-soluble MNPs. PEGylated MNPs were achieved by adding a mixture of water-soluble MNPs and NH_4OH solution to NH_2-PEG_{5000}-NH_2 aqueous solution. After PEGylation, cyclic Arg-Gly-Asp-$_D$-phe-Cys peptide (RGD) was attached to the PEGylated MNPs for tumor targeting. To conjugate PEGylated MNP with RGD (RGD-PEG-MNP), water-soluble PEGylated MNPs were incubated with 4-(N-maleimidomethyl)cyclohexane-1-carboxylic acid 3-sulfo-N-hydroxysuccinimide ester sodium salt (sulfo-SMCC) dissolved in dimethyl sulfoxide (DMSO), and then the cRGDfC solution was added with stirring. Fe^{3+} and $^{64}Cu^{2+}$ were further chelated to produce PA/MR/PET multimodal images. $FeCl_3$ in PBS or $CuCl_2$ in buffer solution was added to the RGD-PEG-MNP and then incubated at 40 °C. By using the Fe^{3+} or $^{64}Cu^{2+}$ chelated RGD-PEG-MNP, in vivo multimodal images of U87MG tumor-bearing mice were acquired with PA/US, PET/CT, and MRI (Fig. 11.27b–d). In the PA/US overlaid images, the US images represent structural information in grayscale, while the PA images represent targeted tumor cells in pseudo-color. For PET/CT overlaid images, coronal and transversal CT images (grayscale) and PET images (pseudo-color) were acquired. MR images are represented in both gray and pseudo-color. Tumor uptake of MNPs is clearly visualized in the PA, PET, and MR images.

M. Lee et al. synthesized another bioinspired polymer based on the melanoidin, which is present in foods including coffee, bean paste, and soy sauce [80]. Glucose-glycine-melanoidin (GG-melanoidin) was synthesized by incubating glucose and glycine dissolved in water with stirring at 37 °C for 2 weeks (Fig. 11.28a). The pH of the GG-melanoidin solution was controlled to 7.4 by using NaOH solution. Because of the strong optical absorption, biocompatibility, and biodegradability of GG-melanoidin, it has great advantages as a contrast agent for PAI. Figure 11.28b shows depth-encoded PA images obtained before and after intradermal injection of GG-melanoidin. After injection, the initially invisible SLN is dyed with GG-melanoidin. The location of the SLN is clearly identified in PA images.

In this section, we have reviewed various organic polymeric nanostructures. These organic nanostructures are biocompatible, size-adjustable, photostable, and

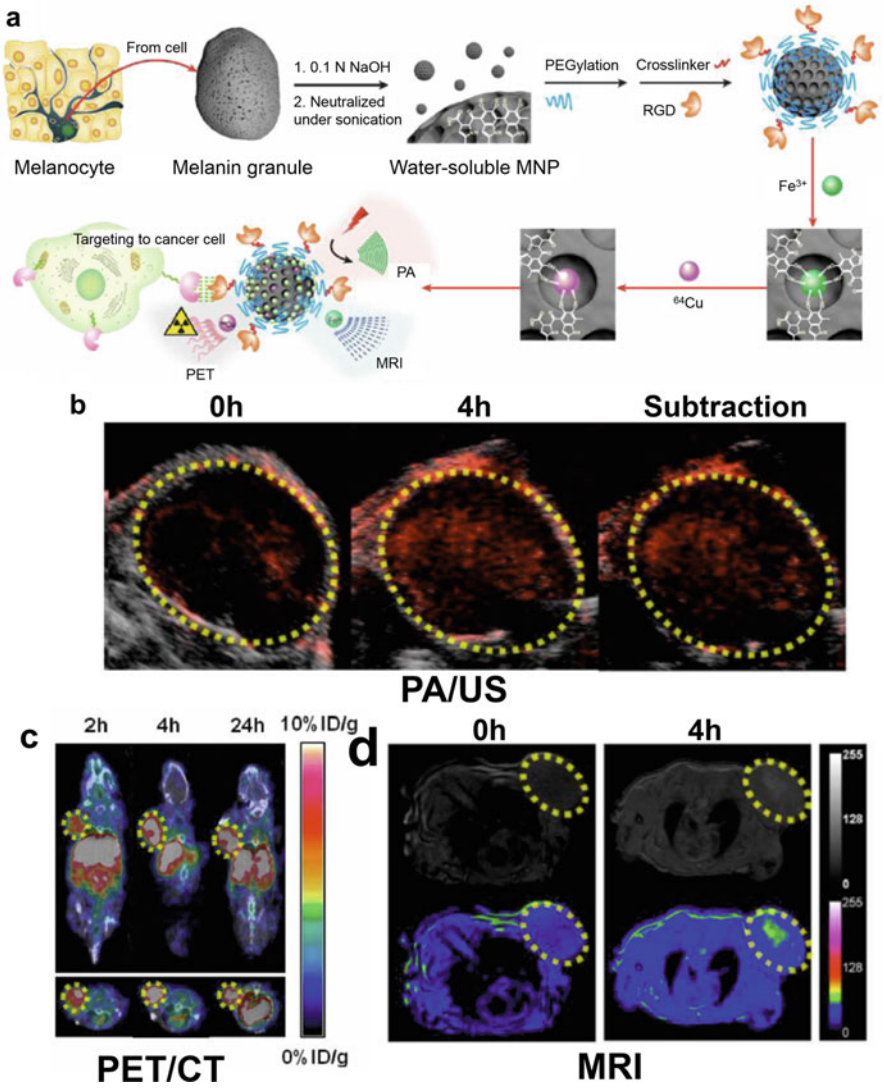

Fig. 11.27 (**a**) Schematic of MNP synthesis. (b)-(d) Overlaid images of U87MG tumor-bearing mice (**b**) PA/US, (**c**) PET/CT, and (**d**) MR. The yellow dashed circle represents tumor region. MNP, melanin nanoparticle; PA, photoacoustic; PET, positron emission tomography; MRI, magnetic resonance imaging; US, ultrasound imaging; and CT, X-ray computed tomography (Reprinted with permission from Ref. [79])

free from heavy metal toxicity. By synthesizing optically absorbing organic polymeric nanostructures, various biocompatible PA contrast agents have been developed and evaluated. The organic nanostructures' characteristics, including their excitation wavelength, PA sensitivity, FL quantum yield, size, multimodal imaging capability, and therapeutic capability, are summarized in Table 11.3.

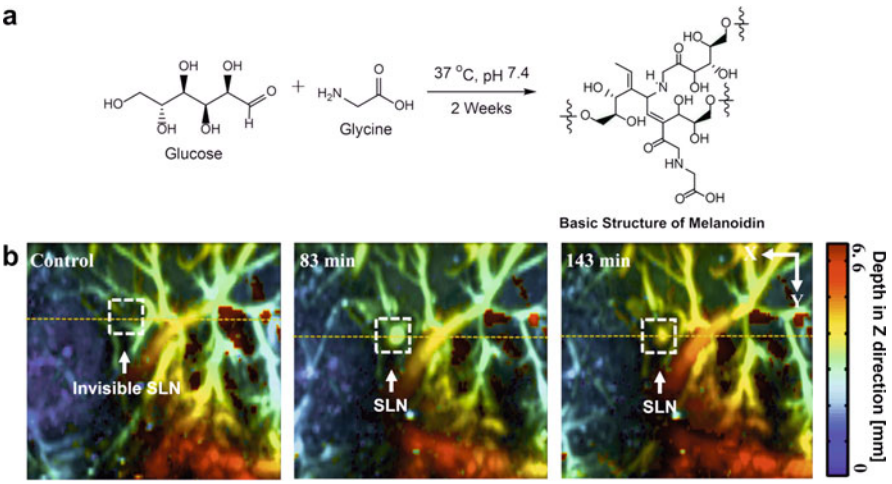

Fig. 11.28 (**a**) Schematic representation of GG-melanoidin. (**b**) Depth-encoded photoacoustic maximum amplitude projection images of a sentinel lymph node (SLN) before and after intradermal injection of GG-melanoidin (Reprinted with permission from Ref. [80])

5.2 Potential Applications of Contrast-Enhanced Photoacoustic Imaging

Visualizing molecular information about cancer is crucial because it improves diagnostic accuracy, helps create an efficient treatment plan, and allows monitoring therapeutic efficacy. For PAI visualization in biomedical research, molecular cancer imaging using various contrast agents has been extensively explored in the last decades [81–83]. Recent trends in biomedical applications include the development and evaluation of contrast agents that treat cancerous tissues through PTT and/or PDT, in addition to providing contrast-enhanced PA images. As another example, the visualization of the digestive or urinary tract, where the most common diseases occur, has recently been explored [21, 77, 84].

5.2.1 Photoacoustic Image-Guided Theranostics

As introduced in the previous section, PTT or PDT effects have been widely studied for various contrast agents. Both therapies have a similar therapeutic approach, in which light is absorbed by a photosensitizer and the absorbed light energy is released in two different ways to kill diseased cells. In PDT, the absorbed light reacts with photosensitive chemicals and releases highly reactive forms of oxygen, which cause cell death through cytotoxic effects [85, 86]. In PTT, the absorbed light energy is released as thermal energy, which raises the local temperature enough to destroy cells [87, 88]. Because the light absorption and heat dissipation processes of PTT are identical to those of PA wave generation, a large number of PA contrast agents have been developed for PTT. From the basic principles of energy transduction from light to heat, the amount of heat generation is determined by the quantum yield. Most PA

Table 11.3 Excitation wavelength, PA sensitivity, FL quantum yield, size, multimodal imaging capability, and therapeutic capability of organic polymeric nanostructures. NP, nanoparticle; PA, photoacoustic; FL, fluorescence; MR, magnetic resonance; PET, positron emission tomography; CT, X-ray computed tomography; and PTT, photothermal therapy

	Excitation λ [nm]	PA sensitivity	FL quantum yield [%]	Size [nm]	Multimodal imaging capability	Therapeutic capability
SPN1	660	≤ 5 μg/mL	0.100	~46	PA, FL	–
SPN2	635	≤ 5 μg/mL	0.005	~46	–	–
SPN3	712	≤ 5 μg/mL	0.010	~46	–	–
SPN4	748	≤ 2 μg/mL	0.001	~46	–	–
PFTTQ NP	800	≤ 50 μg/mL	~0	~50	–	PTT
PPy NP	808	< 10 μg/mL	~0	~46	–	PTT
Nanonap	707 or 860	< 133 μg/mL	~0	~20	PA, PET	–
Melanin NP	680	< 0.625 μM	~0	~10	PA, MR, PET, CT	–
GG-melanoidin	680	< 0.625 μM	~0	~10	–	PTT

contrast agents have high non-radiative quantum yield (which is 1 − FL quantum yield), but some PA contrast agents have intermediate quantum yields and therefore can be used for both PDT and PTT.

Various gold nanoparticles (AuNPs), due to their strong optical absorption in the NIR range, have been investigated as both PTT and PA contrast agents. Under laser illumination, AuNPs can generate excessive heat through localized surface plasmon resonance (LSPR), which leads to PTT, not just contrast enhancement in PAI. Various types of AuNPs, including gold nanospheres [89–91], gold nanoshells [92, 93], gold nanorods [94–97], and gold nanocages [98, 99], have been developed for PA-guided PTT. AuNPs are regarded as photostable and biocompatible compared to other metal-based nanostructures. However, as previously mentioned, AuNPs are not biodegradable and may raise long-term toxicity concerns. Therefore, instead of pursuing AuNPs further, developing organic nanostructures that have strong NIR absorption and photothermal heat conversion is critical for applying PTT technology to clinical practice.

The Pdots/Ce6@lipid-Gd-DOTA micelles introduced in the previous section consist of a photosensitizer (Ce6) for PDT and an NIR absorption material (Pdots) for PTT and PA contrast [69]. In addition, both Pdots and Ce6 photosensitizer have strong optical absorption at the NIR wavelength of 670 nm; therefore combined PTT and PDT can be achieved by using a single laser irradiation. To evaluate the synergic effect of PTT and PDT on Pdots/Ce6@lipid-Gd-DOTA micelles, HepG2-tumor-bearing mice were treated with four different procedures. Each group was treated by 670-nm laser irradiation after intratumoral injection of PBS (no treatment), free Ce6 (for PDT), Pdots@lipid micelles (for PTT), or Pdots/Ce6@lipid-Gd-DOTA micelles (for combined PDT and PTT) (Fig. 11.29). The temperature did not increase

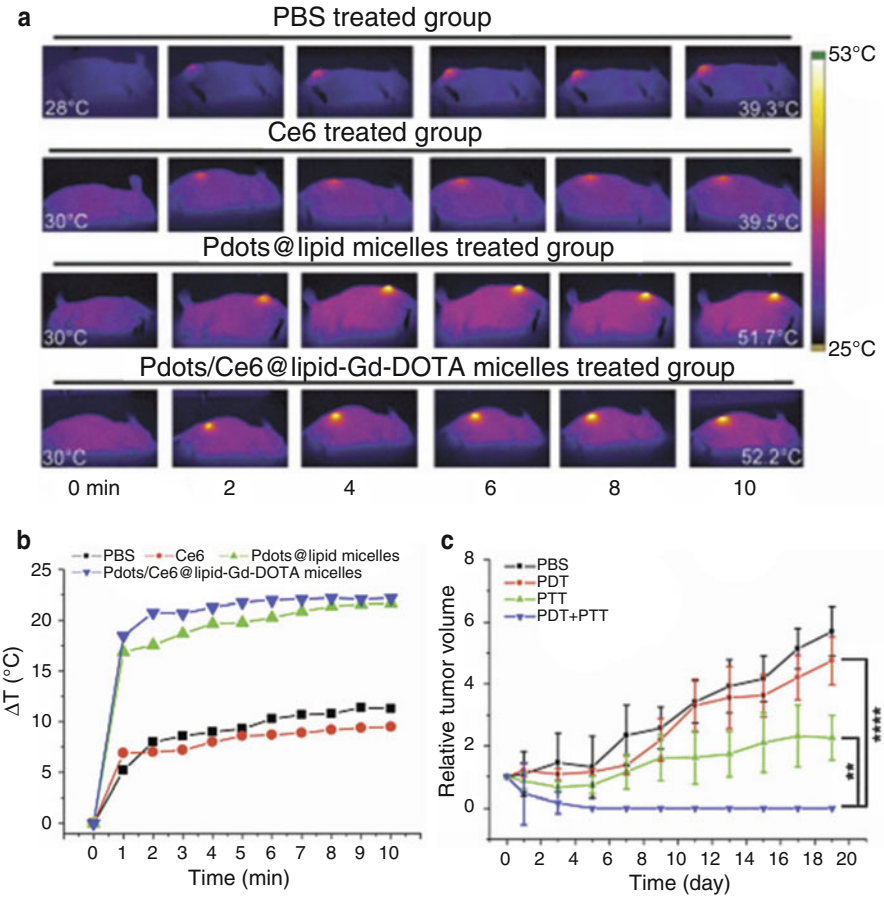

Fig. 11.29 (**a**) Thermographic images of tumor-bearing nude mice after treatment. (**b**) Temperature changes during treatment. (**c**) Relative volume of tumors after treatments (**$p < 0.01$, ****$p < 0.0001$) (Reprinted with permission from Ref. [69])

significantly in the PDT group because most of the absorbed energy was transferred to produce reactive oxygen species. In contrast, rapid temperature increases at the tumors were observed in the PTT and PDT/PTT groups. The relative tumor volumes were measured for 19 days to assess therapeutic efficacy. Compared with the control group and PDT group, the PTT and PDT/PTT groups showed delayed tumor growth. In particular, the PDT/PTT group showed much more effective treatment result in terms of tumor volume.

PPy NPs also can be a therapeutic agent for photothermal treatment of HeLa cells (Fig. 11.30) [76]. HeLa cells and PPy NPs were co-incubated for 6 h and then irradiated with an NIR laser (808 nm, 6 W/cm^2) for 0, 3, 5, and 10 min. After the treatment, substantial cell death was observed near PPy NPs, and the cell death area expanded with increasing laser irradiation time.

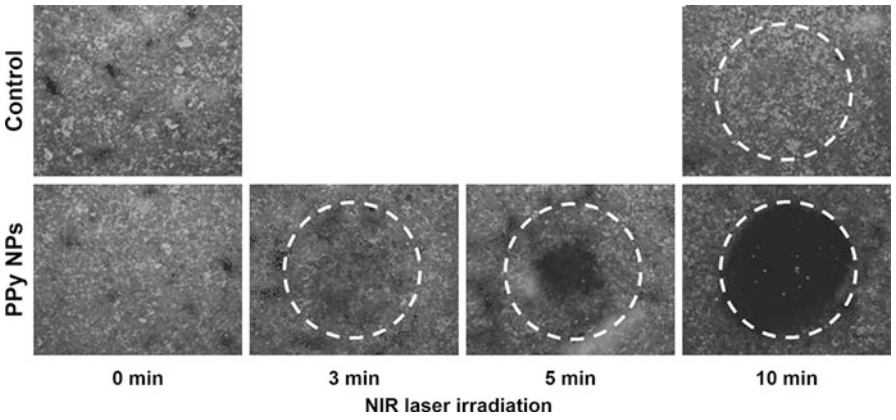

Fig. 11.30 Photothermal treatment of HeLa cells with PPy NPs under NIR laser. The white dashed circle outlines the laser irradiation area. PPy NP, polypyrrole nanoparticle; and NIR, near infrared (Reprinted with permission from Ref. [76])

GG-melanoidin, an organically bioinspired polymer, was further modified for PTT tumor ablation [80]. Fe ions were chelated by adding GG-melanoidin solution into $FeCl_3 \cdot 6H_2O$ solution and incubating the mixture with stirring for 1 h. The Fe^{3+} chelated GG-melanoidin (GG-melanoidin/Fe^{3+}) exhibited improved NIR absorption. The in vivo photothermal effect of melanoidin complexes was monitored by an infrared camera under NIR laser (808 nm, 2 W/cm^2) irradiation after injection of PBS, GG-melanoidin, and GG-melanoidin/Fe^{3+} (Fig. 11.31a). The temperature increase of GG-melanoidin/Fe^{3+} is more rapid and reached a higher temperature than that of GG-melanoidin. To evaluate therapeutic efficacy, PBS, GG-melanoidin, and GG-melanoidin/Fe^{3+} were intratumorally injected into B16F10 melanoma-bearing mice and irradiated with an NIR laser (808 nm, 2 W/cm^2) for 10 min to perform PTT (Fig. 11.31b). Under this laser irradiation, both GG-melanoidin and GG-melanoidin/Fe^{3+} completely ablated tumors. The GG-melanoidin was further applied to photothermal lipolysis, which can be useful for obesity therapy or plastic surgery. In vivo lipolysis was performed on C56bl/6 mice that had been fed high-fat foods for 10 weeks prior to subcutaneous injection of GG-melanoidin. To monitor the photothermal treatment, PA images with laser wavelengths of 1210 nm (where lipids absorb light dominantly) and 1300 nm (control) were acquired (Fig. 11.31c). After PTT treatment with an NIR laser (808 nm, 2 W/cm^2) for 10 min, a decreased PA signal in the lipolysis area was clearly observed. The lipolysis of the GG-melanoidin-injected area with laser irradiation was also verified by H&E-stained images (Fig. 11.31d).

5.2.2 Contrast-Enhanced Photoacoustic Imaging of Small Animal Gastrointestinal Tracts

As another application of PAI, contrast-enhanced imaging of gastrointestinal tracts has recently been studied. Digestive diseases are commonly diagnosed in a hospital,

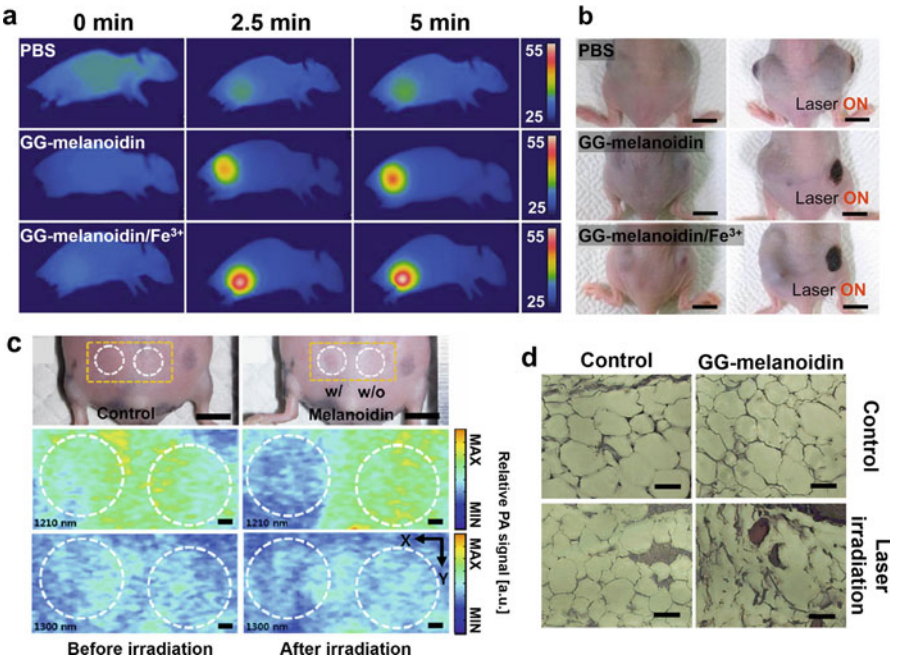

Fig. 11.31 (**a**) Images acquired from an infrared camera, showing the change in temperature after laser irradiation of subcutaneously injected PBS, GG-melanoidin, and GG-melanoidin/Fe^{3+}. (**b**) Photographs of mice before and after the photothermal ablation cancer therapy with laser irradiation at 808 nm. (**c**) Photographs and photoacoustic images of subcutaneous lipids before and after photothermal treatment. (**d**) H&E-stained images of the treated area (Reprinted with permission from Ref. [80])

and the ambulatory care visit rate for patients with digestive diseases has increased in the last decade [100]. Dysfunction in the gastrointestinal (GI) tract is usually monitored to diagnose various intestinal diseases. Clinically, conventional X-ray or CT is utilized for this purpose, but ionizing radiation may cause potential side effects. In this section, we discuss recent research in acquiring contrast-enhanced PA images of small animal GI tracts using optically absorbing organic nanostructures.

Nanonaps have been utilized for contrast-enhanced PA imaging of small animal GI tracts due to their robustness in the harsh environment of the stomach and intestine [11, 77]. After oral administration of nanonaps and methylene blue, the excretion rate of the injected dose was measured (Fig. 11.32a). Nanonaps were completely excreted in the feces due to their relatively large size (the 20 nm size of nanonaps prevents diffusion through membranes) and structure (the PEO of F127 prevents bioadsorption). By contrast, methylene blue was absorbed and partially excreted in the urine, but mostly remained in the body. PA images of GI tracts in mice and rats were noninvasively acquired after oral administration of nanonaps (Fig. 11.32b–c). Before administration, only blood vessels were visualized. However, after oral administration, blood vessels were concealed because the contrast of

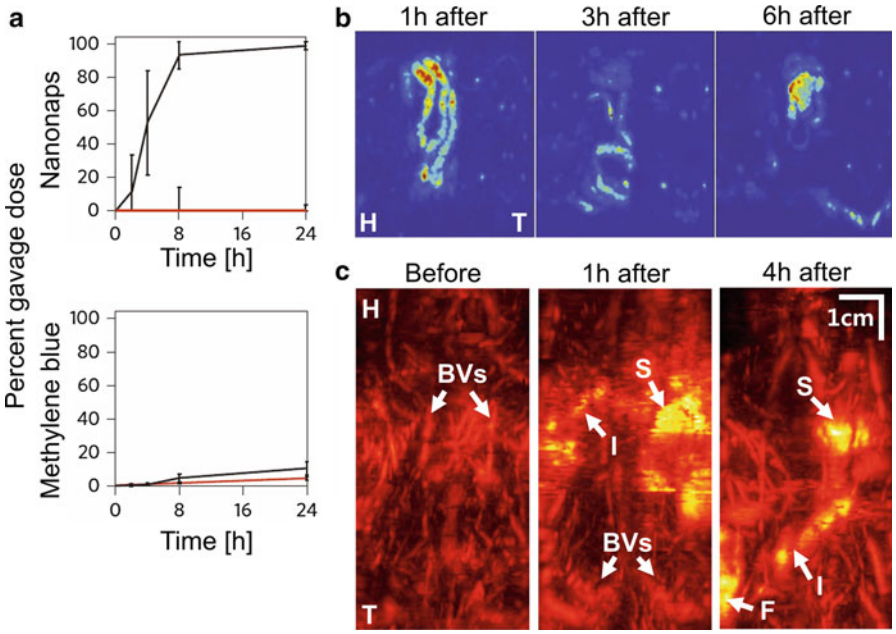

Fig. 11.32 (**a**) Excretion of nanonaps and methylene blue in feces (black) and urine (red). (**b**) and (c) PA images of gastrointestinal tracts in a mouse (**b**) and a rat (**c**). H, head; T, tail; BV, blood vessel; S, stomach; I, intestine; and F, feces (Reprinted with permission from Refs. [11, 77])

the nanonaps was dominant. The flow of nanonaps in the GI tract was visualized by obtaining PA images several times.

GG-melanoidin also has been used for contrast-enhanced GI tract imaging [80]. Because melanoidin presents in various foods, such as coffee, soy sauce, and bean paste, GG-melanoidin has great potential for contrast-enhanced GI tract imaging. To acquire such images of the GI tract, healthy Balb/c nude mice were imaged before and after oral administration of GG-melanoidin (Fig. 11.33). The flow of GG-melanoidin through the initially invisible GI tract was clearly visualized. GG-melanoidin was completely excreted in the feces at 78 h after administration, and the GI tract was again invisible.

5.2.3 Contrast-Enhanced Photoacoustic Cystography

Cystography, a standard method for visualizing bladders, conventionally uses contrast-enhanced X-ray, CT, and MRI [101–103]. However, these methods suffer from ionizing radiation or lack of sensitivity. Photoacoustic cystography with organic dyes, including methylene blue and ICG, has recently been investigated (Fig. 11.34) [84, 104–106]. The bladders of healthy mice were filled with methylene blue or ICG for PA cystography, and in vivo PA images were noninvasively acquired. The contrast of the bladders was significantly enhanced after transurethral injection of methylene blue or ICG. The position of the bladder was verified in cross-sectional images.

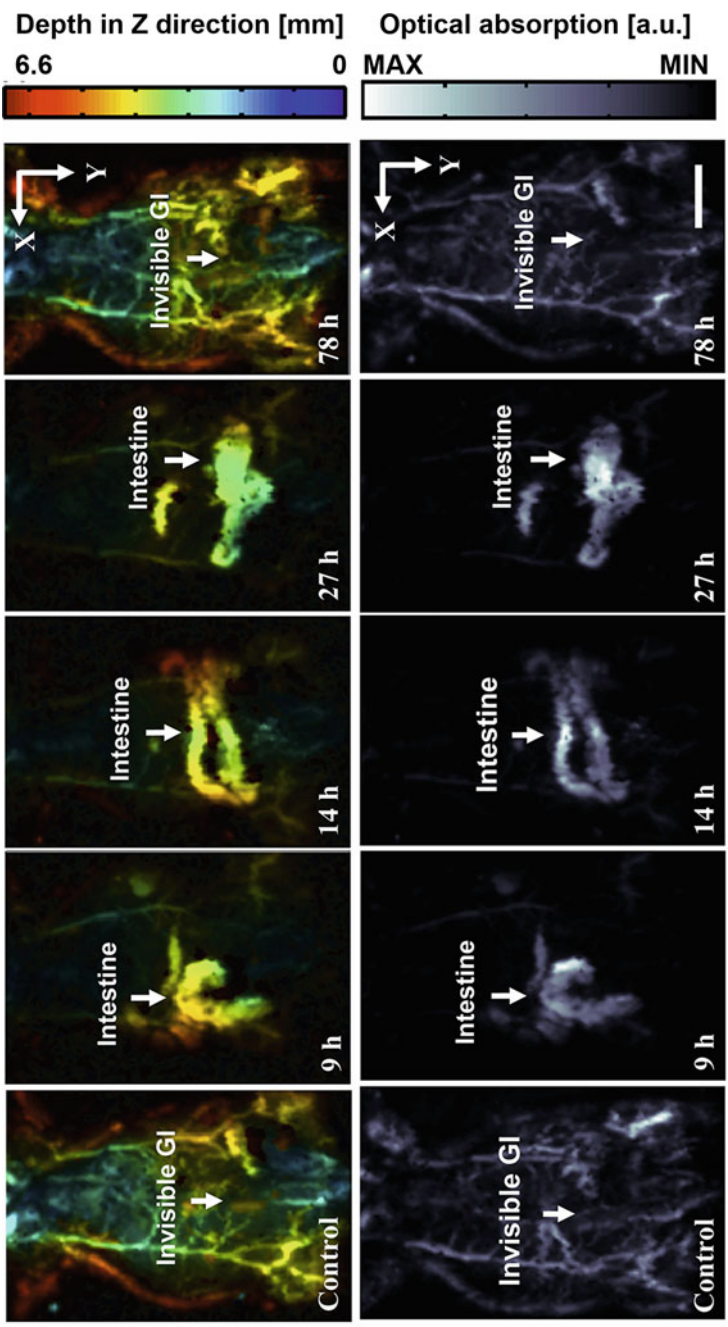

Fig. 11.33 Contrast-enhanced photoacoustic images of mouse gastrointestinal tracts with oral administration of GG-melanoidin (scale bar = 10 mm). GI, gastrointestinal (Reprinted with permission from Ref. [80])

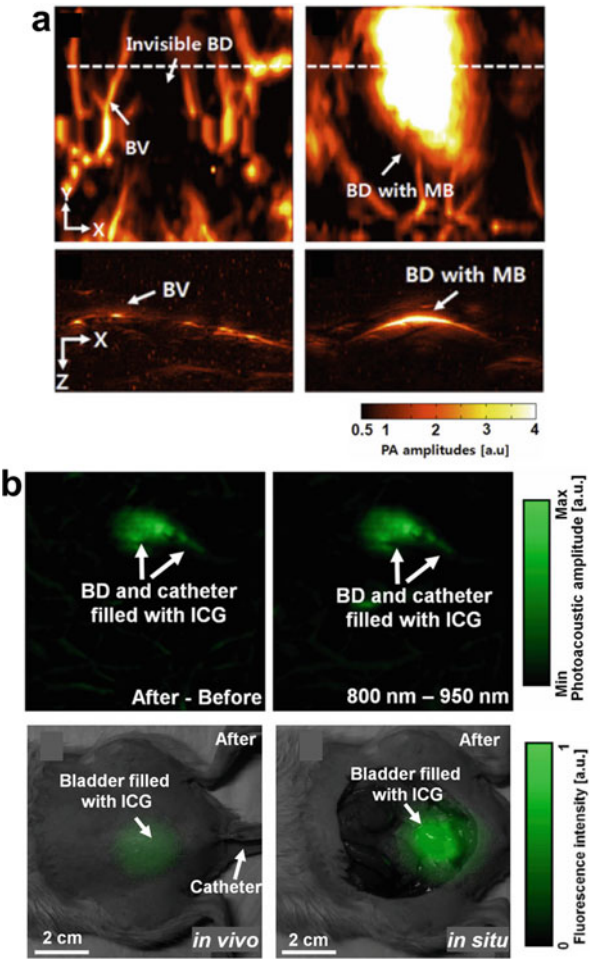

Fig. 11.34 (**a**) In vivo photoacoustic cystography using methylene blue. BD, bladder; BV, blood vessel; and MB, methylene blue. (**b**) Photoacoustic and fluorescence images of rat bladders using ICG. ICG, indocyanine green (Reprinted with permission from Refs. [104, 106])

Since the FL quantum yield of ICG varies with its concentration, FL images of the bladders were also obtained (Fig. 11.34b). Because of its noninvasiveness, non-ionization, and biocompatibility, PA cystography with organic dyes could be a promising approach for clinical bladder imaging.

6 Conclusions and Future Perspective

In this chapter, various types of PAI systems and recent trends in PA contrast agents have been reviewed, accompanied by a number of example applications. PAI is an emerging biomedical imaging modality that offers several advantages by combining optical and ultrasound imaging concepts. Because it can uniquely acquire multiscale images by controlling the acoustic and optical foci, PAI can image a wide range of

scales. In recent decades, various PAI systems have been developed and applied for contrast-enhanced imaging, molecular cancer imaging, drug delivery monitoring, and therapeutic efficacy evaluation. To facilitate biomedical studies with PA images, various types of contrast agents have also been developed, including organic dyes, metallic nanostructures, and carbon nanotubes.

Current and future trends in PAI center on its clinical applications. Since the imaging mechanism of PAI is similar to that of conventional USI, it is relatively easy to develop clinical equipment for PA imaging. Recently, a variety of clinical PAI systems have been developed [11, 12, 32, 53, 107], and clinical studies of such diseases as human breast cancers and thyroid cancers have been conducted [82, 108, 109]. Accompanying these trends, clinically relevant contrast agents, including colored microbubbles, liposomal nanoformulations, and organic polymers, have been developed and evaluated for contrast-enhanced PAI. Although PAI is not yet used in clinical settings, it has great potential as a medical diagnostic tool. Because it is noninvasive, non-ionizing, cost-efficient, and capable of providing functional imaging, it is expected that PAI will become a primary imaging tool for both clinical practice and basic science research.

References

1. Balas C (2009) Review of biomedical optical imaging – a powerful, non-invasive, non-ionizing technology for improving in vivo diagnosis. Meas Sci Technol 20(10):104020
2. Kim C, Favazza C, Wang LV (2010) In vivo photoacoustic tomography of chemicals: high-resolution functional and molecular optical imaging at new depths. Chem Rev 110(5):2756–2782
3. Beard P (2011) Biomedical photoacoustic imaging. Interface Focus 1:602. https://doi.org/10.1098/rsfs.2011.0028
4. Wang LV, Hu S (2012) Photoacoustic tomography: in vivo imaging from organelles to organs. Science 335(6075):1458–1462
5. Kim J, Park S, Lee C, Kim JY, Kim C (2015) Organic nanostructures for photoacoustic imaging. ChemNanoMat 2:156
6. Yao J, Maslov KI, Shi Y, Taber LA, Wang LV (2010) Vivo photoacoustic imaging of transverse blood flow by using Doppler broadening of bandwidth. Opt Lett 35(9):1419–1421
7. Pramanik M, Wang LV (2009) Thermoacoustic and photoacoustic sensing of temperature. J Biomed Opt 14(5):054024–054027
8. Lee C, Jeon M, Jeon MY, Kim J, Kim C (2014) In vitro photoacoustic measurement of hemoglobin oxygen saturation using a single pulsed broadband supercontinuum laser source. Appl Opt 53(18):3884–3889
9. Kim C, Erpelding TN, Jankovic L, Wang LV (2011) Performance benchmarks of an array-based hand-held photoacoustic probe adapted from a clinical ultrasound system for non-invasive sentinel lymph node imaging. Philos Trans R Soc A Math Phys Eng Sci 369 (1955):4644–4650
10. Kim C, Erpelding TN, Jankovic L, Pashley MD, Wang LV (2010) Deeply penetrating in vivo photoacoustic imaging using a clinical ultrasound array system. Biomed Opt Express 1(1):278–284
11. Kim J, Park S, Jung Y, Chang S, Park J, Zhang Y, Lovell JF, Kim C (2016) Programmable real-time clinical photoacoustic and ultrasound imaging system. Sci Rep 6:35137

12. Heijblom M, Steenbergen W, Manohar S (2015) Clinical photoacoustic breast imaging: the Twente experience. IEEE Pulse 6(3):42–46
13. Fakhrejahani E, Torii M, Kitai T, Kanao S, Asao Y, Hashizume Y, Mikami Y, Yamaga I, Kataoka M, Sugie T (2015) Clinical report on the first prototype of a photoacoustic tomography system with dual illumination for breast cancer imaging. PLoS One 10(10): e0139113
14. Smith AM, Mancini MC, Nie S (2009) Second window for in vivo imaging. Nat Nanotechnol 4 (11):710
15. Kim C, Song KH, Gao F, Wang LV (2010) Sentinel lymph nodes and lymphatic vessels: noninvasive dual-modality in vivo mapping by using indocyanine green in rats – volumetric spectroscopic photoacoustic imaging and planar fluorescence imaging 1. Radiology 255(2):442–450
16. Wang X, Ku G, Wegiel MA, Bornhop DJ, Stoica G, Wang LV (2004) Noninvasive photoacoustic angiography of animal brains in vivo with near-infrared light and an optical contrast agent. Opt Lett 29(7):730–732
17. Ku G, Wang LV (2005) Deeply penetrating photoacoustic tomography in biological tissues enhanced with an optical contrast agent. Opt Lett 30(5):507–509
18. Kim C, Cho EC, Chen J, Song KH, Au L, Favazza C, Zhang Q, Cobley CM, Gao F, Xia Y (2010) In vivo molecular photoacoustic tomography of melanomas targeted by bioconjugated gold nanocages. ACS Nano 4(8):4559–4564
19. Srivatsan A, Jenkins SV, Jeon M, Wu Z, Kim C, Chen J, Pandey RK (2014) Gold nanocage-photosensitizer conjugates for dual-modal image-guided enhanced photodynamic therapy. Theranostics 4(2):163–174
20. Li W, Cai X, Kim C, Sun G, Zhang Y, Deng R, Yang M, Chen J, Achilefu S, Wang LV (2011) Gold nanocages covered with thermally-responsive polymers for controlled release by high-intensity focused ultrasound. Nanoscale 3(4):1724–1730
21. Jeon M, Jenkins S, Oh J, Kim J, Peterson T, Chen J, Kim C (2014) Nonionizing photoacoustic cystography with near-infrared absorbing gold nanostructures as optical-opaque tracers. Nanomedicine 9(9):1377–1388
22. De La Zerda A, Zavaleta C, Keren S, Vaithilingam S, Bodapati S, Liu Z, Levi J, Smith BR, Ma T-J, Oralkan O (2008) Carbon nanotubes as photoacoustic molecular imaging agents in living mice. Nat Nanotechnol 3(9):557–562
23. Shashkov EV, Everts M, Galanzha EI, Zharov VP (2008) Quantum dots as multimodal photoacoustic and photothermal contrast agents. Nano Lett 8(11):3953–3958
24. Zerda Adl, Liu Z, Bodapati S, Teed R, Vaithilingam S, Khuri-Yakub BT, Chen X, Dai H, Gambhir SS (2010) Ultrahigh sensitivity carbon nanotube agents for photoacoustic molecular imaging in living mice. Nano Lett 10(6):2168–2172
25. Maslov K, Stoica G, Wang LV (2005) In vivo dark-field reflection-mode photoacoustic microscopy. Opt Lett 30(6):625–627
26. Jeon M, Kim J, Kim C (2014) Multiplane spectroscopic whole-body photoacoustic imaging of small animals in vivo. Med Biol Eng Comput 54(2):283–294 https://link.springer.com/article/10.1007%2Fs11517-014-1182-6
27. Hu S, Maslov K, Wang LV (2011) Second-generation optical-resolution photoacoustic microscopy with improved sensitivity and speed. Opt Lett 36(7):1134–1136
28. Maslov K, Zhang HF, Hu S, Wang LV (2008) Optical-resolution photoacoustic microscopy for in vivo imaging of single capillaries. Opt Lett 33:929
29. Li C, Aguirre A, Gamelin J, Maurudis A, Zhu Q, Wang LV (2010) Real-time photoacoustic tomography of cortical hemodynamics in small animals. J Biomed Opt 15(1):010509
30. Brecht H-P, Su R, Fronheiser M, Ermilov SA, Conjusteau A, Oraevsky AA (2009) Whole-body three-dimensional optoacoustic tomography system for small animals. J Biomed Opt 14(6):064007–064008
31. Xia J, Chatni MR, Maslov K, Guo Z, Wang K, Anastasio M, Wang LV (2012) Whole-body ring-shaped confocal photoacoustic computed tomography of small animals in vivo. J Biomed Opt 17(5):0505061–0505063

32. Luís Deán-Ben X, Razansky D (2014) Adding fifth dimension to optoacoustic imaging: volumetric time-resolved spectrally enriched tomography. Light: Sci Appl 3(1):e137
33. Razansky D, Buehler A, Ntziachristos V (2011) Volumetric real-time multispectral optoacoustic tomography of biomarkers. Nat Protoc 6(8):1121–1129
34. Kruger RA, Lam RB, Reinecke DR, Del Rio SP, Doyle RP (2010) Photoacoustic angiography of the breast. Med Phys 37(11):6096–6100
35. Needles A, Heinmiller A, Sun J, Theodoropoulos C, Bates D, Hirson D, Yin M, Foster FS (2013) Development and initial application of a fully integrated photoacoustic micro-ultrasound system. IEEE Trans Ultrason Ferroelectr Freq Control 60(5):888–897
36. Zafar H, Breathnach A, Subhash HM, Leahy MJ (2015) Linear-array-based photoacoustic imaging of human microcirculation with a range of high frequency transducer probes. J Biomed Opt 20(5):051021
37. Kim JY, Lee C, Park K, Lim G, Kim C (2015) Fast optical-resolution photoacoustic microscopy using a 2-axis water-proofing MEMS scanner. Sci Rep 5:7932
38. Yao J, Wang L, Yang J-M, Maslov KI, Wong TT, Li L, Huang C-H, Zou J, Wang LV (2015) High-speed label-free functional photoacoustic microscopy of mouse brain in action. Nat Methods 12(5):407–410
39. Gamelin J, Maurudis A, Aguirre A, Huang F, Guo P, Wang LV, Zhu Q (2009) A real-time photoacoustic tomography system for small animals. Opt Express 17(13):10489–10498
40. Lin L, Xia J, Wong TT, Li L, Wang LV (2015) In vivo deep brain imaging of rats using oral-cavity illuminated photoacoustic computed tomography. J Biomed Opt 20(1):016019
41. Tsyboulski DA, Liopo AV, Su R, Ermilov SA, Bachilo SM, Weisman RB, Oraevsky AA (2014) Enabling in vivo measurements of nanoparticle concentrations with three-dimensional optoacoustic tomography. J Biophotonics 7(8):581–588
42. Ermilov S, Su R, Conjusteau A, Anis F, Nadvoretskiy V, Anastasio M, Oraevsky A (2016) Three-dimensional optoacoustic and laser-induced ultrasound tomography system for preclinical research in mice: design and phantom validation. Ultrason Imaging 38(1):77–95
43. Dima A, Burton NC, Ntziachristos V (2014) Multispectral optoacoustic tomography at 64, 128, and 256 channels. J Biomed Opt 19(3):036021
44. Taruttis A, Morscher S, Burton NC, Razansky D, Ntziachristos V (2012) Fast multispectral optoacoustic tomography (MSOT) for dynamic imaging of pharmacokinetics and biodistribution in multiple organs. PLoS One 7(1):e30491
45. Ma R, Taruttis A, Ntziachristos V, Razansky D (2009) Multispectral optoacoustic tomography (MSOT) scanner for whole-body small animal imaging. Opt Express 17(24):21414–21426
46. Taruttis A, Herzog E, Razansky D, Ntziachristos V (2010) Real-time imaging of cardiovascular dynamics and circulating gold nanorods with multispectral optoacoustic tomography. Opt Express 18(19):19592–19602
47. Kruger RA, Kuzmiak CM, Lam RB, Reinecke DR, Del Rio SP, Steed D (2013) Dedicated 3D photoacoustic breast imaging. Med Phys 40(11):113301
48. Manohar S, Kharine A, van Hespen JC, Steenbergen W, van Leeuwen TG (2005) The Twente Photoacoustic Mammoscope: system overview and performance. Phys Med Biol 50(11):2543
49. Asao Y, Hashizume Y, Suita T, Nagae K-i, Fukutani K, Sudo Y, Matsushita T, Kobayashi S, Tokiwa M, Yamaga I (2016) Photoacoustic mammography capable of simultaneously acquiring photoacoustic and ultrasound images. J Biomed Opt 21(11):116009
50. Fehm TF, Deán-Ben XL, Ford SJ, Razansky D (2016) In vivo whole-body optoacoustic scanner with real-time volumetric imaging capacity. Optica 3(11):1153–1159
51. Erpelding TN, Kim C, Pramanik M, Jankovic L, Maslov K, Guo Z, Margenthaler JA, Pashley MD, Wang LV (2010) Sentinel lymph nodes in the rat: noninvasive photoacoustic and US imaging with a clinical US system. Radiology 256(1):102–110
52. Sivasubramanian K, Pramanik M (2016) High frame rate photoacoustic imaging at 7000 frames per second using clinical ultrasound system. Biomed Opt Express 7(2):312–323
53. Wang D, Wang Y, Wang W, Luo D, Chitgupi U, Geng J, Zhou Y, Wang L, Lovell JF, Xia J (2017) Deep tissue photoacoustic computed tomography with a fast and compact laser system. Biomed Opt Express 8(1):112–123

54. Sonavane G, Tomoda K, Makino K (2008) Biodistribution of colloidal gold nanoparticles after intravenous administration: effect of particle size. Colloids Surf B: Biointerfaces 66(2):274–280
55. Lindner JR (2004) Microbubbles in medical imaging: current applications and future directions. Nat Rev Drug Discov 3(6):527–533
56. Jeon M, Song W, Huynh E, Kim J, Kim J, Helfield BL, Leung BY, Goertz DE, Zheng G, Oh J (2014) Methylene blue microbubbles as a model dual-modality contrast agent for ultrasound and activatable photoacoustic imaging. J Biomed Opt 19(1):016005
57. Huynh E, Lovell JF, Helfield BL, Jeon M, Kim C, Goertz DE, Wilson BC, Zheng G (2012) Porphyrin shell microbubbles with intrinsic ultrasound and photoacoustic properties. J Am Chem Soc 134(40):16464–16467
58. Huynh E, Jin CS, Wilson BC, Zheng G (2014) Aggregate enhanced trimodal porphyrin shell microbubbles for ultrasound, photoacoustic, and fluorescence imaging. Bioconjug Chem 25(4):796–801
59. Wilson K, Homan K, Emelianov S (2012) Biomedical photoacoustics beyond thermal expansion using triggered nanodroplet vaporization for contrast-enhanced imaging. Nat Commun 3:618
60. Hannah A, Luke G, Wilson K, Homan K, Emelianov S (2013) Indocyanine green-loaded photoacoustic nanodroplets: dual contrast nanoconstructs for enhanced photoacoustic and ultrasound imaging. ACS Nano 8(1):250–259
61. Peer D, Karp JM, Hong S, Farokhzad OC, Margalit R, Langer R (2007) Nanocarriers as an emerging platform for cancer therapy. Nat Nanotechnol 2(12):751–760
62. Malam Y, Loizidou M, Seifalian AM (2009) Liposomes and nanoparticles: nanosized vehicles for drug delivery in cancer. Trends Pharmacol Sci 30(11):592–599
63. Beziere N, Lozano N, Nunes A, Salichs J, Queiros D, Kostarelos K, Ntziachristos V (2015) Dynamic imaging of PEGylated indocyanine green (ICG) liposomes within the tumor microenvironment using multi-spectral optoacoustic tomography (MSOT). Biomaterials 37:415–424
64. Lozano N, Al-Ahmady ZS, Beziere NS, Ntziachristos V, Kostarelos K (2015) Monoclonal antibody-targeted PEGylated liposome-ICG encapsulating doxorubicin as a potential theranostic agent. Int J Pharm 482(1):2–10
65. Lovell JF, Jin CS, Huynh E, Jin H, Kim C, Rubinstein JL, Chan WC, Cao W, Wang LV, Zheng G (2011) Porphysome nanovesicles generated by porphyrin bilayers for use as multimodal biophotonic contrast agents. Nat Mater 10(4):324–332
66. Rieffel J, Chen F, Kim J, Chen G, Shao W, Shao S, Chitgupi U, Hernandez R, Graves SA, Nickles RJ (2015) Hexamodal imaging with porphyrin-phospholipid-coated upconversion nanoparticles. Adv Mater 27:1785
67. Liu TW, MacDonald TD, Shi J, Wilson BC, Zheng G (2012) Intrinsically copper-64-labeled organic nanoparticles as radiotracers. Angew Chem Int Ed 51(52):13128–13131
68. Sreejith S, Joseph J, Lin M, Menon NV, Borah P, Ng HJ, Loong YX, Kang Y, Yu SW-K, Zhao Y (2015) Near-infrared squaraine dye encapsulated micelles for in vivo fluorescence and photoacoustic bimodal imaging. ACS Nano 9(6):5695–5704
69. Zhang D, Wu M, Zeng Y, Liao N, Cai Z, Liu G, Liu X, Liu J (2016) Lipid micelles packaged with semiconducting polymer dots as simultaneous MRI/photoacoustic imaging and photodynamic/photothermal dual-modal therapeutic agents for liver cancer. J Mater Chem B 4(4):589–599
70. Pu K, Shuhendler AJ, Jokerst JV, Mei J, Gambhir SS, Bao Z, Rao J (2014) Semiconducting polymer nanoparticles as photoacoustic molecular imaging probes in living mice. Nat Nanotechnol 9:233
71. Pu K, Mei J, Jokerst JV, Hong G, Antaris AL, Chattopadhyay N, Shuhendler AJ, Kurosawa T, Zhou Y, Gambhir SS (2015) Diketopyrrolopyrrole-based semiconducting polymer nanoparticles for in vivo photoacoustic imaging. Adv Mater 27(35):5184–5190

72. Liu J, Geng J, Liao L-D, Thakor N, Gao X, Liu B (2014) Conjugated polymer nanoparticles for photoacoustic vascular imaging. Polym Chem 5(8):2854–2862
73. Kang B, Yu D, Dai Y, Chang S, Chen D, Ding Y (2009) Cancer-cell targeting and photoacoustic therapy using carbon nanotubes as "bomb" agents. Small 5(11):1292–1301
74. Zha Z, Deng Z, Li Y, Li C, Wang J, Wang S, Qu E, Dai Z (2013) Biocompatible polypyrrole nanoparticles as a novel organic photoacoustic contrast agent for deep tissue imaging. Nanoscale 5(10):4462–4467
75. Hong JY, Yoon H, Jang J (2010) Kinetic study of the formation of polypyrrole nanoparticles in water-soluble polymer/metal cation systems: a light-scattering analysis. Small 6(5):679–686
76. Zha Z, Yue X, Ren Q, Dai Z (2013) Uniform polypyrrole nanoparticles with high photothermal conversion efficiency for photothermal ablation of cancer cells. Adv Mater 25(5):777–782
77. Zhang Y, Jeon M, Rich LJ, Hong H, Geng J, Zhang Y, Shi S, Barnhart TE, Alexandridis P, Huizinga JD (2014) Non-invasive multimodal functional imaging of the intestine with frozen micellar naphthalocyanines. Nat Nanotechnol 9(8):631–638
78. Lee C, Kim J, Zhang Y, Jeon M, Liu C, Song L, Lovell JF, Kim C (2015) Dual-color photoacoustic lymph node imaging using nanoformulated naphthalocyanines. Biomaterials 73:142–148
79. Fan Q, Cheng K, Hu X, Ma X, Zhang R, Yang M, Lu X, Xing L, Huang W, Gambhir SS (2014) Transferring biomarker into molecular probe: melanin nanoparticle as a naturally active platform for multimodality imaging. J Am Chem Soc 136(43):15185–15194
80. Lee MY, Lee C, Jung HS, Jeon M, Kim KS, Yun SH, Kim C, Hahn SK (2015) Biodegradable photonic melanoidin for theranostic applications. ACS Nano 10:822
81. Agarwal A, Huang S, O'Donnell M, Day K, Day M, Kotov N, Ashkenazi S (2007) Targeted gold nanorod contrast agent for prostate cancer detection by photoacoustic imaging. J Appl Phys 102(6):064701
82. Manohar S, Vaartjes SE, van Hespen JC, Klaase JM, van den Engh FM, Steenbergen W, Van Leeuwen TG (2007) Initial results of in vivo non-invasive cancer imaging in the human breast using near-infrared photoacoustics. Opt Express 15(19):12277–12285
83. Song J, Kim J, Hwang S, Jeon M, Jeong S, Kim C, Kim S (2016) "Smart" gold nanoparticles for photoacoustic imaging: an imaging contrast agent responsive to the cancer microenvironment and signal amplification via pH-induced aggregation. Chem Commun 52(53):8287–8290
84. Kim C, Jeon M, Wang L (2011) Nonionizing photoacoustic cystography in vivo. Opt Lett 36(18):3599
85. Saini R, Poh CF (2013) Photodynamic therapy: a review and its prospective role in the management of oral potentially malignant disorders. Oral Dis 19(5):440–451
86. Chen J, Keltner L, Christophersen J, Zheng F, Krouse M, Singhal A, Wang S-s (2002) New technology for deep light distribution in tissue for phototherapy. Cancer J 8(2):154–163
87. Huang X, Jain PK, El-Sayed IH, El-Sayed MA (2008) Plasmonic photothermal therapy (PPTT) using gold nanoparticles. Lasers Med Sci 23(3):217–228
88. Huang X, El-Sayed IH, Qian W, El-Sayed MA (2006) Cancer cell imaging and photothermal therapy in the near-infrared region by using gold nanorods. J Am Chem Soc 128 (6):2115–2120
89. Huang P, Lin J, Li W, Rong P, Wang Z, Wang S, Wang X, Sun X, Aronova M, Niu G (2013) Biodegradable gold nanovesicles with an ultrastrong plasmonic coupling effect for photoacoustic imaging and photothermal therapy. Angew Chem 125(52):14208–14214
90. Lu W, Melancon MP, Xiong C, Huang Q, Elliott A, Song S, Zhang R, Flores LG, Gelovani JG, Wang LV (2011) Effects of photoacoustic imaging and photothermal ablation therapy mediated by targeted hollow gold nanospheres in an orthotopic mouse xenograft model of glioma. Cancer Res 71(19):6116–6121
91. Jing L, Liang X, Deng Z, Feng S, Li X, Huang M, Li C, Dai Z (2014) Prussian blue coated gold nanoparticles for simultaneous photoacoustic/CT bimodal imaging and photothermal ablation of cancer. Biomaterials 35(22):5814–5821

92. Liu H, Chen D, Li L, Liu T, Tan L, Wu X, Tang F (2011) Multifunctional gold nanoshells on silica nanorattles: a platform for the combination of photothermal therapy and chemotherapy with low systemic toxicity. Angew Chem 123(4):921–925
93. Li M-L, Wang JC, Schwartz JA, Gill-Sharp KL, Stoica G, Wang LV (2009) In-vivo photoacoustic microscopy of nanoshell extravasation from solid tumor vasculature. J Biomed Opt 14(1):010507
94. Yang H-W, Liu H-L, Li M-L, Hsi I-W, Fan C-T, Huang C-Y, Lu Y-J, Hua M-Y, Chou H-Y, Liaw J-W (2013) Magnetic gold-nanorod/PNIPAAmMA nanoparticles for dual magnetic resonance and photoacoustic imaging and targeted photothermal therapy. Biomaterials 34(22):5651–5660
95. Chen Y-S, Frey W, Kim S, Kruizinga P, Homan K, Emelianov S (2011) Silica-coated gold nanorods as photoacoustic signal nanoamplifiers. Nano Lett 11(2):348–354
96. Chen Y-S, Frey W, Kim S, Homan K, Kruizinga P, Sokolov K, Emelianov S (2010) Enhanced thermal stability of silica-coated gold nanorods for photoacoustic imaging and image-guided therapy. Opt Express 18(9):8867–8878
97. Tong L, Wei Q, Wei A, Cheng JX (2009) Gold nanorods as contrast agents for biological imaging: optical properties, surface conjugation and photothermal effects. Photochem Photobiol 85(1):21–32
98. Moon GD, Choi S-W, Cai X, Li W, Cho EC, Jeong U, Wang LV, Xia Y (2011) A new theranostic system based on gold nanocages and phase-change materials with unique features for photoacoustic imaging and controlled release. J Am Chem Soc 133(13):4762–4765
99. Chen J, Glaus C, Laforest R, Zhang Q, Yang M, Gidding M, Welch MJ, Xia Y (2010) Gold nanocages as photothermal transducers for cancer treatment. Small 6(7):811–817
100. Everhart JE, Ruhl CE (2009) Burden of digestive diseases in the United States part I: overall and upper gastrointestinal diseases. Gastroenterology 136(2):376–386
101. Han K, Choi H, Jung D, Park S, Cho K, Joung J, Seo H, Chung J, Lee K (2011) A prospective evaluation of conventional cystography for detection of urine leakage at the vesicourethral anastomosis site after radical prostatectomy based on computed tomography. Clin Radiol 66(3):251–256
102. Morgan DE, Nallamala LK, Kenney PJ, Mayo MS, Rue LW (2000) CT cystography: radiographic and clinical predictors of bladder rupture. Am J Roentgenol 174(1):89–95
103. Wang Z, Lee CS, Waltzer WC, Liu J, Xie H, Yuan Z, Pan Y (2007) In vivo bladder imaging with microelectromechanical-systems-based endoscopic spectral domain optical coherence tomography. J Biomed Opt 12(3):034009
104. Jeon M, Kim J, Kim C (2013) Photoacoustic cystography. J Vis Exp 76:e50340–e50340
105. Koo J, Jeon M, Oh Y, Kang HW, Kim J, Kim C, Oh J (2012) In vivo non-ionizing photoacoustic mapping of sentinel lymph nodes and bladders with ICG-enhanced carbon nanotubes. Phys Med Biol 57(23):7853
106. Park S, Kim J, Jeon M, Song J, Kim C (2014) In vivo photoacoustic and fluorescence cystography using clinically relevant dual modal Indocyanine green. Sensors 14(10):19660–19668
107. Su R, Ermilov S, Liopo A, Oraevsky A (2013) Laser optoacoustic tomography: towards new technology for biomedical diagnostics. Nucl Instrum Methods Phys Res Sect A 720:58–61
108. Kitai T, Torii M, Sugie T, Kanao S, Mikami Y, Shiina T, Toi M (2014) Photoacoustic mammography: initial clinical results. Breast Cancer 21(2):146–153
109. Dogra VS, Chinni BK, Valluru KS, Moalem J, Giampoli EJ, Evans K, Rao NA (2014) Preliminary results of ex vivo multispectral photoacoustic imaging in the management of thyroid cancer. Am J Roentgenol 202(6):W552–W558

Dendrimer-Based Nanoplatforms for SPECT Imaging Applications

12

Lingzhou Zhao, Xiangyang Shi, and Jinhua Zhao

Contents

L. Zhao · J. Zhao (✉)
Department of Nuclear Medicine, Shanghai General Hospital, Shanghai Jiao Tong University School of Medicine, Shanghai, People's Republic of China
e-mail: zhaojinhua1963@126.com

X. Shi (✉)
College of Chemistry, Chemical Engineering and Biotechnology, Donghua University, Shanghai, People's Republic of China

CQM-Centro de Química da Madeira, Universidade da Madeira, Funchal, Portugal
e-mail: xshi@dhu.edu.cn

C. S. S. R. Kumar (ed.), *Nanotechnology Characterization Tools for Biosensing and Medical Diagnosis*, https://doi.org/10.1007/978-3-662-56333-5_12

1 Definition of the Topic

Dendrimers can be functionalized with multiple imaging and therapeutic moieties to establish dendrimer-based nanoplatforms for various applications. In this chapter we describe the recent progress in dendrimer-based nanomaterials for SPECT imaging applications with different purposes.

2 Overview

Dendrimers provide viable platforms for molecular imaging of organs and other target-specific diseases due to their unique and well-defined molecular architecture. Recent innovations in dendrimer nanotechnology have led to a rapid development of multi-functional radiolabeled nanoparticles for diagnosis and therapy of diseases. In this chapter, we review the recent advances in dendrimer-based nanosystems for SPECT imaging applications including single-mode SPECT imaging, dual-mode SPECT/CT, SPECT/MR, and SPECT/optical imaging and theranostics of cancer or other diseases.

3 Introduction

Precision becomes one of the core values in today's healthcare environment [1, 2]. Medical imaging, an essential technology in this context, providing precise imaging information, constantly deepens the understanding and instructs the treatment of many diseases [3–6]. During the last several decades, the number of imaging technologies and their applications in clinical practice have unprecedentedly increased. Currently, numerous imaging modalities are being used in biomedical and clinical settings for diagnostic and therapy purposes, including magnetic resonance (MR) imaging [7–11], computed tomography (CT) [12–16], positron emission tomography (PET) [17–19], single photon emission computed tomography (SPECT) [20, 21], and optical imaging [22, 23]. Among these, SPECT, PET, and optical imaging are known as functional imaging modalities, while CT and MRI are normally utilized to acquire anatomical information [24, 25].

Although each imaging modality is being continuously developed and improved for disease diagnosis, prognosis, or therapy monitoring, they are applied with intrinsic advantages and limitations [17, 26–28]. For example, optical imaging has a comparatively high sensitivity, whereas its absorption and scattering properties of tissue components limit the penetration depth to less than 10 mm [28]. PET and SPECT both are quantitative imaging techniques with high sensitivity and ability of observing physiological processes, but spatially limited in resolution [17]. MRI and CT are relatively insensitive imaging techniques but show operation convenience and extreme spatial resolution [26, 27]. Clearly, no single modality provides all of the required information. Hence, dual or multimode imaging approaches that combine functional and anatomic imaging into a single superposed image have emerged to integrate their advantages of

each imaging modality [29–31], and numerous efforts have been devoted to develop multimodality imaging techniques over the last decade [32–34]. Up to now, PET/CT and SPECT/CT with high fusion accuracy are the most successful paragons and have revolutionized medical diagnosis in many fields [35–37]. Lately, PET/MRI, a new diagnostic method with an excellent soft tissue contrast and less radiation dose than PET/CT, has been well developed and used for clinical imaging [38, 39]. These hybrid imaging techniques have gained wide acceptance as powerful tools in preclinical and clinical applications; however, few new imaging agents have been provided for multimodal hybrid imaging during the last decade. Therefore, a number of researchers are attempting to exploit versatile imaging platforms for early diagnosis, accurate prognosis, precision imaging, and image-guided drug delivery [40–42].

Recent progresses in nanotechnology have enabled the development of various advanced imaging agents. By virtue of the unique electrical, magnetic, and optical properties of nanomaterials, a variety of multifunctional nanosystems have been designed and manufactured as contrast agents for different imaging applications [42–45]. These nanosystems not only present enhanced contrast imaging effects, low toxicity, and prolonged circulation time but also possess active targeting ability by means of modification with targeting molecules. Among the developed nanomaterials, dendrimers have been praised as promising platforms to build multiple types of contrast agents due to their exquisite structures [46–48]. In this chapter, we will describe the use of dendrimer-based nanosystems for SPECT imaging including single-mode SPECT imaging, dual-mode SPECT/CT, SPECT/MR, and SPECT/optical imaging and theranostics of cancer or other diseases. To the best of our knowledge, this is the first review article specifically describing the progress of dendrimer-based SPECT agents and their applications in different aspects.

4 Experimental and Instrumental Methodology

4.1 Dendrimers

Dendrimers, a class of highly branched, monodispersed, synthetic macromolecules with well-defined architecture and composition, have highly controllable size and surface properties, which are quite different from linear polymers [49–51]. Dendrimers with nanometer-scale dimensions are composed of three components: a central core, a highly branched interior, and an exterior surface with functional groups. The unique features of dendrimers afford the varied combination of these components to form various functional nanoparticles (NPs) with different shapes, sizes, and modifications for materials sciences and biomedical applications [52]. Especially in the field of medical imaging, the plentiful terminal groups on the dendrimer periphery can be easily modified with multiple imaging moieties to provide dual-mode and multimode imaging functionalities within a single dendrimer molecule [46–48]. Similarly, the generation-dependent physical size of dendrimers may be used to tune their excretion behavior and imaging time, to optimize the payloads of different imaging elements, and to adjust the passive targeting

behavior through enhanced permeability and retention (EPR) effect [53–55]. In order to increase the aggregation in specific areas, such as tumors, dendrimers are able to be conjugated with specific targeting ligands to improve their specificity and cellular uptake [56, 57]. Besides, the attached surface groups affect the solubility and biocompatibility of dendrimers [15, 58]. Through appropriate surface modification, dendrimers are able to have high water solubility and improved biocompatibility. These characteristics may impart the dendrimer-based contrast agents a better application prospect in clinical practice than conventional small molecular contrast agents.

4.2 Preparation of Dendrimer-Based Nanoplatforms

Dendrimer-based contrast agents can be prepared in a variety of ways. For instance, dendrimers are able to connect with iodinated small molecular CT contrast agents, fluorescent molecules, gadolinium (Gd) or radionuclide chelators for CT [59–61], fluorescence [62–64], MR [65–67], and radionuclide-based imaging [68–72]. In addition, dendrimers can be utilized as either templates or stabilizer to construct gold (Au) or iron oxide NPs for CT [52] or MR imaging [73, 74], and functionalized dendrimers can also be assembled onto preformed iron oxide NPs for MR imaging [25, 75]. Furthermore, the versatile dendrimer nanotechnology allows for the incorporation of different types of contrast agents for dual or multimodality imaging. For instance, Au NPs can be formed using dendrimers as templates, and then Gd, radionuclide chelator complexes, or fluorescent molecules can be further modified on the surface of dendrimers for CT/MR [76, 77], SPECT/CT [69], or CT/MR/optical imaging applications [34]. The facile modification of dendrimer surface with different substances and convenient strategies used to generate multifunctional nanoparticles render the dendrimers with great advantages and capacities for different imaging applications.

5 Key Research Findings

5.1 SPECT Imaging

SPECT is a nuclear medicine imaging technique using single photon radionuclides which emit gamma (γ) rays in the energy range of approximately 75 to 360 keV [78, 79]. SPECT imaging with extremely high sensitivity is applicable to tomographic and quantitative functional information in a living subject [35]. For SPECT imaging, small amounts of compounds were labeled by radionuclides called radiotracers which can be applied as noninvasive diagnostic agents. Following administration of radiotracers to a patient, the γ-rays from radionuclides can be directly measured by SPECT detectors. Generally, radionuclides used in SPECT imaging include technetium-99 m (^{99m}Tc), indium-111 (^{111}In), iodine-123 (^{123}I), and galium-67 (^{67}Ga) with half-lives varying from several hours to a few days [80]. Among those, ^{99m}Tc is so far the most used radionuclide in SPECT imaging [81–83]. This is due to its latent chemical properties for labeling and highly attractive physical properties such as

appropriate half-life (6.02 h) and low-energy γ-ray (140 keV), which is favorable for both effective imaging and radiation safety. Furthermore, ^{99m}Tc can be conveniently obtained from a ^{99}Mo/^{99m}Tc generator with low production cost [82].

Over the last several decades, diethylenetriaminepentaacetic acid (DPTA) chelator [84–86], an aminopolycarboxylic acid consisting of a diethylenetriamine backbone with five carboxymethyl groups, has played a significant role in the field of SPECT imaging applications [87–89]. The dendrimer scaffolds conjugated with DTPA can be readily labeled with various radionuclides, such as ^{99m}Tc and ^{111}In. For instance, Zhang et al. reported the synthesis and SPECT imaging of ^{99m}Tc-labeled dendrimer-based nanoparticles using generation 5 (G5) polyamidoamine (PAMAM) dendrimers as a template [90]. In this study, dendrimers were first partially acetylated (Ac) to improve solubility and reduce nonspecific cellular uptake. Then folic acid (FA) was linked on the surface of PAMAM dendrimers as a targeting molecule to FA receptor (FAR)-overexpressing cancer cells, and multiple DTPA chelators were conjugated for ^{99m}Tc labeling. The formed ^{99m}Tc-G5-Ac-FA-DTPA conjugate had a radiochemical yield up to 98.9%, excellent stability, and rapid blood clearance. Preferential uptake in the FAR-positive tumors was confirmed by biodistribution and micro-SPECT imaging studies in KB tumor-bearing nude mice. In the following work, the same authors investigated the effects on the uptake of ^{99m}Tc-labeled dendrimers in tumors using different FA linking strategies [91]. PEGylated FA and FA were respectively modified onto the surface of acetylated G5 PAMAM dendrimers, followed by linking DTPA chelators for the labeling of ^{99m}Tc to form ^{99m}Tc-G5-Ac-pegFA-DTPA and ^{99m}Tc-G5-Ac-FA-DTPA. Both of the biodistribution and micro-SPECT imaging studies showed that PEGylated FA dendrimer conjugate had higher specific accumulation in tumor than that of ^{99m}Tc-G5-Ac-FA-DTPA, while no obvious uptake of radiolabeled dendrimer without folic acid was observed in tumor (Fig. 12.1). These results demonstrated that indirect FA conjugation through PEG spacer was able to enhance the accumulation in tumors more significantly than direct FA conjugation via EDC chemistry. Subsequently, they attempted to employ avidin instead of folic acid on dendrimer surface to decrease the accumulation of ^{99m}Tc-labeled conjugate in the kidneys [92]. It seemed that this method was able to gain a low uptake in the kidney but very high accumulation in the liver and spleen.

Beyond the use of ^{99m}Tc, ^{111}In is another promising radionuclide for SPECT imaging, which is produced in a cyclotron from the proton irradiation reaction of cadmium [93]. ^{111}In with a decay mode of electron capture emits 173 and 247 keV γ-rays and has a relatively long half-life (2.8 days) [94–96]. Like ^{99m}Tc, ^{111}In can be effectively chelated by DTPA ligands [97]. Kojima et al. synthesized ^{111}In-labeled DTPA-conjugated polymers using G4 acetylated PAMAM dendrimer (Ac-den) and collagen peptide-conjugated dendrimer (CP-den) (Fig. 12.2a, b) and investigated their behaviors in vivo by micro-SPECT imaging following subcutaneous injection into tumor-bearing mice, respectively (Fig. 12.2c) [98]. These ^{111}In-DTPA-bearing dendrimers were largely retained at the injection site for at least 1 day. Notably, because of higher molecular weight, the retention time of CP-den-DTPA was longer than that of Ac-den-DTPA. Thus, thanks to the prolonged retention around the subcutaneous injection site, these polymers with controlled-release drug delivery systems might be beneficial for long-term treatment.

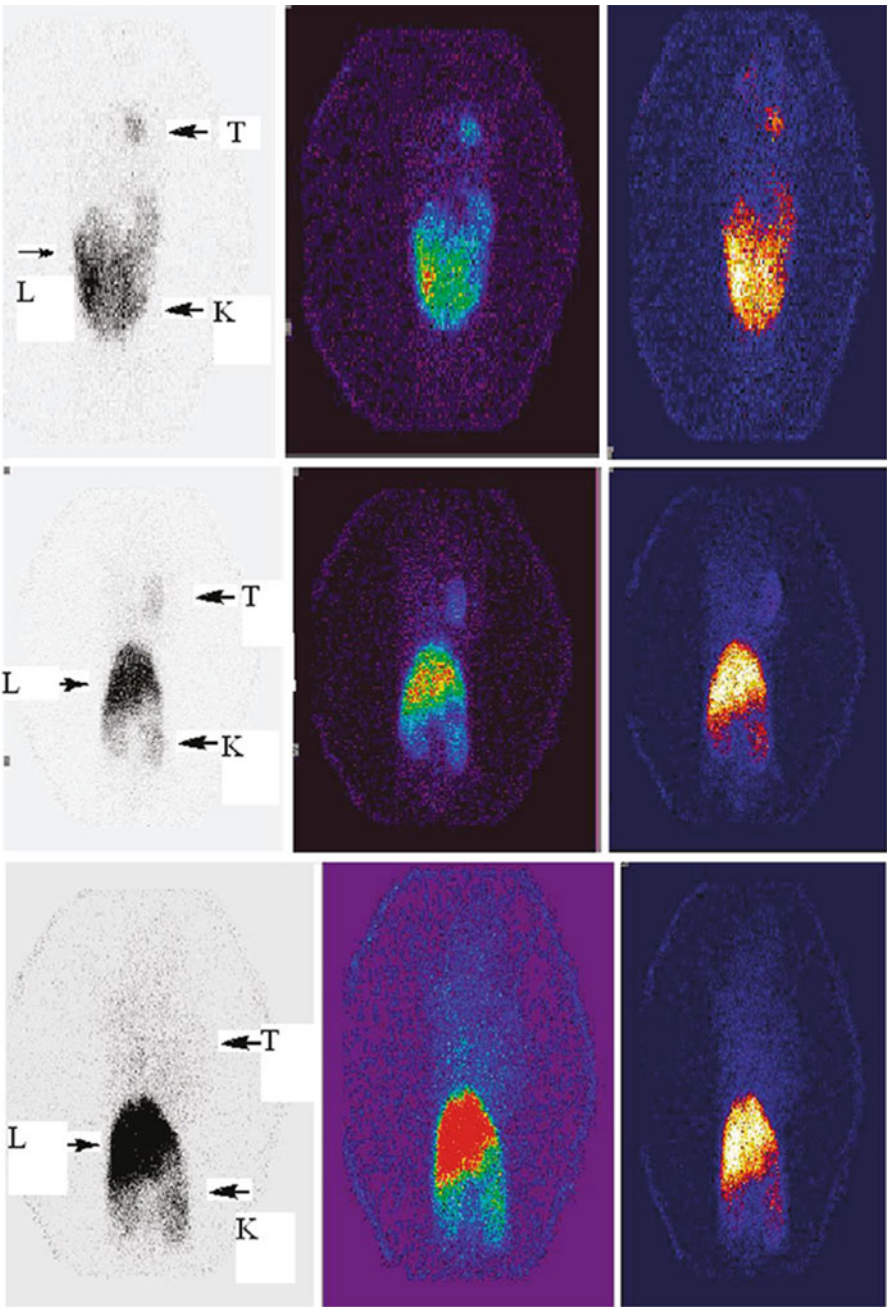

Fig. 12.1 Micro-SPECT images of KB-bearing nude mice at 4 h: *T*, tumor; *L*, lungs; *K*, kidney ((upper) ^{99m}Tc-G5-Ac-pegFA-DTPA, (middle) ^{99m}Tc-G5-Ac-FA-DTPA, (lower) ^{99m}Tc-G5-Ac-DTPA)) (Reprinted (adapted) with permission from Ref. [91]. Copyright (2010) American Chemical Society)

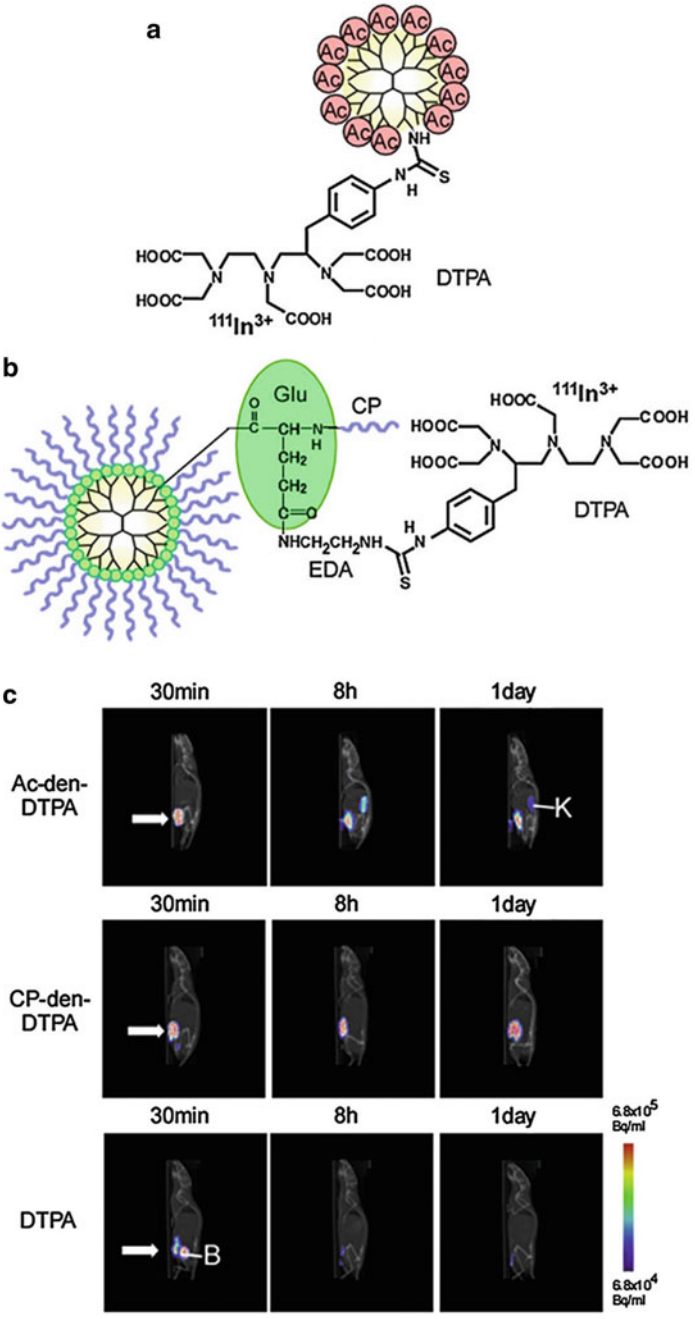

Fig. 12.2 (**a**) ^{111}In-labeded acetylated (Ac) dendrimer with DTPA (Ac-den–DTPA), (**b**) ^{111}In-labeded collagen peptide-conjugated (CP) dendrimer with DTPA (CP-den–DTPA), (**c**) SPECT/CT imaging of mice subcutaneously injected with Ac-den-DTPA, CP-den-DTPA, and unconjugated

The lymphatic system, especially the sentinel lymph node (SLN), plays a vital role in the metastatic spread of various cancer cells [99–101]. Within the fields of cancer therapy and diagnosis, a great deal of attention has been attracted in the noninvasive imaging of SNL using dendrimer-based nanoparticles [102, 103]. For example, Sano et al. prepared ^{111}In-labeled G4 PAMAM dendrimers conjugated with DTPA, polyethyleneimine (PEI), and γ-polyglutamic acid (γ-PGA) and evaluated their feasibilities as nanoprobes for SPECT imaging of SLN [104]. It seemed that the synthesized ^{111}In-DTPA-G4/PEI/γ-PGA with high biocompatibility could be highly taken up by macrophage cells in vitro comparable to the ^{111}In-DTPA-G4/PEI without γ-PGA modification, which might be due to the mechanisms of phagocytosis and γ-PGA-specific pathway. Intradermal administration of ^{111}In-labeled dendrimer conjugates into rat footpads, when compared with ^{111}In-DTPA-G4/PEI and ^{111}In-DTPA-G4/PEI/γ-PGA, the latter had a relative fast clearance from the injection site, significantly higher radioactive uptake in the first draining popliteal LN, and low radioactivity in the other tissues including the liver, spleen, and kidneys, which was confirmed by micro-SPECT imaging studies (Fig. 12.3). Subsequently, Niki et al. systematically evaluated 12 types of different generations (G2, G4, G6, and G8) of dendrimers with different terminal groups (amino, carboxyl, and acetyl) to determine the optimal one for sentinel lymph node imaging [105]. The SPECT imaging studies showed that high-generation (greater than G4) PAMAM dendrimers with carboxyl-termini were able to significantly accumulate at the SLN, which might have important effects on the development of dendrimer-based SLN imaging agents and SLN-targeted drug carriers.

5.2 SPECT/CT Imaging

CT is known as one of the most useful imaging techniques in modern research and clinical settings, which can be applied in the detection of tissues, organs, and blood vessels [106–108]. CT contrast agents are regularly introduced in order to improve contrast and acquire desirable imaging quality. Commercially available CT contrast agents are usually iodinated small molecules with the drawbacks of rapid clearance from blood after injection, latent renal toxicity at a relatively high concentration, and nonspecificity to tissues and organs, which restricts the scope of applications [45].

Recently, there is great interest in the development of dendrimer-based nanoparticles for CT imaging to overcome these drawbacks caused by the small molecular iodinated contrast agents [109–111]. Due to unique structural features of

Fig. 12.2 (continued) DTPA at different times after injection. Arrows indicate the injection site, and L, K, and B indicate the liver, kidney, and bladder, respectively (Reprinted (adapted) with permission from Ref. [98]. Copyright (2014) Elsevier)

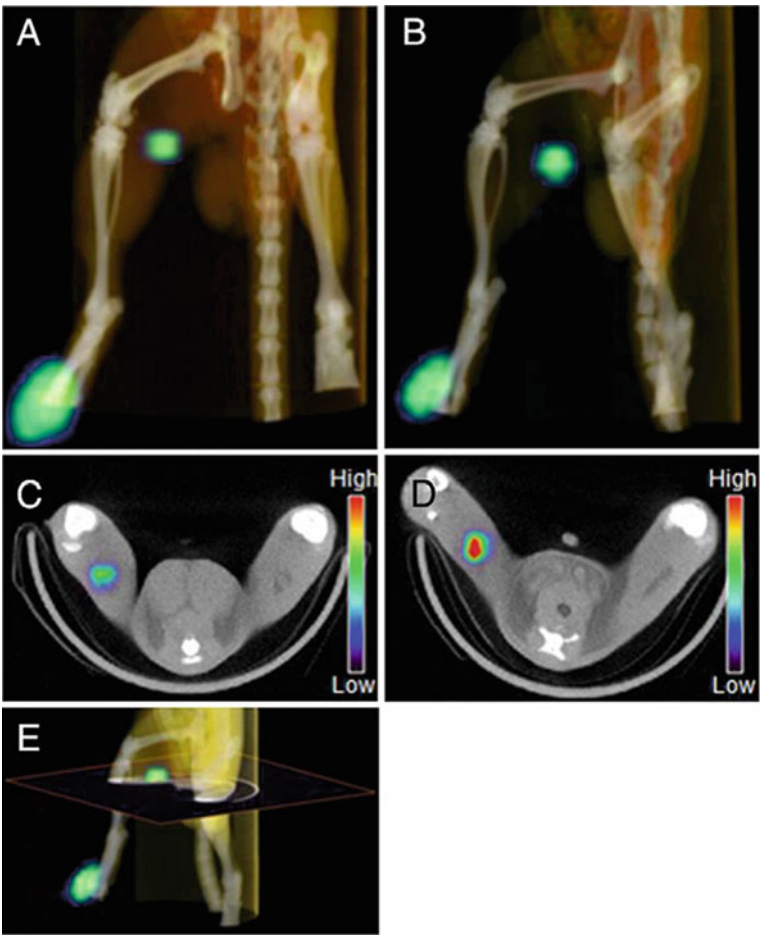

Fig. 12.3 SPECT/CT images (**a**–**e**) after the injection of ^{111}In-DTPA-G4/PEI (**a**, **c**) or ^{111}In-DTPA-G4/PEI/γ-PGA (**b**, **d**) into footpads of SD rats (DTPA-G4: 10 μg/mL, 1.0–1.7 MBq/200 μL in 5% glucose/rat). Panels (**c**) and (**d**) are 2D transaxial images including lymph nodes constructed from 3D images (**a** and **b**) as shown in (**e**). ^{111}In-DTPA-G4/PEI/γ-PGA (**b**, **d**) clearly visualized the popliteal lymph nodes (sentinel LNs in this model) compared to ^{111}In-DTPA-G4/PEI (**a**, **c**) (Reprinted (adapted) with permission from Ref. [104]. Copyright (2014) Elsevier)

dendrimers, the developed dendrimer-based CT contrast agents can also be labeled with ^{99m}Tc for SPECT/CT imaging to afford diagnosis accuracy. For instance, Criscione et al. conjugated triiodinated moieties and ^{99m}Tc on the surface of G4 PAMAM dendrimers modified with *m*PEG (Fig. 12.4) [112]. The iodinated dendritic NPs with a diameter of 12.4 nm displayed similar X-ray attenuation properties to the small molecule iodinated contrast agents (Omnipaque 350) routinely used in clinical

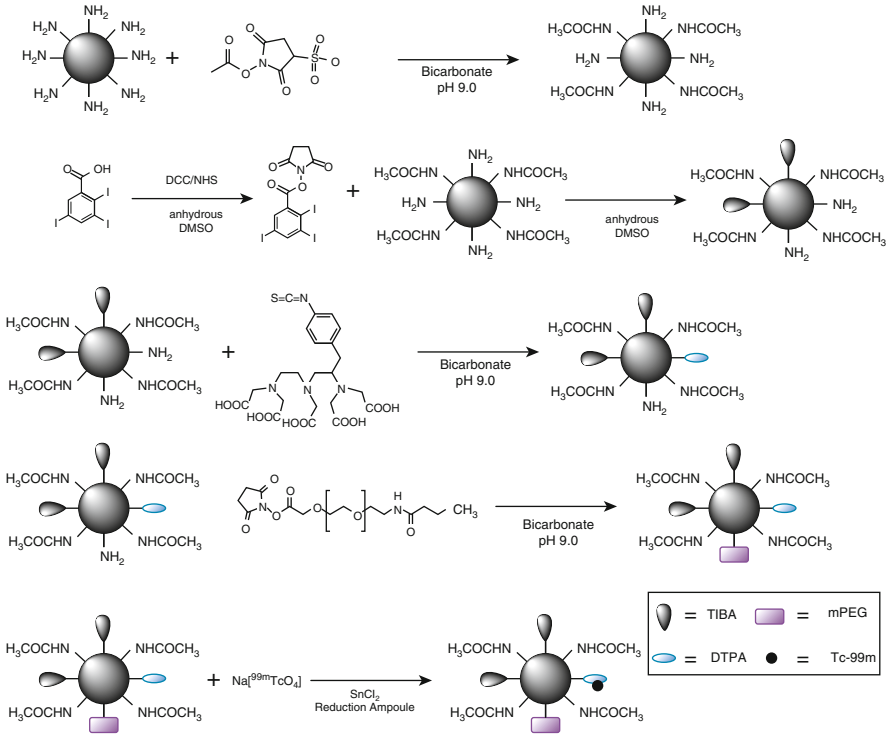

Fig. 12.4 Schematic of the synthesis of ^{99m}Tc-labeled G4-[[[[Ac]-TIBA]-DTPA]-mPEG12] (Reprinted (adapted) with permission from Ref. [112]. Copyright (2011) American Chemical Society)

applications and possessed long enough intravascular residence time, favorable contrast-to-noise ratio for serial intravascular, and blood pool imaging with both SPECT and CT. However, further evaluations of this potential SPECT/CT agent including toxicity in vitro and in vivo have not been investigated in the literature.

Meanwhile, Au NPs have received great attention as CT contrast agents due to their higher atomic number than that of iodine for iodine-based small molecular contrast agents, stronger X-ray attenuation coefficient, and better biocompatibility than iodine-based CT contrast agents [13, 113–115]. In a recent study, Shi and coworkers reported ^{99m}Tc-labeled multifunctional dendrimer-entrapped gold nanoparticles (Au DENPs) for tumor-targeted SPECT/CT imaging using amine-terminated G2 PAMAM dendrimers as templates [69]. The low-generation dendrimers were functionalized with DTPA via an amide linkage and targeting ligand FA via a PEG spacer and then used to entrap Au core NPs (Fig. 12.5). The developed Au DENPs with an average Au core diameter of 1.6 nm had excellent solubility in water, satisfactory stability, and biocompatibility in a given concentration range. Biodistribution and SPECT/CT imaging studies further demonstrated that

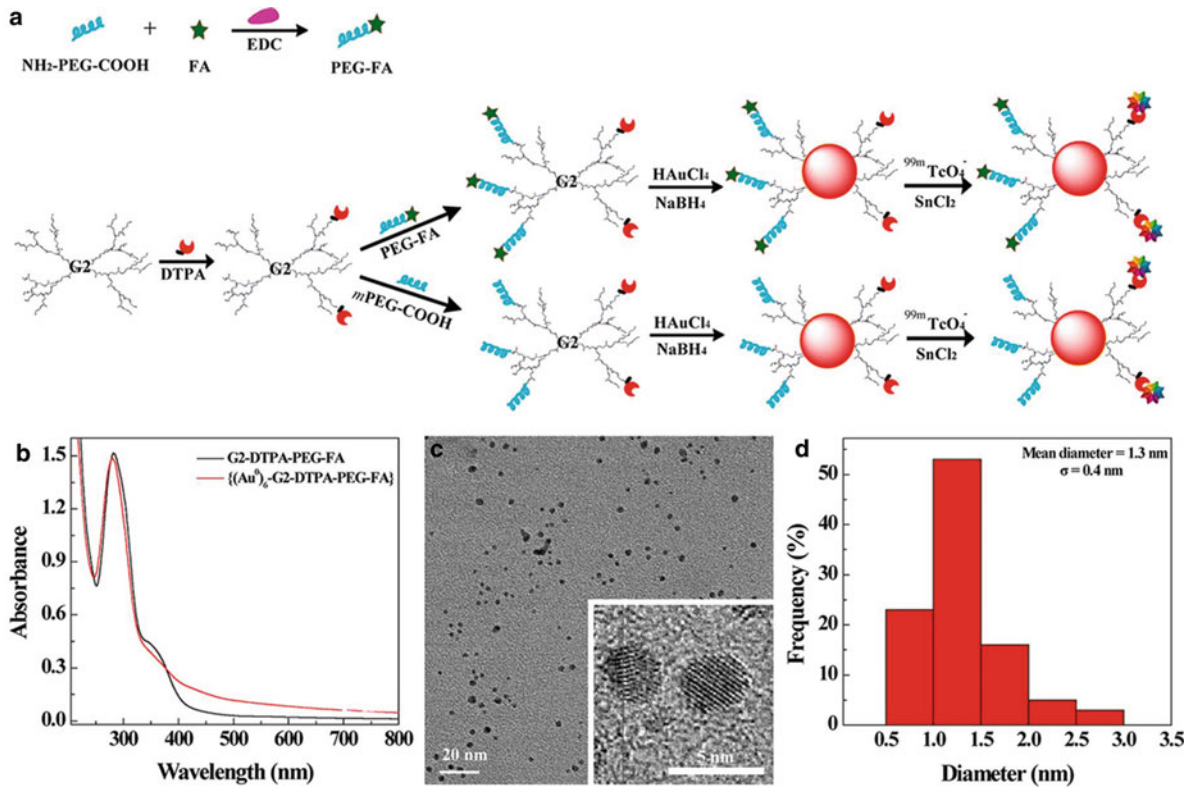

Fig. 12.5 (**a**) Schematic illustration of the synthesis of FA-PEG-COOH segment, $(Au_0)_6$-G2-DTPA(^{99m}Tc)-PEG-FA ENPs, and $(Au_0)_6$-G2-DTPA(^{99m}Tc)-mPEG DENPs. (**b**) UV-vis spectra of G2-DTPA-PEG-FA and $(Au_0)_6$-G2-DTPA-PEG-FA DENPs. (**c**) TEM image and (**d**) size distribution histogram of the

the formed multifunctional Au DENPs had a great potential to be utilized as an effective and economic nanoplatform for dual-mode imaging of FAR-overexpressing tumors (Fig. 12.6).

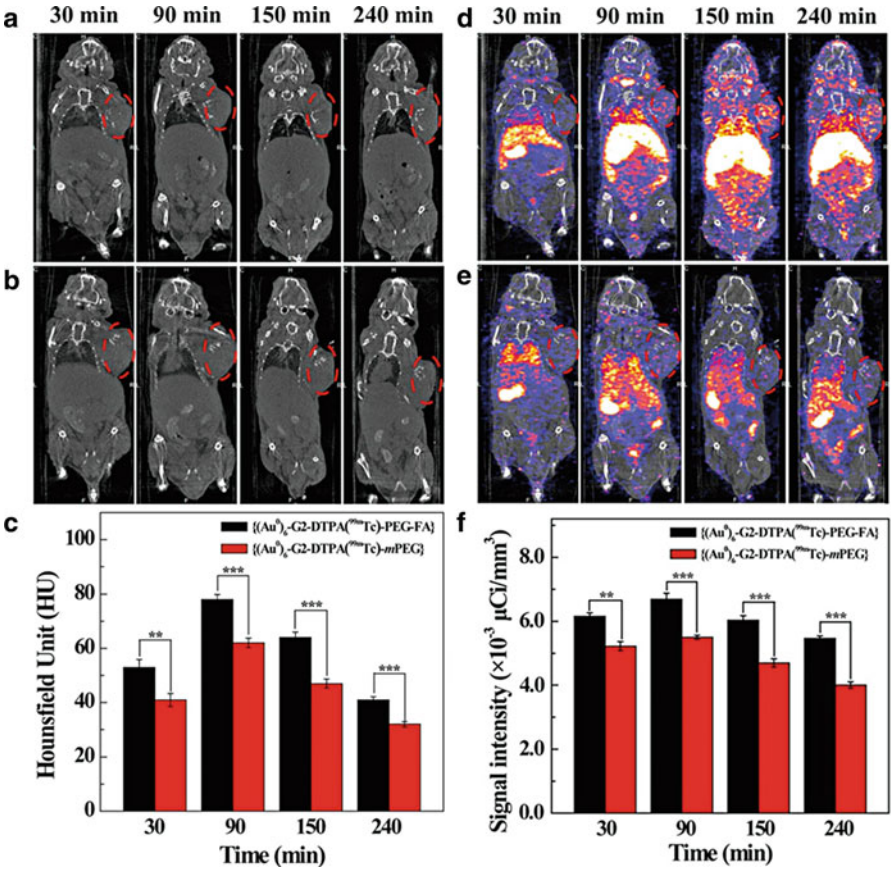

Fig. 12.6 In vivo CT images (**a** and **b**) and signal intensity (**c**) of tumors after intravenous injection of the $\{(Au^0)_6$-G2-DTPA(^{99m}Tc)-PEG-FA$\}$ (**a**) or $\{(Au^0)_6$-G2-DTPA(^{99m}Tc)-mPEG$\}$ (**b**) DENPs ([^{99m}Tc] = 740 MBq·mL^{-1}, [Au] = 0.08 M, in 100 μL PBS) at different time points postinjection. In vivo SPECT/CT images of tumors (**d** and **e**) and SPECT signal intensity of tumors (**f**) after intravenous injection of the $\{(Au^0)_6$-G2-DTPA(^{99m}Tc)-PEG-FA$\}$ DENPs (**d**) or $\{(Au^0)_6$-G2-DTPA (^{99m}Tc)-mPEG$\}$ DENPs (**e**) ([^{99m}Tc] = 740 Bq·mL^{-1}, [Au] = 0.08 M, in 100 μL PBS) at different time points postinjection. The dashed red circles indicate the tumor sites (Reprinted (adapted) with permission from Ref. [69]. Copyright (2016) American Chemical Society)

Fig. 12.5 (continued) $(Au_0)_6$-G2-DTPA-PEG-FA DENPs. Inset in panel c shows the high-resolution TEM image of the Au core particles (Reprinted (adapted) with permission from Ref. [69]. Copyright (2016) American Chemical Society)

5.3 SPECT/MR Imaging

MR imaging has been evolved as an indispensable imaging technique for clinical diagnosis due to its admirable spatial resolution, noninvasive nature, and no ionizing radiation [116, 117]. Similarly to CT imaging, contrast agents are commonly required in clinical MR applications to improve the visibility of internal tissue or organ structures. The most generally used compounds for contrast enhancement are Gd (III)-based small molecules, which also suffer from some disadvantages including rapid excretion [55], relatively low contrast effect [118], possible renal damage [119], and lack of sufficient sensitivity and specificity [120]. Taking advantage of the superiorities of dendrimers discussed above, a lot of dendrimer-based MR contrast agents have been prepared to eliminate the defects of Gd-based contrast agents [65, 121, 122]. In most cases of T_1-weighted MR imaging, dendrimers serve as scaffolds to load multiple copies of small molecular Gd(III) complexes, typically Gd(III) chelated with tetraazacyclododecane tetraacetic acid (DOTA) [65] or DPTA [121, 122]. Then these dendrimers containing Gd(III) can be further labeled with radionuclides for dual-mode SPECT/MR imaging. Interestingly, except nonradioactive ^{157}Gd used as MRI contrast agent, ^{147}Gd ($E_\gamma = 229$ keV, $t_{1/2} = 38.1$ h) is γ-ray-emitting radionuclides which may be exploited for SPECT imaging [123]. Recently, Rahmania et al. reported radiogadolinium(III) DOTA-based PAMAM G3 dendrimers linked with monoclonal antibody trastuzumab as a SPECT/MR imaging agent for diagnosis of HER-2-positive breast cancer [123]. It seemed that the radiogadolinium-labeled dendrimers had good radiochemical purity and stability. However, more detailed investigation of this SPECT/MR agent including toxicity and performance in vitro and in vivo has not been performed in this study. In a recent study, Luo et al. developed a facile approach to prepare a manganese (Mn) and ^{99m}Tc-coloaded dendrimeric nanoprobe for tumor-targeted SPECT/MR imaging applications [68]. G5 PAMAM dendrimers were used as a platform to link FA and DOTA, followed by complexation with Mn(II) for T_1-weighted MR imaging and simultaneously labeling with ^{99m}Tc for SPECT imaging both via DOTA chelation. The formed multifunctional dendrimer-FA conjugates before ^{99m}Tc labeling had good water solubility, cytocompatibility, and stability and were able to rapidly accumulate and reach the peak value in the tumor region within 2 h for MR imaging (Fig. 12.7), which was also confirmed by SPECT imaging (Fig. 12.8). These results revealed that this nanoprobe could be used for specific SPECT/MR imaging of cancer cells in vivo.

5.4 SPECT/Optical Imaging

Fluorescence imaging provides unique advantages in terms of high sensitivity, multiplex detection capabilities, and inexpensiveness. Nevertheless, it primarily depends on suitable markers such as fluorescent dyes or proteins, with good stability, excellent biocompatibility, and high specificity and sensitivity to ensure the images with splendid temporal and spatial resolution [48]. With the quite rigid molecular structure, dendrimers have the blue fluorescence emission property

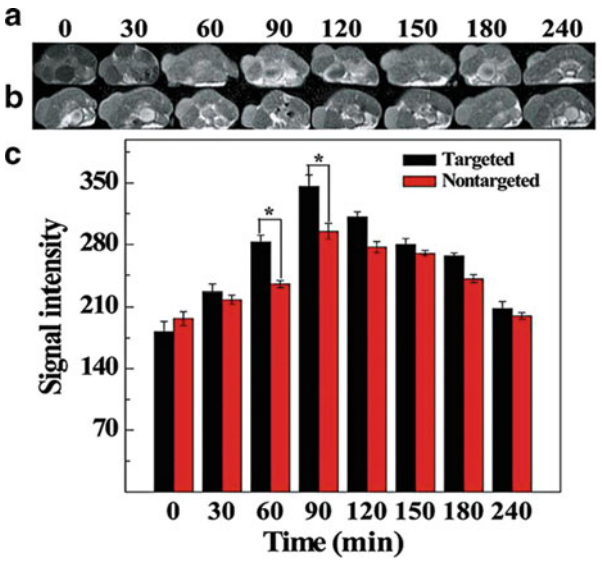

Fig. 12.7 In vivo T_1-weighted MR images (**a** and **b**) and signal intensity (**c**) of tumors after intravenous injection of the nontargeted G5.NHAc-FI-DOTA(Mn) (**a**) or targeted G5.NHAc-FI-DOTA(Mn)-FA (**b**) dendrimers (300 mg Mn, in 0.3 mL PBS) at different time points postinjection (Ref. [68] – Reproduced by permission of The Royal Society of Chemistry)

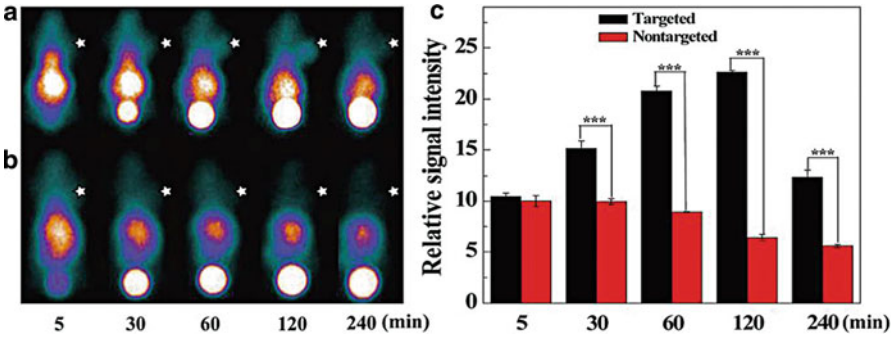

Fig. 12.8 In vivo SPECT images (**a** and **b**) and SPECT signal intensity (**c**) of tumors after intravenous injection of the targeted G5.NHAc-FI-DOTA(Mn/^{99m}Tc)-FA (**a**) and nontargeted G5.NHAc-FI-DOTA(Mn/^{99m}Tc) (**b**) dendrimers (3 mCi ^{99m}Tc, in 0.2 mL PBS) at different time points postinjection (Ref. [68] – Reproduced by permission of The Royal Society of Chemistry)

[124, 125]; however, the intrinsic fluorescence quantum yield is quite low and unsuitable for clinical applications. Therefore, dendrimer-based nanomaterials have been broadly investigated as fluorescence imaging agents in order to enhance the fluorescence quantum yield [124]. In general, fluorescent molecules can be readily modified onto the surface or be loaded within the interior of dendrimers as fluorescence probes. To achieve different imaging purposes, these probes can be subsequently labeled with ^{99m}Tc for dual-mode SPECT/fluorescence imaging. For instance, Tsuchimochi et al. developed PAMAM G3 dendrimer-coated silica nanoparticles loaded with ^{99m}Tc and indocyanine green

(ICG) for SPECT/NIR imaging of SNL [126]. The formed PAMAM-coated silica nanoparticles with a diameter of 30–50 nm were injected into the tongue of rats. In the animal studies, these nanoparticles were able to clearly depict sentinel lymph nodes in real time with the use of dual-mode imaging.

5.5 Theranostics

The rapid development of imaging techniques and drug delivery systems has offered opportunities in a relatively new area called "theranostics" [127, 128]. For theranostics, it is essential to combine diagnostic and therapeutic functionalities into a single system, to develop more precise and personalized therapies for various diseases. A convenient way in constructing theranostic agents is to load therapeutic functions on existing imaging nanoprobes. Besides various imaging applications, dendrimer-based nanomaterials have been known with this capability and used as carriers for drug, gene, and therapeutic radionuclide delivery [46, 128]. Among massive therapeutic radionuclides, ^{131}I is one of the most common therapeutic radionuclides in the clinic, because of its relative long half-life (8.01 days) and appropriate beta radiation energy (606 keV) for radiotherapy [70, 129, 130]. Moreover, ^{131}I emits a γ-ray (364 keV) for SPECT imaging which renders its feasibility for theranostic applications. While another important radioisotope of iodine, ^{125}I with less energy γ-ray (35.5 keV) is poorly suited for imaging but convenient for radioimmunoassay test, implantation therapy, and method development due to its long half-life (60.1 days) [131, 132].

Merkel et al. reported a family of triazine dendrimers as nonviral gene delivery systems with high transfection efficacy [133, 134]. Then these flexible triazine dendrimer-based siRNA complexes were synthesized for gene delivery systems and labeled with ^{111}In via DTPA for SPECT imaging to identify efficient siRNA delivery in vivo [135]. Interestingly, simulated thermodynamic approach was employed to explain the interactions of dendrimers with siRNA and compared with the experimental data including siRNA complexation, complex stability, size, and zeta potentials. In their following work, Lee et al. designed and developed a G3 triazine dendrimer with 8 PEG chains and 16 paclitaxel groups (Fig. 12.9) [136]. Molecular dynamic simulations revealed that the water penetration and accessibility of novel complexes were better than their previous constructs, but the computed dimension of complexes was significantly smaller than the 15.8 nm obtained from experiment. Slow and identical release of paclitaxel was observed in plasma in drug release studies. Biodistribution and SPECT/CT imaging of ^{125}I–labeled complexes suggested significant persistence in the vasculature with slow clearance and high tumor uptake while low levels of radiolabeled dendrimer in the lung, liver, and spleen (Fig. 12.10). In another study, Xiao et al. reported a multifunctional telodendrimer-based micelle system for SPECT imaging and delivery of chemotherapy agents [137]. The telodendrimer was covalently modified with ^{125}I for SPECT/CT imaging and loaded with ^{14}C–paclitaxel for pharmacokinetics and biodistribution studies, respectively. SPECT/CT imaging showed that ^{125}I–labeling nanomicelles were preferential uptaken

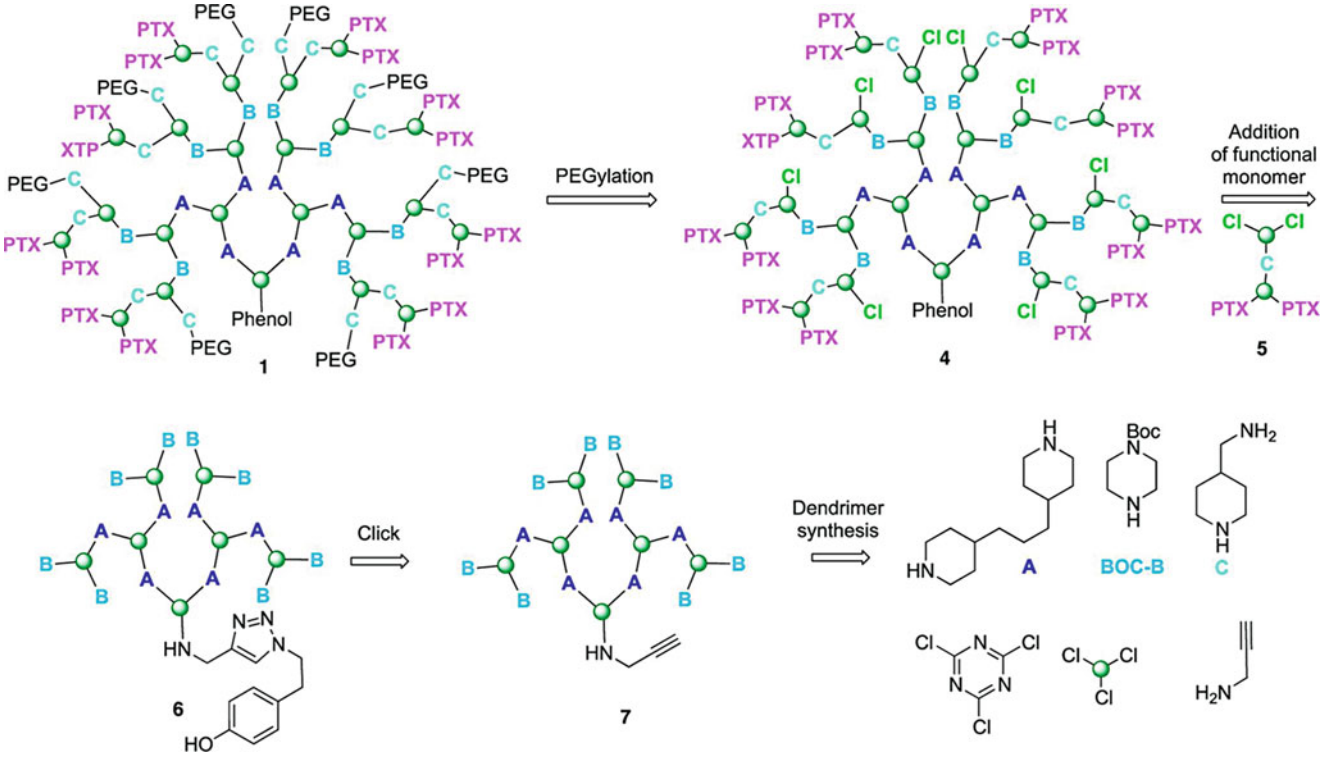

Fig. 12.9 Target 1 derives from a two-step PEGylation procedure of 4. Intermediate 4 results from reaction of the functionalized dichlorotriazine bearing two paclitaxel groups (PTX), 5, with dendrimer 6. Dendrimer 6 comes from click reaction of 7, which derives from some of the building blocks identified (Reprinted (adapted) with permission from Ref. [136]. Copyright (2013) American Chemical Society)

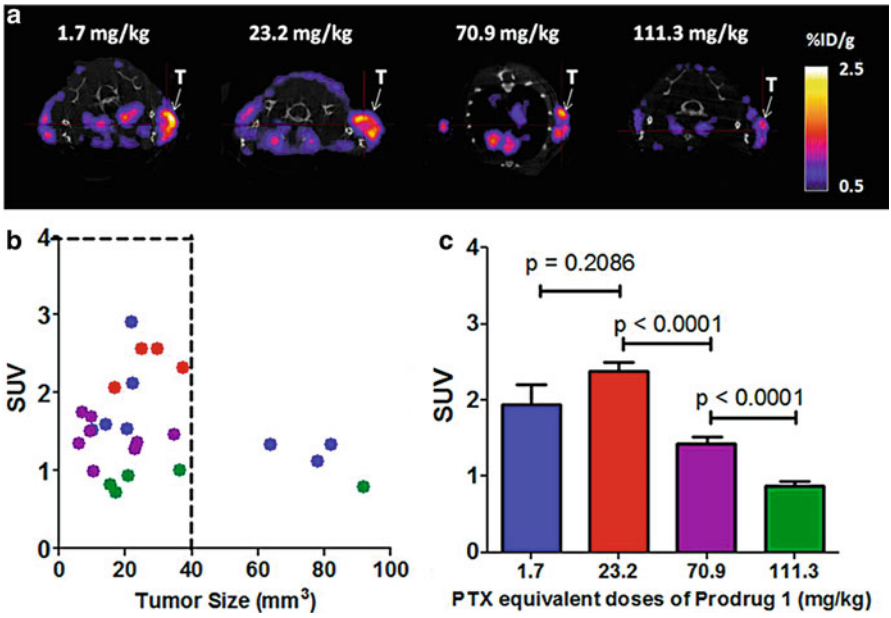

Fig. 12.10 Tumor saturation dose evaluation of ^{125}I-1 in PC-3 tumor-bearing mice: 1.7 mg/kg (blue), 23.2 mg/kg (red), 70.9 mg/kg (purple), and 111.3 mg/kg (green). (**a**) Representative transaxial SPECT/CT images of PC3 tumor in SCID mice (48 h p.i.). Tumors are indicated by white arrows. (**b**) Tumor uptake of ^{125}I-1 versus tumor size. Tumors smaller than 100 mm^3 were selected for the evaluation. (Number of tumors evaluated in each group: 7 (1.7 mg/kg); 5 (23.2 mg/kg); 8 (70.9 mg/kg); 5 (111.3 mg/kg)). (**c**) Tumor uptake levels of the four dosing groups in tumors smaller than 40 mm^3. (Number of tumors evaluated in each group: 4 (1.7 mg/kg); 5 (23.2 mg/kg); 8 (70.9 mg/kg); 4 (111.3 mg/kg)). SUV is standardized uptake value of the labeled prodrug (Reprinted (adapted) with permission from Ref. [136]. Copyright (2013) American Chemical Society)

by tumor tissues with slow clearance, and the biodistribution data of ^{14}C–paclitaxel-loaded nanomicelles also confirmed the increased accumulation at the tumor site with slower pharmacokinetics than Taxol. The results suggested that nanomicelle-loaded paclitaxel might be used as a promising nanocarrier for imaging-guided drug delivery.

In a recent study, Shi group and the coworkers reported a series of multifunctional dendrimers labeled with ^{131}I for targeted SPECT imaging and radiotherapy of different cancers [70, 129, 130]. In these studies, G5 amine-terminated PAMAM dendrimers were used as platforms to be sequentially conjugated with PEG, targeting agent biotoxins or FA, and 3-(4-hydroxyphenyl)propionic acid-OSu (HPAO). These were followed by acetylation of the remaining dendrimer terminal amines and radiolabeling with ^{131}I directly through HPAO to form the targeted theranostic dendrimeric nanoplatforms (Fig. 12.11). The formed ^{131}I–labeled multifunctional dendrimers with good cytocompatibility and organ compatibility could be used as promising nanoplatforms for SPECT imaging and radiotherapy of different types of MMP2 or FAR-overexpressing cancers (Fig. 12.12).

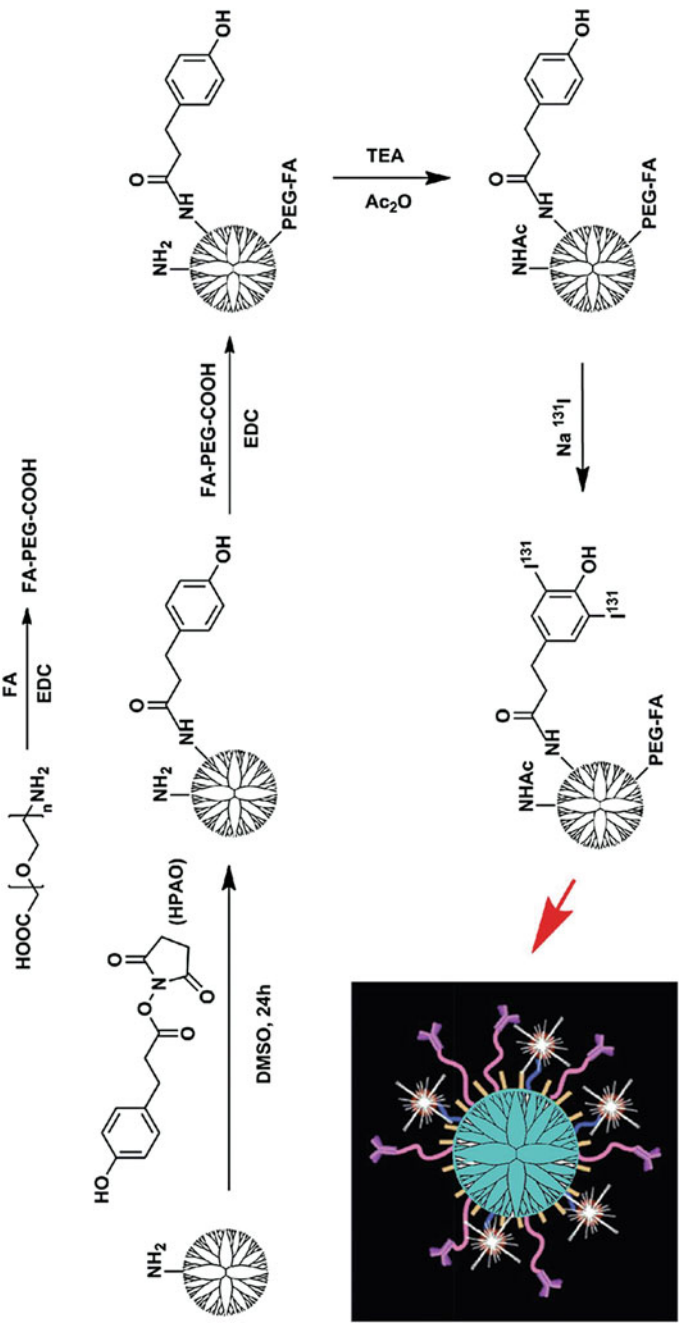

Fig. 12.11 Schematic illustration of the synthesis of the ^{131}I–G5·NHAc-HPAO-PEG-FA dendrimers (Ref. [129] – Reproduced by permission of The Royal Society of Chemistry)

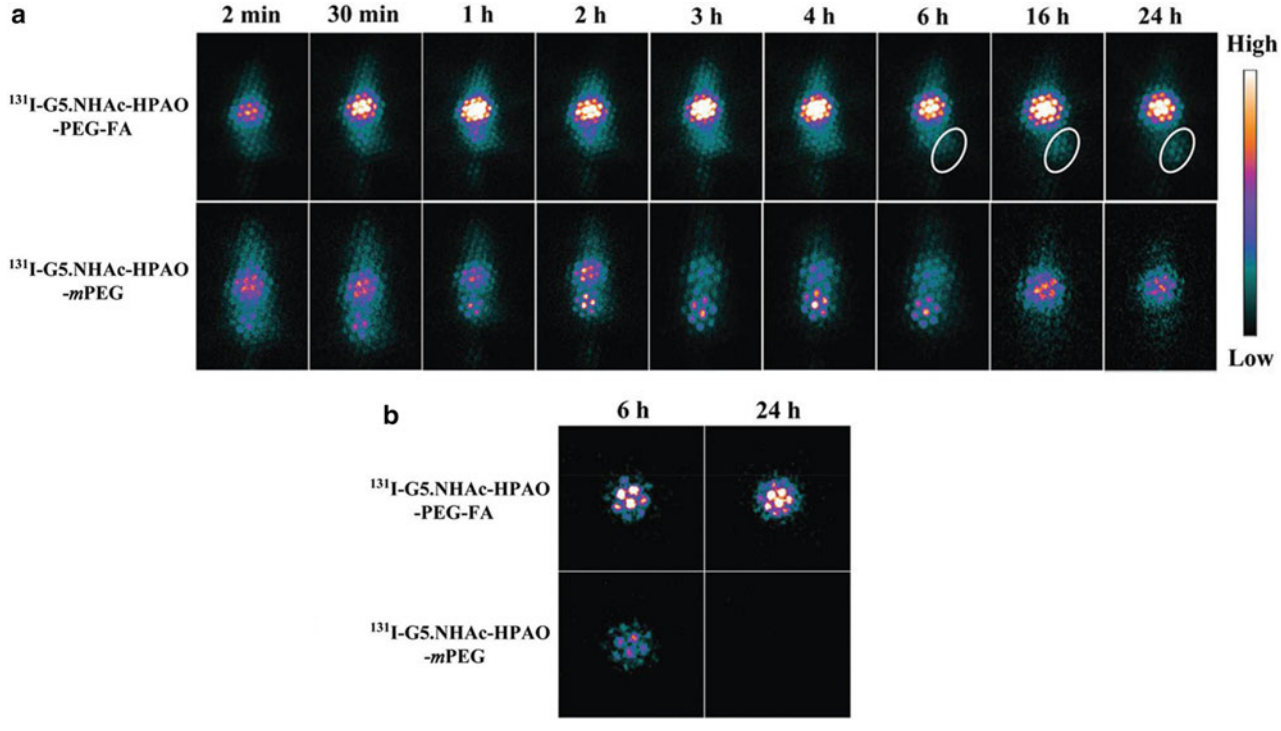

Fig. 12.12 SPECT images of the nude mice bearing C6 xenografted tumors at different time points post-intravenous injection of the ^{131}I–G5·NHAc-HPAO-PEG-FA and ^{131}I–G5·NHAc-HPAO-mPEG dendrimers (tumor site was marked by white circle) (**a**) and SPECT images of ex vivo tumors (**b**) (Ref. [129] – Reproduced by permission of The Royal Society of Chemistry)

6 Conclusion and Future Perspectives

In summary, we have reviewed the use of dendrimer-based nanoplatforms for SPECT imaging applications including single-mode SPECT imaging, dual-mode SPECT/CT, SPECT/MR, and SPECT/optical imaging and theranostic applications. In view of the unique structural features of dendrimers, abundant dendrimer-based nanomaterials as platforms can be formed since they can be functionalized with fluorescent dyes, iodinated CT contrast agents, Gd, and radionuclides on the periphery and can be used to entrap, stabilize, or assemble Au and metal oxide nanoparticles, generating all sorts of imaging agents. The functionalized dendrimers have been used for imaging of blood pool, lymph nodes, major organs, cancer, and other biological systems. Importantly, these developed dendrimer-based imaging agents can be further modified with targeting ligands to improve specificity and selectivity and loaded drugs, genes, or therapeutic radionuclides for theranostic applications, which is of great importance for precise cancer diagnosis and imaging-guided drug delivery applications.

In spite of comprehensive investigation on dendrimer-based nanoplatforms, this growing area of research still remains largely underground, and a great number of challenges are needed to be explored [48, 127]. For instance, the toxicity of dendrimer-based contrast agents is one of inevitable issues, particularly the large molecule systems with slow clearance and latent renal damage from Gd-containing dendrimeric nanoparticles. In addition, more types of dendrimer-based nanoplatforms should be developed in order to satisfy different requirements. For instance, to expand the scope of imaging, radionuclides can be modified on the surface of dendrimer-based iron oxide NPs for SPECT and T_2-weighted MR imaging. Furthermore, with the ability to equip therapeutic modules in dendrimer platforms via many different approaches, it is requisite to develop various multifunctional dendrimers by integrating drugs, genes, or therapeutic radionuclides into dendrimer-based imaging agents for theranostic applications.

Acknowledgments This research is financially supported by the National Natural Science Foundation of China (81671712, 81401440), the Program for Professor of Special Appointment (Eastern Scholar) at Shanghai Institutions of Higher Learning, and the Sino-German Center for Research Promotion (GZ899). L. Zhao thanks the support from the Shanghai Sailing Program (16YF1409300).

References

1. Collins FS, Varmus H (2015) A new initiative on precision medicine. N Engl J Med 372 (9):793–795
2. Jameson JL, Longo DL (2015) Precision medicine – personalized, problematic, and promising. N Engl J Med 372(23):2229–2234
3. Weissleder R, Pittet MJ (2008) Imaging in the era of molecular oncology. Nature 452 (7187):580–589
4. Pysz MA, Gambhir SS, Willmann JK (2010) Molecular imaging: current status and emerging strategies. Clin Radiol 65(7):500–516

5. Kircher MF, Hricak H, Larson SM (2012) Molecular imaging for personalized cancer care. Mol Oncol 6(2):182–195
6. Naumova AV, Modo M, Moore A, Murry CE, Frank JA (2014) Clinical imaging in regenerative medicine. Nat Biotechnol 32(8):804–818
7. Chan KW-Y, Wong W-T (2007) Small molecular gadolinium(III) complexes as MRI contrast agents for diagnostic imaging. Coord Chem Rev 251(17–20):2428–2451
8. Li J, Zheng L, Cai H, Sun W, Shen M, Zhang G, Shi X (2013) Polyethyleneimine-mediated synthesis of folic acid-targeted iron oxide nanoparticles for in vivo tumor MR imaging. Biomaterials 34(33):8382–8392
9. Jin R, Lin B, Li D, Ai H (2014) Superparamagnetic iron oxide nanoparticles for MR imaging and therapy: design considerations and clinical applications. Curr Opin Pharmacol 18:18–27
10. Li L, Gao F, Jiang W, Wu X, Cai Y, Tang J, Gao X, Gao F (2016) Folic acid-conjugated superparamagnetic iron oxide nanoparticles for tumor-targeting MR imaging. Drug Deliv 23 (5):1726–1733
11. Mustafa R, Zhou B, Yang J, Zheng L, Zhang G, Shi X (2016) Dendrimer-functionalized laponite nanodisks loaded with gadolinium for T1-weighted MR imaging applications. RSC Adv 6(97):95112–95119
12. Suzuki H, Oshima H, Shiraki N, Ikeya C, Shibamoto Y (2004) Comparison of two contrast materials with different iodine concentrations in enhancing the density of the aorta, portal vein and liver at multi-detector row CT: a randomized study. Eur Radiol 14(11):2099–2104
13. Hainfeld JF, Slatkin DN, Focella TM, Smilowitz HM (2006) Gold nanoparticles: a new X-ray contrast agent. Br J Radiol 79(939):248–253
14. Popovtzer R, Agrawal A, Kotov NA, Popovtzer A, Balter J, Carey TE, Kopelman R (2008) Targeted gold nanoparticles enable molecular ct imaging of cancer. Nano Lett 8 (12):4593–4596
15. Peng C, Zheng L, Chen Q, Shen M, Guo R, Wang H, Cao X, Zhang G, Shi X (2012) PEGylated dendrimer-entrapped gold nanoparticles for in vivo blood pool and tumor imaging by computed tomography. Biomaterials 33(4):1107–1119
16. Zhang Y, Wen S, Zhao L, Li D, Liu C, Jiang W, Gao X, Gu W, Ma N, Zhao J, Shi X, Zhao Q (2016) Ultrastable polyethyleneimine-stabilized gold nanoparticles modified with polyethylene glycol for blood pool, lymph node and tumor CT imaging. Nanoscale 8(10):5567–5577
17. Ametamey SM, Honer M, Schubiger PA (2008) Molecular imaging with PET. Chem Rev 108 (5):1501–1516
18. Fletcher JW, Djulbegovic B, Soares HP, Siegel BA, Lowe VJ, Lyman GH, Coleman RE, Wahl R, Paschold JC, Avril N, Einhorn LH, Suh WW, Samson D, Delbeke D, Gorman M, Shields AF (2008) Recommendations on the use of 18F-FDG PET in oncology. J Nucl Med 49 (3):480–508
19. Mosconi L, Mistur R, Switalski R, Tsui WH, Glodzik L, Li Y, Pirraglia E, De Santi S, Reisberg B, Wisniewski T, de Leon MJ (2009) FDG-PET changes in brain glucose metabolism from normal cognition to pathologically verified Alzheimer's disease. Eur J Nucl Med Mol Imaging 36(5):811–822
20. Brindle K (2008) New approaches for imaging tumour responses to treatment. Nat Rev Cancer 8(2):94–107
21. Shirani J, Dilsizian V (2011) Nuclear cardiac imaging in hypertrophic cardiomyopathy. J Nucl Cardiol 18(1):123–134
22. Wang G, Stender AS, Sun W, Fang N (2010) Optical imaging of non-fluorescent nanoparticle probes in live cells. Analyst 135(2):215–221
23. Hellebust A, Richards-Kortum R (2012) Advances in molecular imaging: targeted optical contrast agents for cancer diagnostics. Nanomedicine (Lond) 7(3):429–445
24. James ML, Gambhir SS (2012) A molecular imaging primer: modalities, imaging agents, and applications. Physiol Rev 92(2):897–965
25. Cai H, Li K, Shen M, Wen S, Luo Y, Peng C, Zhang G, Shi X (2012) Facile assembly of Fe_3O_4@Au nanocomposite particles for dual mode magnetic resonance and computed tomography imaging applications. J Mater Chem 22(30):15110–15120

26. Herschman HR (2003) Molecular imaging: looking at problems, seeing solutions. Science 302 (5645):605–608
27. Hoffman JM, Gambhir SS (2007) Molecular imaging: the vision and opportunity for radiology in the future. Radiology 244(1):39–47
28. Luo S, Zhang E, Su Y, Cheng T, Shi C (2011) A review of NIR dyes in cancer targeting and imaging. Biomaterials 32(29):7127–7138
29. Beyer T, Townsend DW, Brun T, Kinahan PE, Charron M, Roddy R, Jerin J, Young J, Byars L, Nutt R (2000) A combined PET/CT scanner for clinical oncology. J Nucl Med 41(8):1369–1379
30. Keidar Z, Israel O, Krausz Y (2003) SPECT/CT in tumor imaging: technical aspects and clinical applications. Semin Nucl Med 33(3):205–218
31. Jennings LE, Long NJ (2009) 'Two is better than one'-probes for dual-modality molecular imaging. Chem Commun (24):3511–3524
32. Ogawa M, Regino CAS, Seidel J, Green MV, Xi W, Williams M, Kosaka N, Choyke PL, Kobayashi H (2009) Dual-modality molecular imaging using antibodies labeled with activatable fluorescence and a radionuclide for specific and quantitative targeted cancer detection. Bioconjug Chem 20(11):2177–2184
33. Li K, Wen S, Larson AC, Shen M, Zhang Z, Chen Q, Shi X, Zhang G (2013) Multifunctional dendrimer-based nanoparticles for in vivo MR/CT dual-modal molecular imaging of breast cancer. Int J Nanomedicine 8:2589–2600
34. Chen J, Sun Y, Chen Q, Wang L, Wang S, Tang Y, Shi X, Wang H (2016) Multifunctional gold nanocomposites designed for targeted CT/MR/optical trimodal imaging of human non-small cell lung cancer cells. Nanoscale 8(28):13568–13573
35. Mariani G, Bruselli L, Kuwert T, Kim EE, Flotats A, Israel O, Dondi M, Watanabe N (2010) A review on the clinical uses of SPECT/CT. Eur J Nucl Med Mol Imaging 37(10):1959–1985
36. Thrall MM, DeLoia JA, Gallion H, Avril N (2007) Clinical use of combined positron emission tomography and computed tomography (FDG-PET/CT) in recurrent ovarian cancer. Gynecol Oncol 105(1):17–22
37. Chiti A, Kirienko M, Grégoire V (2010) Clinical use of PET-CT data for radiotherapy planning: what are we looking for? Radiother Oncol 96(3):277–279
38. Delso G, Fürst S, Jakoby B, Ladebeck R, Ganter C, Nekolla SG, Schwaiger M, Ziegler SI (2011) Performance measurements of the Siemens mMR integrated whole-body PET/MR scanner. J Nucl Med 52(12):1914–1922
39. Drzezga A, Souvatzoglou M, Eiber M, Beer AJ, Fürst S, Martinez-Möller A, Nekolla SG, Ziegler S, Ganter C, Rummeny EJ, Schwaiger M (2012) First clinical experience with integrated whole-body PET/MR: comparison to PET/CT in patients with oncologic diagnoses. J Nucl Med 53(6):845–855
40. Liong M, Lu J, Kovochich M, Xia T, Ruehm SG, Nel AE, Tamanoi F, Zink JI (2008) Multifunctional inorganic nanoparticles for imaging, targeting, and drug delivery. ACS Nano 2(5):889–896
41. Rubel C, Hao H, Weibo C (2015) Image-guided drug delivery with single-photon emission computed tomography: a review of literature. Curr Drug Targets 16(6):592–609
42. Guo R, Shi X (2012) Dendrimers in cancer therapeutics and diagnosis. Curr Drug Metab 13 (8):1097–1109
43. Chen X, Gambhir SS, Cheon J (2011) Theranostic nanomedicine. Acc Chem Res 44(10):841
44. Namiki Y, Fuchigami T, Tada N, Kawamura R, Matsunuma S, Kitamoto Y, Nakagawa M (2011) Nanomedicine for cancer: lipid-based nanostructures for drug delivery and monitoring. Acc Chem Res 44(10):1080–1093
45. Lusic H, Grinstaff MW (2013) X-ray-computed tomography contrast agents. Chem Rev 113 (3):1641–1666
46. Mintzer MA, Grinstaff MW (2011) Biomedical applications of dendrimers: a tutorial. Chem Soc Rev 40(1):173–190
47. Sun W, Mignani S, Shen M, Shi X (2016) Dendrimer-based magnetic iron oxide nanoparticles: their synthesis and biomedical applications. Drug Discov Today 21(12):1873–1885

48. Qiao Z, Shi X (2015) Dendrimer-based molecular imaging contrast agents. Prog Polym Sci 44:1–27
49. Tomalia DA, Baker H, Dewald J, Hall M, Kallos G, Martin S, Roeck J, Ryder J, Smith P (1985) A new class of polymers: starburst-dendritic macromolecules. Polym J 17 (1):117–132
50. Bosman AW, Janssen HM, Meijer EW (1999) About dendrimers: structure, physical properties, and applications. Chem Rev 99(7):1665–1688
51. Tomalia DA, Fréchet JMJ (2002) Discovery of dendrimers and dendritic polymers: a brief historical perspective. J Polym Sci Part A Polym Chem 40(16):2719–2728
52. Shen M, Shi X (2010) Dendrimer-based organic/inorganic hybrid nanoparticles in biomedical applications. Nanoscale 2(9):1596–1610
53. Tang J, Sheng Y, Hu H, Shen Y (2013) Macromolecular MRI contrast agents: structures, properties and applications. Prog Polym Sci 38(3–4):462–502
54. Kobayashi H, Brechbiel MW (2005) Nano-sized MRI contrast agents with dendrimer cores. Adv Drug Deliv Rev 57(15):2271–2286
55. Kobayashi H, Kawamoto S, Jo S-K, Bryant HL, Brechbiel MW, Star RA (2003) Macromolecular MRI contrast agents with small dendrimers: pharmacokinetic differences between sizes and cores. Bioconjug Chem 14(2):388–394
56. Hong S, Leroueil PR, Majoros IJ, Orr BG, Baker JR Jr, Banaszak Holl MM (2007) The binding avidity of a nanoparticle-based multivalent targeted drug delivery platform. Chem Biol 14(1):107–115
57. Shukla R, Hill E, Shi X, Kim J, Muniz MC, Sun K, Baker JR (2008) Tumor microvasculature targeting with dendrimer-entrapped gold nanoparticles. Soft Matter 4(11):2160–2163
58. Shi X, Wang S, Sun H, Baker JR (2007) Improved biocompatibility of surface functionalized dendrimer-entrapped gold nanoparticles. Soft Matter 3(1):71–74
59. Cao Y, Liu H, Shi X (2015) Targeted CT imaging of cancer cells using PEGylated low-generation dendrimer-entrapped gold nanoparticles. J Control Release 213:e138–e139
60. Zhou B, Zheng L, Peng C, Li D, Li J, Wen S, Shen M, Zhang G, Shi X (2014) Synthesis and characterization of PEGylated polyethylenimine-entrapped gold nanoparticles for blood pool and tumor CT imaging. ACS Appl Mater Interfaces 6(19):17190–17199
61. Wang H, Zheng L, Peng C, Shen M, Shi X, Zhang G (2013) Folic acid-modified dendrimer-entrapped gold nanoparticles as nanoprobes for targeted CT imaging of human lung adencarcinoma. Biomaterials 34(2):470–480
62. Talanov VS, Regino CAS, Kobayashi H, Bernardo M, Choyke PL, Brechbiel MW (2006) Dendrimer-based nanoprobe for dual modality magnetic resonance and fluorescence imaging. Nano Lett 6(7):1459–1463
63. Kim Y, Kim SH, Tanyeri M, Katzenellenbogen JA, Schroeder CM (2013) Dendrimer probes for enhanced photostability and localization in fluorescence imaging. Biophys J 104 (7):1566–1575
64. Taratula O, Schumann C, Duong T, Taylor KL, Taratula O (2015) Dendrimer-encapsulated naphthalocyanine as a single agent-based theranostic nanoplatform for near-infrared fluorescence imaging and combinatorial anticancer phototherapy. Nanoscale 7(9):3888–3902
65. Bryant LH Jr, Jordan EK, Bulte JWM, Herynek V, Frank JA (2002) Pharmacokinetics of a high-generation dendrimer–Gd-DOTA. Acad Radiol 9(Suppl 1):S29–S33
66. Wen S, Li K, Cai H, Chen Q, Shen M, Huang Y, Peng C, Hou W, Zhu M, Zhang G, Shi X (2013) Multifunctional dendrimer-entrapped gold nanoparticles for dual mode CT/MR imaging applications. Biomaterials 34(5):1570–1580
67. Nwe K, Bernardo M, Regino CAS, Williams M, Brechbiel MW (2010) Comparison of MRI properties between derivatized DTPA and DOTA gadolinium–dendrimer conjugates. Bioorg Med Chem 18(16):5925–5931
68. Luo Y, Zhao L, Li X, Yang J, Guo L, Zhang G, Shen M, Zhao J, Shi X (2016) The design of a multifunctional dendrimer-based nanoplatform for targeted dual mode SPECT/MR imaging of tumors. J Mater Chem B 4(45):7220–7225

69. Li X, Xiong Z, Xu X, Luo Y, Peng C, Shen M, Shi X (2016) 99mTc-labeled multifunctional low-generation dendrimer-entrapped gold nanoparticles for targeted SPECT/CT dual-mode imaging of tumors. ACS Appl Mater Interfaces 8(31):19883–19891
70. Zhao L, Zhu J, Cheng Y, Xiong Z, Tang Y, Guo L, Shi X, Zhao J (2015) Chlorotoxin-conjugated multifunctional dendrimers labeled with radionuclide 131I for single photon emission computed tomography imaging and radiotherapy of gliomas. ACS Appl Mater Interfaces 7(35):19798–19808
71. Seo JW, Baek H, Mahakian LM, Kusunose J, Hamzah J, Ruoslahti E, Ferrara KW (2014) 64Cu-labeled lyp-1-dendrimer for PET-CT imaging of atherosclerotic plaque. Bioconjug Chem 25(2):231–239
72. Ghai A, Singh B, Panwar Hazari P, Schultz MK, Parmar A, Kumar P, Sharma S, Dhawan D, Kumar Mishra A (2015) Radiolabeling optimization and characterization of 68Ga labeled DOTA–polyamido-amine dendrimer conjugate – animal biodistribution and PET imaging results. Appl Radiat Isot 105:40–46
73. Bulte JWM, Douglas T, Witwer B, Zhang S-C, Strable E, Lewis BK, Zywicke H, Miller B, van Gelderen P, Moskowitz BM, Duncan ID, Frank JA (2001) Magnetodendrimers allow endosomal magnetic labeling and in vivo tracking of stem cells. Nat Biotechnol 19(12):1141–1147
74. Strable E, Bulte JWM, Moskowitz B, Vivekanandan K, Allen M, Douglas T (2001) Synthesis and characterization of soluble iron oxide–dendrimer composites. Chem Mater 13 (6):2201–2209
75. Shi X, Thomas TP, Myc LA, Kotlyar A, Baker JJR (2007) Synthesis, characterization, and intracellular uptake of carboxyl-terminated poly(amidoamine) dendrimer-stabilized iron oxide nanoparticles. Phys Chem Chem Phys 9(42):5712–5720
76. Zhou B, Xiong Z, Zhu J, Shen M, Tang G, Peng C, Shi X (2016) PEGylated polyethylenimine-entrapped gold nanoparticles loaded with gadolinium for dual-mode CT/MR imaging applications. Nanomedicine 11(13):1639–1652
77. Chen Q, Wang H, Liu H, Wen S, Peng C, Shen M, Zhang G, Shi X (2015) Multifunctional dendrimer-entrapped gold nanoparticles modified with RGD peptide for targeted computed tomography/magnetic resonance dual-modal imaging of tumors. Anal Chem 87(7):3949–3956
78. Shaw LJ, Iskandrian AE (2004) Prognostic value of gated myocardial perfusion SPECT. J Nucl Cardiol 11(2):171–185
79. Gnanasegaran G, Ballinger JR (2014) Molecular imaging agents for SPECT (and SPECT/CT). Eur J Nucl Med Mol Imaging 41(1):26–35
80. Cutler CS, Hennkens HM, Sisay N, Huclier-Markai S, Jurisson SS (2013) Radiometals for combined imaging and therapy. Chem Rev 113(2):858–883
81. Madsen MT (2007) Recent advances in SPECT imaging. J Nucl Med 48(4):661–673
82. Eckelman WC (2009) Unparalleled contribution of technetium-99m to medicine over 5 decades. J Am Coll Cardiol Img 2(3):364–368
83. Khalil MM, Tremoleda JL, Bayomy TB, Gsell W (2011) Molecular SPECT imaging: an overview. Int J Mol Imaging 2011:796025
84. Niendorf HP, Dinger JC, Haustein J, Cornelius I, Alhassan A, Clauß W (1991) Tolerance data of Gd-DTPA: a review. Eur J Radiol 13(1):15–20
85. Weinmann HJ, Brasch RC, Press WR, Wesbey GE (1984) Characteristics of gadolinium-DTPA complex: a potential NMR contrast agent. Am J Roentgenol 142(3):619–624
86. Brix G, Semmler W, Port R, Schad LR, Layer G, Lorenz WJ (1991) Pharmacokinetic parameters in CNS Gd-DTPA enhanced MR imaging. J Comput Assist Tomogr 15(4):621–628
87. Lorberboym M, Lampl Y, Sadeh M (2003) Correlation of 99mTc-DTPA SPECT of the blood–brain barrier with neurologic outcome after acute stroke. J Nucl Med 44(12):1898–1904
88. McLarty K, Cornelissen B, Cai Z, Scollard DA, Costantini DL, Done SJ, Reilly RM (2009) Micro-SPECT/CT with 111In-DTPA-pertuzumab sensitively detects trastuzumab-mediated her2 downregulation and tumor response in athymic mice bearing MDA-MB-361 human breast cancer xenografts. J Nucl Med 50(8):1340–1348

89. Bar-Shalom R, Yefremov N, Guralnik L, Keidar Z, Engel A, Nitecki S, Israel O (2006) SPECT/CT using 67Ga and 111In-labeled leukocyte scintigraphy for diagnosis of infection. J Nucl Med 47(4):587–594
90. Zhang Y, Sun Y, Xu X, Zhu H, Huang L, Zhang X, Qi Y, Shen Y-M (2010) Radiosynthesis and micro-SPECT imaging of 99mTc-dendrimer poly(amido)-amine folic acid conjugate. Bioorg Med Chem Lett 20(3):927–931
91. Zhang Y, Sun Y, Xu X, Zhang X, Zhu H, Huang L, Qi Y, Shen Y-M (2010) Synthesis, biodistribution, and microsingle photon emission computed tomography (SPECT) imaging study of technetium-99m labeled pegylated dendrimer poly(amidoamine) (PAMAM)−folic acid conjugates. J Med Chem 53(8):3262–3272
92. Xu X, Zhang Y, Wang X, Guo X, Zhang X, Qi Y, Shen Y-M (2011) Radiosynthesis, biodistribution and micro-SPECT imaging study of dendrimer–avidin conjugate. Bioorg Med Chem 19(5):1643–1648
93. Mirzaii M, Seyyedi S, Sadeghi M, Gholamzadeh Z (2010) Cadmium electrodeposition on copper substrate for cyclotron production of 111In radionuclide. J Radioanal Nucl Chem 284 (2):333–339
94. Mamede M, Saga T, Ishimori T, Higashi T, Sato N, Kobayashi H, Brechbiel MW, Konishi J (2004) Hepatocyte targeting of 111In-labeled oligo-DNA with avidin or avidin–dendrimer complex. J Control Release 95(1):133–141
95. Bindslev L, Haack-Sørensen M, Bisgaard K, Kragh L, Mortensen S, Hesse B, Kjær A, Kastrup J (2006) Labelling of human mesenchymal stem cells with indium-111 for SPECT imaging: effect on cell proliferation and differentiation. Eur J Nucl Med Mol Imaging 33(10):1171–1177
96. Wong KK, Cahill JM, Frey KA, Avram AM (2010) Incremental value of 111-in pentetreotide SPECT/CT fusion imaging of neuroendocrine tumors. Acad Radiol 17(3):291–297
97. Castaldi P, Rufini V, Treglia G, Bruno I, Perotti G, Stifano G, Barbaro B, Giordano A (2008) Impact of 111In-DTPA-octreotide SPECT/CT fusion images in the management of neuroendocrine tumours. Radiol Med 113(7):1056–1067
98. Kojima C, Niki Y, Ogawa M, Magata Y (2014) Prolonged local retention of subcutaneously injected polymers monitored by noninvasive SPECT imaging. Int J Pharm 476(1–2):164–168
99. Keshtgar MRS, Ell PJ (1999) Sentinel lymph node detection and imaging. Eur J Nucl Med 26 (1):57–67
100. Xie Y, Bagby TR, Cohen MS, Forrest ML (2009) Drug delivery to the lymphatic system: importance in future cancer diagnosis and therapies. Expert Opin Drug Deliv 6(8):785–792
101. Ryan GM, Kaminskas LM, Porter CJH (2014) Nano-chemotherapeutics: maximising lymphatic drug exposure to improve the treatment of lymph-metastatic cancers. J Control Release 193:241–256
102. Koyama Y, Talanov VS, Bernardo M, Hama Y, Regino CAS, Brechbiel MW, Choyke PL, Kobayashi H (2007) A dendrimer-based nanosized contrast agent dual-labeled for magnetic resonance and optical fluorescence imaging to localize the sentinel lymph node in mice. J Magn Reson Imaging 25(4):866–871
103. Jain R, Dandekar P, Patravale V (2009) Diagnostic nanocarriers for sentinel lymph node imaging. J Control Release 138(2):90–102
104. Sano K, Iwamiya Y, Kurosaki T, Ogawa M, Magata Y, Sasaki H, Ohshima T, Maeda M, Mukai T (2014) Radiolabeled γ-polyglutamic acid complex as a nano-platform for sentinel lymph node imaging. J Control Release 194:310–315
105. Niki Y, Ogawa M, Makiura R, Magata Y, Kojima C (2015) Optimization of dendrimer structure for sentinel lymph node imaging: effects of generation and terminal group. Nanomedicine 11(8):2119–2127
106. Willi AK (2006) X-ray computed tomography. Phys Med Biol 51(13):R29
107. Mattrey RF, Aguirre DA (2003) Advances in contrast media research. Acad Radiol 10 (12):1450–1460
108. Hallouard F, Anton N, Choquet P, Constantinesco A, Vandamme T (2010) Iodinated blood pool contrast media for preclinical X-ray imaging applications – a review. Biomaterials 31 (24):6249–6268

109. Liu H, Wang H, Xu Y, Shen M, Zhao J, Zhang G, Shi X (2014) Synthesis of PEGylated low generation dendrimer-entrapped gold nanoparticles for CT imaging applications. Nanoscale 6 (9):4521–4526
110. Wang H, Zheng L, Guo R, Peng C, Shen M, Shi X, Zhang G (2012) Dendrimer-entrapped gold nanoparticles as potential CT contrast agents for blood pool imaging. Nanoscale Res Lett 7 (1):190
111. Peng C, Qin J, Zhou B, Chen Q, Shen M, Zhu M, Lu X, Shi X (2013) Targeted tumor CT imaging using folic acid-modified PEGylated dendrimer-entrapped gold nanoparticles. Polym Chem 4(16):4412–4424
112. Criscione JM, Dobrucki LW, Zhuang ZW, Papademetris X, Simons M, Sinusas AJ, Fahmy TM (2011) Development and application of a multimodal contrast agent for SPECT/CT hybrid imaging. Bioconjug Chem 22(9):1784–1792
113. Xu C, Tung GA, Sun S (2008) Size and concentration effect of gold nanoparticles on X-ray attenuation as measured on computed tomography. Chem Mater 20(13):4167–4169
114. Shi X, Lee I, Baker JR (2008) Acetylation of dendrimer-entrapped gold and silver nanoparticles. J Mater Chem 18(5):586–593
115. Guo R, Wang H, Peng C, Shen M, Pan M, Cao X, Zhang G, Shi X (2010) X-ray attenuation property of dendrimer-entrapped gold nanoparticles. J Phys Chem C 114(1):50–56
116. Jordan LC, McKinstry RC, Kraut MA, Ball WS, Vendt BA, Casella JF, DeBaun MR, Strouse JJ (2010) Incidental findings on brain magnetic resonance imaging of children with sickle cell disease. Pediatrics 126(1):53
117. Beets-Tan RGH, Beets GL (2004) Rectal cancer: review with emphasis on MR imaging. Radiology 232(2):335–346
118. Raymond KN, Pierre VC (2005) Next generation, high relaxivity gadolinium MRI agents. Bioconjug Chem 16(1):3–8
119. Yang C-T, Chuang K-H (2012) Gd(iii) chelates for MRI contrast agents: from high relaxivity to "smart", from blood pool to blood-brain barrier permeable. Med Chem Commun 3 (5):552–565
120. Cheng C-Y, Ou K-L, Huang W-T, Chen J-K, Chang J-Y, Yang C-H (2013) Gadolinium-based CuInS2/ZnS nanoprobe for dual-modality magnetic resonance/optical imaging. ACS Appl Mater Interfaces 5(10):4389–4400
121. Langereis S, de Lussanet QG, van Genderen MHP, Meijer EW, Beets-Tan RGH, Griffioen AW, van Engelshoven JMA, Backes WH (2006) Evaluation of Gd(III)DTPA-terminated poly (propylene imine) dendrimers as contrast agents for MR imaging. NMR Biomed 19 (1):133–141
122. Cheng Z, Thorek DLJ, Tsourkas A (2010) Gadolinium-conjugated dendrimer nanoclusters as a tumor-targeted T1 magnetic resonance imaging contrast agent. Angew Chem Int Ed Engl 49 (2):346–350
123. Rahmania H, Mutalib A, Ramli M, Levita J (2015) Synthesis and stability test of radiogadolinium(III)-DOTA-PAMAM G3.0-trastuzumab as SPECT-MRI molecular imaging agent for diagnosis of HER-2 positive breast cancer. J Radiat Res Appl Sci 8(1):91–99
124. Lee WI, Bae Y, Bard AJ (2004) Strong blue photoluminescence and ECL from OH-terminated PAMAM dendrimers in the absence of gold nanoparticles. J Am Chem Soc 126 (27):8358–8359
125. Wang D, Imae T (2004) Fluorescence emission from dendrimers and its pH dependence. J Am Chem Soc 126(41):13204–13205
126. Tsuchimochi M, Hayama K, Toyama M, Sasagawa I, Tsubokawa N (2013) Dual-modality imaging with 99mTc and fluorescent indocyanine green using surface-modified silica nanoparticles for biopsy of the sentinel lymph node: an animal study. EJNMMI Res 3(1):33
127. Xie J, Lee S, Chen X (2010) Nanoparticle-based theranostic agents. Adv Drug Deliv Rev 62 (11):1064–1079
128. Ma Y, Mou Q, Wang D, Zhu X, Yan D (2016) Dendritic polymers for theranostics. Theranostics 6(7):930–947

129. Zhu J, Zhao L, Cheng Y, Xiong Z, Tang Y, Shen M, Zhao J, Shi X (2015) Radionuclide 131I-labeled multifunctional dendrimers for targeted SPECT imaging and radiotherapy of tumors. Nanoscale 7(43):18169–18178
130. Cheng Y, Zhu J, Zhao L, Xiong Z, Tang Y, Liu C, Guo L, Qiao W, Shi X, Zhao J (2016) 131I-labeled multifunctional dendrimers modified with BmK CT for targeted SPECT imaging and radiotherapy of gliomas. Nanomedicine 11(10):1253–1266
131. Vugmeyster Y, DeFranco D, Szklut P, Wang Q, Xu X (2010) Biodistribution of [125I]-labeled therapeutic proteins: application in protein drug development beyond oncology. J Pharm Sci 99(2):1028–1045
132. Shao X, Zhang H, Rajian JR, Chamberland DL, Sherman PS, Quesada CA, Koch AE, Kotov NA, Wang X (2011) 125I-labeled gold nanorods for targeted imaging of inflammation. ACS Nano 5(11):8967–8973
133. Merkel OM, Mintzer MA, Sitterberg J, Bakowsky U, Simanek EE, Kissel T (2009) Triazine dendrimers as nonviral gene delivery systems: effects of molecular structure on biological activity. Bioconjug Chem 20(9):1799–1806
134. Mintzer MA, Merkel OM, Kissel T, Simanek EE (2009) Polycationic triazine-based dendrimers: effect of peripheral groups on transfection efficiency. New J Chem 33 (9):1918–1925
135. Merkel OM, Zheng M, Mintzer MA, Pavan GM, Librizzi D, Maly M, Höffken H, Danani A, Simanek EE, Kissel T (2011) Molecular modeling and in vivo imaging can identify successful flexible triazine dendrimer-based siRNA delivery systems. J Control Release 153(1):23–33
136. Lee C, Lo S-T, Lim J, da Costa VCP, Ramezani S, Öz OK, Pavan GM, Annunziata O, Sun X, Simanek EE (2013) Design, synthesis and biological assessment of a triazine dendrimer with approximately 16 paclitaxel groups and 8 PEG groups. Mol Pharm 10(12):4452–4461
137. Xiao W, Luo J, Jain T, Riggs JW, Tseng HP, Henderson PT, Cherry SR, Rowland D, Lam KS (2012) Biodistribution and pharmacokinetics of a telodendrimer micellar paclitaxel nanoformulation in a mouse xenograft model of ovarian cancer. Int J Nanomedicine 7 (9):1587–1597

In Vivo Near-Infrared Fluorescence Imaging Based on Polymer Dots

13

Yixiao Guo and Liqin Xiong

Contents

List of Abbreviations

AIE	Aggregation-induced-emission
BODIPY	Phthalocyanine- and boron dipyrrin
BRET	Bioluminescence resonance energy transfer
BSA	Bovine serum albumin
BTE	Bisthienylethene derivative, 1,2-bis(2,4-dimethyl-5-phenyl-3-thienyl)-3,3,4,4,5,5-hexafluoro-1-cyclopentene
BTTP	5,7-bis(5-bromo-2-thienyl)-2,3-dimethylthieno[3,4-b] pyrazine

Y. Guo · L. Xiong (✉)
Nano Biomedical Research Center, School of Biomedical Engineering, Med-X Research Institute, Shanghai Jiao Tong University, Shanghai, China
e-mail: xiongliqin@sjtu.edu.cn

C. S. S. R. Kumar (ed.), *Nanotechnology Characterization Tools for Biosensing and Medical Diagnosis*, https://doi.org/10.1007/978-3-662-56333-5_13

BTTPF	BTTP copolymized with 2,7-bis(4,4,5,5-tetramethyl-1,3,2-dioxaborolan-2-yl)-9,9-bis[30-(dimethylamino)propyl] fluorine
C_7-FA	Homemade heptylamine modified folate
CN-PPVs	Cyanosubstituted derivatives of poly(p-phenylenevinylene)
CPDP-FA NPs	CP-loaded DSPE-PEG-folic acid nanoparticles
cRGD	Cyclic RGD peptides
cvCP	Anovinylene-backboned conjugated polymers
cvPDs	Cyanovinylene-backboned polymer dots
CZ	3,6-dibromo-9-(2-butyloctyl)-9H–carbazole
Dox	Doxorubicin
DPPF	poly{3-(5-(9-hexyl-9-octyl-9H-uoren-2-yl)thiophen-2-yl)-2,5-bis(2-hexyldecyl)-6-(thiophen-2-yl)pyrrolo[3,4-c]pyrrole-1,4(2H,5H)-dione}
DSPE	2-distearoyl-sn-glycero-3-phosphoethanolamine
DSPE-PEG_{2000}	1,2-distearoyl-sn-glycero-3-phosphoethanolamine-N-[methoxy(polyethylene glycol)-2000]
DSPE-PEG-NH_2	1,2-distearoyl-sn-glycero-3-phosphoethanolamine-N-[amino(polyethylene glycol)-2000]
DTT	2,6-dibromo-4,4-dihexyl-4H-cyclopenta[1,2-b:5,4-b'] dithiophene
EPR	Enhanced permeability and retention
FRET	Fluorescence resonance energy transfer
MEH-PPV	poly[2-methoxy-5-(2-ethylhexyloxy)-1,4-phenylenevinylene]
NanoDRONE	Dual-color SPN-based NIR nanoprobe for the detection of RONS
NIR775	Silicon 2, 3-naphthalocyanine bis(trihexylsilyloxide)
PCFDP	[9,9′-dihexyl-2,7-bis(1-cyanovinylene)fluorenylene-alt-co-2,5-bis(N,N′-diphenylamino)-1,4-phenylene]
PCPDTBT	poly[2,6-(4,4-bis-(2-ethylhexyl)-4H–cyclopenta[2,1-b;3,4-b0]dithiophene)-alt-4,7(2,1,3-benzothiadiazole)]
PD-1	PS-PEG-COOH modified MEH-PPV polymer dots
PD-2	PSMA modified MEH-PPV polymer dots
PD-3	PS-PEG-COOH modified and Luc-8 conjugated MEH-PPV polymer dots
PD-4	PS-PEG-COOH modified and RGD conjugated MEH-PPV polymer dots
PD-5	PS-PEG-COOH modified, RGD and Luc-8 conjugated MEH-PPV polymer dots
PDTPDTT	poly[5-octyl-1-(5-(4,4,9,9-tetrakis(4-hexylphenyl)-4,9-dihydro-s-indaceno[1,2-b:5,6-b0]dithiophen-2-yl)thiophen-2-yl)-3-(thiophen-2-yl)-4H–thieno[3,4-c]pyrrole-4, 6(5H)-dione]
PEG-NH_2	Methoxypolyethylene glycol amine 2000

PFBT	poly(9,9-dioctylfluorene-alt-benzothiadiazole) average Mn 10,000–20,000
PFBTDBT10	poly[(9,9-dihexylfluorene)-co-2,1,3-benzothiadiazole-co-4,7-di(thiophen-2-yl)-2,1,3-benzothiadiazole]
PFVBT	poly[9,9-bis(6′-(N,N-dimethylamino)hexyl)fluorenyldivinylenealt-4,7-(2,1,3,-benzothiadiazole)]
PIDT-DBT	poly{[4,4,9,9-tetrakis(4-(octyloxy)phenyl-4,9-dihydro-s-indaceno[1,2-b:5,6-b′]dithiophene)]-alt-co-[4,7-di(thiophen-2-yl)-2,1,3-benzothiadiazole]}
PLGA-PEG-FOL	poly(lactic-co-glycolic acid)-poly(ethylene glycol)-folate
PSBTBT	poly[2,6-(4,40-bis(2-ethylhexyl)dithieno[3,2-b:20,30-d]silole)-alt-4,7(2,1,3-benzothiadiazole)]
PSMA	poly(styrene-alt-maleic anhydride)
PS-PEG-COOH	Polystyrene-graft-ethyleneoxide functionalized with carboxyl groups
$PtTFPPBr_2$	Platinum(II) meso-bis(pentafluorophenyl)bis-(4-bromophenyl) porphyrin
RONS	Reactive oxygen and nitrogen species
ROS	Reactive oxygen species
SPNs	Semiconducting polymer nanoparticles
TC6FQ	5,8-Bis(5-bromo-4-hexylthiophen-2-yl)-6,7-difluoro-2,3-bis-(3-(hexyloxy)phenyl)quinoxaline
TEOS	Tetraethyl orthosilicate
TFPP	meso-bis(pentafluorophenyl)bis-(4-bromophenyl)porphyrin
TPE-TPA-DCM	2-(2,6-Bis((E)-4-(phenyl(4′-(1,2,2-triphenylvinyl)-[1,1′-biphenyl]-4-yl)amino)styryl)-4H–pyran-4-ylidene)malononitrile

1 Definition of the Topic

Conjugated polymer dots emerge as attractive molecular imaging nanoprobes in living animals because of their excellent optical properties including bright fluorescence intensity, excellent photostability, high emission rates, and low intrinsic cytotoxicity. In this chapter we focused on the preparation of near-infrared (NIR)-emitting polymer dots by nano-precipitation method (matrix-encapsulation method), miniemulsion method, and in situ colloidal Knoevenagel polymerization methods and their applications for in vivo NIR fluorescence imaging, including imaging of lymphatic basins, tumors, zebrafish, and oxygen.

2 Overview

Polymer dots exhibited such advantageous features as compared to other nanosized platforms: extraordinary fluorescence brightness, superior photostability, high emission rate, minimal toxicity to cells and tissues, noninvasive nature, real-time monitoring

capacity, etc. Those unique capabilities render polymer dots very promising in the investigation of cancer diagnosis and imaging, tumor growth monitoring, fluorescence-guided surgery and hypoxia evaluation, and other biomedical applications.

However, polymer dots as nanoprobes for fluorescence imaging still has some inherent limitations, such as interferences with light absorption, scattering and autofluorescence from living tissues, limited penetration depth, and unspecific uptake in the liver and spleen after intravenous injection. To address the abovementioned challenges, some strategies have been used to optimize their performance of in vivo applications:

1. Enhancing the NIR fluorescence intensity using bioluminescence resonance energy transfer (BRET), fluorescence resonance energy transfer (FRET), aggregation-induced emission (AIE), silica protection layer, etc.
2. Tuning the emission wavelength to make it migrate to conventional NIR region or the second infrared window (1000–17,000 nm)
3. Enhancing the photostability using encapsulation matrix such as modified PEG, BSA, dextran, etc.
4. Enabling the tumor targeting ability such as enhanced permeability and retention (EPR) effect, folate, or RGD functionalization
5. Establishing the fluorescence switch such as pH sensitivity, photostimulation, and enzyme activity
6. Cooperating with other modalities such as magnetic resonance imaging, photoacoustic imaging, and so on

In this chapter, we reviewed and discussed the in vivo NIR fluorescence imaging applications of a series of polymer dots and some recent solid findings based on them in each subsequent session. The discussion and review generally consist of preparation of NIR-emitting polymer dots based on MEH-PPV, CN-PPV, cvCP, TPE-TPA-DCM, TFPP, TPTBPF, and a series of benzothiadiazole (BT)-based (PFBT, CZBT, PCPDBT, PDTTBT, PIDT-DBT, etc.) polymer dots and applications of these polymer dots for in vivo imaging of lymphatic basins, tumors, zebrafish, and oxygen. The aforementioned strategies are also addressed in corresponding sessions (Scheme 13.1).

3 Introduction

Fluorescence imaging has become a powerful technique to visualize biology in its native physiological settings in a living subject [1–3] and has been used in clinics for image-guided surgery in cancer patients [4, 5]. Besides quantum dots, metal nanoclusters, carbon nanomaterials, up-conversion nanophosphors, and silicon nanomaterials, conjugated polymer dots are one of the most promising nanoprobes and contributed to the advance of fluorescence imaging. Conjugated polymer dots have π-electron-delocalized backbones, and their formation of spherical nanoparticles results from collapse of hydrophobic polymer chains owing to substantial decrease

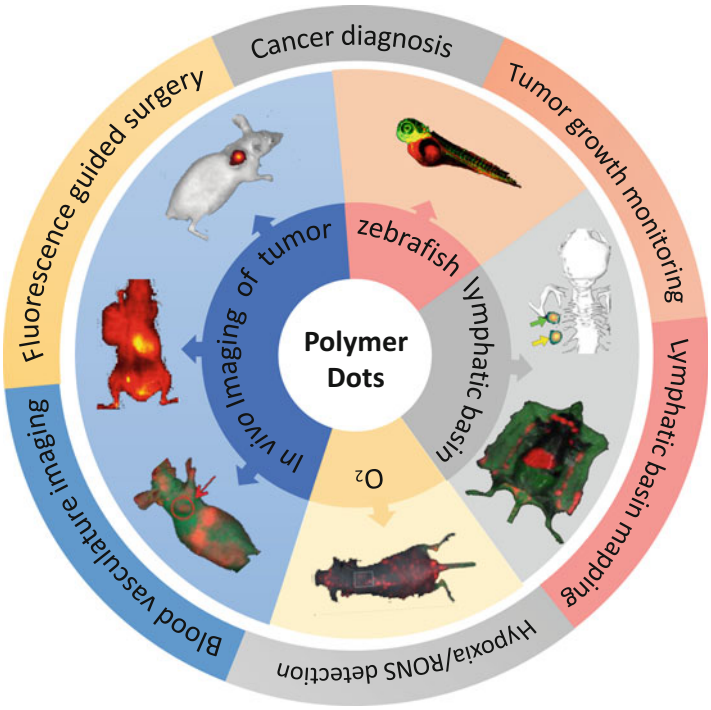

Scheme 13.1 The schematic illustration of the applications of the polymer dots for in vivo near-infrared fluorescence imaging on various animal models [26, 30–32, 37, 41]

in solvent hydrophobicity upon going from organic solvents to water. In addition to their large absorption coefficients, bright fluorescence intensity, excellent photostability, and high emission rates, the completely organic and biologically inert components of polymer dots represent another advantage, which intrinsically circumvents the issue of heavy metal ion-induced toxicity to living organisms, and thus potentially possess good biocompatibility [6–8]. Recently, polymer dots have been demonstrated for in vitro sensing, labeling, imaging, and drug delivery, as examined in a number of recent reviews [9–17].

However, only a few studies about the whole-body fluorescence imaging of polymer dots in living subjects are reported, mainly due to the challenge on the design of polymer dots that show strong and narrowband emissions in the near-infrared (NIR) region. Application of NIR fluorescence in biology enormously enhances the sensitivity of in vivo measurements and optical imaging because monitoring NIR fluorescence minimizes interference from autofluorescence in biological tissues.

Noticing that there exist very few related review articles, this chapter introduced the synthesis and application of the NIR fluorescence imaging based on NIR-emitting polymer dots for the first time. This part consists of the design and preparation of NIR-emitting polymer dots by nano-precipitation method (matrix-

encapsulation method) [18–37], miniemulsion method [21, 38, 39], and in situ colloidal Knoevenagel polymerization methods [40, 41] and in vivo NIR fluorescence imaging applications of these polymer dots, including lymph node mapping [30, 40, 41], tumor vascular imaging [25–31], tumor-targeted imaging [19–24, 30, 33, 38, 39], tumor cell tracking [32, 34, 35], imaging of zebrafish [26–29], and imaging of oxygen [36, 37, 42].

4 Experimental and Instrumental Methodology

4.1 Preparation of Near-Infrared-Emitting Polymer Dots

To date, NIR polymer dots are prepared mainly by nano-precipitation method (matrix-encapsulation method) [18–37], miniemulsion method [21, 38, 39], and in situ colloidal Knoevenagel polymerization methods [40, 41].

4.1.1 Nano-precipitation Method

Chiu lab described a versatile and simple method for tuning the fluorescence properties of poly(9,9-dioctylfluorene-co-benzothiadiazole) (PFBT) polymer dots by doping the hydrophobic matrix of PFBT with hydrophobic dyes using a nanoscale precipitation method. In a typical procedure, a tetrahydrofuran (THF) solution containing 50 μg/mL of PFBT, 50 μg/mL of PS-PEG-COOH, and 0.2 μg/mL of NIR775 dye was prepared. A 5-mL aliquot of the mixture was then quickly dispersed into 10 mL of water under vigorous sonication. The extra THF was evaporated at an elevated temperature (lower than 100 °C) with the protection of nitrogen gas. The THF-free polymer dots solution was filtrated through a 0.2-μm cellulose membrane filter and adjusted to the appropriate concentration [18].

This strategy offers several important advantages: (1) The hydrophobic matrix of polymer dots effectively disperses and stabilizes the doped dyes and allows the dyes to be used in an aqueous environment. (2) The functional groups present on the surface of polymer dots allow the dye-doped nanoparticles to be labeled with a wide range of biomolecules. (3) Polymer dots act as extremely efficient light harvesters that greatly enhance the brightness of the doped dyes. (4) Polymer dots offer amplified energy transfer to the dopant, thus enabling efficient tuning of the emission properties of polymer dots using the dopant.

Using this strategy, NIR-emitting MEH-PPV polymer dots were prepared by encapsulating the NIR dye, silicon 2,3-naphthalocyanine bis(trihexylsilyloxide) (NIR775), into the matrix of MEH-PPV polymer dots (Scheme 13.2) [30–32, 35]. The NIR fluorescence emission is produced based on a fluorescence resonance energy transfer (FRET) system utilizing NIR775 as an acceptor and MEH-PPV polymers as a donor. MEH-PPV are constructed of numerous fluorescent residues that form a large conjugated system and also exhibit very fast intra- and interchain photoexcitation transport (exciton diffusion). This structure allows the excitons to move along the polymer chain until they encounter a quencher molecule. This migration of excitons facilitates the FRET from the MEH-PPV polymer to the

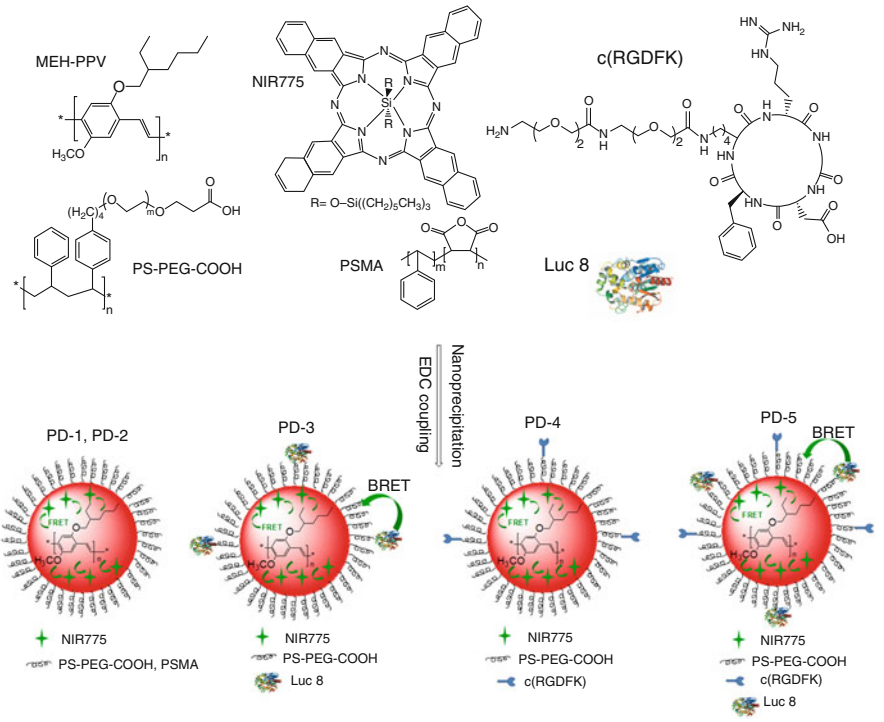

Scheme 13.2 Chemical structures of MEH-PPV, polystyrene-graft-ethyleneoxide functionalized with carboxyl groups (PS-PEG-COOH), poly(styrene-alt-maleic anhydride) (PSMA), NIR775, c (RGDFK), and Luc8, and the schematic depicts the preparation of the NIR polymer dots. PD-1, PS-PEG-COOH modified polymer dots; PD-2, PSMA modified polymer dots; PD-3, PS-PEG-COOH modified and Luc-8-conjugated polymer dots; PD-4, PS-PEG-COOH modified and RGD conjugated polymer dots; PD-5, PS-PEG-COOH modified, RGD and Luc-8-conjugated polymer dots. The biochemical energy generated from the Luc8-catalyzed oxidation of coelenterazine transfers initially to the MEH-PPV polymer and is then relayed to doped NIR775 dye to produce NIR emission. Surface ligands, PS-PEG-COOH or PSMA, coat the nanoparticle to improve water solubility and biocompatibility. Tumor targeting ligands such as cyclic RGD peptides are conjugated to the polymer dots surface for in vivo cancer imaging [30–32]

NIR775 dye over even relatively long distances. The amplified FRET process is further favored by the large extinction coefficient of the NIR775 (5.2×10^5 M^{-1} cm^{-1}). Additionally, the hydrophobic nature of the NIR775 and the polymer dot matrix ensure close interaction between the acceptor dye and the donor matrix, which also enhanced efficient FRET. Therefore, the highly efficient FRET was observed despite the poor spectral overlap between the MHE-PPV's fluorescence and the NIR775's absorbance. Furthermore, FRET resulted in a large Stokes shift (>300 nm) between the excitation and emission maxima and thus can effectively reduce the high fluorescence background during in vivo imaging. Under excitation at 468 nm, these NIR polymer dots exhibited distinctive MEH-PPV emission at 595 nm with a shoulder at 644 nm and a strong and narrowband NIR

peak at 778 nm with a full width at half maximum (FWHM) as narrow as 20 nm. These prepared NIR polymer dots displayed long-term colloidal stability and photostability in water at 4 °C for at least 9 months [31].

The self-luminescing NIR emission is produced based on an energy transfer relay that integrates bioluminescence resonance energy transfer (BRET) and fluorescence resonance energy transfer (FRET). The good overlap between the MEH-PPV absorption and Luc8 (an eight-mutation variant of *R. reniformis* luciferase) emission suggests that efficient BRET can occur. Following BRET from Luc8 to the polymer matrix, FRET could occur between the polymer matrix and the doped NIR fluorophore. This BRET-FRET relay process produces self-luminescing NIR polymer dots, enabling in vivo near-infrared imaging without external light excitation. Upon addition of coelenterazine, in addition to the emission of Luc8 at 480 nm, two new emission peaks at 594 nm (relatively weak, from MEH-PPV matrix) and 778 nm (strongest, from NIR775) were detected.

Based on this synthesis method, we also synthesized NIR775-doped PFBT polymer dots for tumor imaging [33]. The heptylamine modified folic acid (C_7-FA) was chosen as a specific ligand for the folate receptor and physically blended with PFBT and PEG-COOH or PEG-NH_2 to form polymer dots. In a typical procedure, a solution of THF containing 125 μg/mL of PFBT, 125 μg/mL of PEG-COOH or PEG-NH_2, and 25 μg/mL of C_7-FA was prepared. An aliquot of the mixture (2 mL) was then quickly dispersed into 10 mL of water under vigorous sonication. Extra THF was evaporated at an elevated temperature (below 90 °C) under the protection of nitrogen.

Pu lab reported a straightforward one-pot synthetic approach to construct middle silica layer-coated multilayered polymer dots (SPN-M) (Scheme 13.3) [29]. The synthesis procedure is based on nano-precipitation method. Before the addition of silane-PEG2000 (50 mg), tetraethyl orthosilicate (TEOS) (90 μL) was added to form the silica layer outside the polymer core (PDTPDTT, PSBTBT, DPPF, and PCPDTBT). Due to the silica layer's protection, polymer core and water molecules' interaction was reduced and thus enhanced the fluorescence of polymer dots in aqueous solution. This strategy well engineered the emission intensity of polymer dots for subsequent in vivo imaging.

4.1.2 Miniemulsion Method

According to the transitions of solvent extract between oil phase and water phase during the polymer dots synthesis, miniemulsion method is divided into single emulsion method (water-in-oil) and double emulsion method (water-in-oil-in-water) [21, 38, 39].

Shen lab reported a kind of pH-responsive conjugated polymer dots, poly{9,9-bis(N,N-dimethylpropan-1-amino)-2,7-fluorene-alt-5,7-bis(thiophen-2-yl)-2,3-dimethylthieno[3,4-b]pyrazine} (BTTPF) dots for in vivo doxorubicin (Dox) delivery and monitoring (Scheme 13.4) [39]. The NPs encapsulating DOX and BTTPF were prepared via a single emulsion (oil-in-water) solvent evaporation/extraction method. Briefly, m-dextran (50 mg), DOX (0.08 mg), and BTTPF (0.08 mg) were dissolved in dichloromethane (DCM) (0.6 mL). This solution was added to 2 mL of polyvinyl alcohol (PVA) solution

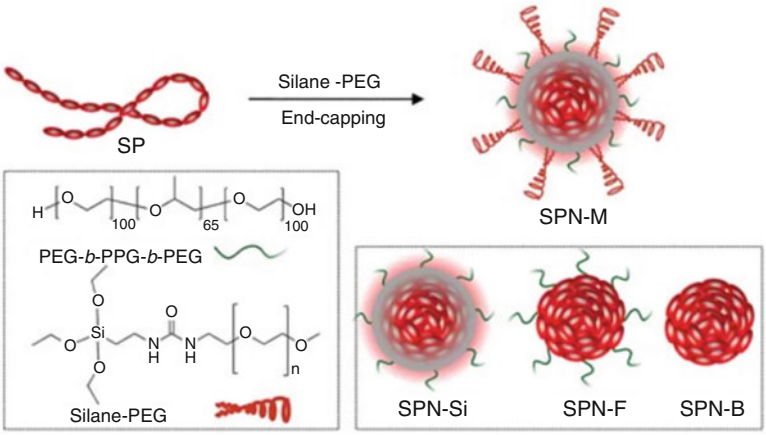

Scheme 13.3 Schematic illustration of the preparation of SPNs [29]

(3%) and sonicated for 45 cycles (1 s each with a duty cycle of 60%). The resulting emulsion was poured into 10 mL of the second PVA solution (0.3%) and stirred at room temperature for 2 h allowing the organic solvent to evaporate. The NPs were collected by centrifugation (13,000 rpm, 15 min), and the supernatant was conserved for calculating the encapsulation efficiency (EE) of the NPs. The collected NPs were washed with distilled water three times and then dried by lyophilization and stored at 4 °C. Hydrophilic PVA encapsulated hydrophobic m-dextran and hydrophobic payloads (DOX and BTTPF) to construct FRET system between Dox and BTTPF. Due to the pH sensitivity of m-dextran, FRET could be turned "on" and "off" along with the degradation of polymer dots. Therefore, Dox release could be monitored by the BTTPF.

Liu lab fabricated a series of dual-modal fluorescent-magnetic nanoparticles with surface folic acid by co-encapsulation of FR/NIR-emissive conjugated polymer (PFVBT) and lipid-coated iron oxides (IOs) into a mixture of poly(lactic-co-glycolic acid)-poly(ethylene glycol)-folate (PLGA-PEG-FOL) and PLGA (Scheme 13.5) [21]. Among these polymer dots, OA (oleic acid)-IO-loaded polymer dots were synthesized via double emulsion method (water-in-oil-in-water). In brief, an aqueous solution of OA-IOs (1 mg of Os) was emulsified into 5 mL of dichloromethane solution containing 1 mg of PFVBT, 5 mg of PLGA-PEG-FOL, and 45 mg of PLGA to form water-in-oil emulsion using a probe sonicator (XL2000, Misonix Incorporated, NY, 20 W for 30 s) over an ice bath. The water-in-oil emulsion was further mixed with an aqueous solution of PVA (0.5% w/v), followed by sonicating at 18 W output for 90 s. The obtained water-in-oil-in-water emulsion was then stirred at room temperature overnight to evaporate dichloromethane. The formed NP suspension was washed with Milli-Q water through centrifugation for three times before collecting the final product.

Lipid like OA was employed for IOs coating and separated them from polymers to minimize fluorescence quenching. Therefore, fluorescence and T_2-weighted magnetic resonance dual-modal imaging were achieved by PFVBT and IOs, respectively.

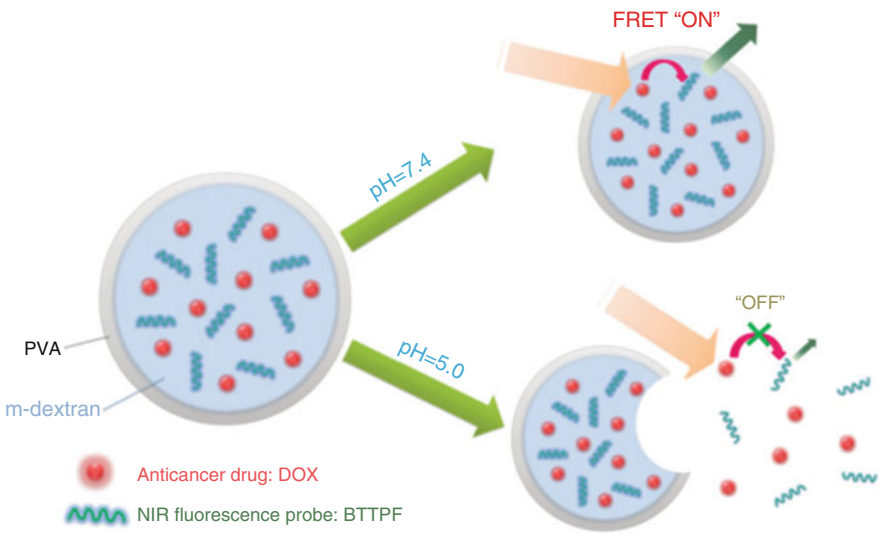

Scheme 13.4 pH-responsive and NIR-emissive polymer nanoparticles as carriers for anticancer drug DOX: fluorescence signal difference under mildly acidic or physiological conditions [39]

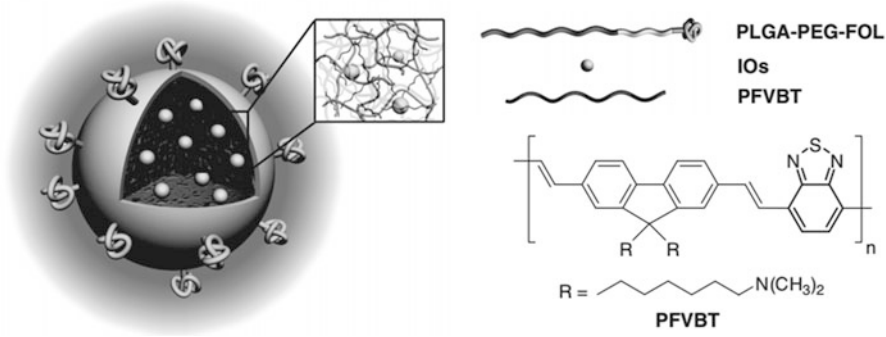

Scheme 13.5 Illustration of the conjugated polymer-based fluorescent-magnetic NP and the chemical structure of PFVBT [21]

4.1.3 In Situ Colloidal Method

Using in situ colloidal Knoevenagel method, polymer dots could be directly synthesized in the aqueous phase without applying any harmful organic solvents. Therefore, this method could avoid potential toxicity of polymer dots during their synthesis procedure [40, 41].

Kim lab reported a kind of cyanovinylene-backboned polymer dots (cvPDs) for lymph node mapping based on this method (Scheme 13.6) [40]. 2,5- Bis(octyloxy) terephthalaldehyde (25.8 mg, 60 mmol, Aldrich Chemical) and p-xylylene dicyanide (10.3 mg, 60 mmol, TCI) were dissolved in Tween 80 (1 g, Sigma Chemical) with

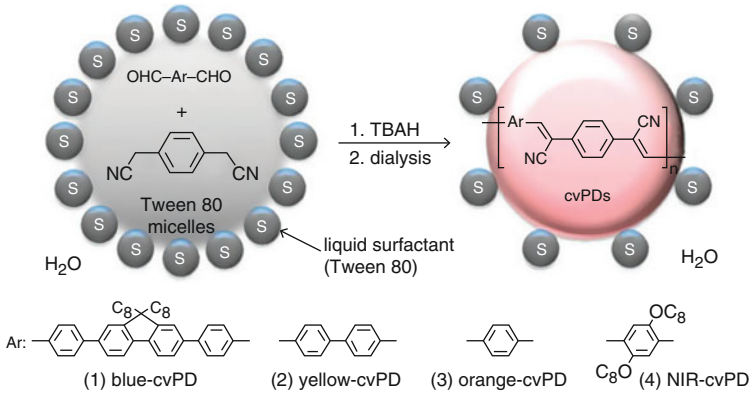

Scheme 13.6 Schematic diagram depicting colloidal synthesis of cyanovinylene-backboned polymer dots (cvPDs) through tetrabutylammonium hydroxide (TBAH)-catalyzed Knoevenagel condensation in the hydrophobic core of solvent-free aqueous micelles [40]

gentle heating. The cooled mixture (0.3 g) was mixed with Milli-Q water (5 mL) under sonication into a transparent micellar dispersion. Polymerization was initiated by adding 0.2 mL of tetrabutylammonium hydroxide (1.0 M in methanol, Aldrich Chemical) and conducted overnight under magnetic stirring at room temperature. Unreacted monomers, catalyst, and excess surfactant were removed by dialyzing the reaction mixture against Milli-Q water in a cellulose ester membrane (cut-off = 300 kDa) for 48 h, to afford a red-colored clear dispersion of fluorescent polymer nanoparticles that can be used as is for the in vivo applications.

4.2 UV Absorption and Fluorescence Spectra Characterization

UV absorption and fluorescence spectra are the major optical characterization methods of NIR polymer dots. They could provide requisite information for constituent identification and quantitative analysis of NIR polymer dots.

As shown in Fig. 13.1a, UV absorption of PD-1 was recorded on an Agilent 8453 ultraviolet-vis spectrometer. 1 mL polymer dots solution was added into the quartz cuvette after baseline correction, and then the spectrum was scanned from 300 nm to 800 nm. The peaks at 503 nm and 778 nm are corresponding to the characteristic absorption of MEH-PPV and NIR775.

As shown in Fig. 13.1b, fluorescence and bioluminescence emission spectra were collected with a FluoroMax-3 (Jobin Yvon Inc.) and corrected for wavelength-dependent detector sensitivity as described by the company. 1 mL polymer dots solution was added into the quartz cuvette, and emission spectrum was collected under excitation at 490 nm.

The UV-vis absorption and fluorescence emission spectra of the different SPNs illustrated in Scheme 13.4 are shown in Fig. 13.2. UV-vis spectra were recorded on a

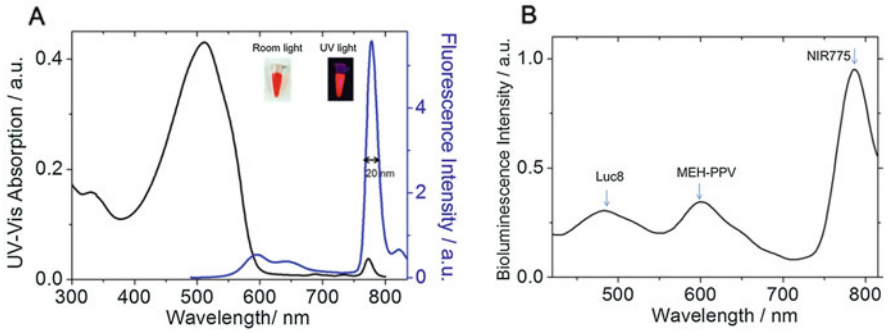

Fig. 13.1 (**a**) UV-vis absorption and fluorescence spectra of PD-1 polymer dots. Insets are the room light and UV light photographs of PD-1 polymer dots. The fluorescence photograph was obtained under 365 nm UV excitation, which showed red emission from the MEH-PPV. (**b**) Bioluminescence emission spectrum of PD-3 polymer dots in PBS buffer [30–32, 35]

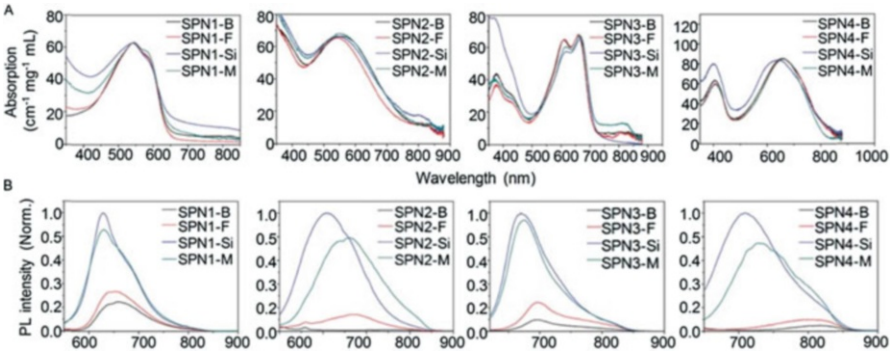

Fig. 13.2 (**a**) Optical properties of SPNs. UV-vis absorption and (**b**) fluorescence spectra [29]

Shimadzu UV-2450 spectrophotometer. Fluorescence measurements were carried out on a FluoroLog 3-TCSPC spectrofluorometer (HORIBA Jobin Yvon). Different SPNs (SPN1–SPN4) have different UV absorption bands from 400 nm to 800 nm (Fig. 13.2a). As for fluorescence emission spectra (Fig. 13.2b), there exhibits distinct intensity enhancement after silica coating of the polymer dots (SPN-Si and SPN-M).

The UV-vis absorption and fluorescence emission spectra of the NIR fluorescent polymer dots illustrated in Scheme 13.4 are shown in Fig. 13.3 [39]. The concentration of DOX and BTTPF in supernatant conversed was determined by measurement of UV-vis absorption at 480 and 570 nm compared to the standard curves using a MAPADA UV-1800 UV-vis spectrophotometer, and then the mass of DOX and BTTPF encapsulated was calculated. Fluorescence spectra of all samples were obtained using a steady-state spectrofluorometer (HORIBA Jobin Yvon FM-4NIR).

The UV-vis absorption and fluorescence emission spectra of the dual-modal fluorescence and magnetic resonance imaging, surface folic acid-functionalized

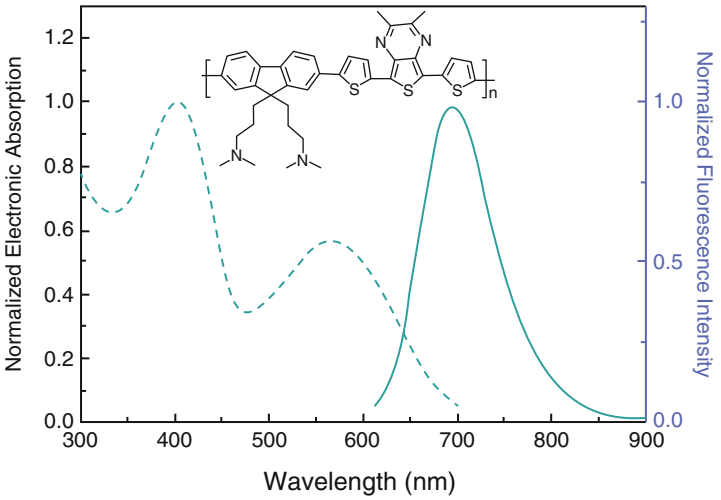

Fig. 13.3 Normalized electronic absorption (dash line) and fluorescence emission (solid line) spectra of BTTPF in DCM [39]

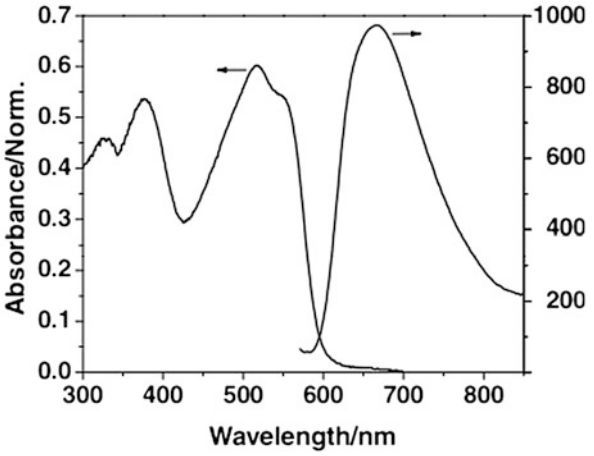

Fig. 13.4 UV-vis absorption and fluorescence spectra of FMCPNPs aqueous suspension ($\lambda_{ex} = 518$ nm) [21]

NPs (FMCPNPs), reported by Liu lab (Scheme 13.5) are shown in Fig. 13.4 [21]. The UV-vis absorption spectra of NP suspensions were collected on a Shimadzu UV-1700 spectrophotometer. The fluorescence spectra of NP aqueous suspensions were measured using a fluorometer (LS-55, Perkin Elmer, USA) with an excitation wavelength of 518 nm.

The UV-vis absorption and fluorescence emission spectra of the NIR-cvPDs illustrated in Scheme 13.6 are shown in Fig. 13.5. Absorption (transmittance) and photoluminescence spectra of cvPDs dispersed in water or 100% serum were acquired using a UV-visible spectrometer (Agilent 8453) and a fluorescence spectrophotometer (Hitachi F-7000, wavelength calibrated for excitation and emission), respectively.

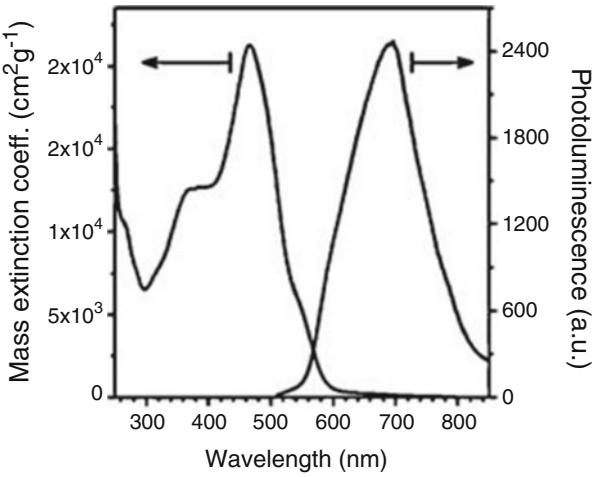

Fig. 13.5 Mass extinction coefficient and photoluminescence spectra of water-dispersed NIR-cvPDs [40]

4.3 In Vivo Near-Infrared Imaging Methodology

In recent years, many kinds of in vivo optical imaging systems have been applied in various research. Some of them are commonly used and well-commercialized devices including IVIS Spectrum (Caliper Life Sciences, Inc.) [30–35, 37, 41, 42], Maestro in vivo fluorescence imaging system (CRi, Inc., Woburn, USA) [21–24, 39], Kodak imaging system (Kodak Image Station 4000MM) [36, 40], and confocal laser scanning microscopy (Zeiss LSM 700 [26–28]; Leica TSC SP8, Germany [29]). Some devices are home-built, for example, Dai Hongjie and co-workers built an imaging system which consists of a 2D InGaAs camera (Princeton Instruments, 2D OMA-V). The excitation was provided by an optical fiber-coupled 808-nm diode laser (RMPC Lasers) [25].

The IVIS Spectrum is one of the most advanced and widely used in vivo optical imaging systems. It consists of imaging chamber, CCD camera, and custom-designed lens. Not only can it quantitate and localize 3D fluorescent and bioluminescent sources in vivo, but it can import and automatically co-register CT or MR images yielding anatomical context (IVIS Spectrum User's Guide, Caliper Life Sciences, Inc.). For bioluminescence and fluorescence imaging, IVIS system can image and quantify all commonly used fluorophores, including fluorescent proteins, dyes, and conjugates.

As shown in Figs. 13.6–13.7, 13.9, 13.10b, 13.13–13.14, and 13.18–13.20, IVIS system was adopted for lymph node imaging and tumor imaging. In lymph node imaging study, mice were anesthetized with 2.5% isoflurane, and PD-2 (~20 μg) were administered to nude mice by tail-vein catheterization using the Vevo

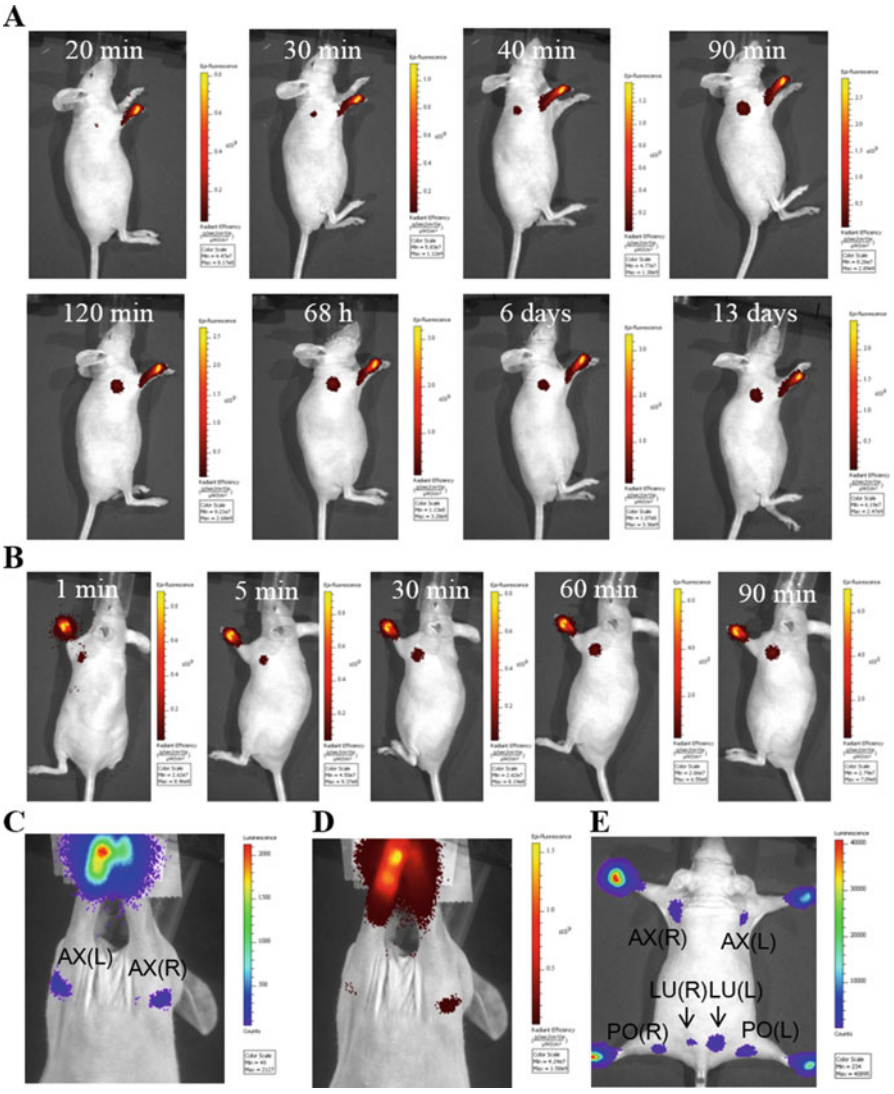

Fig. 13.6 Fluorescence and bioluminescence imaging of lymphatic basins in mice by local injection. Time-dependent in vivo fluorescence imaging of axillary lymph node in the mice with injection of PD-2 (10 μg) (**a**) and PD-1 (1 μg) (**b**) intradermally in the forepaws. (**c**) Bioluminescence and (**d**) fluorescence imaging of lymphatic basins in a mouse 10 min after the injection of PD-3 intradermally in the forepaws. (**e**) Bioluminescence imaging of lymphatic basins in a mouse with injection of PD-3 (2 μg) intradermally in the forepaws. All bioluminescence images were acquired with 10-s exposure time; AX, axillary lymph node; LU, lumbar lymph node; PO, popliteal lymph node; L, left; R, right [30]

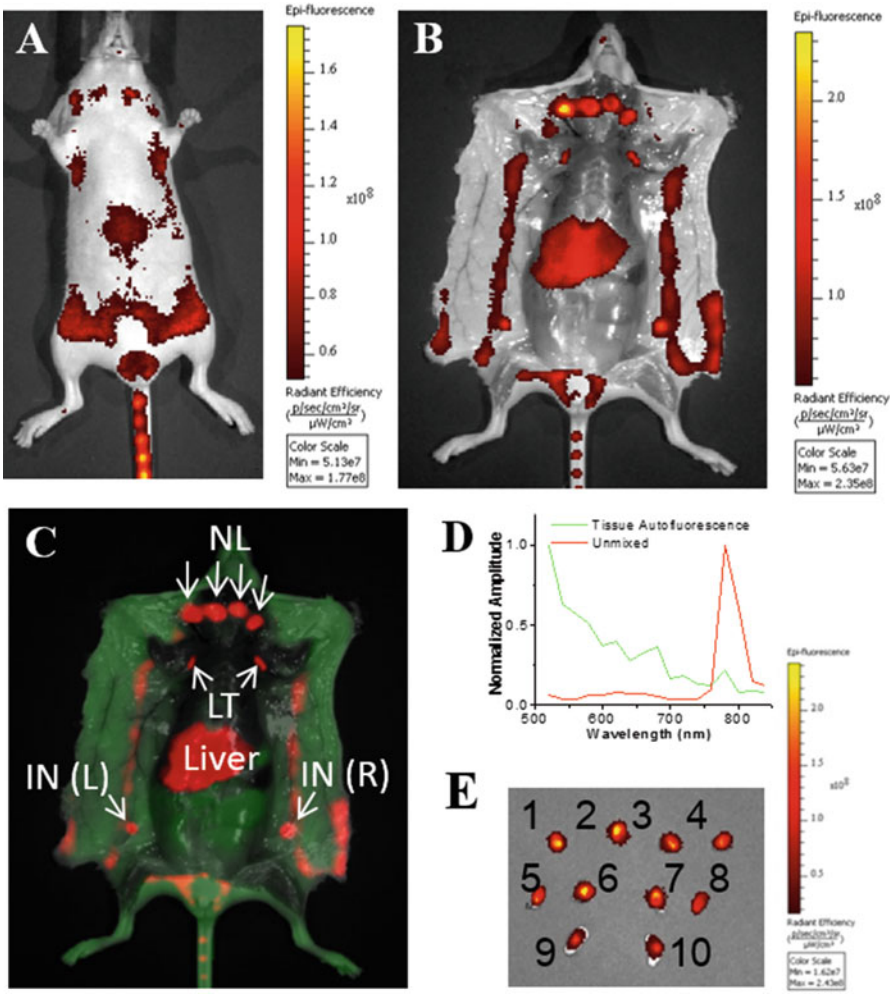

Fig. 13.7 Fluorescence imaging of lymphatic basins in mice by tail-vein injection. (**a**–**c**) Fluorescence imaging of a mouse 24 h after the tail-vein injection of PD-1 (20 μg). (**b**, **c**) Superficial skin was removed before imaging but peritoneum was left intact. (C) Autofluorescence is coded in green and PD-1 signal in red; AX, axillary lymph node; IN, inguinal lymph node; L, left; LT, lateral thoracic lymph node; NL, neck lymph nodes; R, right. (**d**) Fluorescence spectra of tissue autofluorescence (green) and the unmixed polymer dots signal (red) in the mouse. (**e**) Fluorescence image of lymph nodes excised from the mouse: 1–4, NL; 5, AX (left); 6, LT (left); 7, LT (right); 8, AX (right); 9, IN (left), 10, IN (right) [30]

MicroMarker TVA (Vascular Access) Cannulation Kit (VisualSonics). The tail vein was further flushed with 100 mL of PBS buffer. At 24 h after injection, mice were killed, dissected to locate the lymph nodes of interest, and imaged using an IVIS spectrum imaging system immediately (excitation, 465 ± 15 nm; emission,

780 ± 10 nm). Alternatively, ~10 μL of PD-3 NPs (~2 μg each) were administered to the forepaws via intradermal injections. Within 10 min of injection, mice received an intravenous injection of 10 μg of coelenterazine for in vivo bioluminescence imaging (acquisition time, 10 s; no emission filter). Following bioluminescence imaging, in vivo fluorescence imaging was carried out (excitation, 465 ± 15 nm; emission, 780 ± 10 nm).

In the tumor imaging assay, U87-MG cells (2×10^6 cells per site) were implanted subcutaneously into the left shoulder of 4- to 5-week-old female nude mice (Charles River Breeding Laboratories). When the tumors reached the size of 2–8 mm in diameter (2–3 weeks after implantation), the tumor-bearing mice were subjected to biodistribution and imaging studies. In vivo and ex vivo fluorescence imaging was performed with an IVIS spectrum imaging system (excitation, 465 ± 15 nm filter; emission, collected from 520 to 840 nm with a bandwidth of 20 nm). For bioluminescence imaging, the mice were imaged after tail-vein injection of coelenterazine (20 μg per mouse in 20 μL of methanol and 80 μL of phosphate buffer). Images were acquired without filters.

For tumor vasculature imaging, U87-MG cells (5×10^6 cells/site) or H1299 cell (5×10^6 cells/site) were implanted subcutaneously into the left shoulder (stomach position) of 5-week-old female athymic nude mice, respectively. At 20 days after implant, the tumor-bearing mice were subjected to imaging studies. NIR polymer dots synthesized and stored at 4 °C up to 9 months. Athymic nude mice (n = 3) were administered the NIR polymer dots (~50 μg per mouse) through tail-vein injection. At 24 h postinjection, the mice were imaged using an IVIS spectrum imaging system with a 465 ± 15 nm excitation filter and a 780 ± 10 nm emission filter.

To test the difference in sensitivity between the fluorescence and bioluminescence of NIR polymer dots, the prepared Luc8-conjugated NIR polymer dots with different concentrations (3 μg, 0.6 μg, 0.3 μg, 0.06 μg) were subcutaneously injected into a nude mouse. The mouse was imaged immediately after an intravenous injection of 10 μg of coelenterazine for bioluminescence imaging with a 1-minute acquisition time for the no emission filter and a 3-minute acquisition time for the NIR emission filter (780 ± 10 nm). Following bioluminescence imaging, in vivo fluorescence imaging was carried out with a 2-second acquisition time (excitation, 465 ± 15 nm; emission, 780 ± 10 nm). Quantify the in vivo fluorescent signals as total radiant efficiency ([photons/sec/cm^2/sr]/ [μW/cm^2]) within a circular region of interest (ROI) using Living Image software.

Except IVIS systems, Kodak in vivo imaging system was used for tumor hypoxia imaging (Fig. 13.24) [36], and confocal laser microscope was applied for zebrafish imaging (Fig. 13.22) [29].

Huang lab [36] conducted the in vivo tumor hypoxia luminescence imaging experiment on a modified Kodak in vivo imaging system. The xenon lamp (100 W) was used as the excited source, collocating with a band-pass filter (410 ± 15 nm). The luminescence signals were collected at 660 ± 13 nm, and an Andor DU897 EMCCD as the signal collector. The mice were intratumorally injected with the FP-Pdots solution (10 μL, 2 mg/mL) without being deoxygenized. For the purpose of comparison, the mice were subcutaneously injected with the

FP-Pdots probe at the same condition. Images of luminescent signals were analyzed with Kodak Molecular Imaging Software.

Due to the small and transparent body of zebrafish, they could be imaged by confocal laser microscope. Pu lab [29] conducted the in vivo imaging of zebrafish larvae model using confocal laser scanning microscopy. In brief, after anesthetization of the zebrafish larvae 48 h postfertilization in fish medium with 0.01% tricaine, SPN2-M or SPN2-Si (20 μg mL^{-1}, 3 nL) was microinjected into the perivitelline space between the periderm and the yolk using microinjection equipment. 1 h after microinjection, bright-field and fluorescence images of the zebrafish were obtained using a confocal laser microscope.

5 Key Research Findings

5.1 Imaging of Lymphatic Basins

The lymphatic system plays a crucial role in immune responses to foreign antigens and tumors and in tumor metastasis in human and rodent models. The NIR polymer dots were applied to map lymph nodes in vivo [30, 40, 41].

The NIR polymer dots PD-2 (~10 μg) were introduced into the forepaws of mice via intradermal injections; the axillary lymph node (AX) could be readily visualized noninvasively by NIR fluorescence (Fig. 13.6a). Compared with PSMA modified PD-2, PS-PEG-COOH modified PD-1 showed faster AX detection even at lower concentration (~1 μg) (Fig. 13.6b).

Similarly, the self-luminescing NIR polymer dots PD-3 (~2 μg) were introduced into the forepaws of mice via intradermal injections. Within 10 min of injection, the AX could be readily visualized noninvasively by bioluminescence imaging (Fig. 13.6c). When followed by in vivo fluorescence imaging, lower fluorescent signals were obtained at the AX in comparison with bioluminescence imaging (Fig. 13.6d). After PD-3 were injected into all four paws (each at ~2 μg), all AX in the same mouse were clearly visualized by bioluminescence imaging (Fig. 13.6e).

Furthermore, the PD-1 polymer dots allow highly efficient labeling of all the lymph nodes in the lymphatic networks after a single tail-vein injection. At 24 h after injection of the PD-1 into nude mice, the mice were imaged before and after removed superficial skin. Strong NIR fluorescence signals were detected in the lymphatic networks: neck lymph nodes, axillary lymph nodes (AX), lateral thoracic lymph nodes, and inguinal lymph nodes (IN) (Fig. 13.7) [30].

Sentinel lymph node (SLN) is the first group of lymph nodes receiving metastatic cancer cells by direct lymphatic drainage from a primary tumor. Accurate identification of SLNs is the prerequisite of the success of cancer diagnosis and surgery. The utilization of fluorescent polymer dots could serve as a promising candidate for SLN mapping.

Kim lab reported a series of conjugated polymer dots by in situ colloidal Knoevenagel polymerization in the aqueous phase without using any harmful organic solvent [40]. These cyanosubstituted derivative (CN-PPV)-based polymer dots were tuned throughout the broad spectral window by varying the aromatic

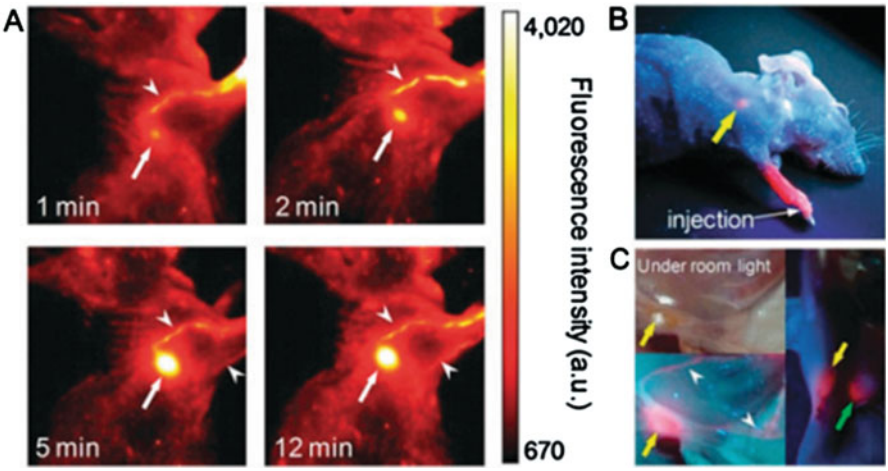

Fig. 13.8 (**a**) Pseudo-color NIR fluorescence images of a mouse (n = 10) injected intradermally with NIR-cvPDs (10 μL of 1.7 mg mL^{-1}) into the right paw. Imaging time points after injection are shown. Arrows and arrowheads indicate axillary lymph node and lymphatic vessels, respectively. The filter set used is TRITC excitation (535 nm) and Cy5.5 emission (700 nm). (**b**–**c**) True-color fluorescence photographs of a cvPD-injected mouse (10 μL of 0.17 mg mL^{-1}, intradermally into the right paw), taken under UV excitation by a 365-nm handheld lamp (1–2 mW cm^{-2}). The mouse was photographed noninvasively at 90 min postinjection (**b**) and subjected to incision for fluorescence-guided surgical inspection (**c**). Two SLNs, axillary and lateral thoracic nodes, and lymphatic vessels are indicated by yellow and green arrows and arrowheads, respectively [40]

structure of the monomers and thus presented multicolor fluorescence. The different color was considered to be useful for simultaneous imaging of plural molecular targets. NIR-cvPDs (TEM, 50 nm) were chosen for in vivo fluorescence SLN mapping which exhibited a broad absorption band and a large Stokes-shifted red-to-NIR fluorescence emission peaking at 693 nm. It should be noted that they also estimated the mass extinction which as high as 21,300 cm^2 g^{-1}. Mass extinction is a light absorptivity per mass concentration representing the light gathering power per injection dose. When NIR-cvPDs were administered intradermally into the forepaw pad of a mouse, fast movement of the fluorescence flow along lymphatic vessels could be clearly detected by a digital imaging system (Fig. 13.8a). Immediately after injection, NIR-cvPDs drained rapidly from the interstitial site of injection into the lymphatics and the front of the migration arrived at an AX in ca. 1 min. Subsequently migrating entities accumulated at the regional lymph node without any sign of outflow toward the next tier nodes, to give clear-cut SLN images.

Kim lab [41] devised a kind of high-performance binary nanococktails for lymph node mapping, and their fluorescence could be turned “on” and “off” by alternate photochromic switching. In these cvCP-aggregated nanococktails, cvCP was fluorescence emitter, and bisthienylethene derivatives (BTE) were the photoswitching modulator. By periodical UV or visible illumination, the molecule structure of BTE reversibly went through “Ring-open” or “Ring-off,” resulting in the efficiency

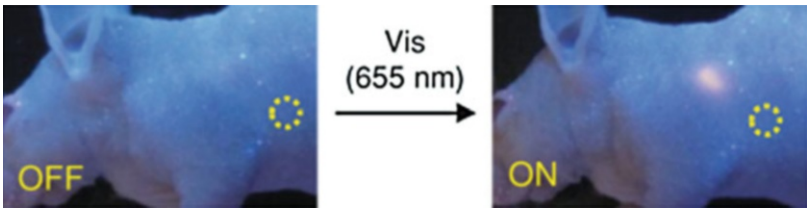

Fig. 13.9 True-color images of a mouse (n = 5, the number of independent experiments) injected intradermally with switched-off DOP-NC into the left forepaw (0.08 mg/kg bodyweight). The images were taken at 5 min postinjection under UV excitation by a 365-nm handheld lamp (1–2 mW cm^{-2}) before (left) and after (right) red laser irradiation (655 nm, 5 min). Circles indicate the laser-illuminated position [41]

change of the intraparticle FRET. Therefore, the nanococktails exhibited bright fluorescence "on" and no fluorescent state "off." DOP-NC, one of the devised nanococktails (NC), emitted fluorescence at 720 nm and was chosen for in vivo lymph node mapping (Fig. 13.9). Switched-off DOP-NC was injected intradermally into the forepaw pad of a mouse, and at 5 min postinjection, red laser (655 nm) was employed on a spot around the axilla. Bright signal was clearly located in a subcutaneous SLN by naked eye, suggesting the occurrence of photoswitching reaction. 3D reconstruction and ex vivo results confirmed the efficient and precise mapping of axillary and brachial nodes. The study validated the aforementioned nanococktails are promising in photoswitchable NIR fluorescence imaging for biomedical in vivo lymph node mapping.

5.2 Imaging of Tumor

5.2.1 Imaging of Tumor Vasculature

Smaller nanoprobes are often more desirable due to their favorable biodistribution characteristics in in vivo experiments. The NIR polymer dots with ultrasmall size (sub-5 nm in diameter) were prepared for in vivo imaging [31].

The transmission electron microscopy (TEM) image showed that the NIR polymer dots were quite monodispersed with an average diameter of 3.6 ± 0.4 nm (Fig. 13.10a). However, dynamic laser scattering (DLS) data showed an average hydrodynamic diameter of NIR polymer dots reached ~30 nm. For in vivo tumor vasculature imaging, the NIR polymer dots PD-1 (~25 μg per mouse) prepared after 3 months, 6 months, and 9 months were injected intravenously into nude mice bearing a human glioblastoma U87-MG tumor on the left shoulder (stomach position), respectively. Thirty minutes postinjection, strong NIR fluorescence signal was clearly observed in the U87-MG tumor vasculature of the mice (Fig. 13.10b). It is observed that the prepared NIR polymer dots were not uptaken by live U87-MG cells in vitro, but accumulating in the U87-MG tumor in vivo. It is probably because tumor tissue vasculatures are leaking and hyperpermeable allowing preferential accumulation of nanoparticles in the tumor vasculature and tumor interstitial space (called passive

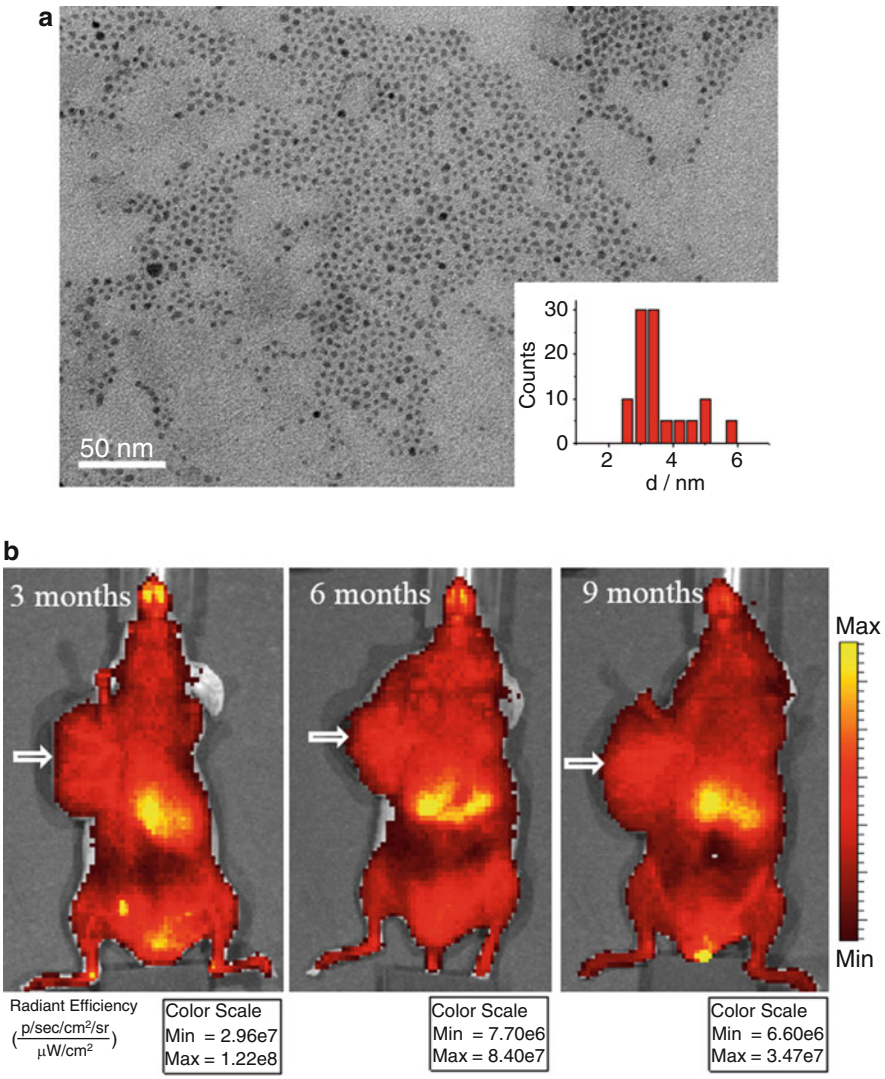

Fig. 13.10 NIR polymer dots with ultrasmall size were used for imaging tumor vasculature in vivo. (**a**) The transmission electron microscopy (TEM) image of PD-1. Inset, the average diameter of the NIR polymer dots obtained from the TEM result. (**b**) In vivo fluorescence imaging of U87-MG tumor-bearing mice (tumors are indicated by white arrows) by the tail-vein injection of PD-1 prepared after 3 months, 6 months, and 9 months, respectively [31]

nanoparticle tumor targeting). In particular, no obvious fluorescence intensity changes were detected among the three mice, indicating excellent long-term photostability of the NIR polymer dots for in vivo imaging.

In addition to tumor vasculature, polymer dots could also be designed for blood vessels and even capillaries in the second infrared window (1.0–1.7 μm).

Due to the tissue's depth and its autofluorescence around the vessels, optical wavelength in the conventional NIR region (400–750 nm) could not penetrate the tissues leading to suboptimal sensitivity and poor signal-to-noise ratio, while in vivo fluorescence imaging in the second near-infrared window could afford deep tissue penetration and high special resolution, owing to the reduced photon scattering.

Dai lab [25] reported a kind of conjugated polymers with intrinsic fluorescence >1000 nm through donor-acceptor (D-A) (donor, benzo[1,2-b:3,4-b0]difuran; acceptor, fluorothieno-[3,4-b]thiophene) alternating copolymerization. Non-covalent functionalization was achieved by PEG coating to afford water solubility and biocompatibility. The yielded pDA-PEG nanoparticles were intravenously injected into mouse's femoral artery, and the ultrafast NIR-II imaging of the arterial blood flow was carried out on a home-built imaging setup consisting of a 2D InGaAs camera (Princeton Instruments, 2D OMA-V).

Fast-moving flow front in the femoral artery was clearly observed as the NIR-II-emitting pDA-PEG entered the hind limb (Fig. 13.11). The average femoral blood flow velocity was quantified by plotting the distance traveled by the flow front as a function of time, showing an overall linear increase with an average blood velocity of 4.36 cms^{-1}. Then waveform blood flow pattern with pDA was resolved by NIR-II fluorescence imaging, and then the mouse heart rate (290 beats/min) was measured from the NIR-II fluorescence oscillations. Thus, the high brightness of the conjugated polymer achieved temporal and high spatial resolution NIR-II imaging with rich details of blood flows and cardiac cycles in vivo.

5.2.2 Imaging of Tumors Based on EPR Effect

In our studies, FRET was applied for tuning the emission wavelength of the polymer dots for deeper tissue penetration in living body (PD1–5). Besides, polymer dots possessing FRET characteristic could also be applied for in vivo drug releasing monitoring.

In Gu's [39] report, FRET was applied for fluorescence tracking of antitumor drug (doxorubicin). Hydrophilic polyvinyl alcohol (PVA) was adopted to encapsulate hydrophobic modified dextran (m-dextran) and hydrophobic payloads (doxorubicin and BTTPF) by using a single emulsion technique. The doxorubicin encapsulating efficiency reached 95.13 ± 0.08%. Doxorubicin, emitting red fluorescence at 590 nm, serves as the donor, and BTTPE serves as the acceptor. Under physiological condition, the nanoparticle structure is stable and FRET is "on," while in the mild acidic aqueous environment, m-dextran is expected to hydrolyze and results in the degradation of the polymer dots and then release of the payload containing the doxorubicin and BTTPF. After the tail-vein injection of the polymer dots, NIR fluorescence signal at 690 nm in tumor tissue was barely detected on the H22 tumor-bearing mice until 16th day postinjection (Fig. 13.12). It indicated that the polymer dots could monitor the drug release in a noninvasive and real-time way.

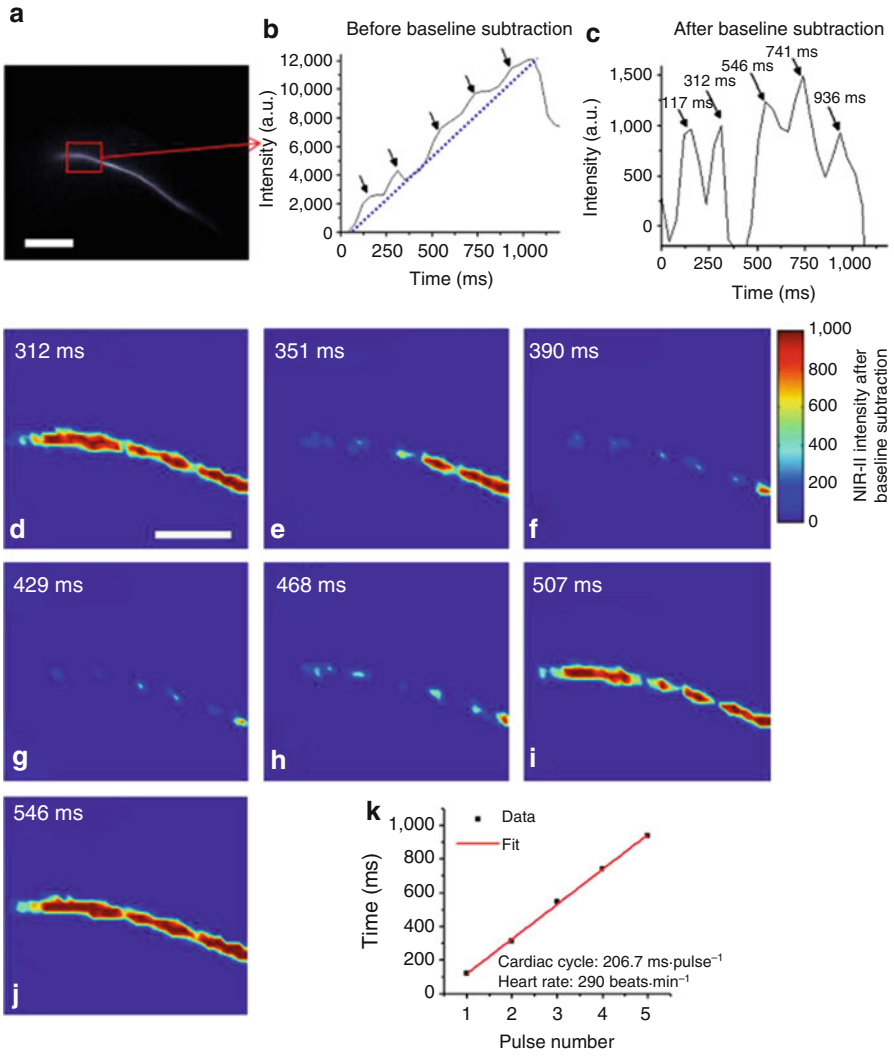

Fig. 13.11 Resolving waveform blood flow pattern with pDA. (**a**, **b**) An NIR-II fluorescence image (**a**) of the mouse femoral artery, where the fluorescence intensity inside the ROI red box is integrated and plotted as a function of time in **b**, showing an increasing profile with humps corresponding to ventricular ejections of cardiac cycles. The scale bar in a indicates 5 mm. (**c**) NIR-II fluorescence intensity plotted as a function of time, after a linear increasing baseline is subtracted from the plot shown in **b**, featuring five cardiac cycles in the plot. (**d**–**j**) Time course NIR-II fluorescence images of the red box area shown in a, after subtraction of a time-dependent linearly increasing background given by the baseline in **b**. Note that these seven images correspond to a complete cardiac cycle from 312 to 546 ms. See Supplementary Movie 2 for a video showing the real-time evolution of the linear background-subtracted fluorescence intensity. The scale bar in d indicates 1 mm, which applies to all images of **d**–**j**. (**k**) Time point of NIR-II fluorescence spikes corresponding to ventricular ejections shown in c, plotted over several heart pulses (black squares). The data are fitted to a linear function with its slope of 206.7 ms per pulse corresponding to the period of each cardiac cycle [25]

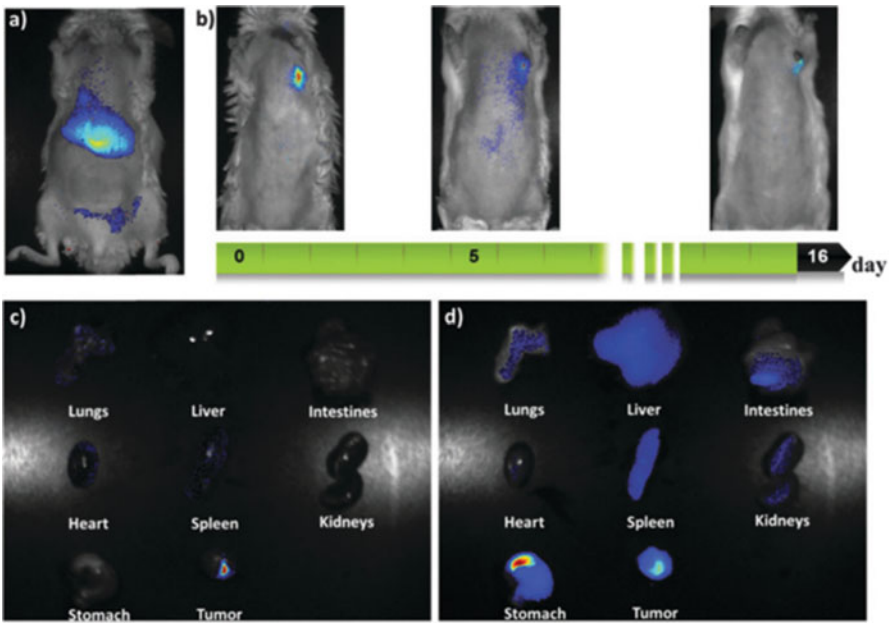

Fig. 13.12 (**a**) NIR image of the mouse following intravenous injection with the NPs (ex = 595 nm). (**b**) NIR images of the subcutaneous tumor-bearing mouse following subcutaneous injection with the NPs (ex = 455 nm). Ex vivo NIR fluorescence imaging on tumor tissue and major organs of mouse with a (**c**) 455-nm and (**d**) 595-nm excitation source (detection wavelengths, 680–780 nm for BTTPF) [39]

5.2.3 Imaging of Tumors Based on Folate and RGD Targeting

Folate and RGD are the most widely applied tumor targeting ligands in polymer dots functionalization. Here, we will give some examples of the design of tumor-targeted polymer dots based on this strategy [21, 23, 25, 30, 33].

RGD peptides have a strong affinity for the cell adhesion receptor integrin $\alpha_v\beta_3$, which has a pivotal role in tumor angiogenesis, and have been used for in vivo imaging of a variety of cancers. Cyclic RGD peptides are conjugated to the polymer dots surface for imaging human glioblastoma U87-MG tumor xenografts in nude mice.

RGD conjugated NIR polymer dots PD-4 were injected intravenously into nude mice bearing a U87-MG tumor (~8 mm in diameter) on the left shoulder, and the mice were imaged at multiple time points postinjection (Fig. 13.13a). The in vivo fluorescence spectrum of the PD-4 was collected from 520 to 840 nm with a bandwidth of 20 nm and an excitation of 465 nm. As early as 5 min postinjection, enhanced NIR fluorescence signal (780 nm) was observed in the U87-MG tumor and gradually increased over time. There was significant fluorescence signal from the skin after 1 h, which complicated the detection of small size tumors.

The self-luminescing NIR polymer dots PD-5 can emit NIR light in the presence of the substrate of Luc8, coelenterazine, without external excitation and therefore

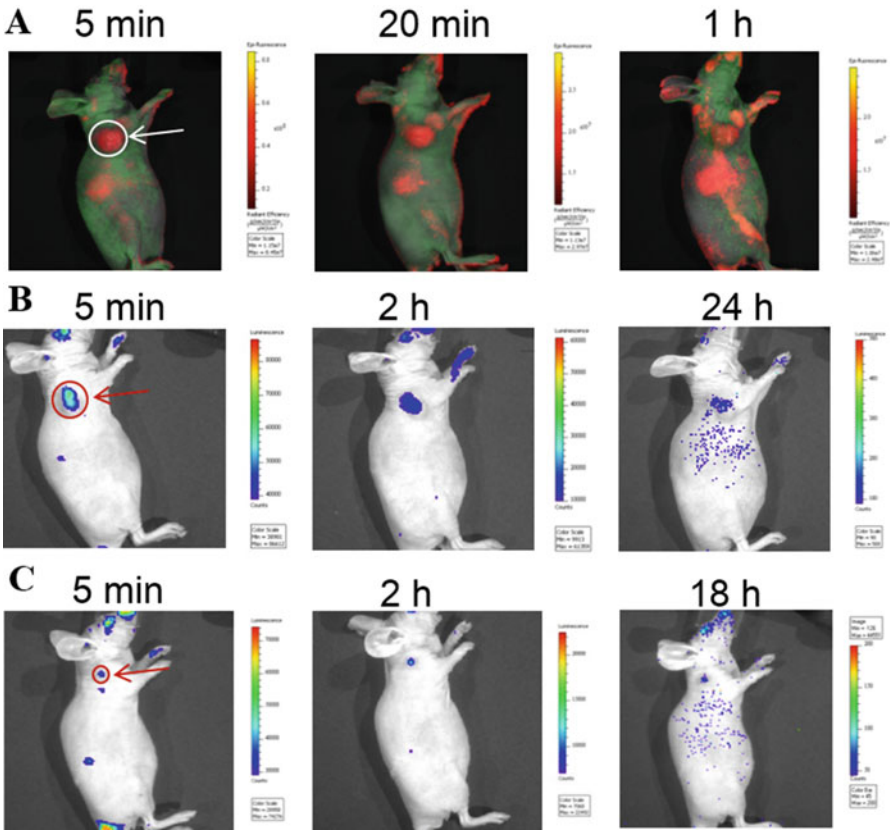

Fig. 13.13 Time-dependent in vivo imaging of U87-MG tumors in mice by the tail-vein injection of NIR polymer dots. (**a**) Fluorescence imaging of mouse with a tumor of ~8 mm in diameter (indicated by a white arrow and circle) by the tail-vein injection of PD-4. Bioluminescence imaging of mice with small tumors of ~5 mm (**b**) and ~2 mm (**c**) in diameter (indicated by red arrows and circles) by the tail-vein injection of PD-5 [30]

can provide further advantages in comparison with PD-4. After tail-vein injection of PD-5, mice were imaged serially by bioluminescence imaging. At 5 min post-injection, strong bioluminescence emission was observed in the U87-MG tumor (~5 mm in diameter) with little signal from other tissues. The bioluminescence signal ratio between the tumor and background was estimated from region of interest measurements to be above 100 at 2 h (Fig. 13.13b). Furthermore, the efficiency of PD-5 in imaging smaller tumors (tumor size of 2–3 mm in diameter) (Fig. 13.13c) was tested. A strong bioluminescence signal was still observed in the U87-MG tumor of the mice at 5 min, 2 h, and 18 h. The self-luminescing feature provided excellent tumor-to-background ratio for imaging very small tumors.

We devised a type of heptylamine modified folate (C7-FA)-functionalized PFBT polymer dots for in vivo tumor imaging [33]. The homemade C7-FA was designed

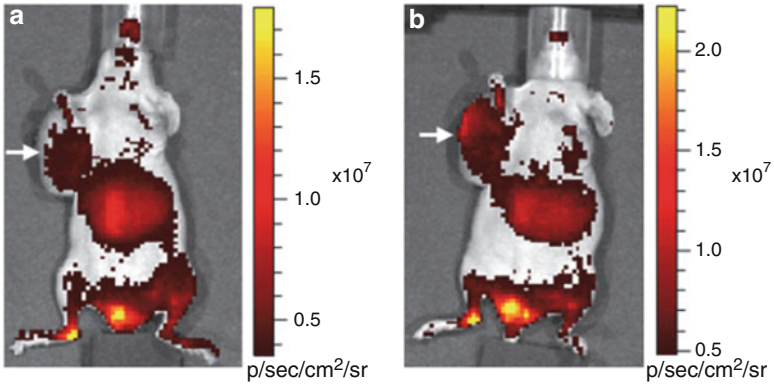

Fig. 13.14 In vivo fluorescence imaging of H1299 tumor-bearing mouse after 0.5 h (**a**) and 24 h (**b**) injection with the NIR775-doped FA-PFBT-COOH polymer dots [33]

for active targeting to tumor tissues. PFBT, as the high emissive polymer core, was encapsulated with PEG-COOH or PEG-NH_2 which utilized their ideal photostability in water. NIR dye (NIR-775) was doped to migrate the emission wavelength to 780 nm for in vivo imaging via FRET with PFBT. H1299 tumor-bearing mice were intravenously injected with FA-PFBT-COOH at a dose of 50 μg per mouse (Fig. 13.14). At 24 h postinjection, fluorescence signal in the tumor was increased with an enhanced signal-to-noise ratio of 19.4. The imaging results indicated the synthesized C7-functionalized PFBT polymer dots have promising potential on in vivo fluorescence tumor targeting.

Liu lab [23] reported a kind of conjugated polymer (CP)-loaded DSPE-PEG-folic acid nanoparticles (CPDP-FA NPs). The polymer nanoparticles show bright FR/NIR fluorescence (27% quantum yield) in the far-red/near-infrared region (>650 nm) which offers a unique window for bioimaging with low biological autofluorescence and high tissue penetration. In addition, the particles possess larger Stokes shift of 233 nm in aqueous solution as compared to commercially available quantum dots (Qdot 655) and organic dyes like Fluor 555. Folate-functionalized PEG as encapsulation matrix along with enhanced permeability and retention (EPR) effect facilitate the particles have target ability to accumulate in the tumor tissues. High fluorescence intensity was observed in the tumor region of H-22 tumor (~150 mm^3)-bearing mice (Fig. 13.15). Moreover, the in vivo toxicity evaluation demonstrated that CPDP-FA NPs have no obvious in vivo toxicity and can serve as an effective FR/NIR fluorescent theranostic agent for in vivo imaging and cancer diagnosis.

In addition to in vivo fluorescent imaging, polymer dots could be further developed as a multimodal imaging platform. Liu lab developed a dual-modal fluorescent-magnetic NP by co-encapsulation of conjugated polymer and iron oxides (IOs) [21]. The folate-functionalized platform shows folate receptor-overexpressed cancer cell (H-22) targeting ability. Tumor tissue (300 mm^3) signal was clearly collected both

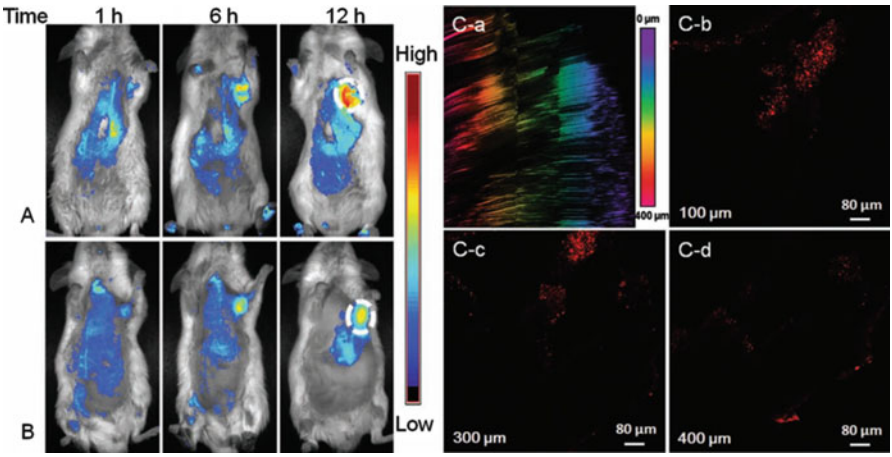

Fig. 13.15 One-photon excited in vivo noninvasive fluorescence imaging of H22 tumor-bearing mice after intravenous injection of (**a**) FTTDNPs and (**b**) TTDNPs at the same NP concentration of 1 nM. The white circles mark the tumor sites. (**C-a**) 3D two-photon fluorescence image of C6 tumor from the mouse that was intratumorally injected with FTTDNPs. (**C-b**) 100 μm, (**C-c**) 300 μm, and (**C-d**) 400 μm deep images from the C6 tumor. The images were recorded upon 800-nm excitation with 600–780 nm band-pass filter [23]

in fluorescent imaging and T_2-weighted MR imaging at 6 h and 5 h postinjection, respectively (Fig. 13.16). The studies indicated that polymer dots could be developed as a promising imaging agent not only for fluorescent imaging but also other modalities in living body.

Recently, aggregation-induced emission (AIE) feature has been discovered by many research groups for their imaging and therapeutic application in polymer nanosystem. Those luminogens, with AIE feature, are non-emissive in dilute solution but are induced to luminesce strongly when aggregated through a mechanism of the restriction of intramolecular rotation. According to Liu's research, 2-(2,6-bis((E)-4-(phenyl(4′-(1,2,2-triphenylvinyl)-[1,1′-biphenyl]-4-yl)amino)styryl)-4H–pyran-4-ylidene) malononitrile (TPE-TPA-DCM) shows the novel phenomenon of AIE feature when in the aggregate state [24]. TPE-TPA-DCM nanoparticles were formulated by using bovine serum albumin (BSA) as the polymer matrix. In the PL spectra of TPE-TPA-DCM in THF/water mixture, PL intensity (660 nm) drastically increased when the water fraction was over 40%. The result verified its efficient AIE feature. Intracellular imaging, photostability, and cytotoxicity were demonstrated in MCF-7 cells, and the results showed fluorogen-loaded BSA NPs were high emissive with good photostability and low cytotoxicity. In vivo test was carried out in H22 tumor (400 mm^3)-bearing mice (Fig. 13.17). After the intravenous injection of folate-functionalized fluorogen-loaded BSA NPs, tumor signal could be collected after 3 h. And up to 28 h postinjection, the signal became prominent, in sharp contrast to ambient part of the mouse body, indicating its promising application perspective for cancer diagnosis.

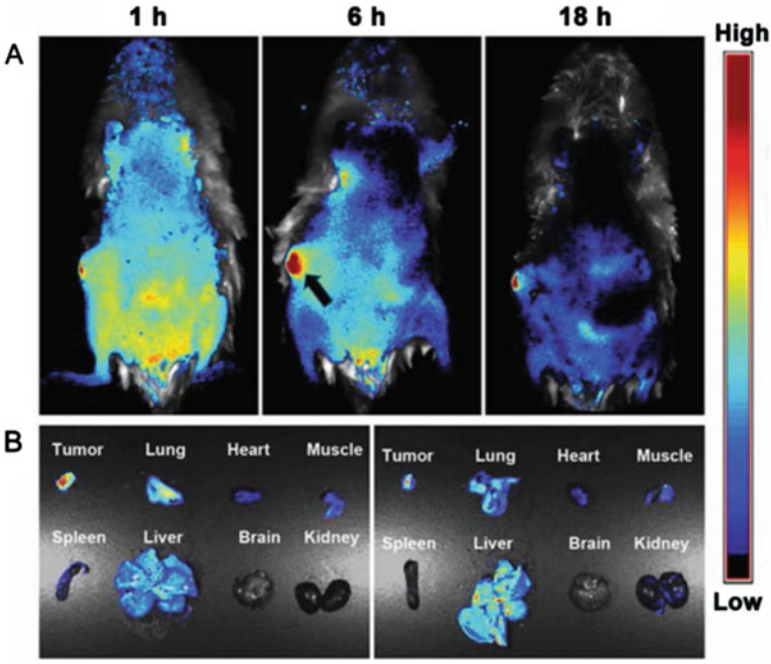

Fig. 13.16 (**a**) Representative in vivo fluorescence images of mouse injected with FMCPNPs acquired at 1 h, 6 h, and 18 h postinjection. (**b**) Fluorescence images of various organs from the mice treated with FMCPNPs (left) and MCPNPs (right), respectively, at 12 h postinjection [21]

5.2.4 Tumor Cell Tracking

The NIR775 dye-doped MEH-PPV polymer dots system was further used as fluorescent nanoprobes for the in vitro HeLa cell labeling and in vivo long-term HeLa tumor tracking [32].

Approximately 100% of HeLa cells were labeled with polymer dots PD-1 by direct cell labeling method under the fluorescence microscope. To investigate the long-term labeling capability and toxicity of the NIR polymer dots PD-1, 2×10^5 HeLa cells treated with 20 μg of PD-1 were subcutaneously injected into a nude mouse. The mouse was imaged at different time after injection (Fig. 13.18). The NIR polymer dot remains 75% of its fluorescence upon 7 days injection and still retains 28% of fluorescence after 23 days, indicating the durable brightness and long-term photostability of the NIR polymer dots. Moreover, ex vivo imaging of tumors showed that strong NIR fluorescence signal was detected in almost the whole region of the tumor, suggesting that the NIR polymer dots could be inherited by daughter cells.

The difference in sensitivity between fluorescence and bioluminescence of NIR polymer dots PD-3 was also studied. The prepared Luc8-conjugated NIR polymer dots PD-3 with different concentration (3 μg, 0.6 μg, 0.3 μg, 0.06 μg) were

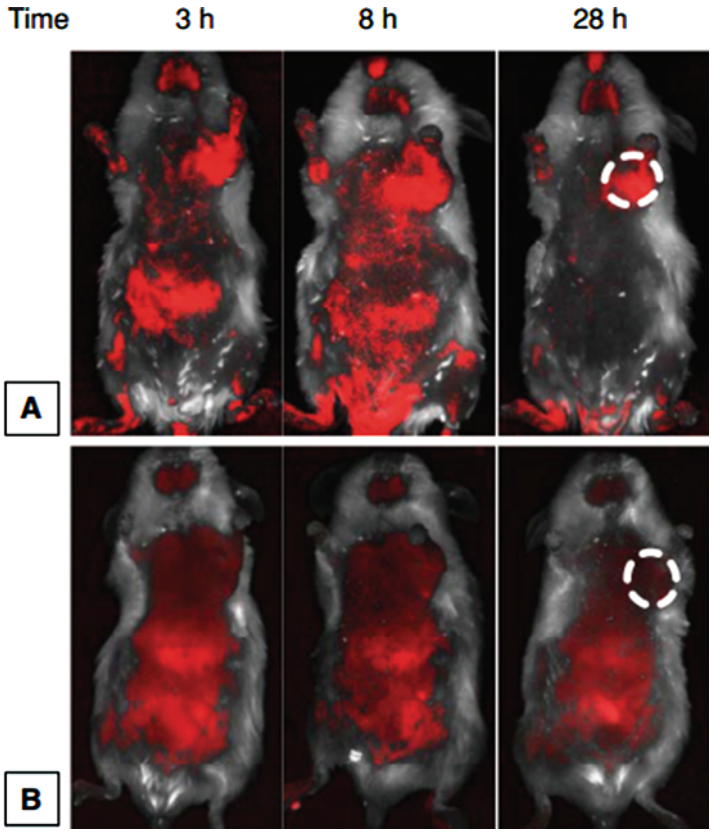

Fig. 13.17 (**a**, **b**) In vivo noninvasive fluorescence imaging of H22 tumor-bearing mice after intravenous injection of fluorogen-loaded BSA NPs (with TPE-TPA-DCM loading of 0.86 wt%) (**a**) and bare TPE-TPA-DCM NPs (**b**) at the same fluorogen concentration. The white circles mark the tumor sites [24]

subcutaneously injected into a nude mouse. The mouse was imaged immediately after an intravenous injection of 10 μg of coelenterazine for bioluminescence imaging with 1 minute acquisition time for no emission filter and 3 min acquisition time for NIR emission filter (780 ± 10 nm). Following bioluminescence imaging, in vivo fluorescence imaging was carried out with 2-second acquisition time (excitation, 465 ± 15 nm; emission, 780 ± 10 nm) (Fig. 13.18b). Intense NIR fluorescence signals were clearly visualized in the four injection sites, while bioluminescence imaging showed no obvious signal in the injection of 0.06 μg. Although bioluminescence imaging showed higher signal-to-background ratio, the NIR fluorescence imaging observed higher luminescence intensity even at low concentration. Besides, compared to NIR bioluminescence imaging, NIR fluorescence imaging based on PD-3 as a probe decreased the exposure time by >90-fold, which benefited the monitoring of quick interactions of cells.

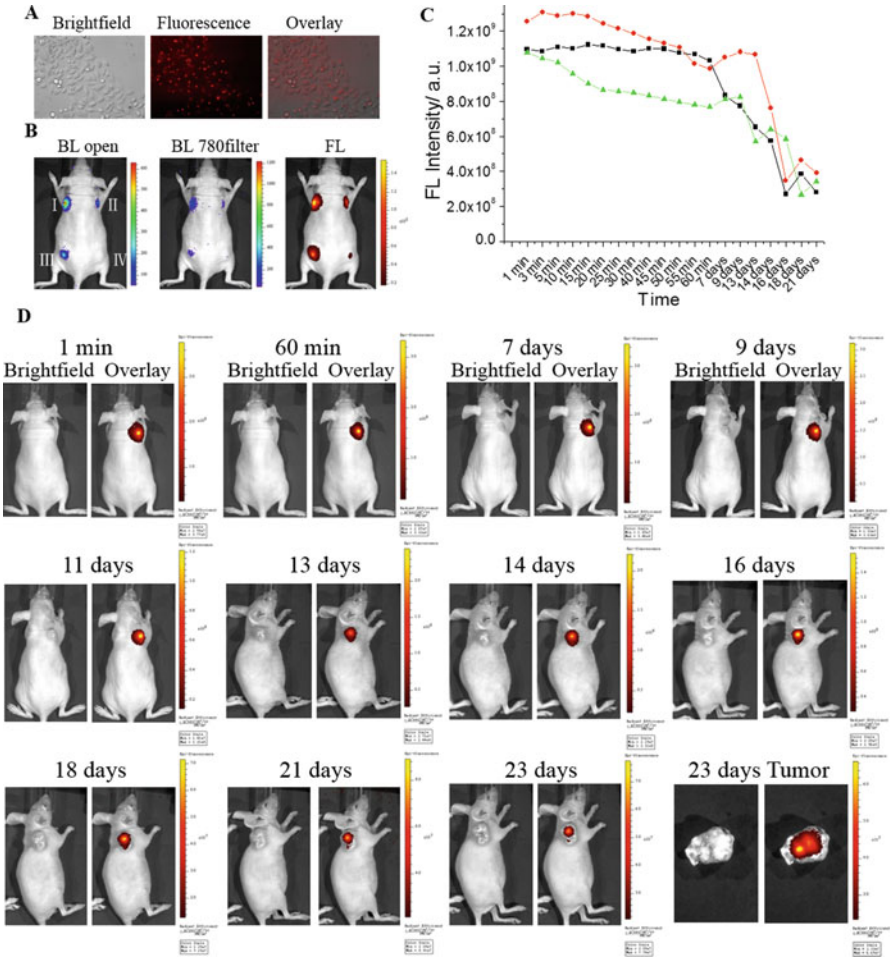

Fig. 13.18 NIR polymer dots were used for the in vitro HeLa cell labeling and in vivo long-term HeLa tumor tracking. (**a**) Fluorescence imaging of HeLa cells labeled with PD-1. (**b**) In vivo bioluminescence (BL) and fluorescence (FL) imaging of the mouse with injection of different concentrations of PD-3 subcutaneously (I, 3 μg; II, 0.3 μg; III, 0.6 μg; IV, 0.06 μg). (**c**) Region of interest (ROI) analysis of the fluorescence intensity of PD-1-labeled HeLa cells in the mice over time. (**d**) Time-dependent in vivo bright-field and fluorescence imaging of the mouse with injection of PD-1-labeled HeLa cells and ex vivo fluorescence imaging of the tumor excreted from the mouse after 23 days injection [32]

Liu lab reported a kind of PIDT-DBT-Tat nanoparticles for long-term in situ monitoring of live tumor growth in FR/NIR wavelength region [34]. PIDT-DBT was capsulated with modified PEG chains and the human immunodeficiency virus type 1 (HIV-1) trans-acting transcriptional activator was conjugated with the NPs by click reaction. In vitro cell tracing ability was conducted on HepG2 live cancer cells using cytometry. 53.1% of the cells were still efficiently labeled, while the labeling rate was

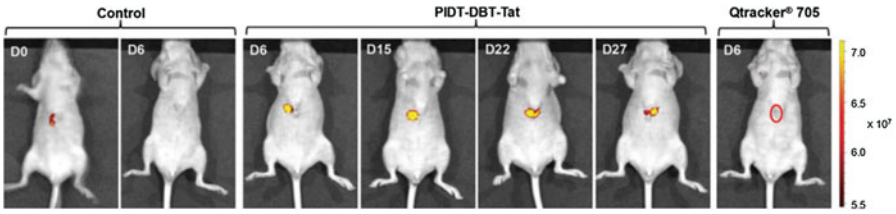

Fig. 13.19 Representative in vivo fluorescence images of the mouse transplanted with 4×10^6 of HepG2 cells labeled by PIDT-DBT-Tat NPs and Qtracker 705. The control images were obtained from a nude mouse that underwent the same surgical operation without injection of labeled HepG2 cells. The images were taken on designated days post cell injection ($\lambda_{ex} = 640$ nm, 720/20 nm filter) [34]

23.5% at day 7 when cells were treated with PIDT-DBT-Tat nanoparticles. Moreover, the labeling efficiency of PIDT-DBT-Tat nanoparticles showed great enhancement as compared to bare PIDT-DBT nanoparticles which indicated that conjugation of Tat peptide on NPs surface is essential to enhance the internalization of the NPs into living cells. The in vivo fluorescent imaging was carried out on HepG2 tumor-bearing mice, and the results showed that PIDT-DBT-Tat nanoparticles could monitor liver tumor growth for more than 27 days in a real-time manner (Fig. 13.19).

Polymer dots which possess persistent fluorescence open up an avenue of image acquisition for time-delay imaging, thus eliminating tissue autofluorescence associated with fluorescence imaging [35].

Rao lab reported NIR-775-based MEH-PPV polymer dots for tumor cell tracking [35]. Persistent luminescence in tumor tissue was still detectable at 24 h post-injection by subcutaneous administration. In this study, they proposed the mechanism of the persistent luminescence in polymer nanoparticles: The nanoparticles are first excited, and the excitation energy is trapped within the semiconducting layer of the polymer before released from the trap after activation energy (heat) is applied. Part of the relaxation energy from the energy trap may be transferred to the near-infrared dye NIR-775 and emit persistent luminescence from the nanoparticle and the near-infrared dye. Moreover, the in vivo systemic persistent luminescence imaging showed that whole-body signal vanished within 60 min after intravenous injection (Fig. 13.20). The timely clearance of the polymer dots out the body indicated its safety and potential perspective for long-time cancer cell tracking in clinical usage.

5.3 Imaging of Zebrafish

Zebrafish, a kind of model animal, possess several advantages as experiment living body in in vivo fluorescence imaging research: (1) Transparency of the zebrafish embryos allows for direct observation. (2) Zebrafish are evolutionarily close to human and can also be done in a large scale with low cost.

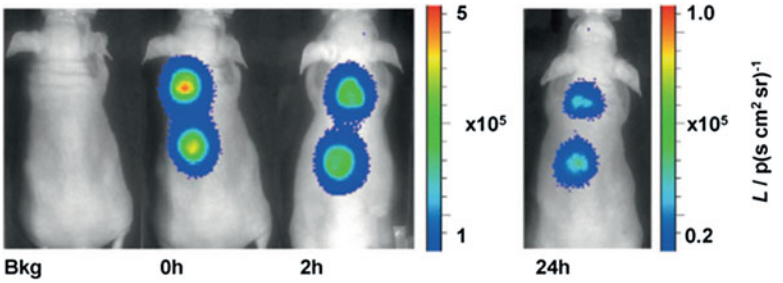

Fig. 13.20 In vivo optical persistent luminescence imaging of a mouse before (Bkg) and after (0 h) subcutaneous injection of nanoparticles (≈16 μg) that had been excited prior to injection. At 2 h and 24 h later, the subcutaneous injection site was exposed to white light for 3 min first before the collection of persistent luminescence (in the absence of any excitation light) [35]

Chan lab [26–28] reported a series of quinoxaline, benzothiadiazole (BT), and donor-bridge-acceptor-based multicolor semiconducting polymer nanoparticles (Pdots) in succession for in vivo biological imaging. These NIR-emitting polymer dots possessed high photostability and brightness.

Quinoxaline-based Pdots can be up to eight times brighter than Qdots655. In vivo imaging studies were all conducted on zebrafish. In the BT-based polymer nanosystem, BT as the acceptor and various kinds of donors were incorporated to tuning their emission wavelengths. Those BT-based fluorescent semiconducting copolymers (PDTTBT, Si-PFBT, PFBT, etc.) were synthesized by introducing different types of donors for energy transfer via Suzuki polymerization, and the tunable emission wavelength varied from 550 nm to NIR (760 nm). The Pdots were functionalized using carboxyl group and subsequently coupled with streptavidin for specific cellular targeting and in vivo microangiography imaging on zebrafish. Si-PCPDBT Pdots (λ_{max}^{em}, 720 nm) were injected into the sinus venous of the zebra larva. The fluorescent signal was immediately distributed in the blood stream and the signal intensity lasted 2 h without leakage after injection. Compared with the signal from eGFP-expressing endothelial cell, prominent fluorescence of the Pdots were revealed in the lumen of the vessels. Moreover, from the close view, the trunk vasculatures of the zebrafish were clearly marked and imaged by Pdots. The synthesized Pdots (0–4 nM) exhibited no obvious toxicity on zebrafish embryo within 49 h. Those findings showed this series of BT-based Pdots can be widely applied for basic biological studies and biomedical imaging.

In order to optimize the near-infrared fluorescence emission of polymer dots, they further designed and synthesized donor-bridge-acceptor-based polymer dots with narrowband and high near-infrared emission. These polymer dots have a high fluorescence quantum yield of 33% with a Stokes shift of more than 200 nm. The emission full width at half maximum of the Pdots can be as narrow as 29 nm, about 2.5 times narrower than that of inorganic quantum dots at the same emission wavelength region. The average per-particle brightness of the Pdots is at least three times larger than that of the commercially available quantum dots. They

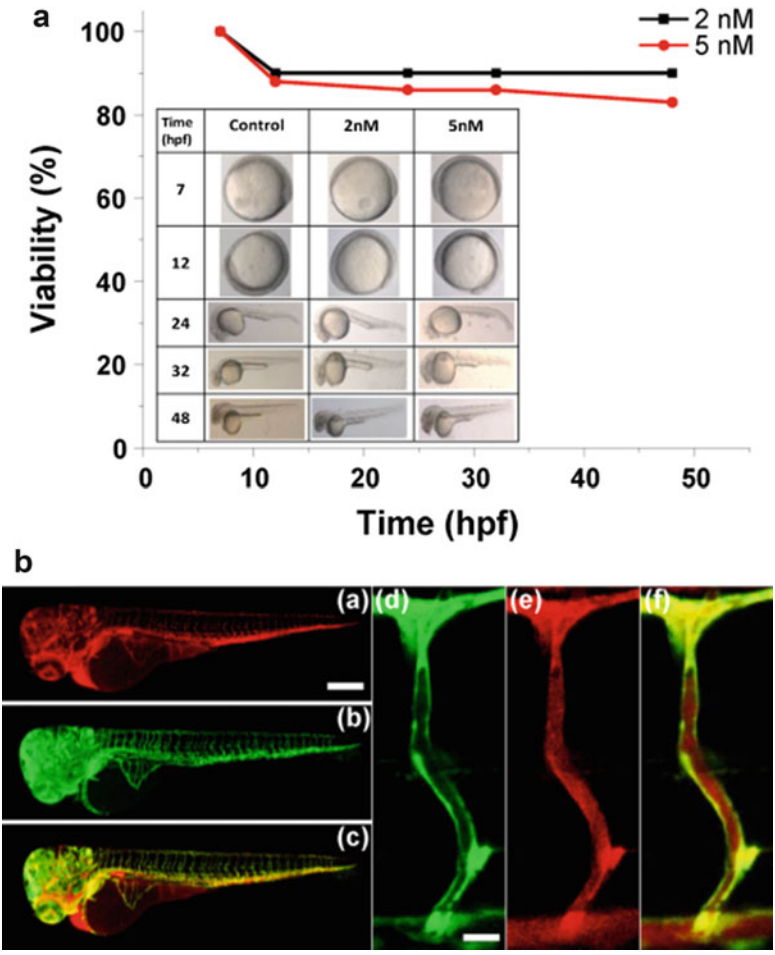

Fig. 13.21 (**a**) Biotoxicity assessment of Pdots by the zebrafish model. Time course recording morphology of zebrafish embryos exposed to 2 and 5 nM Pdot solutions in the period of 0–48 h postfertilization (hpf). (**b**) Zebrafish microangiography by injection of PF-TC6FQ-BODIPY Pdots into 3 days postfertilization Tg(*kdrl*:*e*GFP) zebrafish embryos. The global view of zebrafish vessels and Pdot images is shown in the left panels (**a**–**c**), and a close view of the trunk vasculature (intersegmental vessel) is shown in the right panels (**d**–**f**). Green emission is from endothelial cells expressing eGFP, while red emission is from Pdots. Scale bars represent 200 μm in **a**–**c** and 60 μm in **d**–**f**, respectively [28]

inserted π-bridge segments into polymer backbones to gain the absorption in the visible regions (400–600 nm). They integrated phthalocyanine- and boron dipyrrin (BODIPY)-containing NIR monomers into the polymers to achieve narrowband emissions. Among these polymer dots, PF-TC6FQ-BODIPY-COOH was functionalized with FA-PEG-NH_2 for tumor targeting. Besides zebrafish (Fig. 13.21), the folate-functionalized polymer dots were injected into $SKOV_3$

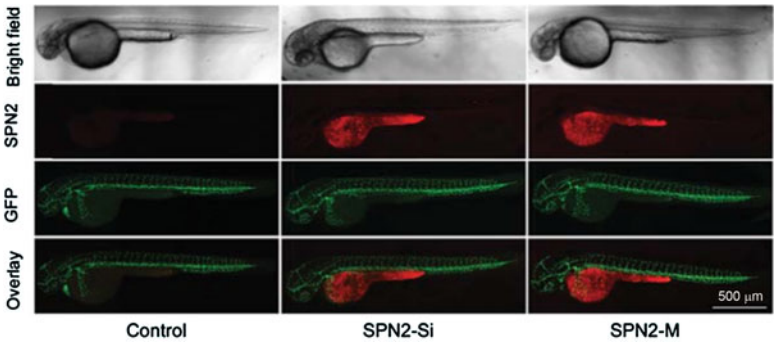

Fig. 13.22 CLSM images of zebrafish larvae 48 h postfertilization after microinjecting SPN2-Si or SPN2-M (20 mg mL^{-1}, 3 nL) for 18 h [29]

tumor-bearing mice for long-term observation and tracking. NIR fluorescent polymer dots retained 32% of their fluorescence even 36 days after injection. The high brightness with narrowband emission, good biocompatibility, and excellent stability of these NIR Pdots have demonstrated their promising potential for in vivo multiplexed biological detection and imaging.

Pu lab [29] reported a type of multilayered semiconducting polymer nanoparticles (SPNs-M) for NIR imaging in zebrafish and mice. The multilayered SPNs consist of a SP-based core, middle silica protection layer, and outer PEG-based corona. Silica layer and PEG corona play a crucial role in enhancing the NIR fluorescence by up to ~100-fold and reducing nonspecific interactions, respectively. According to the PL spectra, the fluorescence intensity dramatically increased with the presence of the silica layer as compared to other control groups. The author's explanation is that silica layer effectively reduces the interaction between the SP core and water molecules and provides a relatively less polar environment. The in vivo imaging of SPNs-M was conducted on a zebrafish larvae model using confocal laser scanning microscopy. After 48 h postinjection of SPN2-Si and SPN2-M into the zebrafish, red fluorescence can be detected for both SPNs in the yolk sac (Fig. 13.22). Average fluorescence intensity for SPN2-M injected zebrafish was 1.14-fold higher than that of SPN2-Si injected zebrafish. Moreover, no obvious morphology and pericardium edema were observed in those SPNs injected zebrafish. These proof-of-concept applications indicate that the synthesized SPNs may serve as the promising candidate for in vivo NIR fluorescence imaging.

5.4 Imaging of O_2

5.4.1 Imaging of Hypoxia and O_2 Distribution

Hypoxia has been studied to be related to various diseases, such as solid tumors, retinal lesion, and brain diseases. As we all knew that the oxygen concentration in some solid tumors is around 4% and even decrease to zero locally, it is important to

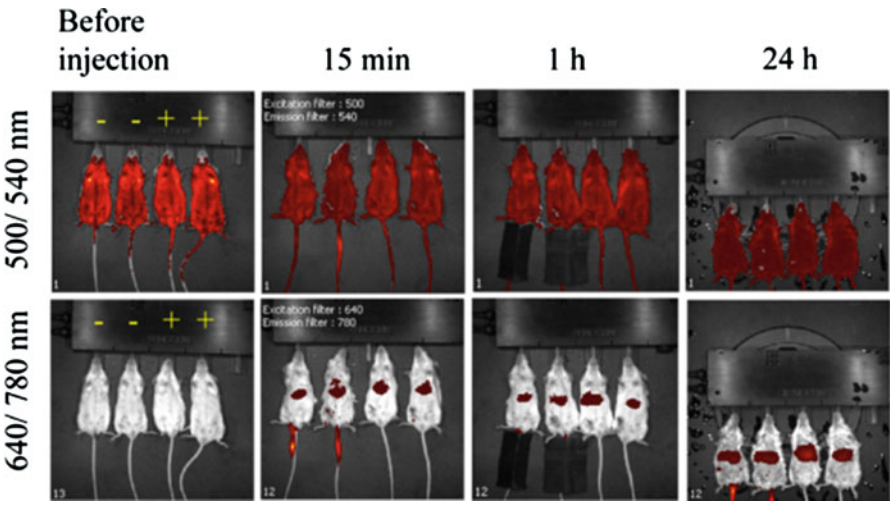

Fig. 13.23 In vivo imaging of nanoparticles SII-0.2$^-$ and SII-0.2$^+$ (indicated as "−" and "+," respectively) in Balb/c mice over time. Two different spectral channels are shown (top and bottom rows) [42]

monitor the O_2 concentration in living body. In vivo fluorescence imaging provides a noninvasive and sensitive approach to map the O_2 distribution in living animals.

Among the reported polymer dots in O_2 mapping [36, 37, 42], Pt(II)-porphyrin, a kind of popular O_2 indicator, have been widely discovered and applied due to its high O_2 sensitivity by utilizing the energy transfer between the triplet excited state of the metal complex and the triplet ground state of O_2. Its long luminescence decay times (1–1000 μs) allow lifetime-based O_2 sensing which can be realized by phase- or time-resolved fluorometry. Dmitriev and Borisov's group [42] described a class of polymer dots for high-resolution, ratiometric intensity and phosphorescence lifetime-based imaging of O_2 that consist of a substituted conjugated polymer acting as a FRET antenna (donor) and a fluorescent reference (acceptor) Pt-porphyrin (PtTFPP or PtTPTBPF). The devised nanoparticles (SI, SII) emitted at 780 nm and displayed adequate sensitivity over the whole physiological range (0–20 kPa O_2). Cationic and anionic charged nanoparticles (SII-0.2$^+$, SII-0.2$^-$) were injected in the tail vein of a mouse and analyzed live animals on an animal imager at different time points within 24 h (Fig. 13.23). Spectral unmixing showed predominant accumulation of the nanoparticles in the liver. The ex vivo analysis on a two-photon microscope applied excitation at 750 nm. O_2-sensitive (Pt(II)-porphyrin) and polymer reference (polyfluorene) signals were detectable down to 70–100 μm. An increase of the ratio signal (650/430) from 0.8 to 1.1 reflects increased tissue deoxygenation over 20 μm depth. These current results indicated the potential applications of the O_2-sensitive polymer dots on cancer biology, immunology, and other biomedical fields.

Huang lab [36] also reported a kind of Pt(II)-porphyrin-based fluorescent/phosphorescent (FP) dual-emissive conjugated polymer dots for hypoxia bioimaging.

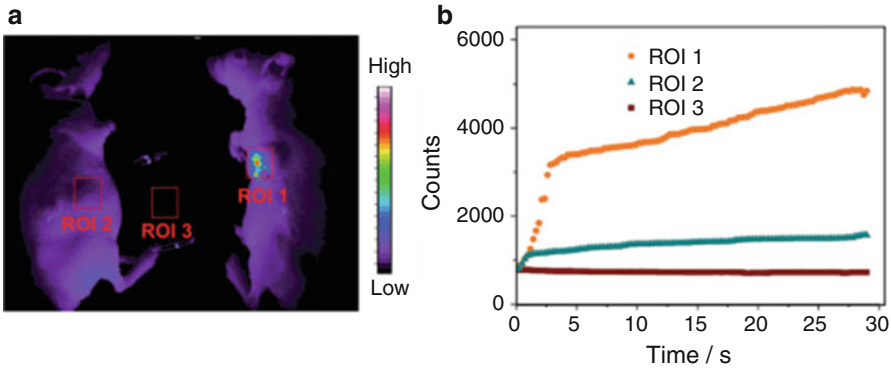

Fig. 13.24 (**a**) Luminescence imaging in vivo of a tumor-bearing mouse (ROI 1) and the control nude mouse (ROI 2) after injection of the FP-Pdots. (**b**) The change in luminescence intensity of the marked regions (ROI 1, ROI 2, and ROI 3) following different times after injection of the FP-Pdots into the nude mice. A xenon lamp was used as the excitation source, collocating with a band-pass filter (410 ± 15 nm) [36]

The FP-Pdots were self-assembled by the Pt(II)-porphyrin (O_2-sensitive) and conjugated polyelectrolyte (O_2-insensitive). FRET could occur from the donor (conjugated polyelectrolyte) to the acceptor (Pt(II)-porphyrin) which significantly enhanced the sensitivity. O_2 sensitivity was measured by the emission intensity at 656 nm from 0% to 21%. The radiometric O_2 sensing of the FP-Pdots was analyzed quantitatively based on the data of phosphorescence intensities according to the Stern-Volmer equation. Luminescence imaging of tumor hypoxia was conducted in nude mice. In vivo and ex vivo luminescence imaging were achieved using a modified Kodak in vivo imaging system (Fig. 13.24). The luminescence signals were collected at 660 ± 13 nm. The mice were intratumorally injected with the FP-Pdots solution (10 μL, 2 mg mL^{-1}) without being deoxygenized. High signal-to-noise emission intensity within the tumor area can be detected and imaging dynamic curves also confirmed the luminescence increase inside of the tumor. The PF-Pdots' performance demonstrated their oxygen sensitivity and can be adopted as in vivo tumor hypoxia probes.

5.4.2 Imaging of Reactive Oxygen and Nitrogen Species

The elevated generation of reactive oxygen and nitrogen species (RONS) is a hallmark of many pathological processes ranging from acute and chronic bacterial infections to chronic diseases such as cancer, cardiovascular disease, and arthritis. Rao lab [37] reported a dual-color SPN-based NIR nanoprobe (NanoDRONE) for the detection of RONS in inflammatory microenvironment in living mice. NanoDRONE consisted of a RONS-inert polymer core (energy donor) covered by RONS-sensitive fluorophore molecules (energy acceptor) thus established a FRET system. FRET was turned on in the absence of RONS and the polymer dots mainly emitted at 818 nm, while in the presence of RONS, FRET was turned off and the polymer dots

emitted mainly at 655 nm. NanoDRONE was applied to the RONS imaging in peritonitis mice induced by intraperitoneal (i.p.) injection of LPS. After 30 min postinjection, the fluorescence intensities of the LPS-treated mice were 2.7 times higher than saline-treated mice.

Then NanoDRONE was injected intravenously to test its systemic performance. Organs of the reticuloendothelial system (RES) such as the liver and spleen did not display higher nanoparticle uptake than non-reticuloendothelial tissues, suggesting the ability of NanoDRONE to evade RES uptake (Fig. 13.25a). On a bacterial

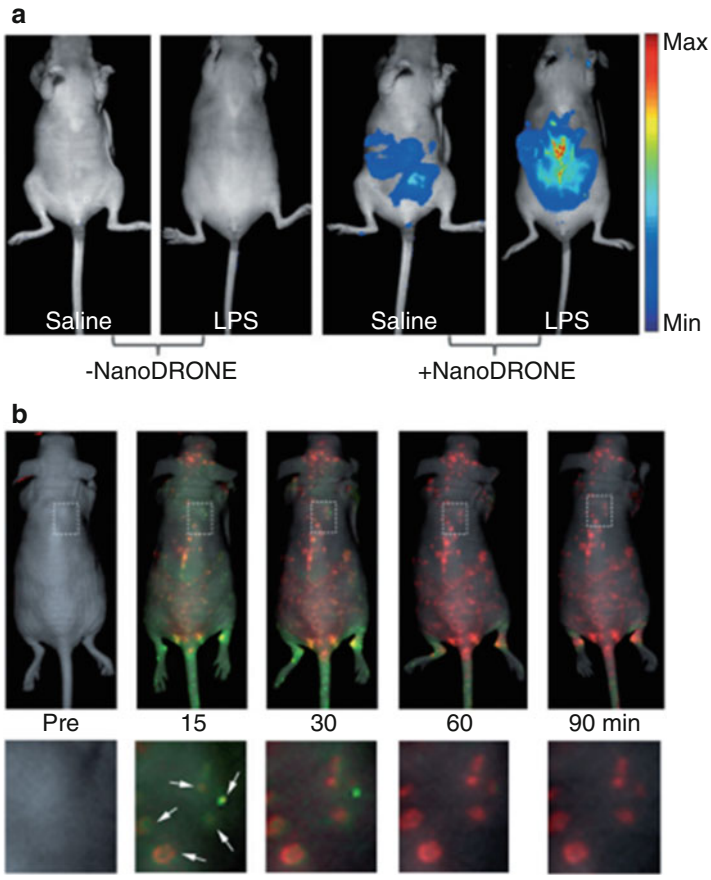

Fig. 13.25 (**a**) In vivo imaging of RONS with NanoDRONE in a LPS-induced acute peritonitis mouse model. Saline (n = 4) and LPS (n = 4) were administered i.p., followed 4 h later by i.p. administration of NanoDRONE. Images were acquired before and 30 minutes after particle administration. (**b**) Imaging RONS with NanoDRONE in mice with spontaneous systemic *C. bovis* bacterial infection. Overlaid images of activated (red) and unactivated (green) NanoDRONE following i.v. administration to mice with spontaneous infections (n = 4). Enlargements of the regions indicated by dashed white boxes are given below each corresponding image. White arrows indicate localized regions of bacterial infection [37]

infected mice model, NanoDRONE was found to first accumulate in the infected region within 15 minutes through the EPR effect and then progressively be induced to change from inactivated (green) to activated (red) states by microenvironmental RONS in the bacterial infected regions, with complete probe activation by 60 min (Fig. 13.25b). The systemic performance demonstrated that the nanoprobe could detect RONS in the inflammation region and its fluorescence spectrum in the NIR region allows real-time tracking and differentiation of probe activation from accumulation in living mice and thus validates its potential on RONS-based biomedical application.

6 Conclusion and Future Perspective

The NIR-emitting polymer dots exhibited unique capabilities for in vivo imaging, such as good biocompatibility, durable brightness, excellent long-term photostability, and high sensitivity, as demonstrated by the studies summarized in this review. These properties are crucial for imaging in living animals but do not all exist in other optical imaging probes such as organic dyes and metallic nanoparticles (such as QDs).

As reviewed in each session, various polymer dots have been discovered for in vivo fluorescence imaging of lymph nodes, tumors, or oxygen in mice and fluorescence imaging of zebrafish. Scientific and reasonable functionalization methods enable polymer dots to meet various biomedical requirements in living body. The prominent results in those animal models encourage us to invest more enthusiasm to promote and optimize the polymer dots application in clinical practice.

In addition, when properly designed, a single polymer dot might be able to simultaneously show capabilities of multimodal imaging (such as chemi−/bioluminescence, photoacoustic, MRI) and therapy (such as photothermal and photodynamic therapies), which will provide unprecedented simplicity in designing a single nanoparticle-based multimodality image-guided therapy agent. Polymer dots thus represent a multifunctional nanoplatform that facilitates the preclinical investigation of physiological and pathological processes in living subjects.

While polymer dots hold great promises for in vivo imaging, there are important issues that should be addressed before their advance to potential clinical translations, for instance, the unspecific uptake in the liver and relatively long circulation time by the tail-vein injection. Strategies such as synthesis of a size smaller than the physiologic pore size of filtration slit in the glomerular capillary wall (5 nm) are effective in reducing the uptake in the organs and being rapidly cleared out through urinary excretion. In addition, potential leakage of the doped dyes from the polymer dot matrix was initially a concern. More synthetic strategies such as incorporating the NIR dye into the polymer backbone and side chains, introducing moieties to induce intramolecular and intermolecular energy transfer, are effective in shifting the emission of polymer dots to the NIR region [28]. Thereby, new chemistry for the preparation of ultrasmall, biodegradable, and high-performance NIR-emitting polymer dots is highly demanded for their advance toward potential clinical applications.

References

1. Ntziachristos V, Ripoll J, Wang LHV, Weissleder R (2005) Looking and listening to light: the evolution of whole-body photonic imaging. Nat Biotechnol 23(3):313–320
2. Contag CH, Bachmann MH (2002) Advances in in vivo bioluminescence imaging of gene expression. Annu Rev Biomed Eng 4:235–260
3. Wagnieres GA, Star WM, Wilson BC (1998) In vivo fluorescence spectroscopy and imaging for oncological applications. Photochem Photobiol 68(5):603–632
4. van Dam GM, Themelis G, Crane LM, Harlaar NJ, Pleijhuis RG, Kelder W, Sarantopoulos A, De Jong JS, Arts HJ, Van der Zee AG, Bart J, Low PS, Ntziachristos V (2011) Intraoperative tumor-specific fluorescence imaging in ovarian cancer by folate receptor-α targeting: first in-human results. Nat Med 17(10):1315–1319
5. Vahrmeijer AL, Hutteman M, van der Vorst JR, Van de Velde CJ, Frangioni JV (2013) Image-guided cancer surgery using near-infrared fluorescence. Nat Rev Clin Oncol 10(9):507
6. Pecher J, Mecking S (2010) Nanoparticles of conjugated polymers. Chem Rev 110(10):6260–6279
7. Tian ZY, Yu JB, Wu CF, Szymanski C, McNeill J (2010) Amplified energy transfer in conjugated polymer nanoparticle tags and sensors. Nanoscale 2(10):1999–2011
8. Massey M, Wu M, Conroy EM, Algar WR (2015) Mind your P's and Q's: the coming of age of semiconducting polymer dots and semiconductor quantum dots in biological applications. Curr Opin Biotechnol 34:30–34
9. Zhu CL, Liu LB, Yang Q, Lv FT, Wang S (2012) Water-soluble conjugated polymers for imaging, diagnosis, and therapy. Chem Rev 112(8):4687–4735
10. Pu K, Chattopadhyay N, Rao J (2016) Recent advances of semiconducting polymer nanoparticles in in vivo molecular imaging. J Control Release 240:312–322
11. Wu CF, Chiu DT (2013) Highly fluorescent semiconducting polymer dots for biology and medicine. Angew Chem Int Ed 52(11):3086–3109
12. Peng HS, Chiu DT (2015) Soft fluorescent nanomaterials for biological and biomedical imaging. Chem Soc Rev 44(14):4699–4722
13. Li K, Liu B (2014) Polymer-encapsulated organic nanoparticles for fluorescence and photoacoustic imaging. Chem Soc Rev 43(18):6570–6597
14. Pu KY, Liu B (2011) Fluorescent conjugated polyelectrolytes for bioimaging. Adv Funct Mater 21:3408–3423
15. Feng L, Zhu C, Yuan H, Liu L, Lv F, Wang S (2013) Conjugated polymer nanoparticles: preparation, properties, functionalization and biological applications. Chem Soc Rev 42(16):6620–6633
16. Chan YH, Wu PJ (2015) Semiconducting polymer nanoparticles as fluorescent probes for biological imaging and sensing. Part Part Syst Charact 32(1):11–18
17. Li J, Liu J, Wei CW, Liu B, O'Donnell M, Gao X (2013) Emerging applications of conjugated polymers in molecular imaging. Phys Chem Chem Phys 15(40):17006–17015
18. Jin Y, Ye F, Zeigler M, Wu C, Chiu DT (2011) Near-infrared fluorescent dye-doped semiconducting polymer dots. ACS Nano 5(2):1468–1475
19. Pu KY, Shuhendler AJ, Valta MP, Cui L, Saar M, Peehl DM, Rao JH (2014) Phosphorylcholine-coated semiconducting polymer nanoparticles as rapid and efficient labeling agents for in vivo cell tracking. Adv Healthc Mater 3(8):1292–1298
20. Ding D, Liu J, Feng G, Li K, Hu Y, Liu B (2013) Bright far-red/near-infrared conjugated polymer nanoparticles for in vivo bioimaging. Small 9(18):3093–3102
21. Li K, Ding D, Huo D, Pu K, Thao NNP, Hu Y, Li Z, Liu B (2012) Conjugated polymer based nanoparticles as dual-modal probes for targeted in vivo fluorescence and magnetic resonance imaging. Adv Funct Mater 22(15):3107–3115
22. Ding D, Li K, Qin W, Zhan R, Hu Y, Liu J, Tang BZ, Liu B (2013) Conjugated polymer amplified far-red/near-infrared fluorescence from nanoparticles with aggregation-induced emission characteristics for targeted in vivo imaging. Adv Healthc Mater 2(3):500–507

23. Geng J, Li K, Ding D, Zhang X, Qing W, Liu J, Tang BZ, Liu B (2012) Lipid-PEG-folate encapsulated nanoparticles with aggregation induced emission characteristics: cellular uptake mechanism and two-photon fluorescence imaging. Small 8(23):3655–3663
24. Wei Q, Ding D, Liu J, Yuan WZ, Hu Y, Liu B, Tang BZ (2012) Biocompatible nanoparticles with aggregation-induced emission characteristics as far-red/near-infrared fluorescent bioprobes for in vitro and in vivo imaging applications. Adv Funct Mater 22:771–779
25. Hong G, Zou Y, Antaris AL, Diao S, Wu D, Cheng K, Chen X, Zhang C, Liu B, He Y, Wu JZ, Yuan J, Zhang B, Tao Z, Fukunaga C, Dai H (2014) Ultrafast fluorescence imaging in vivo with conjugated polymer fluorophores in the second near-infrared window. Nat Commun 5:4206
26. Liu HY, Wu PJ, Kuo SY, Chen CP, Chang EH, Wu CY, Chan YH (2015) Quinoxaline-based polymer dots with ultrabright red to near-infrared fluorescence for in vivo biological imaging. J Am Chem Soc 137(32):10420–10429
27. Liou SY, Ke CS, Chen JH, Luo YW, Kuo SY, Chen YH, Fang CC, Wu CY, Chiang CM, Chan YH (2016) Tuning the emission of semiconducting polymer dots from green to near-infrared by alternating donor monomers and their applications for in vivo biological imaging. ACS Macro Lett 5(1):154–157
28. Ke CS, Fang CC, Yan JY, Tseng PJ, Pyle JR, Chen CP, Lin SY, Chen J, Zhang X, Chan YH (2017) Molecular engineering and design of semiconducting polymer dots with narrow-band, near-infrared emission for in vivo biological imaging. ACS Nano. https://doi.org/10.1021/acsnano.7b00215
29. Zhu H, Fang Y, Zhen X, Wei N, Gao Y, Luo KQ, Xu C, Duan H, Ding D, Chen P, Pu K (2016) Multilayered semiconducting polymer nanoparticles with enhanced NIR fluorescence for molecular imaging in cells, zebrafish and mice. Chem Sci 7(8):5118
30. Xiong LQ, Shuhendler AJ, Rao JH (2012) Self-luminescing BRET-FRET near-infrared dots for in vivo lymph-node mapping and tumour imaging. Nat Commun 3:1193
31. Xiong LQ, Cao FW, Cao XM, Guo YX, Zhang YM, Cai X (2015) Long-term-stable near-infrared polymer dots with ultrasmall size and narrow-band emission for imaging tumor vasculature in vivo. Bioconjug Chem 26(5):817–821
32. Xiong LQ, Guo Y, Zhang Y, Cao F (2016) Highly luminescent and photostable near-infrared fluorescent polymer dots for long-term tumor cell tracking in vivo. J Mater Chem B 4:202–206
33. Cao F, Xiong LQ (2016) Folic acid functionalized PFBT fluorescent polymer dots for tumor imaging. Chin J Chem 34:570–575
34. Liu J, Li K, Liu B (2015) Far-red/near-infrared conjugated polymer nanoparticles for long-term in situ monitoring of liver tumor growth. Adv Sci 2(5):1500008
35. Palner M, Pu K, Shao S, Rao J (2015) Semiconducting polymer nanoparticles with persistent near-infrared luminescence for in vivo optical imaging. Angew Chem Int Ed Engl 54(39):11477–11480
36. Zhao Q, Li F, Huang W (2015) Fluorescent/phosphorescent dual-emissive conjugated polymer dots for hypoxia bioimaging. Chem Sci 6(3):1825–1831
37. Pu K, Shuhendler AJ, Rao J (2013) Semiconducting polymer nanoprobe for in vivo imaging of reactive oxygen and nitrogen species. Angew Chem Int Ed Engl 52(39):10325–10329
38. Li DD, Wang JX, Ma Y, Qian HS, Wang D, Wang L, Zhang G, Qiu L, Wang YC, Yang XZ, Donor-Acceptor Conjugated A (2016) Polymer with alternating isoindigo derivative and bithiophene units for near-infrared modulated cancer thermo-chemotherapy. ACS Appl Mater Interfaces 8(30):19312–19320
39. Yu JC, Chen L, Zhang YQ, Yao XK, Qian CG, Huang J, Zhu S, Jiang XQ, Shen QD, Gu Z (2014) pH-responsive and near-infrared-emissive polymer nanoparticles for simultaneous delivery, release, and fluorescence tracking of doxorubicin in vivo. Chem Commun 50(36):4699–4702
40. Kim S, Lim CK, Na J, Lee YD, Kim K, Choi K, Leary JF, Kwon IC (2010) Conjugated polymer nanoparticles for biomedical in vivo imaging. Chem Commun 46(10):1617

41. Jeong K, Park S, Lee YD, Lim C, Kim J, Chung BH, Kwon IC, Park CR, Kim S (2013) Conjugated polymer/photochromophore binary nanococktails: bistable photoswitching of near-infrared fluorescence for in vivo imaging. Adv Mater 25(39):5574–5580
42. Dmitriev RI, Borisov SM, Düssmann H, Sun S, Müller BJ, Prehn J, Baklaushev VP, Klimant I, Papkovsky DB (2015) Versatile conjugated polymer nanoparticles for high-resolution O_2 imaging in cells and 3D tissue models. ACS Nano 9(5):5275–5288

Index

C. S. S. R. Kumar (ed.), *Nanotechnology Characterization Tools for Biosensing and Medical Diagnosis*, https://doi.org/10.1007/978-3-662-56333-5

D